Cardiac Imaging

A Multimodality Approach

Manfred Thelen
Raimund Erbel
Karl-Friedrich Kreitner
Joerg Barkhausen

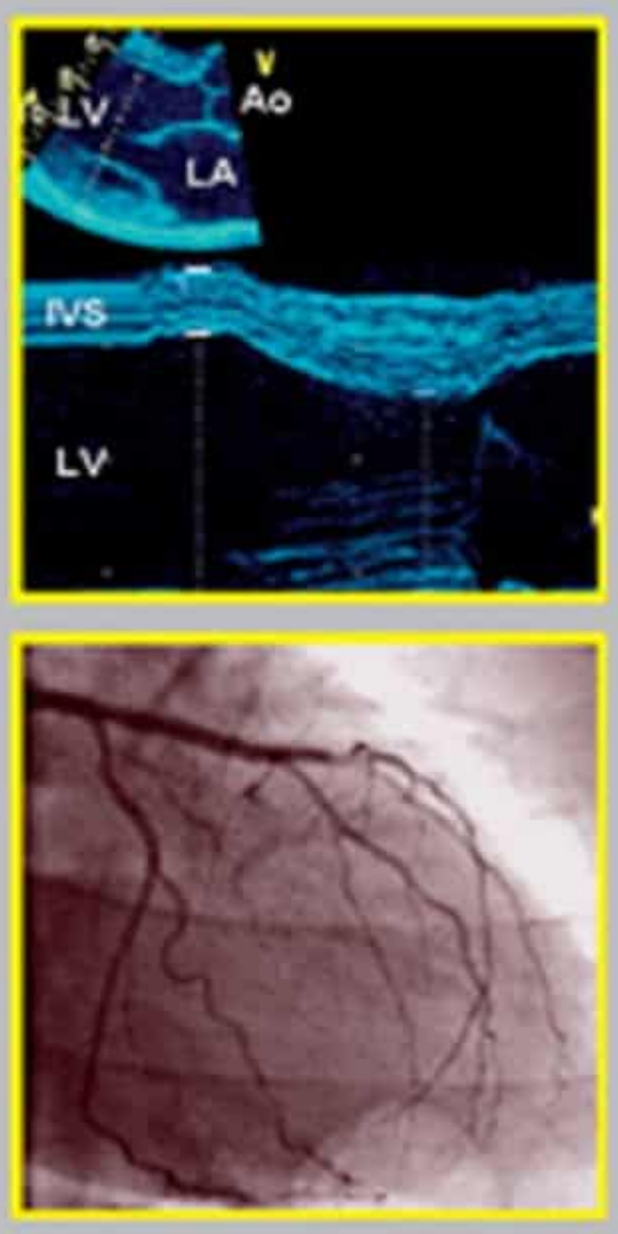

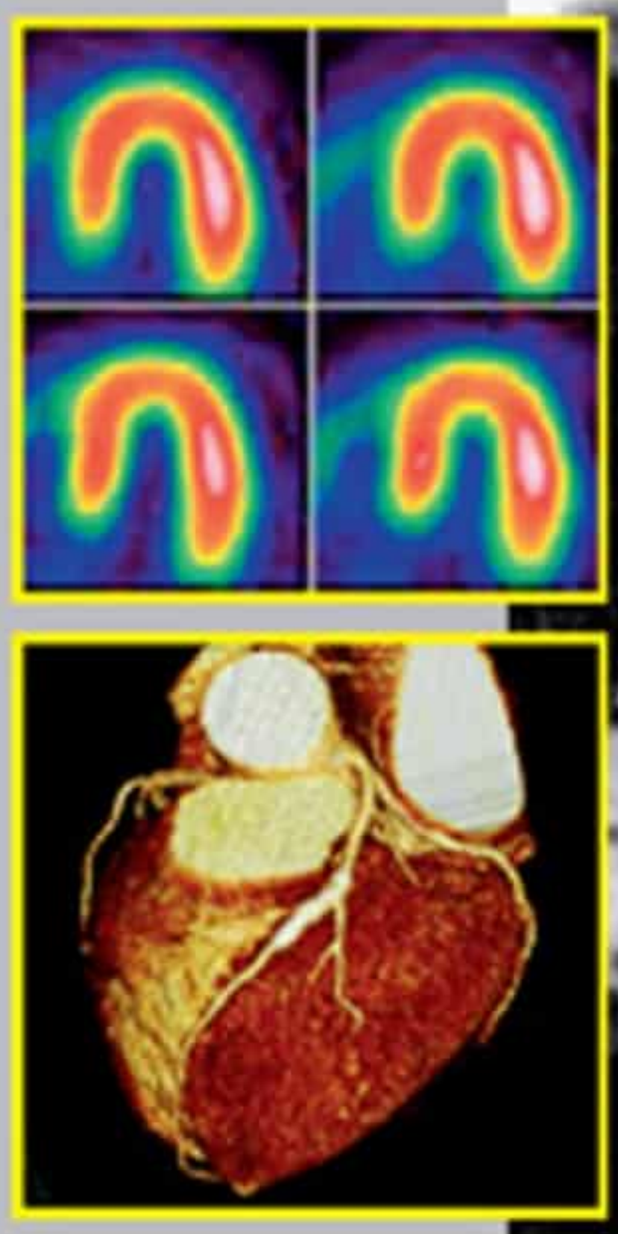

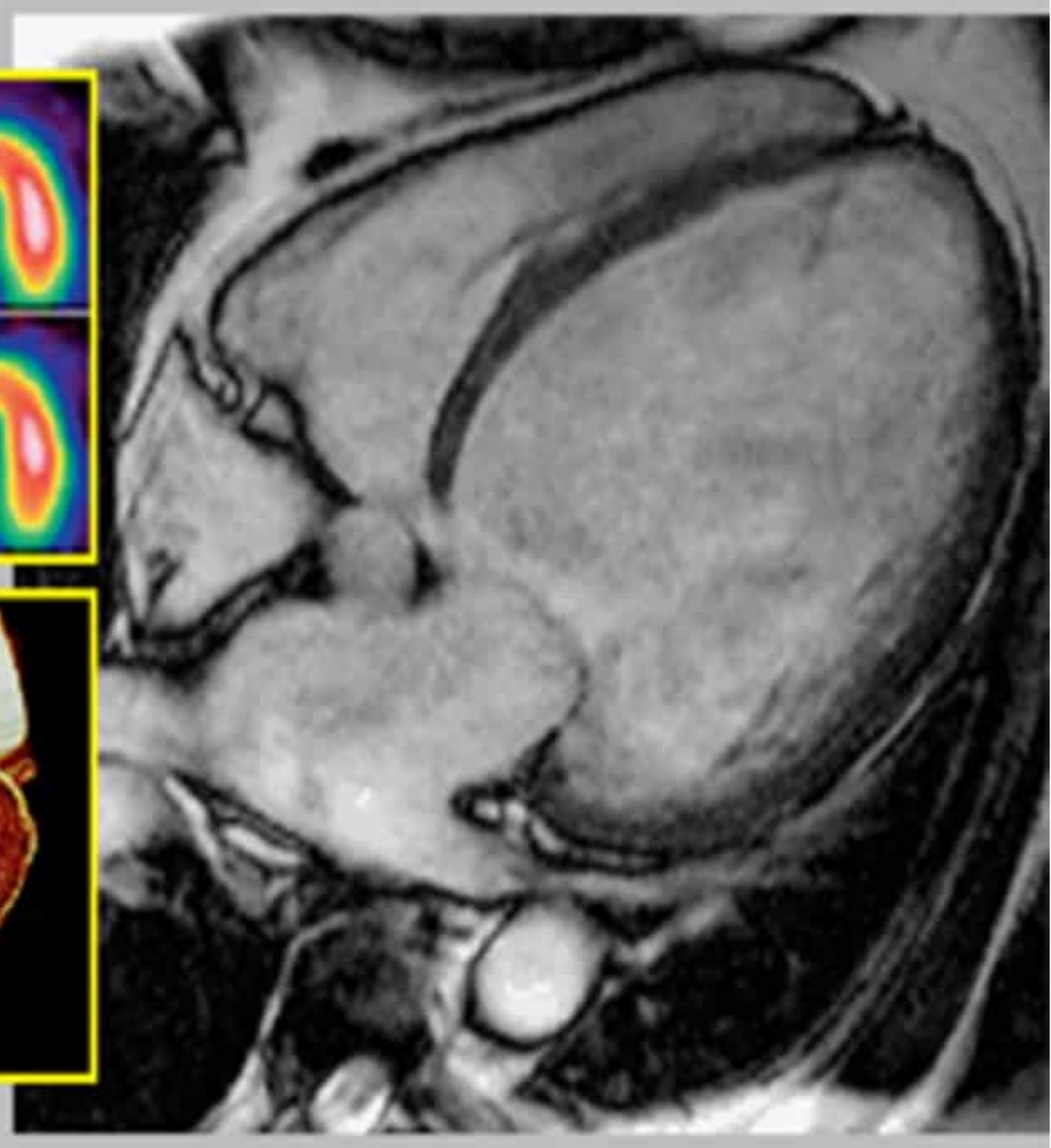

Thieme

h

Cardiac Imaging

A Multimodality Approach

Edited by

Manfred Thelen, MD
Professor Emeritus of Radiology
Johannes Gutenberg University Hospital
Mainz, Germany

Raimund Erbel, MD
Professor of Cardiology
Department of Cardiology
West German Heart Center Essen
University Hospital Essen
Essen, Germany

Karl-Friedrich Kreitner, MD
Professor of Radiology
Clinic and Polyclinic for Diagnostic and Interventional Radiology
Johannes Gutenberg University Hospital
Mainz, Germany

Joerg Barkhausen, MD
Professor of Radiology
Department of Radiology and Nuclear Medicine
University Hospital Schleswig-Holstein, Campus Lübeck
Lübeck, Germany

With contributions by
N. Abegundewardene, J. Barkhausen, A. Bockisch, F. Breuckmann, C. Bruch, O. Bruder, T. Buck, H. Eggebrecht, R. Erbel, C.U. Herborn, G. Horstick, P. Hunold, K. Koch, K.-F. Kreitner, S. Ley, A. Magedanz, K. Nassenstein, B. Pflicht, S.J. Rosenbaum-Krumme, K. Sattler, T. Schlosser, A. Schmermund, W. Schreiber, M. Thelen, T. Voigtlaender, M. Vosseler, K.-U. Waltering

608 illustrations

Thieme
Stuttgart · New York

Library of Congress Cataloging-in-Publication Data

Bildgebende Kardiodiagnostik. English
Cardiac imaging : a multimodality approach / edited by Manfred Thelen ... [et al.] ; with contributions by N. Abegundewardene ... [et al.].
XXp. ; XXcm.
Includes bibliographical references and index.
ISBN 978-3-13-147781-1 (alk. paper)
1. Heart--Imaging. 2. Heart--Diseases--Diagnosis. I. Thelen, Manfred. II. Title.
[DNLM: 1. Heart Diseases--diagnosis. 2. Diagnostic Imaging--methods. WG 141 B585c 2009a]
RC683.5.I42B5513 2009
616.1'20754–dc22
2008038221

This book is an authorized and revised translation of the German edition published and copyrighted 2007 by Georg Thieme Verlag, Stuttgart, Germany. Title of the German edition: Bildgebende Kardiodiagnostik mit MRT, CT, Echokardiographie und anderen Verfahren.

Translator: Terry Telger, Fort Worth, Texas, USA

Illustrator: Otto Nehren, Achern, Germany

Cover design: Thieme Publishing Group
Typesetting by F3 Media, Weil im Schönbuch, Germany
Printed in Germany by Grammlich, Pliezhausen
ISBN 978-3-13-147781-1 1 2 3 4 5 6

Contributors

Nico Abegunewardene, MD
Second Medical Clinic and Polyclinic
Johannes Gutenberg University Hospital
Mainz, Germany

Joerg Barkhausen, MD
Professor of Radiology
Department of Radiology and Nuclear Medicine
University Hospital Schleswig-Holstein, Campus Lübeck
Lübeck, Germany

Andreas Bockisch, MD, PhD
Professor of Nuclear Medicine
Department of Nuclear Medicine
University Hospital Essen
Essen, Germany

Frank Breuckmann, MD
Department of Cardiology
West Germany Heart Center Essen
University Hospital Essen
Essen, Germany

Christian Bruch, MD
Medical Clinic and Polyclinic
Muenster University Hospital
Muenster, Germany

Oliver Bruder, MD
Supervising Physician
Department of Cardiology
Elisabeth Hospital Essen
Essen, Germany

Thomas Buck, MD, FACC, FESC
Associate Professor and Supervising Physician
Department of Cardiology
West Germany Heart Center Essen
Essen University Hospital
Essen, Germany

Holger Eggebrecht, MD, FESC
Supervising Physician
Department of Cardiology
West Germany Heart Center Essen
University Hospital of Essen
Essen, Germany

Raimund Erbel, MD
Professor of Cardiology
Department of Cardiology
West German Heart Center Essen
University Hospital Essen
Essen, Germany

Christoph U. Herborn, MD, MBA
Associate Professor of Radiology
University Medical Center Hamburg-Eppendorf
Hamburg, Germany

Georg Horstick, MD
Associate Professor of Cardiology
Head of Pharmacology
Sanofi-Aventis Deutschland GmbH
TD Cardiovascular Diseases
Frankfurt, Germany

Peter Hunold, MD
Supervising Physician
Department of Diagnostic and Interventional Radiology
and Neuroradiology
University Hospital Essen
Essen, Germany

Katja Koch, MD
Specialist
Clinic and Polyclinic for Diagnostic and Interventional
Radiology
Johannes Gutenberg University Hospital
Mainz, Germany

Karl-Friedrich Kreitner, MD
Professor of Radiology
Clinic and Polyclinic for Diagnostic and Interventional
Radiology
Johannes Gutenberg University Hospital
Mainz, Germany

Sebastian Ley, MD, Specialist
Clinic and Polyclinic for Diagnostic
and Interventional Radiology
Ruprecht Karl University Hospital
Heidelberg, Germany

Annett Magedanz, MD, Specialist
Bethany Cardiovascular Center
Frankfurt, Germany

Kai Nassenstein, MD
Specialist
Department of Diagnostic and Interventional
Radiology and Neuroradiology
University Hospital Essen
Essen, Germany

Bjoern Plicht, MD
Department of Cardiology
West Germany Heart Center Essen
University Hospital Essen
Essen, Germany

Sandra Julia Rosenbaum-Krumme, MD
Supervising Physician
Department of Nuclear Medicine
University Hospital Essen
Essen, Germany

Katherine Sattler, MD
Department of Cardiology
West Germany Heart Center Essen
University Hospital Essen
Essen, Germany

Thomas Schlosser, MD
Supervising Physician
Department of Diagnostic and Interventional
Radiology and Neuroradiology
University Hospital Essen
Essen, Germany

Axel Schmermund, MD, FESC
Associate Professor of Cardiology
Bethany Cardiovascular Center
Frankfurt, Germany

Wolfgang Schreiber, MD
Professor and Head of Medical Physics Section
Clinic and Polyclinic for Diagnostic and
Interventional Radiology
Johannes Gutenberg University Hospital
Mainz, Germany

Manfred Thelen, MD
Professor Emeritus of Radiology
Johannes Gutenberg University Hospital
Mainz, Germany

Thomas Voigtlaender, MD
Associate Professor of Cardiology
Bethany Cardiovascular Center
Frankfurt, Germany

Markus Vosseler, MD
Second Medical Clinic and Polyclinic
Johannes Gutenberg University Hospital
Mainz, Germany

Kai-Uwe Waltering, MD
Supervising Physician
Clinic for Diagnostic and Interventional Radiology
Hospital Essen-Mitte
Essen, Germany

Preface

Diagnostic imaging of the heart has a long tradition in Germany, starting over a century ago with the discovery of Wilhelm Conrad Röntgen, which forms the basis for all radiographic techniques of cardiac imaging. Another milestone was the development of cardiac ultrasonography, which began in Germany during the 1940s and was perfected by Edler and Hertz, who recorded the first tracings of the heart based on ultrasound reflection. Professor Sven Effert introduced the method in Germany and was instrumental in gaining national and international recognition. Other key milestones were the development of computed tomography and magnetic resonance imaging.

The creation of this book was motivated by a desire to combine expert knowledge from the two medical specialties of cardiology and radiology, which have been responsible for tremendous advances in the diagnosis of heart diseases.

A third essential field in developing cardiac imaging is medical physics, which has fostered fascinating developments based on work that gained several Nobel Prize awards to physicists. Equally essential is the sectional imaging triad of echocardiography, computed tomography, and magnetic resonance imaging, whose basic physical principles have contributed to the current worldwide high level of development through systematic advances in medical technology.

Against this background of innovations and advances, it has been a genuine pleasure for the editors and authors to compile a synopsis of modern cardiac imaging and summarize the advances in this field, which are most clearly reflected in sectional imaging modalities. The new role of nuclear medicine imaging (PET-CT) is also considered in this context. Despite the profound insights that modern techniques have provided into the pathological anatomy of the heart and especially its function, conventional radiographs are far from obsolete and are available for almost every patient. Radiographs should not be ordered indiscriminately, however; this relatively low-cost and well-tolerated study should be applied critically and selectively. Recognizing that decades of experience in the analysis of chest radiographs should be fully exploited, we open this book by reviewing the basic aspects of conventional radiography.

It takes more than a detailed knowledge of sectional imaging studies to maintain high medical standards and obtain certification. It is also necessary to have well-planned organizational and communication structures within and among the different specialties as well as a command of current and traditional knowledge in order to achieve a true “state of the art status.”

Manfred Thelen
Raimund Erbel
Karl-Friedrich Kreitner
Joerg Barkhausen

Acknowledgments

Even in the age of internet-based media, the printed page still has an undisputed role in medical education. Information technology is less a competitor of books than a tool to enhance the visual impact of a book and make its contents more accessible to the reader.

Cardiac Imaging takes full advantage of these modern capabilities, particularly in its illustrations, which were processed with the aid of digital image processing techniques.

This has all been made possible by the ambitious and dedicated support of Thieme Medical Publishers under the direction of Dr. Albert Hauff and his colleagues. The editors and authors express special thanks to the project manager of this book, Ms. Susanne Huiss, and to Ms. Martina Dörsam, who was responsible for production of the book. We are also grateful to Dr. Christian Urbanowicz, who outlined the cost parameters for the book so that it could be presented in its current form.

The editors and authors thank all of our colleagues at hospitals and other institutions who helped compile the superb illustrations for this book. We are grateful to the entire staff at the Echocardiography Laboratory of the Department of Cardiology, University of Essen, and especially to Ms. Christiane Plato, the medical technologist at that institution. We extend special thanks to our colleagues Björn Plicht, Alexander Lind, Philip Kahlert, and Dirk Böse for their help in compiling the illustrations.

Dr. Peter Hunold, Dr. Thomas Schlosser, Ms. Lena Schäfter, and Mr. Kai Reiter of the Department of Diagnostic and Interventional Radiology, Essen University Hospital, were instrumental in the preparation of this book, and their help is gratefully acknowledged.

We express thanks to Ms. Ine Mayer and Ms. Josefine Kestel, radiology technologists at the Department of Diagnostic and Interventional Radiology university hospital Mainz, and we thank our photographer, Ms. Anne Marie Keuchel, for her conscientious and dedicated work.

Manfred Thelen
Raimund Erbel
Karl-Friedrich Kreitner
Joerg Barkhausen

Abbreviations

Note: Abbreviations used in the illustrations are explained in this list of abbreviations. Abbreviations used in the text and tables are also listed. Any abbreviation used without explanation may be identified in this list. For clarity and as an aide-memoire, some abbreviations are expanded at their use within the text.

ABI	Ankle-brachial index
ACB	Aortocoronary bypass
ACE	Angiotensin-converting enzyme
ACVB	Aortocoronary venous bypass
AHA	American Heart Association
AI	Aortic insufficiency
AIDS	Acquired immunodeficiency syndrome
AMI	Acute myocardiac infarction
AML	Anterior mitral valve leaflet
Ao	Aorta
Ao asc.	Ascending aorta
Ao desc.	Descending aorta
A-P	Anteroposterior
ARDS	Acute respiratory distress syndrome
ARVC	Arrhythmogenic right ventricular cardiomyopathy
ARVD	Arrhythmogenic right ventricular dysplasia
AS	Aortic stenosis
ASD	Atrial septal defect
A. subc.	Subclavian artery
AoV	Aortic valve
A.U.	Arbitrary units
AV	Arteriovenous/ aortic valve
AV fistula	Arteriovenous fistula
AVM	Arteriovenous malformation
AVOA	Aortic valve orifice area
BCT	Brachiocephalic trunk
BMI	Body mass index
bpm	Beats per minute
BSA	Body surface area
bw	Body weight
CA	Cardiac apex
CAD	Coronary artery disease
CE MRA	Contrast-enhanced MR angiography
CE MRI	Contrast-enhanced MR imaging
CFR	Coronary flow reserve
CHD	Coronary heart disease
CNR	Contrast-to-noise ratio
CO	Cardiac output
CoA	Coarctation of the aorta
COPD	Chronic obstructive pulmonary disease
CRP	C-reactive protein
CSA	Cross-sectional area
CT ratio	Cardiothoracic ratio
CT	Computed tomography, computed tomogram
CTA	CT angiography
CTCA	CT coronary angiography
CTEPH	Chronic thromboembolic pulmonary hypertension
CVP	Central venous pressure
CW Doppler	Continuous-wave Doppler
DA	Direct angiography
DCM	Dilated cardiomyopathy
DD	Differential diagnosis
DSA	Digital subtraction angiography
DSCT	Dual-source computed tomography
EBCT	Electron-beam computed tomography
ECG	Electrocardiogram
EDD	End-diastolic diameter
EDV	End-diastolic volume
EF	Ejection fraction
EPSS	E-point septal separation (in echocardiography)
EROA	Effective regurgitant orifice area
ESD	End-systolic diameter
ESV	End-systolic volume
Fr	French [gauge]
FA	Flip angle
FDG	Fluorodeoxyglucose
FFR	Fractional flow reserve
FFRmyo	Fractional myocardial flow reserve
FFT	Fast Fourier transform
FL	False lumen
FLASH	Fast low-angle shot
FOV	Field of view
FS	Fat saturation, fractional shortening
GEA	Gastroepiploic artery
Gd	Gadolinium
Gd-BOPTA	Gadolinium benzyloxypropionic tetraacetate
Gd-DOTA	Gadolinium tetraazacyclododecanetetraacetic acid
Gd-DTPA	Gadolinium diethylenetriaminepentaacetic acid
GE	Gradient echo
GRAPPA	Generalized autocalibrating partially parallel acquisition

HASTE	Half-Fourier acquisition single-shot turbo spin echo
HCM	Hypertrophic cardiomyopathy
HIV	Human immunodeficiency virus
HNCM	Hypertrophic nonobstructive cardiomyopathy
HOCM	Hypertrophic obstructive cardiomyopathy
HR	Heart rate
HU	Hounsfield unit
IAS	Interatrial septum, atrial septum
ICD	Intracoronary Doppler ultrasound
ICU	Intensive care unit
IMA	Internal mammary artery
IMH	Intramural hematoma
IR GRE	Inversion recovery-gradient echo
IR	Inversion recovery
IRAD	International Registry of Aortic Dissection
IRP	Isovolumic relaxation period
ISFC	International Society and Federation of Cardiology
IV	Intravenous
IVS	Interventricular septum
IVUS	Intravascular ultrasound
LA	Left atrium
LAO	left anterior oblique
LA pressure	Left atrial pressure
LAD	Left anterior descending coronary artery
LBBB	left bundle branch block
LCA	Left coronary artery
LCC	left coronary cusp
LCX	Left circumflex artery
LE	Late enhancement
LIMA	Left internal mammary artery
LV	Left ventricle, left ventricular
LVEDP	Left ventricular end-diastolic pressure
LVEDV	Left ventricular end-diastolic volume
LVEF	Left ventricular ejection fraction
LVESD	Left ventricular end-systolic diameter
LVESV	Left ventricular end-systolic volume
LVNC	Left ventricular noncompaction
LVOT	Left ventricular outflow tract
LVSV	Left ventricular stroke volume
MaxPG	Maximum pressure gradient
MBF	Myocardial blood flow
MCE	Myocardial contrast echocardiography
MI	Mitral insufficiency; myocardial infarction
MIBG	Metaiodobenzylguanidine
MIBI	Methoxyisobutylisonitrile
MIP	Maximum intensity projection
MM	Myocardial mass
MO	Microvascular obstruction
MPG	Mean pressure gradient
MPI	Myocardial performance index
MPR	Multiplanar reformatting
MPRI	Myocardial perfusion reserve index
MRA	MR angiography
MRCA	MR coronary angiography
MR	Magnetic resonance
MRI	Magnetic resonance imaging
MS	Mitral stenosis
MS-CT	Multislice CT
mSv	Millisievert
MV	Mitral valve
MVA/MVOA	Mitral valve orifice area
NCC	Noncoronary cusp
OCT	Optical coherence tomography
OSAS	Obstructive sleep apnea syndrome
PA	Pulmonary artery
P-A	Posteroanterior
PAI	Plasminogen activator inhibitor
PAOD	Peripheral arterial occlusive disease
PAP	Pulmonary arterial pressure
PAPVC	Partial anomalous pulmonary venous connection
PAS	Pulmonary arterial sarcoma
PAU	Penetrating aortic ulcer
PAVM	Pulmonary arteriovenous malformation
PCH	Pulmonary capillary hemangioma
PE	Pericardial effusion
PEA	Pulmonary endarterectomy
PET	Positron emission tomography
PFO	Patent foramen ovale
PH	Pulmonary hypertension
PHT	Pressure half-time
PI	Pulmonary valve insufficiency, pulmonary insufficiency
PISA	Proximal isovelocity surface area
PIVB	Posterior interventricular branch of right coronary artery
PLVED	Pressure in left ventricle at end diastole (left ventricular end-diastolic pressure)
PL	Pleural effusion
PLB	Posterolateral branch
PML	Posterior mitral valve leaflet
PPG	Peak pressure gradient
P(RA)	Right atrial pressure
PROCAM	Prospective Cardiovascular Münster Study
PRVED	Pressure in right ventricle at end diastole (right ventricular end-diastolic pressure)
PSIR	Phase-sensitive inversion-recovery
PTCA	Percutaneous transluminal coronary angioplasty
PTE	Pulmonary thromboendarterectomy

PV Pulmonary vein, pulmonary valve
PVS Pulmonary venous sarcoma
PW Posterior wall
PW Doppler Pulsed-wave Doppler

QP Pulmonary circulation
QS Systemic circulation

RA Right atrium
RA pressure Right atrial pressure
RAO projection Right anterior oblique projection
RAP Right atrial filling pressure
RCA Right coronary artery
RCC Right coronary cusp
RCM Restrictive cardiomyopathy
RCX Circumflex coronary artery
RF Radiofrequency
RIMA Right internal mammary artery
rMBF Regional myocardial blood flow
rMBV Regional myocardial blood volume
ROI Region of interest
RstAC Rest attenuation corrected
RV Right ventricle
RVEDV Right ventricular end-diastolic volume
RVEF Right ventricular ejection fraction
RVESV Right ventricular end-systolic volume
RVOT Right ventricular outflow tract

SAM Systolic anterior motion
SAR Specific absorption rate (W/kg)
SE Spin echo
SENSE Sensitivity encoding
SNR Signal-to-noise ratio
SPAMM Spatial modulation of magnetization
SPAP Systolic pulmonary arterial pressure
SPECT Single-photon emission computed tomography
SPGR Fast spoiled gradient-echo acquisition
Spiral CT Spiral computed tomography
SR Saturation recovery
SSFP Steady-state free precession
STIR Short-tau inversion recovery
StrAC Stress attenuation corrected
SV Stroke volume
SVC Superior vena cava

T Tesla
T2 prep T2 preparation pulse
TA Acquisition time
TAA Thoracic aortic aneurysm
TAPVC Total anomalous pulmonary venous connection
TASH Transcoronary ablation of septal hypertrophy
Tc Technetium
TDE Tissue Doppler echocardiography
TDI Tissue Doppler imaging
TE Echo time
TEE Transesophageal echocardiography
TEI Time ejection index
TI Inversion time, tricuspid insufficiency
TL True lumen
TlCl Thallium chloride
TP Pulmonary trunk
TR Repetition time
TS Tricuspid stenosis
TSE Turbo spin echo
TTE Transthoracic echocardiography
TV Tricuspid valve
TVI Tricuspid valve insufficiency

VCATS Volume coronary angiography with targeted scans
VCi Inferior vena cava
VCs, Vcs Superior vena cava
Venc Encoding velocity
Vm Mean velocity
Vmax Maximum velocity
VOA Valve orifice area
VR Volume rendering
VRT Volume rendering technique
VSD Ventricular septal defect
VTI Velocity-time integral

WHO World Health Organization
WMSI Wall motion score index

Contents

I Imaging Modalities

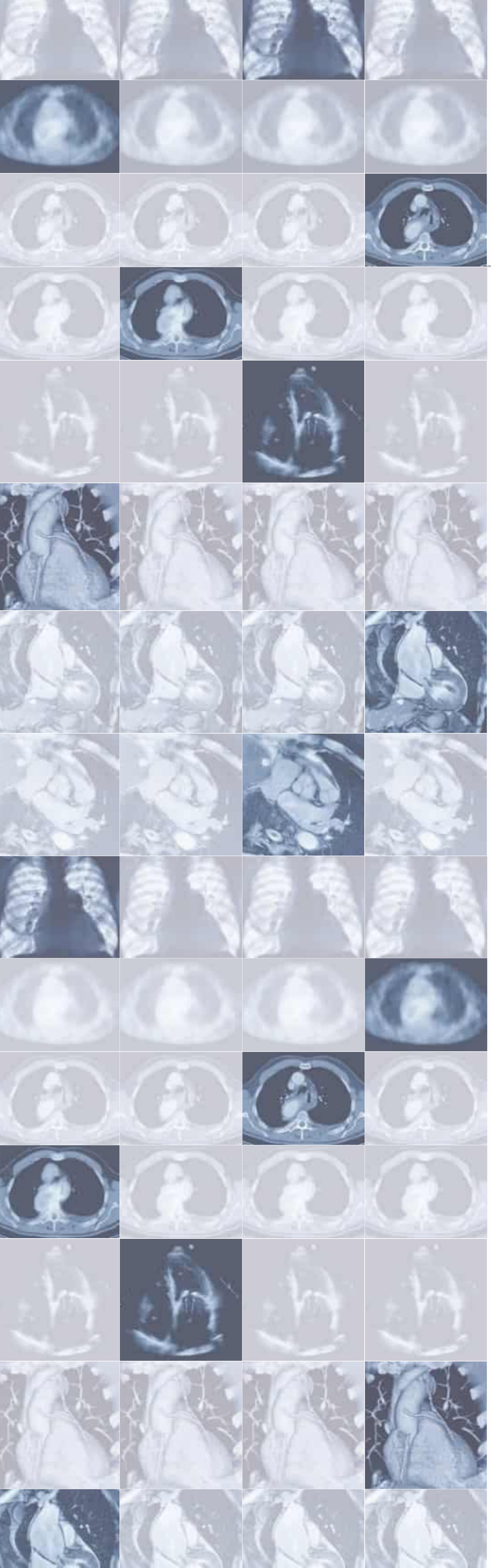

I

Imaging Modalities

1 Conventional Radiography

M. Thelen

Clinical Manifestations of Heart Diseases

In cardiology as in other specialties, the indication for examining the heart is based on patient complaints.[1–8] In this section the main clinical manifestations of heart diseases are briefly reviewed from a differential diagnostic standpoint. Conventional X-ray films of the chest, or projection radiographs, are a basic tool in the differential diagnostic investigation of these symptom complexes.[8]

Chest Pain

This complaint is almost always related to heart disease. It typically induces fear of an imminent life-threatening heart attack. If the pain is of brief duration, it is referred to as a typical episode of angina pectoris.

Essential Point
Approximately one-third of patients with myocardial ischemia, especially diabetics, do not experience chest pain.

If the pain lasts longer than 15 minutes, extracardiac causes should also be considered. The differential diagnosis of chest pain is thus highly complex:

- Angina pectoris (myocardial ischemia), myocardial infarction
- Hypertrophic cardiomyopathy
- Dilated cardiomyopathy
- Arrhythmias
- Acute pericarditis (pericarditis sicca)
- Mitral valve prolapse
- Aortic aneurysm
- Aortic dissection
- Massive pulmonary embolism
- Small or moderate pulmonary embolism combined with pulmonary infarction
- Pneumothorax
- Pleuritis sicca
- Pneumonia
- Broad range of esophageal disorders
- Broad range of musculoskeletal disorders
- Broad range of abdominal diseases in which pain is projected to the chest
- Neurogenic diseases (neuralgia, radicular syndromes, herpes zoster)
- Functional cardiac complaints

The differential diagnosis of chest pain is extremely challenging. The establishment of a chest pain unit in the emergency room, chiefly in university hospitals, is an initiative aimed at addressing this problem.

Edema

Edema results from an imbalance between the quantity of fluids, salts, and proteins which leave and re-enter the capillary system. It may be a manifestation of heart disease. A classic example is biventricular heart failure, which may develop as a result of myocardial, pericardial, or valvular heart disease, as well as of other cardiac lesions.

Dyspnea

Dyspnea, or respiratory distress, is characterized by very different degrees of severity; it may occur during rest or exercise, and may be position-dependent (orthopnea) or may present as an abnormal respiratory pattern. The underlying cause may be a disturbance of ventilation, gas exchange, or lung perfusion.

In addition to pulmonary causes, various cardiac abnormalities may be the underlying symptoms of respiratory distress. Possible causes include pulmonary outflow obstruction or left-sided heart failure as a result of myocardial, valvular, or coronary heart disease.

Cyanosis

Cyanosis is a reflection of insufficient pulmonary oxygen uptake or peripheral oxygen depletion. Pulmonary cyanosis may be caused by:

- Ventilatory impairment
- Diffusion impairment
- Increased intrapulmonary venous admixture of blood in unventilated but perfused lung areas, or the arteriovenous shunting of blood.

Cardiac central cyanosis may be caused by:

- Congenital heart defects with a right-to-left shunt
- Congenital defects with decreased pulmonary blood flow

These heart defects lead to central cyanosis. This condition is to be distinguished from peripheral cardiac cyanosis, in which cardiac output is reduced by myocardial insufficiency or caused by congestion, e.g., mitral stenosis).

Arrhythmias

Tachycardiac arrhythmias are present when the rate of ventricular contractions increases to 100 bpm or more. They may occur in association with:

- Primary defects of the impulse conduction system (e.g., congenital anomalies)
- Coronary heart disease
- Myocardial diseases
- Valvular heart diseases
- Severe left ventricular dysfunction
- Pericardial diseases
- Right ventricular dysplasia (cardiomyopathy)

Hypertension

The potential causes of hypertension are extremely diverse. The most important causes are listed below:

- Decreased elasticity of the aorta and great vessels due to atherosclerosis
- Coarctation of the aorta
- Conditions causing an increase in stroke volume and cardiac output
- Heart failure
- Renal causes

Over time, all of these conditions lead to cardiac symptoms which may be reflected in a change in the cardiac silhouette.

Hypotension

Primary forms of cardiac hypotension result from a decrease in cardiac output due to

- Impaired myocardial contractility (heart failure)
- Cardiac arrhythmias (bradycardiac and tachycardiac)
- Impaired diastolic filling of the heart
- Valvular heart disease

The most common form of acute cardiac hypotension is cardiogenic shock due to myocardial infarction or severe heart failure. Chronic cardiovascular forms of hypotension are associated with the following conditions:

- Aortic valve disease
- Mitral valve disease
- Aortic arch syndrome
- Constrictive pericarditis

Syncope

Brief syncopal episodes lasting 1 minute or less may have a cardiac cause. The cause may be mechanical, relating to abnormalities of left ventricular emptying or filling. Syncope may also result from septal defects (including atrial septal defects), as well as thrombus formation in the left atrium associated with mitral stenosis.

The following mechanical causes of syncope can be differentiated by imaging studies:

- Abnormalities of left ventricular emptying
- Abnormalities of left atrial emptying
- Aortic stenosis
- Hypertrophic obstructive cardiomyopathy
- Heart failure
- Myocardial infarction

Conventional radiography continues to have an established place even with the availability of modern electrophysiology, echocardiography, invasive cardiac testing, and sectional imaging modalities such as CT and MRI, although its role needs to be redefined.[9–18] Thus, sophisticated cardiological tests are not state of the art unless standard biplane chest films are also obtained. Radiographs are also widely used in the follow-up of cardiac status. This applies to the follow-up of conservative and interventional therapies and, in particular, to preoperative treatment planning or perioperative monitoring and follow-up after surgical intervention.[6,19–21]

The information necessary for understanding and interpreting a normal chest radiograph is derived from specific pathophysiological parameters that are based on changes in hemodynamics.

Radiographic Anatomy

The standard projections for cardiac radiography are the frontal (posteroanterior, P-A) projection and the left lateral projection (with an esophagogram). A plain radiograph of the heart is a summation image of the individual cardiac chambers. The cardiac borders and their shape changes are therefore the sole indicators in determining the location of the individual cardiac chambers and assessing their size in radiographs. The structures that form the borders of the heart cannot always be conclusively identified, even when all standard views are obtained (**Fig. 1.1**).[22]

Frontal (P-A) Radiograph

The following structures normally form the cardiac borders in the frontal radiograph:

- Left side of mediastinum (from above downward):
  - Distal portion of the aortic arch
  - Main pulmonary artery trunk
  - Left atrial appendage (part of the left atrium)
  - Left ventricle
- Right side of mediastinum (from above downward):
  - Superior vena cava
  - Right atrium

The protrusion located below the aortic arch on the P-A radiograph is termed the pulmonary segment. This is an arch-shaped structure formed by the pulmonary trunk and not by the conus pulmonalis, which is located below the pulmonary valves. The pulmonary segment may be very prominent owing to dilatation of the pulmonary artery.

Lateral Radiograph

The lateral radiograph shows the following topography:

- Anterior structures (from above downward):
  - Ascending aorta
  - Pulmonary trunk
  - Right ventricle

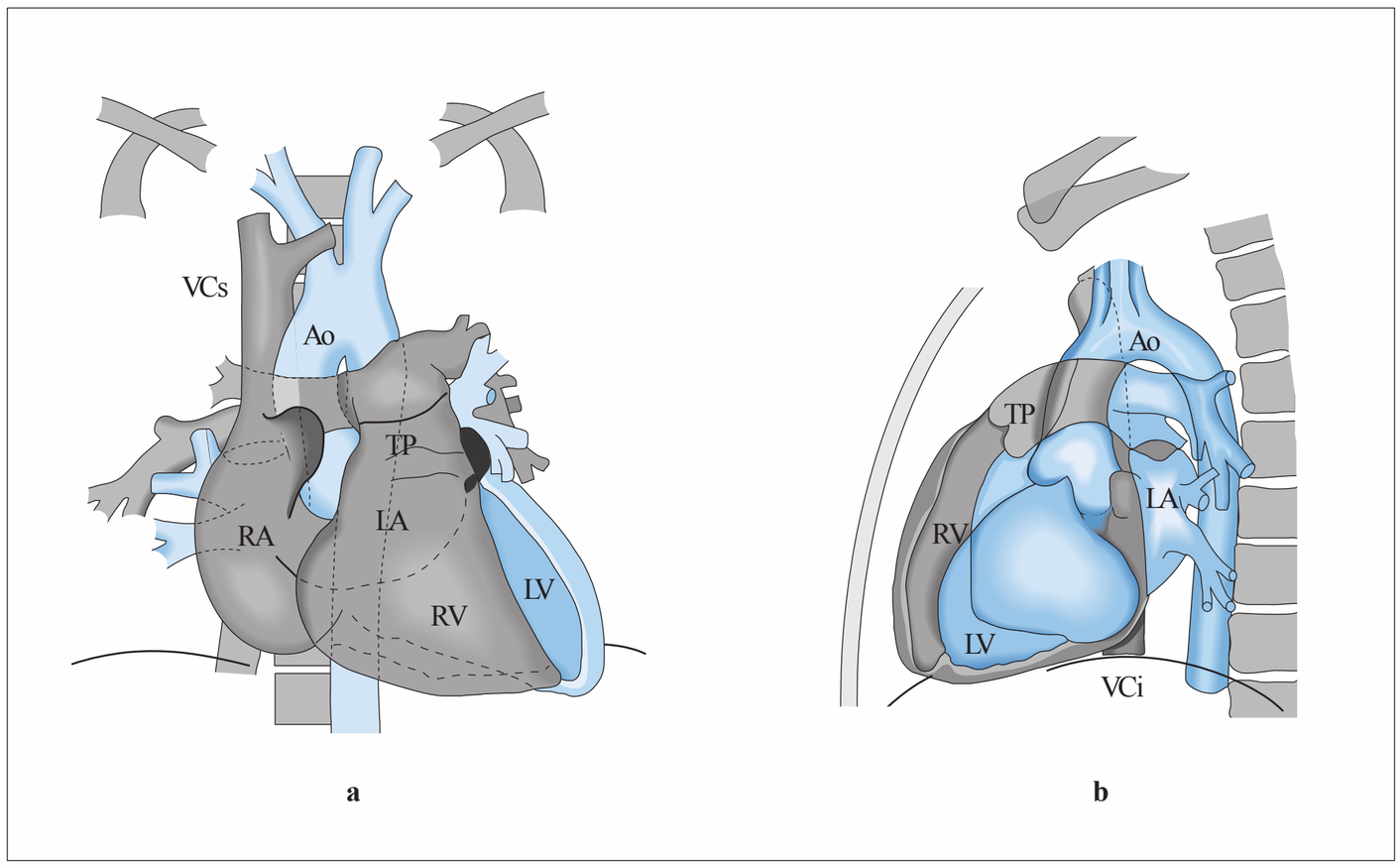

Fig. 1.1a, b Diagrammatic representation of the radiographic anatomy of the heart.
a P-A radiograph.
b Lateral radiograph.

The retrosternal space normally appears as a narrow space between the anterosuperior border of the heart and the anterior chest wall.

- Posterior structures (from above downward):
  - Descending aorta and pulmonary vessels
  - Left atrium
  - Left ventricle
  - Inferior vena cava

The space between the posterior cardiac border and vertebral column represents the retrocardiac space. The space bounded by the left atrium, vertebral column, and aortic arch (superior vascular pedicle) is called the aortic window. If the aortic window is notably devoid of structures, this indicates the presence of small main pulmonary arteries. The close relationship between the esophagus and left atrium explains why an enlarged left atrium causes circumscribed posterior displacement of the esophagus in the lateral chest radiograph.

Given the typical location and arrangement of the cardiac chambers, the enlargement of specific chambers may produce characteristic changes in the size and shape of the cardiac silhouette that can be identified in the various projections.[23–25]

Radiographic Technique

P-A View

Conventional radiographic examination of the heart begins with a P-A projection, which is obtained when the patient is first admitted. A left lateral radiograph at full inspiration shows an overview of the anterior and posterior cardiac borders and may yield important information on the relative sizes of the cardiac chambers.[26]

Oblique Views[24]

Today, the traditional right anterior oblique (RAO) and left anterior oblique (LAO) views of the chest are important only in angiocardiography. They are no longer included in a standard radiographic series.

Contrast Radiography of the Esophagus

Oral contrast radiography of the esophagus, especially in the lateral projection, is useful for evaluating the position of the aortic arch, the course of the descending aorta, and anomalies of the aortic arch vessels. It is also useful in the assessment of the size of the left atrium on the posterior border of the heart.

Preliminary Fluoroscopy[27,28]

Cardiac fluoroscopy, in which different projections are obtained by rotating the patient, is used to screen for cardiac calcifications and to evaluate the motion of the cardiac borders. Despite its demonstrable value, fluoroscopy is rarely included in routine cardiac imaging. It can supply information on:

- Severely calcified coronary vessels
- Calcified cardiac valves
- Calcifications of the myocardium, pericardium, or fibrous ring
- Movement and location of implanted pacemaker leads
- Wobbling or other instability of implanted valves or valve rings (**Fig. 1.2**)

Enlargement of the Cardiac Chambers

Right Ventricle

P-A View When the right ventricle is enlarged, it expands upward in the direction of its outflow tract and from right (posterior) to left (anterior), and to the side (**Fig. 1.3**). This displaces the pulmonary artery upward, causing it to occupy most of the concavity of the cardiac waist in the P-A view. This type of cardiac silhouette is referred to as a right ventricular configuration. It is a common normal finding in children and is very infrequently found in healthy adolescents and adults. At the same

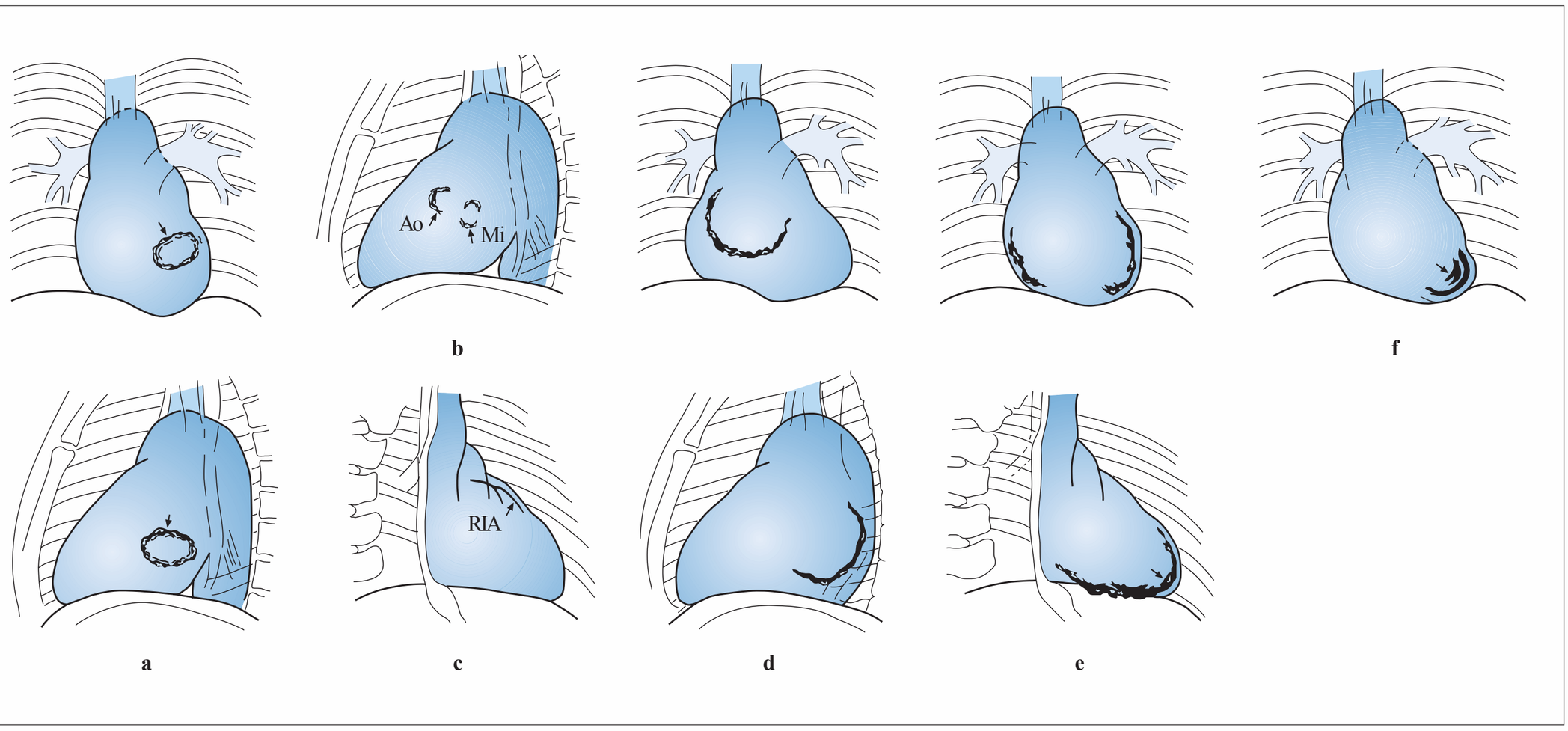

Fig. 1.2 a–f Sites of occurrence of intracardiac calcifications (diagrammatic representation).
a Calcified mitral valve annulus; P-A and lateral views.
b Calcification of the aortic and mitral valve; lateral view.
c Calcification of the LAD and left coronary artery; RAO view.
d Calcification of the left atrial wall; P-A and lateral views.
e Calcification of the pericardium, calcifying pericarditis; P-A and RAO views.
f Calcified myocardial aneurysm; P-A view.

time, the associated rotation of the heart toward the left side shifts the left ventricle more or even completely toward the posterior side of the heart. The right ventricle may expand on the anterior side of the heart and, in rare cases, forms the left border of the cardiac silhouette (**Fig. 1.4**).

Essential Point
Dilatation of the right ventricle rotates the heart to the left, shifting the left ventricle posteriorly about the cardiac axis.

Lateral View In the left lateral view, dilatation of the right ventricle leads to narrowing and obliteration of the retrosternal space. This is considered a reliable sign of right ventricular enlargement. When enlargement is extreme, the left ventricle is shifted so far posteriorly that it may cause narrowing of the retrocardiac space near the diaphragm (**Fig. 1.5**).

Left Ventricle[29–31]

P-A View Enlargement of the left ventricle expands the heart downward, backward, and toward the left side. The cardiac silhouette in the P-A view appears broadened, and the cardiac

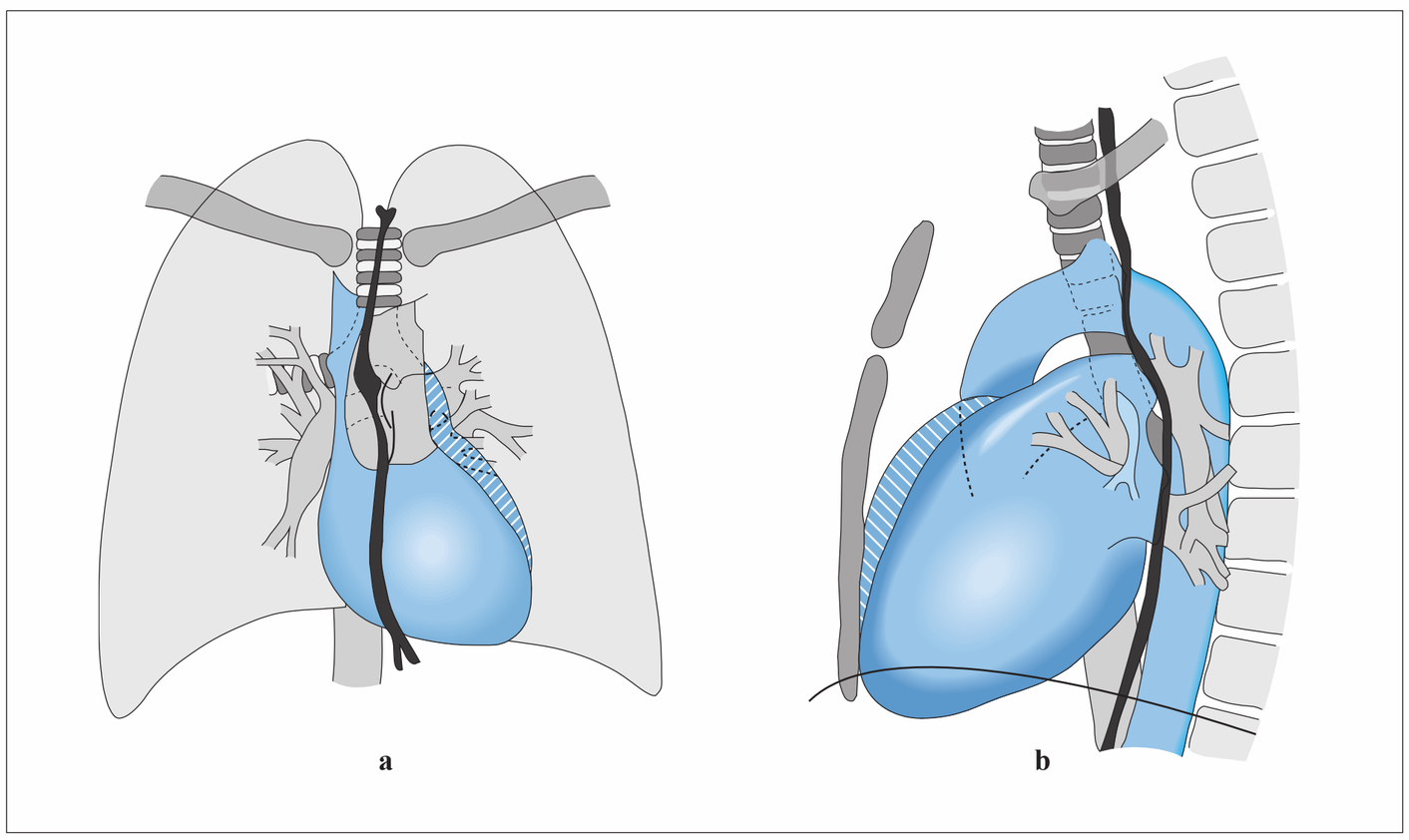

Fig. 1.3 a, b Change in cardiac shape caused by pronounced enlargement of the right ventricle.
a P-A radiograph.
b Lateral radiograph.

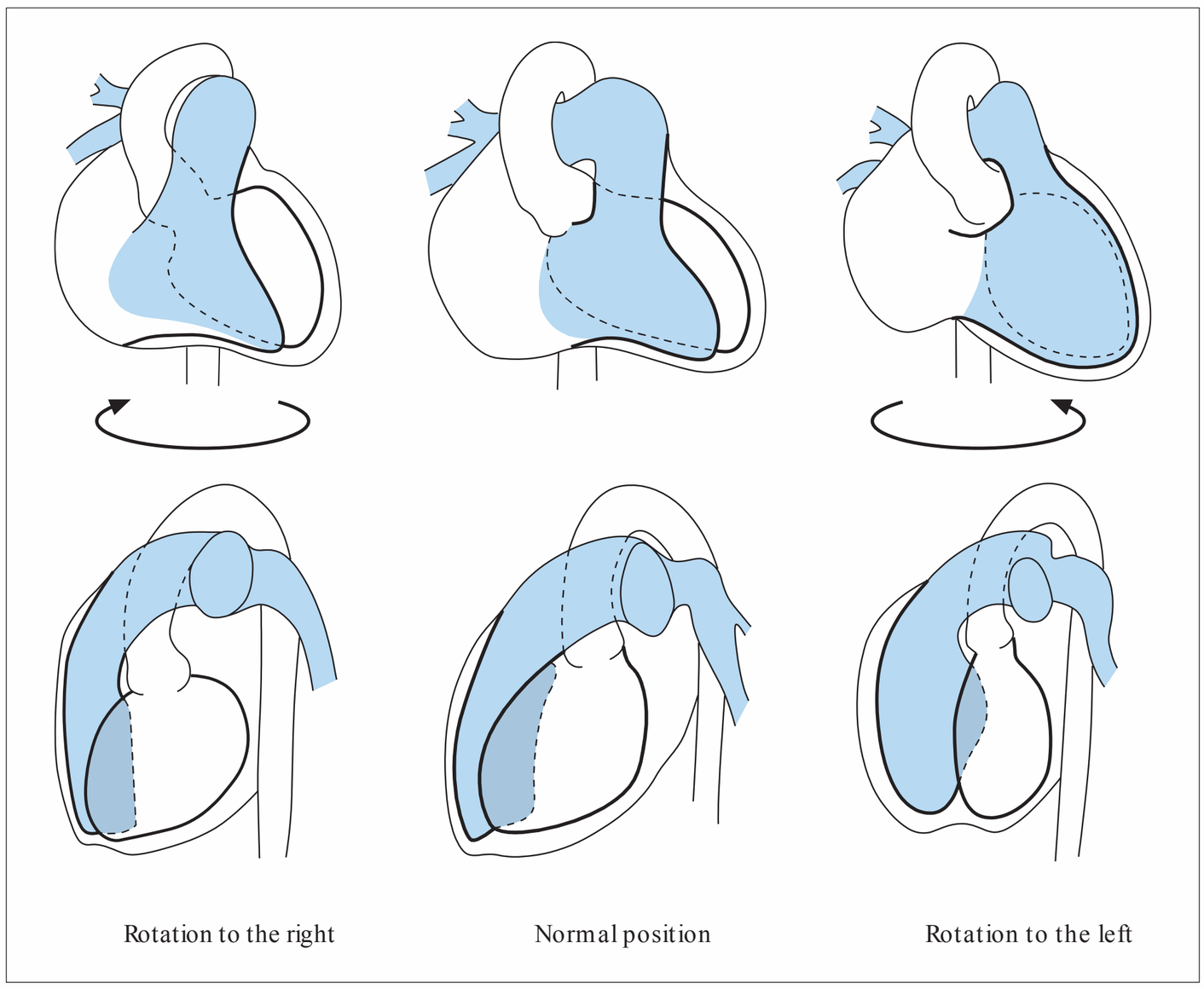

Fig. 1.4 Diagrammatic representation of the change in cardiac shape caused by significant rotation to the right (left ventricular dilatation) and to the left (right ventricular dilatation) compared with the normal position.

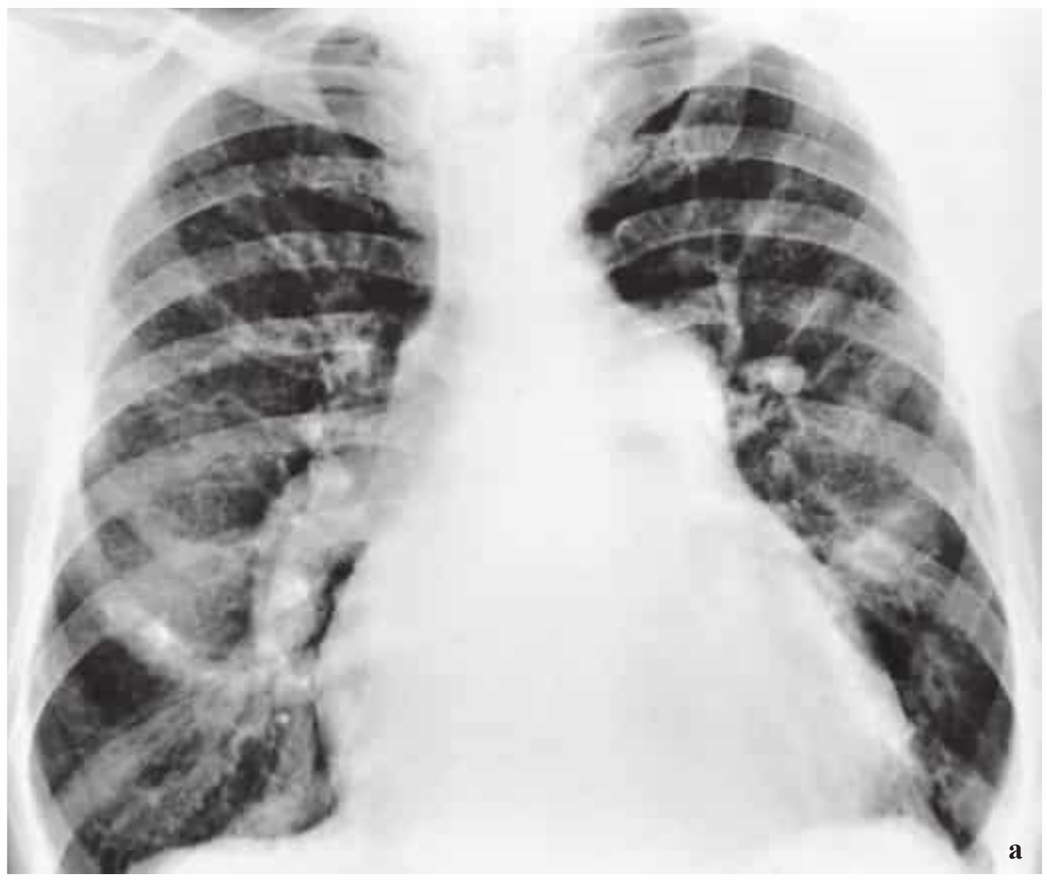

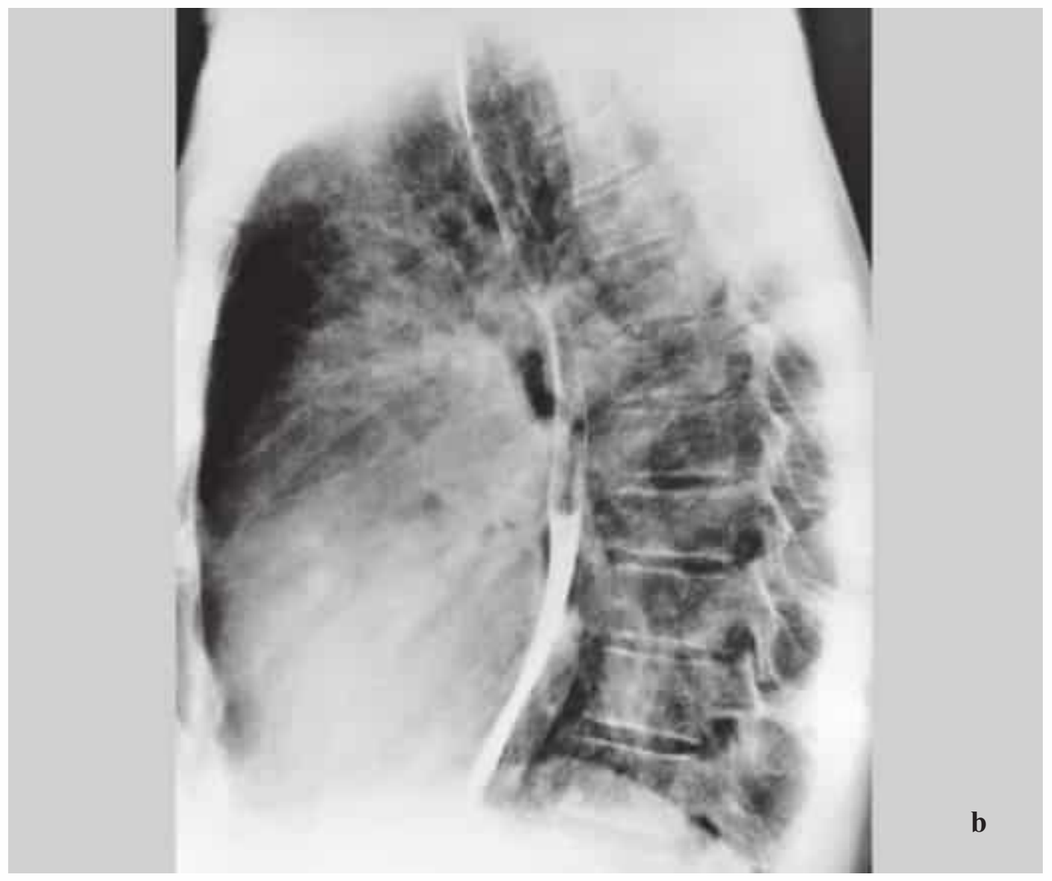

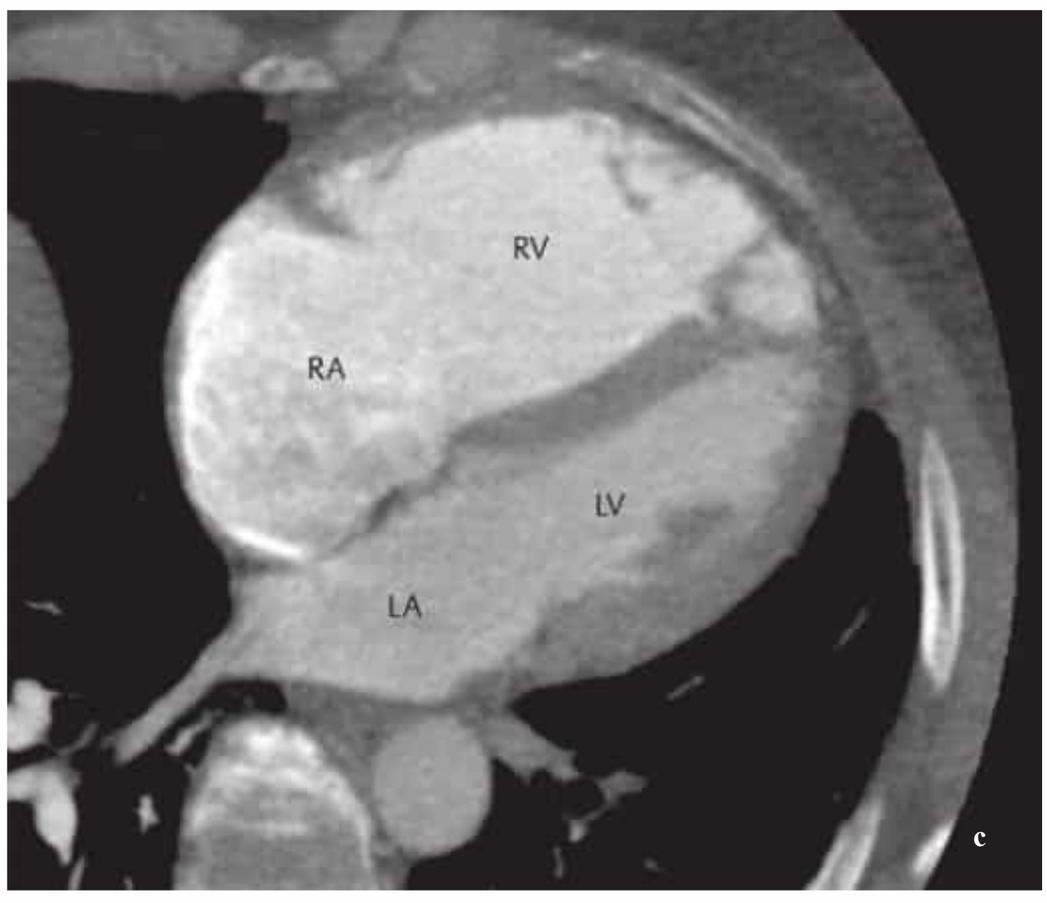

Fig. 1.5 a–c Pronounced right ventricular configuration in stage III cor pulmonale. With the heart rotated to the left, the dilated right ventricle forms the anterior cardiac border. It also extends to the left cardiac border, displacing the left ventricle posteriorly (**c**). Typical signs of pulmonary hypertension are:

- Prominence of the pulmonary segment
- Large central pulmonary arteries
- Cardiac rotation due to right ventricular dilatation.

a P-A radiograph.
b Left lateral radiograph with esophagogram.
c Cardiac CT scan at the level of the ventricular plane demonstrates the dilated right ventricle, the nearly horizontal orientation of the septum, and posterior displacement of the left ventricle.

waist is accentuated. This pattern is generally described as an aortic or left ventricular configuration. With few exceptions (congenital heart defects, e.g., Fallot-type cardiac anomalies), it is typical of left ventricular enlargement (**Figs. 1.6, 1.7**).

Essential Point
The P-A view is useful in distinguishing between dilatation of the right and left ventricles, as it enables one to differentiate between a right ventricular configuration of the cardiac silhouette and an aortic or left ventricular configuration.

Lateral View Narrowing of the retrocardiac space is an indicator of left ventricular enlargement in the left lateral radiograph. The left ventricle is definitely enlarged if it extends more than 18 mm past the inferior vena cava. The enlarged left ventricle may displace the lower portion of the barium-filled esophagus, forming a posterior convexity, or it may slide back past the esophagus without altering its course.

Right Atrium[32]

P-A View Normally the right atrium forms almost the entire right border of the cardiac silhouette in the P-A view. An enlarged right atrium forms a convex protrusion toward the right, which may be most conspicuous at the upper right cardiac border (**Fig. 1.8**). The enlarged right atrium also expands toward the left side, however, and broadening of the heart on the right side is thus not directly proportional to the degree of atrial dilatation.

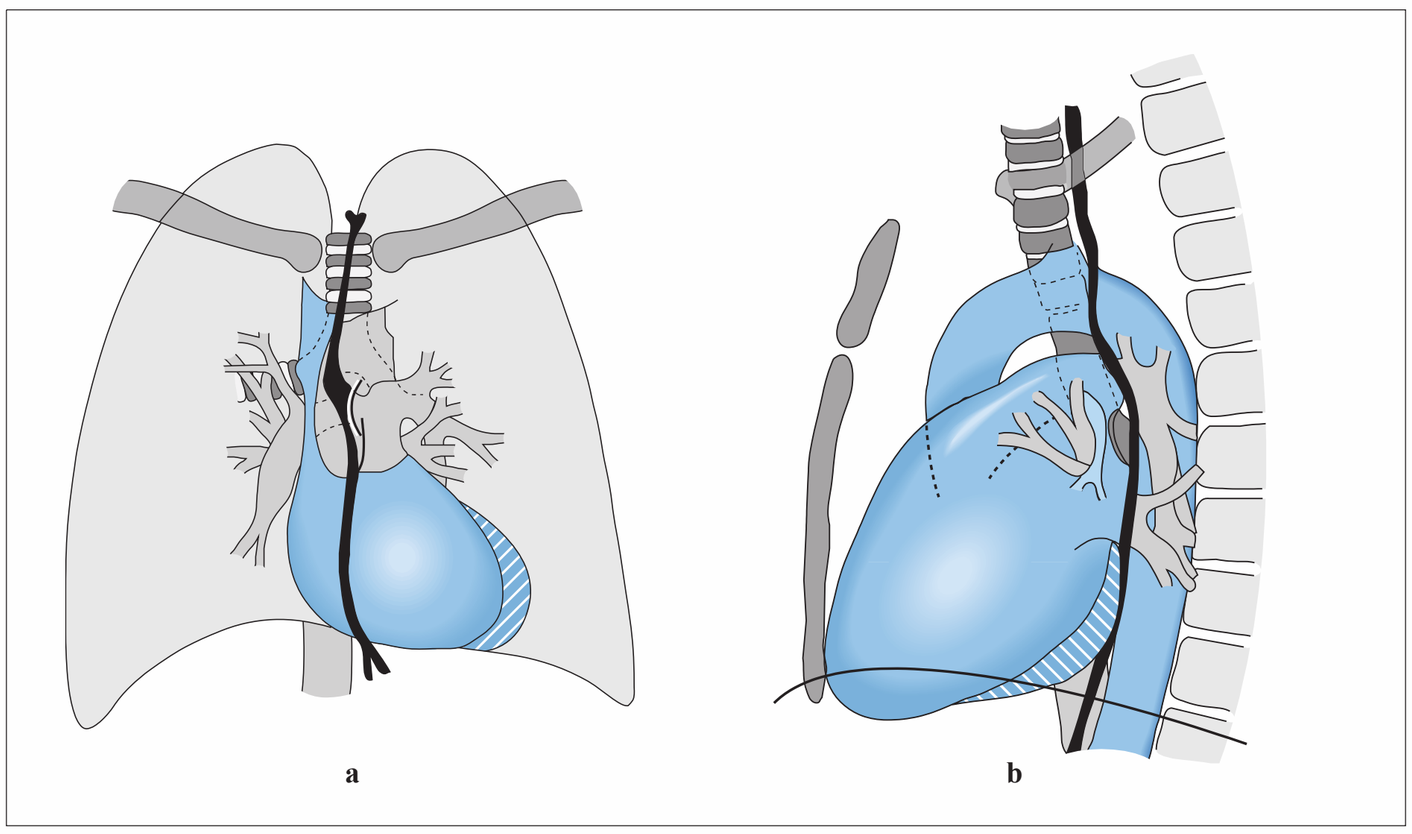

Fig. 1.6 a, b Change in cardiac shape caused by left ventricular enlargement in the P-A radiograph (**a**) and lateral radiograph (**b**).

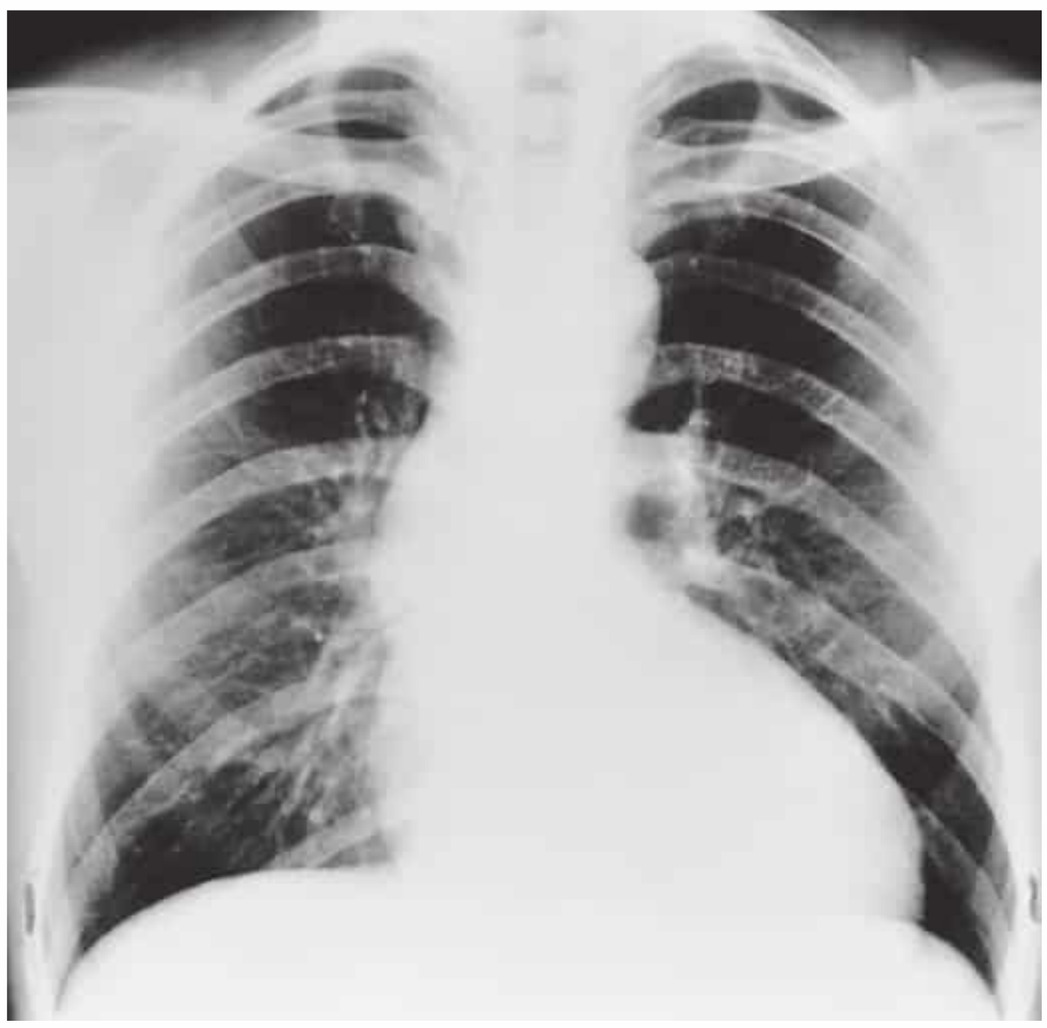

Fig. 1.7 Typical aortic or left ventricular configuration in a patient with combined aortic valve disease with left ventricular dilatation. The ascending aorta is expanded because of a jet effect resulting from aortic stenosis.

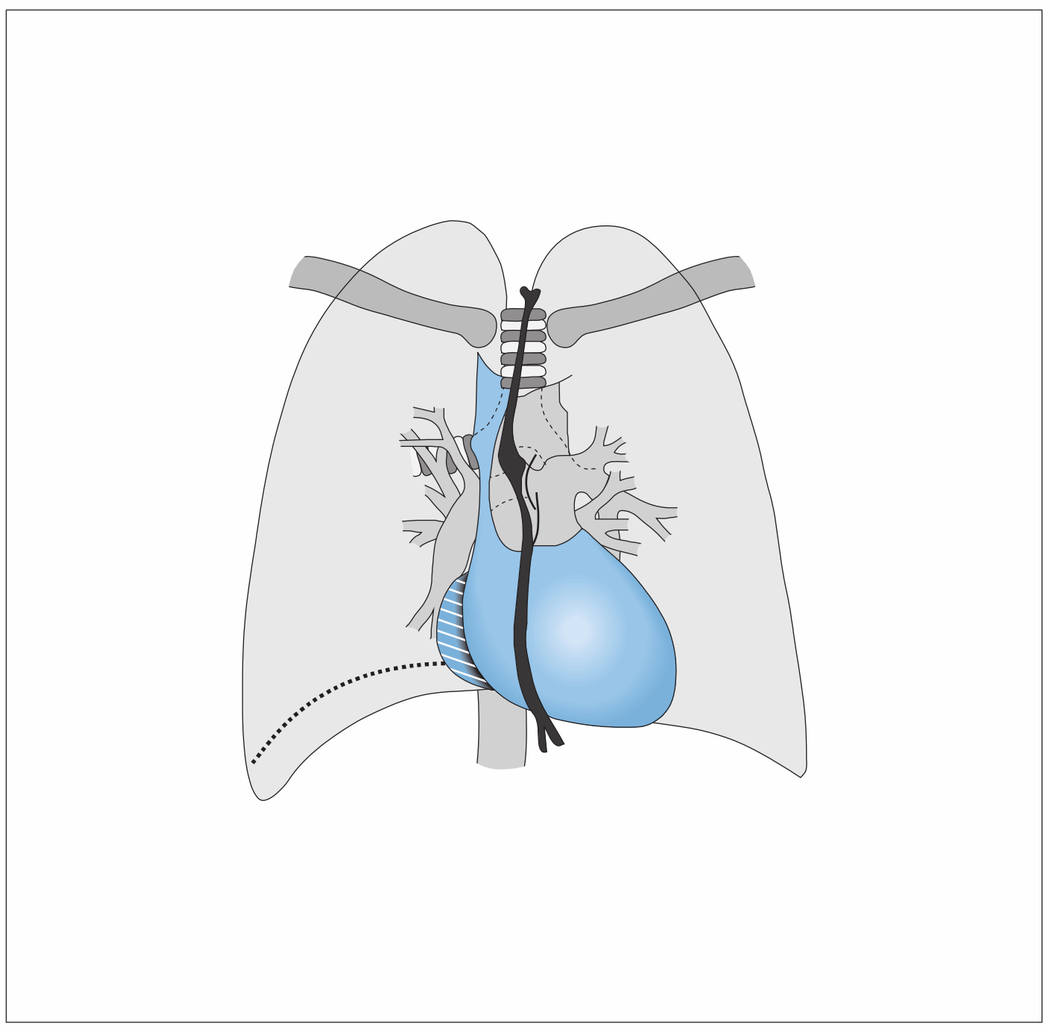

Fig. 1.8 Change in cardiac shape caused by dilatation of the right atrium.

Lateral View In the left lateral view an enlarged right atrium causes no apparent cardiac abnormalities and no esophageal displacement.

Left Atrium[33–38]

When the left atrium is enlarged, it expands posteriorly in accordance with its location on the posterior heart wall. It may also project toward the right side, and less commonly it may broaden the left side of the cardiac silhouette. Because the left atrium is located in close proximity to the esophagus, dilatation of the left atrium always leads to circumscribed displacement of the barium-filled esophagus. The size of the left atrium can be determined on an upright contrast radiograph of the esophagus in the left lateral projection taken at full inspiration.

When the dilated left atrium is viewed in the frontal chest radiograph, the superimposed positions of the left and right atria often create a double contour along the upper right cardiac border, especially taken with harder x-rays or digitally postprocessed images. A markedly enlarged left atrium may even project past the right cardiac border. On the left side, the enlarged left atrium may fill out the cardiac waist or create a lateral protrusion. The esophagus below the tracheal bifurcation is displaced by a markedly dilated left atrium to the right and only infrequently to the left. Extreme dilatation of the left atrium may displace the left main bronchus upward or even narrow it, causing an increase in the tracheal bifurcation angle (normally ~70°). Enlargement of the left atrium is most easily detected in radiographs following routine opacification of the esophagus (**Figs. 1.9, 1.10**).

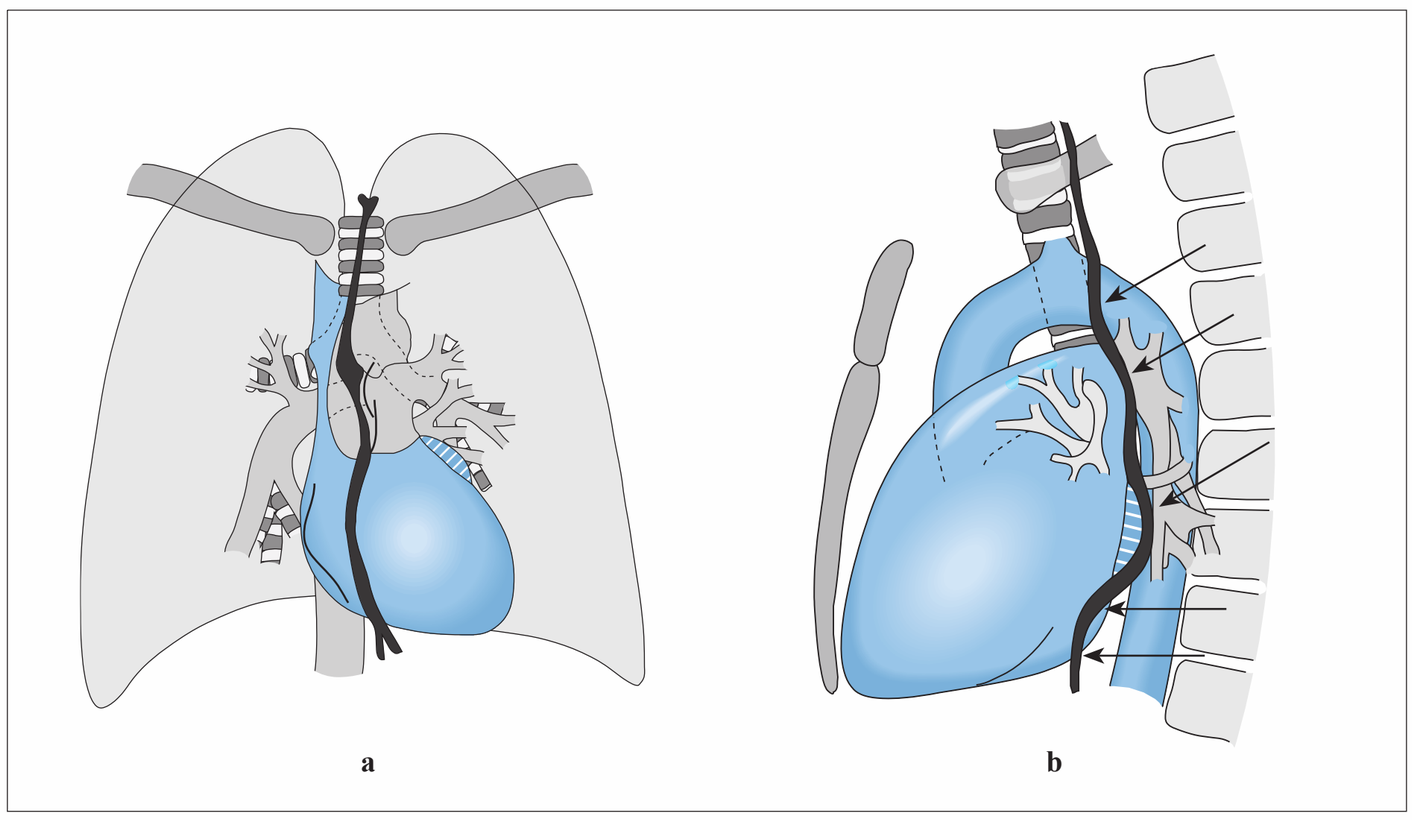

Fig. 1.9 a, b Change in cardiac shape due to enlargement of the left atrium, which displaces the opacified esophagus posteriorly and toward the right side.
a PA radiograph.
b Lateral radiograph.

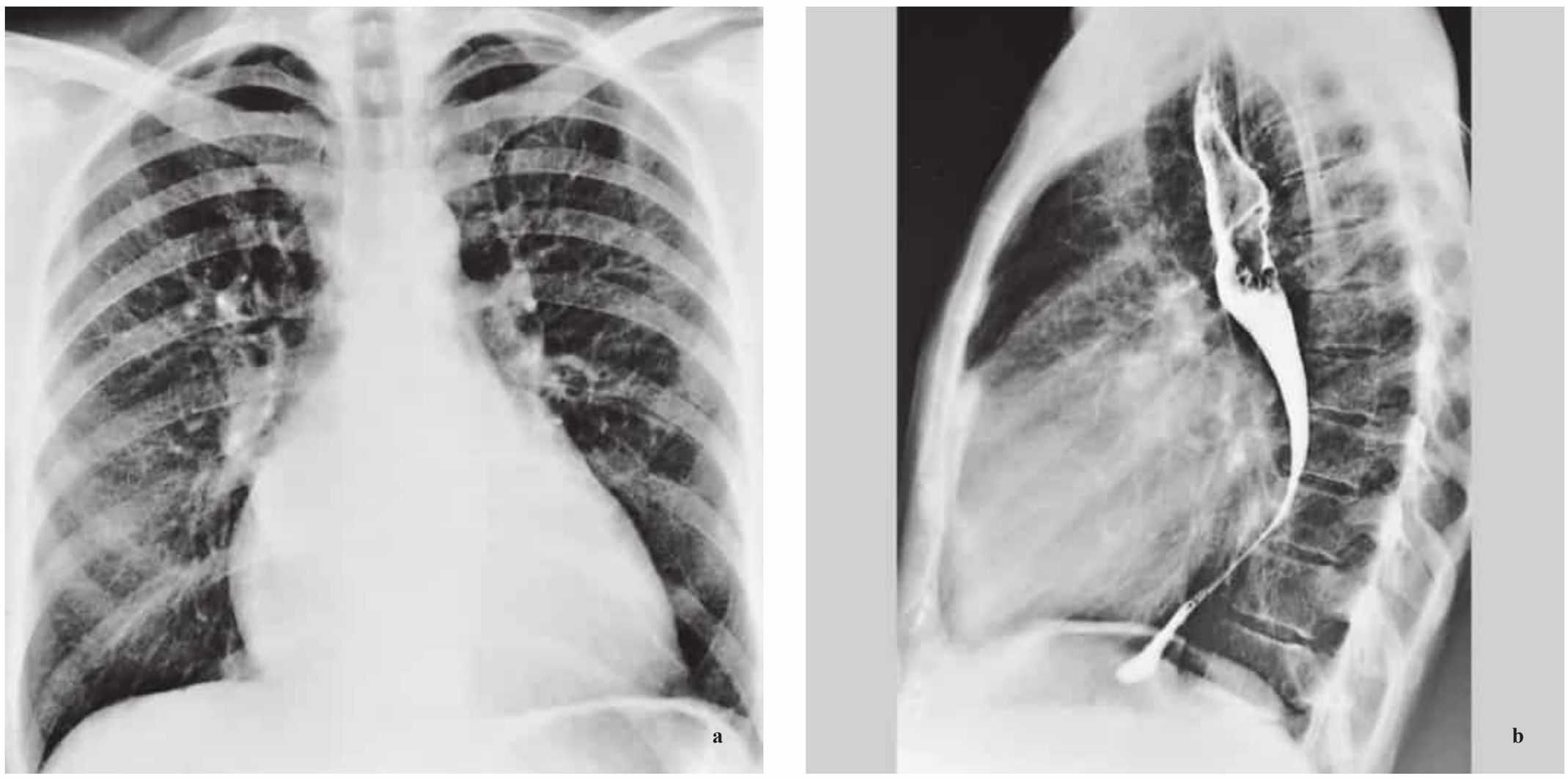

Fig. 1.10 a, b Combined mitral valve defect with predominant stenosis. PA chest radiograph (**a**) and left lateral radiograph with an esophagogram (**b**). Enlargement of the left atrium is manifested by a double contour along the right cardiac border, a prominent atrial appendage, and deep indentation and posterior curving of the opacified esophagus.

It should be noted that barium opacification of the esophagus may prove troublesome in subsequent tests such as angiocardiography (contrast material in the transverse colon superimposed over the heart), and therefore a barium swallow is frequently omitted.

Combined Change[39–48]

Enlarged cardiac chambers may displace other normal-sized cardiac segments in ways that are difficult to interpret. For example, a significantly dilated right ventricle may displace the left ventricle posteriorly, making it difficult to assess the size of the left ventricle in the presence of a markedly enlarged right ventricle (e.g., combined mitral valve disease). Similarly, a severely dilated left atrium may displace the right ventricle forward. Even when the left atrium is definitely enlarged, this does not necessarily signify mitral valve disease. Impairment of blood flow through the mitral valve may have other causes, such as a fixed or floating atrial tumor or a large thrombus in the left atrium, resulting in obstruction of the mitral valve. In some cases this can lead to marked enlargement of the left atrium.[22,49] The degree of dilatation depends on its duration and the hemodynamic effects of the lesion. Thus, echocardiography has replaced radiography for routine clinical measurements of the cardiac chambers, although chest films still provide important initial information on the nature of the underlying heart disease (**Figs. 1.11, 1.12**).

Radiographic Determination of Cardiac Size[50–59]

Radiographically visible enlargement of the heart is an important indicator of heart disease. Although there is no established correlation between cardiac size and the severity of heart disease, the presence of an abnormally enlarged heart and especially its progression over time can still provide important information. Cardiac size is determined on a standard chest radiograph with a 2-m film-focus distance, which will display the heart in its approximate actual size.

Cardiac size is determined by measuring the transverse diameter of the heart, i.e., the horizontal distance between the outermost right and left cardiac borders on the P-A chest radiograph measured from the midline. The ratio of the transverse cardiac diameter to the transverse thoracic diameter (measured between the inner rib margins at the level of the right hemidiaphragm at normal inspiration) is termed the cardiothoracic (CT) ratio. The CT ratio for a normal-sized heart should not exceed 1:2.

When the heart is viewed in supine radiographs (e.g., taken under ICU conditions), it appears enlarged owing to the decreased film–focus distance (1 m) and greater object–film distance (posterior cassette). The elevated position of the diaphragm also causes apparent transverse broadening of the heart. Thus, in evaluating the size of the heart (e.g., after cardiac surgery) it is helpful, though not strictly necessary, to have a preoperative bedside radiograph available to enable a meticulous comparison of the pre- and postoperative chest radiographs.[60]

Essential Point
The CT ratio in supine radiographs is of limited value in determining cardiac size, but can be useful in follow-up examinations.

Since the advent of sonographic, angiographic, computed tomographic, and magnetic resonance methods for determining cardiac volume and the size of the individual cardiac chambers, chest radiographs have become obsolete for cardiac volumetry.

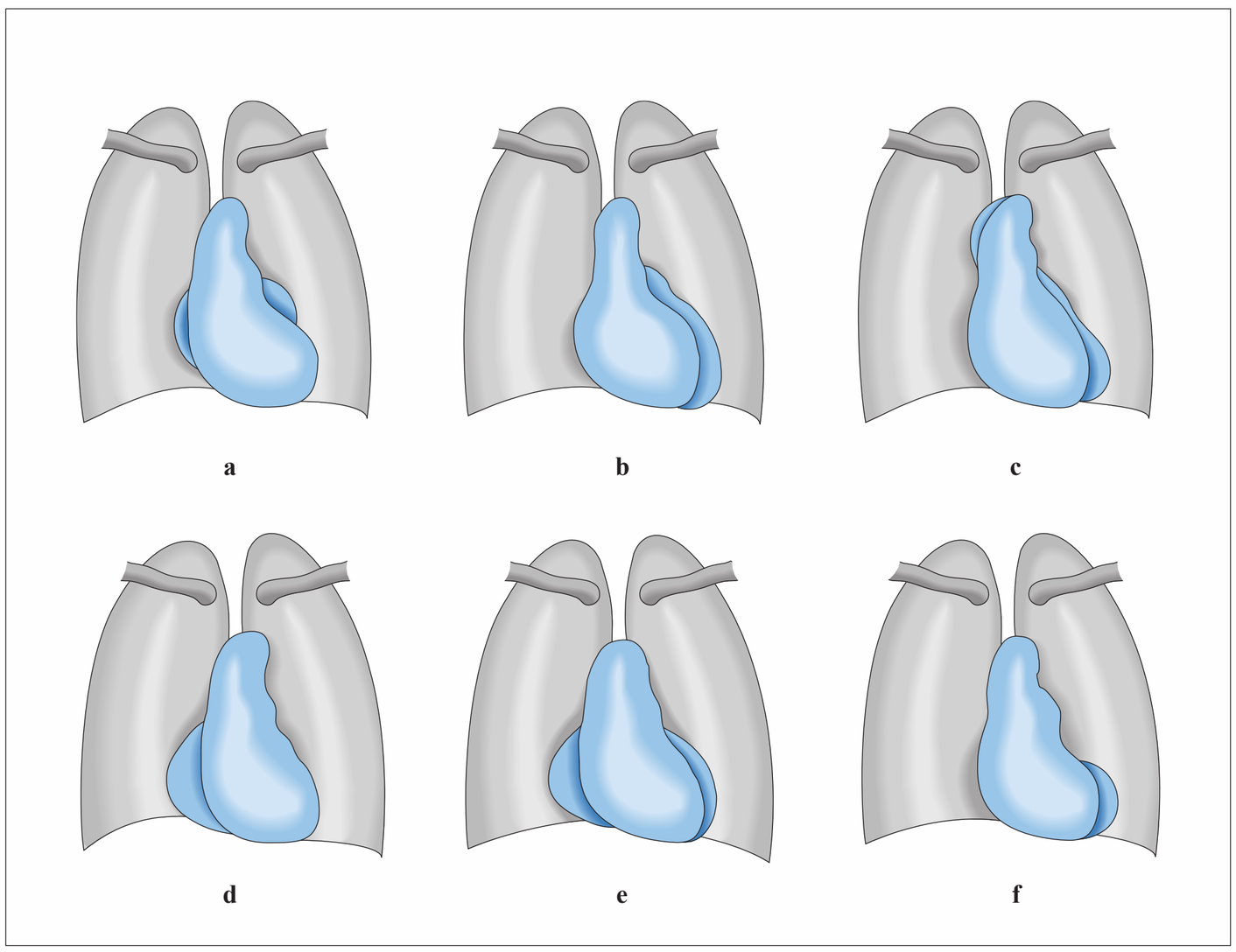

Fig. 1.11 a–f Schematic representation of the change in cardiac configuration associated with acquired valvular diseases (from Bücheler E, Lackner K-J, Thelen M. Einführung in die Radiologie. Thieme, Stuttgart, 2006. Fig. 6.23, p. 350).
a Mitral stenosis.
b Mitral insufficiency.
c Aortic valve disease.
d Tricuspid stenosis.
e Tricuspid insufficiency.
f Pulmonary valve disease.

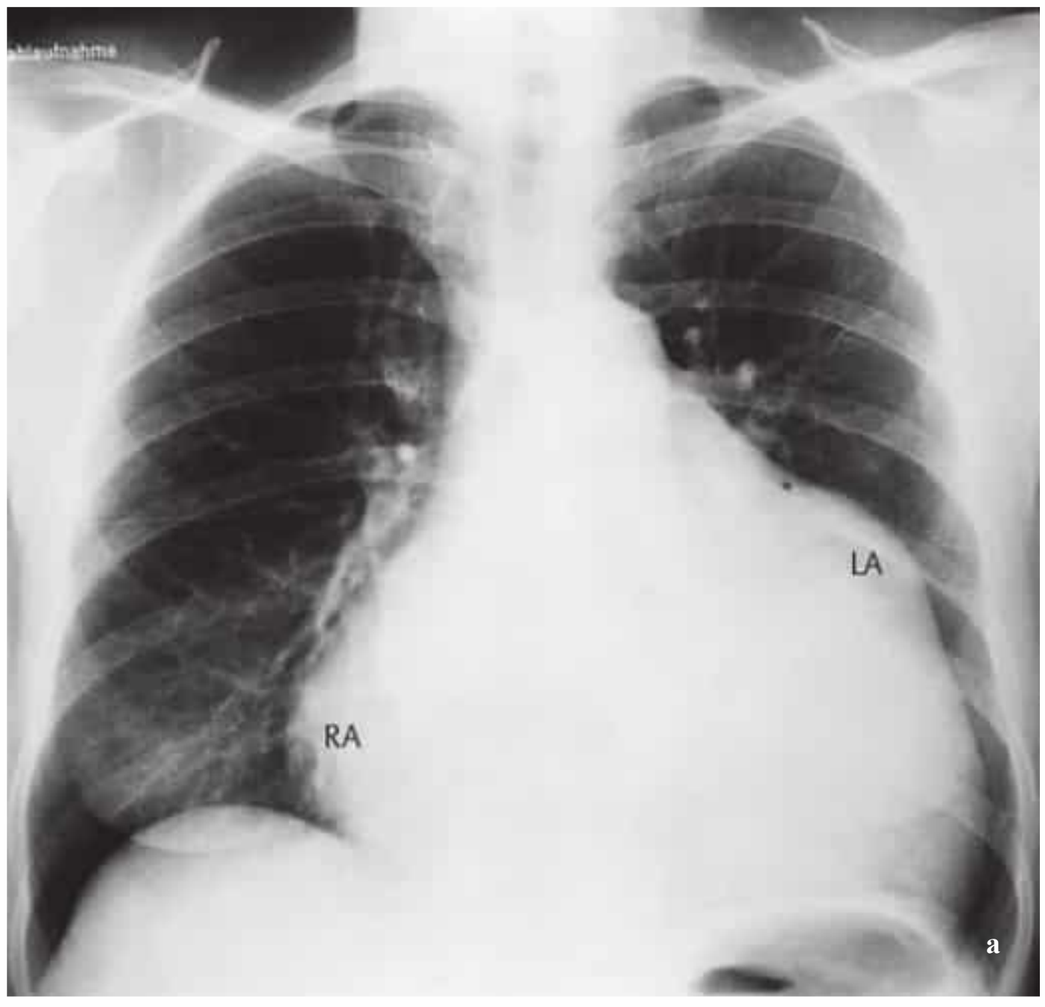

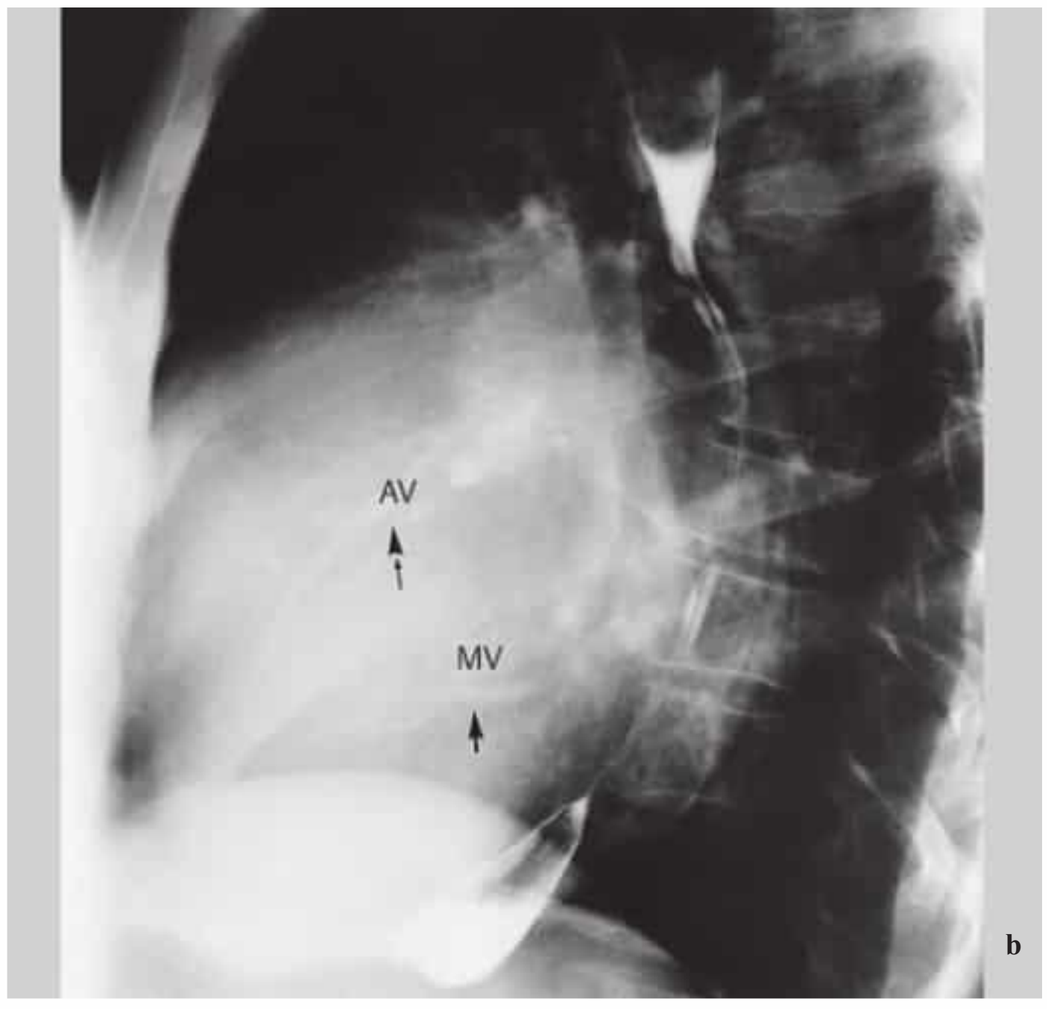

Fig. 1.12 a, b Multivalvular disease (combined aortic, mitral, and tricuspid valve disease).

a PA radiograph **b** Lateral radiograph with esophagogram.

- Prominent right cardiac border due to enlargement of the right atrium (RA).
- Significantly enlarged left atrium (LA) causes convexity of the cardiac waist and is viewed as a faint double contour on the right cardiac border.
- Massive cardiac dilatation is also present at the ventricular level.
- Lateral radiograph shows right ventricular outflow tract dilatation and displacement toward the retrocardiac space.
- The left ventricle occupies the retrocardiac space completely.
- The esophagus is curved posteriorly by the enlarged left atrium.
- Calcification of the aortic (AV) and mitral (MV) valves.

Cardiac Hypertrophy and Dilatation

Ventricular hypertrophy is the basic mechanism through which the heart compensates for an increased load.[61–63]

Pressure Overload

Pressure overload on the heart is characterized by an increase in systolic wall tension. The initial cardiac manifestation is wall thickening, followed by concentric myocardial hypertrophy with an associated reduction of inner volume. Some dilatation may also occur as an adaptive response to chronic pressure overload, although it does not yet constitute myogenic dilatation. Hypertrophy is always the dominant initial response of the heart to an isolated pressure overload.

Volume Overload

Volume overload, characterized by increased diastolic wall tension of the dilated ventricles, leads to elongation of the myocardial fibers followed by eccentric hypertrophy with an expanded inner volume. Volume overload causes less wall thickening than pressure overload. The dominant feature of volume overload is therefore dilatation, while hypertrophy is secondary.[64]

Underlying Diseases

Tables 1.1 and 1.2 list the most common underlying diseases leading to left- and right-sided cardiac enlargement, illustrated here for diseases causing a pressure or volume overload.

Importance of Pulmonary Vasculature in Cardiac Diagnosis[18,65]

Because of the low intravascular pressures in the pulmonary circulation, gravity has a much greater effect on blood flow in the lung than in the systemic circulation. Hydrostatic pressures are added to the intravascular pressures in the lower lung zones. Because of these effects, blood flow in the lower lung zones is three times greater than in the upper zones. Accordingly, pulmonary vascular markings appear larger in the basal than in the apical lung in the P-A radiograph. A reduction in the caliber of the basal vessels indicates a redistribution of blood flow that may signify the presence of pulmonary or cardiac disease. This phenomenon, described as upper lobe blood diver-

Table 1.1 Examples of diseases causing pressure and volume overload of the left heart

Pressure overload
- Aortic stenosis
- Coarctation of aorta
- Systemic arterial hypertension

Volume overload
- Aortic insufficiency
- Mitral insufficiency
- Ventricular septal defect
- Patent ductus arteriosus
- Aortopulmonary window
- AV fistula

Table 1.2 Causes of pressure and volume overload of the right ventricle

Pressure overload of the right ventricle

Frequent causes—pulmonary arterial hypertension due to:
- Primary parenchymal lung disease
- Primary or secondary pulmonary vascular obstruction
- Shunt lesions
- Severe mitral valve disease
- Severe aortic valve disease
- Pulmonary congestion due to left-sided heart failure

Rare causes:
- Pulmonary stenosis

Volume overload of the right ventricle

Frequent causes:
- Atrial septal defect
- Anomalous pulmonary venous return

Rare causes:
- Tricuspid insufficiency
- Pulmonary insufficiency
- Ventricular septal defect

sion is, however, appreciated only in upright P-A radiographs (**Table 1.3**, **Fig. 1.13**).

Pulmonary Congestion

When normal venous return from the lungs to the heart is impaired, this leads to congestion of blood flow in the pulmonary veins. The earliest sign of this process is a visible increase in the caliber of the upper lobe veins. The increase in left ventricular filling pressure leads to a rise of pulmonary venous and pulmonary capillary pressure, altering the balance between capillary fluid extravasation and reabsorption in favor of extravasation. The resulting increase in tissue pressure eventually leads to a reduction of blood flow in the basal lung zones. This redistribution of blood flow is manifested by enlarged arteries and veins in the upper lung zones and by small vessels in the lower zones. This consequence of decreased left ventricular inflow can be appreciated in the plain chest radiograph, which also shows enlargement of the left atrium.

In patients with severe mitral valve stenosis or chronic heart failure (**Table 1.4**), there is an additional active arterial vasoconstriction with intimal proliferation, leading to a rise in pulmonary arterial pressure.[66–68] Radiographs show signs of pulmonary arterial hypertension with large central pulmonary arteries and narrow peripheral arteries. As this state continues to progress, marked by a growing imbalance between fluid extravasation and reabsorption, fluid begins to accumulate in the pulmonary interstitium. This is followed by the entry of fluid into the alveoli and finally into the bronchioles. As this occurs, the clinical picture progresses from acute dyspnea to manifest pulmonary edema (**Table 1.5**, **Fig. 1.14**).[69]

Table 1.3 Radiographic appearance of pulmonary vasculature because of changes in pulmonary pressure as a result of congenital or acquired heart disease

Large apical veins and arteries (upper lobe blood diversion)	Pulmonary venous hypertension due to early mitral stenosis, heart failure, or atrial tumor
Narrow basal veins, large apical veins, small peripheral arteries, large central arteries	Pulmonary arterial hypertension due to late mitral stenosis, chronic heart failure
Large arteries and veins in all lung zones	Hyperemia due to ASD, VSD, ductus arteriosus, etc.
Narrow peripheral arteries and veins, large central pulmonary arteries	Severe pulmonary arterial hypertension with vascular proliferation due to ASD, VSD, or ductus arteriosus
Small central and peripheral arteries and veins	Hypemia due, for example to pulmonary stenosis, Ebstein anomaly, pericardial effusion, heart defects with a right-to-left shunt (Fallot group), relative tricuspid insufficiency based on right-sided heart failure
Narrow peripheral arteries, large central pulmonary arteries	Pulmonary arterial hypertension due to pulmonary sarcoidosis, pneumoconiosis, panarteritis nodosa, primary pulmonary hypertension

Table 1.4 Principal causes of chronic heart failure

- Loss of contractile muscle mass (myocardial infarction, coronary heart disease)
- Persistent pressure overload (hypertension, aortic stenosis, coarctation of the aorta, pulmonary hypertension, pulmonary stenosis, congenital heart disease with elevated right ventricular pressure)
- Persistent volume overload (valvular insufficiency, congenital heart disease, vascular malformations with right-to-left shunt, arteriovenous fistulas, Paget disease)
- Abnormal heart rate (hypercritical tachycardia, abnormal bradycardia, arrhythmias)
- Noncoronary cardiomyopathy (myocarditis, dilated cardiomyopathy, toxic and metabolic cardiomyopathies, endocrine myocardial alteration)
- Impaired ventricular filling (restrictive cardiomyopathies, constrictive pericarditis, storage diseases, cardiac tumors, cardiac thrombi)

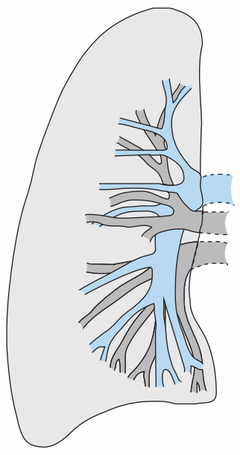 **a** Veins and arteries smaller in upper lung zones than in lower lung zones	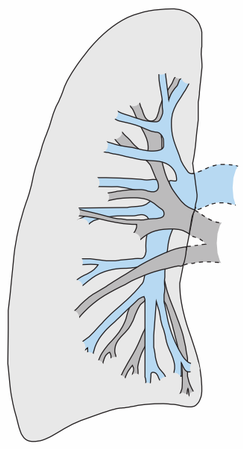 **b** Large apical veins and arteries: upper lobe blood diversion	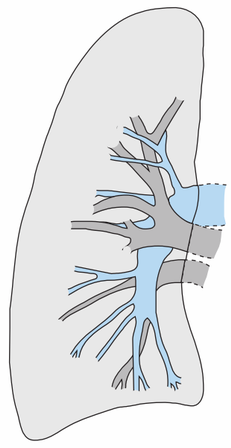 **c** Narrow basal veins, large apical veins, small peripheral arteries, large central arteries	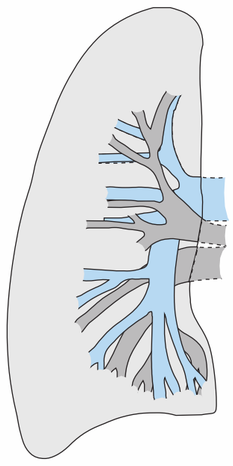 **d** Large veins and arteries in all lung zones
Normal findings	Pulmonary venous hypertension due to early mitral stenosis, heart failure, atrial tumor, or decompensated aortic stenosis	Pulmonary arterial hypertension due to late mitral stenosis or chronic heart failure	Hyperemia due to, e.g. ASD, VSD, patent ductus, etc.

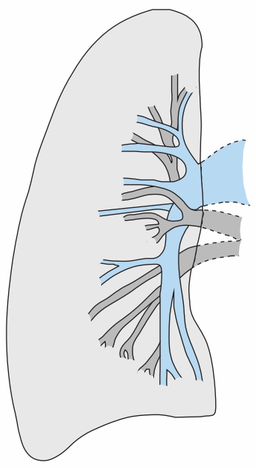 **e** Narrow peripheral veins and arteries, large central pulmonary arteries	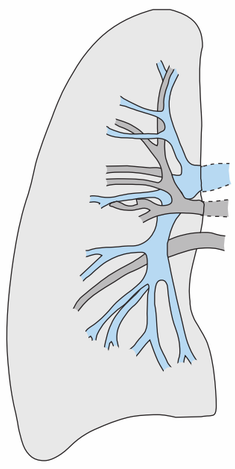 **f** Narrow central and peripheral veins and arteries	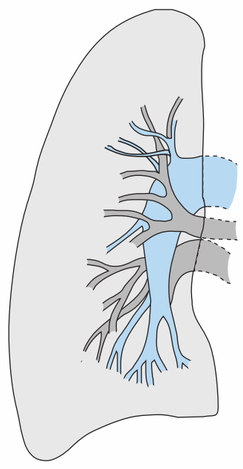 **g** Small peripheral arteries, large central pulmonary arteries
Severe pulmonary arterial hypertension with vascular proliferation due to ASD, VSD, or patent ductus	Hypoemia due to, e.g. pulmonary stenosis, Ebstein anomaly, pericardial effusion, heart defects with right-to-left shunt (Fallot group), relative tricuspid insufficiency based on right-sided heart failure	Pulmonary arterial hypertension due to pulmonary sarcoidosis, pneumoconiosis panarteritis nodosa, primary pulmonary hypertension

Fig. 1.13 a–g Changes in pulmonary vasculature due to altered pulmonary hemodynamics (gray = vein, blue = artery).

a Normal vascular pattern.

b Pulmonary venous congestion with large upper lobe veins and reduced calibers of lower lobe vessels.

c Pulmonary arterial hypertension due to chronic pulmonary congestion, with large central pulmonary arteries, slightly enlarged upper lobe veins, and narrow peripheral arteries and veins.

d Pulmonary hyperemia with enlargement of pulmonary arteries and peripheral arteries and veins due to increased blood flow.

e Pulmonary arterial hypertension as a result of persistent hyperemia.

f Small peripheral and central vessels due to decreased pulmonary blood flow.

g Pulmonary arterial hypertension (parenchymal cor pulmonale) with small peripheral vessels and large central pulmonary arteries.

Table 1.5 Principal causes of acute heart failure and cardiogenic shock, which may be accompanied by pulmonary edema

Myocardium	• Myocardial infarction • Septal rupture • Advanced cardiomyopathy • Myocarditis
Valve apparatus	• Decompensated valvular heart disease • Papillary muscle rupture • Chordae tendineae rupture
Pericardium	• Ventricular tamponade due to hemopericardium • Ventricular wall rupture • Effusion
Cardiac rhythm	• Severe tachycardia • Bradycardia
Outflow tract	• Hypertensive crisis • Massive pulmonary artery embolism • Dissecting aortic aneurysm

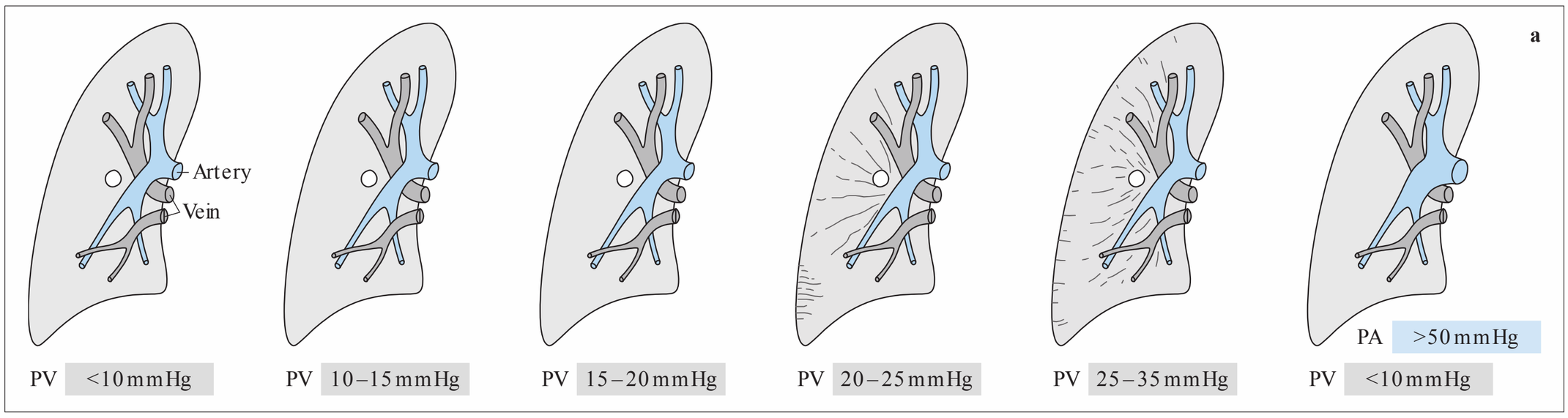

Fig. 1.14 a–e **a** Radiographic changes in the pulmonary vasculature and interstitium resulting from increased pulmonary venous pressure (diagrammatic representation).
b Normal pulmonary blood flow.
c Pulmonary hyperemia. Ventricular septal defect due to postinfarction rupture of the septum.
d Pulmonary congestion with Kerley B lines (arrow).
e Decreased pulmonary vascular markings with small, indistinct peripheral pulmonary vessels (hyperlucent lung) in a patient with hemodynamically significant pericardial effusion.

Decreased Pulmonary Blood Flow

The lung may show signs of diminished blood flow with small central and peripheral vessels in the frontal chest radiograph, indicating a decrease in the blood supply to the lung. Possible causes include hemodynamically significant pulmonary stenosis, congenital heart defects with a primary right-to-left shunt (e.g., Fallot group), Ebstein anomaly, rare primary tricuspid insufficiency, hemodynamically significant pleural effusion, and relative tricuspid insufficiency resulting from global heart failure (**Table 1.6**).

Pulmonary Hyperemia

A general increase in pulmonary blood flow (active pulmonary hyperemia, not to be confused with pulmonary congestion) due to intracardiac or extracardiac shunting of blood leads to volume overload, causing dilatation of all the pulmonary arteries and veins. Over time, this increased pulmonary blood flow induces endothelial hyperplasia at the arteriolar level with intimal fibrosis in the small vessels. The subsequent rise in vascular resistance eventually leads to pulmonary arterial hypertension, with large central pulmonary arteries, narrow peripheral arteries, and a reversal of the cardiac shunt (**Table 1.7**).

Pulmonary Arterial Hypertension (Cor Pulmonale)[70,71]

The cardiac causes of pulmonary arterial hypertension are to be distinguished from pulmonary hypertension resulting from a primary lung disease (**Table 1.8**; see Other Forms of Pulmonary Arterial Hypertension, Chapter 12, p. 256). The signs of pulmonary arterial hypertension in these cases (large central pulmonary arteries with peripheral pruning of vessels) are accompanied by signs of the underlying disease. The central pulmonary arteries are considered to be enlarged if the width of the right descending pulmonary artery is greater than 16 mm.

In a chronic obstructive syndrome with emphysema, the lung shows a generalized increase in radiolucency (**Table 1.9**). This state is characterized by a destruction of interalveolar septa and loss of the capillary bed, leading to precapillary pulmonary arterial hypertension. The pulmonary hypertension that develops in interstitial lung disease (e.g., sarcoidosis, pneumoconiosis) or panarteritis nodosa of the lung is based on a decrease in pulmonary vasculature. The peripheral arterial branches appear narrowed, and the veins are also reduced in caliber as a result of diminished venous return. The pulmonary hypertension imposes an increased pressure load on the right ventricle, leading by definition to a state of cor pulmonale.

Table 1.6 Principal causes of decreased pulmonary blood flow

- Heart defects with a right-to-left shunt (Fallot symptom complex)
- Hemodynamically significant pulmonary stenosis
- Ebstein anomaly
- Organic tricuspid insufficiency
- Relative tricuspid insufficiency developing as a result of global heart failure
- Hemodynamically significant pericardial effusion

Table 1.7 Principal causes of pulmonary hyperemia

Intracardiac	• Ventricular septal defect (including septal rupture after myocardial infarction)
	• Atrial septal defect
	• Anomalous pulmonary venous return
Extracardiac	• Patent ductus arteriosus
	• Aortopulmonary window
	• Coronary fistula to pulmonary circulation
	• Large peripheral AV shunts (including large hemodialysis fistulas)

Table 1.8 2004 Venice Classification of Pulmonary Arterial Hypertension

Pulmonary arterial hypertension (PAH)	• Sporadic, familial
	• Associated with collagen diseases, toxins, HIV, or PHT
	• Significant venous or capillary involvement
PAH associated with diseases of the left heart	• LV dysfunction, mitral or aortic valve disease
PAH associated with hypoxia and/or respiratory diseases	• COPD, interstitial lung disease, SAS, alveolar hypoventilation, alveolocapillary dysplasia, congenital heart disease
PAH associated with chronic thromboembolism or emboli	• Proximal and distal thromboembolic or embolic obstruction of PAH
Miscellaneous	• Sarcoidosis, histiocytosis X, lymphangiomatosis, extrinsic compression

Table 1.9 Causes of cor pulmonale

Pulmonary vascular diseases	Large or multiple emboli	Decrease in cardiac output due to acute obstruction
	Small emboli, vasculitis, extensive lung destruction (ARDS)	Pulmonary hypertension due to extensive hypoxia and microvascular obstruction
	Moderately large or recurrent emboli, primary pulmonary hypertension, dietary or drug-induced vasculopathy	Pulmonary hypertension due to vascular obstruction, with low or normal cardiac output
Respiratory diseases	Obstructive: • Chronic bronchitis and emphysema • Chronic bronchial asthma	Pulmonary hypertension due to hypoxia, straightening and loss of vessels, external impairment of cardiac filling after pulmonary hyperinflation, with normal or increased cardiac output
	Restrictive: • Intrinsic interstitial fibrosis, lung resection • Extrinsic: obesity, myoedema, muscle weakness, kyphoscoliosis, lower airway obstruction, decreased respiratory drive at high altitudes	• Hypertension due to hypoxia, torsion, and loss of vessels; normal or diminished cardiac output • Hypertension due to alveolar hypoxia, normal or increased cardiac output

The radiographic hallmarks of pulmonary arterial hypertension are as follows:

- Dilatation of the main pulmonary artery trunk (prominent pulmonary segment)
- Enlargement of the central pulmonary arteries. This sign is particularly important in follow-up examinations which show a increasing diameter of the right descending pulmonary artery not previously present.
- Pruning of vessels, i.e., rapid tapering of vascular calibers from the enlarged lobar arteries (second-order vessels) to the narrowed segmental arteries (third-order vessels).
- Narrowing of the peripheral arteries and veins. The frontal chest film shows almost no vascularity in the peripheral subcostal lung, which appears abnormally lucent. This decrease in peripheral vascularity is among the most common signs of pulmonary artery hypertension.

Lymphatic System

Interstitial lung edema is associated with an increased removal of excess tissue fluid via lymphatic channels. As a result, these lymphatics are distended and become radiographically visible owing to the summation effect of overlapping projections. There are several disorders in which lymphatic structures may become visible in the P-A chest radiograph:

- Pulmonary venous hypertension relating to mitral valve disease, chronic or acute left heart failure, or pulmonary edema
- Primary lymphatic diseases
- Neoplasias (e.g., carcinomatous lymphangiitis)

Kerley A and B lines in the chest radiograph (**Fig. 1.15**) represent the summation images of many thickened lymphatic channels and septa. Kerley A lines are linear opacities ~1 mm thick and several centimeters long which radiate from the hila into the central portion of the lung. Kerley B lines are located in the periphery of the lung. They appear as thin, horizontal lines ~1 cm long and are commonly found near the costophrenic angle. They represent thickened interlobar septa and distended lymphatics. Confluent Kerley B lines (severe forms of pulmonary venous hypertension in mitral stenosis) lead to a reticular pattern of interstitial lung markings.[27,72]

In cases of severe chronic pulmonary venous congestion (especially with severe mitral stenosis), pigment deposition may occur in basal portions of the pulmonary interstitium (hemosiderin due to erythrocyte migration), giving rise to ossified foci of hemosiderin fibrosis. These basal foci are differentiated from calcified tuberculous lesions in that the latter are located primarily in apical lung zones.

Pleural Effusion

Pleural effusion may develop as a result of pulmonary edema or stasis-related intra-abdominal fluid collections (ascites), due partly to a rise in pulmonary venous pressure and partly to ve-

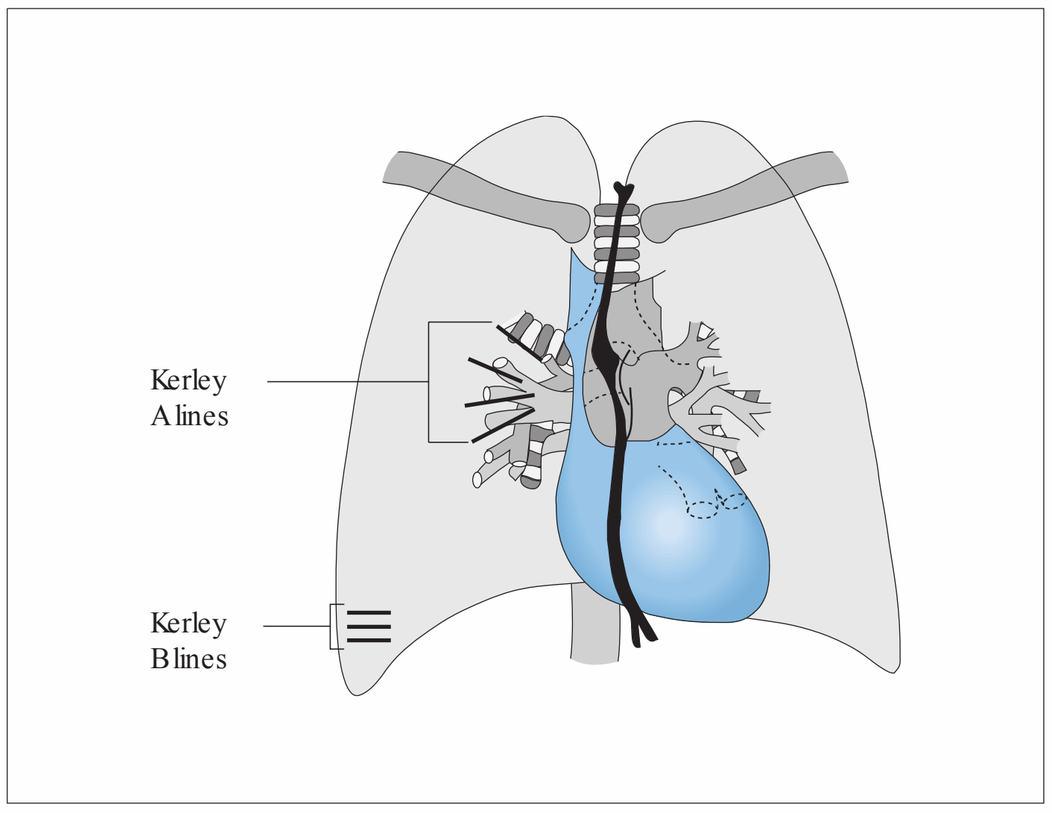

Fig. 1.15 Diagrammatic representation of Kerley lines associated with fluid accumulation in the pulmonary interstitium.

nous hypoxia, leading to increased capillary permeability. The earliest radiographic sign of pleural effusion is a thickening of the pleura between the pulmonary lobes (pleural edema). Increasing fluid transudation subsequently leads to pleural effusion of varying extent. The location of the effusion is position dependent: it may overlie the diaphragm or may appear as a crescent-shaped accumulation along the lateral chest wall in the upright patient. Pleural effusions may also be subpulmonary without separation of the lateral pleural layers. This type of effusion, especially when small, is not detectable in the P-A chest radiograph. A subpulmonary effusion is best documented by positioning the patient on the affected side. Pleural effusions are more common on the right than the left side, as a larger pleural surface area is available for fluid transudation on the right side. Moreover, intra-abdominal fluid (ascites in right-sided heart failure) can drain directly into the right pleura from the abdominal cavity via lymphatic connections.

Cardiac Malposition

The most common type of cardiac malposition is dextrocardia, in which the major portion of the heart is located to the right of the vertebral column. Three forms are distinguished:

- Inversion (mirror-image dextrocardia)
- Dextroversion
- Dextroposition

Inversion Mirror-image dextrocardia occurs relatively often as an isolated anomaly in the absence of associated heart defects. A mirror image of normal cardiac anatomy, it is usually accompanied by inversion of the abdominal organs so that the stomach bubble is visualized below the right hemidiaphragm (complete transposition of the viscera).

Dextroversion Dextroversion is usually accompanied by congenital heart disease and is characterized by rotation of the heart toward the right side. The right ventricle is shifted upward and to the right, while the left ventricle is shifted downward and forward, creating a prominent bulge in the upper right portion of the cardiac silhouette. A cardiac apex cannot be identified in the P-A radiograph. The aortic arch occupies a typical location on the left side. This finding differentiates dextroversion from inversion, in which the aortic arch is on the right side.

Dextroposition In dextroposition, the heart is displaced or deviated to the right owing to an extracardiac abnormality, such as a left diaphragmatic hernia or right-sided pleural thickening.

Heart Failure

Acute Heart Failure[73–75]

In heart failure of acute onset, clinical manifestations are characterized by an abrupt decline in cardiac output. The dominant features include acute pulmonary congestion or edema and arterial hypotension.

Acute heart failure, which presents in severe cases as cardiogenic shock and pulmonary edema, most commonly results from a significant loss of contractile tissue following an acute myocardial infarction or, less commonly, diffuse myocarditis. Another cause is an acute stress on the unconditioned heart, as, for example, a critical rise in arterial pressure; the sudden rupture of cardiac valves, papillary muscle or chordae tendineae; an acute septal perforation; severe acute arrhythmias; or a sudden pressure rise in the pulmonary circuit due to pulmonary embolism (**Table 1.5**).

The acuteness of these events allows no time for morphological adaptation of the heart, and chest radiographs show a marked discrepancy between massive pulmonary edema and a normal-sized heart.

Chronic Heart Failure[76–82]

In chronic heart failure several compensatory mechanisms are often able to maintain the arterial pressure at an adequate level for a period of years.

The most frequent causes of chronic heart failure are:

- Coronary heart disease
- Hypertension
- Cardiomyopathies

Less frequent causes are valvular heart disease and inflammatory or toxic cardiac injury, which may damage the myocardium so severely that its contractile function is permanently impaired. Chronic heart failure may also result from a decrease in cardiac filling or stroke volume due to a cause other than primary muscular disease (e.g., constrictive pericarditis or impaired filling as a result of massive endocardial thickening). The resulting chronic pressure and volume overload initially recruit cardiac and peripheral compensatory mechanisms which sustain an adequate cardiac output. Accordingly, the initial adaptive mechanisms to pressure and volume overload do not produce radiographically visible changes, and chest films show no abnormalities in the early stages of chronic heart failure. It is not until later stages, when the adaptive mechanisms are accompanied by dilatation, that radiographs show pathognomonic structural alterations which initially involve the left heart, next the pulmonary circulation, and finally the right heart. As the adaptive mechanisms begin to fail, contractile dysfunction develops, leading to myogenic dilatation. This dilatation is identical to ventricular contractile dysfunction and myocardial insufficiency.

Essential Point

Adaptations to pressure and volume overload generally cause no chest film abnormalities in the early stage. Typical radiographic changes do not appear until adaptive mechanisms are accompanied by dilatation of the cardiac chambers. Particular attention should be given to adaptive cardiac dilatation to accommodate greater volumes.

Radiographic Features

It is generally agreed that there is no strong correlation between the degree of radiographically detectable cardiac enlargement and the functional performance of the ventricle or ventricles.[83,84] This problem is particularly apparent after a

recent myocardial infarction. Nevertheless, a radiographically normal-sized heart may be associated with contractile dysfunction of the left ventricle, which may lead to marked pulmonary congestion and even interstitial or alveolar pulmonary edema on the chest radiograph.[85,86]

Essential Point
Even in massive acute heart failure, the heart may initially maintain a normal size.

It is important clinically to note that interstitial edema, unlike alveolar edema, does not produce audible abnormalities on chest auscultation, at least in the early stages. Its radiographic detection is important, however, because interstitial edema is an early sign of cardiac decompensation (**Figs. 1.16, 1.17**). Alveolar pulmonary edema is characterized by the presence of focal, rounded acinar shadows 3–7 mm in diameter located predominantly in the basal lung zones. In more advanced forms the shadows may coalesce to form larger opacities, occasionally with a positive air bronchogram. This may progress to almost complete opacification of the lung, requiring differentiation from secondary obstructive pneumonia or pneumonia in the strict sense. It should be emphasized that pulmonary opacities in patients with heart failure are too often interpreted as inflammatory pneumonia and that pulmonary congestion would be sufficient to account for the lung findings. These cases represent a source of considerable diagnostic uncertainty.

At the same time, pronounced left ventricular enlargement in the chest radiograph resulting from cardiomyopathy or aortic valve disease is not always an expression of myocardial contractile dysfunction (**Fig. 1.18**).

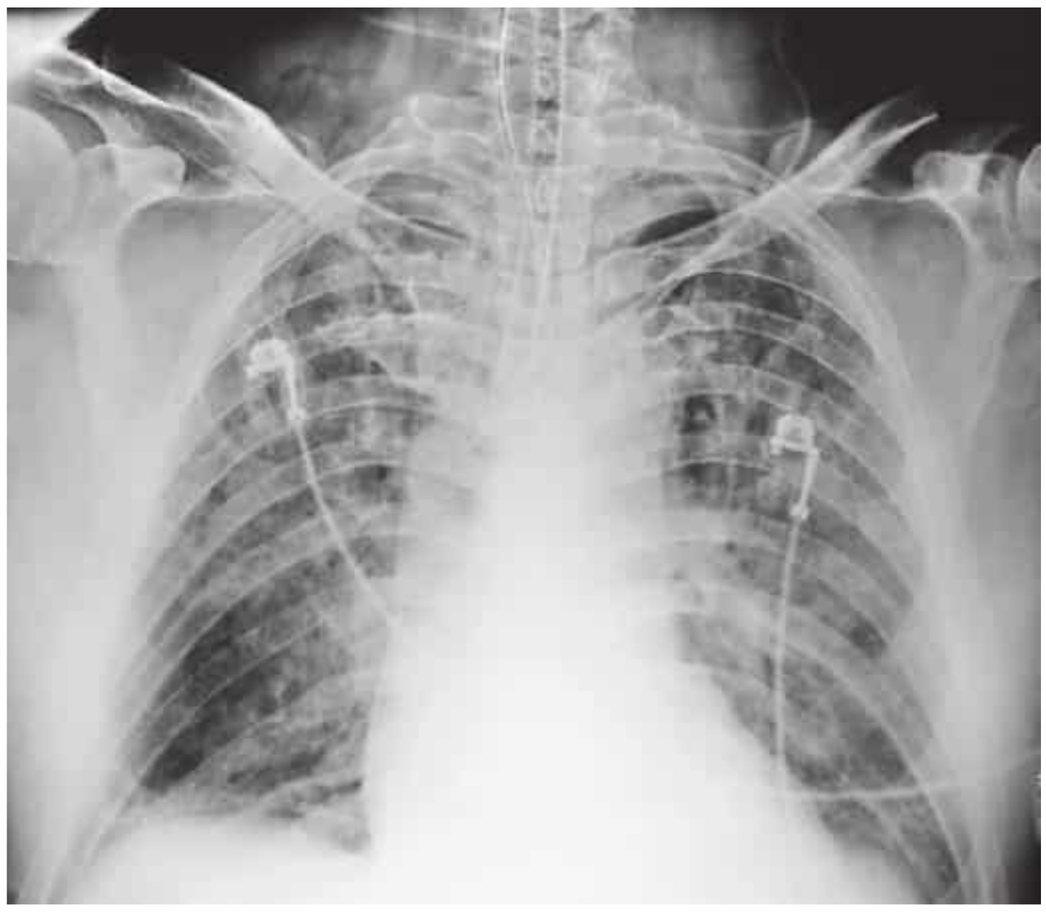

Fig. 1.16 Supine chest radiograph. Recent anterior wall infarction following coronary artery bypass graft. Acute left-sided heart failure. Although cardiac size is normal for a supine radiograph, interstitial lung edema is nevertheless present. Apart from some fine, moist rales, no abnormal finding on auscultation.

Except in cases with very pronounced cardiac enlargement, the radiographic evaluation of functional performance is based largely on the presence of congestive signs (**Fig. 1.19**). These signs include mild to moderate enlargement of the left atrium and the detection of various grades of pulmonary congestion and edema. The redistribution of blood flow is evidenced by dilatation of the upper lobe vein. Normally this dilatation is not present and is detectable earlier and more reliably in the right upper lobe than in the left upper lobe. Interstitial fluid transu-

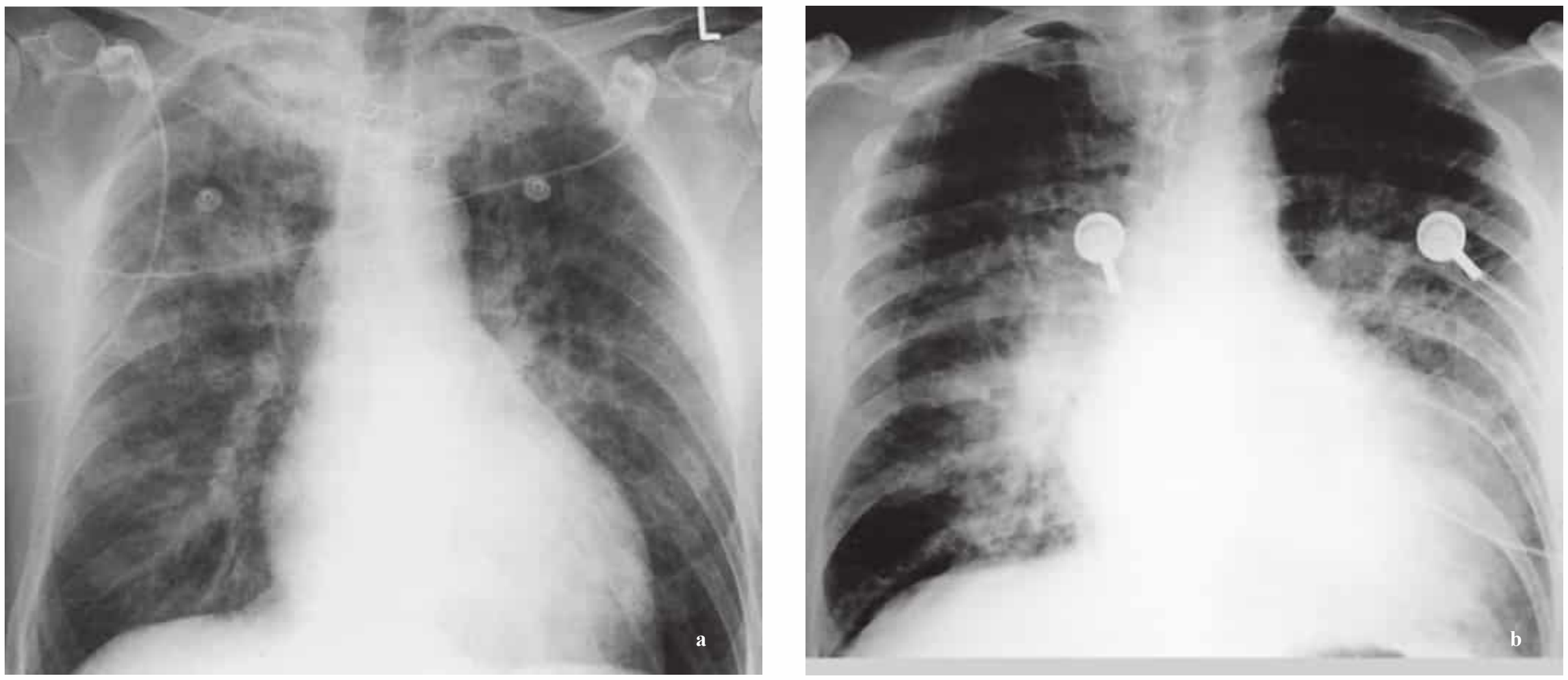

Fig. 1.17 a, b Supine chest radiographs.
a Status following ACVB. Recent myocardial infarction. Acute left-sided heart failure. Cardiac dilatation, interstitial lung edema (unremarkable auscultation findings).
b Radiograph after a recent posterior wall infarction shows cardiomegaly with progression from interstitial to alveolar pulmonary edema (very marked auscultation findings).

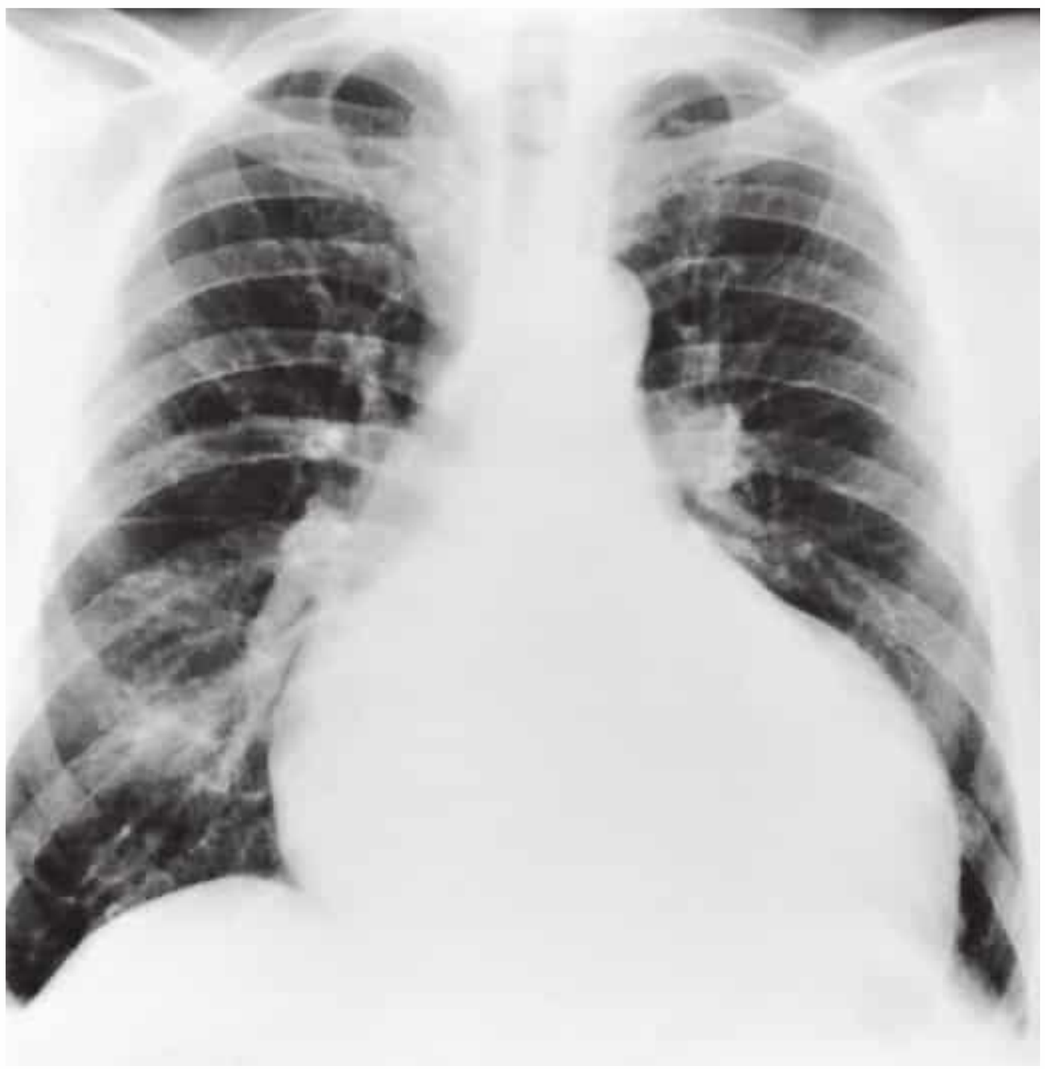

Fig. 1.18 P-A chest radiograph. Dilated cardiomyopathy in a patient with alcoholic cirrhosis of the liver. Myogenic dilatation predominantly affects the left heart. There are no signs of pulmonary congestion.

dation is manifested by haziness in the basal and peripheral lung zones, with indistinct vascular structures. Additional signs are costodiaphragmatic septal lines, known as Kerley B lines, and perihilar Kerley A lines, which are the radiographic correlate of distended lymphatics (**Fig. 1.13**). Another reliable sign of interstitial fluid accumulation is thickening and indistinctness of the bronchial wall in end-on views of the anterior upper lobar segmental bronchi.[87]

Left Heart Failure

Chronic left heart failure is generally characterized by forward and backward failure. The following stages of backward failure, which result from the impaired pumping function of the heart, can be recognized in conventional radiographs:

- Highly variable degree of left ventricular enlargement (mild to severe)
- Mild to moderate enlargement of the left atrium
- Enlargement of the upper lobe veins (more pronounced on the right side than on the left)
- Haziness of the basal and peripheral lung zones with indistinct vascular outlines (incipient fluid transudation)
- Kerley A and B lines (summation effect from distended lymphatics)
- Thickened and indistinct bronchial wall in end-on views of anterior upper lobe segmental bronchi (bronchial wall edema)
- Sharply delineated pleural lines (pleural edema)
- Restriction of arterial blood flow in the lower zones (active vasoconstriction and interstitial tissue proliferation)
- Pulmonary arterial hypertension with narrow peripheral pulmonary vessels and large central vessels (rare late stage)

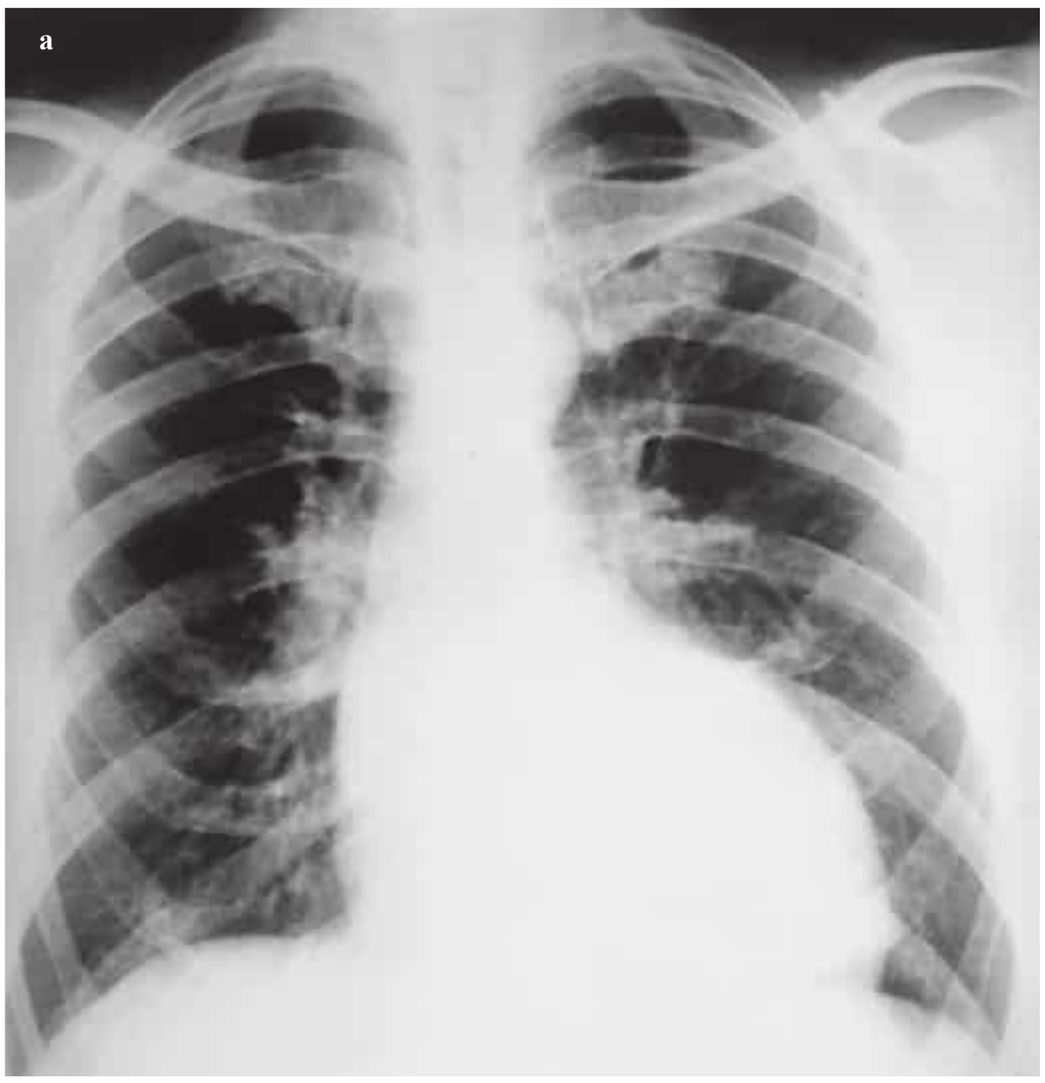

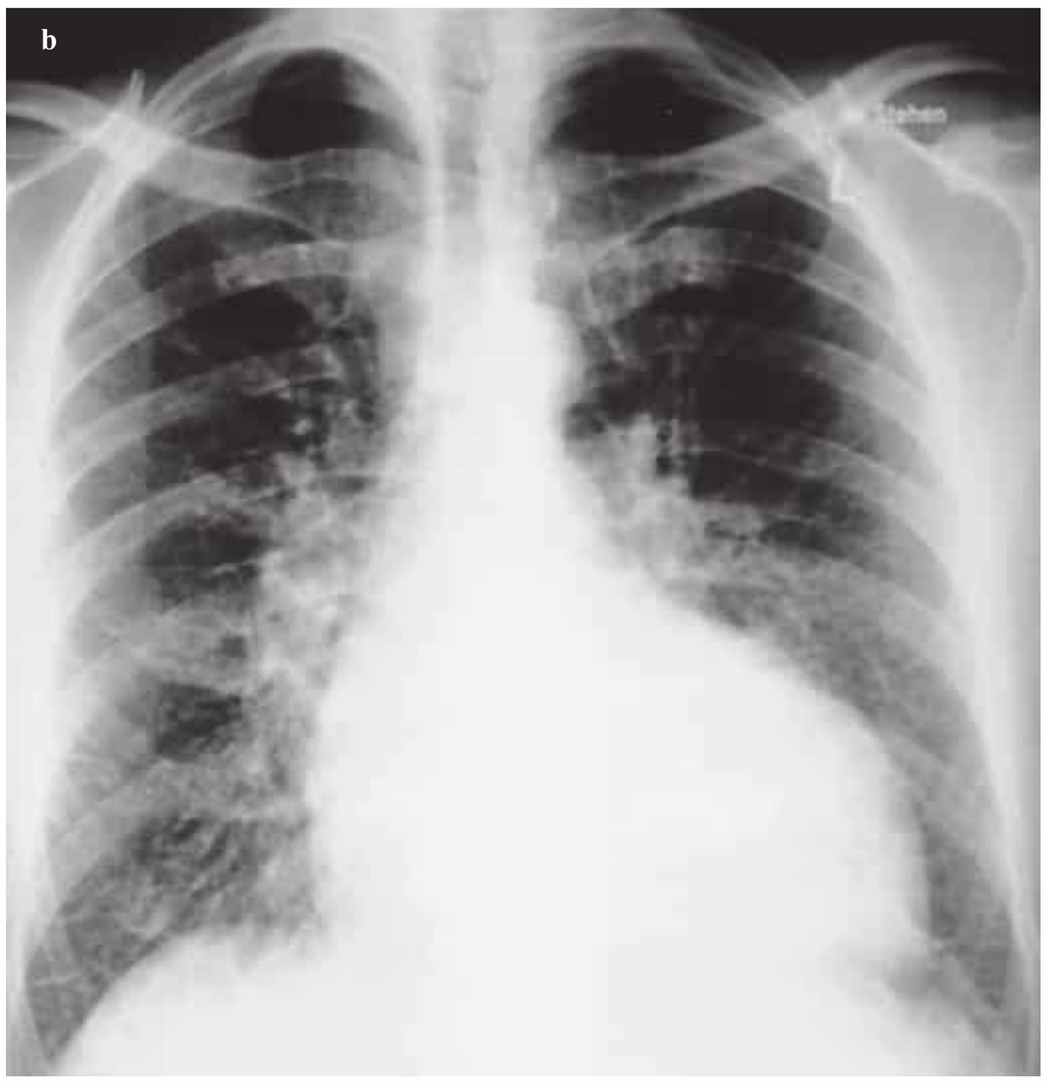

Fig. 1.19 a, b Follow-up examination. **a** Cardiomyopathy with dilatation of the left ventricle. **b** Radiograph at 2 years shows progressive myogenic dilatation of the heart with definite signs of pulmonary congestion and interstitial edema (Kerley lines) consistent with chronic left heart failure.

Right Heart Failure[88–90]

Acute right heart failure may be the immediate cause of death from pulmonary embolism. As the vascular resistance in the lung increases, there is a proportionate increase in right ventricular wall tension. Depending on the degree of the acute pressure rise, this increased wall tension may suddenly progress to right ventricular dilatation and dysfunction. The elevated right ventricular pressure causes the interventricular septum to protrude into the initially normal left ventricle, compressing it. As left ventricular filling declines, it causes a fall in the left ventricular output and systemic arterial pressure, leading to decreased perfusion of the coronary vessels and myocardial ischemia. In the worst case, this may result in circulatory collapse and death.

Chronic right heart failure is the end point of a chronic volume overload with primary dilatation of the right ventricle, secondary dilatation in response to a primary pressure overload, or direct myocardial injury.

Radiographic Features

Pressure overload and volume overload can both lead to right-sided heart failure. The radiographic signs of right ventricular failure appear much later in a pressure-loaded than in a volume-loaded heart. An initially healthy myocardium can compensate for high pressures up to 80 mmHg or more without enlarging or altering the shape of the heart. Changes in the pulmonary vasculature are the only detectable abnormalities. But as the pressure load continues over time, the heart undergoes structural alterations manifested by elongation of the right outflow tract in the lateral radiograph (narrowing of the retrosternal space). The increasing enlargement of the right ventricle causes the cardiac silhouette to broaden toward the left side as the heart rotates in a clockwise direction, causing the right ventricle to occupy a left anterior position and moving the left ventricle posteriorly. This enlargement of the right ventricle then becomes an expression of impaired myocardial function.

Essential Point
An initially healthy myocardium can compensate for elevated right ventricular pressures (up to 80 mmHg or more) without altering the shape of the heart.

Right ventricular enlargement in response to a volume overload is to be interpreted differently. Enlargement of the right ventricle by expansion of its cavity represents an adaptation to the altered hemodynamics associated with the volume overload and is not yet an expression of myocardial dysfunction.

In the presence of a significant, sustained volume overload, however, myocardial function does become impaired. Cardiac size is borderline or enlarged. With elongation of the outflow tract, the conus arteriosus and pulmonary trunk are displaced upward, and the cardiac waist is effaced. Enlargement and elongation of the inflow tract cause the heart to expand toward the left side, the rotation effect again causing the right ventricle to move forward as the left ventricle moves posteriorly. The anteroposterior cardiac diameter is often so enlarged that the subdiaphragmatic triangle (vena cava triangle) is narrowed, as it is with an enlarged left ventricle (**Table 1.2, Fig. 1.20**).[91,92]

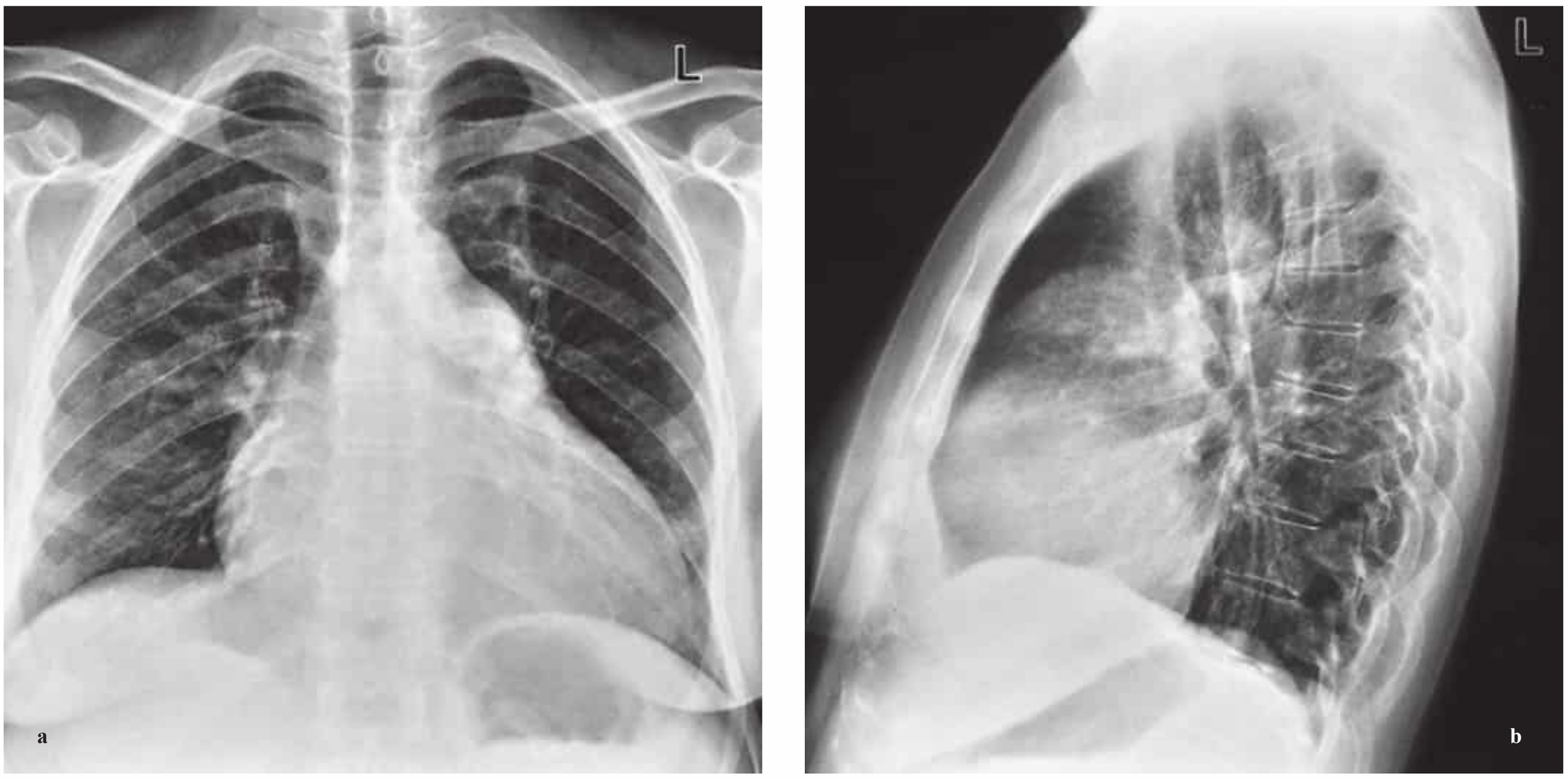

Fig. 1.20 a, b Recurrent pulmonary emboli with a pronounced pressure overload of the right ventricle.

a Prominent left cardiac border caused by the large, anteriorly situated right ventricle (heart is rotated to the left). Convex cardiac waist (enlargement of the main pulmonary artery trunk).

b Lateral radiograph shows narrowing of the retrosternal space (upward displacement of the right ventricular outflow tract). The vena cava triangle is occupied by the left ventricle, which is displaced posteriorly but is not dilated.

Essential Point
Enlargement of the volume-loaded heart is to be interpreted differently from that in a pressure-loaded heart. Enlargement of the cardiac chambers in response to volume overload is a reflection of adaptive dilatation, i.e., the cardiac enlargement can still be fully compensated. The most striking example is the "athlete's heart."

The chest radiograph merits particular attention in pulmonary embolism. A normal or almost normal radiograph in a patient with respiratory distress does not exclude pulmonary embolism. The diagnosis of these cases is aided by noting radiographic abnormalities in the pulmonary vascular tree (**Fig. 1.21**).

Global Heart Failure[93–98]

If the functional capacity of the left ventricle is so severely impaired that it allows blood to reflux into the left atrium and pulmonary vasculature, i.e., if the left ventricle can no longer deliver the necessary volume and pressure output leading to marked signs of pulmonary congestion, the right ventricle will naturally be affected. The difficulties of evaluating right ventricular performance have been mentioned above. Progressive enlargement of the right atrium due to relative tricuspid insufficiency, widening of the superior vena cava and azygos vein, a right-sided or bilateral pleural effusion, or elevation of the right hemidiaphragm due to hepatomegaly may be the only signs that the myocardial contractility of the right ventricle has also become impaired. Thus, concomitant myogenic dilatation of the left and right ventricles, or global heart failure, can be diagnosed from radiographic findings if a right-sided pleural effusion is present in addition to mild or moderate pulmonary congestion. Right ventricular enlargement is confirmed, and the confidence of this diagnosis increased in the presence of obliteration of the cardiac waist in the P-A view and narrowing of the retrosternal space in the lateral view. Because of the right-sided failure, pulmonary congestion is usually less pronounced than in patients with isolated left heart failure. A regression of pleural effusion, pulmonary congestion, and cardiac enlargement indicates improvement in the performance of both ventricles.

On initial examination, a heart in global failure cannot always be distinguished radiographically from one with organic mitral valve disease, especially if the left atrium is enlarged. The regression of congestive symptoms and cardiac enlargement (including left atrial dilatation) in response to cardiac therapy is suggestive of primary myogenic dilatation and does not support a diagnosis of primary valvular disease.

Pulmonary congestion due to contractile dysfunction of the left ventricle will eventually lead to a secondary pressure overload on the right ventricle. Whether secondary right heart failure will supervene on primary left-sided failure depends both on the functional capacity of the right ventricle and on the timing of possible improvement in left ventricular performance. In patients with chronic pulmonary congestion, which ultimately leads to pulmonary fibrosis and induration, the pressure load on the right ventricle is evidenced by the pulmonary vascular changes described above.

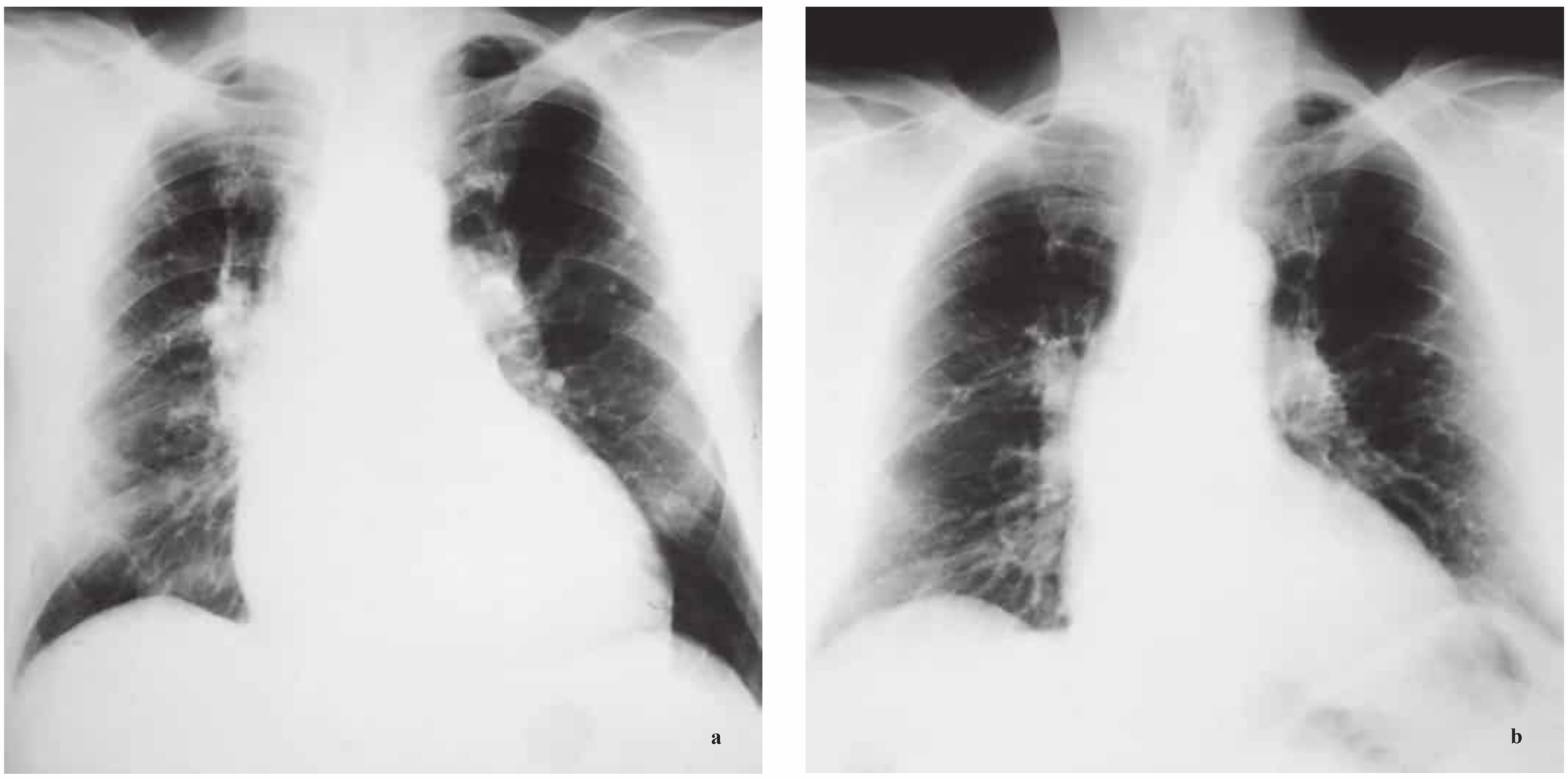

Fig. 1.21 a, b Chronic recurrent pulmonary embolism. Status at 2-year follow-up after pulmonary thromboendarterectomy.
a Preoperative chest radiograph shows dilatation of the main pulmonary artery trunk (convex cardiac waist) with enlargement of the central pulmonary arteries, pruning of arteries in the left upper and lower lung zones, and narrow peripheral pulmonary arteries in the left lung.
b Partial regression of signs 2 years after PTE.

Coronary Heart Disease

Acute Myocardial Infarction[51,61,99–107]

The accurate determination of cardiac size can be difficult in the acute stage of myocardial infarction because the quality of bedside supine radiographs is limited and a film–focus distance of 1 m will in itself cause the heart to appear enlarged. The hemodynamic changes associated with left-sided heart failure can still be clearly appreciated in the lung fields, however.

The change in cardiac size and shape caused by an acute myocardial infarction depends on the size and location of the infarction and the severity of any previous myocardial damage. A heart that was not enlarged before the infarction may still be completely normal in size following the infarction. A relative large infarction, however, will usually cause prominence of the left cardiac border that requires differentiation from pericardial effusion.

The severity of left ventricular dysfunction is manifested on radiographs by abnormal pulmonary vascular markings and in some cases by pleural effusion. More than half of patients with acute myocardial infarction show a variable degree of pulmonary congestion (mild to severe). A relationship also exists between radiographic changes and quantitative parameters that can be measured with a flow-directed catheter. An elevated diastolic pulmonary arterial pressure (>18 mmHg) can be inferred from radiographic signs of increased pulmonary pressure. If signs of pulmonary congestion are noted, the pressure is higher than 20 mmHg; if alveolar pulmonary edema is present, the pressure exceeds 30 mmHg. When cardiac enlargement is accompanied by a pleural effusion, this is also a reliable indicator of increased left ventricular filling pressure. With few exceptions, a normal radiographic appearance of the lungs makes it unlikely that there is significant left ventricular dysfunction with a rise in pulmonary capillary pressure to more than 20 mmHg.

The radiographic indicators of left heart failure and cardiac size can also supply important prognostic information. Thus, the development of diffuse alveolar pulmonary edema after myocardial infarction indicates a very poor prognosis, whereas a normal heart/lung ratio with no signs of pulmonary congestion in the postinfarction period is associated with very low mortality.

Essential Point
The development of pulmonary edema shortly after myocardial infarction is a poor prognostic sign. Pulmonary congestion or edema in this situation should always be differentiated from overhydration due to intravenous infusion or renal disease.

Chronic Myocardial Infarction

The size of the heart in the chronic phase after myocardial infarction depends on the location and size of the infarction, the status of the residual myocardium, possible associated ischemia at the periphery of the infarction, or the presence of multivessel disease. The same applies to changes in the lung, and especially the pulmonary vascular markings. A normal cardiac size does not exclude incipient enlargement of the left ventricle. Not infrequently, however, incipient left ventricular enlargement is marked by an asymmetric cardiac silhouette with a prominent left cardiac border. Marked broadening of the heart toward the left side indicates that the left ventricle has sustained significant damage. The left atrium may also be enlarged owing to increased end-diastolic pressure associated with the left ventricular dysfunction. The pulmonary pressure may also be elevated, placing an increased load on the right ventricle and causing enlargement of that chamber. Right ventricular enlargement may, however, also be due to a right ventricular infarction.

A cardiac aneurysm visible in plain chest films (**Fig. 1.22**) indicates severe, extensive damage to the left heart. An aneurysm may develop within a few weeks after myocardial infarction. Radiographs are important in the detection of relatively large aneurysms, although plain films are not useful in the diagnosis of dyskinesia and akinesia. The same is true of small- and medium-sized myocardial aneurysms, which are difficult or impossible to detect on X-ray films. This is due partly to the difficulty of identifying aneurysms located on the posterior wall or septum. Another problem is that aneurysms in the apical heart region are often projected into the abdominal shadow and are difficult to recognize as aneurysms. Anterior aneurysms located in the territory of the left anterior descending coronary artery (LAD) are the easiest to diagnose on radiographs. An aneurysm produces a focal bulge on the left cardiac border, thus deforming the left ventricle, which is expanded to the left. In rare cases radiographs may show calcification in the aneurysm wall.

Cardiomyopathies[107–112]

The revised WHO classification of cardiomyopathies published in 1996 defines cardiomyopathy as a collective term for diseases of the myocardium associated with cardiac dysfunction. The classification of cardiomyopathies into dilated, hypertro-

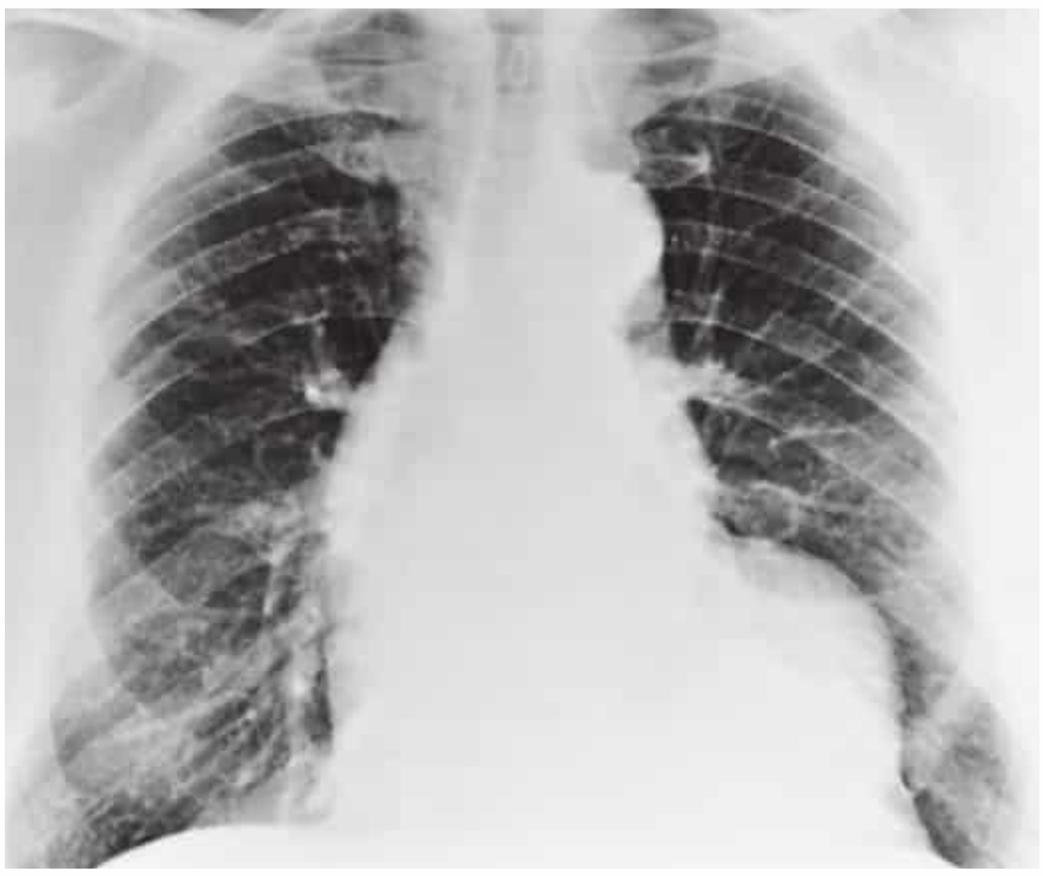

Fig. 1.22 Aneurysm on the left cardiac border following myocardial infarction.

phic, restrictive, and unclassified forms is retained in the revised classification, and arrhythmogenic right ventricular cardiomyopathy has been added as a new separate entity. The group of specific cardiomyopathies has been restructured. While the diseases are classified mainly according to pathophysiological criteria, the classification also takes into account etiological and pathogenetic aspects whenever possible (**Table 1.10**).

Table 1.10 Revised WHO classification of cardiomyopathies[a]

Dilated cardiomyopathy (DCM)	• Idiopathic cardiomyopathy • Familial/genetic cardiomyopathy, inflammatory cardiomyopathy • Special forms of specific cardiomyopathies
Hypertrophic cardiomyopathy (HCM)	• Hypertrophic obstructive cardiomyopathy • Secondary restrictive cardiomyopathy
Restrictive cardiomyopathy	• Primary restrictive cardiomyopathy • Secondary restrictive cardiomyopathy
Arrhythmogenic right ventricular dysplasia (ARVD)	–
Unclassified cardiomyopathy	• Fibroelastosis • Systolic contractile dysfunction without vascular dilatation • Mitochondrial cardiomyopathies
Specific cardiomyopathies	• Ischemic cardiomyopathy • Valvular cardiomyopathy • Hypertensive superior mesenteric plexus • Inflammatory cardiomyopathy – Collagen diseases – Rheumatic carditis – Disseminated lupus erythematosus – Dermatomyositis – Scleroderma – Rheumatoid heart disease • Toxic cardiomyopathies – Alcohol – Medications – Uremia • Metabolic and endocrine diseases – Hyper- or hypothyroidism – Pheochromocytoma – Amyloidosis (primary or secondary) – Diabetes mellitus – Infiltrative diseases: – Fabry disease, mucopolysaccharidosis, neoplasms, hemochromatosis, glycogen storage diseases • Immunological cardiomyopathies – Medications – Serum sickness – Postcardiotomy syndrome • Neuromuscular diseases – Friedrich ataxia – Myotonic muscular dystrophy – Progressive muscular dystrophy – Myasthenia gravis • Peripartum cardiomyopathy • Tachycardia-induced cardiomyopathies • Physical myocardial injury – Radiation, trauma, electric shock, heat stroke

[a] Richardson P. et al. Circulation 1996;93:841–842.

Conventional Radiography

Different forms of cardiomyopathy cannot be differentiated on conventional chest radiographs. In the initial stage of the disease, radiographs may still show a normal-sized heart even if other imaging modalities already show definite abnormalities. As a rule, patients with dilated cardiomyopathy are characterized by predominantly left-sided or generalized cardiac enlargement, which is initially not accompanied by pulmonary congestion. When the cardiomyopathy progresses to the decompensation stage, detectable cardiac dilatation is accompanied by typical signs of lung congestion. Stages are found ranging from interstitial to alveolar edema, and effusions are detected in the lymph spaces, interlobar spaces, and pleural cavities (**Fig. 1.23**).

Pulmonary vascular markings are of some diagnostic importance. While normal vascular markings do not exclude an increased diastolic filling pressure at rest or during exercise, it is very likely that left ventricular contractile dysfunction has not yet developed when normal pulmonary vascular markings are seen. Enlarged perihilar arterial vessels in both lungs and accentuated arterial markings in the upper and midlung zones may result exclusively from a decrease in left ventricular compliance. Associated contractile dysfunction should be excluded.

■ Systemic Hypertension

Hypertension is the principal risk factor for stroke and is among the major risk factors for coronary heart disease, chronic heart failure, peripheral occlusive disease, and chronic renal failure (**Table 1.11**).

Chronic hypertension is characterized by a rise in peripheral resistance leading to hypertensive end-organ damage in the heart such as:

- Angina pectoris or myocardial infarction
- Heart failure
- Left ventricular hypertrophy

Typical hypertension-induced cardiac lesions are coronary microangiopathy in intramural arteries and structural changes in the myocardium with left ventricular hypertrophy and eventual myocardial fibrosis. The clinical picture is often determined by additional atherosclerotic macroangiopathy involving the epicardial coronary arteries. This acceleration of atherosclerosis occurs not only in the coronary system but throughout the circulatory system including the aorta, carotid arteries, and peripheral vasculature. Renal changes consist of nephrosclerosis, and involvement of the interlobar arteries and arteri-

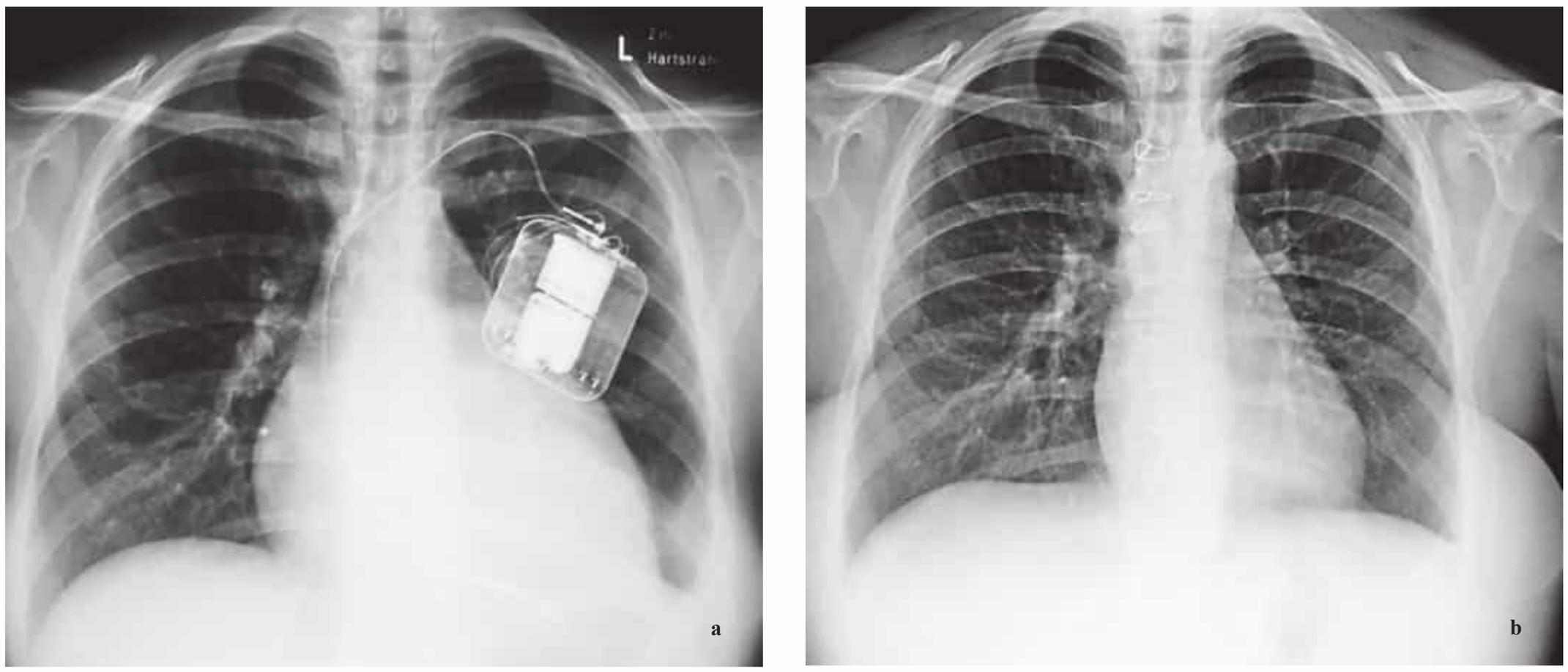

Fig. 1.23 a, b Dilated cardiomyopathy with signs of global decompensation before (**a**) and after (**b**) heart transplantation.

oles eventually leads to focal necrosis of those vessels. Hypertension is perpetuated by atherosclerotic renal atrophy.

The sustained pressure load on the left ventricle from the increased peripheral resistance initially leads to concentric left ventricular hypertrophy, which is characterized by thickened ventricular walls with a normal or small cardiac chamber and an increased cardiac mass. Ventricular function is still normal at this stage.

Over time, the left ventricle undergoes further dilatation with a gradual increase in end-diastolic volume. If the ejection fraction declines, this signifies a decrease in left ventricular contractility and pump function and heralds progression to myogenic contractile dysfunction, with all its attendant sequelae.

Radiographic Features

In the presence of concentric left ventricular hypertrophy alone, the chest radiograph almost never shows enlargement of the cardiac borders. Radiographic changes are first seen when dilatation supervenes in the absence of myogenic dysfunction. Ventricular dilatation in the P-A radiograph leads to prominence of the left cardiac border with preservation of the cardiac waist, the "aortic configuration" (**Fig. 1.24**). Posterior expansion of the left ventricle is best appreciated in the lateral view. The increased pressure load is manifested by aortic elongation or aortic sclerosis.

With the progression of left ventricular failure, the raised end-diastolic pressure leads to pulmonary congestion accompanied by mild enlargement of the left atrium (relative mitral insufficiency). The earliest sign in the lung of left ventricular failure is enlargement of the right upper lobe veins. Increasing retrograde blood flow into the pulmonary venous system leads to interstitial edema (Kerley B lines, pleural edema) and later to intra-alveolar edema with effusion formation in the pleural space and interlobar fissure, and an eventual rise in peripheral resistance due to vascular fibrosis in the interstitium. With

Table 1.11 Classification of arterial hypertension

Forms of hypertension	Relative frequency
Primary (essential) forms of hypertension	Approximately 95 %
Secondary hypertension	Approximately 5 %
Renal causes • Renal parenchymal disease – Chronic glomerulonephritis – Diabetic nephropathy – Chronic interstitial nephritis • Renovascular diseases – Uni- or bilateral renal artery stenosis – Segmental or polar artery stenoses – Renal artery aneurysm, renal infarction, arteriovenous fistula • Unilateral renal diseases – Renal carcinoma, renin-producing tumor, etc. • Previous renal transplantation	
Endocrine causes • Adrenomedullary forms – Pheochromocytoma (30%extra-adrenomedullary) • Adrenocortical forms – Primary hyperaldosteronism and other forms of mineralocorticoid hypertension • Cushing syndrome • Thyroid diseases – Hyperthyroidism – Hypothyroidism (in ~ 20%of cases) • Primary hyperparathyroidism (in ~ 50%of cases) – Monogenetic (familial) forms – Coarctation of the aorta – Neurogenic cause • Loss of baroreflex function, etc. – Obstructive sleep apnea syndrome (OSAS)	
Not assigned to chronic arterial hypertension in the strict sense • Drug-induced hypertension	

continued persistence of left heart failure and pulmonary congestion, pulmonary arterial hypertension develops, resulting in pressure overload and enlargement of the right ventricle, and causing progressive obliteration of the cardiac waist in the P-A radiograph (expanded conus pulmonalis). The lateral radiograph shows progressive narrowing of the retrosternal space. When the right ventricle eventually decompensates, the transverse diameter of the heart expands to the right through dilation of the right atrium. This is accompanied by a decrease in pulmonary vascular markings. At this stage pleural effusions and enlargement of the superior vena cava provide definitive evidence of right heart failure.

Pulmonary Arterial Hypertension (Cor Pulmonale)[113–118]

Cor pulmonale denotes a change in the configuration of the heart based on right ventricular hypertrophy as a result of underlying pulmonary disease.

In acute cor pulmonale, right ventricular dilatation is essentially the only radiographic sign observed. Possible causes include pneumonia and extensive pulmonary emboli (see Chapter 12).

The findings of chronic cor pulmonale are stagedependent. Right ventricular hypertrophy and dilatation may be seen as a result of chronic obstructive syndrome, chronic bronchitis, pulmonary emphysema, pulmonary fibrosis, pneumonectomy, or recurrent emboli. The reduced oxygen tension leads to pulmonary vasoconstriction with subsequent pulmonary arterial hypertension due to the rise in peripheral resistance (Euler–Liljestrand reflex). This parenchymal type of primary arterial hypertension is distinguished from primary vascular pulmonary hypertension, which develops as a result of primary vascular disease, thus yielding two main categories of cor pulmonale: parenchymal and vascular. It should also be noted that the term "cor pulmonale" is inaccurate for describing secondary pulmonary arterial hypertension caused by persistent mitral or aortic valve disease, left heart failure, or a shunt lesion, even though the right heart and pulmonary artery undergo similar morphological changes.

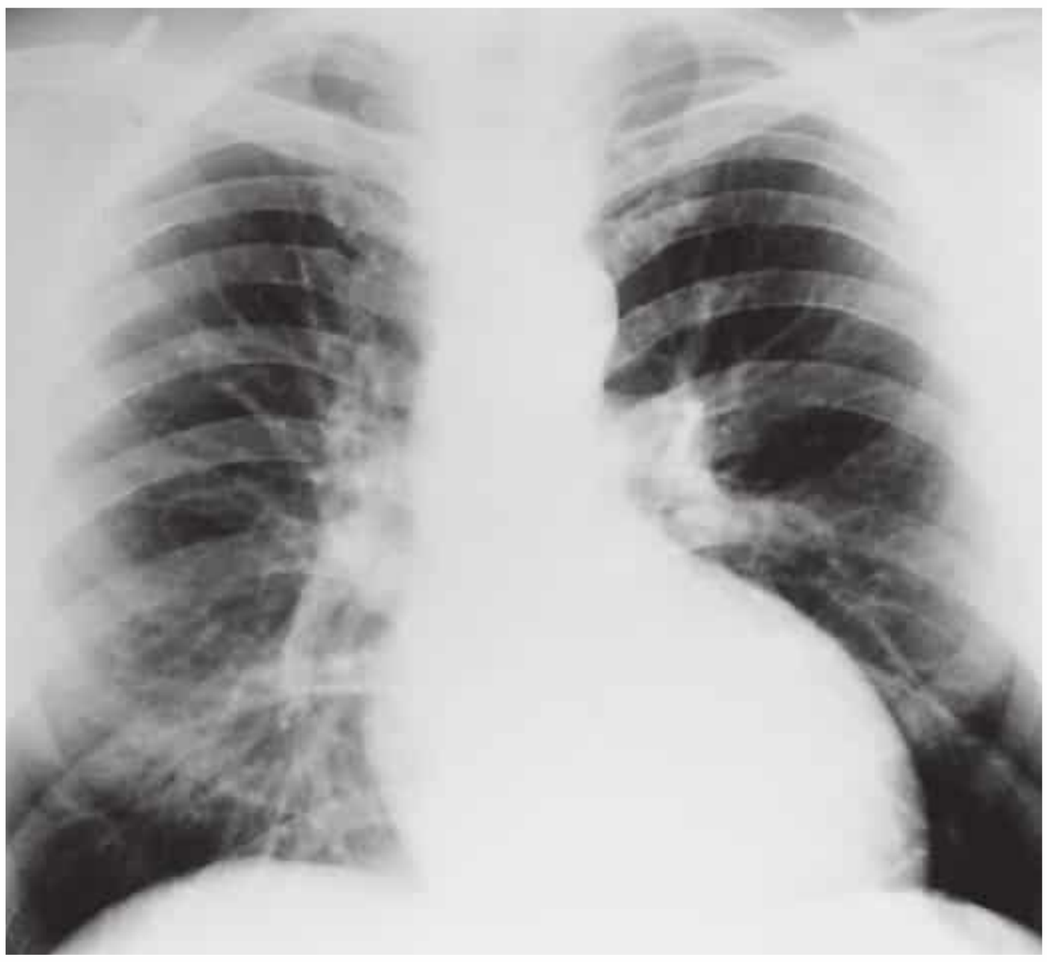

Fig. 1.24 Chronic arterial hypertension. The heart shows a typical "aortic" or left ventricular configuration due to myogenic dilatation of the left ventricle. Signs of cardiac decompensation are not yet present.

It is remarkable and even paradoxical that while radiographs in severe parenchymal lung diseases with a high pulmonary artery pressure do show signs of hypertension in the pulmonary vessels, the cardiac silhouette is narrowed rather than enlarged. These hearts are compressed by the massive emphysematous and fibrotic changes in the lung parenchyma caused by the underlying disease ("dirty lung"), which prevent cardiac dilatation. However, this squeezing effect does not alter or mitigate the cardiac pathology (**Fig. 1.25**).

Essential Point
Radiographs in severe parenchymal lung diseases with high pulmonary arterial pressures show signs of pulmonary hypertension in the lung vessels. The cardiac silhouette may, paradoxically, be narrow.

Pericardium

The pericardium consists of a visceral layer (epicardium) and a parietal layer (pericardium). Its diaphragmatic part is firmly adherent to the diaphragm beneath the heart. The pericardium is attached superiorly to the aorta and pulmonary artery and may be reflected onto the divisions of those vessels. The pericardium has an anterior fibrous attachment to the sternum and is bounded laterally by mediastinal pleura on both sides. The pericardial cavity normally contains 20–50 mL of fluid. The pericardium prevents sudden dilatation of the cardiac chambers during exercise and hypervolemia, and it permits atrial filling during ventricular systole by maintaining a negative intracardiac pressure. Additionally, the pericardium maintains the heart in its anatomical position while stabilizing the position of the great vessels. Pericarditis can have numerous causes (**Table 1.12**).[119]

Radiographic Features

Conventional radiographs cannot contribute to the etiological classification of pericardial diseases, but they do have a role in clinical classification. Pericarditis may occur in either a fibrinous (dry pericarditis) or an exudative form with pericardial effusion. The life-threatening form is an effusion leading to pericardial tamponade. Most cases of acute pericarditis heal with the formation of adhesions between the parietal and visceral layers and between the pericardium and surrounding structures. A small number of patients develop clinical manifestations of chronic nonconstrictive pericarditis, which is characterized by chronic effusions, progressive fibrosis, and some degree of calcification. When associated with hemodynamically insignificant adhesions, this condition is also referred to as chronic adhesive pericarditis.

If an acute pericardial effusion raises the intrapericardial pressure, the stroke volume is decreased and there is a

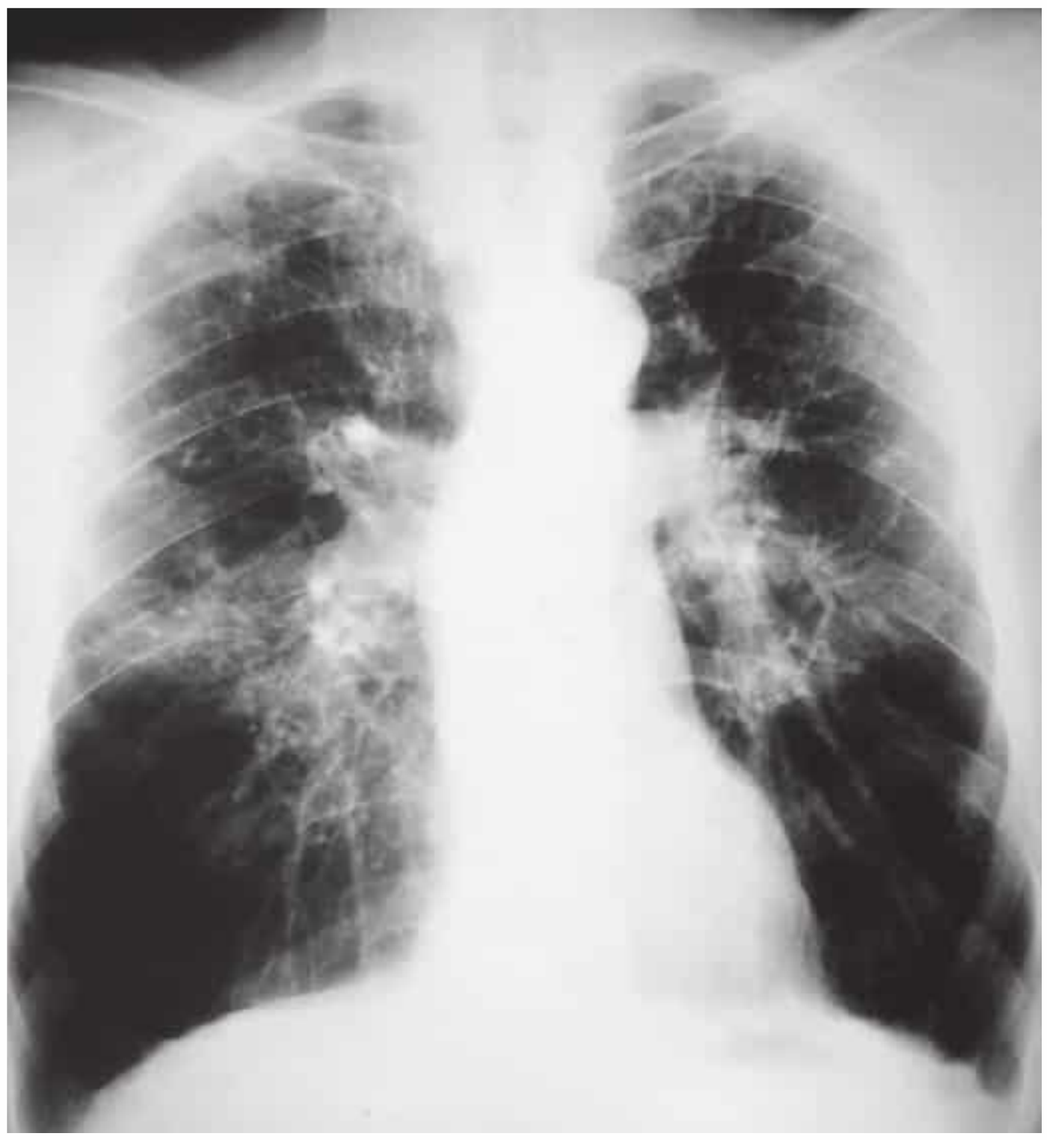

Fig. 1.25 "Dirty lung" in COPD. The pulmonary vessels show signs of pulmonary hypertension (abnormally enlarged central pulmonary arteries). Narrow cardiac silhouette.

compensatory rise in heart rate. The systemic arterial pressure falls, and the blood pressure amplitude is diminished. When the pressure in the pericardial cavity reaches ~20 mmHg, ventricular filling can no longer occur. When the volume of pericardial fluid exceeds 200–300 mL, a life-threatening pericardial tamponade may develop. Inflow to the right atrium is obstructed, resulting in decreased perfusion of the lungs.

Essential Point
Approximately 200 mL of fluid must be present before a pericardial effusion can be detected in chest radiographs.

Chronic pericarditis associated with chronic fibrinous inflammation and limited chronic effusions do not produce adverse hemodynamic effects.

Pure fibrinous pericarditis without effusion is not detectable by conventional radiography or even CT. A fluid collection in the pericardial space which exceeds 200 mL can generally be detected on chest radiographs, but only CT scans can differentiate among hydro-, hemo- and chylopericardium.

A large intrapericardial fluid collection of sudden onset causes generalized enlargement of the cardiac silhouette with acute cardiophrenic angles, as the pericardial sac has no time to adapt to the increased intrapericardial volume. Widening of the superior vena cava in the chest film due to obstruction of venous inflow merely represents an additional inconventional radiographic presentation. Since pulmonary blood flow is diminished, the lung shows increased lucency and the pulmonary vessels are reduced in caliber (**Fig. 1.26**).

Table 1.12 Classification of pericarditis

Clinical classification

I. Acute pericarditis (<6 weeks)
- Fibrinous
- Exudative (or hemorrhagic)

II. Subacute pericarditis (6 weeks to 6 months)
- Constrictive exudative
- Constrictive

III. Chronic pericarditis (>6 months)
- Constrictive
- Exudative
- Adhesive (nonconstrictive)

Etiological classification

I. Infectious pericarditis
- Viral (coxsackie A and B, echovirus, mumps, adenovirus, hepatitis, HIV)
- Pyrogenic (Pneumococcus, Streptococcus, Staphylococcus, Neisseria, Legionella)
- Tuberculous
- Mycotic (histoplasmosis, coccidiomycosis, Candida, blastomycosis)
- Other infections (syphilitic, parasitic)

II. Noninfectious pericarditis
- Acute myocardial infarction
- Uremia
- Neoplasia
  – Primary tumors (benign or malignant)
  – Pericardial metastases
- Myxedema
- Cholesterol
- Chylopericardium
- Trauma
  – Penetrating chest wall
  – Nonpenetrating
- Aortic aneurysm (penetrating the pericardial sac)
- Postirradiation pericarditis
- Familial Mediterranean fever
- Familial pericarditis
- Acute idiopathic

III. Pericarditis most likely associated with hypersensitivity reactions or autoimmunity
- Rheumatic fever
- Collagen diseases (systemic lupus erythematosus, rheumatoid arthritis, scleroderma, acute rheumatic fever, Wegener granulomatosis)
- Drug-induced pericarditis (procainamide, hydralazine, phenytoin, isoniazid, doxorubicin)

IV. Posttraumatic
- Postmyocardial infarction syndrome (Dressler syndrome)
- Postpericardiotomy syndrome
- Posttraumatic

Viewed in the lateral projection, a large pericardial effusion will almost completely occupy the anterior and posterior portions of the chest. Another sign in this projection is the "epimyocardial fat line," an anterior crescent-shaped lucent zone located between the epicardium and pericardium.

If the pericardial effusion takes a more chronic course and does not obstruct the inflow of blood, there will be generalized enlargement of the cardiac silhouette with obliteration of the cardiac waist and a relatively narrow aorta which contrasts sharply with the broad cardiac shadow. Both cardiophrenic angles are wide and obtuse. Moreover, since the intrapericardial pressure is not increased, signs of superior vena cava compression are not observed. With a serofibrinous or hemorrhagic pericardial effusion in end-stage renal disease, radiographs do not show a hyperlucent lung, but instead demonstrate a "fluid lung" owing to the presence of excessive lung water.

Constrictive Pericarditis[120–123]

Constrictive pericarditis can result from scar formation in the end stage of pericarditis, regardless of whether the pericarditis has an inflammatory or traumatic cause. If these scars calcify, the condition is known as calcific constrictive pericarditis or "armored heart." Of course, this "armor" may also result from heavy fibrous plaque formation in the absence of detectable calcification.

In many cases the cause of constrictive pericarditis cannot be established. Tuberculosis has become less common as an etiological factor.

Constrictive pericarditis impedes systolic and diastolic changes in the ventricular volumes. This means that systolic contraction and diastolic filling of the heart are both impaired. Because the pericardial constriction predominantly affects the right heart, in many cases the dominant signs are based on obstructed venous inflow to the right heart (portal hypertension, ascites). If the left ventricle is predominantly affected, the functional result will be the same as in mitral stenosis, and is also associated with pulmonary congestion.

Radiographic Features

Severe constrictive pericarditis may be accompanied by a normal-sized or enlarged heart in the chest radiograph. Cardiac size depends on the presence or absence of associated myogenic dilatation. It is important to determine whether constrictive pericarditis coexists with heart failure, to ensure an accurate assessment of the degree of possible postoperative ventricular dilatation. The diagnosis of constrictive pericarditis is confirmed by the detection of calcium deposits in the pericardium. These deposits are found in more than 50% of patients with a severe grade of inflammatory pericarditis. The pericardial calcifications (calcific constrictive pericarditis) are rarely homogeneous and are located predominantly on the atrioventricular constrictions, on very mobile portions of the ventricles, and on the diaphragmatic part of the pericardium. Overall, the calcifications tend to occur with greater frequency on the right ventricle.

Enlargement of the left atrium due to impaired diastolic filling of the left ventricle is occasionally seen in constrictive pericarditis. This may have the same functional effects as mitral stenosis and is occasionally associated with pulmonary venous congestion.

The pulsations of the cardiac borders are diminished when viewed fluoroscopically. Rotational fluoroscopy can differentiate pericardial calcifications from calcifications of the pleura, calcified cardiac thrombi, myocardial plaques, myocardial aneurysms, cardiac valves, annulus calcifications, and calcified coronary arteries (**Fig. 1.27**).

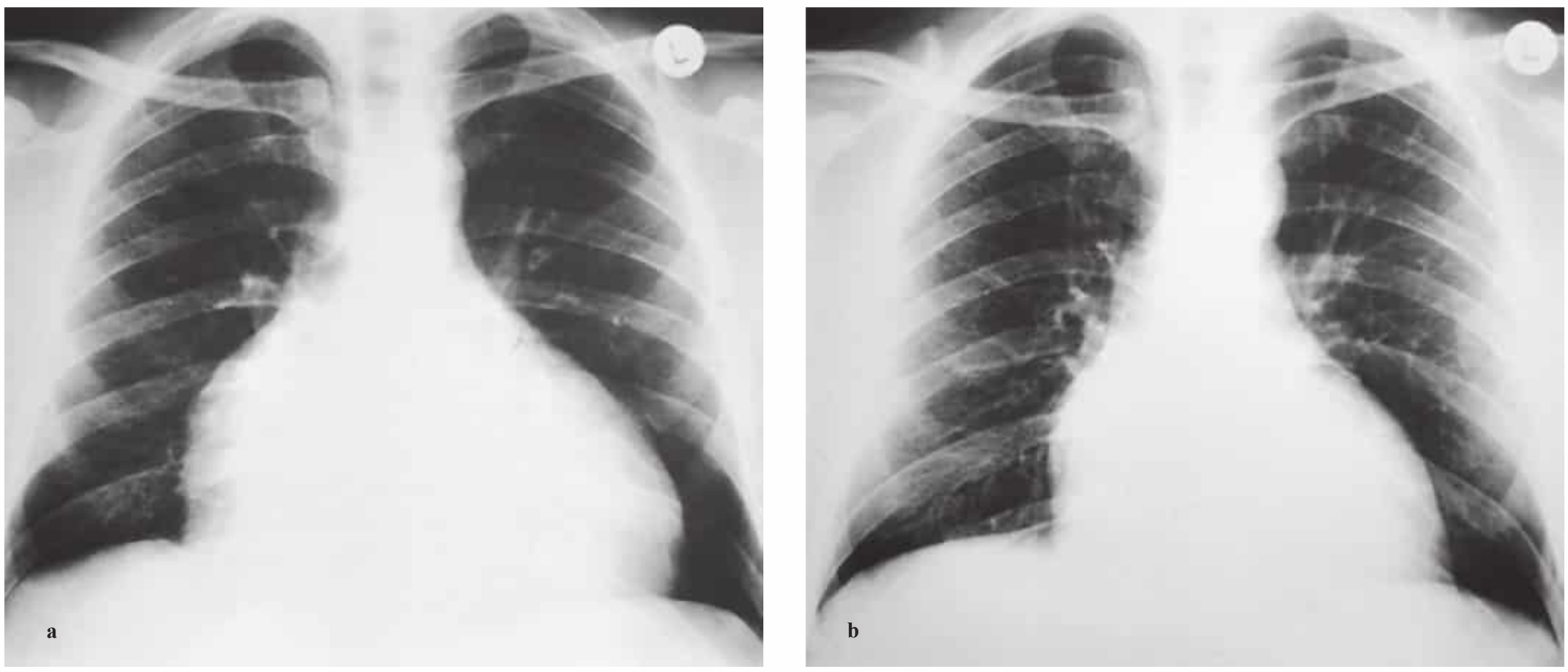

Fig. 1.26 a, b Large pericardial effusion before (**a**) and after (**b**) pericardiocentesis. The marked enlargement of the cardiac silhouette regresses following aspiration of the pericardial effusion. The hyperlucent lung fields (decreased pulmonary blood flow) again show normal pulmonary vascular markings following pericardiocentesis.

Aorta

The most important primary vascular disease in humans is atherosclerosis, which is particularly impressive when it involves the aorta. This is reflected in the weight of the aorta, which normally increases from ~22 g to 58 g between 20 and 60 years of age.[40,124] Only ~15 % of this weight increase is based on lipoid deposition, however, and up to 80 % results from connective tissue proliferation. The diameter of the aorta in adults is ~3 cm at its origin, 2.5 cm in its descending thoracic portion, and 1.8–2 cm at the abdominal level.

Because the aorta is constantly subjected to high pulsation pressures and shearing forces, it is highly susceptible to injury from mechanical trauma. Additionally, the aorta is more prone to rupture than other vessels, especially during the development of a dilated aneurysm. The wall tension of the aorta is intrinsically high according to the Laplace law, which states that wall tension is proportional to the product of pressure and vessel radius.

Congenital Anomalies

Rare congenital anomalies of the aorta may be incidental findings in standard chest X-rays or may similarly be detected during barium examination of the esophagus (see Chapter 13, p. 264).

Right Descending Aorta

A right-sided aortic arch may pass in front of the right main bronchus and descend on the right side (anterior type), or it may angle behind the right main bronchus and then pass behind the esophagus to descend on the left side (posterior type).

Radiographic Features

The chest radiograph shows widening of the right upper mediastinum. The P-A esophagogram shows a typical right-sided indentation of the esophagus at that level.

Double Aortic Arch

In the pathological variant of the double aortic arch, the left arch passes in front of the trachea and esophagus, while the right arch passes behind these structures. Both arches then merge to form the left descending aorta.

Radiographic Features

The double aortic arch causes widening of the upper mediastinum in the P-A radiograph. The barium-filled esophagus shows characteristic indentations in its right and left borders. In the lateral radiograph, the esophagus is displaced anteriorly by the aortic arch, which passes behind the esophagus from left to right.

Coarctation of the Aorta

Coarctation of the aorta may occur in an infantile (preductal) or adult (postductal) form. A collateral circulation must develop between the pre- and poststenotic aortic segments to surmount the stenosis. Less than 50 % narrowing of the aortic lumen is not hemodynamically significant. The prestenotic dilatation may assume aneurysmal proportions.

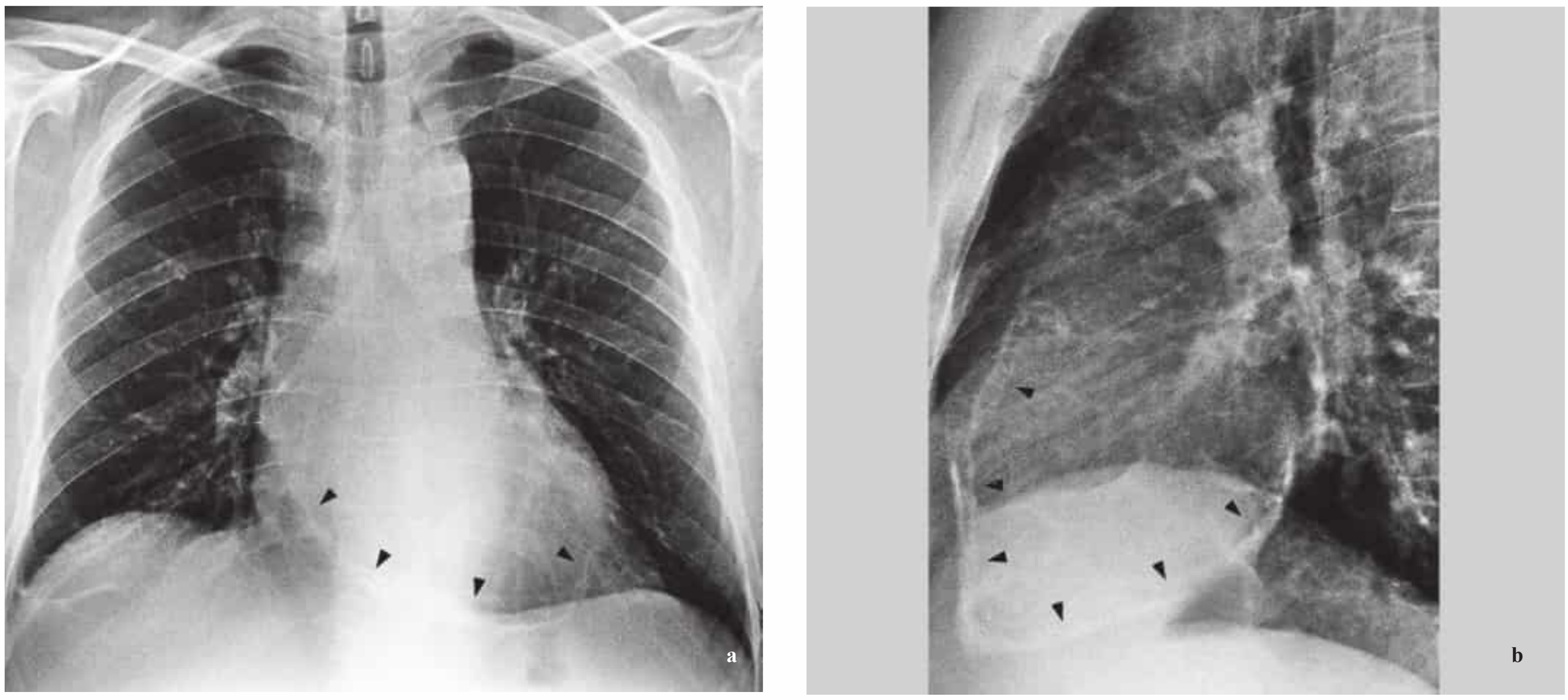

Fig. 1.27 a, b P-A (**a**) and lateral (**b**) radiographs in calcific constrictive pericarditis show shell-like calcification along the left cardiac border (**a**) and anterior and posterior calcified shells extending to the cardiac apex (**b**).

Radiographic Features

Isolated coarctation of the aorta imposes a pressure load on the left ventricle. It initiates an early ventricular hypertrophy and subsequent dilatation with a typical change in the outline of the cardiac silhouette (aortic or left ventricular configuration).

The contours of the upper mediastinum provide important information. The ascending aorta is frequently widened. The enlarged left subclavian artery appears as a shallow protrusion directed upward and to the left. At the level of the stenosis is a notch corresponding to the indentation in the outer aortic wall. This notch is accentuated if the descending aorta is dilated past the stenosis (epsilon sign).

Oral barium contrast examination of the esophagus, which may yield information on collateralization as well as pre- and poststenotic dilatation, has been replaced by modern sectional imaging modalities.

Rib notches caused by enlarged intercostal arteries are an important aid in radiographic diagnosis (**Fig. 1.28**).

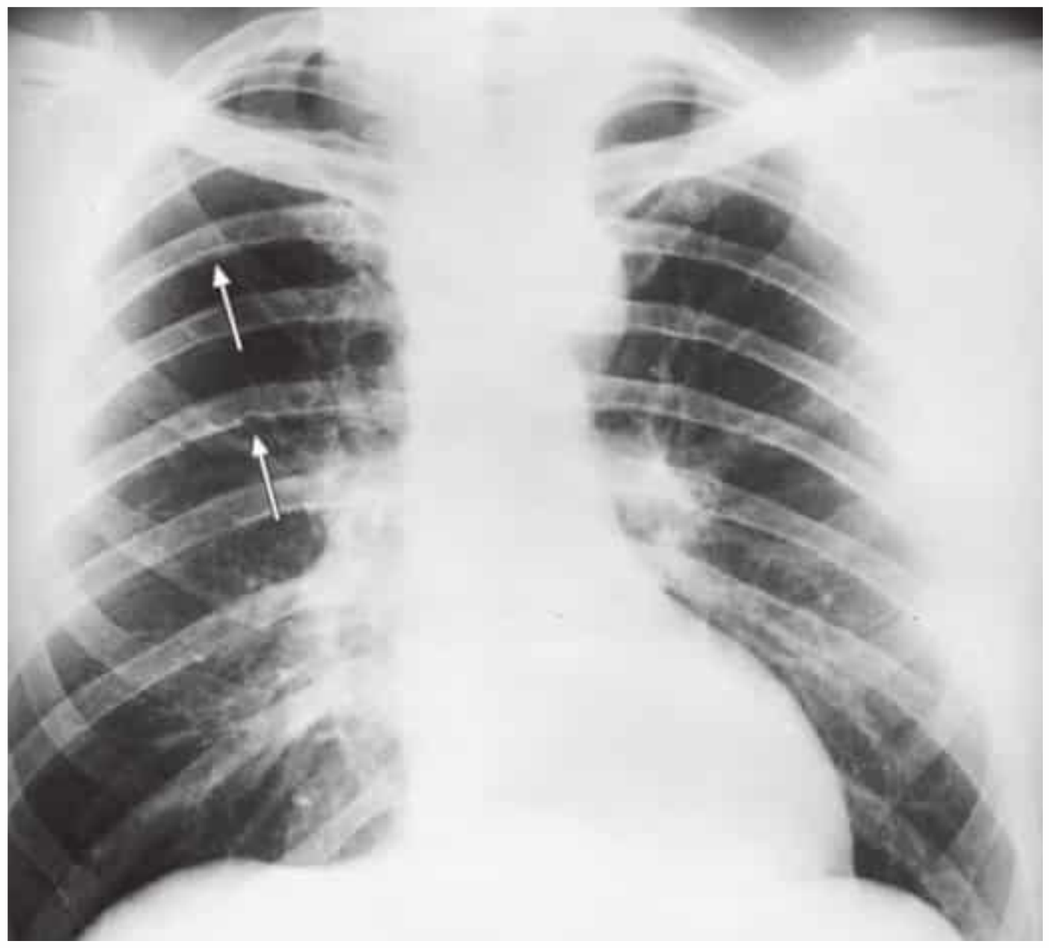

Fig. 1.28 Hemodynamically significant postductal coarctation of the aorta.
- Aortic or left ventricular configuration at still-normal cardiothoracic ratio.
- Enlarged aortic arch.
- "epsilon sign" (notching of the descending aorta at the isthmus level with poststenotic dilatation).
- Rib notching (arrows).

Essential Point
Widening of the upper mediastinum due to an anomaly of the thoracic aorta should not be mistaken for a mediastinal tumor.

Aortic Sclerosis, Aortic Dilatation, Aortic Elongation, Aorta Angusta

Aortic Sclerosis In its advanced stage, aortic sclerosis is marked by calcium deposits in the vessel wall. Calcium deposits in the aortic arch are viewed tangentially in the P-A chest film, where they are clearly visible as rounded or crescent-shaped densities. The detection of severely calcified sclerosis of the ascending aorta can provide the surgeon with important information prior to aortocoronary bypass surgery.

Aortic Dilatation Diffuse dilatation of the thoracic aorta appears in conventional chest radiographs as prominence of the ascending aorta (upper right cardiac border) and a protrusion in the left mediastinal border (course of the ascending aorta). Additional calcium deposits in the vessel wall delineate the course of the vessel with particular clarity (**Table 1.13**).

Aortic Elongation Elongation of the aorta is manifested in radiographs by upward displacement of the apex of the aortic arch. In pronounced cases the aortic arch extends past the upper sternal border and shows a markedly tortuous course (kinking).

Aorta angusta A narrow aortic arch (aorta angusta) is the expression of a decreased stroke volume, which may result from severe mitral stenosis, hemodynamically significant pericardial effusion, or hypoplasia in a setting of congenital heart disease.

Aortic Aneurysm

Aortic aneurysm is defined as a circumscribed dilatation of the aorta. A true aneurysm involves all three layers of the vessel wall. It is distinguished from a false aneurysm (pseudoaneurysm), in which the intima and media are ruptured and the dilatation is bounded only by the adventitia and sometimes by a perivascular hematoma. Aneurysms can be classified by their external appearance. A fusiform aneurysm involves the entire circumference of the aorta, leading to diffuse dilatation. In contrast, a saccular aneurysm involves only one side of the vessel, forming a protrusion in the vessel wall.

Table 1.13 Differential diagnosis of enlargement of the thoracic aorta

- Aortic stenosis, valvular (ascending aorta only)
- Aortic insufficiency, valvular
- Aortitis
- Atherosclerosis
- Aortic aneurysm
- Aortic dissection (may show double contour)
- Coarctation of the aorta (ascending aorta and aortic arch only)
- Hypertension
- Patent ductus arteriosus
- Marfan syndrome
- Ehlers–Danlos syndrome
- Osteogenesis imperfecta
- Pseudoxanthoma elasticum
- Subvalvular aortic stenosis
- Tricuspid atresia with transposition of the great vessels
- Tetralogy of Fallot
- Pseudotruncus arteriosus
- Truncus arteriosus
- Ventricular septal defect with right-to-left shunt
- Arteriovenous malformations and acquired fistulas

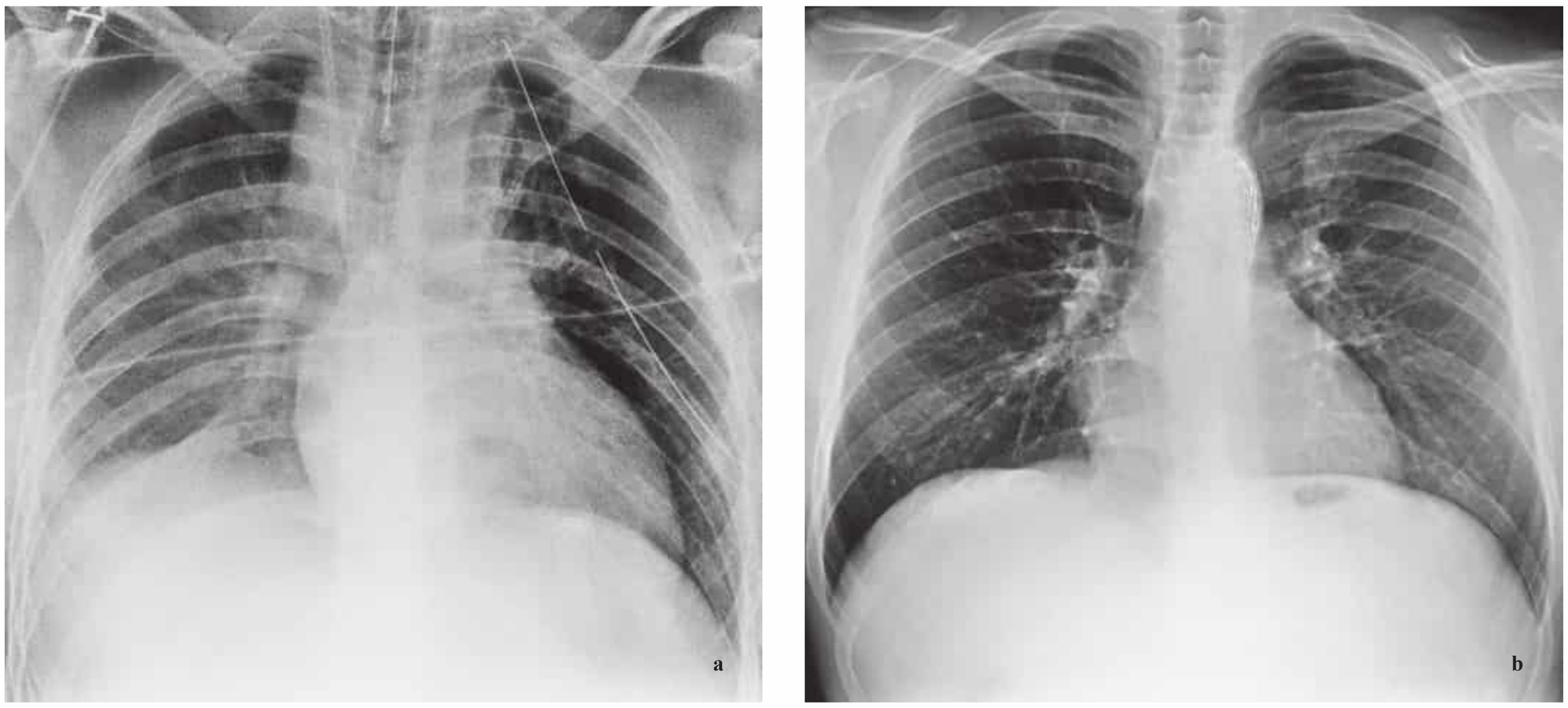

Fig. 1.29 a, b Severe chest contusion in a patient with polytrauma.
a Supine chest radiograph shows bilateral widening of the upper mediastinum by mediastinal hematoma due to a ruptured aortic arch.
b P-A radiograph with normal appearance of the mediastinum following stent repair of the aortic rupture.

Radiographic Features

In the P-A chest radiograph, a thoracic aortic aneurysm forms a bulge in the outer contour of the ascending aorta, aortic arch, or descending aorta. Diagnosis is aided by the presence of shell-like calcifications in the aneurysm wall.

A **traumatic aortic rupture**[125] (**Fig. 1.29**) or an **aneurysm rupture** into the mediastinum or pleural space, for example, is almost always a life-threatening complication. Spontaneous perforations may also occur in vessels with a normal diameter.

Aortic Dissection

Aortic dissection is caused by a tear in the circumference of the aorta. Usually this occurs along the right lateral wall of the ascending aorta, where hydraulic shear stresses are very high. The initiating event is most likely a medial hemorrhage, which disrupts the intima and allows luminal blood to dissect into the vessel wall. Another common site is the descending thoracic aorta directly below the ligamentum arteriosum. The pulsatile blood flow along the aorta leads to a tear in the elastic lamellar plates of the aorta and creates a false lumen. The dissection usually propagates down the descending aorta and into its major branches, but it may also propagate upward into the cervical vessels. A second, distal intimal rupture may also occur, allowing re-entry of the blood from the false lumen into the true lumen (**Table 1.14**).

With a dissection of the ascending aorta, the chest radiograph often shows widening of the upper mediastinum. A pleural effusion (usually on the right side) may also be present. Dissection of the thoracic descending aorta also causes mediastinal widening on the chest film. Additionally, the thoracic descending aorta may appear wider than the ascending aorta.

Table 1.14 Dissecting aneurysm

Etiological factors
• Hypertension • Atherosclerosis • Syphilitic mesaortitis • Erdheim–Gsell cystic medial necrosis • Mycotic aortitis • Marfan syndrome • Thoracic trauma

Various groups of authors have published classifications of aortic dissection. In addition to the DeBakey and Stanford classifications (see **Fig. 13.15**), a new classification has been developed which combines aspects of previous classifications, adds new subdivisions, and places greater emphasis on pathoanatomical changes (see **Table 13.1** and **Fig. 13.14**).

References

1. Bouillot JL, Fingerhut A, Paquet JC, Hay JM, Coggia M. Are routine preoperative chest radiographs useful in general surgery? Eur J Surg 1996;162:597–604
2. Boxt LM, Reagan K, Katz J. Normal plain film examination of the heart and great arteries in the adult. J Thorac Imaging 1994;9:208–218
3. Braunwald E. Heart Diseases. Philadelphia: Saunders; 1980.
4. Buenger RE. Five thousand acute care/emergency department chest radiographs: comparison of requisitions with radiographic findings. J Emerg Med 1988;6:197–202
5. Fauci AS, Braunwald E, Isselbacher KJ, et al. Harrisons Innere Medizin. McGraw-Hill; 1999.
6. Garcia-Miguel FJ, Garcia Caballero J, Gomez de Caso-Canto JA. Indications for thoracic radiography in the preoperative evaluation for elective surgery. Rev Esp Anestesiol Reanim 2002;49:80–88
7. Siegenthaler W. Klinische Pathophysiologie. Stuttgart: Thieme; 2001.
8. Siegenthaler W. Differenzialdiagnose Innerer Krankheiten. Stuttgart: Thieme; 2005.
9. Haas M. Biomarker bei Herzinsuffizienz. Kardiologie up2date 2005;1: 23–40.
10. Hauber B, Gohring S, Reifart N. Thoracic radiography as routine within cardiological diagnosis? Dtsch Med Wochenschr 1997;122:396–399
11. Hoppe UC, Böhm M, Dietz R, et al. Leitlinien zur Therapie der chronischen Herzinsuffizienz. Z Kardiol 2005;94:488
12. Hubbell FA, Greenfiled S, Tyler JL, Chetty K, Wyle FA. The impact of routine admission chest x-ray films on patient care. N Engl J Med 1985; 312:209–213
13. Hurst JW. The examination of the heart: the importance of initial screening. Dis Mon. 1990;36:245–313
14. Just H. Clinical diagnosis of heart failure. Ther Umsch 2000;57:293–297
15. Krayenbühl HP, Kübler W. Kardiologie in Klinik und Praxis. Vol. 2. Stuttgart: Thieme; 1981.
16. Steiner RM, Gross GW, Flicker S, Salazar A, Baron M, Loessner A. Congenital heart disease in the adult patient: the value of plain film chest radiology. J Thorac Imaging 1995;10:1–25
17. Strain DS, Kinasewitz GT, Vereen LE, George RB. Value of routine daily chest x-rays in the medical intensive care unit. Crit Care Med 1985;13:534–536
18. Tape TG, Mushlin AL. How useful are routine chest x-rays of preoperative patients at risk for postoperative chest disease? J Gen Intern Med 1988;3:15–20
19. Ishaq M, Kamal RS, Aqil M. Value of routine pre-operative chest x-ray in patients over the age of 40 years. J Pak Med Assoc 1997;47:279–281
20. Maffessanti M, Berlot G, Bortolotto P. Chest roentgenology in the intensive care unit: an overview. Eur Radiol 1998;8:69–78
21. Restrepo CS, Diethelm I, Lemos JA, et al. Cardiovascular complications of human immunodefiiency virus infection. Radiographics 2006;26: 213–231
22. Meshan I. Analyse der Röntgenbilder. Vol. 2. Stuttgart: Enke; 1982.
23. Dietlen J. Über Größe und Lage des normalen Herzens und ihre Abhängigkeit von physikalischen Bedingungen. Dt. Arch Klin Med 1907;88:55
24. Ensor RE, Fleg JL, Kim YC, de Leon EF, Goldman SM. Longitudinal chest X-ray changes in normal men. J Gerontol 1983;38:307–314
25. Neufang KF, Krug B, Lorenz R, Steinbrich W. Can digital luminescent radiography substitute for conventional x-ray technics in chest radiography? Rofo 1990;152:501–509
26. Duerinckx AJ. Plain film/MR imaging correlation in heart disease. Radiol Clin North Am 2004;42:515–541
27. Kim HK, Park SJ, Suh JW, et al. Association between cardiac valvular calcification and coronary artery disease in a low-risk population. Coron Artery Dis 2004;15:1–6
28. Woodruff JH. Calcified heart valves: comparison of methods for their demonstration. Radiology 1962;79:384
29. Chikos PM, Figley MM, Fisher L. Correlation between chest film and angiographic assessment of left ventricular size. AJR Am J Roentgenol 1977;128:367–373
30. Jung G, Landwehr P, Schanzenbacher G, Faeber B, Lackner K. Value of thoracic radiography in the assessment of cardiac size. A comparison with left ventricular cardiography. Rofo 1995;162:368–372
31. Klatte EC, Tampas JT, Campbell JA, Lurie PR. Roentgenographic manifestations of aortic stenosis and aortic valvular insufficiency. AJR Am J Roentgenol 1962;88:57
32. Klatte EC, Tampas JP, Campbell JA. Evaluation of right atrial size. Radiology 1963;81:48
33. Amplatz K. The roentgenographic diagnosis of mitral and aortic valvular disease. Am Heart J 1962;64:556
34. Bayer OFL, Wolter HH, Rippert R, Augath D, Beier D. Zur Pathophysiologie und Klinik der Mitralstenose. Z Kreisl Forsch. 1954;21:383
35. Higgins CB, Reinke RT, Jones NE, Broderick T. Left atrial dimension on the frontal thoracic radiography: a method for assessing left atrial enlargement. AJR Am J Roentgenol 1978;130:251
36. Kelley MJ, Elliott LP, Shulman ST, Ayoub EM, Victorica BE, Gessner ICH. The significance of the left atrial appendage in rheumatic heart disease. Circulation 1976;54:146–153
37. Neufang KF, Carstens V. Der vergrößerte linke Vorhof bei Mitralvitien – Vergleich nativröntgendiagnostischer Zeichen und Meßmethoden. Rontgenblatter 1981;34:280
38. Velusamy M, Mullens mL, Harrell JE, Talley JD. The chest x-ray in mitral stenosis. J Ark Med Soc 1995;91:604–605
39. Bücheler E, Lackner K, Thelen M. Einführung in die Radiologie. Stuttgart: Thieme; 2006
40. Buddecke E. Angiochemische Abwandlung des Aortenbindegewebes. Verh dt Ges Kreisl Forsch. 1958;34:143.
41. Burgener FA, Kormano M. Differential diagnosis in conventional Radiology. Stuttgart: Thieme; 1985.
42. Krestin GP, Carsten V. Diagnostische Aussagekraft der Roentgennativdiagnostik für die Beurteilung der Haemodynamik nach kombiniertem Aortenmitralklappenersatz. Röntgenblätter 1982;35:398
43. Kuhn HM. Die Bedeutung der konventionellen Röntgenuntersuchung des Thorax für die Herzdiagnostik. Rontgenpraxis 1982;33:111–132
44. Lipton MJ, Coulden R. Valvular heart disease. Radiol Clin North Am 1999;37:319–339
45. Newell JD, Higgins CB, Kelley MJ. Radiographic-echocardiographic approach to acquired heart disease: diagnosis and assessment of severity. Radiol Clin North Am 1980;18:387–409
46. Raphael MJ, Donaldson RM. The plain chest x-ray in acquired heart disease in adults. Br J Hosp Med 1987;37:211–219
47. Roskamm H, Hilsmann H, Reindell H. Neuere Untersuchungen zur Form des Herzens in den verschiedenen Altersstufen. Radiologe 1967;6:168
48. Ruttley MS. The chest radiograph in adult heart valve disease. J Heart Valve Dis 1993;2:205–217
49. Oryoji A, Kwara T, Hara H, Aoyagi S, Kosuga K, Ohishi K. Left atrial free-floating ball thrombus in a patient without mitral valve disease. Nippon Kyobu Geka Gakkai Zasshi 1993;41:699–703
50. Baron MG. The cardiac silhouette. J Thorac Imaging. 2000;15:230–242
51. Christie D, Gardner A. Radiologic heart volume and subsequent mortality. Acta Radiol Diagn (Stockh) 1979;20:66–69
52. Cleland JG, Swedberg K, Follath F, et al. The EuroHeart Failure survey programme—a survey on the quality of care among patients with heart failure in Europe. Part 1. Eur Heart J 2003;24:442–463
53. Klebzig H, Frisch P. Roentgenologische Herzvolumenbestimmung in Klinik und Praxis. Stuttgart: Thieme; 1965.
54. Linzbach AJ. Die quantitative Anatomie des normalen und vergrößerten Herzens im Hinblick auf die Herzinsuffizienz. Verh dt Ges Kreisl Forsch. 1950;16:43.
55. Linzbach AJ. Die pathologische Anatomie der röntgenologisch feststellbaren Form- und Größenveränderung des menschlichen Herzens. Fortschr Röntgenstr. 1952;77:1
56. Lipton MJ, Boxt LM. How to approach cardiac diagnosis from the chest radiograph. Radiol Clin North Am 2004;42:487–495
57. Reindell H, Roskamm H. Herzkrankheiten. Berlin: Springer; 1977.
58. Schad H, Künzler R, Onat T. Differentialdiagnose kongenitaler Herzfehler. Synopsis von Röntgenbild, Elektrokardiogramm und Phonokardiogramm. Stuttgart: Thieme; 1963.
59. Thurn P. Zur Röntgenologischen Volumenmessung des Herzens. Fortschr Röntgenstr. 1959;90:290
60. Milne E, Pistolesi M. Reading the chest radiography. St. Louis, MO: Mosby; 1993.
61. Reindell H, Bubenheimer P, Dickhuth HH, Görnandt L. Funktionsdiagnostik des Herzens. Stuttgart: Thieme; 1988.
62. Reindell H, Musshoff K, Gebhardt W, König K, Roskamm H. Die Dynamik des gesunden und kranken Herzens als Grundlage einer Beurteilung seiner Größe und Form. Radiologe 1967;6:169
63. Zdansky E. Röntgendiagnostik des Herzens und der großen Gefäße. Vienna: Springer; 1962.
64. Felix R, Weiand G. Diagnose und Differentialdiagnose des großen Herzens. Radiologe 1979;19:51

65. Chang CHJ. The normal roentgenographic measurement of the right descending pulmonary in 1085 cases. AJR Am J Roentgenol 1962; 87:929
66. Brahms O, Kleinsorg H, Kochsiek K, Voth H. Zur roentgenologischen Beurteilung der pulmonalen Hypertonie bei Mitralvitien. Klin Wochenschr 1964;42:1005
67. Bruwer AJ. Practical value of therapeutic posterioanterior roentgenogram and roentgenoscopy in certain types of heart disease. AJR Am J Roentgenol 1956;75:664
68. Lavender JP, Doppman J, Shawson H, Steiner RE. Pulmonary veins in left ventricular failure and mitral stenosis. Br J Radiol 1962;35:293
69. Stender HS, Shermuly W. Das interstitielle Lungenödem im Röntgenbild. Fortschr Röntgenstr. 1961;95:461
70. Dash H, Lipton MJ, Chatterjee K, Parmley WW. Estimation of pulmonary artery wedge pressure from chest radiograph in patient with congestive cardiomyopathy and ischaemic cardiomyopathy. Br Heart J 1980;44:322
71. de Groot MR, Turkstra F, van Marwijk Kooy M, Oostdijk AH, van Beek EJ, Buller HR. Value of chest x-ray combined with perfusion scan versus ventilation/perfusion scan in acute pulmonary embolism. Thromb Haemost 2000;83:412–415
72. Esch D, Thurn P. Zur Pathogenese und diagnostischen Bedeutung der kostodiaphragmalen Septumlinien bei der Mitralstenose. Fortschr Roentgenstr. 1957;87:7
73. Becker AE, Anderson RH. Pathologie des Herzens. Stuttgart: Thieme; 1985.
74. Cascade PN, Kantrowitz A, Wajszcuk WJ, Rubenfire M. The chest x-ray in acute left ventricular power failure: an aid to determining prognosis of patients supported by intraaortic balloon pumping. AJR Am J Roentgenol 1976;126:1147–1154
75. Goebel N, Gander M, Wellauer J, Hess OM. Die Korrelation zwischen Laevokardiogramm und Nativröntgenbild bei der Herzmuskelinsuffizienz. Fortschr Röntgenstr. 1979;130:14
76. Richter C, Cobet H, Richter K. Are thoracic radiographs in the recumbent position useful in the diagnosis of chronic left heart insufficiency? Comparison of x-ray findings with left ventricular hemodynamics. Rofo. 1986;145:428–431
77. Schillinger M, Domanovits H, Paulis M, et al. Clinical signs of pulmonary congestion predict outcome in patients with acute chest pain. Wien Klin Wochenschr 2002;114:917–922
78. Schinz HR. Radiologische Diagnostik in Klinik und Praxis. Stuttgart: Thieme 1983.
79. Teschendorf W, Anacker H, Thurn P. Röntgenologische Differentialdiagnostik. Vol. 1. Stuttgart: Thieme; 1977.
80. Thurn P. Haemodynamik des Herzens im Röntgenbild. Stuttgart: Thieme 1977.
81. Thurn P. Die röntgenologische Beurteilung der Leistungsfähigkeit des Herzens. Fortschr Röntgenstr. 1959;90:1
82. Weil J, Schunkert H. Rational diagnosis of chronic heart failure. Z Arztl Fortbild Qualitatssich 2003;97:105–112
83. Linzbach AJ. Die Herzdilatation. Klin Wschr. 1951;29:621
84. Petrie MC. It cannot be cardiac failure because the heart is not enlarged on the chest x-ray. Eur J Heart Fail 2003;5:117–119
85. Jackson F. The radiology of acute pulmonary oedema. Br Heart J 1961;13:503
86. Pfister SA, Muller C, Wiesner W. What is your diagnosis? Pulmonary edema in acute left heart failure. Schweiz Rundsch Med Prax 2003; 92:265–270
87. Milne EN, Pistolesi M, Miniati M, Giuntini C. The radiologic distinction of cardiogenic and noncardiogenic edema. AJR Am J Roentgenol 1985; 144:879–894
88. Schwarzbach W, Schmidt J. The thoracic x-ray picture in chronic right cardiac insufficiency. Arch Kreislaufforsch 1968;56:71–88
89. Shamsham F, Mitchell J. Essentials of the diagnosis of heart failure. Am Fam Physician 2000;61:1319–1328
90. Stanford W, Galvin JR. The radiology of right heart dysfunction: chest roentgenogram and computed tomography. J Thorac Imaging 1989;4:7–19
91. Hammermeister KE, Chikos PM, Fisher L, Dodge HAT. Relationship of cardiothoracic ratio and plain film heart volume to late survival. Circulation 1979;59:89–95
92. Hannibal D, Neufang KF, Mager G, Vogel U, Klocke RK. The place of thoracic plain film in the assessment of left heart insufficienca. Aktuelle Radiol. 1992;2:86–91
93. Baumstark A, Swensson RG, Hessel SJ, et al. Evaluation of the radiographic assessment of pulmonary venous hypertension in chronic heart disease. AJR Am J Roentgenol 1984;142:877
94. Frommhold W, Stender HS, Thurn P. Radiologische Diagnostik in Klinik und Praxis. Vol. 2. Stuttgart: Thieme; 1983.
95. Grosse-Brockhoff F. Klinische Pathologie der erworbenen Herzklappenfehler. Verh dt Ges Kreisl Forsch. 1954;20:19.
96. Philbin EF, Garg R, Danisa K, et al. The relationship between cardiothoracic ratio and left ventriuclar ejection fraction in congestive heart failure. Digitalis Investigation Group. Arch Intern Med 1998;158:501–506
97. Slutsky RA, Brown JJ. Chest radiographs in congestive heart failure: response to therapy in acute and chronic heart disease. Radiology. 1985; 154:577–580
98. Steinbach HL, Keats TE, Sheline PD. The roentgen appearance of the pulmonary veins in heart failure. Radiology 1955;65:157
99. Battler A, Karliner JS, Higgins CB, et al. The initial chest x-ray in acute myocardial infarction. Circulation 1980;61:1004–1009
100. Franken T, Thelen M, Thurn P. Röntgenuntersuchung des Thorax beim akuten Myokardinfarkt. Fortschr Röntgenstr. 1975;122:29
101. Franken T, Sewing B, Esser H, Gerlach F, Hildenbrand G. The value of radiographic examinations of the thorax in acute myocardial infarction. Fortschr. Röntgenstr. 1978;128:385–391
102. Hemingway H, Shipley M, Christie D, Marmot M. Cardiothoracic ratio in healthy middle aged men an independent predictor of coronary heart disease mortality. Eur Heart J 1998;19:859–869
103. Hemingway H, Shipley M, Christie D, Marmot M. Cardiothoracic ratio in healthy middle aged men and independent predictor of coronary heart disease mortality? BMJ 1998;316:1353–1354
104. Kutateladze NM, Kvaliashvili Iu A, Kemulariia M, Khvichiia N, Tsertsadze SV. The x-ray-picture of pulmonary circulation in the course of acute myocardial infarct. Vestn Rentgenol Radiol. 1989;Jul-Aug;(4):5–8. [In Russian]
105. Stein PD, Lewinson H, Potts KH. Cardiac size and left ventricular performance. Lack of correlation with silhouette measurement. JAMA 1974;229:1614
106. Tsallagova ZS, Savchenko AP. X-ray characteristics of heart failure in patients with acute myocardial infarction. Vestn Rentgenol Radiol. 1997; Sep-Oct;(5):4–7. [In Russian]
107. Wynne J, Braunwald E. The cariomyopathies and myocarditides. In: Isselbacher K, et al, eds. Harrison's Principles of Internal Medicine. 14th ed. New York: McGraw-Hill; 1998.
108. Böhm M, Kilter H. Kardiomyopathien. Berlin: Springer; 2006.
109. Chapman AH, Raphael MJ, Steiner RE, Oakley CM. Unusual chest x-ray appearances in hypertrophic cardiomyopathy. Clin Radiol 1978;29: 9–16
110. Kübler W, Kuhn H, Loogen F. Die Kardiomyopathien. Ihre Einteilung nach ätiologischen und klinischen Gesichtspunkten. Z Kardiol 1973; 62:3
111. Rezus C, Boiculese LV, Rezus E, et al. Cardio-thoracic index: marker of the clinical course of alcoholic dilated cardiomyopathy. Rev Med Chir Soc Med Nat Iasi 2003;107:802–808
112. Sharkey SW, Lesser JR, Zenovich AG, et al. Acute and reversible cardiomyopathy provoked by stress in women from the United States. Circulation 2005;111:472–479
113. Chhabra SK, De S. Clinical significance of hilar thoracic index and width of right descending branch of pulmonary artery in chronic obstructive pulmonary disease. Indian J Chest Dis Allied Sci 2004;46:91–97
114. Esch D, Thurn P. Zur Diagnose der pulmonalen Hypertonie im gewöhnlichen Röntgenbild. Fortschr Roentgenstr. 1959;90:434
115. Kanemoto N, Furuya H, Etoh T, Sasamoto H, Matsuyama S. Chest roentgenograms in primary pulmonary hypertension. Chest 1979;76:45
116. Laack TA, Goyal DG. Pulmonary embolism: an unsuspected killer. Emerg Med Clin North Am 2004;22:961–983
117. Satoh T, Kyotani S, Okano Y, Nakanishi N, Kunieda T. Descriptive patterns of severe chronic pulmonary hypertension by chest radiography. Respir Med 2005;99:329–336
118. Thurn P. Die Röntgenaufnahme des Cor pulmonale. Schweiz Rundsch Med Prax 1970;59:1506
119. Maisch B, Seferowic PM, Ristic AD, et al. Guidelines on the diagnosis and management of pericardial diseases. Eur Heart J 2004;25:587
120. Cornell SH, Rossis NP. Roentgenographic findings in constrictive pericarditis. AJR Am J Roentgenol 1965;102:301

121. Hilger HH, Schaede A, Düx A, Thurn P. Zur Diagnostik, Differentialdiagnostik und Haemodynamik der Pericarditis constrictiva, der sog. idiopathischen Myokardhypertrophie und der Endokardfibrose. Arch Kreisl Forsch. 1962;38:260
122. Lange RL, Boticelli JT, Tsagaris TJ, Walker JA, Gani M, Bustamente RA. Diagnostic signs in compressive cardiac disorders. Circulation 1966; 33:763
123. Wood P. Chronic constrictive percarditis. Am J Cardiol 1961;7:48
124. Meyer WM. Das Aortengewicht in seiner Beziehung zum Alter, Körpergewicht und Herzgewicht. Gerontologie 1963;8:105–113
125. Mirvis SE. Diagnostic imaging of acute thoracic injury. Semin Ultrasound CT MR 2004;25:156–179

Further Reading

Erbel R, Alonso F, Coileau C, et al. Diagnosis and management of aortic dissection. Recommendations of the Task Force on Aortic Dissection. Eur Heart J 2001;22:1642

Gerok W, Huber Ch, Meinerz Th, Zeidler H. Die Innere Medizin. Stuttgart: Schattauer; 2000

Kerley P. Lung changes in acquired heart disease. AJR Am J Roentgenol 1958;80:256

Matsuyama S, Watabe T, Kuribayashi S, et al. Plain radiographic diagnosis of thrombosis of left atrial appendage in mitral valve disease. Radiology. 1983;146:15–20

Reinbold WD, Kasper W, Wollschlager H, Lindenberger D, Kropelin T. X-ray changes in the thoracic organs in acute heart infarct. Radiologe 1988;28:417–421

Sharma S, Bhargava A, Krishnakumar R, Rjani M. Can pulmonary venous hypertension be graded by the chest radiograph? Clin Radiol 1998; 53:899–902

Young JW, Andersen BL, Reinig JW. Oblique chest film: value in routine and selective use. AJR Am J Roentgenol 1984;142:69–72

2 Echocardiography

R. Erbel

Basic Principles of Echocardiography

Echocardiography is a procedure in which the heart and surrounding vessels are examined with **ultrasound**. Ultrasound is a mechanical wave that requires a medium in which to propagate and is characterized by alternating compression and decompression of the medium. The audible range of ultrasound waves is from 8000 to 20000 Hz (cycles per second). Ultrasound frequencies of 2–7 MHz, or sometimes as high as 45 MHz, are used in cardiac imaging.

Piezoelectric crystals are used to produce ultrasound waves. These act by transforming electrical energy into mechanical energy and vice versa (**Fig. 2.1**).

Ultrasound waves are reflected at interfaces. The reflection may be partial or complete, depending on the structure encountered by the waves.

Essential Point
The greater the density difference between the interfaces, the greater the reflection.

Because air reflects up to 99% of incident ultrasound waves, a medium must be used to couple the transducer to the body surface. Other factors that affect the amplitude of the reflected echo are the insonation angle, surface texture, and penetration depth. The deeper the structure is located, the greater the need to amplify the returning echoes.

Essential Point
The higher the frequency of the sound, the less its penetration depth.

Because of this depth relationship, transducers operating in the 2–4 MHz range are used in adults while 5- to 7-MHz transducers are preferred in children. Transducers are now available that can be operated over a variable frequency range of 2–7 MHz. The sound energy densities used in human patients are safe and do not pose a health risk.

At present, phased-array transducers are used almost exclusively for echocardiography. This type of transducer provides up to a 90° sector angle with steering and focusing options within that range. The array consists of 64 to 256 piezoelectric crystals that can be individually excited with electrical impulses to generate ultrasound waves. The crystals then receive the reflected waves and covert them back into electrical signals.

Time-delayed excitation of the crystals creates a broad ultrasound wavefront that can be steered by varying the time delays between successive excitations. Other technical means can be used to filter the ultrasound signals that are returned from a specific direction and from a specified depth. The ultrasound beam can be focused by applying excitation pulses to the outer crystals earlier than to the more central crystals. With advances in microtechnology, transducers have already been developed that can provide real-time 3D imaging based on the simultaneous excitation of 3000 separate elements with parallel processing of the signals. Parallel data processing has resulted in higher image frame rates for 2D and 3D echocardiography and for tissue Doppler echocardiography.

Ultrasound waves may undergo multiple reflections between an interface and the transducer. If the first reflection is disregarded and the second or third reflected ultrasound signal (2nd or 3rd harmonic) is evaluated, it is possible to achieve better suppression of near-field signals and obtain a clearer image. This technique is particularly important for endocardial delineation and can be used with or without ultrasound contrast agents.

The **broadband scattering** of ultrasound waves reflected at interfaces can also be evaluated. The cardiac-phase–dependent change in these scattered echoes has been used to differentiate viable ischemic tissue from scar tissue, to detect graft rejection, and to characterize cardiomyopathies. Reproducibility is poor, however. This technique, called integrated backscatter, is used

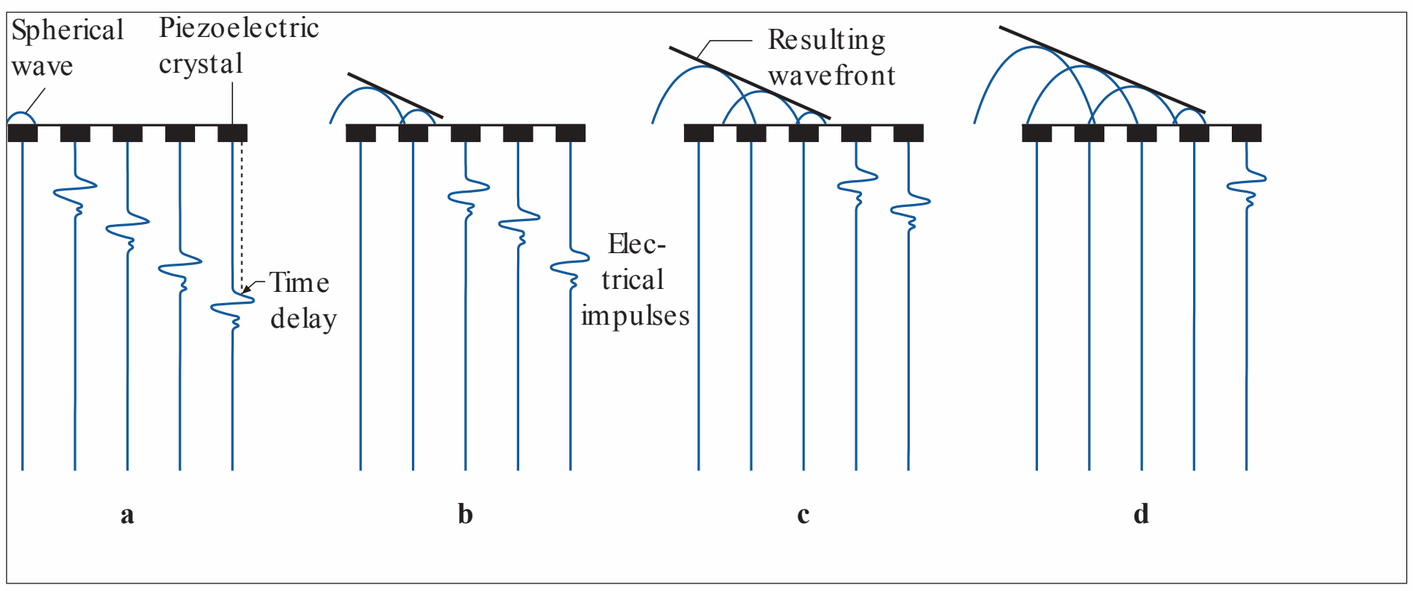

Fig. 2.1 Two-dimensional echocardiography. Diagrams show the principle of electronic ultrasound scanning with a phased-array transducer. The ultrasound wavefront can be steered by applying electrical impulses to the crystals with a time delay.

in automated border detection and tracking during cardiac motion ("acoustic quantification," "color kinesis").

Basic Principles of Ultrasound Imaging

Distances can be determined in ultrasound images by assuming that ultrasound has a velocity of 1540 m/s in tissue. Most scanners emit ultrasound pulses 1 µs long and receive the reflected ultrasound waves during the next 999 µs, resulting in a pulse frequency of 1000 s^{-1}. If ultrasound waves are continuously transmitted and received and the deflections are recorded over time, a motion-mode (M-mode) image is obtained. If numerous ultrasound pulses are transmitted and received with a phased-array transducer, a two-dimensional echocardiogram (2D image) is produced.

The reflected sound waves returning to the transducer can be displayed on an oscilloscope in three forms:

- **A-mode**: Amplitude display in which the intensity of the reflected ultrasound waves is displayed as a vertical deflection along a baseline.
- **B-mode:** Reflected A-mode ultrasound signals are displayed as spots of varying brightness (**b**right mode) proportional to the intensity of the reflected ultrasound signal.
- **M-mode:** The motion of the B-mode spots is displayed over time.

Types of Echocardiography

M-Mode Echocardiography

The M-mode display is still used today, whereas A-mode imaging has fallen from use. The M-mode display has an extremely high temporal resolution that permits the tracking of interfacial echoes over time. One M-mode beam can be displayed in the 2D image (**Fig. 2.2**), and two M-mode beams can be displayed in some systems. To facilitate analysis, tissue depth is indicated in 1-cm increments on a vertical scale, while time calibration marks are spaced at half-second intervals along the M-mode scan. An ECG is recorded simultaneously with the M-mode trace to allow temporal correlation. A phonocardiogram is also recorded if necessary. A simultaneous respiratory curve is recorded to check for signs of tamponade, pericardial constriction, or restrictive cardiomyopathy. Concomitant pressure measurements are also useful for certain applications but are generally reserved for scientific studies.

M-mode echocardiography includes a standard sweep from the aortic valve across the mitral valve to the apex of the left ventricle. M-mode traces are documented at specific, characteristic sites.

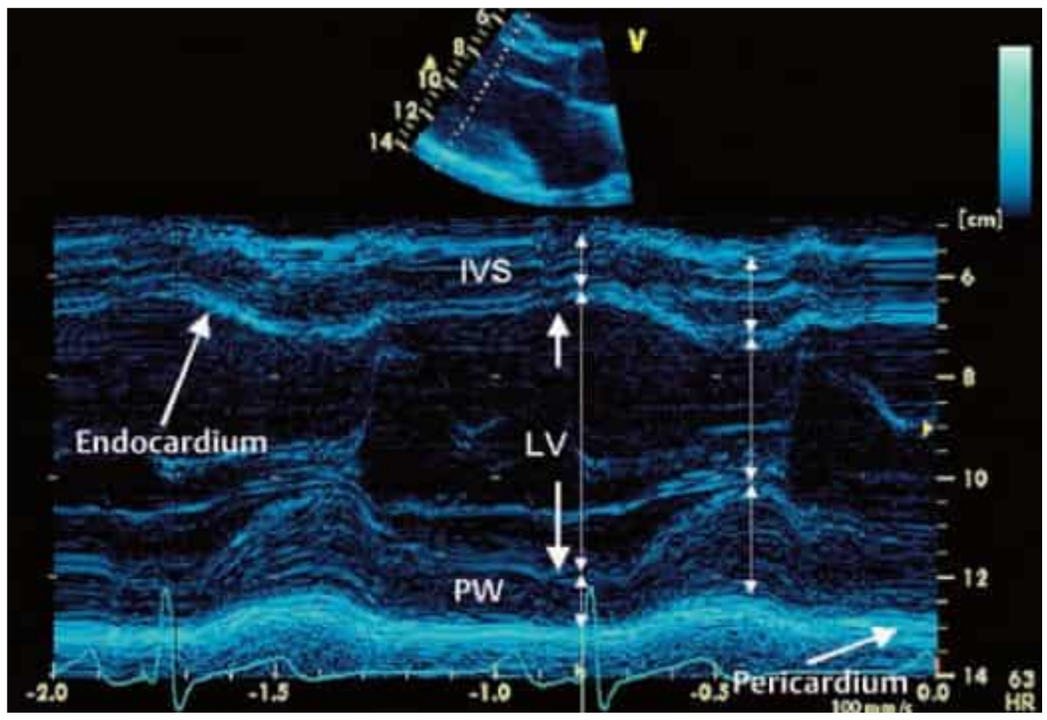

Fig. 2.2 2D-based M-mode recording.

Two-Dimensional Echocardiography

Two-dimensional echocardiography allows a section of tissue to be imaged in real time, usually over a 90° sector. The typical frame rate is 25/s, but parallel image processing can achieve frame rates up to 100/s. Even higher rates can be obtained by narrowing the sector angle. Echocardiography has the highest temporal resolution of all clinical imaging modalities.

Acoustic Quantification and Color Kinesis

Acoustic quantification employs the real-time detection of interfaces—in this case the boundary between the myocardium and its cavity—to quantify global and regional myocardial function. It permits the beat-by-beat tracking of cardiac wall motion. The addition of color encoding, called "color kinesis," makes it possible to track the velocity of endocardial border motion by encoding both the direction and velocity of the motion. The frame rate is about 25/s. This method is particularly useful in stress echocardiography.

Three-Dimensional Echocardiography

Three-dimensional echocardiography has developed rapidly during the past 15 years. Today it is no longer restricted to off-line analysis but is available in real time, thanks to improvements in transducer geometry and parallel data processing (matrix array).

The following methods are available in 3D echocardiography:

- Offline reconstruction
  - External reference systems
    - Mechanical arm
    - Acoustic locator
    - Electromagnetic sensor
  - Internal reference system
    - Linear transducer motion
    - Sweep motion
    - Transducer rotation
- Real-time 3D imaging

Offline reconstruction has assumed special importance because it helps the cardiac surgeon in the preoperative planning of cardiac valve surgery. It can provide moving images of the heart that are otherwise unavailable to surgeons.

The new matrix transducer (**Fig. 2.3**) contains 3000 individual crystal elements operating at 2–4 MHz. These elements are used for both the transmission and reception of signals to image the moving heart.

The advantage of a 3D volume data set over a 2D data set is that virtual sections through the heart can be generated in numerous planes, and the image of the heart itself can be freely rotated and displayed in arbitrary planes. As in MRI and CT, 3D echocardiography permits the quantitative assessment of chamber volumes, ventricular mass, and other cardiac parameters. It also permits the visualization of Doppler signals in three planes.

Three-dimensional echocardiography is particularly useful for structure identification, the diagnosis of valvular disease and structural cardiac pathology, and the detection of ischemia during stress echocardiography. At present 3D echocardiography is still limited in its spatial and temporal resolution, but this is gradually improving with the development of faster computers and more powerful computer processors. In the future 3D data sets will be used in the planning and virtual testing of cardiac surgical procedures.

Three-dimensional images also have training applications, as they can be used to simulate transducer positioning relative to the heart (www.sonocard.de).

Ultrasound Stethoscope

Miniaturization and digital technology have led to a decrease in the size of ultrasound systems and to the development of battery-powered instruments for portable use (**Fig. 2.4**). This type of instrument is called an ultrasound stethoscope because it is useful not only for physical examination and auscultation but also for bedside echocardiography.

These systems have been expanded with capabilities that include transesophageal echocardiography (TEE). Ultrasound stethoscopes can already provide a prompt and accurate diagnosis of pericardial effusion, decreased ejection fraction, cardiac hypertrophy, and valvular diseases such as aortic and mitral stenosis. These findings can be an important aid to surgical planning; for example, permitting the fast and reliable detection of conditions such as right heart enlargement, a hyperdynamic circulatory state, and complications of acute myocardial infarction. Any lingering questions can be investigated later by a detailed transthoracic or transesophageal study of the heart.

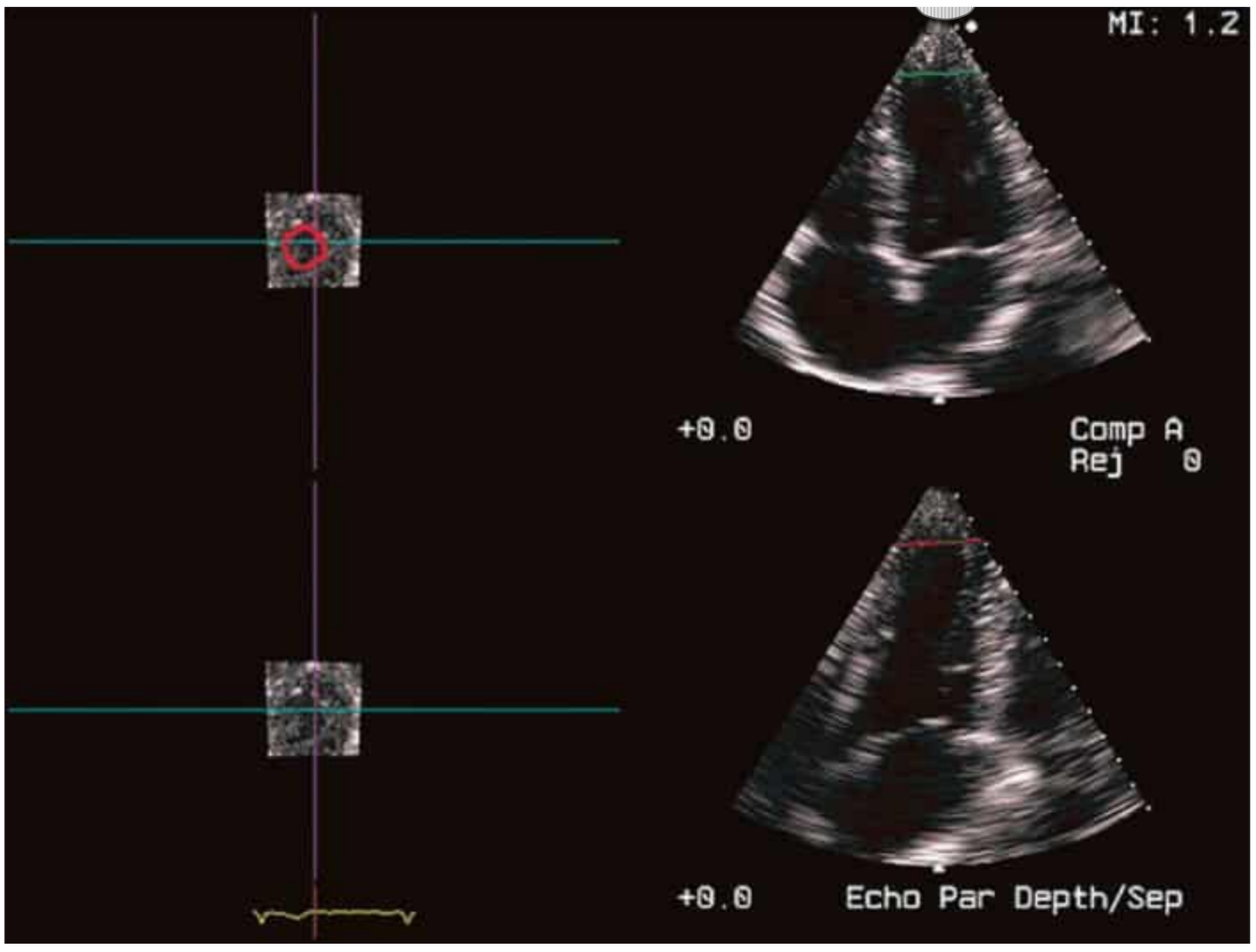

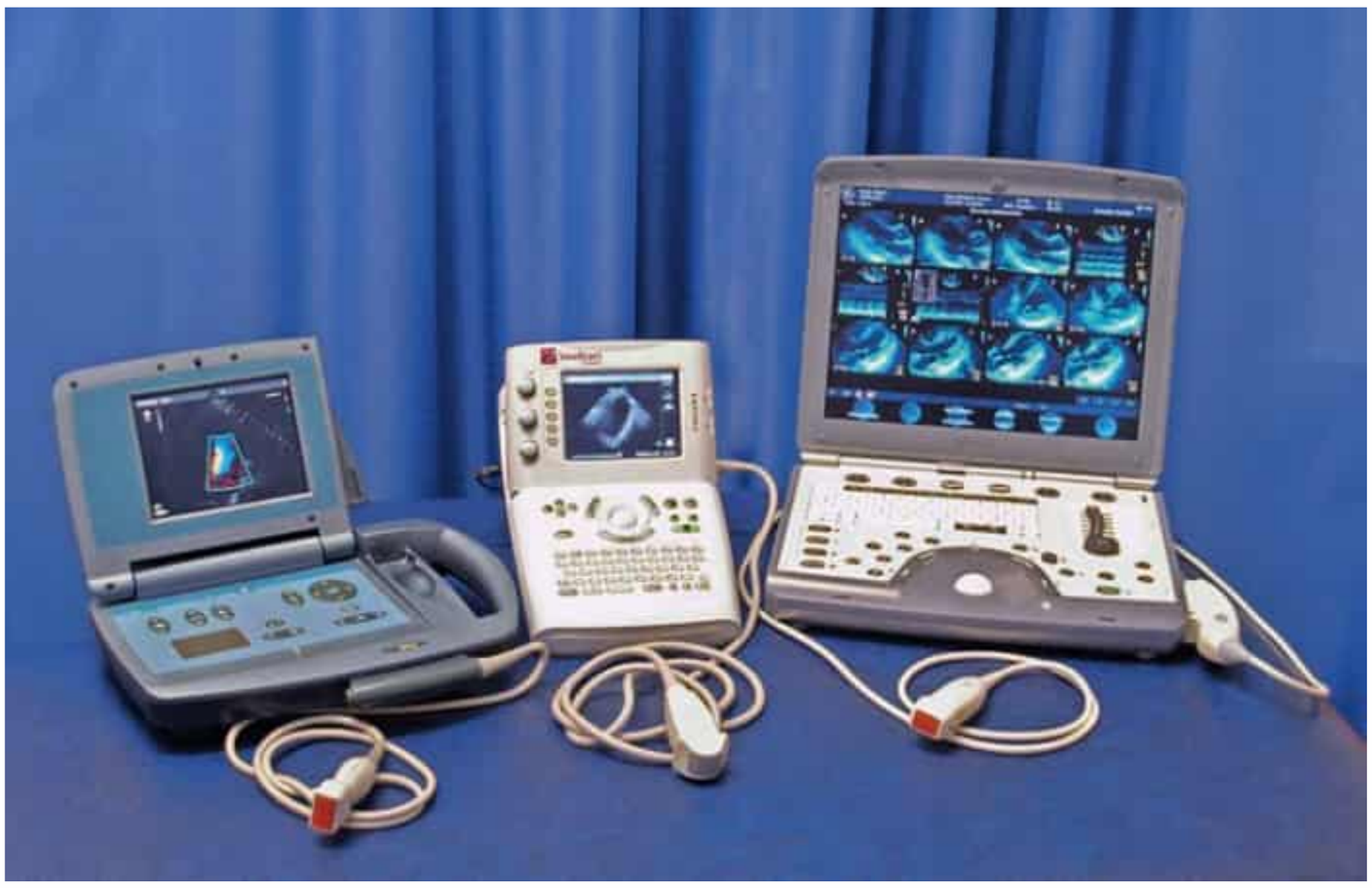

Fig. 2.4 Miniaturized ultrasound systems for bedside or ambulatory imaging (Optigo, Philips Sonoline, ViVid I GE).

Specific Applications of Echocardiography

Contrast Echocardiography

When an ultrasound beam encounters air, almost all of the sound is reflected at the air interface. For this reason, even the tiniest bubbles and cavitations in the blood or myocardium are visible in an ultrasound image. The ultrasound signal is enhanced, a property that is used mainly to amplify a weak Doppler signal.

Any injection of saline solution, medications, or infusions may produce microbubbles that are detectable with ultrasound. Various methods are used to produce these contrast agents for echocardiography.

Ultrasound contrast agents for the right heart:

Saline. Saline solution (5–8 mL) is drawn into a 3-way stopcock and syringe system and mixed with 1 mL of air. The air–saline mixture can immediately be injected intravenously to accentuate ultrasound contrast in the right heart. Shunt flow is detected by noting microcavitation at the level of the interventricular or interatrial septum. Washout effects may be seen in the presence of a right-to-left shunt. Caution should be exercised when right–left shunts of the heart are present because of the problem of potential neurological side-effects.

Gelatin solution (Gelifundol, Braun, Melsungen, Germany) gelatin solution prepared in house). This solution agitates better than saline, and it is unnecessary to draw air into the syringe. The residual air present in the 3-way stopcock is sufficient to produce dense opacification, which is confirmed when the clear, yellowish liquid turns cloudy. Only 0.5–1 mL of the solution must be injected to produce good contrast enhancement in the right heart. This method is widely utilized, has excellent reproducibility, and is nontoxic at the recommended dose. After five cardiac cycles, the solution may cause slight opacification of the left atrium after passing through the lung.

Echovist 300 (Bayer-Schering AG, Berlin). Echovist is the only agent that is currently approved for contrast echocardiography of the right heart and pulmonary circulation. Good enhancement is obtained with the agent, which must be prepared strictly according to instructions provided.

Other contrast agents. Other contrast agents, such as injected radiographic contrast agents, Cardiogreen, and infusion solutions can also produce echocadiographic contrast.

Ultrasound contrast agents for the left heart:

Levovist (Bayer-Healthcare Schering AG, Leverkusen, Germany). Contrast agents with extremely small microbubbles on the order of 4–8 μm have been developed that will opacify the left heart following intravenous injection. The agent is supplied in an injection bottle in granular form. It is dissolved in 20 mL of water, shaken, drawn into a syringe, and injected into a peripheral vein.

Optison (GE Healthcare, Amersham, UK). Optison is supplied in a bottle as a milky-white solution but was recently withdrawn from the market. Similar agents in current use are Sulfur hexafluoride, **SonoVue** (Bracco-Altana, Milan, Italy) and Perflutren, **Luminity** (Bristol-Myers Squibb, Medical Imaging, New York).

New approaches that show promise in oncology are also being applied to cardiology. These include binding pharmacological agents to microbubbles and releasing them in the cardiovascular system by specific stimuli (e.g., shock waves or ultrasound), or using antibodies to bind agents to specific receptors in the heart identified by their contrast-enhanced effect. This may be done to detect endothelial dysfunction, fibrin deposition, thrombus formation, or allograft rejection as well as to provide a mechanism for local delivery of medication and for gene delivery as in antisense therapy.

Stress Echocardiography

Resting myocardial perfusion in patients with coronary heart disease is not decreased until a stenosis has reduced the luminal diameter by more than 90 % Stress testing is used to induce a reduction of myocardial perfusion, which is possible when the stenosis is >75 % Stress echocardiography can be used for the detection of coronary artery disease, the localization of decreased blood flow, and the quantification of its effects. Stress echocardiography is also useful for risk stratification in coronary patients. The indications for stress echocardiography are the same as in nuclear medicine imaging. Stress echocardiography should always be done in clinically suspicious cases with a negative stress ECG, as its sensitivity is 85–90 %, which is 20–25 %higher than calculated for the stress ECG.

Numerous stress protocols have been proposed and are based on the use of physical exercise or a pharmacologically induced increase of oxygen demand or perfusion heterogeneity.

For exercise stress echocardiography (maximum increase in O_2 consumption), it is advantageous to test the patient in a semi-sitting position (**Fig. 2.5**). The ECG and echocardiogram are recorded simultaneously, and the development of wall motion abnormalities can be detected at an early stage. The echocardiogram is not taken after the end of exercise (e.g., after treadmill exercise), because at this point an induced wall motion abnormality may quickly disappear (reversible ischemia) within few seconds (<60 s).

A pharmacological stress can be induced by the infusion of dobutamine, with or without atropine, to raise the heart rate to a maximal level.

Vasodilation can be induced with dipyridamole or adenosine to test for a coronary steal effect. While these methods are also popular in nuclear medicine studies, they appear to be inferior to other techniques. The goal is not to increase O_2 consumption (as with dobutamine) but to induce a "steal effect" in which the heterogeneous blood flow will trigger wall motion abnormalities.

In the resting state, autoregulation maintains coronary perfusion (which occurs mainly during diastole) within a constant range of 80–220 mmHg. The administration of dipyridamole or adenosine leads to a dilatation of the resistance vessels, the normal autoregulation is abolished, and a linear relationship can be found between pressure and perfusion (**Fig. 2.6**). The coronary flow reserve (CFR) is calculated by determining the ratio of the maximum flow increase to resting perfusion at a given pressure. Because the pressure remains constant after adenosine, the CRF can be calculated on the basis of the Doppler analysis of flow velocities.

The **lower normal tolerance value** is 3.0, with a range from 4 to 6.

When stress testing is done with dobutamine (**Fig. 2.7**), myocardial viability can also be assessed. Viable but ischemically compromised myocardium will show functional abnormalities at rest that improves with low-dose dobutamine and may decreases at higher dosages. The accuracy of dobutamine echocardiography for detecting viable myocardial function is in the range of 85–90 %, comparable to that of positron emission tomography (PET), which is the "gold standard" for the detection of viability though its role may be taken over by magnetic resonance imaging.

Digital imaging techniques are best for stress echocardiography, as they permit the simultaneous display of resting and stress results side by side and provide greater analytical accuracy. The use of contrast agents, especially in stress echocardiography, also helps to improve discrimination by improving endocardial border delineation.

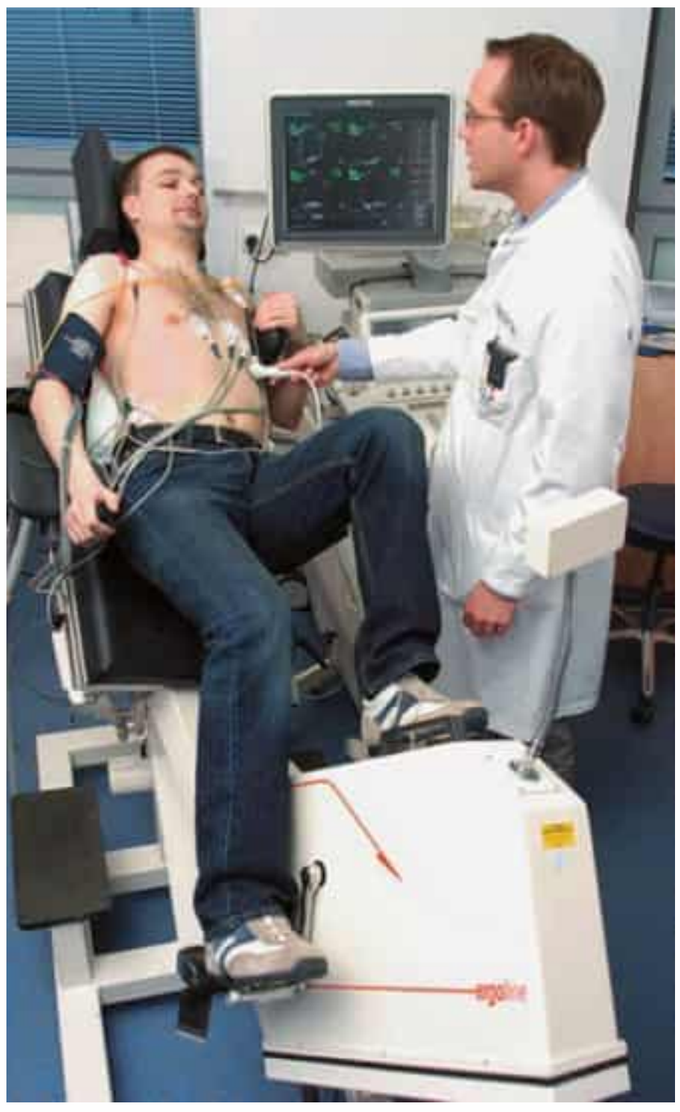

Fig. 2.5 Semi-sitting position for stress echocardiography with equipment for simultaneous ECG monitoring and echocardiography. Exercise stress is advantageous as it produces a maximum rise in O_2 consumption.

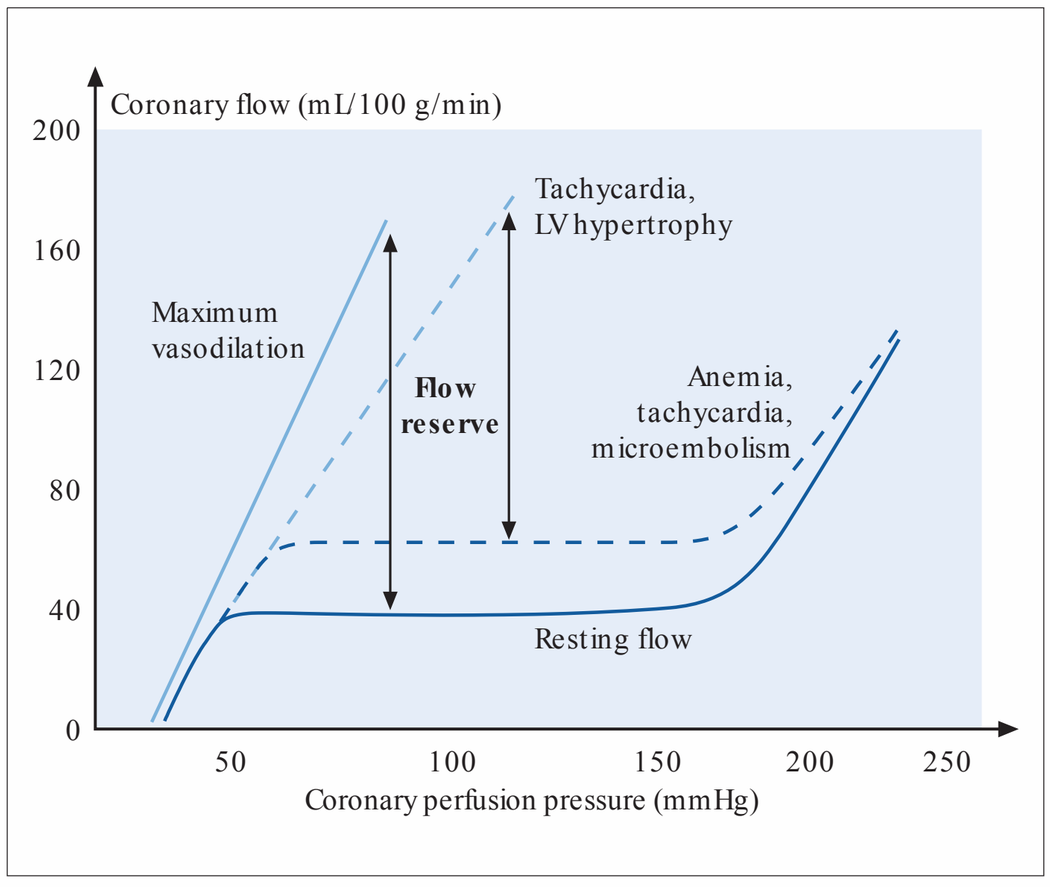

Fig. 2.6 Autoregulation of coronary perfusion. Constant conditions between 50 and 180 mmHg at rest (lower curve) versus linear relationship after dilation of the resistance vessels. A possible increase in the resting flow velocity or a fall in the maximum flow velocity will diminish the coronary flow reserve (CFR) between the curves for a given initial pressure.

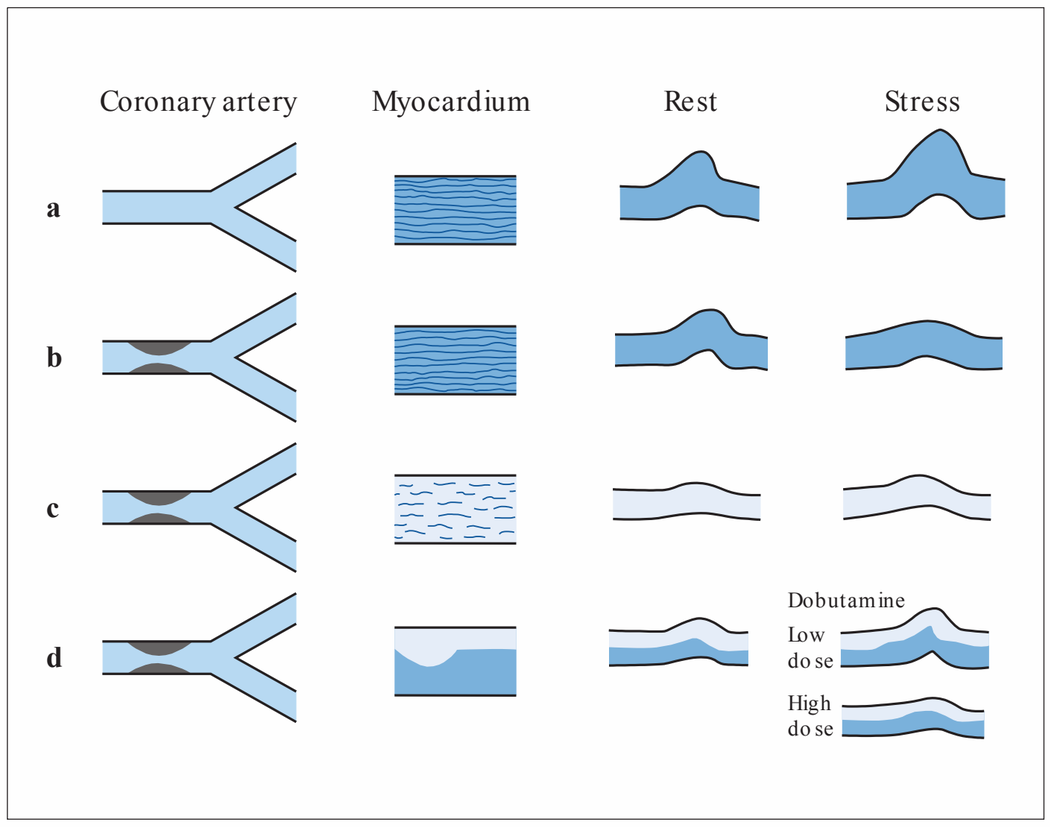

Fig. 2.7 a–d Dobutamine stress.
a Normal. **b** Ischemia. **c** Scar. **d** Viable myocardium.

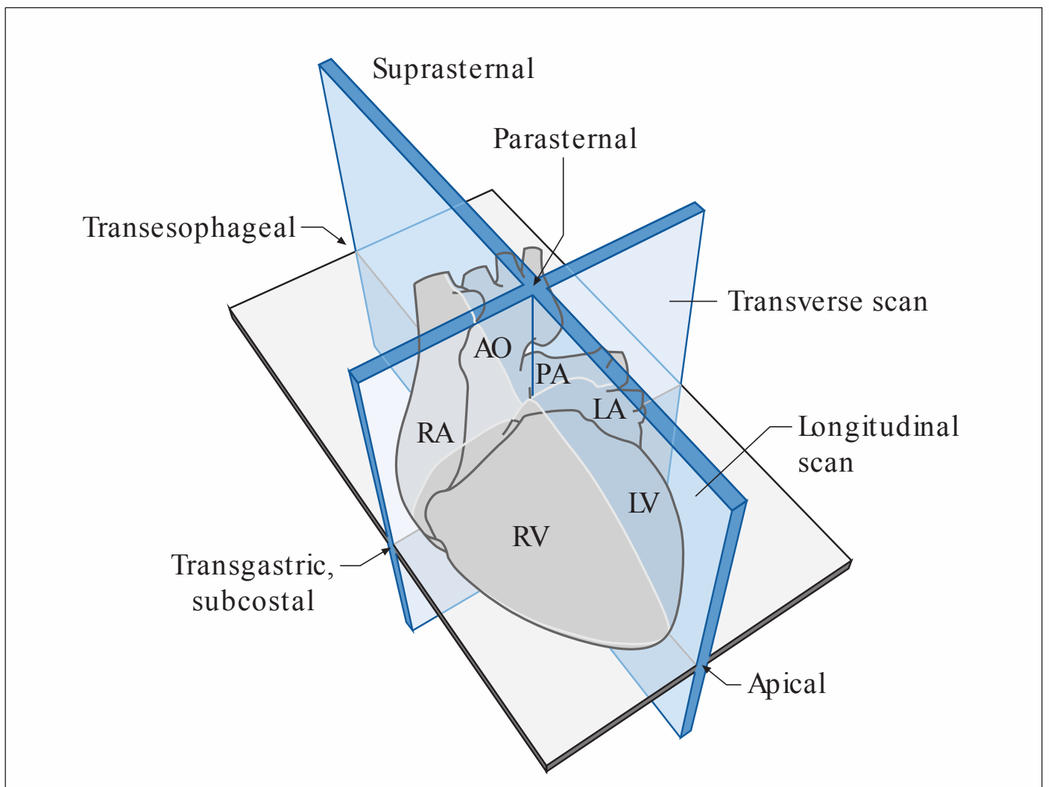

Fig. 2.8 Diagram showing the three standard scan planes used by TTE/TEE. Transgastric and transesophageal planes: four-chamber view, short axis, long axis.

Transesophageal Echocardiography

With the miniaturization of ultrasound transducers, flexible probes tipped with ultrasound crystals can now be introduced into the esophagus and stomach—orally or via the nose—to scan the heart and great vessels from various locations.

The transducer can be rotated from a transverse to a longitudinal scan, rotating the imaging plane by up to 180°. Numerous transverse and longitudinal sections can be acquired in this way (**Fig. 2.8**). The angle setting is indicated on the monitor. The endoscope tip is freely deflectable in all three planes, making it possible to optimize contact with the mucosa and also optimize the Doppler signals. Owing to the small penetration depth and high transducer frequency, the TEE probe can provide exceptionally detailed views that are even useful for surgical decision making. The real-time 3D-capable probes further improve the application to TEE.

The risk of TEE is less than that of other endoscopic procedures, since biopsy samples are not obtained. Generally no problems will arise when standard precautions are followed.

The examination can be done with or without sedation (e.g., 2–10 mg midazolam) and is particularly easy to perform intraoperatively and in ventilated intensive-care patients. The tolerance of the probe is further improved when the nasal route is chosen. The main limiting factors are esophageal strictures, tumors, and diverticula. The transesophageal endoscope can be used in all situations where an endoscope can be introduced.

TEE is appropriate in acute emergency situations, critically ill patients, and intraoperative imaging. The Swan–Ganz catheter is used less frequently since the advent of TEE. New insights have been gained into the pathophysiology of acute aortic syndrome, and new discoveries have been made regarding prosthetic valves, endocarditis, and pulmonary embolism. Transesophageal echocardiography has become a standard procedure in intensive care units. TEE is a useful aid for management in critically ill patients. Intraoperative ultrasound is also used to direct surgeons in valve reconstructions, endoscopic procedures, and congenital heart disease.

Miniaturized endoscopes can also be passed transnasally. Pediatric probes are commonly used for this purpose. These probes can even be introduced at drainage sites to monitor cardiac function during the postoperative period and nowadays in neonates.

Intraoperative Echocardiography

Echocardiography can be performed intraoperatively using a transesophageal, an epicardial, or an epiaortic approach. Epicardial scanning is used mainly to detect diseases of the ascending aorta and may function as a “third eye” for the surgeon.

An interesting innovation is postoperative subcostal ultrasound using a drain for probe access.

Intracardiac Echocardiography

Ultrasound catheters with a built-in single mechanical rotating element (9 MHz, 9 Fr catheter) or phased-array transducer (5.5–10 MHz, 10 Fr catheter) are available for intracardiac and intravascular echocardiography. The phased-array probe can in addition provide flow information. The transducers have a resolution of 100–150 µm. Ultrasound catheters are introduced over guidewires.

Especially promising is a new 8 Fr catheter with a linear transducer array for longitudinal scanning of the heart and vessels. Because the catheter itself is steerable in three planes, it can provide detailed, high-resolution information. The new intravascular ultrasound probe allows flexible steering in all directions (**Fig. 2.9**), eliminating the need for a guidewire. The aorta can be imaged by scanning from the inferior or superior vena cava, or the probe can be advanced into the aorta itself. This device is particularly useful for directing interventional procedures with less radiation exposure, such as repairs of atrial septal defects and patent foramen ovale, intra-aortic fenestration, and intra-aortic or intracardiac biopsy. Transseptal puncture is

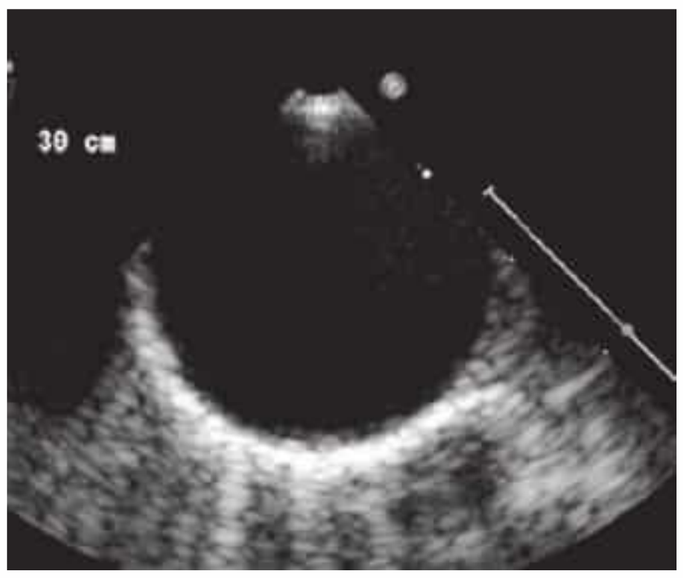

also facilitated by intracardiac echocardiography. The disadvantages of TEE for such applications as imaging of the ascending aorta are not found for intracardial ultrasound.

Examination Techniques

Transthoracic Echocardiography

An optimal transthoracic echocardiographic examination requires imaging in the left lateral decubitus position, as this moves the heart closer to the chest wall and gives better access for scanning the parasternal and apical planes.

The supine position is best for suprasternal and subcostal echocardiograms. From each transducer position, longitudinal and transverse views are obtained by angulation and rotation of the transducer (**Fig. 2.10**). The gray-scale and gain settings should be optimized to obtain the best delineation of interfaces, which is provided in newer systems automatically. Images are acquired at end-expiration with simultaneous ECG monitoring. 2D echocardiography also directs the orientation of M-mode echocardiograms as well as Doppler and color Doppler imaging.

Transesophageal Echocardiography

The preparations for TEE are the same as for gastroscopy. The patient should be fasting for at least 4 hours and receives local pharyngeal anesthesia. Sedation with midazolam, propofol, or a similar agent is recommended. An IV line is placed and heart rate, blood pressure, and oxygen saturation are continuously monitored. The ultrasound probe is fitted with a bite block to prevent probe damage. A rubber sleeve provides electrical isolation and prevents infections. The echo probes must be stored under sterile conditions. The procedure should be explained to the patient and informed consent should be obtained on the previous day, but the examination can be done immediately in an emergency situation.

After the echo probe has been passed into the esophagus, it is first advanced to the gastric level to obtain transverse and longitudinal scans of the left ventricle and right ventricle. It is then drawn back into the esophagus and maneuvered in transverse and longitudinal planes to identify the superior and inferior vena cava and the coronary sinus.

Next the operator scans the right atrium and right atrial appendage as well as the tricuspid valve and right ventricle. A longitudinal section displays the right ventricular outflow tract with the pulmonary valve and main pulmonary trunk. The pulmonary veins are located first in transverse and then in longitudinal sections, and the left atrial appendage is identified. Next the mitral valve and left ventricular inflow tract are imaged in transverse and longitudinal planes, followed by the left ventricular outflow tract and the aortic valve. The probe is withdrawn further to image the ascending aorta, the origin of the coronary arteries, the main pulmonary artery trunk, and the right pulmonary artery. It is more difficult to image the left

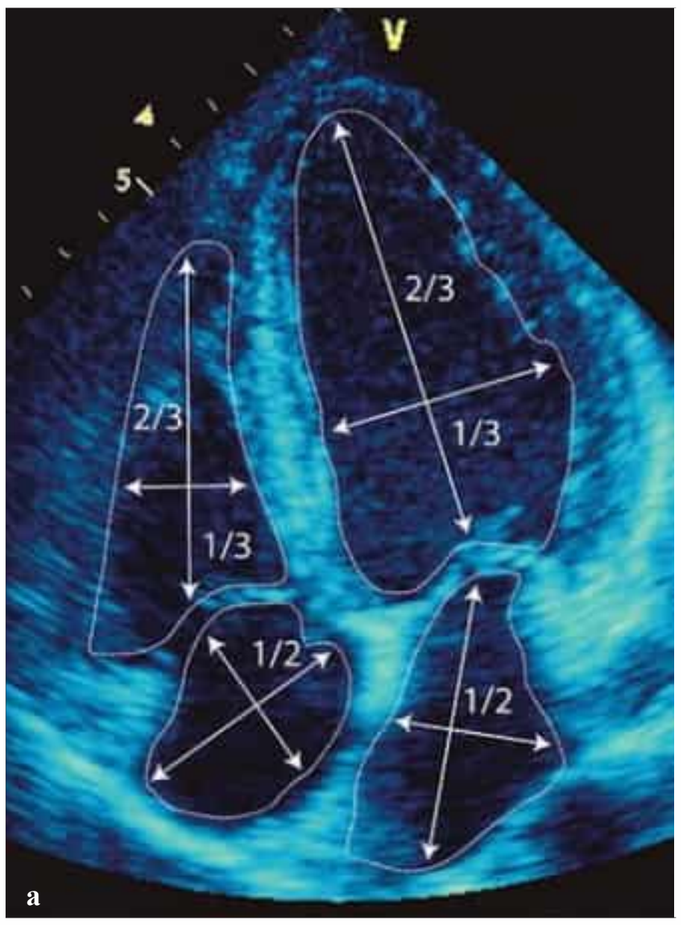

pulmonary artery and right pulmonary veins owing to the interposition of the trachea and left main bronchus.

Rotating the probe to scan behind the heart brings the descending thoracic aorta into view. That vessel is surveyed in a series of transverse and longitudinal sections (measured in centimeters aboral distance) from the stomach to the aortic arch, scanning as far as the origin of the subclavian artery. The ascending part of the aortic arch is a "blind spot" not accessible to transesophageal scanning owing to interposition of the trachea.

Quantification Using M-Mode and 2D Echocardiography

M-Mode Echocardiography

Echocardiography is a technique that can yield not only qualitative information but also quantitative data related to dimensions and temporal relationships. Two-dimensional echocardiography provides spatial orientation and guidance for orthogonal scan alignment that avoids erroneous measurements based on tangential planes of section.

The reference values for M-mode echocardiography are listed in **Table 2.1**.

Despite the availability of 3D echocardiography, M-mode echocardiography is still the most widely used technique for the determination of left ventricular muscle mass, both clinically and in research studies.

The diastolic diameter of the left ventricle measured in the short-axis view provides the basis for calculating the LV volume and LV myocardial mass.

Volume (V) of the left ventricle:

$$V = (\pi/6)L \times D^2$$

Assuming that the ventricle has an ellipsoidal shape with $L=2D$ and taking the value of $\pi/6$ as 1.047, we can simplify the formula to:

$$V = 1.047 \times D^3$$

By adding the thickness of the posterior wall and interventricular septum (T_{PW}, T_{IVS}), we can calculate the total muscle volume of the left ventricle (**Fig. 2.11**).

The ventricular volume can be subtracted from the total volume to obtain the LV muscle mass:

$$\text{Myocardial volume} = 1.047\,(D + T_{PW} + T_{IVS})3 - D^3 - 13.6/m_2\,\text{BSA}$$

$$\text{LV mass (grams)} = (1.04 \times \text{myocardial volume}) \times 0.8 + 0.6$$

where 1.04 g/mL is the specific gravity of the myocardium and 0.8 is the correction factor.

Normal values for the **left ventricular muscle mass:**

- $<134\ g/m^2$ in males
- $<110\ g/m^2$ in females

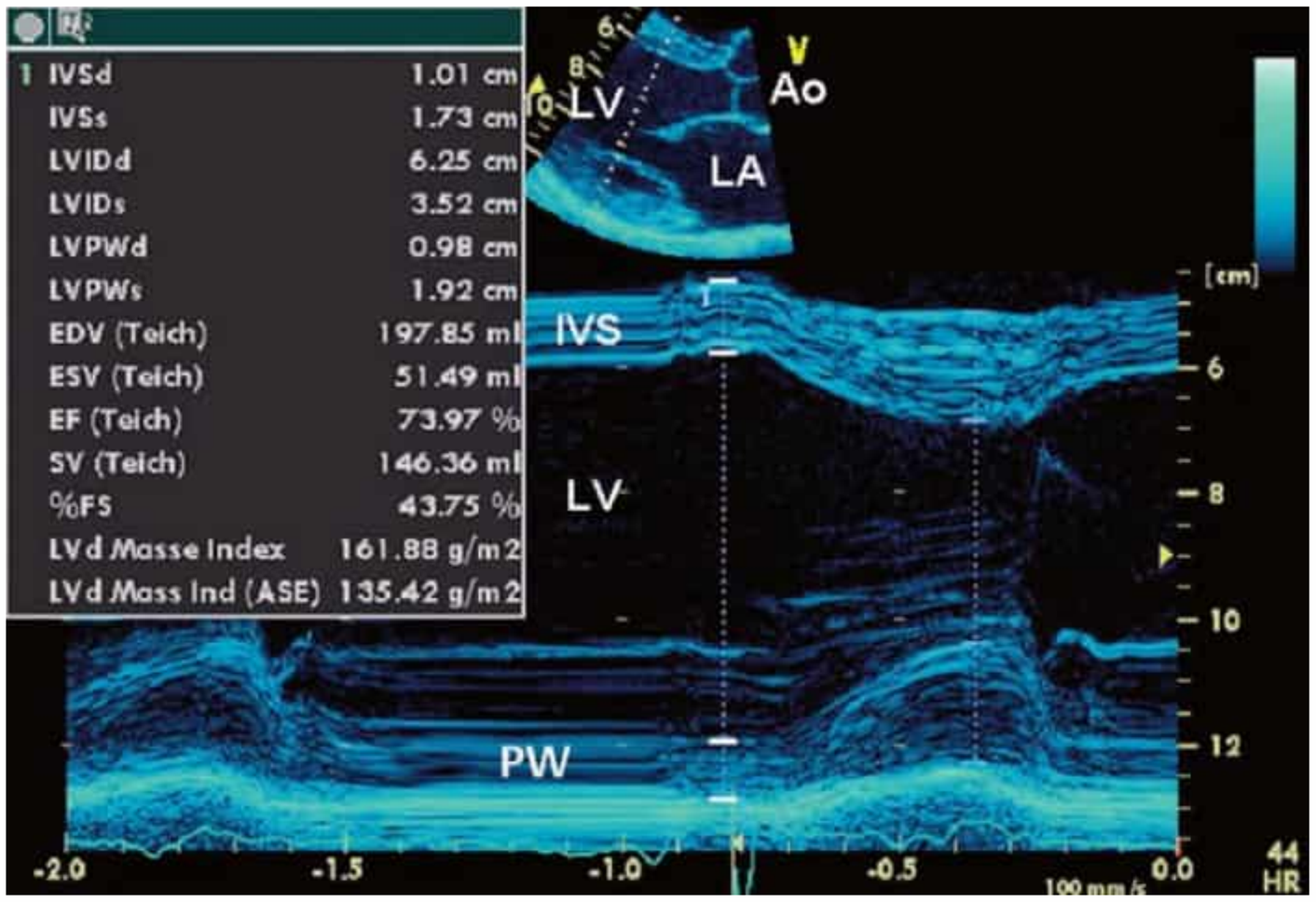

Fig. 2.11 M-mode echocardiogram of the left ventricle. The bars indicates the borders used in the Penn method of calculating LV muscle mass. This method is based on the thickness of the ventricular septum and posterior wall. It excludes the endocardial and pericardial echo thicknesses, which are included in diameter measurements for the calculation of LV volume.
Teich = Teichholz formula,
ASE = American Society of Echocardiography,
IVS = intervertricular septon,
LVID = left ventricular diameter,
LVPW = LV Posterior Wall,
EDV = end-diastolic volume,
ESV = end-systolic volume,
SV = stroke volume,
FS = fractional shortening,
d = diastole,
s = systole.

Two-Dimensional Echocardiography

Two-dimensional echocardiography is a routine tool in cardiac testing. Diameters can be precisely determined (**Figs. 2.10, 2.12**) and fractional shortening can be calculated, especially when the endocardium is optimally delineated in plain images or after contrast administration.

It is important to note that in many cases an apical transducer position will not insonate the cardiac apex, but will scan a site above the anatomical apex at the level of the left ventricular outflow tract (**Fig. 2.13**). This results in tangential scan planes that tend to underestimate volume and overestimate the myocardial muscle mass.

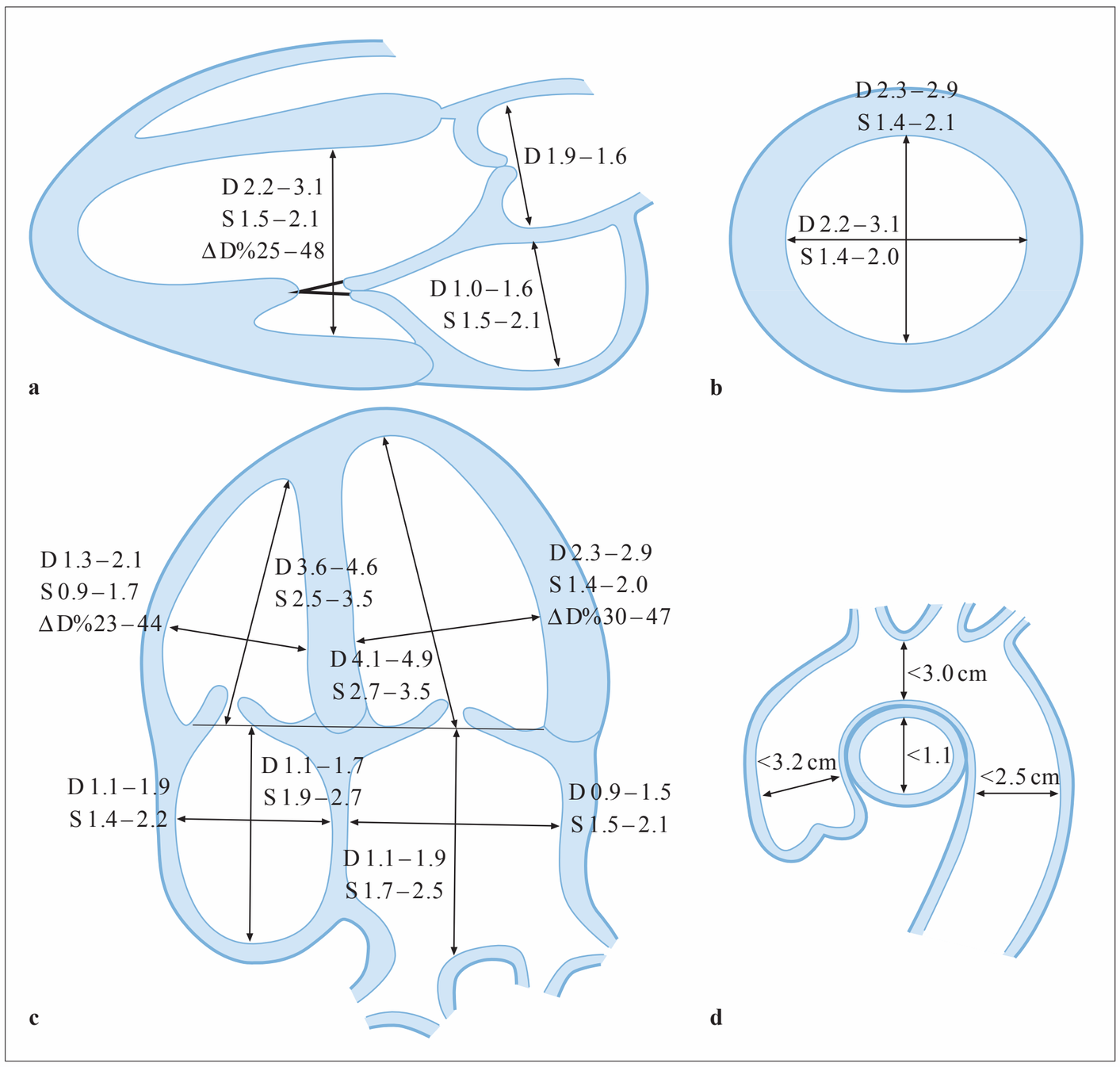

Fig. 2.12 a–d Determination of cardiac and aortic diameters (cm^2) in various scan planes. Values given corrected for body surface area (m^2).

Volume of the Left Ventricle

The mathematical model for volume calculation is an ellipsoid of revolution. The volume of the left ventricle is best determined using the disk summation method in one or two planes in order to calculate the volume of an ellipsoid of revolution. This is also called the "modified Simpson method" in the literature, although there is no mathematical connection with Simpson's rule for volume determination using a summation of trapezoids. In the disk summation method (**Fig. 2.14**), the cross-sectional area of the ventricle is determined in one or more planes and its volume is calculated from the thickness of the disks. The more disks are used, the more accurate the volume determination. The biplanar method is superior to the single-plane method. Each ventricle should be divided into at least 12 transverse disks.

The area–length method is less accurate than the disk summation method. The ellipsoid method is even less accurate.

Table 2.2 lists the reference values and normal limits for left ventricular volume determination based on 2D echocardiography.

Table 2.2 Reference values for left ventricular volumes and ejection fraction

Author	N	Methods	EDV	ESV	EF
			(mL/m^2)	(mL/m^2)	(%)
Triulzi et al. 1985	62	A_2/AL method	70 ± 26	25 ± 13	64 ± 10
	55	$A_2 + A_4$/biplane	73 ± 21	28 ± 11	62 ± 8
	39	$A_1 + A_2$/biplane	71 ± 24	23 ± 11	68 ± 8
	52	$A_2 + A_4$/cylinder	84 ± 18	28 ± 9	67 ± 7
Wahr et al. 1983	52	Simpson's rule	55 ± 10	18 ± 6	67
Erbel et al. 1985	55	$A_1 + A_2$/biplane disk summation	M: 66 ± 8 F: 60 ± 12	26 ± 5 25 ± 7	59 ± 6 58 ± 6

A_1 = A plane, longitudinal scan = RAO scan.
A_2 = B plane = 2-chamber view.

Volume of the Right Ventricle

Right ventricular volume is more difficult to determine because the right ventricle is not a rotational ellipsoid but a somewhat flattened, shell-shaped structure that abuts the left ventricle. The biplane disk summation method is often used in the literature but is imprecise. A new type of calculation is the subtraction method, in which the total volume of the left and right ventricles including the interventricular septum (IVS) is determined, and the volume of the left ventricle and IVS is subtracted from the whole.:

$$RV = (LV + IVS + RV) - (LV + IVS)$$

Three-dimensional echocardiography has helped to reduce the problem of geometry in the determination of left and right ventricular volumes, but does not eliminate the fundamental problem of the underestimation of ventricular volumes.

Volume of the Left Atrium

The determination of left atrial (LA) volume has proved particularly important in recent years, as the LA volume has been identified as a risk factor for atrial fibrillation and cardiovascular morbidity and mortality. It is not enough to determine the diameter alone, as this underestimates the longitudinal extent of the atrium. The disk summation method and the area–length method can both be used (**Fig. 2.15**) in order to take into account the 3D structure of the left atrium. Additionally, an ellipsoid method has been published that does not require contouring of the atrium:

$$V_{LA} = (\pi/6) \times D \times L \times S$$

where *D* is the diameter of the left atrium in the parasternal M-mode view, *L* is the longitudinal dimension of the atrium in the four-chamber view, and *S* is the transverse dimension in the apical long-axis view.

Three-dimensional echocardiography can also be used for the determination of left atrial volume.

Normal value: < 30 mL/m^2 BSA.

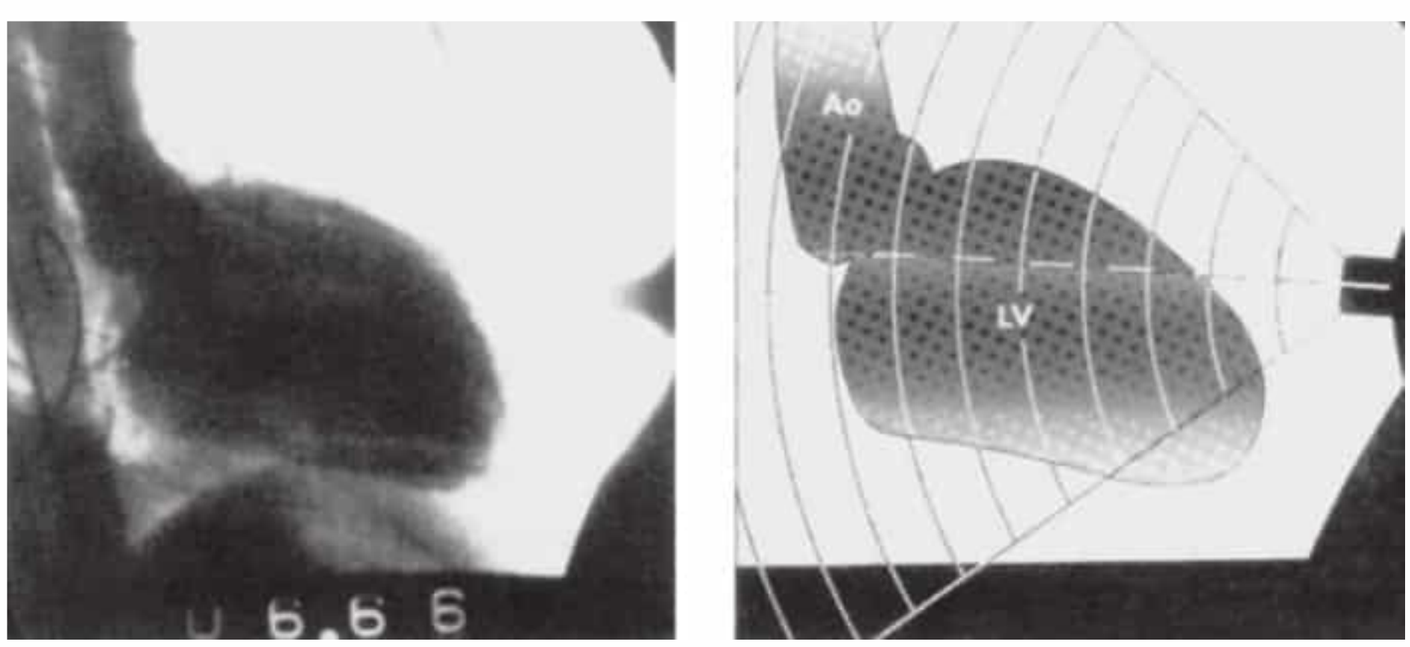

Fig. 2.13 LV angiogram illustrates the transducer position for apical long-axis scanning of the heart, resulting in a tangential plane of section (right panel).

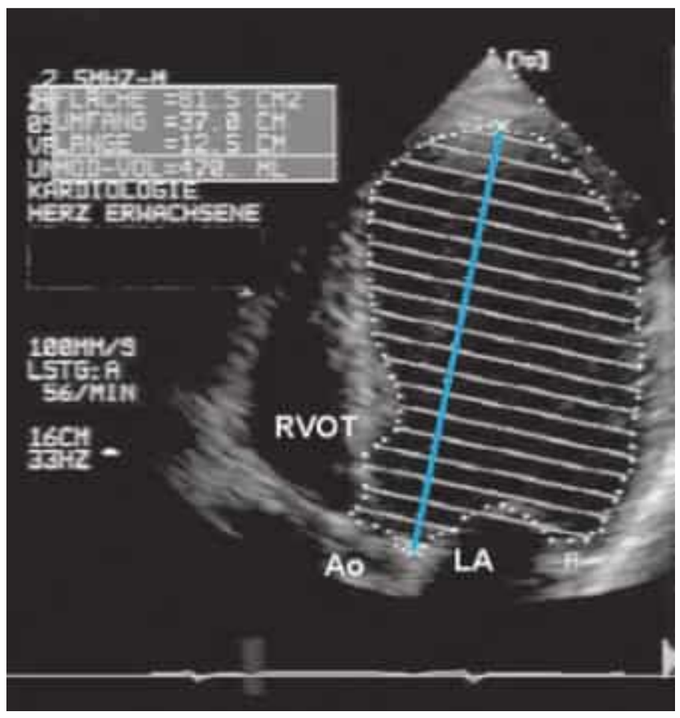

Fig. 2.14 Illustration of the method of disks (disk summation method) for determining left ventricular volume.

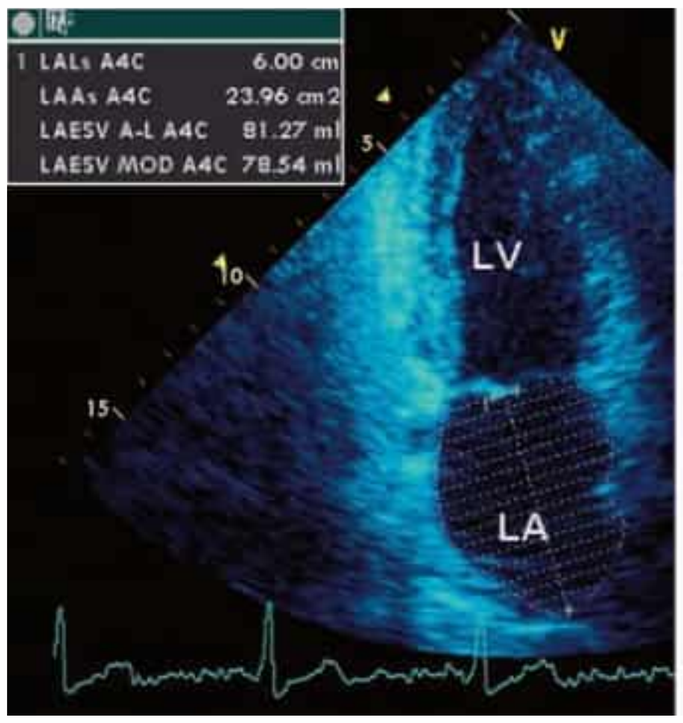

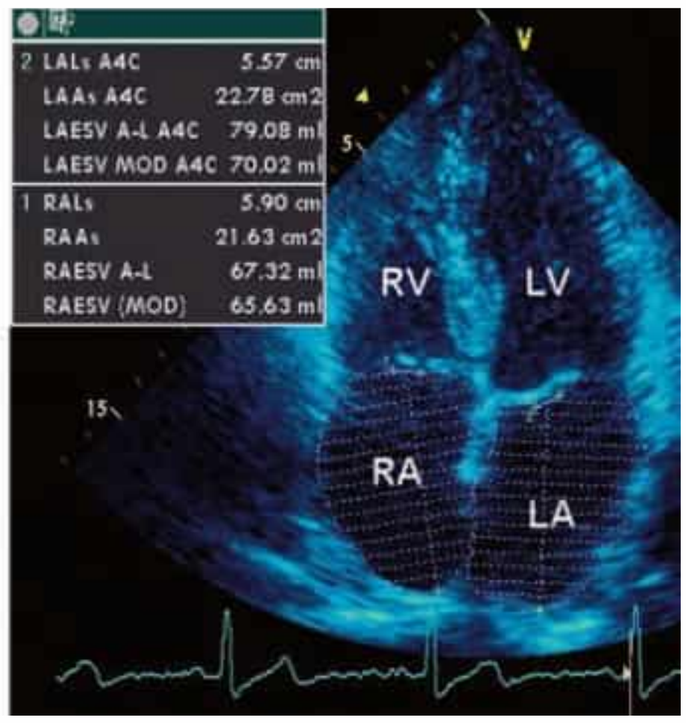

Fig. 2.15 Illustration of left and right atrial volume determination at end systole.

Principles of Doppler Echocardiography

Doppler echocardiography is based on the principle of the phase shift that occurs in ultrasound waves that encounter a moving object. The degree of the phase shift depends on the velocity of the moving object and is directly proportional to it. If the object is moving toward the transducer, the ultrasound signals move closer together; if it is moving away from the transducer, the signals are spaced farther apart.

$$\Delta f = \frac{2f_t \times v \times \cos\theta}{c}; \quad v = \frac{c \times \Delta f}{2f_t \times \cos\theta}$$

where Δf is the Doppler frequency shift, f_t is the transducer frequency, v is the velocity of the moving object, cos θ is the angle between the ultrasound beam and the direction of object motion, and c is the sound velocity in tissue.

If the measured Doppler velocity exceeds a certain value called the Nyquist limit, an apparent reversal of velocity occurs that is visible in the frequency spectrum. This means that an attempt should be made to find an optimum position for the transducer, which should have the lowest possible operating frequency and should be placed as close to the object as possible.

The Nyquist effect is familiar in "American Western" movies when wagon wheels appear to spin backward while the wagon is moving forward. This "sampling error" occurs when the wheels are turning faster than the frame rate of the movie camera.

Pulsed Doppler

Pulsed Doppler ultrasound can measure velocity at a pre-specified location within the imaging sector. This is accomplished by transmitting intermittent ultrasound pulses and receiving only the signals returned from a specified depth. One disadvantage of this method is that the velocity that can be detected is strictly limited by the Nyquist frequency. This problem has been somewhat reduced by the use of high pulse transmission frequencies combined with filters that can separate high-amplitude low-velocity signals in the tissue from Doppler flow signals with a low amplitude and high velocity.

Continuous-Wave Doppler

In continuous-wave (CW) Doppler, some of the transducer crystals transmit sound waves while others continuously receive the reflected ultrasound signals. CW Doppler is not subject to the Nyquist limit, but one drawback is that it measures velocity all along the ultrasound beam and not just at a designated point. It is necessary and helpful, therefore, to check the orientation of the beam in the 2D echocardiogram. CW Doppler is essential in the quantification of congenital and acquired valvular heart disease and is necessary for determining pressure gradients and contractility parameters (**Fig. 2.16**).

When flow velocity is recorded in a spectrum over time (T) and divided by the flow duration, the resulting time–velocity integral (TVI) can be determined:

$$\mathrm{TVI} = \sqrt{(\mathrm{cm})}$$

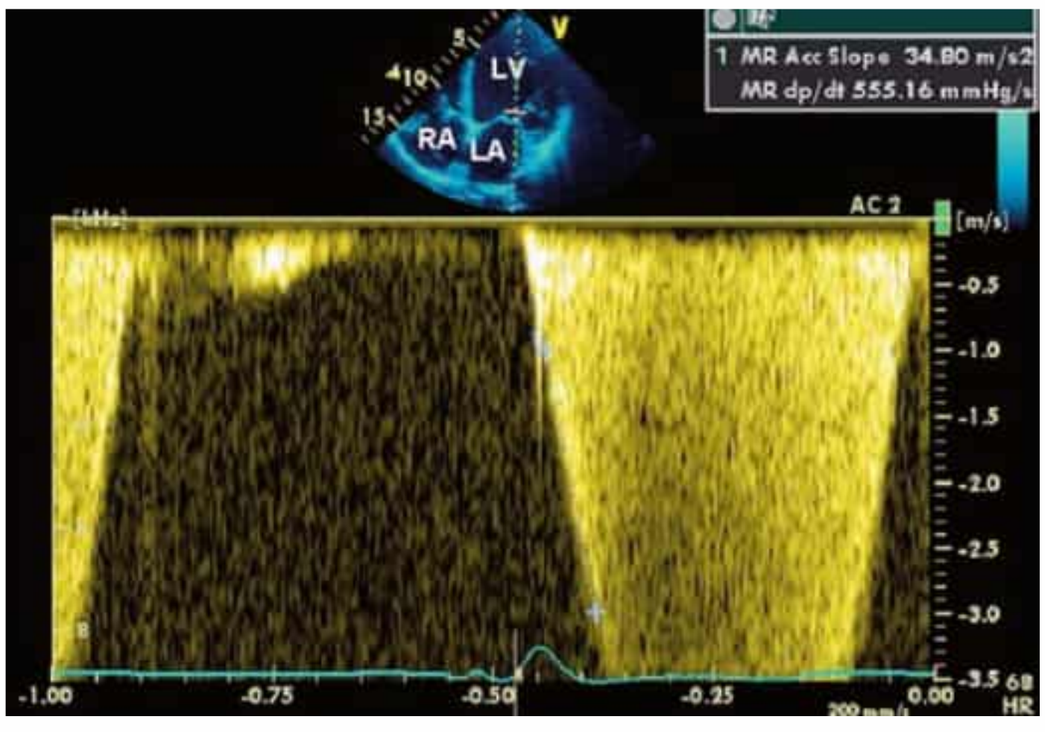

Fig. 2.16 Continuous-wave Doppler in the four-chamber view in case of mitral regurgitation (MR). The beam extends from the left ventricular apex to the roof of the left atrium. The contractility parameter (dP/dt) is calculated from the interval between the time points corresponding to velocities of 1 m/s and 3 m/s in mm Hg/s.

Modified and simplified Bernoulli equation:

$\Delta P = 4 \times V^2$

where ΔP is the pressure gradient and V is maximum flow velocity.

Color Doppler

When flow information is acquired over the entire imaging sector, color encoding can be used to indicate the velocity and direction of the flow (**Fig. 2.17**). Flow can be analyzed by superimposing the color Doppler information over the 2D echocardiographic image. Discrimination is accomplished with a special autocorrelation technique. A mosaic pattern of color pixels is used to indicate flow of increased variance (turbulence). Flow directed toward the transducer is encoded in red, and flow away from the transducer is encoded in blue. (This convention contrasts with the original astronomical observations of Edwin Hubble, who noted a red shift in stars moving away from the earth and a blue shift in stars moving toward the earth.) Three-dimensional color Doppler analysis requires a high-speed computer that can provide a frame rate of 25 images per second and more.

Color Doppler M-Mode Echocardiography

Just as M-mode echocardiography is derived from the 2D ultrasound image, it is also possible to record color-encoded Doppler information along a time axis. This information (**Fig. 2.18**) can be used to analyze temporal relationships and determine, for example, the duration of regurgitant flow across a heart valve and the velocity of the inflow pattern for assessing diastolic heart failure.

Tissue Doppler Echocardiography

Tissue Doppler echocardiography is a special form of color Doppler echocardiography in which filters are used to detect signals with high amplitudes and low velocities. This technique is used to study the patterns of cardiac wall motion and contractions over time.

The velocity of motion within the myocardium is displayed, and other structures are also visualized. This method is used to obtain information on global and regional myocardial function and synchronicity. Individual regions can be interrogated by determining pulsed or color Doppler velocities within the myocardium. Tissue Doppler is limited by its angle dependence.

Tissue Doppler can identify and differentiate structures based on their motion patterns:

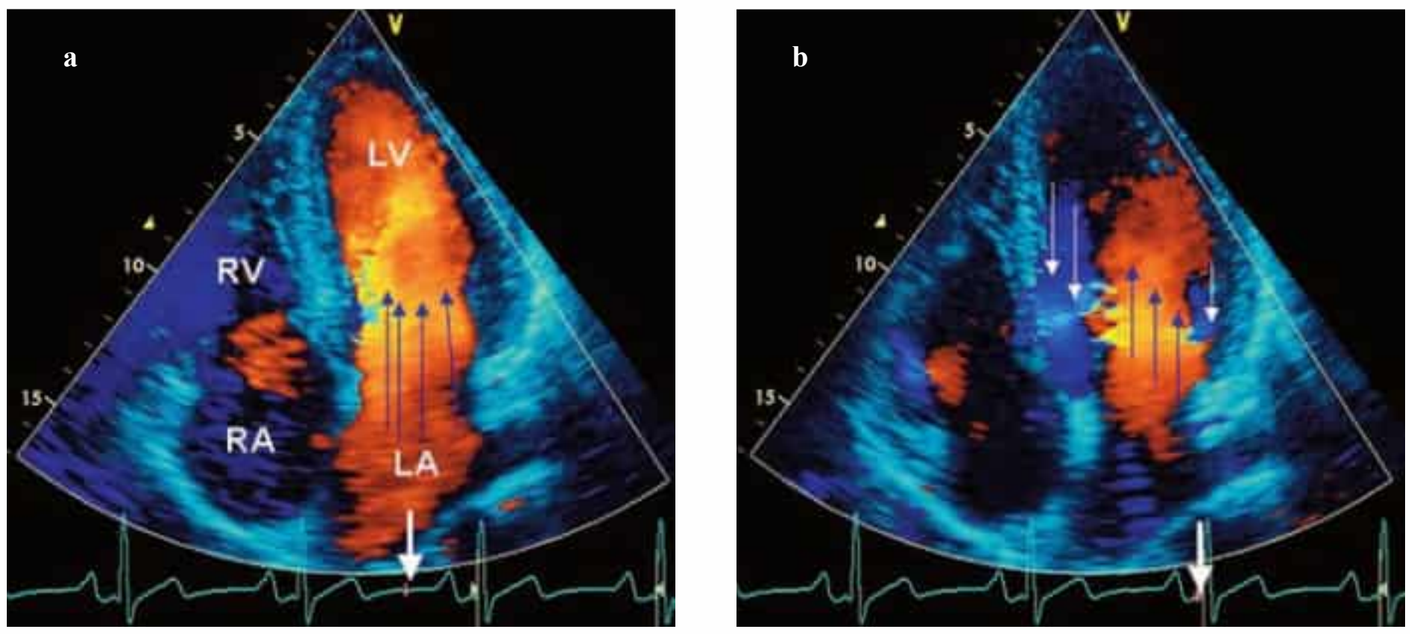

Fig. 2.17 a, b Color Doppler images acquired during rapid ventricular filling (E wave, **a**) and atrial filling (A wave, **b**). Aliasing causes a color reversal in the left image but is absent at the lower velocity in the right image. The arrow indicates the phase of the cardiac cycle in the ECG trace.

- **Incoherent motion:** motion unrelated to the cardiac cycle or cardiac structures (**Fig. 2.19**). Typical of vegetations, free-floating thrombi, and Chiari network.
- **Coherent motion:** temporal phase shift between tissue and abnormal structures such as thrombi and tumors (Newton's law relating to mass inertia).
- **Concordant (parallel) motion:** wall thickening, intramural hematomas, and posttraumatic valvular disease move parallel to cardiac structures with no time lag.

A recent innovation in tissue Doppler imaging is to display the stress–strain relationship. This feature takes into account myocardial fiber angle and shortening and permits an exceptionally detailed analysis of myocardial function and ventricular synchrony or asynchrony.

Reference Values for Doppler Echocardiography

Transvalvular Flow Velocity

Transmitral flow from the left atrium into the left ventricle is interrogated with pulsed Doppler between the mitral valve tips in the apical four-chamber or long-axis view. Transmitral flow is laminar with an approximate velocity of 1 m/s. Normally there is an early maximum flow velocity (E wave) that occurs during rapid passive filling of the left ventricle, followed by a second wave (A wave) during late ventricular filling that results from atrial contraction. Flow velocity is low during the diastasis between the two waves.

Flow velocity across the mitral valve is affected by the compliance of the left ventricle and atrium and is also subject to pericardial influences. Besides the peak velocities corresponding to the E and A waves, it is standard practice also to determine the E/A ratio and the deceleration time (DT) from the peak of the E wave to the baseline. The E/A ratio is significantly greater than 1.5 in young patients, declines with aging, and is less than 1 in elderly patients.

Table 2.3 lists the reference values for transvalvular flow velocity in adults and children.

The flow velocity in the left ventricular outflow tract is sampled at a standard site 1 cm below the aortic valve. Flow across the tricuspid valve closely resembles transmitral flow in its waveform and spectrum. The flow velocities proximal and distal to the pulmonary valve are the same as those recorded at the aortic valve.

Table 2.3 Reference values for transvalvular flow velocities (cm/s)

	Adults		Children	
	Mean value	Range	Mean value	Range
Mitral valve	90	60–130	100	80–130
Tricuspid valve	50	30–70	60	50–80
Pulmonary valve	75	60–90	90	70–110
Aortic valve	135	100–170	150	120–180
Left ventricular outflow tract	100	70–110	100	70–120

Pulmonary Venous Flow Velocity

Waveforms can usually be recorded from the right and left superior pulmonary veins (PV) in the four-chamber view using pulsed Doppler TTE/TEE. It is easier to assess pulmonary venous flow with transesophageal or intracardiac ultrasound.

In a normal pulmonary venous inflow spectrum, the S wave is higher than the D wave and a small A wave is also present (**Fig. 2.20**). When the left ventricular filling pressure increases, the S-wave velocity declines while the D-wave velocity rises, simultaneously the retrograde wave velocity of the A wave increases owing to enhanced atrial contraction. In normal individuals the amplitude of the A wave is usually less than 20 cm/s and its duration is shorter than that of the A wave in the transmitral inflow spectrum.

Normal values: $S > D$, A_{PV} shorter than A_{MV}, $A < 20$ cm/s.

Tissue Doppler Echocardiography

If there are no significant changes in left ventricular contraction and no severe regional wall-motion abnormalities, the motion and velocity of the mitral valve annulus reflect the pres-

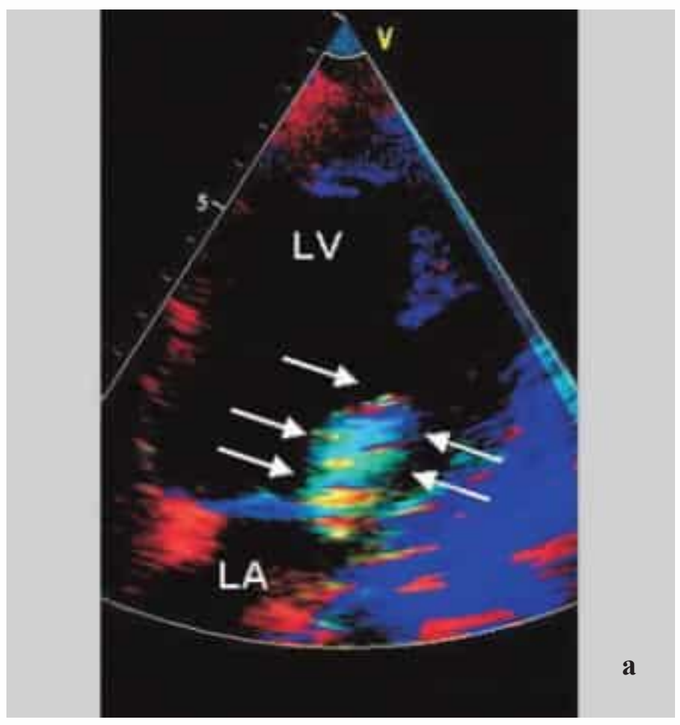

Fig. 2.19 a, b Tissue Doppler echocardiography (TDE) of abnormal structures in the heart.
a Incoherent motion of a mitral valve vegetation (arrows).
b Coherent motion of a thrombus in the left ventricular apex (arrows).

sure differential between the left atrium and left ventricle and depend very little on flow. The velocity of the mitral annulus can be determined with tissue Doppler (**Fig. 2.21**).

Normal value: >10 cm/s.

The mitral annulus moves in the apical 4-chamber view toward the left ventricular apex in systole and away from it in diastole. The systolic velocity of the lateral portion of the mitral annulus correlates very closely with the maximum rate of left ventricular pressure rise. The determination of lateral mitral annulus velocity in the 4-chamber view is very important in the analysis of diastolic ventricular function, as this velocity helps to differentiate a pseudonormalization pattern of the left ventricular inflow velocity from a normal pattern.

Color Doppler Visualization of Transmitral Inflow

The better the heart functions, the more rapid the inflow of blood from the left atrium to the left ventricle. Color Doppler M-mode echocardiography is excellent for demonstrating this flow. The upslope pattern of transmitral inflow into the left ventricle is determined as a basis for describing diastolic function. The flow velocity is calculated from the flow propagation rate in the M-mode image.

Normal value: >45 cm/s.

Strain Rate Imaging

There have been several attempts to introduce velocity, displacement, strain rate, and strain imaging based on gray scale information, using **speckle tracking** as well as other gray scale information in advanced mathematical treatments. Additionally, experimental work is being done using **tracking in RF data**, as reported by Amundsen BH (Norwegian University of Science and Technology, Trontheim).

Thus, the terms velocity imaging, displacement imaging, strain rate imaging, and strain imaging should not be used synonymously with tissue Doppler but should be used with respect to the method employed, and the qualification "by tissue Doppler," "by speckle tracking," or whatever application is used, should be added.

The general physical principles of velocity and displacement versus deformation (strain rate, strain) apply, although each method may have different limitations and pitfalls—for tissue Doppler, typically angle deviation and lateral resolution; for gray scale imaging, typically frame rate—according to Støylen.

- **Strain:** Strain means "stretching." The definition is extended to mean "deformation." The concept of strain is complex, but linear strain can be defined by the Lagrangian formula:

$$\varepsilon = \frac{L - L_0}{L_0} = \frac{\Delta L}{L_0}$$

where ε is strain, L_0 is baseline length, and L is the instantaneous length at the time of measurement. Thus strain is the extent of deformation of an object relative to its original length.

- **Strain rate:** The strain rate (indicated by the addition of a dot above the symbol for strain) is the rate at which the deformation occurs, i.e., the change in deformation or strain per unit time.

$$\dot{\varepsilon} = \frac{\Delta \varepsilon}{\Delta t}$$

The unit of strain rate is /s, or s^{-1}.

- **Myocardial strain:** The term strain was first used in relation to the heart by Mirsky and Parmley to describe myocardial deformation. Transmural strain is nothing more than wall thickening. Transmural strain rate is the same as the transmural velocity gradient, as pointed out by Støylen. The transmural strain rate is reflected by the velocity gradient, strain per time unit approximates velocity per length unit.
- **Speckle tracking:** The basic principle of speckle tracking is based on the interference of the reflected ultrasound giving rise to an irregular (random) speckled pattern (Støylen). The random distribution of the speckles ensures that each region of the myocardium has a unique pattern. The speckles follow

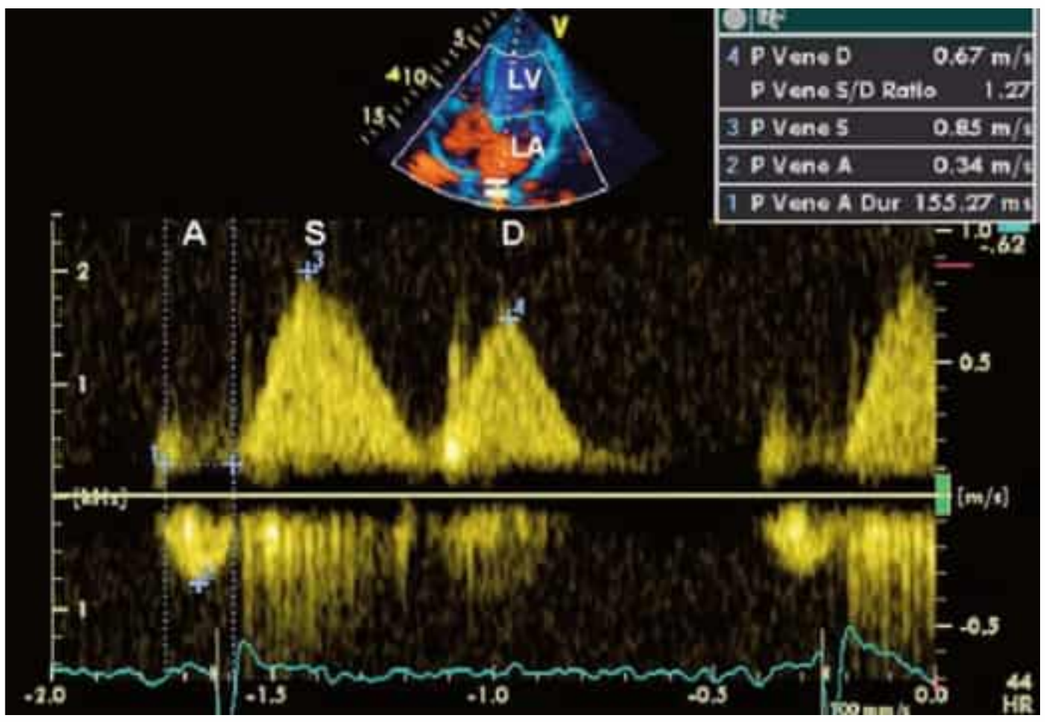

Fig. 2.20 Pulsed Doppler spectrum from the pulmonary veins (PV) shows a normal S-wave amplitude in systole that is higher than the D wave in diastole and a retrograde A wave that is <20 cm/s and is shorter than the A wave in pulsed Doppler of mitral inflow.

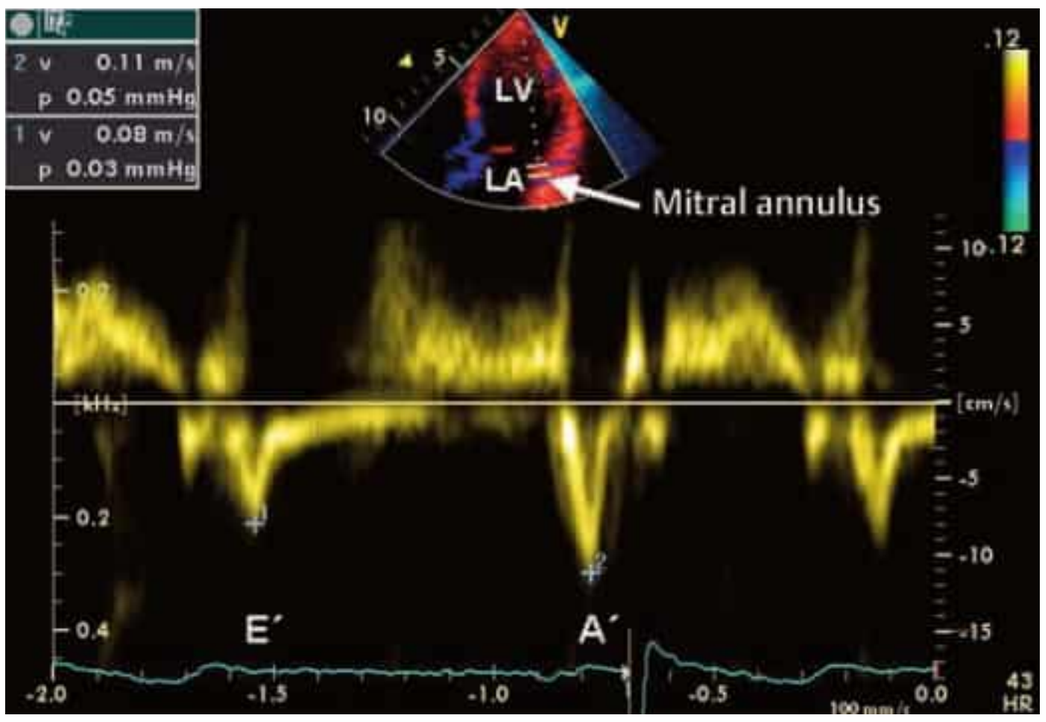

Fig. 2.21 Tissue Doppler of the lateral mitral annulus velocities in the 4-chamber view with a high A′ wave and low E′ wave.

the motion of the myocardium. As the myocardium moves from one frame to the next, the position of the speckles shifts constantly. A defined region (kernel) can be defined in one frame, and a search algorithm will be able to recognize the position within the next frame with similar pattern. Motion of one kernel can thus be measured throughout one heart cycle. Velocity can be derived from the motion curve or calculated as the movement divided by the frame interval (Støylen). With two kernels, the relative displacement per distance can be derived. This is equal to strain. One way of using this approach, is to place a defined region of interest in the myocardium at the segmental borders and measure segmental strain and strain rate directly by changes in segment length. This is true segmental strain rate, an angle independent measure, eliminating the insonation angle problems discussed by Støylen. It therefore represents true longitudinal strain.

Echocardiographic Assessment of Hemodynamics

Both M-mode and 2D echocardiography can provide information on hemodynamic abnormalities, including specific disorders (**Table 2.4**).

Table 2.4 Indirect M-mode and 2D echocardiographic signs and hemodynamic abnormalities

Echocardiographic finding	Pathology
Mitral valve leaflet flail	Aortic insufficiency
C wave during closure of mitral or tricuspid leaflets (A–C)	Increased LA or RA pressure
Systolic forward motion of mitral leaflet	LVOT obstruction or pseudo-obstruction
Premature mitral valve closure	High left ventricular filling pressure
Premature midsystolic aortic valve closure	Evidence of HOCM
Early systolic aortic valve closure	Fixed subaortic stenosis
Midsystolic pulmonary valve closure	Pulmonary hypertension
Dilated inferior vena cava with decreased inspiratory caliber change	Increased RA pressure, increased flow pressure in right ventricle
Absent A wave and systolic W shape of pulmonary valve in M-mode	Pulmonary hypertension
Diastolic collapse of the RA and/or RV	Cardiac tamponade
Abnormal (paradoxical) septal motion	CHD, previous ACVB, previous heart operation, elevated RV pressure
Early diastolic dip-plateau pattern of septal motion	Constrictive pericarditis

LA = left atrium, RA = right atrium, RV = right ventricle, LVOT = left ventricular outflow tract.

Stroke Volume and Cardiac Output

Volume flow is equal to the product of cross-sectional area (CSA) and Time velocity Integral (TVI):

$$\text{Volume flow} = \text{CSA} \times \text{V}$$

Flow velocity varies in different phases of the cardiac cycle, and therefore the instantaneous flow velocities must be integrated (sum of individual velocities = time-velocity integral, TVI) in order to calculate the total amount of volume flow.

Stroke Volume

$$\text{SV (mL)} = \text{CSA (mm}^2\text{)} \times \text{TVI (mm)}$$

Modern echo systems have software that allows them to bypass a Doppler spectral analysis of flow velocities and calculate the VTI directly. The cross-sectional area of the left ventricular outflow tract is most commonly used to calculate the stroke volume (SV), but other sites may also be used. For practical reasons, the cross-section is assumed to be circular and its area (CSA) is calculated from its diameter (*D*).

$$\text{CSA} = \pi\,(\text{D}/2)^2 = 0.785\,(\text{D})^2$$

$$\text{SV (mL)} = 0.785\,(\text{D})^2 \times \text{TVI}$$

The cardiac output (CO) is determined by multiplying heart rate (HR) by stroke volume:

$$\text{CO (L/min)} = \text{SV (mL)} \times \text{HR (bpm)}$$

The cardiac index (CI) is defined as the cardiac output divided by body surface area (BSA):

$$\text{CI (L/min/m}^2\text{)} = \text{CO (L/min)} / \text{BSA (m}^2\text{)}$$

Regurgitant Volume

Volumetric Method

The total volume flow (*Q*) that passes through an incompetent valve consists of the SV and the regurgitant volume:

$$\text{Regurgitant volume} = \text{Q} - \text{SV}$$

The regurgitant volume in aortic insufficiency is calculated by subtracting the mitral valve inflow volume from the total volume determined in the left ventricular outflow tract.

In cases of severe aortic regurgitation, the pressure difference between the aorta and left ventricle falls rapidly during diastole, and this is associated with an increase in deceleration velocity. The degree of regurgitation can be calculated from the steepness of the decline in flow velocity.

The regurgitant fraction is the regurgitant volume expressed as a percentage:

$$\text{Regurgitant fraction (\%)} = (\text{Q} - \text{SV}) / \text{Q} \times 100\,(\%)$$

Proximal Isovelocity Surface Area (PISA) Method

The total regurgitant volume is calculated from the effective regurgitant orifice area (EROA) and the velocity–time integral (**Fig. 2.22**):

$$\text{Regurgitant volume} = \text{EROA} \times \text{VTI}_{\text{reg}}$$

EROA is determined with the PISA method. All blood flowing through the orifice area shows a uniform velocity (isovelocity) contour at one site. The flow can be calculated from the distance of this curve from the valve orifice and the surface area of the hemisphere ($2\pi r^2$). The product of surface area and aliasing velocity (V_{ai}) yields the instantaneous flow volume:

$$\text{Volume flow} = 2\pi r^2 \times V_{ai}$$

EROA is now calculated by dividing the volume flow by the regurgitant velocity.

Mitral Regurgitation

$$\text{EROA} = \frac{\text{Volume flow}}{V_{MR}} = 2\pi r^2 \frac{V_{ai}}{V_{MR}}$$

$$\text{Regurgitation volume} = 2\pi r^2 \frac{V_{ai}}{V_{MR}} \ \text{VTI}_{MR}$$

Aortic regurgitation is calculated in a similar way.

Shunt Flow

The relationship between pulmonary and systemic blood flow is important for estimating the degree of a shunt. The magnitude of intracardiac shunt flow is expressed as the ratio of pulmonary circulation (Q_P) to systemic (Q_S) circulation. Q_P is calculated over the right ventricular outflow tract $(\text{CSA} \times \text{TVI})_{\text{RVOT}}$, while Q_S is calculated over the left ventricular outflow tract $(\text{CSA} \times \text{TVI})_{\text{LVOT}}$:

$$Q_P/Q_S = (\text{CSA} \times \text{TVI})_{\text{RVOT}} / (\text{CSA} \times \text{TVI})_{\text{LVOT}}$$

Pressure Gradients

Doppler flow velocities enable us to calculate instantaneous pressure gradients across stenotic valves and pressure-limiting defects. These pressure gradients (ΔP) can be calculated using the Bernoulli equation:

$$\Delta P\,(\text{mmHg}) = 4 \times V^2$$

V is the maximum flow velocity in m/s at the stenotic valve and is determined with CW Doppler. The Doppler-measured pressure gradients represent the maximum pressure differential and are usually smaller than the peak-to-peak pressure changes determined during catheter withdrawal in a cardiac catheterization laboratory. As a result, the mean pressure gradient correlates better with hemodynamic measurements in the catheterization laboratory. The maximum and mean pressure gradients can be calculated without having to analyze the Doppler spectral waveform. The equation can only be used when a stenosis is present, otherwise the calculations are misleading.

Valve Orifice Area

Three methods are available for calculating valve orifice area: pressure half-time, continuity equation, and PISA analysis in addition to the planimetry of the valve area in cross-sectional images.

Pressure Half-Time

In mitral stenosis, the pressure gradient is highest during opening of the mitral valve and falls continuously thereafter (**Fig. 2.23**). The fall in transmitral pressure can be expressed as the time it takes for the pressure gradient across the mitral valve to fall to half its maximum value—the pressure half-time (PHT, $P_{1/2}$). This also represents the time for the corresponding fall in flow velocity.

$$P_{1/2} = \tfrac{1}{2} P_{max} = 4(V_{t1/2})^2 - \tfrac{1}{2}\ 4\ (V_{max})^2$$

$$V_{t1/2} = V_{max} / \sqrt{2} \qquad \text{or} \qquad V_{max}/1.4$$

The pressure half-time is calculated from the deceleration time and is always 0.29 of the DT (time constant obtained by the conversion of velocity to pressure).

$$\text{PHT} = 0.29\ \text{DT}$$

Mitral valve orifice area (MVA): The area of the mitral valve orifice is calculated with the aid of an empirically derived time constant:

$$\text{MVA}\,(\text{cm}^2) = 220/\text{PHT} = 220/(0.29\ \text{DT})$$

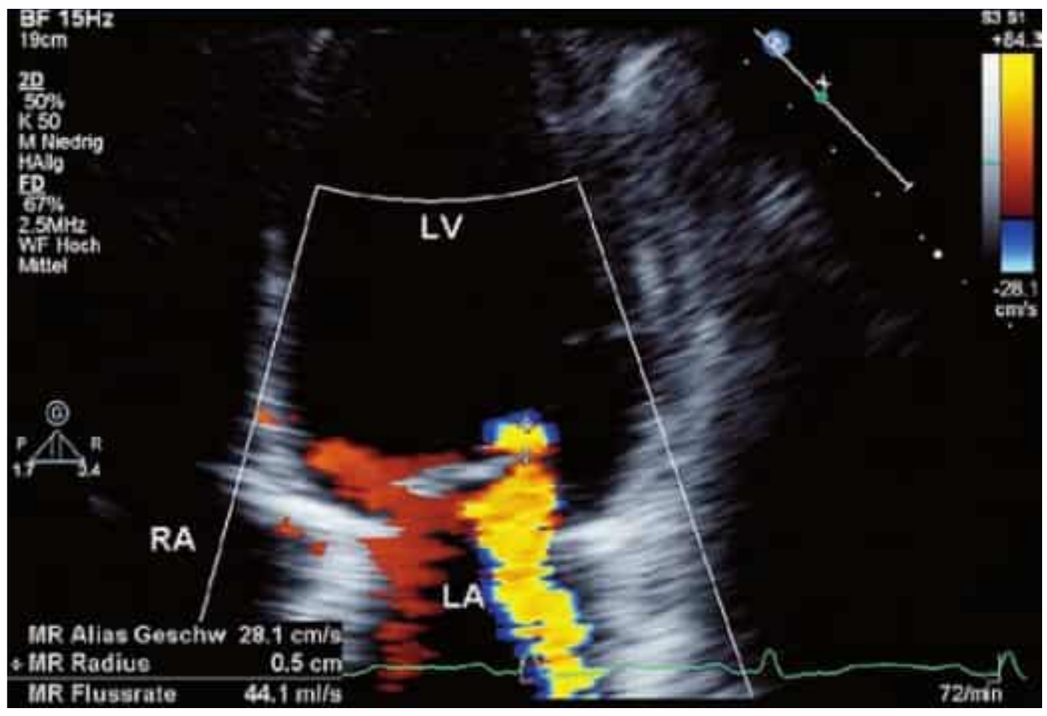

Fig. 2.22 PISA method for the quantification of regurgitation.

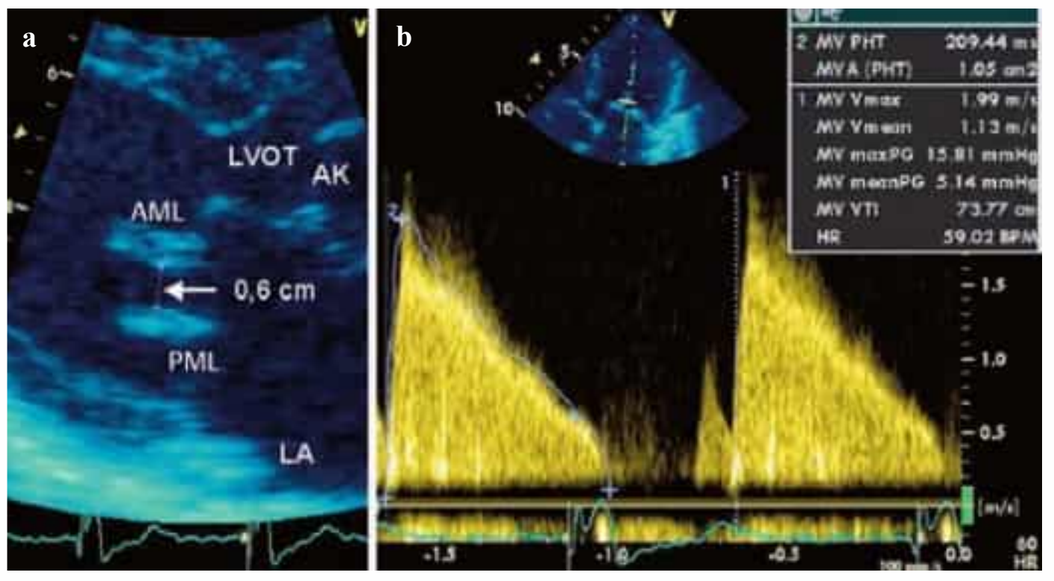

Fig. 2.23 a, b Pressure half-time (PHT) measurement of the mitral valve (MV). **a** Mitral stenosis. **b** Gradient calculated from the PHT.

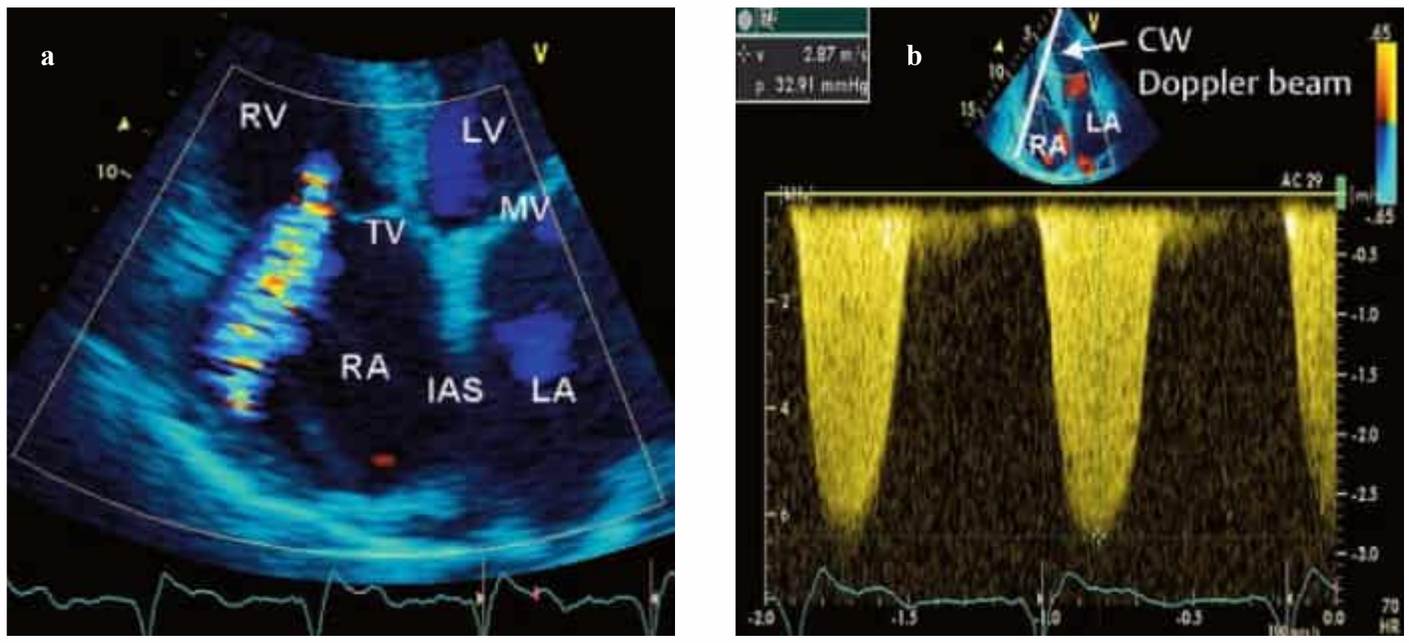

Fig. 2.24 a, b CW Doppler imaging of the tricuspid valve (TV). The pressure gradient is calculated from maximum flow velocity. With the addition of right atrial pressure (RA), the systolic ventricular pressure of the RV is determined. In the absence of pulmonary stenosis (very rare), the systolic pulmonary arterial pressure CPAs) can be determined with this formula: TV gradient 33 mmHg + RA = PAs .

Continuity Equation

Inertial mass determines the principle by which the equation is used to calculate the cross-sectional area (CSA) of a valve orifice.

$$CSA_1 \times TVI_1 = CSA_2 \times TVI_2$$

The flow velocity–time integral proximal to the stenosis (TVI_1) and within the stenosis (TVI_2) and the CSA proximal to the stenosis (CSA_1) are determined and substituted into the equation to calculate the area of the stenosis (CSA_2):

$$CSA_2\ (cm^2) = CSA_1 \times TVI_1/TVI_2 = SV/TVI_2$$

The orifice area of the stenotic aortic valve can be calculated as SV/TVI_{AV} and that of the mitral valve as SV/TVI_{MV}.

PISA Method

The PISA method can also be used to calculate the mitral valve orifice area:

$$MVA = 2\pi r^2 \frac{V_{ai}}{V_{max}\ (MV)} \times (\alpha/180°)$$

When there is an angle α between the inflow direction and beam direction, a correction factor (α/180°) is used.

Intracardiac Pressures

Doppler echocardiography can be used as an alternative to cardiac catheterization for the assessment of intracardiac hemodynamic variables. This requires optimum insonation conditions and a parallel beam alignment relative to the blood flow (**Fig. 2.24**).

Right Ventricular Pressure

Right ventricular systolic pressure can be determined by analyzing the systolic regurgitant jet across the tricuspid valve. The simplified Bernoulli equation is used to calculate RV pressure. The estimated right atrial filling pressure (RAP) is added (**Fig. 2.24**):

$$RVSP = 4(V_{max})^2 + RAP$$

The RAP can be estimated taking into account the size of the inferior vena cava and the collapsibility during inspiration (**Table. 2.5**):

This principle is the basis for all intracardiac pressure measurements. The Doppler signal can be enhanced with an echo contrast agent. Even in healthy individuals, a regurgitant flow signal, though slight, can usually be recorded during closure of the tricuspid valve.

Left Ventricular Filling Pressure

Mitral valve. A regurgitant signal can also be detected across the mitral valve (MR), and the filling pressure of the left ventricle (LVEDP) can be determined. RRs/d is the systolic or diastolic blood pressure measured at the right arm.

$$LVEDP = RRd - 4(V_{MR})^2$$

Mitral stenosis. When mitral stenosis is present, the LA pressure is also calculated with the formula

$$LAP = RRs - 4(V_{MR})^2$$

Other Calculations

Aortic insufficiency. In aortic insufficiency, the diastolic pressure reflects the gradient between the aorta and left ventricle.

$$LVEDP = RRd_{cuff} - 4(V_{ARend\ diastole})^2$$

where RRd is the diastolic blood pressure taken at the right arm.

Ventricular septal defect. In the presence of a ventricular septal defect, color Doppler can detect the jet and permit optimum alignment of the ultrasound beam. The pressure gradient is determined with CW Doppler. The following calculations are used:

$$RVSP = RRs_{cuff} - 4(V_{LV-RV})^2$$

Table 2.5 Right atrial pressure estimation

Pressure	IVC size	Collapsibility
<5 mmHg	Normal	High
0–10	Enlarged	High
10–15	Enlarged	Normal
10–20	Enlarged	Low
Unknown	Normal	Low

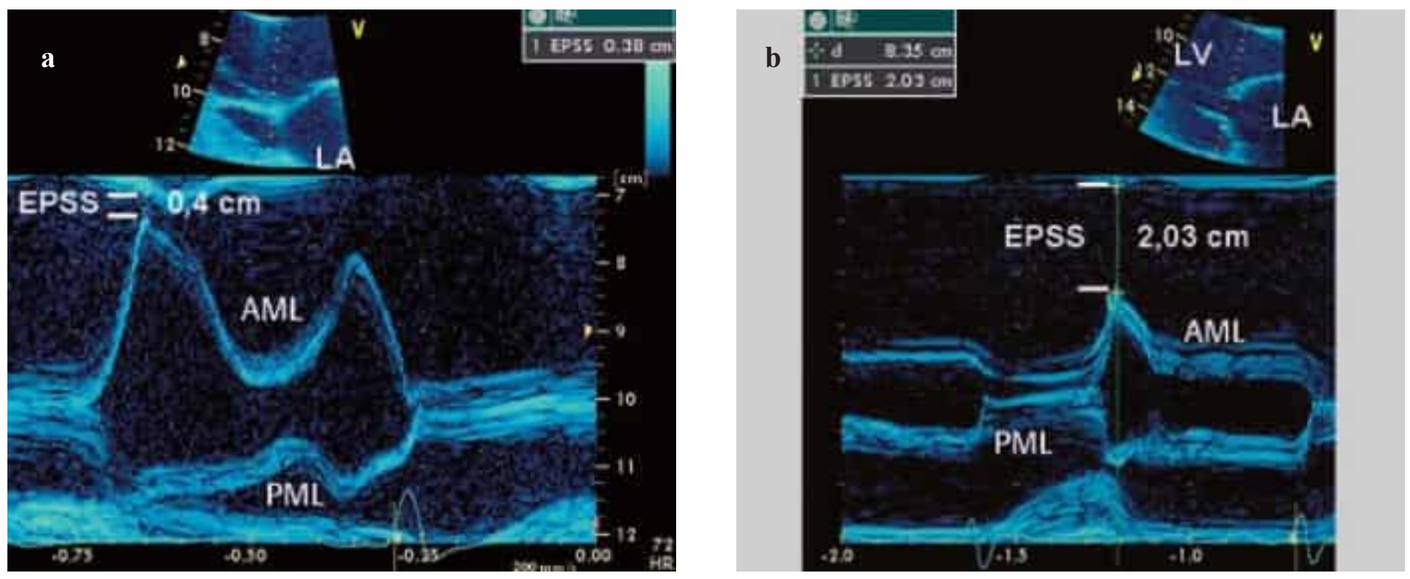

Fig. 2.25 a, b E-point separation of the mitral valve from the septum (EPSS).
a Normal finding (EPSS <0.7 cm).
b Abnormal finding in chronic myocarditis (EPSS = 2.03 cm).

where $V_{LV–RV}$ is the flow velocity across the interventricular septal defect.

Gradient in the outflow tract. With a pressure gradient in the outflow tract of the left ventricle, the following formula applies:

$$LVSP = RRs_{cuff} + LVOT\ gradient$$

Right ventricular pressure. The right ventricular pressure can be determined from the calculated left ventricular pressure:

$$RVDP = LVEDP - 4(V_{LV–RV})^2_{diast}$$

Pulmonary arterial pressure. In the absence of right ventricular obstruction, the pulmonary arterial pressure can also be calculated.

Systolic pulmonary arterial pressure: in patients with pulmonary stenosis (PS)

$$PASP = RVSP + RAP$$

Diastolic pulmonary arterial pressure: (Pulmonary artery regurgitation end-diastolic velocity) = VPR end-diastole

$$PADP = 4(V_{PR\ end\text{-}diastole})^2 + RAP$$

Assessment of Left Ventricular Function

The assessment of left ventricular function is among the most frequent indications for echocardiography. In addition to global and regional systolic function, global and regional diastolic function can also be determined.

Global Left Ventricular Function

M-Mode Echocardiography

M-mode echocardiography can provide data that are useful in the assessment of left ventricular function. **Table 2.6** lists other specific signs in the M-mode echocardiogram. The mitral valve E-point septal separation (EPSS) is illustrated in **Fig. 2.25**.

Left ventricular diameters are determined at end diastole and end systole. Two-dimensional echocardiography is used to direct orthogonal positioning of the M-mode cursor in the left parasternal long- and short-axis planes. Ventricular diameters are recorded at a standard site between the papillary muscle tip and the tip of the mitral valve leaflet.

End-diastolic diameter (EDD) = diameter at start of QRS complex

End-systolic diameter (ESD) = diameter at maximum inward excursion of the posterior wall of the left ventricle (smallest LV diameter)

It should be noted that during isovolumetric contraction the left ventricle changes from an ellipsoidal shape to a spherical shape, with an associated expansion of the region of interest. To reduce errors, the diastolic diameter is determined at the start of the QRS complex.

The diameters are used to determine the fractional shortening (FS) of the left ventricle:

$$FS\ (\%) = [(EDD - ESD) / EDD] \times 100$$

For determination of left ventricular volumes, it should be noted that these volumes are dependent on heart rate. The volume decreases by a certain amount for each 10 bpm rise in heart rate (**Table 2.7**).

The increase in ventricular wall thickness is an important contractility parameter. Wall thickening is calculated from the

Table 2.6 M-mode echocardiographic signs of LV dysfunction

A–C (point A to point C of mitral valve leaflet closure after atrial contraction)	Signs of increased left ventricular PLVED
Premature closure of the aortic valve	Obstruction of left ventricular outflow tract
Decreased systolic motion of the anterior and posterior walls of the aorta	Decreased stroke volume
Late systolic inward motion of the aortic leaflets	Reduced LV function (EF, low SV)

Table 2.7 Dependence of LV volumes on heart rate

Parameter	Change per 10 bpm	
	Normal cardiac function	Ventricular dysfunction
End-systolic volume	4 mL	6 mL
End-diastolic volume	2 mL	1 mL
Stroke volume	2 mL	5 mL
Ejection fraction	1 %	2 %

end-diastolic wall thickness (WTh_{ED}) and end-systolic wall thickness (WTh_{ES}).

$$\Delta\%WTh = \frac{WTh_{ES} - WTh_{ED}}{WTh_{ES} \times 100}$$

Determination of the left ventricular muscle mass is described on page 41.

Two-Dimensional Echocardiography

The end-diastolic and end-systolic volumes of the left ventricle are determined in the apical long-axis view, which should optimally display the left ventricular outflow tract while showing as little of the right ventricular outflow tract as possible. Both the inflow and outflow tract should appear in this long-axis view of the left ventricle. The cardiac apex should be clearly defined. It should not be rounded and should taper to the apex. A rounded apex may signify an abnormality of ventricular contraction, or it may result from a very tangential scan plane through the apex. Besides the long-axis view, the ventricle is also imaged in the two-chamber and four-chamber views to obtain optimum visualization of all segments. Remember that the anatomical apex measures only 3–5-mm thickness.

Care should be taken that the longitudinal axis of the left ventricle is parallel and centered in the imaging sector:

$$EF\,(\%) = [(EDV - ESV) / EDV] \times 100$$

where EDV is end-diastolic volume, ESV is end-systolic volume, and EF is the ejection fraction.

Doppler Parameters for the Assessment of Systolic Function

Various Doppler parameters have been proposed for the assessment of cardiac systolic function. The stroke volume and cardiac output can be determined, as can the ejection time and contractility (see Chapter 7). The flow velocity in the left ventricular outflow tract is not generally determined because it is very load-dependent. Tissue Doppler echocardiography has confirmed earlier studies with implanted markers at the basal and apical cardiac segments suggesting that the base of the heart moves toward the apex much more than the apex moves toward the base. Most contraction occurs along a line connecting the base with the apex with a center of gravity at the border from the first to the second third of this distance. The movement of the base can be measured as the movement of the mitral annulus, which has a total excursion of approximately 10–13 mm. This value is useful in the assessment of cardiac contraction.

Tei Index

The Tei index is determined by recording the mitral-valve inflow velocity and the Doppler flow profile in the left ventricular outflow tract but can also be calculated from M-mode recordings of the mitral and aortic valve. The index is calculated by determining the time from mitral valve closure to mitral valve opening, subtracting the ejection time (ET), and dividing by the ejection time. The index can be determined for both the right and left ventricles.

The reference range for a normal Tei index is 0.29–0.48 with an upper limit of 0.49 (0.4 ± 0.05).

Normal value: <0.49.

The index proposed by Tei et al. has become an essential parameter in the clinical assessment of left ventricular function. Functional changes in the left ventricle can be detected with high reproducibility. The Tei index is particularly useful for detecting functional changes relating to cardiomyopathies and cardiotoxic medications and for prognostic assessment.

A unique feature of this index is that it takes into account both systolic and diastolic intervals, making it more accurate than the determination of systolic intervals alone, which once had broad diagnostic applications.

Left Ventricular Contractility

Rate of LV pressure rise and fall. A mitral regurgitation Doppler spectrum is recorded, and the time interval between the 1 m/s and 3 m/s velocities is determined. Spectra should be recorded at 100 m/s or preferably 200 mm/s. The basis for calculation is the Bernoulli equation. When the mitral regurgitation signal is detected, the following formulas can be used to calculate the contractility parameter dp/dt_{max} and the relaxation parameter dp/dt_{min}:

$$dp/dt_{max} = 4[(V_2^2) - (V_1^2)] \times 1000/\Delta t$$

$$dp/\,dt_{max} = 4(3)^2 - 4(1)^2 \times 1000/\Delta t$$

$$dp/dt_{max}\,(mmHg/s) = 32\,000/\Delta t$$

$$dp/dt\,(mmHg/s) = 32\,000/dt$$

where dt = time interval and $32 = (4 \times 3^2 - 4 \times 1^2)$.

Normal values:

- Normal: >1200 mmHg/s.
- Borderline: 1000–1200 mmHg/s.
- Reduced <1000 mmHg/s.

The same method can be used to assess right ventricular contractility.

Assessment of Right Ventricular Function

The global function of the right ventricle is best described by the Tei index, because the complex geometry of the ventricle does not permit the reliable determination of its volume. Functional analysis of the right ventricle is based on the opening of the tricuspid valve and an analysis of the flow velocity across the pulmonary valve.

Assessment of Regional Ventricular Function

Qualitative analysis is based on the degree of wall motion or preferably on the change in wall thickness. Regional LV function can be described as follows (**Fig. 2.26**):

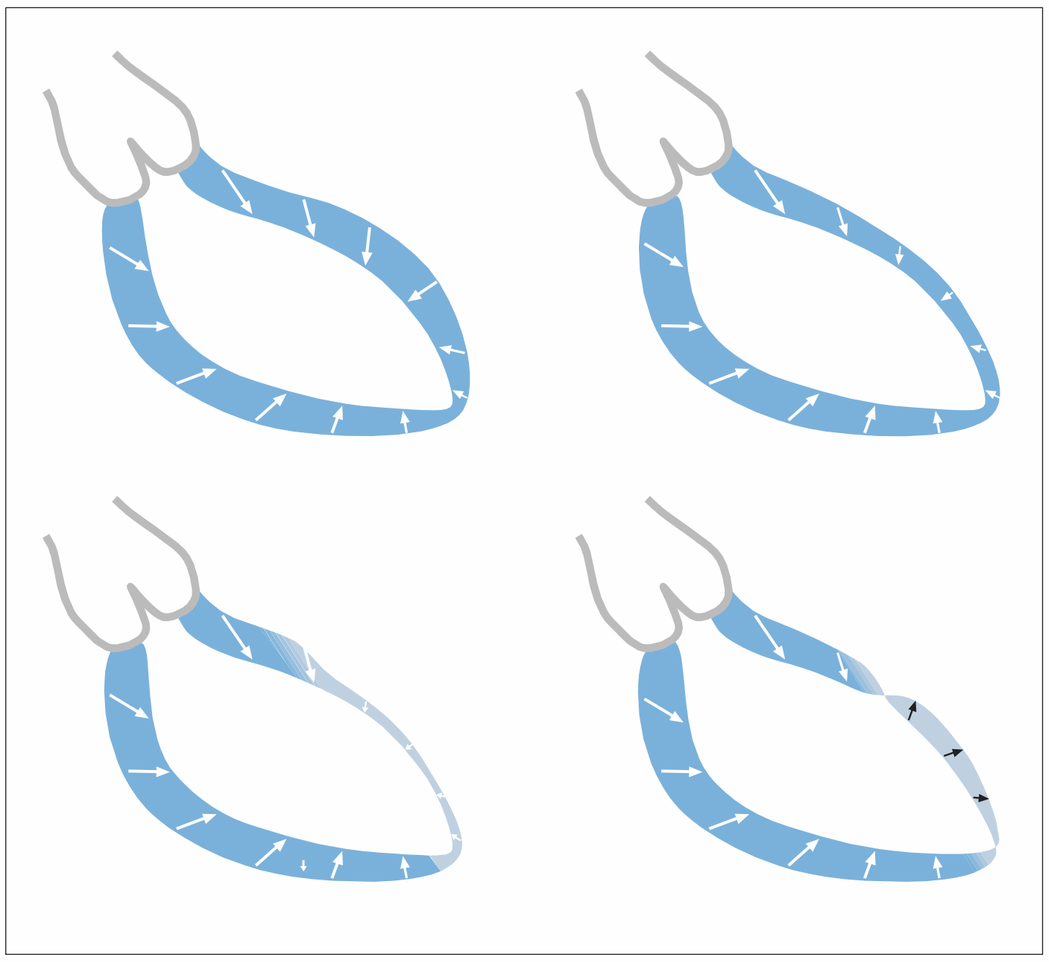

Fig. 2.26 a–d Diagram illustrating various wall-motion abnormalities. **a** Normal contraction. **b** Hypokinesia. **c** Akinesia. **d** Dyskinesia.

- Normal function = 1
- Hypokinesia = 2 (decreased contraction, less than 25 %shortening)
- Akinesia = 3 (±5% wall motion excursion)
- Dyskinesia or aneurysmal ventricular contour = 4 (outward wall motion)

For semiquantitative analysis, the points assigned to each of the above conditions are added together. The ventricle is subdivided into 17 segments:

- six basal segments
- six midventricular segments
- four apical segments
- one apex

When contraction is evaluated by segments, the values for each segment are added together and divided by 17 to obtain a semiquantitative score.

Quantitative wall-motion analyses, while useful in scientific investigations, have not yet come into clinical use. The semiquantitative analysis, however, is extremely useful in the interpretation of stress examinations.

The individual wall regions can be assigned to specific coronary artery territories so that the affected vessels can be identified (**Fig. 2.27**). It should be noted, however, that variants in the coronary artery distribution (left or right dominance) limit the value of the prediction with regard to the right coronary artery or left circumflex artery. The involvement of more than one segment confirms the diagnosis of a wall-motion abnormality.

In stress testing, only wall-motion abnormalities that arise or worsen in more than one segment are interpreted as positive, indicating the presence of coronary heart disease. It is important to consider the sequence of events that is initiated by ischemia, beginning with relaxation abnormalities and diastolic dysfunction and progressing later to systolic contraction ab-

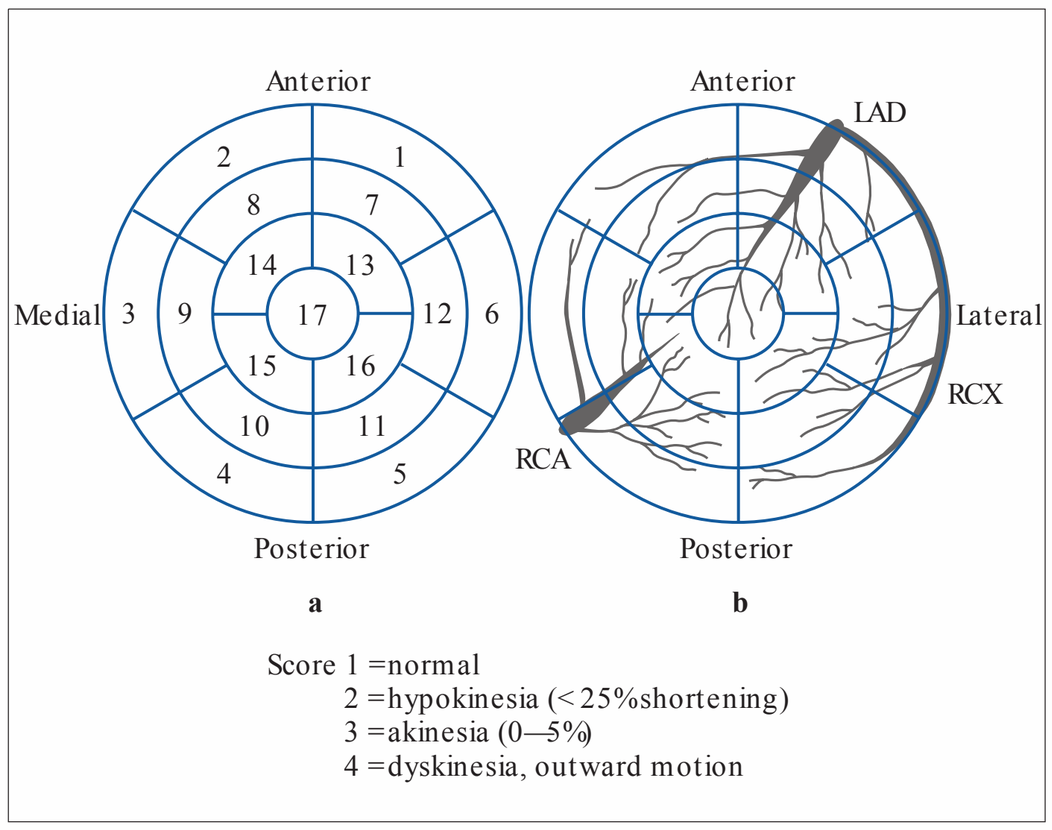

Fig. 2.27 a, b Left ventricular segmentation and vascular distribution. Diagram of the 17-segment model of the left ventricle with six basal segments, six midventricular segments, and five apical segments.

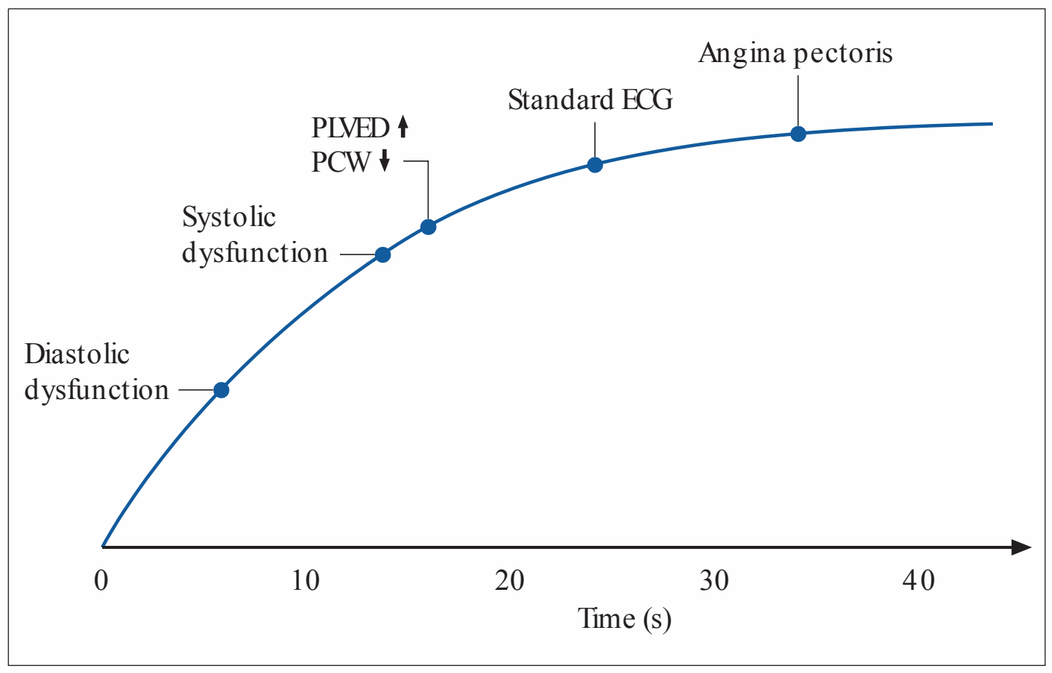

Fig. 2.28 Impairment of myocardial perfusion. A reduction in blood flow induced by a coronary intervention, spontaneous coronary spasms, or stress testing, for example, may initiate an ischemic cascade. The cascade is not always complete, and in 70 %of cases it does not progress to angina pectoris.

normalities (**Fig. 2.28**). This is followed by ST–T segment changes in the ECG and angina pectoris. But ischemia does not always produce changes of this extent. Only about 30 %of all ischemic episodes are associated with angina pectoris, which is more likely to occur in diabetics.

Wall-motion abnormalities do not always result from stenosis of the epicardial arteries, which must be greater than 50 % diameter stenosis (75 %area stenosis) to be hemodynamically significant. They may also result from small-vessel disease induced by spontaneous or iatrogenic microembolism due to plaque disruption. Myocarditis and cardiomyopathies are also included in the differential diagnosis. Contrast agents are successfully used to improve endocardial border delineation and used in pharmocodynamic studies.

Three-dimensional reconstructions or 3D real-time images can be analyzed to plot regional function curves (**Fig. 2.29**). The peaks and partial values vary but show a synchronous overall pattern. Additionally, the cardiac muscle fibers have

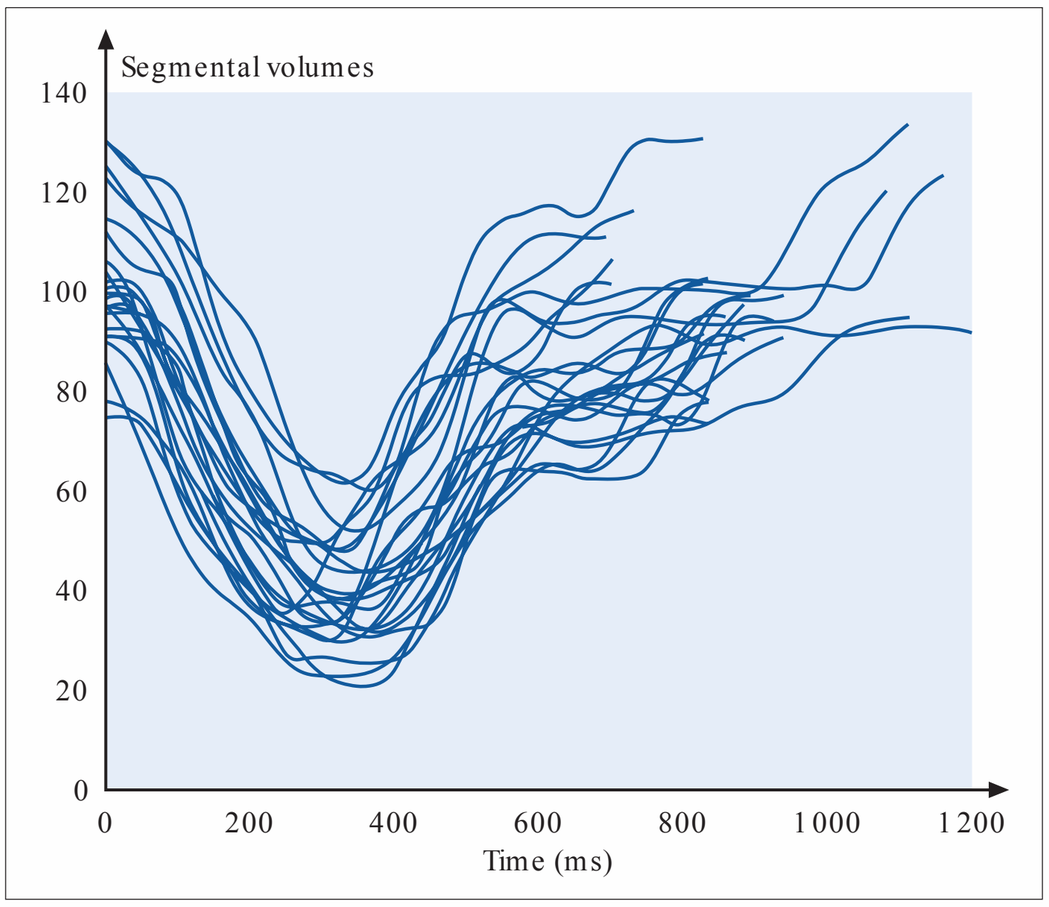

Fig. 2.29 Real-time 3D echocardiography. Segmental volume–time curves.

varying excursions that produce a rotational motion of 3–5°. The base of the heart twists toward the apex.

Tissue Doppler and stress–strain analyses are used in an attempt to quantify regional myocardial function. This is an effective technique in stress echocardiography. Ischemia is associated with the occurrence of postsystolic inward excursions that produce an asynchronous pattern of contraction and relaxation.

There is much current interest in methods for detecting the presence of intraventricular or interventricular asynchrony. This can be accomplished by tissue Doppler analysis of the septum and lateral wall and by temporal analysis of the start of the ejection phase in the LVOT and RVOT.

Diastolic Ventricular Function

The assessment of left ventricular diastolic function is based on determining the filling pressure of the ventricle. The symptoms and prognosis correlate better with diastolic than systolic functional parameters, especially with respect to exertional dyspnea.

LV Diastolic Function

Impairment of left ventricular diastolic function is classified into four grades of severity (see below). Analysis is based on the pulsed Doppler determination of transmitral and pulmonary venous flow velocities and on tissue Doppler imaging and CW color Doppler M-mode echocardiography.

Grade I Diastolic Dysfunction

Grade I diastolic dysfunction is diagnosed in cases where myocardial relaxation is impaired but the diastolic pressure in the left atrium and left ventricle is still normal (**Fig. 2.30**). The pressure changes lead to a prolonged isovolumetric relaxation period with a decrease in mitral inflow velocity during the E wave, a prolonged DT, and an increased A-wave amplitude, which can be interpreted as a compensatory mechanism for increased atrial contraction.

The E/A ratio is less than 1, and pulmonary venous flow shows a diminished S wave and a rising D wave. E′ is reduced in the tissue Doppler echocardiogram, and color M-mode shows a reduction of antegrade left ventricular inflow.

Abnormal relaxation is a typical pattern occurring in diastole of the aging heart. This phase shows the earliest evidence of diastolic dysfunction, as, for example, in younger patients with arterial hypertension. Most patients are asymptomatic at rest and have only mild complaints during exercise.

Grade II Diastolic Dysfunction

When the diastolic function of the left ventricle declines further, the left atrial pressure rises and the left atrium enlarges. The size of the left atrium is the principal indicator of abnormal left ventricular function in patients with normal mitral valve morphology. The transmitral flow pattern normalizes as the flow velocity restores a normal-appearing E/A wave ratio. This "pseudonormal" flow pattern (grade II) is a transition pattern from impaired relaxation to restrictive filling. In certain clinical conditions this flow pattern may be confusing and requires differentiation from a normal pattern. Pseudonormal filling is a typical finding in patients who are regularly followed for heart diseases such as amyloidosis and cardiomyopathies, but it can be difficult to recognize. There are several ways to differentiate a normal filling pattern from grade II pseudonormalization, in which patients experience exertional dyspnea and have moderate functional impairment (NYHA class IIb–III).

The following criteria are used in identifying a pseudonormal (grade II) pattern:

- The left atrium is mildly enlarged.
- The A wave in the pulmonary venous flow signal has an amplitude >20 cm/s and is longer than the pulsed Doppler A wave of mitral inflow.
- The E′ wave in tissue Doppler is decreased compared with A′.
- The transmitral E/E′ ratio is >10.
- Color Doppler M-mode trace shows a reduced flow velocity in the left ventricle with a transmitral propagation velocity <45 cm/s.
- Decreased left ventricular filling in response to provocative testing with nitroglycerin or a Valsalva maneuver.
- Abnormal relaxation parameter dP/dt_{min}, indicating reduced left ventricular relaxation.

Grade III Diastolic Dysfunction

Patients with a grade III restrictive filling pattern have severe dyspnea on even mild exertion and severe functional impairment (NYHA class III–IV).

As the compliance of the left ventricle continues to decline, there is further deterioration of left ventricular diastolic function with a rise in left ventricular filling pressure and left atrial

Diastolic dysfunction		I		II	III reversible IV irreversible
LV diastolic function		Normal	Abnormal relaxation	Pseudonormal	Restriction
Mitral inflow	E/A (cm/s)	> 1	< 1	1 – 2	> 2
Mitral inflow	DT (ms)	< 220	> 220	150 – 200	< 150
LVOT, MV	IVRT (ms)	< 100	> 100	60 – 100	< 60
Pulmonary vein	S/D	≥ 1	≥ 1	< 1	> 1

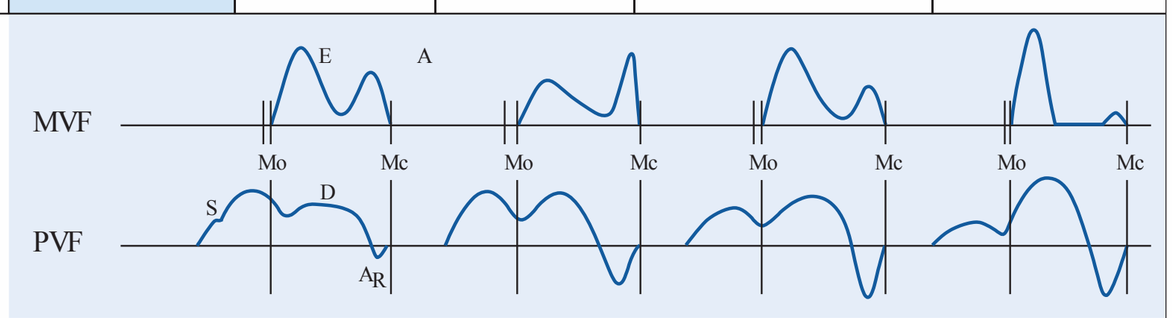

Fig. 2.30 Classification of diastolic dysfunction.

pressure. A restrictive filling pattern develops. As the pressure in the left atrium increases, the mitral valve opens earlier and isovolumetric relaxation time is reduced. This leads to a very rapid pressure rise in the left ventricle, with shortening of inflow and DT. The E/A ratio is greater than 2. The diastolic pulmonary venous flow signal shows an increased D-wave amplitude relative to the S wave. Atrial contraction shows high regurgitation and a longer A wave compared with the A wave of mitral valve inflow.

The tissue Doppler echocardiogram shows a decrease in wall velocities, which fall below 5 cm/s. Color Doppler M-mode shows a further decrease in flow propagation rate.

■ Grade IV Diastolic Dysfunction

When an agent such as a vasodilator is used in a patient with a restrictive filling pattern, that pattern will convert to a pseudonormal pattern if the functional impairment is reversible (grade III). If the restrictive filling is constant and irreversible, it is classified as grade IV diastolic dysfunction. If mitral annulus velocity during the A wave is still greater than 5 cm/s, the dysfunction is usually reversible (**Table 2.8**). The reversibility can be tested using vasodilators such as nitroglycerin.

Estimation of Left Ventricular Filling Pressure

Various parameters can be used to estimate the filling pressure of the left ventricle (**Table 2.9**).

The E-wave flow velocity is determined mainly by the pressure in the left atrium during opening of the mitral valve and reflects the filling rate of the left ventricle. A high, narrow E-wave amplitude generally signifies a high LA pressure, while a low E-wave signifies a low LA pressure. When left ventricular systolic dysfunction is present, a high E/A ratio greater than 2 indicates a high LA pressure, while a low E/A ratio indicates a low LA pressure. If the left atrial pressure is elevated owing to abnormal compliance of the left ventricle, the DT is shortened. A DT < 150 ms signifies a mean LA pressure of approximately 20 mmHg. It should be noted, however, that relaxation is very rapid in young patients and that the left ventricle has high compliance in this population. This accounts for the high amplitude of the E wave and short DT that are observed in young patients. Young people are free of complaints and have good exercise tolerance.

The tissue Doppler mitral annulus velocity is increased in these patients, whereas it is reduced in patients with diastolic

Table 2.8 Assessment of diastolic function

	Normal	Decreasing relaxation	Restrictive filling
IVRT (ms) <40 years	70 ± 12	>110	<60
>40 years	80 ± 12	>110	<60
DT (ms)	200 ± 32	>240	<150
E wave (ms)	0.85 ± 0.15	<0.50	>120
A wave (ms)	0.55 ± 0.15	<0.80	30
E/A	>1	<1	>2

Table 2.9 Identification of patients with elevated left ventricular filling pressure

- Enlargement of the left atrium
- Decreased function of the left atrium
- LV enlargement and hypertrophy
- E/A ratio >2.0
- DT < 150 ms[a]
- PVF: S/D < 40 %
- PVF A_g amplitude > 35 cm/s
- PVF A_g duration 30 ms > transmitral A duration
- E/E′ ratio > 10[a]
- Color Doppler M-mode left ventricular inflow velocity < 40 cm/s[a]
- E/PV ratio < 2

PV = Pulmonary vein, PVF = Pulmonary vein flow.
[a] Also used in atrial fibrillation.

Table 2.10 Estimation of left ventricular filling pressure

- **Sinus rhythm**
  1.9 + 1.24 (E/E′) 5,27 (E/Pv) + 4.66
- **Sinus rhythm + (LV dysfunction)**
  1.85 DR – 0.15 F + 1.9
- **Sinus tachycardia**
  1.55 + 1.47 (E/E′)
- **Atrial fibrillation**
  6.49 + 0.82 (E/E′)

dysfunction. On the other hand, patients with dilatation of the left atrium and left ventricle always have an increased filling pressure and are symptomatic.

It is difficult to identify patients that have only mild functional impairment and show pseudonormalization of their mitral valve inflow pattern. Analysis of the pulmonary venous flow signal (PV) is particularly helpful in this situation. When dysfunction is present, the S/D ratio and systolic forward flow are diminished. If the S/D ratio is <40%, the pulmonary capillary wedge pressure is >18 mmHg.

Other parameters such as the amplitude and duration of the A wave are also helpful in pulmonary venous flow analysis. When LV dysfunction is present, there is a premature cessation of transmitral flow and flow reversal occurs in the pulmonary vein. If A-wave flow velocity in the pulmonary vein is greater than 35 cm/s and its duration is >30 ms compared with the A wave of mitral valve inflow, this indicates that the diastolic left ventricular filling pressure has reached a level higher than 15 mmHg. Analysis of the pulmonary venous flow signal is often difficult, however, and measurements are more difficult to perform when the heart rate is elevated. Analysis of the mitral annulus and of M-mode color Doppler inflow into the left ventricle (flow propagation) may be helpful in these cases (**Fig. 2.17**). If the E/E′ ratio is greater than 10, the left ventricular filling pressure is higher than 15 mmHg. A ratio less than 8 means that the left ventricular filling pressure is normal. The E/E′ ratio can be determined in nearly all patients, and it can be analyzed in patients with sinus tachycardia and atrial fibrillation.

An E/PV ratio <2 also suggests an elevated left ventricular filling pressure. Various formulas have been presented to calculate, rather than just estimate, left ventricular filling pressure (**Table 2.10**).

Further Reading

Agricola E, Oppizzi M, De BM, et al. Multiplane transesophageal echocardiography performed according to the guidelines of the American Society of Echocardiography in patients with mitral valve prolapse, flail, and endocarditis: diagnostic accuracy in the identification of mitral regurgitant defects by correlation with surgical findings. J Am Soc Echocardiogr 2003;16:61–66

Admunsen BH, Helle-Valle T, Edvardsen T, et al. Noninvasive myocardial strain measurement by speckle tracking echocardiography: validation against sonomicrometry and tagged magnetic resonance imaging. J Am Coll Cardiol. 2006 Feb 21;47(4):789-93. Epub 2006 Jan 26

Appleton CP, Galloway JM, Gonzales MS, et al. Estimation of left ventricular filling pressures using 2-dimensional and Doppler echocardiography in adult patients with cardiac disease. J Am Coll Cardiol 1993;22:1972–1982

Appleton CP, Hatle LK, Popp RL. Relation of transmitral flow velocity patterns to left ventricular diastolic function. New insights from a combined hemodynamic and Doppler echocardiographic study. J Am Coll Cardiol 1988;12:426–440

Bach DS, Armstrong WF, Donovan CL, Mueller DW. Quantitative Doppler tissue imaging for assessment of regional myocardial velocities during transient ischemia and reperfusion. Am Heart J 1996;132:721–725

Banerjee A, Brook MM, Klautz RJM, Teitel DF. Nonlinearity of the left ventricular and systolic wall stress velocity of fibrous shortening relations in young pigs: a potential pitfall in ist use as a single beat index of contractility. J Am Coll Cardiol 1994;23:514–524

Bargiggia GS, Bertucci C, Recusani F, et al. A new method for estimating left ventricular dP/dt by continuous wave Doppler-echocardiography. Validation studies at cardiac catheterization. Circulation 1989;80:1287–1292

Bartel T, Müller S, Caspari G, Erbel R. Intracardiac and intraluminal echocardiography: Indications and standard approaches. Ultrasound Med Biol 2002;28:997–1003

Bartel T, Müller S, Nesser HJ, Mohlenkamp S, Bruch C, Erbel R. Usefulness of motion patterns identified by tissue Doppler echocardiography for diagnosing various cardiac masses, particularly valvular vegetations. Am J Cardiol 1999;84:1428–1433

Bartel T, Müller S, Reich D, Gassmann B, Bruch C, Erbel R. Evaluation of hemodynamic determinance of quantitative tissue Doppler echocardiography in the assessment of left ventricular function. Echocardiography 1999;16:481–489

Becher H. Contrast echocardiography: clinical applications and future prospects Z Kardiol 1994;83:658.

Brennecke R, Erbel R. Stand der echokardiographischen Bildgebung. Z Kardiol. 1998;87:75–80

Brunazzi MC, Chirillo F, Pasqualini M, et al. Estimation of left ventricular diastolic pressures from precordial pulsed Doppler analysis of pulmonary venous mitral flow. Am Heart J 1994;128:293–300

Buck T, Hunold P, Wentz KU, Tkalec W, Nesser HJ, Erbel R. Tomographic three-dimensional echocardiographic determination of chamber size and systolic function in patients with left ventricular aneurysm. Comparison to magnetic resonance imaging, cineventriculography, and two-dimensional echocardiography. Circulation 1997;96:4286–4297

Buck T, Plicht B, Erbel R. Current recommendations on echocardiographic evaluation of the severity of mitral regurgitation: Standardization and practical application using a scoring system. Herz 2006;31(1):30–37

Carr KW, Engler LR, Forsythe JR, Johnson AD, Gonsink W. Measurement of left ventricular ejection fraction by mechanical cross sectional echocardiography. Circulation 1979;59:1196–1206

Castello R, Vaughn M, Dressler FA, et al. Relation between pulmonary venous flow and pulmonary wedge pressure. Influence of cardiac output. Am Heart J 1995;130:127–134

Cerqueira MD, Weissman NJ, Dilsizian V, et al. Standardized myocardial segmentation and nomenclature for tomographic imaging of the heart: a statement for healthcare professionals from the Cardiac Imaging Committee of the Council on Clinical Cardiology of the American Heart Association.

Cheitlin MD, Armstrong WF, Aurigemma GP, et al. ACC/AHA/ASE 2003 guideline update for the clinical application of echocardiography--summary article: a report of the American College of Cardiology/American Heart Association Task Force on Practice Guidelines (ACC/AHA/ASE Committee to Update the 1997 Guidelines for the Clinical Application of Echocardiography). J Am Coll Cardiol 2003;42:954–970

Clark RD, Korcuska K, Cohn K. Serial echocardiographic evaluation of left ventricular function in valvular disease, including reproducibility guidelines for the real studies. Circulation 1980;62:564–575

Colan SD. Borow KM, Neumann A. Left ventricular and systolic wall stress – velocity of fibrous shortening relation: A low indepent index of myocardial contractility. J Am Coll Cardiol 1984;4:715–724

Crouse LJ. Sonicated serum albumin in contrast echocardiography: improved segmental wall motion depicition and implications for stress echocardiography. Am J Cardiol 1992;69:42H–45H

Crouse LJ, Cheiref J, Hanly DE, et al. Opacification and boarder delineation improvement in patients with suboptimal endocardial boarder definition in routine echocardiography: results of the phase III albunex multicenter trial. J Am Coll Cardiol 1993;22:1494–1500

Daniel WG, Erbel R, Kasper W, et al. Safety of transesophageal echocardiography. A multicenter survey of 10,419 examinations. Circulation 1991;83:817–821

Darmon PL, Hillel Z, Mogtader A, et al. Cardiac output by transesophageal echocardiography using continuous wave Doppler across the aortic valve. Anesthesiology. 1994;80:796–805

Davila JC, Sanmarco ME. An analysis of the fit of mathematical models applicable to the measurement of left ventricular volume. Am J Cardiol 1966;18:31–42

Devereux RB, Reichek N. Echocardiographic determination of left ventricular mass in man. Anatomic validation of the method. Circulation 1977;55:613–618

Douglas PS, Reichek N, Plappert T, et al. Comparison of echocardiographic methods for assessment of left ventricular shortening and wall stress. J Am Coll Cardiol 1987;9:945–951

Eaton LW, Moughan WL, Shoukas AA, Weiss JL. Accurate volume determination in the isolated ejecting canine left ventricle by two dimensional echocardiography. Circulation 1979;60:320–326

Enriquez-Sarano M, Miller FA, Hayes SN, Bailey KR, Tajik AJ, Seward JB. Effective mitral regurgitant orifice area: clinical use and pitfalls of the proximal isovelocity surface area method. J Am Coll Cardiol 1995;25:703–709

Epperlein S, Wittlich N, Mohr-Kahaly S, Erbel R, Meyer J. Echokardiographische online Volumetrie mittels akustischer Quantifizierung – Vergleiche zur manuellen echokardiographischen Analyse und Cineventrikulographie. Z Kardiol 1994;83:658–665

Erbel R, Brenneke R, Görge G, et al. Möglichkeiten und Grenzen der 2-D Echokardiographie in der quantitativen Bildanalyse. Z Kardiol 1989; 78(Suppl. 7):131–142

Erbel R, Krebs W, Henn G, et al. Comparison of single-plane and biplane volume determination by 2-dimensional echocardiography. Eur Heart J 1982;3:469–480

Erbel R, Neuhaus KL, Spiller P, Benn M, Kreuzer H. Beeinflussung der systolischen und diastolischen Ventrikelfunktion durch Kontrastmittelinjektion in den linken Ventrikel. Z Kardiol 1976;65:305–318

Erbel R, Schweizer P, Richter HA, Krebs W, Meyer J, Effert S. Vergleich zwischen monoplaner und biplaner 2-dimensionaler echoklardiographischer Volumenbestimmung bei asymmetrischen Ventrikeln. Z Kardiol 1980;69:231

Erbel R, Schweizer P, Henn G, Meyer J, Effert S. Apical two-dimensional echocardiography: normal values for single- and bi-plane determination of left ventricular volume and ejection fraction. Dtsch med Wilhr 1982;107:1872-7

Erbel R, Schweizer P, Krebs W, Langenhaar J, Meyer J, Effert S. Effects of hear rate changes on left ventricular volume end ejection fraction: A 2-dimensional echocardiographic study. Am J Cardiol 1984;53:590–597

Erbel R, Schweizer P, Krebs W, Meyer J, Effert S. Sensitivity and specificity of 2-dimensional echocardiography in detection of impared left ventricular function. Eur Heart J 1984;5:477–489

Erbel R, Schweizer P, Krebs W, Pyhel N, Meyer J, Effert S. Monoplane und biplane 2-D echokardiographische Volumenbestimmung des linken Ventrikels, II. Untersuchung bei koronarer Herzerkrankung. Z Kardiol 1981; 70:436–444

Erbel R, Schweizer P, Lambertz H, et al. Echoventriculography – a simultaneous analysis of 2-dimensional echocardiography and cine ventriculography. Circulation 1983;67:205–215

Erbel R, Schweizer P, Meyer J, Grenner H, Krebs W, Effert S. Bestimmung der Volumina und der Ejektionsfraktion des linken Ventrikels aus dem 2-D Echokardiogramm bei Patienten mit koronarer Herzerkrankung. Z Kardiol 1980;69:52–61

Erbel R, Schweizer P, Meyer J, Krebs W, Effert S. Regional myocardial function in coronary artery disease at rest and during atrial pacing. Eur J Cardiol 1980;11(3):183–199

Erbel R, Schweizer P, Meyer J, Krebs W, Yalkinoglu Ö, Effert S. Sensitivity of cross sectional echocardiography in detection of impared global and regional left ventricular function: prospective study. Int J Cardiol 1985;7:375–389

Erbel R, Schweizer P, Pyhel N, et al. Quantitative Analyse regionaler Kontraktionsstörungen des linken Ventrikels im 2-D Echokardiogramm. Z Kardiol 1980;69:562–572

Erbel R, Schweizer P. Diagnostischer Stellenwert der Echokardiographie bei der koronaren Herzerkrankung. 1. M-Mode Echokardiographie. Z Kardiol 1980;69:391–397

Feigenbaum H, Corya BC, Dillon JC, et al. Role of echocardiography in patients with coronary disease. Am J Cardiol 1976;37:775–786

Feinberg MS, Hopkins WE, Davila-Roman VG, et al. Multiplane transesophageal echocardiographic Doppler imaging accurately determines cardiac output in critically ill patients. Chest 1995;107:769–773

Folland ED, Parisi AF, Moynihan PF, Johns DR, Feldman CL, Tow DE. Assessment of left ventricular ejection fraction and volumes by real time, 2-dimensional echocardiography. A comparison of cineangiography and radio nuclide techniques. Circulation 1979;60:760–766

Gibson DG. Measurement of left ventricular volumes in men by echocardiography comparison the biplane angiographs. Br Heart J 1971;33: 614–620

Gopal AS, Keller AM, Rigling R, King DL Jr, King DL. Left ventricular volume and endocardial surface area by 3-dimensional echocardiography. Comparison with 2-dimensional echocardiography and nuclear magnetic resonance imaging in normal subjects. J Am Coll Cardiol 1993; 22:258–270

Gorcsan J 3rd, Morita S, Mandarino WA, et al. Two dimensional echocardiographisc automatic boarder detection accurately reflex changes in left ventricular volume. J Am Soc Echocardiogr 1993;6:482–489

Gorcsan J 3rd, Romond JA, Mandarino WA, et al. Assessment of left ventricular performance by one-line pressure area relations using echocardiographic automated border detection. J Am Coll Cardiol 1994;23:242–252

Gorcsan J 3rd, Snow FR, Paulsen W, Nixon JV. Non invasive estimation of left atrial pressure in patients with congestive heart failure and mitral regurgitation by Doppler echocardiography. Am Heart J 1991;121:858–863

Gorcsan J, Strum DP, Mandarino WA, et al. Quantitative assessment of alterations in regional left ventricular contractility with colour coded tissue Doppler echocardiography: comparison with sonomicrometry and pressurevolume relation. Circulation 1997;95:2423–2433

Greim CA, Roewer N, Schulte AM, Esch J. Assessment of changes in left ventricular wall stress in the end-systolic pressure-area product. Br J Anaesth 1995;75:583–587

Gueret P, Meerbaum S, Wyatt HL, Uchijama T, Lang PW, Corday E. 2-dimensional echocardiographic quantitation of left ventricular volumes and ejection fraction. Importance of accounting for dyssynergy in short axis reconstruction models. Circulation 1980;62:1308–1318

Harrison MR, Clifton GD, Berk MR, De Maria HM. Effect of blood pressure after load on Doppler echocardiographic measurements of left ventricular systolic function in normal subjects. Am J Cardiol 1989;64:905–908

Hatle L, Angelsen BAJ. Doppler ultrasound in cardiology: physical principles and clinical applications. 2nd ed. Philadelphia: Lea&Febiger, 1985

Helak JW, Reichek N. Quantitation of human left ventricular mess ans volume by 2-dimensional echocardiography: in vitro anatomic validation. Circulation 1981;63:1398–1407

Hickman HO, Weyman AE, Wann LS, et al. Cross sectional echocardiography of the cadiac apex. Circulation 1977;56 (Suppl III-153):1977.

Hoffman BF, Bindler E, Suckling IE. Post extra-systolic potentiation of contraction in cardiac muscle. Am J Physiol 1956;185:95–102

Hoffmann R, von Bardeleben S, ten Cate F, et al. Assessment of systolic left ventricular function: a multi-centre comparison of cineventriculography, cardiac magnetic resonance imaging, unenhanced and contrast-enhanced echocardiography. Eur Heart J 2005;26:607–616

Hugenholtz PG, Wagner HR, Sandler H. An in vivo determination of left ventricular volume. Circulation 1968;37:489–508

Hundley WG, Kizilbash AM, Afridi I, Franco F, Peshock RM, Grayburn PA. Administration of an intravenous perfluorocarbon contrast agent improves echocardiographic determination of left ventricular volumes and ejection fraction: comparison with cine magnetic resonance imaging. J Am Coll Cardiol 1998;32:1426–1432

Jenni R, Vieli SO, Anliker M, Krayenbuehl HP. Estimation of left ventricular volume from apical orthogonal 2-dimensional echocardiograms. Eur Heart J 1981;2:217–225

Jongbloed MR, Schalij MJ, Zeppenfeld K, Oemrawsingh PV, van der Wall EE, Bax JJ. Clinical applications of intracardiac echocardiography in interventional procedures. Heart 2005;91:981–990

Kan G, Visser CA, Lie KI, Durrer D. Left ventricular volumes and ejection fraction by single plane 2-dimensional apex echocardiography. Eur Heart J 1981;2:339–343

Kass DA, Beyar R. Evaluation of contractile state by maximal ventricular power divided by the square of end-diastolic volume. Circulation 1991;84:1689–1708

Khouri SJ, Maly GT, Suh DD, Walsh TE. A practical approach to the echocardiographic evaluation of diastolic function. J Am Soc Echocardiogr 2004;17:290–297

King DL, Jaffee CC, Schmidt DH, Ellis K. Left ventricular volume determination by cross-sectional cardiac ultrasonography. Radiology 1972;104: 201–202

Kücherer HF, Muhiudeen IA, Kusumoto FM, et al. Estimation of mean left atrial pressure form transesophageal pulse Doppler echocardiography of pulmonary venous flow. Circulation 1990;82:1127–1139

Lang RM, Bierig M, Devereux RB, et al. Recommendations for chamber quantification: a report from the American Society of Echocardiography's Guidelines and Standards Committee and the Chamber Quantification Writing Group, developed in conjunction with the European Association of Echocardiography, a branch of the European Society of Cardiology. J Am Soc Echocardiogr 2005;18:1440–1463

Marwick TH, Nemec JJ, Pashkow FJ, Stewart WJ, Salcedo EE. Accuracy and limitations of exercise echocardiography in a routine clinical setting. J Am Coll Cardiol 1992;19:74–81

Mock MB, Ringqvist I, Fisher LD, et al. Survival of medically treated patients in coronary artery surgery study (CASS) registry. Circulation 1982;66: 562–568

Mohr-Kahaly S, Erbel R, Zotz R, Duwe L, Schreiner G, Meyer J. Linksventrikuläre Kontrastechokardiographie mittels Gelifundol. Z Kardiol 1987;76: 699–705

Moir S, Marwick TH. Combination of contrast with stress echocardiography: a practical guide to methods and interpretation. Cardiovasc Ultrasound 2004;2:15

Müller S, Bartel T, Baumann G, Erbel R. Preliminary report: evaluation of 3-dimensional echocardiographic volumetry by simultaneous thermal dilution in coronary heart disease. Cardiology 1996;87:552–559

Müller S, Bartel T, Katz MA, Pachinger O, Erbel R. Partial cut-off of the left ventricle: Determinants and effects on volume parameters assessed by real-time 3-D echocardiography. Ultrasound Med Biol 2003;29:25–30

Müller S, Bartel T, Schürger D, Gasmann G, Erbel R. Quantitative tissue Doppler in comparison with 2-dimensional and Doppler echocardiographic indices in normal subjects. Int J Cardiol 1997;61:183–192

Mulvagh SL, DeMaria AN, Feinstein SB, Burns PN, Kaul S, Miller JG. Contrast echocardiography: Current and future applications. J Am Soc Echocardiogr 2000;13:331–342

Mulvagh SL, Foley DA, Aeschbacher BC, Klarich KK, Seward JB. Second harmonic imaging of an intravenously administrated echocardiographic contrast agent. J Am Coll Cardiol 1996;27:1519–1525

Murray JA, Johnston W, Reid JM. Echocardiographic determination of left ventricular dimensions, volumes and performance. Am J Cardiol 1972; 30:252–257

Nagueh SF, Kopelen HA, Quinones MA. Assessment of left ventricular filling pressures by Doppler in the presence of atrial fibrillation. Circulation 1996;94:2138–2145

Nagueh SF, Middleton KJ, Kopelen HA, et al. Doppler tissue imaging: a non invasive technique for evaluation of left ventricular relaxation and estimation of filling pressures. J Am Coll Cardiol 1997;30:1527–1533

Olzhausen von K, Schuler G, Haueisen H, Leinberger H, Mehmel HC, Kübler W. Messung der LV-Ejektionsfraktion mittels 2-dimensionaler mechanischer apex Echokardiographie. Z Kardiol 1980;69:232

Poelaert J, Schmidt C, Van Aken H, et al. A comparison of transesophageal echocardiographic Doppler across the aortic valve and a termodilution technique for estimating cardiac output. Anaesthesia 1999;54:128–136

Pozzoli M, Capomolla S, Pinnan G, et al. Doppler schocardiographiy reliably predict pulmonary artery wedge pressure regurgitation. J Am Coll Cardiol 1996;27:883–893

Previtali M, Lanzarini L, Fetiveau R, et al. Comparison of dobutamine stress echocardiography, dipyridamole stress echocardiography and exercise stress testing for diagnosis of coronary artery disease. Am J Cardiol 1993;72:865–870

Quinones MA, Waggoner AD, Reduto LA, et al. A new, simplified and accurate method for determining ejection fraction with 2-dimensional echocardiography. Circulation 1981;64:744–753

Recusani F, Bargiggia GS, Yoganathan AP, et al. A new method for quantification of regurgitant flow rate using color flow imaging of the flow convergence region proximal to a discrete orifice: an in vitro study. Circulation 1991;83:594–604

Reichek N, Wilson J, St John Sutton M, et al. Non invasive determination of left ventricular end-systolic stress: validation of the method and initial applications. Circulation 1982;65:99–108

Sagawa K, Suga H, Shoukas AA, et al. Endystolic pressure/volume ratio: a new index of ventricular contractility. Am J Cardiol 1977;40:748–753

Sahn DJ. Instrumentation and physical factors related to visualization of stenotic and regurgitant jets by Doppler color flow mapping. J Am Coll Cardiol 1988;12:1354–1365

Sapin PM. Schröder KM, Gopal AS, Smith MD, DeMaria AN, King DL. Comparison of 2-dimensional and 3-dimensional echocardiography with cineventriculography for measurements of left ventricular volumes in patients. J Am Coll Cardiol 1994;24:1054–1063

Schiller NB, Aquatella H, Ports TA, et al. Left ventricular volume from pared biplane 2-dimensional echocardiograms. Circulation 1979;60:547–555

Schiller NB, Shah PM, Crawford M, et al. Recommendations for quantitation of the left ventricle by 2-dimensionl echocardiography. J Am Soc Echocardiogr 1989;2:358–367

Schwarz KQ, Chen X, Steinmetz S, Phillips D. Harmonic imaging with levovist. J Am Soc Echocardiogr 1997;10:1–10

Seward JB. Cardiovascular ultrasound imaging. Curr Opin Cardiol 1988;3: 912–921

Seward JB, Douglas PS, Erbel R, et al. Hand-carried cardiac ultrasound (HCU) device: Recommendations regarding new technology. A report from the echocardiography task force on new technology of the nomenclature and standards committee of the American society of Echocardiography. J Am Soc Echocardiogr 2002;15:369–373

Sheikh K, Smith SW, Von Ramm O, Kisslow J. Real time 3-dimensional echocardiography: feasibility and initial use. Echocardiography 1991; 8:119–125

Siu SC, Rivera JM, Guerrero JL, et al. Three-dimensional echocardiography in vivo validation of left ventricular volume in function. Circulation 1993;88:1715–1723

Spencer KT, Bednarz J, Rafter PG, Korcarz C, Lang RM. Use of harmonic imaging without echocardiographic contrast to improve 2-dimensional image quality. Am J Cardiol 1998;82:794–799

Stein PD, Sabbah NH. Rate of change of ventricular power, and indicator of ventricular performance during ejection. Am Heart J 1976;91:219–227

Sugeng L, Weinert L, Thiele K, Lang RM. Real-time three-dimensional echocardiography using a novel matrix array transducer. Echocardiography 2003;20:623–635

Sun JP, Pu M, Foud FM, et al. Automated cardiac output measurement by speciotemporal integration of colour Doppler data. Circulation 1997; 95:932–939

Suriani RJ, Neustein S, Shore-Lesserson L. Konstadt. Intraoperative transesophageal echocardiography during noncardiac surgery. J Cardiothorac Vasc Anesth 1998;12:274–280

Tei C, Ling LH, Dujardin KS, Hodge DE, et al. Doppler index combining systolic and diastolic myocardial performance: Clinical value in cardiac amyloidosis. J Am Coll Cardiol 1996;28:658–664

Tei C, Dujardin KS, Hodge DE, et al. New index of combined systolic and diastolic cardiac performance: a simple and reproducible measure of cardiac function. A study in normals and dilated cardiomyopathy. J Am Coll Cardiol 1995;26:357–366

Tei C, Nishimura RA, Seward JB, et al. Non invasive Doppler-derived myocardial performance index: correlation with simultaneous measurements of cardiac catheterization measurements. J Am Soc Echocardiogr 1997;10:169–178

Teichholz LE, Cohen MV, Sonnenblick EH, Gorlen R. Study of left ventricular geometry and function by B-scan ultrasonography in patients with and without asynergy. N Engl J Med 1974;291:1220–1226

Teichholz LE, Kreulen T, Hermann MV, Gorlin R. Problems in echocardiographic volume determinations: Echocardiographic – angiographic correlations in the presence or absence of asynergy. Am J Cardiol 1976;37:7–11

Thys DM, Hillel Z, Goldman ME, et al. A comparison of hemodynamic indices derived by invasive monitoring and 2-dimensional echocardiography. Anaesthesiology. 1987;67:630–634

Voigt JU, Arnold MF, Karlsson M, et al. Assessment of regional longitudinal myocardial strain rate derived from doppler myocardial imaging indexes in normal and infarcted myocardium. J Am Soc Echocardiogr 2000;13:588–598

Wyatt HL, Heng MK, Mehrbaum S, Gueret P, Dula E, Corday E. Cross-sectional echocardiography. II. Analysis of mathematic models for quantifying volume of the formalin-fixed left ventricle. Circulation 1980;61: 1119–1125

Wyatt HL, Heng MK, Mehrbaum S, Hestenes J, Davidson R, Corday E. Quantification of volumes in asymmetric left ventricles by 2-d echocardiography. Circulation 1978;58(Suppl II):188–192

Wyatt HL, Mehrbaum S, Heng MK, Gueret P, Corday E. Cross-sectional echocardiography. III. Analysis of mathematic models quantifying volume of symmetric and asymmetric left ventricles. Am Heart J 1980;100:821–828

Yamamoto K, Nishimura RA, Chaliki HP, et al. Determination of left ventricular filling pressure by Doppler echocardiography in patients with coronary artery disease: critical role of left ventricular systolic function. J Am Coll Cardiol 1997;30:1819–1826

Zeidan Z, Erbel R, Barkhausen J, Hunold P, Bartel T, Buck T. Analysis of global systolic and diastolic left ventricular performance using volume – time curves by real-time 3D echocardiography. J Am Soc Echocardiogr 2003; 16:29–37

3 Angiography

H. Eggebrecht

The invasive procedure of angiography is useful in establishing a diagnosis in several cardiac diseases. In addition to selective contrast visualization of the cardiac chambers and coronary arteries, cardiac catheterization enables direct pressure measurements, the measurement of oxygen saturation, and the detection of intracardial shunts. Angiography can further define the full length of the aorta and its branches such as the carotid artery. Digital subtraction angiography (DSA) and electronically enhanced digital imaging techniques are used to improve the quality of the examination. Catheter angiography continues to be the gold standard for vascular imaging, yet the number of conventional angiograms has declined in recent years owing to advances in modern noninvasive procedures such as MR angiography and CT angiography. It can be expected that the number of purely diagnostic catheter angiograms for vascular imaging will continue to decline in the future. Through advances in fast CT scanning in particular, noninvasive imaging of the coronary arteries is also becoming an increasingly important alternative to invasive coronary angiography. Nevertheless, angiography will continue to have an important role in the planning and conduct of interventional procedures. It is to be expected that therapeutic angiography, in contrast to diagnostic angiography, will play an increasingly important role owing to the more frequent detection of abnormalities as a result of the increasing use of noninvasive techniques.[1]

Cardiac Catheterization Technique for Pressure and Oxygen Measurements and for Angiocardiography

Except in emergency indications (e.g., acute myocardial infarction), **informed patient consent** with disclosure of possible risks and complications should be obtained at least 24 hours before angiocardiography. At that time the patient should be asked about allergies, anticoagulant therapy, and possible pregnancy and thyroid complaints.

The access site of choice for cardiac catheterization is the **femoral artery**. This allows retrograde catheterization of the aorta, left ventricle, and all arterial vascular regions of interest. An alternative to the inguinal approach is to introduce the catheter through a brachial or radial artery access. This approach is particularly useful when transfemoral catheterization is not possible (e.g., in patients with severe peripheral arterial occlusive disease [PAOD]). The main advantage of the approach described is that it allows the patient to ambulate immediately after the procedure.

Right heart catheterization can be accomplished through a cubital, jugular, or the femoral vein. This permits pressure and oxygen-saturation measurements in the pulmonary circulation, in the right ventricular inflow and outflow tracts, and at various levels in the right atrium. An atrial septal defect or anomalous pulmonary vein terminations can also be catheterized by this approach. Cardiac output can be determined by the thermodilution method or measured indirectly by the Fick principle. Access through the internal jugular vein may be advantageous for right ventricular biopsy.

Transseptal cardiac catheterization is generally accomplished through the right femoral vein. A Brockenbrough needle is passed through the interatrial septum, allowing pressure and oxygen-saturation measurements to be taken in the pulmonary veins, left atrium, and left ventricle. This approach is used in particular for diagnostic confirmation, but also for interventional procedures such as balloon angioplasty for mitral valve stenosis. The pressure gradient between the left atrium and left ventricle can be measured simultaneously with a second catheter introduced through the femoral artery and passed in retrograde fashion into the left ventricle.

As a rule, angiocardiography is performed under **local anesthesia**. General anesthesia is required only in rare cases. The femoral artery is usually anesthetized with 10 mL of a local anesthetic solution (e.g., 1% lidocaine). Even smaller amounts may suffice at alternative sites, such as the radial or brachial artery. After a skin wheal has been raised to the left and right of the proposed insertion site, anesthesia of the deep soft-tissue layers is recommended for femoral artery catheterization. An extra-long needle (e.g., a spinal needle) should be used in obese patients.

A **direct percutaneous approach** to the access vessel is made with a suitable beveled needle, which may be open or fitted with an inner stylet. **Retrograde puncture** of the femoral artery is generally accomplished in slim patients with superficial vessels, but may be difficult in obese patients, or those with severe PAOD.

The femoral artery is punctured in the lacuna vasorum in the right or left groin area lateral to the vein, above the median portion of the femoral head.

Essential Point

The inguinal ligament is an unsuitable landmark because the targeted common femoral artery runs above it in ~ 80% of cases. Puncturing the femoral artery above the inguinal ligament may cause initially unnoticed (retroperitoneal) bleeding that is extremely difficult to control by manual compression.

The **angle of needle insertion** depends on the thickness of the soft-tissue layer to be penetrated. A very flat needle angle is generally used in slim patients, while a more vertical angle (up to 90°) is used in obese ones. The needle tip should ideally

enter the artery at the first attempt. Multiple puncture attempts increase the risk of complications such as hematomas and arteriovenous fistulas.

Care should be taken to puncture only the **anterior vessel wall**. Puncture of the posterior vessel wall is unfavorable for later manual compression and may lead to retroperitoneal hematoma in a transfemoral approach. A strong, pulsating jet of blood confirms correct intravascular needle placement.

Following successful puncture, the access site is secured by inserting a guidewire (usually with a 0.035-inch diameter) through the needle and into the vessel. The guidewire may initially be advanced without fluoroscopic guidance, taking care that it is advanced gently and without resistance. A Judkins J-wire is most commonly used. In severe PAOD—with or without stenosis—the inserted wire may become snared in atherosclerotic plaque. This may require using a special wire with hydrophilic coating, or a straight or slightly curved tip.

After removal of the puncture needle, a **sheath** is inserted into the vessel using Seldinger technique to establish access for angiographic catheterization. The use of a sheath permits various catheters to be introduced as desired without causing additional vascular trauma, and with practically no blood loss. A sheath ~10 cm long is adequate for most diagnostic catheterizations. Longer sheaths can be used if there is significant elongation or kinking of the access vessel (usually the femoral/iliac artery). With technical advances in miniaturization, it has become possible to use sheaths of considerably smaller diameters. Today, 4 Fr and 5 Fr sheaths are most commonly used in diagnostic cardiac catheterizations. Larger sheaths up to 12 Fr or 14 Fr are used for therapeutic angiography (e.g., in angioplasty for coarctation of the aorta).

A variety of disposable plastic catheters with various shapes and curvatures are available for accessing the targeted vascular region. A **pigtail catheter** is essential for imaging the cardiac chambers as well as for aortography. A calibrated pigtail catheter with radiopaque centimeter markings is suitable for aortography to facilitate later quantitative analysis of the angiograms.

The catheter is threaded into the vessel over the **guidewire**. This technique poses fewer risks than advancing the catheter without a wire, which carries a substantial risk of perforation. When the catheter has reached the vessel selected for angiography, the guidewire is withdrawn and the catheter is flushed with heparinized saline solution.

Essential Point

Contrast medium can be safely injected only when arterial blood is flowing freely from the catheter. Furthermore, there should be no significant damping of the arterial pressure trace.

Before angiography is initiated, correct catheter placement should be confirmed by a **test injection** of several milliliters of contrast medium.

After angiography is completed, the arterial sheath is removed and the insertion site is manually compressed for ~15 minutes until complete **hemostasis** is achieved. Additionally, a compression dressing is usually applied and left in place for 12–24 hours, depending on the size of the arterial sheath. The insertion site may also be closed with a "closure device," an increasingly popular option which permits early mobilization even of anticoagulated patients and lowers the risk of post-procedure vascular complications.[2]

Cardiac Catheterization Measurements

Pressure Measurements

The systolic pressures in the left and right ventricles rise in response to a resistance load in the dependent circulation (e.g., aortic stenosis, coarctation of the aorta, pulmonary stenosis, hypertension). Impaired ventricular function is associated with an increase in end-diastolic pressures. Stenosing valvular lesions and stenoses in larger vessels can be quantified by the simultaneous measurement of pre- and poststenotic pressure differences (e.g., in aortic stenosis). The pulmonary capillary wedge pressure is measured with a balloon catheter carried by the bloodstream (antegrade) into the pulmonary circulation. When the balloon catheter has reached the "wedge" position, the catheter tip measures the pressure in the venous circulatory system distal to the insufflated balloon (the pulmonary veins), which corresponds roughly to the mean pressure in the left atrium. In the absence of mitral valve disease, this pressure equals the left ventricular end-diastolic blood pressure, thereby making it possible to monitor the left ventricular filling pressure.

Oxygen Saturation Measurements

By measuring oxygen saturation at various sites in the pulmonary circulation, we can detect and locate shunt connections between the right and left heart and between the great vessels. We can further quantify the shunt flow. In patients with an atrial septal defect or anomalous pulmonary venous return, the oxygen content of the blood in the right atrium is higher than in the vena cava. In the presence of an isolated ventricular septal defect, the oxygen content in the right ventricle is higher than in the right atrium. With a patent ductus arteriosus, the oxygen content in the pulmonary artery is higher than in the right heart.

Cardiac Output and Derivative Parameters

Cardiac output is measured by the thermodilution method or according to the Fick principle. The thermodilution method uses a pulmonary artery catheter that has an extra port with a separate lumen (central venous lumen) ~30 cm proximal to the catheter tip, and a thermistor probe mounted to the tip. A bolus of cold saline solution is injected, inducing a continuous temperature change that is converted to a change in voltage. When the temperature difference, injection volume, and integral of the voltage change are known, the cardiac output can be calculated using the Stewart–Hamilton formula:

$$CO\ (L/min) = (1.08) \times CT\ (60) \times VI \times (TB - TI)/(1.22 \times TB(t)\ dt)$$

where CT = correction factor, 60 = s/min, VI = injection volume, TI = injection time, TB = blood temperature, 1.22 = compensation factor for the area integrated down to 30% of the peak temperature difference, and TB(t) dt = the integral for blood-temperature change.

The thermodilution method is used today in fully computerized bedside instruments and in all intensive care units.

The Fick principle for measuring cardiac output uses oxygen as an indicator. The uptake or release of an indicator by an organ equals the product of blood flow times and the arteriovenous concentration difference. When oxygen uptake is known (from spirometry), the cardiac output can be calculated with the following formula by measuring the arteriovenous oxygen difference:

$$CO = O_2 \text{ uptake } (mLO_2/min) \,/\, \text{arteriovenous } O_2 \text{ difference } (mLO_2 / L\text{blood})$$

Because the pulmonary veins are accessible only by the transseptal route and the O_2 concentration measured in the aorta equals the pulmonary venous oxygen concentration (in the absence of shunt flow), the arterial O_2 saturation is used to calculate cardiac output.

Detection of Shunt Lesions

The following congenital heart lesions can be directly detected by catheterization combined with oxygen saturation measurements and angiography:

- Atrial septal defect
- Anomalous pulmonary venous terminations on the right atrium
- High and low ventricular septal defects
- Patent ductus arteriosus

Selective Angiocardiography

In selective angiocardiography, contrast medium is injected directly into a cardiac chamber or central vessel through an angiographic catheter (usually a pigtail catheter) so that the passage of contrast medium can be tracked through all or part of the heart and great vessels.

The heart is imaged in two planes (biplane RAO/LAO projections or biplane posterior/left lateral views). Digital images are acquired at a high frame rate (generally 25/s) to compensate for the rapid motion of the heart.

Left Ventricular Angiography

Selective left ventricular angiography is usually done as a routine component of coronary angiography and is useful in the assessment of left ventricular systolic function (**Fig. 3.1**). Left ventricular angiography should precede coronary angiography, because the contrast injection used for coronary angiography may exert a negative inotropic effect and could thus mimic impairment of ventricular function. In addition to the qualitative assessment of regional wall motion abnormalities, this study permits the quantitative computer-assisted determination of end-systolic volume, end-diastolic volume, and stroke volume. These quantities can be used to determine the ejection fraction as a parameter of global systolic function. Left ventricular angiography has further importance in the assessment of mitral regurgitation, which may, however, be an artifact caused also by extrasystoles or the indwelling catheter.

Indications for selective left ventricular angiography:

- Assessment of regional and global left ventricular function
- Left ventricular aneurysm formation after myocardial infarction
- Cardiomyopathies
- Aortic valve disease
- Mitral valve disease
- Ventricular septal defect with a left-to-right shunt

Right Ventricular Angiography

Selective right ventricular angiography is used primarily to evaluate pulmonary and tricuspid valve diseases. Right ventricular angiography is also performed in patients with complex congenital cardiac anomalies. In most cases the right heart is catheterized in an antegrade direction through the femoral vein. A pigtail catheter is generally used for this procedure.

Indications for selective right ventricular angiography:

- Investigation of pulmonary hypertension
- Pulmonary valve disease
- Tricuspid valve disease
- Tricuspid atresia
- Complex congenital heart disease with a right-to-left shunt (e.g., tetralogy of Fallot, defects associated with shunt reversal)
- Constrictive pericarditis
- Right myocardial infarction
- Arrhythmogenic right ventricular dysplasia

Aortography

Aortography is used for the invasive diagnosis of aortic diseases and for planning their management (**Fig. 3.2**).[3] Angiography of the ascending aorta is employed to assess aortic insufficiency, and is further used in cardiac catheterizations to assess the patency of venous bypasses (**Fig. 3.3**). Abdominal aortography is done in patients with suspected infrarenal abdominal aortic aneurysm or proximal renal artery stenosis. This procedure may be done within the framework of cardiac catheterizations (**Fig. 3.4**).

The ascending aorta, aortic arch, and proximal descending aorta are imaged in the 60° LAO projection, while the thoracoabdominal and infrarenal aorta are imaged in the 0° (A-P) projection. Using a catheter with calibration marks facilitates subsequent quantitative analysis of lengths and diameters.

Indications for selective aortography (Guideline for Diagnostic Coronary Angiography of the German Cardiology Society) are as follows[4]:

- Aortic valve diseases
- Suspected aortic diseases (aortic aneurysm, aortic dissection, coarctation of the aorta)
- Previous venous bypass surgery, to locate the bypass during coronary angiography

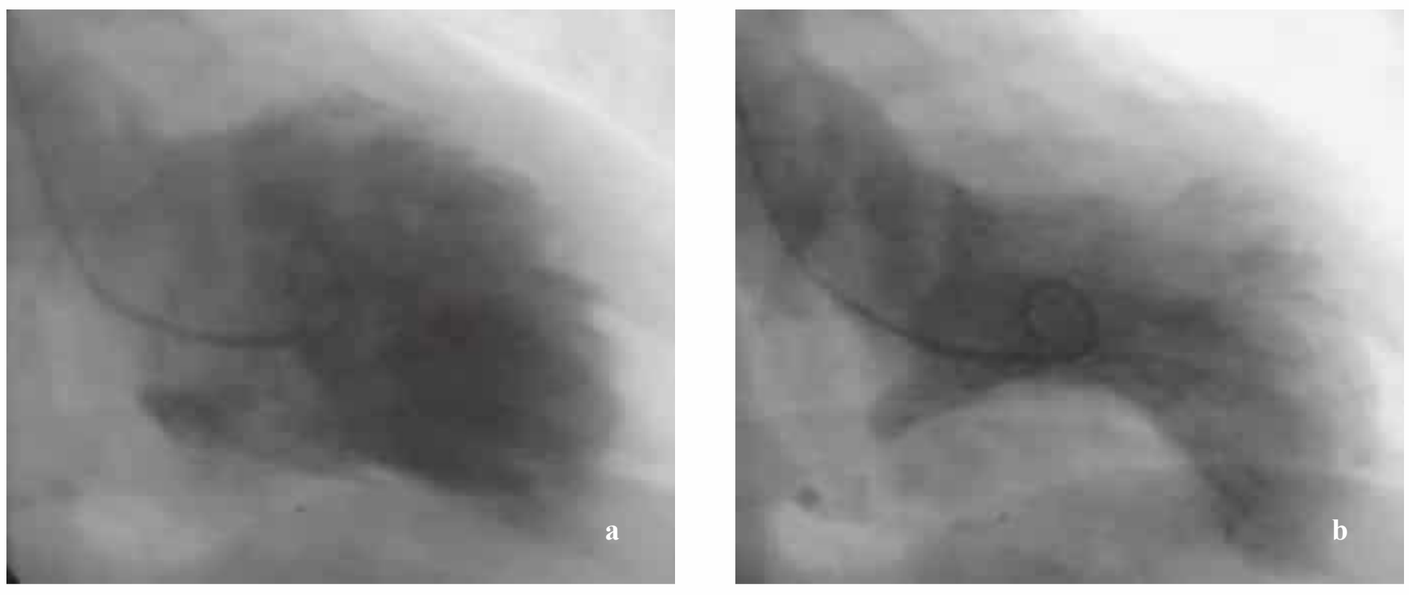

Fig. 3.1 a, b Selective left ventricular angiograms in diastole (**a**) and systole (**b**) show severe akinesia of the apical anterior wall following an acute ST-elevation infarction of the anterior wall.

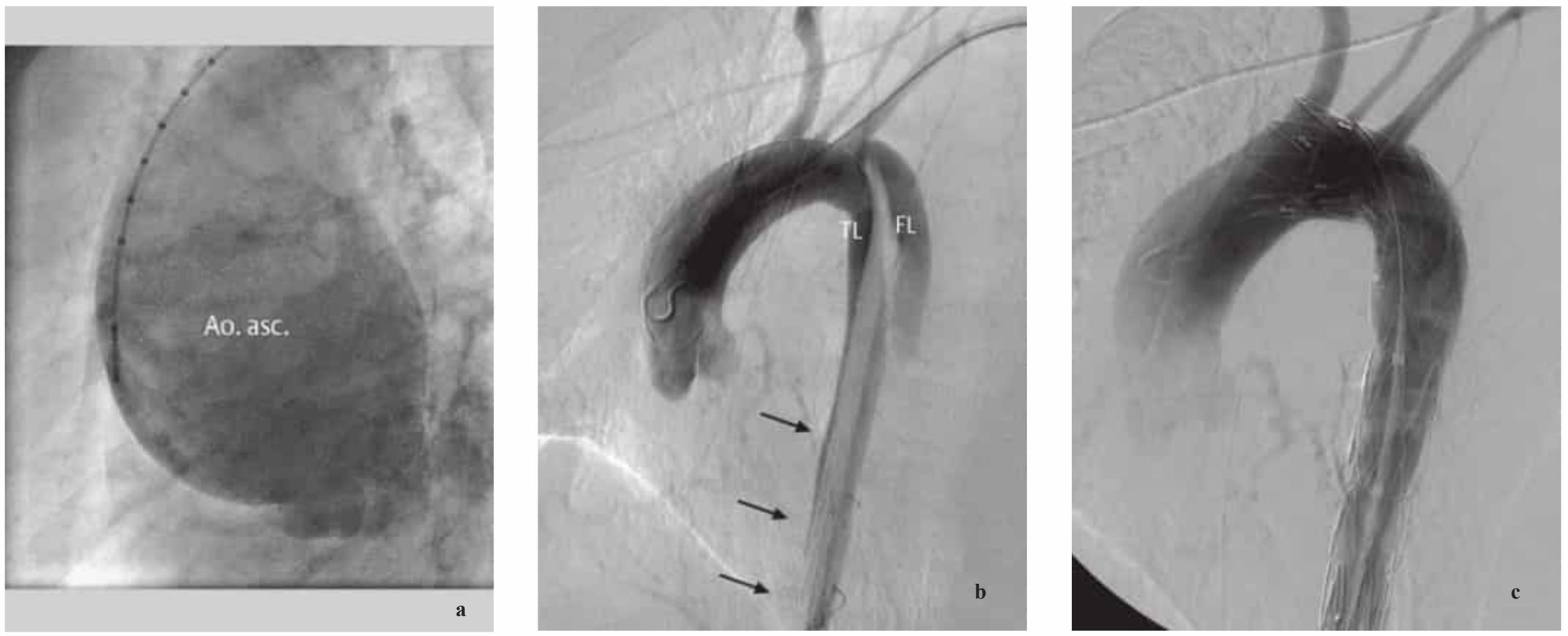

Fig. 3.2 a Selective angiography of the ascending aorta. Digital angiogram of an extensive aneurysm of the ascending aorta.
b, c Acute type B dissection and rupture of the descending thoracic aorta in a 40-year-old female patient.
b DSA of the thoracic aorta in the LAO projection. An endovascular stent (arrows) has been placed in the aorta with a transfemoral catheter but has not yet been deployed. The type B dissection starts immediately past the origin of the left subclavian artery. The angiographic catheter has been inserted through the left brachial artery.
c DSA after stent deployment shows complete occlusion of the false lumen and effective sealing of the entry site. The image confirms patency of the supra-aortic vessels.

Pulmonary Angiography

Although for many years selective pulmonary angiography was the gold standard in the diagnosis of pulmonary embolism, in recent years it has been superseded by multislice CT. However, pulmonary angiography continues to be used in patients with pulmonary embolism, as it provides both an opportunity for mechanical catheter fragmentation of the embolus and local lytic therapy. Pulmonary angiography is further employed in patients with chronic recurrent pulmonary embolism, as it not only yields characteristic vascular findings but also permits the assessment of pulmonary hemodynamics in the same session. In cases where retrograde catheterization of the aortic valve is not possible, pulmonary angiography can also be used to evaluate left ventricular function by obtaining follow-through images after pulmonary transit of the contrast medium.

Indications for selective pulmonary angiography:

- Pulmonary embolism
- Pulmonary hypertension
- Pulmonary valve disease
- Pulmonary AV fistula
- Tumors of the left atrium
- Left ventricular opacification in conditions preventing retrograde catheterization of the aortic valve (e.g., high-grade aortic stenosis, previous mechanical aortic valve replacement)
- Pulmonary AV shunts

Contraindications for Angiocardiography

The main contraindications are:

- Severe contrast medium allergy
- Acute, decompensated heart failure
- Hyperthyroidism
- Impaired renal function

Complications of Angiocardiography

Angiocardiography represents an invasive examination. Complications may consist of local access-site complications (e.g., postprocedure hemorrhage, hematoma, thrombosis, embolism, vascular occlusion, AV fistula formation, pseudoaneurysm formation), cardiac complications (arrhythmias, ECG changes), and complications resulting from contrast medium administration (renal failure requiring dialysis, allergic reactions).

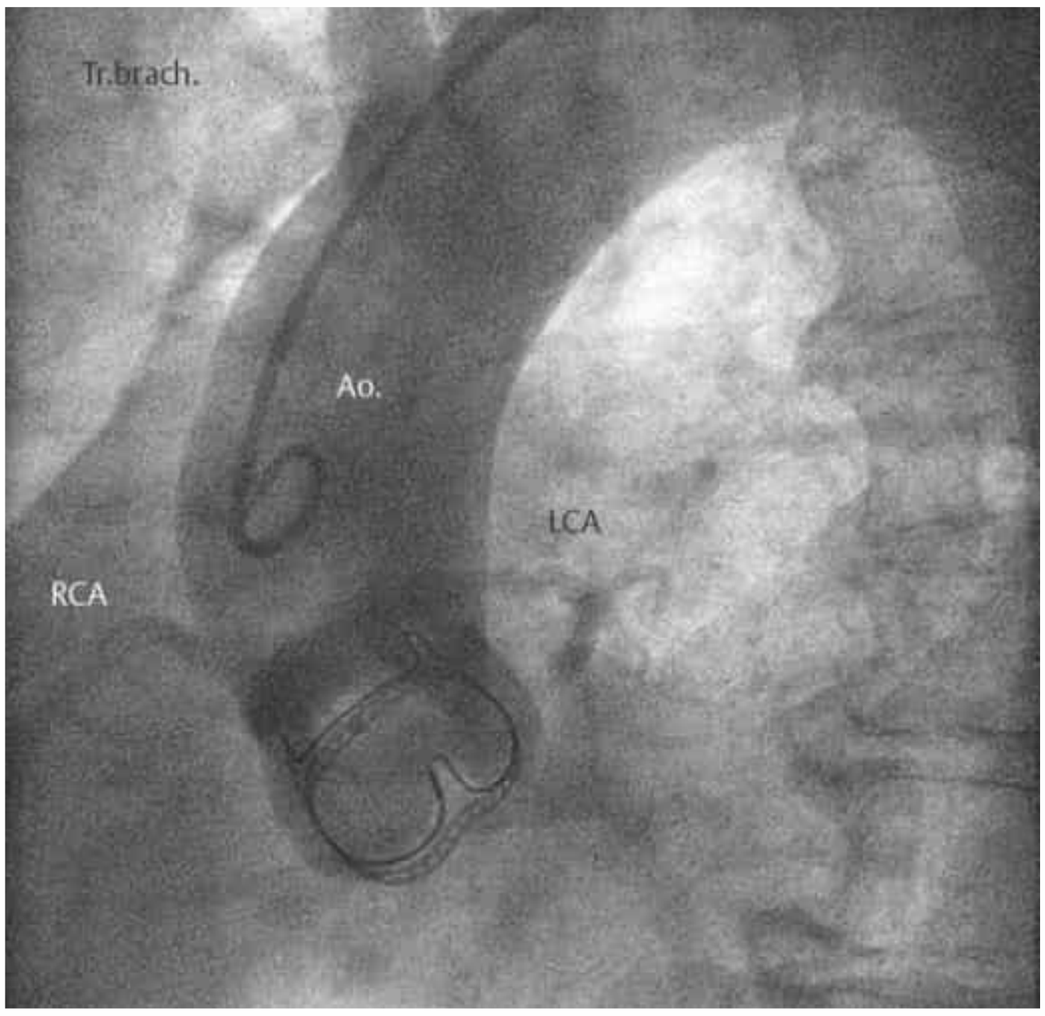

Fig. 3.3 Selective digital angiography of the ascending aorta following aortic valve replacement. The biological aortic valve prosthesis occupies a normal position without evidence of reflux.

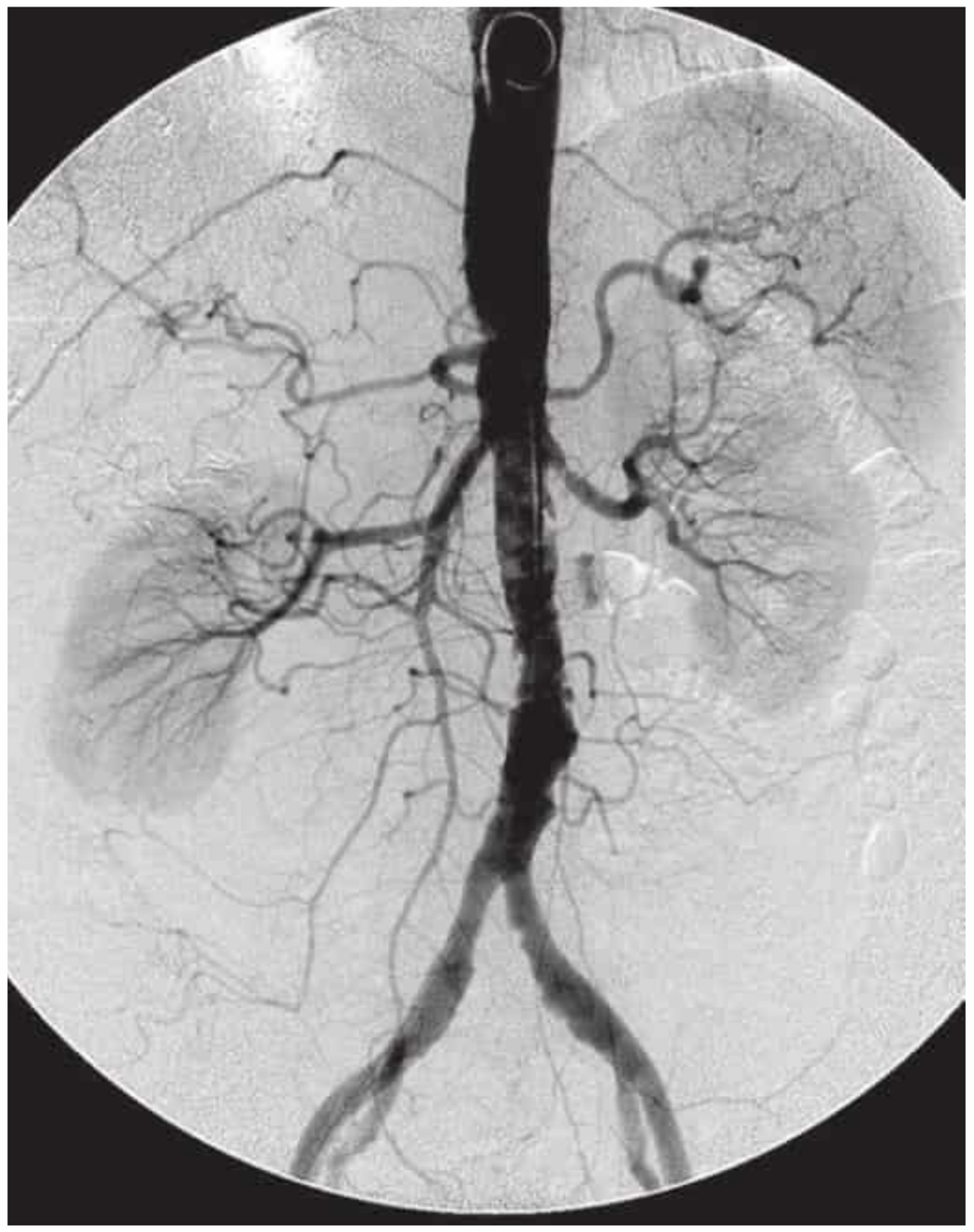

Fig. 3.4 Selective DSA of the abdominal aorta demonstrates severe atherosclerotic wall changes in the infrarenal aorta and proximal iliac vessels. The relatively high-grade left renal artery stenosis represents an incidental finding.

Coronary Angiography

Diagnostic cardiac catheterization is the current gold standard for the **morphological evaluation of coronary anatomy**. In 2003 a total of 652 781 coronary angiographies were performed in Germany.[1] Visualization of the epicardial coronary vessels is indicated in patients with clinical suspicion of significant coronary heart disease based on clinical symptoms, prior history, and noninvasive diagnostic test results. Coronary angiography can determine the:

- Location
- Length
- Degree, and
- Type of an obstructive lesion (atheroma, thrombus, dissection, spasm, myocardial bridge)

in the epicardial arteries. The coronary microcirculation can also be angiographically evaluated based on blood flow patterns (slow flow phenomenon, myocardial blush, or TIMI [Thrombolysis In Myocardial Infarction] status).

Coronary angiography can be performed through a **transfemoral approach** (Judkins technique) or a **transbrachial/transradial approach**. The main advantage of the transfemoral approach is the relatively straightforward technique of femoral artery puncture.

The Sones method involving brachial artery cutdown is rarely used today. The advantage of the Sones technique is that the entire protocol—selective visualization of the right and left coronary arteries and left ventriculography—can be performed with a single catheter. Another advantage is that the patient can ambulate immediately after the procedure.

Each segment of the coronary vessels should be imaged in two mutually perpendicular planes whenever possible. The standard investigation is supplemented with additional views if necessary. Visualization of the left coronary artery generally requires a minimum of six projections, while the right coronary artery necessitates at least two. The purpose of different projection planes is to obtain profile views of the coronary arteries and their branches, so that the extent and degree of stenoses, vascular pathomorphology, and collateral channels can be accurately assessed. Images are acquired at a frame rate of 12.5/s using the digital technique.

The angiographically "healthy" coronary artery exhibits smooth margins. Abnormal signs are increased vascular tortuosity (e.g., due to persistent arterial hypertension) and coarse wall irregularities suggestive of diffuse coronary sclerosis (**Figs. 3.5, 3.6**). Stenoses may be circumscribed (eccentric, concentric) or segmental.

Indications for selective coronary angiography (Guideline for Diagnostic Coronary Angiography of the German Cardiology Society)[4]:

- **Class I** indications (usefulness clearly outweighs the risk, no further tests are needed, and the procedure is definitely indicated):
  - Angina pectoris of CCS Class III or IV under therapy (Class I indication)
  - High-risk criteria on noninvasive testing, regardless of severity of angina pectoris
  - Patients with acute coronary syndrome

- Heart failure with impaired LV function and angina pectoris or confirmed ischemia
- Patients selected for heart transplantation
- Patients resuscitated from sudden cardiac death
- Persistent monomorphic ventricular tachycardia (>30 s)
- Nonsustained polymorphic ventricular tachycardia (<30 s)

• **Class IIa** indications (usefulness outweighs the risk, further tests are needed, and the procedure or therapy is appropriate):

- Angina pectoris of CCS Class III or IV which improves to CCS I or II with antianginal therapy
- Angina pectoris of CCS Class I or II with intolerance or lack of response to medical therapy or recurrent angina pectoris despite medical therapy
- Deterioration of stress test findings (using the same protocol)
- Patients with angina and suspected coronary heart disease (moderate or high pretest probability) who cannot undergo stress testing owing to disability or comorbidity
- Suspected high-grade stenosis in the proximal vascular segments or left main trunk on multislice spiral CT angiography
- Individuals who require definitive exclusion of coronary heart disease for occupational reasons (e.g., pilots or bus drivers where the presence of CHD poses a risk to others) when CHD is suspected on the basis of abnormal stress tests, high-risk features, or other risk features
- Unexplained reduction in LV function
- Normal LV function in a patient with recurrent heart failure
- Reduction in LV function or increase in LV diameter (by the same test) in patients with known CHD
- Patients with HOCM and angina pectoris

Complications of selective coronary angiography. The potential complications are similar to those of angiocardiography. There is an additional risk of coronary arterial injury due to intramural injection or catheter-induced dissection. Furthermore, the intracoronary injection of air or thrombi may cause an acute myocardial infarction requiring emergency bypass surgery.

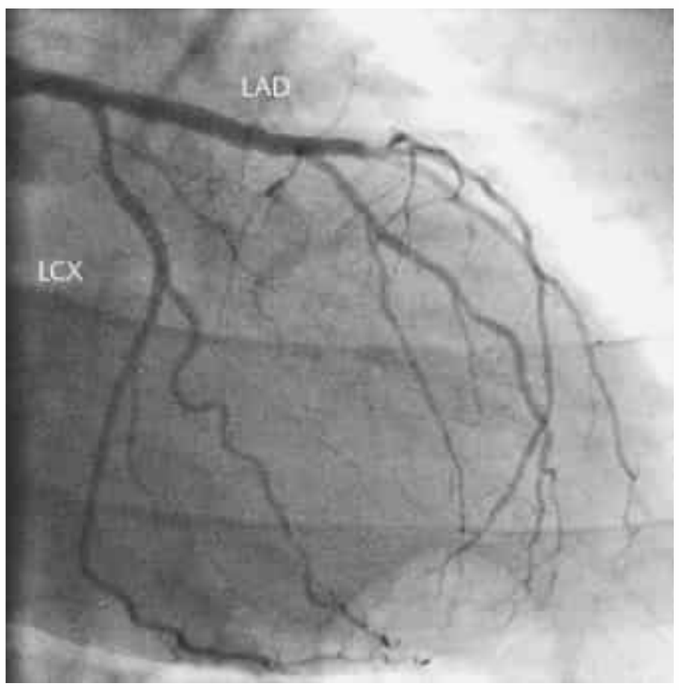

Fig. 3.5 Selective angiography of the left coronary artery demonstrates the main trunk, LAD, and LCX with a low-grade proximal stenosis.

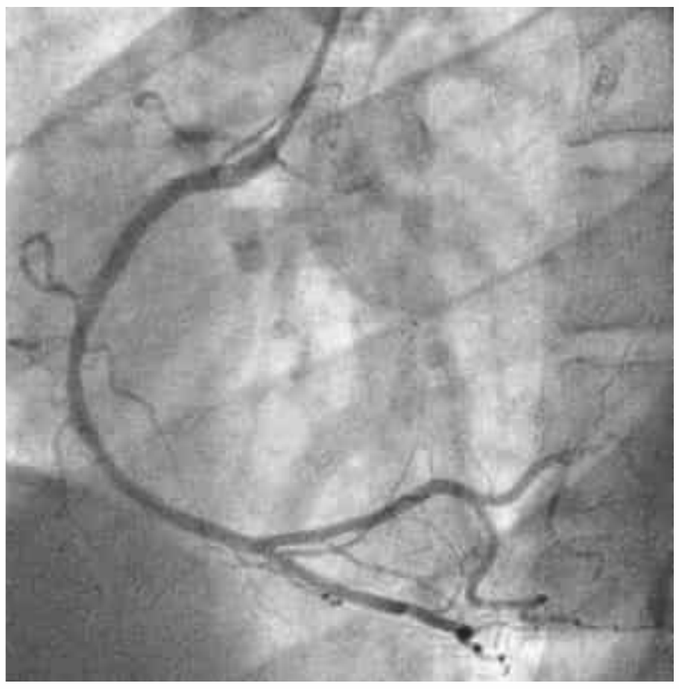

Fig. 3.6 Selective angiography of the right coronary artery.

Special Invasive Imaging Techniques

Intravascular Ultrasound

Intravascular ultrasound (IVUS) has become the established gold standard in recent years for the evaluation of:

- Vessel lumina
- The vessel wall
- Atherosclerotic morphology

An invasive sectional imaging modality, IVUS is used in the catheterization laboratory or angiography suite as an adjunct to angiocardiography to obtain more detailed information. Various catheters are used depending on whether the study targets small-caliber coronary arteries, large-caliber peripheral vessels, or the aorta. The tip of the catheter is fitted with ultrasound crystals that operate at frequencies from 10 to 40 MHz and thus have a variable range and resolution.

In addition to mechanical ultrasound systems with a rotating transducer at the catheter tip, electronic catheter systems with a cylindrical array of slender acoustic ultrasound elements arranged around the catheter tip are available. Both systems can provide detailed cross-sectional images of the vessel lumen and wall.

The catheters are wire-guided and have an outer diameters ranging from 2.5 Fr (coronary IVUS) to 8.2 Fr (aortic IVUS). The coronary IVUS catheter is introduced into the coronary vessel with a guide catheter threaded over a wire 0.014 inch in diameter (the same type as used in coronary interventions). The IVUS catheter is then withdrawn manually, or preferably with an automated device, at a rate of 1 mm/s, permitting entire coronary vessels as small as 1.0 mm to be scanned. The data obtained during automated pullback can later be used to generate a 3D reconstruction of the coronary vessel. A recent innovation in coronary IVUS is so-called "virtual histology," in which the radiofrequency dataset that forms the basis for the IVUS image is subjected to spectral analysis. A computerized comparison with existing datasets acquired by histological in-vitro validation permits individual plaque structures to be classified as fibrous, lipid-rich, mixed, or calcified.[5] The IVUS catheter for evaluating peripheral vessels and the aorta has a larger lumen than the coronary IVUS catheter and is generally inserted directly into the vessel over a 0.035-inch wire without using a guide catheter. The vessel is surveyed by manual catheter withdrawal.

As a supplement to angiocardiography, IVUS has the ability to define intraluminal structures (e.g., intimal flaps) in high detail and visualize wall structures (e.g., atherosclerotic plaques) (**Fig. 3.7**). IVUS has better spatial resolution than angiography and can resolve structures as small as 150–170 µm, enabling it to detect **slight intimal thickening** that is not yet visible in angiograms.[6,7] Thus, coronary heart disease can be diagnosed at an earlier stage with IVUS than with coronary angiography alone.[8]

In 1995, Stary et al. described a pathoanatomical staging system for **coronary plaque formation**[9] that was later reproduced by IVUS findings in vivo.[10] IVUS provides important additional physiological information in patients with **myocardial bridging**.[11] It further permits a more accurate assessment of **calcification** in coronary stenosis. This is particularly helpful in coronary interventions and may prompt modification of the intervention strategy. IVUS is also useful in the examination of patients with **aortic diseases**, most of which involve the aortic wall and are thus inadequately depicted in conventional angiograms.

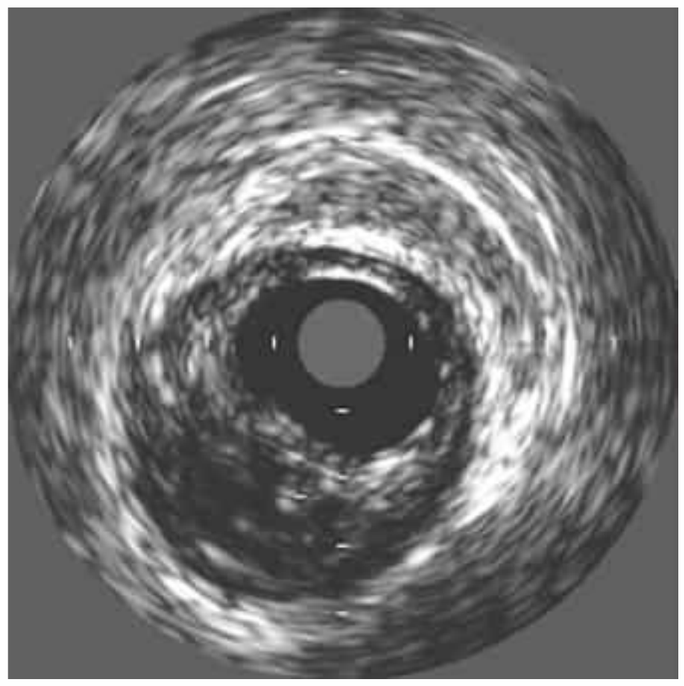

Fig. 3.7 Intravascular ultrasound image of complicated plaque formation (Stary type Va) with high-grade narrowing of the perfused lumen.

Essential Point
As an example, the false lumen of an aortic dissection can be demonstrated only indirectly by angiography. Intramural hematoma is angiographically occult because it does not communicate with the perfused lumen.

IVUS is superior to TEE in that it can evaluate the **entire aorta**. This permits diagnostic information of CT quality to be obtained in the catheterization laboratory.

Koschyk et al. found that IVUS was useful in the guidance of **aortic stent-graft implantation**, providing information complementary to angiography and even superior to that obtained with TEE.[12] However, IVUS is limited by the lack of color Doppler capabilities, which would be useful, for example, in locating sites of communication between the true and false lumen. The AcuNav ultrasound catheter is a promising innovation in this regard.[13] This catheter-based 8 Fr ultrasound system has all the color duplex and Doppler capabilities of a traditional echocardiographic system. Unlike IVUS, the AcuNav system generates sector images with a maximum range of 15 cm. The system has various applications, such as monitoring intracardiac procedures in pediatric and adult cardiology (e.g., interventional umbrella occlusion of an atrial septal defect) to spare patients the discomfort of TEE.[14] This system is further used in electrophysiological pulmonary vein ablations for the treatment of atrial fibrillation. In this procedure the catheter is advanced into the right atrium via the femoral vein, and the target structures are scanned from that location. Because this catheter system is not wire-guided like IVUS, the catheter must be carefully manipulated under continuous fluoroscopic guidance.

IVUS can also be used transvenously to monitor interventional procedures such as **balloon fenestration** of the abdominal aorta.[15] Initial attempts have already been made to use the system intra-arterially, for example, in the **evaluation of aortic dissection**. The color Doppler capabilities of the system may make it superior to angiography in detecting very small communications between the true and false lumina.

Intracoronary Doppler

Intracoronary Doppler ultrasound (ICD) can supply important information on **coronary blood flow and physiology** during diagnostic cardiac catheterization. Intracoronary Doppler can also be used to assess the hemodynamic significance of a coronary stenosis.

Initially, 3 Fr catheters with annular crystals at the tip were the only probes available for ICD, but these catheters were limited in their ability to evaluate flow velocity in small and stenotic coronary vessels. Development of the **ultrasound Doppler wire** represents a significant advance because it can be used in place of a standard 0.014-inch guidewire, and because a fast Fourier transform (FFT) analysis can be done to determine maximum and mean coronary blood flow velocity. The ultrasound crystal at the distal end of the Doppler wire has a sample volume located 5 mm from the wire tip.

Extensive knowledge of coronary physiology and pathophysiology is necessary to understand and interpret intracoronary Doppler findings. **Homeostatic regulation** describes the relationship between intracoronary pressure and coronary blood flow. This means that an increase in coronary perfusion pressure does not cause an increase in coronary flow over a wide range of values. The pressure must fall below a critical threshold of ~80 mmHg before coronary flow decreases, and it must rise above a critical level of 200 mmHg before coronary flow increases.[16] Autoregulation of the coronary vascular system can be partially or completely eliminated with vasodilators (adenosine, papaverine, moxaverine, dipyridamole, radiographic contrast media). Treatment with these agents leads to a maximal increase in blood flow, which then correlates directly with the coronary perfusion pressure.[17] This corresponds to the physiological situation of a maximum rise in oxygen consumption during physical exercise, for example. The ratio of coronary blood flow during maximum vasodilation to coronary blood flow at rest is described as the coronary flow reserve.

Various factors may affect autoregulation. For example, resting blood flow is elevated in patients with hyperthyroidism, tachycardia, and hypertension, while the maximum flow increase is reduced in patients with tachycardia, prior myocardial

infarction, and microvascular perfusion disorders. ICD can determine the coronary flow velocity reserve, defined as the ratio of maximum hyperemic blood flow velocity to resting flow velocity. For clinical applications, the velocity reserve in the coronary vessels correlates very closely with the coronary flow reserve.[18] Maximum coronary hyperemia is induced by an intracoronary bolus injection or by continuous peripheral venous infusion of adenosine. A coronary flow velocity reserve of 3.0, corresponding to a 300%increase in the resting blood flow velocity, is considered normal.

The **indications** for intracoronary Doppler scanning include:

- Chest pain
- An abnormal stress test with a normal coronary angiogram

These findings may result from **coronary microangiopathy**, which occurs as an isolated condition in up to 20%of patients, but is frequently combined with coronary macroangiopathy. Abnormalities of the coronary microcirculation have been described based on coronary vascular changes in arterial hypertension, diabetes mellitus, hyperlipoproteinemia, and rheological and extravascular components. The diagnosis of coronary microangiopathy cannot be established in the catheterization laboratory on the basis of coronary angiography alone but requires additional function studies such as intracoronary Doppler flowmetry.

Intracoronary ultrasound is also useful in assessing the hemodynamic significance of an angiographically moderate **coronary stenosis**. Borderline stenoses (50–70%luminal narrowing) pose a special diagnostic and therapeutic challenge in the catheterization laboratory with regard to determining whether the stenosis is a flow-limiting lesion which can adequately account for the patient's complaints.[19] This can be accomplished by relating the coronary flow velocity reserve in a nonstenosed reference vessel to the coronary velocity reserve distal to the coronary stenosis. A ratio <0.75 suggests that the stenosis is hemodynamically significant.[20] This indicates the potential value of adding a functional assessment of the coronary circulation in coronary macroangiopathy to the standard morphological vascular assessment made in the cardiac catheterization laboratory.

Intracoronary ultrasound can also be applied in **coronary interventions** to assess the outcome of the interventional therapy, i.e., to determine whether coronary blood flow has been improved. If a decreased flow velocity reserve is found after PTCA or stent implantation, the patient may require an additional interventional procedure (e.g., redilation with a larger balloon).

Intracoronary Doppler scanning continues to be helpful in the functional evaluation of **myocardial bridging** to assess the hemodynamic significance of systolic vascular compression.

Intracoronary Pressure Wire

Comparable to intracoronary ultrasound, an intracoronary pressure wire is used during diagnostic cardiac catheterization to determine whether a **coronary stenosis** is causing a hemodynamically significant reduction in coronary blood flow. Pijls et al. have introduced the concept of fractional flow reserve (FFR_{myo}), an index which is virtually identical to the coronary flow reserve and can be easily and accurately determined with a pressure wire.[21] The FFR has a well-validated cutoff value of 0.75 for hemodynamically significant stenosis. Determination of the FFR also eliminates the need to take a measurement in a healthy reference vessel as required in intracoronary Doppler.

The FFR is determined by measuring the pressure gradient across a coronary stenosis with a pressure wire introduced into the stenosed coronary vessel. The pressure gradient is measured in relation to the aortic pressure during maximal coronary hyperemia induced by adenosine. A ratio of less than 0.75 indicates the presence of a hemodynamically significant stenosis.[22]

References

1. van Buuren F, Mannebach H, Horstkotte D. 20th report of performance data from heart catheterization laboratories in Germany. 2003 results of a collaborative survey by the Committee of Clinical Cardiology and the Interventional Cardiology (for ECS) and Angiology Study Groups of the German Society of Cardiology-Cardiovascular Research. Z Kardiol 2005;94(3):212–215
2. Eggebrecht H, Haude M, Woertgen U, et al. Systematic use of a collagen-based vascular closure device immediately after cardiac catheterization procedures in 1,317 consecutive patients. Catheter Cardiovasc Interv 2002;57(4):486–495
3. Erbel R, Alfonso F, Boileau C, et al. Task Force on Aortic Dissection, European Society of Cardiology. Diagnosis and management of aortic dissection. Eur Heart J2001;22(18):1642–1681
4. http://www.dgk.org/leitlinien
5. Nair A, Kuban BD, Tuzcu EM, Schoenhagen P, Nissen SE, Vince DG. Coronary plaque classification with intravascular ultrasound radiofrequency data analysis. Circulation 2002;106(17):2200–2206
6. Mintz GS, Nissen SE, Anderson WD, et al. American college of cardiology clinical expert consensus document on standards for acquisition, measurement and reporting of intravascular ultrasound studies (IVUS). J Am Coll Cardiol 2001;37(5):1478–1492
7. Baumgart D, Liu F, Haude M, Görge G, Ge J, Erbel R. Acute plaque rupture and myocardial stunning in patient with normal coronary arteriography. Lancet 1995;346:193–194
8. Erbel R, Ge J, Bockisch A, et al. Value of intracoronary ultrasound and Doppler in the differentiation of angiographically normal coronary arteries: a prospective study in patients with angina pectoris. Eur Heart J 1996;17:880–889
9. Stary HC, Chandler AB, Dinsmore RE, et al. A definition of advanced types of atherosclerotic lesions and a histological classification of atherosclerosis. Circulation 1995;92:1355–1374
11. Ge J, Erbel R, Rupprecht HJ, et al. Comparison of intravascular ultrasound and angiography in the assessment of myocardial bridging. Circulation 1994;89(4):1725–1732
12. Koschyk DH, Nienaber CA, Knap M, et al. How to guide stent-graft implantation in type B aortic dissection? Comparison of angiography, transesophageal echocardiography, and intravascular ultrasound. Circulation 2005;112(9 Suppl):I1260–1264
13. Caspari GH, Muller S, Bartel T, Koopmann J, Erbel R. Full performance of modern echocardiography within the heart: in-vivo feasibility study with a new intracardiac, phased-array ultrasound-tipped catheter. Eur J Echocardiogr 2001;2(2):100–107
14. Bartel T, Konorza T, Arjumand J, et al. Intracardiac echocardiography is superior to conventional monitoring for guiding device closure of interatrial communications. Circulation 2003;107(6):795–797
15. Bartel T, Eggebrecht H, Ebradlidze T, Baumgart D, Erbel R. Images in cardiovascular medicine. Optimal guidance for intimal flap fenestration in aortic dissection by transvenous two-dimensional and Doppler ultrasonography. Circulation 2003;107(2):e17–e18
16. Gould KL, Kirkeeide R, Buchi M. Coronary flow reserve as a physiological measure of stenosis severity, I: relative and absolute coronary flow reserve during changing aortic pressure; II: determination from angiographic stenosis dimensions under standardized conditions. J Am Coll Cardiol 1990;15:459–474
17. Kern MJ, Syndrome X. Understanding and evaluating the patient with chest pain and normal coronary arteriograms. Heart Dis Stroke 1992;1: 299–302
18. Baumgart D, Haude M, Birgelen Cv C, Ge J, Gorge G, Erbel R. Assessment of ambiguous coronary lesions by intravascular ultrasound. Int J Cardiovasc Intervent 1999;2(1):3–12
19. Baumgart D, Haude M, Goerge G, et al. Improved assessment of coronary stenosis severity using the relative flow velocity reserve. Circulation 1998;98(1):40–46
20. Baumgart D, Haude M, Liu F, Ge J, Goerge G, Erbel R. Current concepts of coronary flow reserve for clinical decision making during cardiac catheterization. Am Heart J 1998;136(1):136–149
21. Pijls NH, De Bruyne B, Peels K, et al. Measurement of fractional flow reserve to assess the functional severity of coronary-artery stenoses. N Engl J Med 1996;334(26):1703–1708
22. Verberne HJ, Piek JJ, van Liebergen RA, Koch KT, Schroeder-Tanka JM, van Royen EA. Functional assessment of coronary artery stenosis by doppler derived absolute and relative coronary blood flow velocity reserve in comparison with (99 m)Tc MIBI SPECT. Heart 1999;82(4):509–514

Further Reading

Mintz GS, Painter JA, Pichard AD, et al. Atherosclerosis in angiographically "normal" coronary artery reference segments: an intravascular ultrasound study with clinical correlations. J Am Coll Cardiol 1995;25(7): 1479–1485

4 Nuclear Medicine Imaging

A. Bockisch, K. Sattler, and S. J. Rosenbaum-Krumme

Basic Principles

Nuclear medicine has several applications in cardiac diagnosis, the most common being the assessment of left ventricular perfusion and myocardial viability. Imaging is generally performed with SPECT-capable gamma cameras (SPECT=single-photon emission computed tomography) or a positron emission tomography (PET) scanner. PET is the superior technique because of its better image quality and higher spatial resolution. While image quality and resolution are of less importance in the assessment of perfusion and viability, they have considerable importance in the evaluation of circumscribed anatomical structures, as in plaque imaging, for example. SPECT and PET use different types of radiotracer for imaging: gamma emitters and positron emitters, respectively. Different tracers have different kinetics and image more or less different physiological processes. Today there are more SPECT-capable gamma cameras than PET scanners available for patient care.

All nuclear medicine imaging is concerned primarily with the **left ventricle**. The right ventricle has a considerably smaller muscle mass with less perfusion and less energy consumption than the left ventricle, which makes it less accessible to scintigraphic investigation.

Myocardial Scintigraphy

Examination Technique

Myocardial scintigraphy is a noninvasive study which provides information on myocardial perfusion and myocardial viability.

Myocardial scanning is performed at **rest** and under **stress conditions**. The exact scan protocol depends on the type of radiotracer used (see p. 69, **Table 4.2**). It should be emphasized that nuclear medicine imaging evaluates function. Accordingly, the results of myocardial scintigraphy vary depending on diet, medication, physical conditioning, and so on. Optimum nuclear medicine testing for the presence and severity of coronary heart disease requires maximum age-appropriate stress conditions and the avoidance of negative chronotropic or antianginal medications (β-blockers, nitrates). On the other hand, scintigraphy can be used during medical therapy to determine the effect of the medication on myocardial perfusion. Ergometric stress is preferred in all patients who can tolerate exercise. Pharmacological stress can be used in patients who are uncooperative or cannot perform an ergometric protocol for noncardiac reasons (e.g., arthritis, amputation, neurological disease). Pharmacological stress can be induced with agents that cause coronary hyperemia (adenosine, dipyridamole) or agents that increase myocardial contractility (dobutamine).

Essential Point

To detect ischemia with high sensitivity, negative chronotropic and antianginal medications (β-blockers, nitrates) should be discontinued before testing. Exercise to maximum tolerance is encouraged.

SPECT technique is recommended for all nuclear medicine stress testing. Multihead gamma cameras should be used to improve the count statistics. Because of the eccentric location of the heart in the body, it is advantageous to position the gamma cameras at right angles (90° configuration) rather than opposite each other (180° configuration). Special "cardiac SPECT gamma cameras" are not widely available, and their costs are justified only at a sufficiently high level of usage.

In the simplest acceptable form of myocardial SPECT imaging, standard planes of section are calculated along the long, short, and transverse axes of the left ventricle. The results are displayed in a "bull's-eye" format, in which the left ventricle is depicted as a series of apical to basal segments arranged in a circular pattern. The segments are numbered according to the 17-segment model of the left ventricle described by the American Heart Association.[1]

These images routinely contain attenuation artifacts because the emitted photons are scattered or absorbed depending on the path length within the body. Photon attenuation in obese patients may cause apparent areas of decreased tracer uptake in the posterior heart wall, and in large-breasted women it can mimic decreased uptake in the anterolateral heart wall. These effects should not be misinterpreted as a perfusion defect (**Table 4.1**). **Attenuation correction** is a technique enabling the measurement of soft-tissue attenuation with the aid of an external source.[2] Attenuation correction thus requires an additional transmission scan with an external radiation source. The transmission and emission images—the actual SPECT images—are then used to compute attenuation-corrected scans. Attenuation correction improves the image quality and diagnostic accuracy of myocardial scintigraphy. The superiority of attenuation-corrected scans over uncorrected scans has been documented in several clinical studies and does not depend on the body mass index of the individual patient.[3]

ECG gating increases the logistic efforts of myocardial SPECT. In addition, it enables the evaluation of left ventricular function. In this technique, special software-based algorithms are used to define the wall contours of the myocardium. Ventricular volume is determined in each of the cardiac phases and is used to calculate the left ventricular ejection fraction. Wall motion and wall thickening can also be visualized. It has been shown that adding functional data to the perfusion data facilitates both the identification of patients with multivessel CHD, and assessment of the severity of ischemia due to persistent LV

Table 4.1 Uptake patterns associated with different findings in myocardial scintigraphy

	Normal finding	Ischemia	Scar
Stress scans	Normal	Decreased	Decreased
Rest scans	Normal	Normal	Decreased

dysfunction in poststress images. It further allows an assessment for the prediction of cardiac events.[4] ECG-gated data can also help narrow the differential diagnosis in cases where an attenuation artifact cannot be excluded. For example, when a wall-motion abnormality is detected in a wall segment with equivocal perfusion findings, it can be assumed that the segment is ischemic.

On the whole, gated SPECT images are more cost intensive in terms of quality control. It should also be noted that, with regard to technical aspects, myocardial SPECT image quality depends significantly on the count statistics in the image, i.e., on the administered activity and length of the examination. Neither of these values can be arbitrarily increased, setting limits on what can be accomplished with the technical improvements described above.

Essential Point
Whenever possible, gated SPECT with attenuation correction should be used in myocardial scintigraphy.

Tracers

Various radiotracers are available for myocardial scintigraphy, all of which have one property in common: within the range of physiological flow, all radiotracers are extracted from the blood in proportion to blood flow and become concentrated in myocardial cells. Because of their different kinetics, the tracers available for myocardial scintigraphy also require different imaging strategies.

Thallium Chloride

Thallium chloride Tl^{201} (TlCl) is extracted by myocardial cells in proportion to blood flow. It is distinguished from other tracers by its **high extraction in low-flow conditions**, and has the longest range of **linear uptake** even under high-flow conditions. As a result, TlCl permits the most sensitive viability assessment of chronically ischemic myocardium and defines the extent of perfusion abnormalities most accurately.

Nevertheless, thallium 201 is an unfavorable nuclide for perfusion scanning, both in terms of the half-life and energy of the emitted photons. The relatively high radiation exposure (**Table 4.2**) limits the activity that can be applied and results in a "noisy" image. Thus, the interpretation of TlCl perfusion scans requires considerable experience and a well-defined image processing routine to avoid inaccurate findings due to image artifacts. Another problem with thallium chloride is that the low applicable activity of this tracer greatly limits its suitability for gated SPECT imaging.

TlCl is actively transported into cells by the Na^{+}–K+ pump mechanism and leaves the cells very slowly by passive diffusion. This redistribution or "washout" of the agent is advantageous in that approximately similar stress-induced perfusion changes are detected globally in all myocardial segments. TlCl is injected intravenously approximately 1 minute before the end of exercise. Stress imaging begins immediately after the end of exercise, and the redistribution scan is obtained 3–4 hours later. Redistribution of the activity eliminates the need for an additional tracer injection (**Fig. 4.1**). Because the ischemic myocardium has not always recovered by 3 hours postinjection, it may be necessary to obtain a rest scan approximately 24 hours after application to differentiate ischemia from a fixed thallium defect present in both the stress and redistribution scans.

Sestamibi

Sestamibi is labeled with the metastable isotope technetium 99 m (Tc^{99}), which makes it ideal for radionuclide imaging. With a gamma emission of 140 keV and physical half-life of 6 hours, it causes only moderate radiation exposure. Despite the markedly lower radiation exposure compared with TlCl, the images are sharper and have good count statistics. Sestamibi (synonym for MIBI) can also be used in conjunction with gated SPECT imaging to obtain additional ventriculographic data.

Sestamibi has a flow-proportional uptake in myocardial cells and is concentrated in the mitochondria. In a typical examination, and even for several hours, redistribution does not occur. Two injections are therefore necessary, one for rest and one for stress imaging.

The two tests should ideally be done on different days. Since Tc^{99m} has a half-life of 6 hours, approximately 5 %of the original activity is still present in the heart the following day, causing little if any interference with the second test if the rest images are obtained first. However, in view of the fact that a two-day examination would delay diagnosis and increase logistical costs,

Table 4.2 Radiopharmaceuticals and radiation exposure[a]

Radiopharmaceutical	Half-life of nuclide	Characteristic activity (MBq)	Critical organ and dose (mGy/MBq)	Effective dose equivalent (mSv/MBq)
Thallium chloride Tl^{201}	73 h	75–150	0.54 kidney	0.23
Technetium Tc^{99m} sestamibi	6.0 h	750–1100	0.036 gallbladder	0.0085
Technetium Tc^{99m} tetrofosmin	6.0 h	750–1100	0.031 gallbladder	0.0067
(^{18}F)FDG	110 min	200–370	0.17 urinary bladder	0.027
^{82}Rb	75 s	1400	0.01 kidney	0.0005
(^{13}N)NH_3	10 min	700	0.008 bladder wall	0.0027

[a] Lines 1–4 in accordance with AWMF guidelines.

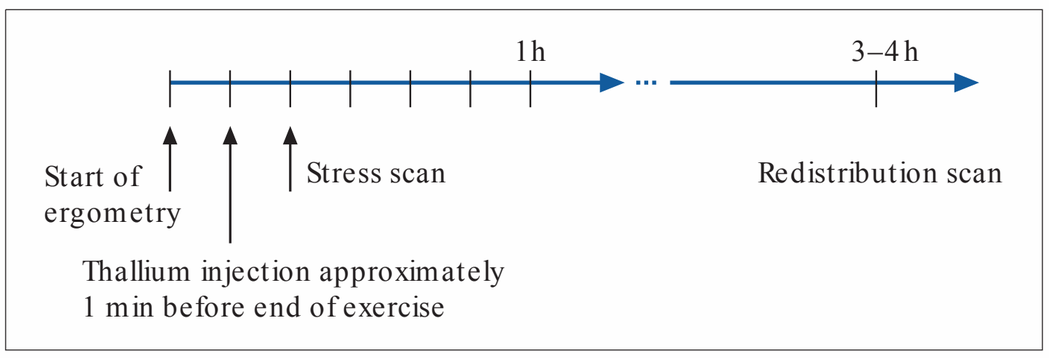

Fig. 4.1 Typical protocol for thallium myocardial scintigraphy. A single injection of thallium chloride Tl^{201} is sufficient for stress and rest scans. The nuclide is redistributed after the end of exercise, allowing a rest scan to be obtained after a standard interval of~ 3–4 hours.

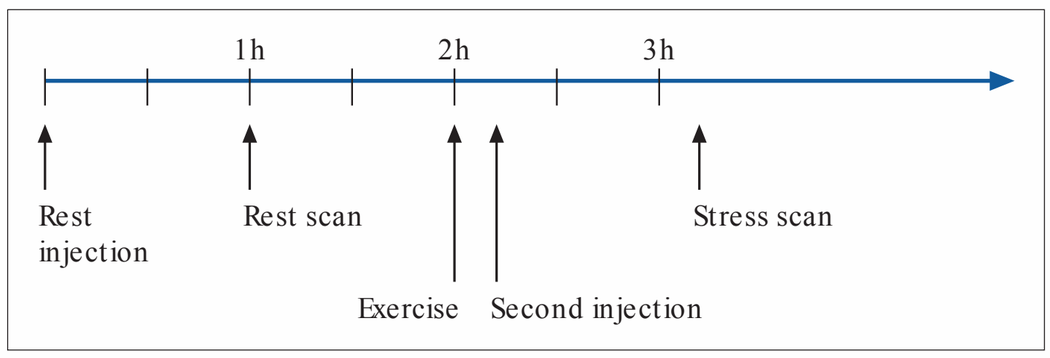

Fig. 4.2 Typical protocol for technetium Tc^{99m} sestamibi myocardial scintigraphy. Another option is a two-day protocol in which rest scans are obtained on day 1 and stress scans on day 2.

a one-day protocol has become standard. In this case rest scans are obtained first with ~200 MBq of technetium Tc^{99m} sestamibi, and stress scans are obtained at the earliest 2 hours later with ~600 MBq (**Fig. 4.2**). Because blood flow is usually at least twice as high during exercise as at rest, the activity from the rest study contributes only up to 5 %to the stress study without distorting the results.

Tetrofosmin

Tetrofosmin has properties similar to those of sestamibi, but because of its shorter biological half-life in the heart, the time window between injection and imaging is smaller than with sestamibi. Furthermore, tetrofosmin has a better heart/liver ratio owing to its more rapid hepatic clearance. Tetrofosmin, unlike TlCl, is not redistributed because it undergoes rapid chemical transformation to a compound that is no longer extracted by myocardial cells, and therefore two injections are required. All other statements pertaining to sestamibi also apply to tetrofosmin.

Interpretation of Scintiscans

Before the findings are analyzed, the acquired data should be subjected to quality control. Errors most commonly result from the patient's movements during imaging. Motion artifacts can be excluded following examination of the raw data, and the scans can be repeated if necessary. This option is limited in thallium stress tests because of the redistribution of TlCl.

The uptake of the injected radionuclide depends on myocardial perfusion and viability. Myocardial scintigraphy permits not only the early noninvasive detection of coronary heart disease (CHD) but also the quantification of myocardial ischemia. It therefore has two main indications:

- Investigation of suspected CHD
- Prognostication in patients with known or suspected CHD

Tracer uptake is evaluated at rest and during stress. If a hemodynamically significant stenosis is present, its effects will be augmented under stress conditions because a portion of the flow reserve is already used up at rest. Because decreased uptake under stress conditions may result either from a relative reduction in blood flow or from a decrease in myocyte mass, rest scans must be obtained to differentiate between these findings. **Table 4.1** summarizes the uptake patterns that may be found in rest and exercise scans (**Figs. 4.3, 4.4**).

One potential problem, especially in sestamibi scanning, is the presence of increased activity in the hepatobiliary system and gastrointestinal tract. These areas may abut the inferior heart wall and yield an inaccurate finding of increased or decreased uptake in the reconstructed images, making evaluation of the posterior wall difficult. This may occur despite the stimulation of biliary secretion (a fatty meal, choleretics) or the use of prokinetic agents. Currently there are no technical solutions for the correction of this problem, and the scans should be repeated at a later time if gastrointestinal uptake causes serious image degradation.

Clinical Significance of Myocardial Scintigraphy

Myocardial scintigraphy permits the earliest possible quantitative detection of a perfusion abnormality at the cellular level, thereby documenting the hemodynamic significance of a stenotic lesion. From a prognostic standpoint, a normal stress myocardial perfusion scan implies an excellent medium-term prognosis with less than a 1 %risk of cardiovascular complications per year.[5] As the extent and severity of a stress-induced abnormality increase, there is a significant rise in the risk of cardiac death and other major cardiac events. The choice of therapeutic modality (medical therapy versus revascularization) is influenced by the severity and extent of ischemia and affects the likelihood of future severe cardiac events. It has been shown for extended abnormalities that the incidence of cardiac death is significantly lower after revascularization than with medical therapy. Conversely, medical therapy is associated with a higher survival rate in patients with less severe scintigraphic abnormalities.[6]

Myocardial scintigraphy is also useful in determining the functional significance of a known coronary stenosis and in evaluating the response to coronary revascularization or medical therapy. At a sensitivity of 91 %and specificity of 87 %, corresponding to a diagnostic accuracy of 91 %(reference: >50 % diameter stenosis in angiography), myocardial scintigraphy meets the criteria for a clinically valid diagnostic procedure.

As in all examinations, the value of myocardial scintigraphy depends on patient selection and, as in other nuclear medicine studies, on patient preparation. Myocardial scintigraphy is particularly useful in patients who are at moderate risk for CHD. A positive result in these patients would be an indication for further measures, whereas a negative result would justify a wait-and-see approach or conservative management.

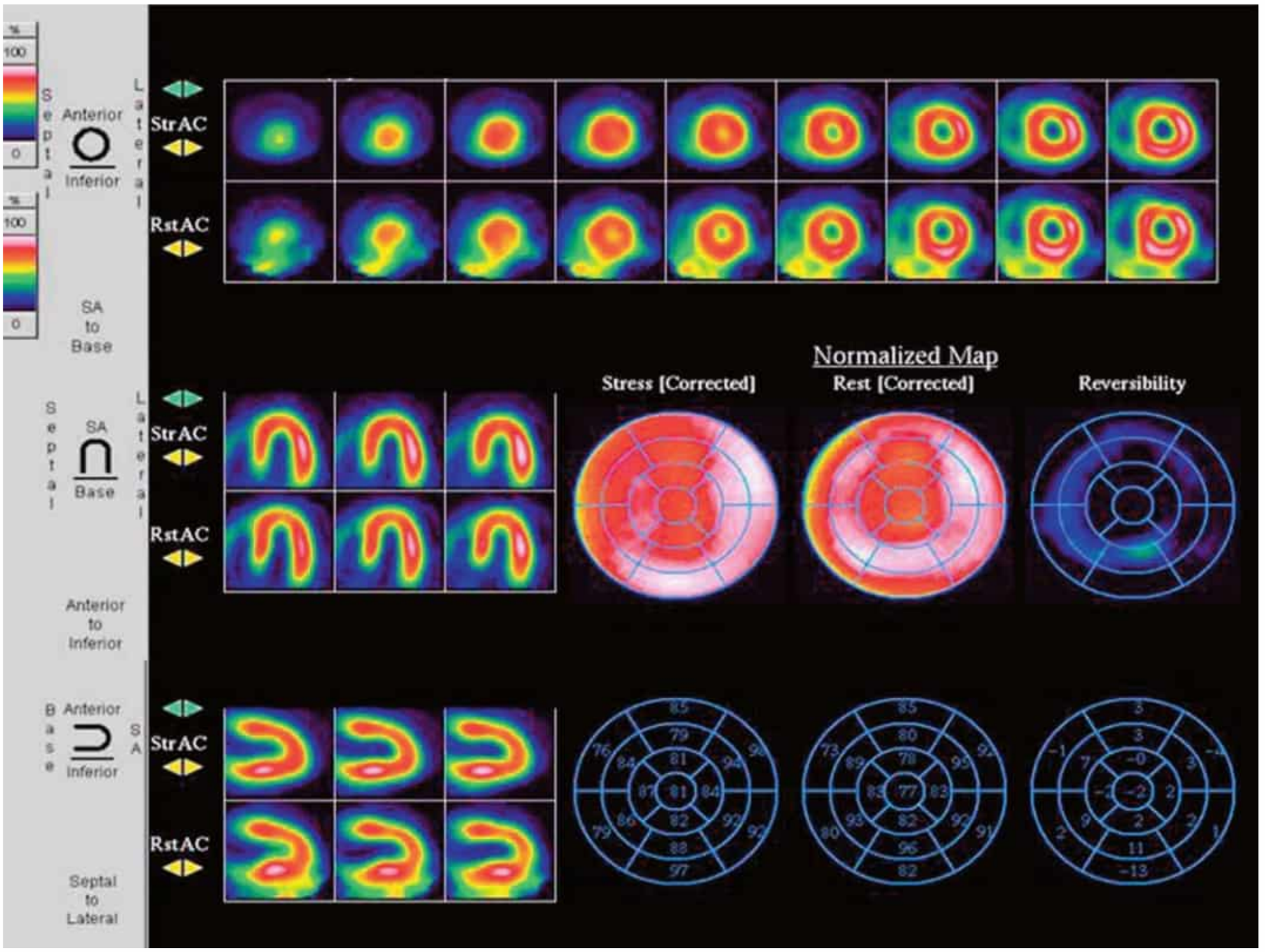

Fig. 4.3 Normal findings in myocardial scintigraphy.
The images in the top row are short-axis stress scans of the left ventricle; in the row directly below them are the corresponding rest scans. Lower left: representative coronal oblique and sagittal stress and rest scans.
The bull's eyes demonstrate homogeneous perfusion during exercise (left) and at rest (center) in a color-coded format (top row) and quantitative segmental format (bottom row). The reversibility bull's eye (right) indicates the extent of ischemia. In the case illustrated, only minor position-related changes are seen.
Far left: definition of the color scale and orientation of the sections. The segmental bull's-eye format follows the American Heart Association scheme[16]; the orientation of the bull's eyes corresponds to that of the short-axis sections.
Str AC = stress attenuation corrected, Rst AC = rest attenuation corrected, Corrected = attenuation corrected display, SA = cardiac apex.

The medical conditions that may be encountered are illustrated by two groups of patients: older patients with diabetes mellitus and women. Myocardial ischemia is frequently asymptomatic in older diabetics and becomes symptomatic only at an advanced stage. The DIAD study (Detection of Ischemia in Asymptomatic Diabetics), conducted in patients 50–75 years of age with type 2 diabetes mellitus and no signs of CHD, showed that clinically asymptomatic ischemia was present in 22% of the patients examined.[7]

Women with coronary heart disease often have a different cardiac symptomatology from male patients. This frequently delays diagnosis in women,[8] although CHD remains one of the leading causes of death among women in western countries. In symptomatic women with a moderate to high risk of CHD, myocardial scintigraphy is excellent for the investigation of CHD, yielding results of comparable sensitivity, specificity, and prognostic significance to those obtained in males. Myocardial scintigraphy in asymptomatic women is a valuable adjunct to ergometric testing, which may result in false-positives more often in women than in men.[9] Women are less frequently referred for noninvasive testing than men, however. This led the American Heart Association to issue a consensus statement and take a position on noninvasive cardiac testing in this patient group.[10]

Positron Emission Tomography

Examination Technique

Positron emission tomography (PET) is frequently used synonymously with FDG (fluorodeoxyglucose)-PET, a test for assessing viability. In fact perfusion tracers and tracers for viability assessment are both available for PET scanning. Combined with the superior spatial resolution of PET, this results in images of very high quality compared with SPECT. The main disadvantages of PET are its higher cost, the limited availability of PET technology, and higher logistical cost due to the short tracer half-lives.

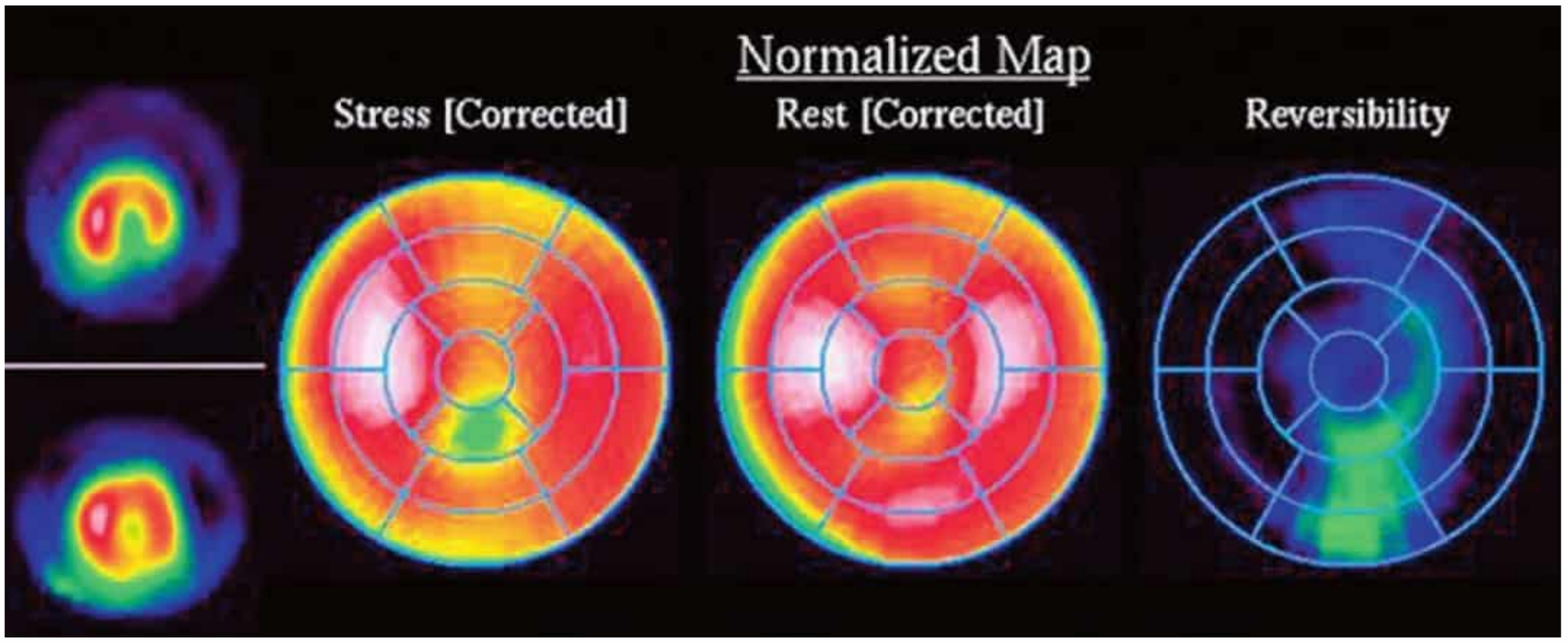

Fig. 4.4 Scintigraphic detection of stress-induced, reversible ischemia in the apical posterior wall. Stress scans demonstrate a perfusion defect in the apical posterior wall that is not present at rest. A positive finding area appears at the corresponding site in the reversibility display. Far left: poststress image above, rest image below. Designations, segments and orientation of the bull's eyes, orientation of the short-axis scans, and color scale are the same as in **Fig. 4.3**.

Cardiac FDG-PET is the gold standard for the evaluation of **myocardial viability in conjunction with perfusion data**. Left ventricular dysfunction due to CHD is associated with a rising mortality risk as the dysfunction becomes more severe. In many cases this condition leads to functional compromise of viable myocardial cells rather than to an irreversible myocardial scar. Because the cells may undergo functional recovery after blood flow is restored, hibernating myocardium should be referred for revascularization to prevent irreparable changes, improve left ventricular function, and lower the mortality risk.

For FDG-PET imaging, the myocardial metabolism should be shifted toward **glucose utilization** to achieve good visualization of the heart and promote homogeneous FDG uptake in healthy myocardium. Various protocols have been described for this purpose. The simplest form involves oral glucose loading with 50–100 g of glucose 1 hour before FDG administration. In diabetics, however, a poor result is achieved in ~30 % of cases when this regimen is used. Unsatisfactory myocardial visualization with FDG is occasionally observed even in patients with no history of diabetes. Oral glucose loading which is individually adjusted based on repeated blood sugar determinations after glucose administration and FDG application at a falling blood sugar level yields good results but is logistically demanding. Even more elaborate is the euglycemic hyperinsulinemic "clamp technique" with continuous glucose and insulin infusion adjusted to the blood sugar level. This technique was long considered the gold standard. The administration of a nicotinic acid derivative (acipimox, 250 mg; Byk, The Netherlands) 3 hours and again 1.5 hours before FDG administration also yields good results, comparable with those achieved with euglycemic clamping.[11]

At our institution, the nicotinic acid derivative acipimox is used in preparation for FDG-PET imaging. It is suitable for both diabetics and nondiabetics. When the first dose of acipimox is administered, aspirin is given in addition to suppress a possible flush reaction. A glucose-rich, fat-free meal between the two doses of acipimox leads to increased FDG uptake in patients with normal fasting blood sugar levels. Data acquisition begins ~60 minutes after the intravenous administration of FDG (**Fig. 4.5**).

Patient preparation and exercise stress are the same for perfusion imaging as described for myocardial scintigraphy. Again, the exact protocol depends on the properties of the tracer. Because most tracers are very short-lived, very high activities can be administered without causing relevant radiation exposure.

Tracers

FDG is used for the visualization of myocardial glucose metabolism. The intracellular uptake of FDG is similar to that of glucose, but it is not metabolized further and therefore it accumulates within the cells. Because the myocardial metabolism has several distinctive features, standard preparations are required for FDG-PET. Various myocardial energy substrates have been identified: fatty acids, glucose, lactate, ketone bodies, and glutamate. The relative contributions of these molecules depend on the current energy demand. A high uptake of FDG occurs in ischemic tissue because fatty acid metabolism is reduced while glucose metabolism is increased. In addition, a high insulin level increases FDG uptake by lowering the blood sugar level and reducing free fatty acids. Conversely, a high fatty acid level leads to increased insulin resistance and thus to a decline in FDG uptake.

Several perfusion tracers are available for PET; for example, rubidium, ammonia, and radiolabeled water.

The uptake of rubidium 82 (^{82}Rb) by myocytes is analogous to that of potassium. The radionuclide "rubidium 82" is eluated from an sr 82/rb 82 generator and does not require production in a cyclotron. Because its physical half-life is only 75 s, the stress must be applied in the course of the PET examination

and must be maintained at a constant level. A pharmacological stress is generally used because of the motion artifacts induced by exercise stress.

Ammonia is labeled with ^{13}N, which is produced with a cyclotron. Because ^{13}N has a short half-life (10 minutes), the cyclotron and PET scanner must be in close proximity to each other. Ammonia diffuses into the myocytes where it binds metabolically to nitrogen.

Scanning with ^{15}O labeled water this is a technically demanding process which is primarily reserved for scientific studies.

Interpretation of PET

Myocardial tissue can be classified into various metabolic patterns based on the dual criteria of perfusion and function (**Table 4.3**, **Figs. 4.6, 4.7**). FDG-PET can differentiate between a myocardial scar and hibernating myocardium in patients with either a fixed perfusion defect (decreased uptake on stress and rest scans) or stress-induced ischemia on myocardial scintigraphy that is not completely reversible. While a myocardial scar consists of nonviable myocardial cells and connective tissue, hibernating myocardium consists of viable tissue that is metabolically compromised because of reduced blood flow.

The images obtained with perfusion tracers are interpreted analogously to myocardial scintiscans (**Table 4.1**).

Clinical Significance of PET

Based on the assessment of myocardial viability by FDG-PET, it can be predicted whether patients will benefit from a revascularization procedure (angioplasty or bypass) or should be referred for a different therapy.[12] Patients with left ventricular dysfunction due primarily to myocardial scarring will not benefit from revascularization. Correspondingly, it has been shown that patients with left ventricular dysfunction who underwent revascularization without prior investigation of myocardial viability had a significantly higher mortality rate in the ensuing 12 months than patients selected for revascularization based on the assessment of myocardial viability.[12]

In a comparative study of thallium chloride, sestamibi, ammonia, FDG, and stress echocardiography in the detection of hibernating myocardium, FDG-PET was found to be the superior predictive parameter, as well as the only independent parameter with a high predictive value.

The clinical significance of perfusion results is independent of the use of gamma-camera nuclides or PET tracers.

Special Nuclear Medicine Studies

MIBG Scintigraphy

Dysfunction of the myocardial autonomic nervous system is considered a risk factor for increased mortality in heart failure. Metaiodobenzylguanidine (MIBG), a norepinephrine analogue, can be used to assess adrenergic cardiac activity based on the function of presynaptic sympathetic nerve endings. Its value in the prediction of cardiac events has been documented.[13] Evaluation of the integrity of cardiac sympathetic innervation with MIBG is also employed in various neurological investigations such as the differentiation of Parkinson disease from multisystem atrophy syndromes.

Plaque Imaging

Inflammation and the extent of macrophage infiltration are important predictors of plaque rupture and thus of thromboembolic events. Thus, plaque composition is a more important predictor of plaque-associated events than plaque size. It is therefore essential to identify these vulnerable plaques with imaging techniques. FDG-PET is a promising modality in this regard. Studies in animal models have shown that the macrophage density in atherosclerotic plaques correlates with the noninvasively determined uptake of FDG. The determination of vascular FDG uptake therefore provides a noninvasive modality for the characterization of vascular inflammation.[14] A study in human patients has shown that inflammatory atherosclerotic plaques in larger vessels are associated with increased FDG uptake.[15] The proximity of the often pronounced FDG uptake in the myocardium to FDG uptake in coronary plaque may pose a technical challenge, but alternative tracers for plaque visualization have thus far not been developed for clinical use.

Table 4.3 Myocardial tissue classification based on function, perfusion, and metabolism

Tissue classification	LV function	Perfusion	Metabolism
Normal	Normal	Normal	Normal or non-homogeneous
Ischemia	Normal or slightly decreased	Reduced during exercise, normal at rest	Increased or normal
Stunned	Impaired	Normal	Variable
Hibernating	Impaired	Absent or reduced during exercise and at rest	Normal or increased
Scar	Impaired	Absent or reduced during exercise and at rest	Absent or reduced

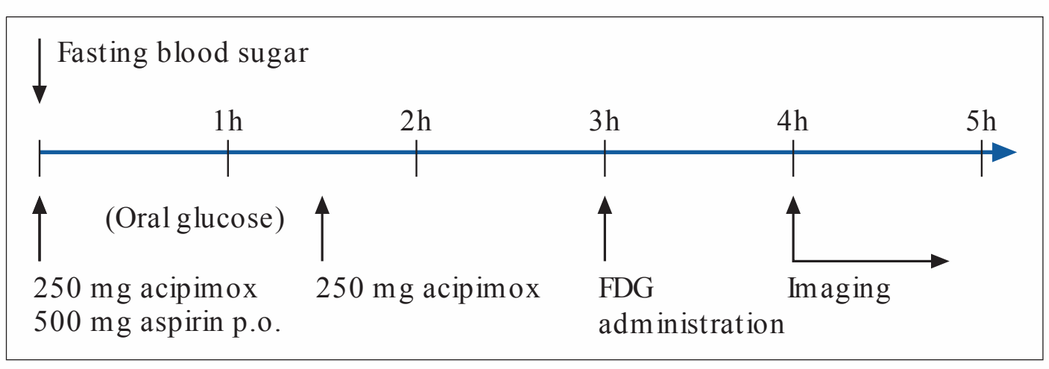

Fig. 4.5 Protocol for myocardial FDG-PET at our institution. The nicotinic acid derivative acipimox is used in both diabetics and nondiabetics to optimize the myocardial metabolism. Two doses are to be given 3 hours and 3.5 hour before FDG administration. The first dose is given in parallel to aspirin to inhibit skin flush. A glucose-rich, fat-free meal between the two acipimox doses leads to increased FDG uptake in patients with normal fasting blood glucose levels.

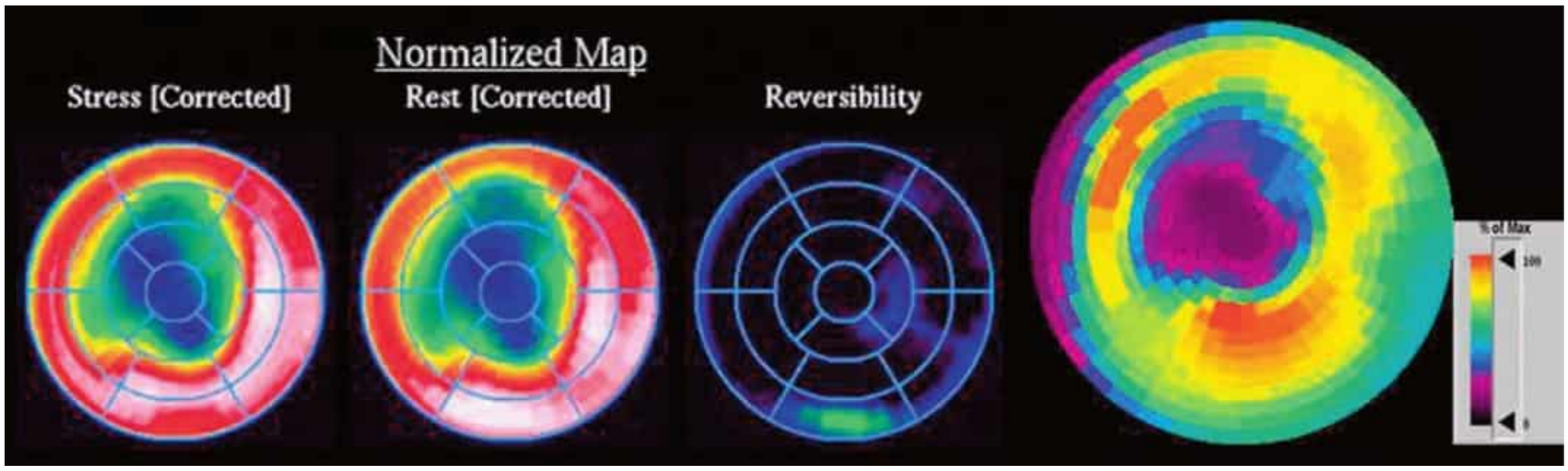

Fig. 4.6 Example of a myocardial scar (fixed, irreversible area of decreased uptake with no evidence of viability on [18F]FDG-PET) on the cardiac apex and adjacent portions of the posterior and anterior walls and periapical septal wall. Designations, scintigraphy color scale, segments, and bull's-eye orientation are the same as in **Fig. 4.3**.

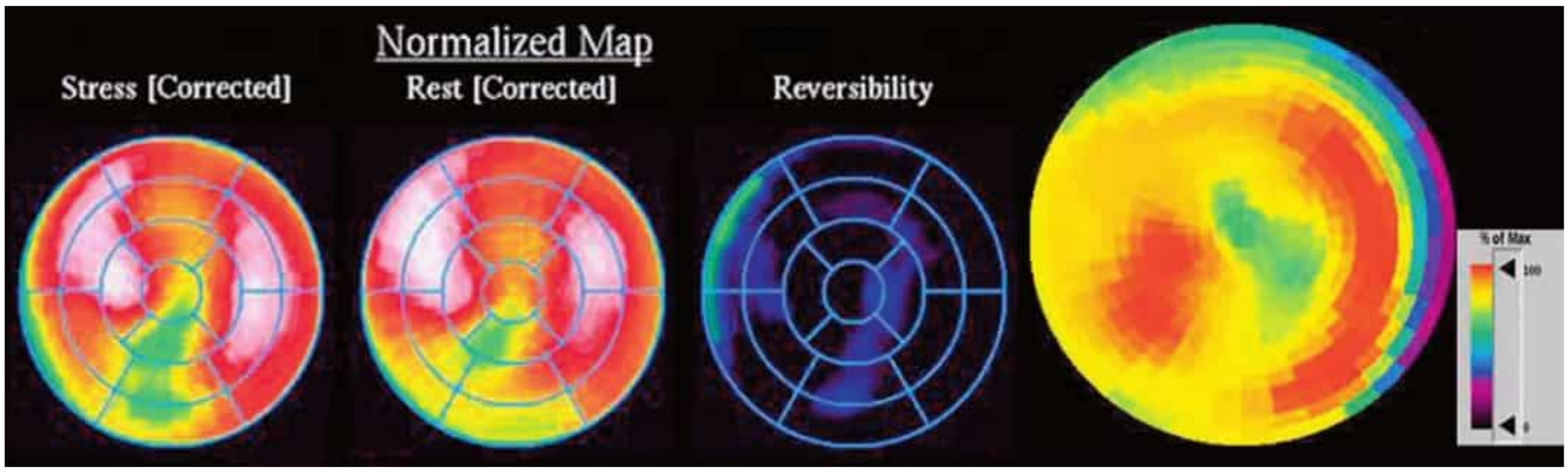

Fig. 4.7 Hibernating myocardium. Scintigraphy shows a fixed, irreversible perfusion defect in portions of the cardiac apex and adjacent posterior wall. [18F]FDG-PET shows normal to slightly increased glucose utilization in this area consistent with ischemic myocytes. Reversible stress-induced ischemia is further found in areas of the basal and midposterior wall. Designations, scintigraphy color scale, segments, and bull's-eye orientation are the same as in **Fig. 4.3**.

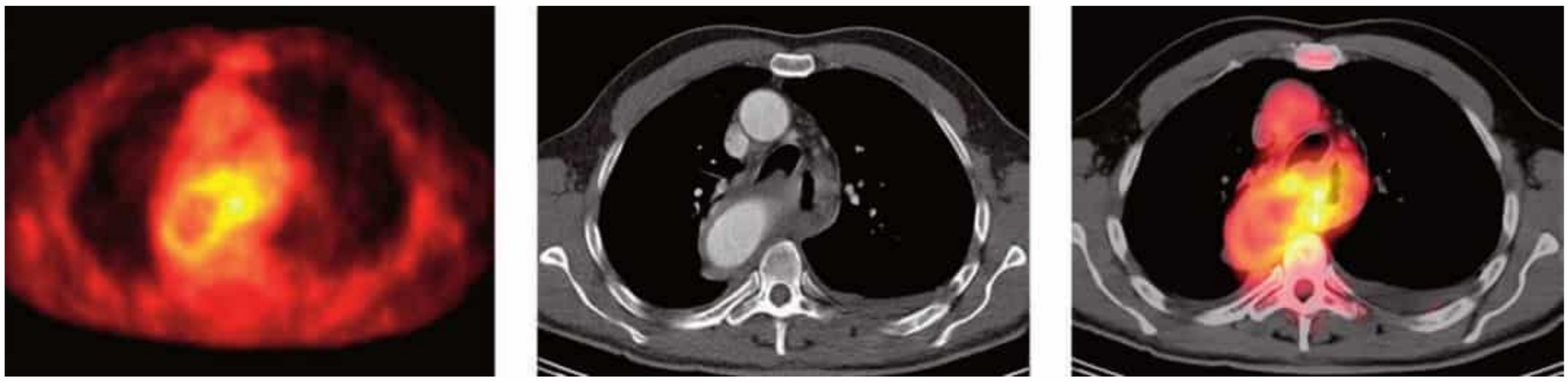

Fig. 4.8 A 60-year-old male patient with clinical inflammatory parameters. FDG-PET image (left) shows a marked, ring-shaped area of increased nuclide uptake. The configuration of this area, but not its location, may indicate extended aortitis.
Corresponding CT scan (center) from the PET/CT examination shows marked wall thickening and abnormal contrast enhancement of the aortic wall with dextroposition of the aortic arch and descending aorta as a normal variant. PET/CT coregistration (right) of both modalities permits definitive morphological classification of the hypermetabolic pathology detected by PET, indicting a florid inflammatory process in the thickened aortic wall. Metabolic quantification permits subsequent evaluation of treatment response. (With kind permission of Dr. Kühl, Department of Radiology, Essen University Hospital, Germany.)

The use of PET/CT for plaque imaging, rather than PET alone, offers the advantage of direct anatomical correlation, i.e., more strongly enhancing areas can be directly assigned to a specific vascular segment.

In the aorta and other large vessels, FDG has already established itself as an effective tracer for the detection of circumscribed inflammatory changes (**Fig. 4.8**).[16] This agent can also detect the significantly increased glucose utilization occurring in systemic forms of angiitis. Successful therapy leads to a normalization of findings, which can be documented at an early stage by inflammatory PET imaging with FDG.

References

1. Cerqueira MD, Weissman NJ, Dilsizian V, et al. Standardized myocardial segmentation and nomenclature for tomographic imaging of the heart: a statement for healthcare professionals from the cardiac imaging committee of the council on clinical cardiology of the American Heart Association. Circulation 2002;105:539–542
2. Bateman TM, Cullom S. Attenuation correction single-photon emission computed tomography myocrdial perfusion imaging. Semin Nucl Med 2005;35:37–51
3. Hendel R. Attenuation correction: eternal dilemma or real improvement? Q J Nucl Med Mol Imaging 2005;49:30–42
4. Sciagra R, Leoncini M. Gated single-photon emission computed tomography. The present-day "one-stop-shop" for cardiac imaging. Q J Nucl Med Mol Imaging 2005;49:1–3
5. Thomas GS, Miyamoto MI, Morrello AP 3 rd, et al. Technetium 99 m sestamibi myocardial perfusion imaging predicts clinical outcome in the community outpatient setting. The Nuclear Utility in the Community (NUC) Study. J Am Coll Cardiol 2004;43:213–223
6. Hachamovitch R, Berman D. The use of nuclear cardiology in clinical decision making. Semin Nucl Med 2005;35:62–72
7. Wackers FJ, Young LH, Inzucchi SE, et al. Detection of ischemia in asymptomatic diabetics investigators. Detection of silent myocardial ischemia in asymptomatic diabetic subjects: the DIAD study. Diabetes Care 2004;27:1954–1961
8. Patel H, Rosengren A, Ekman I. Symptoms in acute coronary syndromes: does sex make a difference? Am Heart J 2004;148:27–33
9. Blumenthal RS, Becker DM, Yanek LR, et al. Detecting occult coronary disease in a high-risk asymptomatic population. Circulation 2003; 107:702–707
10. Mieres JH, Shaw LJ, Arai A, et al. Role of noninvasive testing in the clinical evaluation of women with suspected coronary artery disease: consensus statement from the cardiac imaging committee, council on clinical cardiology, and the cardiovascular imaging and intervention committee, council on cardiovascular radiology and intervention, American Heart Association. Circulation 2005;111:682–696
11. Bax JJ, Visser FC, Poldermans D, et al. Safety and feasibility of cardiac FDG SPECT following oral administration of Acipimox, a nicotinic acid derivative: Comparison of image quality with hyperinsulinemic euglycemic clamping in nondiabetic patients. J Nucl Cardiol 2002;9:587–593
12. Travin MI, Bergmann SR. Assessment of myocardial viability. Semin Nucl Med 2005;35:2–16
13. Merlet P, Benvenuti C, Moyse D, et al. Prognostic value of MIBG imaging in idiopathic dilated cardiomyopathy. J Nucl Med 1999;40:917–923
14. Tawakol A, Migrino R, Hoffmann U, et al. Noninvasive in vivo measurement of vascular inflammation with F-18 fluorodeoxyglucose positron emission tomography. J Nucl Cardiol 2005;12:294–301
15. Davies JR, Rudd JH, Fryer TD, et al. Identification of culprit lesions after transient ischemic attack by combined 18F fluorodeoxyglucose positron-emission tomography and high-resolution magnetic resonance imaging. Stroke 2005;36:2642–2647
16. Kuehl H, Eggebrecht H, Veit P, et al. Imaging in patients with acute aortic syndrome: use of PET/CT to identify patients at risk. RSNA 2005, 91st Scientific Assembly and Annual Meeting. Scientific program. November 27–December 1, McCormick Place, Chicago: p. 181.

Further Reading

Mohan HK, Livieratos L, Gallagher S, Bailey DL, Chambers J, Fogelman I. Comparison of myocardial gated single photon emission computerised tomography, planar radionuclide ventriculography and echocardiography in evaluating left ventricular ejection fraction, wall thickening and wall motion. Int J Clin Pract 2004;58:1120–1126

Mowatt G, Brazzelli M, Gemmell H, et al. Systematic review of the prognostic effectiveness of SPECT myocardial perfusion scintigraphy in patients with suspected or known coronary artery disease and following myocardial infarction. Nucl Med Commun 2005;26:217–229

Nowak B, Stellbrink C, Schaefer W, et al. Comparison of regional myocardial blood flow and perfusion in dilated cardiomyopathy and left bundle branch block: role of wall thickening. J Nucl Med 2004;45:414–418

Zipoli A. Prognostic value of combined perfusion and function by stress technetium-99 m sestamibi gated SPECT myocardial perfusion imaging in patients with suspected or known coronary artery disease. Am J Cardiol 2005;95:1351–1357

Coronary Calcium Determination

A. Schmermund, T. Schlosser, A. Magedanz, and T. Voigtlaender

The prognostic significance of coronary artery calcium has been recognized for many years, but the application of cardiac computed tomography (CT) first enabled a reproducible, quantitative determination of coronary calcium. CT can detect calcifications and define their spatial extent. The **quantification of coronary artery calcium** is an important issue because a definite relationship exists between the extent of coronary atherosclerosis and the extent of coronary calcium. More coronary calcium is associated with a greater risk of cardiovascular events such as myocardial infarction and cardiac death (**Fig. 5.1**). Conversely, the absence of coronary calcium correlates with a very low cardiovascular risk, at least in the 45- to 74-year age group. Based on these relationships, coronary calcium determination has been incorporated into the guidelines for cardiovascular risk assessment of the major professional societies in Europe and the United States.[1–3]

To make an accurate coronary calcium determination consistent with published guidelines, it is important to understand the technical capabilities and limitations of CT. Despite efforts of users and manufacturers to establish uniform standards, differences in the algorithms used for quantification of coronary calcium and the use of different types and generations of CT scanners have made it difficult to compare calcium determinations published by different authors. This should be considered in the interpretation and reporting of coronary calcium findings.

Essential Point

Coronary calcium is a largely specific expression of coronary atherosclerosis. Because of the correlation between the extent of calcification and the extent of atherosclerosis, the accurate quantitative determination of coronary calcium is an important concern.

Examination Techniques

Coronary Calcium Determination by Electron-Beam Computed Tomography

Electron-beam computed tomography (EBCT) was conceived in the late 1970s and introduced clinically in the early 1980s. The first cardiac CT scanners had image acquisition times of 50–100 ms per slice.[4] In 1990, Agatston et al. published a proposed algorithm for the quantitative determination of coronary artery calcium.[5] This algorithm was later called the Agatston score (**Fig. 5.2**). Although based on EBCT, it still has major importance today because almost all data on the prognostic implications of coronary artery calcium have been acquired using EBCT technology and the Agatston score.

EBCT differs from modern CT in that it employs a **greater distance between the cathode and anode**, approximately 3 m. This design eliminates mechanical motion of the X-ray tube. The only rotating component is the electron beam that generates the X-rays. The electron beam is electromagnetically steered to sweep in a 210° range across the anode, called the target ring. The sudden deceleration of the electrons (as in every CT scanner) results in the emission of X-rays, which emerge from the anode beneath the patient, pass through the

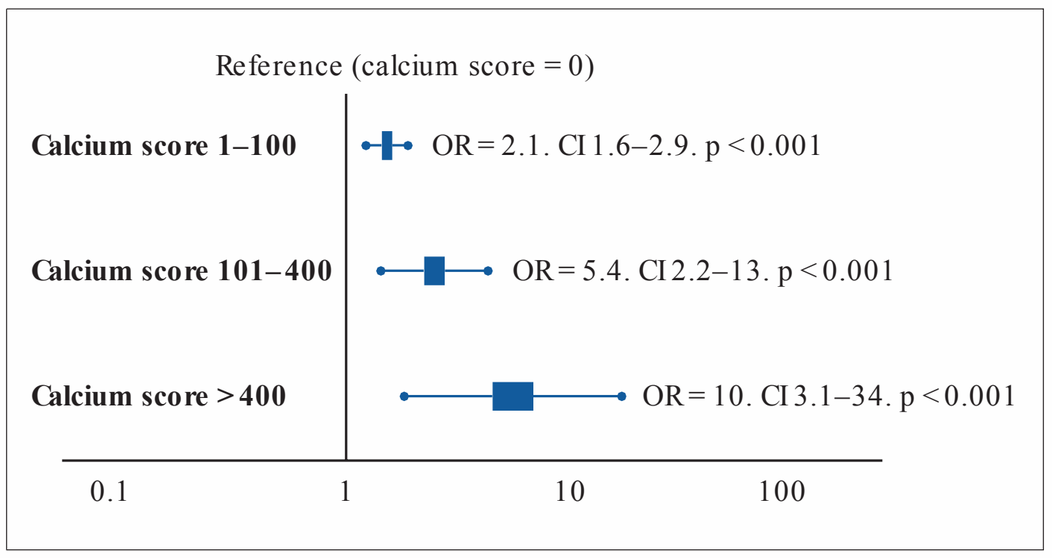

Fig. 5.1 Meta-analysis of four studies on calcium scores and cardiovascular risks. A total of 3970 asymptomatic patients were followed for an average of 3.6 years (13 000 person years) (after Pletcher[5a]).

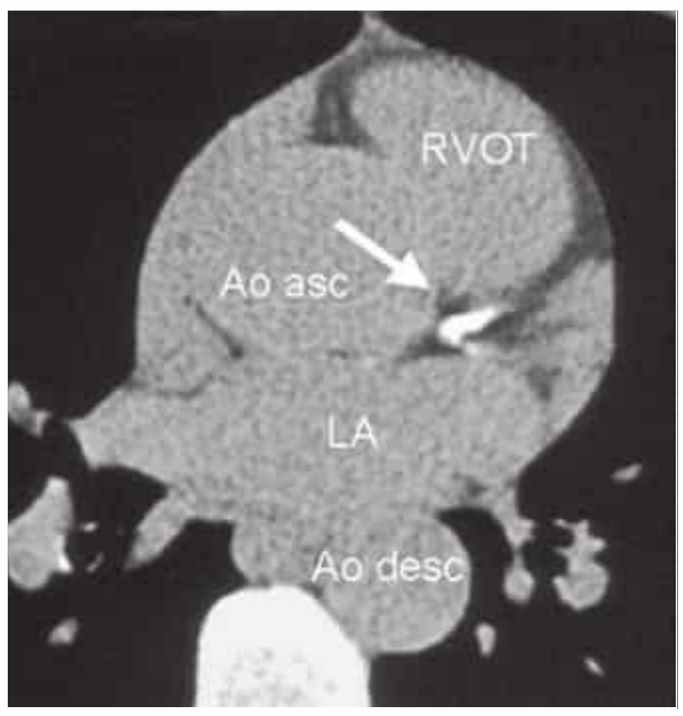

patient's body, and are registered by a detector array linked to a digital measuring system.

Single-slice image acquisition is generally used for coronary calcium determination by EBCT. Prospective ECG triggering is used to acquire image slices at a designated point in the cardiac cycle, usually at 40 %or 80 %of the R–R interval. The slice thickness is 3 mm, and the image acquisition time is 100 ms. In most cases, 30–40 contiguous slices are acquired from the pulmonary artery bifurcation to the cardiac apex. Overlapping slices can improve spatial resolution in the longitudinal *z*-axis, but this requires a longer scan time with a greater likelihood of respiratory motion and artifacts.

One advantage of EBCT over modern CT scanners is **lower radiation exposure**, which is in the range 0.5–1.0 mSv. For many years the very **short image acquisition time** was a unique feature of EBCT and has recently been equaled only by up-to-date CT units. The single-slice scanning technique of EBCT is a disadvantage, however, as it requires a long breath hold that may exceed 30–40 s depending on the number of slices and the patient's heart rate. Additionally, the abrupt movements of the scanner table necessary for contiguous slices are a potential source of motion artifacts. On the whole, EBCT has not become widely utilized despite its groundbreaking cardiac applications and still short acquisition time, due primarily to its high costs and limited clinical applications.

Agatston Calcium Score

The Agatston calcium score, introduced in 1990, still has an important role owing to its proven prognostic significance. This is all the more remarkable when we consider that the score was instituted on an arbitrary basis without scientific foundation. For purposes of Agatston scoring, a calcification is defined as an area of increased CT density measured in **Hounsfield units** (HU, named for the CT pioneer Sir Geoffrey Hounsfield). The CT density of water is 0 HU, and the density of air is – 1000 HU. Coronary calcifications cause greater X-ray attenuation, leading to values considerably greater than 0 (up to ~600).

The Agatston score defines the lower threshold for calcifications as a value >2 SD above the mean density of blood, corresponding to 130 HU. The area of the lesion is calculated in mm^2 based on the number of contiguous pixels (numbering at least 2) that show calcific density. Additionally, the lesion is assigned a "density factor" of 1–4 based on its maximum calculated CT density. The density factor is 1 if the CT density is between 130 and 199 HU, 2 for a CT density between 200 and 299 HU, 3 for a density between 300 and 399 HU, and 4 for a density of 400 HU or more. The Agatston calcium score is a dimensionless quantity defined as the product of lesion area times density factor (**Fig. 5.2**). The lesions distributed throughout the coronary tree are added together to yield a total score.

Experimental validation studies have shown that, despite the arbitrary criteria used in the Agatston calcium score, the score shows good agreement with the true extent of vascular calcification as measured by histomorphometry or weight after 3 days' heat treatment.[6] Nevertheless, the Agatston calcium score does not always have good reproducibility, especially in small lesions. This is due mainly to ambiguities inherent in the density factor. If the maximum density of a lesion is measured at 198 HU, the density factor is equal to 1. If the maximum density is measured at 201 HU, the density factor is 2. Assuming a lesion area of 8 mm^2, the calcium score would be 8 in the first case and 16 in the second case. Several studies on the interscan variability of the Agatston calcium score suggest that the score should be at least 30–50 to achieve acceptable interscan variability.

When the Agatston calcium score is determined with a multislice CT scanner (MSCT), the difference in imaging technology must be taken into account. Modern CT scanners all have a thinner slice thickness than the traditional 3-mm slice thickness of EBCT. Accordingly, comparable protocols must be applied to transfer the Agatston score to these scanners. The calcium scores determined with a 4-slice CT scanner appear to correlate quite well with the calcium scores determined by EBCT.[7,8] However, protocol selection and slice thickness are crucial. Given these circumstances, the determination of coronary calcium mass is becoming an increasingly important test as it is largely independent of the type of scanner used.

Essential Point

Electron-beam computed tomography was first used specifically for cardiac CT imaging and established the principle of coronary calcium determination based on the Agatston score. This quantitative coronary calcium score is the basis for most sectional and prognostic studies on the importance of coronary calcium determination.

Volume Calcium Score

The volume calcium score was specially developed to allow a more precise calcium score determination in **progression studies**. This score does not employ a density factor. As in the Agatston calcium score, a CT density higher than 130 HU is considered to indicate calcium. As the name suggests, the volume score is obtained by determining the volume of the calcified lesion. Isotropic interpolation of the original data is used in an effort to achieve greater accuracy.[9] Using the original dataset, measurements are taken at various points within the slice corresponding to the size of the pixels in the cross-sectional plane (e.g., 0.51 mm in the 26-cm^2 field of view of traditional EBCT). The density values are assumed to have a linear distribution so that the interpolated voxels can be calculated. These calculations are performed automatically with software currently available. Although the volume score has been successfully used in several progression studies, its advantages over the Agatston score appear to be small. Comparative studies have not shown that the volume score is more reproducible than the Agatston score.[10] As a result, application of the volume score has basically been limited to scientific progression studies.

Calcium Mass Determination

Calcium mass can be determined accurately and reproducibly by scanning a **calibrated phantom** that contains cylinders with varying, precisely defined calcium masses. In this way a calibration factor can be determined and the calcium mass can be

measured in milligrams. Today this analysis is generally included in the processing software of modern MSCT scanners. Comparative studies have shown that calcium mass determination remains very stable across different imaging protocols, slice thicknesses, and acquisition times, while the Agatston calcium score may show considerable variation.[11] The calcium mass in milligrams measured in the coronary tree is in a ratio of ~1:4.5 to the dimensionless Agatston score, depending on the image acquisition protocol. Determination of the coronary calcium mass will assume greater importance in the future because it provides internationally comparable measurements that are independent of CT technology and image acquisition protocols.

Essential Point
Differences in the quantification of coronary calcium relating to different scanners and algorithms can largely be avoided by using an algorithm calibrated to calcium masses measured in a phantom. Given this advantage, calcium mass determination is assuming an increasingly important role.

Coronary Calcium Determination by Multislice CT

Modern MSCT technology produces a true volumetric dataset, as the continuous rotation of the X-ray tubes yields overlapping datasets that can be processed in thin slices.[12] This reduces partial volume effects and the slices can be reduced to a submillimeter thickness, resulting in true isotropic resolution. Additionally, data can be acquired continuously throughout the cardiac cycle, making it possible to reconstruct images at various points in time and eliminate motion artifacts during certain phases of the cardiac cycle. The radiation dose can be reduced by "tube current modulation," i.e., periodic lowering of the tube current during cardiac cycle phases in which imaging data are not acquired (**Fig. 5.3**). Meanwhile, MSCT imaging permits the prospective triggering of image acquisition at a predefined point in the cardiac cycle. The radiation dose is in the range 1.0–3.0 mSv, depending on the particular scanner and protocol.

Regarding procedural recommendations on coronary calcium determination by MSCT, the importance of the shortest possible acquisition time and a slice thickness of 3 mm or less should be emphasized.[13] The currently available multislice scanners (usually 16 slices or more) offer sufficient image quality for this purpose. Recommendations differ regarding the prospective ECG triggering of image acquisition and the retrospective ECG gating of acquired images that is used in most spiral scanners. The advantages of spiral scanning (true volumetric dataset, variable timing of image reconstructions) result in better reproducibility and thus greater validity of the findings, but spiral scans also expose the patient to a somewhat higher radiation dose. Both protocols (retrospective gating, prospective triggering) have been used successfully in the Multi-Ethnic Study of Atherosclerosis.[14]

Essential Point
The image quality of modern MSCT scanners permits the accurate quantification of coronary calcium. With continuous spiral scanning, image acquisition can be timed to any point in the cardiac cycle by the retrospective selection of sectional images for analysis (retrospective gating). Another option is prospective ECG triggering, in which data are acquired at a predefined point in the cardiac cycle as in EBCT. Continuous spiral scanning yields the best image quality, and prospective triggering provides the best reduction in radiation dose.

Interpretation

As in CT coronary angiography, when the calcium score is determined by spiral CT the examination should be followed by suitable data reconstructions to minimize artifacts that could distort the calcium score. For example, motion artifacts from calcified plaques may cause blurring of the calcifications in systolic reconstructions (smearing or blurring artifacts). Various phenomena may be observed, depending on the size of the calcified plaques. The density of small plaques may fall below the 130 HU threshold owing to blurring artifacts, with the result that the analytic software no longer recognizes them as calcified lesions (**Fig. 5.4**). Motion artifacts also affect the quantification of large calcified plaques. Blurring artifacts in this case lead to overestimation of the actual score. The degree of overestimation depends on the amplitude of the motion.

Essential Point
Selection of the reconstruction interval in retrospective gating can influence coronary calcium determination (over- or underestimating the actual amount of calcium). This effect is less pronounced in the latest generation of scanners than in older instruments.

Distortion of the calcium score due to artifacts is especially likely to occur in patients with a very high heart rate. It is best to examine patients with a heart rate of ~60 bpm. If necessary, β-blockers should be given orally or intravenously before the

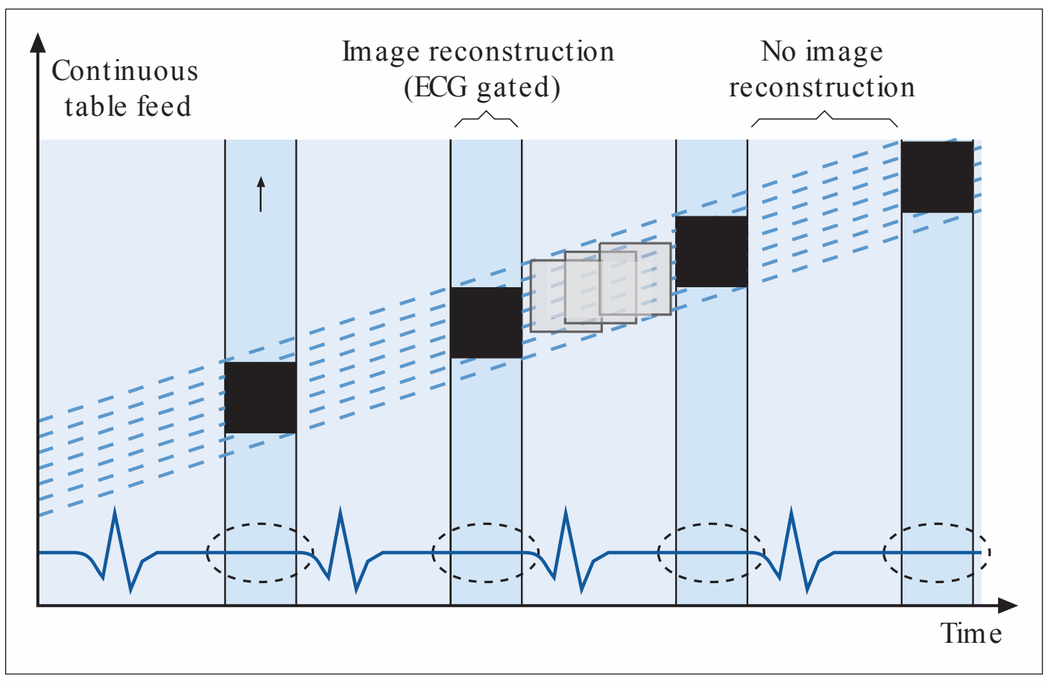

Fig. 5.3 Principle of multislice spiral CT. Continuous table feed moves the patient through the rotating beam, which simultaneously scans multiple slices within the body. The acquisition of image information occurs at designated times in the cardiac cycle, typically within the end diastole. These image acquisition times are indicated by black rectangles and broken-line ovals in the diagram. The radiation is reduced between acquisitions.

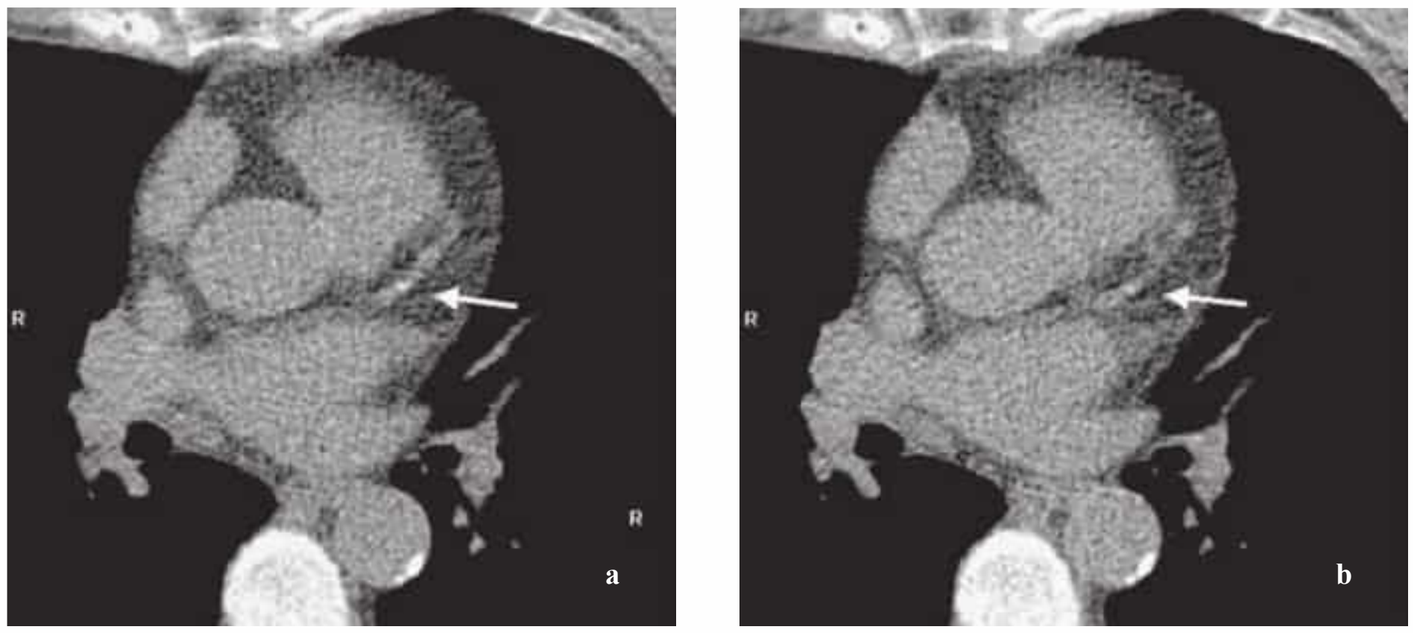

Fig. 5.4 a, b Images of the cardiac base (64-slice MSCT). The image reconstructed at 55 % of the R–R interval shows a calcified lesion in the proximal left anterior descending artery (arrow in **a**). However, image reconstruction at 70 % of the R–R interval results in a density below the cutoff value of 130 HU and the lesion is no longer depicted as a calcification (arrow in **b**).

test to lower the heart rate to the target range. Caution is urged in patients who have coronary stents or have undergone coronary bypass surgery, because stents and clips cannot always be distinguished from coronary calcium, resulting in overestimation of the calcium score. The accuracy of calcium score determination is limited in both groups of patients. Also, scanning conditions are often compromised in patients with cardiac pacemakers, and artifacts from the pacemaker leads can be particularly troublesome in evaluations of the right coronary artery.

Scanning Protocol

Table 5.1 reviews typical image acquisition protocols with retrospective gating for multislice CT scanners in current use.

Reporting of Coronary Calcium Findings

A standard scheme should be followed in the reporting of coronary calcium findings. The examination itself must conform to the minimum requirements and quality criteria noted above to produce a meaningful report. We recommend the following 9-point scheme in reporting the findings of a coronary calcium examination:

1. Give clinical information regarding the patient's symptoms, prior cardiac history, and risk factors.
2. State the basic clinical question (e.g., "risk stratification").
3. Give methodological details with regard to scanning technology (EBCT, MSCT), manufacturer, scanner type, and calcium mass determination and a brief description of the calibration method.
4. Indicate basic scan parameters with regard to slice pattern (contiguous, overlapping), slice thickness, coverage (scan volume should always cover the entire coronary system), slice acquisition with prospective or retrospective ECG gating, and any deviations from the recommended tube current (mAs) and voltage (kV).
5. Describe the image quality as good or degraded owing to artifacts (respiratory artifacts, extrasystoles). Indicate "noise" in the aorta (state mean density and standard deviation in the aortic root).
6. Indicate the method of coronary calcium quantification (Agatston calcium score, volume calcium score, calcium mass) for the entire coronary system and separately for the left main stem, left anterior descending artery, left circumflex coronary artery, and right coronary artery.
7. Evaluate extracoronary cardiac calcifications and aortic calcium.
8. Indicate age and sex percentiles, and classify the finding by stating the source (own series or drawn from the literature).
9. Make a risk assessment based on coronary calcium quantification and percentiles.

Outlook

Although rapid advances in CT technology with changes in hardware, image acquisition protocols, and analytical software pose an obstacle to uniform measurements at the present time, there has still been a marked overall improvement in the image quality and reproducibility of coronary calcium determination. Besides technical advances, this stems partly from the efforts of users to establish comparable protocols as well as standard interpretation and reporting schemes. The determination of coronary calcium mass has an important role in this regard, and there has been steady progress toward more reproducible examinations with increasingly shorter image acquisition times and thinner slices.[15] The Agatston calcium score will continue to be important, as it is the measure upon which current

Table 5.1 Protocol for coronary calcium determination with multislice CT for different numbers of available detector rows

Detector rows	4	16	32/64
Collimation	4 × 2.5 mm	16 × 0.75 mm	32/64 × 0.625 mm
Rotation time	500 ms	370–420 ms	330–400 ms
Tube current	300 mAs	300 mAs	150 mAs
Tube voltage	80 kV	80 kV	120 kV
Effective dose	~ 1 mSv	~ 1 mSv	~ 1 mSv
Slice thickness	3 mm	3 mm	3 mm
Slice overlap	1.5 mm	1.5 mm	1.5 mm
Kernel	e.g., B35 f	e.g., B35 f	e.g., B35 f
ECG pulsing	Yes	Yes	Yes

prognostic data and percentiles in various groups of selected and unselected patients are based.

The challenge for the future is no longer the question of how coronary calcium determination can be performed with precision. As more and better data are acquired, the real challenge is to define the role of this examination within the context of other methods of risk stratification. This requires the uniform application of coronary calcium determination with a widely comprehensible scheme for the reporting of findings.

CT Coronary Angiography

T. Schlosser

Principle of Computed Tomography

The basic principle of computed tomography (CT) is that a narrow **X-ray beam** passes through the patient's body from various directions. The attenuation of the X-ray beam is measured along each of the beam paths by **detectors**, and a mathematical process (filtered back projection) is used to calculate the attenuation coefficient at each point in the scanned section. The relative attenuation values are expressed in Hounsfield units (HU) and represented as a gray-scale image. The Hounsfield scale ranges from –1000 HU for air through 0 HU for water and has no upper limit (it is ~1500 HU for compact bone).

CT angiography of the coronary vessels can be performed with **electron beam CT** (EBCT) or with a **multislice spiral CT** (MSCT) system. In "conventional" CT, the X-ray tube moves around the patient. In EBCT, however, the electrons generated in an electron gun are aimed at a tungsten target, and the resulting X-ray emissions are directed through the patient to the detector rings. In theory, EBCT is capable of demonstrating the larger, proximal coronary arteries, but there are major practical limitations such as relatively low spatial resolution, dose limits, high cost, and limited availability.

For these reasons, CT angiography of the coronary vessels is performed almost exclusively with multislice (multidetector) spiral CT systems. There are two basic requirements for CT imaging of the heart:

- High temporal resolution to prevent motion artifacts
- High spatial resolution to define even small anatomical structures like the coronary arteries

This has become possible through rapid advances in CT technology during the past 15 years.

The revolution in CT began in 1991 with the introduction of **spiral CT**. Until then, CT scanning was a stop-and-shoot technique in which the patient table was advanced a short distance, paused for the acquisition of a single slice, then advanced again. Even with a large slice thickness of 5–10 mm, a complete thoracic examination took 5–10 minutes and required numerous breath holds. Spiral CT, on the other hand, acquires image data during continuous table motion, enabling the entire thorax to be scanned as a 3D volume in a single breath hold. Meanwhile the rotation time of the X-ray tube has been dramatically shortened.

In 1999, a CT system with four detector rows and a gantry rotation time of 500 ms was introduced that allowed ECG-triggered imaging of the heart. Scanners with 16 detector rows and a gantry rotation time of 420 ms were introduced two years later, making it possible for the first time to make a detailed evaluation of the heart and coronary arteries. Systems with 64 detector rows and gantry rotation times as short as 330 ms have been available since mid-2004. By end of 2007 initial results of 256-detector-row CT have been published and recently a 320-slice CT has been launched.

Whereas scanners with more detector rows are able to improve coverage per rotation and spatial resolution the introduction of dual-source computed tomography (DSCT) in 2006 has significantly improved the temporal resolution of ECG-gated multidetector-row cardiac computed tomography. DSCT scanners are equipped with two tubes and detectors at 90° to each other in a single gantry rotating at 330 ms.

Additionally, in-vitro studies have shown that new detector technologies such as flat-panel CT scanners can provide significantly greater spatial resolution than traditional CT systems.[16] This technology is expected to provide greater robustness for imaging of the coronary arteries, especially in patients with a high heart rate.[17]

Patient Preparation

History

Before the examination, a **history** should be taken that includes the patient's complaints, course of illness, and previous diagnostic procedures. In planning and interpreting the examination, it is essential to question the patient about any **implanted stents** or **previous cardiac surgery**. A standard questionnaire may be useful for this purpose.

Informed Consent

Except in determinations of calcium score, IV contrast administration is necessary in all cardiac CT examinations. The patient must be informed about **possible adverse events related to the contrast agent** prior to the examination. Advanced kidney disease and hyperthyroidism should be ruled out prior to contrast administration.

Owing to the relatively high radiation exposure from cardiac CT, preparations should be made to expedite the examination. All parts of the examination should be explained to the patient beforehand (e.g., breathing instructions over a loudspeaker, breath holding, lying quietly, etc.), and it may be helpful to rehearse them with the patient prior to scanning.

Heart Rate

A **sinus rhythm** is necessary for optimal image quality. The target heart rate is less than 65 bpm and ideally should be below 60 bpm. This prolongs the diastolic rest phase of the cardiac cycle, during which images can be acquired without motion artifacts. If this target rate is not achieved, the heart rate should be lowered with β-blockers unless contraindicated (e.g., 95 mg

of metaprolol, 5 mg of bisoprolol orally 1 hour before the start of the examination, or up to 4 × 5 mg metaprolol IV immediately before the CT scan). To avoid nondiagnostic examinations, patients with tachycardia or severe arrhythmias should not be scanned.

Essential Point

CT coronary angiography requires at least a 64-slice CT scanner with a gantry rotation time <500 ms.[18,19] Patients should be informed about the risk of contrast reactions and radiation exposure. The target heart rate during the examination is <65 bpm and can be reduced with β-blockers if necessary.

Planning the Examination

An ECG is recorded concurrently with CT imaging so that image data can be assigned to specific phases of the cardiac cycle after the examination. The ECG electrodes should be placed infraclavicularly on each side and on the left lateral chest wall. The scan volume for imaging the native coronary vessels should extend from the carina to the diaphragm. To image an aortocoronary or arterial bypass, coverage should be extended to the origin of the internal mammary artery from the subclavian artery (**Fig. 5.5**).

A noncontrast scan to detect or exclude **coronary artery calcium** may be advised to identify patients with significant calcifications that would hamper interpretation of the contrast-enhanced scans. Depending on the amount and distribution of coronary calcium, it may be necessary to dispense with CT coronary angiography (CTCA) owing to the difficulty of luminal evaluation in heavily calcified coronary vessels. If the Agatston score is greater than 400, the indication for CTCA should be closely scrutinized and the examination should be withheld when necessary.

Data acquisition in CTCA is done with a spiral scanner with a tube rotation time of 500 ms or less. Temporal resolution equals approximately one-half the rotation time. Accordingly, a 64-slice scanner with a tube rotation time of 330 ms has a temporal resolution of 165 ms. In the latest generation of scanners (DSCT), a temporal resolution of ~83 ms can be achieved. Temporal resolution can be further improved by segmented reconstruction of the scan data from more than one cardiac cycle. However, multisegment reconstructions can adversely affect image quality in some circumstances, as in patients with a fluctuating heart rate.

The **collimation** should be 1 mm or less, and submillimeter collimation is definitely preferred on the basis of current data. The collimation is set to 0.75 mm on a 16-slice CT scanner and as low as 0.5 mm on a 64-slice scanner. Overlapping slices are reconstructed following data acquisition. The tube voltage should be 120 kV, as higher voltages would cause needlessly high radiation exposure. The radiation dose can be further reduced by ECG-triggered modulation of the tube current. This means that the tube current is lowered by up to 80 %in cardiac phases not used for image reconstruction. Dose reduction by up to 40 %can be achieved with this technique.

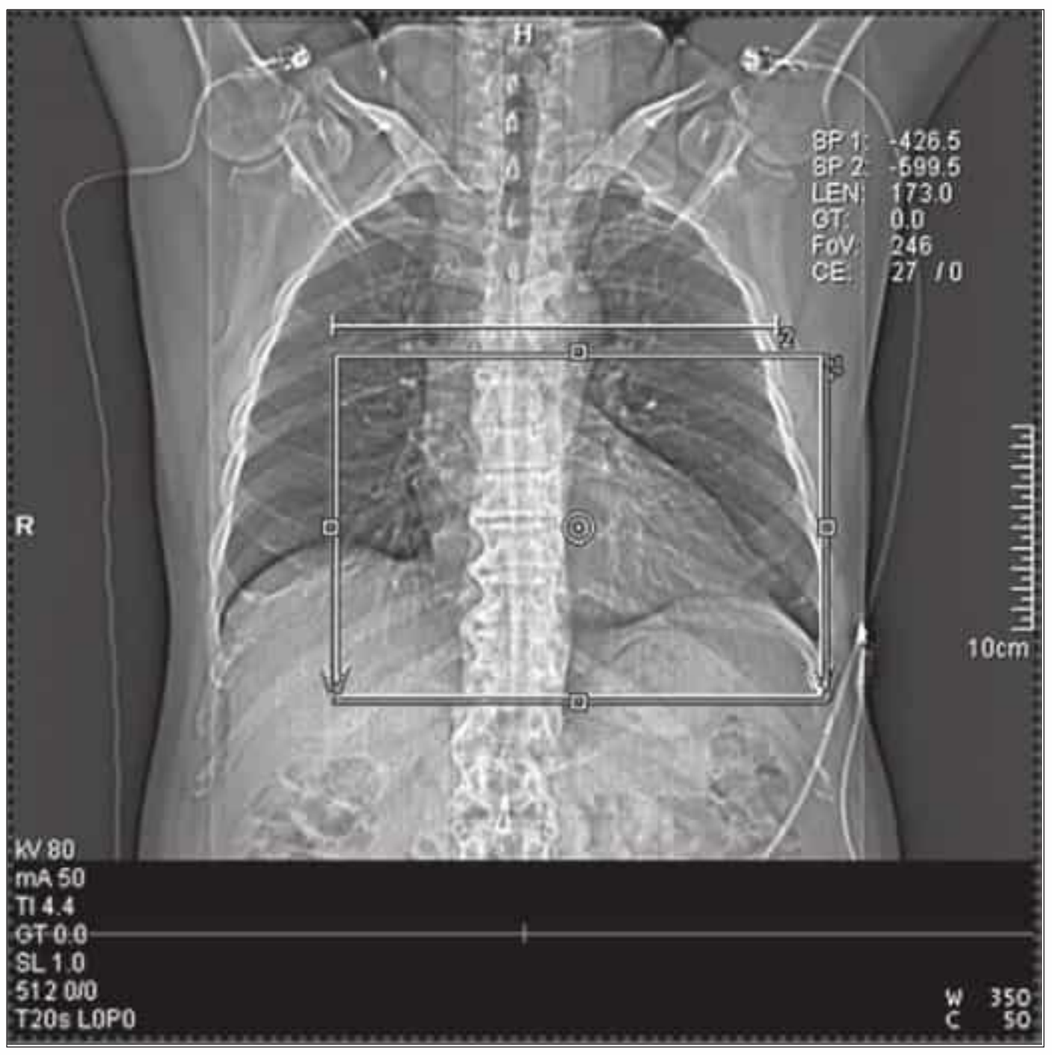

Fig. 5.5 A scout image is used to plan the examination and set the boundaries of the scan volume. For imaging the noncontrasted coronary vessels, coverage extends from the carina to the diaphragm.

Contrast Media

The **iodine concentration** of the contrast medium used for CT coronary angiography should be between 300 and 400 mg/mL. The contrast should be administered with an automated injector, preferably one that allows for variable phase injections and the subsequent administration of a saline flush. With a 16-slice CT scanner, good results have been achieved with a biphasic contrast injection protocol starting with 50 mL of contrast medium at a flow rate of 4 mL/s, followed by 30–70 mL of contrast medium injected at 2.5 mL/s, and finally a 30–50 mL NaCl bolus injected at 2.5 mL/s.[20,21] In clinical studies with 64-slice CT scanners, a monophasic protocol was used in which 80–100 mL of contrast medium was injected at a rate of up to 5 mL/s.[22,23] Thus, the contrast dose can be reduced by using a scanner equipped with more detector rows.

Optimum enhancement of the coronary arteries is an essential prerequisite for diagnostic CTCA. Because the time window for this enhancement is very narrow and varies in different patients, the timing of data acquisition after contrast injection must be accurately determined. Basically two methods are available for determining the scan delay after contrast injection. First, the circulation time can be determined before CTCA by injecting a small amount of contrast medium and taking reference scans in the ascending aorta at 1-second intervals. The time interval to opacification of the aorta is then used as the scan delay for CTCA. The second method, called bolus tracking, consists of analyzing CT density at 1-second intervals in a reference slice in the ascending aorta during contrast injection. When the density exceeds a predefined threshold value of 150 HU, for example, the CTCA scan starts automatically.

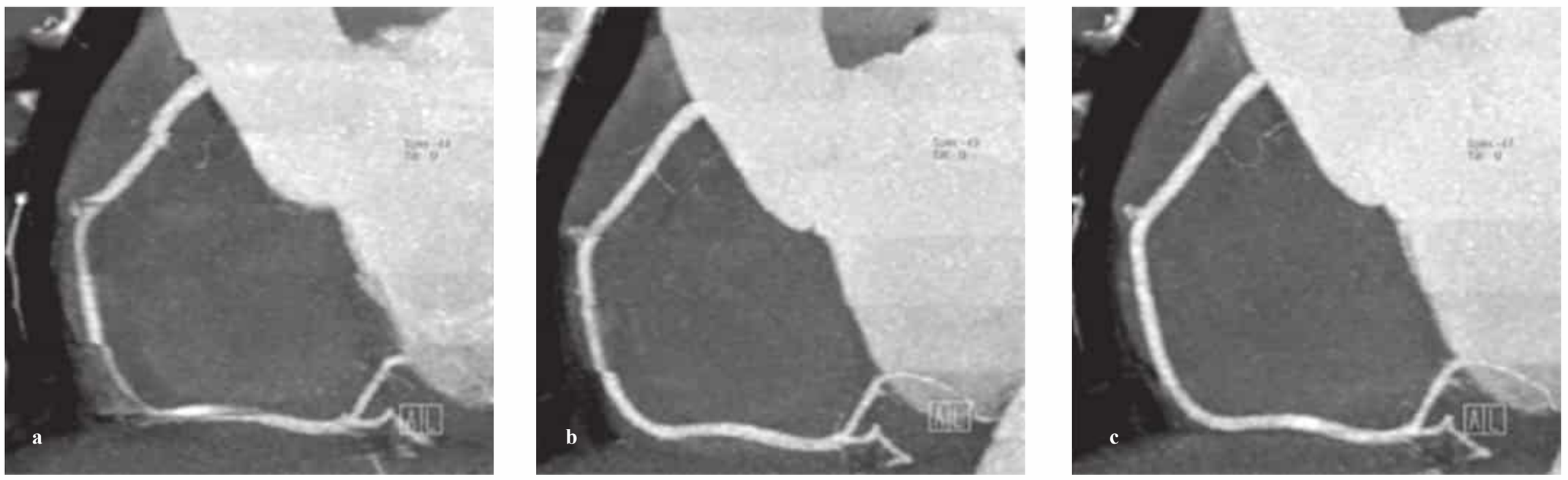

Fig. 5.6 a–c Effect of reconstruction interval on image quality. Maximum intensity projection of the right coronary artery.

a An image reconstructed at 55 % of the R–R interval shows marked motion and stair-step artifacts, resulting in nondiagnostic image quality.

b Better image quality is obtained at 65 % of the R–R interval, but the image is still difficult to interpret.

c Image reconstructed at 70 % of the R–R interval. The entire course of the RCA is clearly displayed without artifacts.

Examination Technique

The ECG and heart rate should be rechecked just prior to CT scanning. A pharmacologically induced fall in heart rate should be monitored, especially after the administration of very short-acting β-blockers such as esmolol, and scanning is initiated when the minimum rate is reached. The ECG should then be monitored during the examination to quickly establish the cause of possible image artifacts such as triggering errors due to arrhythmias. It is also advisable to watch the patient's chest during the scan to detect sources of error such as body movements and breathing during data acquisition.

CT coronary angiography should be performed with breath-hold technique. Data acquisition at full inspiration is best, since patients can hold their breath longer in that phase, resulting in fewer motion artifacts. The total scan time ranges from 12 to 40 s and depends on the scan volume, the number of detector rows, and the gantry rotation speed.

Interpretation

Following data acquisition, it is necessary in most cases to reconstruct various datasets at different points in the cardiac cycle to minimize **motion artifacts** (**Fig. 5.6**). In patients with a low heart rate, mid-diastole is usually the most favorable point for image reconstruction. End-systolic reconstructions are also advantageous at higher heart rates, however. It is good practice to reconstruct and store various datasets for different coronary vessels. Mid-diastolic reconstructions (at 60 %, 65 %, and 70 % of the R–R interval) are usually sufficient when a 64-slice or DSCT scanner is used.

Most CT systems have various algorithms available for further processing and multidimensional rendering of the axial image data. **Multiplanar reformatting** (MPR) can be performed on axial scans to yield coronal, sagittal, oblique, and even curved planes of section. Maximum intensity projections (MIP, **Fig. 5.6**) make it possible to view the scanned volume from any desired angle. The MIP is a summation image, however, in which the maximum CT value along the projection is assigned to every point in the imaging plane. This technique is particularly useful for increasing contrast between small vessels and their surroundings. In volume rendering technique (VRT, **Fig. 5.7**), a color and an opacity are assigned to every CT value in one or more selected density ranges. This technique can provide realistic-looking 3D reconstructions of the heart and vessels. VRT can be used, for example, to survey potentially complex cardiovascular anatomy (e.g., after multiple bypass operations).

Essential Point

Volume-rendered images are useful for obtaining a quick overview, but abnormalities found in volume-rendered images should be verified in axial images, MPRs, or thin-slice MIPs, which form the basis for image analysis.

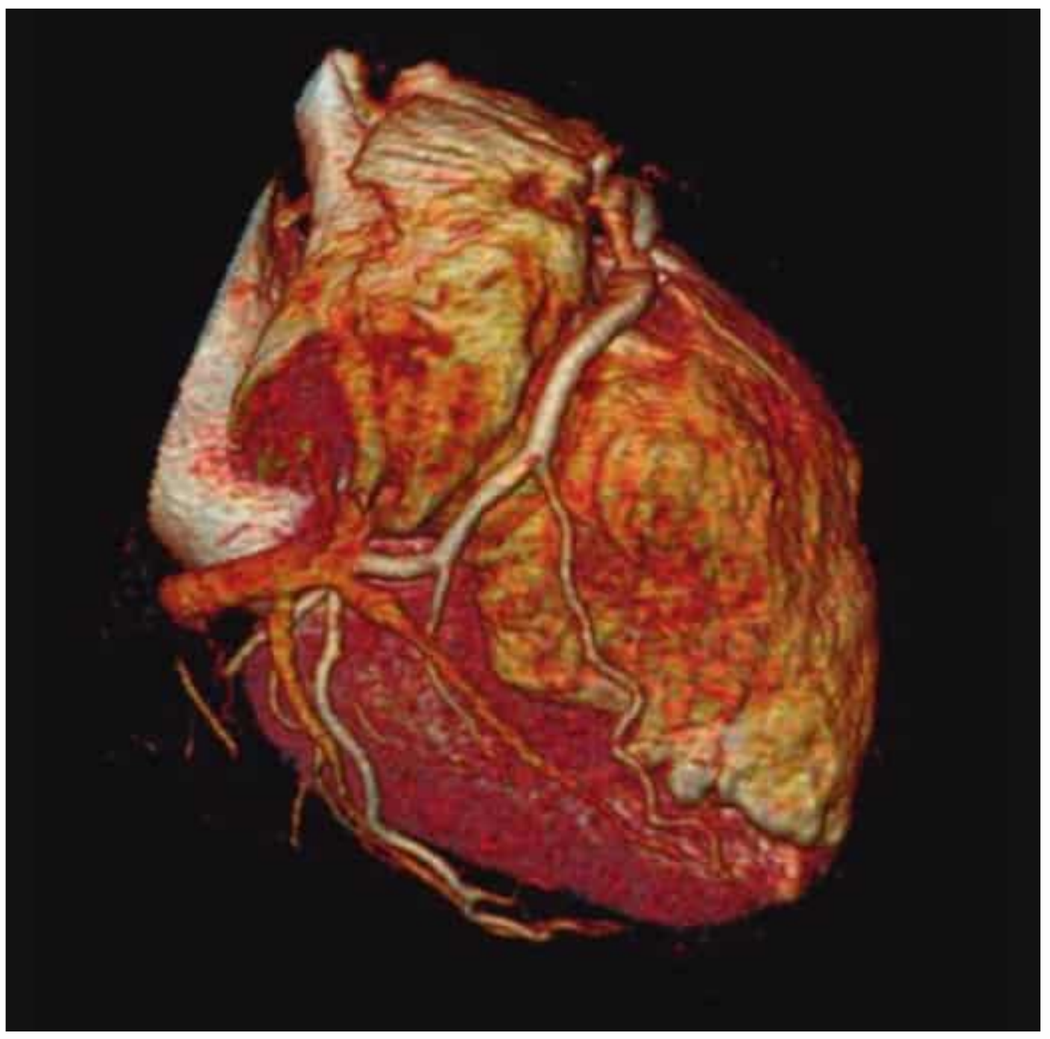

Fig. 5.7 Volume-rendered image from a CT coronary angiography dataset acquired with a 64-slice CT scanner. The image excludes a stenosis of the right coronary artery.

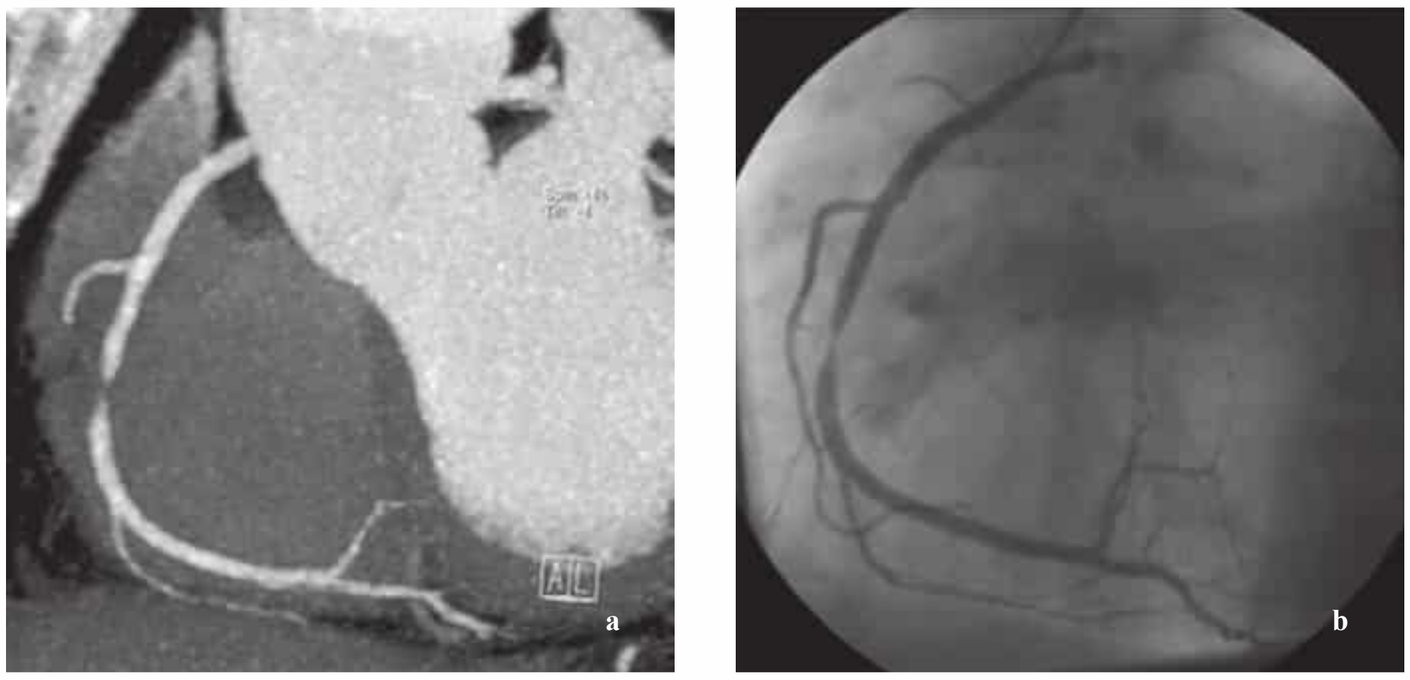

Fig. 5.8 a, b High-grade stenosis in the midportion of the RCA, diagnosed by CT coronary angiography (**a**). The finding was confirmed by subsequent invasive coronary angiography (**b**).

The most frequent causes of undiagnosed or false-positive stenoses are:

- Motion artifacts, especially in the right coronary artery
- Heavy calcifications in the LAD artery
- Masking of the circumflex artery by opacified venous structures

The degree of stenosis is difficult to evaluate with CTCA, but high-grade stenoses can be detected with high sensitivity (**Fig. 5.8**). Mild or moderate stenoses are often overestimated, however, especially in small-diameter vessels.

Venous bypass vessels tend to have a larger diameter than native coronary vessels, move less during cardiac activity, and are less calcified, generally making them easier to evaluate than native vessels. On the other hand, arterial IMA bypasses in particular may be difficult to evaluate owing to radiopaque clip material distributed along the course of the bypass.

Clinical Applications

The **indications** for coronary artery imaging have not been clearly defined because of a previous lack of large controlled studies.[17–19,22] The possible applications of CT coronary angiography are as follows:

- Exclusion of coronary heart disease in patients with a low or moderate pretest probability
- Visualization of coronary anomalies
- Evaluation of aortocoronary bypass grafts

Meanwhile, several studies have investigated the diagnostic accuracy of multislice CT compared with invasive catheter angiography.

Assessability of the coronary segments was markedly limited in studies where 4-slice CT scanners were used and β-blockers were not always administered before scanning.[24–26] In more recent studies where 12- or 16-slice CT scanners were used and β-blockers were consistently given to lower the heart rate, **assessability of the coronary arteries** was significantly improved, and only up to 12% of the coronary segments were considered nonassessable.[27–31] It is reasonable to expect that the introduction of the latest generation of CT scanners with 64-slice or DSCT technology will lead to further improvement of image quality (**Fig. 5.7**). Subsequent studies have demonstrated that coronary angiography with 64-section CT provides diagnostic image quality within a wide range of heart rates. Moreover, reducing average heart rate and heart rate variability is beneficial for reducing artifacts.[32] The following factors will continue to limit assessability of the coronary arteries:

- Motion of the patient
- Arrhythmia or frequent extrasystoles
- Respiratory artifacts
- Heavy vascular calcifications
- Coronary stents
- Beam-hardening artifacts due to high concentrations of contrast material in the superior vena cava
- Pacemaker electrodes

In most studies conducted with 16-slice CT scanners, only vessels as small as 2 mm or 1.5 mm were assessed. Of those vessels some segments had to be excluded owing to poor image quality. The sensitivities in these studies ranged from 72% to 95% and the specificities from 86% to 97% (positive predictive value 72–80%, negative predictive value 97–98%) (**Fig. 5.9**).[28–31] The latest studies done with 64-slice scanners yielded similar sensitivities and specificities, but all coronary segments were

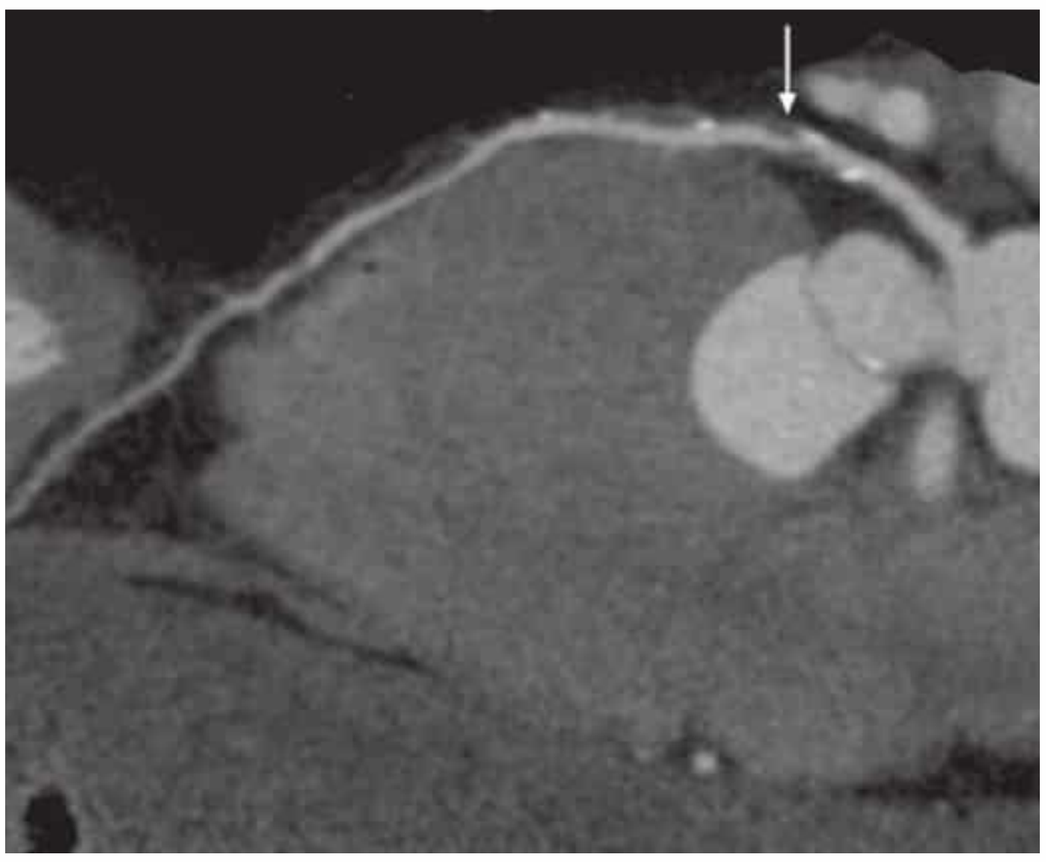

Fig. 5.9 Curved MPR of the LAD in a 58-year-old man with a 70% stenosis due to a mixed plaque (arrow) confirmed by catheter angiography.

analyzed in these studies including vessels <1.5 mm in diameter.[33,34]

CT coronary angiography cannot only detect high-grade coronary stenoses but can also demonstrate noncalcified plaques and differentiate between lipid-rich and fibrous plaques. A high lipid content indicates a vulnerable plaque that may rupture and lead to coronary thrombosis (**Fig. 5.10**).

Another application of CT coronary angiography is in the investigation of **coronary anomalies**, which are found in up to 0.6 % of coronary angiograms. CTA of the coronary arteries is superior to conventional angiography in defining the proximal course of the coronary arteries. Of particular interest are anomalies that may cause a reduction in blood flow or sudden cardiac death, such as the left coronary artery arising from the right coronary sinus or the right coronary artery arising from the left coronary sinus and coursing between the ascending aorta and right ventricular outflow tract. In these anomalies the coronary artery may become compressed between the great vessels leading to myocardial ischemia, especially during exercise. Volume rendering techniques and curved MPRs are particularly useful in these cases for detecting the anomaly and defining its course (**Fig. 5.11**).

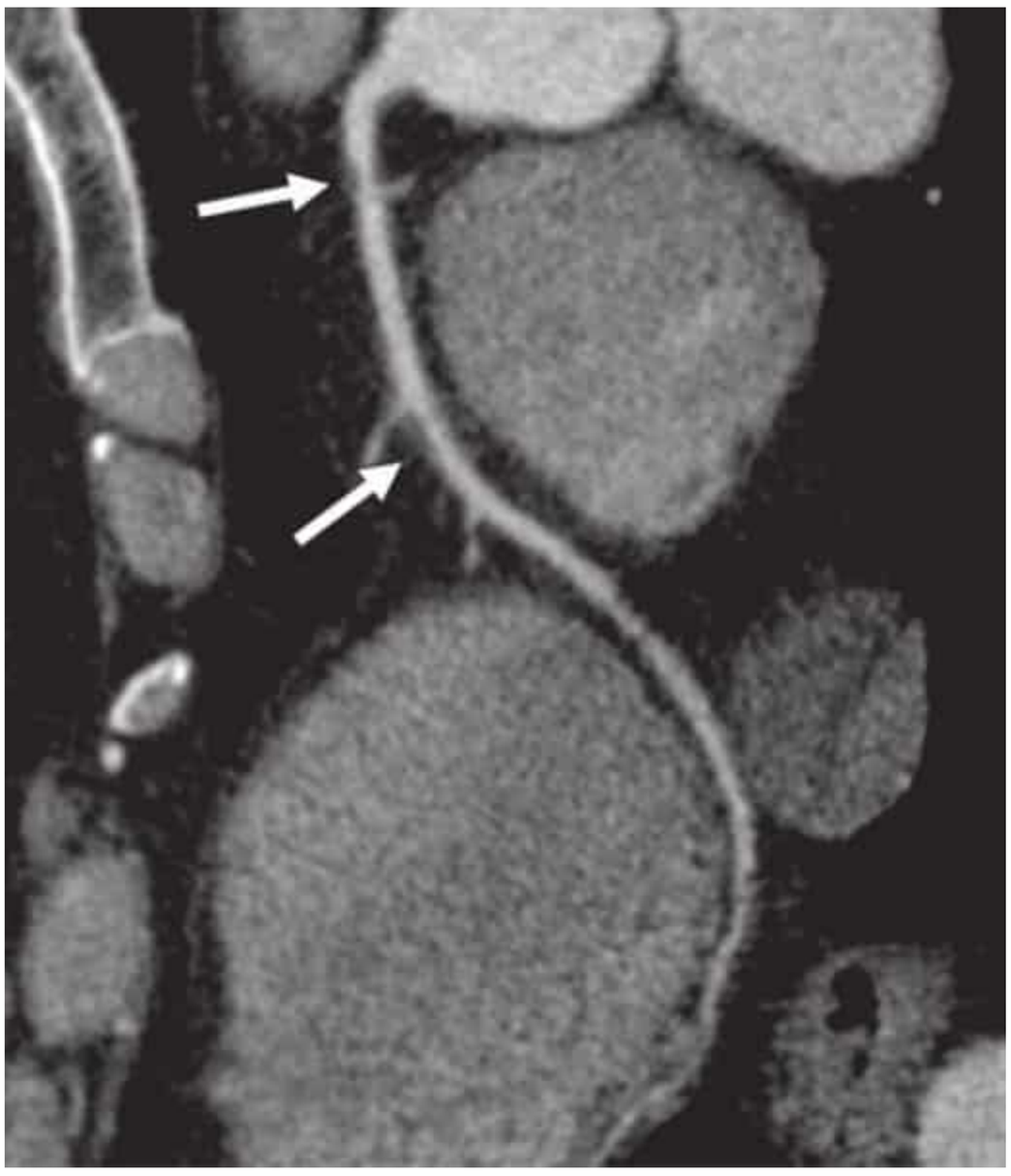

Essential Point
CT coronary angiography can detect coronary anomalies and coronary stenoses with high sensitivity and specificity. Assessability can be limited by motion artifacts, heavily calcified vessels, and stents.

CT Angiography of the Great Vessels

K. Koch

Basic Physical Principles

The introduction of spiral CT has opened up new possibilities in vascular imaging compared with conventional sequential CT. Since the X-ray tube rotates continuously around the patient while the table moves through the scanner, the X-ray beam traces a spiral path relative to the patient. This permits seamless scanning of the body region of interest. The scanning process yields a volume dataset from which axial slices can be computed upon completion of the actual examination.

Because spiral CT shortens the examination time compared with conventional CT, the scanned region can be evaluated in specific perfusion phases after IV contrast administration owing to improved utilization of the contrast bolus. This is critically important in CT angiography (CTA). The applications of CTA have been greatly expanded by engineering advances, with gantry rotation times in the subsecond range (down to ~330 ms) and by the introduction of multislice CT (MSCT), which currently allows the parallel acquisition of up to 64–256 slices in the spiral mode. MSCT can examine substantially larger volumes than single-slice spiral CT with approximately the same or even better spatial resolution, or it can scan the same volumes with significantly higher spatial resolution along the *z*-axis.[35,36]

Methodological Requirements

Noncontrast CT images are of very limited value for vascular investigations. Ultimately they can show only the course and diameter of the vessels, vascular calcifications, and fresh hemorrhagic areas. All further investigations require IV contrast injection. Besides visualizing the perfused lumen, contrast-enhanced images can supply information on the vessel wall, possible thrombus formation, and the relationship of the vessel to surrounding structures.

The contrast medium for CTA can be injected through a peripheral vein with an 18G needle. The risks include the usual ones for contrast medium, particularly contrast allergy. Patient preparations for CTA are similar to those in other contrast-enhanced studies and include the disclosure of information on contrast risks and an assessment of renal and thyroid function.

Examination and Analysis Techniques

The imaging protocol and analysis techniques may vary considerably depending on the clinical question. For this reason, the clinical question should be clearly formulated to allow for proper planning. For example, if the patient is examined for an aortic aneurysm, data acquisition should be initiated when maximum contrast is present in the aorta, after the contrast medium has passed through the pulmonary circulation. But if the patient is being examined for a suspected pulmonary embolism, the arteries of the pulmonary tree should be maximally enhanced with as little contamination from pulmonary veins or systemic arteries as possible. In most cases, longitudinal scan coverage from the supra-aortic vessels to the diaphragm is satis-

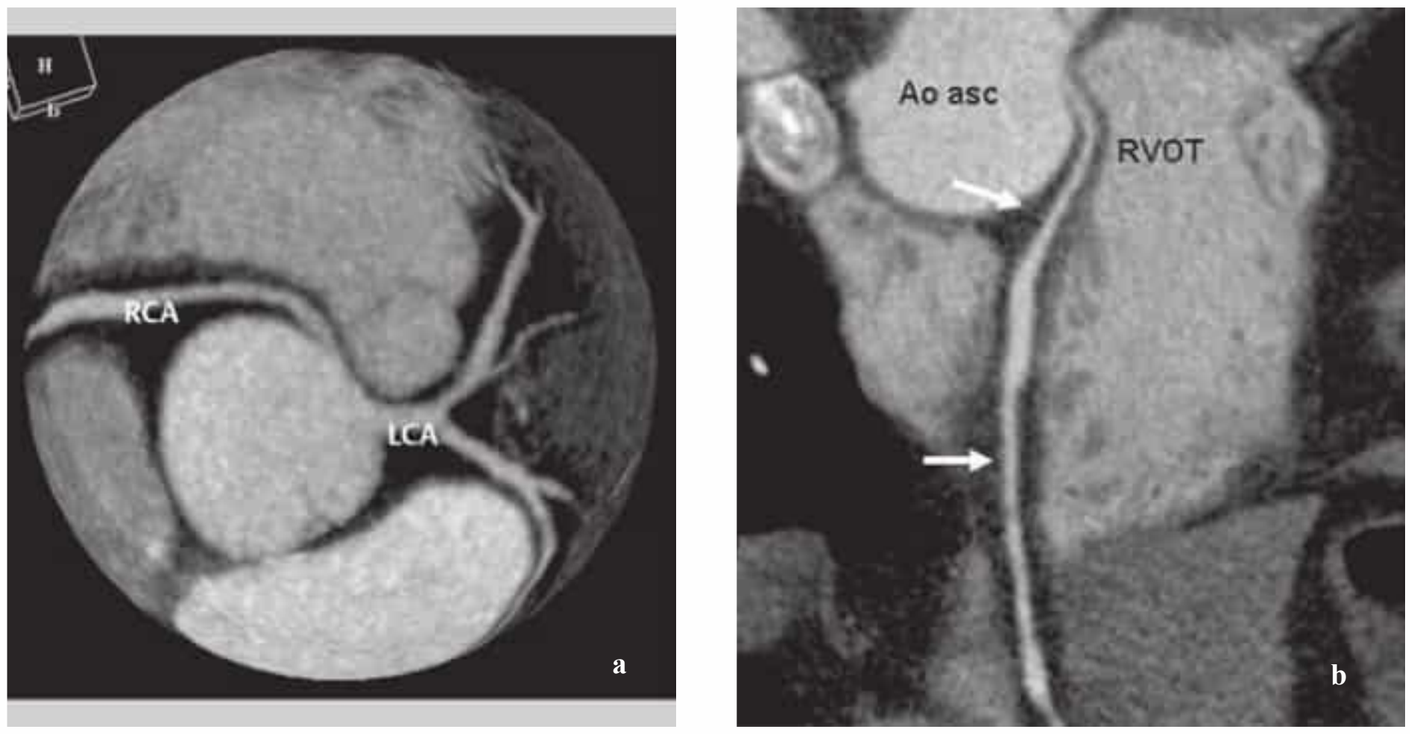

Fig. 5.11 a, b **a** Anomaly of the right coronary artery (RCA) arising from the left coronary sinus. **b** The vessel (arrows) runs between the ascending aorta and right ventricular outflow tract (RVOT). The patient underwent bypass surgery.

factory for CTA of the thoracic vessels. If the patient is being evaluated for aortic dissection, however, the entire aorta should be scanned to evaluate the abdominal side branches in case the dissection extends into the abdominal aorta. A slice thickness of 1–3 mm is desirable for all CT angiographic examinations of the thoracic vessels. **Table 5.2** lists the main parameters for CT scanning of the major thoracic vessels based on the guidelines of the German Radiology Society.[37]

Contrast Medium

Contrast administration should be individually tailored to each patient to achieve optimum enhancement of the targeted vascular region. The arterial phase of enhancement is generally of greatest interest in CTA. It provides good delineation of the perfused vessel lumen. Venous-phase imaging may also be of interest in selected cases, as in patients with an aortic dissection or aortic rupture, to detect opacification of the less-perfused false lumen or extravasation of contrast into a periaortic or pericardial hematoma.

Contrast medium should be administered with a power injector so that the medium can be administered at a sufficiently high, predefined flow rate—usually in the range 3–5 mL/s. Isotonic saline solution should also be injected at the same rate immediately after contrast administration. The purpose of this saline flush is to propel the contrast medium forward, keep the bolus compact, and prolong the enhancement plateau. It can also reduce the necessary contrast dose. A biphasic injection protocol can be used for scanning longer vascular segments such as the complete aorta. In this technique the initial portion of contrast material is injected at a higher flow rate, such as 4 mL/s, to produce a rapid density increase in the vessel. The second portion is then injected at a lower rate, such as 2–3 mL/s, to prolong the enhancement plateau and maintain optimum contrast until the end of the scan. The injection rate for the subsequent saline flush equals that of the second-phase contrast injection.

Finally, optimum vascular imaging requires good coordination of contrast administration, the start of CT data acquisition, and the circulation time of the patient. This coordination is aided by injecting a test bolus to measure how long it takes the contrast medium to arrive in the vascular region of interest. This is done by injecting a small amount of contrast medium, usually ~20 mL, and determining the time to maximum visual contrast wash-in based on reference scans taken at specified time intervals (e.g., every 2 s). This information is then used to calculate the delay time for CT data acquisition after the start of contrast injection. When a test bolus is used, care has to be taken to use the same flow parameters as for the actual angiographic scans. Most modern CT scanners also feature automated bolus triggering. In this mode the scanner automatically detects arrival of intravascular contrast in a preselected reference slice in the region of interest by the rise of CT density, at which point it automatically initiates CT data acquisition. This reduces the total administered dose of contrast medium by eliminating the need for a test bolus.

Table 5.2 Scan parameters for CTA of the great vessels

Scan volume	
• Thoracic aorta	• Diaphragm up to and including the supra-aortic branches
• Pulmonary artery	• Diaphragm to pulmonary apex • Pulmonary embolism: at least from the aortic arch to the diaphragmatic surface of the heart
Necessary views or planes	Transverse slices; multiplanar reformatting if needed
Collimation	≤3 mm
Slice thickness	≤3 mm
Field of view	Adapted to course of vessel
Matrix	≥512
Image acquisition/ reconstruction	• Spiral technique is essential • ECG gating is obligatory only for imaging the aortic root; otherwise ECG is not essential
Intravenous contrast medium	• Essential • Automated injection pump (flow rate at least 2 mL/s) • Intravascular enhancement at least 200 HU

Essential Point

When imaging is done with a modern multislice CT scanner, especially a 16-, 40-, or 64-slice system, the scan time may be considerably shorter than with single-slice CT. There is a risk that data acquisition will "outrun" the contrast bolus, especially in patients with poor cardiac function. This means that scanning concludes before the entire vascular segment is opacified, and the final images will still be unenhanced. This risk is higher with bolus triggering than with a test bolus. Because the circulation time is determined before actual contrast administration when a test bolus is used, it is still possible to adapt the CTA scan protocol to the individual circulation time of the patient.

ECG-Correlated Image Reconstruction

Motion artifacts due to transmitted cardiac pulsations may occur in CTA of the thoracic vessels. They are particularly common in the ascending aorta, where pulsations can cause fluctuations in the aortic diameter. The vessel then shows typical double contours and streak artifacts that hamper evaluation, making it particularly difficult to detect or rule out an aortic dissection or rupture (**Fig. 5.12**).

These pulsation artifacts can be minimized by ECG-correlated image reconstruction (**Fig. 5.13**).[38] Two methods are available for this:

- Retrospective ECG gating
- Prospective ECG triggering

In prospective ECG triggering, scanning is initiated at an operator-selected delay time following detection of the R wave. This method is suitable only for sequential image acquisition, and is not used in CTA. In retrospective ECG gating, an ECG is recorded simultaneously with CT data acquisition. After scanning is completed, series of axial images can be reconstructed retrospectively from the volume dataset at arbitrary points in the cardiac cycle. It should be noted, however, that the scan time is generally longer in ECG-gated examinations because a slower table speed is used. This is necessary to ensure that image information is available for every portion of the scanned region at every point in the cardiac cycle.[39] Thus, images free of pulsation artifacts can be generated at various points in the cardiac cycle. Whereas images in mid-diastole are most suitable for evaluating the ascending aorta and aortic arch, images in late diastole give the best image quality for evaluating the pulmonary arteries.[40]

Interpretation

CT angiograms of the great thoracic vessels are analyzed interactively on the basis of a combination of axial images and postprocessed views. The latter consist mainly of multiplanar reformatting (MPRs) and maximum intensity projections (MIPs), which have an angiogram-like appearance (**Fig. 5.14**). Multiplanar views make it easier to determine the exact location and extent of abnormalities. Special analytical software provides sectional images that are precisely orthogonal to the vessel axis. Quantities such as degree of stenosis, vascular diameters, and aneurysm size can be accurately determined in this way. Three-dimensional reconstructions using surface- or volume-rendering techniques (VRT) make it easier to depict complex 3D relationships and are helpful in the presentation of findings (**Fig. 5.15**). The advantage of VRT is that it provides 3D information while preserving information on the CT densities of the individual structures.

Essential Point

Overlapping image reconstruction in CTA (slice increment less than the reconstructed slice thickness) will improve postprocessed image quality compared with contiguous reconstruction (increment equals the slice thickness).

Clinical Applications

CTA is a simple and fast tool for vascular imaging. It is less costly and less invasive than conventional angiography, and it can demonstrate not only the vessel lumen but also the vessel wall and surrounding structures, revealing possible significant associated findings (**Fig. 5.16**).

CTA has numerous applications in routine clinical investigations of morphological changes in large vessels, both as a standalone modality and as an adjunct to other modalities such as conventional angiography, MRI, and ultrasound.

In life-threatening emergencies such as pulmonary embolism, symptomatic aortic aneurysm, aortic dissection, and aortic rupture, CTA has become the imaging procedure of choice at many institutions owing to the short examination time, the ease of patient monitoring during the examination, and the modest requirements in terms of patient compliance.[37,41,42]

Aortic Aneurysm and Aortic Dissection

CTA makes it possible to evaluate the overall diameter of the aorta and also the diameter of the perfused lumen. Additionally, it can define the extent of partial thrombosis, if present, and can detect calcifications in the vessel wall or the parietal thrombus (**Fig. 5.16**).

With an aortic dissection, CTA can generally define the dissection flap and discriminate between the true and false lumina, although these structures cannot be positively differentiated in all cases.

Essential Point

In patients with a suspected aortic dissection or a large, partially thrombosed aortic aneurysm, a test bolus may be preferable to bolus triggering in some cases. This is because when the region of interest for bolus triggering is placed in the plain reference scan, the true and false lumina cannot be differentiated. If the region of interest is placed in a false lumen that is thrombosed or has extremely slow flow, the optimum time for initiating data acquisition will be missed.

Additionally, the entry and reentry sites can often be identified, and the origins of the aortic side branches and their relationship to the dissected vessel lumen can be evaluated (**Fig. 5.17**). Complications such as rupture, hematoma, aneurysmal expansion, and side-branch involvement, especially that of the coronaries, are also demonstrable by MS-CT.

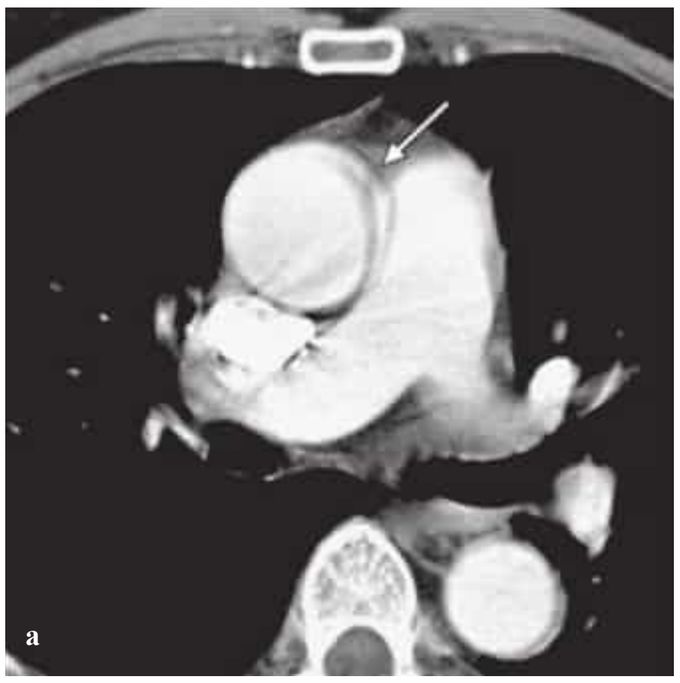

Fig. 5.12 a, b When the ascending aorta is imaged without ECG gating, pulsation artifacts (arrow) appear in the axial image (**a**) and in the coronal reconstruction (**b**).

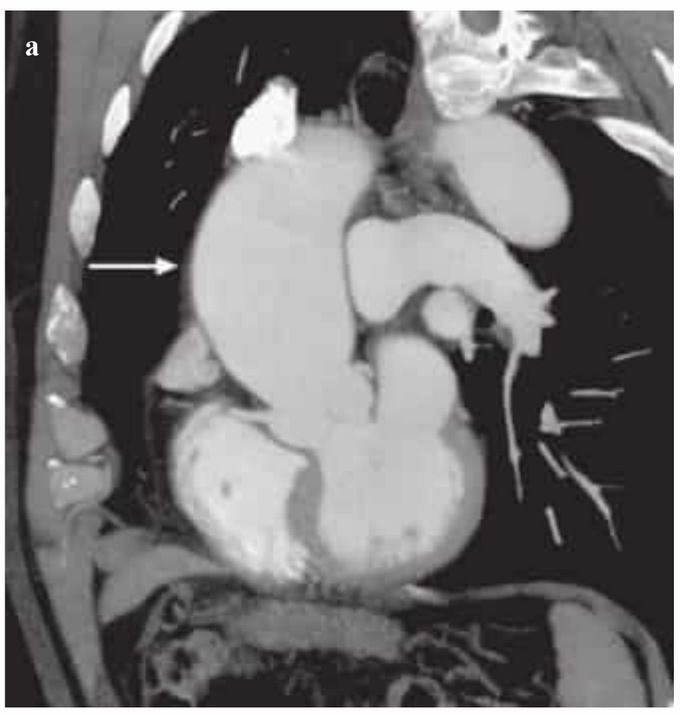

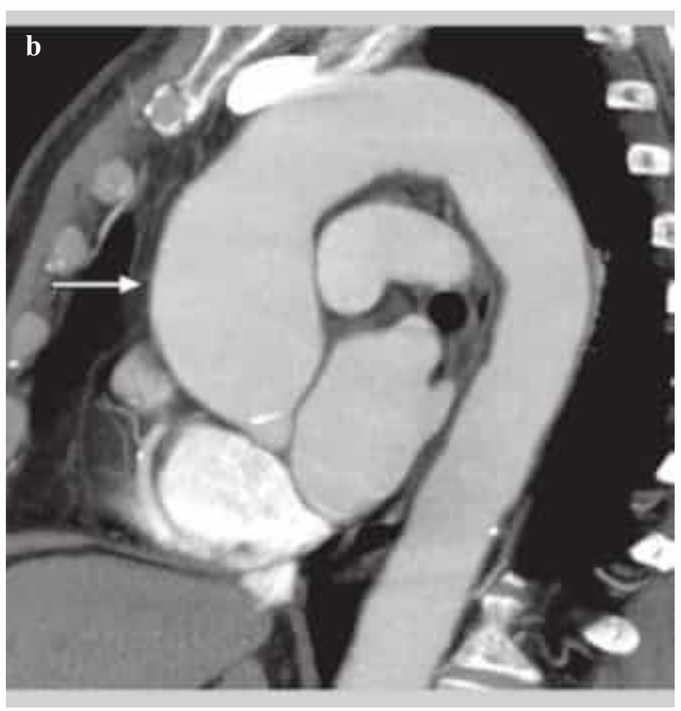

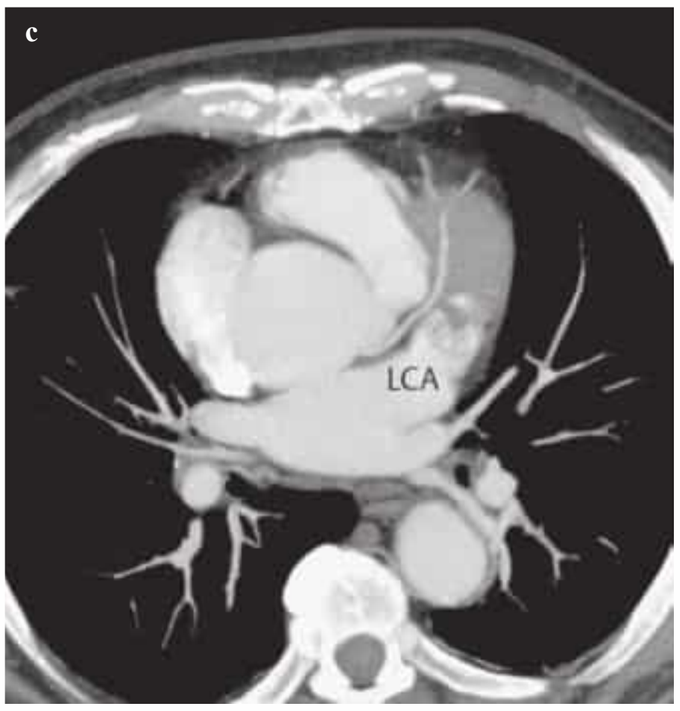

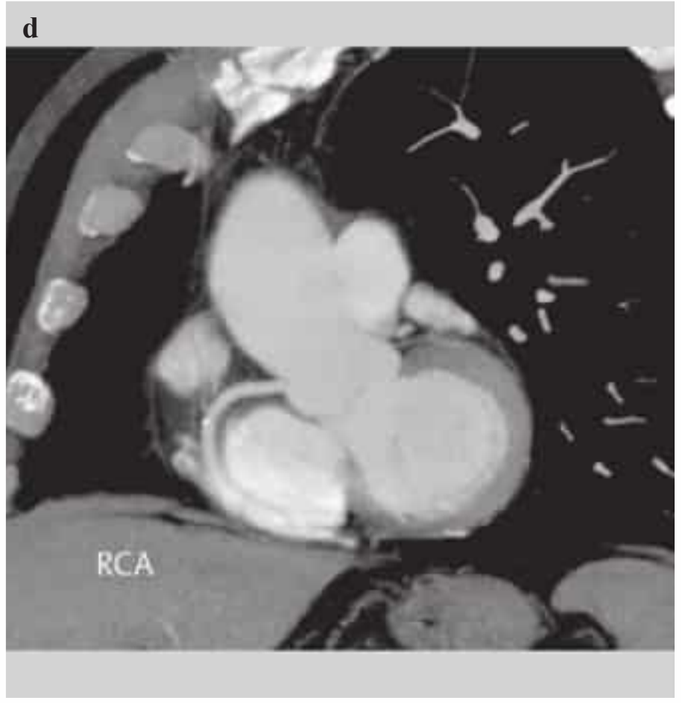

Fig. 5.13 a–d ECG-gated images of the ascending aorta are free of pulsation artifacts and demonstrate an aneurysm distal to the sinotubular junction (arrow). Coronal (**a**) and parasagittal reconstruction (**b**). The proximal portions of the coronary arteries (**c, d**) can also be evaluated when ECG gating is used.

Besides its applications in primary diagnosis and follow-up, CTA can also aid in planning the interventional or operative treatment of aortic aneurysms and dissections to determine the exact size of an aneurysm including parietal thrombosis and to evaluate vessel wall status, the course of the vessel, and its relationship to neighboring structures.

Essential Point

When a type A dissection is suspected, ECG-gated CTA is very useful for minimizing pulsation artifacts in the ascending aorta. ECG gating prolongs the scan time relative to ungated imaging, however, and this must be taken into account during contrast administration.

Traumatic Aortic Injuries

Aortic injuries are discovered in ~0.3 % of patients who have sustained blunt chest trauma. CTA can detect aortic rupture in only 20 % of patients with a mediastinal hematoma.[43] Most frequently a pseudoaneurysm formation is found. Its typical site is the left lateral aspect of the proximal descending aorta at the attachment of the ligamentum arteriosum.

Acute Pulmonary Embolism

Pulmonary artery CTA has become the imaging procedure of choice in patients with acute pulmonary embolism.[44–46] CTA in this condition demonstrates filling defects in the pulmonary

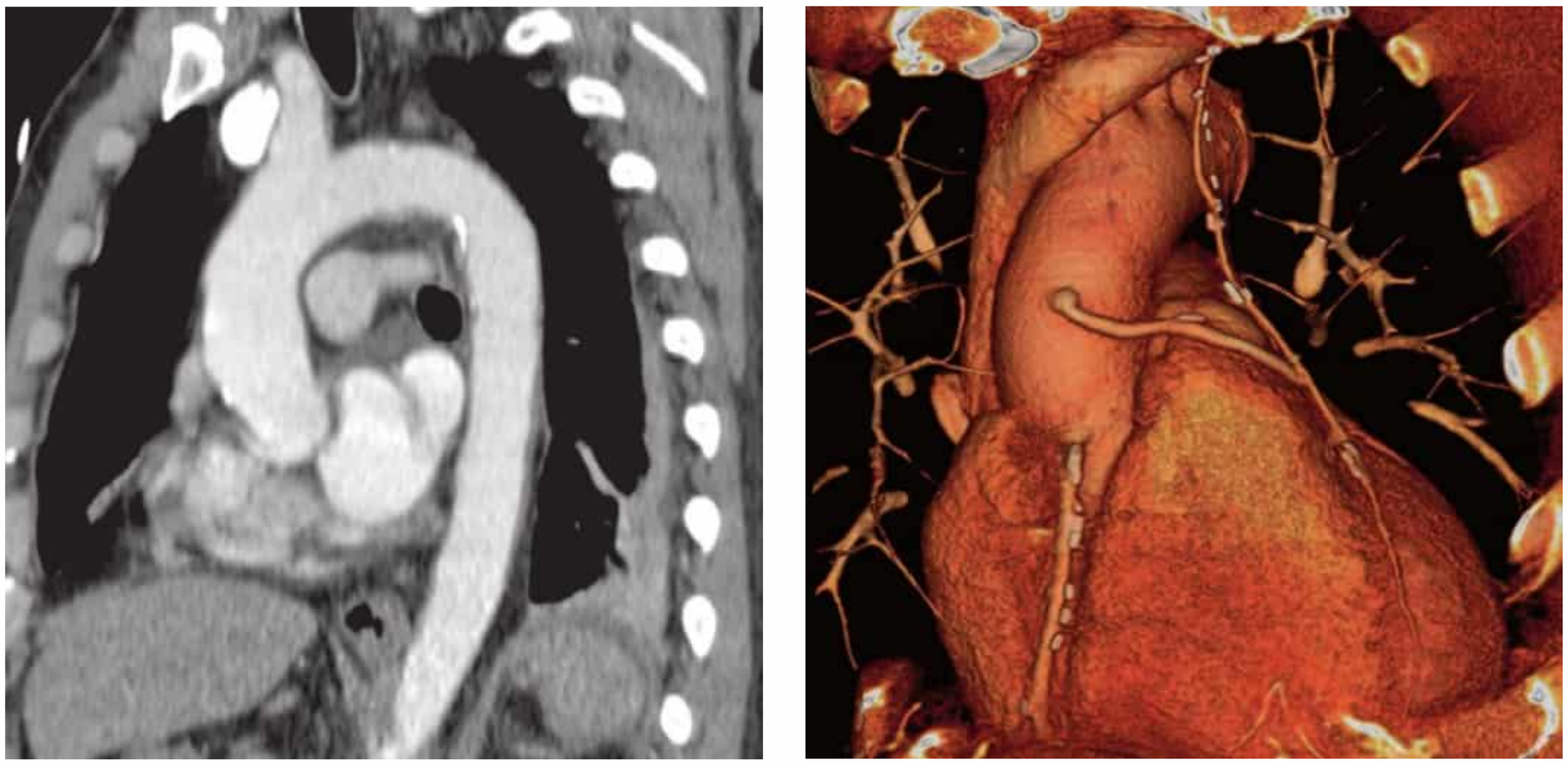

Fig. 5.14 Multiplanar reformatting (MPR) of the thoracic aorta in an oblique sagittal section.

arteries. Fresh emboli appear as arterial filling defects located anywhere from the main pulmonary trunk down to the level of the segmental and subsegmental arteries. They are frequently lodged at vascular bifurcations, appearing as a partially occlusive filling defect outlined by contrast medium (**Fig. 5.18**). Total occlusions are less common. There may also be signs of right-heart overload with enlargement of the right ventricle and atrium.

Essential Point
When pulmonary embolism is detected, the pelvic vasculature should be screened to look for possible deep venous thrombosis as the cause of the pulmonary embolism. The pelvic vessels should be scanned in a late venous phase using the contrast bolus given for pulmonary CTA.

Chronic Thromboembolic Pulmonary Hypertension

Pulmonary CTA is also used in the diagnosis of chronic thromboembolic pulmonary hypertension (CTEPH).[44,47–49] Typical manifestations of CTEPH are right heart enlargement, enlarged pulmonary arteries, thrombotic deposits on the vessel walls, and vascular occlusions. VRT and MIPs can aid in the detection of vascular pruning and cutoffs. Chronic recurring pulmonary embolism typically produces mosaic oligemia in the lung parenchyma, appearing on CTA as areas of decreased ventilation and reduced vascular calibers due to hypoperfusion and vasoconstrictor effects.

Vascular Anomalies and Visualization of Complex Anatomy

CTA can be used in patients with anatomically complex anomalies of the aorta, pulmonary arteries, pulmonary veins, and supra-aortic branches (**Figs. 5.19, 5.20**). It can also be helpful in patients with multiple previous cardiovascular operations to define topographic relationships and direct the planning of additional surgery.

Rare Applications

Less frequent applications of CTA include the imaging of vascular changes in vasculitis, which may consist of vessel wall changes (wall thickening, aneurysmal dilatation) and intraluminal processes (arterial thrombosis), and the evaluation of pulmonary aneurysms with a variety of causes (congenital, infectious, postoperative, iatrogenic due to catheter manipulations).[50]

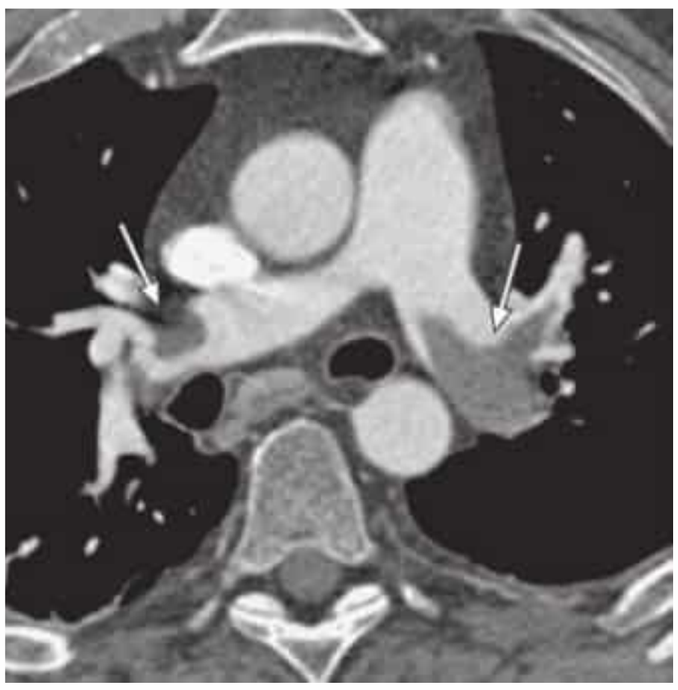

References

1. Graham I, Atar D, Borch-Johnson K, et al. European guidelines on cardiovascular prevention in clinical practice: full text. Fourth Joint Task Force of the European Society and other Societies on Cardiovascular Disease Prevention in Clinical Practice. Eur J Cardiovasc Prev Rehabil 2007;14(Suppl 2):S1–S113
2. Erbel R, Möhlenkamp S, Kerkhoff G, Budde T, Schmermund A. Non-invasive screening for coronary artery disease: calcium scoring. Heart 2007; 93(12):1620–1629
3. Greenland P, Bonow RO, Brundage BH, et al. ACCF/AHA 2007 clinical expert consensus document on coronary artery calcium scoring by computed tomography in global cardiovascular risk assessment and in evaluation of patients with chest pain: a report of the American College of Cardiology Foundation Clinical Expert Consensus Task Force (ACCF/AHA Writing Committee to Update the 2000 Expert Consensus Document on Electron Beam Computed Tomography). Circulation 2007;115:402
4. Boyd DP, Gould RG, Quinn JR, Sparks R, Stanley JH, Herrmannsfeldt WB. A proposed dynamic cardiac 3-D densitometer for early detection and evaluation of heart disease. IEEE Trans Nucl Sci 1979;26:2724–2727
5. Agatston AS, Janowitz WR, Hildner FJ, et al. Quantification of coronary artery calcium using ultrafast computed tomography. J Am Coll Cardiol 1990;15:827–832

5a. Pletcher MJ, Tice JA, Pignone M, Browner WS. Using the coronary artery calcium score to predict coronary heart disease events: a systematic review and meta-analysis. Arch Intern Med. 2004 Jun 28; 164(12):1285-92

6. Schmermund A, Möhlenkamp S, Erbel R. Coronary calcium and its relationship with coronary artery disease. Cardiol Clin 2003;21:521–534
7. Becker CR, Kleffel T, Crispin A, Knez A, Young J, Schoepf UJ. Coronary artery calcium measurement: agreement of multirow detector and electron beam CT. AJR Am J Roentgenol 2001;176:1295–1298
8. Schmermund A, Erbel R, Silber S. Age and gender distribution of coronary artery calcium measured by 4-slice-computed tomography in 2030 individuals with no symptoms of coronary artery disease. Am J Cardiol 2002;90:168–173
9. Callister TQ, Cooil B, Raya SP, et al. Coronary artery disease: Improved reproducibility of calcium screening with an electron-beam CT volumetric method. Radiology 1998;208:807–814.
10. Achenbach S, Ropers D, Möhlenkamp S, et al. Variability of repeated coronary artery calcification measurements by electron beam tomography. Am J Cardiol 2001;87:210–213
11. Hong C, Becker CR, Schoepf UJ, Ohnesorge B, Bruening R, Reiser MF. Coronary artery calcium: Absolute quantification in nonenhanced and contrast-enhanced multi-detector row CT studies. Radiology 2002; 223:474–480
12. Schoepf UJ, Becker CR, Ohnesorge BM, Yucel EK. CT of coronary artery disease. Radiology 2004;232:18–37
13. Schroeder S, Achenbach S, Bengel F, et al. Cardiac computed tomography: indications, applications, limitations, and training requirements:

Report of a Writing Group deployed by the Working Group Nuclear Cardiology and Cardiac CT of the European Society of Cardiology and the European Council of Nuclear Cardiology. Eur Heart J 2008;29(4): 531–556 Epub 2007 Dec 15.
14. Carr JJ, Nelson JC, Wong ND, et al. Calcified coronary artery plaque measurement with cardiac CT in population-based studies: standardized protocol of Multi-Ethnic Study of Atherosclerosis (MESA) and Coronary Artery Risk Development in Young Adults (CARDIA) study. Radiology 2005;234:35–43
15. Schlosser T, Hunold P, Schmermund A, et al. Coronary artery calcium score: influence of reconstruction interval at 16-detector row CT with retrospective electrocardiographic gating. Radiology 2004;233:586–589
16. Mahnken AH, Seyfarth T, Flohr T, et al. Flat-panel detector computed tomography for the assessment of coronary artery stents: phantom study in comparison with 16-slice spiral computed tomography. Invest Radiol 2005;40:8–13
17. Flohr TG, McCollough CH, Bruder H, et al. First performance evaluation of a dual-source CT (DSCT) system. Eur Radiol 2006;16:256–268
18. Arbeitsgruppe "Cardio CT" der Deutschen Gesellschaft für Kardiologie, Herz- und Kreislaufforschung. http://cardio-ct.dgk.org
19. Deutsche Röntgengesellschaft. Leitlinien für den Einsatz der CT in der Diagnostik des Herzens. Fortschr Roentgenstr. 2004;176:632–637
20. Flohr TG, Schoepf UJ, Kuettner A, et al. Advances in cardiac imaging with 16-section CT systems. Acad Radiol 2003;10:386–401
21. Heuschmid M, Küttner A, Flohr T, et al. [Visualization of coronary arteries in CT as assessed by a new 16 slice technology and reduced gantry rotation time: first experiences] RoFo 2002;174:721–724
22. Pugliese F, Mollet NR, Runza G, et al. Diagnostic accuracy of non-invasive 64-slice CT coronary angiography in patients with stable angina pectoris. Eur Radiol 2006 Mar;16(3):575–582.Epub 2005 Nov 16
23. Nikolaou K, Rist C, Wintersperger BJ, et al. 64-detector-row computed tomography of the coronary arteries: Initial experience. Eur Radiol 2005;15:209
24. Achenbach S, Giesler T, Ropers D, et al. Detection of coronary artery stenoses by contrast-enhanced, retrospectively electrocardiographically-gated, multislice spiral computed tomography. Circulation 2001; 103:2535–2538
25. Kuettner A, Kopp AF, Schroeder S, et al. Diagnostic accuracy of multidetector computed tomography coronary angiography in patients with angiographically proven coronary artery disease. J Am Coll Cardiol 2004;43:831–839
26. Nieman K, Oudkerk M, Rensing BJ, et al. Coronary angiography with multi-slice computed tomography. Lancet 2001;357:599–603
27. Achenbach S, Moselewski F, Ropers D, et al. Detection of calcified and noncalcified coronary atherosclerotic plaque by contrast-enhanced, submillimeter multidetector spiral computed tomography: a segment-based comparison with intravascular ultrasound. Circulation 2004; 109:14–17
28. Kuettner A, Trabold T, Schroeder S, et al. Noninvasive detection of coronary lesions using 16-detector multislice spiral computed tomography technology: initial clinical results. J Am Coll Cardiol 2004;44:1230–1237
29. Mollet NR, Cademartiri F, Nieman K, et al. Multislice spiral computed tomography coronary angiography in patients with stable angina pectoris. J Am Coll Cardiol 2004;43:2265–2270
30. Nieman K, Cademartiri F, Lemos PA, et al. Reliable noninvasive coronary angiography with fast submillimeter multislice spiral computed tomography. Circulation 2002;106:2051–2054
31. Ropers D, Baum U, Pohle K, et al. Detection of coronary artery stenoses with thin-slice multi-detector row spiral computed tomography and multiplanar reformatting. Circulation 2003;107:664–666
32. Leschka S, Wildermuth S, Boehm T, et al. Noninvasive coronary angiography with 64-section CT: effect of average heart rate and heart rate variability on image quality. Radiology 2006;241(2):378–385
33. Leschka S, Alkadhi H, Plass A, et al. Accuracy of MSCT coronary angiography with 64-slice technology: first experience. Eur Heart J 2005;26:1482–1487
34. Raff GL, Gallagher MJ, O'Neill WW, et al. Diagnostic accuracy of noninvasive coronary angiography using 64-slice spiral computed tomography. J Am Coll Cardiol 2005;46:552–557
35. Duddalwar VA. Multislice CT angiography: a practical guide to CT angiography in vascular imaging and intervention. Br J Radiol 2004;77(Suppl 1):S27–S38
36. Rubin GD. MDCT imaging of the aorta and peripheral vessels. Eur J Radiol 2003;45(Suppl 1):S42–S49
37. Kreitner K-F, Sandstede J. CT des Herzens: Aktuelle Leitlinien. Fortschr Roentgenstr. 2004;176:632–637
38. Cademartiri F, Pavone P. Advantages of retrospective ECG-gating in cardio-thoracic imaging with 16-row multislice computed tomography. Acta Biomed 2003 Dec;74(3):126–130
39. Ohnesorge BM, Becker CR, Flohr TG, Reiser MF. Multi-slice CT in Cardiac Imaging. Berlin: Springer; 2002: 24–48.
40. Hofmann LK, Zou KH, Costello P, Schoepf UJ. Electrocardiographically gated 16-section CT of the thorax: cardiac motion suppression. Radiology 2004;233(3):927–933
41. Coulam CH, Rubin GD. Acute aortic abnormalities. Semin Roentgenol 2001;36(2):148–164
42. Tatli S, Yucel EK, Lipton MJ. CT and MR imaging of the thoracic aorta: current techniques and clinical applications. Radiol Clin North Am 2004;42(3):565–585
43. Prokop M, Galanski M. Spiral and Multislice Computed Tomography of the Body. Stuttgart: Thieme; 2003: 83–108, 825–928.
44. Filipek MS, Gosselin MV. Multidetector pulmonary CT angiography: advances in the evaluation of pulmonary arterial diseases. Semin Ultrasound CT MR 2004;25(2):83–98
45. Reid JH. Multislice CT pulmonary angiography and CT venography. Br J Radiol 2004;77(Suppl 1):S39–S45
46. Wittram C, Mahler MM, Yoo AJ, Kalra MK, Shepard JA, McLoud TC. CT angiography of pulmonary embolism: diagnostic criteria and causes of misdiagnosis. Radiographics 2004;24(5):1219–1238
47. Coche E, Verschuren F, Hainaut P, Goncette L. Pulmonary embolism findings on chest radiographs and multislice spiral CT. Eur Radiol 2004;14:1241–1248 10.1007/s00330–003–2203–2
48. Collomb D, Paramelle PJ, Calaque O, et al. Severity assessment of acute pulmonary embolism: evaluation using helical CT. Eur Radiol 2003; 13(7):1508–1514 10.1007/s00330–002–1804–5
49. Ley S, Kauczor HU, Heussel CP, et al. Value of contrast-enhanced MR angiography and helical CT angiography in chronic thrombembolic pulmonary hypertension. Eur Radiol 2003;13(10):2365–2371 10.1007/s00330–003–1878–8
50. Kierse R, Jensen U, Helmberger H, Muth G, Rieber A. Value of multislice CT in diagnosis of pulmonary artery pseudoaneurysm from Swan-Ganz catheter placement. J Vasc Interv Radiol 2004;15(10):1133–1137

Further Reading

Prokop M. Multislice CT angiography. Eur J Radiol 2000;36(2):86–96

6 Magnetic Resonance Imaging

Planning the Examination

K. Nassenstein

The basic principle of magnetic resonance imaging (MRI) is that the magnetic moments of the protons in a sample become aligned when exposed to a static magnetic field. When brief radiofrequency pulses are applied to the sample, energy is transferred to the protons, which then release the energy in the form of electromagnetic waves. These waves are detected with special receiver coils and undergo a complex mathematical process (Fourier transformation) that converts them into images. This chapter is not concerned with the technical principles of MRI, which can be found in the literature,[1–3] but with the specific practical aspects of **cardiac MRI**.

System Requirements

A high-performance scanner should be used for cardiac MRI to ensure a good **signal-to-noise ratio** (SNR) and rapid **data acquisition**. Morphological and functional studies require at least a 1.0-T system, but 1.5-T systems are better for all cardiac MRI examinations and are essential for perfusion studies and MR coronary angiography.[4] In recent years, 3.0-T systems have also been employed for cardiac imaging. They can theoretically double the SNR[5] but also cause other problems such as an increase in the specific absorption rate (SAR) and increased susceptibility artifacts.[5,6]

Special phased-array surface coils are available for data acquisition. Placed directly on the chest wall, they contain a variable number of coil elements, depending on the manufacturer, and provide a homogeneous B_1-field over a large field of view. An MR-compatible contrast injector should always be used for studies such as first-pass perfusion imaging or MR angiography that require the rapid injection of contrast material.[4]

Patient Preparation

Before the examination, the patient should receive an **explanation of the procedure** that briefly covers the following points:

1. Basic structure of the scanner (a long, relatively narrow "tube")
2. Basic principle of the examination ("magnetic field," "no radiation")
3. Approximate length of the examination
4. Importance of lying still and following breath-hold commands
5. Explanation of contraindications
6. Risks of intravenous contrast administration, if required

Essential Point
A thorough explanation will increase patient compliance, improve image quality, and shorten the examination time.

To ensure a safe examination, the **contraindications** to MRI should be carefully explained. **Table 6.1** lists frequent contraindications to cardiac MRI. Stents and artificial heart valves are not a contraindication to MRI.

After the procedure has been explained and contraindications have been excluded, the patient is positioned supine in the scanner and the ECG electrodes are applied. A good ECG signal is essential for obtaining MR images of good quality. Correct placement of the ECG electrodes and good contact between the electrodes and skin are necessary to eliminate ECG artifacts and provide accurate triggering for image acquisition. The quality of the ECG signal can be improved by using disposable electrodes and, if necessary, by shaving the skin.

Essential Point
If the initial ECG signal is of poor quality, it may be improved by reattaching the ECG electrodes. This should be done repeatedly if necessary, since good triggering is essential for good image quality.

Pulse Sequences

Various sequences are available for image acquisition. A sequence is a combination of radiofrequency and gradient pulses that produce a resonance signal from which images are constructed. Image contrast can be manipulated by varying the design and different parameters of the pulse sequences including repetition time, echo time and flip angle. Image contrast can also be varied by combining basic sequences with preparation pulses (fat saturation, inversion recovery, saturation recovery, T2 prep). The main types of sequences will be briefly described below. Details can be found in the following sections.

Table 6.1 Contraindications to MRI[173]

Absolute contraindications	• Cardiac pacemaker • ICD • Neurostimulator • Cochlear implant • First-trimester pregnancy
Relative contraindications	• Claustrophobia • Intracranial aneurysm clips (individual counseling required) • Metallic foreign objects (individual counseling required) • Second- or third-trimester pregnancy

Dark-Blood Sequences

Dark-blood pulse sequences suppress flowing blood, causing the vascular lumen and the heart chambers to appear black. The simplest type in this group are spin-echo (SE) sequences, but they are rarely used in modern cardiac imaging because of the long acquisition times (too long for breath holding). Turbo spin-echo (TSE) sequences permit the acquisition of single slices during one breath hold and show excellent contrast properties.[7] They are used for tissue characterization in cardiac tumors, for example, and for the detection of myocardial edema. Single-shot turbo spin-echo sequences are even faster, enabling a complete stack of slices to be acquired during a single breath hold, but they provide less contrast than turbo spin-echo sequences. This type of sequence can be used to obtain a quick overview of anatomical structures.

Bright-Blood Sequences

Flowing blood has high signal intensity in bright-blood sequences. Gradient-echo (GE) sequences are a prime example. Because they have a considerably shorter acquisition time than SE sequences, they are suitable for dynamic imaging with high temporal and spatial resolution. However, cine MRI for the assessment of cardiac function is today done almost exclusively with steady-state free-precession (SSFP) sequences,[8] which are even faster and provide a better signal-to-noise and contrast-to-noise ratio.[9,10]

Planning the Examination

Diagnostic MRI of the heart is performed in multiple standard orientations. Because the position of the heart in the chest is subject to marked anatomical variations (**Fig. 6.1**), the standard imaging planes are defined in relation to the cardiac axes rather than the orthogonal body axes. The standard orientations for cardiac MRI are derived from the scan planes used in echocardiography. To ensure complete visualization of the complex cardiac anatomy, the standard imaging planes described below should always be prescribed in a cardiac MR examination.

Basic Protocol for Cardiac MRI

Scanning Extracardiac Structures

Examination of the heart itself should be preceded by axial scans of the entire thorax. Coronal views can additionally be obtained if needed. These survey scans are helpful for the subsequent prescription of standard double-oblique cardiac scans. They are also useful in the detection of anatomical variants or abnormalities involving the major thoracic vessels, mediastinum, lungs, and chest wall. Single-shot turbo spin-echo sequences and single-shot steady-state free-precession sequences can provide a rapid overview of the entire thorax in a single breath hold.

Essential Point

Cardiac MRI is more than just MR imaging of the heart! Attention should always be given to extracardiac pathologies.

Standard Double-Oblique Sections of the Heart

Double-oblique scan planes are angled to conform to the intrinsic cardiac axes. They can reproducibly display the complex anatomical structures of the heart, and they can rapidly detect morphological and functional changes in the heart using relatively few sequences.

Essential Point

A consistent routine should be followed in the prescription of standard cardiac scans. At each step along the way, the operator should carefully determine whether the current scan plane is correctly positioned, because each sectional plane builds upon the preceding plane.

The steps involved in prescribing the standard scan planes are described below.

Survey Scan 1

Survey scans are performed with fast single-shot SSFP or single-shot TSE sequences, which permit the acquisition of multiple scans in a single breath hold. In the initial step, survey scans centered at the heart are acquired in axial, sagittal, and coronal planes. (**Fig. 6.2**).

Survey Scan 2

A second scan parallel to the ventricular septum is prescribed from the axial survey scan. The second scan passes through the center of the mitral valve and through the left ventricular apex, thus defining the left ventricle in its maximum longitudinal extent (**Fig. 6.3a**). The left atrium, mitral valve, and left ventricle are displayed in this scan (**Fig. 6.3b**).

Survey Scan 3

The first double-oblique scan is prescribed from the single-oblique scan above. This plane is perpendicular to the second survey scan and passes through the left ventricular apex and center of the mitral valve (**Fig. 6.4a**). Both atria and both ventricles are depicted in this scan (**Fig. 6.4b**).

Short-Axis Views

The acquisition of double-oblique short-axis views is based on the third survey scan. Multiple short-axis sections are acquired perpendicular to survey scan 3 (**Fig. 6.5**) and to the ventricular septum (**Fig. 6.5b**).

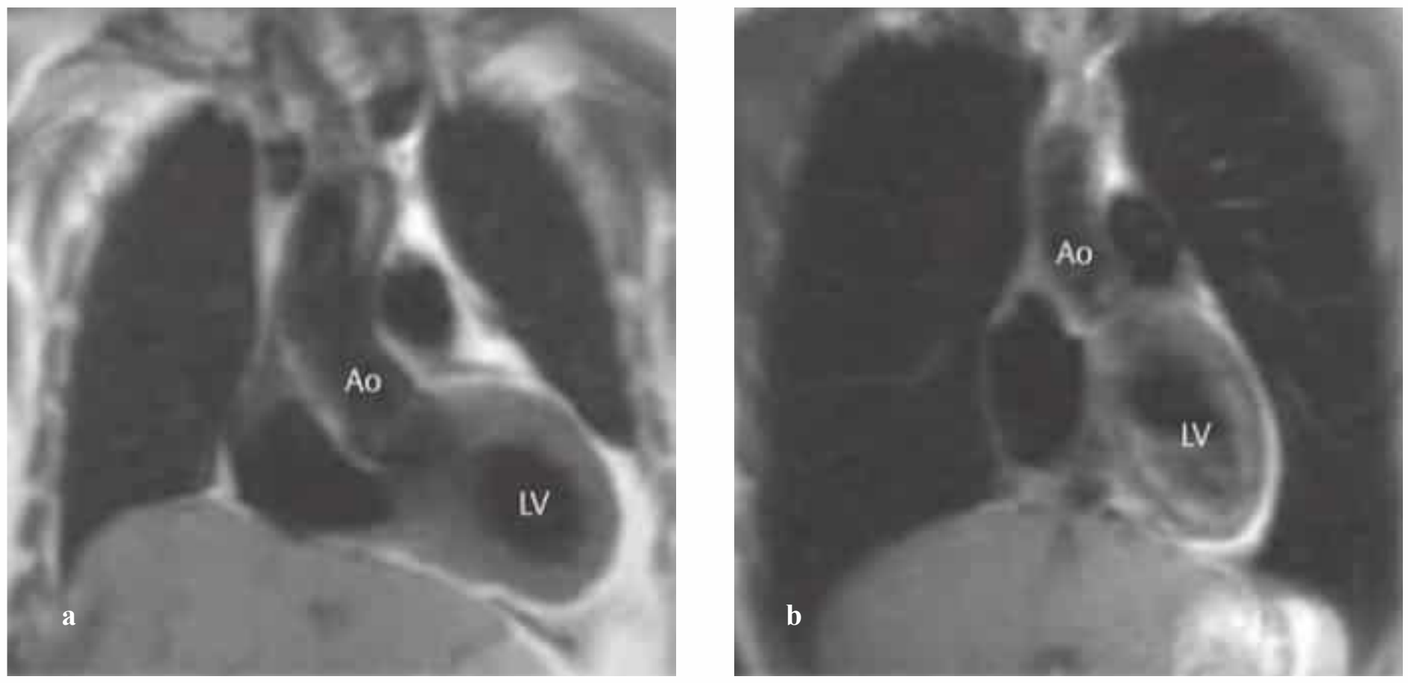

Fig. 6.1 a, b Marked variability of cardiac position relative to the body axes.
a Heart broadly apposed to the diaphragm.
b Upright cardiac position in the chest.

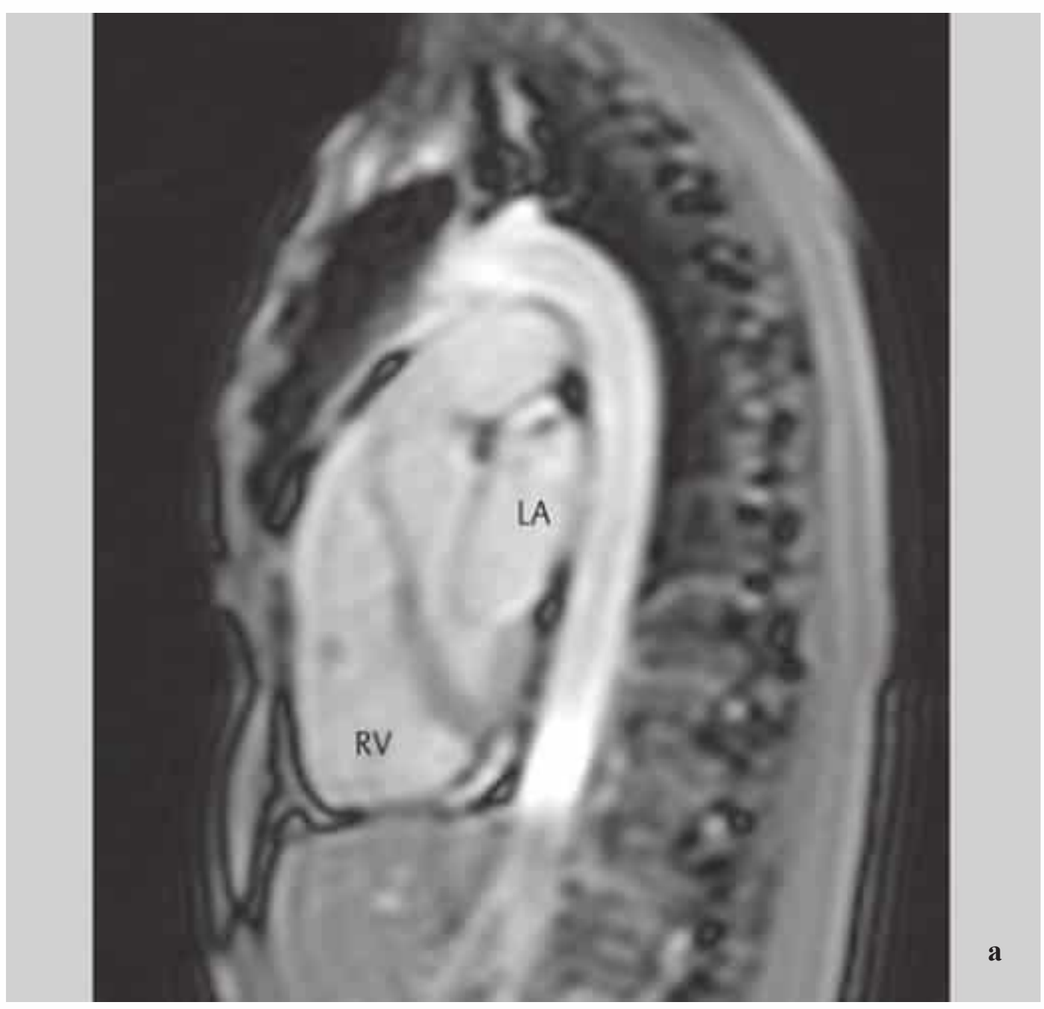

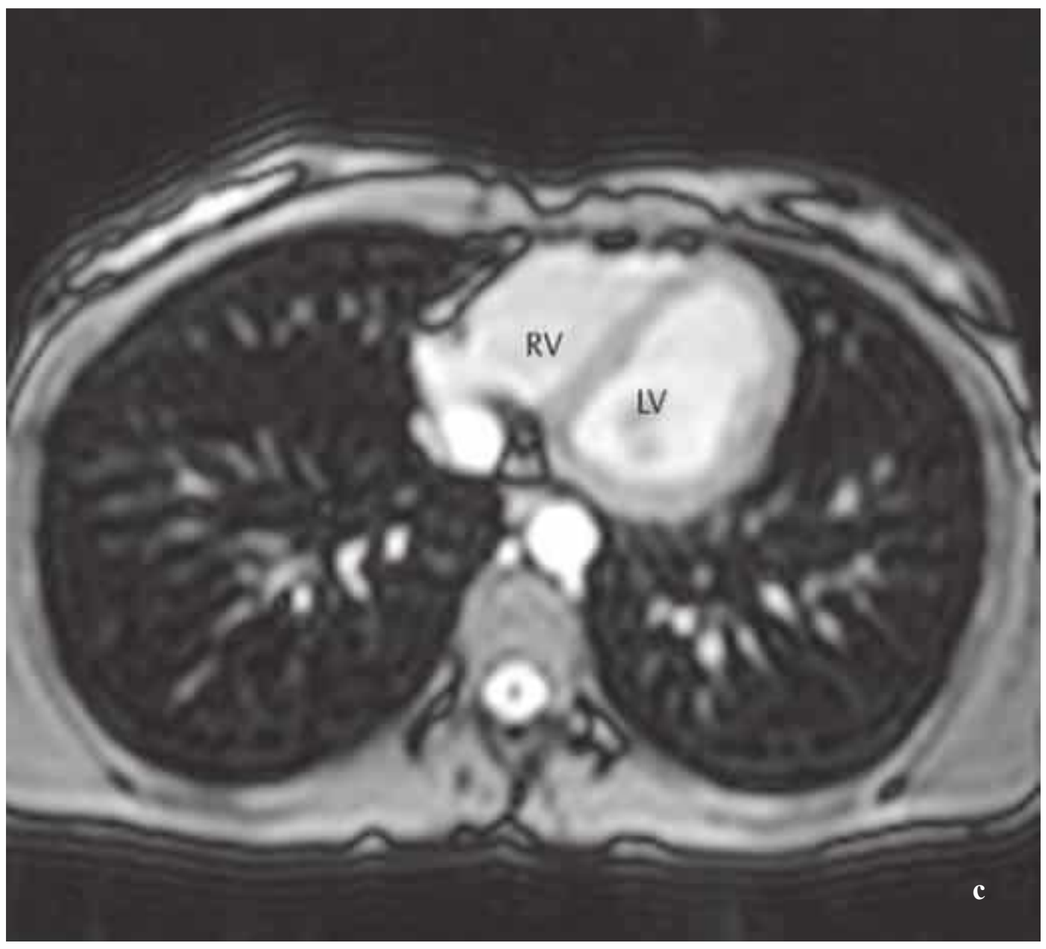

Fig. 6.2 a–c Step 1: The heart is imaged at low spatial resolution in sagittal (**a**), coronal (**b**), and axial (**c**) planes.

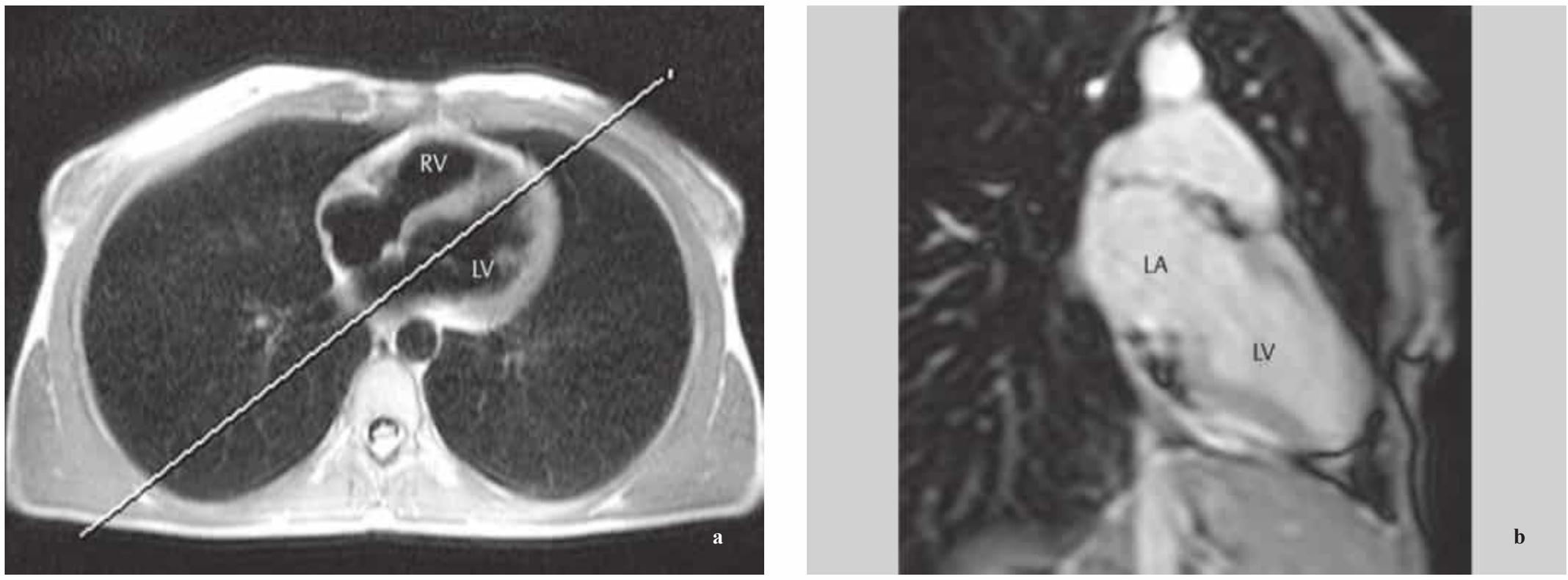

Fig. 6.3 a, b Step 2: Prescription of a second survey scan (**b**) based on the first survey scan (**a**), passing through the left ventricular apex and the center of the mitral valve.

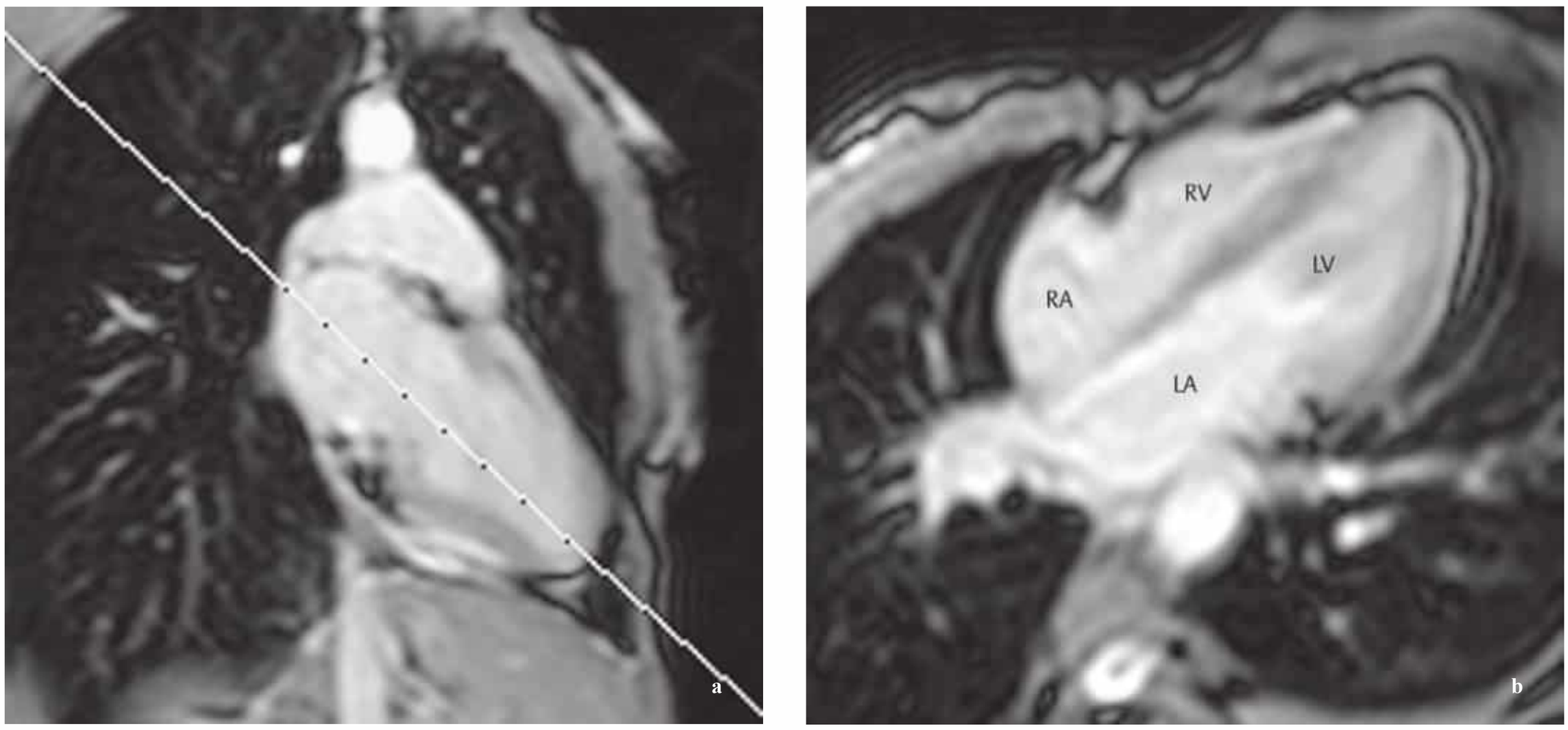

Fig. 6.4 a, b Step 3: A third survey scan (**b**) is prescribed perpendicular to the second survey scan, which displays the left atrium and left ventricle (**a**). Survey scan 3 passes through the left ventricular apex and the center of the mitral valve.

Essential Point

The left ventricular myocardium should appear circular in correctly prescribed short-axis sections. If the short-axis sections are not perpendicular to the long axis of the left ventricle, the ventricular myocardium will have an oblong shape.

Short-axis views are usually acquired from base to apex with cine SSFP sequences to display all of the left and right ventricle (maximum slice thickness 8 mm). These contiguous short-axis sections are the basis for determining the left ventricular volume.

Essential Point

Incorrectly prescribed short-axis sections can lead to errors in volume determination.

Four-Chamber View (Horizontal Long Axis of the Left Ventricle)

Prescription of the four-chamber view, also called the horizontal long axis of the left ventricle, is based on the double-oblique short-axis views. The prescribed plane is perpendicular to the short-axis sections and is oriented to demonstrate the maximum transverse extent of the right and left ventricles while showing none of the left ventricular outflow tract (**Fig. 6.6a**). The four-chamber view is acquired with a cine SSFP sequence. It is useful for evaluating both atria, the mitral and tricuspid valves, and both ventricles (**Fig. 6.6b**).

Essential Point

The plane position should also be checked on survey scan 2 to make sure the plane aligns through the cardiac apex and the center of the mitral valve.

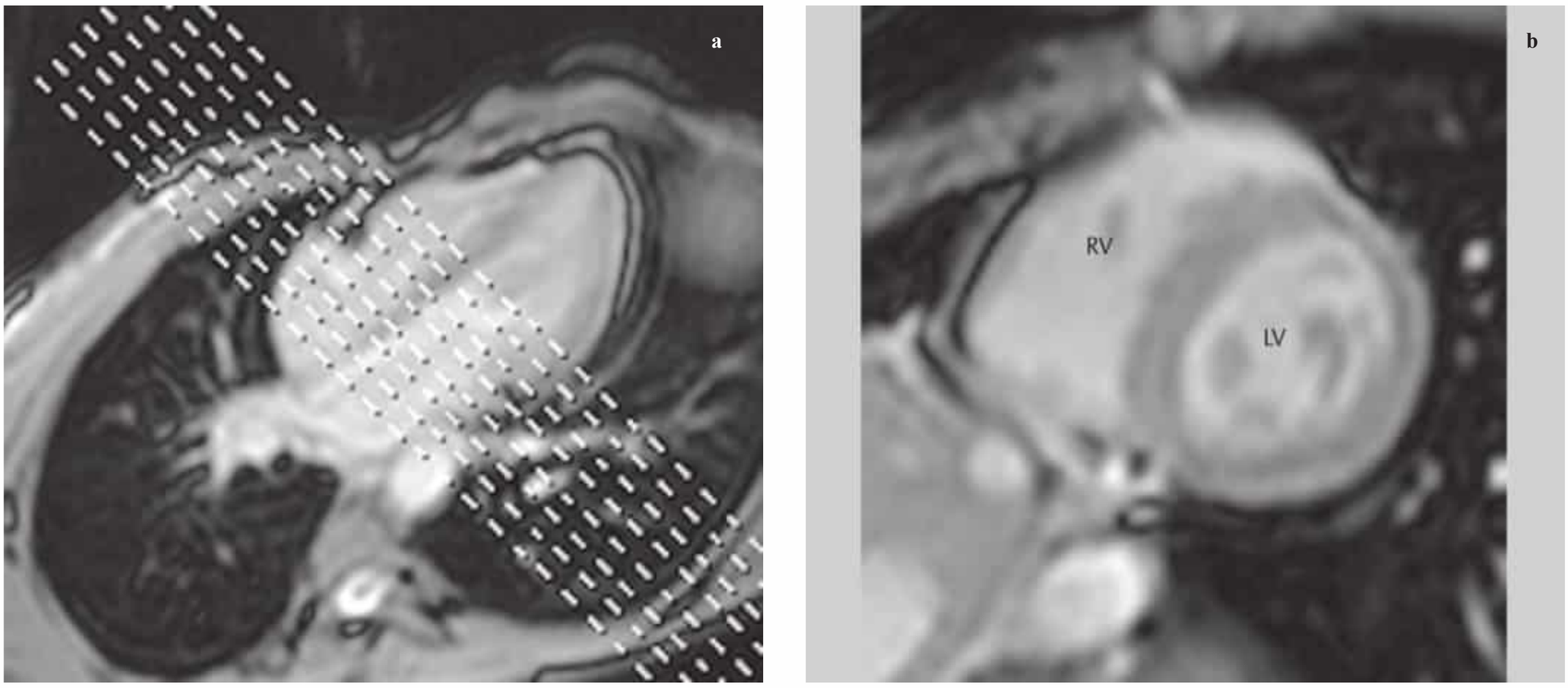

Fig. 6.5 a, b Step 4: Prescription of short-axis views (**b**) perpendicular to the third survey scan (**a**) and to the ventricular septum.

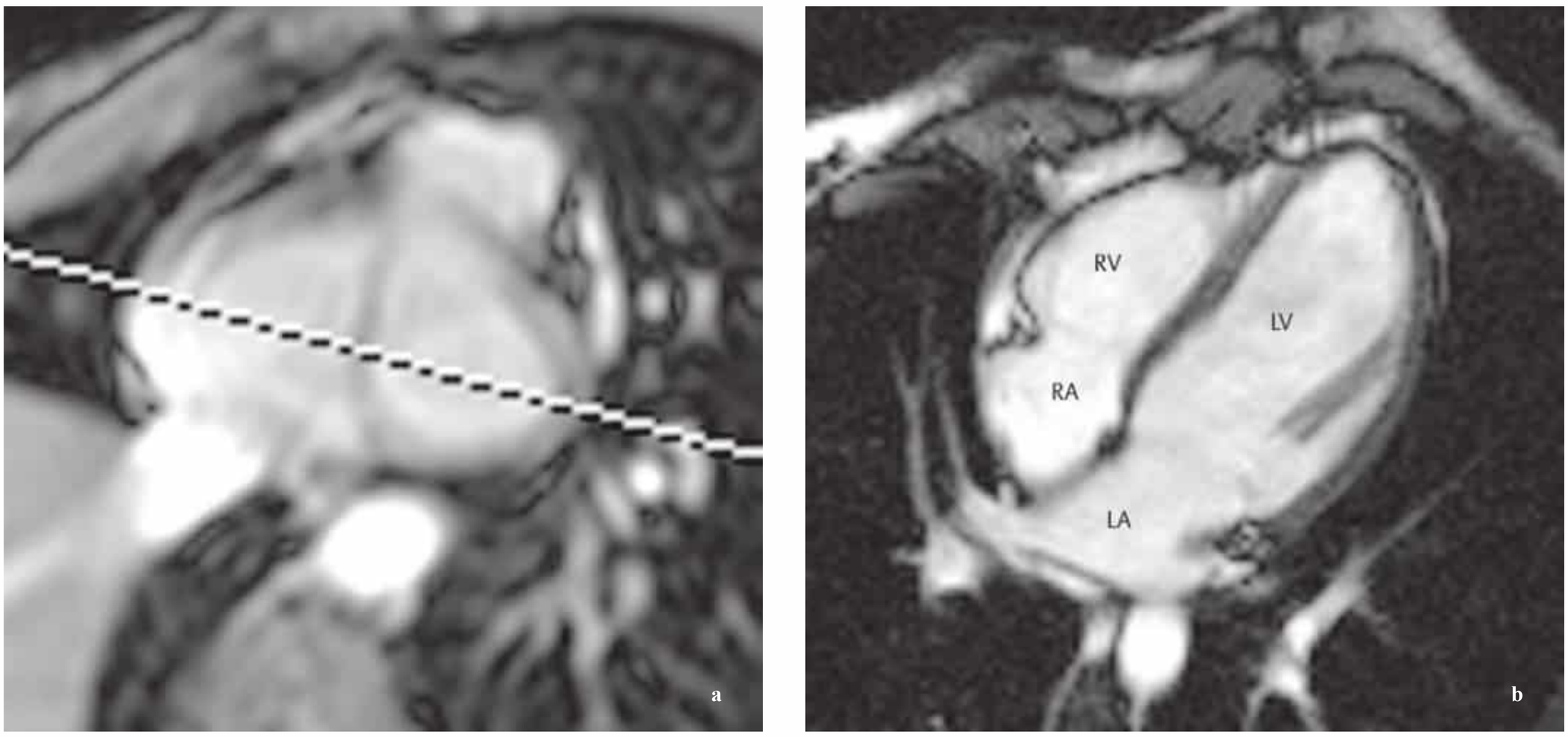

Fig. 6.6 a, b Step 5: Prescription of the double-oblique four-chamber view (**b**) from a basal short-axis view (**a**). The section is angled to display the greatest transverse extent of both ventricles while excluding the left ventricular outflow tract.

Two-Chamber View (Vertical Long Axis)

The two-chamber view is directed perpendicular to the four-chamber view (**Fig. 6.7a**), passes through the left ventricular apex, and cuts the midpoint of the mitral valve. Acquired with a cine SSFP sequence, it is used to evaluate the left atrium, mitral valve, and left ventricle (**Fig. 6.7c**).

Essential Point

The basal short-axis sections (**Fig. 6.7b**) provide an additional reference for checking the prescription of the two-chamber view.

Left Ventricular Inflow and Outflow Tract (LVOT, Three-Chamber View)

The LVOT is prescribed from the basal short-axis view (**Fig. 6.8a**), which already displays the aortic valve and aortic bulb, and from the four-chamber view (**Fig. 6.8b**). The prescribed plane is perpendicular to the short-axis view, passes through the left ventricular apex, and is angled so that it passes through the center of the aortic valve. The three-chamber view demonstrates the left atrium, mitral valve, left ventricle, aortic valve, and ascending aorta, thus displaying the left ventricular inflow and outflow tract (**Fig. 6.8c**).

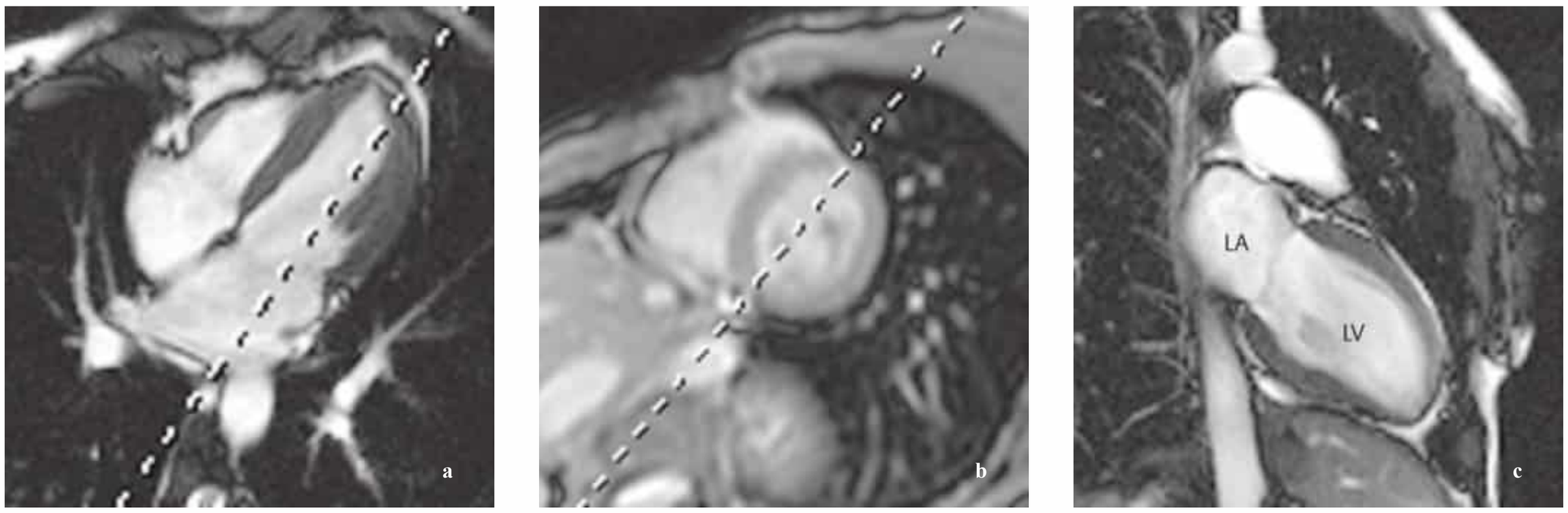

Fig. 6.7 a–c Step 6: Prescription of the double-oblique two-chamber view (**c**) from the four-chamber view (**a**) and short-axis view (**b**). The section passes through the left ventricular apex and the center of the mitral valve.

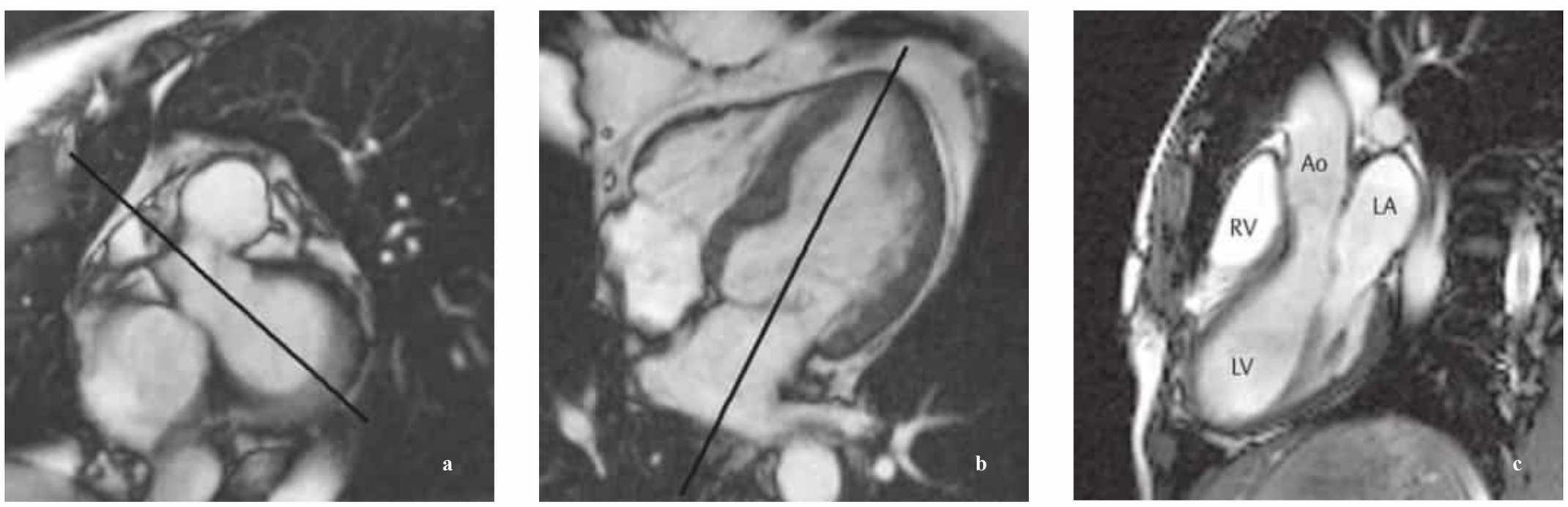

Fig. 6.8 a–c Step 7: Prescription of the three-chamber view (LVOT, **c**) from a basal short-axis section (**a**) and the four-chamber view (**b**) The section is prescribed perpendicular to the short-axis view passing through the center of the aortic valve and the LV apex.

Extended Scan Protocol

Some clinical questions may also require imaging in additional planes. This is particularly true in the evaluation of complex cardiac anomalies, right ventricular diseases (e.g., arrhythmogenic right ventricular dysplasia), and valvular heart diseases.

Axial Cine-SSFP Sequences

Scanning the entire heart in axial cine-SSFP sequences can be very helpful for visualizing complex anomalies of the heart and great vessels and for right ventricular volumetry.

Essential Point
Axial cine-SSFP sequences permit a more accurate and reproducible determination of right ventricular volume because the tricuspid valve can be defined more accurately than in short-axis sections.

Right Ventricular Vertical Long Axis

The right ventricular vertical long-axis view (two-chamber view of the right heart) demonstrates the right atrium, tricuspid valve, and right ventricle. This section is perpendicular to the four-chamber view and passes through the center of the tricuspid valve and the apex of the right ventricle.

Tricuspid Valve

The orifice of the tricuspid valve can be evaluated in basal short-axis sections. For the quantification of tricuspid inflow, the scan plane must run strictly parallel to the tricuspid valve plane. This view of the tricuspid valve is prescribed from the four-chamber view and right ventricular vertical long-axis view, which display the tricuspid valve in two mutually perpendicular planes.

Mitral Valve

The mitral valve orifice can be evaluated in basal short-axis sections. The measurement of mitral valve inflow is analogous to the quantification of tricuspid inflow. Prescription of the scan plane is based on the four-chamber view and left ventricular two-chamber view, which display the mitral valve in two mutually perpendicular planes. The acquisition plane must be parallel to the mitral valve plane.

Essential Point
The scan plane for the quantification of mitral and tricuspid inflow must be proximal to the valve (i.e., in the atrium). This eliminates artifacts that would result from valve motion across the acquisition plane.

Aortic Valve

For flow quantification or planimetry of the orifice area (**Fig. 6.9c**), the aortic valve must be imaged parallel to its annular plane. The imaging plane must be prescribed from two mutually perpendicular planes in which the aortic valve is displayed. In the planes acquired in a standard protocol, the aortic valve appears only in the three-chamber view (LVOT, **Fig. 6.9b**). The first step, then, is to prescribe a second plane perpendicular to the three-chamber view and valvular plane, passing through the center of the aortic valve (**Fig. 6.9a**). This gives two mutually perpendicular planes for defining a new plane parallel to the aortic valve plane (**Fig. 6.9a–c**). A high-resolution cine SSFP sequence should be used for planimetry of the orifice area.

Essential Point
Overlapping slices with high spatial and temporal resolution are best for quantification of the aortic valve orifice area. Because the valve moves perpendicular to the scan plane, the optimum scan position cannot always be accurately predicted. Orifice area should be measured in the section that most clearly displays the opened valve.

Phase-contrast imaging for the quantification of aortic volume flow should be performed in the ascending aorta, making certain that the valve leaflets do not extend into the imaging plane.

Pulmonary Valve and Right Ventricular Outflow Tract

Unlike the aortic valve, the pulmonary valve does not appear in the standard sections of the basic protocol. Consequently the right ventricular outflow tract must be displayed separately, analogously to the three-chamber (LVOT) view. This section is prescribed from a coronal slice in which the RVOT is displayed longitudinally and the main trunk of the pulmonary artery is cut transversely. This plane is then angled to obtain a longitudinal section of the right ventricular outflow tract.

Essential Point
The "three-point method" can also be used for prescription of the RVOT. In this method the scan plane is defined by three fixed reference points—one at the center of the tricuspid valve, one at the center of the pulmonary valve, and one at the right ventricular apex.

Analogously to visualization of the aortic valve, a second view of the outflow tract is displayed perpendicular to the prescribed plane. Both of these RVOT planes are then used to prescribe a plane that is exactly parallel to the pulmonary valve. This plane can be used for the quantification of pulmonary flow and planimetry of the valve orifice area.

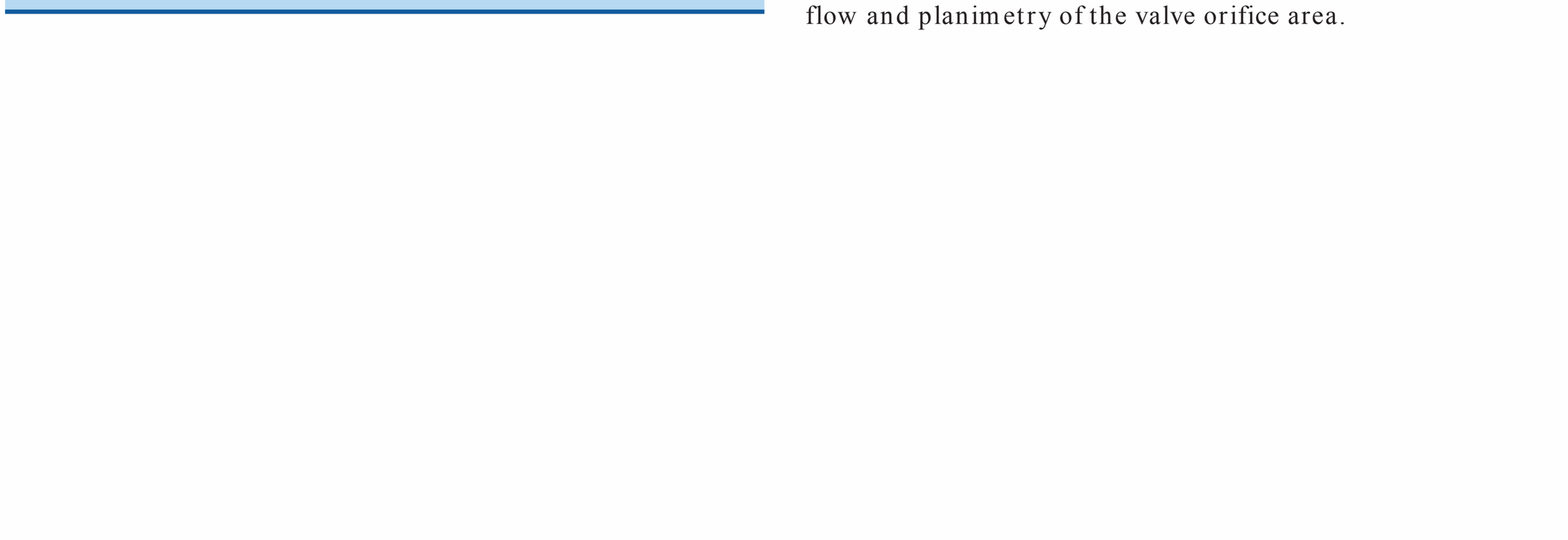

Fig. 6.9 a–c Prescription of the aortic valve view (**c**) from the left ventricular outflow tract displayed in two orthogonal planes (**a, b**). The section is parallel to the aortic valve plane. This slice (**c**) clearly demonstrates the three valve cusps and the valve orifice area.

Morphology

K.-U. Waltering

As a result of the increased availability of scanning equipment as well as technical advances, MRI has become the established standard for morphological imaging of the heart. Cardiac MRI has several important advantages over other imaging modalities:

- Capacity for three-dimensional imaging
- Ability to scan in arbitrary planes
- No need for an acoustic window
- Excellent soft-tissue contrast
- Lack of radiation exposure
- Ability to evaluate paracardiac and thoracic structures in addition to cardiac structures

Typical indications for cardiac MR examinations for a primary morphological investigation are cardiac and paracardiac masses, congenital heart diseases, and variants in cardiovascular anatomy.[11,12]

Pulse Sequences

All pulse sequences for morphological cardiac imaging should be acquired with ECG triggering.[13,14] The sequences traditionally used for this purpose are spin-echo (SE) sequences, which consist of a 90° pulse followed by a 180° radiofrequency refocusing pulse to produce a resonance signal after echo time TE. In ECG-gated SE sequences, one k-space line is acquired per image and R–R interval. Because an image matrix of $n \times 256$ requires n k-space lines and thus an acquisition time of n heartbeats, ECG-triggered spin-echo sequences cannot be acquired with breath holding. Although SE sequences are important in understanding the techniques described below, they are no longer used in routine clinical imaging.[15]

The sequences most commonly used to evaluate cardiac and paracardiac morphology are dark-blood turbo or fast SE sequences, using either segmented or single-shot data acquisition schemes. In segmented sequences, multiple k-space lines are collected per heart beat, but information from multiple cardiac cycles is still used for image reconstruction.[16] In single-shot sequences, the complete information for an image is acquired during a single R–R interval.

Alternative to TSE sequences are extremely fast bright blood SSFP sequences, which can acquire multiple slices or a single slice at different phases of the cardiac cycle (cine MRI) in a single breath hold (see pp. 104–110).[17] Another important technique for morphological investigations is contrast-enhanced 3D MRA, which is described more detailed in a later section, pp. 127–133.[18]

Turbo or Fast Spin-Echo Sequences

Today, ECG-gated turbo or fast spin-echo sequences (TSE) are predominantly used for the visualization of cardiac anatomy. This type of sequence can be used to acquire both T1- and T2-weighted images, with or without fat suppression. In contrast to spin-echo sequences, multiple k-space lines are acquired after one excitation during each heartbeat. The number of lines per heartbeat is called the turbo factor or echo train length. Typically this number is ~7–9 for T1-weighted sequences and ~20 for T2-weighted sequences. As a result, data acquisition is ~10–20 times faster than in SE sequences, making it possible to acquire turbo or fast spin-echo images in a single breath hold.[19]

Essential Point
In patients who have difficulty with prolonged breath holding, the acquisition time can be shortened by using parallel imaging techniques.

T1-weighted sequences employ a short echo time (TE=5–15 ms), and the repetition time (TR) is set to deliver one excitation per heartbeat. Fat has high signal intensity on T1-weighted images, while fluids are displayed with low signal intensity (**Fig. 6.10a**).

T2-weighted sequences employ a long echo time (TE>50 ms), and the selected TR must be long enough (two or three R–R intervals) to allow sufficient signal recovery to occur before the next acquisition. Stationary fluids appear bright on T2-weighted images, and many pathological changes show increased signal intensity due to tissue edema (**Fig. 6.10b**). Dark-blood TSE sequences can be combined with fat suppression to provide optimum contrast in T2-weighted images. In theory, this can be done in either of two ways. The first method exploits the fact that protons in fat and protons in water have slightly different resonance frequencies and therefore can be excited independently of each other (frequency-selective fat suppression). This requires an extremely homogeneous magnetic field, but unfortunately this degree of homogeneity cannot always be achieved. For this reason, routine cardiac MRI usually employs a second method of fat suppression (**Fig. 6.10c**) in which an inversion pulse is applied before the actual excitation, and acquisition begins at the moment when, ideally, the fatty tissue has lost all of its longitudinal magnetization (fat suppression with an inversion pulse).

Essential Point
TSE sequences, unlike SE sequences, allow for single slice acquisition during breath holds. Image contrast is manipulated by varying the repetition and echo times. Fat has high signal intensity in T1-weighted sequences, while fluids (e.g., edema, CSF) appear hyperintense in T2-weighted sequences.

Many pathological processes (tumors, inflammatory changes) show increased **contrast enhancement**. This enhancement can be demonstrated by T1-weighted imaging (**Fig. 6.10d**). Fat-suppressed T1-weighted sequences improve image contrast and are typically used to facilitate the detection of enhancement after contrast administration. Since almost all normal tissues have low signal intensity in these sequences, even small enhancing lesions can be easily detected.[20]

Flowing blood normally has little or no signal intensity in TSE sequences, because moving structures are not subjected to the 90° and 180° pulses necessary to produce a resonance signal. A proton in the blood that is within the excited slice at the

time of the 90° pulse will move out of that slice by the time the 180° pulse is applied. Consequently its spin is not refocused, and it does not emit a signal. But because this effect depends on flow velocity and does not always produce complete suppression of the blood signal, ECG-gated TSE sequences are usually combined with dark-blood preparation so that the cardiac chambers and vessel lumina will appear as signal voids.[16,21]

Essential Point

- A pericardial effusion, which should appear hyperintense (bright) on T2-weighted TSE images, actually appears black owing to fluid motion using dark-blood preparation.
- Very slow-flowing blood in the apex of the left ventricle or in a ventricular aneurysm sometimes appears hyperintense, even when dark-blood preparation is used. These "slow-flow artifacts" should not be mistaken for masses or intramyocardial edema.

Dark-blood preparation consists of a nonselective inversion pulse applied at the time of the R wave, followed immediately by a slice-selective inversion pulse. Starting from an equilibrium state (**Fig. 6.11a**), the first pulse inverts the longitudinal magnetization in the body (**Fig. 6.11b**), and the second pulse returns it to its initial position within the targeted slice (**Fig. 6.11c**). Now when the next excitation is applied, only the protons in the reinverted slice will produce a signal.

Both inversion pulses must be synchronized to the **R wave** so that they are applied before the start of ventricular contraction. Two effects then occur during cardiac contraction:

- First, the blood in the atria and ventricles is exchanged.
- Second, the reinverted parts of the myocardium move out of the image slice (**Fig. 6.11d**)

This is followed by a **delay time** in which the myocardium, by late diastole, reassumes its exact starting position at the time of the R wave. The reinverted parts of the myocardium reenter the image slice and can emit a resonance signal, while the blood in that slice has been completely exchanged and does not produce a signal (**Fig. 6.11e**).

If the acquisition is timed too early, the myocardium will not have enough time to return to its initial position during the R wave, and the myocardium within the image slice will not be reinverted, causing signal voids to appear within the myocardium. If the acquisition is timed too late, the dark-blood preparation will be less effective.[20]

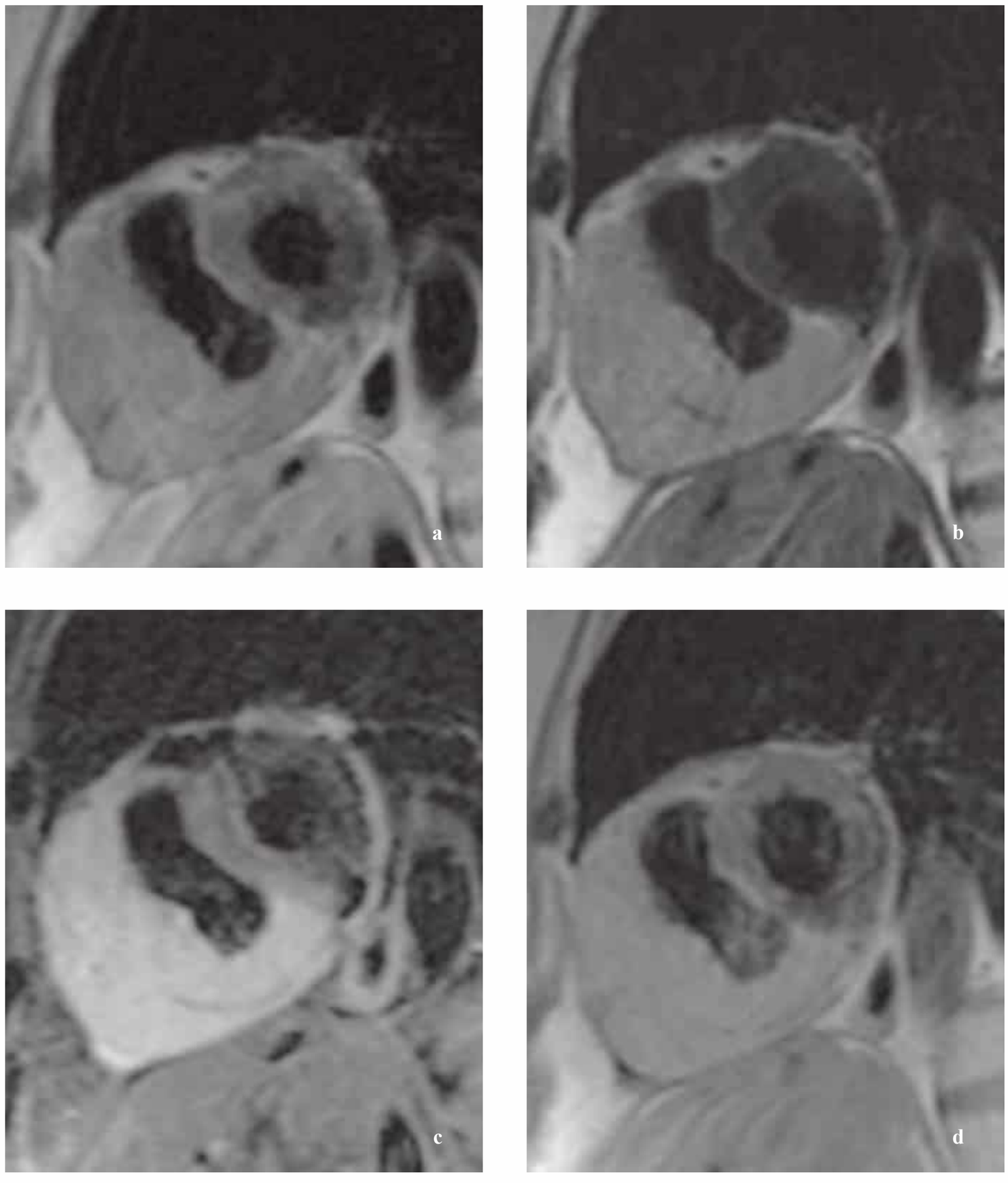

Fig. 6.10 a–d Short-axis views in a patient with intrapericardial lymphoma. T1-weighted (**a**) and T2-weighted (**b**) dark-blood TSE images and a T2-weighted sequence with fat saturation (**c**). All the sequences show a homogeneous, well-circumscribed mass compressing the right ventricle. The T1-weighted image after contrast administration (**d**) shows homogeneous enhancement.

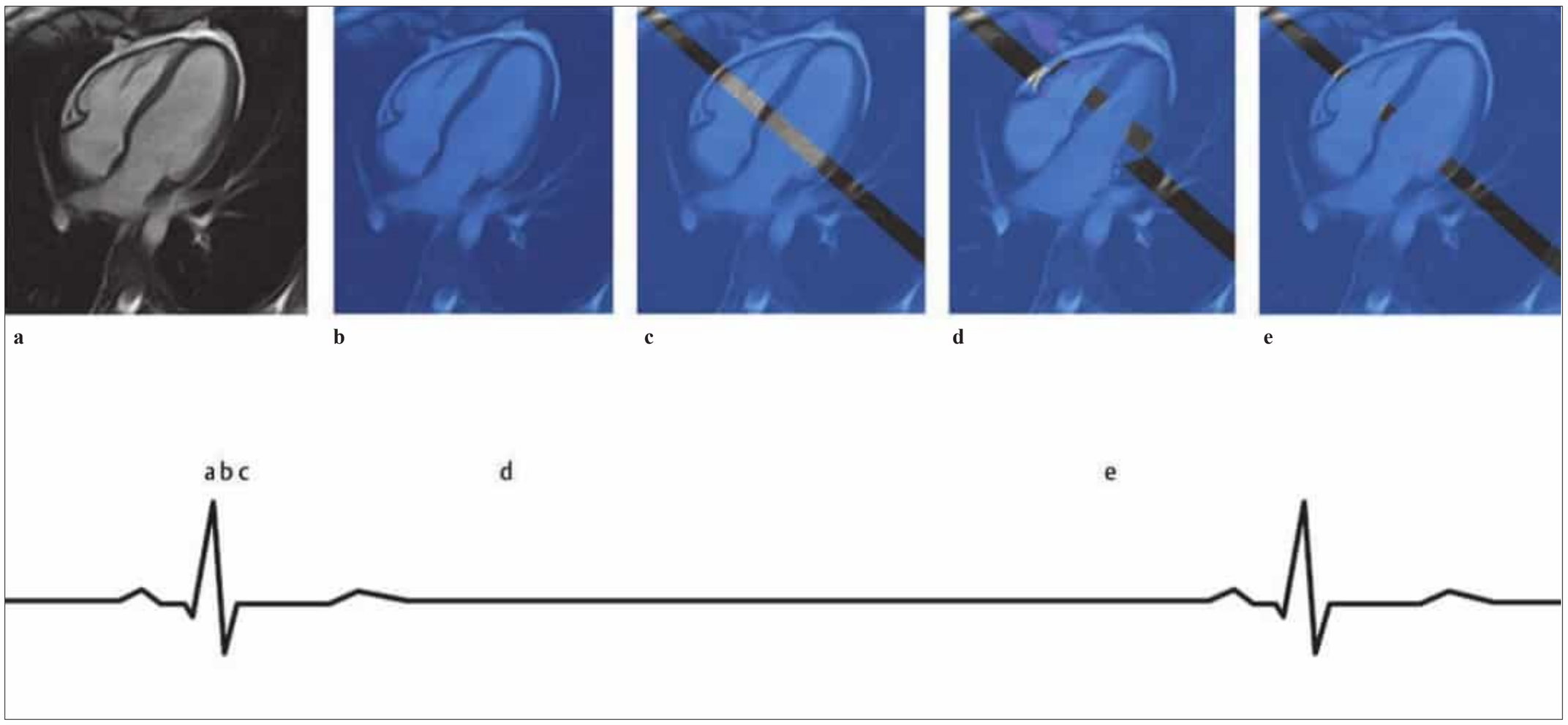

Fig. 6.11 a–e Prescription of a dark-blood TSE sequence in the short-axis plane based on an image in the four-chamber view (**a**). See text for explanations. The blue-shaded areas represent inverted spins. Letters indicate the timing of each image relative to the R–R interval.

Essential Point

The optimum delay time and thus the optimum acquisition time after the R wave are difficult to determine. It is often helpful to analyze cardiac motion in a cine sequence to determine the time taken until the ventricle has returned to its configuration at the time of the R wave. In some cases, however, the only solution is to shift the data acquisition window in 30- to 50-ms increments in late diastole (by trial and error) until good image quality is obtained, but this may be difficult or even impossible in uncooperative or arrhythmic patients.

For assessment of cardiac morphology uncooperative or arrhythmic patients can better be imaged with single-shot TSE sequences. After a single excitation, all the data for one image are acquired within a time window of several hundred milliseconds during one R–R interval. This sequence makes it possible to image the entire thorax in a single breath hold and is extremely resistant to arrhythmias and motion artifacts. The very short acquisition times are achieved at the cost of SNR by filling slightly more than half of k-space and calculating the rest of the data (half-Fourier acquisition).[22]

Essential Point

Single-shot TSE sequences provide a good overview of the heart, mediastinum, and lung in a single breath hold and should be included in every cardiac MRI protocol.

Single-shot TSE sequences also have significant **disadvantages**:

- Limited spatial resolution
- Low signal-to-noise ratio

Moreover, image contrast cannot be manipulated to the degree that it can in segmented TSE sequences. The repetition time is equal to one or two R–R intervals, depending on heart rate. Short echo times (~20 ms) are typically used to obtain an acceptable signal, resulting in proton-density-weighted images only.

Essential Point

These proton-density-weighted images cannot reliably detect or exclude myocardial edema in a setting of acute infarction or myocarditis.

Steady-State Free-Precession Sequences

Steady-state free-precession (SSFP) sequences are characterized by extremely **short repetition and echo times** (TR ~3 ms), allowing for very fast acquisitions. Blood has high signal intensity, and the sequences are very insensitive to flow artifacts. Image contrast is determined by the ratio of T2 to T1 and cannot be significantly altered. As a result, these sequences are not suitable for the tissue characterization of tumors or other lesions.[23]

Single-shot SSFP sequences can image the entire thorax in one breath hold, providing a particularly good view of vascular structures. Cine SSFP sequences, which permit the acquisition of single slices or a stack of slices depending on spatial and temporal resolution, can provide both morphological and functional information (see the section on Function, p. 104).[24]

Normal Anatomy

Axial images that cover the entire thorax are an essential part of every cardiac examination because they yield important information on paracardiac structures, which often are not completely visualized in cardiac imaging.

Essential Point
A cardiac MRI examination involves more than just cardiac imaging. It should also permit other intrathoracic and abdominal structures to be evaluated.

Figure 6.12 shows a series of axial single-shot TSE images from the aortic arch to the diaphragm. It should be possible to assess the position and diameter of the great vessels and the size and location of the heart. Additionally, the mediastinum and lung should be consistently evaluated to ensure that masses are not overlooked. While these images are not comparable to CT in the detection of intrathoracic masses, they are definitely superior to conventional biplane radiographs. Bony structures and thoracic soft tissues should also be evaluated, and the imaged abdominal organs should be checked for possible abnormalities.[25]

Variants and Anomalies

In any deviation from the norm, but especially in complex cardiac anomalies, a systematic image analysis should be conducted so that the anatomical structures can be positively identified.

A systematic image analysis includes the determination of atrial situs, the position of the ventricles, the position of the great vessels, and the evaluation of atrioventricular and ventriculoatrial connections. In an individual with normal situs, the heart is in the left hemithorax; the liver, gallbladder, and inferior vena cava are on the right side; the spleen and stomach are on the left side; and the superior and inferior venae cavae terminate in the right atrium. With complete situs inversus, all the viscera show a mirror-image transposition, and atrial situs is easily determined based on the position of the abdominal organs.[26] Complete situs inversus is present in 0.01 %of the population.

Situs inversus is not always complete. The position of the abdominal organs is of little help in this situation, and other analytic criteria must be used. A precise evaluation of the atrial appendages may be helpful in differentiating between the left and right atrium: The right atrial appendage typically has a triangular shape and is broadly attached to the atrium, whereas the left atrial appendage has a more tubular shape and has a narrow attachment to the atrium.

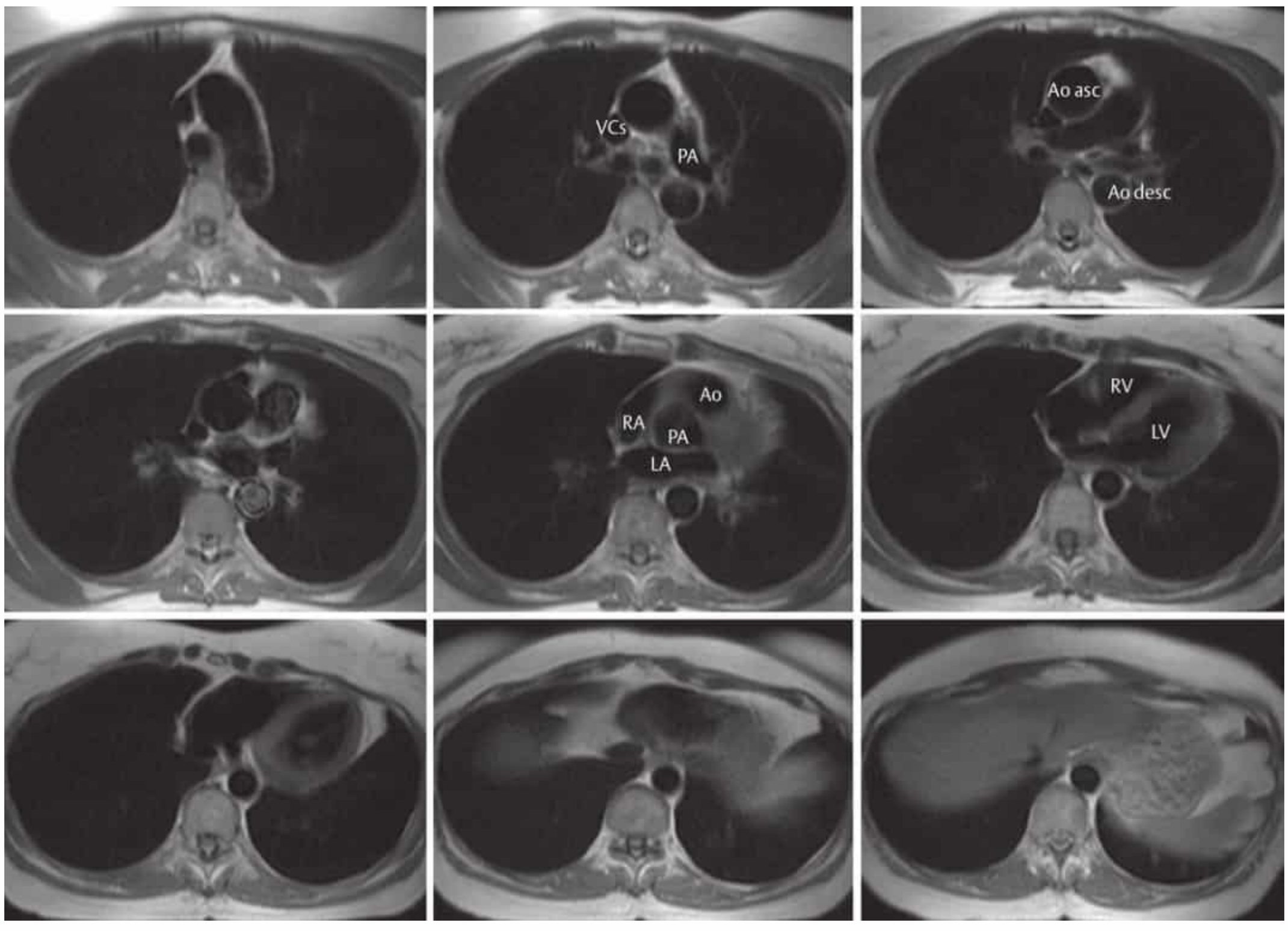

Fig. 6.12 Axial dark-blood TSE sequence to demonstrate the cardiovascular structures.

Atrial situs is most accurately evaluated based on the **position of the bronchi and pulmonary arteries**. With normal situs, the main bronchus on the right side is shorter than on the left and has a more vertical orientation. The right pulmonary artery runs anterior and lateral to the bronchus (eparterial bronchus), and the right lung is divided into three lobes (**Fig. 6.13**). The main bronchus on the left side is longer and more horizontal, the left pulmonary artery is cranial to the bronchus (hyparterial bronchus), and the lung has only two lobes. With situs inversus, a morphologically left bronchus and left lung are present on the right side and a morphologically right bronchus and right lung are present on the left side.

This analysis permits the diagnosis of situs ambiguus (heterotaxy syndrome), which may occur in two variants: right isomerism and left isomerism. In left isomerism, each lung consists of two lobes and the pulmonary artery is cranial to the bronchus on each side. The abdominal changes are variable, but typically there is a centrally placed liver, polysplenia, interruption of the inferior vena cava (hepatic veins open directly into the right atrium), and azygos continuation. Right isomerism is characterized by the presence of morphologically right lungs and bronchi on both sides. Again the abdominal changes are variable, but it is common to find a central liver, asplenia, and a left-sided inferior vena cava.[27]

Essential Point
Attention is given to the lungs and bronchi, not the abdominal organs, in the diagnosis of atrial situs variants.

Based on the definition of atrial situs, a systemic analysis should include evaluation of the ventricles. Normally the left and right ventricles are easily distinguishable from each other by their position and muscle mass. However, this is often not possible in complex anomalies and additional morphological criteria are needed. The right ventricle is more strongly trabeculated than the left ventricle and contains the moderator band, a broad muscular connection linking the midventricular or apical septum to the ventricular apex (**Fig. 6.14**). The morphologically right ventricle also has a muscular ring separating the tricuspid valve from the pulmonary valve. In the morphologically left ventricle, on the other hand, the mitral valve and aortic valve abut directly upon each other with no intervening musculature (**Fig. 6.15**). Additionally, the left ventricle has a smooth septum without any trabecula.

Normally the inflow tract of the morphologically right ventricle is located to the right of the inflow tract of the morphologically left ventricle (D loop). If the positions of the ventricles are reversed (L loop), the inflow tract of the morphologically right ventricle is situated to the left of the inflow tract of the morphologically left ventricle (**Fig. 6.15**).[28]

Essential Point
The more muscular ventricle is not always a left ventricle!

After the ventricles, the position of the great vessels is next evaluated. Normally the aorta is posterior and to the right of the pulmonary artery at the level of the aortic and pulmonary valves (**Fig. 6.12**). In L-transposition, the aorta is anterior and to the left of the pulmonary artery. In D-transposition it is anterior and to the right of the pulmonary artery. In a type I double-outlet right ventricle, the aorta and pulmonary artery are located side by side (**Fig. 6.16**).[29]

Essential Point
Combined anomalies are a frequent occurrence. When situs inversus is combined with L-transposition, the aorta is anterior and to the right of the pulmonary artery. The potential for combined anomalies requires a systematic, step-by-step image analysis.

Finally, attention is given to the intersegmental connections. The atrioventricular connections are concordant when the right atrium is connected to the right ventricle and the left atrium is connected to the left ventricle. They are discordant when the right atrium communicates with the left ventricle and the left atrium communicates with the right ventricle. Similarly, the ventriculoarterial connections may be concordant (LV → Ao, RV → PA) or discordant (LV → PA, RV → Ao).

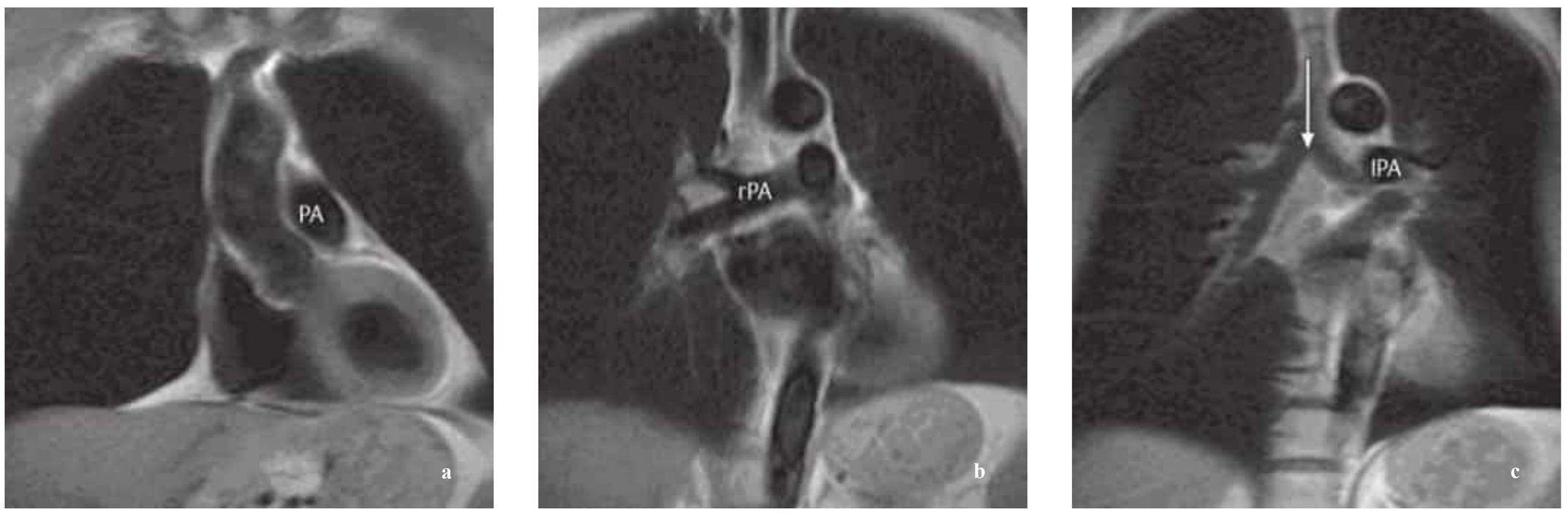

Fig. 6.13 a–c Anterior (**a**), central (**b**), and posterior (**c**) coronal dark-blood TSE images. The right pulmonary artery (rPA) arises from the pulmonary trunk and runs anterior to the right main bronchus. The longer and more horizontal left main bronchus arises from the carina (arrow) below the left pulmonary artery (lPA).

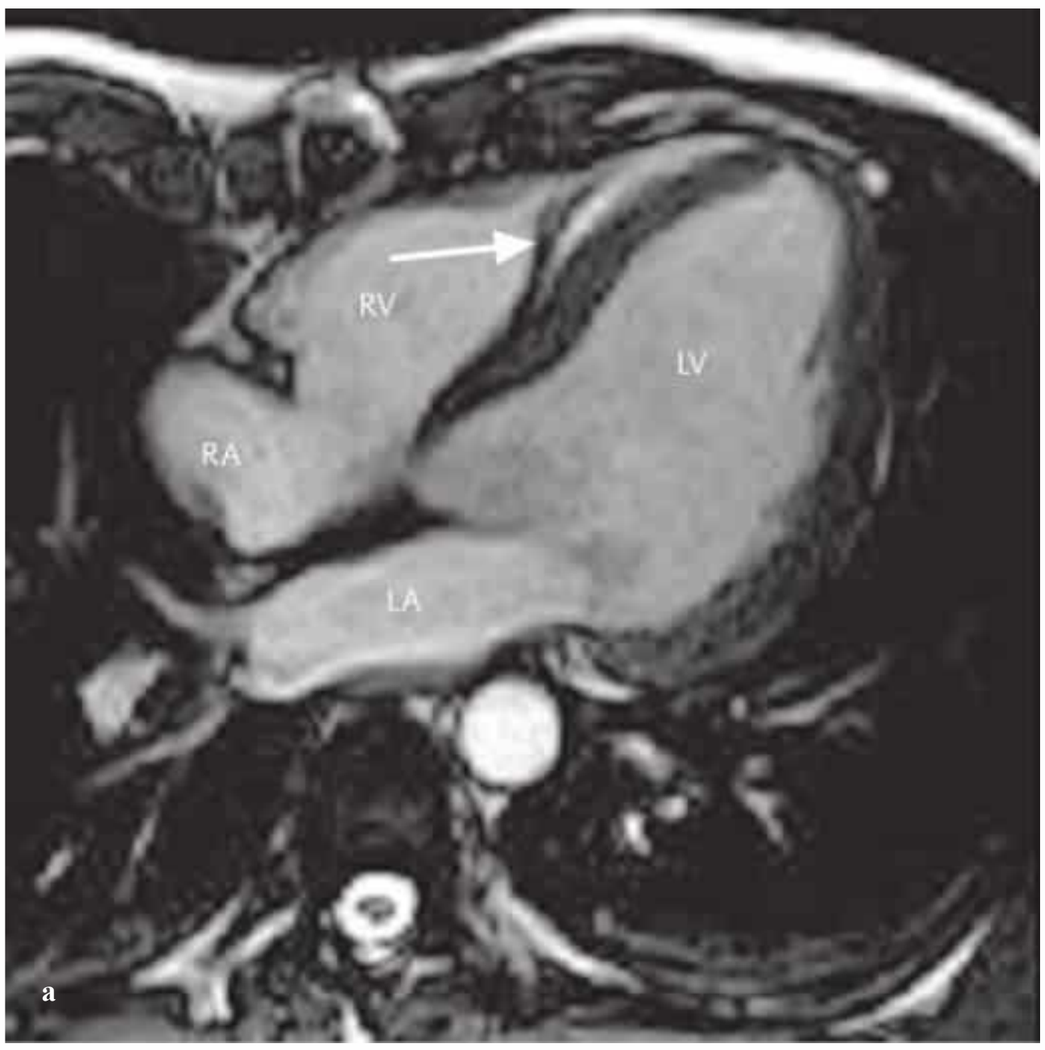

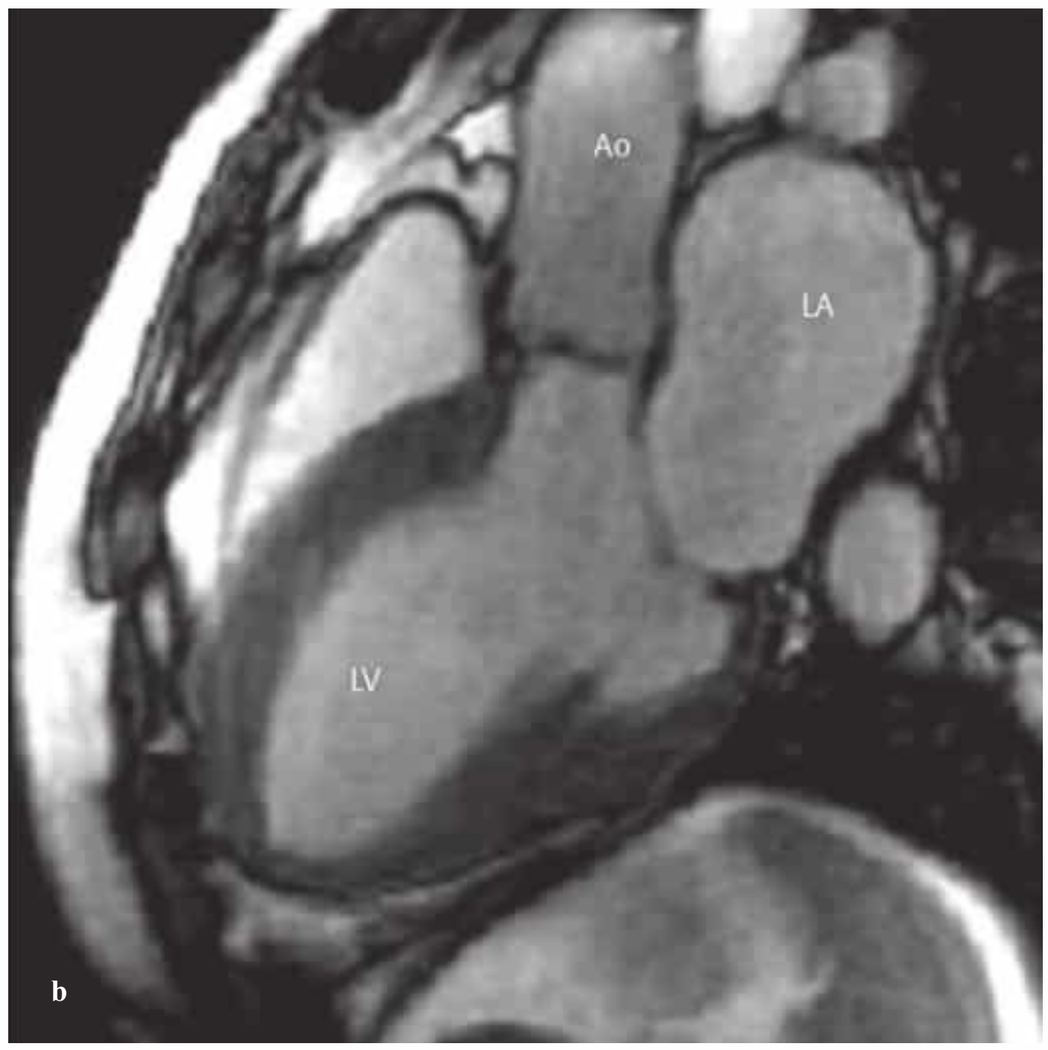

Fig. 6.14a, b Morphologically normal heart (**a**). The smooth-bordered septum is visible in the left ventricle, and the moderator band (arrow) is visible on the right side. The three-chamber view (**b**) shows a direct connection between the mitral valve and aortic valve in the left ventricle.

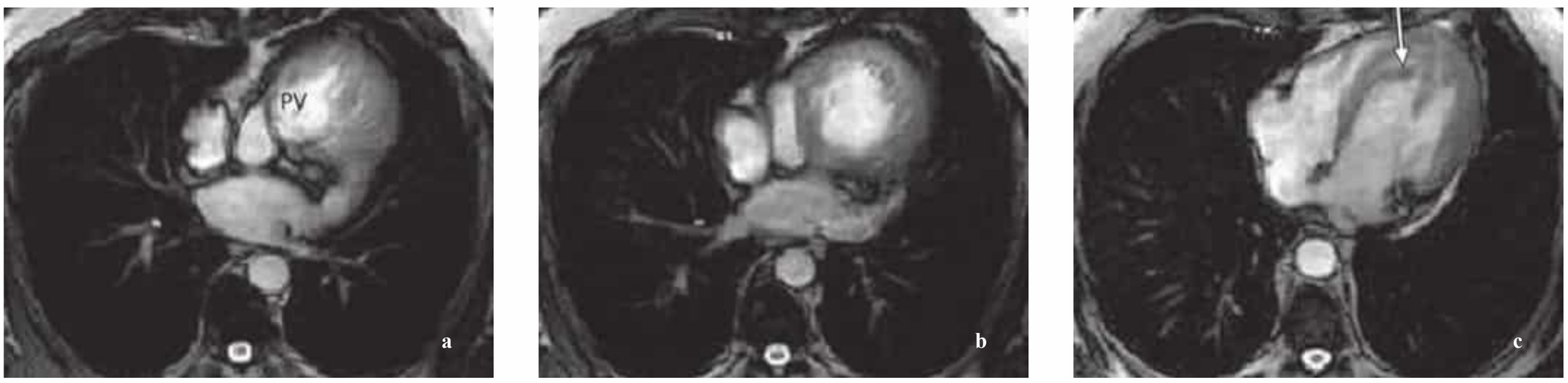

Fig. 6.15a–c images in a patient with L-transposition. Below the valve (**a**) within the outflow tract is a complete muscular ring (**b**) separating the pulmonary valve from the AV valve (**c**). The more muscular, systemic ventricle also shows a moderator band (arrow), positively identifying it as a morphologically right ventricle.

Other variants may occur in which, for example, one ventricle is connected to both vessels (RV → Ao, PA) as in a double-outlet right ventricle, or both ventricles communicate with one vessel (RV, LV → truncus arteriosus).[30]

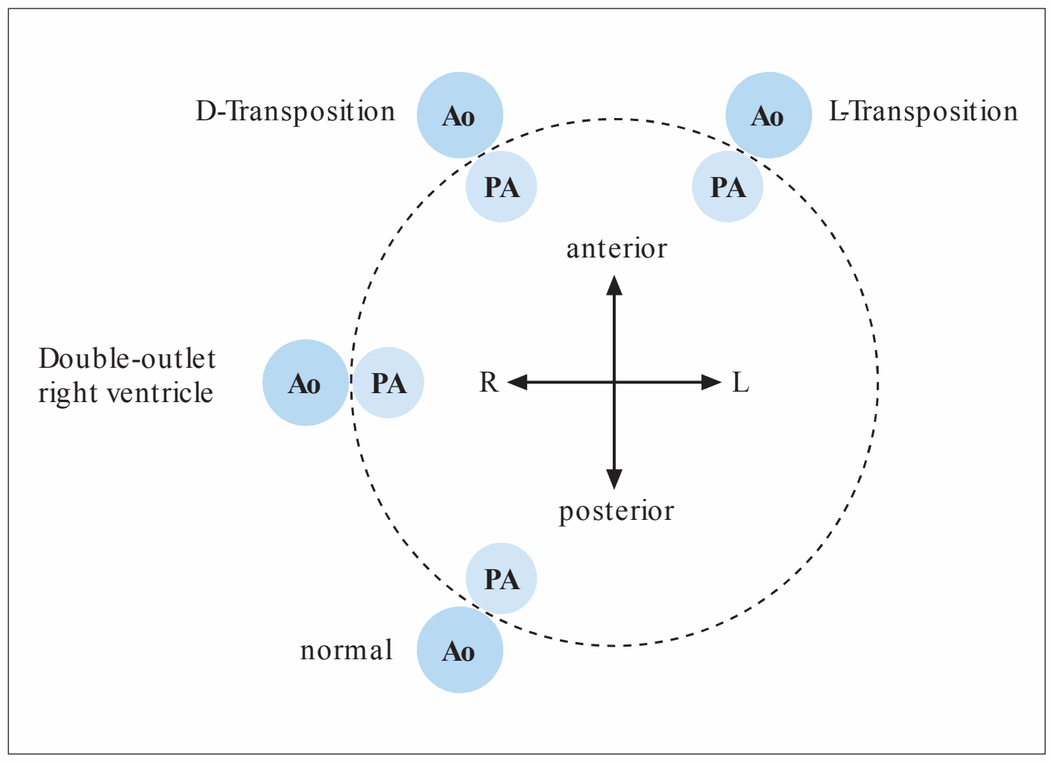

Fig. 6.16 Diagrammatic representation of the position of the vessels at the level of the aortic and pulmonary valves.

Function

S. Ley and K.-F. Kreitner

A variety of cardiological parameters are established in the detection and prognosis of acquired and congenital heart diseases such as CHD, myocardial infarction, and congenital anomalies. These parameters include the following:

- Ventricular volume
- Ejection fraction
- Regional wall-motion abnormalities (quantitative and qualitative)
- Location and size of intracardiac shunt volumes

In recent years, MRI has become the sectional imaging modality of choice for functional evaluation of the heart. Advances in equipment and pulse sequences have led to marked improvements in temporal and spatial resolution, permitting the detailed visualization of anatomy and the accurate measurement of functional parameters. MRI is also an effective follow-up modality owing to its lack of radiation exposure, high quantitative accuracy, and good reproducibility.[31,32]

Analysis of Cardiac Function

Ventricular Volumes

The quantitative analysis of LV function is based on the determination of end-systolic volume (ESV) and end-diastolic volume (EDV). These quantities can be used to calculate the following parameters:

- The stroke volume (SV), where SV=EDV – ESV
- The ejection fraction (EF), where EF=(EDV – ESV)/EDV
- The global functional parameter of cardiac output (CO), where CO=SV × heart rate

The myocardial mass (MM) should also be determined, as it has been recognized as an independent predictor of cardiac mortality.[33] It is calculated by multiplying the myocardial volume by the specific mass of muscle tissue: MM=myocardial volume ×1.05 g/mL. Comparability of findings can be improved by normalizing the results to the body surface area (BSA) of the patient.

The DuBois formula is used to calculate body surface area[34]:

$$BSA\,(m^2) = 0.007184\,(m^2/kg \times cm) \times \text{body height (cm)}^{0.725} \times \text{body weight (kg)}^{0.425}$$

The Simpson method is widely used to determine end-systolic and end-diastolic volumes with MRI. This is based on the acquisition of short-axis slices along the cardiac long axis. The volume of each short-axis slice is determined in end systole and end diastole by multiplying its area and thickness (each slice should be 6–10 mm thick, with an interslice gap not exceeding 20 % of the slice thickness), and the volumes are added together to give the total ventricular volume. Unlike the area–length method and other formulas, the Simpson method is independent of geometrical assumptions and therefore most accurately reflects the anatomy of the ventricles.[35]

This independence is a major advantage in examining the right ventricle, which has a complex geometry, and in examining a left ventricle that has undergone remodeling owing to myocardial infarction or other disease. It has also been shown that excluding the papillary muscles from the left ventricular volume can improve the accuracy of the measurements. For practical reasons, however, the papillary muscles are often included as part of the left ventricular cavity. Based on current literature,[34,35] the Cardiac Imaging Committee of the German Radiology Society has established sequence- and sex-dependent normal values for left ventricular functional parameters (**Table 6.2**). The age of the patient also has a significant effect on these values.

Essential Point

The Simpson method is used to determine end-systolic and end-diastolic volumes in MRI. It divides the heart into a series of contiguous short-axis slices. The quantitative analysis of LV function is based on the determination of end-systolic volume (ESV) and end-diastolic volume (EDV). These values are used to calculate the stroke volume (SV), ejection fraction (EF), and cardiac output (CO). The myocardial mass (MM) should also be determined, as it is an independent predictor of cardiac mortality.

Wall Motion Analysis

Cardiac wall motion can be analyzed qualitatively and quantitatively by imaging the heart in one or more cross-sectional planes over the cardiac cycle. This is done by acquiring successive images of the same slice at different phases of the cycle. The left ventricle is divided into multiple segments along the various cardiac axes. Clinically, this involves the use of a 17-segment model that is an extended version of the 16-segment model used in echocardiography[36] (**Fig. 6.17**). For a qualitative description, the wall motion of each segment is assigned to a

Table 6.2 Normal values for ventricular volumes determined with different pulse sequences

Ichikawa[43]		**LVEDV (mL)**	**LVESV (mL)**	**LVEF (%)**
Short axis	SSFP	150.7 ±31.9	59.5 ±20.4	60.8 ±9.6
	SPGR	130.7 ±24.9	50.2 ±16.5	61.7 ±9.9
Long axis	SSFP	142.2 ±36.4	55.6 ±20.3	61.8 ±8.3
	SPGR	125.4 ±32.4	49.8 ±20.0	61.4 ±8.3
Angiography		153.2 ±34.6	58.1 ±19.6	62.6 ±7.7
Lund[44]		LVEDV (mL)	LVESV (mL)	LVEF (%)
Short axis	SSFP	131 ±20	52 ±14	79 ±10
Grothues[47]		RVEDV (mL)	RVESV (mL)	RVEF (%)
	FLASH	153 ±34	58 ±20	63 ±7

LVEDV = left ventricular end-diastolic volume; LVESV = left ventricular end-systolic volume; LVEF = left ventricular ejection fraction; RVEDV = right ventricular end-diastolic volume; RVESV = right ventricular end-systolic volume; RVEF = right ventricular ejection fraction; SSFP = steady-state free precession; SPGR = fast spoiled-gradient-echo acquisition.

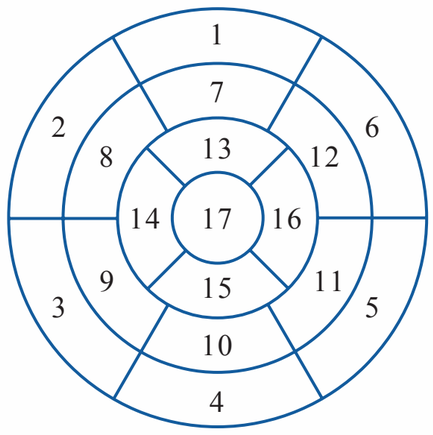

Fig. 6.17 The 17-segment model is an extension of the 16-segment model used in echocardiography.[70]

1	Basal anterior	10	Midinferior
2	Basal anteroseptal	11	Midinferolateral
3	Basal inferoseptal	12	Midanterolateral
4	Basal inferior	13	Apical anterior
5	Basal inferolateral	14	Apical septal
6	Basal anterolateral	15	Apical inferior
7	Midanterior	16	Apical lateral
8	Midanteroseptal	17	Apex
9	Midinferoseptal		

specific category (normokinetic, hypokinetic, akinetic, dyskinetic).

Technical Requirements

The use of surface coils significantly improves signal amplitudes and resolution in cardiac MRI. Multielement surface coils are best for this purpose, as they permit the use of parallel imaging techniques.[37–39]

ECG triggering is necessary to reduce motion artifacts and acquire images in different cardiac phases. This ECG synchronization may be prospective or retrospective. In prospective triggering, data acquisition is initiated by detection of the Q-wave of the QRS complex. The last 10% of the R–R interval are excluded from the data acquisition window to avoid artifacts due to the variable physiological length of the R–R interval. In retrospective gating, the untriggered MR data and ECG signals are acquired continuously throughout the R–R interval. The phase-encoding gradient is incremented each time an R wave is detected. Prior to Fourier transformation, the k-space lines are assigned to the correct phases in the cardiac cycle. This technique covers the entire R–R interval, which also permits a detailed analysis of diastolic function.

If an adequate trigger signal is not recorded with the chest wall lead, another option is to perform peripheral pulse oximetry using a photoplethysmograph connected to a finger. The delay between the R wave and maximum peripheral pulse wave ranges from 150 to 500 ms, depending on the heart rate. Images acquired immediately after the peak in the peripheral pulse wave are assigned to diastole. Systole is located at the end of the trigger period. Systolic images can be acquired only when retrospective gating is used; otherwise that phase is cut off.

Essential Point

Multielement surface coils are best for cardiac MRI. They also allow the use of parallel imaging techniques like SENSE and GRAPPA. A good ECG trigger signal is essential for reducing motion artifacts and for dynamic cine imaging. Recording signals with a finger photoplethysmograph leads to a 150–500 ms delay between the R wave and trigger signal, depending on the patient's heart rate.

Pulse Sequences

The basic sequences for myocardial motion analysis are gradient-echo (GE) sequences with segmented data acquisition. The myocardium has low signal intensity in GE sequences while blood flowing into the slice has high signal intensity. The implementation of k-space segmentation was the basic requirement for cine image acquisition using breath-hold technique.

"Flow compensation" is a technique that can reduce the phase loss of blood entering the slice. It gives the blood a more homogeneous signal intensity, making it easier to discriminate between myocardium and blood. This is true only with laminar flow, however. Turbulent flow cannot be compensated and leads to signal voids. These voids are advantageous, as they provide markers for the detection of valvular stenosis or regurgitation as well as ventricular and atrial septal defects (see **Fig. 6.22**).

A major disadvantage is that the TR must be relatively long (~8 ms) to allow unsaturated blood to enter the imaging plane. Moreover, the contrast between blood and myocardium is diminished if blood flow is reduced owing to global impairment of cardiac function or local wall-motion abnormalities. This can make it difficult to quantify wall-motion abnormalities, as it is difficult to identify the exact boundary between the myocardium and cardiac cavity.

These problems were eliminated by the introduction of SSFP (steady-state free precession) sequences. The hallmark of these sequences is that the residual magnetization still present from the previous excitation is refocused and superimposed over the magnetization excited in the next phase-encoding step. If all the gradients are balanced (nulled) at the time the RF pulse is applied and the repetition time is equal to twice the echo time, the echoes will overlap in time. Contrast in SSFP sequences is determined by the ratio of T2 to T1 at flip angles >45° and therefore does not depend on unsaturated spins flowing into the slice. The echo time and repetition time in SSFP sequences can be greatly shortened compared with FLASH gradient-echo sequences, depending on the gradient system. This reduces the acquisition time and results in higher contrast-to-noise and signal-to-noise ratios.[40] This also permits the more accurate quantification of wall-motion abnormalities compared with FLASH gradient-echo sequences[41] (**Fig. 6.18**).

ECG-triggered sequences do not provide acceptable image quality in patients with arrhythmias. One solution in these cases is real-time imaging. Real-time images can be acquired without ECG triggering and can be produced at a frame rate of 20 or more per second with the latest techniques. Real-time MRI can accurately detect wall-motion abnormalities owing to its high temporal resolution and the high contrast between

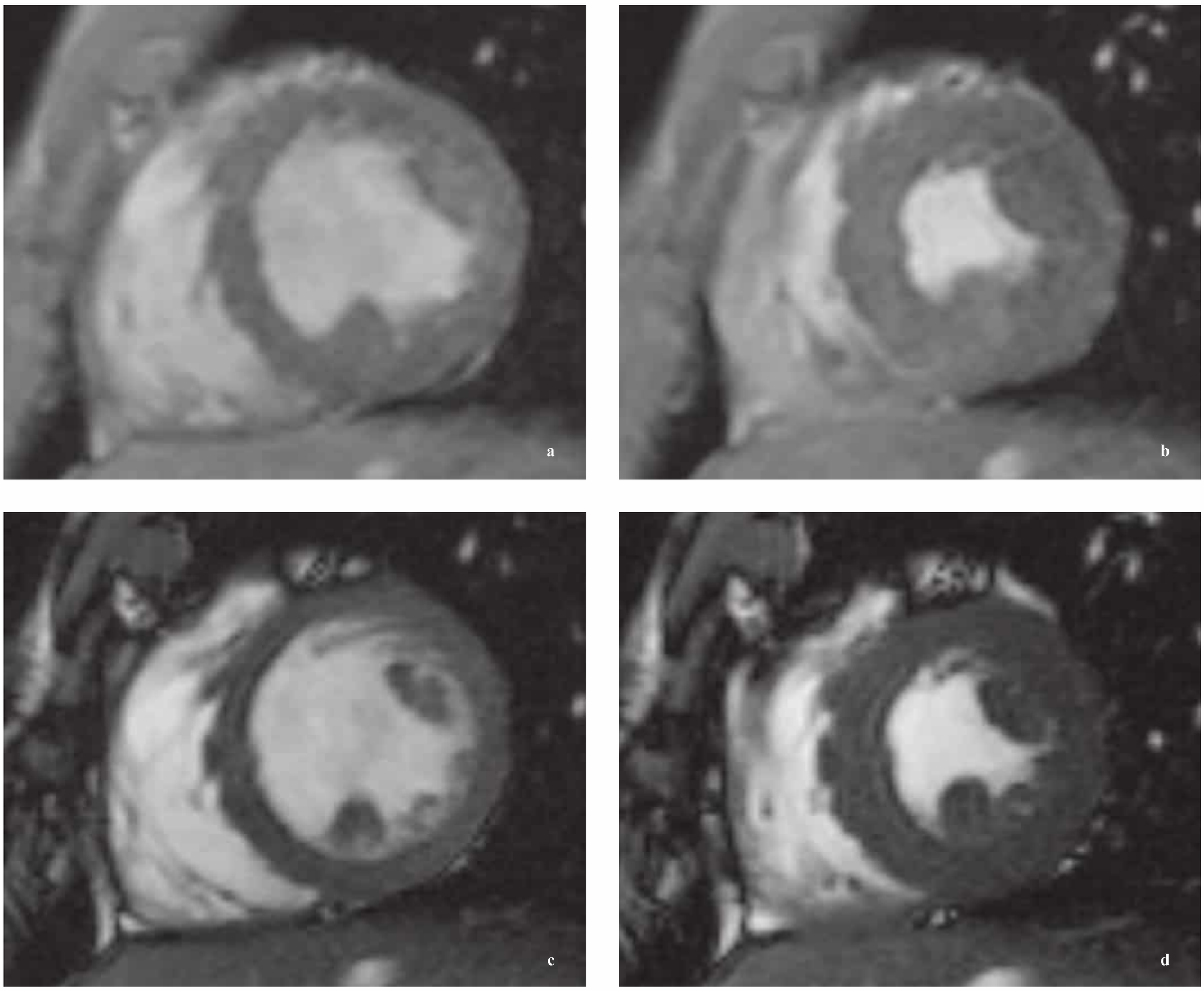

Fig. 6.18 a–d Short-axis images of the heart in diastole (**a, c**) and in systole (**b, d**) acquired with a FLASH 2D cine sequence (upper row) and a SSFP cine sequence (lower row). Besides better delineation of the myocardium and papillary muscles, the SSFP sequence also provides better temporal resolution.

blood and myocardium, even in areas with abnormal wall motion.

Essential Point

SSFP is a fast gradient-echo sequence in which the residual magnetization left from the previous excitation is refocused and superimposed over the magnetization excited in the next phase-encoding step. The acquisition time is significantly shorter than in traditional GE sequences. The contrast-to-noise and signal-to-noise ratios are higher, and wall-motion abnormalities can be quantified with greater accuracy.

Accuracy and Reproducibility

The FLASH sequences described above were used in the first validation studies comparing MRI and echocardiography. As SSFP sequences evolved, it was found that they were just as accurate in evaluating the functional parameters of the heart (interstudy variability between FLASH and true-FISP stroke volume was 0.6 mL, and variability in end-diastolic left ventricular volume was 1.2 mL in healthy subjects) (**Fig. 6.18**).[41] Turbulent flow like that associated with valvular disease and atrial or ventricular septal defects can also be visualized (see **Fig. 6.22**) owing to local turbulence-induced inhomogeneities of the magnetic field.[42]

The parameters determined with the SSFP sequence have shown better agreement with the results of left ventricular angiography than values measured with the FLASH gradient-echo sequence[43,44] (**Table 6.2**). A slice thickness <10 mm, an interslice gap <3 mm, a temporal resolution <50 ms, and a maximum pixel size <1.5 mm × 3.0 mm^2 have been identified as minimum requirements for the assessment of cardiac function.[35] **Table 6.3** shows the differences in left ventricular functional parameters between GE and SSFP sequences and also between males and females.[45] Interobserver variability and interstudy variability for the end-diastolic LV volume range from <1 %to 5.2 %[32,46]

Large standard deviations with a 6–16 % range of variation have been found (by 2D FLASH) in determinations of the right ventricular ejection fraction[47,48] (**Table 6.2**). In one study on

right ventricular volumetry using GE and SSFP sequences, the SSFP sequence showed definite advantages in terms of interobserver and intraobserver variability.[49] Interobserver variability for the GE sequence showed a standard deviation of 14.4 %(SV) versus 9.1 % for the SSFP sequence. The standard deviation of intraobserver variability for SV was 12 % for the GE sequence and 5.4 %for the SSFP sequence.

Essential Point
SSFP imaging permits the accurate, reproducible quantification of left ventricular volumes and ejection fraction. Determination of the right ventricular ejection fraction is subject to a relatively high standard deviation owing to the anatomical configuration of that chamber. Real-time SSFP techniques lead to significant underestimation of the EDV and SV.

Stress Imaging

Functional deficits may occur during stress that are not detectable at rest. MRI pharmacological stress testing with dobutamine (high-dose protocol) is most commonly used in the detection of ischemia-induced abnormalities of wall motion. It is more reproducible than stress echocardiography and is not examiner-dependent.[50,51]

During the MRI examination, dobutamine is administered in incremental doses that are increased every 3 minutes (5, 10, 20, 30, and 40 µg/kg BW/min). At each dose level, a cine acquisition is obtained in all standard cardiac axes (**Fig. 6.19**). The injection is terminated when the heart rate reaches 85 %of the age-predicted maximum (= 220 – age × 0.85) or when wall-motion abnormalities appear. If maximal heart rate is not reached, the stress is augmented by the fractionated infusion of 0.25 mg atropine every 2 minutes to a maximum dose of 2 mg.[51]

Most side-effects that occur during high-dose dobutamine stress imaging are mild (anxiety, palpitations, heat sensation, tachypnea). Isolated ventricular extrasystoles are common but are not indicative of CHD and should not prompt termination of the test. Paradoxical hypotensive reactions are not uncommon in response to dobutamine stress (incidence of ~10–20 %). Atrial fibrillation occurs in ~1 %of patients under dobutamine stress. This is a nonspecific response that is spontaneously reversible in most cases by stopping the dobutamine infusion. The main contraindications to dobutamine stress imaging, besides the known contraindications to MRI, are obstruction of the left ventricular outflow tract and significant preexisting ventricular arrhythmia.[52] (Low-dose dobutamine stress testing is described under Chronic Coronary Heart Disease in Chapter 8, p. 187)

A sensitivity of 83–87 %and specificity of 83–86 %have been reported for pharmacological stress MRI in the detection of CHD.[51,52]

A basic disadvantage of exercise stress testing (e.g., on a bicycle ergometer) is its dependence on the motivation, cooperation, conditioning, and general health of the patient, which determine whether the patient can attain the level of exercise that is essential for a sensitive test. Because exercise-induced ischemia and resulting wall-motion abnormalities are very quickly reversible in some patients, the time window for data acquisition is limited to approximately 1 minute after the end of exercise, which greatly limits the practicability of this method for MRI. As a result, physical exercise is of minor importance in the current practice of stress MRI.

Essential Point
Pharmacological stress testing with fast-acting agents that have a short half-life (e.g., dobutamine) is the method of choice for evaluating ischemia-induced wall-motion abnormalities by MRI. This technique has proved to be practical, sensitive, and specific.

Myocardial Tagging

Myocardial tagging is an objective method for the quantitative analysis of myocardial contractility based on the visualization of local tissue deformation.[53]

SPAMM (spatial modulation of magnetization) is the most commonly used tagging technique. A series of closely spaced RF prepulses are applied to the myocardium at different angles. The interference effect of the pulses produces thin saturation bands directed perpendicular to the imaging plane. The arrangement of the saturation lines creates a grid pattern within the image plane (**Fig. 6.20**), and a cine sequence is obtained to show the passive deformation of the grid lines as the myocardium contracts.[54,55] When standard parameters are used (grid lines spaced 7 mm apart), myocardial movements as small as 0.1 mm can be reliably detected.[56] Physiological and pathophysiological tagging studies have shown that the left ventricle undergoes a twisting motion in addition to contraction and

Table 6.3 Absolute normal values for left ventricular functional parameters established for MRI by the Cardiac Imaging Committee of the German Radiology Society.[61] Different normal values are used depending on patient sex and type of sequence. The normal values can also be normalized to body surface area

	SSFP sequence		Gradient-echo sequence	
Parameters	**Males**	**Females**	**Males**	**Females**
EDV (mL)	102–235	96–174	65–171	55–139
ESV (mL)	29–93	27–71	15–66	10–48
EF (%)	55–73	54–74	56–77	61–80
MM (g)	85–181	66–114	119–190	79–141

Table 6.4 Rotation and contraction of the heart in different wall segments determined by myocardial tagging. A negative value indicates clockwise rotation; a positive value indicates counterclockwise rotation (from Kivelitz et al., 2003[71])

	Rotation (°)	Contraction (mm)	Circumferential shortening (%)		
			Subendocardial	Subepicardial	Transmural
Base	–4,2 ± 1.8	4.8 ± 1.1	27.7 ± 8.0	11.6 ± 5.0	19.7 ± 4.7
Midwall	3.4 ± 2.3	4.9 ± 0.5	31.2 ± 7.7	12.8 ± 3.0	22.0 ± 3.4
Apex	10.3 ± 2.3	4.2 ± 0.5	33.2 ± 8.2	15.7 ± 4.5	24.4 ± 3.0

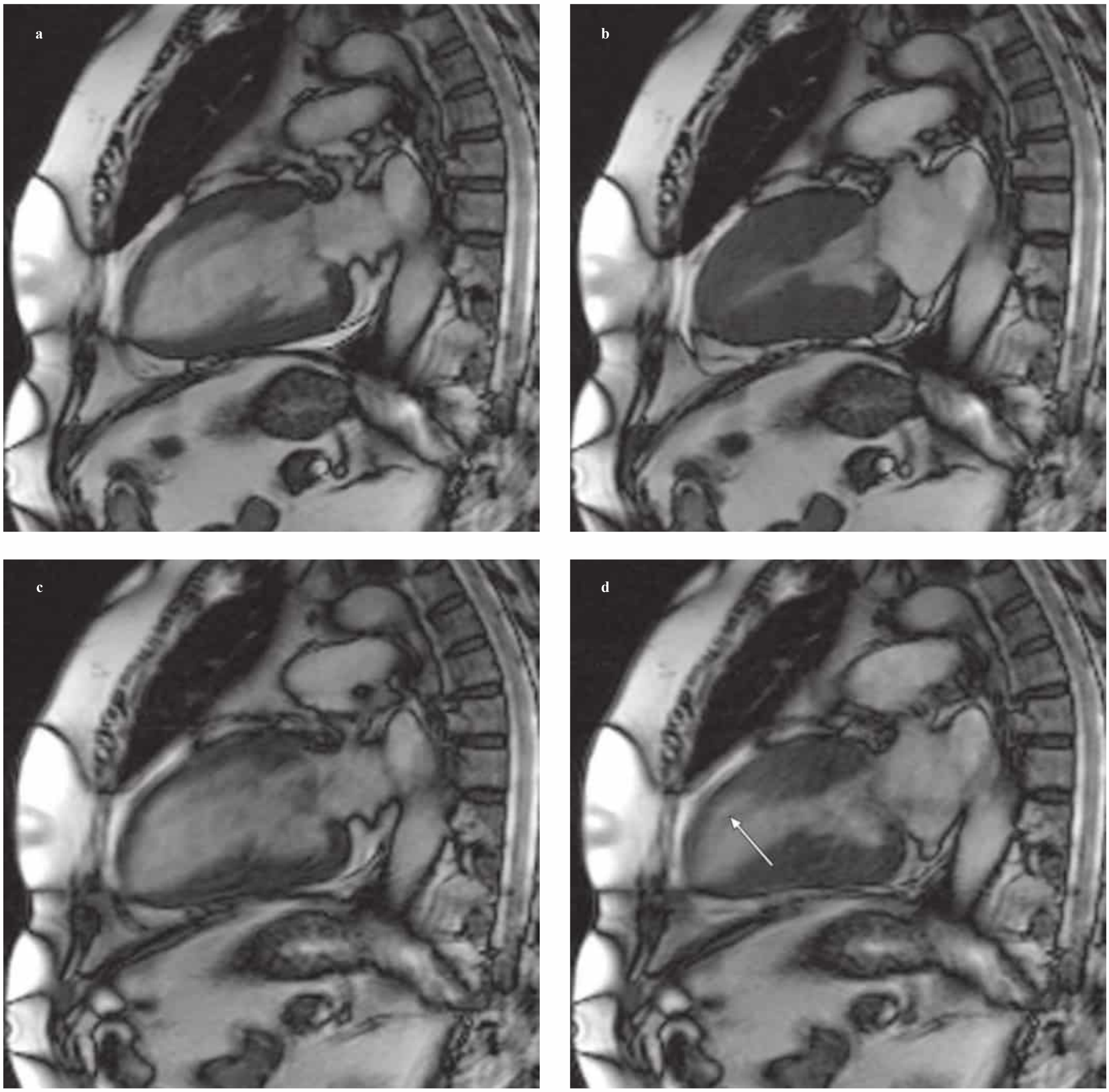

Fig. 6.19 a–d Cine images (vertical long axis) from a stress MRI examination. The images in the left column (**a, c**) were acquired in diastole, the images in the right column (**b, d**) in systole. The upper images, acquired at rest, demonstrate normal wall motion with no evidence of circumscribed abnormalities. The lower images, acquired in the same planes during pharmacological stress (dobutamine), show a definite stress-induced motion abnormality (hypokinesia) in the apical anterior wall (arrow).

rotation (**Table 6.4**).[57–59] Quantitative information requires sophisticated postprocessing of the image data, however, and this continues to be a limiting factor in the clinical application of myocardial tagging.[57]

Essential Point

The myocardium is tagged with saturation lines, and local tissue deformation is measured as an expression of myocardial contractility. This technique has not yet come into routine clinical use because of sophisticated postprocessing requirements.

Flow Measurement

Basic Principles

Flow measurement techniques have been used routinely since the 1980s for the quantification of blood flow in MRI. Unlike stationary spins, moving spins induce a phase shift in the transverse magnetization within a magnetic field gradient. This phase shift, designated ϕ (phi), is roughly proportional to the velocity of the spins, assuming the spins are moving at a constant velocity. The phase shifts are measured in degrees and must lie within a range of ±180°. This means that the user must preset the correct velocity range. The encoding velocity (V_{enc}) is

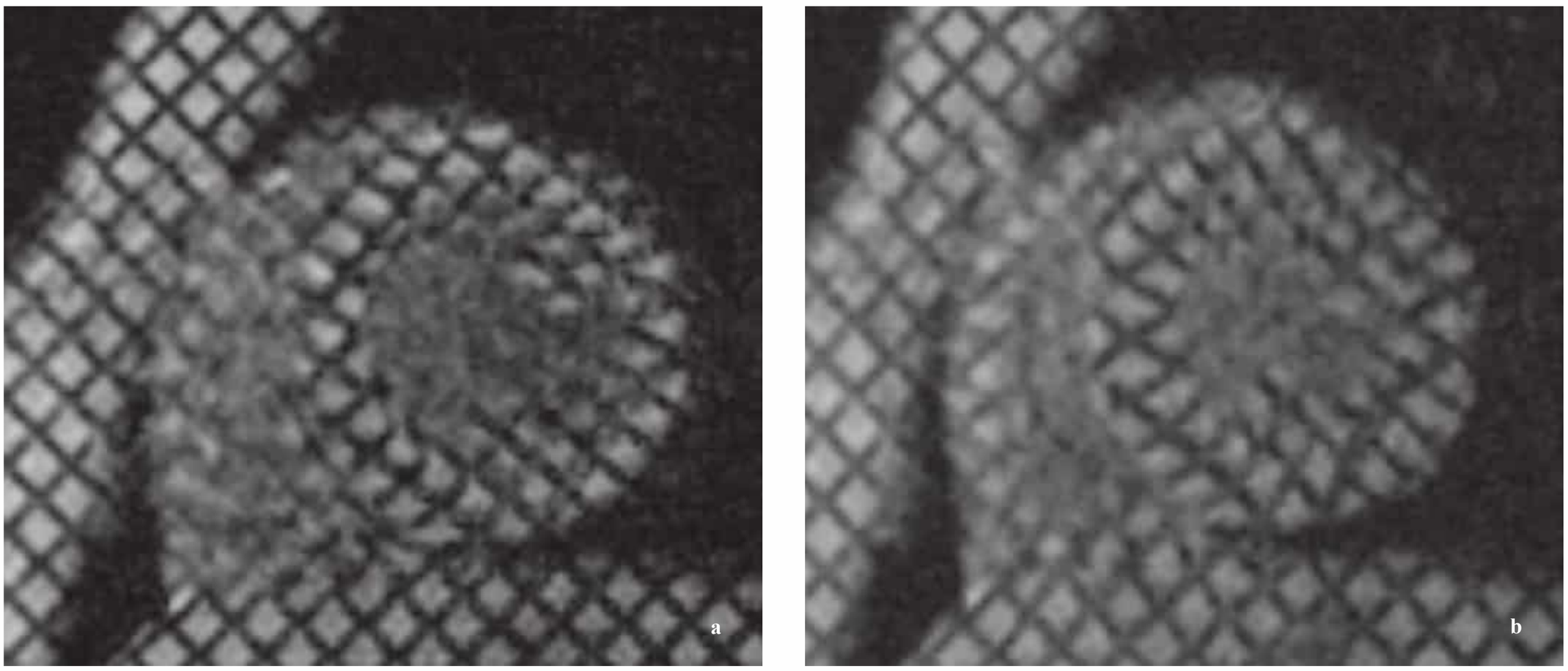

Fig. 6.20 a, b Myocardial tagging in a healthy subject (based on a FLASH 2D cine sequence). The tagged images show symmetrical, uniform distortion of the grid lines (**a** diastole, **b** systole).

entered in cm/s on most systems. Phase-contrast imaging with a 2D GE sequence is most commonly used for flow measurement in MRI. In this method, two datasets are acquired for each voxel. The first dataset contains information on signal intensity (magnitude image) and the second contains phase information (velocity image).

The better the encoding velocity matches the true velocity, the more accurate the resulting velocity information will be. Noise in the phase-contrast image increases with greater values of V_{enc}. This may cause random noise voxels to appear in the vessel lumen, leading to overestimation of velocity. Blood flow, on the other hand, is relatively insensitive to noise voxels because flow represents the sum of all intravascular voxels, and individual voxels have less impact on this averaged quantity. If the encoding velocity is set too low, aliasing will occur. This is a phase inversion in which the aliased voxels display a color opposite to that of the other voxels. Computer algorithms can correct for these errors, provided the true velocity is no more than twice the encoding velocity. In principle, however, it is better to repeat the measurement with a higher V_{enc} setting.[60]

Ideally, the slice position for phase-contrast flow measurement should be orthogonal to the vessel of interest, and this requires a double-oblique slice orientation. The true velocity is reduced by a factor of the cosine of the deviation from a true orthogonal slice (cosα) (measured velocity = true velocity × cosα). Deviations up to 15° are acceptable, as they do not cause a significant deviation from the true velocity or flow. A slice thickness of 6 mm is considered an optimum tradeoff between partial-volume effects and signal-to-noise ratio.[61] The guidelines of the German Radiology Society require a minimum temporal resolution of 50 ms and at least four pixels per vessel cross-section.[35]

Flow measurements in large vessels such as the aorta and pulmonary trunk show very good interobserver reproducibility (difference of 3–6 %)[33,62] (**Table 6.5**).

In healthy subjects, the volume flow determined in the ascending aorta is equal to the volume flow in the pulmonary artery (~70 mL/heart beat; r=0.92). A slight discrepancy between the two measurements results from coronary arterial flow, which comprises ~5 % of the cardiac output. It has also been found that the stroke volume of the right and left ventricles is predicted significantly better by flow measurements than by cine volumetry based on intra- and interobserver variability.[63]

Essential Point

In phase-contrast flow measurements, two image datasets are acquired for each voxel—one with signal intensity information and one with phase information. This permits the absolute quantification of blood flow. Phase-contrast data slightly underestimate the true velocity but show very good agreement with echocardiography.

Table 6.5 Anticipated peak velocities in different vascular systems

Vessel	Peak velocity (cm/s)	Pathologies	Peak velocity (cm/s)
Ascending aorta	100–250	Aortic stenosis	250–800
Descending aorta	100	Valvular insufficiency	200–400
Common carotid artery	80–150	Carotid artery, prestenotic	5–50
Middle cerebral artery	60–140	Intrastenotic	100–500
Basilar artery	40–50	Veins	
Femoral artery	60–80	Portal vein	5–10
Popliteal artery	35–50	Vena cava	5–40

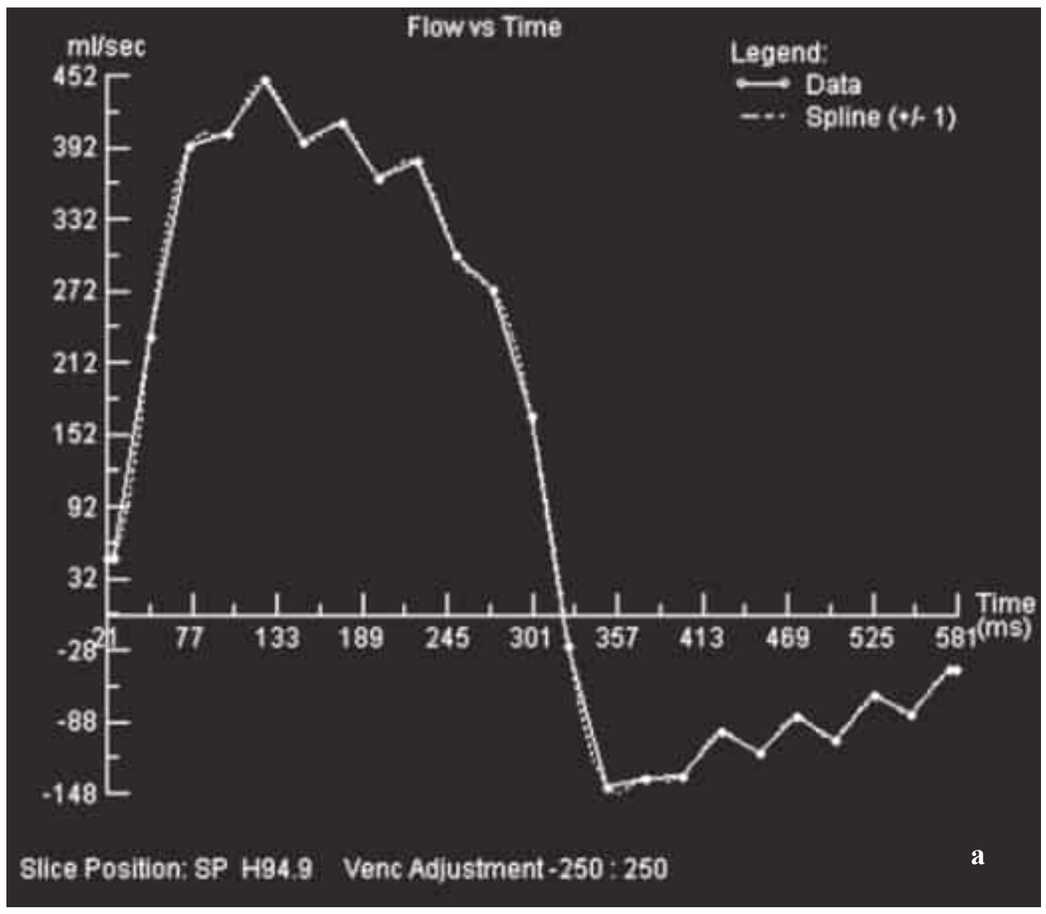

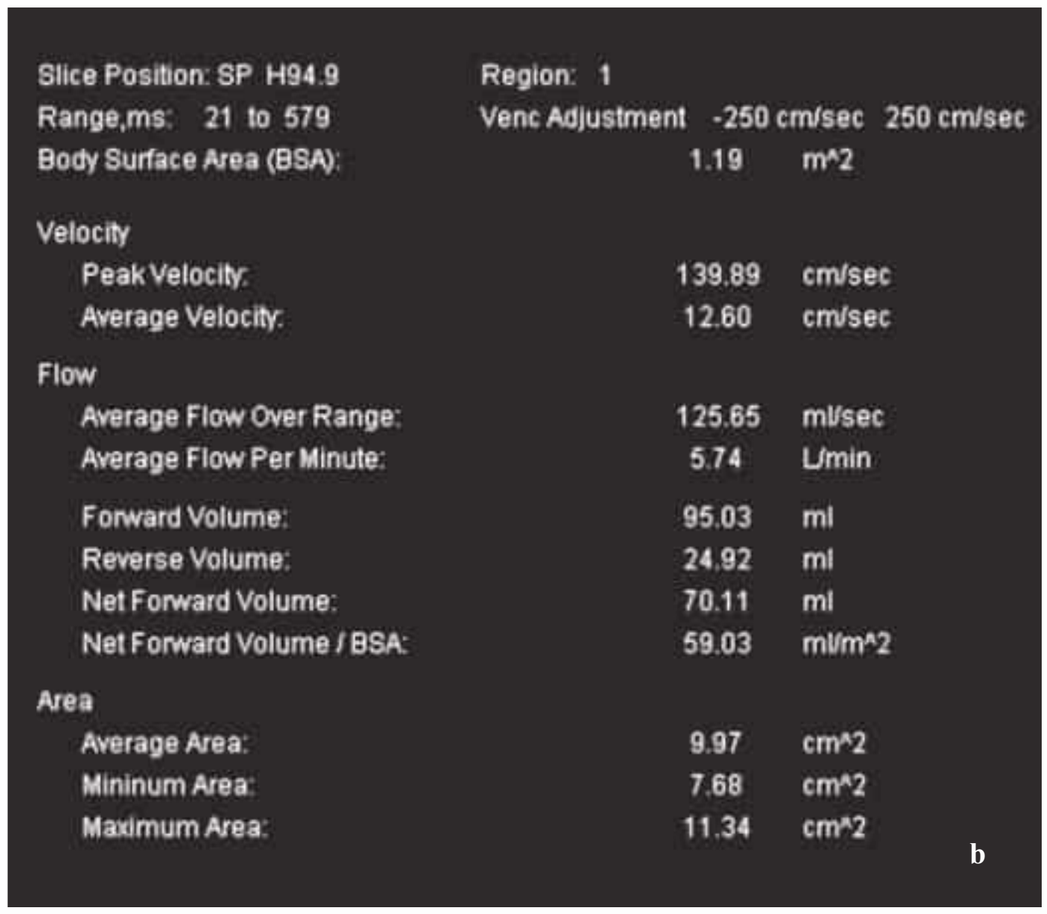

Fig. 6.21 a, b Analysis of a phase-contrast flow measurement performed in the ascending aorta.

a Graphic representation of blood flow over time. The map indicates negative flow during diastole, i.e., the portion of the curve below the horizontal axis represents the regurgitant volume.

b Overall analysis of the flow measurement includes a direct readout of antegrade flow and regurgitant volume data.

Clinical Applications

Intracardiac Shunts

In patients with atrial or ventricular septal defects, blood is exchanged among the cardiac chambers.[64] The hemodynamic significance of an intracardiac left-to-right shunt can be assessed by determining the ratio of blood flow in the pulmonary trunk (Q_p) to that in the ascending aorta (Q_s). A Q_p/Q_s ratio >1.5 indicates the presence of a significant shunt, while a ratio <1.3 means that the shunt is not significant. When $Q_p/Q_s=1$, a shunt is not present. In routine cardiology, the intracardiac shunt volume is determined with invasive techniques such as oximetry[65] and the indicator dilution method. Studies comparing oximetry with MRI flow measurements have shown that MRI has comparatively good accuracy in determining the Q_p/Q_s ratio ($r=0.87–0.91$).[65–68] In daily practice, invasive techniques should be reserved for cases in which MRI is contraindicated.

Valvular Insufficiency

Aortic or pulmonary valve insufficiency can be directly quantified by determining the relationship between antegrade flow during systole and the volume of retrograde flow in diastole.[64,69] In the quantification of aortic insufficiency, the best accuracy is achieved by placing the imaging slice between the aortic valve and the coronary ostia. This limits flow measurement to the regurgitant blood volume passing through the incompetent valve while excluding blood flow through the coronary arteries (**Fig. 6.21**).[70] The measurement error associated with a higher slice position is less when greater degrees of regurgitation are present. Besides volumetry, it is also possible to display an en-face view of the valvular apparatus by performing a bright-blood cine acquisition in the valvular plane. This provides a direct view of the regurgitant jet and valve defect, which can be accurately measured and localized.[71,72]

Mitral valve insufficiency can be quantified by subtracting the systolic flow in the aorta from the diastolic flow through the mitral valve into the left ventricle.[73] A more practical method for routine testing is to determine the SV or "net forward volume" in the ascending aorta by phase-contrast imaging. The difference between this value and the SV of the left ventricle (determined by cine measurements) equals the regurgitant volume across the mitral valve.

Valvular and Vascular Stenosis

Flow measurements can be used to determine the peak pressure gradient across a stenotic lesion such as a valvular stenosis or coarctation of the aorta (**Fig. 6.22**). An orthogonal measurement of the peak velocity jet is essential in this regard. The pressure gradient can then be determined by applying the modified Bernoulli equation[74]:

$$\text{Pressure gradient} = 4 \times V_{max}^{2}$$

In patients with valvular stenosis, it is important to quantify the pre- and posttherapeutic valve orifice area (VOA). The VOA can be demonstrated in cine images that are orthogonal to the valvular plane.[75] Since the valve cusps limit blood flow, the maximum VOA can be measured as an area (planimetry) during systole. VOA determined by MRI correlates very well ($r=0.8$) with values determined by echocardiography.[75]

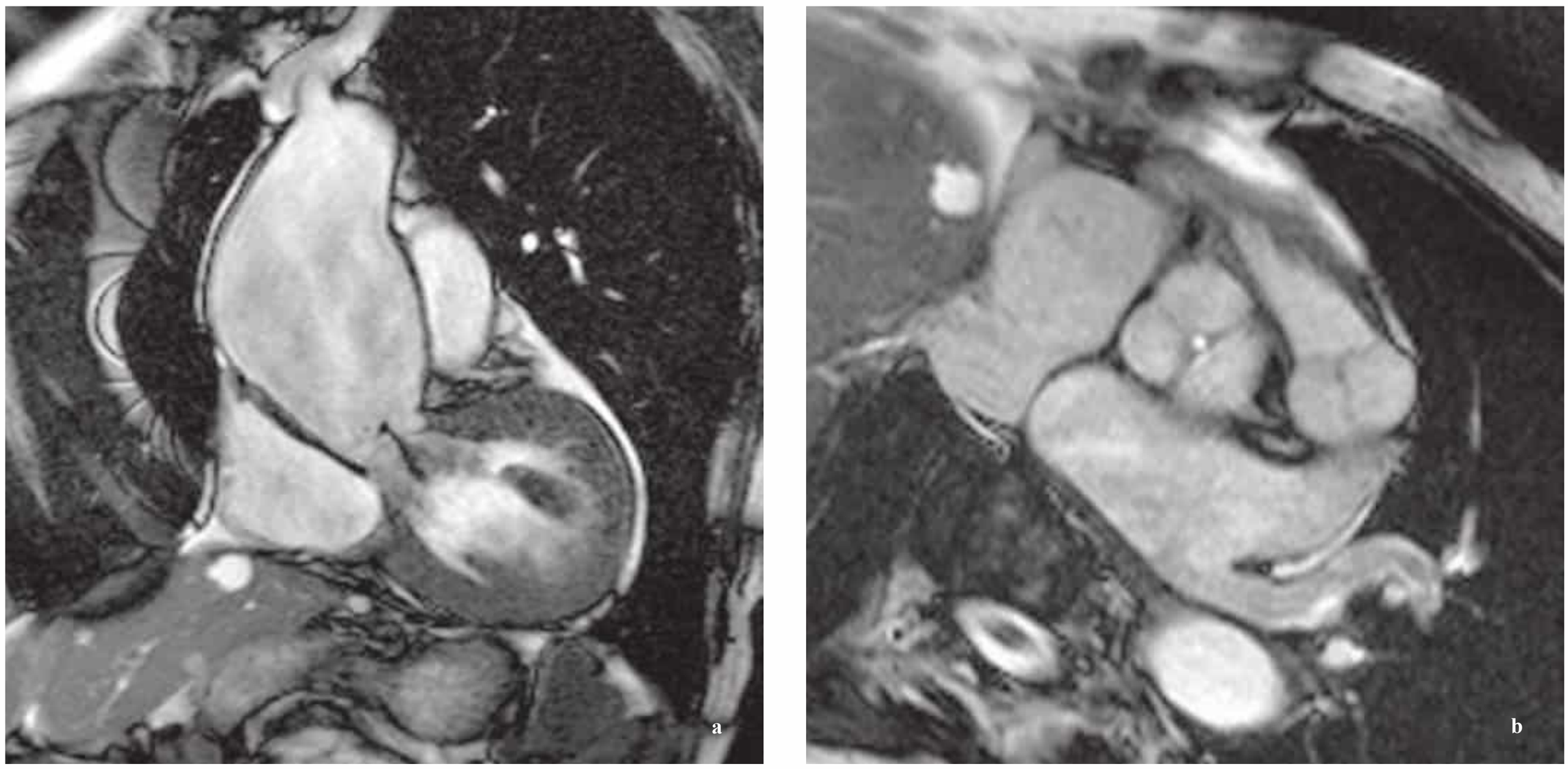

Fig. 6.22 a, b Cine images of the left ventricular outflow tract in a woman with an ascending aortic aneurysm and consecutive aortic insufficiency. The black jet indicates blood regurgitating into the left ventricle through the aortic valve during diastole. The image on the right shows an en-face view of the aortic valve. Blood regurgitates into the ventricle through the white gap at the center of the valve, which results from enlargement of the aortic valve annulus.

Myocardial Perfusion

W. G. Schreiber

An adequate blood supply is crucial for maintaining the function and viability of cells. Modern MRI techniques make it possible not only to examine major feeding and draining vessels by coronary angiography and blood flow measurements but also to investigate tissue microcirculation. The actual exchange of oxygen and nutrients between the blood and tissue takes place in the capillary region. The goal of MR perfusion imaging is to evaluate blood flow at the capillary level without directly visualizing the individual capillaries themselves. It is also reasonable to expect that regional disturbances are more likely to be detected with a spatially resolved technique than in global studies such as coronary artery flow measurements. Moreover, the detection of a stenosis by coronary angiography does not indicate how the lesion affects perfusion in the territory supplied by the stenosed vessel. For example, collaterals may be able to maintain adequate perfusion even in the presence of a relatively high-grade stenosis.

As technical capabilities have increased, greater interest has been focused on myocardial perfusion MRI. The advantage of this modality over established myocardial perfusion methods such as single-photon emission computed tomography (SPECT) and positron emission tomography (PET) is that MR scanners are now available at many institutions and that they do not expose patients to ionizing radiation. When a patient is already in the MR scanner for cardiac imaging, it takes little additional time to carry out perfusion imaging.

The goal of this section is to review the technical and methodological aspects of MR perfusion imaging and its clinical applications. Our scope will be limited to contrast-enhanced perfusion MRI using exogenous contrast agents such as gadolinium chelates. Noncontrast MRI techniques such as arterial spin labeling have been used for the investigation of myocardial perfusion but are of little clinical interest at present owing to long acquisition times and poor image quality.

Physiology

"Perfusion" is a general term denoting the flow of blood or other fluids through the body or specific organs. "Perfusion imaging" in the strict sense deals with the terminal portion of the vascular bed, the capillaries. This is where the primary exchange of oxygen and nutrients takes place between the blood and tissue. The key indicators of perfusion are regional myocardial blood flow (rMBF, in mL/min/100 g myocardium) and regional myocardial blood volume (rMBV, in mL/100 g myocardium). The rMBF is of primary interest in the diagnosis of ischemia because it indicates the amount of fresh, oxygen-rich blood that is available in a given time period for supplying the tissue with oxygen and nutrients and for removing metabolic end products. The normal rMBF at rest is ~80–90 mL/min/100 g of tissue.

The rMBV expresses only the amount of blood present in a tissue; it does not indicate whether the blood is serving any function. Approximately 60–80 %of the capillaries are perfused at rest, and the rMBV is ~13 mL/100 g of tissue.

The myocardial perfusion reserve index (MPRI) denotes the mechanism of myocardial autoregulation that increases MBF through capillary recruitment in response to stress. The purpose of this mechanism is to satisfy the increased oxygen demand of the heart in stress situations. The MPRI in normally perfused myocardium is ~4–5 under experimental conditions, and values

of 2.25–2.50 are measured clinically in response to pharmacological stress. The importance of the MPRI in the diagnosis of ischemia, as in patients with suspected CHD, is based on the fact that the MPRI is a more sensitive indicator than MBF, showing a measurable decline in response to lower grades of stenosis.

It should be noted that the contrast agents used in MRI are distributed entirely to the blood plasma and interstitium, and so they basically indicate plasma flow (unlike agents that bind to erythrocytes and label nutritional blood flow).

Essential Point

Myocardial blood flow (MBF) during stress and especially the myocardial perfusion reserve index (MPRI) are of great clinical interest in perfusion studies, particularly in examinations of patients with suspected CHD.

Principle of Perfusion MRI

First-pass perfusion MRI is based on the bolus injection of a contrast agent into a peripheral vein while a rapid series of heavily T1-weighted MR images of the heart are acquired. The time course of contrast arrival in the myocardium is then determined and analyzed, either by visual interpretation of the first-pass images or by a quantitative or semiquantitative analysis of the enhancement kinetics.

The basic idea is that the MR contrast agent behaves like an indicator, i.e., it dissolves perfectly in the blood plasma without affecting blood flow. Since mixing of the contrast agent with the blood is assumed to be perfect, myocardial blood flow can be evaluated by analyzing the wash-in kinetics of the contrast agent. If the agent shows rapid wash-in and raises the signal intensity to high values, the blood flow is relatively high (**Fig. 6.23**). But if the enhancement in one region is delayed relative to other myocardial regions and produces lower signal intensities, the perfusion in that region must be diminished. The principles of the indicator dilution theory developed in the nineteenth and twentieth centuries can be applied in the (semi)quantitative analysis of perfusion (see below).

The specific aspects of MR perfusion imaging will be examined below in greater detail.

Technological Requirements

MR perfusion imaging has rigorous technological requirements. Since relevant signal changes take place within seconds, high temporal resolution (at least one image per heart beat) is mandatory. Additional requirements are optimum image quality (high signal- and contrast-to-noise ratios), high spatial resolution, and maximum coverage of the heart, which requires multislice capability.

To obtain an acceptable SNR, modern perfusion MRI employs magnetic field strengths of 1.5 T combined with multielement phased-array receive coils. Lower field strengths can be used but lead to compromise between image quality, temporal resolution, and/or contrast dose. Higher field strengths such as 3.0 T are desirable in principle,[76] but associated problems such as the achievement of a uniform signal intensity across the heart and increased specific absorption rate (SAR) have not yet been completely resolved.

Short acquisition times combined with high spatial resolution and coverage require the use of high-performance gradient systems. Minimum gradient system requirements are a maximum gradient strength of 25 mT/m and a slew rate of at least 40 mT/m/ms. Dedicated cardiovascular MRI systems can provide gradient strengths higher than 35 mT/m and slew rates greater than 100 mT/m/ms.

The high intensity and rapid switching of the gradient fields and the short RF pulses often interfere with ECG recordings and may preclude the use of ECG-triggered image acquisition. Possible solutions to this problem are special active ECG electrodes with carbon fiber cables and preamplifiers, special filtering software, or vector ECG gating. As an emergency solution, an Spo_2 finger sensor can be used for pulse triggering as its signals are not affected by MRI.[77]

Essential Point

If a clean ECG trace cannot be obtained (test by positioning the patient in the magnetic field as for an actual examination), an Spo_2 sensor can be used for triggering.

Pulse Sequences

Fast gradient-echo pulse sequences with short echo and repetition times are essentially the only sequences used for modern MR perfusion imaging. T1-weighting is produced by applying a saturation or inversion pulse immediately before image acquisition. Inversion preparation offers the advantage of greater T1-weighting and the ability to suppress selected tissues, such as normal perfused myocardium, by manipulating the inversion time. Saturation preparation, on the other hand, is insensitive to real changes in heart rate, or mistriggering. This can be an important advantage in quantitative and semiquantitative perfusion studies. Selection of the saturation or inversion time—the time from the preparation pulse to readout of the central k-space lines—depends strongly on the proposed method of analysis. For visual analysis, relatively long preparation times (up to 600 ms) can provide acceptable image quality. For quantitative analysis, however, the preparation time should be as short as possible to avoid nonlinearity in the signal equation (see below), although this reduces the SNR.

The most widely used pulse sequences for perfusion MRI are single-shot turbo FLASH sequences,[78–81] SSFP sequences (e.g., TrueFISP[77,82–84]), and segmented gradient-echo sequences (echo planar sequences, echo train length ~4–11).[85–87] Turbo FLASH sequences are very robust but have a relatively poor SNR. SSFP sequences provide better image quality but are more susceptible to artifacts. This also applies to segmented gradient-echo pulse sequences.

The pixel size should be no greater than 3.0 mm × 5.0 mm × 10 mm so that the left ventricular myocardium can be imaged with acceptable spatial resolution. Perfusion deficits are often manifested at the subendocardial level. A true spatial resolution of better than 2.5 mm is desirable for discriminating between endocardial and epicardial tissue.[88,89] At least three or

four slices should provide adequate clinical coverage of the heart in the short-axis plane.

The conflicting requirements in terms of acquisition time on the one hand and spatial resolution/cardiac coverage on the other make the use of parallel imaging techniques like SENSE, GRAPPA, and their variants seem attractive. The potential applications of these techniques in myocardial perfusion imaging are being closely scrutinized, but definitive conclusions cannot yet be drawn. One problem is that all parallel acquisition techniques ultimately reduce the amount of data acquired (i.e., the phase-encoding steps per image), resulting in a deterioration of SNR. Since image quality is often relatively poor even without parallel acquisition techniques, the quality of the results may suffer. However, because fewer phase-encoding lines are acquired in parallel imaging, the linearity of the signal equation (see below) extends to higher concentrations. Therefore, up to 40 %higher dosage of contrast agent may be used to more than compensate for the reduced SNR in parallel imaging.[90]

Imaging Protocol

After localization, planning of the short-axis slice, and data acquisition without contrast administration (e.g., cine imaging), perfusion imaging is generally performed. To avoid problems from the moving heart, perfusion imaging is usually done over 30–40 cardiac cycles using breath-hold technique. Contrast injection into a cubital vein is preceded by approximately five precontrast images, which will serve as a reference for subsequent analysis. The contrast agent should be injected mechanically with an MRI-compatible injector at a flow rate of at least 3 mL/s and preferably 5–10 mL/s. Mechanical injection using a power injector is preferred over manual contrast administration as it is easier to standardize and yields more reproducible results.

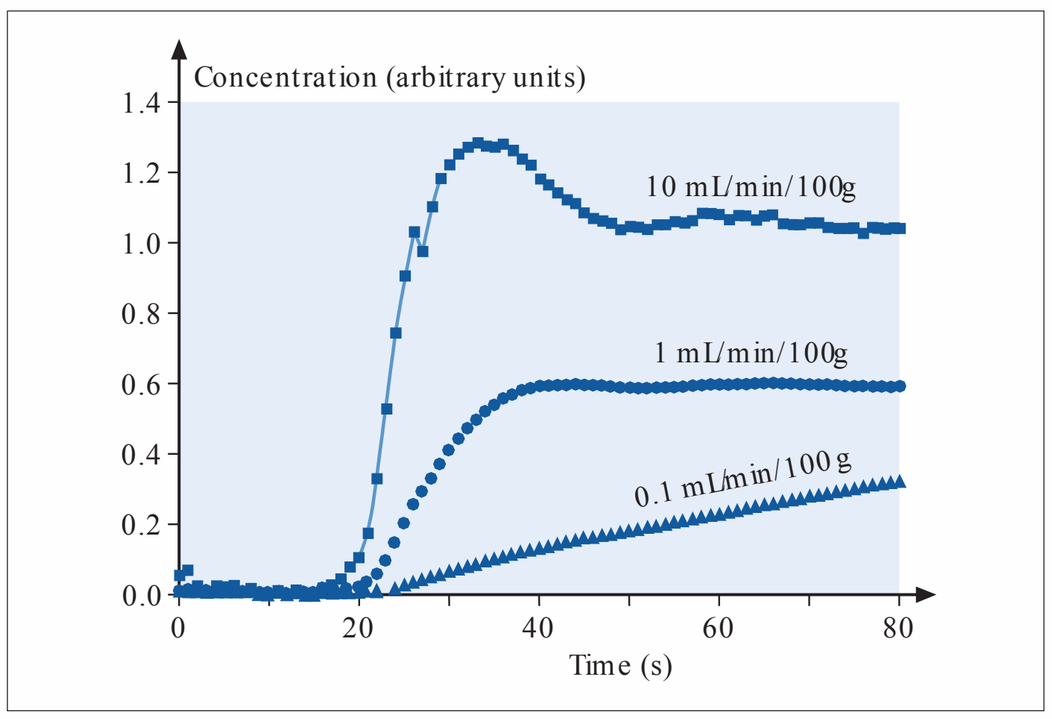

Fig. 6.23 Temporal evolution of the contrast agent concentration during a first-pass perfusion study. If the relation between the signal intensity and the contrast agent concentration is linear, this graph also denotes the temporal evolution of the signal intensity. The higher the blood flow, the steeper the upslope during the wash-in phase. With very low blood flow, the enhancement peak is delayed or does not appear. The middle curve represents normally perfused myocardium. The upper curve represents hyperemia, while the lower curve corresponds to an ischemic condition. The graph is the result of a computer simulation based on actual measurements of left ventricular contrast wash-in and a mathematical model (MMID4).[97]

The contrast agents of choice are gadolinium chelates such as Gd-DTPA. The dosage depends on the application: For visual analysis, the agent is usually administered in a clinical dose of 0.05–0.1 mmol/kg bw. For quantitative analysis, the dose should be reduced to no more than 0.025 mmol/kg bw to avoid the nonlinear region of the signal equation, as this could lead to systematic errors during data analysis.[77] The same dose is recommended for semiquantitative analysis, although doses up to 0.15 mmol/kg bw can still provide clinically reliable measurements.[85]

Essential Point

The standard contrast dose of 0.05–0.10 mmol/kg bw can be used for qualitative perfusion analysis. It should be reduced to 0.025–0.050 mmol/kg bw for semiquantitative analysis. Dosing for quantitative analysis should not exceed 0.025 mmol/kg bw.

Abnormalities of myocardial perfusion are often appreciated only in stress images. Owing to the strong magnetic fields used in MRI, the confined space within the scanner, and the sensitivity of MRI to motion, exercise stress testing using a bicycle ergometer is extremely difficult and is rarely done clinically.

A more practical option is pharmacological stress testing with dobutamine, which increases MBF by raising the heart rate and increasing myocardial contractility. Alternative agents are dipyridamole (0.56 mg/kg bw)[91,92] or adenosine (140 µg/min/kg bw),[80,85,86] which increase myocardial blood flow through vasodilation and thus simulate a stress examination. Dipyridamole has a primary positive inotropic action, in consequence leading to the production of adenosine and, thus, increased MBF.

Adenosine has become very widely used in stress MRI.[93] As a rule, two image acquisitions are performed to determine the perfusion reserve: one before and one during the pharmacological stress so that the effects of the stress can be assessed accurately.[80,86]

For a reliable determination of perfusion reserve, it should be noted that aminophylline, theophylline, and xanthines interact with adenosine. Thus, the test results may be distorted if drugs containing these compounds are taken within 24 hours before testing. The patient is cautioned to avoid xanthine-containing foods (chocolate) and beverages (coffee, tea, cola drinks) for at least 12 hours prior to testing. Otherwise, paradoxical test results may be obtained.

To avoid systematic errors during the second acquisition due to contrast agent still present from the first acquisition, the rest and stress images should be acquired at least 10–20 minutes apart. There may still be an undesired increase in precontrast signal intensity in the second acquisition owing to a delayed enhancement effect.

Because the stress images are the more important source of information, it has been suggested that stress imaging be done before rest imaging or that a stress-only protocol be used that omits the rest images.[85,92] However, when rest images are omitted, problems may arise in the interpretation of potential image artifacts. Thus, low signal intensity due to ischemia may be difficult to distinguish from low signal intensity due to an image

artifact (artifacts are common in rest images), especially in SSFP sequences.

Methods of Analysis

Once the image data have been acquired and transferred to a special computer or evaluation workstation, the images are analyzed. The presence of ischemia may be detected by a pure visual analysis of the image data, depending on clinical requirements, time constraints, and available analytic software. A (semi)quantitative analysis aims for a more precise, numerical, and reproducible evaluation but often requires considerable additional time and effort.

In principle, all analytical methods are based on the graph shown in **Fig. 6.23**. The contrast agent is administered by IV bolus injection, travels through the arterial bloodstream, and enters the myocardium. The initial rapid increase of the signal intensity is called the wash-in phase. It is a result of rapid diffusion of contrast agent from the intravascular to interstitial space. In general, a plateau of relatively constant signal intensity over time (middle curve in **Fig. 6.23**) follows upon the wash-in phase.

In case of myocardial ischemia, contrast wash-in is significantly slower because contrast agent is supplied at a reduced rate. In consequence, a continuous increase of the signal intensity without an enhancement peak is observed during the measurement duration of a single breath hold (30 s or less). Moreover, in this case the signal intensity remains below the signal intensity of normally perfused myocardium, i.e., ischemia shows negative contrast relative to normally perfused myocardium. The more severe the ischemia, the greater the difference in image contrast, and the more delayed is the wash-in. In extreme cases such as an occluded coronary artery (without a collateral blood flow), contrast wash-in does not occur (zero perfusion). A typical perfusion study is illustrated in **Fig. 6.24**.

Essential Point

Qualitative image analysis is a convenient method that is adequate for many clinical questions. If greater accuracy and comparability are needed (e.g., for follow-ups), a semiquantitative analysis of the image data is recommended. At present, a quantitative analysis (in mL/min/100 g) is feasible only for investigational studies.

Visual (Qualitative) Analysis

A purely visual analysis of perfusion images is often satisfactory for clinical purposes. A series of images acquired at different times after contrast injection are scrutinized for hypointense areas during the wash-in phase (**Fig. 6.24**). The images may be analyzed by reading all the individual images in succession or by viewing a cine loop on the computer screen as in cardiac function studies.

The advantage of qualitative analysis is its speed and convenience. It is also relatively robust, for even suboptimal ECG triggering or an incomplete breath hold will still yield meaningful

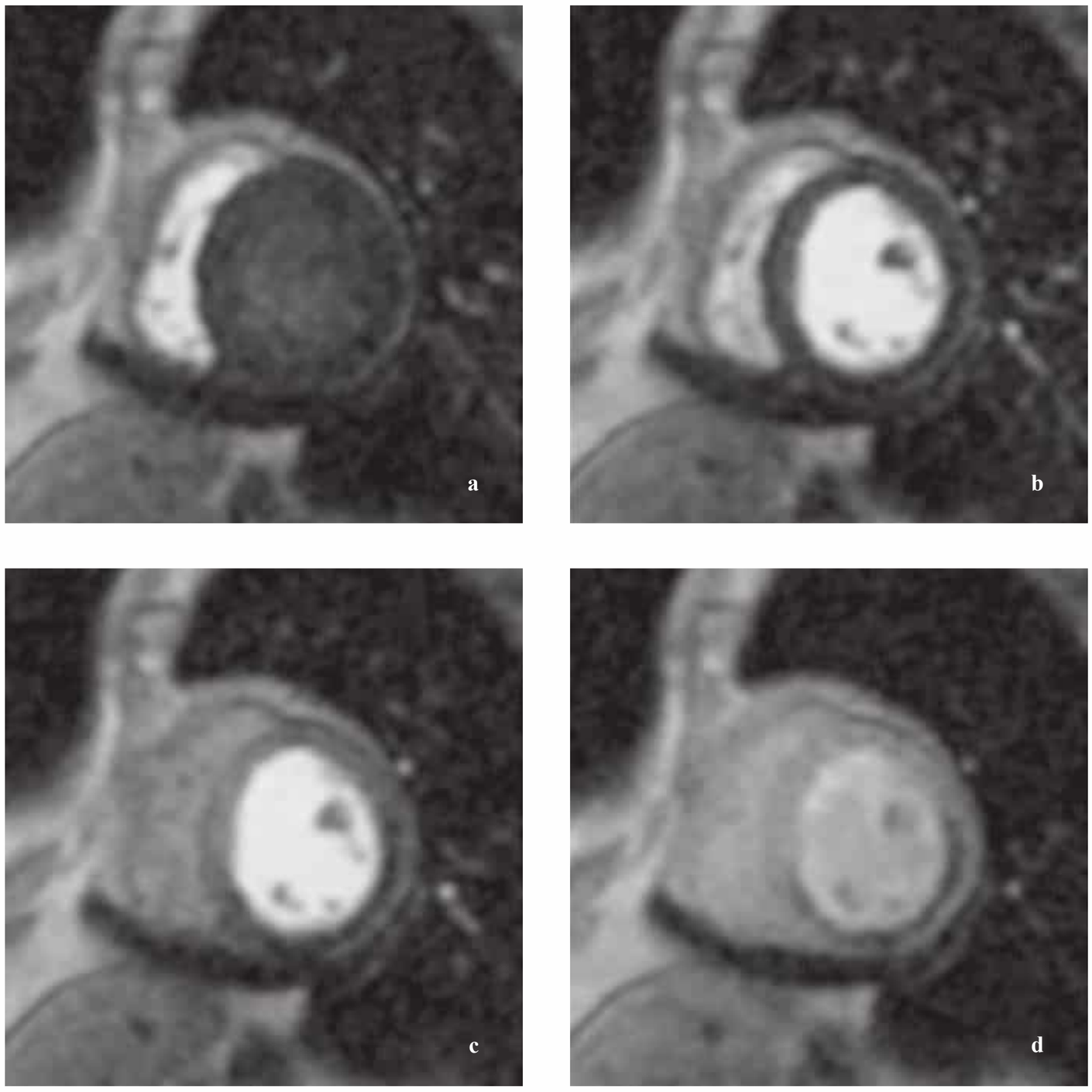

Fig. 6.24 a–d Perfusion imaging with a turbo FLASH pulse sequence in a patient with a subendocardial perfusion defect in the posterior wall. Short-axis slice before contrast agent has entered the left ventricular blood and myocardium (**a**). The high signal intensity is from contrast that has already entered the right ventricle. When the contrast concentration is maximal in the left ventricle (**b**), very little contrast agent has yet entered the myocardium. During the contrast wash-in phase (**c**), marked enhancement is also visible in the myocardium. A subendocardial perfusion defect appears now as a hypointense area in the posterior wall. A similar but faded enhancement pattern is seen near the end of the acquisition (**d**).

studies. Frequently this is not the case with (semi)quantitative methods (see below). Disadvantages are that image interpretation depends strongly on the experience of the reader, and there is a lack of reproducible, standardized numerical data that may be necessary in serial follow-up examinations, for example.

Semiquantitative Analysis

A numerical analysis of the time–intensity curves plotted for specific myocardial segments provides greater accuracy than visual analysis. The time course of signal intensity is plotted and analyzed for each segment (**Fig. 6.25**). The 6- or 8-segment model is generally used. Good ECG triggering and a stable breath-hold period are essential, so that the myocardial contours from the first image can be automatically transferred to all subsequent images in the same slice location. Unless all of these requirements are met, serious analytical errors are apt to occur if, for example, the lung or ventricles move into the region of interest during the acquisition.

Essential Point
Good ECG triggering and stable breath holding are necessary for the semiquantitative and quantitative analysis of perfusion images. Major errors may result if these conditions are not met.

Several different empirical parameters can be derived from the time–intensity curves, such as the maximum percentage rise in signal intensity (relative to myocardial signal intensity before contrast injection) and the "time to peak," which is measured from the start of the image acquisition (or from initial contrast wash-in) to maximum enhancement. But although these parameters are easily determined, they show only an indefinite, indirect correlation with myocardial blood flow (**Fig. 6.23**).

It can be seen from **Fig. 6.23** (and from other studies not referenced here) that the (up-) slope of the wash-in phase correlates with myocardial blood flow. The actual value of this slope depends on several factors (e.g., the T1 relaxation time of the myocardium, the contrast agent, type of sequence, field strength). But if a standardized technique is used for contrast administration (e.g., a power injector), the ratio of the slope during stress (e.g., adenosine) to the slope at rest will provide a good estimation of myocardial perfusion reserve. The effect of varying wash-in conditions (e.g., manual contrast injection or acquisitions on different days) can be eliminated by normalizing the slope values to the upslope of the time–intensity curve in the left ventricle. The perfusion reserve can then be calculated from the normalized slopes:

$$\text{Perfusion reserve} = \frac{\text{(normalized) slope during stress}}{\text{(normalized) slope at rest}}$$

The perfusion reserve is a (patho)physiologically and clinically important parameter that is relatively easy to determine. Clinically, values of 2.25–2.50 are measured in normally perfused myocardium during pharmacological stress. The perfusion reserve is reduced under conditions of ischemia, because myocardial autoregulation can no longer compensate for the decrease in perfusion pressure caused by the stenosis.

The cutoff value for discriminating between normally and abnormally perfused myocardium depends somewhat on the selected acquisition technique and contrast dose. In one study comparing MRI with coronary angiography, a cutoff value of 1.1 yielded a sensitivity of 88 %and a specificity of 90 %in the detection of hemodynamically significant stenosis using the normalized slope method.[86]

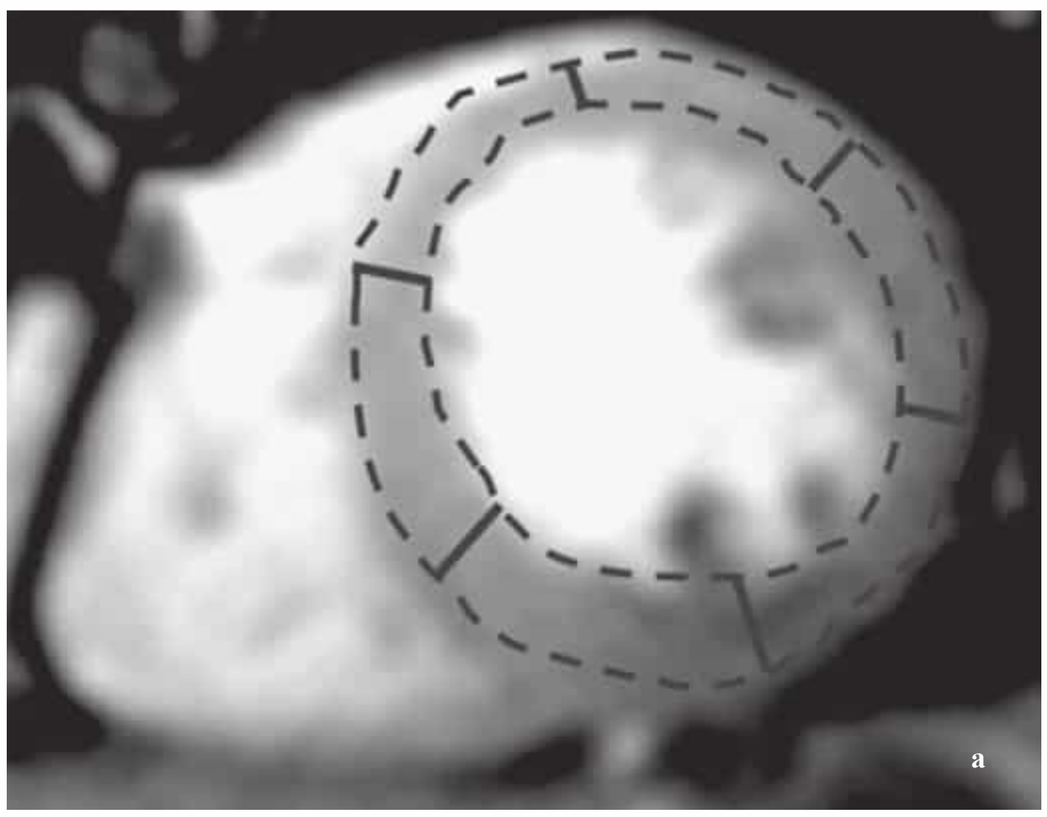

Fig. 6.25 a, b Semiquantitative analysis. The myocardium is divided into six or eight segments (**a**), and a time–intensity curve is plotted for each segment (**b**). This case illustrates a typical time–intensity curve in normally perfused myocardium (relatively high amplitudes) and in an ischemic region (low amplitudes with a somewhat delayed enhancement peak). The results can be expressed numerically by calculating the slope of the wash-in phase (dotted and dashed lines). This slope is proportional to myocardial blood flow (MBF).

Essential Point
The cutoff value for discriminating between a normal and abnormal perfusion reserve depends on the imaging conditions (especially the pulse sequence, type and dose of contrast agent used, and injection protocol). Ideally, a new cutoff should be determined for each center (in multicenter studies) and whenever there is a change in any of the parameters listed. The impact of these parameters can be minimized by proper selection of the contrast dose (≤0.025 mmol/kg b.w.) and by using the normalized perfusion reserve for assessment of myocardial ischemia.

Quantitative Perfusion Analysis

A qualitative or semiquantitative analysis is satisfactory for most clinical questions. True quantification would be desirable for special investigations or scientific studies so that myocardial blood flow can be expressed in actual physiological units (mL blood/min/100 g tissue). Authors have developed a variety of quantitative approaches based on deconvolution methods,[88,94] pharmacokinetic models,[95,96] and more complex tracer kinetic models.[78,80,97,98] Currently these methods are not suitable for routine clinical use because of their prohibitive costs and are outside the scope of our discussion.

Applications

Qualitative analysis has become the mainstay for routine perfusion imaging, especially in the diagnosis of ischemia, and has been utilized in several studies. There is still no standardization of the strongly operator- and manufacturer-dependent examination techniques, however, and this limits the ability to compare and interpret the results at different institutions. Semiquantitative perfusion analysis offers a good compromise in this regard, as it permits a simple examination and interpretation protocol and yields reproducible results.

In one study, semiquantitative perfusion MRI achieved a sensitivity of 91 %and specificity of 94 %in the diagnosis of coronary heart disease compared with ammonia PET. It achieved a sensitivity of 87 %and specificity of 85 %compared with coronary angiography.[92] Similar results were found in a second study comparing perfusion MRI with coronary angiography (88 %sensitivity, 90 %specificity).[86] The advantages of MRI over PET include the good availability of MRI and its relatively high spatial resolution, which even permits the detection of subendocardial perfusion defects.

Comments on Methodology

Myocardial perfusion imaging can provide information on microcirculation when the proper methodology is used. By comparison, coronary angiography (X-ray or MRI) can demonstrate luminal reduction of the coronary vessels but cannot show its hemodynamic significance. At the same time, perfusion imaging cannot provide direct information on the cause of the perfusion defect, although the cause can be indirectly inferred from its effect on perfusion reserve compared with the normal value. Thus, a 70 %stenosis leads to an ~50 %reduction in the coronary flow reserve.[99] MRI can detect the effects of this and even smaller degrees of stenosis[80,100] but it cannot directly show the degree of stenosis or define the extent of atherosclerotic plaque in the vessel wall.

Atherosclerosis begins with the formation of a lesion within the vessel wall, and considerable time passes before significant luminal narrowing occurs. Approximately 85 %of stenoses that lead to myocardial infarction cause less than 70 %luminal narrowing, and 65 %of these stenoses are less than 50 %[101] Naturally it is difficult to detect these low-grade stenoses by perfusion imaging. In the future, it would be desirable to supplement perfusion scans with high-resolution MRI of the coronary vessel walls[102] to provide a comprehensive evaluation of patients with suspected coronary heart disease. It should be noted, however, that high-resolution MRI of coronary vessel walls is not yet practical for routine clinical use.

Delayed Enhancement

P. Hunold

Delayed enhancement (synonym: late enhancement, late gadolinium enhancement) in contrast-enhanced MRI refers to delayed hyperenhancement that is observed during the equilibrium phase following IV contrast administration. Unlike early first-pass imaging, delayed-enhancement imaging does not assess myocardial perfusion but is used in the **detection of myocardial changes** such as scar, edema, necrosis, and fibrosis. Delayed-enhancement imaging has quickly become an established clinical tool owing to its ease of application, robustness, and unique value in differential diagnosis.

Originally, delayed-enhancement imaging was used mainly for viability assessment in acute or chronic myocardial infarction (see Chapter 8 pp. 181 and 187). Its main application in this setting is in differentiating functionally abnormal but viable (hibernating or stunned) myocardium from irreversibly damaged myocardium (scar) in patients with global or regional myocardial dysfunction. This distinction is important prior to revascularization procedures (interventional or bypass surgery) to predict whether regional function will improve after perfusion has been restored. In recent years delayed-enhancement imaging has become the gold standard for addressing this important clinical question.

With its ability to detect subtle structural changes within the myocardium and the typical distribution patterns of delayed enhancement in various diseases, this method is markedly superior to echocardiographic and nuclear medicine techniques in the investigation of myocardial changes. Thus, besides the evaluation of myocardial infarction, various new and interesting indications for delayed-enhancement imaging have emerged in a variety of nonischemic myocardial diseases (especially myocarditis and cardiomyopathies). These applications are described in the chapters dealing with specific cardiac diseases.

Essential Point
Delayed enhancement is found not only in myocardial infarction but also in various other myocardial diseases.

Pathophysiology of Delayed Enhancement

The principle of delayed enhancement in cardiac imaging—the delayed accumulation of contrast agent in the myocardium during the equilibrium phase—was described for iodinated contrast media more than 25 years ago. At that time, CT studies of induced myocardial infarction in an animal model showed that contrast media became concentrated in the infarcted area.[103] The high contrast between infarcted and viable/normal myocardium after IV contrast administration allows for quantification of infarct size.[104]

As early as 1986, the same effect was observed in MR images following IV contrast administration in animal studies.[105] As contrast agents gadolinium (Gd)-based paramagnetic, extracellular agents were used that do not penetrate the intact cell membrane but are distributed entirely in the extracellular space.[106] Today the most widely used compounds are Gd-DTPA, Gd-BOPTA, gadodiamide, and Gd-DOTA. Most clinical experience has been acquired with Gd-DTPA, which was the first clinically approved MRI contrast agent. These compounds shorten the T1 relaxation time, thereby increasing the signal intensity of enhancing tissues in T1-weighted sequences.

In normal healthy myocardium, contrast agents administered by IV injection distribute only in the intravascular and the interstitial space. Owing to redistribution and rapid renal excretion, the blood concentration of the intravenous agent falls rapidly during the initial minutes after injection. The delayed uptake of Gd contrast agent in pathologically altered myocardium, such as an infarcted area, is based on a combination of multiple pathophysiological differences between normal and damaged myocardium (**Table 6.6**).

The most important mechanism of contrast pooling in abnormal myocardium is as follows. Scar tissue and inflammatory or fibrotic myocardium have a larger interstitium compared with normal myocardium, i.e., the extracellular space is enlarged relative to the intracellular space. As a result, an **increased distribution volume** is available for extracellular Gd contrast agents.[107] Additionally, these agents are not only present in greater concentration but are also retained for a longer time.[108]

These effects are of major importance in all entities that show delayed enhancement. The interstitium in acute myocarditis is increased as a result of edema. In acute myocardial infarction, cellular necrosis leads to a loss of cell membrane integrity, allowing contrast material to enter the intracellular space. In chronic changes such as postinfarction scars or myocardial fibrosis with a nonischemic cause, enlargement of the interstitial space is based on the fact that the originally very close-packed, parallel, viable myocardial cells have been replaced by an irregular aggregation of fibrocytes and collagen.

Besides the increased distribution volume, **perfusion differences** are another mechanism that contributes to delayed enhancement. Scar tissue has less blood flow than viable myocardium, resulting in a delay of contrast wash-in[109] and an even greater delay of contrast wash-out. Taken together, these effects cause a significant difference in contrast uptake and signal intensity between normal and abnormal myocardium during the equilibrium phase (5–30 minutes) following contrast administration (**Fig. 6.26**).

Table 6.6 Pathophysiology of delayed enhancement. Various mechanisms for Gd contrast uptake in damaged myocardium during the equilibrium phase after contrast injection

- Enlargement of the interstitial space
- Enlargement of the contrast distribution volume
- Penetration of extracellular contrast agent into cells through membranes damaged by acute necrosis
- Delayed wash-in due to decreased perfusion
- Delayed wash-out

Essential Point
Myocardial abnormalities such as scar tissue, inflammation, or fibrosis increase the distribution volume of extracellular contrast agents. Their accumulation and delayed wash-out lead to significantly greater T1 shortening than in normal myocardium during the equilibrium phase, and this effect can be demonstrated with appropriate sequences.

Pulse Sequences

An optimum pulse sequence for detecting differences in contrast uptake between normal and abnormal myocardium must satisfy various requirements. It must be fast enough to acquire one or more ECG-triggered slices with good spatial resolution during a single breath hold. Additionally, myocardial abnormalities should contrast sharply with normal myocardium and with blood in the ventricular cavity so that even small areas of increased contrast uptake can be identified. The sequence should also be resistant to artifacts.

In 2001, Simonetti et al. designed an optimum sequence that has become standard for this type of investigation.[110] It is described as an ECG-triggered, segmented inversion-recovery turbo gradient-echo sequence. The key improvement over all previously used sequences was the use of an inversion pulse to produce maximum contrast between normal and abnormal myocardium after contrast administration. The parameters for a typical inversion-recovery turbo gradient-echo sequence are shown in **Table 6.7**.

As explained above, contrast material accumulates in a myocardial scar and causes a greater shortening of the T1 relaxation time than in normal myocardium. As a result, longitudinal magnetization relaxes much faster in scar tissue than in normal myocardium following a 180° inversion pulse. As **Fig. 6.27** shows, the longitudinal magnetization of normal and infarcted myocardium are close together at the beginning and end of the relaxation process, resulting in very little image contrast between the two tissues. The greatest difference occurs when the excitation for data acquisition begins at the point where the relaxation curve for normal myocardium crosses the *x*-axis. Because normal myocardium has no longitudinal magnetization at that point in time, it does not produce a signal during the next excitation and appears dark in the image. In other words, the signal from normal myocardium has been "nulled."

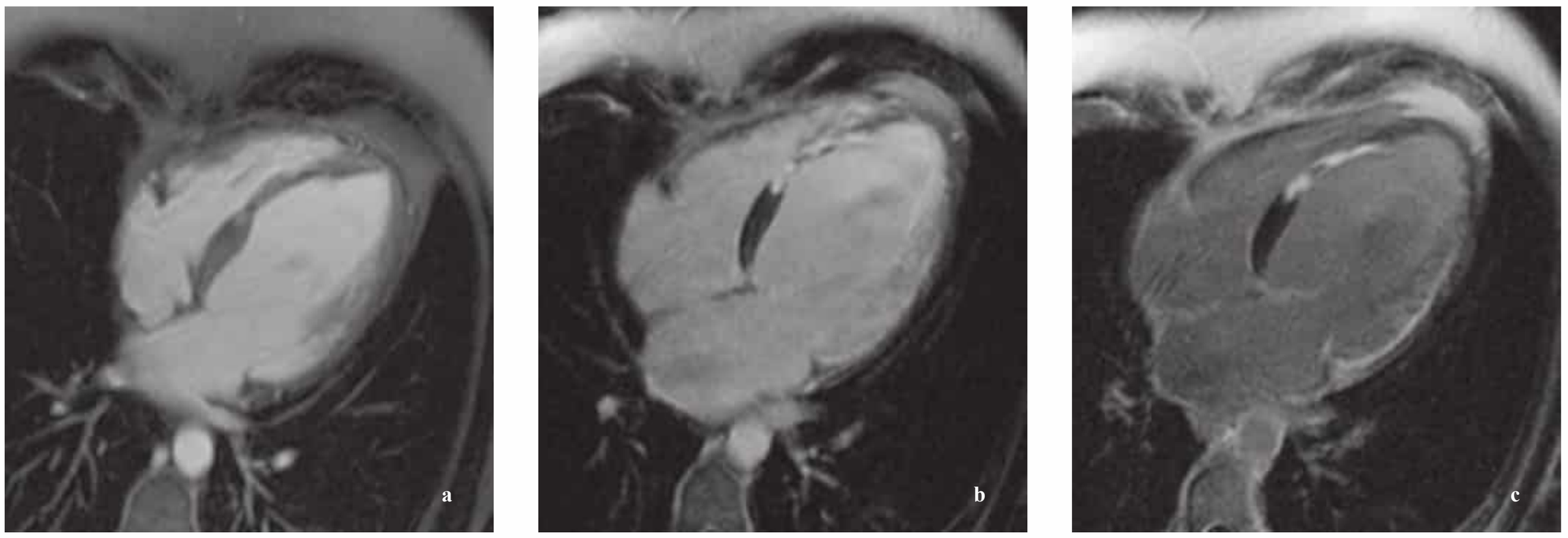

Fig. 6.26 a–c Time-course of the delayed enhancement of a transmural and nontransmural myocardial scar at various times after contrast injection. Fast inversion-recovery gradient-echo images acquired 1 minute (**a**), 6 minutes (**b**), and 12 minutes (**c**) after the injection of 0.2 mmol/kg bw Gd-DTPA. Transmural myocardial scar in the inferoseptal midventricle (segment 9) and a nontransmural myocardial scar in the anterolateral basal and midventricle (segments 6 and 12). The contrast concentration in the blood falls markedly over time. A similar decrease occurs in viable myocardium. Intense, progressive contrast enhancement in the myocardial scars (delayed enhancement) clearly delineates the scar tissue from the ventricular lumen and viable myocardium.

For optimum sequence timing, the delay between the inversion pulse and the acquisition of image data (inversion time, TI) must be individually adjusted (**Fig. 6.28**). The optimum inversion time depends on the administered contrast dose as well as time after contrast administration, because the concentration of contrast agent in the myocardium declines owing to redistribution and renal excretion and requires an incremental lengthening of TI (**Fig. 6.29**).

Essential Point

Improper adjustment of the inversion time may cause bands of high signal intensity to appear at the center of the myocardium. These artifacts should not be mistaken for abnormal delayed enhancement. Correct adjustment of the inversion time (TI) is particularly important for indications that go beyond the detection of infarcts, where it is necessary to detect smaller areas that frequently show less enhancement. If healthy myocardium no longer appears uniformly black several minutes after the optimization of image contrast but is "tiger-striped" or contains midmyocardial hyperintense zones, the TI time should be progressively increased in increments of ~ 20 ms.

TI can also be optimized by using sequences that acquire a series of images with different TI times (TI scout sequence, Look-Locker sequence) during one breath hold after an inversion pulse.[111] The image with optimum contrast can then be selected from the series, and the inversion time for that image can be used for subsequent acquisitions.

Another option is to use phase-sensitive inversion-recovery (PSIR) sequences, which do not require an individual adjustment of TI.[112] Phase-sensitive images are reconstructed in a manner unlike conventional reconstructions of magnitude images that are sensitive to TI settings. The background phase is eliminated so that a constant desired contrast can be maintained.[113] The resulting images have a somewhat artificial appearance and their interpretation involves a learning curve, but they can be an effective alternative for less-experienced examiners.

Various sequences can be used for data acquisition after the inversion pulse. The standard technique is a segmented 2D turbo gradient-echo sequence, acquiring a single slice per breath hold. While considerable time is needed to examine the entire left ventricle (5–10 minutes), this sequence provides the best contrast and image quality of all the pulse sequences. Segmented 3D sequences can acquire multiple slices during one breath hold. The acquisition time is typically longer than in 2D sequences, which may cause increased motion artifacts due to respiratory excursions. Often the images have poorer contrast resolution. Thinner slices can be acquired with 3D sequences.

Another option is single-shot IR-SSFP sequences, in which all the information necessary for a complete image is acquired during one R–R interval after a single inversion pulse. While the attainable spatial resolution is limited with this technique, it is possible to image the entire left ventricle in one breat-hold, and the single-shot acquisition can provide artifact-free images

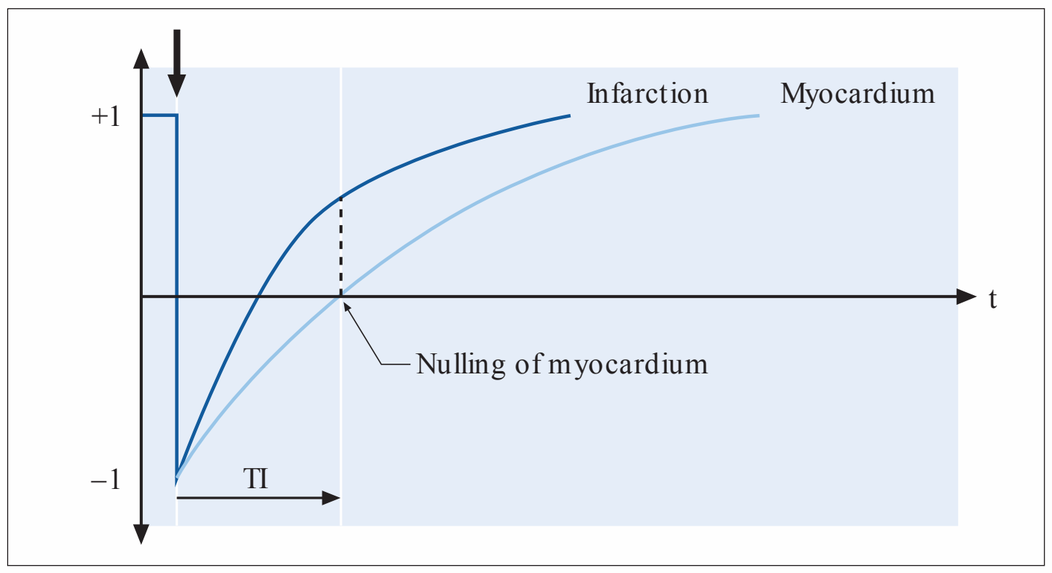

Fig. 6.27 Principle of the inversion recovery preparation pulse. Longitudinal magnetization is plotted over time. The magnetization is turned to negative by a 180° inversion pulse (arrow). The initial state is restored over time, and the magnetization recovers. Owing to the T1-shortening effect of the Gd contrast agent, recovery occurs faster in enhancing myocardial segments (dark blue) than in viable, nonenhancing myocardium (light blue). By adjusting the inversion time TI so that image acquisition takes place when the magnetization from normal myocardium is crossing the horizontal axis, maximum contrast is obtained between enhancing infarction/scar tissue and nonenhancing (viable) myocardium.

even in arrhythmic patients and patients who cannot hold their breath.

Essential Point
Segmented 2D inversion-recovery turbo gradient-echo sequences are the current standard for delayed-enhancement imaging. Single-shot IR-SSFP sequences may be helpful in patients with arrhythmias.

Protocol for Delayed-Enhancement Imaging

The protocol for delayed-enhancement MRI should always include SSFP cine sequences for the analysis of wall motion. The contrast agent can be administered before or after functional imaging; the latter option is, however, preferred.

The main argument for contrast administration before functional imaging is that it shortens the examination time, since the waiting interval between contrast injection and the acquisition of delayed-enhancement images can be utilized to acquire the cine functional sequences. This method has several disadvantages, however. First, the myocardium has higher signal intensity in the SSFP sequences if contrast material has already been administered, and this reduces contrast between the myocardial wall and the left ventricular cavity. Second, an early phase after contrast administration cannot be acquired and utilized for the detection of cardiac thrombi or no-reflow zones in acute infarctions. And third, there is a theoretical risk of missing the optimum time for the acquisition of delayed-enhancement images.

The other, somewhat more time-consuming option is to withhold contrast injection until after functional imaging is completed. This allows us to "monitor" the progression of delayed enhancement to optimize the timing of image acquisition. This method also eliminates the problem of contrast material adversely affecting the contrast in the SSFP cine images. After functional imaging is completed, the total dose of Gd contrast agent (0.1 or 0.2 mmol/kg bw) is administered by bolus injection via a peripheral vein. The "double dose" of 0.2 mmol/kg bw has two measurable advantages over the single dose, besides producing a more vivid image:

Table 6.7 Technical parameters for delayed-enhancement imaging. Example of a typical ultrafast inversion-recovery gradient-echo sequence (turbo FLASH) for the detection of delayed enhancement[110]

Repetition time (TR)	8.0 ms
Echo time (TE)	4.0 ms
Flip angle	20°
Inversion time (TI)	200–260 ms (individually adjusted)
Bandwidth	130 Hz/Px
Echoes/segment	23
Matrix	166 × 256
Temporal resolution	184 ms
ECG triggering	Mandatory
Coils	Surface and body coil
Respiratory triggering	Breath-hold technique

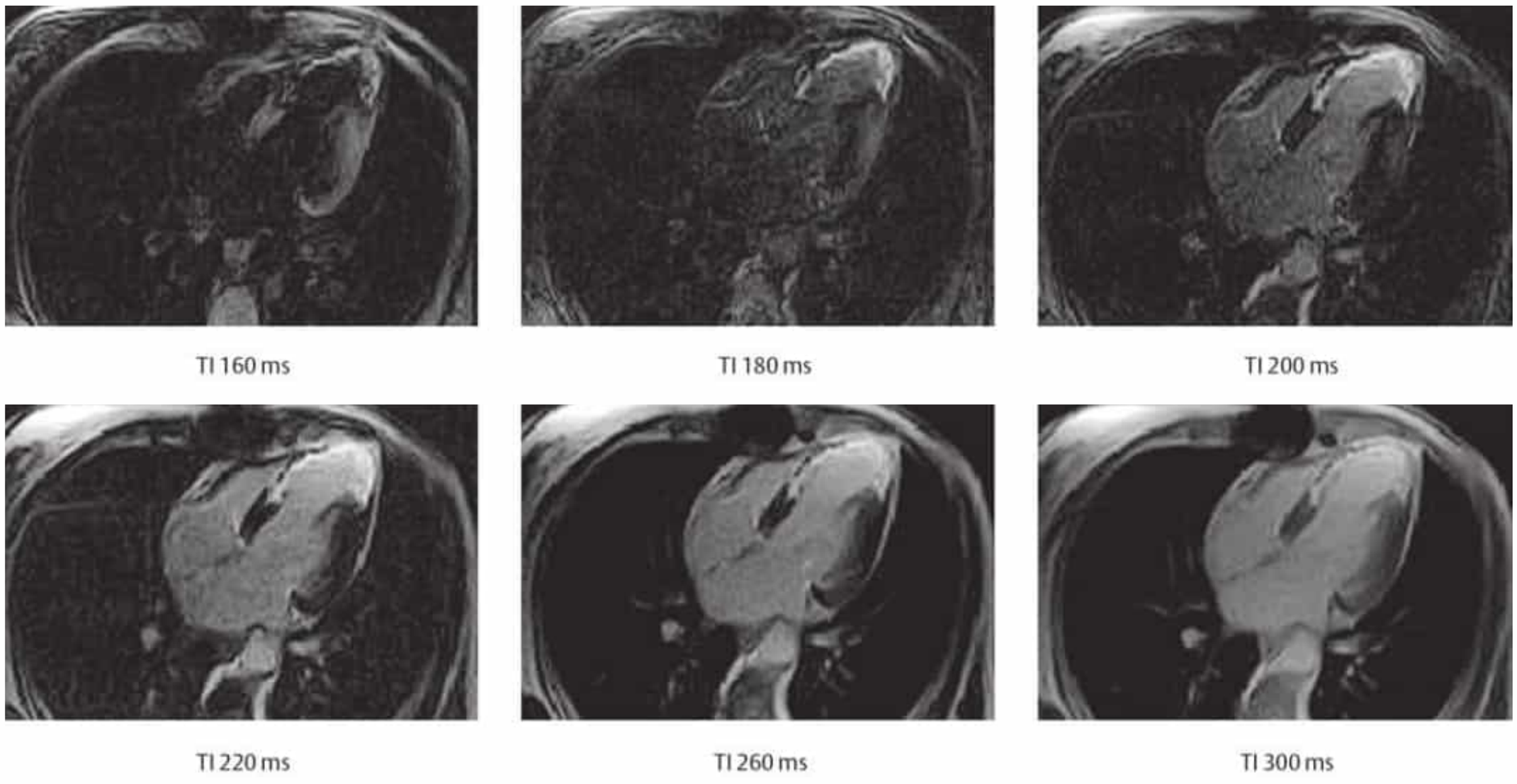

Fig. 6.28 Effect of inversion time (TI) on image contrast. The metal artifacts are from sternal wires from previous bypass surgery. A predominantly transmural scar in the septal and apical myocardial segments is imaged with fast inversion-recovery gradient-echo sequences 10 minutes after injection of 0.2 mmol/kg bw Gd-DTPA. The images were acquired with various inversion times (TI). The optimum TI setting in this example is 260 ms, depicting a uniformly hypointense (nulled) myocardium with very high contrast between normal myocardium and scar.

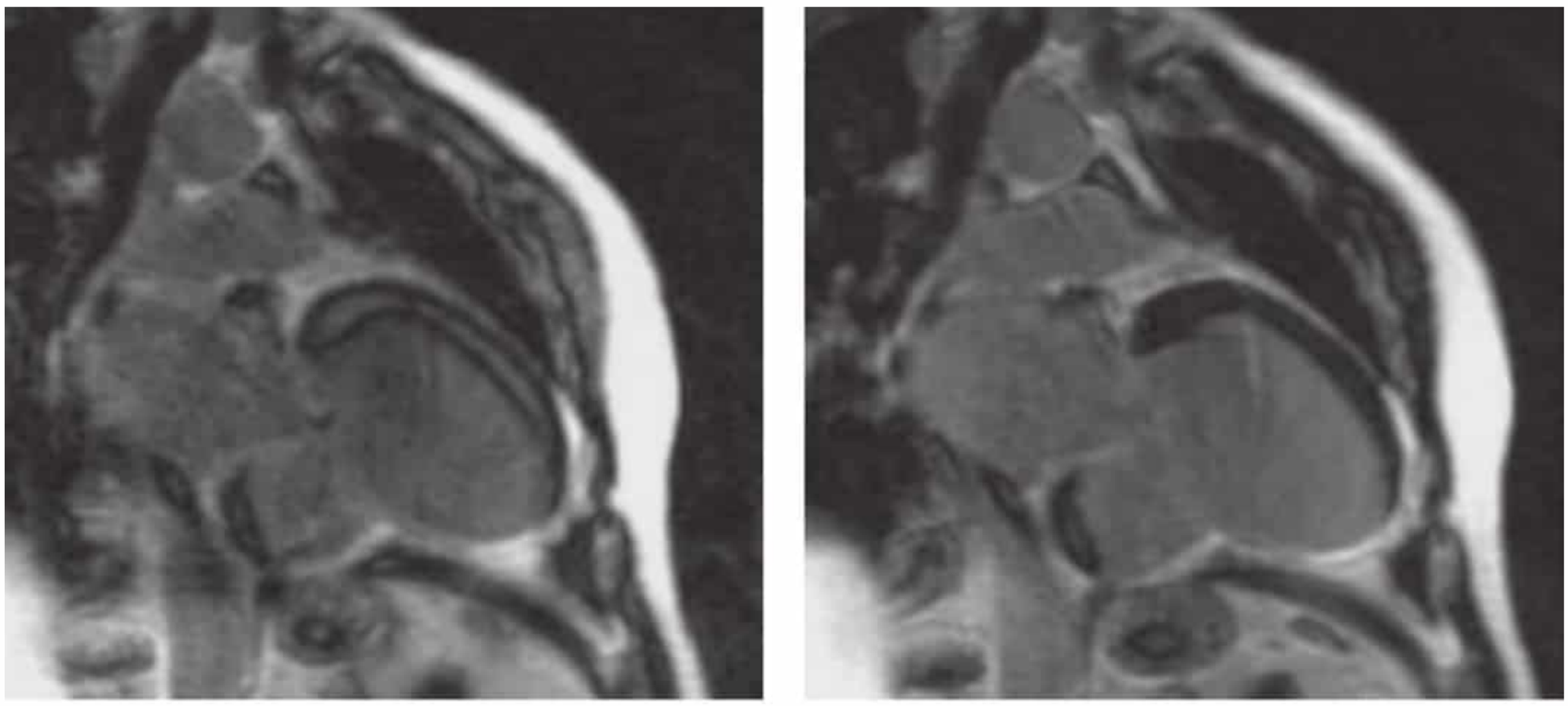

Fig. 6.29 Optimizing the inversion time (TI) during the acquisition. This patient has a large transmural myocardial scar involving the entire inferior wall with a basal aneurysm and overlying thrombus. Fast inversion-recovery GE images 10 minutes after injection of 0.2 mmol/kg bw Gd-DTPA. The image on the left was acquired with a TI of 220 ms. This TI is too short, as the healthy anterior myocardial wall does not show homogeneous low signal intensity. A hyperintense streak is visible within the myocardium. Increasing the TI by 20 ms (right) provides effective, homogeneous nulling of healthy myocardium.

- It increases the contrast between normal and abnormal myocardium.
- A longer time window is available for image acquisition.[114]

The change of image contrast can be observed in selected 2D slices during the initial minutes following contrast administration. Repeating the acquisition every 2 minutes ensures that the optimum time for data acquisition is not missed.

Essential Point
The selected slice position should display an area where abnormal wall motion has been found, as this will increase the likelihood of detecting delayed enhancement. The TI should be set at 200 ms for the initial acquisitions after contrast injection and can then be progressively increased as needed.

The scan delay for achieving optimum image contrast is highly variable and can range from 5 to 15 minutes. The acquisitions employ the inversion-recovery sequence described above and should completely cover both ventricles in short-axis slices with no interslice gaps (**Table 6.7**). The three standard long-axis slices should also be acquired. Identical planes should be imaged for the SSFP cine study and for the inversion-recovery GE sequences so that the slices can be compared. A slice thickness of 8 mm is the best compromise for detecting infarcted areas in the 2D sequences: it minimizes image noise while allowing the entire ventricle to be examined within an acceptable time.

Essential Point
Small areas of delayed enhancement are sometimes difficult to distinguish from artifacts. Apparent abnormalities should always be visualized in two orthogonal planes. Also, the differentiation of artifacts and lesions can sometimes be aided by rotating the phase- and frequency-encoding direction or slightly varying the TI. This will cause artifacts to disappear or change their location, while true abnormalities will remain unchanged.

Delayed Enhancement—From Image to Differential Diagnosis

The phenomenon of delayed enhancement is not specific for myocardial infarction and may be found in various other myocardial diseases.[115] Delayed enhancement in chronic myocardial infarction typically appears as an area of homogeneous hyperenhancement with very well-defined margins that may be confined to the subendocardial layers or may extend across the full thickness of the myocardial wall. This pattern is also seen in association with acute myocardial infarction, but the area of delayed enhancement often presents less well-defined margins. Acute myocardial infarction is in some cases also characterized by the presence of hypointense "no-reflow zones" at the center of the delayed enhancement area. Another important feature of ischemic changes is that the delayed enhancement involves the vascular territories of one of the three main coronary arteries.[116]

Essential Point
Acute and chronic myocardial infarctions invariably involve the subendocardial layer of the myocardium, which manifests delayed enhancement.

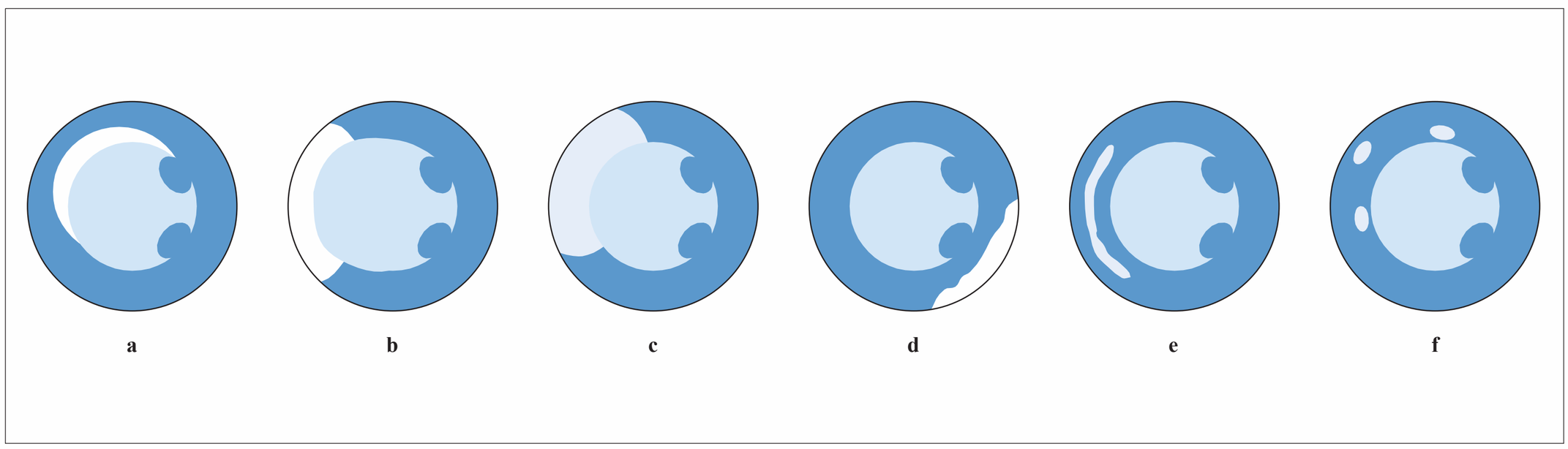

Fig. 6.30 a–f Various patterns of myocardial delayed enhancement, demonstrated by a fast gradient-echo sequence in the equilibrium phase after Gd contrast administration.

a–c Typical patterns of ischemic delayed enhancement.
a Anterior and anteroseptal subendocardial scar in chronic myocardial infarction shows a sharply defined, very hyperintense pattern of delayed enhancement.
b Transmural scar in chronic myocardial infarction shows wall thinning and a sharply defined, very hyperintense pattern of delayed enhancement.
c Faint, somewhat ill-defined transmural pattern of delayed enhancement in an acute or subacute myocardial infarction.
d–f Typical patterns of nonischemic delayed enhancement.
d Subepicardial late enhancement, as in chronic pericarditis or myocarditis.
e Midmyocardial late enhancement, as in dilated cardiomyopathy or chronic myocarditis.
f Speckled pattern of delayed enhancement with lower signal intensities.

While delayed enhancement consistently involves the subendocardial myocardium in ischemic myocardial diseases, it may spare the subendocardial layer in diseases with a nonischemic cause. If delayed enhancement is confined to the subepicardial or midventricular portion of the myocardial wall, it is reasonable to exclude myocardial ischemic damage as the cause.[117] Nonischemic delayed enhancement often appears less sharply defined or may produce a speckled pattern of involvement that does not conform to a particular coronary vascular territory (**Fig. 6.30**). It should be noted that this very heterogeneous group of nonischemic conditions include entities that produce typical patterns of delayed enhancement on MRI.[118] These patterns will be discussed in the chapters dealing with specific diseases.

Essential Point
MRI can advance the differential diagnosis of ischemic and nonischemic myocardial diseases based on typical patterns of delayed enhancement.

Magnetic Resonance Angiography of the Coronary Arteries

C. U. Herborn

MR angiography (MRA) has replaced conventional catheter-based angiography as the imaging modality of first choice for many vascular regions. Although MR coronary angiography (MRCA) can now be applied clinically as a result of technical advances in modern scanner systems,[119] it cannot yet replace cardiac catheterization for most clinical investigations. The problems with MRCA result from the small vessel diameters, the tortuous course of the vessels, and especially the constant motion imposed by respiratory and cardiac activity. MRCA has made significant improvements in spatial resolution and motion-correction algorithms, but the inability to achieve diagnostic image quality in all patients continues to be a problem. Nevertheless, MRCA can be used clinically in the detection or exclusion of coronary anomalies, in Kawasaki disease, and in selected cases for the exclusion of stenosing coronary artery disease (CAD) of the proximal coronary vessels.[120] Current research projects are focused on the use of parallel imaging for fast data acquisition, new strategies for k-space sampling, the use of intravascular contrast agents,[121,122] and imaging at field strengths higher than 1.5 T.[123]

Planning the Examination

Most current experience with MRCA is based on the use of 1.5 T scanners with high-performance gradient systems (slew rate >150 mT/m/ms), and initial reports indicate comparable results with magnets operating at 3.0 T. Scanners with a lower field strength or less powerful gradient systems are not recommended for MRCA.

One of the first decisions to be made is whether to use breath-hold technique or navigator technique (see below) for

MRCA. This is important because data acquisition in breath-hold MRCA is typically performed in inspiration to maximize the length of the breath-hold, whereas data acquisition with navigator gating is performed at end-expiration. Because the three-dimensional (3D) volumes are very thin, especially in breath-hold imaging, accurate scan prescription for complete coverage of the coronary arteries can be done only on scout images that have been obtained in the same respiratory position as the MR angiographic images.

Essential Point
Obtain scout images for breath-hold MRCA in inspiration, whereas scout images for free-breathing navigator MRCA should be obtained in expiration.

Localization of the coronary vessels and prescription of the 3D volumes for the MRCA sequence can be done with fast dark-blood sequences (e.g., half-Fourier acquisition single-shot turbo spin-echo, HASTE) or bright-blood sequences (e.g., steady-state free precession, SSFP), which are usually imaged in axial planes. Multiple 3D MRCA acquisitions are usually obtained in different oblique planes to define the entire coronary system. A para-sagittal slice orientation is recommended for visualization of the right coronary artery (RCA). It is helpful to use a three-point Planscan tool in which the scan plane is defined by three points that can be freely selected. For imaging the RCA, the first point is placed at the RCA ostium, the second in the descending part of the vessel, and the third at the distal part of the RCA.

Essential Point
For MRCA of the right coronary artery the posterior RF coil elements may be switched off to minimize wrap-around artifacts. This allows for a small field of view and better spatial resolution.

The left coronary artery is usually visualized in a para-axial plane (**Fig. 6.31**). When three-point Planscan is used, the first point is placed at the ostium of the left main coronary artery (LCA), the second in the midportion of the left anterior descending artery (LAD), and the third at the junction of the proximal and middle thirds of the left circumflex artery (LCX). Owing to the short acquisition time, additional 3D datasets can be acquired in other orientations during breath holding to visualize all segments or demonstrate abnormalities in a second plane.

An alternative to visualizing the coronary arteries in multiple oblique 3D slabs (volume cardiac angiography with targeted scans, VCATS) is "whole heart" MRCA, in which navigator gating must be used. In this method only one axial 3D volume with almost isotropic voxels is acquired, covering the entire heart from the aortic root to the diaphragm. A successful study requires the use of extremely fast pulse sequences (preferably SSFP) with good contrast, a relatively long data acquisition window during the cardiac cycle, and parallel imaging techniques so that the data can be acquired in an acceptable time, i.e., 5–10 minutes. Initial results in subjects and in patients with suspected CAD are very promising and demonstrate the potential

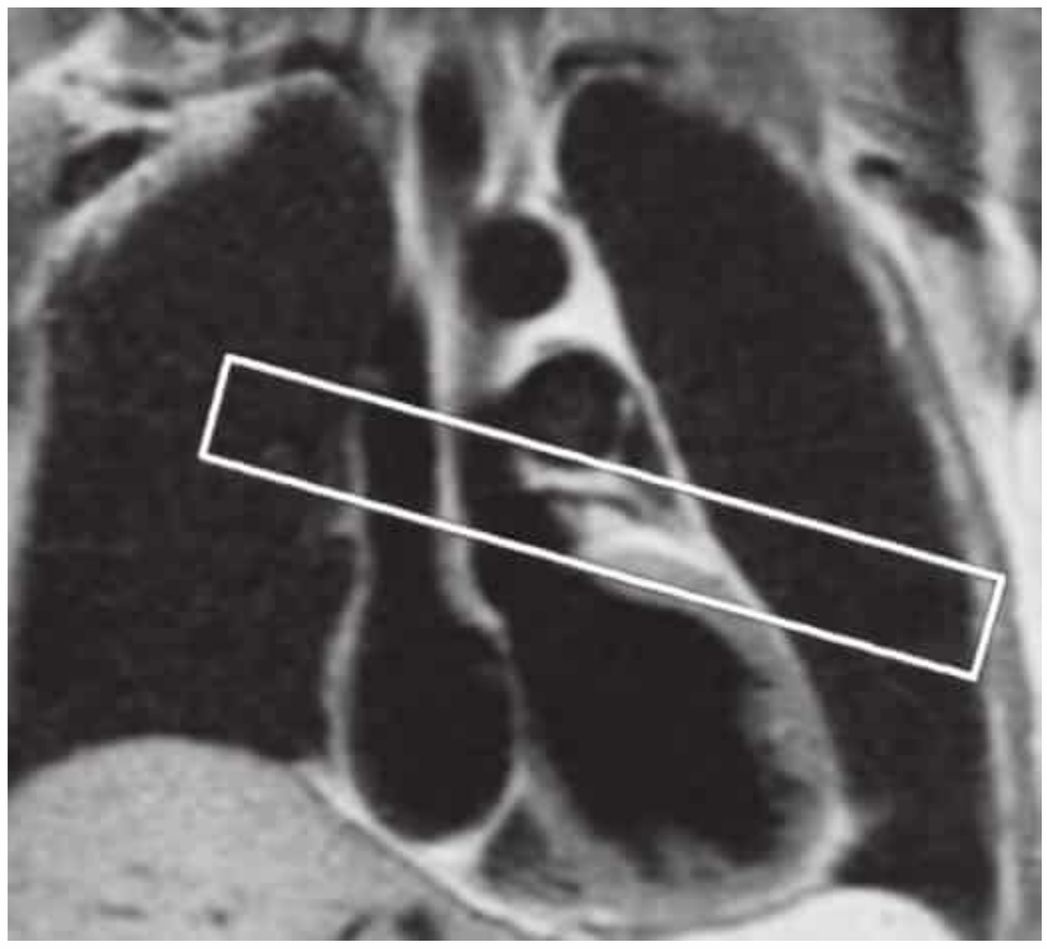

Fig. 6.31 Imaging slab (3D volume, white box) for examination of the left coronary system.

of this technique for coronary artery imaging.[124,125] While this technique simplifies planning, it also has several disadvantages: lower spatial resolution, greater image noise (usually higher acceleration factors for parallel imaging), and still a relatively long acquisition time.

Compensation for Cardiac Motion

ECG triggering is essential to compensate for cardiac motion. Good image quality requires a robust ECG signal and a regular sinus rhythm. Data acquisition typically occurs in mid-diastole during the isovolumetric relaxation phase before the start of the next atrial contraction.

Essential Point
The optimum phase for data acquisition can be determined with a cine SSFP sequence in the four-chamber view. This plane cuts segment 2 of the RCA at an orthogonal angle in the right atrioventricular groove. Because this portion of the RCA undergoes the greatest amplitude of motion, the start and duration of the diastolic rest period are most easily determined in this plane.

The duration of the diastolic rest period varies considerably with the heart rate, and so the length of the data acquisition window within the cardiac cycle requires individual adjustment. If the selected data acquisition window is too short, it will needlessly prolong the total examination time. If the window is too long, motion artifacts will result. The most common data acquisition window setting is from 80 to 150 ms. Breath-hold imaging requires a higher setting because the length of the breath-hold limits the total acquisition time.

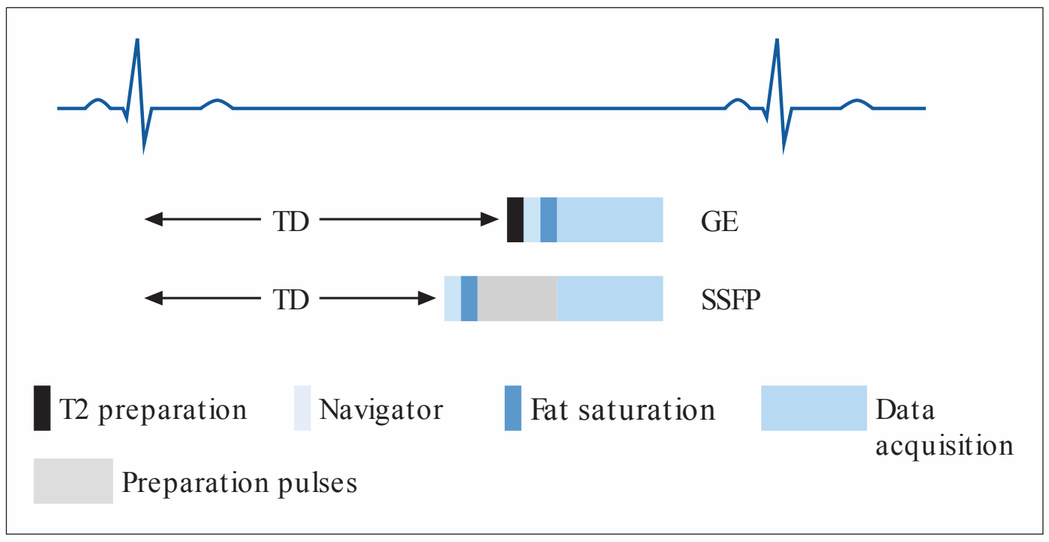

Fig. 6.32 Gradient-echo (GE) sequence and steady-state free precession (SSFP) sequence with corresponding preparation pulses during the R–R interval.

Essential Point
The trigger delay after the R-wave, which must be set in the user interface is not necessarily equal to the start of the diastolic rest period identified in the cine sequence.

The pulse sequence for coronary angiography consists of various components: a navigator pulse, a high-frequency fat suppression pulse, and a T2 preparation pulse and/or high-frequency pulses to produce equilibrium magnetization in SSFP sequences before the start of data acquisition (**Fig. 6.32**). Because these components vary from sequence to sequence and also vary among different manufacturers, generally applicable recommendations cannot be made. It is important to know the precise makeup of the sequence, however, to make sure that the starting point for data acquisition, rather than the start of the preparation pulses, is synchronized to the start of the diastolic rest period.

Essential Point
Because the heart rate may vary during the examination, the optimum data acquisition window should be determined just before the start of the MRCA sequence, and this acquisition should be repeated as needed during the course of the examination.

Compensation for Respiratory Motion

Respiratory motion is compensated by breath-hold imaging or by navigator gating, which permits images to be acquired without breath-holding. Both methods have their advantages and disadvantages, and it is difficult to predict which will yield better results in a particular patient.

Breath-Hold Coronary Magnetic Resonance Angiography

The total acquisition time in breath-hold imaging ranges from 20 s to a maximum of 40 s depending on the ability of the patient to suspend respirations. Thus, the maximum attainable spatial resolution and the number of slices per 3D volume (and therefore the thickness of the 3D slab) are less than when the navigator technique is used.

Essential Point
A navigator should be obtained even in breath-hold imaging.

A navigator should also be used in breath-hold imaging to document the motion of the diaphragm. This makes it possible not only to check the reproducibility of the diaphragm position but also to match the total acquisition time to the maximum duration of a breath-hold. Some patients can maintain a perfect plateau from the start of the breath-hold command through the end of the acquisition (**Fig. 6.33 a**). These patients are the best candidates for breath-hold MRCA. The mean duration of the plateau phase in patients with CAD is ~27 s.[126] In other patients the breath-hold command is followed by an initial drift of the diaphragm, and some time is needed before a plateau is established (**Fig. 6.33 b**). Data acquisition in these patients should be delayed for several seconds after the breath-hold command is given. Two other patterns that may be seen are continuous irregular diaphragm movements or a continuous drift of the diaphragm position. These patterns are encountered in ~20% of patients, and this subset of patients are not good candidates for breath-hold MRCA.

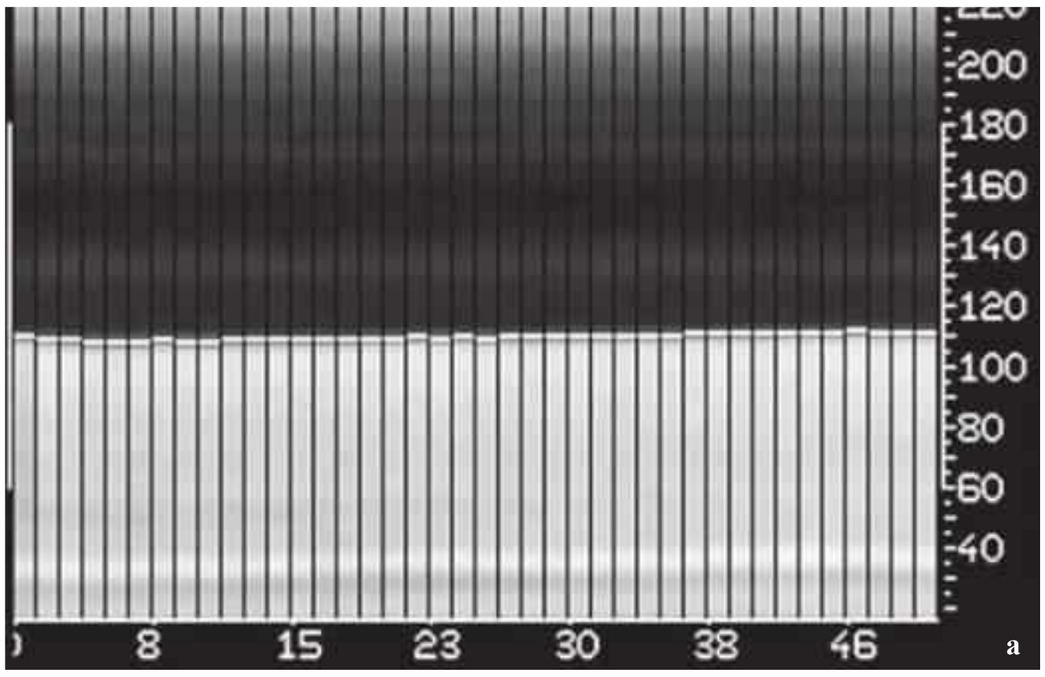

Fig. 6.33 a, b Navigator profiles.
a Perfect breath hold documented with navigator pulses in coronary MRA.
b Deep inspiration is followed by an initial drift of the diaphragm. It takes 8 s for diaphragm position to reach a plateau phase in which angiographic data can be acquired.

Breath-hold MR imaging has several advantages: it saves time, is easy to implement technically, and permits the use of clinically approved extracellular contrast agents, which provide coronary artery visualization only during the arterial phase. On the other hand, the examination depends strongly on the breath-holding ability of the patient.[127]

Free-Breathing Coronary Magnetic Resonance Angiography

In this technique the patient can breathe normally during data acquisition because the motion of the diaphragm is tracked during the examination with navigator echoes, and only data acquired in expiration are utilized for image reconstruction.

The navigator, usually in the form of a cylindrical excitation pulse, is placed on the right hemidiaphragm and tracks the respiratory displacement of the right lung–liver interface in the craniocaudal direction (**Fig. 6.34**). The interface is easily detected automatically and in real time because the liver has high signal intensity and the lung has low signal intensity.

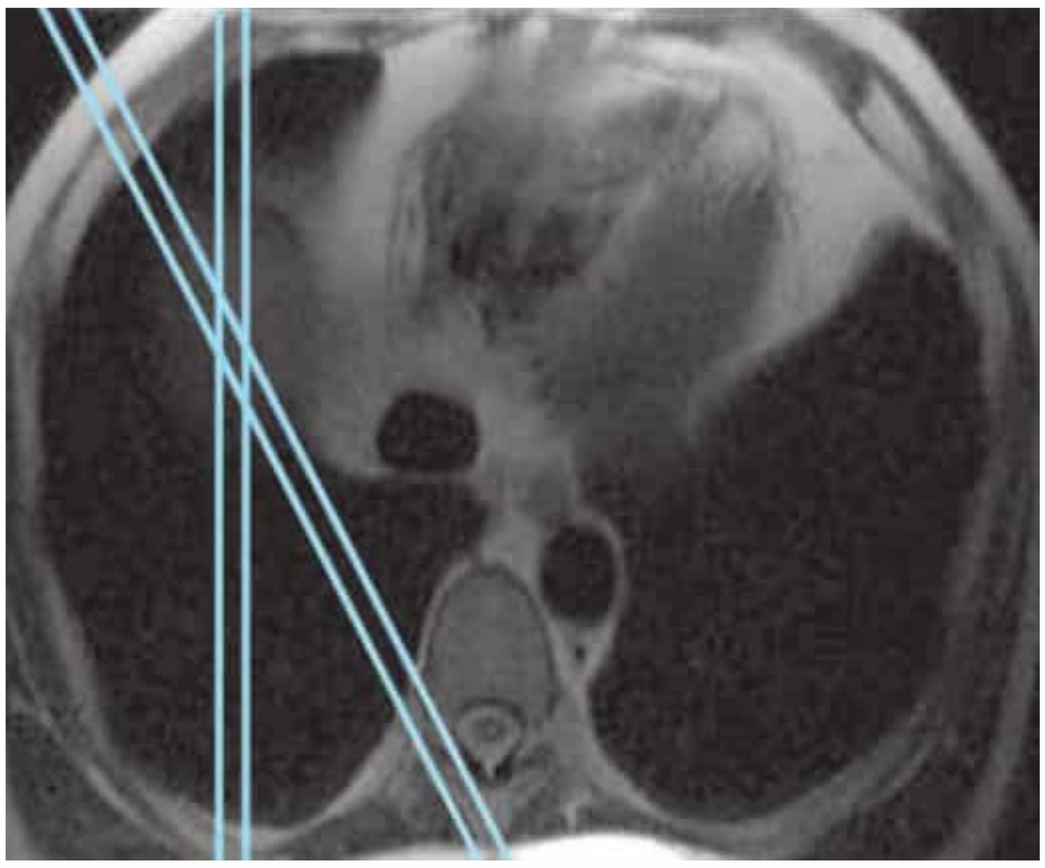

Fig. 6.34 Example of navigator pulses positioned at the liver–diaphragm interface for documentation of diaphragm motion in free-breathing coronary MRA.

Essential Point
Place the navigator precisely on the dome of the right hemidiaphragm, as this site undergoes the greatest excursions and yields the best navigator signal.

During acquisition of the MRCA sequence, it is determined at each heart beat whether the position of the lung–liver interface falls within a user-preset acceptance window. If the interface is inside the acceptance window, the acquired data are used for image reconstruction; otherwise the data are discarded and a new acquisition begins. Generally the acceptance window is a 3- to 5-mm-wide zone at end-expiration (**Fig. 6.35**). Because the navigator is intended to reflect the position of the coronary arteries during actual data acquisition, the position of the navigator pulse within the sequence is critical: it must come immediately before the imaging portion of the sequence.

The advantages of navigator gating are obvious. Spatial resolution is significantly better than in breath-hold imaging and is within the submillimeter range. One disadvantage of navigator gating is the relatively long total acquisition time, which is sometimes difficult to calculate. This is especially true in patients with an irregular breathing pattern and cases where the end-expiratory diaphragm position shifts during the course of the examination.

Essential Point
Decide initially whether to use breath-hold technique or navigator gating. Obtain scout images in inspiration (for breath-hold imaging) or expiration (for navigator gating). Select the optimum data acquisition window in the cardiac cycle and adjust the sequence accordingly. Start the acquisition and hope for good images.

Contrast Mechanisms in Coronary Magnetic Resonance Angiography

The ability to evaluate small structures in MRCA depends on spatial resolution and on the contrast between these structures and their surroundings. In principle, the coronary arteries can be depicted with high or low signal intensity in MRCA. Today

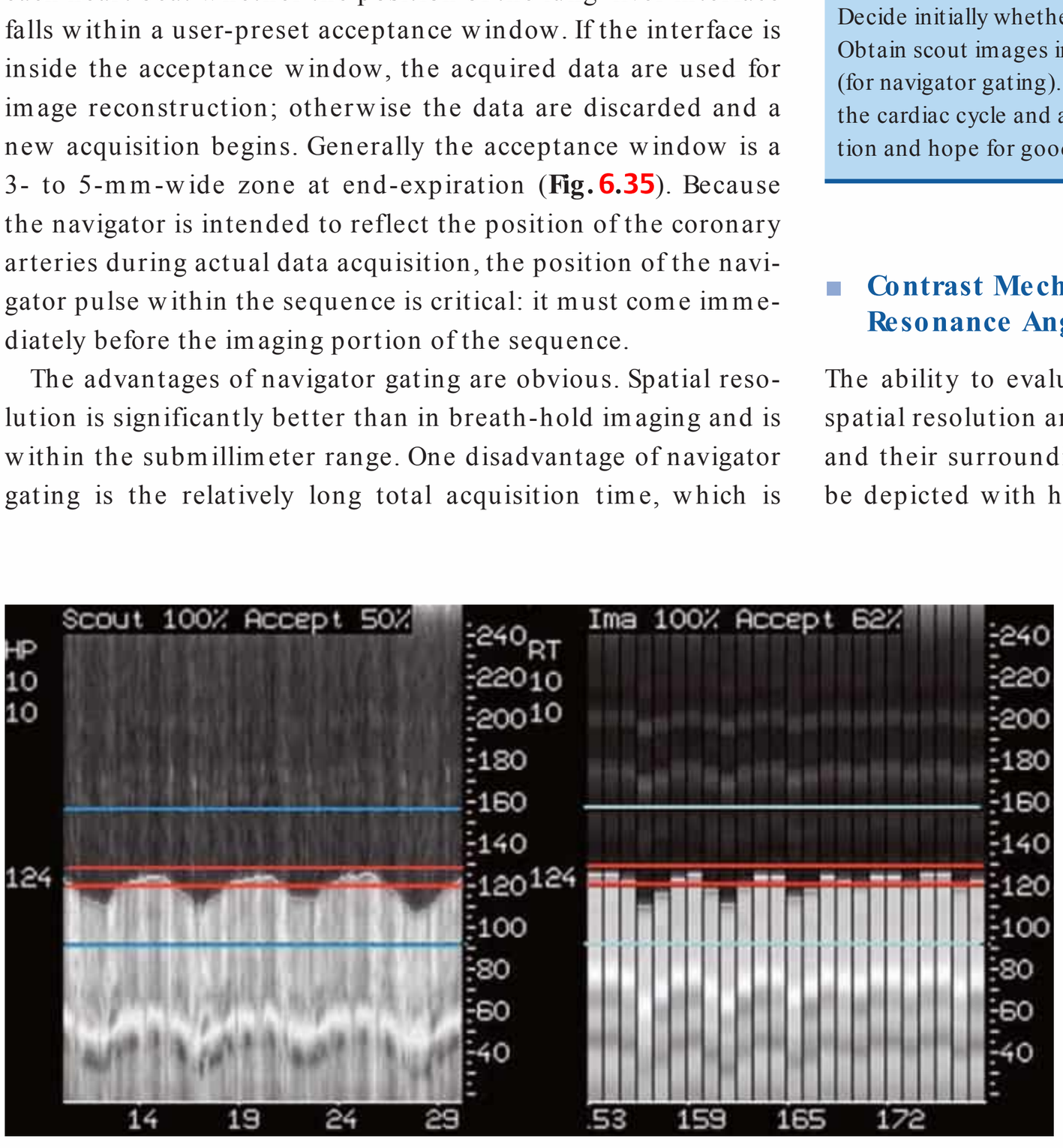

Fig. 6.35 Navigator echoes document diaphragm motion in real time. The red bars indicate the region in which data are accepted for image acquisition.

black-blood sequences are used almost exclusively for investigations of the vessel wall, while bright-blood sequences are used for coronary angiographic imaging.

Because the coronary vessels are partially surrounded by fat and myocardium in their course, it is important to obtain good contrast between the vessels and these other tissues. Contrast between vessels and fat is maximized by starting the sequence with the application of a frequency-selective fat-suppression pulse.[128] This is particularly useful in visualizing the proximal portions of coronary vessels, which are generally surrounded by epicardial fat.

Essential Point

Good fat suppression and a very homogeneous magnetic field are essential for effective MRCA. The scanner should be re-shimmed if necessary or shimmed with a small target volume in the cardiac region.

The more distal coronary segments, especially the LAD, are surrounded more by myocardium than fat, and suppression of the myocardial signal is desirable in that region. This can be done with a T2 preparation pulse consisting of a combination of 90° and 180° pulses. The function of this preparation pulse is to suppress the signal from tissue with a short T2 relaxation time (myocardium: 50 ms). A positive side effect is that deoxygenated blood is also suppressed because of its short T2 time, and this makes it easier to differentiate the coronary arteries from epicardial veins.

Data readout can be done with either gradient-echo (GE) or SSFP sequences, but SSFP sequences are increasingly preferred over older GE sequences owing to their very good signal-to-noise ratio, their immunity to flow effects, and the very short acquisition times. The image contrast obtained with these sequences depends on the T2/T1 ratio in the examined tissue.[129] Because this ratio is markedly higher for blood than for myocardium, the coronary arteries in SSFP sequences appear bright against a relatively dark myocardial background. Because fat also appears extremely bright in SSFP sequences, frequency-selective fat suppression is also necessary (**Fig. 6.36**).

Contrast Agents for Coronary Magnetic Resonance Angiography

Paramagnetic contrast agents shorten the T1 relaxation time of tissues, leading to an improvement of SNR and CNR. In first-pass imaging after intravenous contrast injection, the T1 time of the arterial blood is less than 100 ms. This forms the basis for extremely high-contrast visualization of the vessel lumen. However, currently available extracellular contrast agents diffuse very quickly into the interstitium following IV administration, with the result that MRA can be performed only during the first systemic pass of the agent immediately after the injection.[128,130–132] This time window is adequate for the breath-hold acquisition of 3D image volumes, but these agents are not advantageous for MRCA with navigator gating.

The clinical introduction of new intravascular contrast agents may overcome these limitations in the near future. These compounds remain in the blood for a longer time owing to their molecular size or transient binding to albumin, and consequently a longer time window is available for imaging. This is particularly advantageous for data acquisition with high-resolution navigator sequences.[133] Any desired number of breath-hold or navigator-gated images of all three main coronary arteries can be acquired after a single contrast injection.

Inversion-recovery (IR) sequences are used for data acquisition. The inversion time (TI) is set to null the signal from myocardium. IR sequences must include a navigator-restore pulse to ensure acceptable navigator gating. Initial studies of intra-

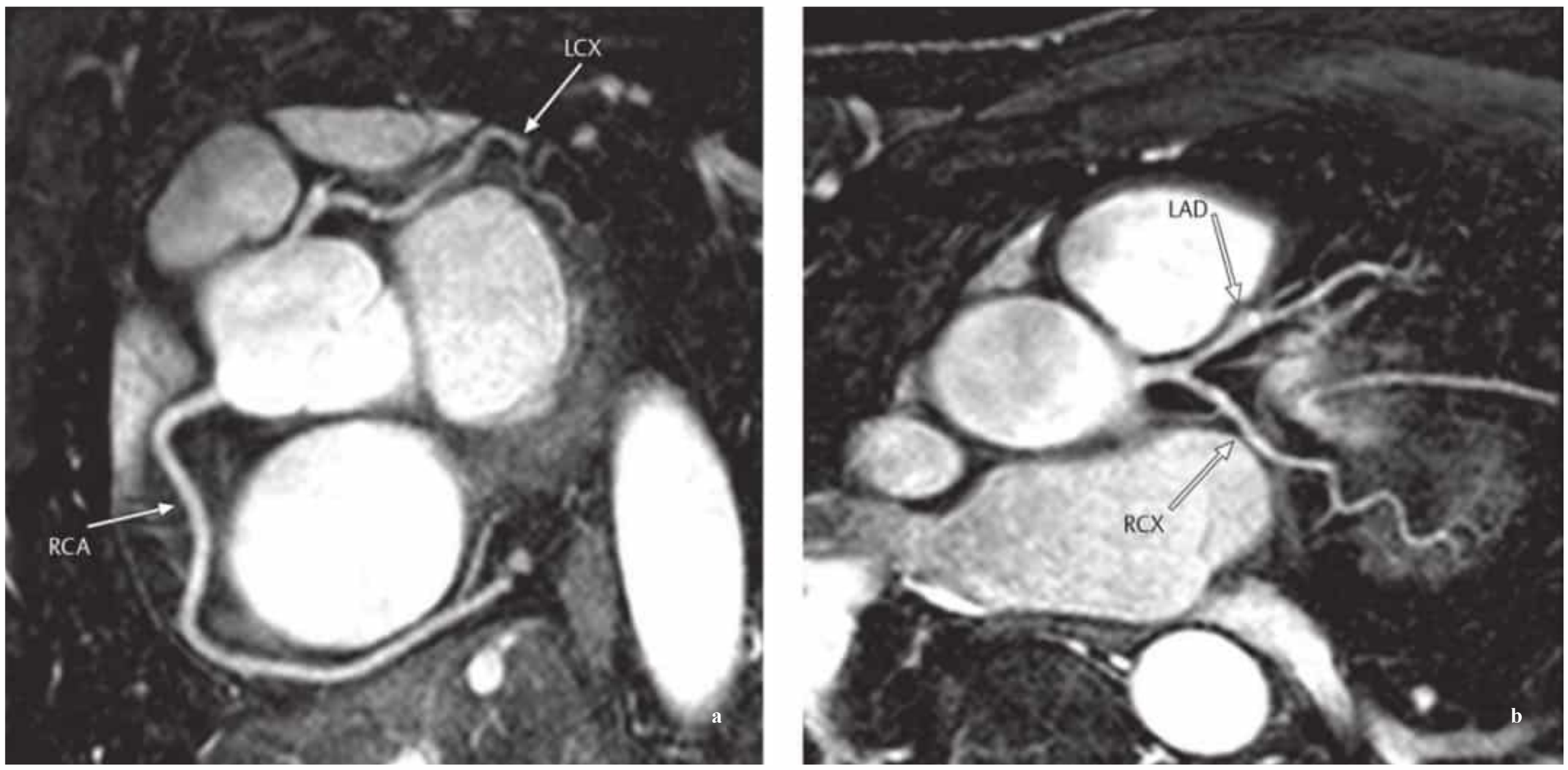

Fig. 6.36 a, b MRCA in a healthy volunteer. A T2-prep 3D SSFP sequence was used for data acquisition, providing a spatial resolution of 0.99 mm × 0.99 mm × 3 mm (with kind permission of R. M. Botnar, Technical University of Munich).

vascular contrast agents in healthy subjects and limited comparisons of conventional coronary angiograms with coronary MRA demonstrate the great potential of these new compounds. Not only can these agents significantly improve the SNR and CNR, but they can also increase the number of assessable coronary segments and improve the delineation of the coronary arteries relative to their surroundings (**Figs. 6.37, 6.38**).[120–122,134]

Clinical Applications

Coronary Artery Disease

To date, two major studies have been published on the use of MRCA in the diagnosis of CAD. Navigator gating was used in both studies. In one study of 107 patients with suspected CAD, Sommer et al. investigated the diagnostic accuracy of high-resolution 3D coronary MRA using navigator correction.[135] Diagnostic image quality was achieved in three-fourths of the cases, and the sensitivity and specificity for stenosis detection in the proximal and middle segments of the main coronary arteries were 88% and 91%, respectively (**Figs. 6.39, 6.40**). Similar results were published by Kim et al., who compared navigator-gated MRCA with the gold standard of conventional angiography in 109 patients and found that MRCA detected CAD with a diagnostic accuracy of 72%[136] Overall, however, MRCA is not yet robust enough for routine clinical use even when it is limited to evaluations of the proximal and middle segments.

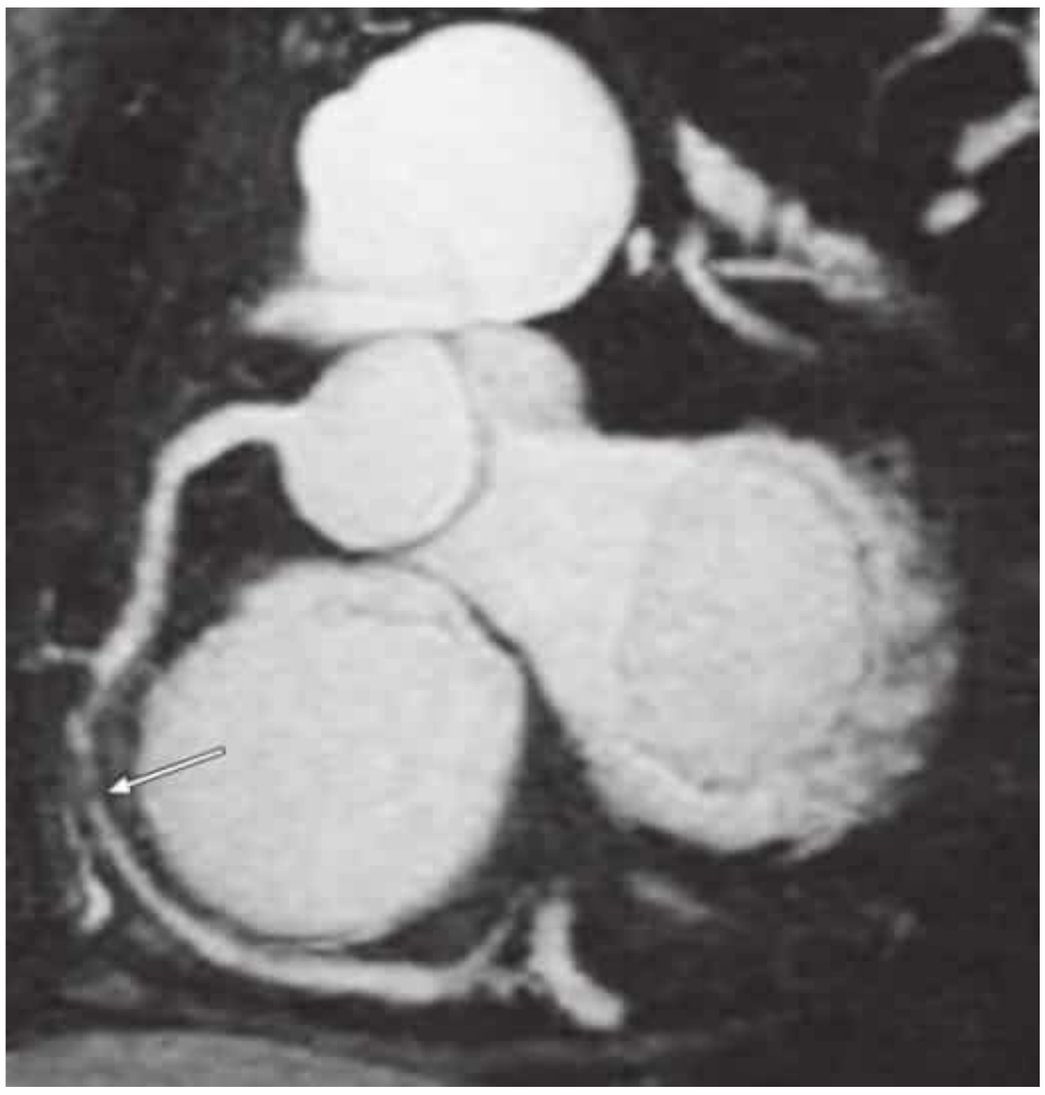

Fig. 6.37 MRCA after the injection of an intravascular contrast agent (Gadomer) demonstrates an ~ 50% stenosis (arrow) in the middle third of the right coronary artery.

Coronary Anomalies

The course of the proximal coronary arteries can be clearly visualized with MRA, permitting the confident detection of anomalies. Coronary anomalies have an estimated incidence of ~0.3–0.8% in the general population, and they have up to 30% incidence in patients with congenital heart disease. In the most common variant, the circumflex artery arises from the right sinus of Valsalva. There is another common variant in which the left coronary artery arises from the right sinus of Valsalva. Then it either passes anterior to the great vessels or courses between the aorta and RVOT. The second variant is called the "malignant type" because the artery may become compressed, especially during stress, leading to myocardial ischemia.[137]

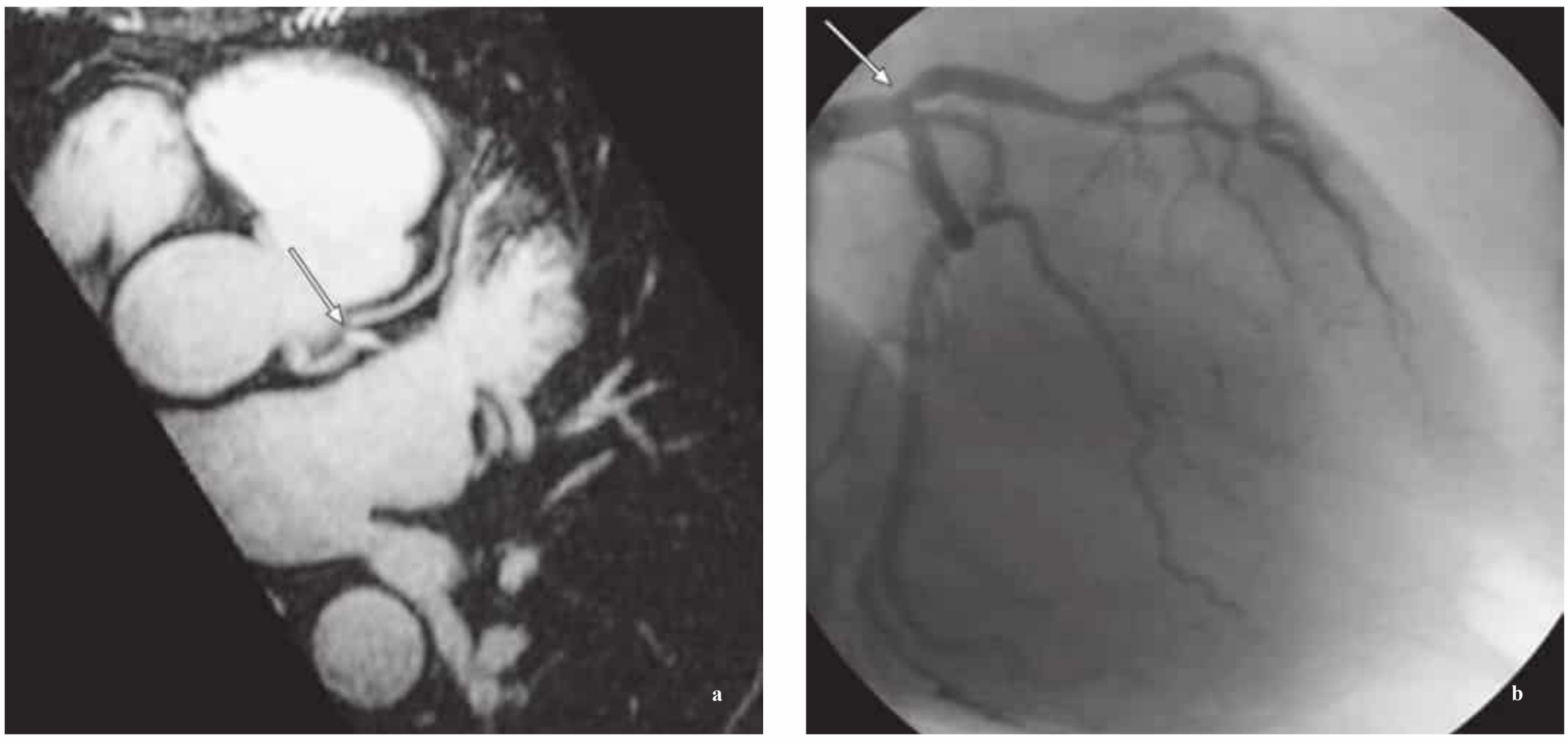

Fig. 6.38 a, b Gadomer-enhanced MRCA shows a stenosis of the left coronary artery at the origin of the circumflex artery (**a**, arrow). Correlative finding in conventional angiography (**b**, arrow).

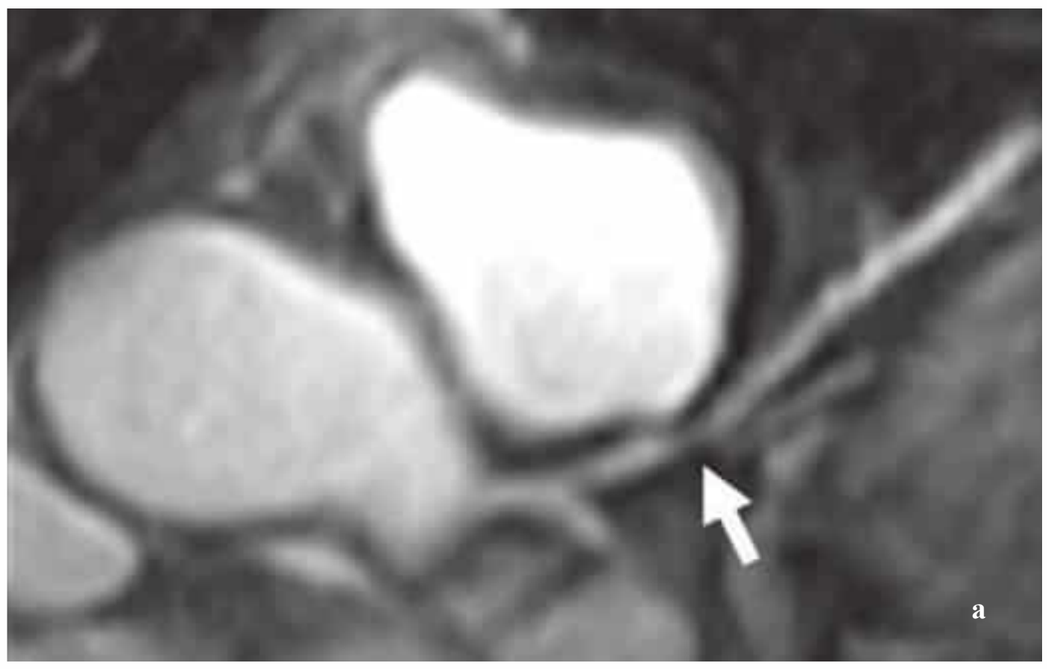

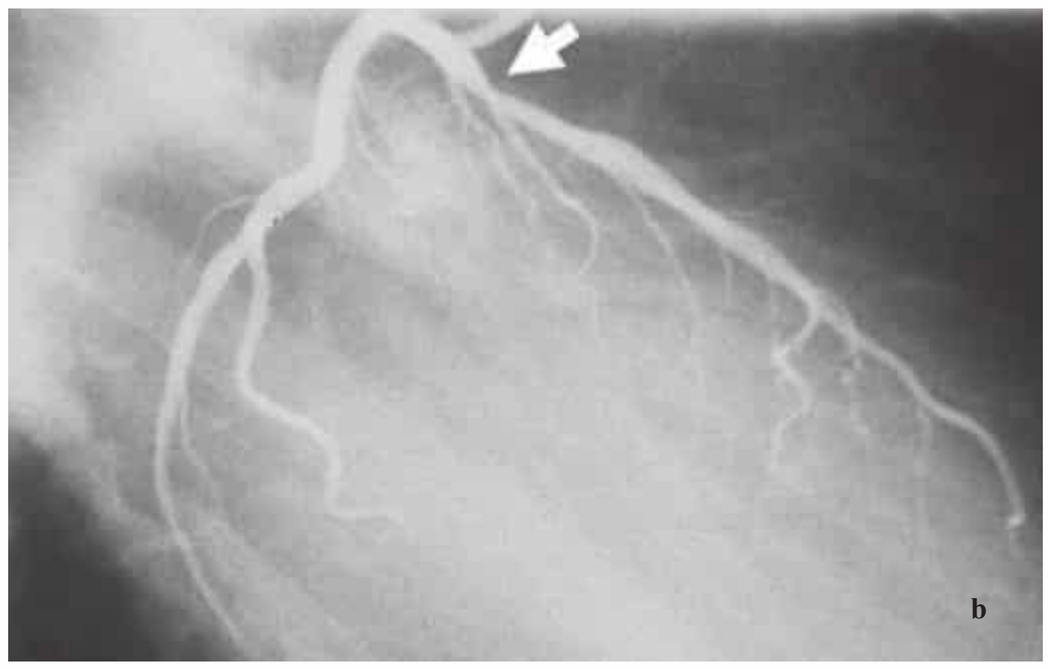

Fig. 6.39 a Unenhanced free-breathing MRCA demonstrates a stenosis in the proximal portion of the left coronary artery (arrow). **b** Finding at the same location on conventional angiography (arrow) (with kind permission of T. Sommer, Bonn University Hospital).

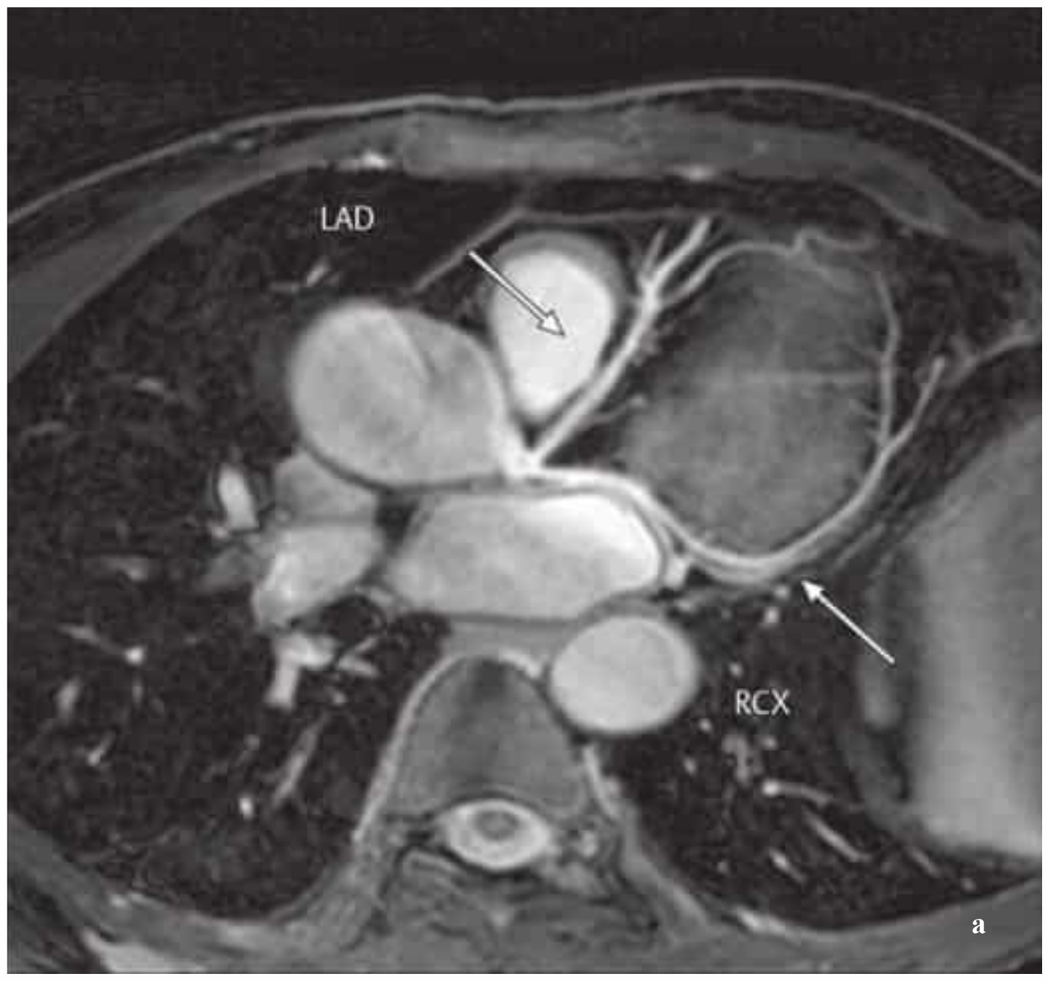

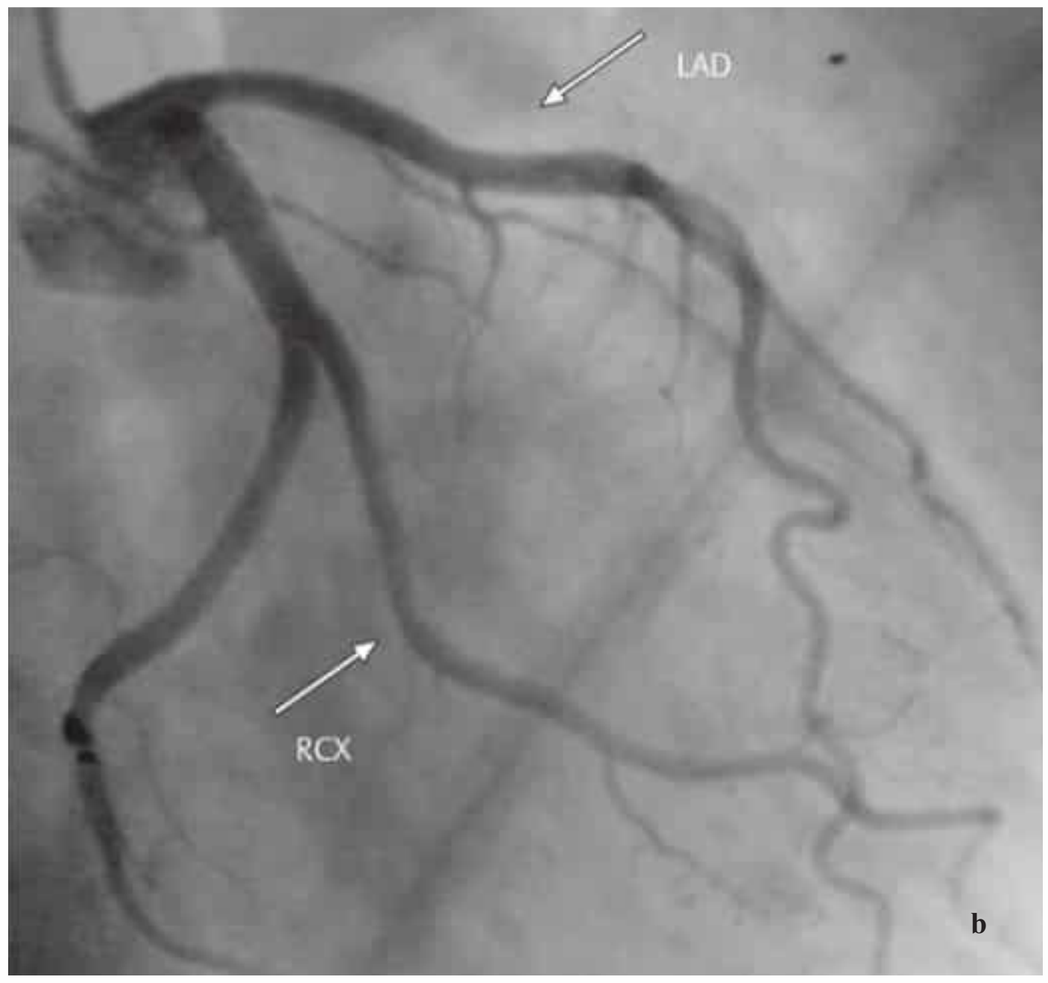

Fig. 6.40 a, b MRCA of the left coronary system in a patient with inflammatory signs and suspected Mediterranean fever shows no apparent abnormalities (**a**). Conventional angiography (**b**) confirms this finding (with kind permission of T. Ibrahim and R. M. Botner, Technical University of Munich).

Kawasaki Disease

Kawasaki disease is a generalized vasculitis of unknown etiology that occurs in small children and may eventually give rise to coronary vascular aneurysms. Subsequent thrombosis of these aneurysms and a reduction in blood flow may lead to myocardial infarction. The aneurysms often reach considerable size, and most are easily detected by MRCA.

Magnetic Resonance Angiography of the Great Vessels

K.-F. Kreitner

Although MRI has been used since its introduction in clinical practice for the investigation of flow effects, the development of clinically useful MR angiography techniques (MRA) did not begin until the mid-1980s. The first techniques to be developed were time-of-flight angiography and phase-contrast angiography. Used without intravenous contrast agents, they were the first techniques that permitted the selective visualization of flowing blood, making it possible to image the interior of vessels. However, they did not reach any clinical significance in the diagnosis of intrathoracic vascular diseases, because the intraluminal signal in both techniques is dependent on complex flow effects. Furthermore, respiratory movements and cardiac pulsations in the chest lead to motion artifacts, and the air-filled lung tissue induces susceptibility artifacts.

With advances in gradient technology, T1-weighted 3D sequences were developed that made it possible to acquire a complete dataset in less than 30 s. These sequences could be acquired during a single breath hold. The heavy saturation of flowing spins requires the use of an effective T1-shortening contrast agent to produce an intraluminal signal that is very bright in relation to the background.[138–141] These enhanced intraluminal signals are virtually independent of flow phenomena, making contrast-enhanced MRA somewhat similar to digital subtraction angiography (**Fig. 6.41**).

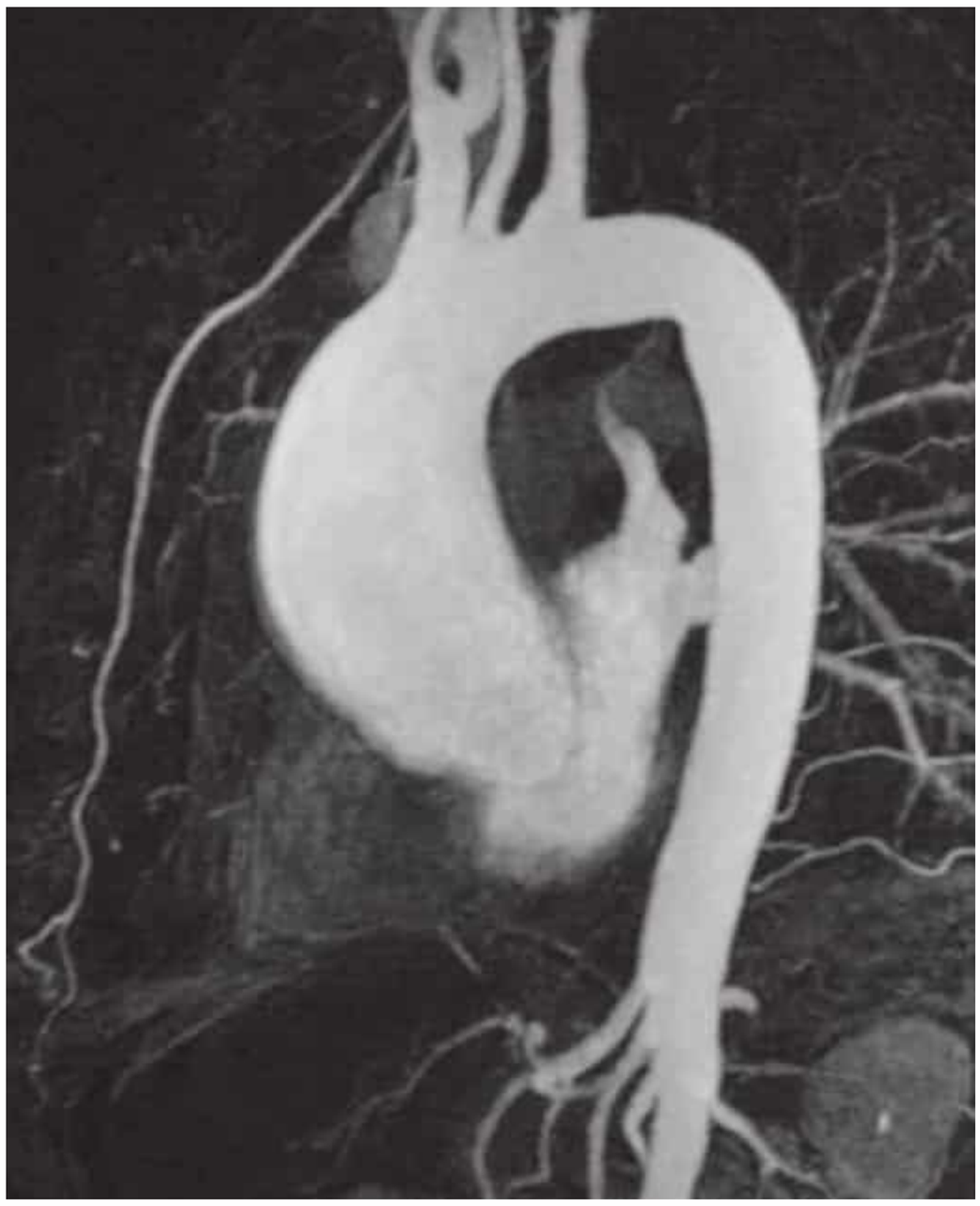

Fig. 6.41 Aneurysm of the ascending aorta in a 65-year-old man. Optimally timed MRA basically limits intravascular enhancement to the aorta and its side branches.

Basic Technical Principles

Scanner Hardware and Software

Although MRA of the great thoracic vessels can be performed successfully at 1.0 T, 1.5 T is considered the standard field strength.[138,139,142] Increasingly, 3.0-T magnets are becoming available for routine clinical imaging, and their use is currently being optimized for thoracic MRA.[143,144]

The speed of an imaging sequence mainly depends on the performance of the gradient system. To achieve short acquisition times, it must be possible to produce magnetic field gradients of very high amplitude that can be switched rapidly on and off. Manufacturers' specifications for maximum amplitudes range from 30 to 45 mT/m with rise times ranging between 100 and 200 mT/m/ms and a maximum field of view (FOV) between 40 and 53 cm.[145–147] Another important parameter is the number of receiver channels that are available to receive the signal from a single surface coil element. While four receiver channels are sufficient for conventional thoracic imaging, additional channels must be available for parallel imaging techniques that are used in modern protocols.[143,148] More recently, receiver coils with up to 32 elements have been introduced.[144]

Pulse Sequences

The standard pulse sequence for contrast-enhanced MRA is a spoiled three-dimensional (3D) T1-weighted gradient-echo sequence. It provides rapid imaging with acceptable resolution and coverage, enabling the images to be acquired during breath holds. The 3D acquisition provides high spatial resolution across the imaged plane with no breaks between the individual partitions.[138,141,142] A "spoiled" sequence is one in which all residual transverse magnetization is destroyed before the next excitation. This increases the T1 weighting of the sequence and increases the contrast between the blood vessels and surrounding tissue.[140]

The repetition time of the MRA sequence should be as short as possible, as this setting will directly affect the acquisition time (TA) of the sequence:

$$TA = N_y \times N_z \times TR \qquad (6.1)$$

where N_y is the number of phase-encoding steps in the y direction, N_z is the number of phase-encoding steps in the z direction (number of partitions), and TR is the repetition time. The TR should be shorter than 5 ms to maintain a reasonable duration of breath holding. High-performance scanners can now achieve TR times of less than 2 ms. This makes it possible to expand anatomical coverage without lengthening the acquisition time or losing spatial resolution, or to improve spatial resolution while maintaining the same degree of coverage. When a very short TR is used, a 3D dataset can be acquired multiple times in succession, resulting in a time-resolved MRA study.[145,149]

Analogously to the TR, the echo time TE should be as short as possible in MRA to minimize artifacts due to flow dephasing (e.g., in high-grade stenoses) and susceptibility differences (air–tissue interface in pulmonary angiography). Usually the TE is less than 2 ms, and high-performance scanners can achieve values less than 1 ms[145,146] (**Fig. 6.42**).

Various other techniques can be used to expedite data acquisition.[139,142,148] The use of partial Fourier techniques is based on the fact that information contained in the upper half of the raw data matrix duplicates information in the lower half. This makes it possible to carry out a complete image reconstruction with equivalent contrast and resolution using only slightly more than 50 % of the raw data, enabling us to modify equation (6.1) as follows:

$$TA = N_y \times N_z \times TR \times 0.6 \qquad (6.2)$$

The cost of this shortcut is reflected in the signal-to-noise ratio, which is decreased by the square root of the time saved (**Fig. 6.42a**).

As an alternative, slightly more than half of the raw data matrix can be scanned in the frequency-encoding direction. This registers only a portion of the complete signal echo. Also know as "fractional echo" or "asymmetric echo," this technique allows a primary reduction of TE, leading secondarily to a shortening of TR.

Zero filling is an interpolation algorithm for improving the apparent resolution of individual images. With a zero filling factor of 2, the raw data matrix is doubled, the new points at the periphery of the matrix are filled with zeroes, and the images are then subjected to Fourier transformation. The use of zero filling does not primarily affect image acquisition, but it prolongs the reconstruction time. When zero filling is done in all three spatial planes with a filling factor of 2, eight times as

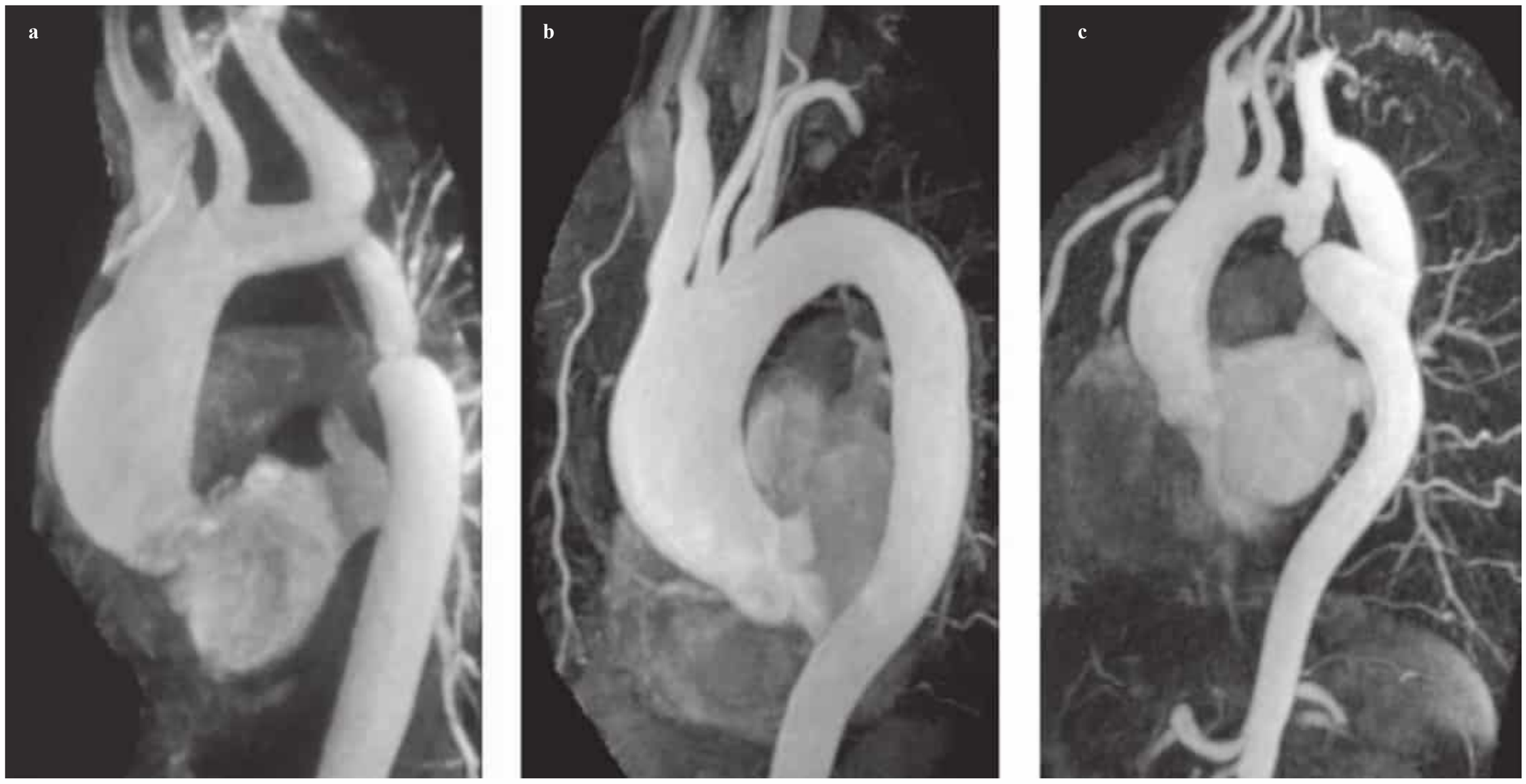

Fig. 6.42 a–c Images showing the evolution of contrast-enhanced MRA in terms of scanner hardware and software. Note the progressive shortening of acquisition times and optimization of injection parameters.

a A total of 20 mL Gd-DTPA was injected at a rate of 2 mL/s, with an acquisition time of 28 s. The voxel size is 0.9 mm × 1.8 mm × 1.5 mm using partial Fourier techniques. A Dacron graft was placed in the proximal descending aorta for coarctation repair in this 65-year-old man.

b A high-performance gradient system and the use of parallel imaging resulted in an acquisition time of 11 s with a total contrast dose of only 15 mL injected at a rate of 4 mL/s. Voxel size is 1.0 mm × 1.0 mm × 1.2 mm. The patient was a 56-year-old man with ectasia of the ascending aorta.

c Time-resolved MRA with temporal resolution of 3.5 s and a total contrast dose of 10 mL injected at a rate of 4 mL/s. Voxel size is 1.3 mm × 1.3 mm × 1.5 mm. This 58-year-old woman underwent a subclavian artery-descending aorta bypass for coarctation of the aorta.

many voxels must be calculated as when interpolation is omitted. But if we assume that an imaging protocol provides sufficient diagnostic information without zero filling, we can use the zero filling strategy to reduce the number of necessary phase-encoding steps (N_y or N_z), which in turn will shorten the acquisition time.

A recent approach to accelerated data acquisition is parallel imaging. In this technique the sensitivity profile of the coil elements used for signal detection is utilized for spatial encoding, so that ultimately the number of phase-encoding steps can be reduced at either the raw-data or image-data level.[148] Prior to application, the sensitivity profile of the coil elements that can be integrated into the imaging sequence must be determined by calibration. An acceleration factor of 2 leads to an ~48 %reduction of acquisition time. The cost of this accelerated acquisition is reflected in the signal-to-noise ratio, which is decreased by a factor of 1/√acceleration factor (**Fig. 6.42b, c**).

Essential Point

The current standard magnetic field strength for contrast-enhanced MRA of the thoracic vessels is 1.5 T. The speed of data acquisition depends critically on the performance of the gradient system. The goal is to shorten the TR and TE times as much as possible. Partial Fourier techniques, zero filling, and parallel imaging have become established techniques for accelerating data acquisition. Parallel imaging requires multiple coil elements for signal detection and a corresponding number of interconnectable receiver channels

Techniques of Examination and Interpretation

Contrast Agents

The extracellular contrast agents that have been approved for clinical use are low-molecular hydrophilic gadolinium chelates. The agents that have been approved in Germany for MR angiography of the thoracic vessels are the open-chain complex Gd-DTPA (Magnevist, Bayer Schering Pharma), gadodiamide (Omniscan, GE Amersham Buchler), and the neutral macrocyclic agent gadobutrol (Gadovist, Bayer Schering Pharma). Gadobutrol is characterized by its double concentration of gadolinium compared with other extracellular contrast agents (1.0 mmol/L), so that only half as much needs to be injected to achieve an equal dose.[146]

The use of extracellular contrast agents temporarily shortens the T1 relaxation time of the blood to values between 30 and 80 ms.[140,141]

Original dose recommendations for MRA of the thoracic vessels were in the range 0.2–0.3 mmol/kg bw or a total dose of 40–60 mL. But with current acquisition times of 15–25 s it is sufficient to administer smaller doses in the range 0.1–0.15 mmol/kg bw, or a total dose of 20 mL.[138,150,151]

Considerable interest has focused on the development of "blood-pool" contrast agents that remain within the blood vessels for an extended period and cause little or no enhancement of extravascular tissues. In MRA of the great vessels, these blood-pool agents could make it possible to examine various regions without the need for additional contrast injection. They

would be particularly useful in the quantification of cardiac perfusion and imaging of the coronary arteries (see p. 111 ff)

Bolus Timing

For successful contrast-enhanced MRA of the thoracic vessels, acquisition of the 3D dataset should coincide with the arrival of the contrast bolus in the vessels of interest.[140,141,150]

Various methods have been described for the optimum timing of contrast-enhanced MRA. In the test bolus method, a small initial bolus is administered to determine the physiological transit time of the contrast agent from injection to its appearance in the ROI so that MR data acquisition can be initiated precisely when the contrast bolus arrives in the target region (**Figs. 6.41, 6.42**).[152] There are also techniques in which continuous SI measurements are taken to time the arrival of the contrast bolus in a predefined test region. When the rise in SI per unit time exceeds a designated threshold, MRA is automatically initiated (e.g., Smart Prep, SmartScan). Another approach is the MR fluoroscopic detection of arrival of the contrast bolus in the target region with manual initiation of the MRA sequence (e.g., CareBolus).

Both methods involve centric rather than linear k-space acquisition, because ideally MRA is initiated to coincide with the peak concentration of gadolinium in the desired vessel. Large clinical studies have confirmed the reliability of these techniques in ensuring diagnostic image quality.[146,150,153] A major advantage of the test bolus method is that it can be used in any MR system and does not require special hardware or software.

The imprecise timing of contrast-enhanced MRA can affect image quality in various ways.[154] If the contrast bolus appears too early in the ROI relative to acquisition of the 3D dataset, the contrast agent will already have washed out by the time imaging is initiated, resulting in the undesired enhancement of veins and/or other vascular and tissue structures.

If the contrast bolus arrives too late, little or no contrast agent will be present in the vascular region of interest. "High-pass filter" artifacts may be observed; these occur when the T1 time of the blood changes rapidly because of contrast wash-in during acquisition of the central k-space lines, which determine image contrast. This results in poor visualization and enhancement of the target vessels, with or without "ringing" artifacts along the vessel walls, making it difficult to detect abnormalities.

Essential Point

For successful contrast-enhanced MRA of the thoracic vessels, acquisition of the 3D dataset should coincide with the arrival of the contrast bolus in the vessels of interest. Strategies for bolus timing include the test bolus method as well as manufacturer-specific automated or semiautomated techniques. The main advantage of the test bolus method is that it does not require special hardware or software.

Planning the Examination

The pulmonary circulation can be imaged in one coronal or two sagittal slice packages[151,155]. In the coronal acquisition, both halves of the lung are imaged simultaneously. Generally, a larger field of view is needed to prevent wrap-around artifacts from the shoulders and apposed arms, and this adversely affects the voxel size of the 3D dataset. Another option is to extend the arms above the head before imaging. The coronal technique is satisfactory for evaluating abnormalities of the pulmonary veins, but a 3D volume 12–14 cm thick cannot cover the entire pulmonary tree, and the voxel size remains anisotropic even when a high-end system is used. These restrictions may be overcome by use of multichannel phased-array coils, parallel imaging techniques, and imaging at 3 T: here, whole coverage of the lung is realizable with acquisition of isotropic voxel sizes of 1 mm × 1 mm × 1 mm in a total of 20 s.[144]

Sagittal data acquisition permits the use of smaller FOVs, which has a favorable effect on voxel size and makes it easier to acquire isotropic voxels. Because of the smaller 3D volume, the acquisition time is shorter than with coronal data acquisition. The main disadvantage of sagittal acquisition is the fact that separate datasets must be acquired for each side, which doubles the required contrast dose[151,155–157] (**Fig. 6.43**).

An oblique sagittal plane is usually recommended for imaging the thoracic aorta. Generally the prescription of this plane is based on the orientation of the aortic arch in the transverse plane. Coronal data acquisition is recommended in cases where it is necessary to investigate the supra-aortic branch vessels or detect congenital anomalies of the aortic arch.[158–160] ECG triggering is not absolutely essential but does improve visualization of the ascending aorta and is therefore recommended in examinations for ascending aortic disease.[150]

In time-resolved contrast-enhanced MRA, the time needed to acquire a 3D dataset can be shortened to less than 4 s, which is a particular advantage in severely dyspneic patients. With the advent of multichannel coil technology, receiver channels and modified strategies for k-space sampling, the reduction of in-plane resolution, using thicker partitions, and decrease of the number of partitions may be minimized.[139,143,145,161] With time-resolved examination techniques, higher injection rates (up to 6 mL/s) should be used with a concomitant reduction in the contrast dose[149] (**Fig. 6.44**). Time-resolved imaging techniques can be useful in congenital vascular malformations (e.g., ductus arteriosus) and aortic dissections (perfusion characteristics of the true and false lumina), and to document steal effects in patients with subclavian artery stenosis.[145,149,162]

The recommended protocol for contrast-enhanced 3D MRA of the thoracic vessels is outlined in **Table 6.8**.

Essential Point

With acquisition times from 10 to 20 s, a contrast dose of 20 mL or 0.1–0.15 mmol/kg bw is generally adequate. The shorter the acquisition time, the higher the recommended injection rate (up to 4 mL/s). A rate up to 6 mL/s is recommended for time-resolved MRA.

Interpretation

The interpretation of thoracic MRA is based on a detailed analysis of the source images. Combined with multiplanar refor-

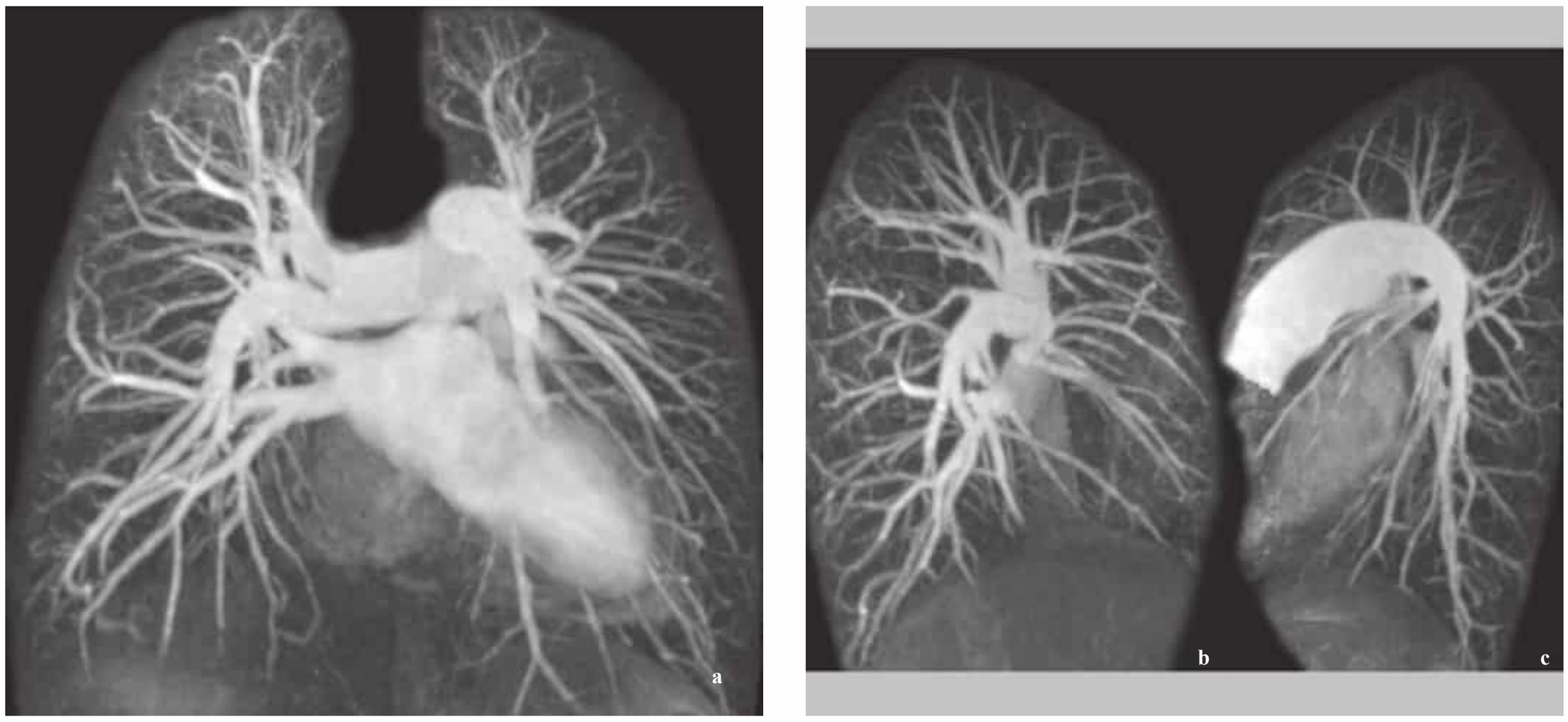

Fig. 6.43 a–c Chronic recurrent pulmonary hypertension in a 45-year-old woman.

a Coronal data acquisition. Despite the use of parallel imaging techniques, the dataset is anisotropic with a voxel size of 1.2 mm × 0.9 mm × 1.4 mm. Acquisition time = 20 s; 20 mL Gd-DTPA injected at a rate of 4 mL/s.

b, c c Separate sagittal acquisitions on each side yield an almost isotropic dataset with a voxel size of 1.2 mm × 1.0 mm × 1.2 mm. Acquisition time = 14 s; 12 mL Gd-DTPA injected at a rate of 4 mL/s.

matting, this makes it possible to determine the presence, location, and three-dimensional extent of vascular abnormalities with a high degree of confidence.[147,150,163,164] One of the most commonly used postprocessing techniques in MRA examinations is the maximum intensity projection (MIP). This technique yields high-resolution projection images that resemble digital subtraction angiograms[147] (**Fig. 6.45**). Projections at various angles can be reconstructed from the volume dataset, providing oblique views that aid in the detection and classification of abnormalities. Manufacturers offer software tools that permit the selective deletion of overlying structures such as the chest wall. Shaded-surface displays also allow for three-dimensional visualization and provide depth cues for the objects depicted. As well as outer-surface displays, inner-surface reconstructions can also be generated to provide intraluminal views. The clinical benefits of "virtual endoscopy" are controversial, however. Image subtraction has proved useful for time-resolved examination techniques, and some manufacturers bundle subtraction algorithms with the standard reconstruction software.[139,145,146]

Clinical Applications

According to the guidelines of the Cardiac Imaging Committee of the German Radiology Society and the recommendations of the Task Force of the European Cardiology Society, contrast-enhanced MRA is considered the first-line technique for imaging the great thoracic vessels, especially in patients with congenital abnormalities.[165,166] The principal anomalies affecting the thoracic aorta are coarctation of the aorta (**Fig. 6.42a, c**) and aortic arch anomalies. In coarctation of the aorta, MR flow measurements can be used to determine pressure gradients as

Table 6.8 Imaging protocol for contrast-enhanced 3D MRA of the great thoracic vessels (modified from the guidelines of the Cardiac Imaging Committee of the German Radiology Society)

Coil	**Target-volume-adapted surface receiver coil system**
Imaging volume	• Thoracic aorta: diaphragm up to and including the supra-aortic vessels • Pulmonary arteries: diaphragm to the apex of the lung
Slice location	Depends on clinical question
Scan parameters: • Slice thickness • FOV • Maximum pixel size • Weighting • Sequences	 • 1.5–4 mm • ≤480 mm • ≤1.9 × 2.7 mm^2 • • T1, spoiled 3D gradient-echo sequence
Respiratory triggering	Breath-hold technique
ECG triggering	Optional; useful in investigations of the ascending aorta
IV contrast agent (Gd chelate)	0.1–0.2 mmol/kg bw, injected at 2–4 mL/s
Additional requirements	Test bolus or bolus tracking Analysis of source images and reconstructions
Postprocessing	Optional: multiplanar reformatting, maximum intensity projection (MIP), volume rendering (VR), subtraction

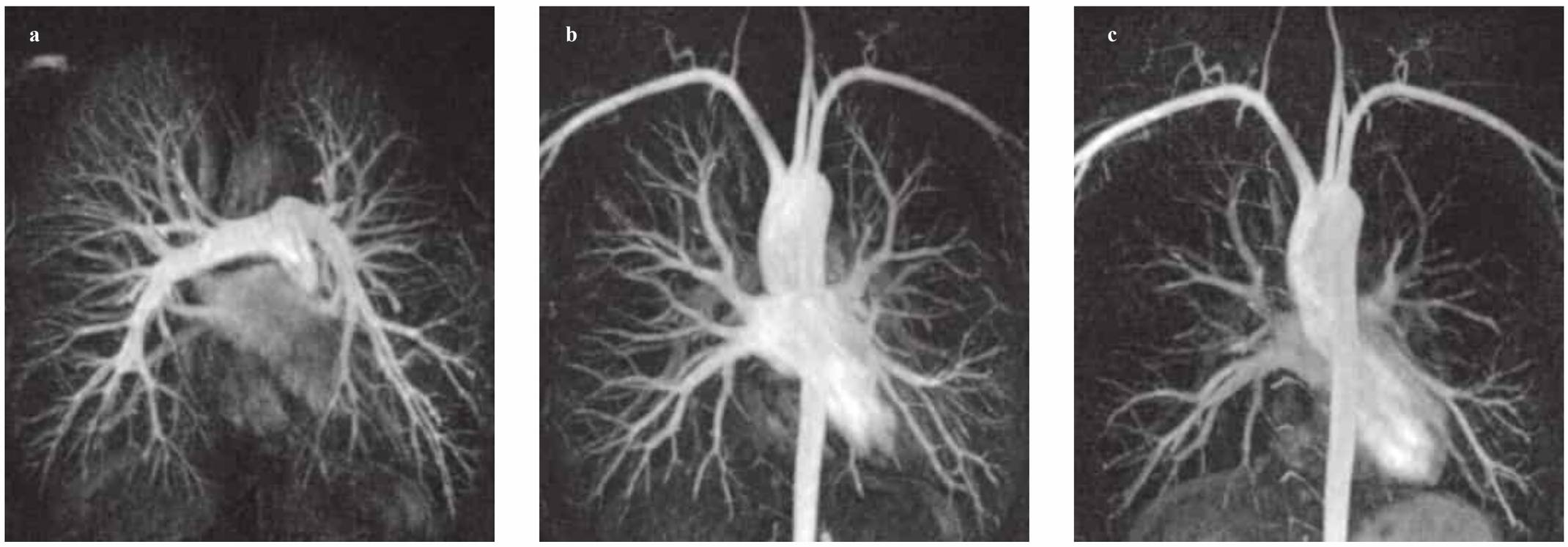

Fig. 6.44 a–c Time-resolved MRA in a 24-year-old man to exclude partial anomalous pulmonary venous return. Acquisition time per 3D dataset = 3.8 s; voxel size = 1.3 mm × 1.3 mm × 2 mm; 8 mL Gd-DTPA injected at a rate of 4 mL/s.

a Predominant enhancement of the pulmonary arteries.
b Predominant enhancement of the pulmonary veins, all of which run normally into the left atrium.
c Predominant enhancement of the thoracic aorta and its branches.

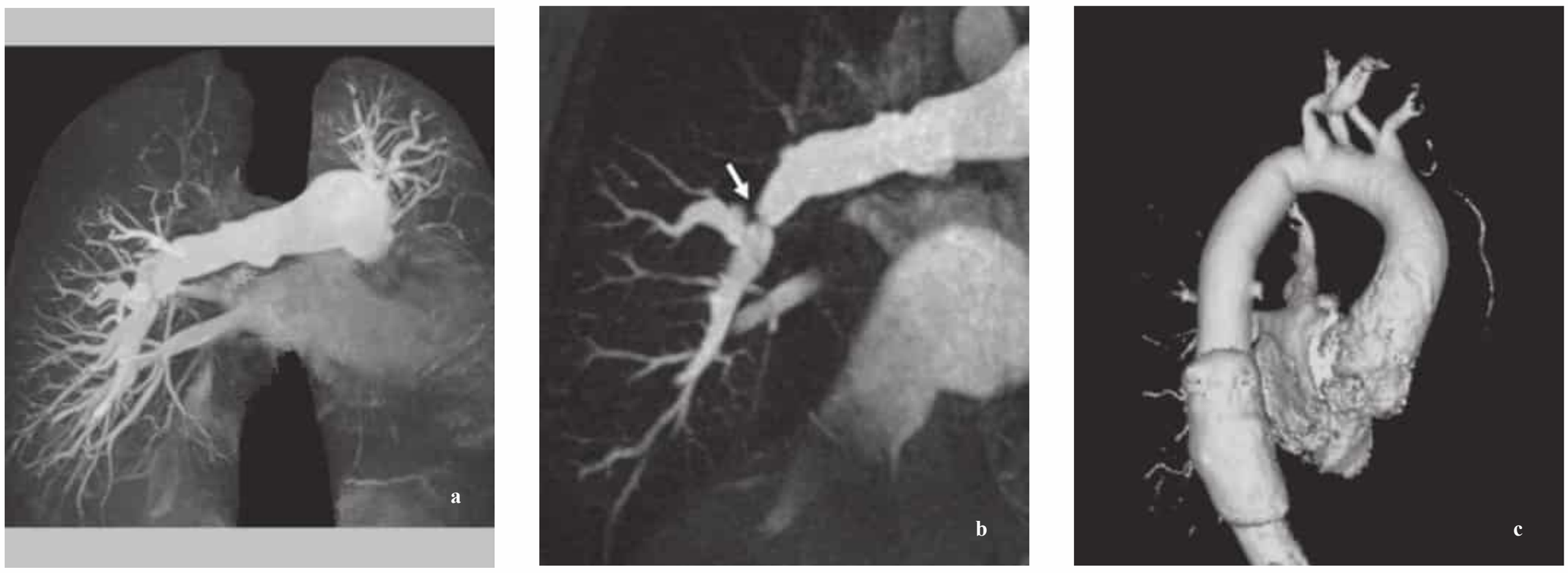

Fig. 6.45 a–c CTEPH in a 34-year-old woman.

a Maximum-intensity projection from a coronal dataset shows central enlargement of the pulmonary arteries with rapid tapering toward the periphery and vascular occlusions in the left lower lobe, lingula, and right upper lobe.
b The characteristic bands in CTEPH (arrow) are clearly depicted by the multiplanar reformatted image.
c Shaded-surface display of the aorta (posterior view) in a 30-year-old woman with Marfan syndrome who underwent replacement of the descending aorta. The image also shows an anomaly of the supra-aortic branches with a common origin for both common carotid arteries and an aberrant right subclavian artery.

well as to evaluate hemodynamically significant re-stenosis following operative or interventional treatment.[167–169]

The most important congenital abnormality of the pulmonary circulation is anomalous pulmonary venous drainage, which may occur as an isolated anomaly or in the setting of cardiac septal defects, tetralogy of Fallot, persistent ductus arteriosus, coarctation of the aorta, or persistent left superior vena cava (**Fig. 6.46**). Contrast-enhanced MRA can define the anatomy of the malformation, and flow measurements can be performed in the ascending aorta and pulmonary trunk to quantify the shunt volume. The heart should be examined in the same sitting to detect or exclude associated anomalies or septal defects. Pulmonary vascular imaging is also important in certain forms of congenital heart disease. This includes patients with truncus arteriosus, aortopulmonary window, or an obstruction of the right ventricular outflow tract:

- Pulmonry atresia
- Tricuspid atresia
- Tetralogy of Fallot
- Unilateral anomalies of the pulmonary arteries ("pulmonary sling")[142,162,168]

Besides evaluating the pulmonary vessels, contrast-enhanced MRA can be used in postoperative patients to evaluate surgically created shunts between the systemic and pulmonary circulations as well as extracardiac conduits. Less frequently it is used in the detection of congenital anomalies such as pulmonary sequestra and pulmonary arteriovenous malformations

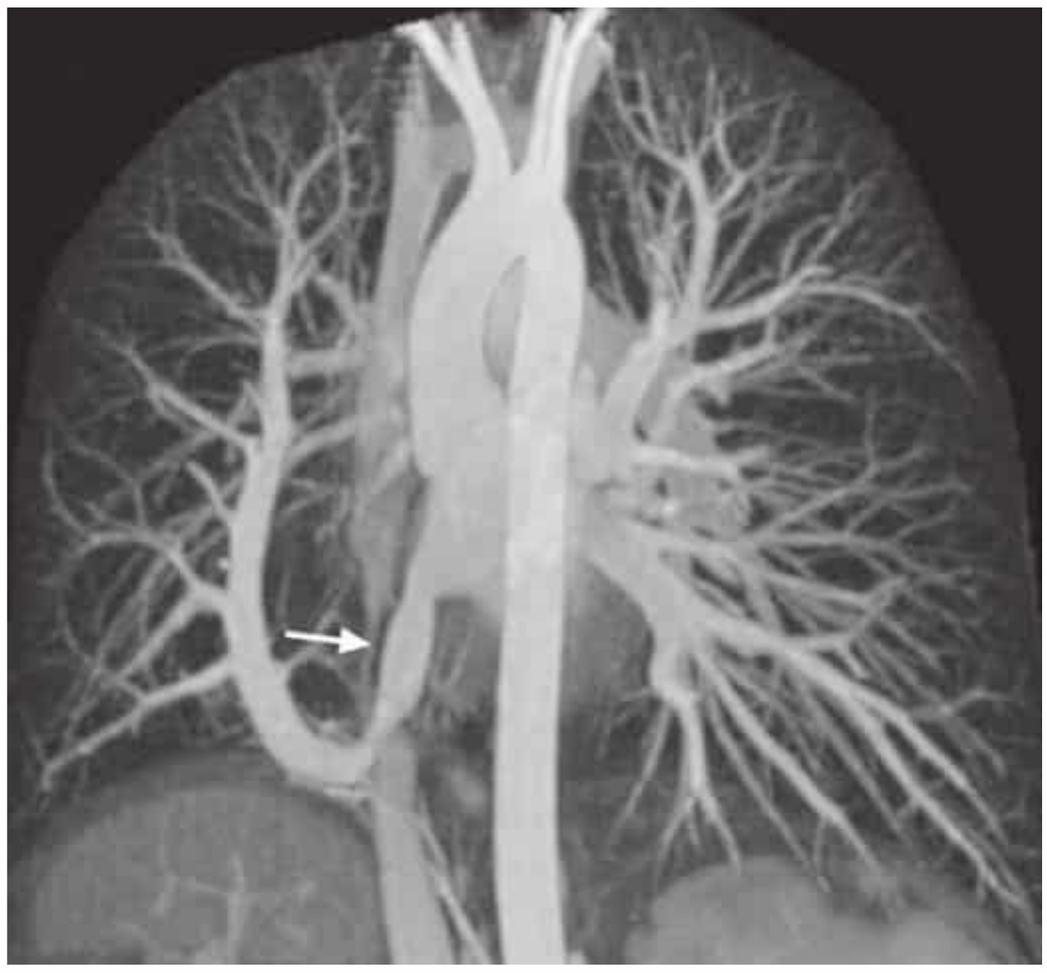

Fig. 6.46 Total anomalous pulmonary venous drainage on the right side (scimitar syndrome) in a 22-year-old woman, surgically corrected with a conduit anastomosed to the left atrium (arrow).

(AVMs). Pulmonary AVMs are particularly common in patients with Rendu–Osler disease. With its ability to characterize the vascular architecture of the malformations, contrast-enhanced MRA can guide the planning of interventional therapies.[161,169]

In acquired diseases, the use of MRI and contrast-enhanced MRA should always be considered in cases where both functional and morphological information are required.[157,170] For example, an aneurysm of the ascending aorta may cause enlargement of the aortic valve annulus, leading to aortic regurgitation that can be quantified with MR techniques (**Fig. 6.41**). Morphological and functional information is also necessary in chronic aortic dissection (**Fig. 6.47**). Inflammations of the great arteries are also considered a primary indication for MRI.[171,172] MRA can be combined with fat-suppressed sequences to detect vessel-wall edema and enhancement after IV contrast administration. MRA can detect expansion and particularly stenosis of the supra-aortic vessels that may be associated with arteritis.

Contrast-enhanced MRA does not have a primary role in the diagnosis of acute pulmonary embolism,[156,157] although it can be used in cases where iodinated contrast media are contraindicated. In patients with chronic recurrent pulmonary embolism (CTEPH, chronic thromboembolic pulmonary hypertension), MRI can aid in assessing operability and can also provide functional information on the regional distribution of perfusion in the lung parenchyma, the extent of bronchosystemic collateral flow, the degree of pressure elevation and vascular resistance in the pulmonary arterial vasculature, and the degree of right-heart overload caused by the obliteration of pulmonary vessels[163] (**Fig. 6.45a, b**). Primary tumors of the pulmonary vasculature are very rare, appearing as intraluminal filling defects that resemble chronic recurrent pulmonary emboli. Delayed images after IV contrast administration show an extremely variable degree of tumor enhancement and are important in differentiating tumors from CTEPH.

Essential Point

Contrast-enhanced MRA of the great thoracic vessels is considered a first-line technique for the investigation of congenital diseases. In acquired diseases, the use of MRI should always be considered when functional information is needed in addition to morphological findings.

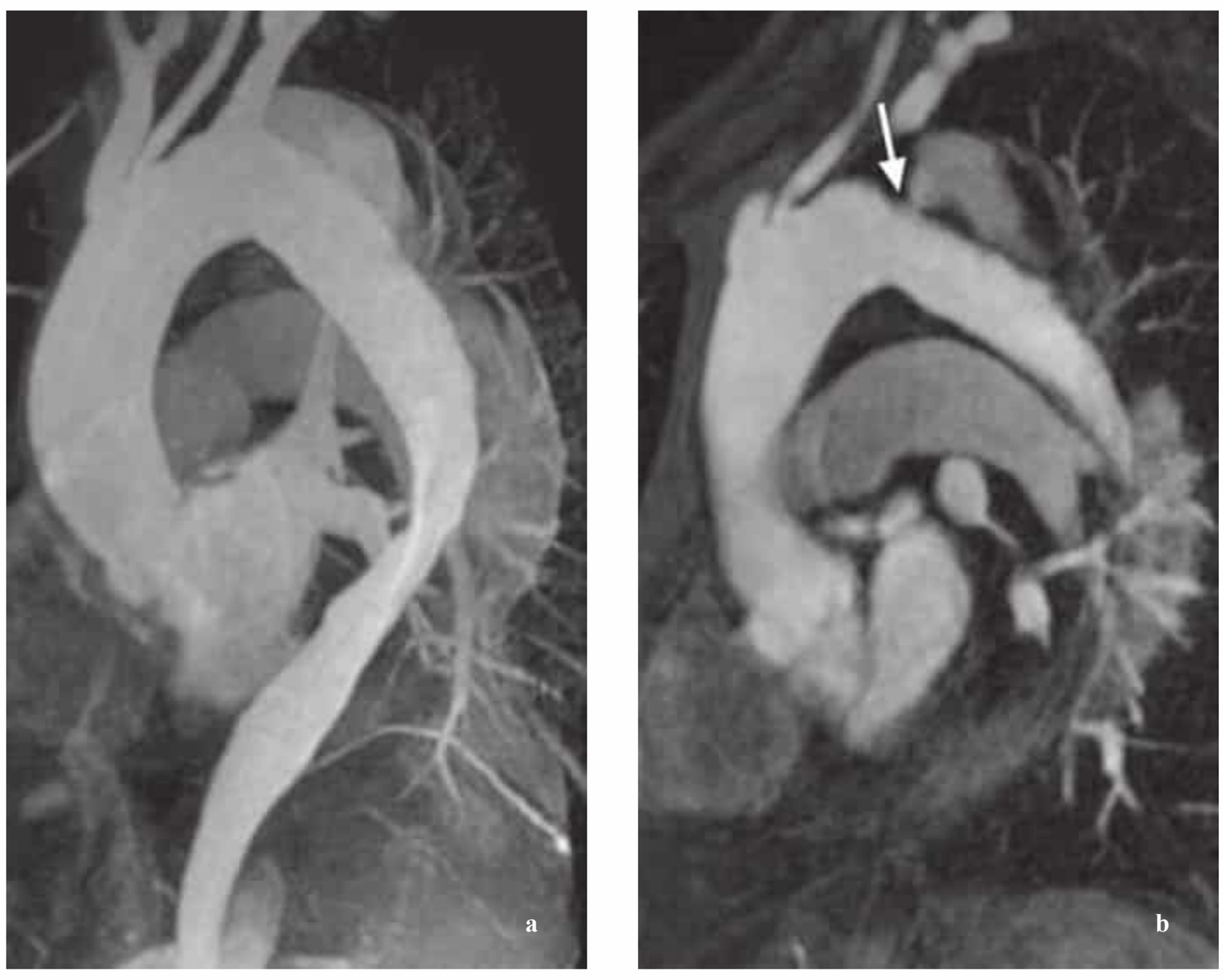

Fig. 6.47 a, b Chronic type B dissection in a 58-year-old man.

a MIP image shows only the better-perfused true lumen of the descending aorta.

b Multiplanar reformatted image demonstrates the entry with smaller contrast filling of the false lumen distal to the origin of the left subclavian artery (arrow).

References

1. Rinck P. Magnetic Resonance in Medicine. The Basic Textbook of the European Magnetic Resonance Forum Magnetresonanz in der Medizin: Lehrbuch des European Magnetic Resonance Forum. Berlin: ABW Wissenschaftsverlag, 2003.
2. Runge V, Nitz WR, Schmeets SH, Faulkner WH, Desai NK. The Physics of Clinical MR. Taught Through Images. Stuttgart, New York: Thieme, 2005.
3. Mitchell DG, Cohen M. MRI Principles. Amsterdam: Elsevier, 2004.
4. ACCF/ACR/SCMR/ASNC/NASCI/SCAI/SIR 2006. Appropriateness criteria for cardiac computed tomography and cardiac magnetic resonance imaging: a report of the American College of Radiology, Society of Cardiovascular Computed Tomography, Society for Cardiovascular Magnetic Resonance; American Society of Nuclear Cardiology, North American Society for Cardiac Imaging, Society for Cardiovascular Angiography and Interventions, and Society of Interventional Radiology. JACC 2006; 48:1475–1497
5. Nayak KS, Cunningham CH, Santos JM, Pauly JM. Real-time cardiac MRI at 3 tesla. Magn Reson Med 2004;51:655–660
6. Atalay MK, Poncelet BP, Kantor HL, Brady TJ, Weisskoff RM. Cardiac susceptibility artifacts arising from the heart-lung interface. Magn Reson Med 2001;45:341–345
7. Winterer JT, Lehnhardt S, Schneider B, et al. MRI of heart morphology. Comparison of nongradient echo sequences with single- and multislice acquisition. Invest Radiol 1999;34:516–522
8. Atkinson DJ, Edelman RR. Cineangiography of the heart in a single breath hold with a segmented turboFLASH sequence. Radiology 1991; 178:357–360
9. Barkhausen J, Ruehm SG, Goyen M, Buck T, Laub G, Debatin JF. MR evaluation of ventricular function: true fast imaging with steady-state precession versus fast low-angle shot cine MR imaging: feasibility study. Radiology 2001;219:264–269
10. Moon JC, Lorenz CH, Francis JM, Smith GC, Pennell DJ. Breath-hold FLASH and FISP cardiovascular MR imaging: left ventricular volume differences and reproducibility. Radiology 2002;223:789–797
11. Pennell DJ, Sechtem UP, Higgins CB, et al. Clinical indications for cardiovascular magnetic resonance (CMR): Consensus Panel report. J Cardiovasc Magn Reson 2004;6:727–765
12. Pohost GM, Hung L, Doyle M. Clinical use of cardiovascular magnetic resonance. Circulation 2003;108:647–653
13. Lanzer P, Barta C, Botvinick EH, Wiesendanger HU, Modin G, Higgins CB. ECG-synchronized cardiac MR imaging: method and evaluation. Radiology 1985;155:681–686
14. Lanzer P, Botvinick EH, Schiller NB, et al. Cardiac imaging using gated magnetic resonance. Radiology 1984;150:121–127
15. Vignaux OB, Augui J, Coste J, et al. Comparison of single-shot fast spin-echo and conventional spin-echo sequences for MR imaging of the heart: initial experience. Radiology 2001;219:545–550
16. Simonetti OP, Finn JP, White RD, Laub G, Henry DA. "Black blood" T2-weighted inversion-recovery MR imaging of the heart. Radiology 1996;199:49–57
17. Barkhausen J, Ruehm SG, Goyen M, Buck T, Laub G, Debatin JF. MR evaluation of ventricular function: true fast imaging with steady- state precession versus fast low-angle shot cine MR imaging: feasibility study. Radiology 2001;219:264–269
18. Debatin JF, Hany TF. MR-based assessment of vascular morphology and function. Eur Radiol 1998;8:528–539
19. Atkinson DJ, Edelman RR. Cineangiography of the heart in a single breath hold with a segmented turboFLASH sequence. Radiology 1991;178:357–360
20. Simonetti OP, Kim RJ, Fieno DS, et al. An improved MR imaging technique for the visualization of myocardial infarction. Radiology 2001;218:215–223
21. Edelman RR, Chien D, Kim D. Fast selective black blood MR imaging. Radiology 1991;181:655–660
22. Semelka RC, Kelekis NL, Thomasson D, Brown MA, Laub GA. HASTE MR imaging: description of technique and preliminary results in the abdomen. J Magn Reson Imaging 1996;6:698–699
23. Huang TY, Huang IJ, Chen CY, Scheffler K, Chung HW, Cheng HC. Are TrueFISP images T2/T1-weighted? Magn Reson Med 2002;48:684–688
24. Carr JC, Simonetti O, Bundy J, Li D, Pereles S, Finn JP. Cine MR angiography of the heart with segmented true fast imaging with steady-state precession. Radiology 2001;219:828–834
25. Vogt FM, Herborn CU, Hunold P, et al. HASTE MRI versus chest radiography in the detection of pulmonary nodules: comparison with MDCT. AJR Am J Roentgenol 2004;183:71–78
26. Fulcher AS, Turner MA. Abdominal manifestations of situs anomalies in adults. Radiographics 2002;22:1439–1456
27. Applegate KE, Goske MJ, Pierce G, Murphy D. Situs revisited: imaging of the heterotaxy syndrome. Radiographics 1999;19:837–852 discussion 853–854
28. Araoz PA, Reddy GP, Thomson PD, Higgins CB. Images in cardiovascular medicine. Magnetic resonance angiography of criss-cross heart. Circulation 2002;105:537–538
29. Akins EW, Martin TD, Alexander JA, Knauf DG, Victorica BE. MR imaging of double-outlet right ventricle. AJR Am J Roentgenol 1989;152: 128–130
30. Haramati LB, Glickstein JS, Issenberg HJ, Haramati N, Crooke GA. MR imaging and CT of vascular anomalies and connections in patients with congenital heart disease: significance in surgical planning. Radiographics 2002;22:337–347 discussion 348–349
31. Mogelvang J, Lindvig K, Sondergaard L, Saunamaki K, Henriksen O. Reproducibility of cardiac volume measurements including left ventricular mass determined by MRI. Clin Physiol 1993;13:587–597
32. Semelka RC, Tomei E, Wagner S, et al. Normal left ventricular dimensions and function: interstudy reproducibility of measurements with cine MR imaging. Radiology 1990;174:763–768
33. Caputo GR, Kondo C, Masui T, et al. Right and left lung perfusion: in vitro and in vivo validation with oblique-angle, velocity-encoded cine MR imaging. Radiology 1991;180:693–698
34. Sandstede J, Lipke C, Beer M, et al. Age- and gender-specific differences in left and right ventricular cardiac function and mass determined by cine magnetic resonance imaging. Eur Radiol 2000;10:438–442
35. Kreitner K-F, Sandstede J. Leitlinien für den Einsatz der MR-Tomographie in der Herzdiagnostik. RoFo. 2004;176:1185–1193
36. Cerqueira MD, Weissman NJ, Dilsizian V, et al. Standardized myocardial segmentation and nomenclature for tomographic imaging of the heart: a statement for healthcare professionals from the Cardiac Imaging Committee of the Council on Clinical Cardiology of the American Heart Association. Circulation 2002;105:539–542
37. Hunold P, Maderwald S, Ladd ME, Jellus V, Barkhausen J. Parallel acquisition techniques in cardiac cine magnetic resonance imaging using TrueFISP sequences: comparison of image quality and artifacts. J Magn Reson Imaging 2004;20:506–511
38. Pruessmann KP, Weiger M, Boesiger P. Sensitivity encoded cardiac MRI. J Cardiovasc Magn Reson 2001;3:1–9
39. Weiger M, Pruessmann KP, Leussler C, Roschmann P, Boesiger P. Specific coil design for SENSE: a six-element cardiac array. Magn Reson Med 2001;45:495–504
40. Thiele H, Nagel E, Paetsch I, et al. Functional cardiac MR imaging with steady-state free precession (SSFP) significantly improves endocardial border delineation without contrast agents. J Magn Reson Imaging 2001;14:362–367
41. Barkhausen J, Ruehm SG, Goyen M, Buck T, Laub G, Debatin JF. MR evaluation of ventricular function: true fast imaging with steady-state precession versus fast low-angle shot cine MR imaging: feasibility study. Radiology 2001;219:264–269
42. Krombach GA, Kuhl H, Bucker A, et al. Cine MR imaging of heart valve dysfunction with segmented true fast imaging with steady state free precession. J Magn Reson Imaging 2004;19:59–67
43. Ichikawa Y, Sakuma H, Kitagawa K, et al. Evaluation of left ventricular volumes and ejection fraction using fast steady-state cine MR imaging: comparison with left ventricular angiography. J Cardiovasc Magn Reson 2003;5:333–342
44. Lund GK, Watzinger N, Saeed M, et al. Chronic heart failure: global left ventricular perfusion and coronary flow reserve with velocity-encoded cine MR imaging: initial results. Radiology 2003;227:209–215
45. Alfakih K, Plein S, Thiele H, Jones T, Ridgway JP, Sivananthan MU. Normal human left and right ventricular dimensions for MRI as assessed by turbo gradient echo and steady-state free precession imaging sequences. J Magn Reson Imaging 2003;17:323–329
46. Shors SM, Fung CW, Francois CJ, Finn JP, Fieno DS. Accurate quantification of right ventricular mass at MR imaging by using cine true fast imaging with steady-state precession: study in dogs. Radiology 2004; 230:383–388
47. Grothues F, Moon JC, Bellenger NG, Smith GS, Klein HU, Pennell DJ. Interstudy reproducibility of right ventricular volumes, function, and mass with cardiovascular magnetic resonance. Am Heart J 2004;147: 218–223

48. Pattynama PMT, Lamb HJ, van der Velde EA, van der Geest RJ, van der Wall EE, de Roos A. Reproducibilty of MRI-derived measurements of right ventricular volumes and myocardial mass. J Magn Reson Imaging 1995;13:53–63
49. Alfakih K, Thiele H, Plein S, Bainbridge GJ, Ridgway JP, Sivananthan MU. Comparison of right ventricular volume measurement between segmented k-space gradient-echo and steady-state free precession magnetic resonance imaging. J Magn Reson Imaging 2002;16:253–258
50. Nagel E, Lehmkuhl HB, Bocksch W, et al. Noninvasive diagnosis of ischemia-induced wall motion abnormalities with the use of high-dose dobutamine stress MRI: comparison with dobutamine stress echocardiography. Circulation 1999;99:763–770
51. Paetsch I, Jahnke C, Fleck E, Nagel E. Current clinical applications of stress wall motion analysis with cardiac magnetic resonance imaging. Eur J Echocardiogr 2005;6:317–326
52. Jahnke C, Nagel E, Gebker R, et al. Prognostic value of cardiac magnetic resonance stress tests: adenosine stress perfusion and dobutamine stress wall motion imaging. Circulation 2007;115(13):1769–1776
53. Zerhouni EA, Parish DM, Rogers WJ, Yang A, Shapiro EP. Human heart: tagging with MR imaging–a method for noninvasive assessment of myocardial motion. Radiology 1988;169:59–63
54. Castillo E, Lima JA, Bluemke DA. Regional myocardial function: advances in MR imaging and analysis. Radiographics 2003;23(Spec No): S127–140.
55. Moore CC, McVeigh ER, Zerhouni EA. Quantitative tagged magnetic resonance imaging of the normal human left ventricle. Top Magn Reson Imaging 2000;11:359–371
56. Masood S, Yang GZ, Pennell DJ, Firmin DN. Investigating intrinsic myocardial mechanics: the role of MR tagging, velocity phase mapping, and diffusion imaging. J Magn Reson Imaging 2000;12:873–883
57. Johnson T, Hahn D, Sandstede J. [Quantitative analysis of left ventricular wall motion with MRI tagging] Radiologe 2004;44:158–163
58. Pai VM, Axel L. Advances in MRI tagging techniques for determining regional myocardial strain. Curr Cardiol Rep 2006;8(1):53–58
59. Moore CC, Lugo-Olivieri CH, McVeigh ER, Zerhouni EA. Three-dimensional systolic strain patterns in the normal human left ventricle: characterization with tagged MR imaging. Radiology 2000;214:453–466
60. Gatehouse PD, Keegan J, Crowe LA, et al. Applications of phase-contrast flow and velocity imaging in cardiovascular MRI. Eur Radiol 2005; 15:2172–2184
61. Lotz J, Meier C, Leppert A, Galanski M. Cardiovascular flow measurement with phase-contrast MR imaging: basic facts and implementation. Radiographics 2002;22:651–671
62. Lee VS, Spritzer CE, Carroll BA, et al. Flow quantification using fast cine phase-contrast MR imaging, conventional cine phase-contrast MR imaging, and Doppler sonography: in vitro and in vivo validation. AJR Am J Roentgenol 1997;169:1125–1131
63. Rominger MB, Dinkel HP, Bachmann GF. Vergleich von schneller MR-Flussmessung in Atemanhaltetechnik in Aorta ascendens und Truncus pulmonalis mit rechts- und linksventrikulärer Cine MR-Bildgebung zur Schlagvoluminabestimmung bei Probanden. Rofo 2002;174:196–201
64. Rebergen SA. Wall EEvd, Helbing WA, de Roos A, Voorthuisen AEv Quantification of pulmonary and systolic blood flow by magnetic resonance velocity mapping in the assessment of atrial-level shunts. Int J Card Imaging 1996;12:143–152
65. Petersen SE, Voigtlander T, Kreitner KF, et al. Quantification of shunt volumes in congenital heart diseases using a breath-hold MR phase contrast technique–comparison with oximetry. Int J Cardiovasc Imaging 2002;18:53–60
66. Kalden P, Kreitner KF, Voigtländer T, et al. Flussquantifizierung von intrakardialen Shuntvolumina unter Verwendung der MR-Phasenkontrast-Technik in Atemanhaltephase. Rofo 1998;169:378–382
67. Colletti PM. Evaluation of intracardiac shunts with cardiac magnetic resonance. Curr Cardiol Rep 2005;7(1):52–58
68. Wang ZJ, Reddy GP, Gotway MB, Yeh BM, Higgins CB. Cardiovascular shunts: MR imaging evaluation. Radiographics 2003;23(Spec No): S181–194. Review.
69. Dulce MC, Mostbeck GH, O'Sullivan M, Cheitlin M, Caputo GR, Higgins CB. Severity of aortic regurgitation: interstudy reproducibility of measurements with velocity-encoded cine MR imaging. Radiology 1992;185:235–240
70. Chatzimavroudis GP, Walker PG, Oshinski JN, Franch RH, Pettigrew RI, Yoganathan AP. Slice location dependence of aortic regurgitation measurements with MR phase velocity mapping. Magn Reson Med 1997; 37:545–551
71. Kivelitz DE, Dohmen PM, Lembcke A, et al. Visualization of the pulmonary valve using cine MR imaging. Acta Radiol 2003;44:172–176
72. Reid SA, Walker PG, Fisher J, et al. The quantification of pulmonary valve haemodynamics using MRI. Int J Cardiovasc Imaging 2002; 18:217–225
73. Fujita N, Chazouilleres AF, Hartiala JJ, et al. Quantification of mitral regurgitation by velocity-encoded cine nuclear magnetic resonance imaging. J Am Coll Cardiol 1994;23:951–958
74. Kunz RP, Oellig F, Krummenauer F, et al. Assessment of left ventricular function by breath-hold cine MR imaging: Comparison of different steady-state free precession sequences. J Magn Reson Imaging 2005; 21:140–148
75. Debl K, Djavidani B, Seitz J, et al. Planimetry of aortic valve area in aortic stenosis by magnetic resonance imaging. Invest Radiol 2005;40: 631–636
76. Cheng ASH, Pegg TJ, Karamitsos TD, et al. Cardiovascular Magnetic Resonance Perfusion Imaging at 3-Tesla for the Detection of Coronary Artery Disease: A Comparison With 1.5-Tesla. J Am Coll Cardiol 2007; 49:2440–2449
77. Schreiber WG, Schmitt M, Kalden P, Mohrs OK, Kreitner KF, Thelen M. Dynamic contrast-enhanced myocardial perfusion imaging using saturation-prepared TrueFISP. J Magn Reson Imaging 2002;16:641–652
78. Jerosch-Herold M, Hu X, Murthy NS, Rickers C, Stillman AE. Magnetic resonance imaging of myocardial contrast enhancement with MS-325 and its relation to myocardial blood flow and the perfusion reserve. J Magn Reson Imaging 2003;18:544–554
79. Panting JR, Gatehouse PD, Yang G-Z, et al. Abnormal subendocardial perfusion in cardiac syndrome X detected by cardiovascular magnetic resonance imaging. N Engl J Med 2002;346:1948–1953
80. Schmitt M, Mohrs OK, Petersen SE, et al. Bestimmung der myokardialen Perfusionsreserve bei KHK-Patienten mit der kontrastmittelverstärkten MRT: Ein Vergleich zwischen semiquantitativer und quantitativer Auswertung. Fortschr Roentgenstr. 2002;174:187–195
81. Wilke N, Jerosch-Herold M, Wang Y, et al. Myocardial perfusion reserve: assessment with multisection, quantitative, first-pass MR imaging. Radiology 1997;204:373–384
82. Fenchel M, Helber U, Simonetti OP, et al. Multislice first-pass myocardial perfusion imaging: Comparison of saturation recovery (SR)-TrueFISP-two-dimensional (2D) and SR-TurboFLASH-2D pulse sequences. J Magn Reson Imaging 2004;19:555–563
83. Hunold P, Maderwald S, Eggebrecht H, Vogt FM, Barkhausen J. Steady-state free precession sequences in myocardial first-pass perfusion MR imaging: comparison with TurboFLASH imaging. Eur Radiol 2004; 14:409–416
84. Schreiber WG, Schmitt M, Kalden P, et al. MR-Perfusionsbildgebung des Herzens mit TrueFISP. Fortschr Roentgenstr. 2001;173:205–210
85. Giang TH, Nanz D, Coulden R, et al. Detection of coronary artery disease by magnetic resonance myocardial perfusion imaging with various contrast medium doses: first European multi-centre experience. Eur Heart J 2004;25:1657–1665
86. Nagel E, Klein C, Paetsch I, et al. Magnetic resonance perfusion measurements for the noninvasive detection of coronary artery disease. Circulation 2003;108:432–437
87. Schwitter J, Debatin JF, von Schulthess GK, McKinnon GC. Normal myocardial perfusion assessed with multishot echo-planar imaging. Magn Reson Med 1997;37:140–147
88. Jerosch-Herold M, Wilke N, Stillman AE. Magnetic resonance quantification of the myocardial perfusion reserve with a Fermi function model for constrained deconvolution. Med Phys 1998;25:73–84
89. Wilke N, Jerosch-Herold M. Assessing myocardial perfusion in coronary artery disease with magnetic resonance first-pass imaging. Cardiol Clin 1998;16:227–246
90. Weber S, Kronfeld A, Kunz RP, et al. Comparison of three accelerated pulse sequences for semiquantitative myocardial perfusion imaging using sensitivity encoding incorporating temporal filtering (TSENSE). J Magn Reson Imaging 2007;26:569–579
91. Ali Raza J, Reeves WC, Movahed A. Pharmacological stress agents for evaluation of ischemic heart disease. Int J Cardiol 2001;81:157–167
92. Schwitter J, Nanz D, Kneifel S, et al. Assessment of myocardial perfusion in coronary artery disease by magnetic resonance: A comparison with positron emission tomography and coronary angiography. Circulation 2001;103:2230–2235
93. Pennell DJ. Cardiovascular magnetic resonance and the role of adenosine pharmacologic stress. Am J Cardiol 2004;94:26D–31D discussion 31D–32D

94. Jerosch-Herold M, Swingen C, Seethamraju RT. Myocardial blood flow quantification with MRI by model-independent deconvolution. Med Phys 2002;29:886–897
95. Larsson HB, Fritz Hansen T, Rostrup E, Sondergaard L, Ring P, Henriksen O. Myocardial perfusion modeling using MRI. Magn Reson Med 1996; 35:716–726
96. Vallee JP, Sostman HD, MacFall JR, et al. MRI quantitative myocardial perfusion with compartmental analysis: a rest and stress study. Magn Reson Med 1997;38:981–989
97. Kroll K. MMID4 Overview. National Simulation Resource, University of Washington 2001; http://nsr.bioeng.washington.edu/NSR/NSRinfo/Documents/mmid4x/1.fm.html
98. Schmitt M, Horstick G, Petersen SE, et al. Quantification of resting myocardial blood flow in a pig model of acute ischemia based on first-pass MRI. Magn Reson Med 2005;53:1223–1227
99. Gould KL, Lipscomb K. Effects of coronary stenoses on coronary flow reserve and resistance. Am J Cardiol 1974;34:48–55
100. Klocke FJ, Simonetti OP, Judd RM, et al. Limits of detection of regional differences in vasodilated flow in viable myocardium by first-pass magnetic resonance perfusion imaging. Circulation 2001;104:2412–2416
101. Smith SC. Risk-reduction therapy: the challenge to change. Circulation 1996;93:2205–2211
102. Yuan C, Kerwin WS. MRI of atherosclerosis. J Magn Reson Imaging 2004;19:710–719
103. Higgins CB, Siemers PT, Schmidt W, Newell JD. Evaluation of myocardial ischemic damage of various ages by computerized transmission tomography. Time-dependent effects of contrast material. Circulation 1979;60:284–291
104. Higgins CB, Siemers PT, Newell JD, Schmidt W. Role of iodinated contrast material in the evaluation of myocardial infarction by computerized transmission tomography. Invest Radiol 1980;15:S176–S182
105. Rehr RB, Peshock RM, Malloy CR, et al. Improved in vivo magnetic resonance imaging of acute myocardial infarction after intravenous paramagnetic contrast agent administration. Am J Cardiol 1986;57:864–868
106. Saeed M, Higgins CB, Geschwind JF, Wendland MF. T1-relaxation kinetics of extracellular, intracellular and intravascular MR contrast agents in normal and acutely reperfused infarcted myocardium using echoplanar MR imaging. Eur Radiol 2000;10:310–318
107. Adzamli IK, Jolesz FA, Bleier AR, Mulkern RV, Sandor T. The effect of gadolinium DTPA on tissue water compartments in slow- and fast-twitch rabbit muscles. Magn Reson Med 1989;11:172–181
108. Inoue S, Murakami Y, Ochiai K, et al. The contributory role of interstitial water in Gd-DTPA-enhanced MRI in myocardial infarction. J Magn Reson Imaging 1999;9:215–219
109. Moran GR, Thornhill RE, Sykes J, Prato FS. Myocardial viability imaging using Gd-DTPA: physiological modeling of infarcted myocardium, and impact on injection strategy and imaging time. Magn Reson Med 2002;48:791–800
110. Simonetti OP, Kim RJ, Fieno DS, et al. An improved MR imaging technique for the visualization of myocardial infarction. Radiology 2001; 218:215–223
111. Gupta A, Lee VS, Chung YC, Babb JS, Simonetti OP. Myocardial infarction: optimization of inversion times at delayed contrast-enhanced MR imaging. Radiology 2004;233:921–926
112. Huber AM, Schoenberg SO, Hayes C, et al. Phase-sensitive inversion-recovery MR imaging in the detection of myocardial infarction. Radiology 2005;237:854–860
113. Kellman P, Arai AE, McVeigh ER, Aletras AH. Phase-sensitive inversion recovery for detecting myocardial infarction using gadolinium-delayed hyperenhancement. Magn Reson Med 2002;47:372–383
114. Petersen SE, Mohrs OK, Horstick G, et al. Influence of contrast agent dose and image acquisition timing on the quantitative determination of nonviable myocardial tissue using delayed contrast-enhanced magnetic resonance imaging. J Cardiovasc Magn Reson 2004;6:541–548
115. Edelman RR. Contrast-enhanced MR imaging of the heart: overview of the literature. Radiology 2004;232:653–668
116. Cerqueira MD, Weissman NJ, Dilsizian V, et al. Standardized myocardial segmentation and nomenclature for tomographic imaging of the heart: a statement for healthcare professionals from the Cardiac Imaging Committee of the Council on Clinical Cardiology of the American Heart Association. Circulation 2002;105:539–542
117. Hunold P, Schlosser T, Vogt FM, et al. Myocardial late enhancement in contrast-enhanced cardiac MRI: distinction between infarction scar and non-infarction-related disease. AJR Am J Roentgenol 2005;184: 1420–1426
118. Bogaert J, Dymarkowski S. Delayed contrast-enhanced MRI: use in myocardial viability assessment and other cardiac pathology. Eur Radiol 2005;15(Suppl 2):B52–B58
119. Achenbach S, Ropers D, Regenfus M, et al. Noninvasive coronary angiography by magnetic resonance imaging, electron-beam computed tomography, and multislice computed tomography. Am J Cardiol 2001; 88:70E–73E
120. Wang Y, Vidan E, Bergman GW. Cardiac motion of coronary arteries: variability in the rest period and implications for coronary MR angiography. Radiology 1999;213:751–758
121. Herborn CU, Barkhausen J, Paetsch I, et al. Coronary arteries: contrast-enhanced MR imaging with SH L 643A–experience in 12 volunteers. Radiology 2003;229:217–223
122. Herborn CU, Schmidt M, Bruder O, Nagel E, Shamsi K, Barkhausen J. MR coronary angiography with SH L 643 A: initial experience in patients with coronary artery disease. Radiology 2004;233:567–573
123. Sommer T, Hackenbroch M, Hofer U, et al. Coronary MR angiography at 3.0 T versus that at 1.5 T: initial results in patients suspected of having coronary artery disease. Radiology 2005;234:718–725
124. Sakuma H, Ichikawa Y, Suzawa N, et al. Assessment of coronary arteries with total study time of less than 30 minutes by using whole-heart coronary MR angiography. Radiology 2005;237:316–321
125. Weber OM, Martin AJ, Higgins CB. Whole-heart steady-state free precession coronary artery magnetic resonance angiography. Magn Reson Med 2003;50:1223–1228
126. Jahnke C, Paetsch I, Achenbach S, et al. Coronary MR imaging: breath-hold capability and patterns, coronary artery rest periods, and beta-blocker use. Radiology 2006;239:71–78
127. Wang Y, Grimm RC, Rossman PJ, Debbins JP, Riederer SJ, Ehman RL. 3D coronary MR angiography in multiple breath-holds using a respiratory feedback monitor. Magn Reson Med 1995;34:11–16
128. Stuber M, Botnar RM, Danias PG, Kissinger KV, Manning WJ. Submillimeter three-dimensional coronary MR angiography with real-time navigator correction: comparison of navigator locations. Radiology 1999;212:579–587
129. Barkhausen J, Ruehm SG, Goyen M, Buck T, Laub G, Debatin JF. MR evaluation of ventricular function: true fast imaging with steady-state precession versus fast low-angle shot cine MR imaging: feasibility study. Radiology 2001;219:264–269
130. Li D, Zheng J, Bae KT, Woodard PK, Haacke EM. Contrast-enhanced magnetic resonance imaging of the coronary arteries. A review. Invest Radiol 1998;33:578–586
131. Wielopolski PA, van Geuns RJ, de Feyter PJ, Oudkerk M. Coronary arteries. Eur Radiol 2000;10:12–35
132. Zheng J, Li D, Bae KT, Woodard P, Haacke EM. Three-dimensional gadolinium-enhanced coronary magnetic resonance angiography: initial experience. J Cardiovasc Magn Reson 1999;1:33–41
133. Li D, Zheng J, Weinmann HJ. Contrast-enhanced MR imaging of coronary arteries: comparison of intra- and extravascular contrast agents in swine. Radiology 2001;218:670–678
134. Stuber M, Botnar RM, Danias PG, et al. Contrast agent-enhanced, free-breathing, three-dimensional coronary magnetic resonance angiography. J Magn Reson Imaging 1999;10:790–799
135. Sommer T, Hofer U, Hackenbroch M, et al. [Submillimeter 3D coronary MR angiography with real-time navigator correction in 107 patients with suspected coronary artery disease] Rofo 2002;174:459–466
136. Kim WY, Danias PG, Stuber M, et al. Coronary magnetic resonance angiography for the detection of coronary stenoses. N Engl J Med 2001; 345:1863–1869
137. Angelini P, Velasco JA, Flamm S. Coronary anomalies: incidence, pathophysiology, and clinical relevance. Circulation 2002;105:2449–2454
138. Carr JC, Finn JP. MR imaging of the thoracic aorta. Magn Reson Imaging Clin N Am 2003;11:135–148
139. Barger AV, Block WF, Toropov Y, Grist TM, Mistretta CA. Time-resolved contrast-enhanced imaging with isotropic resolution and broad coverage using an undersampled 3D projection trajectory. Magn Reson Med 2002;48:297–305
140. Maki JH, Prince MR, Chenevert TC. Optimizing three-dimensional gadolinium-enhanced magnetic resonance angiography. Invest Radiol 1998;33:528–537
141. Saloner D. Determinants of image appearance in contrast-enhanced magnetic resonance angiography. A review. Invest Radiol 1998;33: 488–495
142. Vogt FM, Goyen M, Debatin JF. MR angiography of the chest. Radiol Clin North Am 2003;41:29–41

143. Kramer U, Nael K, Fenchel M, Miller S. Magnetic resonance angiography of chest and abdomen at 3 T. Top Magn Reson Imaging 2007;18:105–115
144. Nael K, Fenchel M, Krisham M, Finn JP, Laub G, Ruehm SG. 3.0 T high spatial resolution contrast-enhanced magentic resonance angiography (CE-MRA) of the pulmonary circulation: initial experience with a 32-channel phased array coil using a high relaxivity contrast agent. Invest Radiol 2007;42:392–398
145. Finn JP, Baskaran V, Carr JC, et al. Thorax: low-dose contrast-enhanced three-dimensional MR angiography with subsecond temporal resolution – initial results. Radiology 2002;224:896–904
146. Goyen M, Ruehm SG. [Contrast-enhanced Magnetic Resonance Angiography]. Bremen-London-Boston: UNI-MED; Publishers 2004
147. Ho VB, Corse WR, Hood MN, Rowedder AM. MRA of the thoracic vessels. Semin Ultrasound CT MR 2003;24:192–216
148. Wilson GJ, Hoogeveen RM, Willinik WA, Muthupillai R, Maki JH. Parallel imaging in MR angiography. Top Magn Reson Imaging 2004;15:169–185
149. Fink C, Ley S, Kroeker R, Requardt M, Kauczor H-U, Bock M. Time-resolved contrast-enhanced three-dimensional magnetic resonance angiography of the chest. Combination of parallel imaging with view sharing (TREAT). Invest Radiol 2005;42:40–48
150. Kreitner K-F, Kunz RP, Kalden P, et al. Contrast-enhanced three-dimensional MR angiography of the thoracic aorta: experiences after 118 examinations with a standard dose contrast administration and different injection protocols. Eur Radiol 2001;11:1355–1363
151. Oberholzer K, Romaneehsen B, Kunz P, Kramm T, Thelen M, Kreitner K-F. [Contrast-enhanced three-dimensional magnetic resonance angiography of the pulmonary arteries with parallel acquisition techniques (iPAT) in patients with CTEPH] – sagittal or coronal data acquisition? Rofo 2004;176:605–609
152. Earls JP, Rofsky NM, DeCorato DR, Krinsky GA, Weinreb JC. Breath-hold single-dose Gadolinium-enhanced three-dimensional MR aortography: usefulness of a timing examination and MR power injector. Radiology 1996;201:705–710
153. Riederer SJ, Bernstein MA, Breen JF, et al. Three-dimensional contrast-enhanced MR angiography with real-time fluoroscopic triggering: design specifications and technical reliability in 330 patient studies. Radiology 2000;215:584–593
154. Lee VS, Martin DJ, Krinsky GA, Rofsky NM. Gadolinium-enhanced MR angiography: artifacts and pitfalls. AJR Am J Roentgenol 2000;175:197–205
155. Meaney JFM, Johansson LOM, Ahlstrom H, Prince MR. Pulmonary magnetic resonance angiography. J Magn Reson Imaging 1999;10:326–338
156. Oudkerk M, van Beek EJR, Wielopolski P, et al. Comparison of contrast-enhanced magnetic resonance angiography and conventional pulmonary angiography for the diagnosis of pulmonary embolism: a prospective study. Lancet 2002;359:1643–1647
157. Van Beek EJ, Wild JM, Fink C, Moody AR, Kauczor HU, Oudkerk M. MRI for the diagnosis of pulmonary embolism. J Magn Reson Imaging 2003;18:627–640
158. Cosottini M, Zampa V, Petruzzi P, Ortori S, Ciono R, Bartolozzi C. Contrast-enhanced three-dimensional MR angiography in the assessment of subclavian artery diseases. Eur Radiol 2000;10:1737–1744
159. Dymarkowski S, Bosmans H, Marchal G, Bogaert J. Three-dimensional MR angiography in the evaluation of thoracic outlet syndrome. AJR Am J Roentgenol 1999;173:1005–1008
160. Soler R, Rodriguez E, Requejo I, Fernandez R, Raposo I. Magnetic resonance imaging of congenital abnormalities of the thoracic aorta. Eur Radiol 1998;8:540–546
161. Mohrs OK, Voigtländer T, Heußel C-P, von Bardeleben S, Düber C, Kreitner K-F. [Morphologic and functional assessment of anomalies of the pulmonary vasculature by rapid MR imaging techniques] Rofo 2002;174:467–473
162. Fenchel M, Saleh R, Dinh H, et al. Juvenile and adult congenital heart disease: time-resolved 3D contrast-enhanced MR angiography. Radiology 2007;244:399–410
163. Kreitner K-F, Ley S, Kauczor H-U, et al. Chronic Thromboembolic Pulmonary Hypertension: Pre- and Postoperative Assessment with Breath-hold Magnetic Resonance Imaging Techniques. Radiology 2004;232:535–543
164. Tatli S, Yucel EK, Lipton MJ. CT and MR imaging of the thoracic aorta: current techniques and clinical applications. Radiol Clin North Am 2004;42:565–585
165. Kreitner K-F, Sandstede J. [Magnetic resonance imaging of the heart: actual guidelines] Rofo 2004;176:1342
166. Task Force Report. The clinical role of magnetic resonance in cardiovascular disease. Eur Heart J 1998;19:19–39
167. Bogaert J, Kuzo R, Dymarkowski S, et al. Follow-up of patients with previous treatment for coarctation of the thoracic aorta: comparison between contrast-enhanced MR angiography and fast spin-echo MR imaging. Eur Radiol 2000;10:1847–1854
168. Eichhorn J, Fink C, Delorme S, Ulmer H. Rings, slings and other vascular abnormalities. Ultrafast computed tomography and magnetic resonance angiography in pediatric cardiology. Z Kardiol 2004;93:201–208
169. Neimatallah MA, Ho VB, Dong Q, et al. Gadolinium-enhanced 3D magnetic resonance angiography of the thoracic vessels. J Magn Reson Imaging 1999;10:758–770
170. Kunz RP, Oberholzer K, Kuroczynski W, Krummenauer F, Thelen M, Kreitner K-F. Assessment of chronic aortic dissection: contribution of different ECG-gated breath-hold MRI techniques. AJR Am J Roentgenol 2004;182:1319–1326
171. Choe YH, Han B-K, Koh E-M, Kim D-K, Do YS, Lee WR. Takayasu's arteritis. Assessment of disease activity with contrast-enhanced MR imaging. AJR Am J Roentgenol 2000;175:505–511
172. Yamada I, Nakagawa T, Himeno Y, Kobayashi Y, Numaon F, Shibuya H. Takayasu arteritis: diagnosis with breath-hold contrast-enhanced three dimensional MR angiography. J Magn Reson Imaging 2000;11:481–487
173. Shellock F. Reference Manual for Magnetic Resonance Safety, Implants, and Devices. Los Angeles, CA: Biomedical Research Publishing, 2005.

Further Reading

Brown DW, Giles WH, Croft JB. Left ventricular hypertrophy as a predictor of coronary heart disease mortality and the effect of hypertension. Am Heart J 2000;140:848–856
Hoffmann R, Lethen H, Marwick T, et al. Analysis of interinstitutional observer agreement in interpretation of dobutamine stress echocardiograms. J Am Coll Cardiol 1996;27:330–336
Jerosch-Herold M, Wilke N, Wang Y, et al. Direct comparison of an intravascular and an extracellular contrast agent for quantification of myocardial perfusion. Int J Card Imaging 1999;15:453–464
Kilner PJ, Firmin DN, Rees RS, et al. Valve and great vessel stenosis: assessment with MR jet velocity mapping. Radiology 1991;178:229–235
Ley S, Kreitner K-F, Morgenstern I, Thelen M, Kauczor H-U. Bronchopulmonary shunts in patients with Chronic Thromboembolic Pulmonary Hypertension: Evaluation by helical CT and MR imaging. AJR Am J Roentgenol 2002;179:1209–1215
Rominger MB, Kluge A, Dinkel HP, Bachmann GF. Vergleich von biventrikulärer MR-Volumetrie und MR-Flussmessungen in Aorta ascendens und Truncus pulmonalis zur intrakardialen Shuntbestimmung. Rofo 2002;174:1380–1386

II

Imaging of Specific Cardiac Diseases

7 Heart Defects and Endocarditis

T. Buck, B. Plicht, T. Schlosser, and R. Erbel

Congenital Heart Disease in Adults

Congenital cardiovascular anomalies are present in 0.8–1 % of all newborns. The number of different anomalies is so large that their complete description would be beyond the scope of this book. This chapter therefore focuses on the capabilities of modern cardiac imaging techniques in the most common types of congenital heart disease in adults—atrial septal defects, patent foramen ovale, and ventricular septal defects.

■ Atrial Septal Defect

Anatomy and Pathophysiology

Atrial septal defects (ASDs) account for ~10 % of all congenital heart diseases and for 22–40 % of congenital heart disease in adults. They are associated with varying degrees of left-to-right shunting of arterialized blood into the pulmonary circulation, depending on the size of the septal defect and the relative pressures. In extreme cases the shunt flow may be several times the volume flow of that in the systemic circulation. Atrial septal defects are primarily characterized by a volume overload on the right heart, which eventually lead to cardiac failure. With a left-to-right shunt above the level of the tricuspid valve, the great dilatory capacity of the pulmonary vessels can forestall a pressure rise in the pulmonary artery and right ventricle. Comparable to the ventricular septal defect however, a functional and/or organic rise in vascular resistance will develop over time in the pulmonary circulation, causing the pressure in the right ventricle to rise. When the pulmonary vascular resistance exceeds that of the systemic circulation in the presence of a ventricular or atrial septal defect, a "shunt reversal" occurs, leading to marked cyanosis. This phenomenon is termed the **Eisenmenger reaction**.

Three etiological types of atrial septal defect are distinguished:

- An **ostium secundum atrial septal defect (ASD II)** is located in the central portion of the atrial septum in the region of the fossa ovalis. It is the most common type, accounting for 60–70 % of atrial septal defects.
- An **ostium primum atrial septal defect (ASD I)** is usually a large defect that comprises 15–25 % of atrial septal defects. It results from a failure of fusion of the septum primum with the endocardial cushion between the atrioventricular valves. As a result, it is commonly associated with mitral valve defects and occasionally with tricuspid valve defects.
- A **sinus venosus atrial septal defect** is present in 5–15 % of cases. It occurs in the posterosuperior portion of the atrial septum between the termination of the superior vena cava and the fossa ovalis. It is frequently associated with anomalous termination of the right pulmonary veins in the right atrium.

Clinical Features

Symptoms

- Generally asymptomatic until the third decade; 70 % of patients are symptomatic by the fifth decade
- Dyspnea, rapid fatigability (manifestations of heart failure).
- Palpitations (in patients with atrial arrhythmias)
- Proneness to respiratory infections
- Approximately 15 % of patients show clinical symptoms of associated mitral insufficiency

Complications

- Atrial fibrillation or flutter
- Mitral insufficiency

Imaging

Echocardiography

2D Echocardiography

- Transthoracic scanning enables direct visualization of the septal defect (excepting sinus venosus defects) (**Fig. 7.1**).
- Transesophageal scanning permits direct visualization of a sinus venosus defect (**Fig. 7.2**).
- Enlargement of the right atrium and right ventricle
- Detection of associated congenital anomalies

3D Echocardiography

- Enables direct visualization of the ASD in the frontal view to assess the location, size, and shape of the defect.
- Can detect an AV canal in patients with ASD I.
- Allows direct visualization of a cleft in the anterior mitral valve leaflet in ASD I.

Color Doppler Echocardiography

- Detection of shunt flow by demonstrating a flow jet through the atrial septum into the right atrium
- Frequently primary detection of a sinus venosus defect is based on an abnormal flow signal near the termination of the superior vena cava (**Fig. 7.2b**).
- Detection of an AV canal in patients with ASD I
- Detection of associated mitral insufficiency in ASD I

Contrast Echocardiography

- Detection of a left-to-right shunt based on the washout phenomenon in the contrast-filled right atrium (**Fig. 7.1b**).

CW Doppler Echocardiography

- Pulmonary hypertension can be diagnosed by assessing the systolic pulmonary artery pressure based on the regurgitant signal from the tricuspid valve.

Essential Point
In the presence of clinical suspicion of a left-to-right shunt at the atrial level, it is possible to overlook a high-sited sinus venosus type of ASD if the atrial septum appears normal. Often a sinus venosus defect can be detected only by multiplanar transesophageal echocardiography in color Doppler mode.

Magnetic Resonance Imaging and Computed Tomography

The standard planes for detecting an ASD in MRI are horizontal long-axis slices and short-axis slices through the heart. Spoiled gradient-echo sequences are preferred. They are of advantage over SE and balanced SSFP sequences in that they can also detect smaller defects by the associated zones of turbulent flow, for example.

Determination of the maximum size of the ASD is essential in selecting patients for interventional repairs, an unsuitable procedure for large defects. Both MRI and multislice CT (MSCT) can document the enlargement of the right atrium and right ventricle (**Fig. 7.3a**). In addition to demonstrating morphologi-

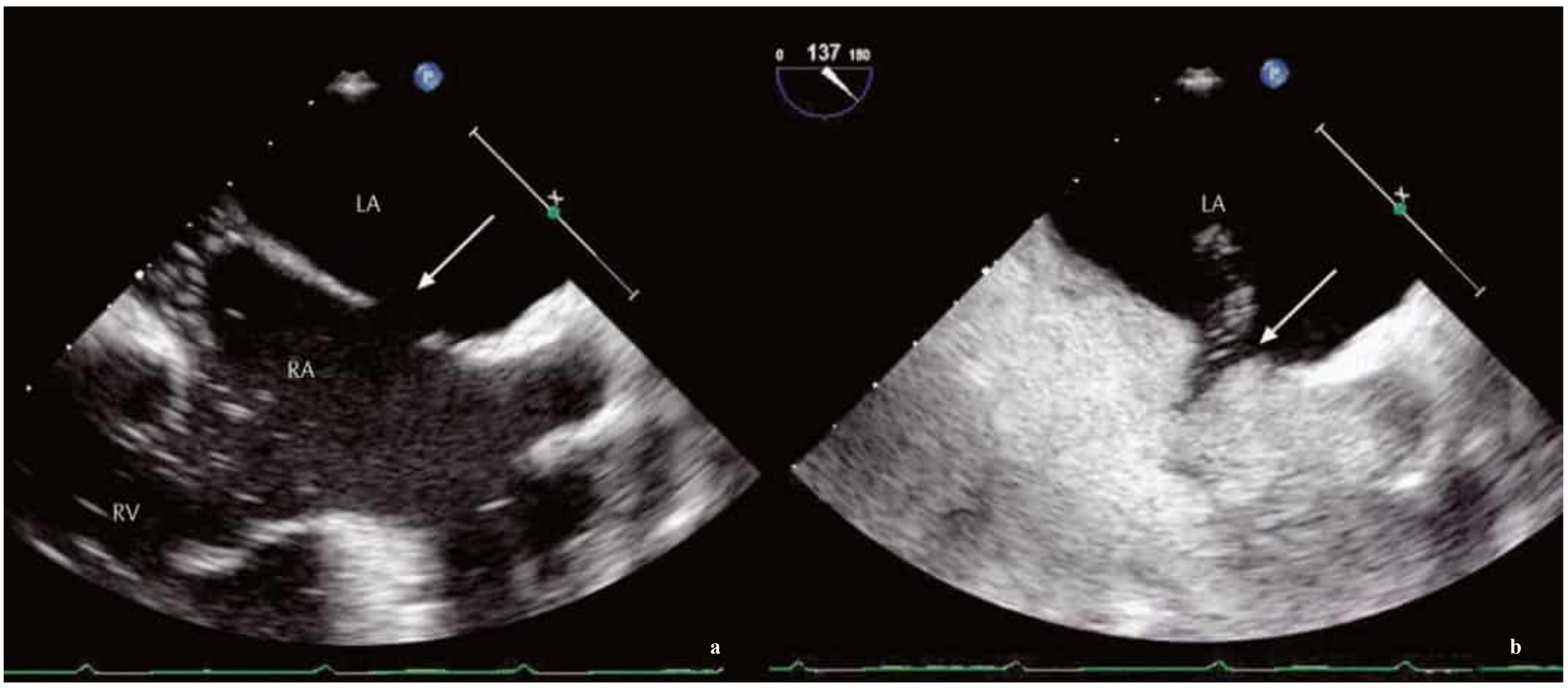

Fig. 7.1 a, b Transesophageal echocardiography of ASD II (arrow).
a Prior to contrast wash-in.
b Typical appearance of the washout phenomenon (arrow) in a left-to-right shunt at the atrial level. Various bubbles can be seen entering the left atrium after passing through the shunt.

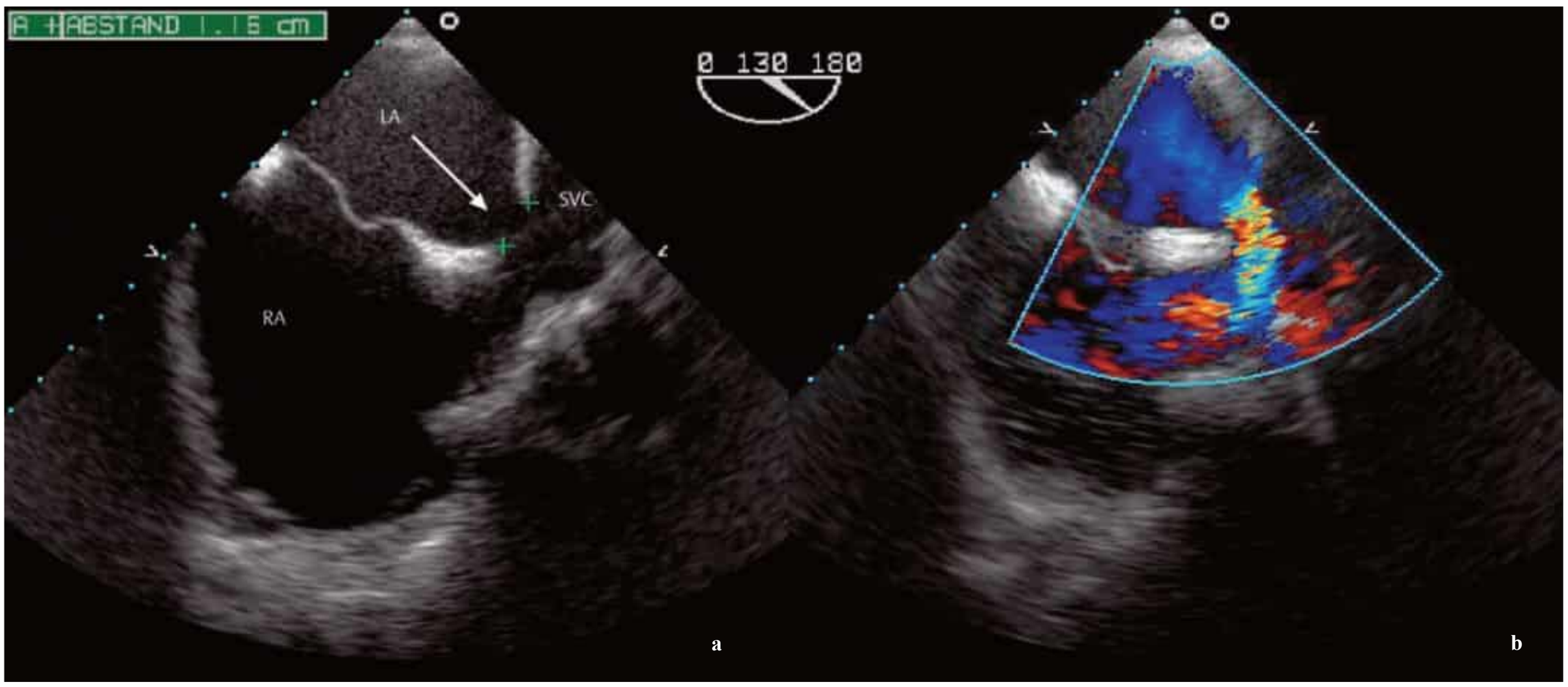

Fig. 7.2 a, b Sinus venosus atrial septal defect documented by transesophageal echocardiography.
a The size of the defect (arrow) is measured at the entry of the superior vena cava into the right atrium.
b Abnormal flow signal detected by color Doppler echocardiography.

cal features, MRI also enables an accurate assessment of the Q_p/Q_s ratio based on flow measurements in the ascending aorta and pulmonary trunk. This ratio is important in selecting patients for operative or interventional repair.[1] The Q_p/Q_s ratio can also be determined using cine MRI to identify right and left ventricular stroke volumes, provided the presence of an additional significant valvular defect can be excluded. MRI and CT additionally detect any anomalous pulmonary venous termination that may be present. Operative treatment is the only option available for correcting this anomaly[2] (**Fig. 7.3b**).

Patent Foramen Ovale

Anatomy and Pathophysiology

Patent foramen ovale (PFO) is a valvelike opening that persists postnatally between the septum primum and secundum in the region of the fossa ovalis owing to failed fusion of these septal elements. A right-to-left shunt at the atrial level may occur spontaneously or in response to a Valsalva maneuver. Autopsy results indicate that PFO has a prevalence of ~25 %in the general population. Its clinical significance is that it places patients at risk for paradoxical emboli. This risk appears to be particularly high in patients with a hypermobile atrial septal aneurysm, which frequently coexists with PFO. Because the opening and volume of the shunt are generally small, hemodynamic complications do not occur.

Clinical Features

Symptoms

- The majority of patients with PFO are asymptomatic.

Complications

- Central or peripheral emboli, stroke, transient ischemic attacks, dizzy spells, migraines

Imaging

Echocardiography

M-Mode Echocardiography

- M-mode can document hypermobile excursions associated with an atrial septal aneurysm (**Fig. 7.4a**).

2D Echocardiography

- Demonstrates the valvelike separation between the septum primum and secundum; but cannot reliably detect patent foramen ovale (2D visualization only by transesophageal scanning).
- Can detect an atrial septal aneurysm (frequently also detectable by transthoracic scanning.

Contrast Echocardiography

- Can reliably detect or exclude patent foramen ovale based on the right-to-left passage of contrast medium, either spontaneously or in response to a Valsalva maneuver (**Fig. 7.4b**).

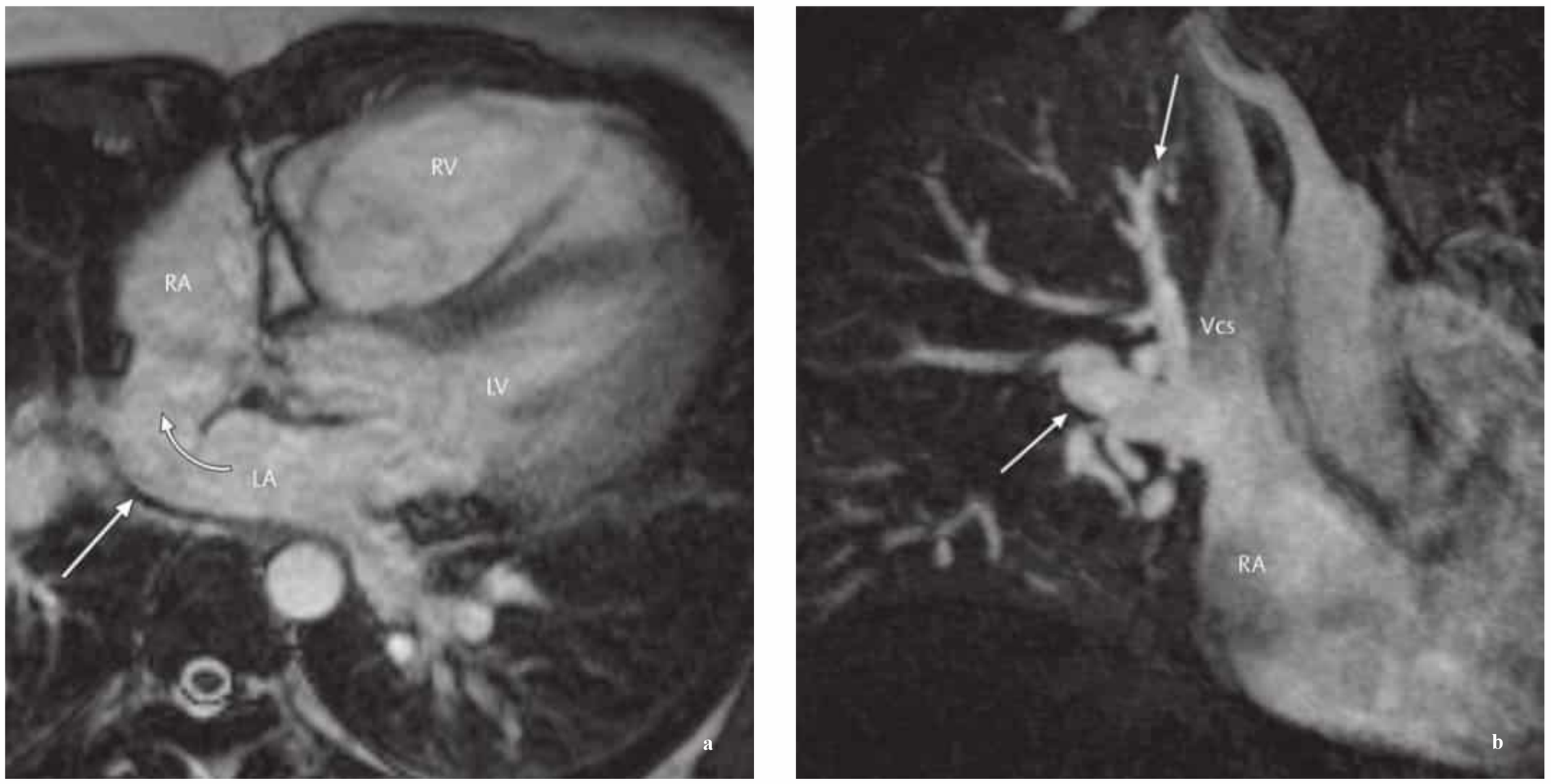

Fig. 7.3a, b Large ASD II in a 32-year-old woman.
a Cine image in the four-chamber view demonstrates the large ASD (arrow).
b Contrast-enhanced 3D MRA further demonstrates partial anomalous pulmonary venous termination on the right side. The upper and middle lobe veins (arrows) open into the superior vena cava.

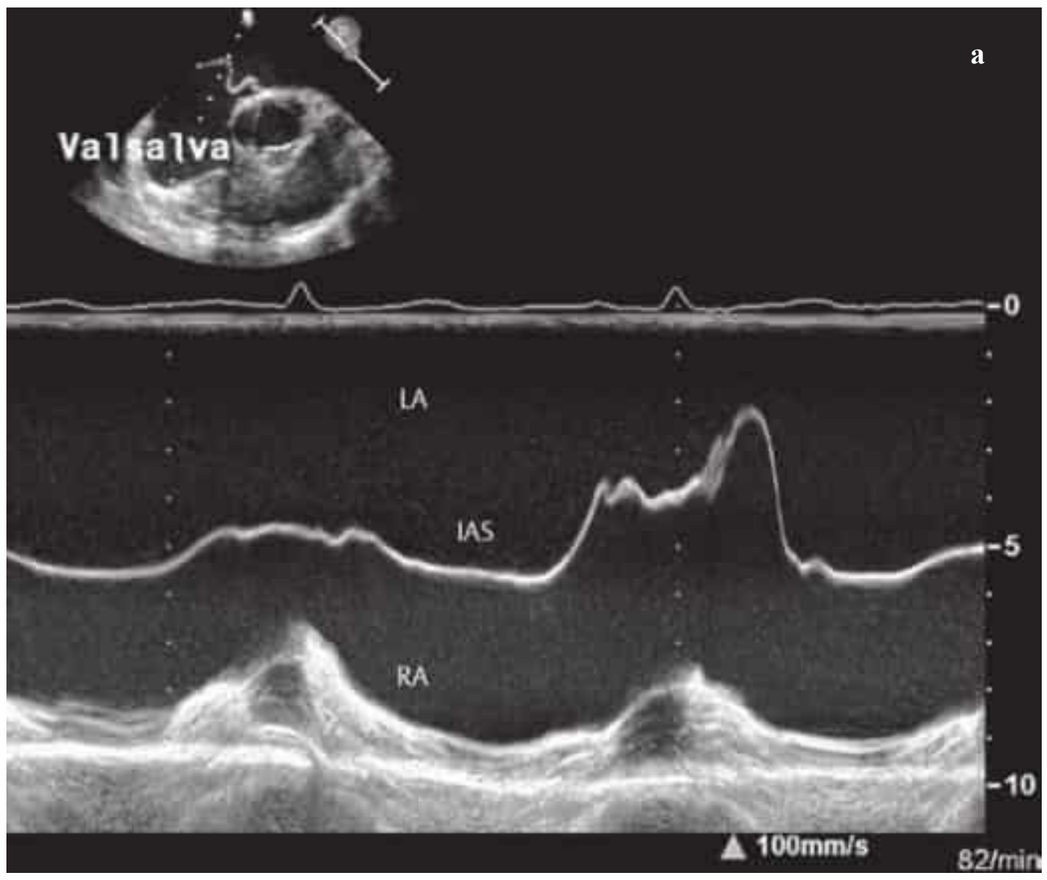

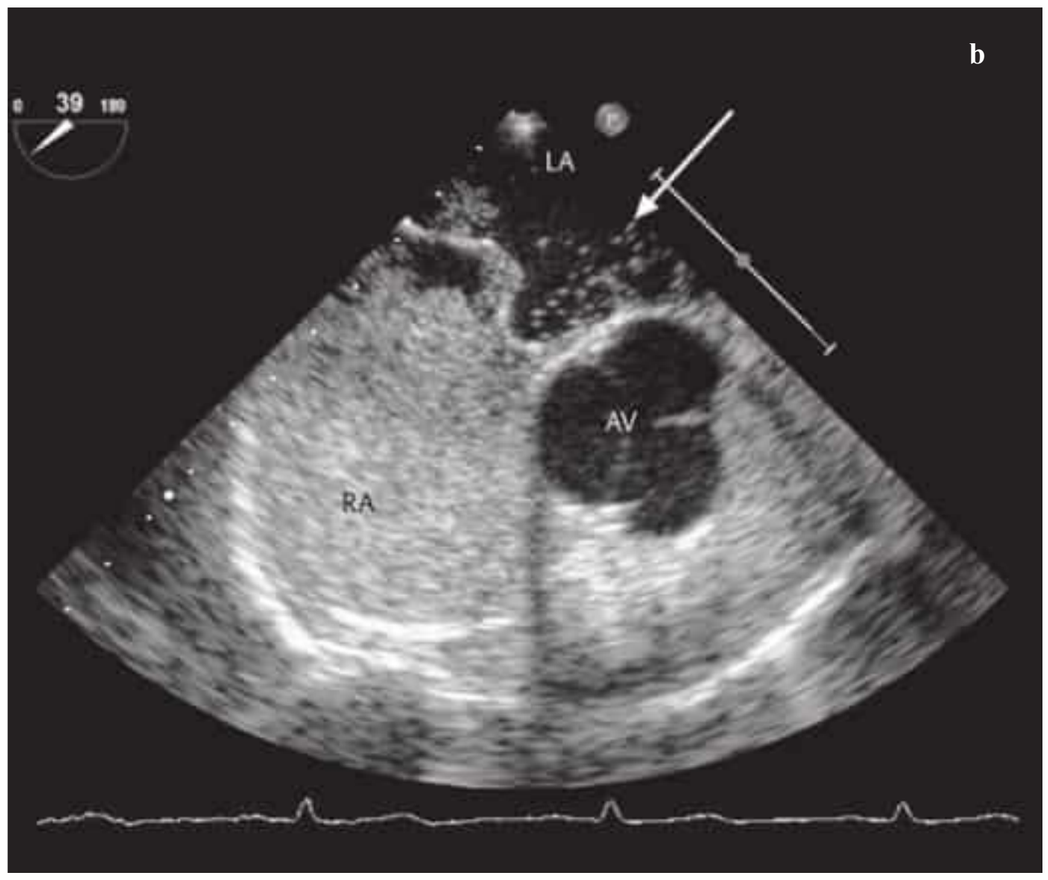

Fig. 7.4 a, b Atrial septal aneurysm with PFO.

a M-mode registration documents the excursion of an atrial septal aneurysm (IAS) in PFO. A Valsalva maneuver significantly increases the amplitude of the excursion.

b Image after IV contrast administration. The passage of contrast medium into the left atrium confirms the presence of a PFO (arrow).

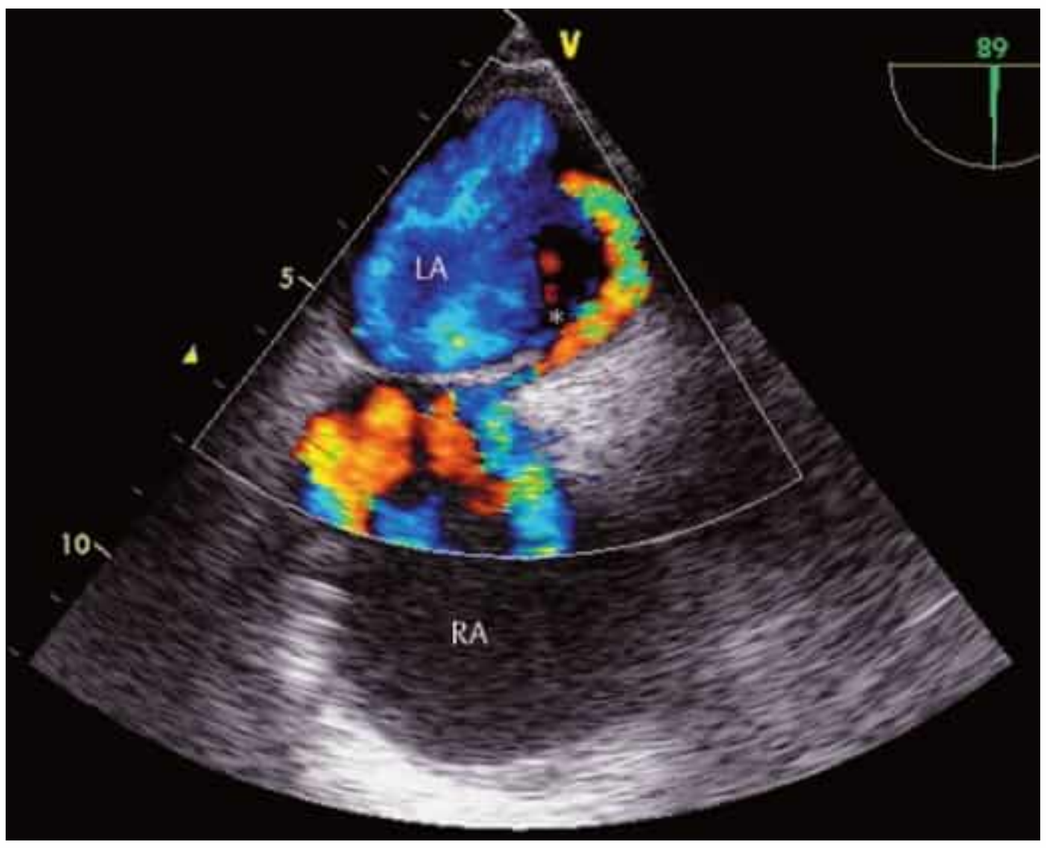

Fig. 7.5 Detection of PFO by transesophageal color Doppler echocardiography, with demonstration of flow through the deflected septum secundum (asterisk).

Color Doppler Echocardiography

- Demonstration of a color Doppler jet from right to left through the patent foramen ovale; however, the definitive exclusion of a patent foramen ovale cannot be conclusively achieved (**Fig. 7.5**).

Essential Point

The reliable detection or exclusion of a patent foramen ovale can be accomplished only following the administration of an echocontrast medium and transesophageal scanning.

In patients with an intact eustachian valve, contrast medium injection through the superior vena cava may significantly reduce contrast wash-in into the atrial septum owing to the concurrent inflow from the inferior vena cava, causing the presence of a patent foramen ovale to be overlooked.

Magnetic Resonance Imaging

Until recently, MRI did not have a role in the diagnosis of PFO. The detection of a hypermobile atrial septal aneurysm is considered to be an indication of the presence of a PFO (**Fig. 7.6**). A very promising approach to the detection of PFO by MRI is to check for premature contrast enhancement of the left atrium, preceding enhancement of the pulmonary veins, while the patient performs a Valsalva maneuver.[3] Further studies are needed in larger patient populations, however.

Ventricular Septal Defect

Anatomy and Pathophysiology

Ventricular septal defect (VSD) accounts for approximately one-fifth of all congenital heart defects. The defects are most commonly located in the membranous portion of the ventricular septum and less frequently in the muscular portion. The hemodynamic and clinical significance of a VSD depend on its size, the shunt volume, and the pulmonary arterial pressure. VSDs smaller than 0.5 cm^2 with a small left-to-right shunt are able to maintain a pressure gradient between the ventricles and generally do not lead to structural cardiac changes. Moderate-sized defects up to 1 cm^2 lead to pressure elevation in the right heart, resulting in pulmonary hypertension due to pulmonary vascular changes. VSDs larger than 1 cm^2 lead to an equalization of pressures between the left and right ventricles. The quantity of pulmonary blood flow, and thus the magnitude of the shunt, are dependent on ventricular function and on the pressure levels in the systemic and pulmonary circulations. In cases with a prolonged volume and pressure load in the pulmonary circu-

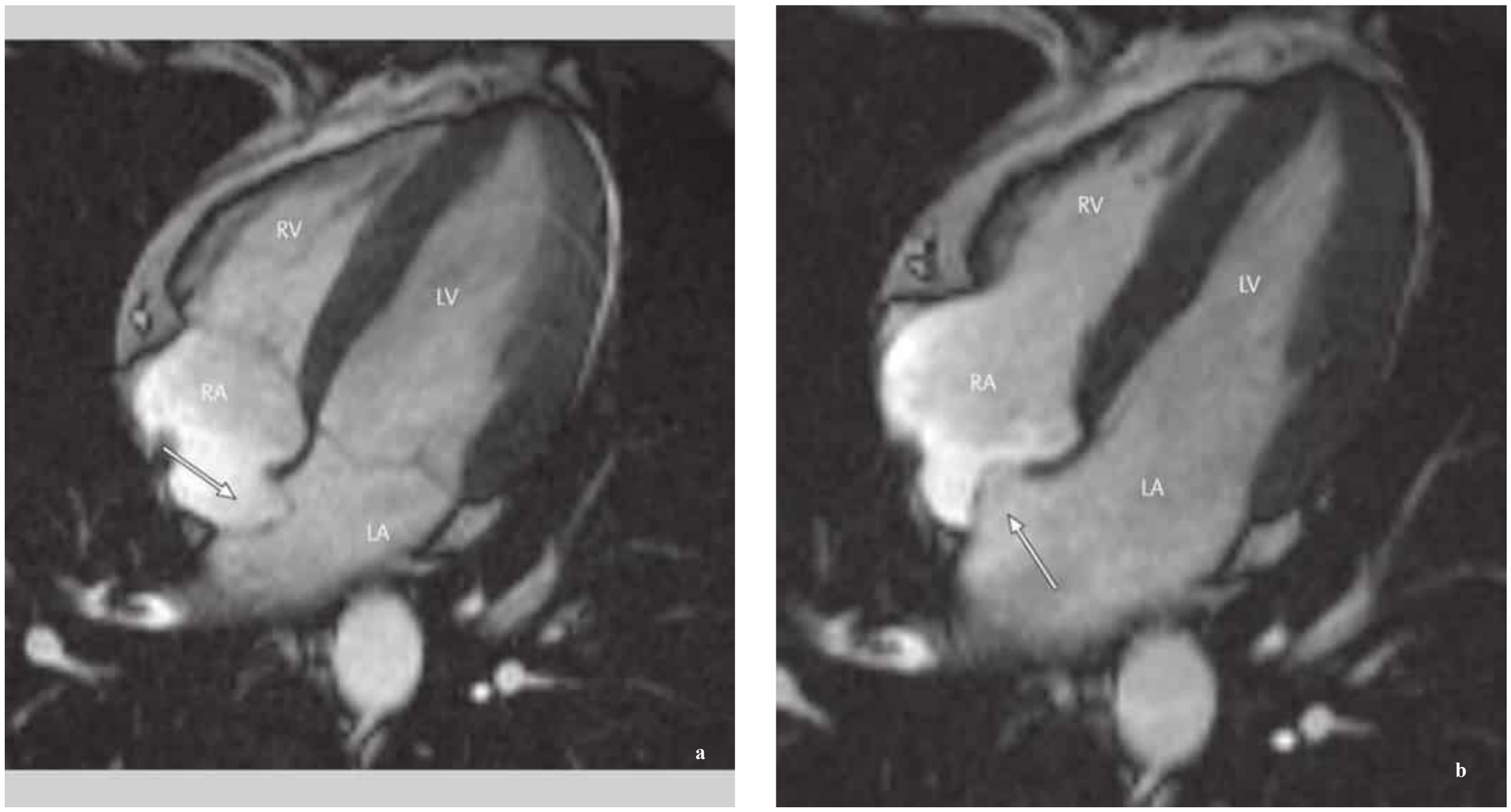

Fig. 7.6a, b Detection of a hypermobile atrial septal aneurysm (arrow). Cine MRI shows the aneurysm bulging into the left atrium during systole (**a**) and into the right atrium in early diastole (**b**).

lation and progressive structural changes in the small pulmonary arteries, an increasing pressure elevation develops in the pulmonary circuit. The pressure in the right ventricle may rise to such a degree that it exceeds the pressure in the left ventricle, thereby reversing the direction of the shunt (Eisenmenger reaction with a right-to-left shunt).

Clinical Features

Symptoms

- Patients with a small ventricular septal defect are frequently asymptomatic.
- Adults with larger VSDs present with dyspnea and rapid fatigability (signifying the volume overload on the left ventricle).
- Cyanosis due to shunt reversal (Eisenmenger reaction)
- Cardiac arrhythmias

Complications

- Development of aortic insufficiency with a high-sited VSD

Imaging

Echocardiography

2D Echocardiography

- Can directly visualize the defect in the membranous or muscular portion of the septum or may show a high-sited defect with an overriding aorta in tetralogy of Fallot (**Fig. 7.7a**).
- Enlargement of the left cardiac chambers (due to volume overload)
- Enlargement of the right cardiac chambers and right ventricular hypertrophy (due to pressure overload in late stages)

3D Echocardiography

- Can accurately define the location, size, and shape of the defect.
- Can define the spatial relationship of the defect to neighboring structures.

Contrast Echocardiography

- Can detect a left-to-right shunt based on the washout phenomenon in the opacified right ventricle.

Color Doppler Echocardiography

- Can detect a VSD with a left-to-right shunt based on the color Doppler jet passing through the defect into the right ventricle (**Fig. 7.7b**).

CW Doppler

- Can determine the pressure gradient between the left and right ventricles to check for pressure equalization.

Essential Point
While defects located near the base of the ventricular septum are relatively easy to detect by echocardiography, the detection of apical muscular defects is often difficult.

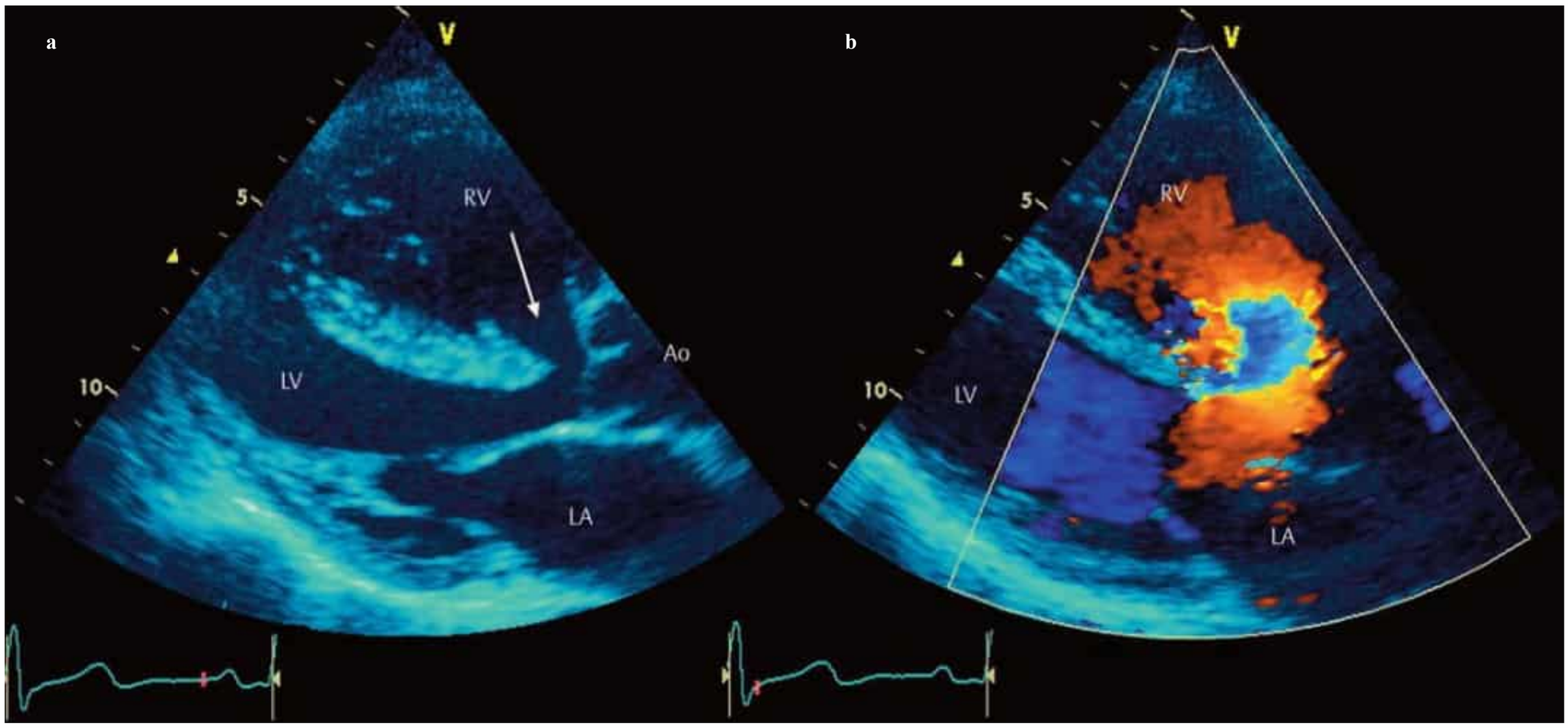

Fig. 7.7 a, b Membranous ventricular septal defect.
a Transthoracic scan of a membranous VSD (arrow) in a woman with tetralogy of Fallot (the overriding aorta can be seen).
b Color Doppler demonstration of shunted blood into the right ventricle.

Magnetic Resonance Imaging and Computed Tomography

Analogous to the diagnosis of ASD, both MRI and CT can accurately detect larger perimembranous and muscular VSDs. The size of the ventricles and atria and the diameters of the pulmonary arteries provide morphological evidence of a right-heart overload or established pulmonary hypertension. Cine MRI can readily document changes in the size of a VSD over the course of the cardiac cycle (**Fig. 7.8**). The magnitude of the resulting left-to-right shunt is of major therapeutic relevance. It can be assessed with MRI by obtaining flow measurements in the ascending aorta and pulmonary trunk to determine the Q_p/Q_s ratio.[1] The detection of a right-to-left shunt in these cases documents shunt reversal due to an Eisenmenger reaction (**Fig. 7.8**).

Essential Point
Noninvasive imaging procedures, especially echocardiography, have replaced invasive cardiac catheterization as the standard method for evaluating valvular heart diseases.

Acquired Valvular Heart Disease

Given the three-dimensional structural complexity of the cardiac valves, the valve-supporting structures, valve motion, and hemodynamic relationships, imaging procedures for investigating acquired valvular heart disease must meet rigorous technical and methodological requirements. With its ability to evaluate a broad spectrum of lesions, its lack of invasiveness, and practical convenience, echocardiography has become the current imaging modality of choice for the morphological and functional evaluation of valvular heart diseases, the assessment of their severity, follow-up, and evaluating associated defects and secondary damage involving the left and right heart. Invasive cardiac catheterization has become obsolete in the primary investigation of valvular heart diseases. In patients with poor echocardiographic image quality, MRI can be used in addition for further evaluation of valvular heart disease.

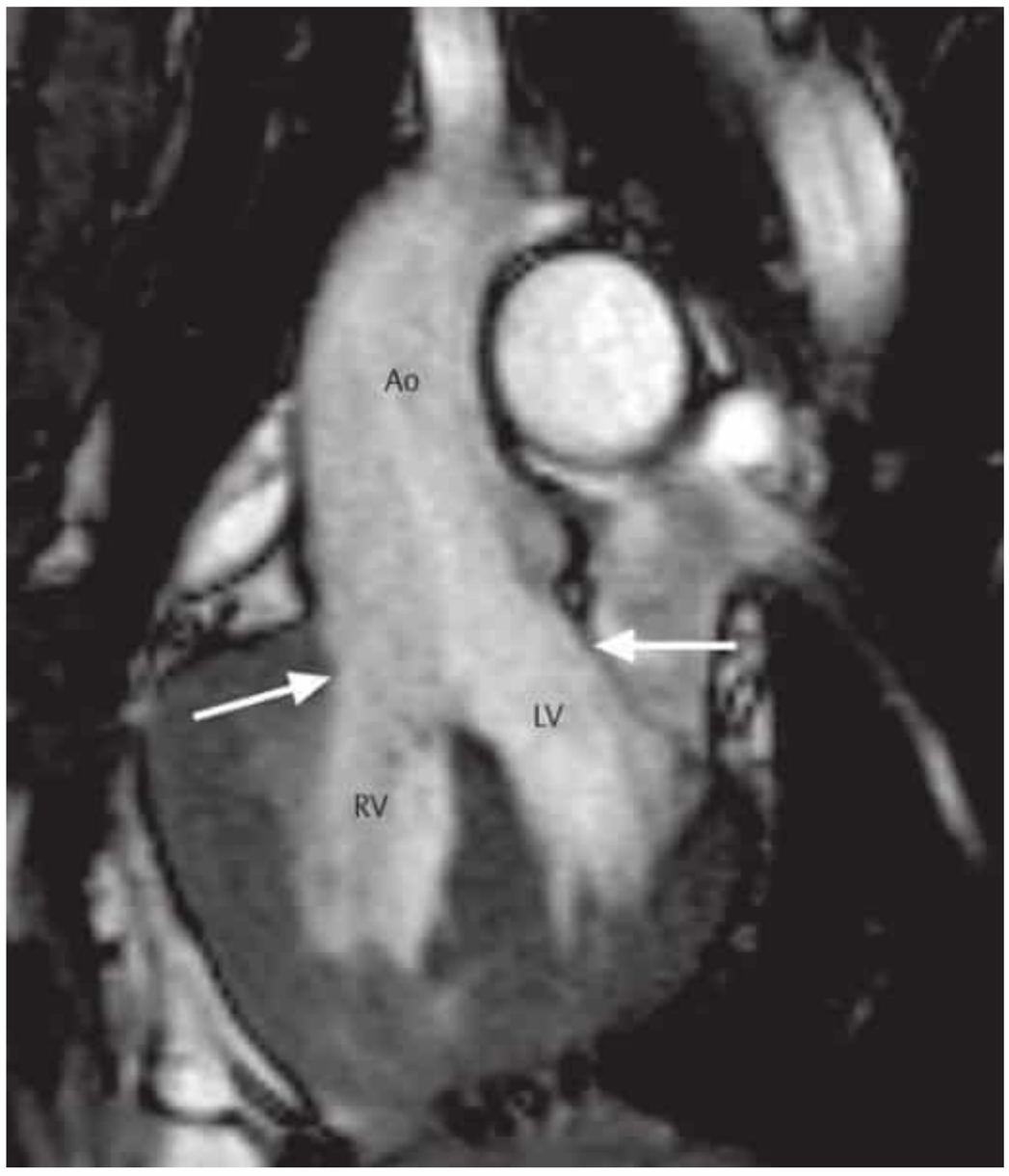

Fig. 7.8 Overriding aorta in a man with tetralogy of Fallot and a large VSD (arrows). Note pronounced right ventricular hypertrophy.

Mitral Stenosis

Etiology

Mitral stenosis is characterized by an obstruction of left ventricular inflow due to abnormal narrowing of the mitral valve orifice. The most frequent cause is **rheumatic fever**, in which an abnormal immune response to group A streptococcal infection leads to degenerative changes in the mitral valve apparatus (**Table 7.1**). A history of rheumatic fever can be elicited in ~60 % of patients with isolated mitral stenosis.[4,5] As rheumatic fever has become less prevalent in western industrialized countries, the incidence of mitral stenosis has also declined. In a Europe-wide survey of patients with valvular heart diseases, mitral stenosis was the fourth most common isolated, left-sided valvular disease, with a prevalence of 12.1 %[6]

The immune process leads to fusion of the valve commissures, thickening and contraction of the valve leaflets, and degeneration of the chordae tendineae.[7] The degenerative changes also hamper valve closure, often resulting in concomitant mitral insufficiency. Mitral stenosis generally takes a progressive course marked by an insidious onset followed later by a greatly accelerated rate of progression.

Less frequent causes are mitral valve involvement by carcinoid syndrome or systemic lupus erythematosus, abnormal calcium metabolism (e.g., dialysis), and mass lesions in the atrium such as myxomas or thrombi.[8]

Pathophysiology

The normal mitral valve orifice has an area of 4–6 cm^2. Mild mitral stenosis is present when the valve orifice area is reduced to 1.5 cm^2, and severe stenosis when the orifice is smaller than 1 cm^2[5,9] (**Table 7.2**). When the mitral valve is narrowed, the pressure in the left atrium rises to values as high as 30 mmHg (normal = 6 mmHg), depending on the degree of stenosis, and the left atrium becomes enlarged.

With severe mitral stenosis (orifice area <1 cm^2), the left atrium dilates to a diameter greater than 6 cm (normal <4 cm). Meanwhile the left ventricle is decompressed owing to lack of atrial inflow and is somewhat reduced in size. The increased pressure in the left atrium leads to retrograde pressure elevation in the pulmonary veins and capillaries.

When the mean pressure in the left atrium rises above 20–25 mmHg, the clinical manifestations of interstitial pulmonary edema may appear. With severe mitral stenosis, the acute rise in the transvalvular pressure gradient during exercise may lead to alveolar pulmonary edema. Chronic exposure of the pulmonary vascular bed to the increased pressure leads to pulmonary venous hypertension and eventually causes pulmonary arterial hypertension and right-heart overload.

The differential diagnosis of atrial dilatation, atrial pressure elevation, and right-heart overload should include diseases such as constrictive pericarditis, severe mitral insufficiency, and congenital shunt lesions.

Most patients with mitral stenosis have combined mitral valve disease with accompanying mitral insufficiency due to degeneration and incompetence of the valve leaflets. The pathophysiological changes in each case are determined by the dominant defect.

Table 7.1 Causes of mitral stenosis

- Rheumatic fever (leading cause; all others are rare)
- Degenerative sclerosis due to abnormal calcium metabolism (chronic hemodialysis)
- Congenital mitral stenosis
- Infective endocarditis
- Systemic lupus erythematosus
- Rheumatoid arthritis
- Malignant carcinoid
- Mucopolysaccharidosis
- Fabry disease
- Whipple disease

Clinical Features

Symptoms (Depending on Severity)

- The majority of patients with a valve orifice area >1.5 cm^2 are asymptomatic.
- Initial symptoms generally develop during physical exercise, stress, febrile infection, or pregnancy:
  - Exertional dyspnea, dyspnea at rest, nocturnal orthopnea
  - Cough, blood-tinged sputum
  - Angina pectoris–like chest pain (due to right ventricular ischemia or coronary embolism)
  - Skipping or racing heartbeat (atrial fibrillation due to overstretching of the atrium)
  - Mitral facies with characteristic pinkish purple patches on the cheeks

Complications

- Atrial fibrillation
- Pulmonary edema
- Thromboembolism
- Infective endocarditis
- Right heart failure

Table 7.2 Grades of severity of mitral stenosis

	Grade I	Grade II	Grade III
MVA	>1.5 cm^2	1.0–1.5 cm^2	<1.0 cm^2
Mean pressure gradient	<5 mmHg	5–10 mmHg	>10 mmHg
Peak pressure gradient	<10 mmHg	10–20 mmHg	>20 mmHg
sPAP	<50 mmHg	≥50 mmHg	≥60–80 mmHg

Summary of various grading criteria based on current guidelines.[4,5]
MVA = mitral valve area, sPAP = systolic pulmonary artery pressure.

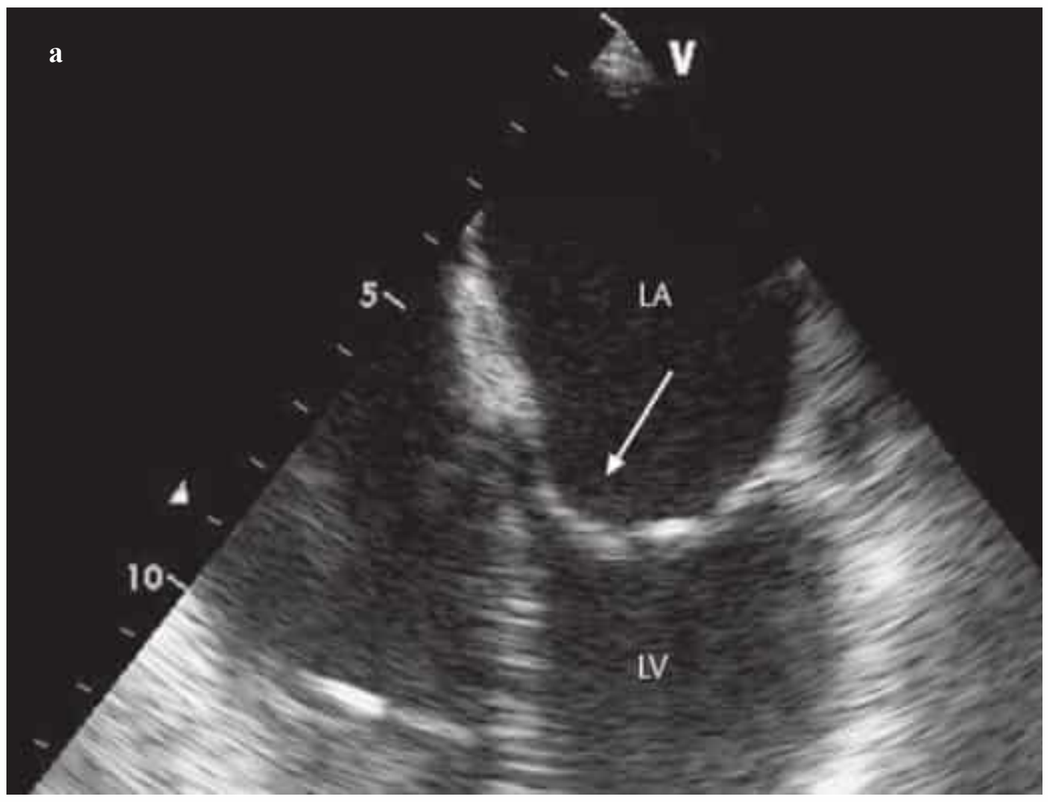

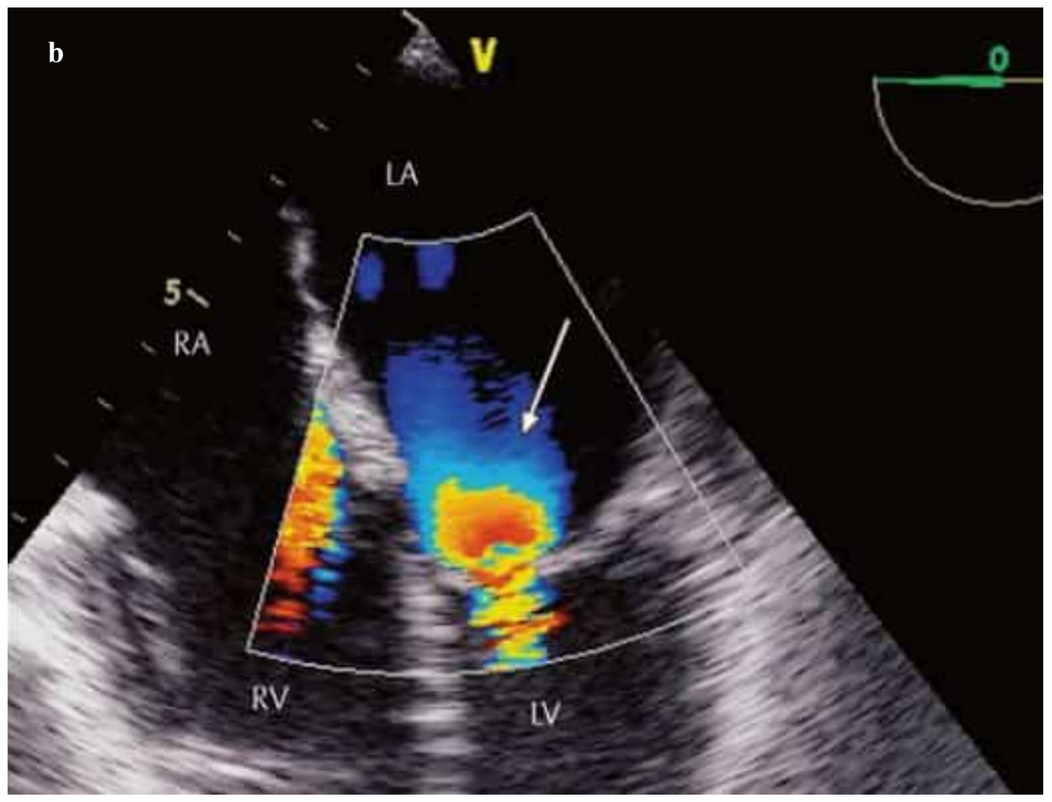

Fig. 7.9 a, b Mitral stenosis.
a Transesophageal echocardiography of postrheumatic mitral stenosis shows typical leaflet doming toward the left ventricle (arrow).
b Color Doppler shows characteristic flow acceleration proximal to the stenotic valve orifice with aliasing (PISA or "peacock eye " pattern, arrow).

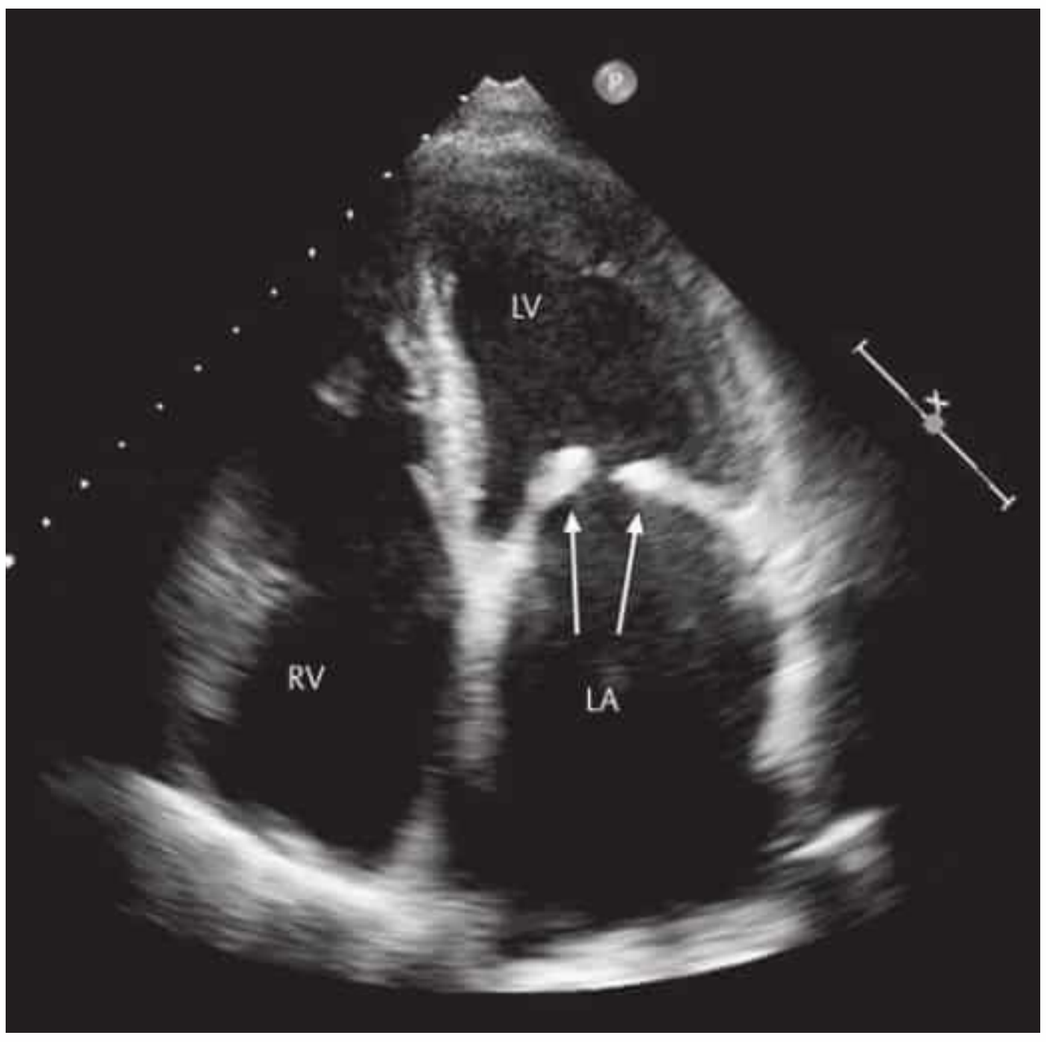

Fig. 7.10 Echocardiographic view of degenerative sclerotic mitral stenosis shows massive leaflet thickening (arrows) and decreased diastolic separation of the leaflets. The left atrium is markedly dilated owing to increased prestenotic pressure.

Imaging

Echocardiography

M-Mode Echocardiography

(This is of minor value in mitral stenosis.)

- Limited separation of the mitral valve leaflets
- Left atrial dilatation

2D Echocardiography

- Characteristic doming of mobile valve leaflets (especially the anterior leaflet, **Fig. 7.9a**)
- Thickened, echogenic, partially immobile mitral leaflets with partial thickening of the chordae tendineae (**Fig. 7.10**) or fusion of the leaflets. Calcification (especially at the commissures) and subvalvular thickening and leaflet thickening will influence the timing and nature of a valvular intervention.[4,5]
- Reduction in the valve orifice area (planimetry in parasternal or transgastric short-axis scans) (**Fig. 7.11**)
- Left atrial dilatation
- Atrial thrombi (defined by TEE)
- Dilatation of the right cardiac chambers and right pulmonary artery
- Spontaneous echo contrast in the left atrium due to slow flow (especially on TEE)
- Other causes of mitral stenosis such as a left atrial tumor (myxoma, sarcoma) (**Fig. 7.12**)

3D Echocardiography

- Three-dimensional visualization of the funnel-shaped mitral stenosis and planimetry of the valve orifice (**Fig. 7.13**)

Color Doppler Echocardiography

- Turbulent flow jet due to accelerated left ventricular inflow
- Proximal flow convergence with PISA phenomenon ("peacock eye" pattern) (**Fig. 7.9b**).
- Calculation of mitral valve orifice area (MVA) based on proximal flow convergence (PISA) and maximum inflow velocity by color Doppler ($MVA = 2\pi r^2 \times v_{Nyquist}/v_{max}$.
- Associated defects (frequently mitral insufficiency)

Pulsed Doppler

- Used only to determine the VTI in the LVOT; does not provide additional information compared with CW Doppler study.

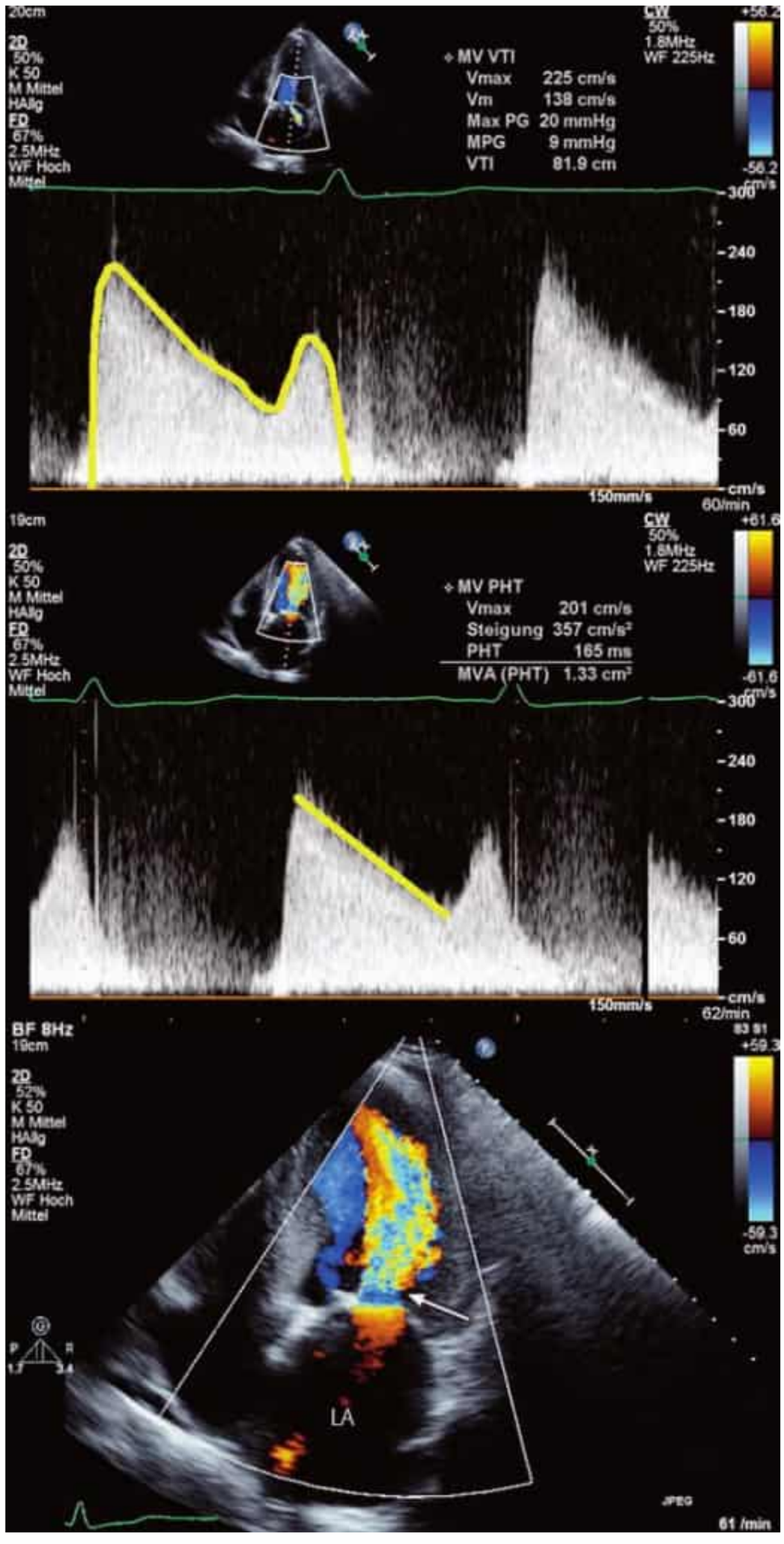

Fig. 7.11 Evaluation of mitral stenosis by Doppler echocardiography, with measurement of the mean pressure gradient (MPG = 9 mmHg, top) and estimation of the valve orifice area (MVA = 1.33 cm^2) based on the PHT (165 ms, center). Imaging in color Doppler mode shows a typical narrow inflow jet with aliasing proximal to the stenosis (bottom, arrow).

CW Doppler

- Mean pressure gradient can be determined with the simplified Bernoulli equation ($\Delta p = 4v^2$) (**Fig. 7.11**).[10]
- Slowing of the decline in velocity, i.e., of the pressure half-time (PHT) (**Fig. 7.11**)
- The PHT can be used to calculate valve orifice area: MVA = 220/PHT (cm^2)[10] (**Fig. 7.11**).
- MVA can be calculated using the continuity equation (MVA = $\text{Area}_{\text{LVOT}} \times \text{VTI}_{\text{LVOT}}/\text{VTI}_{\text{Mitral inflow}})^2$

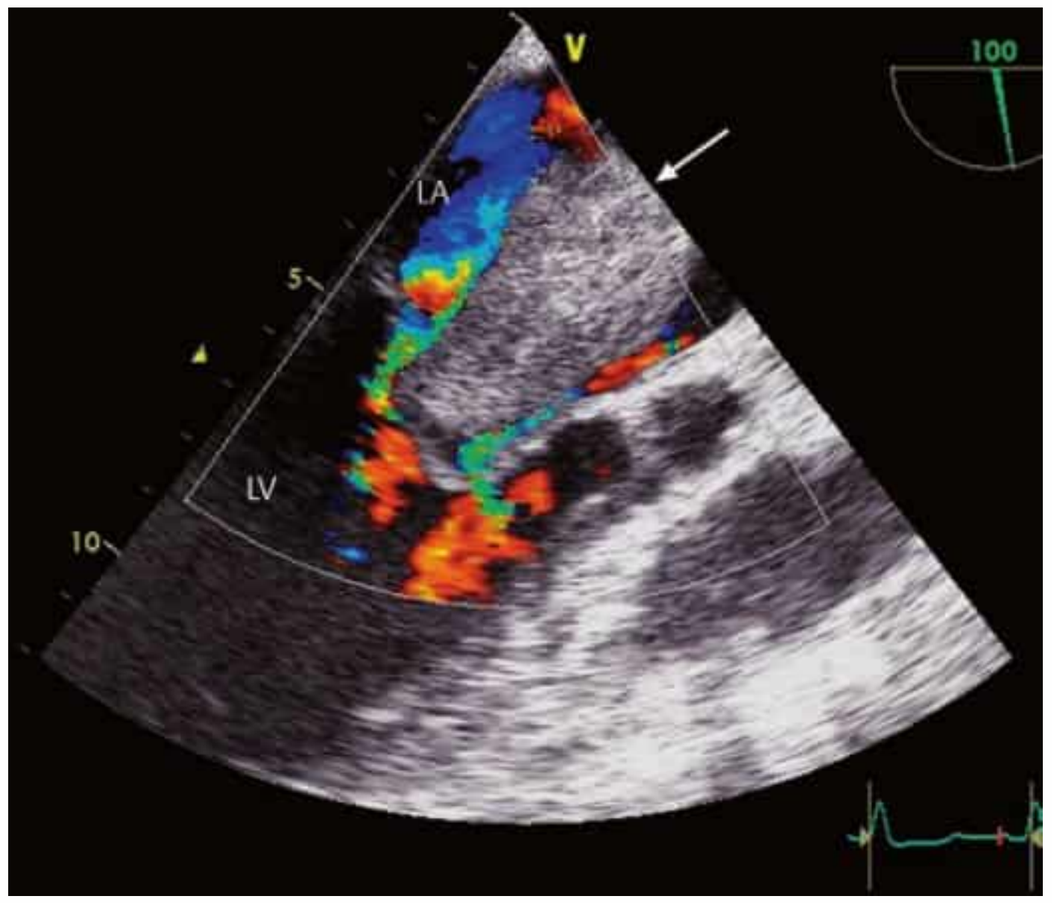

Fig. 7.12 Functional mitral stenosis caused by a left atrial tumor (rhabdomyosarcoma, arrow) obstructing the mitral valve orifice in diastole. Color Doppler demonstrates the reduced flow through the constricted valve.

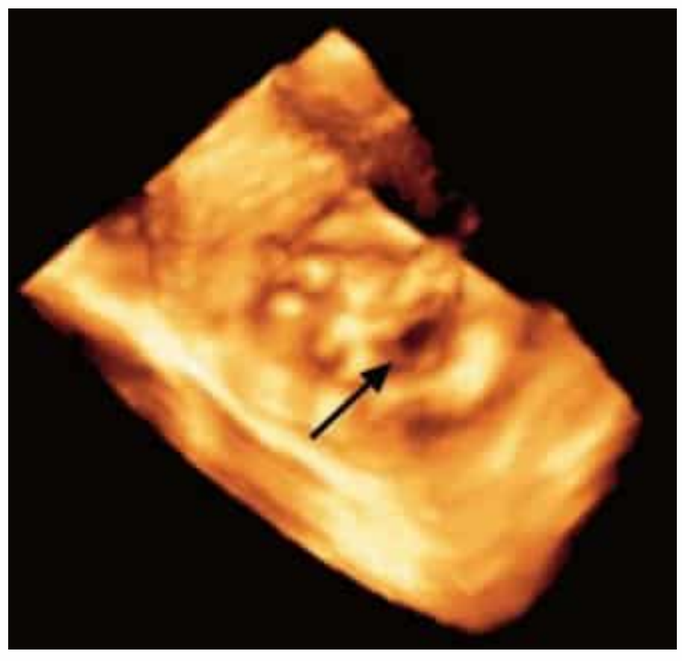

Fig. 7.13 Mitral valve depicted by real-time 3D echocardiography. The bulging valve leaflets and markedly reduced orifice area (arrow) are viewed from the left ventricle.

- The regurgitant signal from the tricuspid valve can be used to determine the systolic pulmonary artery pressure (maximum pressure gradient by Bernoulli equation + estimated atrial pressure).

Stress Echocardiography

- The pressure gradient and clinical manifestations are evaluated during ergometric exercise. (Valvular intervention is indicated in patients with decreased exercise tolerance, a mean transmitral pressure gradient >15 mmHg, and a systolic pulmonary artery pressure >60 mmHg.)

Essential Point

Because the stenosed mitral valve is funnel-shaped, planimetry may overestimate the valve orifice area when performed in a plane proximal to the smallest opening. This error can be avoided by 3D echocardiographic imaging.

A left-to-right shunt at the atrial level must be excluded before using CW Doppler to determine pressure gradient and valve orifice area.

Magnetic Resonance Imaging

MRI has been used in **grading the severity** of mitral stenosis. MRI is inferior to echocardiography in the assessment of valve morphology, especially when transesophageal scanning is used (**Fig. 7.14**).

Recent studies have shown, however, that flow measurements can be used to grade the severity of mitral stenosis, and that MRI planimetry is a reliable method for determining MVA.[11–13] Various authors have found that MRI planimetry may slightly overestimate the valve orifice area compared with echocardiography. MRI can also be successfully used after mitral balloon valvuloplasty, as it reliably detects even slight changes in the valve orifice area.[12]

Mitral Insufficiency

Etiology

In mitral insufficiency, a structural defect in the mitral valve or incomplete closure of the valve leaflets allows blood to regurgitate into the left atrium during systole. After aortic valve stenosis, mitral insufficiency is the second most common valvular heart disease seen in daily practice, accounting for 31.5% of cases.[6] Its prevalence in western industrialized countries is ~19%[14] Mitral insufficiency may have an **organic** or **functional etiology** (**Table 7.3**).

The most frequent organic or **valvular cause** is degenerative mitral insufficiency (MI), in which sclerosis and thickening of the valve leaflets and annulus prevent complete closure of the valve.[6] A special form of degenerative MI occurs in classic mitral valve prolapse, where a congenital abnormality of the connective-tissue matrix leads to myxomatous changes in the valve with elongation of the leaflets and chordae tendineae, ruptured chordae, and annular dilatation, leading to progressive mitral insufficiency.[4,5] This condition is distinguished from a nonclassic prolapse without myxomatous changes. The term flail leaflet describes the fluttering into the left atrium owing to elongation or rupture of the chordae tendineae (**Fig. 7.15**). Infective endocarditis leads to clinically significant mitral regurgitation owing to leaflet destruction and/or abscess formation.

Functional or **relative mitral insufficiency** is present when morphologically normal valve leaflets are unable to coapt owing to a change in the geometry of the valve apparatus as, e.g., in the case of ischemic or dilated cardiomyopathy, with mitral annulus dilatation and papillary muscle displacement (**Fig. 7.15**). A combination of functional and organic causes of mitral insufficiency is frequently present.

The above conditions are to be distinguished from acute mitral insufficiency due to an ischemic or traumatic papillary muscle rupture.

Pathophysiology

Mitral insufficiency leads to volume overload and dilatation of the left ventricle and atrium because of the **regurgitant volume** that moves back and forth between the two left heart chambers. The regurgitant volume depends on the size of the valve orifice and the systolic ventricular pressure. Thus, the severity of mitral insufficiency is increased by enlargement of the mitral annulus owing to ventricular dilatation and increased left ventricular afterload (aortic valve stenosis, arterial hypertension).[4,5]

In chronic mitral insufficiency, the left ventricle and left atrium adapt to the volume overload through compensatory

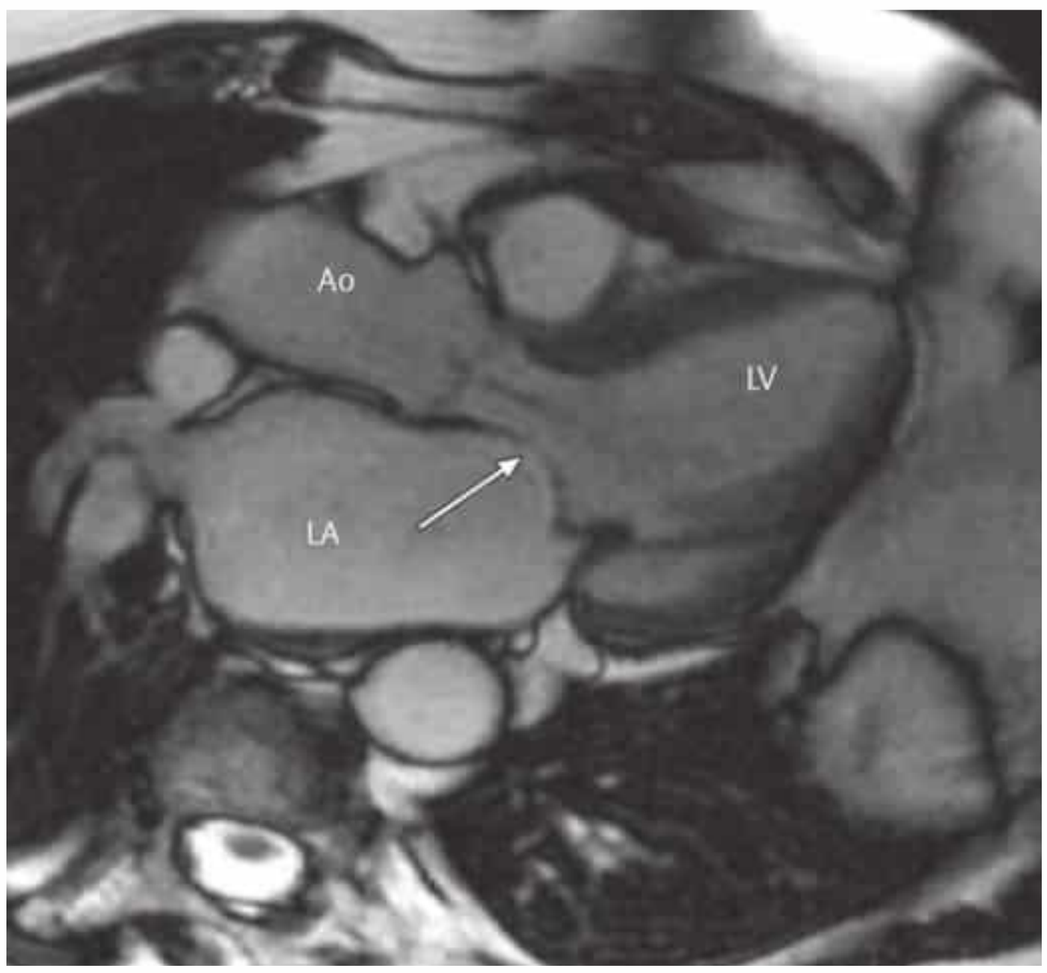

Fig. 7.14 MRI of mitral stenosis and aortic insufficiency in a 68-year-old man. Diastolic image shows both a jet phenomenon below the aortic valve and an abnormally small mitral valve orifice with doming of the anterior mitral leaflet (arrow).

Table 7.3 Causes of mitral insufficiency

Organic (valvular) mitral insufficiency	Acute	• Infective endocarditis • Papillary muscle rupture with an ischemic or degenerative cause • Chordal rupture • Prosthetic valve dysfunction
	Chronic	• Mitral valve degeneration • Mitral valve prolapse (classic, nonclassic, flail leaflet, Barlow disease) • Rheumatic mitral insufficiency • Systemic lupus erythematosus (Libman–Sacks endocarditis) • Carcinoid • Marfan syndrome • Ehlers–Danlos syndrome • Degenerative sclerosis due to abnormal calcium metabolism (chronic hemodialysis) • Dietary products containing fenfluramine (Fen Phen)
Functional mitral insufficiency	Acute	• Acute myocardial infarction • Functional prolapse due to left ventricular volume deficiency
	Chronic	• Dilated cardiomyopathy • Ischemic cardiomyopathy • Annular dilatation

dilatation (increased compliance) (**Fig. 7.16**). The left ventricle undergoes an eccentric hypertrophy, which maintains its stroke volume, and the dilated left atrium is better able to handle the regurgitant volume, thereby reducing the pressure load on the pulmonary circulation. In this compensated stage of mitral insufficiency the majority of patients remain asymptomatic for many years.[4,5] Decompensation occurs at a later stage, when a decline in left ventricular function and left atrial compliance lead to an increased pressure load in the pulmonary circulation.

In cases of severe acute mitral insufficiency, on the other hand, the pressure in the left atrium rises rapidly owing to a lack of compensatory adaptation of the left atrium and ventricle (**Fig. 7.16**). The increased pressure in the left atrium is transmitted directly to the pulmonary tree, resulting in clinical manifestations of dyspnea, pulmonary edema, hemoptysis, or pulmonary hypertension. Concurrently, forward failure develops owing to a decrease in the left ventricular stroke volume delivered to the systemic circulation.

Severe mitral insufficiency is frequently associated with normal or hyperdynamic left ventricular function, because the ejection of the regurgitant volume into the low-pressure pulmonary system relieves pressure on the left ventricle. As a result, left ventricular function cannot be accurately assessed in patients with severe mitral insufficiency.

Mitral insufficiency may be accompanied by mitral stenosis in patients with degenerative sclerotic mitral insufficiency, especially in those with an abnormal calcium metabolism (e.g., dialysis), or with inflammatory rheumatic mitral valve disease. The pathophysiological changes in these cases are again determined by the dominant defect.

Essential Point
Systolic left ventricular function cannot be accurately assessed in severe mitral insufficiency based on imaging of left ventricular contraction.

Clinical Features

Symptoms

- Prolonged tolerance of mitral insufficiency in the absence of symptoms
- Initial signs of dyspnea and fatigability (decreased left ventricular stroke volume) may progress swiftly to orthopnea and nocturnal dyspnea.
- The majority of patients with mitral valve prolapse are asymptomatic. Cardiac arrhythmias, palpitations, syncope, and atypical chest pain are rare complaints which serve as an indication of mitral valve prolapse syndrome.[15]

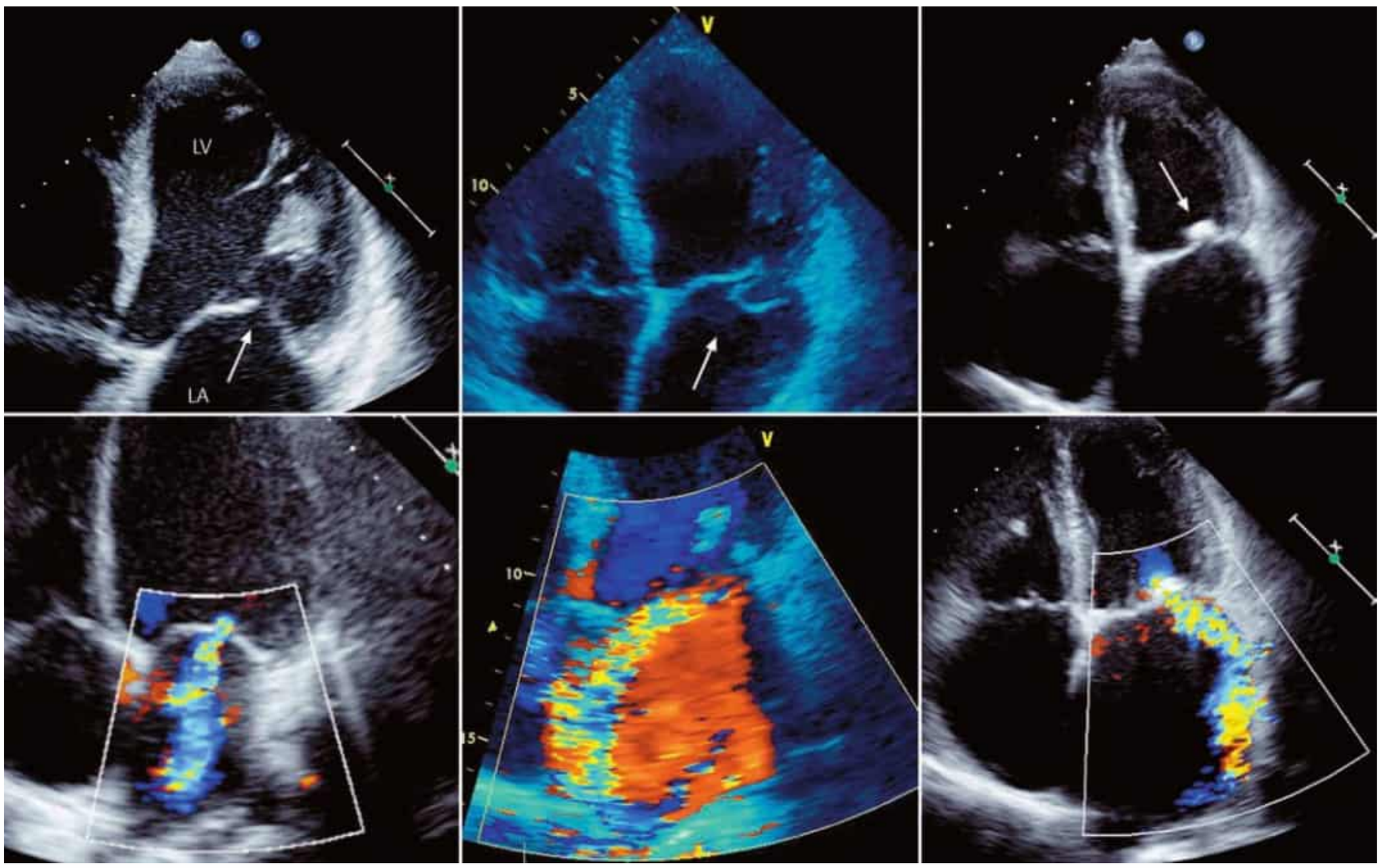

Fig. 7.15 Echocardiographic comparison of different etiologies of mitral insufficiency. Left: functional mitral insufficiency with typical tethering of the mitral leaflets, incomplete valve closure (top, arrow), and a central jet visible on color Doppler (bottom). Center: prolapse of the posterior mitral valve leaflet (arrow) with an eccentric jet on color Doppler. Right: degenerative mitral insufficiency with sclerotic thickening of the leaflet margins (arrow) and an eccentric jet.

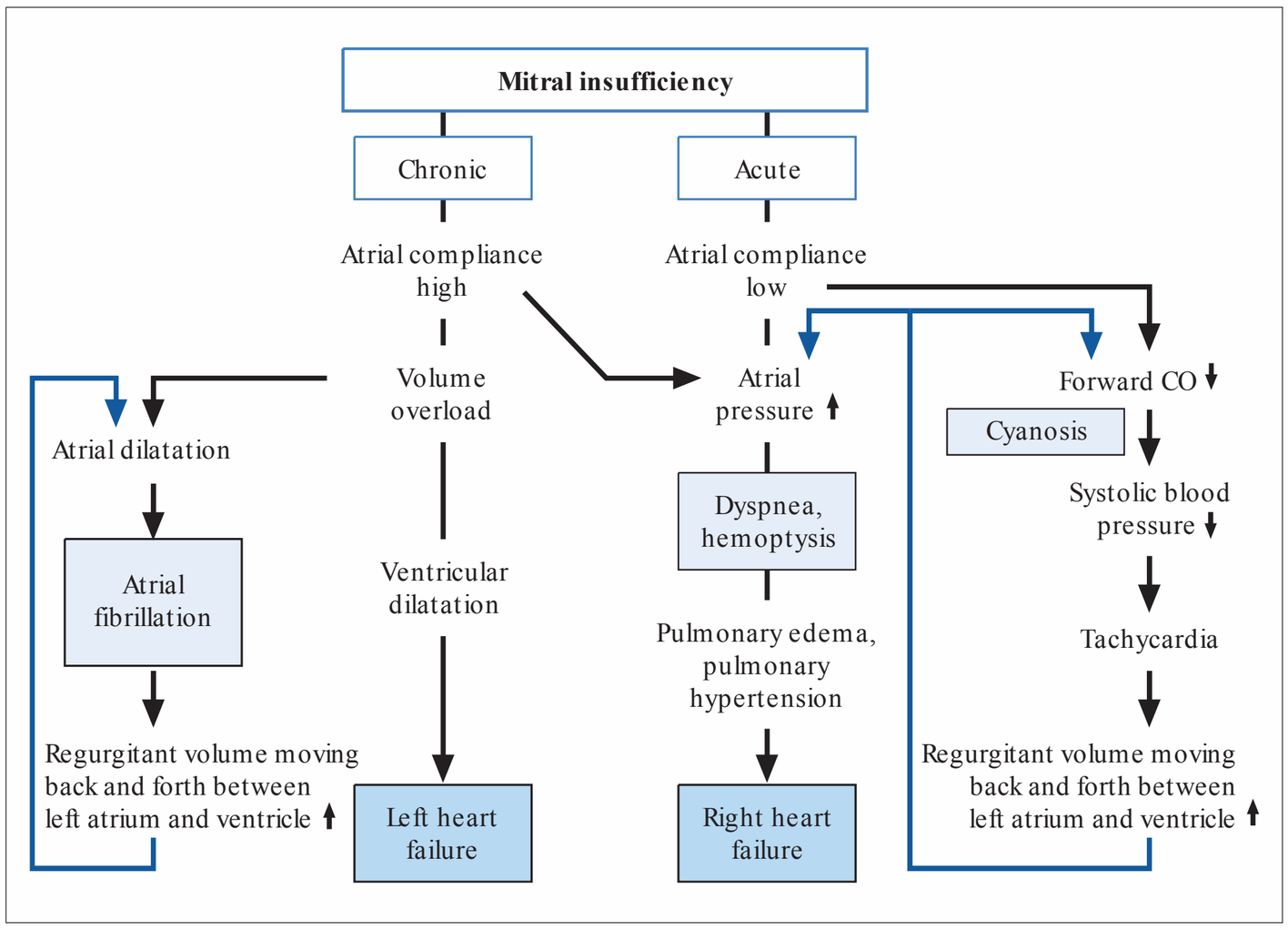

Fig. 7.16 Hemodynamic mechanisms in mitral insufficiency.

- Acute pulmonary edema in acute mitral insufficiency due to rupture of chordae tendineae or papillary muscle

Complications

- Atrial fibrillation
- Thromboembolism
- Endocarditis

Imaging

Echocardiography

M-Mode Echocardiography

(This is of limited value in mitral insufficiency.)

- Abnormal motion of mitral leaflets due to mitral valve prolapse
- Left atrial dilatation[16]

2D Echocardiography

General Findings

- Left atrial dilatation (**Fig. 7.15**)[17]
- Left ventricular dilatation
- Possible signs of right-heart overload
- Possible impairment of left ventricular function

Characteristic Findings

- Functional mitral insufficiency:
  - Tethering of the mitral leaflets due to outward displacement of the papillary muscles (**Fig. 7.15**)[18]
  - Tenting of the mitral leaflets, preventing their coaptation (**Fig. 7.15**)
  - Ventricular dilatation or regional dysfunction
  - Dilatation of the mitral annulus
  - Normal morphological appearance of mitral valve leaflets.
- Degenerative mitral insufficiency:
  - Thickened, echogenic mitral valve leaflets and chordae tendineae (**Fig. 7.15**)
  - Partial immobility of leaflet segments
  - Mitral annular sclerosis
  - Extraneous strand-shaped structures
  - Possible chordae tendineae rupture
- Mitral valve prolapse:
  - Systolic bulging of one or more leaflet segments into the atrium (late or holosystolic) by more than 2 mm beyond the plane of the mitral annulus[15]
  - Localization of affected segments in mitral valve prolapse
  - Myxomatous thickening of the leaflets >5 mm in classic mitral valve prolapse[15]
  - Possible flail leaflet (floating leaflet segment incapable of closure)
  - Dilatation of the mitral annulus
  - Possible chordae tendineae rupture
- Mitral valve endocarditis:
  - Thickening of the mitral leaflets
  - Extraneous floating echoes (vegetations) on the mitral valve and chordae tendineae (**Fig. 7.17**)
  - Abscess cavities
  - Leaflet perforation (**Fig. 7.17**)
- Papillary muscle rupture:
  - Portion of the papillary muscle (usually the head) floats in the left ventricle and protrudes through the mitral valve.

Essential Point

An echocardiographic description of the cause and mechanism of mitral insufficiency is crucial in the therapeutic management of hemodynamically significant MI.

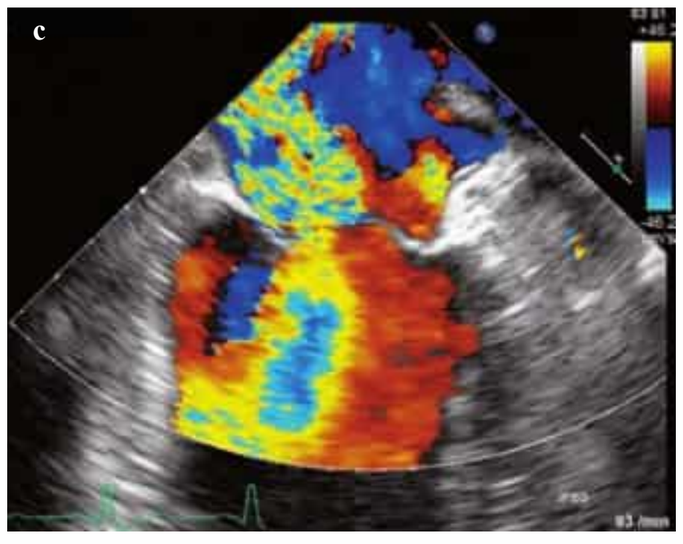

Fig. 7.17 a–c Mitral valve endocarditis.
a Vegetation on the atrial side of the anterior mitral valve leaflet (top, arrow) demonstrated by transesophageal echocardiography.
b The vegetation is delineated by color tissue Doppler.
c Color Doppler view of regurgitant flow through a perforation in the anterior mitral valve leaflet.

3D Echocardiography

- Mitral valve pathology can be evaluated in a surface-rendered en-face (surgical) view of the mitral leaflets from the left atrium (**Fig. 7.18**).
- The pathology (valve leak, prolapse, cleft, etc.) can be accurately localized and sized on the basis of the Carpentier segment model.[19]

Color Doppler Echocardiography

- Can demonstrate the regurgitant jet or multiple jets.
- Can evaluate the size and direction of the regurgitant jet.
- Can determine the proximal width of the jet[16] (**Fig. 7.15**).
- The PISA method can be used to calculate regurgitant volume (**Fig. 7.19**).
- The shape of the valve leak can be determined from the jet dimensions (a narrow jet in the four-chamber view and wide jet in the two-chamber view are typical of incomplete closure along the commissure in functional MI).
- Jet dynamics can be evaluated over the course of systole (late systolic maximum in mitral prolapse, midsystolic minimum in functional MI).

The PISA method can be used to calculate regurgitant volume (**Fig. 7.19**)[16]:

- Regurgitant flow = PISA × $v_{\text{Nyquist}} = 2\pi r^2 \times v_{\text{Nyquist}}$
- EROA = Regurgitant flow/v_{max}
- Regurgitant volume = EROA × VTI
- Regurgitant fraction = Regurgitant volume/filling volume

where PISA is proximal isovelocity surface area; v_{Nyquist} is the Nyquist limit for aliasing in color Doppler; r is the radius of the valve plane up to the Nyquist limit; EROA is the effective regurgitant orifice area; v_{max} is the maximum velocity of the regurgitant signal in CW Doppler; and VTI is the velocity–time integral of the regurgitant signal in CW Doppler.

Essential Point
The severity of mitral insufficiency cannot be reliably graded on the basis of the size of the color Doppler jet alone.
To obtain reliable PISA measurements, the examiner must know the basic principle and limitations of the PISA method.

Tissue Doppler

- Color tissue Doppler can demonstrate the incoherent motion of valvular vegetations (**Fig. 7.17**).

Pulsed Doppler Echocardiography

- The regurgitant volume and effective regurgitant orifice area (EROA) can be determined from the continuity equation based on the velocity–time integral (VTI) of mitral inflow and ventricular outflow.

The **regurgitant volume** and EROA are determined from the continuity equation as follows[16]:

- Method A: Regurgitant volume = [(MV area) × VTI (mitral inflow)] – [(LVOT area) × VTI (ventricular outflow)]
- Method B: Regurgitant volume = LVSV – [(LVOT area) × VTI (ventricular outflow)]

where MV area is the mitral valve area in the annular region determined by biplane calculation (area = π × [d/2 (2CH)] × [d/2 (4CH)]; d is the annular diameter in the two-chamber view [2CH] and four-chamber view [4CH]); VTI (mitral inflow) is the velocity–time integral of the mitral inflow signal; LVOT area is the area of the left ventricular outflow tract (= π[d/2]^2, where d is LVOT diameter); and LVSV is left ventricular stroke volume determined by 2D or 3D volumetry.

Essential Point
Measurement of the regurgitant volume by the continuity method yields highly variable results because of the simplified velocity and cross-sectional flow measurements.

CW Doppler Echocardiography

- The parameter d*p*/d*t* is determined from the Doppler spectrum of the regurgitant signal as an indicator of left ventricular contractility.[20]
- The maximum velocity and VTI are determined to allow computation of the EROA and regurgitant volume (PISA method) (**Fig. 7.19**).[16]
- The amplitude of the CW regurgitant signal reflects the size of the valve leak (not suitable for routine clinical grading of severity).[16]
- The maximum or peak pressure gradient between the left ventricle and atrium is calculated from the Bernoulli equation and the maximum regurgitant flow velocity ($PG_{max} = 4_{Vmax}{}^2$). The difference between the peripherally measured systolic blood pressure and the maximum pressure gradient enables an estimation of left atrial pressure.

Stress Echocardiography

- Can detect and evaluate an increase or decrease in the severity of mitral insufficiency in response to exercise or pharmacological stress.[13]

The contractile reserve can be evaluated in patients with poor left ventricular function (EF <30 %) and severe mitral insufficiency as a prognostic parameter prior to surgical treatment.[21]

Echocardiographic Grading of Mitral Insufficiency

Objective quantitative criteria for echocardiographic grading are the regurgitant volume, regurgitant fraction, and EROA (**Table 7.4**), which are still difficult to determine accurately in routine clinical imaging.[16] The proximal jet width is a semiquantitative parameter that is considered a reliable measure of EROA. The length and area of the jet depend strongly on preload and afterload as well as on system settings. Other grading criteria for mitral regurgitation are atrial size, the eccentricity of the jet, ventricular size and function, pulmonary venous return, as well as morphological criteria such as sclerosis, leaflet mobility, flail leaflet, etc.

The echocardiographic grading of mitral insufficiency can be simplified and standardized by using a scoring system based on current guidelines (**Table 7.5**).[5]

Magnetic Resonance Imaging

In patients with mitral insufficiency, a regurgitant jet extends from the mitral valve into the left atrium during systole (**Fig. 7.20**). The regurgitant volume can be accurately quantified by flow measurement with phase-contrast MRI. This technique enables one to determine both the volume of diastolic inflow across the mitral valve and the ejection volume across the aortic valve.[22] The difference between the two volumes equals the regurgitant volume across the mitral valve. Because the mitral valve may move considerably through the plane of the phase-contrast acquisition during the cardiac cycle relative to the aortic valve, it would be desirable to have software capable of tacking the acquisition plane to valve movements; otherwise there is the risk that the phase-contrast method may underestimate the regurgitant volume. Another possibility for quantifying the regurgitant volume in mitral insufficiency is to determine the difference between the left and right ventricular stroke volumes,[23] provided there are no coexisting defects in other valves.

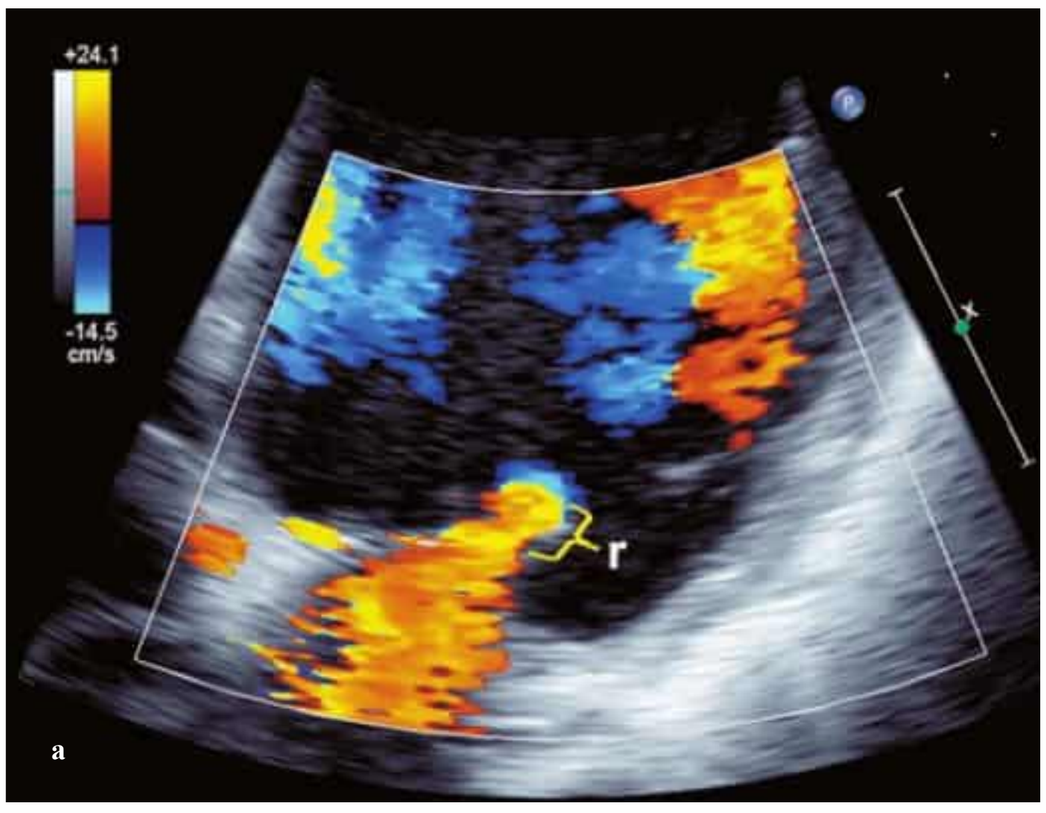

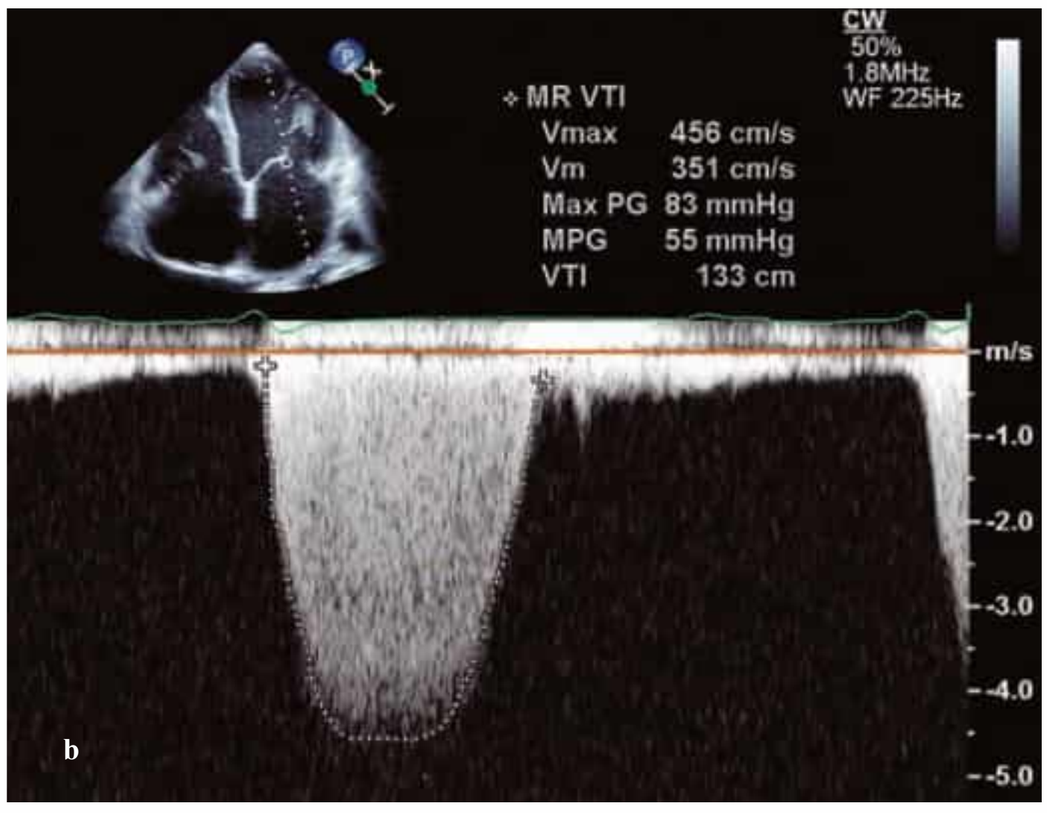

Fig. 7.19 a, b Effective regurgitant orifice area (EROA) and regurgitant volume determined by the PISA method.

a Measurement of the PISA radius (0.9 cm) proximal to the valve orifice (in the left ventricle).

b CW Doppler spectrum of regurgitant flow is used to determine the maximum velocity and velocity–time integral.
Regurgitant flow = $2\pi \times (0.9\,cm)^2 \times 14.5\,cm/s = 73.8\,mL/s$
EROA = $(73.8\,mL/s) / (456\,cm/s) = 0.16\,cm^2$
Regurgitant volume = $0.16\,cm^2 \times 133\,cm = 21.5\,mL$

Aortic Stenosis

Etiology

Aortic stenosis is a condition in which opening of the aortic valve is impaired, usually as a result of degenerative sclerotic valve changes or severe calcification.[14]

Valvular aortic stenosis is the most common form of valvular heart disease, accounting for 43.1 % of cases seen in routine clinical settings.[6] Severe aortic stenosis is present in 2 % of patients of 75 years of age, and in 8 % of individuals aged 85 years.[4,5]

Degenerative changes with sclerotic transformation, shrinkage, and fusion of the valve leaflets, causing a progressive reduction in valve orifice area, are causative in 81.9 % of cases.[6] The second most frequent cause (11.2 %) is (post)rheumatic inflammatory disease, in which an autoimmune response leads to formation of adhesions between the coapting valve margins, transverse shrinkage of the leaflets with abnormal vascularization, and stiffening of the leaflets by organized necrotic tissue. In many cases there is evidence that the degenerative changes in the aortic valve are based on an underlying chronic inflammatory process. Bacterial endocarditis is causative in 0.8 % of patients with known aortic stenosis.

Pathophysiology

The aortic valve has a normal orifice area (AVA) of 3.0–4.0 cm^2. A hemodynamically significant aortic stenosis in which the AVA is reduced by more than half leads to a pressure overload on the left ventricle. Severe aortic stenosis is present when the AVA is reduced to below 1.0 cm^2, or the mean pressure gradient across the aortic valve is ≥40 mmHg (**Table 7.6**).[4,5,5a] The maximum intraventricular pressure load can be estimated by measuring the peripheral systolic blood pressure and adding this value to the peak pressure gradient. With a systolic pressure of 120 mmHg and a peak pressure gradient of 80 mmHg, the maximum intraventricular pressure is as high as 200 mmHg.

Aortic stenosis tends to be gradually progressive, causing an average 0.1–0.3 cm^2 reduction in valve orifice area per year. The left ventricle adapts to the rising pressure load by concentric hypertrophy.[4,5] This is associated with a decline in left ventricular compliance and a rise in end-diastolic pressure, resulting in diastolic dysfunction.

The end stage of the disease is marked by left ventricular dilatation as insufficient oxygen is supplied to the hypertrophic left ventricular myocardium. This leads to further impairment of myocardial contractility, and decompensation occurs with secondary dilatation of the left atrium, pulmonary congestion, and right-sided heart failure.

The majority of patients with aortic stenosis have combined aortic valve disease with associated aortic insufficiency, although aortic stenosis generally represents the dominant defect. In cases where aortic insufficiency predominates, the increased stroke volume from the regurgitant volume leads to a rise in the transvalvular pressure gradient, causing the degree of aortic stenosis to be overestimated.

Table 7.4 Grades of severity of mitral insufficiency

	Grade I	Grade II	Grade III
Jet length	≤⅓ of LA	≤⅔ of LA	>⅔ of LA
Jet area	<4 cm^2; <20 % of LA	4–8 cm^2; 20–40 % of LA	>8 cm^2; >40 % of LA
Prox. jet width	<0.3 cm	0.3–0.7 cm	≥0.7 cm
EROA	<0.2 cm^2	0.2–0.4 cm^2	≥0.4 cm^2; ≥0.2 cm^2 [a]
Regurgitant flow rate	<50 mL/s	50–99 mL/s	100–400 mL/s
Regurgitant volume	<30 mL	30–60 mL	>60 mL; >30 mL[a]
Regurgitant fraction	<30 %	30–50 %	>50 %

Summary of various grading criteria based on current guidelines.[4,5,16]
LA = left atrium, EROA = effective regurgitant orifice area.
[a] In patients with ischemic mitral insufficiency.

Table 7.5 Scoring system for grading mitral insufficiency

Jet size	<4.0 cm^2; <20 % LA (1)	4.0–8.0 m^2; 20–40 % LA (2)	>8.0 cm^2; >40 % LA (3)
Jet direction	Central (1)	Eccentric (2)	
LA size	≤4.0 cm, ≤36 mL (1)	>4.0 cm, >36 mL (2)	
Prox. jet width	<0.3 cm (1)	0.3–0.7 cm (3)	>0.7 cm (5)
Increasing severity			

Grade	I	(I–II)	II	(II–III)	III
Score	4–5	6	7–8	9	10–12

Explanation: The point values (boldface numbers in parentheses) for each of the four grading parameters are added (top) to yield a final score (bottom).[5a]

Table 7.6 Grades of severity of aortic stenosis

	Grade I	Grade II	Grade III
AVA	>1.5 cm^2	1.0–1.5 cm^2	<1.0 cm^2
AVA/BSA (m^2)	>1.0 cm^2/m^2	0.6–1.0 cm^2/m^2	<0.6 cm^2/m^2
Mean pressure gradient	<20 mmHg	20–50 mmHg	>50 mmHg
Peak pressure gradient	<40 mmHg	40–80 mmHg	>80 mmHg
Time to V_{max}	<80 ms		>80 ms

Summary of different grading criteria based on current guidelines.[4,5]
AVA = aortic valve area, BSA = body surface area.

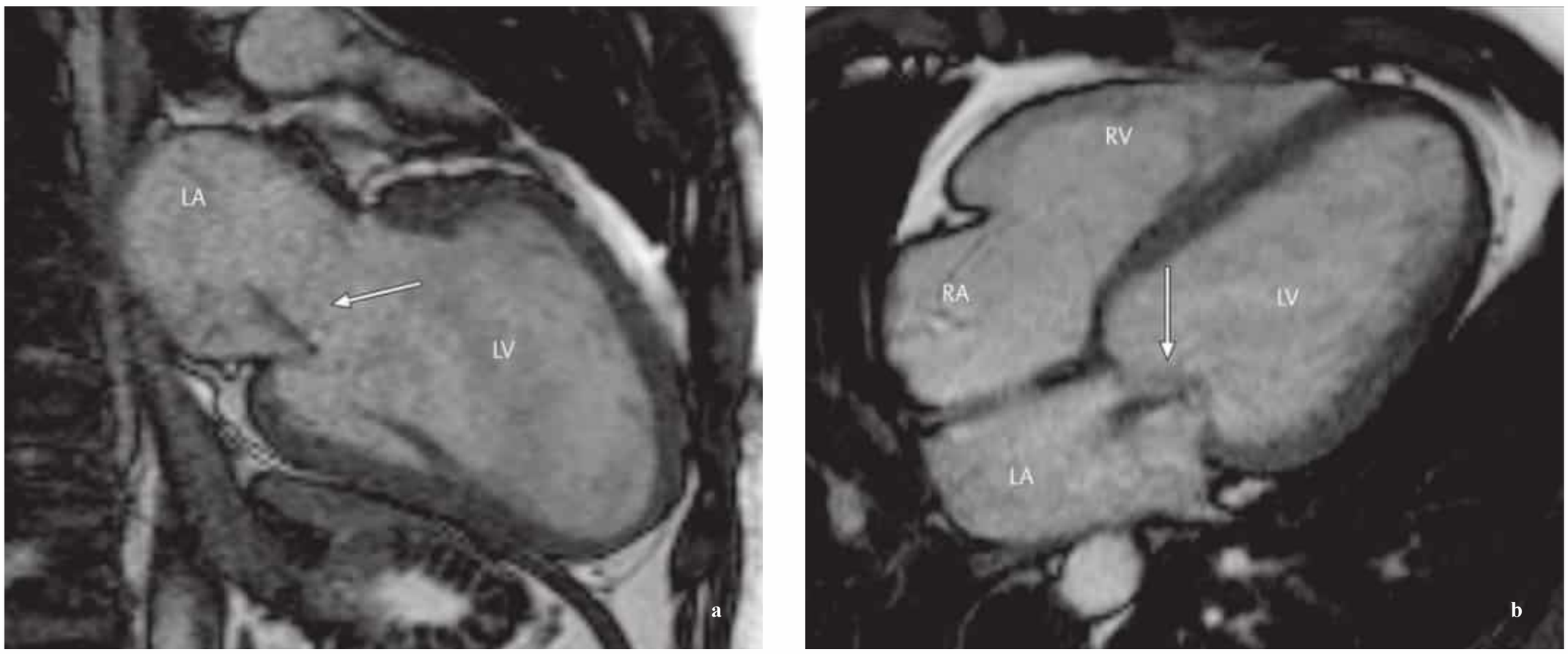

Fig. 7.20 a, b Mitral insufficiency in a 22-year-old man. MRI clearly demonstrates a systolic jet (arrow) regurgitating across the mitral valve into the left atrium. Quantification indicated a regurgitant fraction of 28 %

a Vertical long-axis view.
b Horizontal long-axis view through the left ventricle.

Clinical Features

Symptoms

- Slow progressive course with a long asymptomatic interval
- Decline in exercise tolerance, initially insidious and followed later by exertional dyspnea (late symptom and poor prognostic sign)
- Angina pectoris (increased O_2 consumption by the hypertrophic myocardium, subendocardial ischemia due to increased intraventricular pressure, reduction in coronary perfusion)
- Syncopal attacks and dizzy spells (low output)
- Risk of left ventricular decompensation with pulmonary edema, often occurring acutely in patients with severe aortic stenosis

Complications

- Atrial fibrillation
- Sudden cardiac death from ventricular arrhythmia
- Endocarditis

Imaging

Echocardiography

M-Mode Echocardiography

- Sclerosis and thickening of the valve leaflets with reduced cusp separation (**Fig. 7.21 b**)
- Left ventricular hypertrophy with increased LV muscle mass[17]

2D Echocardiography

- Sclerosis and thickening of the valve leaflets with reduced cusp separation
- Fusion of the valve leaflets (**Fig. 7.21**)
- Planimetry of the anatomical AVA (parasternal short-axis scan or transesophageal echocardiography)
- Basal septal hypertrophy with obstruction of the left ventricular outflow tract
- Assessment of left ventricular function
- Extraneous structures (vegetations or thrombi, detected by transesophageal scanning)

3D Echocardiography

- Allows 3D visualization of aortic valve pathology. The smallest AVA at the level of the valve margins can be determined (orifice area frequently cannot be evaluated in markedly thickened and calcified valves).

Color Doppler

- Turbulence distal to the valve
- Accompanying aortic insufficiency

CW Doppler

- Increased flow velocity due to valvular stenosis (>2.5 m/s) (**Fig. 7.22**)
- Mean and peak pressure gradients can be determined with the simplified Bernoulli equation[14] (**Fig. 7.22**).
- Timing of peak velocity can be determined: early systole (<80 ms)=mild stenosis; late systole (>80 ms)=severe stenosis.

Pressure gradient determination with the Bernoulli equation:

- Pressure gradient = $4_{Vmax}{}^{2}$

where *v* is the maximum flow velocity across the aortic valve measured by CW Doppler.

CW and Pulsed Doppler

The effective AVA can be calculated with the continuity equation[14]:

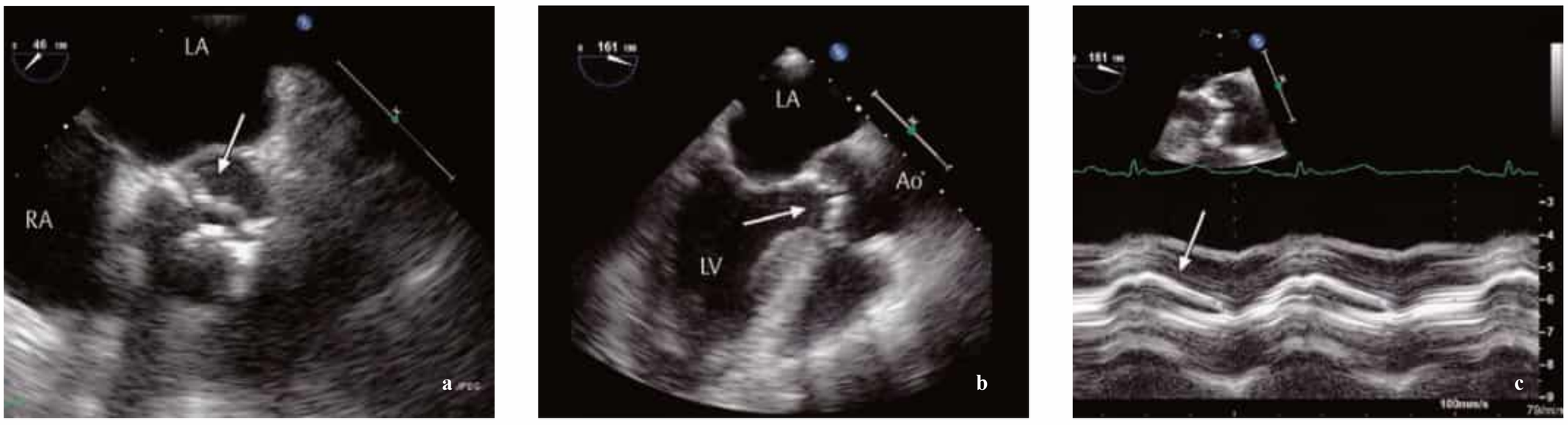

Fig. 7.21 a–c Aortic valve stenosis imaged by transesophageal echocardiography.
a Severely sclerotic aortic valve margins with a small valve orifice area (arrow).
b Lateral view of markedly reduced cusp separation (arrow).
c M-mode registration shows a reduction in systolic valve opening (arrow).

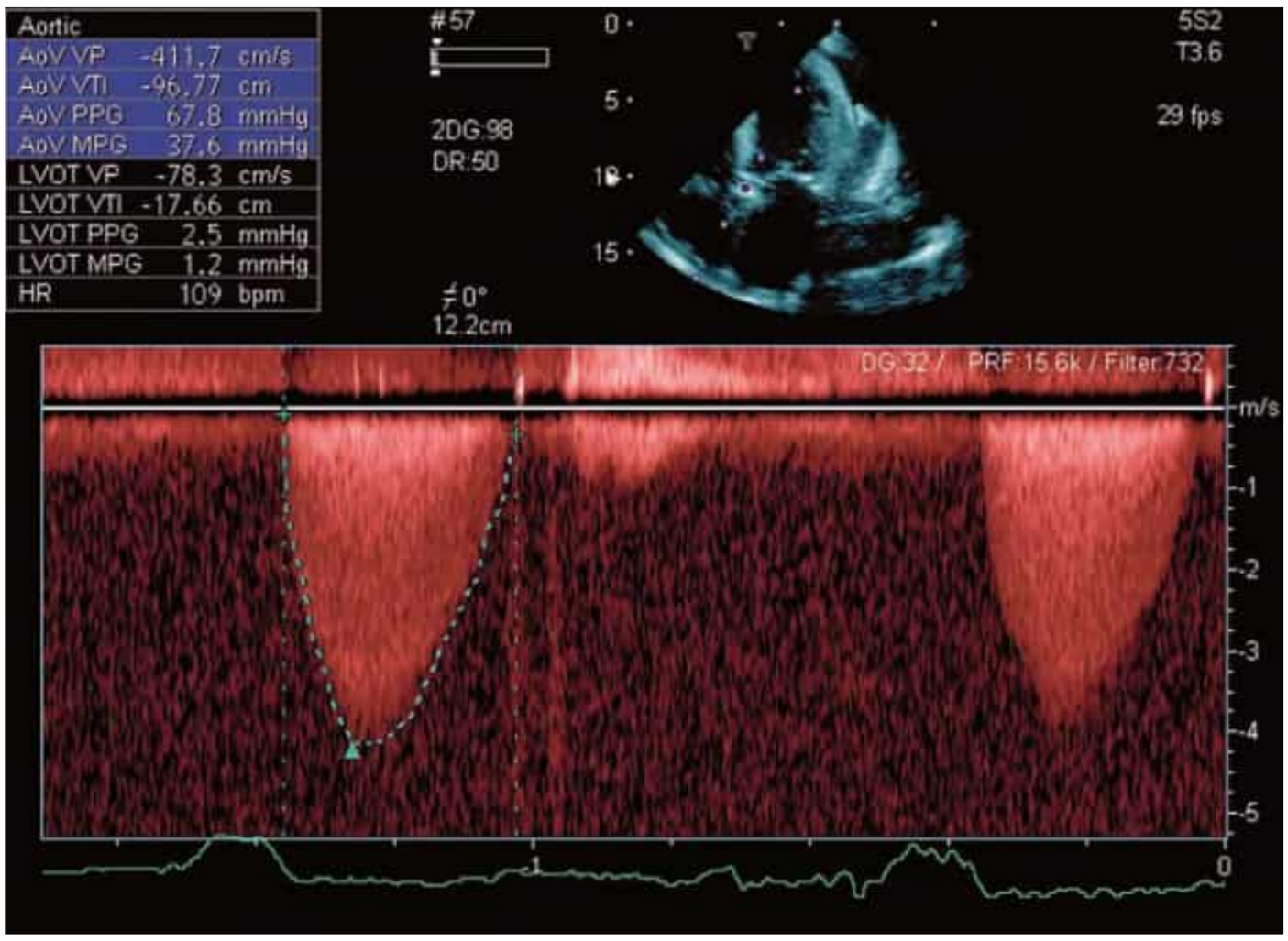

Fig. 7.22 CW Doppler echocardiography of aortic valve stenosis. The modified Bernoulli equation indicates a peak pressure gradient (PPG) of 68 mmHg and a mean pressure gradient (MPG) of 38 mmHg. More than 80 ms is required to reach peak systolic flow. The aortic valve orifice area calculated with the continuity equation is 0.51 cm^2.

- AVA (cm^2)=LVOT area (cm^2) × {VTI [LVOT] (cm)/VTI [CW] (cm)}

where LVOT=left ventricular outflow tract; VTI [LVOT]=velocity–time integral of flow in the LVOT (determined by pulsed Doppler); VTI [CW]=velocity–time integral of flow across the aortic valve (AV) (determined by CW Doppler); and LVOT area=$\pi \times (d[\text{LVOT}]/2)^2$ with d[LVOT]=diameter of the LVOT.

Stress Echocardiography

- Can objectivize severity of aortic stenosis in patients with a reduced AVA and low pressure gradient in the presence of poor left ventricular function.[24]
- Can determine the contractile reserve of the left ventricle as a prognostic parameter.

Essential Point
Because determination of the pressure gradient across a stenotic aortic valve depends significantly on left ventricular function, both pressure gradient and valve orifice area should be determined in every patient.

Magnetic Resonance Imaging

The distinctive feature of aortic valve stenosis in cine MR sequences is a jet extending into the ascending aorta from the aortic valve, a result of phase dispersion due to the increased flow velocities (**Fig. 7.23 a, b**). Jet evaluation alone is insufficient to grade the severity of the stenosis, however.

Two techniques are available for this in MRI[20]: determination of the pressure gradient across the valve by phase-contrast flow measurement, and[9] planimetry of the valve orifice area (AVA).

In **aortic valve planimetry**, the cine sequences should be directed as closely parallel to the aortic valve as possible (**Fig. 7.23 c**). SSFP sequences are advantageous over conventional spoiled gradient-echo sequences owing to their higher spatial and temporal resolution. Initial studies have shown that this technique yields a more consistent image quality, especially compared with TEE. However, it also overestimates the aortic valve orifice area by ~15 %compared with TEE[10,25]—analogously to the determination of the valve orifice area in mitral stenosis.

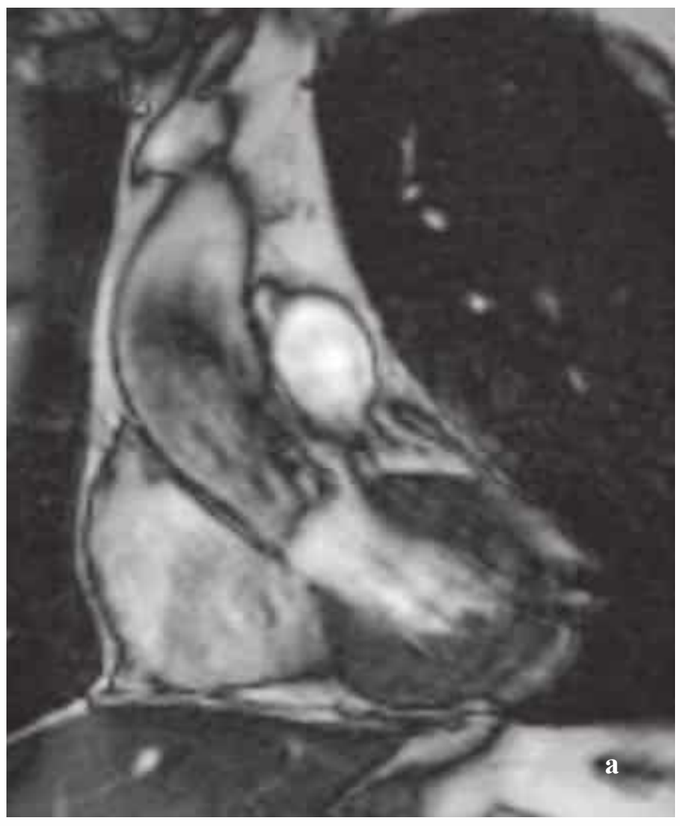

Fig. 7.23 a–d Combined aortic valve disease with predominant stenosis in a 79-year-old man. Phase-contrast flow quantification indicated a peak pressure gradient of 50 mmHg and a regurgitant fraction of 6 %

a, b The systolic jet from the aortic valve into the ascending aorta is consistent with aortic stenosis.

c MRI planimetry shows high-grade aortic stenosis with a valve orifice area of 0.7 cm^2.

d Delayed-enhancement images show fibrotic changes, which are especially pronounced in the posterior lateral wall of the left ventricle (arrow).

The pressure gradient across the stenosis can be determined by MR phase-contrast quantification of flow velocities and use of the Bernoulli equation. The maximum anticipated flow velocity must be present to ensure an accurate determination of flow velocities (see also Chapter 6, p. 104). Underestimation of flow velocity and pressure gradient also occurs in patients with left ventricular pump dysfunction.[26,27] For this reason, left ventricular functional parameters and myocardial mass should be routinely evaluated in all patients. In parallel, delayed-enhancement images after contrast administration are useful in documenting the extent of intramyocardial fibrotic lesions (**Fig. 7.23 d**). The determination of AVA using the continuity equation is largely independent of cardiac function. In this method the orifice area is calculated from the area of the left ventricular outflow tract and from the pre- and postvalvular flow velocities.[26]

Aortic Insufficiency

Etiology

In aortic insufficiency, blood regurgitates through the aortic valve into the left ventricle during diastole. This represents the third most common valve defect in patients with known valvular heart disease, accounting for 13.3 % of cases.[6]

Degenerative processes are the leading cause of aortic insufficiency (50.3 % of cases), followed by (post)rheumatic disease (15.2 %) and valve lesions due to endocarditis (7.5 %).[6] The prevalence of aortic insufficiency in western industrialized countries is higher in males (13 %) than in females (8.5 %).[28] Comparable to mitral insufficiency, aortic insufficiency may be acute or chronic, and may have an organic or a functional cause (**Table 7.7**).

Pathophysiology

Diastolic retrograde flow through an incompetent aortic valve into the left ventricle imposes an acute or chronic volume overload on the left ventricle. The regurgitant volume in this situation depends on the size of the valve defect, the duration of diastole, and left ventricular compliance. In chronic aortic insufficiency, the regurgitant volume induces dilatation of the ventricular cavity. By increasing the stroke volume, the left ventricle can maintain normal pump function during the compensated stage of the disease. The ventricular dilatation leads to a compensatory increase in ventricular muscle mass in the form of eccentric hypertrophy to prevent a rise of wall tension in accordance with Laplace's law. In most cases it takes years for the disease to progress from a compensated to a decompensated stage, which is marked by a rise in end-diastolic left ventricular pressure.[4,5]

Table 7.7 Causes of aortic insufficiency

Organic (valvular) aortic insufficiency	Acute	• Infective endocarditis • Prosthetic valve dysfunction • Paravalvular leak
	Chronic	• Sclerotic valve degeneration • Rheumatic disease • Myxomatous changes with or without prolapse • Ankylosing spondylitis (shortening and thickening of the leaflets and dilatation of the aortic root) • Rheumatoid arthritis • Osteogenesis imperfecta
Functional aortic insufficiency	Acute	• Acute dissection of the ascending aorta (type A)
	Chronic (due to aortic root dilatation)	• Idiopathic • Sinus of Valsalva aneurysm • Ectasia of the ascending aorta • In systemic hypertension • Connective-tissue diseases (Marfan syndrome, Ehlers–Danlos syndrome) • Syphilitic mesaortitis (rare) • Giant cell aortitis • Reiter syndrome • Behçet syndrome

Acute aortic insufficiency generally presents as a severe acute condition. The heart is unable to compensate for the abrupt increase in end-diastolic volume. This causes a rapid and severe rise in end-diastolic filling pressure, leading to an acute pressure rise in the left atrium and pulmonary circulation that may culminate in acute pulmonary edema.

Clinical Features

- The compensated stage of severe, chronic aortic insufficiency remains asymptomatic for several years (the rate of progression to symptom onset or deterioration of left ventricular function is less than 5 %per year).
- Symptom onset is followed by rapid deterioration.
- Rare syncopal episodes (reduced arterial pressure)
- Low incidence of sudden cardiac death (<0.2 %per year)
- Abdominal pain
- Stress-induced tachycardia, palpitations, head nodding in time with the heartbeat (Musset's sign)
- Exertional dyspnea, orthopnea, or nocturnal dyspnea
- Marked increase in blood pressure amplitude (over 100 mmHg with diastolic pressures <60 mmHg in severe aortic insufficiency)
- The incidence of deaths, clinical manifestations, or left ventricular dysfunction is dependent on the left ventricular end-systolic diameter (LVESD): 19 %with LVESD >50 mm, 6 % with LVESD 40–50 mm, 0 %with LVESD <40 mm.[4,5]

Table 7.8 Grades of severity of aortic insufficiency

	Grade I	Grade II	Grade III
Proximal jet width (vena contracta width)	<0.3 cm	0.3 – 0.6 cm	>0.6 cm
PHT	>500 ms	500 – 200 ms	<200 ms
Proximal jet width/LVOT width (×100)	<25 %	25 – 64 %	≥65 %
Effective regurgitant orifice area (EROA)	<0.1 cm²	0.1 – 0.3 cm²	>0.3 cm²
EROA/LVOT area	<5 %	5 – 20 %(I–II) 21 – 59 %(II–III)	≥60 %
Regurgitant volume	<30 mL	30 – 59 ml	≥60 mL

Summary of different grading criteria based on current guidelines.[4,5,16]
PHT = pressure half-life, LVOT = left ventricular outflow tract, EROA = effective regurgitant orifice area.

Imaging

Echocardiography

M-Mode Echocardiography

- Increased contractile amplitudes of the left ventricular septum and posterior wall
- Left ventricular dilatation with an increased end-systolic and end-diastolic diameter. (Aortic valve replacement is indicated in severe, chronic, asymptomatic aortic insufficiency at LVESD >55 mm, or LVEDD >75 mm.)[4,5]
- Determination of left ventricular muscle mass[27]

2D Echocardiography

- Etiological diagnosis (sclerosis, prolapse, functional, endocarditic vegetation, aortic dissection) (**Figs. 7.24—7.26**)
- Assessment of left ventricular dilatation (elliptical versus spherical)
- Determination of left ventricular end-diastolic and end-systolic volumes[17]
- Increased left ventricular contraction due to volume overload
- Determination of the ejection fraction[17]
- Dilatation of the aortic sinus and descending aorta (Marfan syndrome)
- Detection of ascending aortic dissection (transesophageal scanning)

Color Doppler

- Measurement of the proximal jet width (vena contracta width) (**Fig. 7.24**) and proximal jet area (EROA) (**Table 7.8**)[16]
- Ratio of jet width/LVOT diameter and jet area/LVOT area (**Table 7.8**).
- Location of valve leak (valvular or paravalvular)
- The length of the regurgitant jet within the left ventricle enables only a rough assessment of the severity of aortic regurgitation, but it is not useful for the semiquantitative grading of severity (see below)

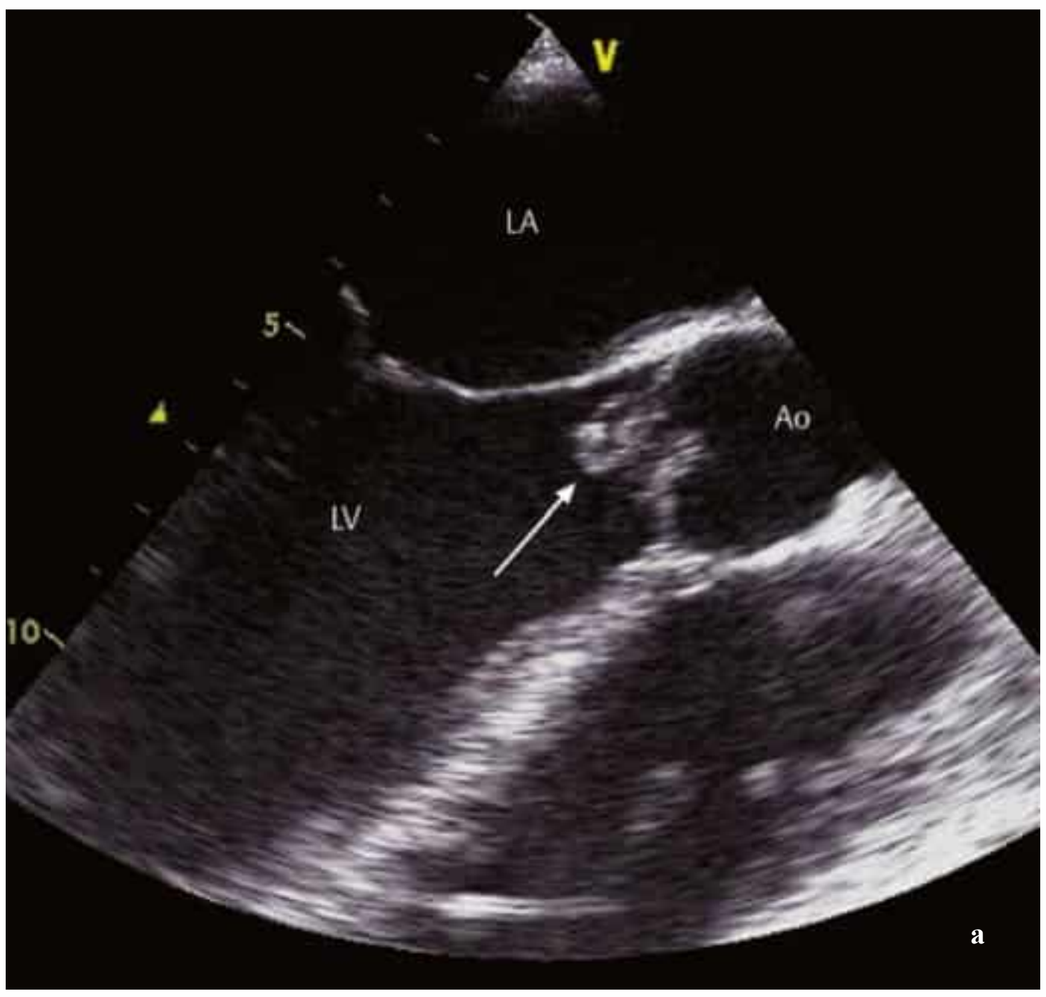

Fig. 7.26 a, b Aortic valve endocarditis.
a Aortic valve endocarditis with pronounced vegetations on the aortic leaflets (arrow). **b** Eccentric regurgitant jet on color Doppler.

Pulsed Doppler

- Suprasternal interrogation of blood flow in the ascending or descending aorta for detection of significant regurgitation

CW Doppler

- Evaluation of signal intensity: high intensity indicates severe aortic insufficiency.
- Measurement of the pressure half-time (PHT).[16]

Essential Point
Because the size of the color Doppler jet in aortic insufficiency depends on the aortic pressures, only the proximal jet width should be used for grading based on assessment of the color Doppler jet.

Magnetic Resonance Imaging

MRI in aortic insufficiency demonstrates a jet extending from the aortic valve into the left ventricle during diastole (**Fig. 7.27**). Determining the size of this area of signal loss permits only a rough estimate of the severity of aortic insufficiency. The regurgitant volume can be established more accurately by determination of the left and right ventricular volumes. The difference between these two volumes is equal to the regurgitant volume. However, this method is reliable only in the absence of other valve disease. The regurgitant volume can also be determined by performing flow measurements in the ascending aorta and pulmonary trunk, although this method also requires the absence of multiple valve disease.[27] An additional method is to determine the regurgitant volume directly by taking a measurement above the aortic valve. As in patients with aortic stenosis, the examination should include left ventricular volumetry to obtain information on muscle mass and the end-diastolic volume index (**Fig. 7.27**).

Combined Mitral and Aortic Valve Disease

Approximately 20 %of patients with acquired left-sided cardiac valve disease have a combination of mitral and aortic valve lesions.[6] In these cases, the individual valve lesions should not be considered in isolation, because they mutually affect each other. It is critically important to evaluate each lesion for its etiology and severity and to determine which one is dominant. This is particularly important preoperatively in deciding whether to perform a double valve repair (**Fig. 7.27**).

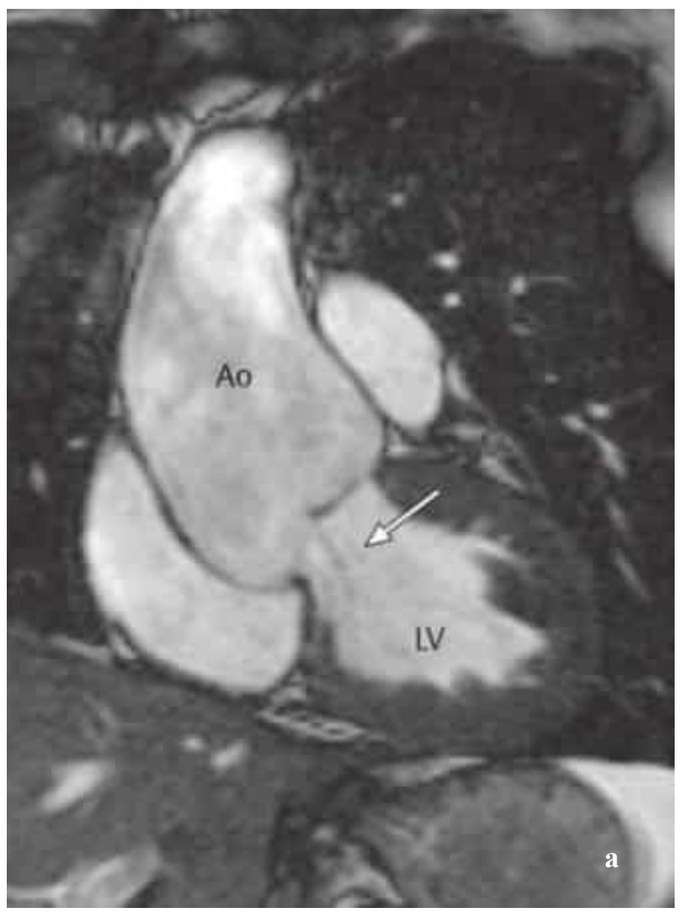

Fig. 7.27 a–d MRI findings in aortic insufficiency.
a, b Aortic insufficiency in a 33-year-old male patient with marfanoid habitus and marked ectasia of the ascending aorta. Cine images show a regurgitant jet directed into the left ventricle and impinging on the anterior mitral valve leaflet (arrow).
c, d Cine MRI of a bicuspid aortic valve with incomplete closure (**d**). The flow measurement sequence indicated a regurgitant fraction of 31 % The end-diastolic volume index of the left ventricle was 108 mL

Pathophysiology

Mitral Stenosis and Aortic Insufficiency (Rare) (Fig. 7.28)

As a rule, mitral stenosis chiefly determines the hemodynamic changes which occur in this combination.[4,5] In patients with severe concomitant aortic insufficiency, impaired ventricular filling may mask the effect of the volume overload on the left ventricle. As a result, evaluation of left ventricular size and determination the PHT of aortic regurgitant flow are not reliable in these cases.

Aortic Valve Stenosis and Mitral Insufficiency (Fig. 7.29)

Functional mitral insufficiency is often present in patients with severe chronic aortic stenosis as a result of the high intraventricular systolic pressure and dilatation of the left heart. The transmitral release of pressure and volume overload from the left ventricle into the low-pressure system, with a decrease in forward stroke volume, may lead to the underestimation of aortic stenosis. The increase in left ventricular contractions caused by this decompression also tends to mask any left ventricular dysfunction that may be present.[4,5]

Aortic Insufficiency and Mitral Insufficiency

Combined aortic and mitral regurgitation are most frequently caused by cardiomegaly with dilatation of the left cardiac chambers leading to functional incompetence of the valves. The compensatory increase in left ventricular contractions in aortic insufficiency may lead to an exacerbation of mitral insufficiency.

Mitral Stenosis and Aortic Valve Stenosis

The most frequent cause of this combination is rheumatic heart disease. The mitral stenosis leads to a reduction in left ventricular filling, causing decreased flow across the aortic valve. The severity of the aortic stenosis is difficult to evaluate in these cases owing to the small aortic valve orifice area and low pressure gradient.[4,5]

Essential Point
Combined aortic and mitral valve lesions may cause the severity of the lesions to be underestimated.

Tricuspid Stenosis

Etiology

Acquired tricuspid stenosis is rare and most commonly results from rheumatic heart disease. The main pathological changes—shortening of the valve leaflets and fusion of the commissures—are the same as in mitral stenosis. It is common for tricuspid insufficiency to coexist with tricuspid stenosis due to shortening and thickening of the chordae tendineae. Acquired forms of tricuspid stenosis may also result from bacterial endocarditis, carcinoid syndrome, endomyocardial fibrosis, or lupus erythematosus.[4,5]

The differential diagnosis in patients with clinical manifestations of tricuspid stenosis should include right atrial masses, such as myxoma or thrombi. Constrictive pericarditis should also be excluded.

Pathophysiology

The normal orifice area of the tricuspid valve is ~6 cm^2. When the orifice becomes significantly narrowed, the mean pressure in the right atrium increases (normal value ~5 mmHg). When the mean pressure gradient between the right atrium and right ventricle is greater than 5 mmHg, severe tricuspid stenosis is present. The pressure gradient across the tricuspid valve leads to rapid dilatation of the right atrium (**Fig. 7.30**), a marked decline in cardiac output, peripheral edema, and signs of hepatic congestion.

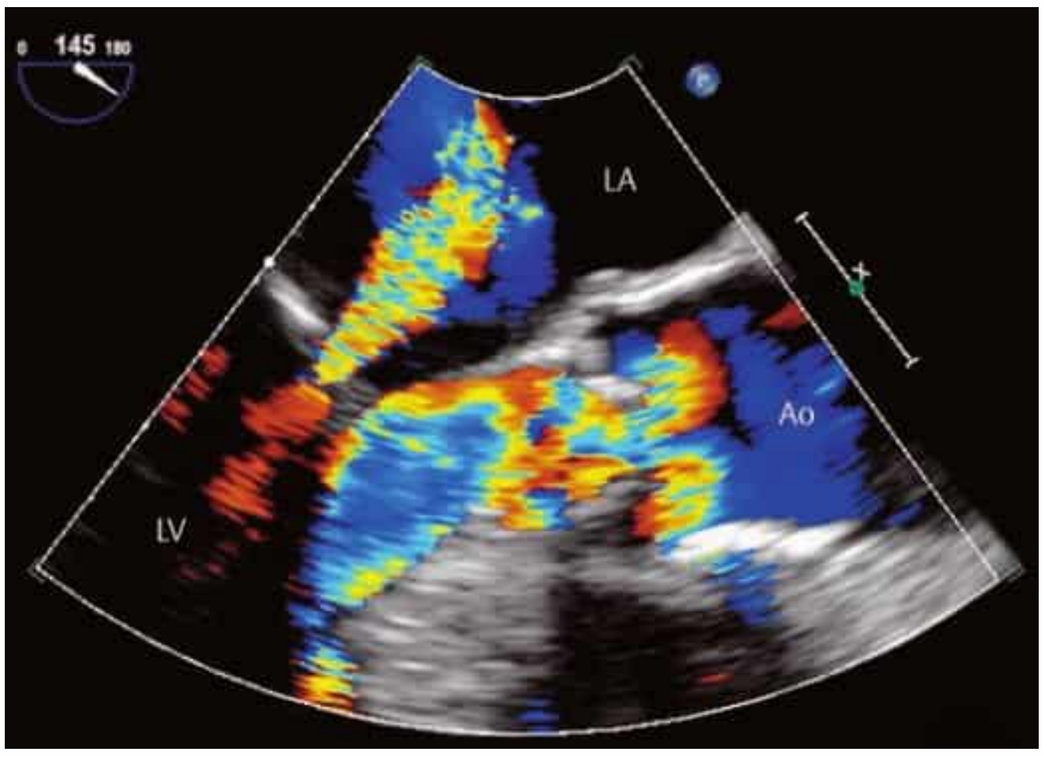

Clinical Features

Symptoms

- Fatigue, decreased exercise tolerance (markedly reduced cardiac output)
- Feeling of fullness, bloating
- Hepatomegaly and positive hepatojugular reflux
- Ascites, edema, anasarca, distended neck veins
- P-dextrocardiale in ECG

Imaging

Echocardiography

2D Echocardiography

- Dilatation of the right atrium (**Fig. 7.30**)
- Abnormal tricuspid valve motion (carcinoid is marked by typical stiff, separated leaflets with combined stenosis and regurgitation) (**Fig. 7.31**).
- Doming of the leaflets (with postinflammatory fusion of the commissures)
- Thickening of the leaflets (**Fig. 7.31**)
- Dilatation and decreased inspiratory collapse of the inferior vena cava

Color Doppler

- PISA phenomenon during tricuspid inflow ("peacock eye" pattern)
- Narrow color Doppler jet caused by accelerated inflow into the right ventricle (**Fig. 7.30**)

CW-Doppler

- Increased flow velocity across the tricuspid valve (**Fig. 7.30**)
- The mean pressure gradient across the tricuspid valve can be determined with the Bernoulli equation (**Fig. 7.30**).
- Determination of the pressure half-time (PHT)
- The tricuspid valve area (TVA) can be estimated from the pressure half-time using the formula TVA=190/PHT.[11]

Essential Point
If the valve leaflets in tricuspid stenosis appear stiff, broadened, and shortened on echocardiography, the differential diagnosis should include carcinoid syndrome.

Tricuspid Insufficiency

Etiology

As in mitral insufficiency, systolic regurgitation into the right atrium across an incompetent tricuspid valve may have a valvular (organic) or functional cause and may be acute or chronic (**Table 7.9**).[4,5]

The incidence of tricuspid insufficiency in western industrialized countries is ~1 % The morbidity and mortality generally depend on the causative disease.

Pathophysiology

Regurgitant flow moves back and forth between the right atrium and right ventricle across the incompetent valve, imposing a volume overload on both cardiac chambers. Relative tricuspid insufficiency is based on an underlying increase in right ventricular pressure, and the volume overload is accompanied by a rise in mean right atrial pressure that rapidly leads to right atrial dilatation. Severe acute or severe chronic tricus-

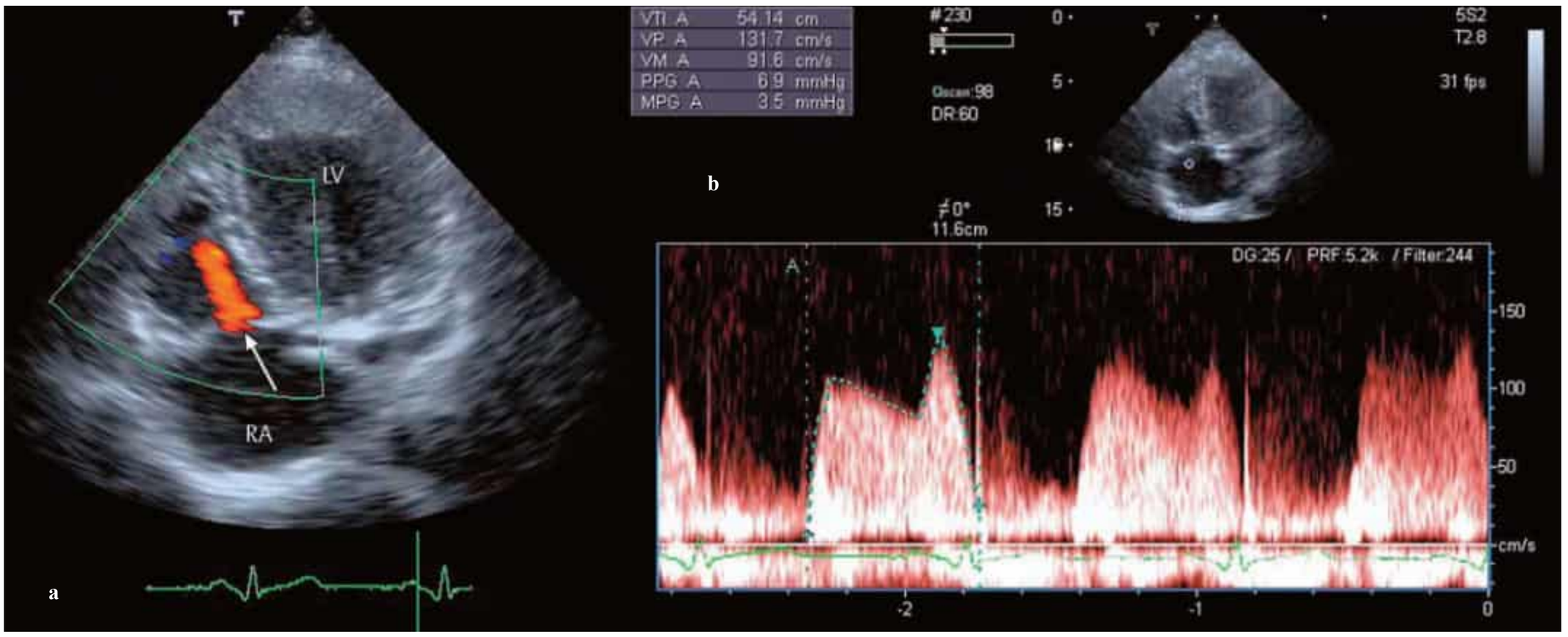

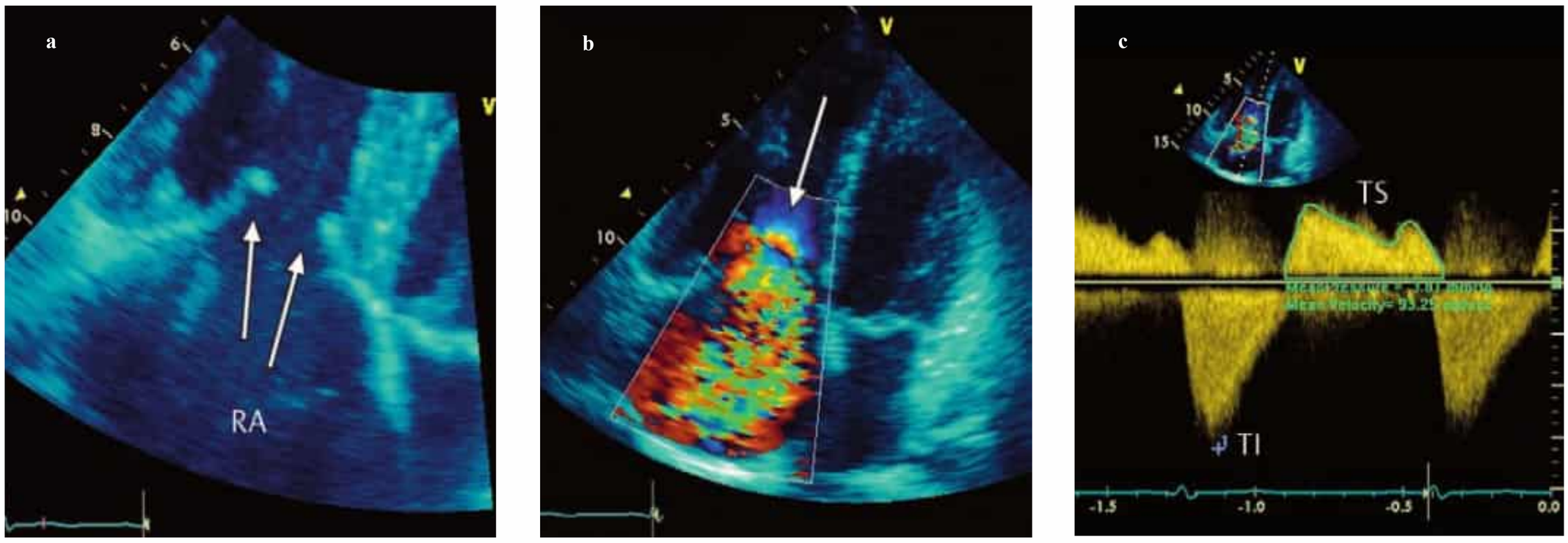

Fig. 7.31 a–c Combined tricuspid stenosis and tricuspid insufficiency in carcinoid syndrome.
a Echocardiographic view of the rigid, fixed, and thickened tricuspid leaflets (arrows).
b Color Doppler shows a large regurgitant jet into the right atrium with a PISA phenomenon on the right ventricle (arrow).
c CW Doppler spectrum shows a systolic regurgitant signal (TI) and diastolic stenotic signal (mean pressure gradient 3.8 mmHg, corresponding to mild-moderate TS).

pid insufficiency produces signs of right-sided heart failure with hepatic congestion, peripheral edema, and ascites.

Clinical Features

Symptoms

- Prolonged asymptomatic course
- Distended neck veins, hepatojugular reflux
- Feeling of fullness due to enlarged liver, possible jaundice
- Edema, ascites
- Cyanosis due to forward failure of the right heart
- Weight loss, cachexia
- Dyspnea in secondary tricuspid insufficiency due to left-sided heart failure with pulmonary congestion and pulmonary hypertension

Complications

- Atrial fibrillation
- Septic embolic pulmonary lesions in bacterial endocarditis

Imaging

Echocardiography

2D Echocardiography

- Enlargement of the right atrium and right ventricle (**Fig. 7.31b**).
- Degenerative changes in the valve apparatus.
- Paradoxical septal motion.
- Detection of extraneous structures (vegetations, thrombi). Transesophageal scanning is indicated in patients with clinical suspicion of endocarditis.
- Prolapse of the valve leaflets

Color Doppler Echocardiography

- Can demonstrate a color Doppler jet in the right atrium (**Fig. 7.31b**).
- Proximal jet width (= vena contracta width)[16] (**Table 7.10**)
- Jet area (of limited value) (**Table 7.10**)
- Regurgitant volume and EROA determined by the PISA method (no standard)
- Detection of reflux into the hepatic veins

CW Doppler

- Systolic pulmonary artery pressure (sPAP) can be estimated with the Bernoulli equation: $sPAP = 4v_{CW}^2 + P_{RA}$, where P_{RA} = mean right atrial pressure = central venous pressure (CVP).[29]
- Estimation of mean right atrial pressure:
  - 5 mmHg = normal RA size
  - 10 mmHg = RA dilated
  - 15 mmHg = RA dilated and IVC congested

Pulsed Doppler Echocardiography

- Can detect systolic reflux into the hepatic veins.

Grading the Severity of Tricuspid Insufficiency

Currently, the severity of tricuspid insufficiency is graded primarily semiquantitatively on the basis of the size and proximal width of the regurgitant jet (**Table 7.10**).[16] Quantitative methods like the PISA method and continuity method for determining regurgitant volume or valve orifice area (EROA) have not yet come into routine clinical use.

Essential Point
Because the size of the tricuspid regurgitant jet depends strongly on systolic pulmonary artery pressure and right ventricular function, the proximal jet width should additionally be considered in grading severity.

Table 7.9 Causes of tricuspid insufficiency

Organic (valvular) tricuspid insufficiency	Acute	• Papillary muscle rupture following acute right myocardial infarction • Bacterial endocarditis due to IV drug abuse • Chest trauma
	Chronic	• Thyrotoxicosis • Rheumatic endocarditis (usually combined with tricuspid stenosis) • Tricuspid valve prolapse • Carcinoid syndrome • Osteogenesis imperfecta • Connective-tissue diseases (Marfan syndrome, Ehlers–Danlos syndrome)
Functional tricuspid insufficiency (due to dilatation of the right cardiac chambers)	Acute	• Right myocardial infarction • Pulmonary embolism
	Chronic	• Ischemic or dilated cardiomyopathy • Cor pulmonale • Decompensated pulmonary stenosis • Decompensated mitral valve defect • Congenital heart disease with left-to-right shunt

Table 7.10 Grades of severity of tricuspid insufficiency

Tricuspid insufficiency: quantitative grading criteria[16]			
	Grade I	**Grade I**	**Grade I**
Jet area	<5 cm²	5–10 cm²	>10 cm²
Proximal jet width (= vena contracta width)	<0.7 cm		≥0.7 cm

■ Pulmonary Valve Stenosis

In view of the fact that pulmonary stenosis is a rare valvular disease and is usually congenital, an in-depth discussion of the defect is beyond the scope of the present work. Other rare causes are involvement by rheumatic endocarditis or carcinoid.

■ Pulmonary Insufficiency

Etiology

Clinically significant pulmonary valve regurgitation is rare. Although functional incompetence due to dilatation of the pulmonary valve annulus in primary or secondary pulmonary arterial hypertension is the most frequent cause, it is rarely severe. Severe regurgitation generally has a valvular etiology. Primary valvular pulmonary insufficiency may be due to rheumatic or bacterial endocarditis, carcinoid syndrome, pulmonary valve prolapse, or valvulotomy.

Pathophysiology

Hemodynamically, isolated pulmonary insufficiency imposes a volume overload on the right ventricle leading to dilatation of the right cardiac chambers. Conversely, functional pulmonary insufficiency may result from dilatation of the right chambers due to right-heart overload, in which case the volume overload exacerbates the functional abnormality of the right ventricle.[16] Backward failure of the right ventricle leads to disturbance of circulation with congestion of the venae cavae, hepatojugular reflux, and edema.

Clinical Features

Symptoms

- Isolated organic pulmonary insufficiency is frequently asymptomatic.
- With relative pulmonary insufficiency, the dominant symptoms are those of the underlying disease.
- Exertional dyspnea
- Rapid fatigability
- Hepatic congestion, peripheral edema, hepatojugular reflux.

Imaging

Echocardiography

2D Echocardiography

- Evaluation of the pulmonary valve with 2D echo is less readily accomplished compared with other valves
- Extraneous floating structures in the region of the pulmonary valve in endocarditis
- Prolapsing leaflets (e.g., in Marfan syndrome)
- Dilatation of the pulmonary valve annulus
- Dilatation of the right ventricular outflow tract
- Sclerotic changes due to combined valve lesions
- Size and function of the right cardiac chambers

Color Doppler Echocardiography

- Can demonstrate the regurgitant jet (**Fig. 7.32d**).
- Limited value in determining jet size for grading severity (**Fig. 7.32d**)[16]
- Proximal jet width for semiquantitative grading (**Fig. 7.32d**)

Pulsed Doppler

- Can detect diastolic retrograde flow through the pulmonary valve.

CW Doppler

- Diastolic pulmonary artery pressure (dPAP) can be estimated by measuring the end-diastolic gradient and adding the estimated mean right atrial pressure (see p. 164).

Magnetic Resonance Imaging

Tricuspid and Pulmonary Valve Diseases

Analogously to aortic and mitral valve diseases, diseases of the tricuspid and pulmonary valves can also be investigated by MRI (**Fig. 7.33**). Imaging of the pulmonary valve is frequently warranted following the surgical correction of congenital heart disease (tetralogy of Fallot, double-outlet right ventricle, etc.) because the pulmonary valve often cannot be adequately evaluated by transthoracic echocardiography. MRI is also useful in the assessment of right cardiac function. Phase-contrast MRI is used for the quantification of pulmonary valve function.

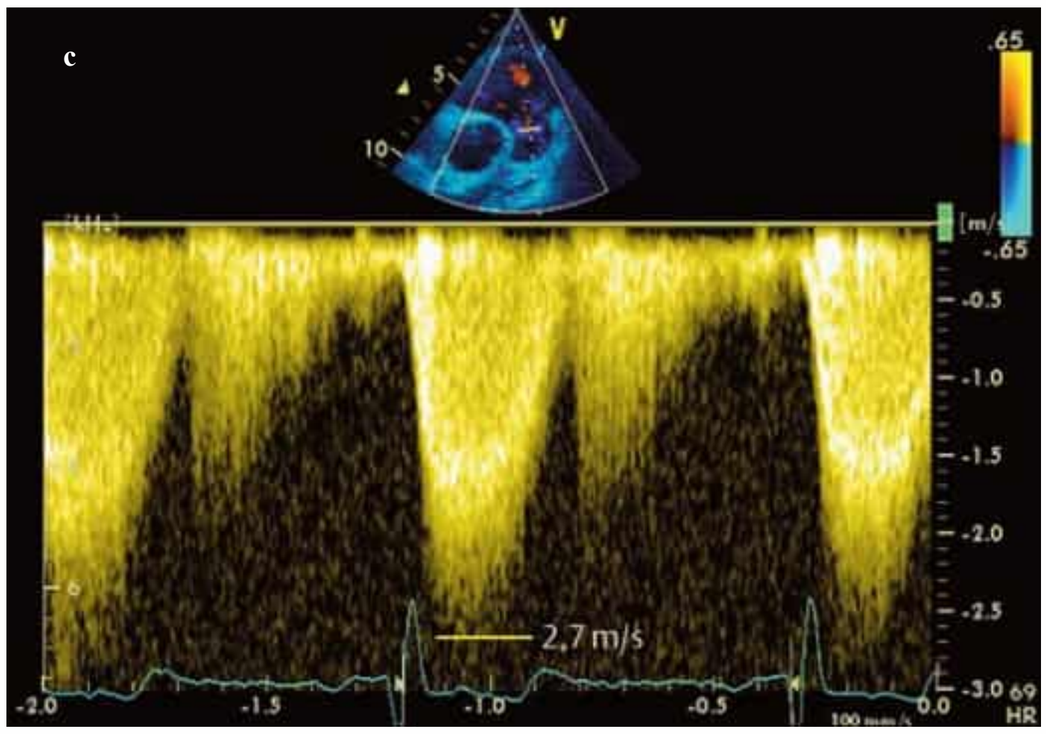

Fig. 7.32 a–d Combined pulmonary insufficiency and stenosis.
a Parasternal short-axis echocardiographic view of the pulmonary valve (arrow).
b Color Doppler shows accelerated flow with a PISA phenomenon proximal to the pulmonary valve (arrow).
c The pressure gradient across the stenotic pulmonary valve is estimated from the Doppler spectral waveform. At a peak velocity of 2.7 m/s, the simplified Bernoulli equation ($PG = 4v^2$) indicates a maximum pressure gradient of 29.2 mmHg, corresponding to mild—moderate pulmonary stenosis.
d Color Doppler view of the regurgitant jet.

Prosthetic Heart Valves

Morphological and functional imaging of prosthetic heart valves is difficult in many cases and requires detailed knowledge of the different types of prosthetic valves and the technical limitations of the various imaging modalities. Today the standard modality for evaluating prosthetic heart valves is echocardiography.[4,5] X-ray fluoroscopy is considered obsolete because of the radiation exposure. MRI of metallic prostheses is limited owing to artifacts. As of today there have been no clinical reports on the capabilities of advanced CT technology for this application.

Pathological Changes

The leading cause of prosthetic valve dysfunction is bacterial endocarditis, usually due to the formation of vegetations in the valve ring region. Associated destructive changes leading to incomplete valve closure, paravalvular regurgitation, or even partial dislodgment of the prosthesis are frequently detected. Further complications include prosthetic valve dysfunction due to abnormal tilting-disk motion, thrombotic stenosis of the prosthesis, the degeneration of bioprosthetic valves, prosthetic dislocation due to suture dehiscence, and prosthetic mismatch with a valve orifice area too small for the patient.[9]

Valve Types

Prosthetic heart valves fall into two main categories: bioprosthetic and mechanical valves (**Fig. 7.34**). Because prosthetic heart valves may be 25 or more years old in some patients, the examiner should be familiar with valve types that are no longer implanted today. Three types can be differentiated:

- Ball-in-cage valves
- Tilting-disk valves
- Double-disk valves[9]

While there are still many patients with tilting-disk valves (e.g., the Björk–Shiley valve) implanted in the past, double-disk valves like the St. Jude have become the current standard for mitral and aortic valve replacement.

The following three main types of bioprosthetic valve are used:

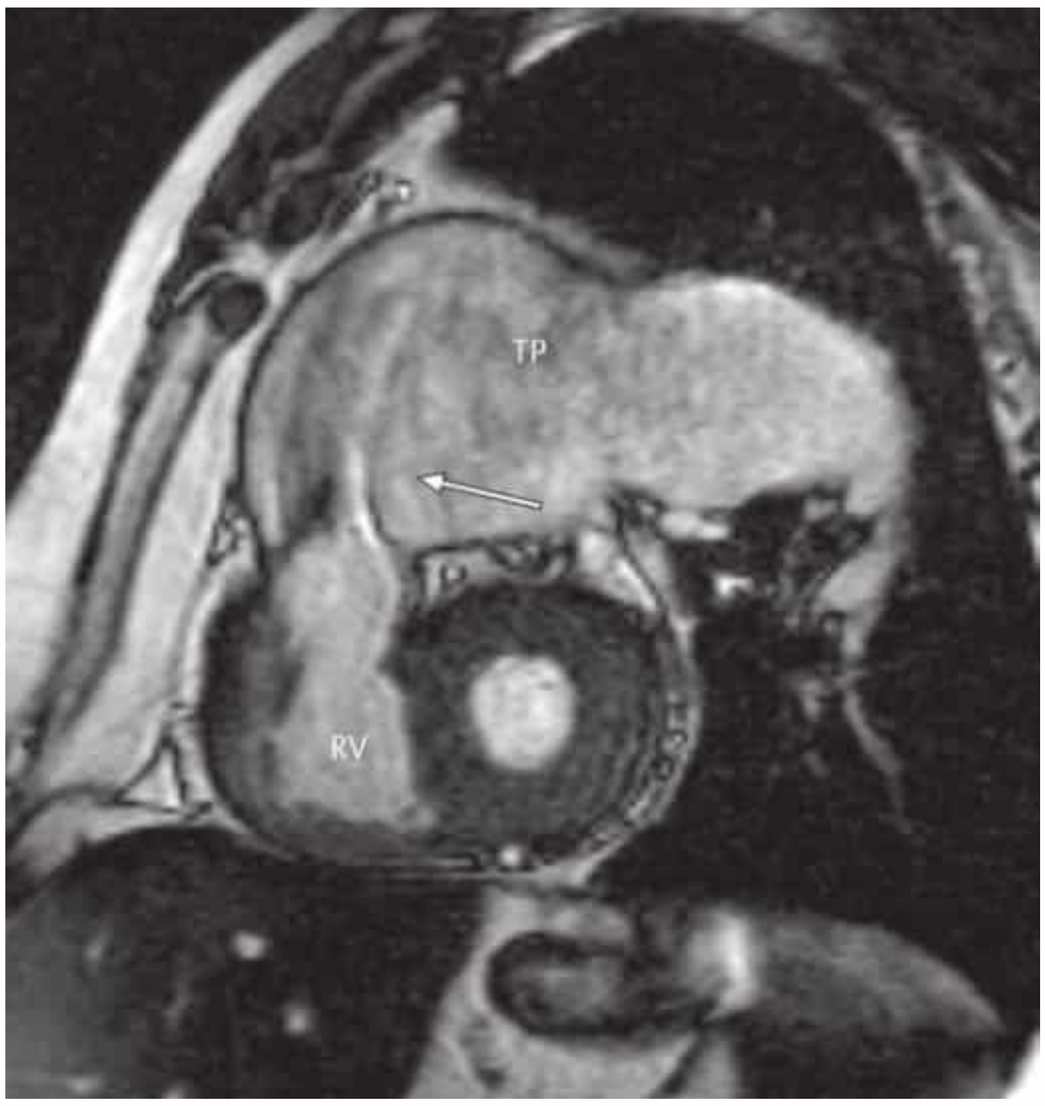

- The most commonly used bioprostheses are porcine valves (e.g., Hancock or Carpentier–Edwards) or bovine pericardial valves (e.g., Mosaic) mounted on a wire frame, or stent.
- Xenograft valves without a stent (e.g., Medtronic Freestyle Stentless)
- Homografts from organ donors

Imaging

Echocardiography

Echocardiography permits a detailed morphological and functional assessment of prosthetic heart valves, especially when transesophageal scanning is used (**Fig. 7.34**).[9] Transesophageal echocardiography is the only imaging technique that allows intraoperative monitoring of the result of a valve implantation. This is particularly important in cases where direct vision is limited, as in minimally invasive cardiac surgery. TEE is further useful as a postoperative follow-up modality for the timely detection of complications (see above).

M-Mode Echocardiography

- Restricted opening of a prosthetic valve may indicate the presence of thrombosis or other mechanical malfunctions.

2D Echocardiography

- Mechanical valves: extraneous perivalvular echoes due to endocarditis and/or thrombosis, asymmetrical valve opening, or restricted opening of a tilting-disk valve.

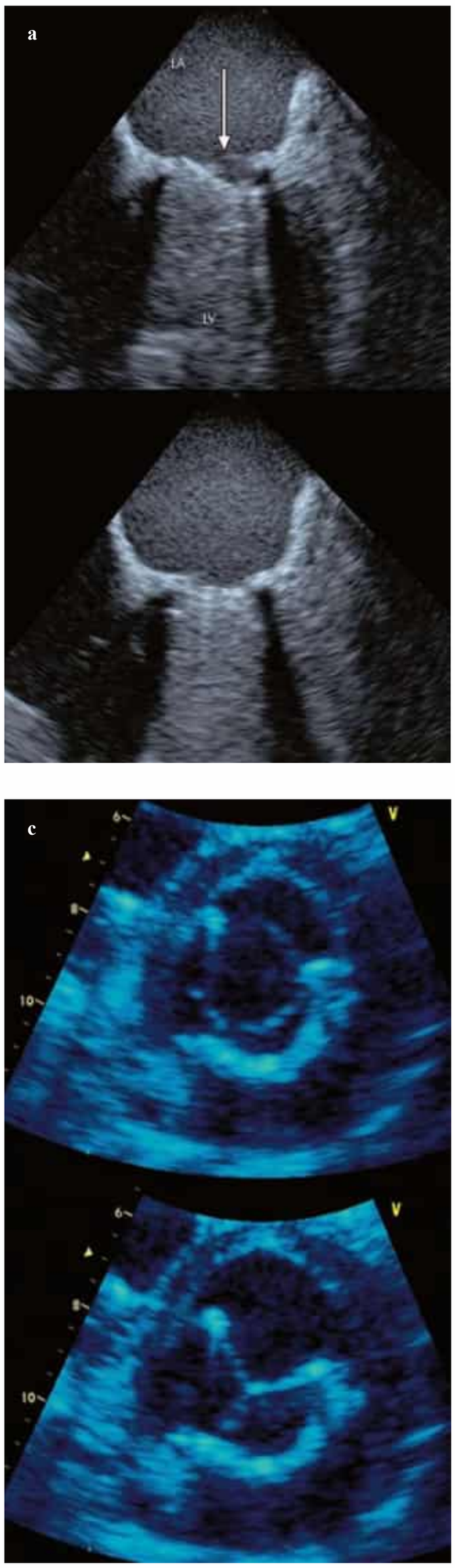

Fig. 7.34a–d Axial views of various prosthetic valve types demonstrated by TEE.
a Tilting-disk mitral valve prosthesis in the open diastolic position (top, arrow) and closed systolic position (bottom).
b Double-disk mitral valve prosthesis. Top: diastolic, parallel open position of the disks (arrow); bottom: closed systolic position.
c Bioprosthetic mitral valve. Top: diastolic opening; bottom: systolic closure.
d Homograft aortic valve (top: longitudinal scan).

- Bioprosthetic valves: Degeneration of a bioprosthesis is marked by the presence of increased echoes on the valves and valve commissures with aging.
- Differentiation of double-disk valves from tilting-disk valves (**Fig. 7.34**). (Different models of a particular valve type cannot be differentiated.)
- 2D echocardiography can detect suture dehiscence and paravalvular abscess formation.

CW and Pulsed Doppler

- Determine the mean pressure gradient across the prosthesis and compare with valve-specific normal values. An increased gradient indicates valve dysfunction.[9]
- Calculate the valve orifice area (as in native aortic and mitral stenosis).[9]

Color Doppler Echocardiography

- Color Doppler can demonstrate regurgitant flow through or around the valve. The leak may be pathological or may relate to the design of the device (**Fig. 7.35**).

- Detection of paravalvular regurgitation
- PISA phenomenon due to design-related flow acceleration or abnormal stenosis in a mitral valve prosthesis, an undersized prosthesis, or annuloplasty
- Color Doppler can document residual insufficiency after a valve reconstruction.

Color Tissue Doppler

- This mode can detect extraneous structures such as thrombi and vegetations based on their incoherent motion (**Fig. 7.36**).

Essential Point

Owing to the metallic components of prosthetic valves and valve rings, echocardiography is the only modality which can reliably assess valve function and paravalvular complications.

The echocardiographic assessment of valve function is often hampered by artifacts in patients with multiple mechanical heart valves.

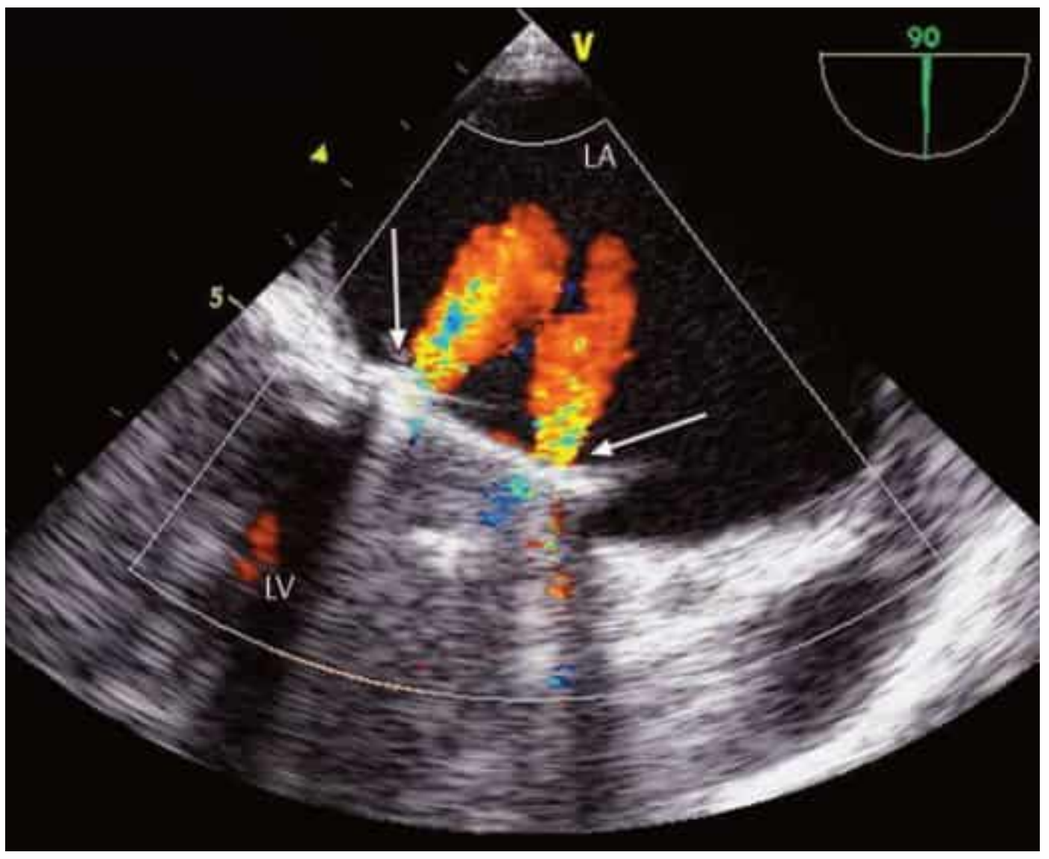

Fig. 7.35 Double-disk valve. Typical color Doppler view shows two regurgitant jets at the disk margins (arrows), a normal finding with this type of valve.

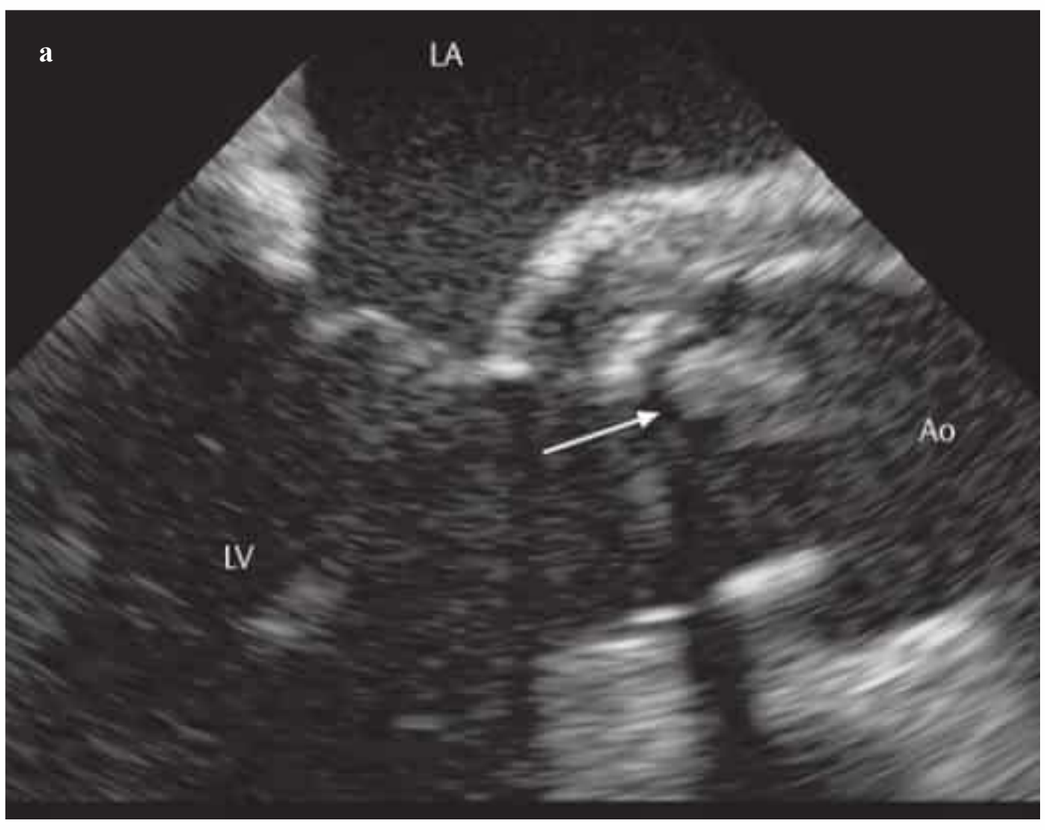

Fig. 7.36 a–d Echocardiography of endocarditis following valve replacement or reconstruction.

a, b Large endocarditic vegetation on the noncoronary leaflet (arrow) of a bioprosthetic aortic valve. Transesophageal longitudinal scan with clear delineation by tissue Doppler (arrow).

c, d Large, elongated vegetation on the inner valve ring following mitral ring implantation, demonstrated by 2D echocardiography and tissue Doppler (arrows).

References

1. Petersen SE, Voigtlander T, Kreitner KF, et al. Quantification of shunt volumes in congenital heart diseases using a breath-hold MR phase contrast technique–comparison with oximetry. Int J Cardiovasc Imaging 2002;18:53–60
2. Mohrs OK, Voigtländer T, Heußel C-P, et al. Morphologische und funktionelle Evaluation pulmonaler Gefäßanomalien mittels schneller MR-Techniken. Rofo. 2002;174:467–473
3. Mohrs OK, Petersen SE, Erkapic D, et al. Diagnosis of patent foramen ovale using contrast-enhanced dynamic MRI: a pilot study. AJR Am J Roentgenol 2005;184:234–240
4. Bonow RO, Carabello RA, Chatterjee K, et al. ACC/AHA 2006 guidelines for the management of patients with valvular heart disease. J Am Coll Cardiol 2006;48:e1–e148
5. Vahanian A, Baumgartner H, Bax J, et al. Guidelines on the management of valvular heart disease: The Task Force on the Management of Valvular Heart Disease of the European Society of Cardiology. Eur Heart J 2007;28:230–268

5a. Buck T, Plicht B, Erbel R., Current recommendations on echocardiographic evaluation of the severity of mitral regurgitation: standardization and practical application using a scoring system. Herz,2006; 31:30–37

6. Iung B, Baron G, Butchart EG, et al. A prospective survey of patients with valvular heart disease in Europe: The Euro Heart Survey on Valvular Heart Disease. Eur Heart J 2003;24:1231–1243
7. Roberts WC, Perloff JK. Mitral valvular disease. A clinicopathologic survey of the conditions causing the mitral valve to function abnormally. Ann Intern Med 1972;77:939–975
8. Bonow RO, Braunwald E. Valvular heart disease. In: Zipes DP, ed. Braunwald's Heart Disease: A Textbook of Cardiovascular Medicine Saunders, Philadelphia. 2005:pp.1553–1563.
9. Baumgartner H. Klappenprothesen. In: Flachskampf FA, Hrsg. Praxis der Echokardiographie. Stuttgart: Georg Thieme; 2002:337–78.
10. Hatle L, Angelsen B, Tromsdal A. Noninvasive assessment of atrioventricular pressure half-time by Doppler ultrasound. Circulation 1979;60: 1096–1104
11. Djavidani B, Debl K, Lenhart M, et al. Planimetry of mitral valve stenosis by magnetic resonance imaging. J Am Coll Cardiol 2005;45:2048–2053
12. Djavidani B, Debl K, Buchner S, et al. MRI planimetry for diagnosis and follow-up of valve area in mitral stenosis treated with valvuloplasty. Rofo. 2006;178:781–786
13. Lin SJ, Brown PA, Watkins MP, et al. Quantification of stenotic mitral valve area with magnetic resonance imaging and comparison with Doppler ultrasound. J Am Coll Cardiol 2004;44:133–137
14. Otto CM. Valvular aortic stenosis: disease severity and timing of intervention. J Am Coll Cardiol 2006;47:2141–2151
15. Freed LA, Levy D, Levine RA, et al. Prevalence and clinical outcome of mitral-valve prolapse. N Engl J Med 1999;341:1–7
16. Zoghbi WA, Enriquez-Sarano M, Foster E, et al. Recommendations for evaluation of the severity of native valvular regurgitation with two-dimensional and Doppler echocardiography. J Am Soc Echocardiogr 2003;16:777–802
17. Lang RM, Bierig M, Devereux RB, et al. Recommendations for chamber quantification: a report from the American Society of Echocardiography's Guidelines and Standards Committee and the Chamber Quantification Writing Group, developed in conjunction with the European Association of Echocardiography, a branch of the European Society of Cardiology. J Am Soc Echocardiogr 2005;18:1440–1463
18. Kono T, Sabbah HN, Stein PD, Brymer JF, Khaja F. Left ventricular shape as a determinant of functional mitral regurgitation in patients with severe heart failure secondary to either coronary artery disease or idiopathic dilated cardiomyopathy. Am J Cardiol 1991;68:355–359
19. Carpentier A, Lessana A, Relland JYM, et al. The „Physio-Ring": An Advanced Concept in Mitral valve Annuloplasty. Ann Thorac Surg 1995; 60:1177–1186
20. Bargiggia GS, Bertucci C, Recusani F, et al. A new method for estimating left ventricular dP/dt by continuous wave Doppler-echocardiography. Validation studies at cardiac catheterization. Circulation 1989;80: 1287–1292
21. Ciampi Q, Villari B. Role of echocardiography in diagnosis and risk stratification in heart failure with left ventricular systolic dysfunction. Cardiovasc Ultrasound 2007;5:34
22. Fujita N, Chazouilleres AF, Hartiala JJ, et al. Quantification of mitral regurgitation by velocity-encoded cine nuclear magnetic resonance imaging. J Am Coll Cardiol 1994;23:951–958
23. Sechtem U, Pflugfelder PW, Cassidy MM, et al. Mitral or aortic regurgitation: quantification of regurgitant volumes with cine MR imaging. Radiology 1988;167:425–430
24. Schwammenthal E, Vered Z, Moshkowitz Y, et al. Dobutamine echocardiography in patients with aortic stenosis and left ventricular dysfunction: predicting outcome as a function of management strategy. Chest 2001;119:1766–1777
25. Debl K, Djavidani B, Seitz J, et al. Planimetry of aortic valve area in aortic stenosis by megnetic resonance imaging. Invest Radiol 2005;40: 631–636
26. Caruthers SD, Lin SJ, Brown P, et al. Practical value of cardiac magnetic resonance imaging for clinical quantification of aortic valve stenosis: comparison with echocardiography. Circulation 2003;108:2236–2243
27. Kozerke S, Schwitter J, Pedersen EM, Boesiger P. Aortic and mitral regurgitation: quantification using moving slice velocity mapping. J Magn Reson Imaging 2001;14:106–112
28. Singh JP, Evans JC, Levy D, et al. Prevalence and clinical determinants of mitral, tricuspid, and aortic regurgitation (The Framingham Heart Study). Am J Cardiol 1999;83:897–902
29. Berger M, Haimowitz A, Van Tosh A, Berdoff RL, Goldberg E. Quantitative assessment of pulmonary hypertension in patients with tricuspid regurgitation using continuous wave Doppler ultrasound. J Am Coll Cardiol 1985;6:359–365

Further Reading

Fawzy ME, Mercer EN, Dunn B, al Amri M, Andaya W. Doppler echocardiography in the evaluation of tricuspid stenosis. Eur Heart J 1989;10:985–990

John AS, Dill T, Brandt RR, et al. Magnetic resonance to assess the aortic valve area in aortic stenosis: how does it compare to current diagnostic standards? J Am Coll Cardiol 2003;42:519–526

Lancellotti P, Lebrun F, Pierard LA. Determinants of exercise-induced changes in mitral regurgitation in patients with coronary artery disease and left ventricular dysfunction. J Am Coll Cardiol 2003;42: 1921–1928

Nakatani S, Masuyama T, Kodama K, Kitabatake A, Fujii K, Kamada T. Value and limitations of Doppler echocardiography in the quantification of stenotic mitral valve area: comparison of the pressure half-time and the continuity equation methods. Circulation 1988;77:78–85

8 Coronary Heart Disease

Subclinical Signs of Coronary Atherosclerosis (Prevention, Screening, and Risk Stratification)

R. Erbel

Early Detection of Coronary Heart Disease

By the year 2015, coronary heart disease will overtake infectious diseases as the leading cause of death in humans. Based on current WHO statistics, ~17 million myocardial infarctions (AMIs) take place each year. Almost 50 %of these patients have no warning signs of an impending AMI, and 60 %of all deaths from AMI occur before the patient reaches the hospital. Patients at risk for AMI can be identified clinically, but the great majority of heart attacks occur in the general population. While these persons have a much lower overall risk than clinical populations, they still suffer absolutely the highest number of heart attack deaths. The ratio of deaths in the general population to deaths in cardiac patients is ~10 :1. Even prominent cardiologists with a specialized knowledge in this field have fallen victim to sudden cardiac death: for example, J. Isner, the father of cardiac genetic research; Ronald W.F. Campell, famous electrophysiologist; and Anthony F. Richards, the father of the BARI Study and rate-adaptive cardiac pacemakers and an authority on malignant cardiac arrhythmias.

After publication of the MONICA Study, the WHO concluded that primary prevention is the only effective way to reduce the prevalence of acute, unexpected cardiac deaths in the general population. This echoes the call of M. Sones, the father of coronary angiography, who spoke at a 1978 conference in Frankfurt, Germany, emphasizing the need to develop methods for the early identification of persons at risk for MI. Interestingly, the topic of that conference was the detection of coronary calcifications by fluoroscopy. To assess the value of invasive and noninvasive methods for the early detection of coronary sclerosis and AMI risk, it is necessary to have a basic understanding of the pathogenesis of coronary atherosclerosis.

Pathogenesis of Atherosclerosis

Like diseases in other vascular regions, the development of coronary atherosclerosis is a gradual process that Stary et al.[1,2] divided into five stages (**Fig. 8.1**). A sixth stage describes the development of complicated plaques. Modifications have been proposed by Virmani et al.[3,4]

The development of atherosclerosis begins in childhood and adolescence (**Fig. 8.2**) with the formation of minute fat deposits. Corresponding to Stary stage II disease, these “fatty streaks” lead to intimal thickening, which is most pronounced at the bifurcations of vessels. Stary stage III is an intermediate stage that shows no signs of progression and is still considered part of the natural aging process. It is pathological only if the stage III lesions show evidence of progression. Typical signs are a continued accumulation of lipid elements and an increase in regional, segmental, eccentric wall thickening that exceeds 300 µm (**Table 8.1**). Stage IV lesions are atheromas, which possess a larger, well-defined lipid core. These lipid pools may be located at a deep level near the media or luminal surface and are separated from the vessel lumen by a fibrous cap. A stage V lesion is a fibroatheroma, which contains increased amounts of collagen that harden and stiffen the vessel. This type is also called stage Va. Heavily calcified lesions are classified as Vb, and predominantly fibrotic lesions are classified as Vc.[1]

Calcifications

Calcium deposits are already present in Stary stage III lesions. First they are intracellular, then extracellular and increase with progression of the disease.[5] Besides purely degenerative processes, intramural hemorrhage is another potential cause of increased calcification in the vessel wall. Intramural hemorrhages also create a nidus for lipid accumulation, which results not only from the infiltration of lipid-laden macrophages but also from the breakdown of erythrocytes, as the wall of red cells are very rich in cholesterol. Thus, intramural hemorrhages are a source of fat accumulation as well as calcification. Potentially extensive wall calcifications may form in stage Vb disease without narrowing the vessel lumen. Coronary calcium reduces the tension at the surface of plaques as long as the fibrous cap is thicker than 100 µm. Calcium, then, is not a late sign but an early sign of coronary atherosclerosis and has a stabilizing effect on the vessel wall. Even if only isolated plaques are detectable, calcifications can be identified in more than 90 % of cases.[5]

Remodeling

Atherosclerosis has its onset during childhood and adolescence. Advanced deposits consistent with stage III–IV lesions are already detectable in 15–20 %of adolescents under 20 years of age and 60 %at the age of 30 years (**Fig. 8.2**).

Studies in US soldiers who died in Korea and Vietnam have confirmed that atherosclerotic lesions, some extensive, have already formed in the coronary vessels by 20–30 years of age. Decades pass without an acute cardiac event, however, as most heart attacks occur between 40 and 64 years of age. This delay is attributable to vascular remodeling, known also as the Glagov phenomenon.[6]

As atherosclerosis progresses in the vessel wall, the surface area of the vessel enlarges (**Fig. 8.3**) to compensate for intimal

Table 8.1 Pathoanatomical and ultrasound-based classification of atherosclerosis (after Erbel et al, 1999[23])

Stary type	Pathoanatomical features	Intravascular ultrasound
I (initial intimal thickening)	Accumulation of lipoprotein in the intima, lipid-laden macrophages. No tissue damage	Single-layer vessel wall with no division into intima, media, and adventitia. The adventitia bounds the vessel as a broad echogenic zone. With aging, the wall acquires a three-layered structure with a visible intima, media, and adventitia as the intima thickens to more than 150 µm, falling within the resolution limits of the scanner
II (fatty streaks) **IIa (progression)** **IIb (progression resistant)**	Accumulation of lipoprotein in the intima, lipid-laden macrophages and smooth muscle cells. Lesions grossly visible as fatty streaks on the surface of vessels	Eccentric three-layered structure in proximal vessel segments with intimal thickening >150 µm
III (preatheroma)	All signs of type II lesions plus multiple extracellular sites lipid accumulation	Progressive, eccentric intimal thickening with narrow zones >300 µm. Rarely, acoustic shadowing due to calcification
IV (atheroma)	All signs of type III lesions plus confluent extracellular lipid zones (lipid core) with massive structural damage to the intima	Eccentric intimal thickening with deep or superficial hyperechoic zones and a fibrous cap. A cap thinner than 100 µm signifies a vulnerable lesion
Va (fibroatheroma)	All types and features of type IV lesions plus collagen and increased smooth-muscle cells	All signs of type IV lesions with progressive thinning of the fibrous cap and more echogenic intimal thickening
Vb (calcified lesion)	Calcifications are the main component of plaque formation	Area of eccentric or concentric intimal thickening with zones of increased echogenicity and acoustic shadowing from calcifications. The degree of calcification is expressed as a percentage of circumference. The calcifications may be deep or superficial
Vc (fibrotic lesion)	Same as type V lesions but consisting mainly of collagen	Eccentric or concentric plaque formation with high-level echoes and possible acoustic shadowing. No reverberations and no hypoechoic zones
VIa (ulcerated plaques)	Ulcerated plaques	Ulcerated plaques. Usually, detectable remnants of the fibrous cap. Communicate with the lumen. Shadowing calcification is usually visible adjacent to and deep within the ulcer
VIb (plaque hematoma or hemorrhage)	Plaque hematoma or hemorrhage with evidence of intramural hemorrhage and numerous remnants of erythrocyte membranes, which are a source of cholesterol deposits. Cholesterol-rich membranes	Detection of an intact intraluminal intimal border with multiple well-defined hypoechoic zones that pulsate with blood flow. Marked pulsatile plaque changes
VIc (plaque thrombosis)	Plaque fissuring or rupture with signs of mural or complete luminal thrombosis	Complete or partial luminal obstruction with granular echoes, irregular luminal boundaries, and free-floating structures. Intraluminal catheter leaves impressions, foot prints in mural thrombus

thickening and forestall luminal narrowing. This compensatory mechanism, called positive remodeling, continues to be effective until plaque formation, which is always eccentric in its early stage, causes 40–45 %cross-sectional luminal narrowing or an increase in the vascular circumference by 60 %[6–8] Negative remodeling may also occur, especially in advanced stages of atherosclerosis but sometimes in the early stage as well. Negative remodeling reduces the cross-sectional area of the vessel in the presence of intimal thickening.[9,10] It is believed to result from scar retraction following injury to the vessel wall. Thus, imaging techniques that define the lumen of vessels usually cannot detect early stages of the disease because they do not image the vessel wall.

The presence of wall irregularities and sites of luminal narrowing usually signifies an advanced atherosclerotic process with a plaque area that exceeds 45 %[11] Hemodynamically significant stenosis that reduces myocardial perfusion during stress is present when more than 75 %cross-sectional luminal narrowing has occurred, corresponding to more than a 50 %reduction in vessel diameter. The corresponding plaque area related to the total vessel area already exceeds 90 %by this stage. This means that an interventional procedure that reduces luminal narrowing by <30 %will usually leave a plaque area of ~70 %[12]

Complicated Plaques

The pathogenesis of acute coronary syndromes—unstable angina, sudden cardiac death, and myocardial infarction—is based on the formation of complicated plaques. Plaque ruptures are

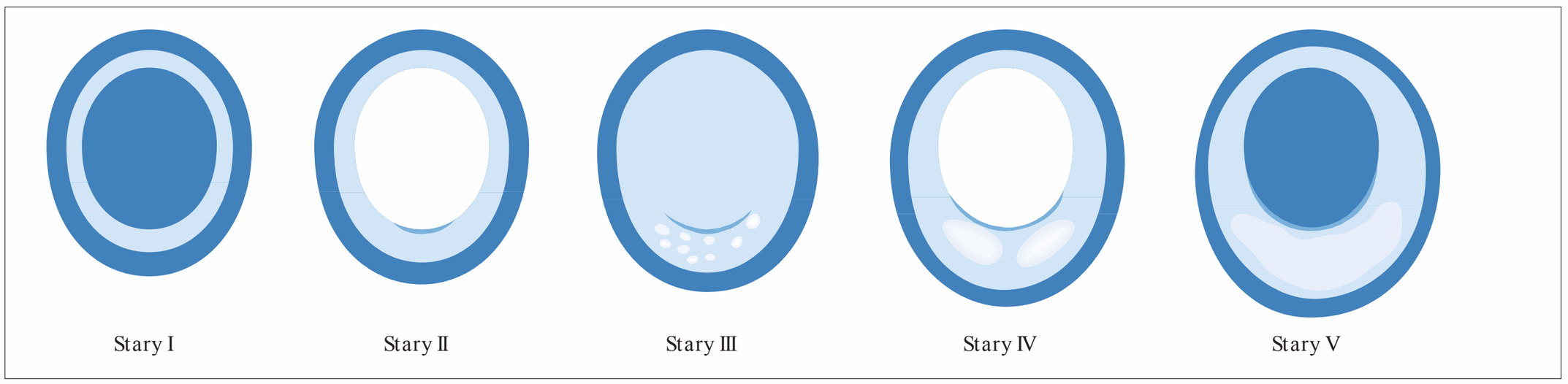

Fig. 8.1 Schematic representation of the progression of atherosclerosis by Stary stages. Stage II and III are characterized by intimal thickening and intermediate lesions with lipid deposits, stage IV by atheroma formation, and stage V by fibroatheroma formation. Plaque rupture may occur in stages IV and V, and plaque erosions may occur at all stages (modified from Naghavi et al., 2006[176]).

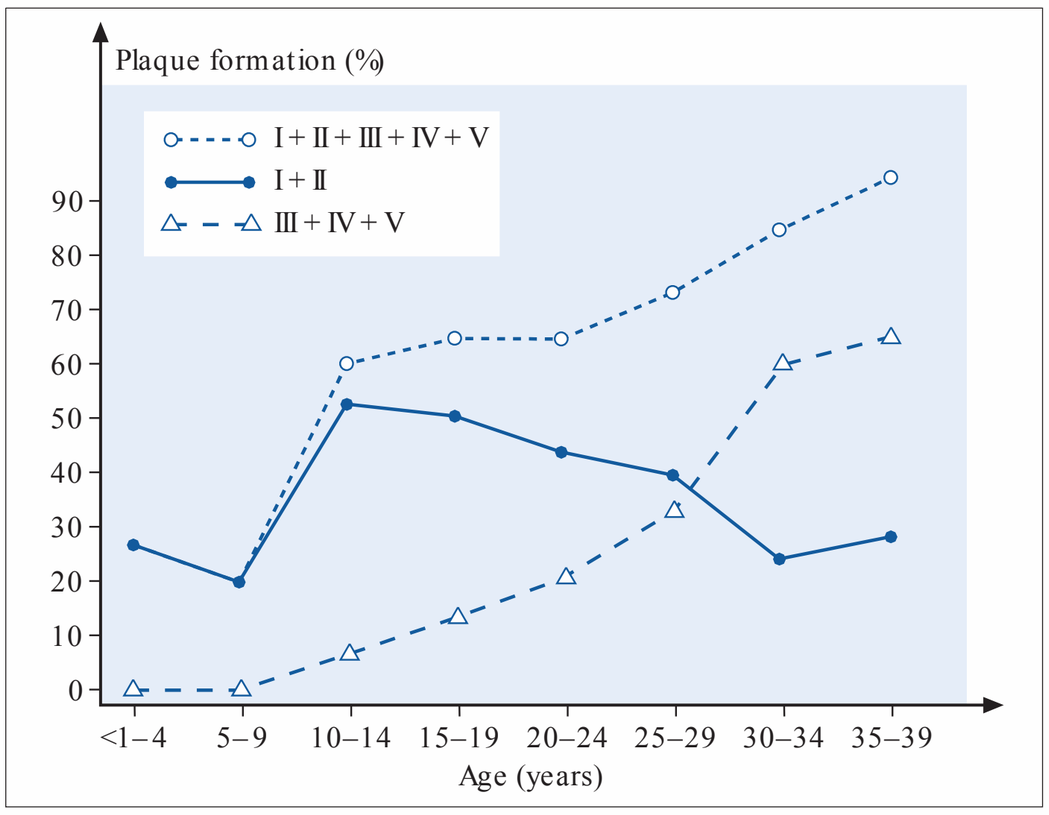

Fig. 8.2 Graphic representation of the frequency of plaque formation at various Stary stages in children, adolescents, and young adults. It is interesting to note that advanced stage IV and stage V lesions are already detectable in adolescents and young adults (after Kolodgie et al., 2004[35]).

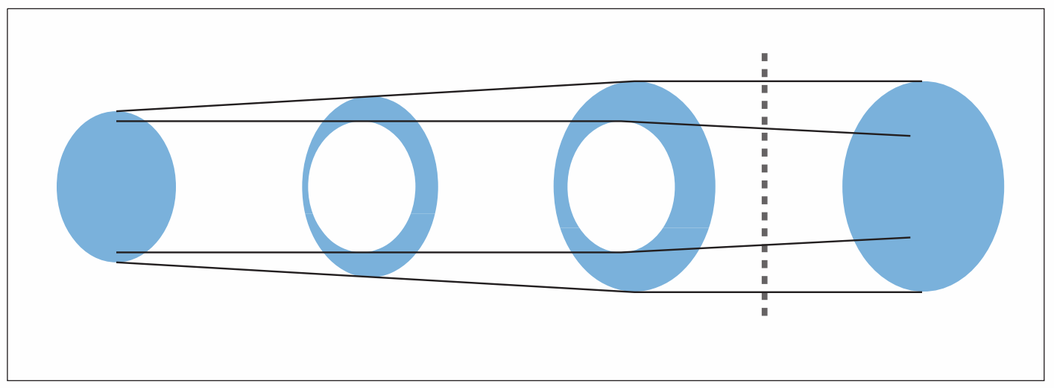

Fig. 8.3 Schematic representation of positive remodeling. As the plaque area in a vessel increases, the vessel expands to maintain its luminal diameter. This mechanism is effective up to 40% cross-sectional luminal narrowing. Beyond that limit, vascular enlargement can no longer compensate for an increase in plaque area, and luminal narrowing occurs. This means that even minimal narrowing of a vessel lumen seen at imaging represents significant plaque formation (after Ge et al., 1993[7]).

present in 65 % of cases, plaque erosions in 35 %, and intraluminal calcium protrusions in less than 5 % of cases.[1,2] Plaque rupture is most likely to occur when:

- A thin fibrous cap (<100 µm) has formed over the atheroma
- Reduced numbers of smooth-muscle cells are present in the cap
- A large atheroma (>40 %) develops
- Signs of inflammation (macrophage infiltration) are present
- The vessel wall has undergone positive remodeling
- Increased vascularity is detectable in the vasa vasorum of the adventitia

This also means that a critical degree of luminal narrowing cannot predict the risk of myocardial infarction, since more than 85 % of infarct-related vessels show less than 75 % luminal narrowing, which is borderline in terms of hemodynamic significance. Moreover, 70 % of vessels show less than 50 % luminal narrowing, which does not reduce myocardial perfusion even during strenuous exercise and does not lead to ECG changes or angina pectoris.[7,13,14] Thus, the early detection of coronary sclerosis must focus on detection of the underlying disease. The detection of critical luminal narrowing comes too late.

When a plaque ruptures, all or part of the atheroma spills into the bloodstream and creates an ulceration in the vessel wall (Stary Va ulcerated plaque). Spontaneous plaque ruptures occur in up to 10 % of otherwise healthy individuals and in up to 25 % of diabetic and hypertensive patients according to forensic data. These changes are present in 65 % of patients with an acute coronary syndrome.

Intramural hemorrhage due to rupture of the vasa vasorum is classified as Stary stage VIb.

Partial or complete mural thrombosis following plaque rupture is classified as Stary stage VIc. This is the causative lesion of unstable angina and acute myocardial infarction. Mural thrombosis is a typical characteristic of unstable lesions. It is more commonly demonstrated by optical coherence tomography (OCT) than angioscopic intravascular ultrasound or angiographic findings would indicate.[15,16]

Stages VIa through VIc are of key importance in the pathogenesis of acute coronary syndromes—a collective term for acute infarction with or without ST segment elevation, sudden cardiac death, and unstable angina pectoris. The symptoms depend on the underlying pathological morphology.

The healing of ruptured plaques leads to thickening of the atherosclerotic wall and is the basis for the progression of coronary sclerosis. Repetitive plaque ruptures that intermittently recur, heal, and add new layers, leading to multiple layering, are the mechanism that drives the progression of coronary atheroma.[3,4]

Detection of Subclinical Atherosclerosis

The earliest abnormality caused by atherosclerotic disease is endothelial dysfunction, which can be detected with special diagnostic techniques. We still do not know the exact degree to which endothelial dysfunction, which is usually detected in the forearm or hand, is indicative of concomitant coronary vascular disease (**Fig. 8.4**).[17]

Early changes associated with atherosclerosis can be reliably detected with intravascular ultrasound (IVUS) (**Fig. 8.5**) and even better with OCT due to the ten times higher resolution. Both complicated and uncomplicated plaques can be identified. Stary stage IV is characterized by atheroma formation and stage Va by fibroatheroma formation (**Figs. 8.5, 8.6**). Lipid cores appear as hypoechoic zones, and calcifications cast acoustic shadows (**Fig. 8.7**). IVUS can also detect plaque formation as an early sign of atherosclerosis in patients who have a normal coronary angiogram. The incidence of normal vessel segments decreases, whereas more patients show advanced lesions type III and IV/V according to the Stary classification (**Fig. 8.8**). Positive remodeling is very clearly demonstrated by IVUS, as a proximal-to-distal analysis of vascular diameter shows the vessel expanding in the area of heaviest plaque formation and narrowing farther distally (**Fig. 8.9**). IVUS can also detect negative remodeling (**Fig. 8.10**).

CT is the best noninvasive modality at present for the early detection of calcified and noncalcified plaques. While contrast administration is unnecessary for detecting calcifications and entails low radiation exposure (<1 mSv in electron beam CT, <3 mSv in multislice CT), the imaging of noncalcified coronary plaques requires contrast injection and therefore exposes the patient to a higher radiation dose. CT can demonstrate vessel enlargement (positive remodeling) in vascular segments where plaque has formed.[18,19] Because calcium deposits form at an early stage of atherosclerosis, positive findings may be seen even before luminal narrowing has occurred. This makes CT an excellent modality for detecting early stages in the progression of coronary atherosclerosis.[20,21]

MRI is most useful for the visualization of noncalcified plaques but is not positive for calcifications. The temporal resolution of MRI is still inadequate for the clinical detection of coronary atherosclerosis. With its ability to define the lumen of coronary vessels, MRI is faced with the same problems as invasive coronary angiography, since 45 %or greater cross-sectional luminal narrowing must be present before there is a visible decrease in luminal diameter. If slight narrowing is detected, it already signifies a considerable plaque burden.

Luminal imaging can also be accomplished with synchrotron radiation, but early diagnosis faces the same obstacles as in coronary angiography (**Fig. 8.11**).

The most sensitive modality for detecting abnormal myocardial perfusion is positron emission tomography (PET) (**Fig. 8.4**). Nuclear medicine studies as well as stress protocols like those used in echocardiography and MRI yield a positive result only if there is at least 70 % lumen reduction (high plaque burden), and their sensitivity is 80–90 % The sensitivity of stress ECG is

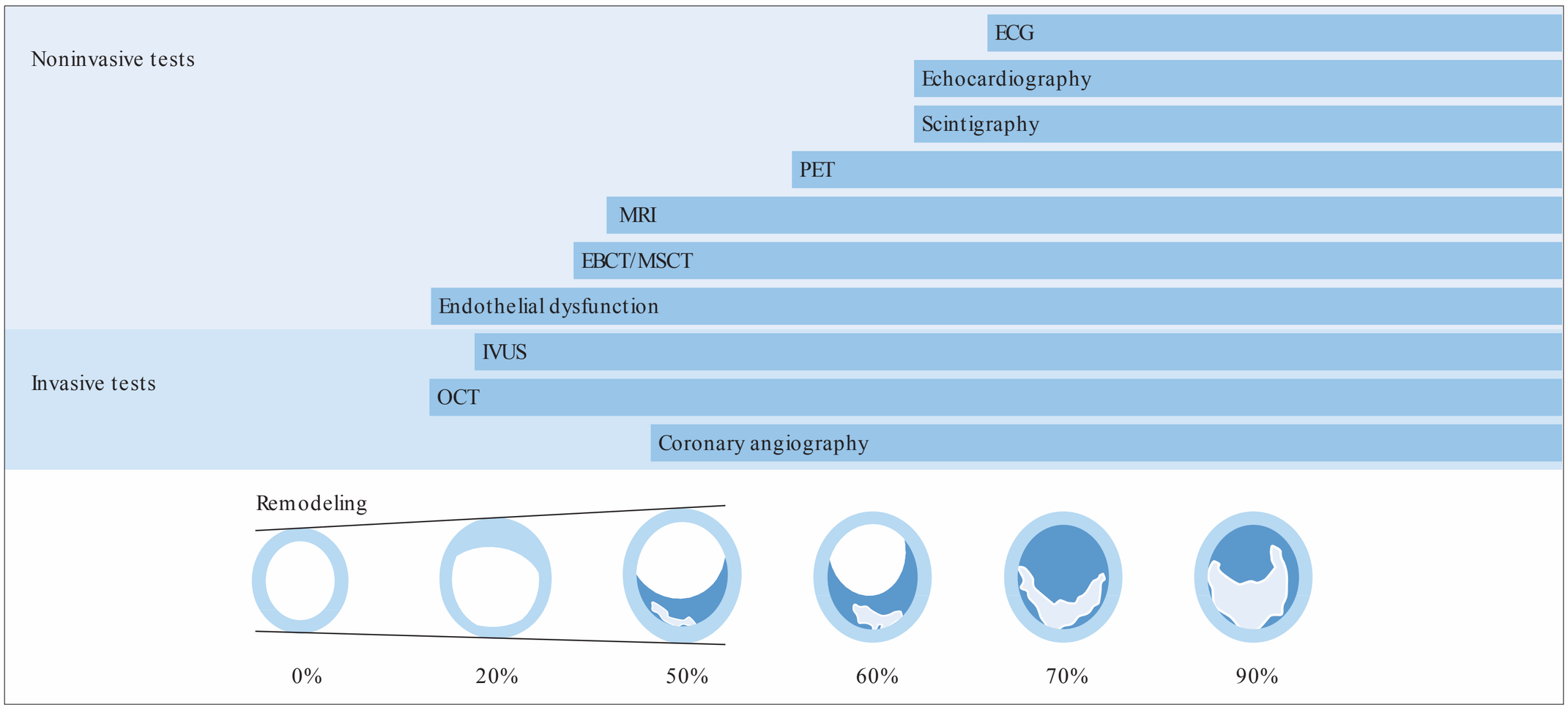

Fig. 8.4 Review of invasive and noninvasive tests for coronary sclerosis and myocardial ischemia, shown in relation to coronary plaque formation and positive remodeling as described by Glagov et al. (1997).[6] The detection of endothelial dysfunction is the first invasive and noninvasive sign of incipient coronary disease. Initial signs can be detected invasively by optical coherence tomography (OCT). Intravascular ultrasound (IVUS) is the most widely used clinical modality for the early detection of coronary sclerosis. Even Stary stage II and III lesions can be visualized. Calcifications can be detected with high sensitivity along with thrombus formation and lipid deposits. Electron-beam CT (EBCT) and multislice CT (MSCT) are the current modalities of choice for detecting coronary calcifications noninvasively. Calcifications are initially intracellular and then extracellular and occur as early as Stary stage III. MRI can also detect plaque formation. As in contrast-enhanced MSCT, noncalcified plaques are more easily detected.
Coronary angiography defines only the vessel lumen and does not become positive until positive remodeling exceeds 45%luminal reduction; a phenomenon valid for all luminographic imaging techniques. Positron emission tomography (PET) is excellent for detecting abnormal myocardial perfusion in cases where more than 50–60%narrowing has occurred. Stress echocardiography and stress myocardial scintigraphy are not positive until luminal narrowing exceeds 75% Stress electrocardiography is 20%less sensitive and does not become positive until flow-limiting stenosis has developed (modified from Erbel et al., 1996[13]).

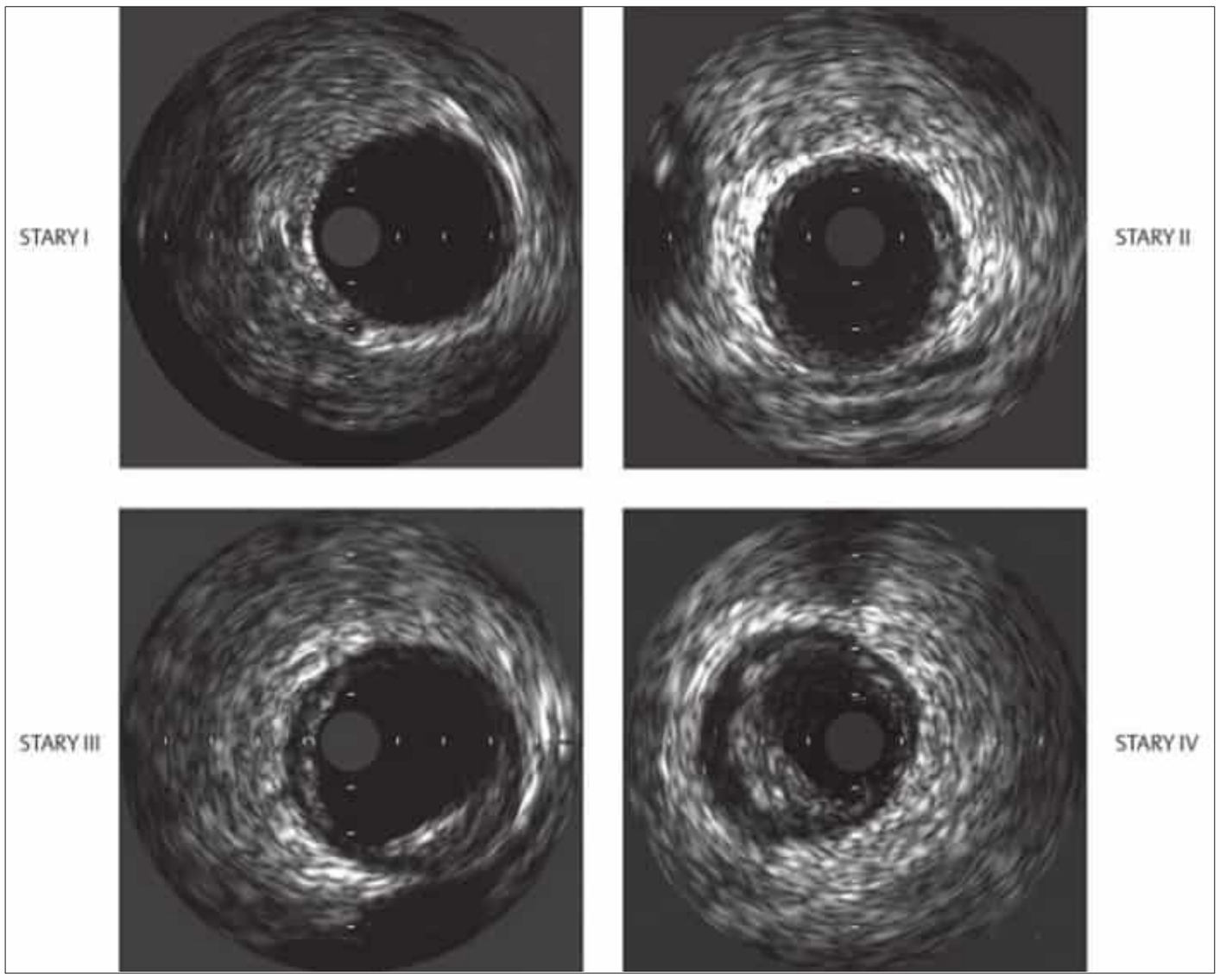

Fig. 8.5 Intravascular ultrasound (IVUS). Images at Stary stages I, II, III, and IV show intimal thickening in stage II, localized eccentric plaque formation in stage III, and eccentric plaque formation with hypoechoic lipid deposits in stage IV (after Erbel 1996[13]).

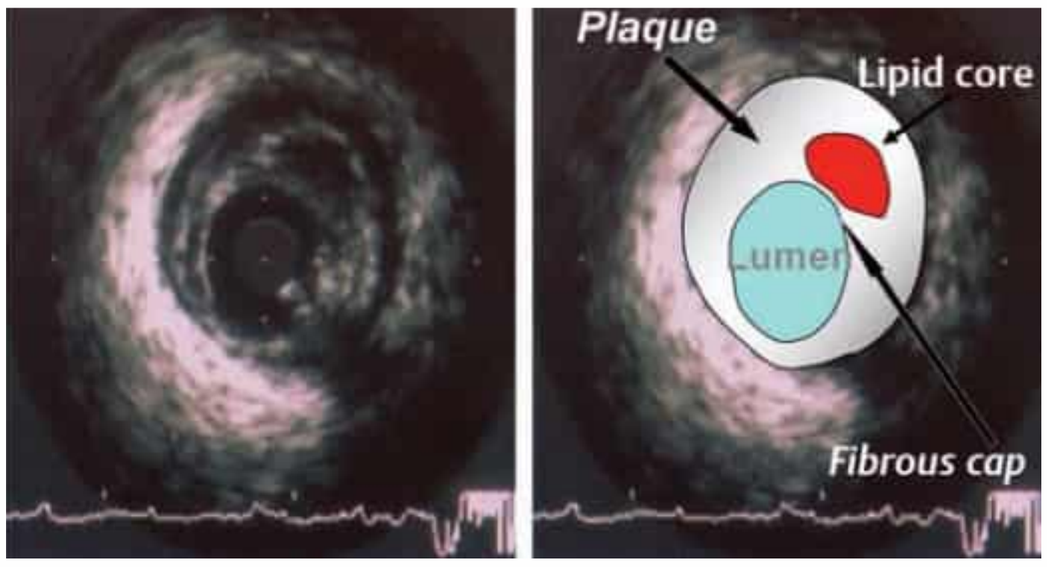

Fig. 8.6 Intravascular ultrasound image and correlative diagram of Stary stage IV/Va plaque formation (atheroma, fibroatheroma). The image (1 mm calibration) shows a large, hypoechoic lipid core with eccentric plaque formation and a typical three-layered vessel wall in which the media appears as a black zone encircling the lumen. The catheter appears as a central structure with a guidewire-induced artifact at the 4 o'clock position. The vulnerable plaque is recognized by its large lipid core, thin fibrous cap, and large atheroma. Vulnerable plaques are also characterized by inflammatory changes, neoangiogenesis, and positive remodeling.

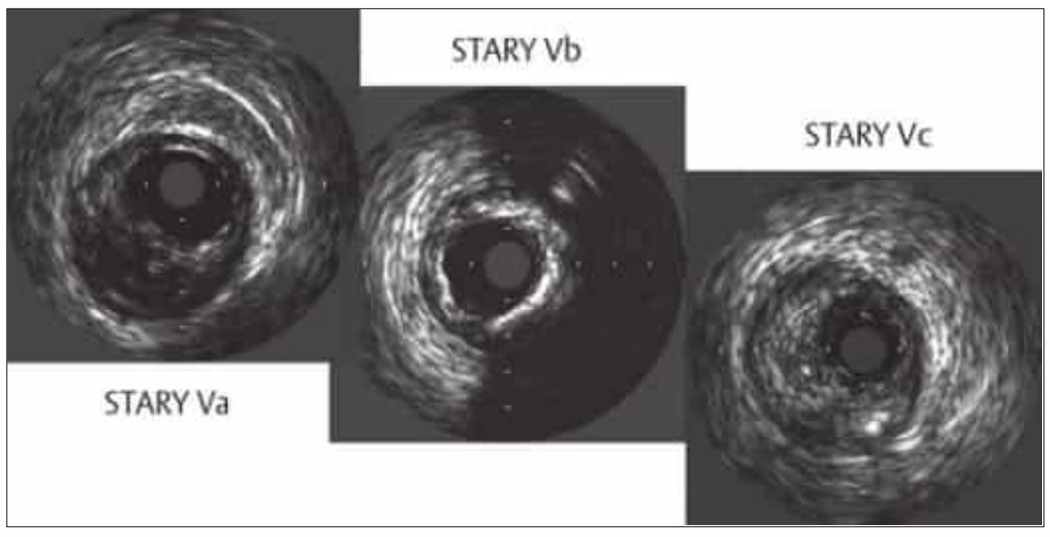

Fig. 8.7 Intravascular ultrasound of Stary stages Va through Vc shows the formation of a fibroatheroma, fibrous cap, thinning of the cap at its margins, and a clear lumen (Va). Extensive calcifications with acoustic shadows and increased echogenicity are observed in stage Vb, and high-level echoes from eccentric plaque are seen in stage Vc of fibrotic plaque formation (after Erbel 1996[13]).

20% lower because decreased blood flow is detectable only when the diameter reduction exceeds 70% and area stenosis exceeds 90% (**Fig. 8.4**). Sensitivity is in the 60–70% range, depending on the clinical population.

Detection of Complicated Plaques

Plaque ruptures appear as aneurysms in lumen-defining techniques such as coronary angiography (**Fig. 8.12**) and MR angiography.[22] Sectional imaging procedures such as IVUS can more accurately define ulcerations and other changes in the vessel wall.[16,23,24]

Intravascular ultrasound can detect intramural hematoma formation (**Fig. 8.13**) in rare cases.[23] This has not yet been accomplished in the coronary vessels with other noninvasive modalities, but MRI has been able to detect intramural hemorrhages in atherosclerotic vessels of the carotid system.

Thrombi can be detected indirectly as filling defects in coronary angiograms and luminograms (**Fig. 8.13**). They should not be mistaken for projecting mural calcifications. Partial and complete thrombosis of the coronary vessels can be detected with IVUS even better by angioscopy and OCT. This technique is not very sensitive in the differentiation of other lesions, however.[11] While IVUS can detect nearly 100% of calcifications (but not microcalcifications), it has 80% sensitivity in detecting atheroma formation and almost 90% sensitivity in detecting fibrotic deposits. Noninvasive imaging techniques are still in the developmental stage as far as the assessment of plaque composition is concerned. They lag well behind the "virtual histology" that can be accomplished with IVUS in clinical settings (**Figs. 8.14, 8.15**).[25–27]

The natural history of plaque ruptures is often marked by a very gradual healing process that is stimulated and initiated by thrombosis at the ulcer base. Intravascular ultrasound studies

have shown that ruptured plaques may persist for many months without causing vascular obstruction. Multiple recurrent microemboli may occur, however, and can lead to significant functional impairment without causing an apparent reduction in blood flow. Microemboli lead to a mismatch between perfusion and function because the functional abnormalities are not accompanied by a corresponding perfusion deficit, at least initially, while induced inflammatory processes perpetuate and exacerbate the functional abnormality over time.[14,28,29] Experimental studies confirm anecdotal clinical reports of functional recovery occurring within 5–10 days after an acute event. Microemboli are particularly likely to be accompanied by cardiac arrhythmias during the initial phase. This observation has important imaging implications, because functional abnormalities of the heart may occur in the absence of detectable luminal narrowing and with little or no evidence of decreased coronary perfusion.[28,30–33] Microemboli may also cause significant impairment of coronary vasomotion.[32]

Both IVUS and angioscopy have shown that plaque ruptures occur frequently in multiple vessels.[34] On average, 2.0–2.5 lesions are detected in each patient.[34,35] Plaque ruptures are also found in 15–20%of patients with stable angina pectoris[35,36]—a finding already noted in previous pathoanatomical studies.[14,36]

Detection of Unstable or Vulnerable Plaques

The goal of modern imaging is to detect "vulnerable" plaques that are most susceptible to rupture.[24,35] The most commonly used imaging procedures in the past were invasive techniques based largely on IVUS. The goal of these procedures is to identify sites in the coronary vessel that are prone to rupture. Patients at risk are extremely difficult to identify clinically because the stenoses that lead to an acute infarction are not flow-limiting lesions. As a result, type IV or type V plaques are rarely diagnosed even with IVUS (**Fig. 8.6**). Most patients who present for examination have already experienced plaque ruptures because they have an acute coronary syndrome. We are still awaiting the results of "virtual histology" (**Figs. 8.14, 8.15**) as a means of identifying coronary vascular sites that display typical features of an unstable lesion.

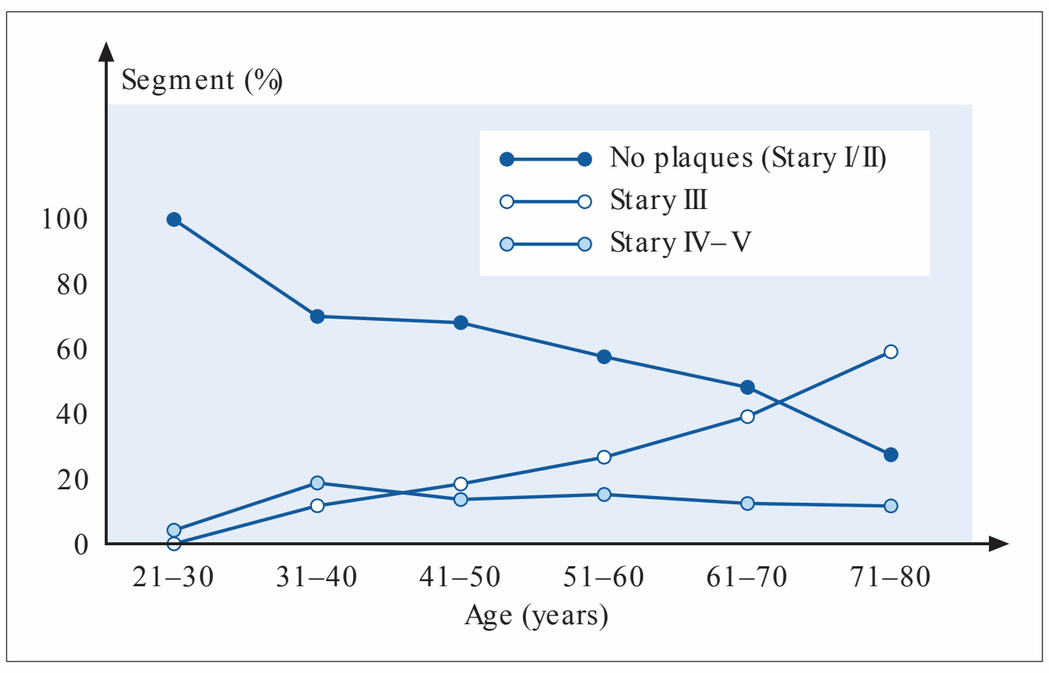

Fig. 8.8 Plaque formation with a normal coronary angiogram. The percentage of imaged segments that show Stary stage III, IV or V plaque formation is plotted against patient age categories.

Thermography is a technique that detects regional temperature elevations caused by the inflammatory reaction that is typically associated with vulnerable plaques. Thermographic imaging has been used clinically, in-vitro studies have documented temperature differences up to 1.5 °C in the carotid arteries. The temperature differences in vivo are smaller but may reach 0.6 to 1 °C. They are higher in an acute infarction than in unstable angina and are reduced by treatment with statins.

Catheter-based spectroscopic and MRI techniques are also being developed for the detection of vulnerable plaques. First studies are also performed using CT and MRT.[37,38]

Angioscopy as well as OCT have been introduced clinically but are still limited to a small number of centers. Angioscopy can distinguish stable plaques from unstable plaques owing to their different color characteristics. Plaque ruptures can be detected, and thrombotic deposits can be diagnosed with high sensitivity, which is highest for OCT.

Preventive Cardiology

Preventive cardiology has reached a new level with the development of methods that allow the detection of subclinical coronary atherosclerosis. An important aspect of preventive cardiology is the identification of risk factors, which is included in the "Check-Up 35" screening program in Germany. A distinction is drawn between modifiable and nonmodifiable risk factors as well as causal, predisposing, and possible risk factors (**Table 8.2**). Heavy smoking, hypertension, hypercholesterolemia, and diabetes mellitus are considered to be causal risk factors, not only because of their link with atherosclerosis but also because treatment of these conditions is associated with a reduction in patient risk. This has not been definitely established for possible risk factors, which include hypertriglyceridemia, hyperhomocysteinemia, and hyperuricemia. Predisposing risk factors include a positive family history. A paternal myocardial infarction before 55 years of age or a maternal myocardial infarction before 60 years of age is considered a predisposing risk factor. Age and sex are classified as predisposing, nonmodifiable risk factors.

Level 1 Screening

Level 1 screening is begun at 40 years of age or sooner in individuals with a very high familial risk. Risk factors are assessed, and it is determined whether there is a prior history of disease in other vascular regions. If there is a positive history of stroke or vascular aneurysm or a current history of peripheral arterial vascular disease, the individual is placed in a high-risk category with an event rate (fatal or nonfatal myocardial infarction) greater than 2%per year (**Fig. 8.16**). Patients with diabetes mellitus are also considered to be at high risk. The various patient data can be combined with tabulated data from the Framingham Study, PROCAM Study, or European Society of Cardiology to calculate a risk score (**Fig. 8.17**). These risk scores are based on large prospective studies that were able to correlate cardiac events with specific constellations of risk factors.

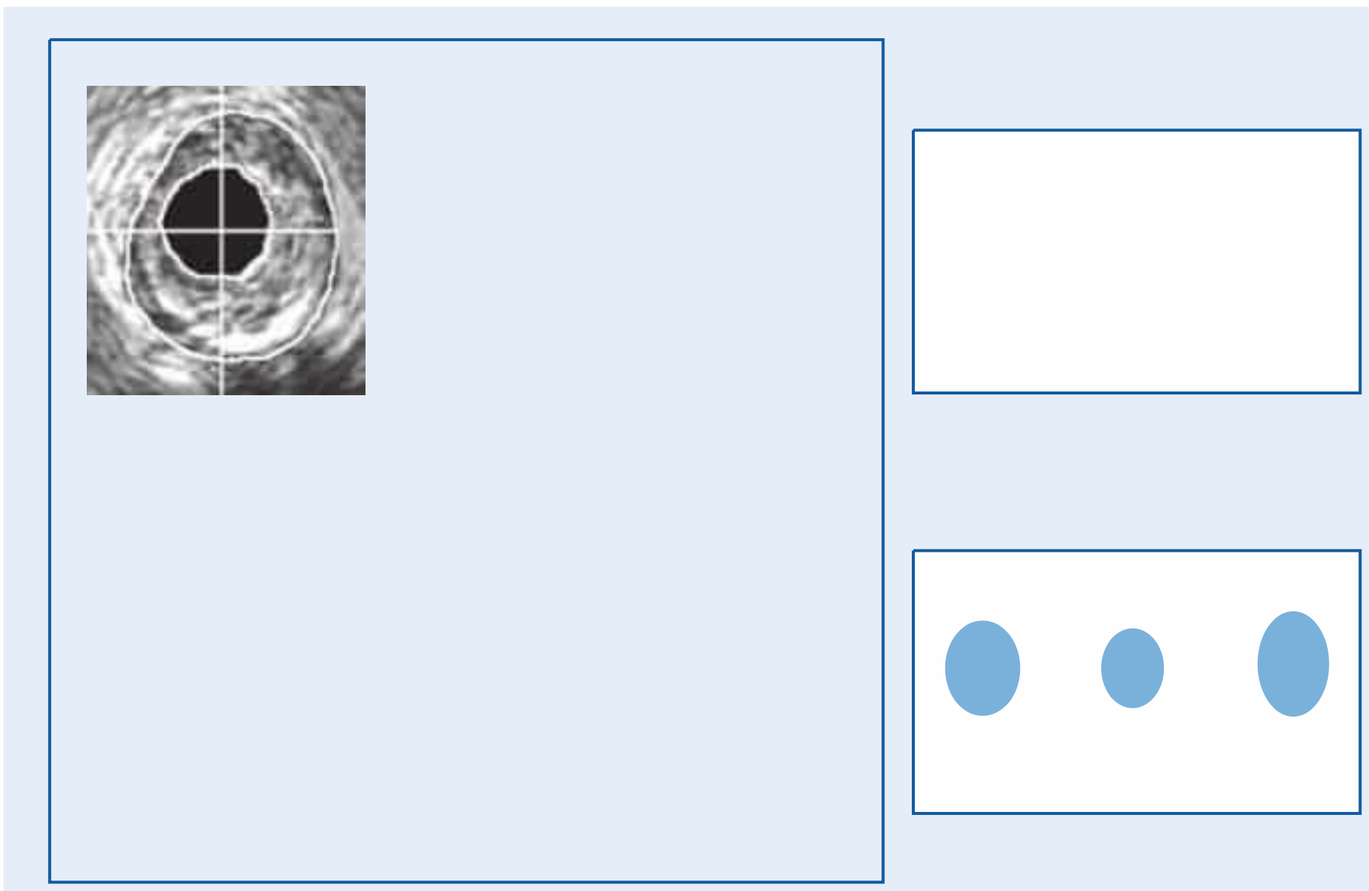

Fig. 8.10 Plaque formation with negative remodeling demonstrated by intravascular ultrasound during distal-to-proximal catheter withdrawal. The largest vascular diameter is not found in the area of greatest luminal narrowing, as the vascular area in that segment is reduced compared with the proximal and distal segments. The smallest vessel diameter based on lumen–adventitia distance is found in the stenotic segment. Lesions with negative remodeling are less vulnerable to plaque rupture.[10]

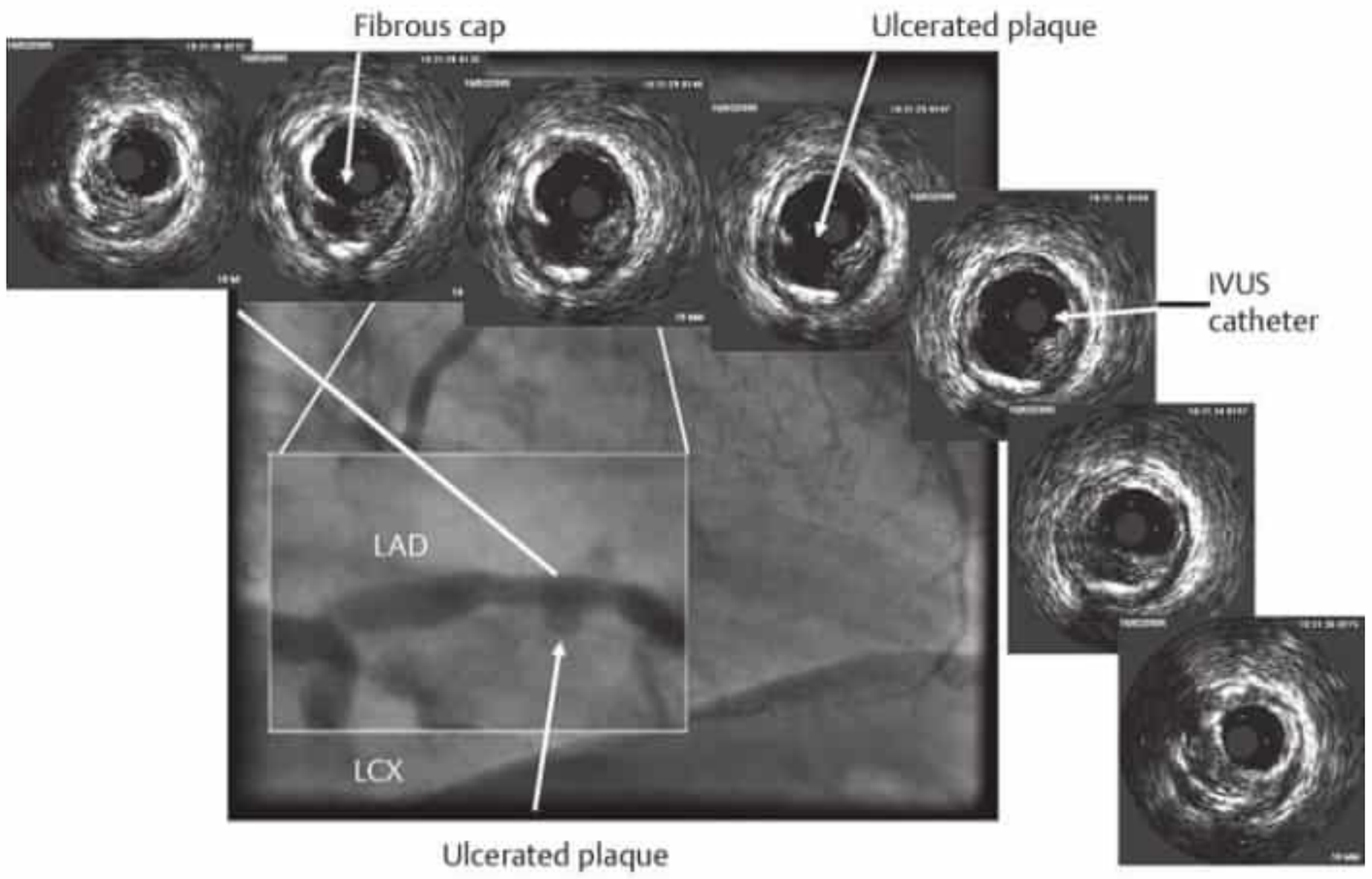

Fig. 8.12 Coronary angiogram shows an enlarged LAD with a ruptured plaque. Proximal-to-distal series of IVUS images (from left to right) demonstrate a ruptured and ulcerated plaque. Remnants of the fibrous cap can be identified along with vascular remodeling (vessel diameter at the plaque rupture site is expanded relative to proximal and distal diameters). (With kind permission of D. Böse, Essen, Germany.)

The 10-year risk is classified as follows:

- Low = less than 10 %
- Intermediate = 10–20 %
- High = greater than 20 %(**Fig. 8.16**)

Level 2

It is recommended that persons with an intermediate risk for cardiac events be screened for signs of subclinical atherosclerosis.[39]

The European Society of Cardiology (**Fig. 8.16**) and German Society of Cardiology have issued the following recommendations:

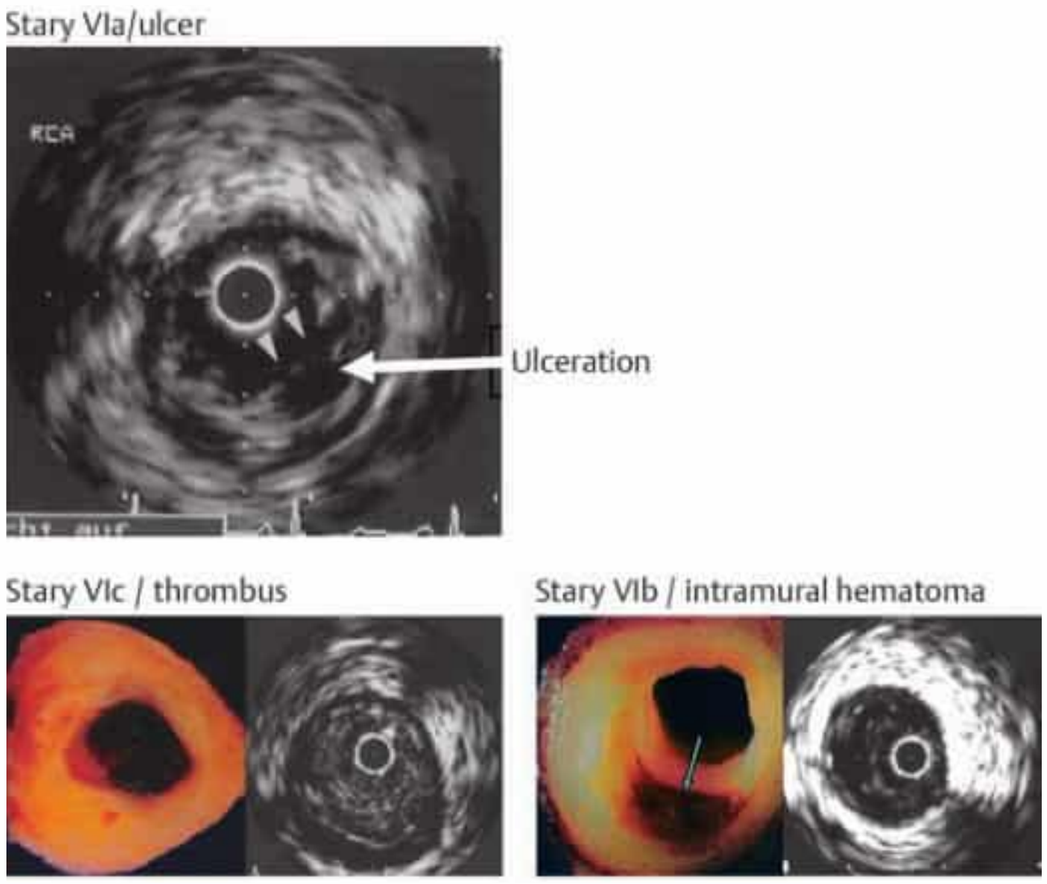

Fig. 8.13 Complicated plaques: IVUS image of Stary VIa ruptured and ulcerated plaque, pathoanatomical view plus IVUS of Stary VIb intramural hemorrhage, and pathoanatomical view plus IVUS of Stary VIc ruptured plaque with complete luminal thrombosis.[13,20,23]

- Use vascular ultrasound to check for signs of sclerosis in peripheral vessels, especially the carotid arteries, and determine the intima-media thickness.
- Determine the ratio of blood pressure readings on the thigh and upper arm (the ankle—brachial index or ABI).
- Check for vascular calcifications with CT.
- Determine high-sensitivity C-reactive protein (hs-CRP test).
- Prescribe a stress ECG for males 45–65 years of age.

To date, **contrast-enhanced CT imaging** has not been recommended for the detection of noncalcified plaques owing to concerns about radiation exposure. If the Agatston score is higher than 100, the risk of myocardial infarction is markedly increased. An Agatston score between 400 and 1000 predicts a substantial event rate.[40,41] There is no strong correlation between risk factors and coronary vascular calcification, and so the detection of vascular calcification may be viewed as an additional "risk factor."[42]

Table 8.2 Risk factors

Causal risk factors	• Hyperlipoproteinemia • Arterial hypertension • Nicotine abuse • Diabetes mellitus
Possible risk factors	• Low HDL • Hypertriglyceridemia • Hyperlipoproteinemia (a) • Hyperhomocysteinemia • Hyperfibrinogenemia • Elevated plasminogen activator inhibitor (PAI) • Increased hs-CRP
Predisposing risk factors	• Obesity • Sedentary lifestyle • Positive family history • Male sex • Insulin resistance • Socioeconomic factors • Psychosocial factors

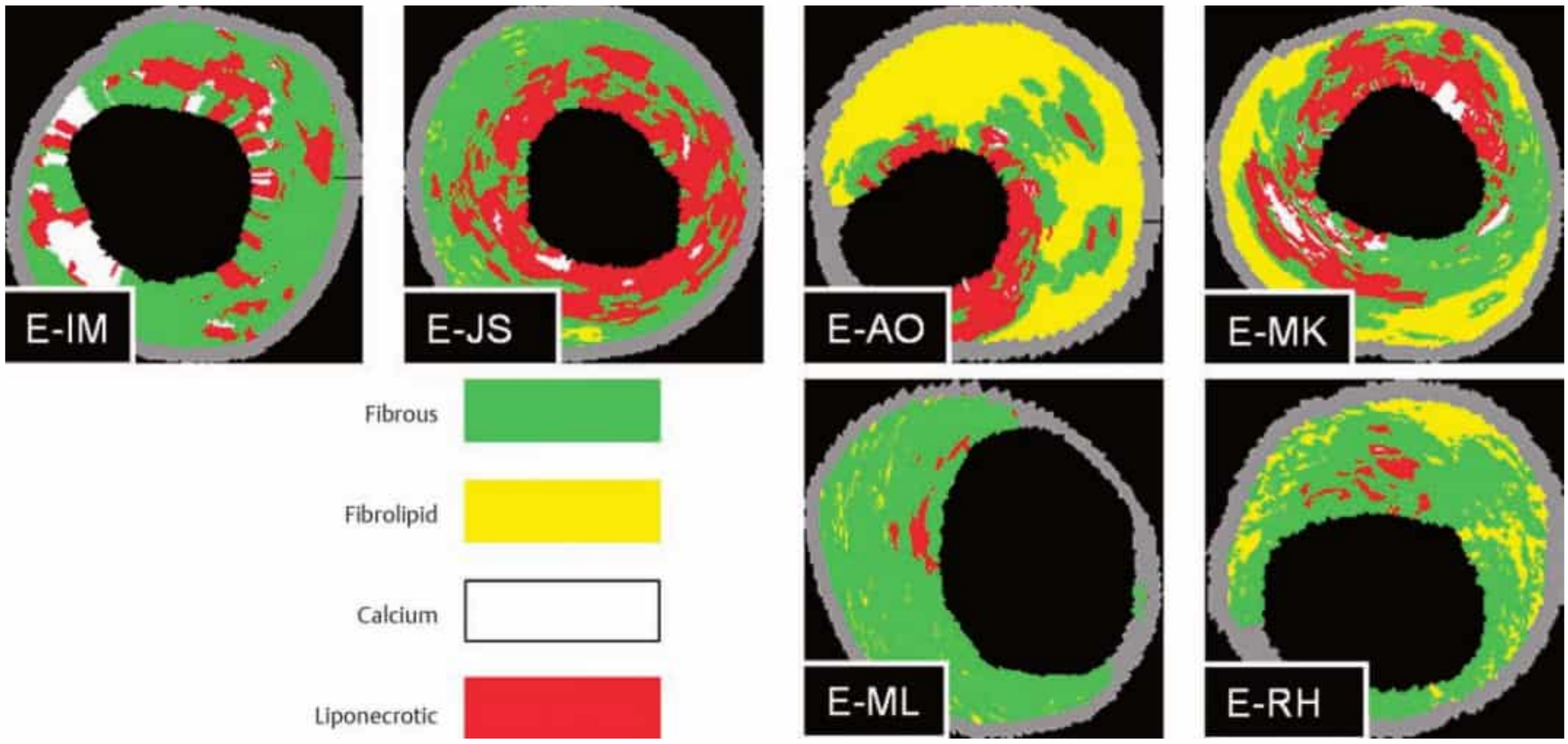

Fig. 8.14 Virtual histology with coronary IVUS. The images show a variety of plaque compositions with fibrous, fibrolipid, calcifying, and liponecrotic components. (With kind permission of D. Böse, Essen, Germany.)

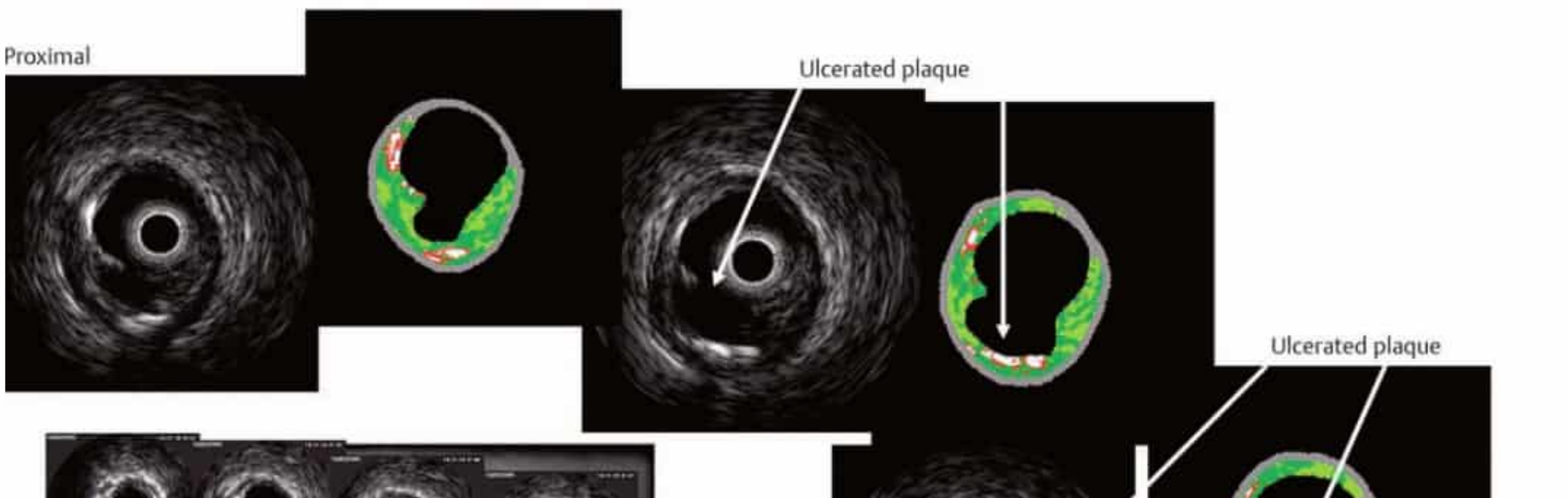

Fig. 8.15 Virtual histology of coronary IVUS images of ruptured plaque (Stary VIa) (see also **Fig. 8.12**). The images show predominantly fibrous and lipid-rich components. Calcifying and liponecrotic elements are found at the base of the ulcerated plaque. Proximal-to-distal series of IVUS images (from upper left to lower right). Arrows = ulcerated plaque. (With kind permission of D. Böse, Essen, Germany.)

Because inflammatory processes are also involved in the pathogenesis of acute coronary syndromes, the determination of C-reactive protein—the high-sensitivity **CRP test**—is recommended so that a differential risk assessment can be made in the low range of CRP concentrations (<1, 1–3, >3 ng/mL).[21,43,44]

Only a weak correlation exists between the detection of atherosclerosis in the cervical vessels and its presence in the coronary vessels. Significant coronary vascular changes may exist in the absence of detectable carotid deposits.

The Heinz–Nixdorf Recall Study is the first large population-based study in Germany to test the predictive value of **electron beam computed tomography**. A total of 4814 participants 45–75 years of age were recruited for the study[45,46] and have been followed over a 5-year period until 2008.

The prevalence of coronary vascular calcifications in the Heinz–Nixdorf Recall Study was 84% in the male participants and 54% in the female participants aged 45–74 years. Twenty percent of the men and 60% of the women had no vascular calcifications. Values >100 were found in ~40% and 15% of the study participants, respectively, and values >400 were found in 16% and 4% Cervical vascular plaques were found in only 43% of participants, and an abnormal ABI index was found in 9% With aging, this percentage rose to 15% in males and to 11% in females.

Stress ECG for risk stratification is recommended in men 45–64 years of age[18,43] but not in women. Physical fitness is measured by overall exercise tolerance and the rate of heart rate recovery after exercise. The decline in heart rate after the conclusion of exercise is evaluated. Heart rate recovery should be 12–15/min measured 1 minute into the recovery phase of the exercise protocol.

The determination of **intima-media thickness** has proved to be a valuable test in large pharmacological studies, but it has not yet come into routine clinical use. Age- and sex-specific factors must be taken into account, but plaque formation is a sign of increased risk.

Current studies are dealing with the question of whether and in what groups the analysis of subclinical atherosclerosis can contribute to the assessment of coronary risk.

It remains unclear whether and at what intervals imaging should be repeated for the detection of subclinical atherosclerosis. It is generally recommended that screening be repeated at 3–5 years if the initial result was negative and the patient is over 45 years of age.

Level 3 Prevention Strategy

After a preliminary examination by the physician, an individual risk assessment is made based on detectable modifiable and nonmodifiable causal risk factors and the prior history of the person examined, who at this preventive stage should not yet be classified as a patient (**Fig. 8.16**). If the risk is determined to be <1%/year, a healthful lifestyle is recommended that includes good nutrition, regular physical exercise, and a low-stress environment. If the risk is deemed to be high, indicating a greater than 2% likelihood of cardiac events per year, the management of risk factors should be optimized to achieve the target values for blood pressure, cholesterol, and HbA1. Usually this will require a combined drug regimen of aspirin therapy, statins, angiotensin-converting enzyme (ACE) inhibitors or angiotensin-receptor antagonists (AT 1), and β-blockers.

In the large group of persons at intermediate risk, where there is a 1–2% likelihood of cardiac events per year, diagnostic tests are aimed at detecting signs of subclinical atherosclerosis. Primary emphasis is placed on the detection of coronary calcifications as a surrogate parameter for coronary plaque formation and on the detection of cardiac atherosclerosis. If vascular calcifications are detected and if they reach a value that ex-

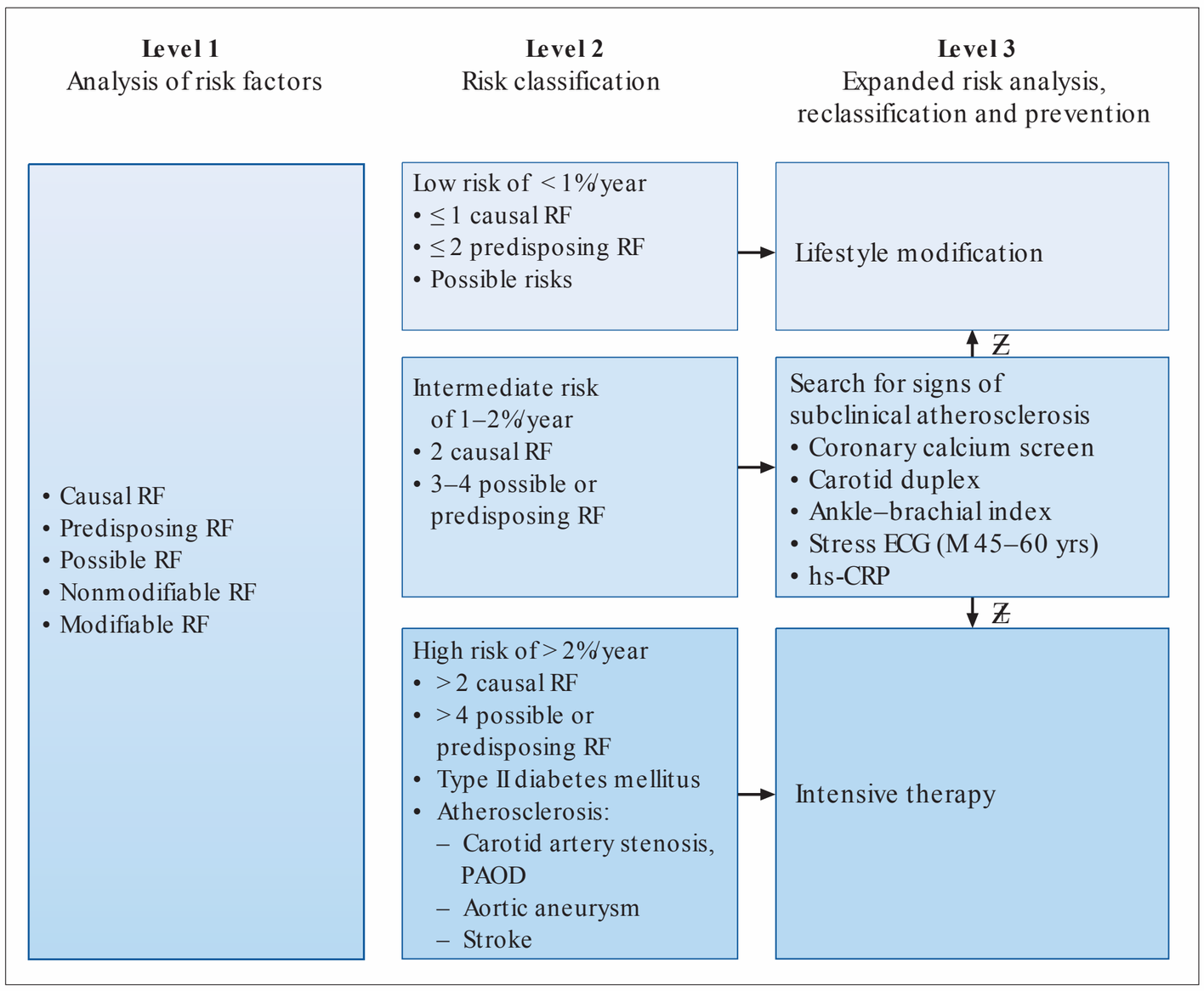

Fig. 8.16 Risk stratification. Level 1: risk analysis for assessing low risk, intermediate risk, and high risk based on determination of risk factors and cardiovascular history. Level 2: risk classification for use of imaging and nonimaging techniques in persons at intermediate risk to check for signs of subclinical atherosclerosis. Level 3: reclassification in those with intermediate risk and lifestyle modification if signs are negative (–) intensive therapy if signs are positive (+)[22,32]

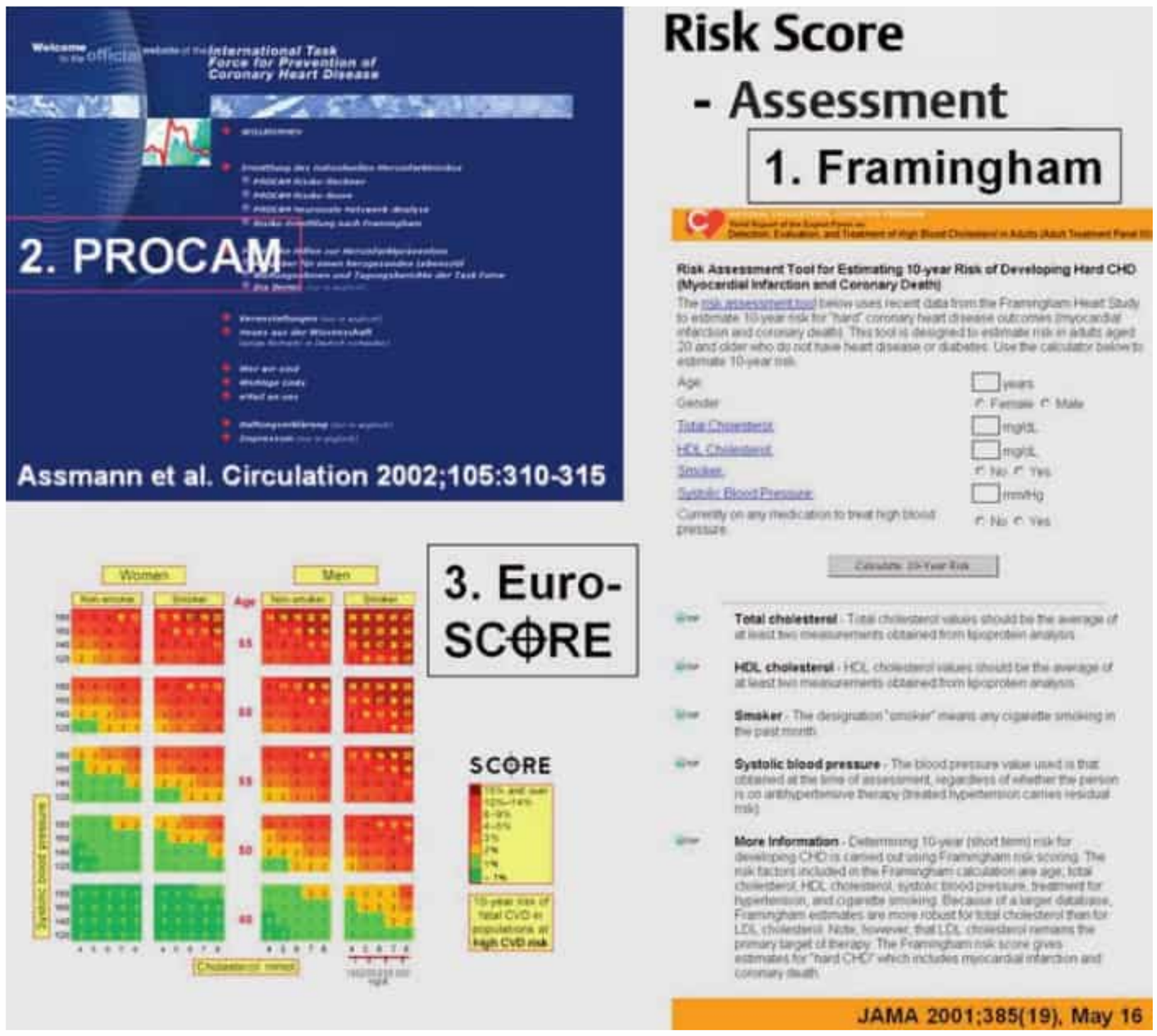

Fig. 8.17 Framingham, PROCAM, and EuroSCORE for risk assessment based on risk factors in level 1 risk stratification.[160,177,178]

ceeds the 75th percentile or an Agatston score of 100, the risk should be adjusted to a level higher than 2%per year. If these signs are absent, the risk is considered to be low. Follow-up examinations for reevaluation should be scheduled every 3–5 years. The patient is counseled to adopt healthier living habits.[18,47]

If an extremely high risk is found, such as an Agatston score >1000 or a percentile value above 90, the patient should be evaluated for ischemic disease by stress ECG and stress echocardiography. Patients with a negative stress ECG should undergo stress scintigraphy or echo cardiography because of the high risk. Cardiovascular events have been documented in up to 20%of high-risk patients within a 1-year period.[40]

Acute Ischemia

G. Horstick, N. Abegunewardene, M. Vosseler, and K.-F. Kreitner

Cardiovascular diseases are the leading cause of death in industrialized western countries. Myocardial infarction is by far the leading cause, although mortality rates have been declining since 1979. Without question, the gain of life expectancy in recent years is attributable to improvements in the treatment of underlying cardiovascular diseases.[48] The multifactorial etiology of myocardial infarction is known, and the assessment of risk factors using the PROCAM score (Prospective Cardiovascular Munster Heart Study) plus additional questions about the patient's lifestyle in the Interheart Study demonstrated a 90% accuracy in the prediction of myocardial infarction.[49]

The heart failure that may result from myocardial infarction has a high mortality rate. It would be desirable, therefore, to have a method that could detect the development of potentially severe heart failure after an acute infarction at an early stage. Cardiac MRI, with its ability to analyze myocardial texture in the early phase after myocardial infarction, can provide this type of information.[50]

Pathophysiology of Myocardial Ischemia in Relation to Cardiac MRI

Infarct Size and Collateral Vessels

In patients with typical anginal symptoms, the diagnosis of myocardial ischemia should be established within 4–6 hours after the onset of complaints so that the causative thrombus can be eliminated and the affected coronary artery can be recanalized. The goal is to prevent myocardial cell death by restoring perfusion as quickly as possible to reduce the size of the infarct.[51]

The classic pathophysiological interpretation of coronary heart disease as an imbalance between oxygen supply and demand has changed in recent years based on research indicating:

- Contractile dysfunction despite the restoration and normalization of perfusion (stunning)[52]
- The recovery of metabolic parameters with persistence of ischemia and depression of myocardial function (hibernation)[53,54]
- The presence of protective endogenous mechanisms (ischemic preconditioning)[55]

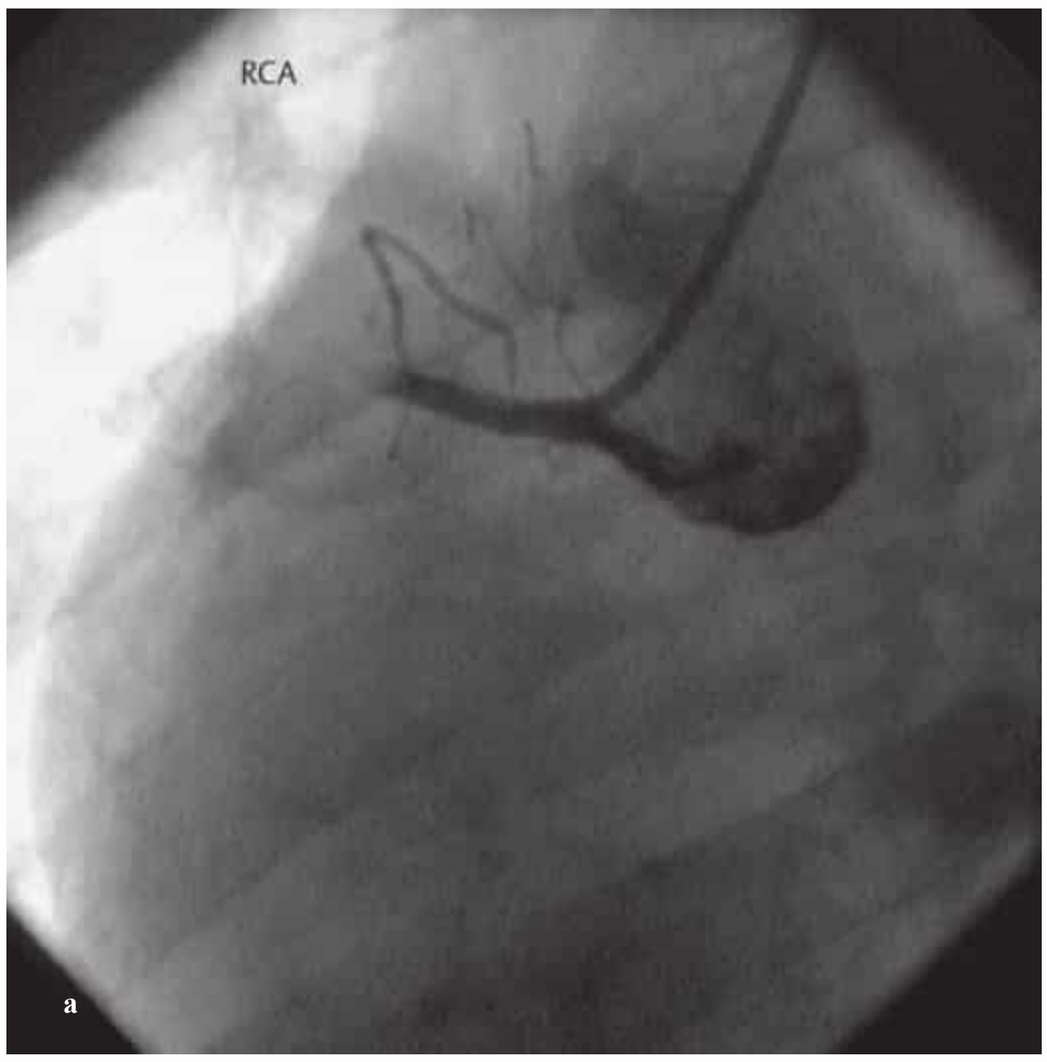

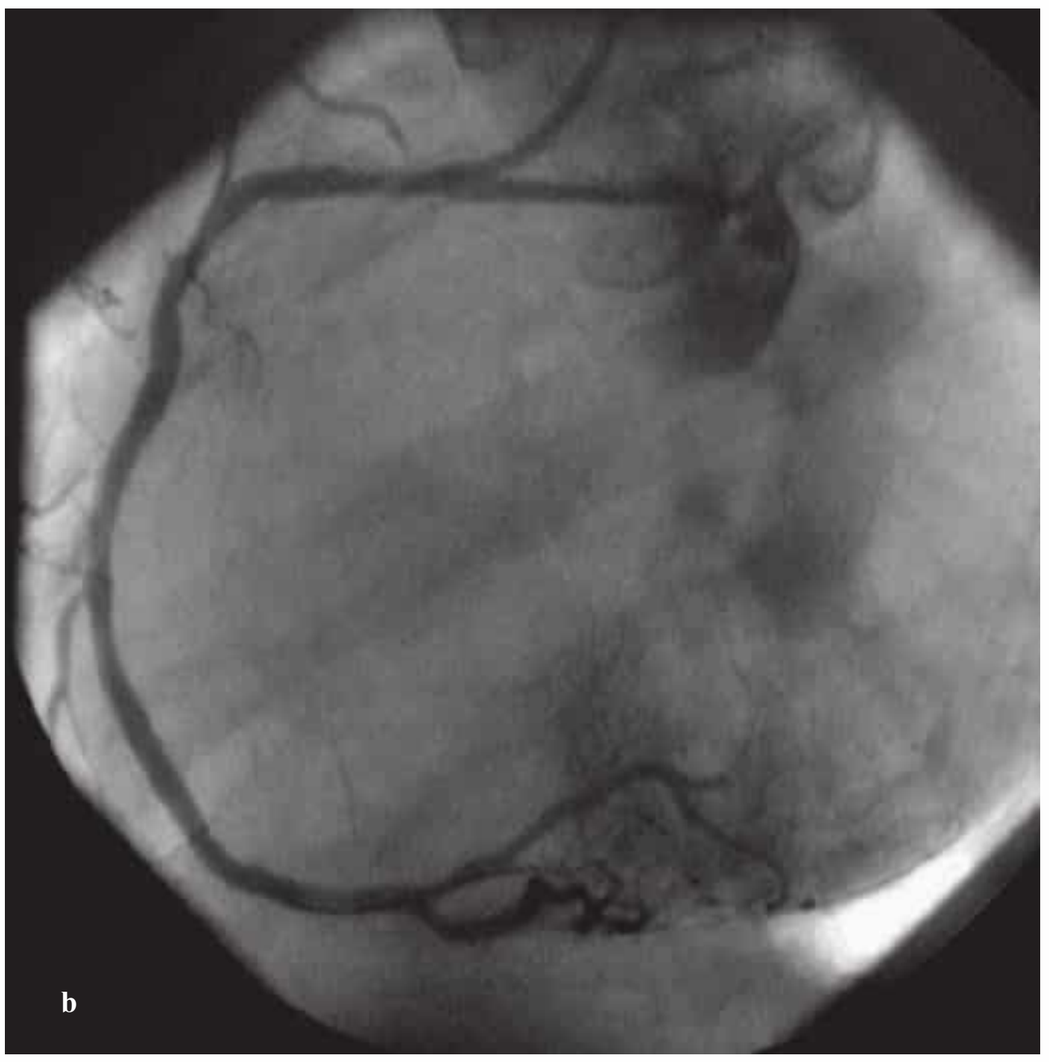

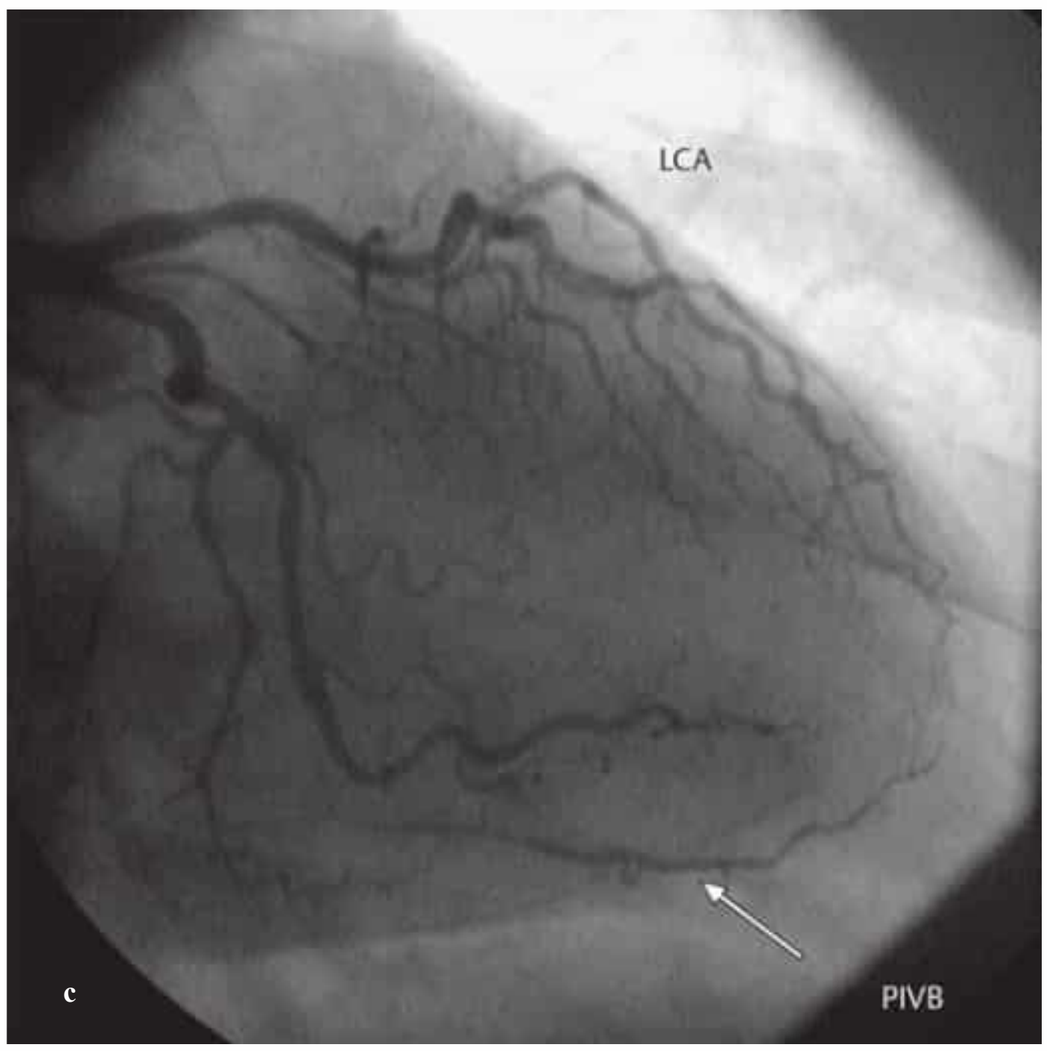

Fig. 8.18 a–f Acute occlusion of the RCA with reperfusion following acute stent PTCA. MR images were acquired 6 months after the intervention.

a Coronary angiogram demonstrates occlusion of the RCA.

b Angiogram after successful recanalization.

c Angiogram of the LCA at the time of RCA occlusion. The PIVB is opacified by collaterals from the LAD.

d Contrast-enhanced MRI of late enhancement in the short-axis view. An area of intact myocardium is identified in the posterior septum.

e Contrast-enhanced MRI in the short-axis view with the RCA schematically superimposed on the image.

f Collateral blood flow to the PIVB prevents postinfarction necrosis of the myocardial cells.

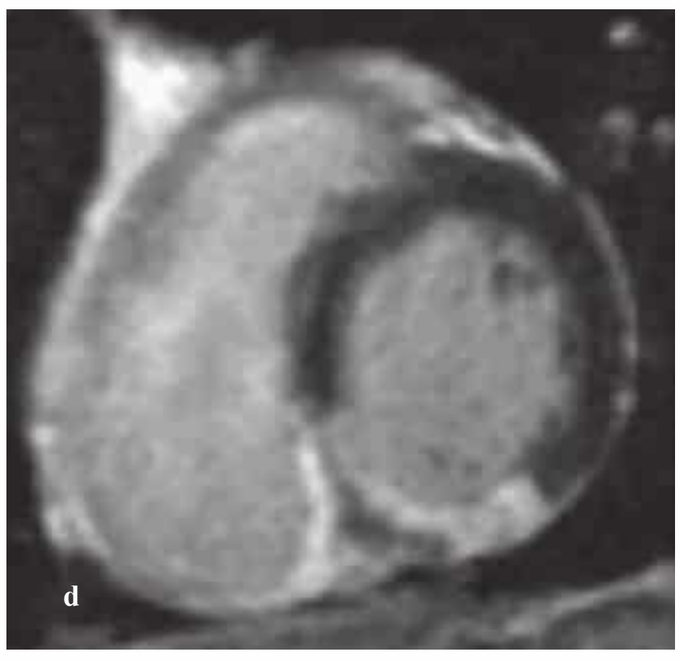

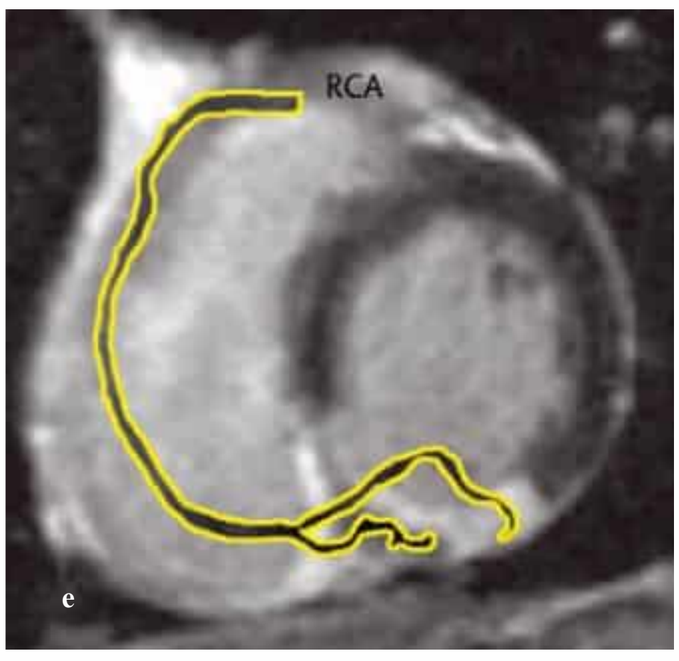

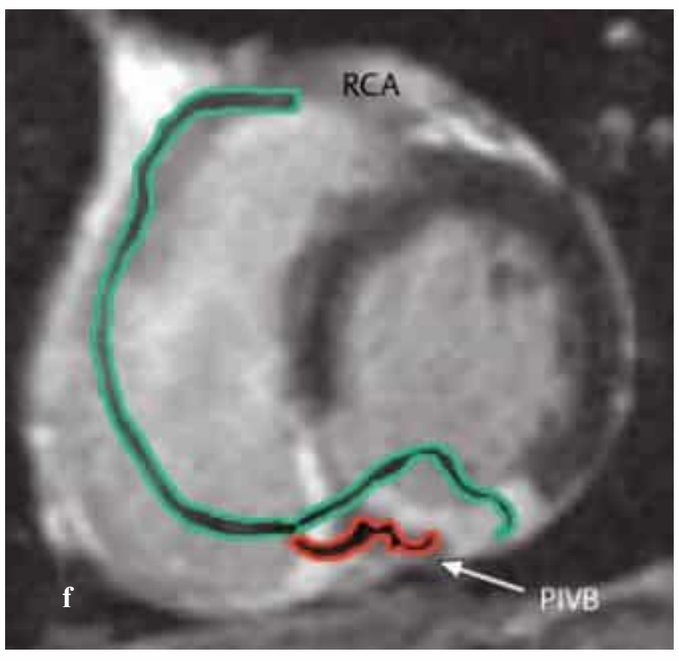

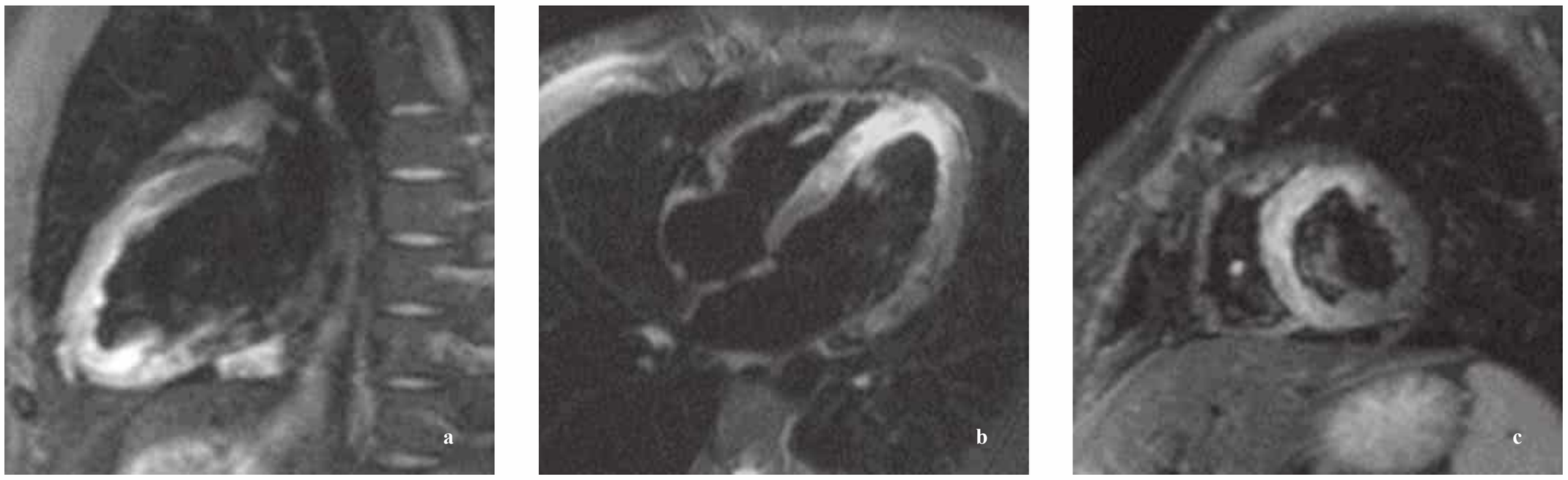

Fig. 8.19 a–c Anterior wall infarction with successful recanalization of the LAD. Images 24 hours after intervention demonstrate successful reperfusion. The anterosuperior infarcted area in the LAD territory appears hyperintense in fat-suppressed sequences (STIR).

a Sagittal long-axis slice through the left ventricle.
b Horizontal long-axis slice.
c Short-axis slice.

Cardiac MRI can demonstrate these phenomena experimentally and under clinical conditions, as after the recanalization of an occluded vessel or in chronic ischemic coronary heart disease. Depending on the development of myocardial collateral vessels, the ischemic area may feature a variety of pathophysiological mechanisms with associated myocardial injury. These mechanisms can be differentiated with MRI (**Fig. 8.18**).

Additionally, studies on the pathophysiology of acute myocardial infarction have documented the effects of inflammatory processes that are known collectively as **reperfusion injury**.[56,57] This term mainly denotes a progression from reversible to irreversible cell damage during reperfusion and the development of microvascular obstruction in a previously occluded or underperfused region. Cardiac MRI can detect these perfusion abnormalities clinically and can also quantitate their severity.[58–61]

On the whole, successful reperfusion of the heart leads to a reduction in mortality. Nevertheless, there are cases in which myocardial reperfusion leads to a paradoxical deterioration of the clinical status with an increase in the size of the infarct and prognostically unfavorable left ventricular dilatation. The exact pathophysiological causes of reperfusion injury as well as postischemic remodeling are not yet fully understood. But with its ability to visualize the myocardium and fibrotic tissue, cardiac MRI can significantly advance our understanding of scar remodeling in the infarcted heart (see **Fig. 8.20**).

The severity of myocardial injury varies in different areas. For example, subepicardial tissue layers can tolerate ischemia for a considerably longer time than subendocardial layers. MRI can demonstrate these subendocardial infarcts better than any other cardiac imaging modality.[62]

Other determinants of myocardial infarct size besides the duration of occlusion are:

- The size of the territory supplied by the occluded artery
- The oxygen demand at the time of the occlusion[63]
- The level of residual blood flow through collateral vessels[64,65] (**Fig. 8.18**)
- The variable ischemic tolerance of the myocardium[55]

Myocardial Metabolism and Contractile Function

Under normal circumstances, the myocardium derives its energy from aerobic glycolysis, the citric acid cycle, and oxidative phosphorylation. When blood flow ceases owing to coronary occlusion, the myocardium consumes physically dissolved oxygen and the oxygen bound to myoglobin within a matter of seconds. Aerobic myocardial metabolism can still take place during this phase. But when a critical oxygen partial pressure (Po_2) is reached and oxidative phosphorylation is curtailed, anaerobic glycolysis is activated and glycolytic flux is increased. Despite the increase in anaerobic glycolysis, the energy yield is limited and an energy deficit develops.

This energy deficit compromises the energy-intensive metabolism of the intracellular membranes, leading to an electrolyte imbalance with intracellular edema. This process appears as a cloudy swelling on light microscopy, while electron microscopy shows distention of the mitochondria and membranes of the endoplasmic reticulum. The edematous tissue shows increased signal intensity in fat-suppressed MRI sequences (**Fig. 8.19**). If the vascular occlusion persists, the duration of ischemia may be sufficient to cause necrosis.

Owing to the presence of native collateral vessels, a mixed situation develops at the periphery of the ischemic area. The collateral vessels can still supply a small amount of oxygen that is sufficient to clear acid metabolites, reduce intracellular acidosis, and increase the glycolytic flux in these areas.[66] This collateral perfusion is sufficient to prevent full-thickness transmural injury (**Fig. 8.18**).

When vascular occlusion occurs, an acute failure of myocardial contractility arises within a few cardiac cycles. Initial hypokinesia with decrease of systolic function is followed swiftly by akinesia. This is usually replaced by dyskinesia after a period up to 2 minutes.

These segmental contraction abnormalities in the form of hypokinesia, akinesia, and dyskinesia can be visualized by echocardiography or cine MRI and myocardial tagging, and they can be quantified by computer-assisted analysis.[67]

Two special types of contraction abnormality can be observed following myocardial ischemia with reperfusion: **myocardial stunning** in cases with complete postischemic restoration of blood flow[3] and **hibernating myocardium** in cases with a sustained perfusion deficit and hypokinesia in the ischemic area.[53] Both conditions may occur after reperfusion of a previously ischemic area mainly in the border zone, and both can cause impairment of cardiac function. Cardiac MRI after myocardial infarction can detect these functional abnormalities of the myocardium depending on the degree of myocardial injury relating to perfusion and wall motion.

Local Pathogenic Mechanisms in Ischemia: Reperfusion

Early Metabolic Abnormalities and Mechanical Cell Damage

Reperfusion injury in the broad sense can be interpreted as a progression from reversible cell damage at the time of reperfusion to a state of irreversible cell damage.[68] Currently there are two state-of-the-art clinical treatment options for the reduction of myocardial injury:

- Acute percutaneous transluminal angioplasty (PTCA)
- Pharmacological thrombolysis[51]

A knowledge of cytotoxic agents and their management during reperfusion can provide an interesting approach to reducing the extent of cell damage and influencing myocardial remodeling after an infarction. From a pharmacological standpoint, we know that myocardial fibrosis can be positively influenced by the administration of aldosterone antagonists, ACE inhibitors, and angiotensin receptor antagonists. Other medical treatment strategies are undergoing preclinical trials. Cardiac MRI is a radiation-free imaging study that can be repeated as often as desired to monitor changes in the myocardium following ischemia and reperfusion.[69,70]

The time course of reperfusion injury can be subdivided into immediate injury (occurring in seconds) and delayed injury (occurring in ~1–5 minutes).[71] There are additional processes that are initiated during this period but do not become apparent for 12–48 hours (e.g., apoptosis) and may have a long-term effect on remodeling during the next 4–8 weeks (scar formation, activation of myofibroblasts).

Initial mechanisms of reperfusion include immediate energy provision and its immediate utilization by reactivation of the ATP-dependent sodium–potassium pump (Na^+-K^+ ATPase), causing an increase in the transmembrane sodium gradient. This mechanism can be visualized by sodium imaging with MRI but currently has only an experimental role.[72]

The rapid normalization of tissue osmolality and tissue pH are additional mechanisms responsible for the immediate development of postischemic intracellular edema, cell swelling, and rupture of the cell membranes.[73] The resulting myocardial edema can be visualized in fat-suppressed MRI sequences (**Fig. 8.19**).[50]

Other mechanisms such as "no reflow"[74] and myocardial hemorrhage[75] that occur acutely after the restoration of coronary blood flow have adverse microcirculatory effects and lead to microvascular obstruction, which can also be demonstrated by MRI (**Fig. 8.20a–d**).[76]

Inflammatory Mechanisms

The early pathogenic mechanisms following reperfusion are accompanied by an increasing interaction between humoral and cellular systems such as surface adhesion molecules[77] with an increase in leukocyte adhesion (e.g., CD-18, ICAM-1) and cellular migration into the extracellular space. These are manifestations of an increasing local cellular inflammatory activity.

In the humoral system, contact activation during the initial minutes after reperfusion evokes an early procoagulant response in both the intrinsic and extrinsic coagulation systems.[78] This leads to endothelial and microvascular dysfunction during the first few minutes after reperfusion.[79,80] Increased free-radical formation also occurs[81] along with activation of the fibrinolytic system, the bradykinin–kinin system, and the complement system.[56,78]

The reperfusion of ischemic myocardium is important not only for the survival of myocardial cells but also for scar formation.[70] Experiments have shown that even late reperfusion can reduce the extent of aneurysm formation in the infarcted area compared with unremitting coronary occlusion.[82] The healing process after reperfusion also includes increased angiogenesis in the ischemic/reperfused area.[83]

Very few clinical data are available on how longer-term damage due to inflammatory activation after ischemia and reperfusion may affect scar formation in left ventricular remodeling. Contrast-enhanced cardiac MRI can provide important information on this process.[50,63]

Viability Assessment in Cardiac MRI

Cardiac MRI is already improving our morphological and functional understanding of the pathophysiological processes (see above) involved in ischemic and reperfused myocardium. From a technological standpoint, all of the imaging sequences necessary for this type of investigation can be completed in ~60 minutes during one examination. The quantitative determination of myocardial fibrosis, the semiquantitative and quantitative measurement of myocardial perfusion, and the investigation of regional and global function parameters can provide a comprehensive assessment of the viability of the myocardium and its varying pathophysiological states. Cardiac MRI is able to discriminate among infarcted nonviable and still viable myocardium, hibernating myocardium, and stunned myocardium.[50]

Myocardial Edema

During the early phase after recanalization, edema develops in the ischemic–reperfused myocardium. This process is characterized by a barrier breakdown with a local capillary leak confined to the reperfused area and a consequent influx of water into the interstitium. This reperfusion edema is demonstrable by MRI (**Fig. 8.19**).[50] By suppressing signals from myocardium and fat, the increased water protons in the myocardium can be used to generate signals.[84] The aggravation of barrier breakdown also contributes to increased contrast uptake in the edematous area (**Fig. 8.21b, c**).

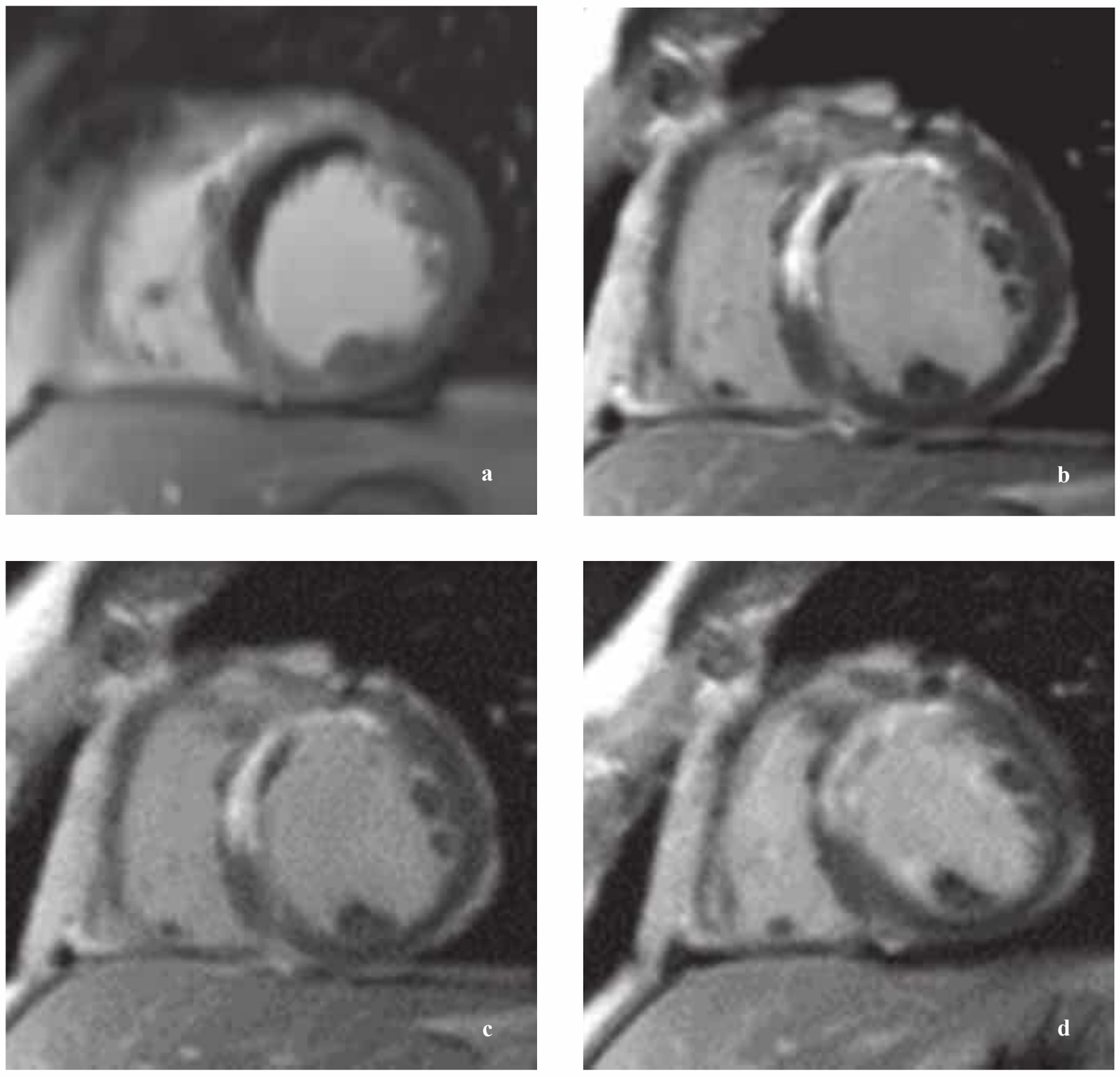

Fig. 8.20 a–c Contrast-enhanced MRI in a patient with myocardial infarction and successful stent PTCA of the LAD.

a, b MRI examination 24 hours after reperfusion.

a Image 2 minutes after contrast administration clearly delineates a central area of signal void (hypoenhancement) indicating microvascular obstruction (MO) with a very narrow hyperenhancing rim (early enhancement).

b Image 10 minute after contrast administration shows a marked decrease in the size of the MO with a larger hyperenhancing rim (late enhancement).

c, d MRI examination 10 days after reperfusion.

c Early images after contrast administration show marked regression of the area of MO (early enhancement).

d Regression of late enhancement.

e MRI 6 months after reperfusion.

f MRI 12 months after reperfusion.

e By 6 months, an MO area is no longer visible after contrast administration.

f Image 12 months postinfarction shows a further decrease in the late enhancement zone. This decrease cannot be attributed entirely to scar contraction in the infarcted area.

Contrast-Enhanced MRI

Paramagnetic contrast agents (e.g., Gd-DTPA) can be used to differentiate myocardium from fibrosis.[85] The fibrotic tissue in a myocardial scar displays late (delayed) hyperenhancement, which distinguishes it from the weak enhancement of viable myocardium (**Figs. 8.18, 8.20**, see also Chapter 6, p. 116 ff).

From a pathophysiological standpoint, different structures in the various tissue compartments are responsible for the variable wash-in and delayed wash-out of contrast medium in viable myocardium and fibrotic and necrotic tissue.[86]

Visualization of a myocardial scar (e.g., after myocardial infarction) depends on the selection of scan parameters for contrast-enhanced (CE-)MRI, the contrast dose, and the timing of image acquisition after contrast administration.[87] A variable degree of late enhancement is also seen during follow-ups of early remodeling processes after myocardial infarction (**Fig. 8.20**).

The extent of late enhancement after consolidation of the myocardial scar is useful in predicting the improvement in regional wall motion that may be expected from successful revascularization by aortocoronary bypass (ACB) surgery or percutaneous balloon dilation (PTCA).[85,88] When transmural late enhancement encompasses 50–75 % of the wall thickness, it is likely that revascularization will produce very little improvement in regional contractility. Greater than 75 % of transmural late enhancement is predictive of no improvement. An inverse correlation also exists between the extent of late enhancement and left ventricular global ejection fraction.[69] There is no direct correlation between the transmural extent of late enhancement after myocardial infarction and the degree of ECG changes in

the acute phase.[69] It has been found that contrast-enhanced MRI is significantly better than nuclear medicine imaging for the detection of small subendocardial infarcts.[62]

When postinfarction CE-MRI is performed in the early phase after contrast administration (early-enhancement imaging at ~2 minutes after contrast injection), areas of microvascular obstruction in the myocardium appear as nonenhancing areas that are much easier to detect than on late-enhancement images taken at ~10–15 minutes after contrast application (**Fig. 8.20**).[50] Moreover, the area of microvascular obstruction appears significantly larger at 2 minutes postinjection than at 10 minutes. The detection of microvascular obstruction also has prognostic implications.[63] The earlier cardiac MRI can be performed after myocardial infarction, with or without recanalization, the more accurately can the individual ischemic area at the time of coronary occlusion (area at risk) be determined.[56] This permits a noninvasive follow-up of myocardial infarction with determination of the nonperfused ischemic area at risk at the time of the occlusion and the scar that will develop in that area with passage of time. Thus, cardiac MRI is the only modality that can noninvasively evaluate the therapeutic effect of ischemia–reperfusion on scar reduction with an acceptable spatial resolution.

Contrast-enhanced cardiac MRI can advance the differential diagnosis of primary and secondary structural myocardial diseases such as dilated cardiomyopathy, hypertrophic cardiomyopathy, arrhythmogenic right ventricular dysplasia, and left ventricular noncompaction (see also Chapter 9).[50] Increased tissue heterogeneity of the measured signal-intensity in CE-MRI of the infarct border zone was strongly associated with the inducibility of ventricular tachycardia.[89]

Perfusion Analysis

The assessment of myocardial perfusion is of key importance in various pathophysiological states that follow ischemia/reperfusion (stunning, infarction, hibernation). The normalization of perfusion after ischemia–reperfusion may preserve the viability of ischemic myocardium.[79]

Both semiquantitative and quantitative contrast-enhanced methods are currently available for the analysis of myocardial perfusion. These methods are important in the noninvasive diagnosis of coronary heart disease as well as other myocardial diseases. The time-varying enhancement of the myocardial tissue can be analyzed with computer software that compares myocardial perfusion at rest and during pharmacological vasodilation (adenosine) to determine the regional perfusion reserve index. Based on the results of various studies, a diminished perfusion reserve with an index less than 1.5 is suspicious for a significant flow reduction due to coronary stenosis.[58,61,90] Perfusion can be quantified with the aid of special algorithms that take into account the distribution of contrast agent in various compartments.[59,91] A very good correlation has been found between experimental flow measurements and flow quantification by cardiac MRI.[60] Clinical studies show that the semiquantitative and quantitative methods yield equally good results.[90]

Meanwhile, improved MRI sequences have made it possible to discriminate between endocardial and epicardial perfusion.[92] In one study, MRI was able to detect subendocardial hypoperfusion in patients with a clinical diagnosis of cardiac syndrome X.[93]

Similar to the myocardial perfusion reserve, the bypass flow reserve can be determined in coronary bypass grafts with phase-contrast MRI to make a functional assessment of the grafts.[94] Technical refinements in pulse sequences also make it possible to determine the flow reserve in non-contrast-enhanced coronary vessels with cardiac MRI.[95]

Established perfusion-reserve tests that compare rest perfusion with adenosine stress perfusion are not recommended for routine testing in the acute phase after myocardial infarction because of limitations on the use of adenosine stress. A much better strategy is to use quantitative methods for the clinical evaluation of resting myocardial blood flow during the early phase after myocardial infarction. Experiments have shown that these methods are also useful in the evaluation of critical myocardial perfusion.[60,79]

Wall-Motion Analysis

Wall-motion analysis with cine MRI provides information on the pathophysiological status of the myocardium after an infarction. Again, routine stress testing is not recommended in the early phase after myocardial infarction because of the consumption of high-energy substrates. As in echocardiography, myocardial wall motion in cine sequences can be analyzed semiquantitatively and quantitatively based on standard segmental models.[67,96] Pharmacological stress can also be used in cardiac MRI but should be avoided in the early period after an infarction.[97,98] The percentage of nondiagnostic scans is significantly lower in stress MRI than in stress echocardiography, however.[99] In routine clinical follow-ups as well as investigational studies, cardiac MRI is excellent for regional and volumetric quantitative measurements and interpretation. The quantification of perfusion, wall-motion analysis, and contrast-enhanced MRI is an effective combination that can discriminate among hibernating, stunned, and infarcted myocardium.

In summary, cardiac MRI can demonstrate the progression of myocardial injury with or without IV contrast administration, depending on the type of sequence used (**Fig. 8.21**).

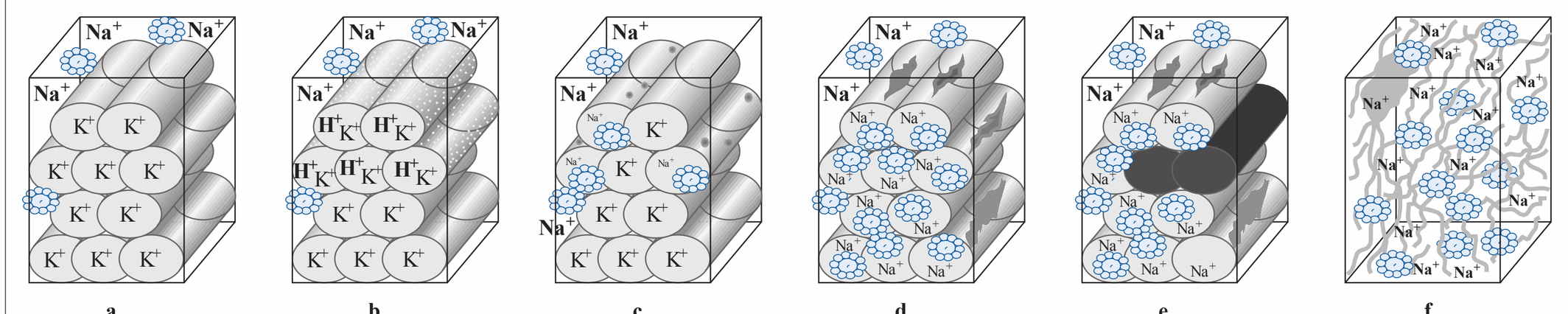

Fig. 8.21 a–f Progressive stages of cellular damage and their effect on contrast-enhanced MR imaging (modified from Mahrholdt et al., 2002[86]).

a Normal cells.

b Membranous capillary leak with water influx into the cell.

c More severe membrane damage with increased influx of water, sodium, and contrast medium.

e Same as **d** plus microvascular obstruction.

f Myocardial fibrosis, scar.

Chronic Coronary Artery Disease

P. Hunold and F. Breuckmann

Chronic coronary artery disease (CAD) is a collective term that includes **chronic myocardial ischemia** and the **late sequelae of myocardial infarction**. Chronic ischemia is characterized by recurrent pain symptoms and may or may not be associated with impairment of left ventricular (LV) function at rest. Thus, additional clinical manifestations of heart failure may be present, depending on LV function.

Essential Point

The goal of noninvasive testing in patients with suspected chronic ischemia is to confirm or exclude CAD so that patients with coronary stenosis can be referred for interventional therapy while patients with normal coronary arteries can be spared diagnostic cardiac catheterization.

Hibernating myocardium is a special form of chronic ischemia in which regional LV function is impaired owing to a persistent reduction of myocardial blood flow. This condition is reversible following reperfusion.[101]

Moreover, the investigation of myocardial scars and their associated sequelae and complications is becoming an increasingly important part of noninvasive cardiac testing. The main goal is to direct the planning of further management, such as revascularization or aneurysmectomy.

Pathophysiology of Chronic Coronary Artery Disease

Chronic Ischemia and Hibernation

Coronary artery disease refers to the manifestations of atherosclerosis in the coronary arteries. The pathophysiology of CAD is marked by a complex interaction of various pathogenic factors and the coexistence of various disease stages[100] (see p. 171).

Stenosis that reduces blood flow in the coronary arteries leads to the development of **myocardial ischemia**, which is characterized by an imbalance between oxygen supply and consumption. The earliest change is a discrepancy of blood flow between the subendocardial and subepicardial portions of the myocardium. Intermediate-term changes are manifested by metabolic dysfunction, impaired diastolic relaxation, and regional dyssynergies of wall motion. Late changes may include segmental systolic wall-motion abnormalities, typical ECG changes, and possible anginal symptoms—although 70% of all ischemic episodes are asymptomatic. This typical progression of ischemia-induced changes is called the ischemic cascade.

A separate pathophysiological entity is **hibernating myocardium**. This typically develops in response to chronic high-grade coronary stenoses or a coronary occlusion with good collateral circulation. It involves a prolonged depression of regional LV function due to hypoperfusion. Energy metabolism adapts to the diminished blood flow to maintain myocardial viability and myocardial function is down-regulated, resulting in a "perfusion–contraction match."[2] Myocardial contractility recovers gradually but completely following reperfusion. In the diagnosis of hibernating myocardium, it is important to note that an inotropic reserve can be recruited in the affected segments. This means that adrenergic stimulation with low doses of dobutamine, for example, will temporarily normalize myocardial contraction. This recruitment has a high metabolic cost, however, and a further reduction in coronary blood flow or prolonged stimulation may precipitate an infarction.

Essential Point

The progression of changes in chronic ischemia is called the ischemic cascade. The symptoms and manifestations depend on the extent of the perfusion deficit. A special form of chronic ischemia is the hibernating myocardium—a reversible depression of regional myocardial function due to a persistent reduction in blood flow.

Scar and Chronic Infarction

A scar is defined biologically as a loss of cellular integrity with impairment of metabolism, function, and external structure. From a clinical cardiological standpoint, the most important property of an intact cardiomyocyte is its ability to contract. **Viable cardiomyocytes** contribute to cardiac impulse conduction and systolic wall thickening, thus helping to maintain the pumping function of the heart. This suggests the clinical definition that viable myocardium, unlike fibrotic scar tissue, is able to contract, provided it is supplied with oxygen and nutrients by adequate myocardial blood flow.

When a scar develops after myocardial infarction, left ventricular remodeling is initiated as a compensatory mechanism. Remodeling can be defined as a change in the size and shape of the left ventricle aimed at maintaining global LV performance despite impairment of regional function (**Fig. 8.22**). But hypertrophy of the noninfarcted segments provides only temporary functional improvement, and progressive remodeling is associated with a deterioration of myocardial function and a worsening prognosis.

The challenge of viability assessment is the characterization of dysfunctional but viable segments within the myocardium. Ischemic or hibernating myocardium, which can undergo functional recovery after the restoration of adequate coronary perfusion (viable by definition), requires differentiation from myocardial infarction, in which necrosis due to prolonged coronary occlusion is eventually transformed into fibrotic tissue (postinfarction scar) consisting mainly of collagen fibers. This tissue has permanently lost its ability to contract and therefore is **nonviable** on the basis of the clinical definition above.

Clinical Features

Chronic ischemia in the setting of CAD usually presents clinically as **stable angina pectoris**. This is defined as reproducible chest discomfort that occurs in response to physical and emotional stress (**Table 8.3**). While angina pectoris may be considered a cardinal symptom of chronic coronary ischemia, the discomfort may be perceived in various ways and with varying degrees of severity in different groups of patient. Notable examples are atypical angina pectoris and silent myocardial ischemia, which commonly affect young and elderly patients as well as women and diabetics. The clinical manifestations of CAD are difficult to interpret in these cases..

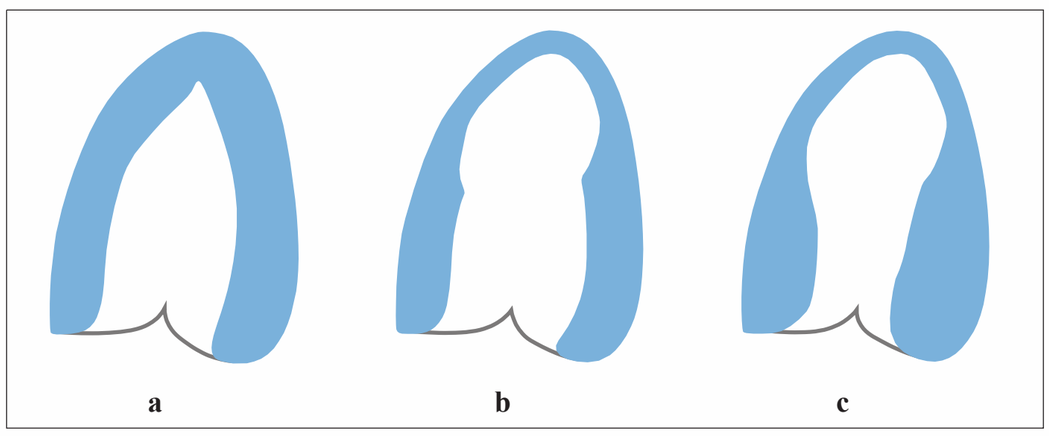

Fig. 8.22 a–c Postinfarction remodeling. Each diagram shows the end-systolic phase of the LV in the four-chamber view.
a Normal ventricle with a uniform increase in wall thickness.
b Apical myocardial infarction. Absence of wall thickening (akinesia) occurs in the apical portions of the septal and lateral wall (AHA segments 14 and 16) and in the apex (segment 17). There is concomitant impairment of global LV function due to the increased LV end-systolic volume.
c Chronic infarction. Remodeling restores global LV function by compensatory hypertrophy of still-viable basal and midventricular myocardial segments.

Diagnosis of Chronic Coronary Artery Disease

Chronic Ischemia

High-Dose Stress Tests

High-dose stress in MRI and echocardiography is a pharmacological stress induced with high doses of an adrenergic agent. **Dobutamine** is the most widely used stressor in routine clinical tests. Dobutamine is a synthetic catecholamine with strong β-adrenergic activity and relatively weak α-adrenergic activity. It exerts a positive inotropic and chronotropic action when administered in low doses (5–10 µg/min/kg bw by continuous infusion).

In response to dobutamine stimulation, the systolic wall thickness in healthy, normally perfused myocardium increases and there is concomitant improvement in both regional and global function.[102] In ischemic myocardium, low doses also induce an improvement in systolic function—a phenomenon called **recruitment of ischemic myocardium**. But if the dobutamine dose is increased to a high level (20–40 µg/min/kg bw by continuous infusion), causing a further increase in myocardial oxygen consumption, the resulting imbalance between oxygen supply and demand induces regional wall-motion abnormalities that confirm ischemia. This type of response—functional improvement at a low dobutamine dose and abnormal wall motion at a high dose—is called a biphasic response and is typical of ischemic but viable myocardium.

In practical stress testing, the dobutamine dose is increased at 3-minute intervals from 5 to 10, 20, 30, and 40 µg/min/kg bw. At each dose level, images are acquired in long- and short-axis sections while the blood pressure is monitored and recorded. If the target heart rate [= (220 – age in years) × 0.85] is not reached with dobutamine stimulation alone, 3 minutes later atropine is added to the maximum dobutamine dose to induce maximal myocardial stress.

Table 8.3 Definition of stable angina pectoris

Location	Retrosternal, radiating (left > right) to jaw, neck, upper abdomen, or back. Some cases have pain elsewhere radiating to the chest. Occasionally chest pain is absent
Precipitating mechanism	Increased cardiac load, rise in blood pressure, tachycardia, physical or emotional stress, cold, overeating, etc.
Sensation	Tightness, pressure, sometimes with burning. May present only as shortness of breath
Duration	Several minutes after precipitating event, no longer than 20 minutes
Additional symptoms	Frequent dyspnea, occasional weakness or fatigue. Improvement in response to nitroglycerine is typical but not specific

Termination criteria for dobutamine stress testing are as follows:

- Reaching the target heart rate [(220 – age in years) × 0.85]
- New occurrence of wall-motion abnormality in more than one myocardial segment (evidence of ischemia=outcome measure)
- Fall in blood pressure (>20 mm Hg from initial reading)
- Severe arterial hypertension (>240/120 mm Hg)
- Severe arrhythmia
- Intolerable side effects such as headache, nausea, or tremor

Intravenous β-blockers (esmolol, metoprolol) are available as antidotes for the very short-acting dobutamine.

Contraindications to dobutamine stress are acute coronary syndrome, ventricular arrhythmias, hypertrophic obstructive cardiomyopathy, severe arterial hypertension, and severe aortic stenosis.

The main technical and logistical requirements for successful dobutamine stress echocardiography or MRI are as follows:

- Continuous ECG monitoring
- Blood pressure monitoring
- Pulse oximetry
- Contact with the patient (microphone, monitor)
- A patient alarm system in the MR scanner
- Emergency equipment and personnel trained in cardiopulmonary resuscitation

Essential Point

Pharmacological stress testing with incremental dobutamine doses is the standard protocol for diagnosing myocardial ischemia. Particular attention is given to logistical requirements such as emergency equipment. Contraindications and termination criteria should be rigorously observed.

Echocardiography

The documentation of regional left ventricular dyssynergy by resting echocardiography is an early, sensitive, and specific marker of ischemia. Consistent with the ischemic cascade model, the initial change after onset of a perfusion abnormality is an ischemia-induced impairment of myocardial relaxation and contraction. The early phase in particular is marked by impaired diastolic function, whose signs include a change in the mitral inflow signal or a reversal or pseudoreversal of the E/A ratio. A regional wall-motion abnormality may be detectable in chronic ischemia.

Stress Echocardiography

Stress echocardiography is used in patients with an unknown coronary status for the detection of CAD and for risk stratification. When coronary status is known, it is used for the localization of ischemia and the evaluation of its extent. In a staged work-up, stress echocardiography can provide additional information on the functional efficacy of coronary revascularization. It has a sensitivity of 75–85 %and specificity of 80–100 % in patients who are good anatomical candidates for echocardiography.[103,104] The extent of wall-motion abnormalities correlates better with functional flow reserve than with the actual degree of stenosis.

The test employs standard imaging planes and a 17-segment wall model, and the results are analyzed at rest, during low-level stress (see Viability Assessment p. 195), during maximal stress, in the early poststress period, and in the recovery period following mechanical or pharmacological stress. The individual myocardial segments are classified as follows according to their contractile function:

- Normokinetic
- Hypokinetic
- Akinetic
- Dyskinetic

The systolic inward motion and thickening of the myocardium are both evaluated (**Table 8.4**).

Essential Point

The quad-screen format gives a simultaneous display of individual wall segments, permitting their direct comparison at various stress levels.

The American Society of Echocardiography has described a semiquantitative index that can be determined to supplement the standard protocol. Called the wall motion score index (WMSI), it is defined as the ratio of the sum of individual segment scores (normokinesia=1, dyskinesia=4) to the number of segments scored. When this index is determined in stress echocardiography, it provides objective information on the location, extent, severity, and ischemic threshold in a setting of chronic myocardial ischemia.

Essential Point

The WMSI is the only standardized assessment in stress echocardiography that supplies reproducible results and valid information on the severity and extent of myocardial ischemia.

Stress echocardiography for detecting ischemia-induced functional abnormalities in CAD is particularly attractive in cases where ergometry cannot be used (bundle branch block, physi-

Table 8.4 Stress-associated changes in various forms of chronic ischemia

Normal myocardium	Stress-induced increase in systolic endocardial inward motion with concomitant wall thickening
Ischemic myocardium	Initial improvement in response to low-dose stress (recruitment), followed by a significant reduction of contractility by at least one category in at least one segment
Stunned myocardium	Stress-induced functional improvement in an initially abnormal area in response to low-dose and high-dose stress (monophasic response)
Hibernating myocardium	Stress-induced functional improvement in an initially abnormal area, with possible deterioration on maximal stress (biphasic response). Contraction improves with low-dose stress, decreases with high-dose stress.
Nonviable myocardium, scar	Akinesia independent of stress

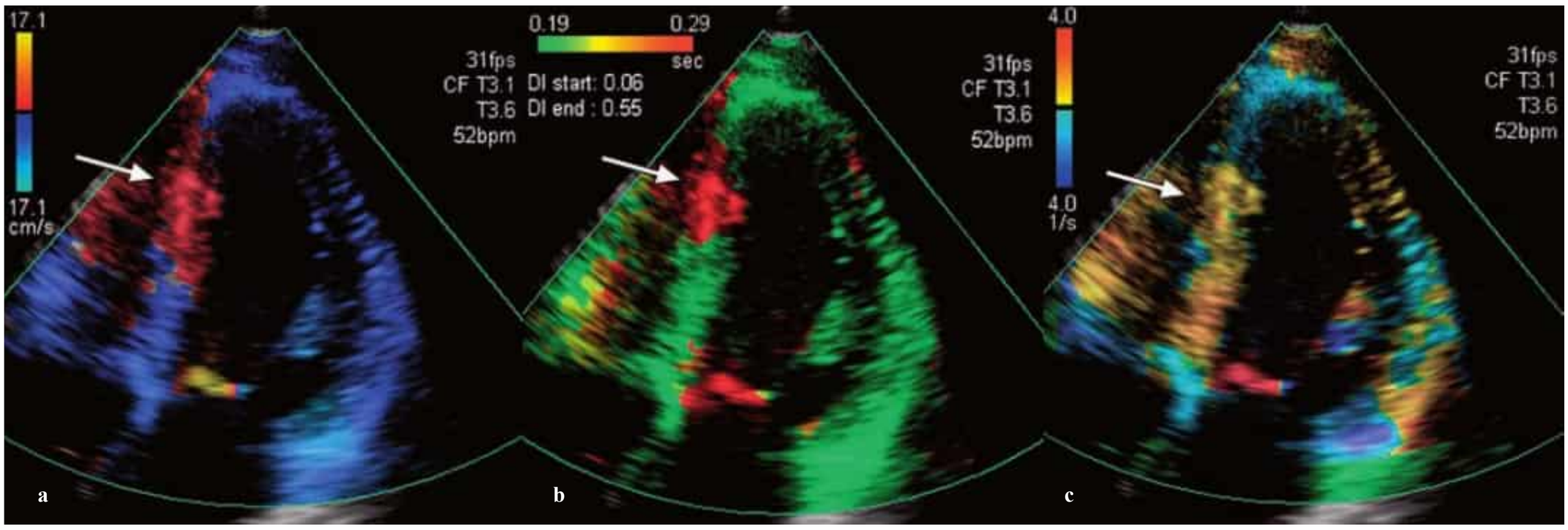

Fig. 8.23 a–c Parametric techniques for imaging myocardial function.
a Tissue Doppler: Functional analysis based on the measurement of myocardial velocity shows an apicoseptal wall-motion abnormality (arrow) in this patient with two-vessel coronary disease and a previous anterior wall infarction.
b Time to peak velocity: Parametric imaging of the time course of myocardial contraction additionally reveals apicoseptal asynchrony (arrow).
c Strain rate imaging shows heterogeneous deformation indicating extensive functional abnormalities throughout the ventricle (arrow).

cal disability, etc.). It can establish the presence of significant ischemia and, if necessary, select patients who require additional invasive testing. Tissue Doppler imaging or tissue Doppler echocardiography (TDI, TDE) can sensitively detect systolic and diastolic changes due to chronic ischemia in CAD and holds great promise for the future, especially when combined with stress echocardiographic techniques. It enables the detection of ischemia-induced diastolic parameters such as motion abnormalities in isovolumetric relaxation or changes in the E/A ratio.

Acoustic Quantification and Color Kinesis

In the past, purely visual or semiquantitative methods have been used in the functional analysis of left ventricular contraction. New techniques allow for a quantitative computer-based analysis. Acoustic quantification involves the automated analysis of myocardial motion in 2D or 3D datasets based on integrated backscatter data analysis to discriminate between the myocardium and the ventricular cavity.[105] The software can automatically detect the endocardial and myocardial borders and superimpose them in the cine image. End-systolic and end-diastolic areas, ventricular volume (Simpson or area–length method), and ejection fraction can be determined in a freely definable region of interest.

Color kinesis adds to the global parameters of acoustic quantification the capability of local color-encoded motion analysis. A single frame acquired at end systole or end diastole can display the same information on endocardial motion as contained in a continuous loop, and this information can be analyzed on the basis of the regional color distribution pattern.

Both methods can be used for rapid documentation in CHD patients and for monitoring global function and volumes in patients with advanced chronic ischemia, although the detection of early ischemic processes has not yet been verified. The advantage of acoustic quantification and color kinesis is that it can provide complete motion information in a single-frame image.

Essential Point
The computer-based analysis in acoustic quantification and color kinesis can more accurately demonstrate wall-motion abnormalities by means of border detection and color encoding. These methods are particularly useful for rapid documentation, ICU monitoring, etc.

Tissue Doppler and Strain Rate Imaging

Tissue Doppler imaging or tissue Doppler echocardiography permits a quantitative analysis of myocardial function based on the measurement of myocardial velocity (**Fig. 8.23a**). In principle, both color Doppler and spectral Doppler information can be used for this purpose, although lower absolute values are obtained with color Doppler datasets. The advantage of color Doppler is its ability to evaluate large image areas. Systolic and diastolic cardiac motion are analyzed with off-line software following data acquisition.

Strain rate imaging is a technique in which the rate of length change in velocity datasets from color tissue Doppler is analyzed on the basis of a spatially normalized velocity gradient (**Fig. 8.23b, c**). Unlike the conventional processing of specific types of subendocardial and subepicardial image information, strain rate imaging gives continuous coverage of a whole color sector. This provides an approach to the direct, comprehensive echocardiographic assessment of myocardial deformation for the objective and quantitative diagnosis of ischemia in patients with coronary heart disease.[106] When the new techniques are applied in chronic CAD, it is possible to detect signs of early ischemia before there is any visual abnormality of contractile function. Strain rate imaging and its diagnostic and therapeutic implications are currently the subject of intensive research.

Essential Point
A very early parameter is the "postsystolic thickening" of ischemic but viable myocardium. This is a significant advance over conventional echocardiographic data.

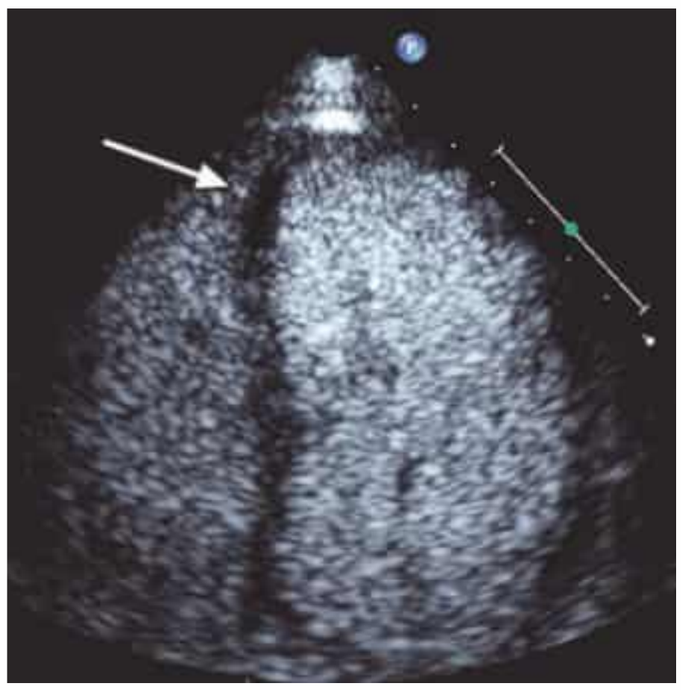

Fig. 8.24 Real-time perfusion contrast echocardiography. Absent or delayed myocardial enhancement after contrast administration signifies a perfusion deficit. This image shows a localized perfusion deficit (arrow) in the apical septal region of a patient with a prior distal LAD occlusion due to single-vessel coronary disease.

Myocardial Contrast Echocardiography

Myocardial contrast echocardiography (MCE) for the analysis of myocardial perfusion is still in the investigational stage. Based on the use of specific transpulmonary echo contrast agents, it uses techniques such as harmonic imaging, power imaging, pulse-inversion imaging, and Doppler imaging to detect abnormalities of myocardial perfusion with high sensitivity and specificity.[107] An irregular increase of echogenicity with decreased segmental enhancement on first-pass imaging is indicative of coronary stenosis (**Fig. 8.24**). Computer-based analysis of enhancement kinetics is used, making it possible to compare the perfusion in different segments. With MCE technology, we are now able to detect perfusion deficits as well as contraction abnormalities.

Essential Point

New quantitative techniques such as acoustic quantification and color kinesis provide better visualization of functional abnormalities in ischemic areas based on the computer analysis of datasets. Color Doppler techniques, strain rate imaging, and myocardial contrast echocardiography also allow for dedicated myocardial function analysis and the detection of perfusion deficits.

Magnetic Resonance Imaging

As in echocardiography, various techniques are available in MRI for the detection of chronic ischemia in CAD. Some resemble echocardiographic techniques because they are based on the same pathophysiological principles. One basic advantage of MRI over echocardiography lies in its consistently high image quality.

Functional Examination at Rest

Every MRI examination in patients with suspected ischemia and CAD should include the determination of global LV function by volumetry, the determination of end-diastolic and end-systolic volumes, and calculation of the ejection fraction (EF). The detection of LV dilatation or a decreased EF in this setting may indicate the presence of ischemia. Because regional functional abnormalities (hypokinesia or akinesia) at rest are at the very end of the ischemic cascade, they are rarely demonstrated (**Fig. 8.25**). Pharmacological stress imaging is frequently necessary for the clinical detection of ischemia.

Dobutamine Stress MRI (High-Dose)

The technical basis for dobutamine stress imaging is cine MRI (see Chapter 6, Function, p. 105) using segmented SSFP sequences. Systolic function is evaluated at rest and in response to dobutamine stimulation. The temporal resolution (acquisition time per image) should be at least 50 ms at rest so that the brief period of end systole can be reliably assessed, and it should be further reduced during the course of the test as the patient's heart rate rises.

Essential Point

Fifteen segments/lines per segment are typically used at rest (k-space lines per image and R–R interval). With a TR of 3 ms, the temporal resolution would be 15 × 3 ms = 45 ms. At each stress level, the number of segments is reduced by 2. This results in a temporal resolution of 7 × 3 ms = 21 ms during maximal stress, permitting an excellent assessment of wall-motion abnormalities.

The left ventricle should be imaged in at least three long-axis slices (horizontal and vertical long axis, three-chamber view) and in one short-axis slice each in the basal, midventricular, and apical thirds. The images are acquired at rest and at each level of pharmacological stress. Wall motion is analyzed by displaying the various stress levels simultaneously on the monitor in a split-screen or quad-screen format (**Fig. 8.26**). Again, regional function is documented by segments using the standard left ventricular segment model of the American Heart Association (AHA).[108]

Many clinical studies and long-term observations have documented the accuracy and reliability of stress MRI. This modality has proved more reliable than stress echocardiography in the detection of significant CAD with 50% or greater coronary stenosis, providing better than 86% sensitivity and specificity.[109] It has also been shown that the documentation of stress-induced ischemia with stress MRI can supply important prognostic information in patients with confirmed or suspected CAD.[110] Despite the better image quality, it should be noted that higher costs and limited equipment availability are potential disadvantages of MRI compared with echocardiography.

The advantages of stress MRI have caused it to become the current reference standard for detection of myocardial ischemia. Owing to its higher costs, however, it is frequently used as a second-line study in cases where stress echocardiography is unrewarding or cannot be performed.

Essential Point

Dobutamine stress MRI for the detection of myocardial ischemia is a practical and robust test that provides greater diagnostic accuracy than stress echocardiography.

Perfusion MRI

The first step in the ischemic cascade of CAD is a decrease in myocardial perfusion. Thus, a noninvasive method for detecting these early perfusion deficits would be extremely useful in the early detection of stenotic CHD. MRI with intravenous con-

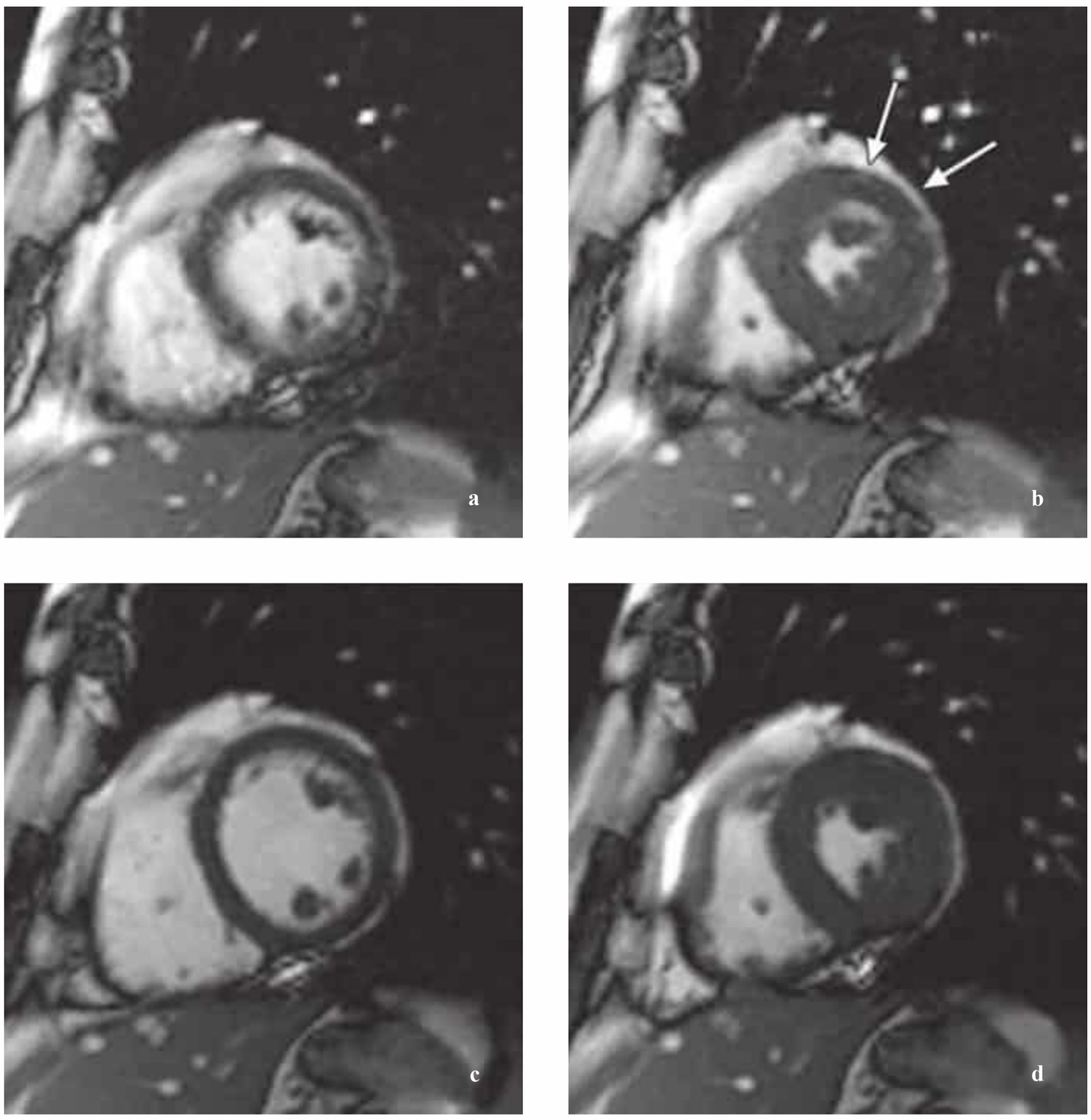

Fig. 8.25 a–d Chronic ischemia due to high-grade LCX stenosis with a resting wall-motion abnormality. Findings before and after revascularization. Short-axis slice through the middle third of the LV acquired with a segmented SSFP cine sequence. End-diastolic (**a**) and end-systolic (**b**) images show severe hypokinesia at the junction of the anterior and anteroseptal segments (arrows) due to chronic ischemia. Images acquired in the same plane after successful revascularization by LCX stenting show a normalization of regional and global LV function (**c, d**).

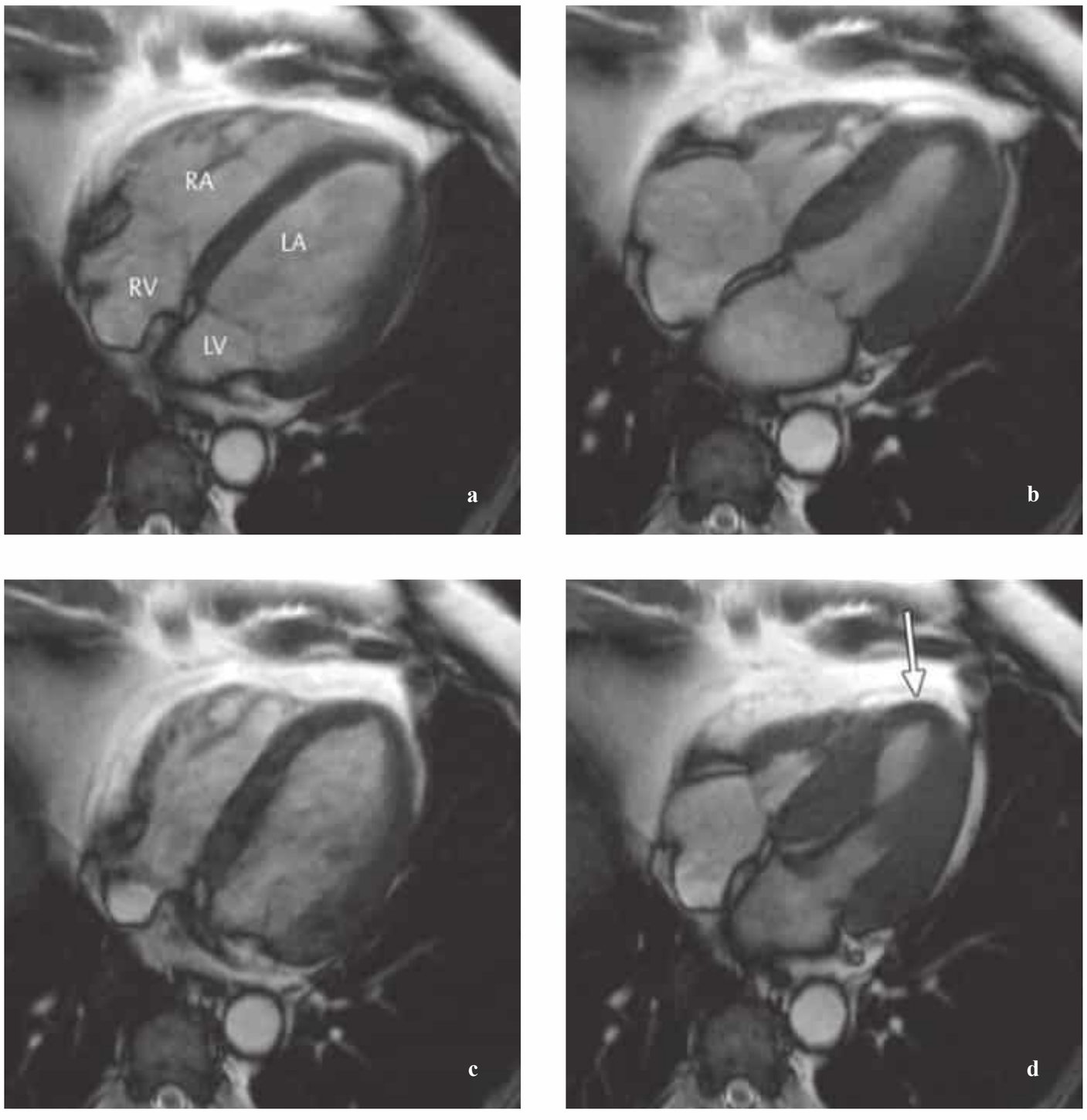

Fig. 8.26 a–d Stress MRI in a patient with chronic ischemia due to high-grade LAD stenosis. Horizontal long-axis images of the LV acquired with a segmented SSFP cine sequence. Rest images at end diastole (**a**) and end systole (**b**) demonstrate normal regional and global wall motion. With high-dose dobutamine stress (40 µg/min/kg bw), akinesia develops in the apical third of the septum and ventricular apex (arrow, AHA segments 14 and 17). The appearance of stress-induced WMA in two segments confirms the diagnosis of ischemia, caused in this case by a high-grade LAD stenosis.

trast material administration meets the criteria for such a method (**Fig. 8.27**).

Perfusion studies are performed with pharmacological stress induced by adenosine or dipyridamole, since the great majority of perfusion abnormalities in viable myocardium are detectable only under stress. Technical specifications and practical aspects are reviewed in Chapter 6, Myocardial Perfusion, p. 111.

Perfusion imaging places rigorous demands on the MRI scanner as far as image contrast and acquisition time are concerned. Despite various technical problems, which exist even with high-end scanners, there have been some very promising technical innovations in recent years that could lead to a clinical breakthrough with perfusion MRI.[111]

Various studies have been performed since the early 1990s using a great variety of sequences and contrast protocols. A very heterogeneous body of data collected from more than 500 patients was reviewed in a meta-analysis in 1999. When the data were analyzed, myocardial perfusion MRI was found to have a sensitivity and specificity of 82±9% and 88±10%, respectively, in the detection of coronary stenosis and myocardial ischemia.[112] In a recently published study, perfusion MRI combined with late-enhancement imaging was found to have a sensitivity and specificity of almost 90% compared with coronary angiography in the detection of significant (>70%) coronary artery stenosis.[113]

Despite these positive results in various studies, only a qualified recommendation can be made for the routine clinical use of adenosine stress perfusion MRI. Frequent problems arise owing to susceptibility artifacts, which can mimic defects, and in patients with three-vessel CAD presenting a homogeneous perfusion deficit affecting the entire myocardium. Another problem is a lack of guidelines with regard to optimum sequences, contrast dose, scanning protocols, post-processing, and the interpretation of findings. Because of these limitations, a direct comparison shows that perfusion MRI with adenosine stress is inferior to dobutamine stress MRI.[114]

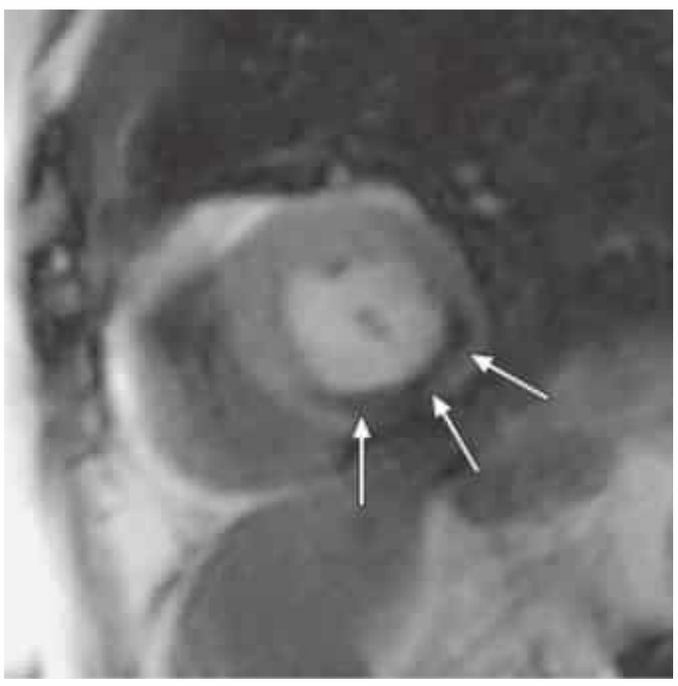

Fig. 8.27 Detection of ischemia by perfusion MRI with adenosine stress. Apical short-axis slice of the LV acquired with a saturation-recovery SSFP sequence (one image per heart beat in each of four short-axis planes) clearly demonstrates a hypointense stripe in the subendocardial layers of the inferior wall (arrows, AHA segment 15) with septal and lateral extension. The cause is a high-grade stenosis of the RCA.

Nuclear Medicine Imaging

Various nuclear medicine imaging techniques are available for the investigation of myocardial ischemia in CHD. The majority are myocardial perfusion studies using:

- Scintigraphy
- Single-photon emission computed tomography (SPECT)
- Positron emission tomography (PET) with various radiotracers

Based on years of experience published in numerous studies, these techniques are currently considered the reference standard for the noninvasive diagnosis of ischemia. Technical specifications and techniques are reviewed in Chapter 4.

The disadvantages of nuclear medicine imaging compared with other modalities are its relatively poor spatial resolution, high cost, and variable degree of exposure to ionizing radiation.

Coronary Angiography

Catheter-based X-ray coronary angiography is still considered the **reference standard** for the diagnostic imaging of CHD. Barring contraindications, invasive angiography is indicated in patients with a diagnosis and/or typical presentation of myocardial ischemia. Coronary angiography is markedly superior to all noninvasive modalities in its spatial and temporal resolution. It provides an opportunity for percutaneous coronary interventions such as PTCA and stenting, and it establishes access for high-resolution intravascular/intracoronary ultrasound (IVUS/ICUS) based on selective intubation and visualization of the coronary arteries. IVUS is a valuable adjunct in patients with equivocal coronary angiographic findings, left main stem disease, and complex lesions. IVUS is also an important aid in planning interventional procedures and managing possible complications.

It should be added that myocardial ischemia in itself, which is expressed by decreased myocardial perfusion, cannot be detected or measured by coronary angiography. When an "intermediate" coronary stenosis is encountered, therefore, it may be necessary to apply one of the above noninvasive techniques for detection of ischemia to assess the functional significance of the stenosis. In the angio suite, lesions associated with intermediate stenosis can additionally be evaluated by intracoronary pressure measurement. A fractional flow reserve (FFR) <0.75 is an indication for intervention.

Computed Tomography

Contrast-enhanced multislice CT of the coronary arteries with retrospective ECG gating emerges as a useful noninvasive clinical tool in detecting coronary artery stenoses. Using the latest generation scanners with 64 or more detector rows, CT coronary angiography will be able to replace X-ray coronary angiography for diagnostic purposes (see p. 111 ff).

Hibernating Myocardium

Low-Dose Stress Testing

In MRI as in echocardiography, pharmacological stress is induced with a low-dose adrenergic agent (low-dose dobutamine stress, 5 and 10 µg/min/kg bw) for the detection of hibernating myocardium. The systolic wall thickness of healthy, normally perfused myocardium increases in response to dobutamine stimulation, and both regional and global function improve.[102] If the myocardium is viable but ischemic, as in hibernating myocardium, low-dose dobutamine will also elicit an improvement in systolic function. Scar tissue, on the other hand, will not show functional improvement even with dobutamine stimulation. Thus, the detection of improved systolic wall thickening in response to adrenergic stimulation is proof of myocardial viability.[115,116]

The equipment and personnel requirements for low-dose dobutamine stress testing are the same as for high-dose stress testing.

Echocardiography

Low-Dose Stress Echocardiography

As described below in greater detail, low-dose stress echocardiography can differentiate between viable but ischemic/hibernating myocardium and scar tissue. Hibernating myocardium typically shows a regional functional abnormality at rest that improves in response to dobutamine.

Magnetic Resonance Imaging

Resting Function and Stress MRI (Low-Dose)

The same principles apply to functional MRI at rest and with dobutamine stress as to echocardiography. Imaging at rest demonstrates a regional disturbance of LV contractile function. The regional function of hibernating myocardial segments improves in response to low-dose dobutamine stress, serving to distinguish it from scar tissue.

As in high-dose stress testing, MRI is advantageous over echocardiography in defining the endocardial boundaries.

Late Enhancement

During the late phase after contrast material administration, hibernating segments do not show late enhancement (delayed enhancement imaging, see Chapter 6, Delayed Enhancement, p. 116) because they consist not of scar tissue but of viable cardiomyocytes whose function is impaired.

On the whole, then, MRI is a useful method for identifying hibernating myocardium without having to rely on other imaging techniques (**Fig. 8.28**). The combination of resting function (regional wall-motion abnormality), low-dose stress (improvement of regional function), and contrast-enhanced delayed images (no late enhancement) can reliably distinguish chronically ischemic or hibernating myocardium from scar tissue.[117]

Essential Point
The detection of late enhancement in chronic ischemia proves a scar, which does not show functional improvement after revascularization.

On the other hand, some functionally abnormal areas that do not show late enhancement, suggesting that they are viable, still do not show functional improvement after revascularization. Several studies have shown that only about two-thirds of segments without late enhancement in severely impaired LV function show functional improvement after adequate revascularization. One-third show no improvement even months after the revascularization procedure. The cause of this phenomenon is not yet fully understood.

Essential Point
Some areas without late enhancement do not show functional improvement after revascularization.

One way to predict whether revascularization will improve a regional wall-motion abnormality without late enhancement is to add a low-dose stress test. If the wall thickens in response to

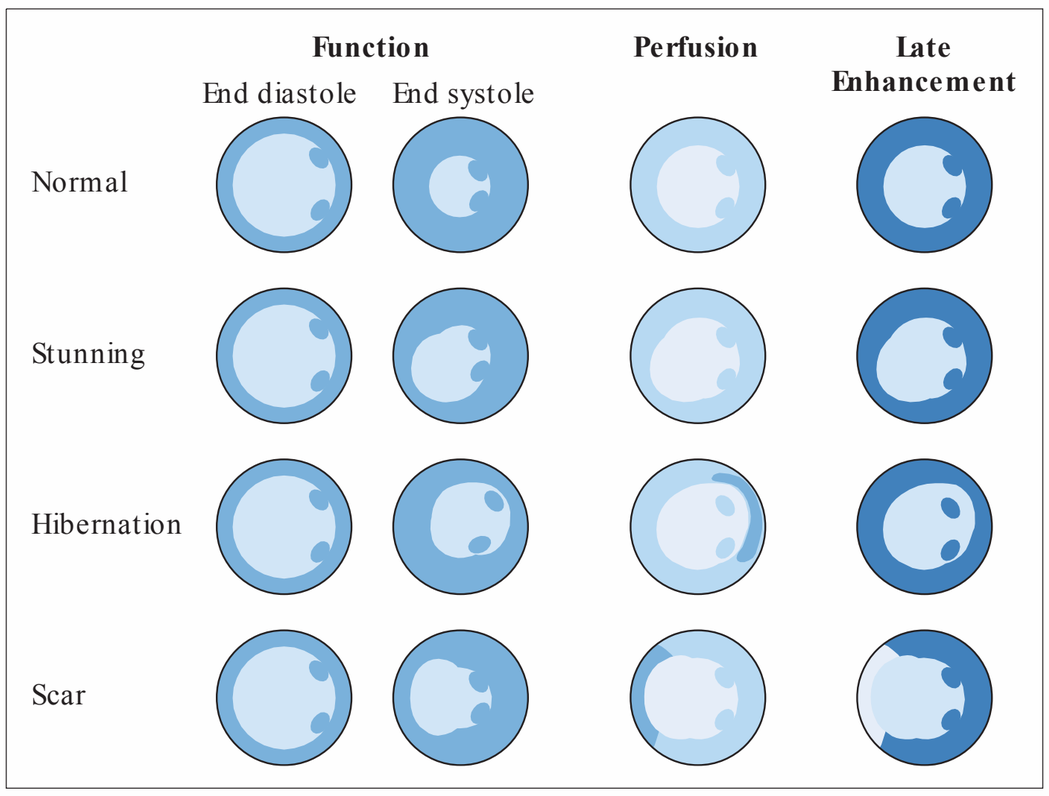

Fig. 8.28 Diagrammatic representation of myocardial behaviour seen in various diseases using various MRI techniques. The “Function” column shows SSFP cine images acquired at end diastole and end systole. “Perfusion” illustrates first-pass perfusion patterns. “Late enhancement" is shown in white. Each image represents a short-axis slice at midventricular level.
Normal myocardium: normal myocardium shows uniform, circumferential wall thickening at end systole and no regional wall-motion abnormalities. There is no perfusion defect, and ubiquitous high signal intensity is seen during contrast wash-in. Late enhancement does not occur.
Stunned myocardium: inferoseptal hypokinesia or akinesia (segment 9) with decreased end-systolic wall thickening and normal, homogeneous first-pass perfusion. The absence of late enhancement indicates viable myocardium.
Hibernating myocardium: anterior and anterolateral hypokinesia or akinesia (segments 7 and 11) with decreased end-systolic wall thickening. The anterolateral dysfunctional area shows a broad subendocardial perfusion defect with decreased signal intensity consistent with ischemia. The absence of late enhancement indicates viable myocardium (no scar).
Scar: anteroseptal and inferoseptal akinesia (segments 8 and 9) with an absence of end-systolic wall thickening. A transmural perfusion defect is visible in the akinetic septal area. Transmural late enhancement throughout the septum (white area) confirms a transmural scar.

stress, it definitely consists of viable, probably hibernating myocardium that should be responsive to revascularization.[116]

Nuclear Medicine Imaging

Hibernation can be diagnosed with various nuclear medicine techniques that selectively image myocardial perfusion: scintigraphy with thallium chloride Tl^{201} or technetium 99 m sestamibi, SPECT and PET imaging with nitrogen 13. Regional LV function should also be assessed using techniques such as echocardiography, MRI, or left ventricular angiography. If desired, the typical perfusion–metabolism mismatch can be demonstrated by fluorine 18 FDG-PET, which shows a paradoxical increase in FDG uptake caused by increased glycolytic activity due to a reduction in blood flow.

The technical specifications and practical aspects of various nuclear medicine imaging techniques are reviewed in Chapter 4.

Nuclear medicine imaging appears to be inferior to MRI, which provides a "one-stop shop" technique for the diagnosis of hibernating myocardium.[118]

Scar and Chronic Infarction

Low-Dose Stress Testing

While ischemic but viable myocardium shows improvement of regional and global function in response to low-dose dobutamine stimulation,[102] a chronic infarct or scar tissue does not show functional improvement on adrenergic stimulation. Thus, the lack of response of systolic wall thickening to low-dose dobutamine confirms the presence of nonviable myocardium, i.e., scar.[115,116]

Echocardiography

Echocardiographic evidence of chronic scarring includes circumscribed areas of hypokinesia, dyskinesia, and akinesia indicative of regional dyssynergy. Despite its ability to detect aneurysms left by an acute or chronic manifestation of coronary heart disease, routine echocardiography at rest provides little therapeutically useful information in patients with chronic infarction. Nevertheless, the test can provide important additional diagnostic and prognostic information, especially in patients with a history of myocardial infarction, heart failure, valvular disease, ventricular hypertrophy, or cardiomyopathy. Stress echocardiography is useful in viability assessment, as it can determine whether functionally abnormal areas consist of nonviable myocardium as opposed to stunned or hibernating myocardium (**Table 8.4**).

Color Kinesis, Tissue Doppler, and Strain Rate Imaging

Besides its use in the diagnosis of ischemia, color kinesis aids in the detection of nonviable tissue by providing better visualization of dyskinetic and/or akinetic areas (**Fig. 8.29**). Tissue Doppler and strain rate imaging are equally useful but are still largely experimental. Additionally, strain rate imaging under low-dose stress conditions can provide a more comprehensive echocardiographic assessment of myocardial deformation for an objective, quantitative viability assessment in patients with chronic CAD.

Essential Point
Tissue Doppler has a special role in evaluating the synchronicity of ventricular contractions in patients undergoing cardiac resynchronization therapy.

Magnetic Resonance Imaging

Two techniques are available for differentiating scar from viable myocardium with unenhanced MRI:

- Morphological evaluation of diastolic and systolic wall thickness at rest
- Systolic wall thickening in response to adrenergic stimulation (generally by pharmacological stress)

Wall Thickness Determination

The simplest method of viability assessment in MRI is to observe myocardial wall thickness and the systolic changes in wall thickness. A myocardial scar is thinner than viable myocardium during all phases of the cardiac cycle, but this discrepancy in wall thickness is most obvious in the end-systolic phase (**Fig. 8.30a, b**). By using end-diastolic wall thickness as a viability criterion in the chronic stage of myocardial infarction and taking 5.5 mm as the cutoff, we can identify viable myocardium with a sensitivity of 92 %and a specificity of 56 %[119] This simple method has not proved reliable, however, because of difficulties in accurately determining wall thickness in the submillimeter range with a spatial resolution greater than 1 mm.

Low-Dose Stress MRI

As stated above, a myocardial area that does not show improved wall thickening in response to low-dose dobutamine stress (5–10 µg/min/kg bw) consists of scar tissue rather than viable myocardium (**Fig. 8.31**).

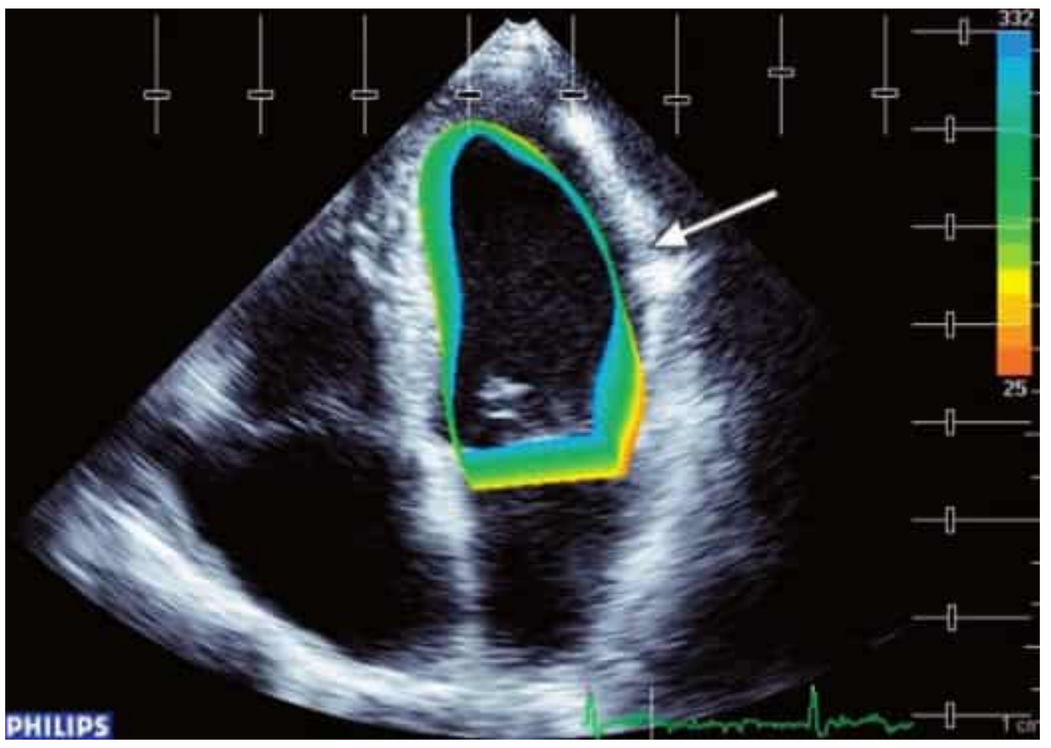

Fig. 8.29 Color kinesis. The color map encodes the inward motion of the endocardial border during contraction (Philips iE33 system). The pattern in this image indicates lateral-wall akinesia (arrow) in a patient with severe three-vessel coronary disease and a prior myocardial infarction in the LCX territory.

Essential Point
MRI techniques without contrast medium have proved to be simple but unreliable (wall thickness determination) or technically complex (low-dose stress MRI).

Late Enhancement

Another very useful technique is MRI with intravenous contrast administration (CE-MRI). Late-enhancement (delayed-enhancement, late-gadolinium-enhancement) imaging has become widely used in recent years owing to its simplicity and robustness. The principle of late enhancement is based on the fact that MRI contrast agents become concentrated in myocardial scars, and that scar tissue is distinguishable from viable, noninfarcted myocardium during the equilibrium phase several minutes after intravenous contrast injection.

Myocardial areas that have sustained irreversible damage appear very hyperintense in equilibrium-phase images and are sharply demarcated from normal myocardium by their delayed hyperenhancement. The location of an infarction can be accurately determined, and the infarcted area can be related to a specific coronary territory based on the AHA segment model.[108]

When used in the chronic stage after myocardial infarction, this technique supplies information on the extent of the definitive myocardial scar. Also, it can reliably distinguish between a transmural and subendocardial infarction, and even the transmural extent of the infarct can be quantified (**Fig. 8.32**). Today it is believed that the volume of late enhancement corresponds to the extent of histologically detectable fibrosis. Long-term follow-ups have shown that the area, transmural extent, and volume of late enhancement in chronic infarction remain constant over time. The simple rule that "bright is dead" appears to be justified in the chronic stage of a myocardial scar (**Fig. 8.33**).

Because the inner layers of the myocardium have higher wall tension and less perfusion than the outer layers, infarctions always begin in the subendocardial layer and spread toward the subepicardium. The extent of this spread depends on the duration and extent of the perfusion deficit during coronary artery occlusion. Several clinical studies have shown that the transmural extent of late enhancement on MRI affects the prognosis for functional recovery after revascularization: Segments that show late enhancement involving more than 50% of the myocardial wall thickness have virtually no chance of functional recovery after revascularization.[120] On the other hand, areas with subendocardial scars involving less than 50% of the wall thickness will improve after revascularization in the majority of cases. This distinction is of major clinical importance because patients who will not show functional improvement after revascularization have a higher perioperative risk and will derive greater benefit from pharmacological therapy.

Essential Point
Ischemic myocardial infarction always involves the subendocardial layer of the myocardial wall. The absence of subendocardial late enhancement indicates a nonischemic myocardial disease.[121]

The "bright is dead" rule applies to chronic myocardial scars; late enhancement means irreversible damage. An area with transmural or near-transmural late enhancement will not show functional improvement after revascularization and does not require further investigation.

If wall-motion abnormalities are associated with only small subendocardial late enhancement or an absence of late enhancement, adding a low-dose dobutamine stress test will improve the accuracy of predicting functional recovery after revascularization.[116]

Several groups have been working on the prognostic value of late enhancement in patients with CAD and chronic infarction. Beyond the prediction of functional recovery after revascularization, recent data suggest also a relation between the extent of late enhancement areas and survival. Infarct size seems to be a stronger predictor of long-term mortality than LV volumes and global function.[122] Even in patients with unrecognized chronic infarction, contrast-enhanced MRI provides incremental prognostic value to major cardiac events and cardiac mortality beyond functional LV parameters. In a 40-month follow-up period, Kwong et al. showed significantly higher survival and event-free survival in patients without late enhancement in MRI compared with those with late enhancement in a study collective with known or suspected CAD and no history of infarction.[123]

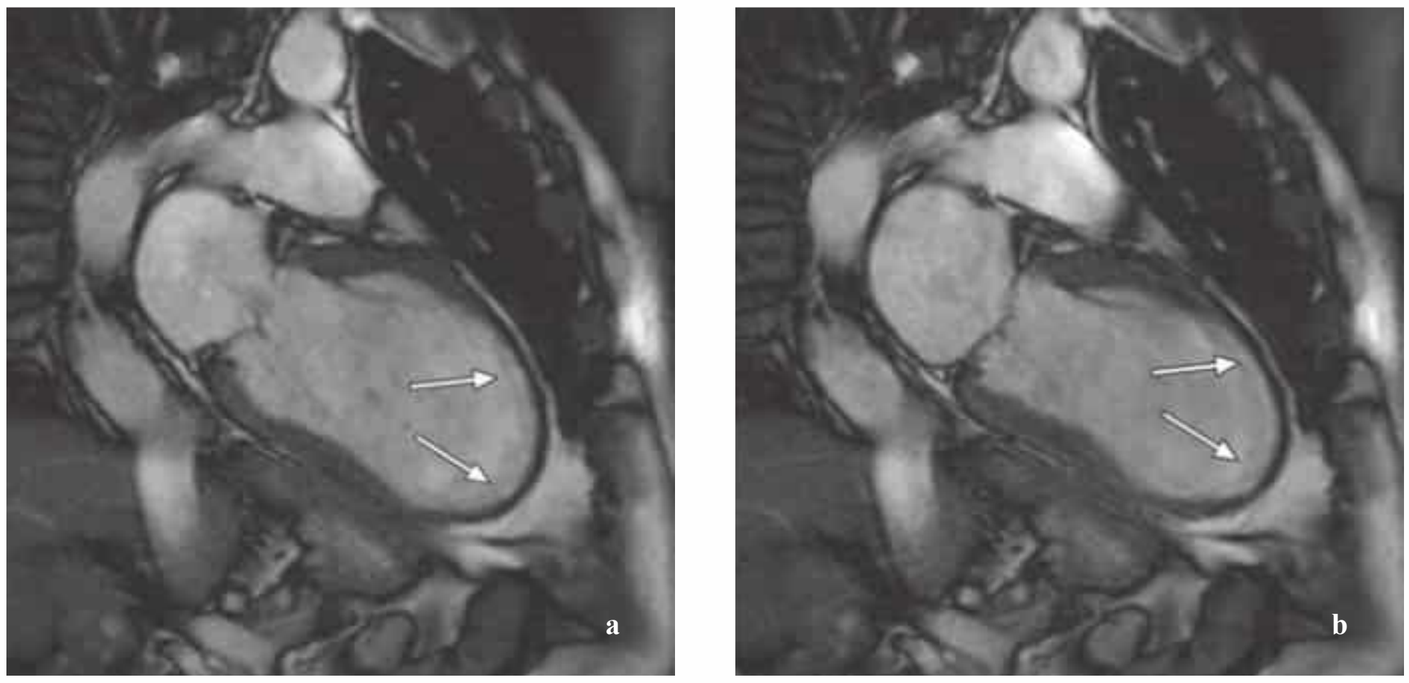

Fig. 8.30 a, b Transmural myocardial scar after an anterior-wall infarction involving the anterior, apical, and inferior apical segments. Resting MRI cine sequence in the two-chamber view at end diastole (**a**) and end systole (**b**) shows akinesia and constant wall thinning to 3 mm in segments 7, 13, 15, and 17 (arrows) with severe impairment of LV global function. Subsequent late-enhancement images (not shown) confirmed a transmural scar.

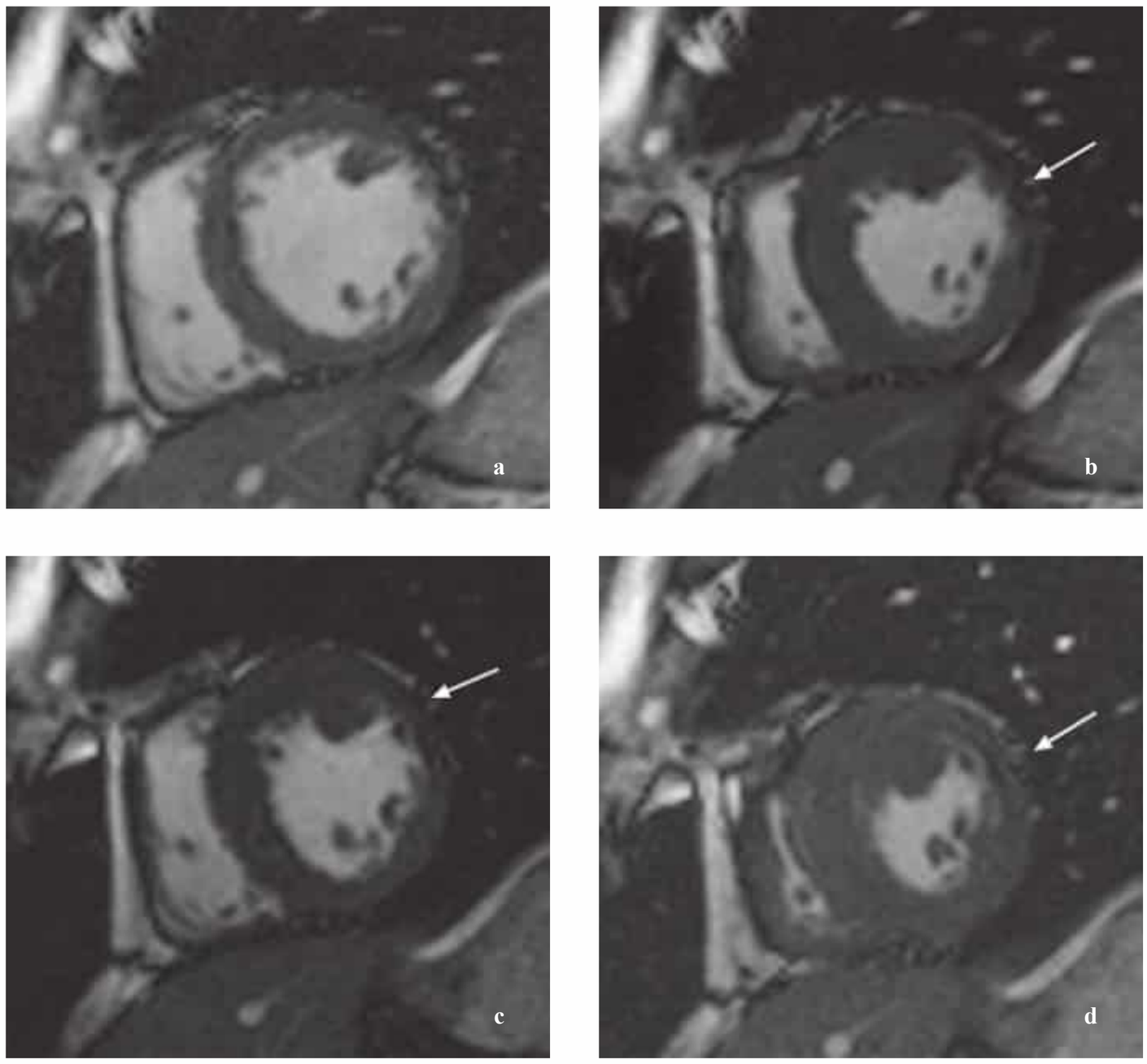

Fig. 8.31 a–d Low-dose dobutamine stress MRI of a transmural myocardial scar. End-diastolic (**a**) and end-systolic (**b**) images from a cine sequence at rest and with low-dose dobutamine stress (10 µg/min/kg bw) (**c, d**). The anterolateral segment (segment 12) shows akinesia and wall thinning at rest and during stress due to a transmural scar (arrows). The remaining, viable segments show normal wall thickening in response to stress.

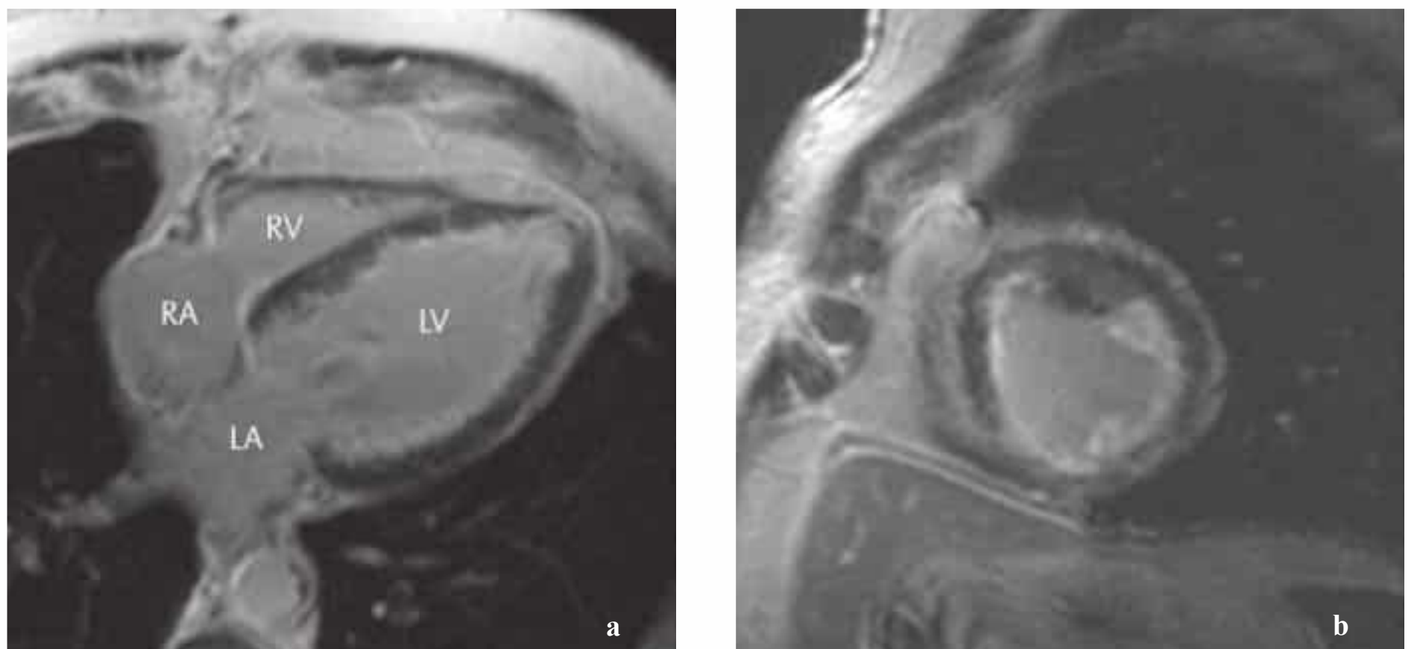

Fig. 8.32 a, b Large subendocardial myocardial scar. Inversion-recovery turbo-FLASH image shows nontransmural late enhancement that occupies the entire subendocardial layer in the four-chamber view (**a**). Apical short-axis slice (**b**) shows a large zone of subendocardial late enhancement in the septal, inferior, and lateral segments 14, 15, and 16 that spans ~ 25–50 % of the wall thickness.

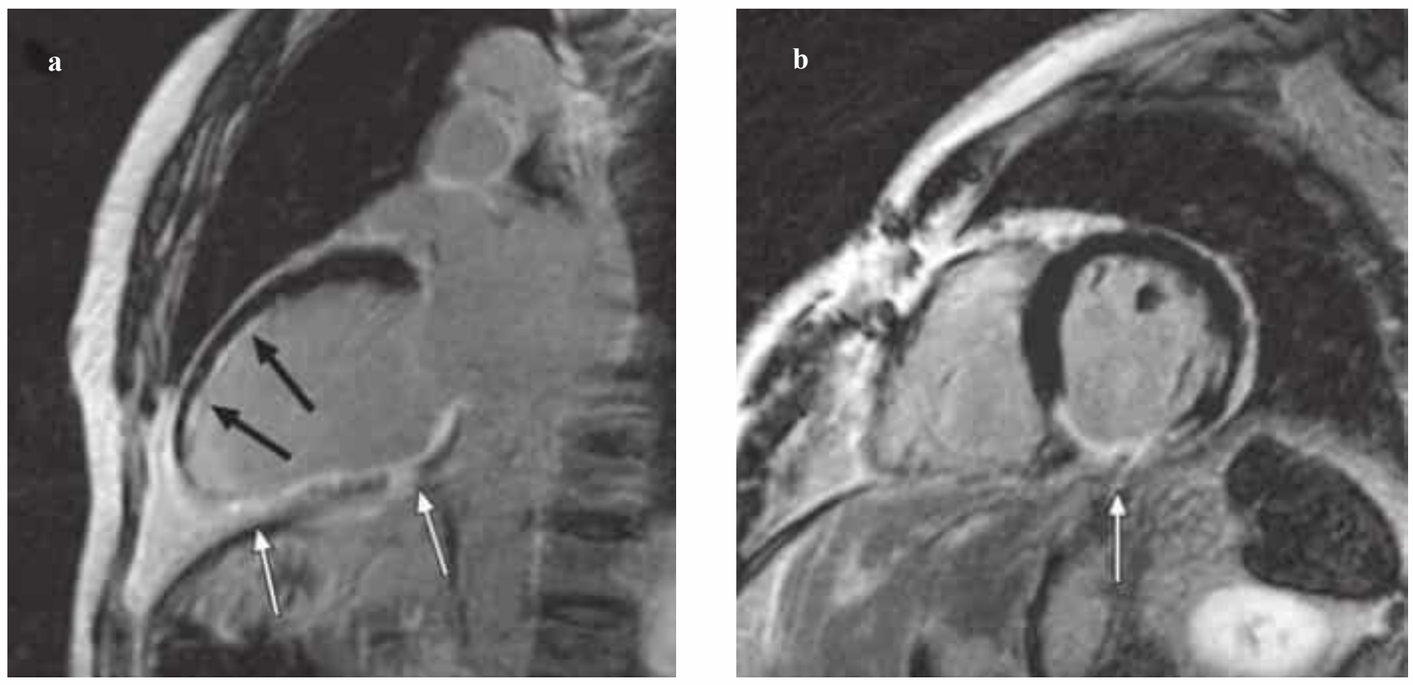

Fig. 8.33 a, b Subendocardial and transmural myocardial scar.

a Two-chamber view shows a narrow zone of subendocardial late enhancement in the midventricular and apical anterior wall (segments 7 and 13, black arrows), predominantly transmural late enhancement (white arrows) in the apical and mid inferior wall (segments 10 and 15), and nontransmural late enhancement in the basal inferior wall (segment 4).

b Transmural late enhancement in the basal inferior wall (segment 4, arrow).

Nuclear Medicine Imaging

Various nuclear medicine techniques are also available for the detection and quantification of myocardial scars. Basically these techniques consist of SPECT and PET imaging. The most reliable technique is PET using radiolabeled glucose as a tracer, i.e., fluorine 18 fluorodeoxyglucose (FDG). The technical specifications and practical aspects of the various techniques are reviewed in Chapter 4.

A significant disadvantage of nuclear medicine techniques compared with MRI is their poorer spatial resolution. As a result, it is not possible in many cases to discriminate between normal myocardium and thin subendocardial scars or to distinguish a broad nontransmural scar from a transmural scar. Several studies have confirmed the greater reliability of MRI, especially in the detection of subendocardial scars.[124–126] Studies comparing revascularization outcomes with preoperative PET and MRI findings have also documented the superiority of MRI (**Fig. 8.34**). This particularly applies to the prediction of functional recovery as proof of viability.[127] For these reasons, MRI will soon replace nuclear medicine imaging as the reference standard for myocardial viability assessment, and MRI will be implemented in official guidelines.[128]

Ventricular Aneurysm

The most severe impairment of myocardial motion is dyskinesia, in which the myocardium bulges outward during systole without undergoing systolic wall thickening. Dyskinesia combined with wall thinning at end diastole and end systole is the hallmark of a ventricular aneurysm in the scarred myocardial wall. Aneurysmal myocardium does not contribute to the pumping action of the heart. Moreover, blood flows from contracting portions of the ventricle into the aneurysm rather than being expelled into the aorta. This flow diversion imposes an additional load on the healthy surrounding myocardium.

Aneurysms may develop in the setting of an acute myocardial infarction owing to necrosis and rapid functional deterioration of the affected myocardium. It is more common, however, for a ventricular aneurysm to form during the fibrotic transformation of a chronic myocardial infarct, especially when transmural scarring has occurred. The fibrotic tissue completely loses its ability to contract, and over time the scar yields to the intraventricular pressure and forms an outpouched area in the heart wall. The blood flow velocity is markedly reduced within a ventricular aneurysm, predisposing to the formation of ventricular thrombi.

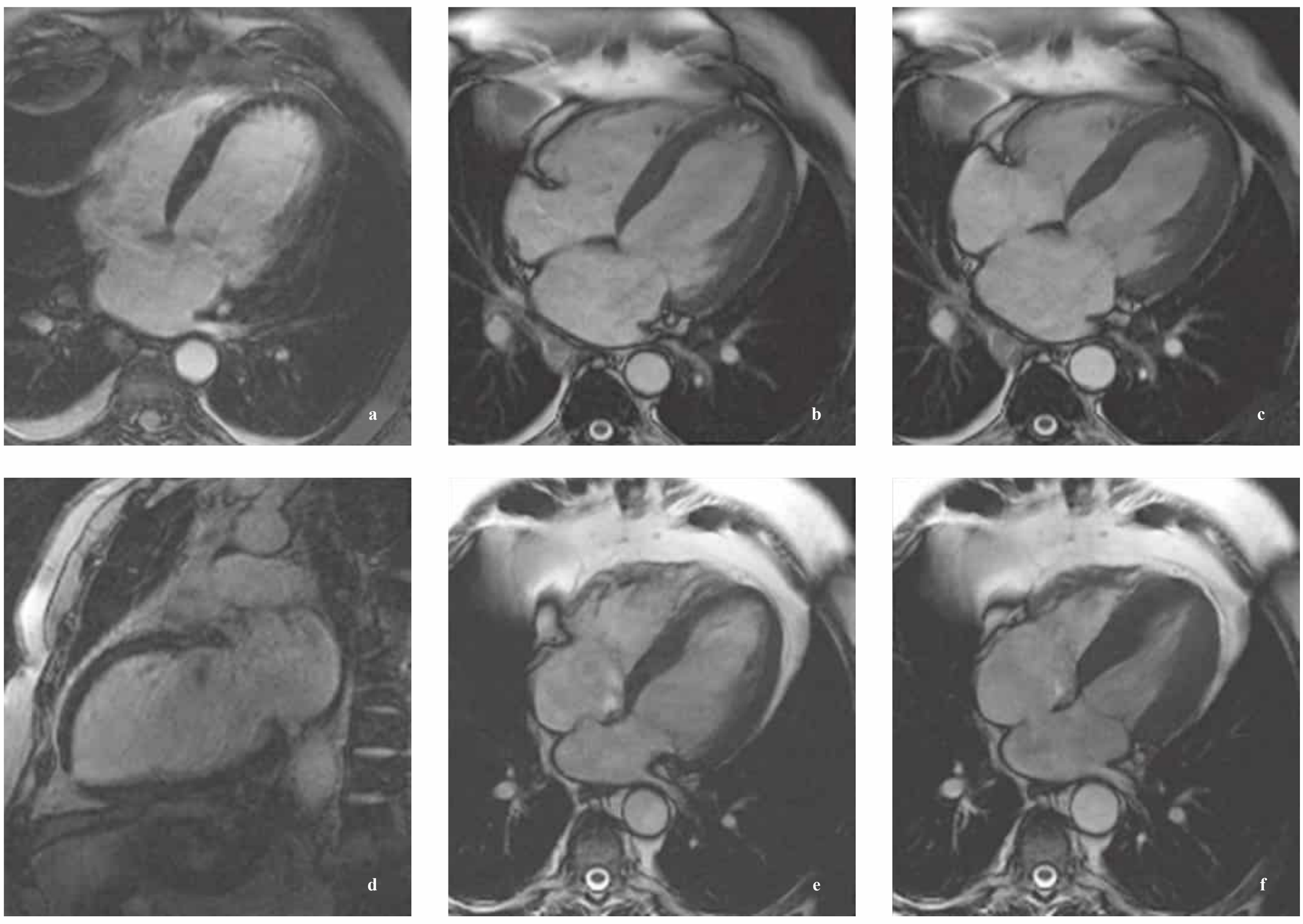

Fig. 8.34 a–f Viability confirmed by functional improvement after coronary bypass surgery and aortic valve replacement in a patient with three-vessel coronary disease and aortic stenosis. Preoperative inversion-recovery turbo FLASH images (**a, d**) show no evidence of late enhancement, indicating myocardial viability. Preoperative cine images at end diastole (**b**) and end systole (**e**) show severe impairment of regional and global LV myocardial function. Images taken 6 months after quadruple bypass surgery and aortic valve replacement show a normalization of LV function (**c**: end diastole, **f**: end systole), proving myocardial viability and confirming the preoperative viability assessment.

There are three indications for the surgical treatment of a ventricular aneurysm (aneurysmectomy):

- Heart failure
- Angina pectoris
- Ventricular arrhythmias

Echocardiography

The echocardiographic findings in ventricular aneurysm consist mainly of dyskinetic wall-motion abnormalities, which are characteristic of ventricular aneurysms. The associated areas of wall thinning can be demonstrated by transthoracic as well as transesophageal scanning. The change in the original shape of the ventricle can also be detected by echocardiography.

Difficulties arise in the echocardiographic volumetry of asymmetrical ventricles. As ventricular geometry changes, the geometric approximations used for long-axis volumetry by the Simpson method are no longer reliable. One solution to this problem is 3D echocardiography with the latest generation of real-time scanners, as this method does not rely on geometric approximations.[129]

Echocardiography often demonstrates "spontaneous" echoes caused by slow blood flow in an aneurysm. Frequently it is difficult to detect flat thrombi on the endocardium and differentiate them from adjacent myocardium owing to their low contrast. Transesophageal echocardiography is definitely superior to transthoracic scanning for identifying these lesions.

Magnetic Resonance Imaging

The characterization of ventricular aneurysms in MRI is based on changes in ventricular geometry and the characteristic dyskinesia observed in **cine sequences**. Both of these findings can be detected reliably and with good contrast. Because MRI is inherently independent of geometric approximations, volumes and global functional parameters can be accurately determined using the standard **disk summation method**.

Late-enhancement MRI can reliably distinguish myocardial scars from viable myocardium. Thus, aneurysms can often be identified by their late enhancement and wall-motion abnormalities, and their size can be accurately determined.

A major advantage of MRI over echocardiography is its ability to detect intraventricular thrombi. Typically thrombi do not enhance after intravenous contrast administration and can be identified by their low signal intensity relative to the hyperintense ventricular lumen. Because thrombi in coronary patients develop almost exclusively in proximity to infarcted myocardium, the enhancing scar tissue makes is easy to distinguish thrombi from the infarcted ventricular wall (**Fig. 8.35**). The superiority of MRI over echocardiography is based on this contrast.[130]

Essential Point

Echocardiography and MRI can reliably detect ventricular aneurysms by demonstrating the typical wall-motion abnormality and change in ventricular geometry. MRI is superior to echocardiography, including transesophageal scans, in the detection of ventricular thrombi.

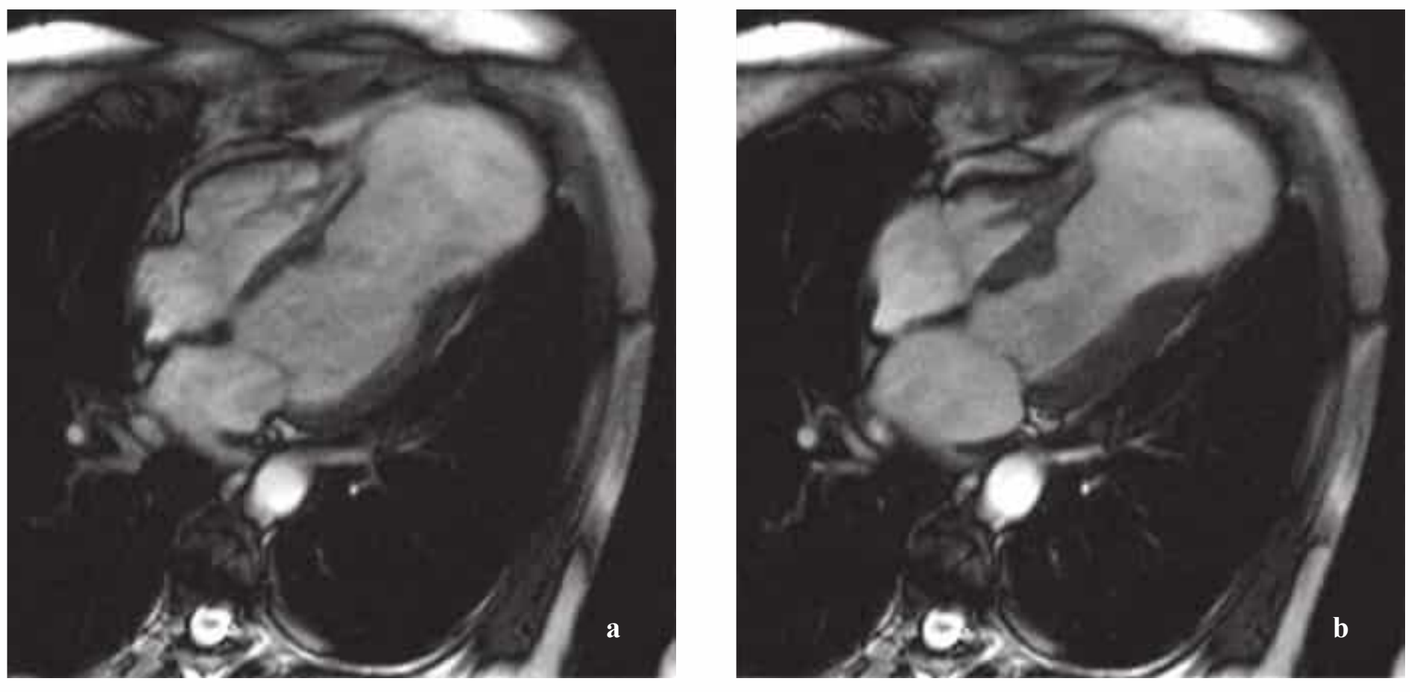

Fig. 8.35 a–d Large LV apical aneurysm with a parietal intraventricular thrombus. Four-chamber view (horizontal long-axis view) of the LV acquired with a segmented SSFP cine sequence. Images at end diastole (**a**) and end systole (**b**) show pronounced wall thinning in the apical half of the ventricle. The systolic image shows no wall thickening and marked dyskinesia of the aneurysm. Inversion-recovery turbo FLASH images in the four-chamber view (**c**) and three-chamber view (**d**) show transmural late enhancement throughout the aneurysm. The three-chamber view also shows a hypointense shell-like deposit in the inferolateral portions of the aneurysm consistent with a thrombus (arrow).

Computed Tomography

Contrast-enhanced multislice CT of the heart with retrospective ECG gating can detect relatively pronounced areas of wall thinning associated with ventricular aneurysms. These datasets can also be used to reconstruct images at various points in the R-R interval, providing functional information on wall-motion abnormalities.

Ventricular thrombi can be accurately detected with CT. Again, the relatively high sensitivity of CT to thrombi is based on the contrast between the high density of contrast-enhanced blood, perfused myocardium, and scar tissue on the one hand, and the low density of the nonenhancing thrombi on the other. The protocols are the same as those used in CT coronary angiography.

Table 8.5 reviews the strengths and weaknesses of the various imaging modalities in the diagnosis of chronic CHD and its entities and gives recommendations on clinical protocols.

Differential Diagnosis of Stenotic Coronary Heart Disease

Syndrome X

Pathophysiology and Symptoms

- Caused by microvascular or endothelial dysfunction
- Presents clinically with angina pectoris

Table 8.5 Overview of various imaging modalities used in chronic CHD and its entities and recommended clinical protocols

Entity	Modality	Strengths and weaknesses	Protocol
Ischemia in chronic CHD	Echocardiography	• Simple, easily available • High-dose stress established • Costs of stress protocol • Frequent poor image quality	Rest and high-dose dobutamine for diagnosis of ischemia
	MRI	• Versatile and reliable • Costs of stress protocol • Perfusion imaging still requires clinical validation	Rest and high-dose dobutamine or perfusion
	Nuclear medicine	• Long scientific track record • Problematic in diabetics • Frequent false-positive results in LV posterior wall • Poor spatial resolution	SPECT or PET
	Coronary angiography	• Standard for coronary artery imaging • Allows for direct intervention • Limited information on LV	
	CT	• No quantification of ischemia • Subtle, noninvasive imaging of coronary artery stenoses	Multislice-CT, contrast-enhanced CTA with ECG gating
Hibernating myocardium	Echocardiography	• Basic work-up • Stress testing is required • Cannot detect scars directly	Rest and low-dose dobutamine
	MRI	Can reliably detect hibernating myocardium without additional tests.	Rest and late enhancement; low-dose dobutamine if desired
	Nuclear medicine	High costs due to need for perfusion and metabolic information: dual examination	
Chronic infarction and scar	Echocardiography	• Stress testing is required • High costs, limited reliability	Low-dose dobutamine
	MRI	New reference standard	Rest function and late enhancement
	Nuclear medicine	Long track record, traditional reference standard	PET
Aneurysms	Echocardiography	Simple and reliable	Rest
	MRI	• Reference standard • Also provides viability information • Reliable thrombus detection	Rest function and late enhancement
	CT	• Functional analysis possible • Relatively high radiation exposure	Multiple reconstructions from contrast-enhanced CTA with ECG gating

Diagnostic Tests and Typical Findings

- Abnormal stress ECG
- Stress tests (stress echocardiography, stress MRI) may show stress-induced wall-motion abnormalities.
- Hypoperfusion can be detected by SPECT and PET imaging, adenosine stress MRI, and myocardial contrast echocardiography.
- No stenoses on coronary angiograms.
- Intravascular ultrasound does not reveal plaque formation. Intracoronary Doppler shows a decreased coronary flow reserve.[131]

Myocardial Bridging

Pathophysiology and Symptoms

- Bridging of myocardial fibers over an epicardial coronary artery segment, causing a normally epicardial artery to become intramyocardial
- Characteristic systolic compression of the coronary artery lumen
- Presents clinically with angina pectoris.
- Complaints are worsened by tachycardia/tachyarrhythmia, hypotension, and vasospasms. Severity depends on the length, thickness, depth, and location of the myocardial bridge and on the presence of left ventricular hypertrophy.

Diagnostic Tests and Typical Findings

- Septal or anterior hypertrophic areas are sometimes detected.
- It is often possible to detect reversible perfusion defects, sometimes with associated wall-motion abnormalities.
- Coronary angiograms (and IVUS) show typical systolic luminal compression.
- Coronary angiograms (and IVUS) of pronounced myocardial bridges show a step-down, step-up phenomenon with an abrupt caliber change in the affected segment.
- CT angiography and MRI may demonstrate the intramyocardial course of the affected coronary artery.

Vasospastic Angina pectoris

Pathophysiology and Symptoms

- Special form with anginal symptoms unrelated to stress
- Triggered by coronary vasospasms, with or without stenoses

Diagnostic Tests and Typical Findings

- ST-segment elevation or depression on ECG
- Coronary angiography shows nonstenotic atherosclerotic plaques in up to two-thirds of affected patients.
- Direct detection of coronary spasms by provocative pharmacological vasomotor testing under direct coronary angiographic control (caution: complex ventricular arrhythmias)
- Other resting, stress, perfusion and viability tests have only a minor diagnostic role.

Postoperative and Postinterventional Imaging

K.-F. Kreitner and G. Horstick

Besides drug therapy, the mainstays in the treatment of CHD are interventional therapy and coronary bypass surgery. In 2005, a total of 271 000 PTCAs were performed in Germany during more than 772 000 left heart catheterizations. In ~85% of cases the PTCA was combined with stent implantation into the affected coronary artery. This represented a 9% increase in PTCAs and a 10% increase in stent implantations over the previous year. Approximately 67 000 bypass operations were performed during the same period, representing a decline of ~1500 operations from the previous year.[132]

Thus, while the numbers of coronary stent implantations have been rising, there has been a corresponding decline in percutaneous coronary interventions and aortocoronary bypass operations. This has been due mainly to the increasing availability and use of drug-eluting stents. Prospective studies comparing bypass surgery and revascularization with drug-eluting stents are already underway and will be helpful in determining which treatment modality is more effective. In all previous comparative studies of bare metal stents versus stents with an antiproliferative coating, the coating invariably led to a significant reduction in re-stenosis and reintervention rates, although a definite mortality benefit with drug-eluting stents has not yet been established.[133–135]

Postoperative Imaging

The need to image coronary bypass grafts is based on their limited lifetime. By just 11 days after bypass surgery, 1.3% of internal mammary artery (IMA) bypass grafts to the LAD artery are occluded, while another 7.8% may show greater than 50% stenosis. By one year postoperatively, 3.4–5.7% of arterial bypass grafts are no longer patent. The occlusion rate at 10 years ranges between 5% and 15%[132,136] The numbers for venous bypass grafts are considerably less favorable: Selective angiographic follow-ups have shown that 15–20% of venous bypass grafts are occluded by one year postoperatively. The 10-year occlusion rate is ~40–50% Graft sclerosis develops in 38% of nonoccluded venous bypass vessels by 5 years and in 75% by 10 years. This sclerosis causes more than 50% luminal narrowing in approximately half of the affected vessels.[136,137]

Given the markedly better long-term results of arterial grafts and the limited availability of IMA vessels (**Fig. 8.36**), surgeons are increasingly turning to alternative arteries for in-situ bypasses and the use of free transfers. Particular interest has centered on the radial and gastroepiploic arteries. Multiple arterial bypass vessels are increasingly being used for complete arterial revascularization.[138,139]

Essential Point

The limited lifetime of coronary bypass grafts makes it necessary to evaluate the bypasses with respect to patency and stenosis. Cardiac anastomoses are particularly vulnerable to stenosis. Arterial bypass grafts have a significantly better long-term prognosis than venous grafts.

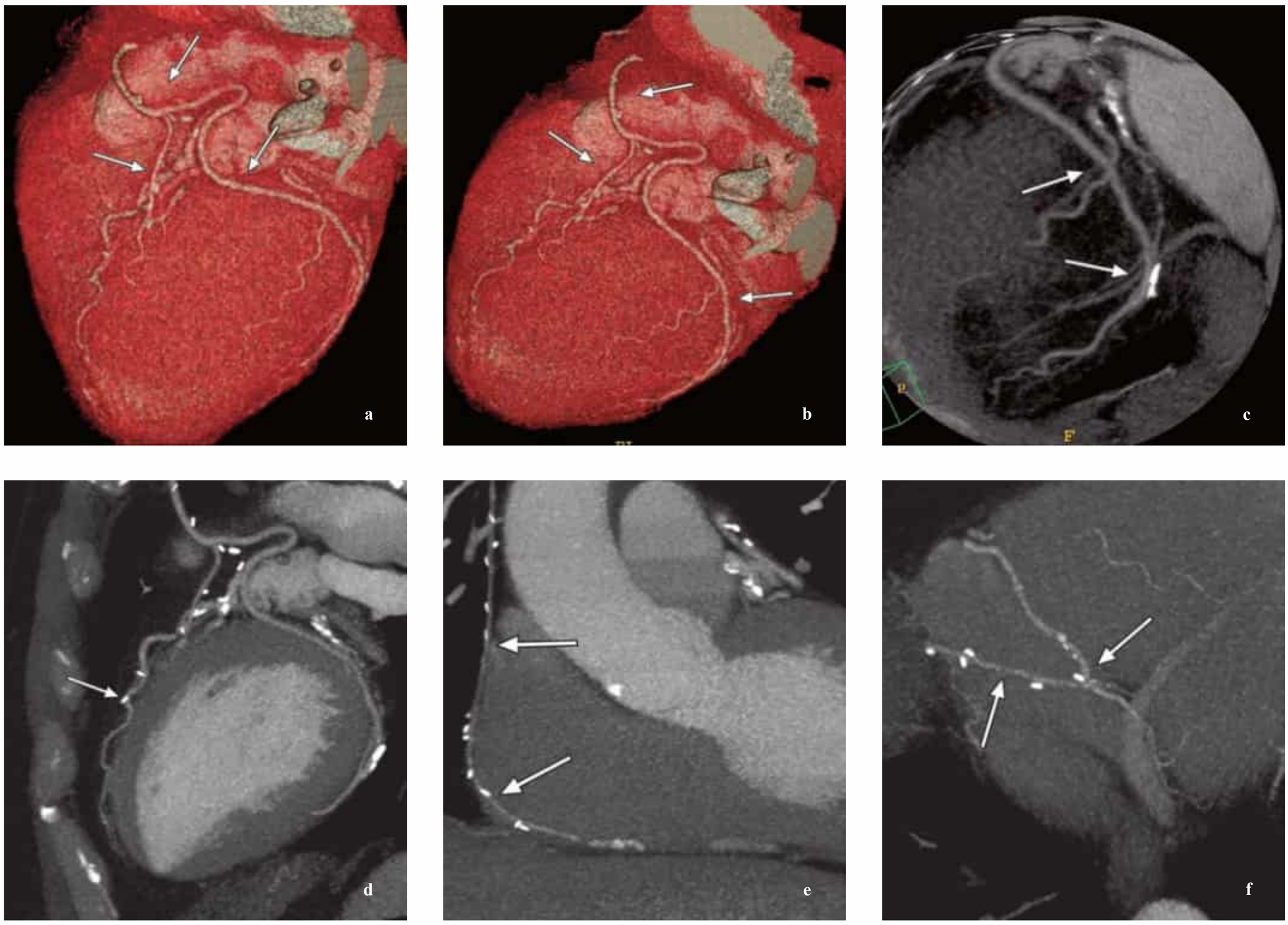

Fig. 8.36 a–f Complete arterial revascularization in a 56-year-old man with one sequential LIMA graft to the PLA 1 and 2 branches, one sequential radial artery T graft to D1 and LAD, and one RIMA graft to the RCA.

a, b Volume-rendered images of the LIMA graft (arrows) and radial artery graft (arrowhead).

c Multiplanar reformatted image shows the anastomoses (arrows) of the LIMA bypass to PLA 1 and 2 with good runoff into the native coronary artery segments.

d Cardiac anastomosis of the radial artery T graft to the LAD (arrow) with a normal appearance of the distal LAD.

e, f Multiplanar reformatting of the RIMA graft (arrows) to the RCA with visualization of the cardiac anastomosis (arrowhead).

The clinical course of the patients correlates with the patency rate of the bypass vessels. Thus, the mortality rate at one year is 2.8 %while the myocardial infarction rate is 4 % Up to 24 %of patients experience recurrent anginal complaints during the first postoperative year. This incidence rises to ~40 %by 6 years. Up to 17.3 %of patients die during the first 8 years after undergoing coronary bypass surgery.[140]

These statistics underscore the importance of repeatedly evaluating coronary bypass grafts for patency and for the presence of hemodynamically significant stenosis. Selective coronary angiography is considered the standard imaging procedure for this application. It can evaluate the status of the native coronary arteries in the same setting, as new clinical complaints may result from progression of the underlying coronary heart disease. Additionally, the functional significance of a stenosis can be assessed during catheter angiography by determining the flow reserve with a Doppler wire. Cardiac catheterization is considered a safe but relatively costly invasive procedure with an ~0.1 %mortality risk that exposes the patient and examiner to ionizing radiation.

MRI and CT are imaging modalities that allow for noninvasive imaging and assessment of coronary bypass grafts.

Computed Tomography

The current technique of choice for the CT imaging of coronary bypass grafts is multidetector row CT. Rotation speeds in the subsecond range (330–500 ms) and the capability for retrospective ECG gating allow bypass vessels to be imaged without artifacts.

The assessment of bypass patency with **four-slice CT systems** has yielded excellent results with sensitivities of 93–100 %and specificities of 94–99 % However, this technology has yielded much less favorable results in the evaluation of:

- Cardiac anastomoses
- Noncontrasted coronary arteries
- The detection of hemodynamically significant bypass stenosis

Table 8.6 Accuracy of 16-slice CT in the detection of patent coronary artery bypass grafts

Author (year)	Patients/ bypasses	Arterial/venous bypasses	Sensitivity (%) total/art./ven.	Specificity (%) total/art./ven.	Assessability of stenoses n (%)	Sensitivity (%)	Specificity (%)
Schlosser et al. (2004)[147]	48/131	40/91	100/100/100	100/100/100	83/112 (74%)	96%	95%
Chiurlia et al. (2005)[145]	52/166	49/117	100/100/100	100/100/100	165/166 (99%)	96%	100%
Salm et al. (2006)[146]	25/67	14/53	100/n.a./n.a.	100/n.a./n.a.	67/67 (100%)	100%	94%
Anders et al. (2006)[143]	32/94	20/74	100/n.a./n.a.	98/n.a./n.a.	78%/84% O1/O2	80/82 O1/O2	85/88 O1/O2
Burgstahler et al. (2006)[144]	13/43	11/32	100/n.a./n.a	93/n.a./n.a	41/43 (95%)	100	100

art. = arterial; ven. = venous; n.a. = not applicable; O1, 2 = observer 1, 2.

In a study by Ropers et al.,[141] only 77 of 124 patent bypass vessels (62%) could be assessed for the presence of hemodynamically significant stenosis. The substantial failure rate was due to arrhythmias and heart rates >65 bpm, metallic clips in the course of the IMA bypass, and respiratory artifacts caused by the very long acquisition time of 40 s.

The assessment of native coronary arteries is also difficult. Nieman et al.[142] analyzed the native coronary arteries in 24 patients with 41 bypass grafts (23 venous and 18 arterial grafts). Of 211 coronary arterial segments, only 146 (69%, observer 1) or 140 (66%, observer 2) could be assessed. The detection of more than 50% luminal reduction yielded a sensitivity of 79–90% and a specificity of 72–75%

Considerably better results are achieved with **16-slice scanners**, which provide a collimation of 16 × 0.5 mm to 16 × 0.75 mm and a higher temporal resolution of 100 ms or less depending on the heart rate. **Table 8.6** shows results from studies in which a 16-slice CT scanner was used and angiographic correlation was obtained.[143–147]

This technology is particularly useful in the evaluation of arterial bypass grafts, where the small vascular diameters and metallic marker clips used in IMA bypasses pose a special challenge. Gurevitch et al. examined 14 patients with 30 bypass grafts (26 arterial and four venous) involving a total of six proximal and 35 coronary anastomoses. CT showed that 29 of the 30 grafts were patent, and excellent visualization of all proximal and distal anastomoses was achieved.[148] Dorgelo et al.[149] studied the assessability of arterial bypass grafts (IMA and gastroepiploic artery [GEA] grafts) and found that CT provided complete graft coverage in more than 90% of the IMA grafts (43/46) and ~70% of the GEA grafts (18/26). The GEA grafts were imaged in a second acquisition at the level of the thoracoabdominal junction with a collimation of 16 × 1.5 mm using the contrast bolus necessary for cardiac imaging.

More than 90% of the native coronary artery segments could also be evaluated in this study.[149] Similar results have been reported by other working groups.[144,146]

These results show that 16-slice CT scanners can provide an acceptable morphological assessment of bypass grafts as well as native coronary arteries down to vessel diameters of ~1.5 mm. On the other hand, heavily calcified native coronary arteries are still difficult to evaluate with this technology.

Modern 40- and 64-slice CT scanners with rotation times ranging between 330 and 420 ms and collimations ranging between 0.5 and 0.625 mm are further improving the visualization of coronary bypass grafts and native coronary arteries. It was shown that these high-end scanners will be particularly useful in the evaluation of cardiac anastomoses and native coronary arteries (**Figs. 8.36, 8.37**).[150–152]

Table 8.7 presents a general protocol for multislice CTA of coronary bypass grafts based on the guidelines developed by the Cardiac Imaging Committee of the German Radiology Society.[153] Today most groups recommend the oral or IV administration of a β-blocker to lower the heart rate to less than 65 bpm, even when a 64-slice scanner is used. This gives the bypass vessels a prolonged relative rest period that is helpful for image reconstruction and analysis, especially in the assessment of cardiac anastomoses and native coronary arteries.

Essential Point

Sixteen-slice CT scanners can accurately evaluate coronary bypass grafts for patency and the presence of significant stenoses, especially of the cardiac anastomoses. The availability of 64-slice CT will further improve visualization of the native coronary arteries. The assessment of heavily calcified vessels remains a problem. Most groups of authors recommend the oral or IV administration of a β-blocker to reduce the heart rate to less than 65 bpm.

Magnetic Resonance Imaging

MRI was used in its early stages for the evaluation of bypass graft patency. Spin-echo and gradient-echo (GE) sequences were most commonly used for this application. Studies using **GE techniques** achieved sensitivities of 93–100% and specificities of 86–88% in the detection of bypass graft patency. An advanced GE technology is **steady-state free-precession**, but results to date indicate that the SSFP sequences are no more

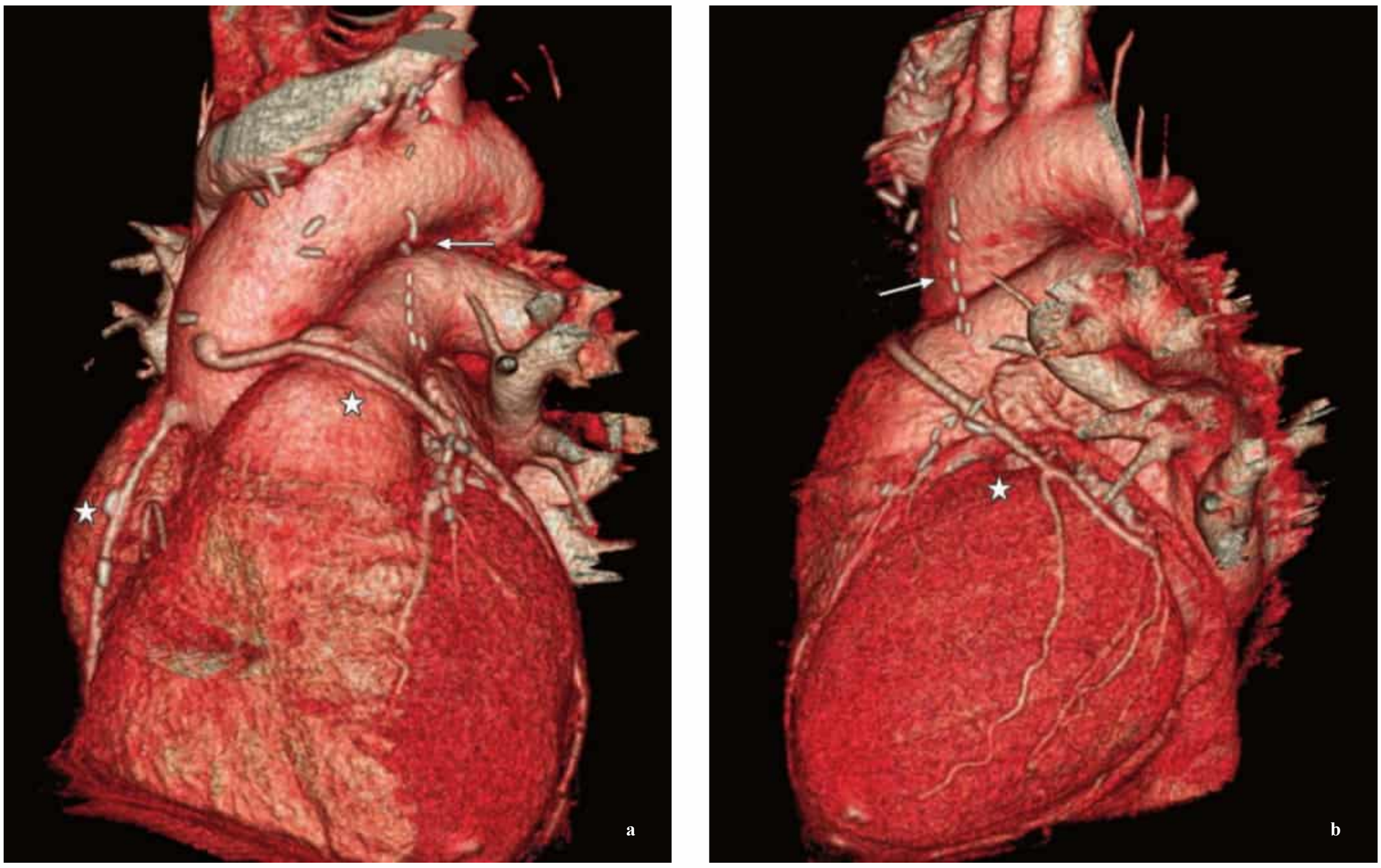

Fig. 8.37 a, b Volume-rendered images in a 62-year-old man with patent venous bypasses (asterisk) to the RCA (single) and LCX (sequential to PLA 1 and 2) and an occluded IMA graft to D1 (arrow). Only the metallic marker clips are visible along the occluded IMA bypass.

Table 8.7 Protocol for CTA of coronary bypass grafts (modified from guidelines of the Cardiac Imaging Committee of the German Radiology Society, Kreitner KF et al., 2004[153])

Scan volume	Superior border of aortic arch to cardiac apex
Requisite views, planes	Axial plus one additional plane
Scan parameters:	
• Collimation	• <1 mm
• Slice thickness	• <1 mm for axial source images, increment less than slice thickness (generally 50% of slice thickness)
• FOV	• ≤3 mm for reconstructions from sternum to spinal column
• Matrix	• ≥512
• Image acquisition	• Diastolic (may vary, depending on bypass vessel of interest)
IV contrast administration	Necessary
Other	• ECG triggering, gating • Bolus timing (test bolus or bolus tracking)
Interpretation	Assessment of patency, cardiac anastomoses, presence of high-grade stenoses, also native coronary arteries based on AHA segment model

accurate than GE sequences in the detection rate of graft patency.[140]

Spin-echo (SE) sequences confirm graft patency by showing an absence of intraluminal signal. Studies with conventional SE sequences, usually T1-weighted, have achieved sensitivities of 73–98 %and specificities of 56–85 % **Single-shot spin-echo** is a technique that allows for breath-hold coronary imaging. Kalden et al. used a 2D T2-weighted HASTE (half-Fourier acquisition single-shot turbo spin-echo) sequence to evaluate 97 coronary bypass grafts in 38 patients. They achieved sensitivities of 96 % (observer 1) and 92 %(observer 2) and specificities of 91 %(observer 1) and 82 %(observer 2) in the detection of patent bypass grafts. Of 97 distal anastomoses, 81 %(observer 1) and 61 % (observer 2) were correctly identified as patent. Interobserver agreement was good (κ=0.68), and agreement with the reference standard of coronary angiography was very good (κ=0.89, observer 1) and good (κ=0.68, observer 2), respectively.[140,154]

The results that can be achieved with contrast-enhanced 3D MRA are summarized in **Table 8.8**.[154–157] The numbers indicate that the patency of coronary bypass grafts can be determined with very high confidence using this technique. Cardiac anastomoses cannot be evaluated without ECG triggering, but they can be evaluated in up to 78 %of cases when prospective ECG triggering is used (**Fig. 8.38**). One problem with 3D CE-MRA is the difficulty of detecting hemodynamically significant stenoses: Two observers in the same study achieved a sensitivity of 64 %and 36 %with a specificity of 98 % Interobserver agree-

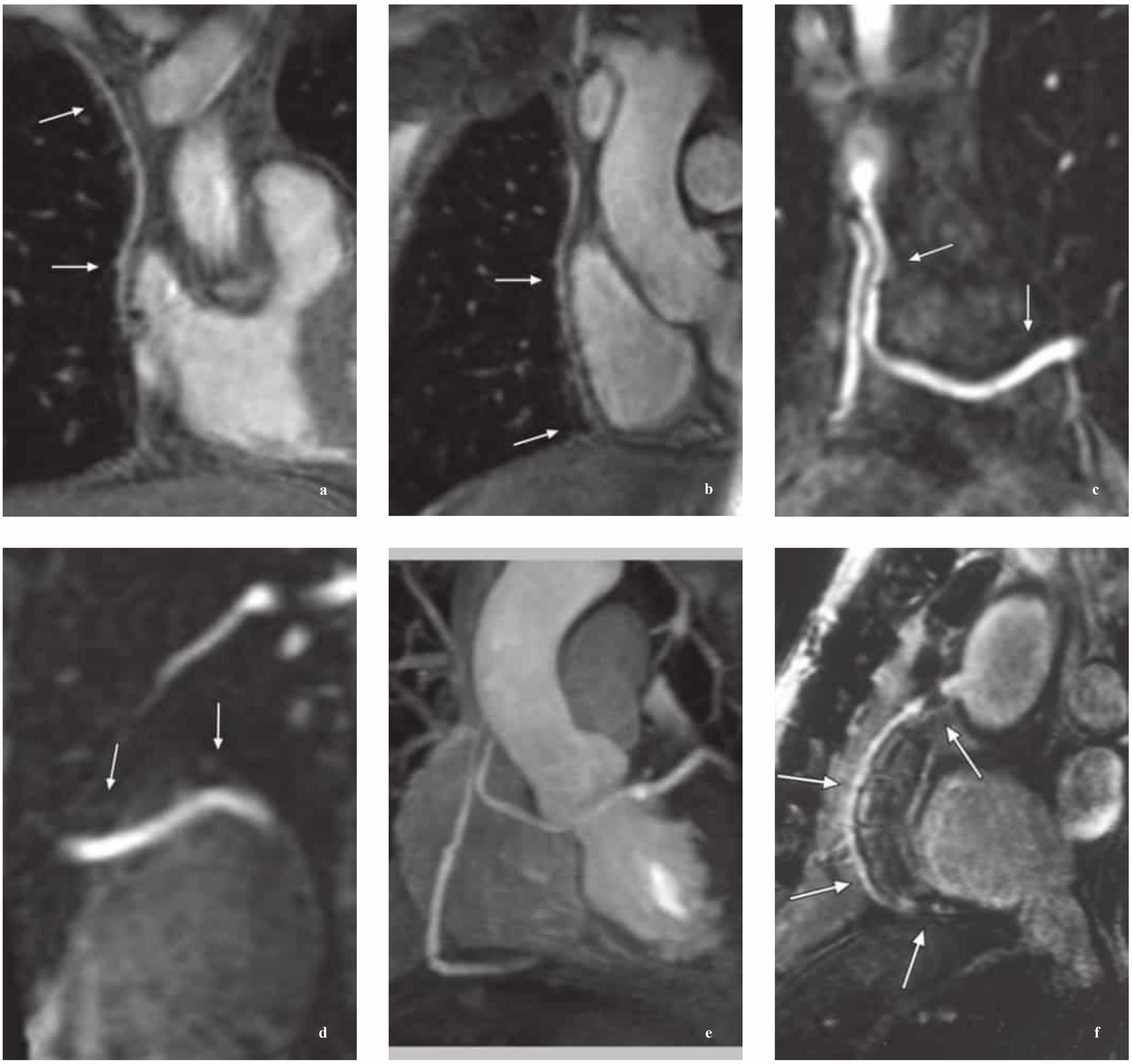

Fig. 8.38 a–f Contrast-enhanced 3D MRA of coronary bypass grafts. **a, b** MPR of a RIMA bypass (arrows) to the RCA. **c–e** MPRs of a sequential venous bypass (arrows) to D1 and PLA (**c, d**) and an MIP from the same dataset showing venous grafts to the RCA and LCX (**e**). **f** MPR of an angiographically confirmed proximal bypass stenosis to the RCA (arrows).

Table 8.8 Results of contrast-enhanced 3D MRA with respect to patency of aortocoronary bypass grafts

Author (year)	Patients, bypasses	Sensitivity (%) observer 1/2	Specificity (%) observer 1/2	Agreement with coronary angiography (κ)	Interobserver agreement (κ)
Vrachliotis et al. (1997)[156]	15/45	86/93	73/93	0.53/0.85	n.a.
Wintersperger et al. (1998)[157]	27/76	95	81	n.a.	n.a.
Kalden et al. (1999)[154]	22/59	93/91	93/93	0.83/0.79	0.87
Kreitner (2001)[155]	31/88	98/95	100/98	0.97/0.89	0.92

n.a. = not applicable.

ment was very low (κ=0.24). This means that 3D CE-MRA cannot detect significant bypass graft stenosis with an acceptable degree of accuracy. A recommended protocol for contrast-enhanced 3D MRA of coronary bypass vessels is outlined in **Table 8.9**.

The detection of significant bypass graft stenosis can be improved by the use of high-resolution, navigator-based 3D MRA. Langerak et al.[158] achieved sensitivity and specificity of 73% and 87%, respectively, in detecting bypass graft stenosis greater than 70% and values of 65% and 82% in detecting stenosis greater than 50%. This study dealt entirely with venous bypass grafts, however, as arterial grafts cannot be assessed for stenosis owing to the susceptibility artifacts induced by the presence of multiple vascular clips. This technique proved no better than 3D MRA in the detection of patent bypass grafts and is considerably more time-consuming.

Essential Point

Morphological MR imaging techniques can provide information on coronary bypass graft patency with a high degree of confidence. The most robust MR technique is contrast-enhanced 3D MRA. The addition of ECG triggering improves the assessability of cardiac anastomoses.

Flow quantification with phase-contrast MRI can also provide information on the patency and functional status of coronary bypass grafts. Important requirements for successful flow measurements in bypass grafts include adequate in-plane resolution, allowing the secure placement of ~3–4 pixels within the vessel lumen. A good a rule of thumb for in-plane resolution is that the ratio of pixel edge length to vessel diameter should be less than 0.5 (**Fig. 8.39**).

The flow sensitivity of the scanner should be set to ~75 cm/s because of the relatively low peak velocities. As for temporal resolution, it should be possible to acquire at least six phases per cardiac cycle. The better the temporal resolution, the more accurately the peak velocities in the bypass graft can be determined.[140,159,160] Patent, nonstenotic bypass grafts display a biphasic flow pattern at rest (given adequate temporal resolution), with bypass grafts to the left coronary artery (LAD or LCX) showing maximal flow in diastole while grafts to the right coronary artery (RCA) show maximal flow in systole. In a study by Ishida et al., a stenotic IMA bypass graft could be identified with 86% sensitivity and 88% specificity by observing peak flow in systole and decreased flow in diastole.[161] Sequential grafts have a greater flow volume on average than single grafts. Studies comparing MR flow measurements with invasive Doppler flow measurements showed a very good correlation between flow rates determined invasively and by phase-contrast imaging.[160,162]

In some cases, a bypass stenosis cannot be diagnosed solely on the basis of reduced flow. Determination of the coronary flow reserve (CFR) and its reduction can provide a measure of the hemodynamic significance of a morphologically detectable stenosis.[163,164] The CFR is determined by evaluating flow at rest and in response to a vasodilator. Adenosine (140 µg/kg bw IV) is administered by brief infusion to induce arteriolar dilatation.

Table 8.9 Protocol for contrast-enhanced 3D MRA of coronary bypass grafts (modified from guidelines of the Cardiac Imaging Committee of the German Radiology Society, Kreitner KF et al., 2004[175])

Coil	Target-volume-adapted surface coil system
Scan volume	Entire heart and ascending aorta
Slice position	Sagittal and/or coronal, taking into account the course of the bypass vessels
Scan parameters:	
• Slice thickness	≤ 2 mm
• FOV	≤ 380 mm
• Maximum pixel size	≤ 1.5 × 2 mm²
Respiratory triggering	Breath-hold technique
ECG triggering	Optional
IV contrast administration	• Breath-hold technique: • 0.1–0.2 mmol/kg bw Gd chelate • Injection rate: 1–4 mL/s
Additional requirements	• Breath-hold technique: test bolus or bolus tracking • Analysis of source images and multiplanar reformatted images
Postprocessing	Optional: multiplanar reformatting, maximum intensity projection, volume rendering, subtraction

A steal phenomenon is observed in the presence of a hemodynamically significant bypass graft stenosis. The vascular bed behind the stenosis is already maximally dilated owing to metabolic autoregulation. As a result, the pharmacologically induced dilatation of normal or minimally stenosed vessels leads to a relative decrease in blood flow followed by an absent or deficient increase in flow through the coronary bypass graft. The advantage of adenosine is its extremely short half-life of 4 s, which allows for excellent control. It should be noted, however, that caffeinated foods and theophylline-containing drugs antagonize the effect of adenosine and should be avoided for at least 24 hours before the stress test. Adenosine administration is contraindicated in patients with a second- or third-degree AV block, sick sinus syndrome, poor medical control of angina pectoris, decompensated heart failure, or a chronic obstructive lung disease with associated bronchospasm.[140]

Studies in normal bypass grafts indicate a coronary flow reserve of 2.4–2.6 for single and sequential grafts.[163] The flow reserve can be successfully determined in ~80% of the grafts examined. Based on a multivariate analysis of mean velocity, peak velocity, peak diastolic and systolic velocities, and coronary flow reserve, sequential grafts with greater than 70% stenosis can be detected with a sensitivity of 94% and a specificity of 71%. The values for single grafts are 96% and 92%, respectively. Coronary flow reserve is a better parameter for detecting or excluding stenosis in single grafts than in sequential grafts (**Fig. 8.39**).[162–164]

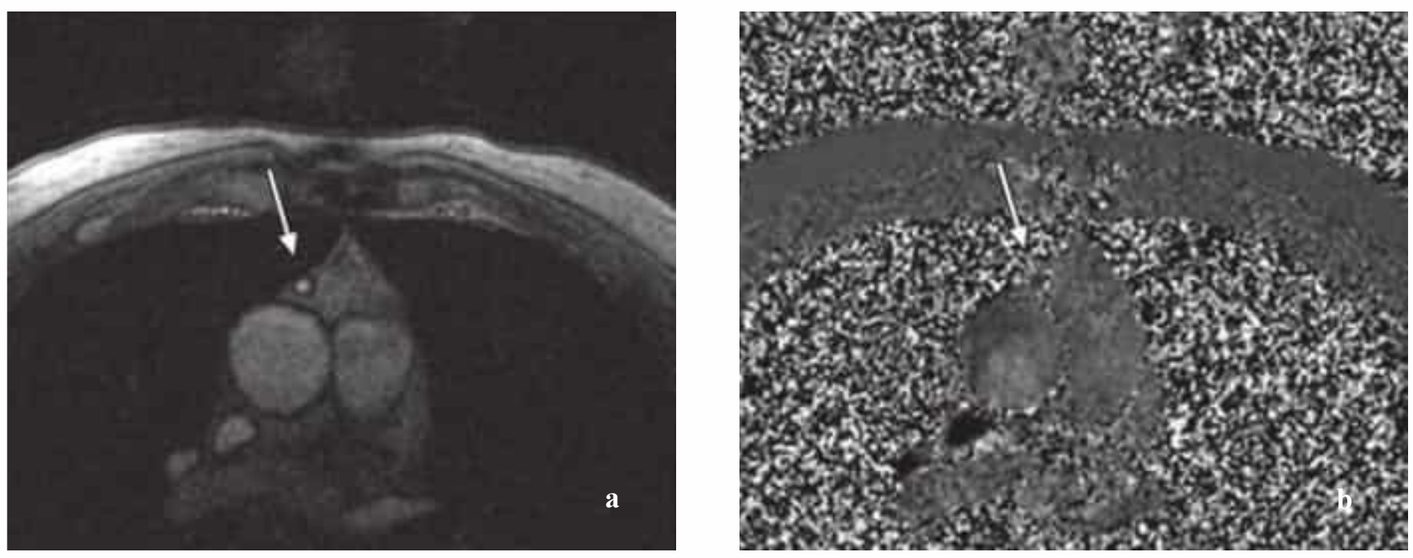

Fig. 8.39 a–c Coronary flow reserve in a venous bypass graft to the LCX.
a, b Magnitude and phase-contrast images of a flow measurement with a temporal resolution of 45 ms (arrow: bypass graft).
c Flow patterns before and after the administration of adenosine show a marked rise of flow rate in a functioning bypass graft.

Essential Point
Flow quantification with phase-contrast MRI before and after the administration of a vasodilator make it possible to determine the important functional parameter of coronary flow reserve. This enables assessment of the hemodynamic significance of a bypass graft stenosis or a stenosis in more distal coronary artery segments. Successful flow measurements require the use of pulse sequences with adequate temporal and spatial resolution.

Recommendations for Clinical Use

The occlusion of a bypass graft does not necessarily lead to a recurrence of angina pectoris, especially in patients with multivessel coronary disease. Usually these patients do not become symptomatic until multiple bypass vessels have become occluded. At the same time, cardiac catheterization generally cannot be recommended for the assessment of graft patency in bypass patients who are clinically asymptomatic. Because multislice CT and MRI are both accurate in the detection of occluded bypass grafts, both modalities are recommended as primary imaging studies in the follow-up of asymptomatic patients who have undergone bypass surgery, especially since almost one-third of patients have an asymptomatic bypass occlusion an average of five years after their surgery.

MSCT and MRI are worthy of consideration in the follow-up of coronary bypass patients with atypical chest discomfort. Often these complaints are not associated with a bypass occlusion or progression of underlying disease, and so repeat cardiac catheterization is withheld, even in older patients, if a bypass occlusion can be confidently detected or excluded noninvasively by MSCT or MRI. MSCT with a 64-slice scanner can also evaluate the progression of the disease in noncontrasted coronary arteries.

Another indication is the assessment of bypass patency in the early postoperative period, especially in cases where new surgical techniques (surgery during beating heart, new anastomotic techniques) have been used and the surgeon wishes to document the technical outcome. MSCT is preferred over MRI in these cases because it can be performed more expeditiously.

On the other hand, patients with recurrence of typical angina pectoris and/or definite evidence of ischemia in another test should be referred at once for left heart catheterization, because even if the bypass vessels are functioning, there may be a

progression of native vascular disease. A few selected cases may require the noninvasive documentation of a patent bypass vessel, especially if the vessel cannot be selectively visualized during catheter examination, but the detection of a functioning bypass will influence further, usually interventional, management (PTA of coronary stenosis with stent insertion).

Appraisal

Based on studies to date, 16-slice and 64-slice CT are superior to MRI in the morphological evaluation of cardiac anastomoses and native coronary arteries and in the detection of bypass graft stenosis.

Unlike CT, MRI can supply information on the functional status of bypass grafts and the coronary vessels past the graft based on the determination of coronary flow reserve. MRI also provides an opportunity to integrate bypass evaluation into a multiparameter protocol that includes the determination of global and regional left ventricular function, myocardial perfusion, perfusion reserve, and viability assessment. Currently this is much more costly than MSCT but permits a more comprehensive evaluation of the heart. It remains to be seen which noninvasive modality will become the established method of choice in the follow-up of patients who have undergone bypass surgery.

Postinterventional Imaging

Data published in the annual Cardiac Report document a steady rise in the number of stent implantations performed during PTCAs in Germany.[165] For example, 230500 stent insertions were performed in 2005, representing 85% of all PTCAs. The success of stent implantation is based on its significantly lower re-stenosis rate compared with PTCA alone, resulting in a reduced number of percutaneous reinterventions.[133,165]

Despite the progress that has been made in lowering re-stenosis rates with conventional stents compared with PTCA alone, randomized studies show that the angiographic re-stenosis rates at 6 months after conventional stent insertion still range from 20% to 40% depending on the patient subgroup and the complexity of the stenosis.[133,135]

The introduction of coated stents that release drugs with antiproliferative properties (drug-eluting stents) has been the most important development in coronary interventions. The most advanced agents are sirolimus and paclitaxel. Initial studies show that stents with an antiproliferative coating can reduce the re-stenosis rate and associated reintervention rate by 50–60%[166,167]—although this does not directly signify a mortality advantage over conventional stents. Moreover, about 10 patients must be treated with a drug-eluting stent to prevent one reintervention.[133]

We may conclude from these figures that patients treated by coronary stenting should undergo repeated follow-ups to evaluate for re-stenosis. The imaging modality of choice is still coronary angiography, which allows for the concomitant treatment of re-stenosis in the same sitting (**Fig. 8.40**). There are still no definite guidelines with respect to the timing of follow-up angiography after stent implantation. In most cases the initial angiographic follow-up is done 6 months after the intervention and stent insertion.

To date, little has been reported on the assessability of coronary stents with multislice CT. Initial clinical and experimental studies using 16- and 64-slice scanners can be summarized as follows[168–173]:

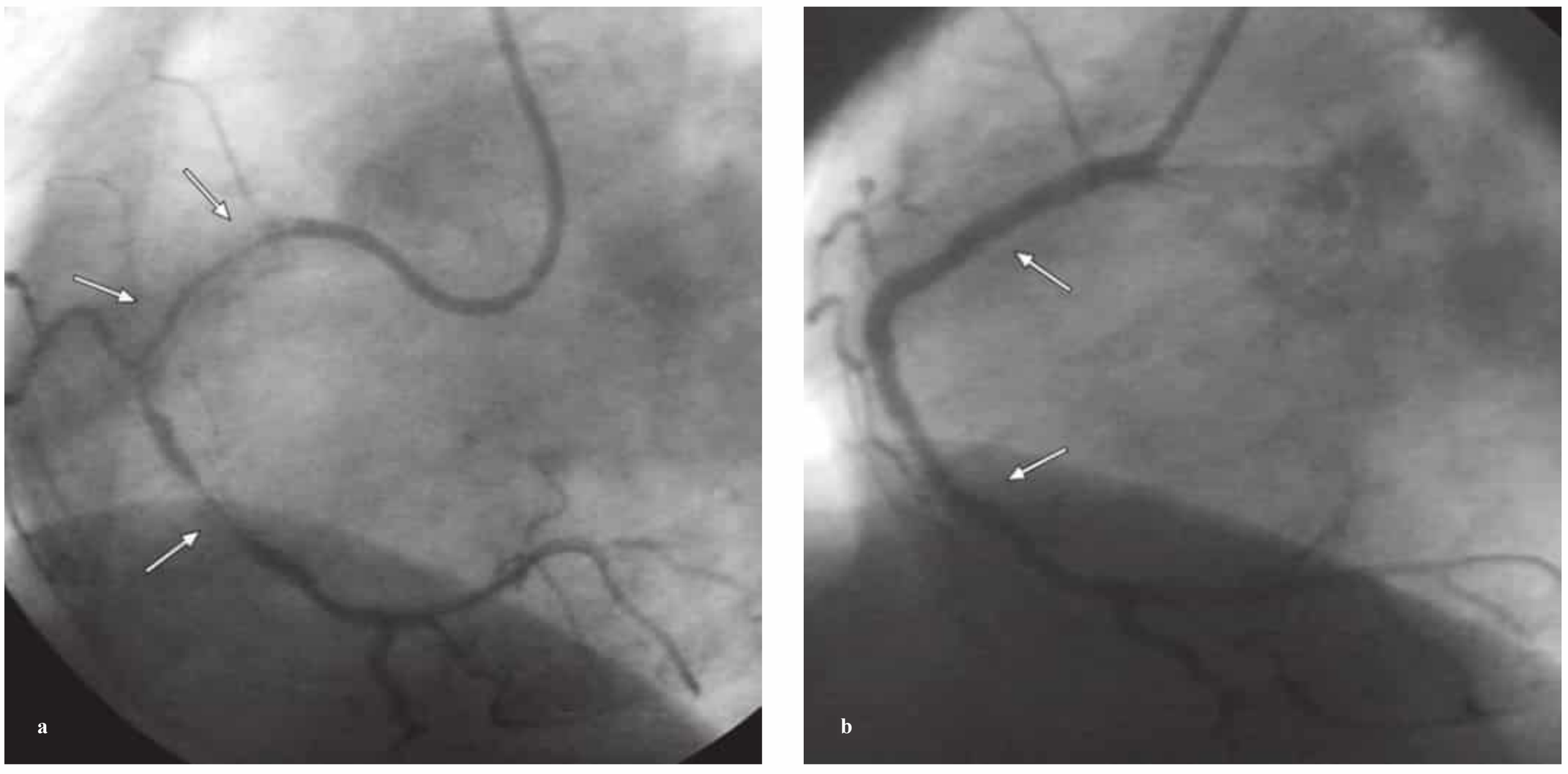

Fig. 8.40 a, b In-stent stenoses (arrows) and their treatment by the implantation of drug-eluting stents in the right coronary artery.

a Coronary angiogram before reintervention.
b Angiogram after new stent insertion documents complete elimination of the stenoses.

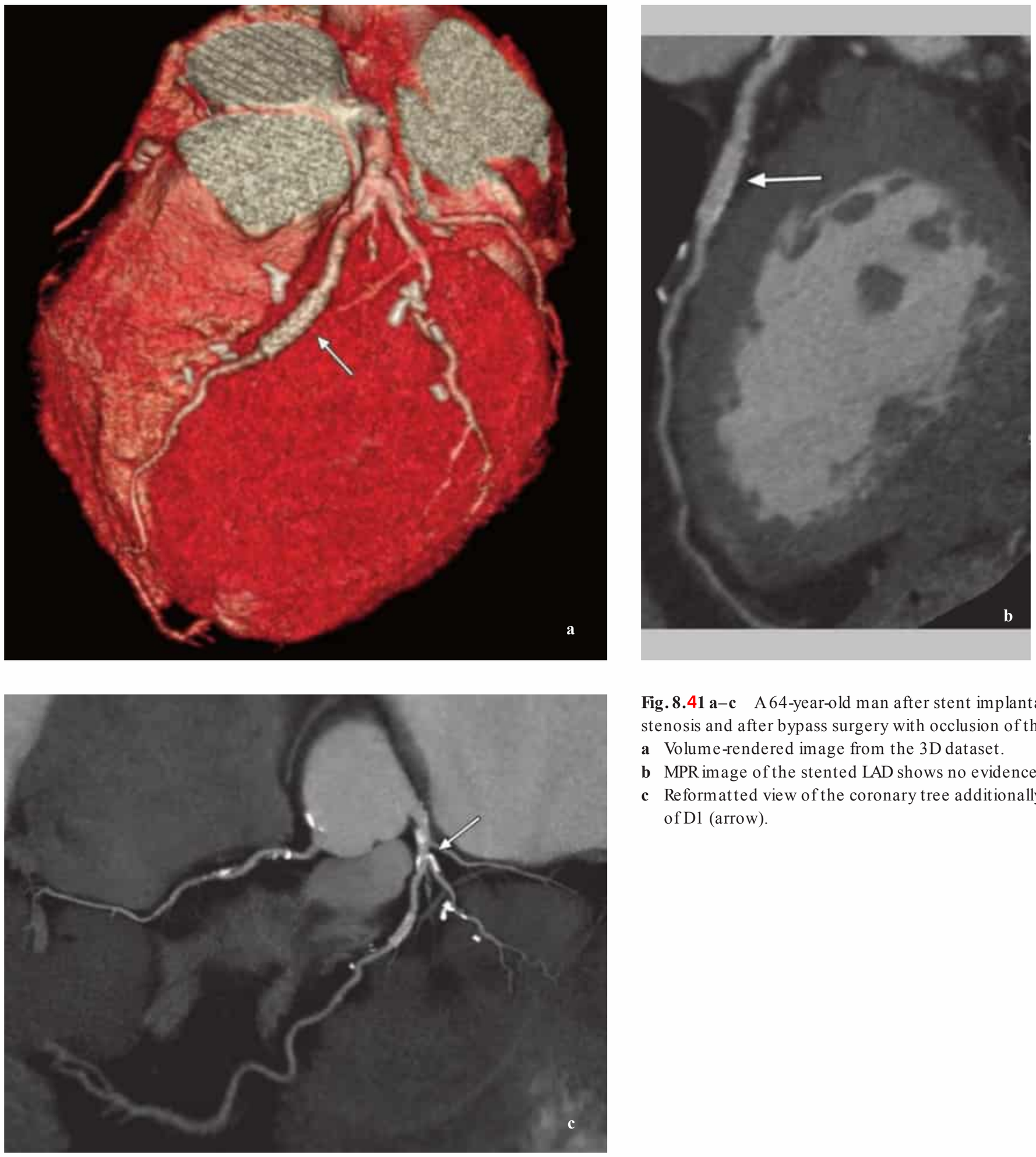

Fig. 8.41 a–c A 64-year-old man after stent implantation (arrow) for an LAD stenosis and after bypass surgery with occlusion of the bypass (D1).
a Volume-rendered image from the 3D dataset.
b MPR image of the stented LAD shows no evidence of in-stent stenosis.
c Reformatted view of the coronary tree additionally shows a proximal stenosis of D1 (arrow).

- Edge-enhancing algorithms facilitate assessment of the stent lumen, which is an important requirement for the detection of in-stent stenosis.
- Stents with a gold coating or gold markings as well as tantalum stents lead to significant beam-hardening artifacts, making it almost impossible to evaluate stents under routine clinical conditions.
- With the increasing availability of 64-slice CT scanners, more than 50 % of the stent lumen can be assessed in the majority of stents in clinical use.[172]

The diameter of implanted stents also plays a major role. In a study of 61 stents implanted in 42 patients, 89 % of the stents with a diameter of 3.5 mm or more could be evaluated for in-stent stenosis.[170] Only 58 % of stents 3 mm in diameter were assessable, and stents 2.5 mm or less in diameter were not assessable. In another study of 47 stents implanted in 42 patients, the presence of greater than 50 % in-stent stenosis or complete obstruction could be detected with a sensitivity of 58 % and a negative predictive value of 89 %[168]

The presence of marked calcifications in the stented vessel wall can also hamper assessability. In a study of 29 patients with a stent in the main trunk of the left coronary artery, the vessel could not be evaluated for re-stenosis in two cases because of calcifications.[169] At present, a general recommendation cannot be made for the routine assessment of implanted coronary stents with MSCT based on available data. It is already clear, however, that the patency of a proximally placed stent more than 3.5 mm in diameter can be accurately assessed even in routine clinical situations.

It is reasonable to predict that the increasing use of 64-slice CT scanners, combined with ongoing advances in stent technology,[174] will further improve our ability to assess coronary stents (**Figs. 8.41, 8.42**), owing particularly to improved

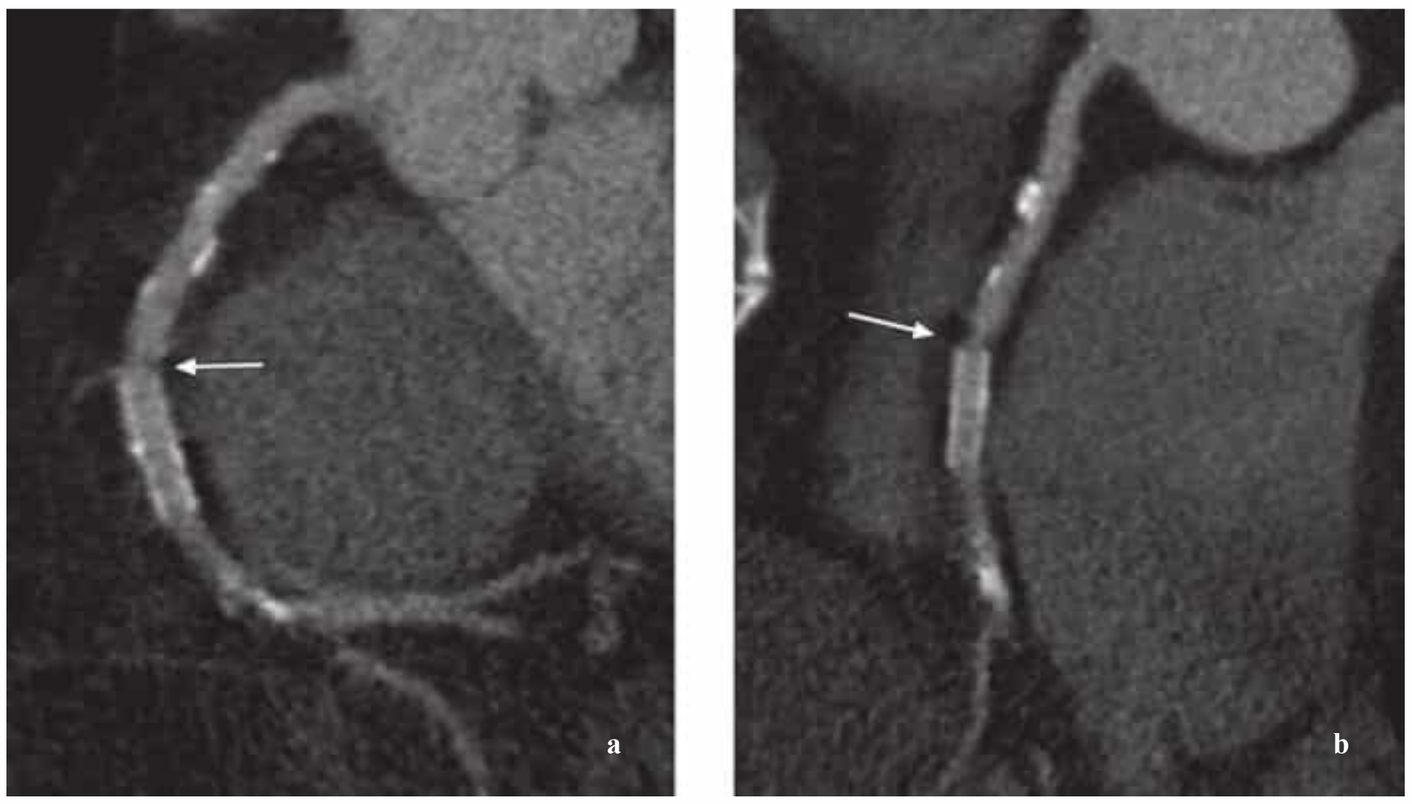

Fig. 8.42 a, b A 59-yearold man after stent placement in the RCA. MPR images of cardiac CTA show a stenosis proximal to the stent (arrow).

temporal and spatial resolution along the *z*-axis. The definitive role of this advanced technology must await the results of additional large-scale studies, which have already been initiated at most centers. When we consider how swiftly MSCT has advanced during the past 5 years, it is not difficult to predict that the follow-up of interventionally treated patients will undergo a paradigm shift in the foreseeable future.

References

1. Stary HC, Chandler AB, Dinsmore RE, et al. A definition of advanced types of atherosclerotic lesions and a histological classification of atherosclerosis. A report from the Committee on Vascular Lesions of the Council on Arteriosclerosis, American Heart Association. Circulation 1995;92:1355–1374
2. Stary HC. Natural history and histological classification of atherosclerotic lesions: an update. Arterioscler Thromb Vasc Biol 2000;20:1177–1178
3. Virmani R, Kolodgie FD, Burke AP, et al. Atherosclerotic plaque progression and vulnerability to rupture: angiogenesis as a source of intraplaque hemorrhage. Arterioscler Thromb Vasc Biol 2005;25(10):2054–2061 Epub 2005 Jul 21.
4. Virmani R, Burke AP, Farb A, Kolodgie FD. Pathology of the vulnerable plaque. J Am Coll Cardiol 2006; 47(8, Suppl)C13–C18
5. Stary HC. The sequence of cell and matrix changes in atherosclerotic lesions of coronary arteries in the first forty years of life. Eur Heart J 1990;11 Suppl E:3–19.
6. Glagov S, Bassiouny HS, Sakaguchi Y, Goudet CA, Vito RP. Mechanical determinants of plaque modeling, remodeling and disruption. Atherosclerosis 1997;131(Suppl):S13–S14
7. Ge J, Erbel R, Zamorano J, et al. Coronary artery remodeling in atherosclerotic disease: an intravascular ultrasonic study in vivo. Coron Artery Dis 1993;4:981–986
8. Gerber TC, Erbel R, Görge G, Ge J, Rupprecht HJ, Meyer J. Extent of atherosclerosis and remodeling of the left main coronary artery determined by intravascular ultrasound. Am J Cardiol 1994;73:666–671
9. Hibi K, Ward MR, Honda Y, et al. Impact of different definitions on the interpretation of coronary remodeling determined by intravascular ultrasound. Catheter Cardiovasc Interv 2005;65:233–239
10. Pasterkamp G, Wensing PJ, Post MJ, Hillen B, Mali WP, Borst C. Paradoxical arterial wall shrinkage may contribute to luminal narrowing of human atherosclerotic femoral arteries. Circulation 1995;91:1444–1449
11. Di Mario C, Görge G, Peters R, et al. Clinical application and image interpretation in intracoronary ultrasound. Study Group on Intracoronary Imaging of the Working Group of Coronary Circulation and of the Subgroup on Intravascular Ultrasound of the Working Group of Echocardiography of the European Society of Cardiology. Eur Heart J 1998;19:207–229
12. Gerber TC, Erbel R, Görge G, Ge J, Rupprecht HJ, Meyer J. Classification of morphologic effects of percutaneous transluminal coronary angioplasty assessed by intravascular ultrasound. Am J Cardiol 1992;70: 1546–1554
13. Erbel R. The dawn of a new era–non-invasive coronary imaging. Herz 1996;21:75–77
14. Falk E, Shah PK, Fuster V. Coronary plaque disruption. Circulation 1995;92:657–671
15. Kubo T, Imanishi T, Takarada S, et al. Assessment of culprit lesion morphology in acute myocardial infarction: ability of optical coherence tomography compared with intravascular ultrasound and coronary angioscopy. Jam Coll Cardiol 2007 Sep 4;50(10):933–939. Epub 2007 Aug 20

16. Ge J, Chirillo F, Schwedtmann J, et al. Screening of ruptured plaques in patients with coronary artery disease by intravascular ultrasound. Heart 1999;81:621–627
17. Gyöngyösi M, Strehblow C, Haumer M, et al. Vascular remodeling in atherosclerotic femoral arteries: three-dimensional US analysis. Radiology 2004;233:366–375
18. Erbel R, Möhlenkamp S, Kerkhoff G, Budde T, Schmermund A. Non-invasive screening for coronary artery disease: calcium scoring. Heart 2007;93:1620–1629
19. Schmid M, Pflederer T, Jang IK, et al. Relationship between degree of remodeling and CT attenuation of plaque in coronary atherosclerotic lesions: An in-vivo analysis by multi-detector computed tomography. Atherosclerosis 2008;197(1):457–564 Epub 2007 Aug 29
20. Ferencik M, Nieman K, Achenbach S. Noncalcified and calcified coronary plaque detection by contrast-enhanced multi-detector computed tomography: a study of interobserver agreement. J Am Coll Cardiol 2006;47:207–209
21. Pohle K, Ropers D, Geitner P, Regenfus M, Daniel WG, Achenbach S. Analysis of coronary calcifications versus Framingham and PROCAM risk assessment in patients with a first myocardial infarction. Int J Cardiol 2006;110:231–236
22. Ambrose JA, Winters SL, Arora RR, et al. Coronary angiographic morphology in myocardial infarction: a link between the pathogenesis of unstable angina and myocardial infarction. J Am Coll Cardiol 1985;6:1233–1238
23. Erbel R, Ge J, Görge G, et al. Intravascular ultrasound classification of atherosclerotic lesions according to American Heart Association recommendation. Coron Artery Dis 1999;10:489–499
24. Schaar JA, Muller JE, Falk E, et al. Terminology for high-risk and vulnerable coronary artery plaques. Report of a meeting on the vulnerable plaque, June 17 and 18, 2003, Santorini, Greece. Eur Heart J 2004; 25:1077–1082
25. Burke AP, Joner M, Virmani R. IVUS-VH: a predictor of plaque morphology? Eur Heart J 2006;27:1889–1890
26. Komatsu S, Sato Y, Ueda Y, et al. Thrombotic occlusion proximal to plaque rupture in acute myocardial infarction: evaluation by intravascular ultrasound and coronary angioscopy. Int J Cardiol 2007;123: e12–e14
27. Nasu K, Tsuchikane E, Katoh O, et al. Accuracy of in vivo coronary plaque morphology assessment: a validation study of in vivo virtual histology compared with in vitro histopathology. J Am Coll Cardiol 2006;47:2405–2412
28. Erbel R, Ge J, Bockisch A, et al. Value of intracoronary ultrasound and Doppler in the differentiation of angiographically normal coronary arteries: a prospective study in patients with angina pectoris. Eur Heart J 1996;17:880–889
29. Heusch G, Schulz R, Haude M, Erbel R. Coronary microembolization. J Mol Cell Cardiol 2004;37:23–31
30. Baumgart D, Liu F, Haude M, Görge G, Ge J, Erbel R. Acute plaque rupture and myocardial stunning in patient with normal coronary arteriography. Lancet 1995;346:193–194
31. Baumgart D, Haude M, Liu F, Ge J, Goerge G, Erbel R. Current concepts of coronary flow reserve for clinical decision making during cardiac catheterization. Am Heart J 1998;136:136–149
32. Leineweber K, Böse D, Vogelsang M, Haude M, Erbel R, Heusch G. Intense vasoconstriction in response to aspirate from stented saphenous vein aortocoronary bypass grafts. J Am Coll Cardiol 2006;47:981–986
33. Qian J, Ge J, Baumgart D, Sack S, Haude M, Erbel R. Prevalence of microvascular disease in patients with significant coronary artery disease. Herz 1999;24:548–557
34. Goldstein JA, Demetriou D, Grines CL, Pica M, Shoukfeh M, O'Neill WW. Multiple complex coronary plaques in patients with acute myocardial infarction. N Engl J Med 2000;343:915–922
35. Kolodgie FD, Virmani R, Burke AP, et al. Pathologic assessment of the vulnerable human coronary plaque. Heart 2004;90:1385–1391
36. Davies MJ, Thomas AC. Plaque fissuring–the cause of acute myocardial infarction, sudden ischaemic death, and crescendo angina. Br Heart J 1985;53:363–373
37. Hoffmann U, Moselewski F, Nieman K, et al. Noninvasive assessment of plaque morphology and composition in culprit and stable lesions in acute coronary syndrome and stable lesions in stable angina by multidetector computed tomography. J Am Coll Cardiol 2006;47:1655–1662
38. Komatsu S, Daniel WG, Achenbach S. Demonstration of clinically silent plaque rupture by dual-source computed tomography. Eur Heart J 2007;28:1667
39. De Backer G, Ambrosioni E, Borch-Johnsen K, et al; Third Joint Task Force of European and Other Societies on Cardiovascular Disease Prevention in Clinical Practice. European guidelines on cardiovascular disease prevention in clinical practice. Eur Heart J 2003;24:1601–1610
40. Möhlenkamp S, Lehmann N, Schmermund A, et al. Prognostic value of extensive coronary calcium quantities in symptomatic males–a 5-year follow-up study. Eur Heart J 2003;24:845–854
41. Shaw LJ, Raggi P, Schisterman E, Berman DS, Callister TQ. Prognostic value of cardiac risk factors and coronary artery calcium screening for all-cause mortality. Radiology 2003;228:826–833
42. Achenbach S, Nomayo A, Couturier G, et al. Relation between coronary calcium and 10-year risk scores in primary prevention patients. Am J Cardiol 2003;92:1471–1475
43. Schmermund A, Erbel R. New concepts of primary prevention require rethinking. Med Klin 2001;96:261–269
44. Wilson PW, Nam BH, Pencina M, D'Agostino RB Sr, Benjamin EJ, O'Donnell CJ. C-reactive protein and risk of cardiovascular disease in men and women from the Framingham Heart Study. Arch Intern Med 2005;165:2473–2478
45. Schmermund A, Möhlenkamp S, Stang A, et al. Assessment of clinically silent atherosclerotic disease and established and novel risk factors for predicting myocardial infarction and cardiac death in healthy middle-aged subjects: rationale and design of the Heinz Nixdorf RECALL Study. Risk Factors, Evaluation of Coronary Calcium and Lifestyle. Am Heart J 2002;144:212–218
46. Schmermund A, Möhlenkamp S, Berenbein S, et al. Population-based assessment of subclinical coronary atherosclerosis using electron-beam computed tomography. Atherosclerosis 2006;185:177–182
47. Erbel R, Möhlenkamp S, Lehmann N, et al; on behalf of the Heinz Nixdorf Recall Study Investigative Group. Sex related cardiovascular risk stratification based on quantification of atherosclerosis and inflammation. Atherosclerosis 2008;197:662–672 Epub 2007 Mar 26.
48. Lenfant C. Shattuck lecture–clinical research to clinical practice–lost in translation? N Engl J Med 2003;349:868–874
49. Yusuf S, Hawken S, Ounpuu S, et al. Effect of potentially modifiable risk factors associated with myocardial infarction in 52 countries (the INTERHEART study): case-control study. Lancet 2004;364:937–952
50. Horstick G, Petersen SE, Voigtlander T, Mohrs OK, Schreiber WG, Kreitner K-F. Kardio-MRT. Die multimodale Funktionsanalyse der Zukunft. Z Kardiol 2004;93(Suppl 4):IV36–IV47
51. Silber S, Albertsson P, Aviles FF, et al. Guidelines for percutaneous coronary interventions. The Task Force for Percutaneous Coronary Interventions of the European Society of Cardiology. Eur Heart J 2005;26: 804–847
52. Braunwald E, Kloner RA. The stunned myocardium: prolonged, postischemic ventricular dysfunction. Circulation 1982;66:1146–1149
53. Heusch G. Hibernating myocardium. Physiol Rev 1998;78:1055–1085
54. Rahimtoola SH. The hibernating myocardium. Am Heart J 1989;117: 211–221
55. Murry CE, Jennings RB, Reimer KA. Preconditioning with ischemia: a delay of lethal cell injury in ischemic myocardium. Circulation 1986;74:1124–1136
56. Horstick G, Heimann A, Gotze O, et al. Intracoronary application of C1 esterase inhibitor improves cardiac function and reduces myocardial necrosis in an experimental model of ischemia and reperfusion. Circulation 1997;95:701–708
57. Kloner RA. Does reperfusion injury exist in humans? J Am Coll Cardiol 1993;21:537–545
58. Al-Saadi N, Nagel E, Gross M, et al. Noninvasive detection of myocardial ischemia from perfusion reserve based on cardiovascular magnetic resonance. Circulation 2000;101:1379–1383
59. Jerosch-Herold M, Wilke N, Stillman AE. Magnetic resonance quantification of the myocardial perfusion reserve with a Fermi function model for constrained deconvolution. Med Phys 1998;25:73–84
60. Schmitt M, Horstick G, Petersen SE, et al. Quantification of resting myocardial blood flow in a pig model of acute ischemia based on first-pass MRI. Magn Reson Med 2005;53:1223–1227
61. Schwitter J, Nanz D, Kneifel S, et al. Assessment of myocardial perfusion in coronary artery disease by magnetic resonance: a comparison with positron emission tomography and coronary angiography. Circulation 2001;103:2230–2235
62. Wagner A, Mahrholdt H, Holly TA, et al. Contrast-enhanced MRI and routine single photon emission computed tomography (SPECT) perfusion imaging for detection of subendocardial myocardial infarcts: an imaging study. Lancet 2003;361:374–379

63. Wu KC, Zerhouni EA, Judd RM, et al. Prognostic significance of microvascular obstruction by magnetic resonance imaging in patients with acute myocardial infarction. Circulation 1998;97:765–772
64. Maxwell MP, Hearse DJ, Yellon DM. Species variation in the coronary collateral circulation during regional myocardial ischaemia: a critical determinant of the rate of evolution and extent of myocardial infarction. Cardiovasc Res 1987;21:737–746
65. Schaper W, Binz K, Sass S, Winkler B. Influence of collateral blood flow and of variations in MVO2 on tissue-ATP content in ischemic and infarcted myocardium. J Mol Cell Cardiol 1987;19:19–37
66. Opie LH. Cardiac metabolism–emergence, decline, and resurgence. Part I. Cardiovasc Res. 1992;26:721–733
67. Hoffmann R, von Bardeleben S, Kasprzak JD, et al. Analysis of regional left ventricular function by cineventriculography, cardiac Magnetic Resonance Imaging, and unenhanced and contrast-enhanced echocardiography. A multicenter comparison of methods. J Am Coll Cardiol 2006;47:121–128
68. Hearse DJ, Humphrey SM, Nayler WG, Slade A, Border D. Ultrastructural damage associated with reoxygenation of the anoxic myocardium. J Mol Cell Cardiol 1975;7:315–324
69. Petersen SE, Horstick G, Voigtlander T, et al. Diagnostic value of routine clinical parameters in acute myocardial infarction: a comparison to delayed contrast enhanced magnetic resonance imaging. Delayed enhancement and routine clinical parameters after myocardial infarction. Int J Cardiovasc Imaging 2003;19:409–416
70. Petersen SE, Voigtlander T, Kreitner KF, et al. Late improvement of regional wall motion after the subacute phase of myocardial infarction treated by acute PTCA in a 6-month follow-up. J Cardiovasc Magn Reson 2003;5:487–495
71. Piper HM, Garcia-Dorado D, Ovize M. A fresh look at reperfusion injury. Cardiovasc Res 1998;38:291–300
72. Kim RJ, Judd RM, Chen EL, Fieno DS, Parrish TB, Lima JA. Relationship of elevated 23Na magnetic resonance image intensity to infarct size after acute reperfused myocardial infarction. Circulation 1999;100:185–192
73. Tranum-Jensen J, Janse MJ, Fiolet WT, Krieger WJ, D'Alnoncourt CN, Durrer D. Tissue osmolality, cell swelling, and reperfusion in acute regional myocardial ischemia in the isolated porcine heart. Circ Res 1981;49:364–381
74. Kloner RA, Ganote CE, Jennings RB. The "no-reflow" phenomenon after temporary coronary occlusion in the dog. J Clin Invest 1974;54:1496–1508
75. Fishbein MC. J YR, Lando U, Kanmatsuse K, Mercier JC, Ganz W. The relationship of vascular injury and myocardial hemorrhage to necrosis after reperfusion. Circulation 1980;62:1274–1279
76. Rochitte CE, Lima JA, Bluemke DA, et al. Magnitude and time course of microvascular obstruction and tissue injury after acute myocardial infarction. Circulation 1998;98:1006–1014
77. Lefer AM, Campbell B, Scalia R, Lefer DJ. Synergism between platelets and neutrophils in provoking cardiac dysfunction after ischemia and reperfusion: role of selectins. Circulation 1998;98:1322–1328
78. Colman RW, Schmaier AH. Contact system: a vascular biology modulator with anticoagulant, profibrinolytic, antiadhesive, and proinflammatory attributes. Blood 1997;90:3819–3843
79. Horstick G, Berg O, Heimann A, et al. Application of C1-esterase inhibitor during reperfusion of ischemic myocardium: dose-related beneficial versus detrimental effects. Circulation 2001;104:3125–3131
80. Ku DD. Coronary vascular reactivity after acute myocardial ischemia. Science 1982;218:576–578
81. Rubanyi GM, Vanhoutte PM. Oxygen-derived free radicals, endothelium, and responsiveness of vascular smooth muscle. Am J Physiol 1986;250:H815–H821
82. Hale SL, Kloner RA. Left ventricular topographic alterations in the completely healed rat infarct caused by early and late coronary artery reperfusion. Am Heart J 1988;116:1508–1513
83. Ren G, Michael LH, Entman ML, Frangogiannis NG. Morphological characteristics of the microvasculature in healing myocardial infarcts. J Histochem Cytochem 2002;50:71–79
84. Laissy JP, Messin B, Varenne O, et al. MRI of acute myocarditis: a comprehensive approach based on various imaging sequences. Chest 2002; 122:1638–1648
85. Kim RJ, Wu E, Rafael A, et al. The use of contrast-enhanced magnetic resonance imaging to identify reversible myocardial dysfunction. N Engl J Med 2000;343:1445–1453
86. Mahrholdt H, Wagner A, Judd RM, Sechtem U. Assessment of myocardial viability by cardiovascular magnetic resonance imaging. Eur Heart J 2002;23:602–619
87. Petersen S, Mohrs O, Horstick G, et al. Influence of contrast agent dose and image acquisition timing on the quantitative determination of non-viable myocardial tissue using delayed contrast-enhanced magnetic resonance imaging. J Cardiovasc Magn Reson 2004;6:541–548
88. Choi KM, Kim RJ, Gubernikoff G, Vargas JD, Parker M, Judd RM. Transmural extent of acute myocardial infarction predicts long-term improvement in contractile function. Circulation 2001;104:1101–1107
89. Schmidt A, Azevedo CF, Cheng A, et al. Infarct tissue heterogeneity by Magnetic Resonance Imaging identifies enhanced cardiac arrhythmia susceptibility in patients with left ventricular dysfunction. Circulation 2007;115:2006–2014
90. Schmitt M, Mohrs OK, Petersen SE, et al. Bestimmung der myokardialen Perfusionsreserve bei KHK-Patienten mit der kontrastmittelverstärkten MRT: Ein Vergleich zwischen semiquantitativer und quantitativer Auswertung. Rofo 2002;174:187–195
91. Kroll K, Wilke N, Jerosch-Herold M, et al. Modeling regional myocardial flows from residue functions of an intravascular indicator. Am J Physiol 1996;271:H1643–H1655
92. Schreiber WG, Schmitt M, Kalden P, et al. MR-Perfusionsbildgebung mit TrueFisp. Rofo 2001;173:205–210
93. Panting JR, Gatehouse PD, Yang GZ, et al. Abnormal subendocardial perfusion in cardiac syndrome X detected by cardiovascular magnetic resonance imaging. N Engl J Med 2002;346:1948–1953
94. Voigtländer T, Kreitner KF, Wittlinger T, et al. MRA und Flussmessung in Koronararterien und koronaren Bypassgefäßen. Z Kardiol 2001;90: 929–938
95. Nagel E, Thouet T, Klein C, et al. Noninvasive determination of coronary blood flow velocity with cardiovascular magnetic resonance in patients after stent deployment. Circulation 2003;107:1738–1743
96. Cerqueira MD, Weissman NJ, Dilsizian V, et al. Standardized myocardial segmentation and nomenclature for tomographic imaging of the heart: a statement for healthcare professionals from the Cardiac Imaging Committee of the Council on Clinical Cardiology of the American Heart Association. Circulation 2002;105:539–542
97. Baer FM, Theissen P, Smolarz K, et al. [Dobutamine versus dipyridamole magnetic resonance tomography: safety and sensitivity in the detection of coronary stenoses] Z Kardiol 1993;82:494–503
98. Nagel E, Lehmkuhl HB, Bocksch W, et al. Noninvasive diagnosis of ischemia-induced wall motion abnormalities with the use of high-dose dobutamine stress MRI: comparison with dobutamine stress echocardiography. Circulation 1999;99:763–770
99. Nagel E, Lehmkuhl HB, Klein C, et al. [Influence of image quality on the diagnostic accuracy of dobutamine stress magnetic resonance imaging in comparison with dobutamine stress echocardiography for the noninvasive detection of myocardial ischemia] Z Kardiol 1999;88:622–630
100. Libby P, Theroux P. Pathophysiology of coronary artery disease. Circulation 2005;111:3481–3488
101. Rahimtoola SH. The hibernating myocardium. Am Heart J 1989;117: 211–221
102. Sklenar J, Ismail S, Villanueva FS, Goodman NC, Glasheen WP, Kaul S. Dobutamine echocardiography for determining the extent of myocardial salvage after reperfusion. An experimental evaluation. Circulation 1994;90:1502–1512
103. Mertes H, Erbel R, Nixdorff U, Mohr-Kahaly S, Kruger S, Meyer J. Exercise echocardiography for the evaluation of patients after nonsurgical coronary artery revascularization. J Am Coll Cardiol 1993;21:1087–1093
104. Mertes H, Sawada SG, Ryan T, et al. Symptoms, adverse effects, and complications associated with dobutamine stress echocardiography. Experience in 1118 patients. Circulation 1993;88:15–19
105. Bosch JG, Reiber JH, van Burken G, Savalle L, Maurincomme E, Helbing WA. Automated contour detection and acoustic quantification. Eur Heart J 1995;16(Suppl J):35–41
106. Voigt JU, Flachskampf FA. Strain and strain rate. New and clinically relevant echo parameters of regional myocardial function. Z Kardiol 2004; 93:249–258
107. Sieswerda GT, Kamp O, Visser CA. Myocardial contrast echocardiography: clinical benefit and practical issues. Echocardiography 2000;17: S25–S36
108. Cerqueira MD, Weissman NJ, Dilsizian V, et al. Standardized myocardial segmentation and nomenclature for tomographic imaging of the heart: a statement for healthcare professionals from the Cardiac Imaging Committee of the Council on Clinical Cardiology of the American Heart Association. Circulation 2002;105:539–542

109. Nagel E, Lehmkuhl HB, Bocksch W, et al. Noninvasive diagnosis of ischemia-induced wall motion abnormalities with the use of high-dose dobutamine stress MRI: comparison with dobutamine stress echocardiography. Circulation 1999;99:763–770
110. Hundley WG, Morgan TM, Neagle CM, Hamilton CA, Rerkpattanapipat P. Link KM. Magnetic resonance imaging determination of cardiac prognosis. Circulation 2002;106:2328–2333
111. Hunold P, Schlosser T, Barkhausen J. Magnetic resonance cardiac perfusion imaging- a clinical perspective. Eur Radiol 2006;16:1779–1788
112. Wilke NM, Jerosch-Herold M, Zenovich A, Stillman AE. Magnetic resonance first-pass myocardial perfusion imaging: clinical validation and future applications. J Magn Reson Imaging 1999;10:676–685
113. Cury RC, Cattani CA, Gabure LA, et al. Diagnostic performance of stress perfusion and delayed-enhancement MR imaging in patients with coronary artery disease. Radiology 2006;240:39–45
114. Paetsch I, Jahnke C, Wahl A, et al. Comparison of dobutamine stress magnetic resonance, adenosine stress magnetic resonance, and adenosine stress magnetic resonance perfusion. Circulation 2004;110:835–842
115. Baer FM, Theissen P, Schneider CA, et al. Dobutamine magnetic resonance imaging predicts contractile recovery of chronically dysfunctional myocardium after successful revascularization. J Am Coll Cardiol 1998;31:1040–1048
116. Wellnhofer E, Olariu A, Klein C, et al. Magnetic resonance low-dose dobutamine test is superior to scar quantification for the prediction of functional recovery. Circulation 2004;109:2172–2174
117. Underwood SR, Bax JJ, vom Dahl J, et al. Imaging techniques for the assessment of myocardial hibernation. Report of a Study Group of the European Society of Cardiology. Eur Heart J 2004;25:815–836
118. Lipton MJ, Bogaert J, Boxt LM, Reba RC. Imaging of ischemic heart disease. Eur Radiol 2002;12:1061–1080
119. Baer FM, Voth E, Schneider CA, Theissen P, Schicha H, Sechtem U. Comparison of low-dose dobutamine-gradient-echo magnetic resonance imaging and positron emission tomography with [18F]fluorodeoxyglucose in patients with chronic coronary artery disease. A functional and morphological approach to the detection of residual myocardial viability. Circulation 1995;91:1006–1015
120. Kim RJ, Wu E, Rafael A, et al. The use of contrast-enhanced magnetic resonance imaging to identify reversible myocardial dysfunction. N Engl J Med 2000;343:1445–1453
121. Hunold P, Schlosser T, Vogt FM, et al. Myocardial late enhancement in contrast-enhanced cardiac MRI: distinction between infarction scar and non-infarction-related disease. AJR Am J Roentgenol 2005;184: 1420–1426
122. Roes SD, Kelle S, Kaandorp TAM, et al. Comparison of myocardial infarct size assessed with contrast-enhanced Magnetic Resonance Imaging and left ventricular function and volumes to predict mortality in patients with healed myocardial infarction. Am J Cardiol 2007;100:930–936
123. Kwong RY, Chan AK, Brown KA, et al. Impact of unrecognized myocardial scar detected by cardiac Magnetic Resonance Imaging on event-free survival in patients presenting with signs or symptoms of coronoary artery disease. Circulation 2006;113:2733–2743
124. Hunold P, Brandt-Mainz K, Freudenberg L, et al. [Evaluation of myocardial viability with contrast-enhanced magnetic resonance imaging–comparison of the late enhancement technique with positronemission tomography] Rofo 2002;174:867–873
125. Klein C, Nekolla SG, Bengel FM, et al. Assessment of myocardial viability with contrast-enhanced magnetic resonance imaging: comparison with positron emission tomography. Circulation 2002;105:162–167
126. Wagner A, Mahrholdt H, Holly TA, et al. Contrast-enhanced MRI and routine single photon emission computed tomography (SPECT) perfusion imaging for detection of subendocardial myocardial infarcts: an imaging study. Lancet 2003;361:374–379
127. Kühl HP, Lipke CS, Krombach GA, et al. Assessment of reversible myocardial dysfunction in chronic ischaemic heart disease: comparison of contrast-enhanced cardiovascular magnetic resonance and a combined positron emission tomography—single photon emission computed tomography imaging protocol. Eur Heart J 2006;27:846–853
128. Selvanayagam JB. Imaging quantification of infarct size. Radiology 2006;239:613
129. Buck T, Schon F, Baumgart D, et al. Tomographic left ventricular volume determination in the presence of aneurysm by three-dimensional echocardiographic imaging. I: Asymmetric model hearts. J Am Soc Echocardiogr 1996;9:488–500
130. Barkhausen J, Hunold P, Eggebrecht H, et al. Detection and characterization of intracardiac thrombi on MR imaging. AJR Am J Roentgenol 2002;179:1539–1544
131. Erbel R, Ge J, Bockisch A, et al. Value of intracoronary ultrasound and Doppler in the differentiation of angiographically normal coronary arteries: a prospective study in patients with angina pectoris. Eur Heart J 1996;17:880–889
132. Berger PB, Alderman EL, Nadel A, Schaff HV. Frequency of early occlusion and stenosis in a left internal mammary artery to left anterior descending artery bypass graft after surgery through a median sternotomy on conventional bypass. Circulation 1999;100:2353–2358
133. Desch S, Schuler G, Niebauer J. Stent implantation or bypass? Current database in patients with stable coronary heart disease. [In German.] Dtsch Med Wochenschr 2005;130:402–407
134. Fischman DL, Leon MB, Baim DS, et al. A radomized comparison of coronary-stent placement and balloon angioplasty in the treatment of coronary artery disease. N Engl J Med 1994;331:496–501
135. Serruys PW, Unger F, Sousa E, et al. Comparison of coronary-artery bypass surgery and stenting for the treatment of multivessel disease. N Engl J Med 2001;344:1117–1124
136. Cameron A, Davis KB, Green G, Schaff HV. Coronary bypass surgery with internal-thoracic-artery-grafts: effects on survival over a 15-year period. N Engl J Med 1996;334:216–219
137. Fitzgibbon GM, Kafka HP, Leach AJ, Keon WJ. Coronary bypass fate and patient outcome: angiographic follow-up of 5,065 grafts related to 1,388 patients during 25 years. J Am Coll Cardiol 1996;28:616–626
138. Lytle BW, Sabik JF. Use of multiple arterial grafts and its effects on long-term outcome. Curr Opin Cardiol 2002;17:594–597
139. Vicol C, Raab S, Beyer M. Die total arterielle Myokardrevaskularisation – Strategie, kurz- und mittelfristige Ergebnisse. Z Kardiol 2003;92:222–228
140. Kreitner K-F, Ehrhard K, Kunz RP, et al. [Non-invasive assessment of coronary bypass grafts – an update] [In German.] Rofo 2004;176:1079–1088
141. Ropers D, Ulzheimer S, Wenkel E, et al. Investigation of aortocoronary artery bypass grafts by multislice spiral computed tomography with electrocardiographic gated image reconstruction. Am J Cardiol 2001; 88:792–795
142. Nieman K, Pattynama PMT, Rensing BJ, van Geuns R-JM, de Feyter PJ. Evaluation of patients after coronary artery bypass surgery: CT angiographic assessment of grafts and coronary arteries. Radiology 2003; 229:749–756
143. Anders K, Baum U, Schmid M, et al. Coronary artery bypass graft (CABG) patency: assessment with high-resolution submillimeter 16-slice multidetector-row computed tomography (MDCT) versus coronary angiography. Eur J Radiol 2006;57:336–344
144. Burgstahler C, Beck T, Kuettner A, et al. Non-invasive evaluation of coronary artery bypass grafts using 16-row multi-slice computed tomography with 188 ms temporal resolution. Int J Cardiol 2006;106:244–249
145. Chiurlia E, Menozzi M, Ratti C, Romagnoli R, Modena MG. Follow-up of coronary artery bypass graft patency by multislice computed tomography. Am J Cardiol 2005;95:1094–1097
146. Salm LP, Bax JJ, Jukema JW, et al. Comprehensive assessment of patients after coronary artery bypass grafting by 16-detector-row computed tomography. Am Heart J 2005;150:775–781
147. Schlosser T, Konorza T, Hunold P, Kühl H, Schmermund A, Barkhausen J. Noninvasive visualization of coronary artery bypass grafts using 16-detector row computed tomography. J Am Coll Cardiol 2004;44:1224–1229
148. Gurevitch J, Gaspar T, Orlov B, et al. Noninvasive evaluation of arterial grafts with newly released multidetector computed tomography. Ann Thorac Surg 2003;76:1523–1527
149. Dorgelo J, Willems TP, van Ooijen PMA, et al. A 16-slice multidetector computed tomography protocol for evaluation of the gastroepiploic artery grafts in patients after coronary artery bypass surgery. Eur Radiol 2005;15:1994–1999
150. Malagutti P, Nieman K, Meijboom WB, et al. Use of 64-slice CT in sympromatic patients after coronary bypass surgery: evaluation of grafts and coronary arteries. Eur Heart J 2007;28:1879–1885 Epub 2006 Jul 17
151. Meyer TS, Martinoff S, Hadamitzky M, et al. Improved noninvasice assessment of coronary artery bypass grafts with 64-slice computed tomographic angiography in an unselected patient population. J Am Coll Cardiol 2007;49:946–950

152. Pache G, Saueressig U, Frydrychowicz A, et al. Initial experience with 64-slice cardiac CT: non-invasive visualization of coronary artery bypass grafts. Eur Heart J 2006;27:976–980
153. Kreitner K-F, Sandstede J. [Cardiac CT: actual guidelines]translated title of German article]. ROEFO Fortschr Roentgenstr 2004;176:632–637
154. Kalden P, Kreitner K-F, Wittlinger T, et al. Assessment of coronary artery bypass grafts: value of different breath-hold MR imaging techniques. AJR Am J Roentgenol 1999;172:1359–1364
155. Kreitner K-F. [Analysis of first-pass bolus geometry in contrast-enhanced MRA of thoracic vessels]. Thesis, Mainz, 2001
156. Vrachliotis TG, Bis KG, Aliabadi D, Shetty AN, Safian R, Simonetti O. Contrast-enhanced breath-hold MR angiography for evaluating patency of coronary artery bypass grafts. AJR Am J Roentgenol 1997;168:1073–1080
157. Wintersperger BJ, Engelmann MG, v Smekal A, et al. Patency of coronary bypass grafts: assessment with breath-hold contrast-enhanced MR angiography – value of a non-electrocardiographically triggered technique. Radiology 1998;208:345–351
158. Langerak SE, Vliegen HW, de Roos A, et al. Detection of vein graft disease using high-resolution magnetic resonance angiography. Circulation 2002;105:328–333
159. Keegan J, Gatehouse PD, Mohiaddin RH, Yang G-Z, Firmin DN. Comparison of spiral and FLASH phase velocity mapping, with and without breath-holding, for the assessment of left and right coronary artery blood flow velocity. J Magn Reson Imaging 2004;19:40–49
160. Langerak SE, Kunz P, Vliegen HW, Jukema JW. Zwinderman, Steedijk P, Lamb HJ, v d Wall EE, de Roos A. MR flow mapping in coronary artery bypass grafts: a validiation study with Doppler flow measurements. Radiology 2002;222:127–135
161. Ishida N, Sakuma H, Cruz BP, et al. MR flow measurement in the internal mammary arteryto-coronary artery bypass graft: comparison with graft stenosis at radiographic angiography. Radiology 2001;220:441–447
162. Langerak SE, Vliegen HW, Jukema JW, Kunz P, Zwinderman AH, Lamb HJ. v d Wall EE, de Roos A. Value of magnetic resonance imaging for the noninvasive detection of stenosis in coronary artery bypass grafts and recipient coronary arteries. Circulation 2003;107:1502–1508
163. Langerak SE. Kunz P, Vliegen HW, Lamb HJ, Jukema JW, v d Wall EE, de Roos A. Improved MR flow mapping in coronary artery bypass grafts during adenosine-induced stress. Radiology 2001;218:540–547
164. Stauder NI, Stauder H, Fenchel M, et al. MR-Angiographie und Flussreservenbestimmung nach minimalinvasiver direkter Koronararterien-Bypass (MIDCAB)-Operation der linken Arteria mammaria interna im Vergleich zur Mehrzeilen-CT. Rofo 2005;177:1094–1102
165. Bruckenberger E. Herzbericht 2005 mit Transplantationschirurgie. 18. Bericht. Sektorenübergreifende Gesundheitsberichterstattung zur Kardiologie und Herzchirurgie in Deutschland, Hannover 2006
166. Moses JW, Leon MB, Popma JJ, et al. Sirolimus-eluting stents versus standard stents in patients with stenosis in a native coronary artery. N Engl J Med 2003;349:1315–1323
167. Stone GW, Ellis SG, Cox DA, et al. A polymer-based paclitaxel-eluting stent in patients with coronary artery disease. N Engl J Med 2004; 350:221–231
168. Cademartiri F, Marano R, Runza G, et al. Non-invasive assessment of coronary artery stent patency with multislice CT: preliminary experience. Radiol Med (Torino) 2005;109:500–507
169. Gilard M, Cornily JC, Rioufol G, et al. Noninvasive assessment of left main coronary stent patency with 16-slice computed tomography. Am J Cardiol 2005;95:110–112
170. Kitagawa T, Fujii T, Tomohiro Y, et al. Noninvasive assessment of coronary stents in patients by 16-slice computed tomography. Int J Cardiol 2005;109:188–194. Epub 2005 Jul 14
171. Mahnken AH, Seyfarth T, Flohr T, et al. Flat-panel detector computed tomography for the assessment of coronary artery stents.Phantom study in comparison with 16-slice spiral computed tomography. Invest Radiol 2005;40:8–13
172. Maintz D, Seifarth H. Raupach r, Flohr T, Rink M, Sommer T, Ozgun M, Heindel W, Fischbach R. 64-slice multidetector coronary CT angiography: in vitro evaluation of 68 different stents. Eur Radiol 2006;16:818–826
173. Seifarth H, Raupach R, Schaller S, et al. Assessment of coronary artery stents using 16-slice MDCT angiography: evaluation of a dedicated reconstruction kernel and a noise reduction filter. Eur Radiol 2005;15:721–726
174. Lind AY, Eggebrecht H, Erbel R. The invisible stent: imaging of an absorbable metal stent mith multislice computed tomography. Heart 2005;91:1604
175. Kreitner K-F, Sandstede J. [Magnetic resonance imaging of the heart: actual guidelines]. [In German.] ROEFO Fortschr Roentgenstr 2004; 176:1185–1193
176. Naghavi M, Falk E, Hecht HS, et al; SHAPE Task Force. From vulnerable plaque to vulnerable patient–Part III: Executive summary of the Screening for Heart Attack Prevention and Education (SHAPE) Task Force report. Am J Cardiol 2006;98:2H–15H
177. Assmann G, Cullen P, Schulte H. Simple scoring scheme for calculating the risk of acute coronary events based on the 10-year follow-up of the prospective cardiovascular Münster (PROCAM) study. Circulation 2002;105:310–315
178. Budoff MJ, Achenbach S, Blumenthal RS, et al. American Heart Association Committee on Cardiovascular Imaging and Intervention. American Heart Association Council on Cardiovascular Radiology and Intervention; American Heart Association Committee on Cardiac Imaging, Council on Clinical Cardiology. Assessment of coronary artery disease by cardiac computed tomography: a scientific statement from the American Heart Association Committee on Cardiovascular Imaging and Intervention, Council on Cardiovascular Radiology and Intervention, and Committee on Cardiac Imaging, Council on Clinical Cardiology. Circulation 2006;114:1761–1791

Further Reading

Conroy RM, Pyörälä K, Fitzgerald AP, et al. SCORE project group. Estimation of ten-year risk of fatal cardiovascular disease in Europe: the SCORE project. Eur Heart J 2003;24:987–1003

Ge J, Liu F, Görge G, Haude M, Baumgart D, Erbel R. Angiographically 'silent' plaque in the left main coronary artery detected by intravascular ultrasound. Coron Artery Dis 1995;6:805–810

Greenland P, Lloyd-Jones D. Time to end the mixed–and often incorrect–messages about prevention and treatment of atherosclerotic cardiovascular disease. J Am Coll Cardiol 2007;50:2133–2135

Greenland P, Smith SC Jr, Grundy SM. Improving coronary heart disease risk assessment in asymptomatic people: role of traditional risk factors and noninvasive cardiovascular tests. Circulation 2001;104:1863–1867

Kannel WB. The Framingham Study: Its 50-year legacy and future promise. J Atheroscler Thromb 2000;6:60–66

Kuijpers D. Diagnosis of coronary artery disease with dobutamine-stress MRI. Eur Radiol 2005;15(Suppl 2):B48–B51

McCrohon JA, Lyne JC, Rahman SL, Lorenz CH, Underwood SR, Pennell DJ. Adjunctive role of cardiovascular magnetic resonance in the assessment of patients with inferior attenuation on myocardial perfusion SPECT. J Cardiovasc Magn Reson 2005;7:377–382

Nikolaou K, Knez A, Rist C, et al. Accuracy of 64-MDCT in the diagnosis of ischemic heart disease. Am J Roentgenol 2006;187:111–117

Sakuma H, Suzawa N, Ichikawa Y, et al. Diagnostic accuracy of stress first-pass contrast-enhanced myocardial perfusion MRI compared with stress myocardial perfusion scintigraphy. Am J Roentgenol 2005;185: 95–102

Schmermund A, Baumgart D, Görge G, et al. Coronary artery calcium in acute coronary syndromes: a comparative study of electron-beam computed tomography, coronary angiography, and intracoronary ultrasound in survivors of acute myocardial infarction and unstable angina. Circulation 1997;96:1461–1469

Schwitter J, Nanz D, Kneifel S, et al. Assessment of myocardial perfusion in coronary artery disease by magnetic resonance: a comparison with positron emission tomography and coronary angiography. Circulation 2001;103:2230–2235

Stary HC. Evolution and progression of atherosclerotic lesions in coronary arteries of children and young adults. Arteriosclerosis 1989; 9(1, Suppl) I19–I32

von Birgelen C, Mintz GS, de Vrey EA, et al. Atherosclerotic coronary lesions with inadequate compensatory enlargement have smaller plaque and vessel volumes: observations with three dimensional intravascular ultrasound in vivo. Heart 1998;79:137–142

9 Cardiomyopathies and Myocarditis

O. Bruder, R. Erbel, and K.-F. Kreitner

Cardiomyopathies

Cardiomyopathies are defined as **primary myocardial diseases** that are diagnosed after the exclusion of valvular, pericardial, and coronary causes. Typical clinical and hemodynamic features must additionally be present before a cardiomyopathy is diagnosed.[1]

Although coronary heart disease is still the leading cause of heart failure, the reported incidence of cardiomyopathies has been rising owing to improved diagnostic methods and heightened awareness.[2] The joint classification of the ISFC (International Society and Federation of Cardiology) and WHO (World Health Organization) defines cardiomyopathies as diseases of the myocardium that are associated with cardiac dysfunction.[3] Primary cardiomyopathies are classified into the following five groups (**Table 9.1**):

- *Dilated cardiomyopathy (DCM)*. Dilated cardiomyopathy is the most common form. It is characterized by dilatation and contraction abnormalities of the left ventricle and presents clinically as heart failure.
- *Hypertrophic cardiomyopathy (HCM)*. Systolic function in HCM is initially intact. The disease is characterized by left ventricular hypertrophy, which is frequently asymmetric and mainly involves the interventricular septum. A special form of HCM is hypertrophic obstructive cardiomyopathy (HOCM) with dynamic narrowing of the left ventricular outflow tract.
- *Restrictive cardiomyopathy (RCM)*. Relatively rare in industrialized western countries, RCM is characterized by an abnormality of left ventricular diastolic relaxation.
- *Arrhythmogenic right ventricular cardiomyopathy (ARVC)*. This is essentially a dysrhythmic condition that is best demonstrated by cardiac MRI.
- *Unclassified cardiomyopathies*. This category includes fibroelastosis and ventricular noncompaction.

Specific or secondary cardiomyopathies result from other cardiac or systemic diseases. Examples are hypertensive, ischemic, valvular, and inflammatory cardiomyopathy. They differ from the primary or idiopathic cardiomyopathies listed above, whose causes are not yet fully understood. Increasingly, however, researchers are describing genetic abnormalities, autoimmune disorders, and chronic forms of myocarditis that contribute to the etiological classification of these diseases (see **Table 1.10**).

Transthoracic echocardiography is the imaging procedure of first choice in cases with satisfactory conditions for ultrasound scanning. This widely available and cost-effective technique provides morphological and functional information on the cardiac chambers and valves that is crucial in narrowing the differential diagnosis. **Invasive coronary angiography** is still necessary for the definitive exclusion of coronary heart disease in patients with dilated cardiomyopathy. **Endomyocardial biopsy** is recommended in patients who have rapidly progressive heart failure and/or may require a change in treatment.

Owing to the delayed inflow and outflow kinetics of damaged ventricular myocardium and the increased distribution volume that is available for extracellular contrast agents, this tissue shows a further rise of T1-weighted signal intensity following the IV injection of gadolinium chelates. The best pulse sequences for this application are segmented gradient-echo sequences with an inversion-recovery prepulse to null the signal of normal myocardium. In delayed images acquired after contrast administration, viable, healthy myocardium shows low signal intensity whereas damaged myocardium shows high signal intensity. This technique, called delayed-enhancement imaging, can detect myocardial damage due to acute and chronic infarction, inflammatory necrosis, and myocardial fibrosis with a spatial resolution superior to all other imaging techniques.[4,5]

Dilated Cardiomyopathy

Epidemiology, Pathophysiology, and Clinical Features

Dilated cardiomyopathies (DCMs) are characterized by **pronounced dilatation of the left ventricle** with **impaired systolic and diastolic function**.

In many cases the right ventricle is also enlarged and functionally impaired. The rare cases in which systolic dysfunction is accompanied by only minimal enlargement of the left ventricle are placed in the category of unclassified cardiomyopathies.

Table 9.1 WHO classification of cardiomyopathies (after Richardson et al., 1996[3])

Main types	• Dilated cardiomyopathy • Hypertrophic cardiomyopathy • Restrictive cardiomyopathy • Arrhythmogenic right ventricular cardiomyopathy • Unclassified cardiomyopathies
Specific cardiomyopathies	• Ischemic cardiomyopathy • Valvular cardiomyopathy • Hypertensive cardiomyopathy • Inflammatory cardiomyopathy • Metabolic cardiomyopathy • Cardiomyopathy in muscular dystrophy • Cardiomyopathy in neuromuscular disorders • Toxic cardiomyopathy • Cardiomyopathy in pregnancy

The **incidence** of DCM is five to eight cases per 100 000 population per year, although this figure does not take into account mild, asymptomatic cases that go unreported. DCM is a common incidental finding in screening examinations.[6] Aside from occasional spontaneous recoveries, DCM in symptomatic patients pursues a chronic progressive course with an annual mortality rate of 11–13 %[2]

Left ventricular dilatation and dysfunction, right ventricular involvement, and maximum oxygen consumption during spiroergometric exercise correlate with the prognosis. Most **secondary cardiomyopathies** (toxic, metabolic, inflammatory, etc.) present functionally as DCM. One example is cardiac hemochromatosis. Hemochromatosis is characterized by an iron overload in parenchymal organs (liver, pancreas, spleen, gonads). The degree of cardiac involvement is highly variable and does not correlate with the involvement of other organs. The cytotoxic effects of iron lead to progressive left ventricular dilatation and dysfunction, which is reversible in response to treatment. Cardiac MRI is particularly useful because the iron overload directly affects magnetic resonance imaging and is easily identified by an early loss of signal intensity in T2-weighted sequences.

The cause remains unclear in over half of patients with DCM. Classified as idiopathic, these cases are attributed to genetic factors, viral myocarditis, and autoimmune mechanisms. For example, genetic mutations with a predominantly autosomal dominant inheritance and very heterogeneous changes in the myocyte cytoskeleton and contractile proteins are found in 25–30 %of patients with dilated cardiomyopathy.[7]

Histological examination reveals pronounced interstitial and perivascular fibrotic changes that occur predominantly in the subendocardium. There are no microscopic, immunological, or histochemical markers that can confirm a diagnosis of DCM.

Imaging

DCM is often noted incidentally on **chest radiographs** (see p. 22). The imaging procedure of choice for initial diagnosis and follow-up is **echocardiography** (**Fig. 9.1**). **Transthoracic echocardiography** is used to assess the size and function of the ventricles and exclude associated valvular and pericardial diseases.

Typical echocardiographic features of DCM are as follows:

- Spherical dilatation of the left ventricle with a normal wall thickness. *Note:* The increased diameter of the left ventricle may still be within normal limits by M-mode echocardiography in the early stage of DCM.
- Enlarged left ventricular outflow tract with increased E-point septal separation (EPSS). That is, the distance between the septum and anterior mitral valve leaflet in early diastole is increased on M-mode examination (normal ≤7 mm).
- Loss of "square wave" opening and premature closure of the aortic valve on M-mode echocardiography in advanced stages.
- Left ventricular systolic dysfunction (global reduction of inward systolic motion and wall thickening) with a decreased ejection fraction.

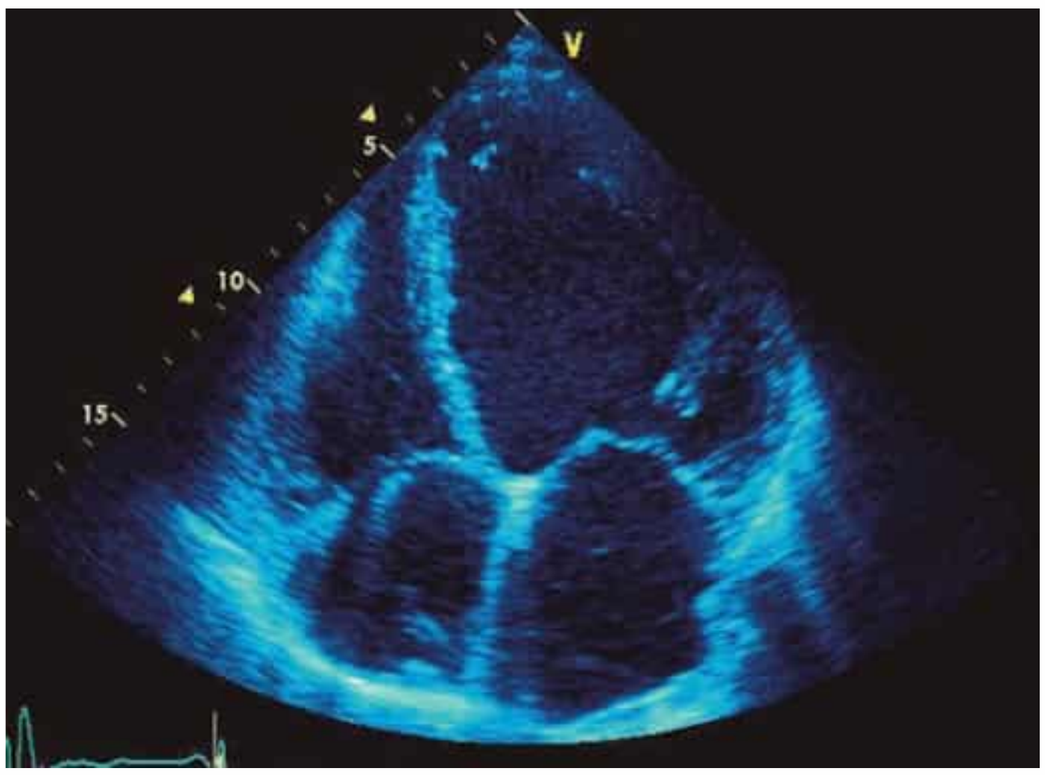

Fig. 9.1 Echocardiography. End-diastolic four-chamber view of a spherically dilated left ventricle in DCM.

- Diastolic dysfunction is another feature of DCM and may range from delayed relaxation to a restrictive filling pattern with a poor prognosis.
- A good parameter for the follow-up of ventricular function is the time ejection index (TEI), or myocardial performance index (MPI), which is determined from the pulsed Doppler waveform of the left ventricular outflow tract and mitral inflow. It is defined as the ratio of the sum of the isovolumetric relaxation and contraction times to the ejection time (normal <0.49).
- Incomplete coaptation of the mitral valve leaflets due to lateralization of the papillary muscles with central mitral valve regurgitation.
- Enlargement of the right ventricle and right atrium with tricuspid regurgitation is an echocardiographic feature of advanced DCM with a poor prognosis.
- Spontaneous echo contrast or left atrial/left ventricular thrombi.

Transthoracic echocardiography is useful in selecting patients with a left bundle branch block and DCM for resynchronization therapy with a biventricular pacemaker system. With its high temporal resolution, this study can supply critical information on the degree of inter- and intraventricular asynchrony. Analysis of myocardial contractions with tissue Doppler is an essential part of this examination.[8]

The following echocardiographic criteria are predictive of a positive response to biventricular pacemaker stimulation:

- Interventricular asynchrony: delay of 40 ms or more between left and right ventricular ejection, determined from the pulsed Doppler waveforms of the left and right ventricular outflow tracts in relation to the ECG.
- Intraventricular asynchrony: contraction delay of at least 130 ms between the anteroseptal and posterior segments on M-mode echocardiography.
- Subjective impression of a "swinging left ventricle" (blood shifting from one side of the ventricle to the other) on B-mode echocardiography (apical four-chamber view).

- More than a 60–80 ms delay between opposing left ventricular segments on tissue Doppler and strain rate imaging.

The advantages of **cardiac MRI** over echocardiography are improved delineation of the myocardium and ventricular cavity, especially in the apical and lateral wall regions of the left ventricle; improved visualization of the right ventricle; and good image quality regardless of patient constitution (**Fig. 9.2**).

With its ability to provide complete and reliable coverage of the left and right ventricles in contiguous short-axis slices, cardiac MRI is the modality of choice for the assessment of regional and global ventricular function. The accurate quantification of end-diastolic and end-systolic ventricular volumes, muscle mass, and ejection fraction on MRI using the Simpson method permits the optimum follow-up of even minor changes[9,10] like those described during treatment with growth hormones or ACE inhibitors.[11]

Ischemic cardiomyopathy is the leading cause of heart failure in elderly patients and the most important condition requiring differentiation from DCM.[6] The differentiation of ischemic and nonischemic cardiomyopathies generally relies on **invasive coronary angiography**. DCM is diagnosed by exclusion based on the absence of coronary stenoses on invasive imaging. The detection of coronary heart disease not only implies a poorer prognosis but also raises other therapeutic options such as interventional or surgical myocardial revascularization, aneurysmectomy, and specific pharmacological therapy with aspirin and statins.

Contrast-enhanced cardiac MRI is also useful in the differentiation of ischemic and nonischemic cardiomyopathies. Thus, areas of delayed enhancement due to an ischemic cause (postinfarction scars) are always subendocardial based on the distribution of myocardial perfusion, whereas delayed enhancement at a subepicardial or intramural site indicates fibrosis due to a nonischemic cause (**Fig. 9.3**).[12]

McCrohon et al. examined 90 patients with clinical signs of stable heart failure and left ventricular systolic dysfunction.[13] Twenty-seven patients were classified as having ischemic cardiomyopathy by angiography, and 63 were classified as having DCM. Subendocardial areas of delayed enhancement were found in all patients (100%) with coronary heart disease. Three patterns of delayed enhancement were found in the patients classified as DCM by angiography: no enhancement (59%), subendocardial enhancement matching the ischemic pattern (13%), or midventricular enhancement (28%). Thus, MRI goes beyond the capabilities of pure "luminography" in catheter angiography and identifies 13% of patients as having left ventricular dysfunction caused by CHD based on an infarction-type pattern of delayed enhancement. The pathogenic mechanism in these cases may be coronary recanalization after infarction

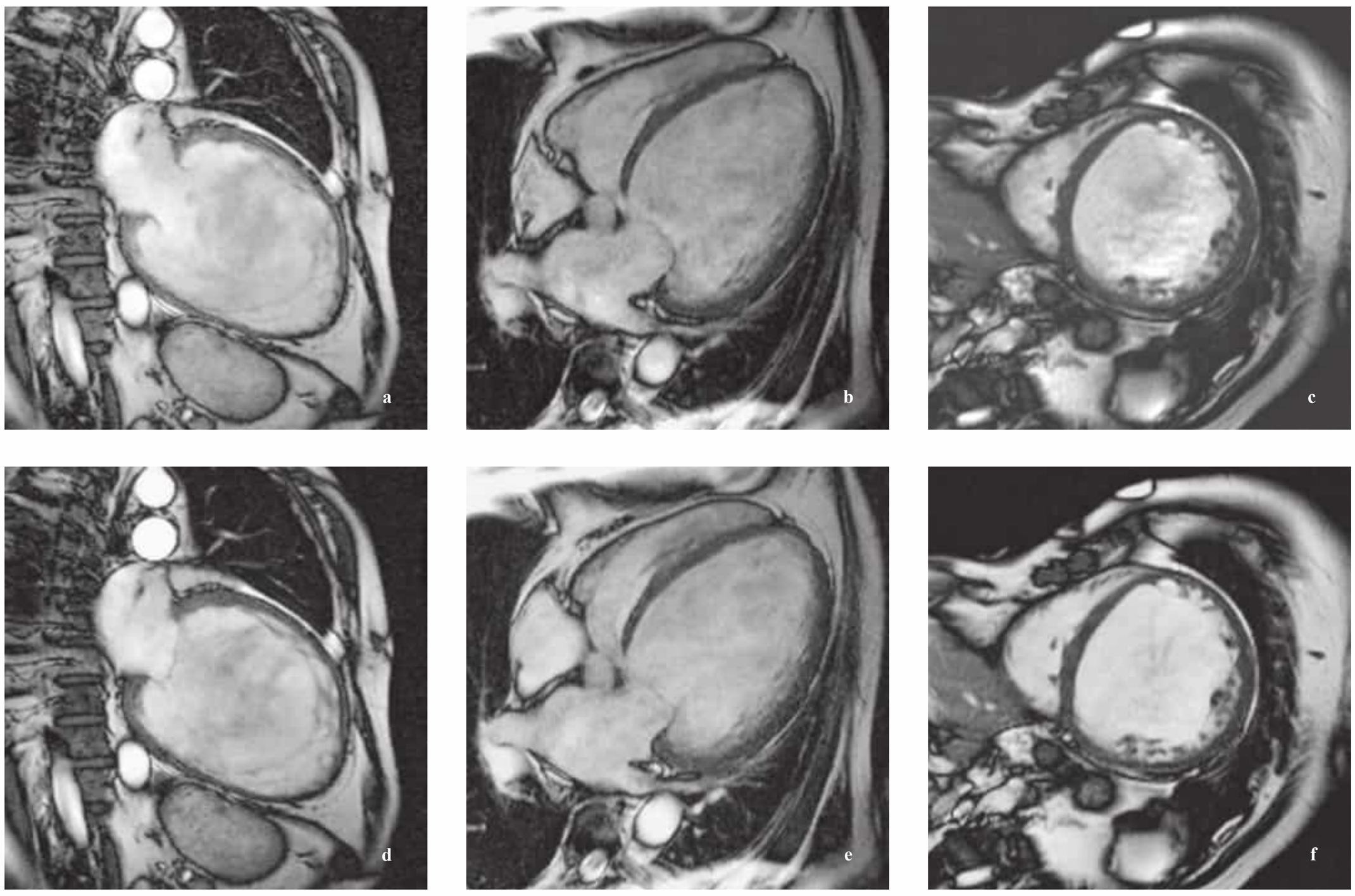

Fig. 9.2 a–f Massive left ventricular dilatation in DCM with an end-diastolic volume of 854 mL and a greatly reduced ejection fraction of 6.4%
a, d Vertical long-axis images in end diastole and end systole.
b, e Horizontal long-axis images in end diastole and end systole.
c, f Sagittal short-axis images in end diastole and end systole.

or coronary embolic events. Midventricular delayed enhancement or absence of delayed enhancement can classify patients with heart failure and left ventricular systolic dysfunction as DCM, probably without a need for invasive testing.

Apart from that, recent studies suggest that the presence and extent of delayed enhancement predict prognosis in DCM.[14]

Myocardial tagging with MRI can demonstrate ventricular asynchrony in patients with left bundle branch block. The detection of delayed-enhancing areas in the potential target area of the left ventricular electrode can explain the lack of response to resynchronization therapy in some patients.[15]

In summary, cardiac MRI can provide the following essential information in the routine clinical investigation of DCM:

- Accurate and reproducible ventricular geometry for optimum follow-up after medical or surgical treatment
- Exclusion of ischemic cardiomyopathy
- Detection and quantification of right ventricular involvement
- Detection of complications such as thrombus or pericardial effusion when echocardiography is unrewarding
- Detection of asynchrony prior to resynchronization therapy in patients with DCM and left bundle branch block (LBBB)

Essential Point

Typical features of DCM are left ventricular dilatation and dysfunction with a normal myocardial wall thickness.

Besides ECG findings of LBBB, it is important to detect inter- and intraventricular dyssynchrony by echocardiography.

MRI permits the accurate quantification of ventricular volumes during follow-up. Delayed-enhancement imaging can noninvasively differentiate between CHD and DCM as the cause of ventricular systolic dysfunction.

Hypertrophic Cardiomyopathy

Epidemiology, Pathophysiology, and Clinical Features

HCM is a **genetically transmitted myocardial disease** that has an autosomal dominant mode of inheritance in at least 50 % of cases and a prevalence of 1 : 500 in the general population.[1]

Various mutations of myocyte contractile proteins lead to compensatory hypertrophy, which is characterized histologically by an irregular array of hypertrophic myocytes, diffuse and focal areas of fibrosis, and abnormal intramural coronary arteries with thickened walls and reduced lumina.

HCM may present **clinically** with angina pectoris, exertional dyspnea, syncope, cardiac arrhythmias, and sudden cardiac death, which often occurs without premonitory signs. HCM is the most common sports-related cause of death in young athletes.[16]

Hypertrophic cardiomyopathy presents on clinical cardiac imaging with myocardial wall thickening, which is disproportionate in relation to the hemodynamic stress (e.g., aortic stenosis or arterial hypertension) of the left ventricle. Two types of HCM are distinguished—**hypertrophic obstructive cardiomyopathy (HOCM)** and **hypertrophic nonobstructive cardiomyopathy (HNCM)**—depending on whether there is dynamic obstruction of the left ventricular outflow tract.

The myocardial hypertrophy in HCM is usually asymmetrical and chiefly affects the interventricular septum and anterolateral free wall of the left ventricle. Approximately 30 % of patients have very circumscribed areas of hypertrophy in other left ventricular segments such as the apical region. Occasionally the right ventricle is also involved. In contrast to DCM, systolic left ventricular function is initially in the normal or even high-normal range. The left ventricle in HCM shows characteristic diastolic dysfunction due to the increased stiffness and impaired relaxation of the hypertrophic myocardium. Left ventricular dilatation and systolic dysfunction subsequently develop as the disease progresses. Impairment of left ventricular diastolic filling leads to marked enlargement and hypertrophy of the left atrium and frequently of the right atrium as well.

In ~25 % of patients with HCM, a dynamic gradient develops in the left ventricular outflow tract (HOCM). It occurs in midsystole as the anterior mitral valve leaflet moves closer to the thickened interventricular septum (Venturi effect). Typically, mitral regurgitation also occurs owing to the forward systolic motion of the anterior mitral valve leaflet.

Imaging

The imaging modality of first choice is **echocardiography**. Typical echocardiographic features of HCM are listed below.

- Asymmetrical septal hypertrophy. The ratio of end-diastolic septal thickness to the thickness of the opposing posterior wall is 1.3 : 1 or more (M-mode).

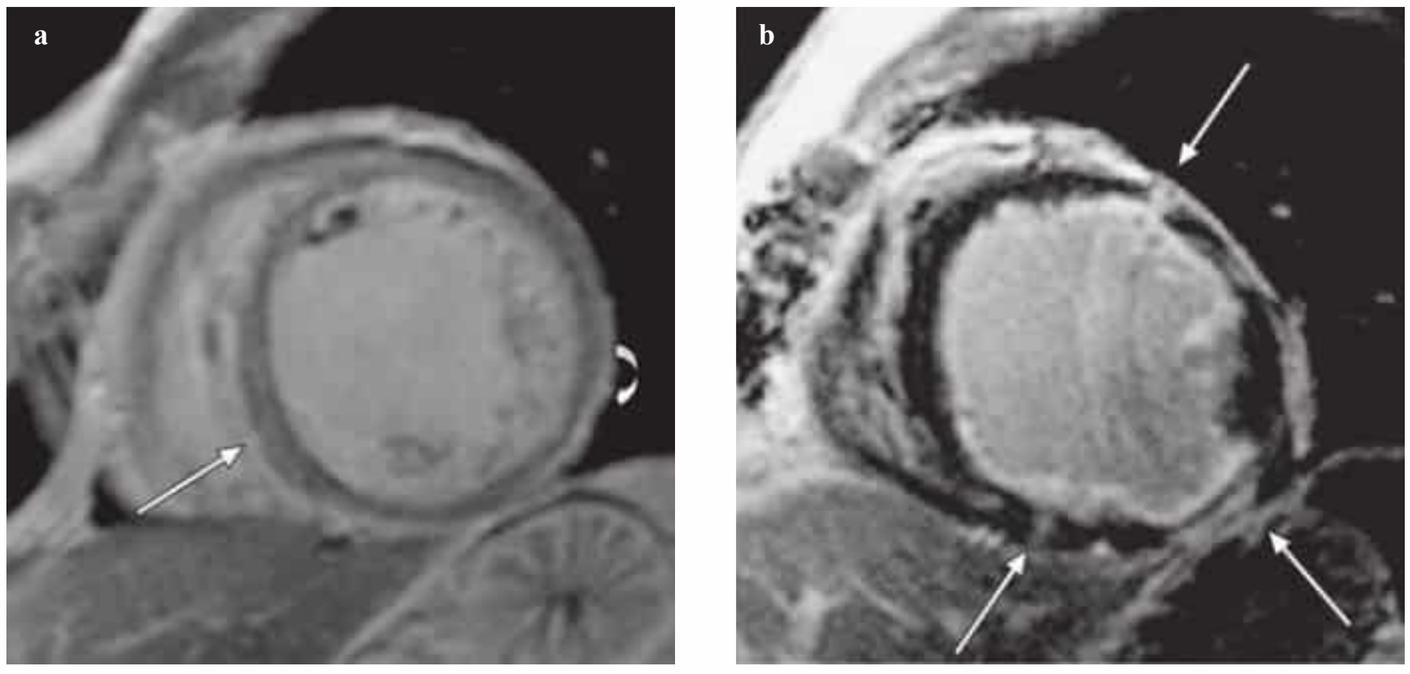

Fig. 9.3 a, b Different patterns of delayed enhancement in DCM and CHD.

a Streaks of midmyocardial (straight arrow) and subepicardial delayed enhancement (curved arrow) in a patient with DCM.

b Subendocardial delayed enhancement (arrows) in ischemic cardiomyopathy in a patient with three-vessel coronary disease.

- Banana-shaped left ventricle in the four-chamber view due to septal hypertrophy.
- Parasternal short-axis views show a smooth transition of left ventricular hypertrophy from maximum involvement in the anterior septum to minimally thickened or normal posterior segments.
- Systolic anterior motion (SAM) of the anterior mitral valve leaflet can usually be observed in 2D long-axis images (**Fig. 9.4**), but M-mode is best for detecting subtle changes and accurately demonstrating the time course, location (chordal, valvular), and degree of septal contact.
- Additional M-mode criteria are midsystolic notching and closure of the aortic valve, and flattened, decreased contraction of the hypertrophic ventricular septum.
- The location of a potential outflow tract obstruction is suggested in color Doppler by the distribution of the hypertrophy and turbulent systolic flow. Pulsed Doppler shows an abnormal increase in systolic flow velocities toward the aortic valve.
- CW Doppler measurements at rest and during stress (ergometry at 75 W, dobutamine) or provocative testing (Valsalva maneuver, nitroglycerin) can accurately quantify the dynamic obstruction of the left ventricular outflow tract. Pressure gradients in excess of 100 mmHg may be documented during stress. Dynamic obstruction of the left ventricular outflow tract (LVOT) typically produces a dagger-shaped signal with a late systolic peak in the CW Doppler waveform over the LVOT.
- Doppler spectra sampled from the outflow tract occasionally indicate presystolic flow, which is attributable to increased atrial contractions arising from left ventricular diastolic dysfunction.
- The systolic anterior motion of the anterior mitral valve leaflet leads to mitral regurgitation, which is detectable by Doppler and color Doppler scanning or by an abnormal position of the papillary muscles.

Rare variants of HCM include the apical form with circumscribed hypertrophy of the apical segments (spadelike appearance in the end-diastolic four-chamber view) and inverted T waves in the left precordial ECG leads. Another variant presents with concentric left ventricular hypertrophy and strictly midventricular obstruction.

The prognosis of HCM depends mainly on the magnitude of the pressure gradient in the left ventricular outflow tract.[17] It depends to a lesser degree on septal thickness and atrial size. Because left ventricular diastolic dysfunction is a dominant feature of HCM, it is important to evaluate the left ventricular inflow pattern across the mitral valve and/or in the left ventricle with **Doppler echocardiography**. Tissue Doppler findings are insensitive to preload and filling pressures. Tissue Doppler measurements of the myocardium close to the mitral annulus can detect diastolic dysfunction of the left ventricle in relatives of HCM patients even before measurable hypertrophy has developed.[18]

Cardiac MRI is superior to echocardiography for imaging the apical and anterolateral left ventricular segments and is the only modality that can detect atypical phenotypes of HCM with circumscribed hypertrophy of those segments (see **Fig. 9.8**).[19] Just as in DCM, cardiac MRI is ideal for the accurate determination and follow-up of volumetric data such as end-diastolic and end-systolic volumes, ejection fraction, and muscle mass. Thus, an important advantage of MRI is its ability to determine muscle mass and assess the distribution of hypertrophy in the segments of the left and right ventricles (**Fig. 9.5**). If echocardiography does not provide acceptable image quality, MRI can also demonstrate possible outflow tract obstruction in cine sequences and quantify them with phase-contrast techniques. Additionally, planimetry can be performed in cross-sectional images of the left ventricular outflow tract (**Fig. 9.6**).

On contrast-enhanced MRI, fibrotic foci in HCM appear as typical intramural streaks or patches of delayed enhancement located in hypertrophic myocardial segments, i.e., predomi-

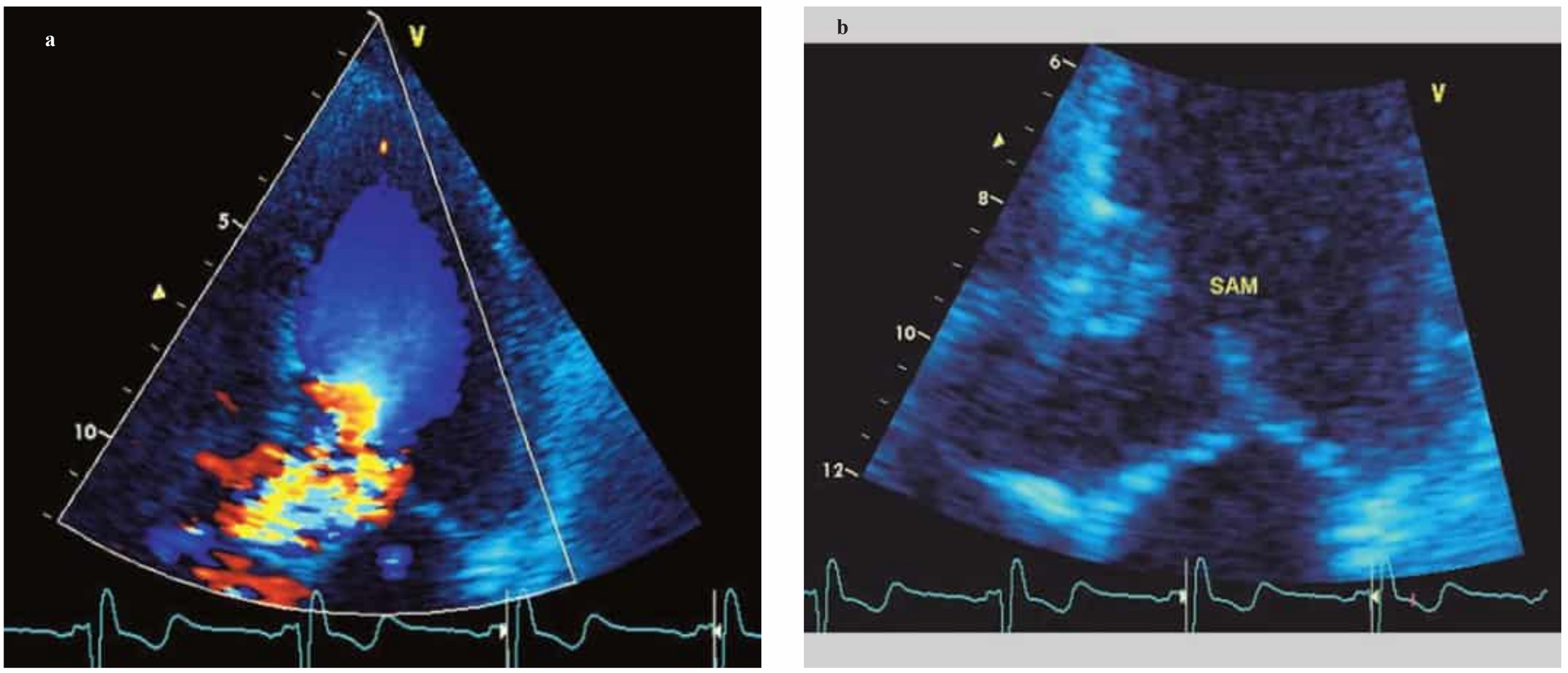

Fig. 9.4 a, b Hypertrophic obstructive cardiomyopathy. Turbulent flow acceleration (aliasing) in the left ventricular outflow tract (**a**) results from dynamic stenosis caused by systolic anterior motion (SAM) of the anterior mitral valve leaflet toward the septum (**b**).

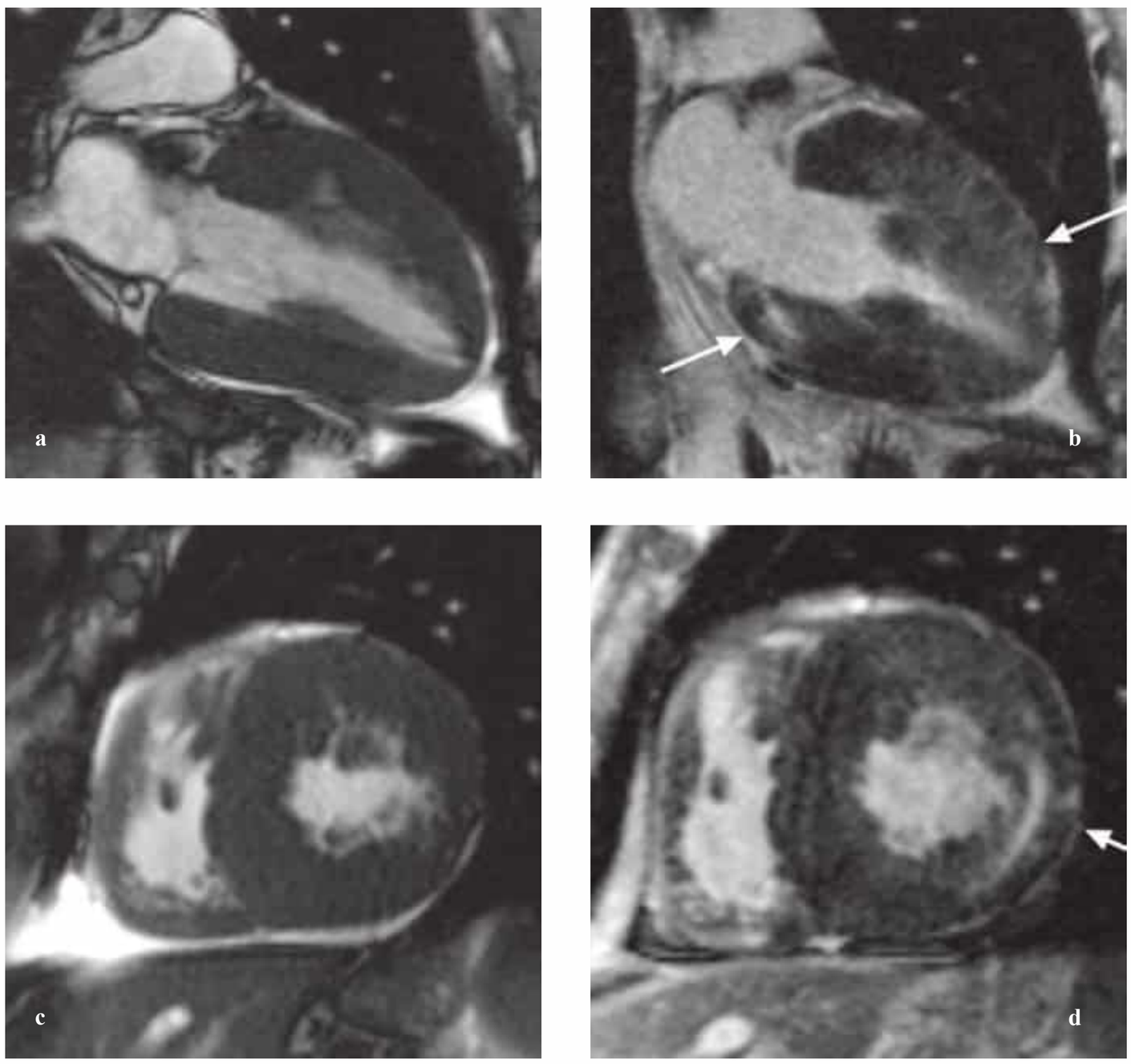

Fig. 9.5 a–d Hypertrophic cardiomyopathy with concentric left and right ventricular hypertrophy. Images after contrast administration (**b, d**) show both a striate pattern and a patchy, diffuse pattern of delayed enhancement consistent with myocardial fibrosis (arrows).
a, b Vertical long axis.
c, d Sagittal short axis.

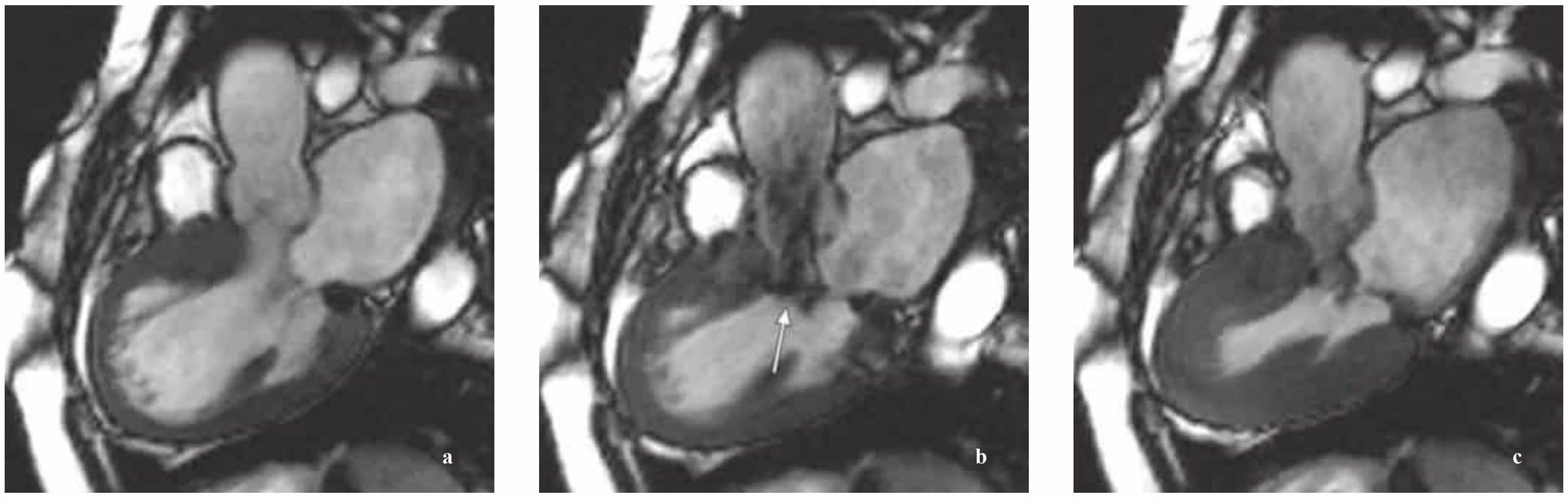

Fig. 9.6 a–c Hypertrophic obstructive cardiomyopathy (HOCM). Thickening of the basal septum (**a**) with systolic obstruction of the left ventricular outflow tract (**b, c**). A conspicuous jet (arrow) results from turbulent flow acceleration between the septum and anterior mitral valve leaflet during systole (**b**).

nantly in the septum.[20] Delayed enhancement in HCM correlates with clinical risk scores and appears to be an independent risk factor and marker for advanced disease (**Fig. 9.7**).

Delayed enhancement is also seen in iatrogenic myocardial necrosis following alcohol embolization or microembolization of a septal arterial branch—a procedure known as transcoronary ablation of septal hypertrophy (TASH).

Gross et al. investigated the cross-sectional area of the left ventricular outflow tract before and after TASH and described the precise anatomical location and extent of necrosis based on delayed-enhancement imaging.[21]

Essential Point

The echocardiographic diagnosis of HCM is based on unexplained left ventricular hypertrophy with initially normal systolic function.
Asymmetrical septal hypertrophy with dynamic obstruction (late systolic peak in CW Doppler) of the left ventricular outflow tract by systolic anterior motion of the mitral valve apparatus is the hallmark of HOCM, which presents clinically with a variable systolic murmur.
Cardiac MRI shows the exact distribution of hypertrophic wall segments and is useful in the detection of atypical forms like the apical and midventricular variants (**Fig. 9.8**). Postcontrast images show delayed enhancement in myocardial fibrosis and in iatrogenic necrosis following interventional septal ablation.

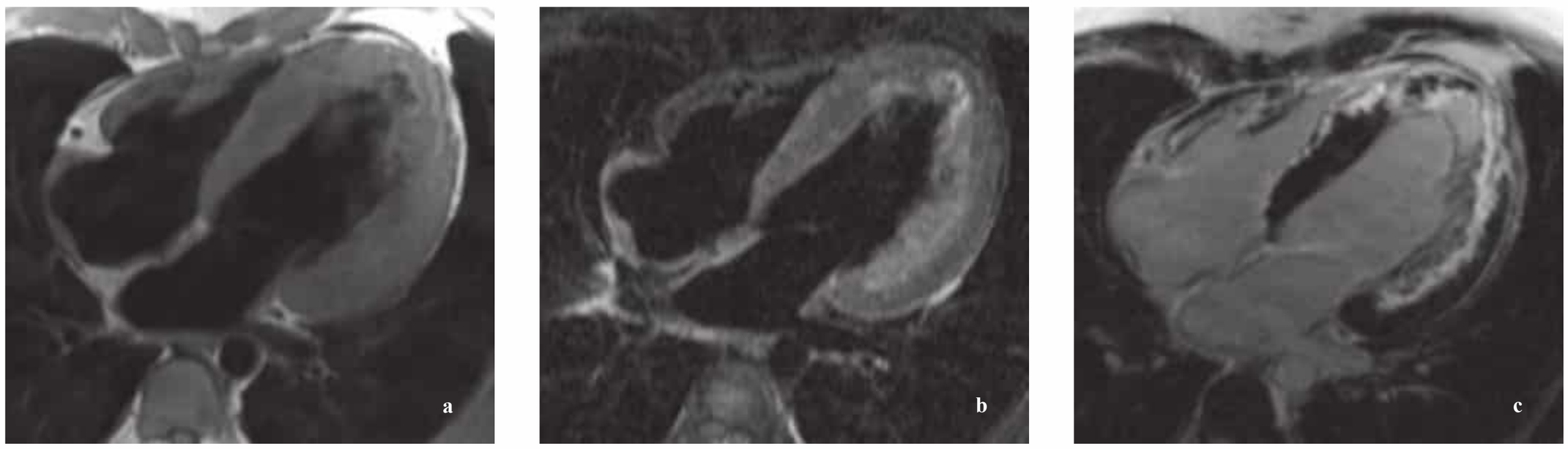

Fig. 9.7 a–c Hypertrophic cardiomyopathy (HCM) with extensive left ventricular involvement and more moderate right ventricular involvement.
a a T1-weighted TSE image.
b Fat-suppressed STIR image.
c Postcontrast image shows fibrosis predominantly involving the left ventricular myocardium and increased trabeculation of the lateral wall and apex.

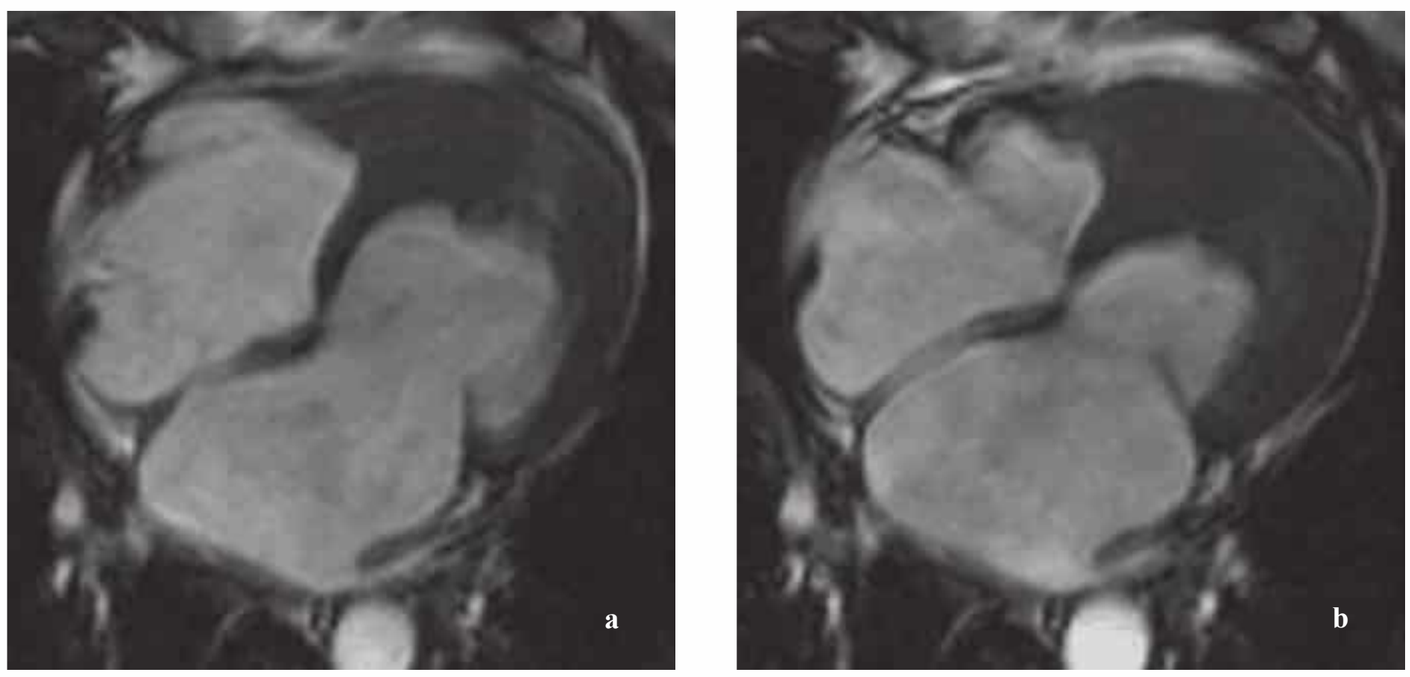

Fig. 9.8 a, b Apical variant of hypertrophic cardiomyopathy.
a End-diastolic four-chamber view.
b End-systolic four-chamber view.

Restrictive Cardiomyopathy

Restrictive cardiomyopathy (RCM) is characterized by **severe diastolic dysfunction** and **normal systolic function**. Generally both atria are greatly dilated, and there is a damming back of blood into the inferior vena cava and hepatic veins. The hemodynamic hallmark of the restrictive cardiomyopathies (RCMs) is an early diastolic pressure dip followed by a plateau in middle and late diastole, resulting in a "dip-and-plateau" or square-root contour of the ventricular pressure curve. RCM is rare in industrialized western countries compared with the dilated and hypertrophic forms.

The main **differential diagnosis** is constrictive pericarditis, which is curable by a relatively simple surgical procedure (pericardectomy). Constrictive pericarditis also presents with abnormal ventricular diastolic function and preservation of systolic function. The diastolic dysfunction is not caused by thickening and increased stiffness of the myocardium, however, but by a secondary compromise of vascular filling due to inflammatory thickening of the pericardium (see also Chapter 11).

Echocardiographic criteria for the differential diagnosis of diastolic dysfunction are as follows:

- Tissue Doppler shows a reduced annular contraction velocity (E_a <10 cm/s) in restrictive cardiomyopathy compared with a high-normal mitral annular velocity (E_a >20 cm/s) in constrictive pericarditis.
- Doppler waveform over the mitral valve shows increased (≥25 %) respiratory variations in the E wave in constrictive pericarditis.

Other reliable features are:

- Enlarged atria
- Pulmonary hypertension due to restriction
- Echogenic pericardial thickening due to constriction

Myocardial fibrosis, infiltration, or endomyocardial fibrosis are the basic pathophysiological processes involved in RCM. The causes of RCM are diverse (**Table 9.2**). Idiopathic RCM, amyloidosis, sarcoidosis, and endomyocardial fibrosis are the forms most commonly seen in routine clinical practice.

The **course** of RCM is usually and progressive with a high mortality. This particularly applies to the idiopathic variant, in which symptomatic treatment for heart failure is the only therapeutic option. In some secondary forms of RCM such as Anderson-Fabry disease and sarcoidosis, specific therapies (enzyme replacement, corticosteroids) are available that can significantly improve the prognosis.[22]

A typical imaging feature in all forms of RCM is **massive enlargement of both atria**. Transthoracic echocardiography is the imaging procedure of first choice for identifying diastolic dysfunction and classifying it as restrictive, the principal tools being tissue Doppler and analysis of the diastolic mitral inflow

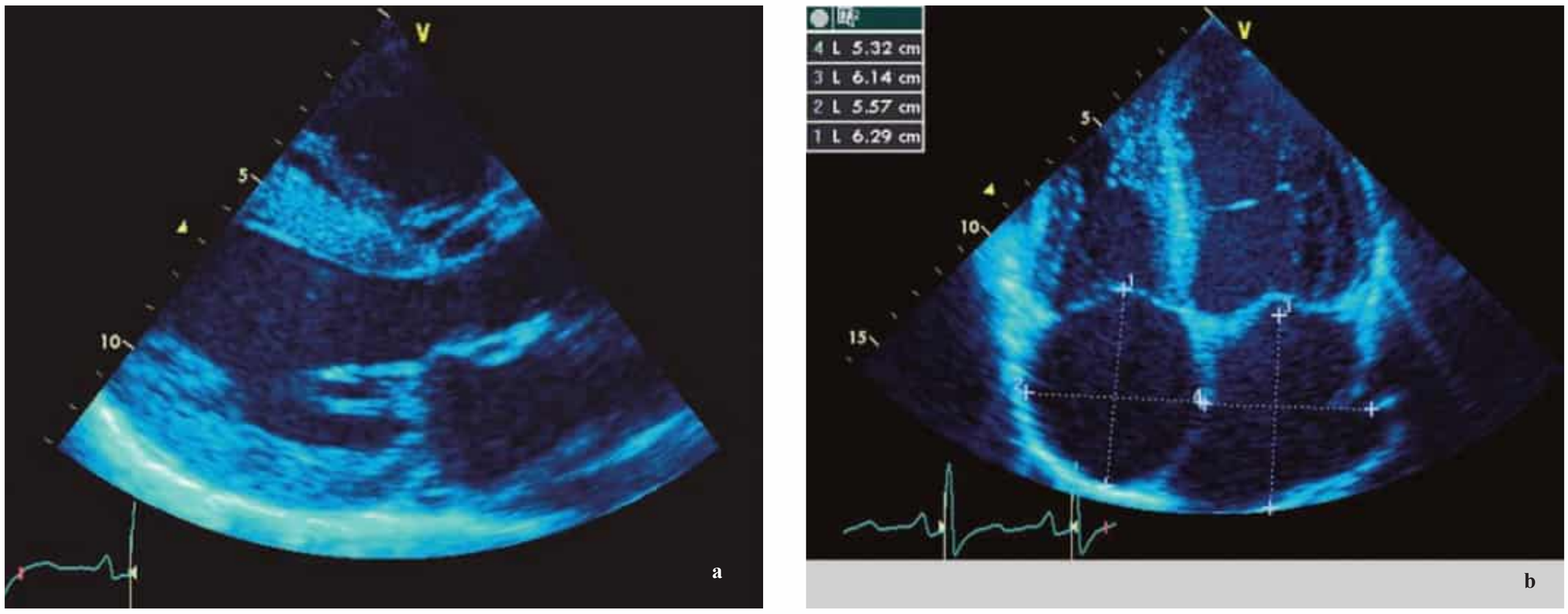

Fig. 9.9 a, b Restrictive cardiomyopathy in a woman with amyloidosis. Transthoracic echocardiography shows left ventricular hypertrophy, thickening of the mitral valve apparatus, and an abnormal myocardial texture.

a Parasternal long-axis view.
b Apical four-chamber view. Dilatation of both atria is also typical of restrictive cardiomyopathy.

Table 9.2 Causes of restrictive cardiomyopathies (RCM)

Noninfiltrative RCM	• Idiopathic cardiomyopathy • Familial cardiomyopathy • Hypertrophic cardiomyopathy • Scleroderma • Pseudoxanthoma elasticum • Diabetic cardiomyopathy
Infiltrative RCM	• Amyloidosis • Sarcoidosis • Gaucher disease • Hurler disease • Fatty infiltration
Storage diseases	• Hemochromatosis • Anderson–Fabry disease • Glycogen storage disease
Endomyocardial cardiomyopathy	• Endomyocardial fibrosis • Hypereosinophilic syndrome • Carcinoid syndrome • Cardiac metastases • Radiotherapy • Anthracyclines • Drug-induced fibrous endocarditis (serotonin, methysergide, ergotamine, busulfan)

waveform. Increasing hypertrophy is a typical feature of infiltrative RCM and storage diseases, which are also reliably diagnosed by echocardiography.

Typical examples of infiltrative cardiomyopathies are

- Cardiac **amyloidosis**
- Cardiac **sarcoidosis**

Amyloidosis

Cardiac involvement is generally present in primary amyloidosis and is the most frequent cause of death. By contrast, clinically significant cardiac involvement in secondary amyloidosis is rare.

Typical **echocardiographic** features of amyloidosis are as follows:

- Increasing left ventricular "hypertrophy" with normal-sized ventricles
- Low voltages in the peripheral ECG leads (voltage-to-mass ratio) contrasting with the "hypertrophy" of the left ventricle
- Progressive thickening of the cardiac valves without significant regurgitation
- Increased echogenicity due to extracellular amyloid deposits with a granular sparkling myocardial texture (**Fig. 9.9a**)
- Marked dilatation of both atria (**Fig. 9.9b**)
- Restrictive pattern of diastolic dysfunction: elevated E wave, small A wave, short deceleration time, and prolonged isovolumetric relaxation time
- Markedly reduced longitudinal contraction velocity in tissue Doppler with a normal ejection fraction

The TEI encompasses systolic and diastolic function and is very useful in the follow-up of infiltrative cardiomyopathies.

Delayed enhancement MRI often shows a very inhomogeneous diffuse or subendocardial pattern of delayed enhancement in ventricular myocardium that has reached an advanced stage of hypertrophy. As a result, effective timing of the inversion pulse usually cannot be accomplished in these patients, and images convey an impression of diffuse hyperenhancement (**Fig. 9.10**).

Sarcoidosis

Sarcoidosis is a systemic granulomatous disease that mainly affects the lung and less commonly involves the skin, lymph nodes, eyes, kidneys, endocrine organs, and nervous system. Within Europe, sarcoidosis is most prevalent in Scandinavia, where its prevalence is 50–60 cases per 100 000 population.[23] Myocardial involvement is present in at least 25 % of sarcoidosis patients and is responsible for 25 % of all deaths. Cardiac

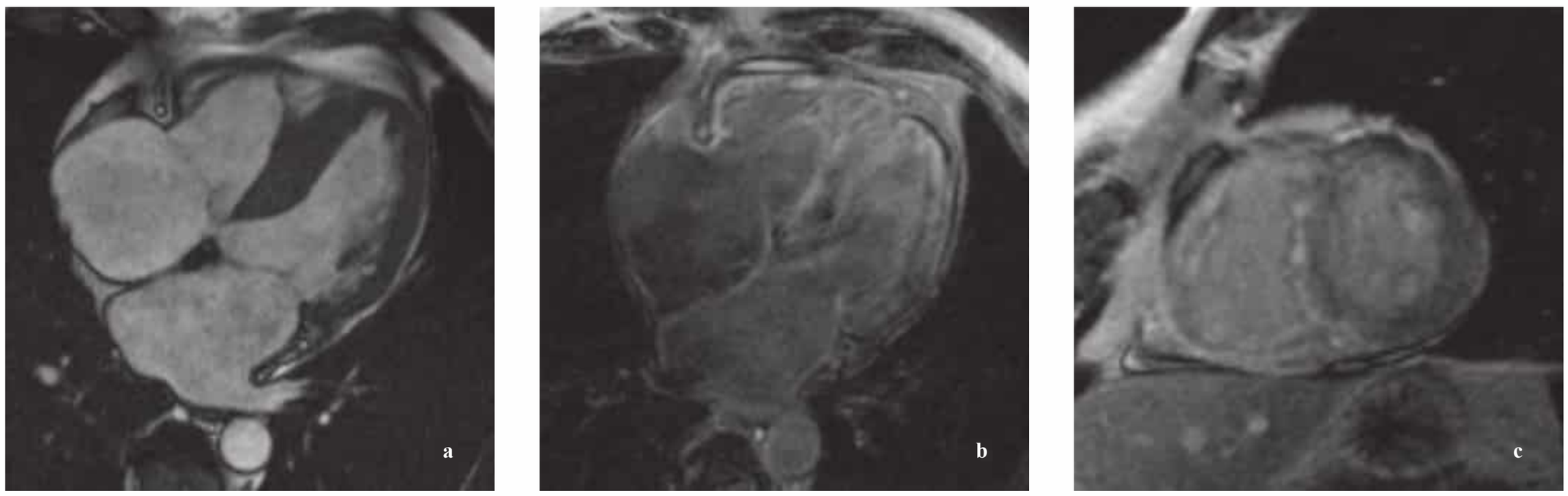

Fig. 9.10 a–c Primary cardiac amyloidosis in a 58-year-old man who presented clinically with decreased exercise tolerance. Echocardiography showed a marked reduction of left ventricular EF. MRI findings raised suspicion of amyloidosis, which was confirmed by biopsy.
a Four-chamber view shows marked enlargement of both atria.
b Amyloid deposits cause diffuse hyperenhancement of the myocardium. Optimum TI adjustment cannot be achieved.
c Sagittal short-axis view.

involvement is more prevalent in Japan and accounts for 85 %of deaths.[24,25]

The **diagnosis** of cardiac sarcoidosis is extremely challenging. In one series, only ~50 %of autopsy-confirmed cases were diagnosed while the patients were alive.[25] Granulomatous infiltration of the myocardium most commonly involves the lateral wall of the left ventricle, the papillary muscles, and the basal ventricular septum. Less common sites are the right ventricle and atrial walls. The leading clinical signs of cardiac sarcoidosis are atrioventricular conduction disorders or ventricular tachycardia, followed by progressive left-sided heart failure and/or chronic cor pulmonale, depending on the location of the granulomatous infiltrates. The Guidelines of the Japanese Ministry of Health (**Table 9.3**) are available to facilitate the clinical diagnosis of cardiac sarcoidosis.[26] Many authors have used these guidelines as a reference standard, although they have not yet been validated in prospective studies.

Approximately half of all patients with systemic sarcoidosis show **surface ECG changes** that range from ST segment elevation to high-grade AV block or ventricular tachycardia. ECG changes have low sensitivity and very poor specificity for diagnosing cardiac involvement, however. Also, no definite correlation has been found between ECG findings, the extent of cardiac involvement, and the individual risk of cardiac death.

Endomyocardial biopsy has high specificity but low sensitivity owing to the predominantly focal infiltration of the myocardium. Sarcoid granulomas occur mainly in the basal myocardium, but most endomyocardial biopsies are taken from the apical portions of the septum. For these reasons, 63 %of right ventricular biopsies and only 47 %of left ventricular biopsies were able to provide an antemortem diagnosis of cardiac sarcoidosis that was later confirmed by postmortem examination.[24]

Septal wall thinning, segmental and global left ventricular systolic dysfunction, moderate valvular regurgitation, pericardial effusion, diastolic dysfunction, and circumscribed thickening of the interventricular septum are typical abnormalities that can be detected by two-dimensional **transthoracic echocardiography**. It is important to detect pulmonary hypertension at Doppler echocardiography, but usually this is possible only in advanced stages. As a result, transthoracic echocardiography is not helpful in the early diagnosis of cardiac involvement.

Table 9.3 Guidelines for the diagnosis of cardiac sarcoidosis[26]

Histological diagnosis	Histopathological detection of noncaseating epithelioid cell granulomas in an endomyocardial biopsy or surgical specimen confirms cardiac sarcoidosis.
Clinical diagnosis	Patients with histologically confirmed extracardiac sarcoidosis are presumed to have cardiac sarcoidosis if criterion (**a**) or at least one of criteria (**b**) through (**e**) is met: **a** Complete right bundle branch block, AV block, ventricular tachycardia, premature ventricular extrasystoles and Q waves or ST segment elevation in surface ECG **b** Left ventricular dilatation, segmental wall thinning, or contraction abnormality **c** Perfusion defect on ^{201}Tl myocardial scans or increased uptake on ^{67}Ga or ^{99m}Tc myocardial scans **d** Increased intracardiac pressures, low cardiac output, or impaired systolic left ventricular segmental or global function on cardiac catheterization **e** Nonspecific interstitial fibrosis or cellular infiltration by endomyocardial biopsy

Cardiac MRI is superior to echocardiography in demonstrating ventricular morphology and function. A particular advantage of MRI is the capacity for tissue characterization with suitable pulse sequences. Myocardial granulomas incite an inflammatory tissue edema that appears hyperintense in T2-weighted fat-suppressed TSE sequences. These areas show delayed enhancement following IV contrast administration.

The delayed enhancement pattern in cardiac sarcoidosis differs from that in CHD by its intramural or subepicardial distribution of markedly high signal intensity (**Fig. 9.11**). Cardiac MRI is more sensitive than myocardial scintigraphy. Using the Guidelines of the Japanese Ministry of Health and Welfare as their reference standard, Smedema et al. found that gadolinium-enhanced MRI had a sensitivity of 100 %and a specificity of 78 %in the diagnosis of cardiac sarcoidosis.[27] Areas of delayed

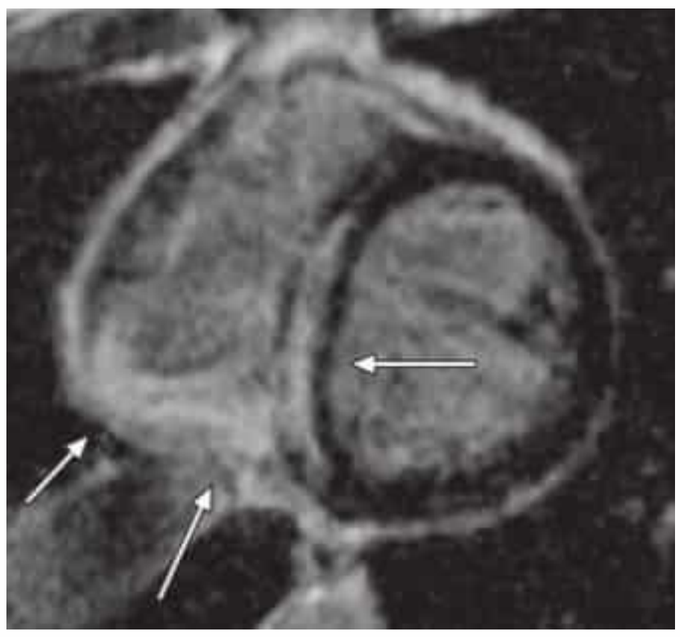

Fig. 9.11 Known sarcoidosis associated with varying AV conduction abnormalities in a 35-year-old woman. MRI detected cardiac involvement with extensive inflammatory infiltrates in the right ventricle and interventricular septum (arrows).

enhancement show a reduction or complete resolution in response to successful therapy.[27,28] Residual areas of delayed enhancement in treated patients and signs of an active inflammatory response are probably indicative of myocardial fibrosis.

In rare cases, restrictive cardiomyopathy is caused by storage diseases such as **Anderson–Fabry disease**, an X-chromosome-linked recessive disorder. The myocardial accumulation of glycosphingolipids leads to hypertrophy of the left and right ventricular myocardium. Left ventricular systolic function in this condition is initially preserved (**Fig. 9.12**). The natural history of untreated disease is characterized by myocardial fibrosis with progressive left ventricular dilatation and dysfunction. The clinical manifestations are those of progressive heart failure: exertional dyspnea, angina pectoris, cardiac arrhythmias, and sudden cardiac death. Unexplained left ventricular hypertrophy found at echocardiography often leads to a presumptive diagnosis of Anderson–Fabry disease.

Contrast-enhanced MRI in advanced cases usually shows a basal, inferolateral, intramural pattern of delayed enhancement indicative of fibrosis[29] (**Fig. 9.13**). But the earliest imaging sign of cardiac Anderson–Fabry disease is a reduction of longitudinal myocardial contraction velocity. This is detectable by echocardiography even before left ventricular hypertrophy can be detected by tissue Doppler or strain rate imaging.

Enzyme replacement therapy in Anderson–Fabry disease leads to a regression of cardiac complaints and complications, an improvement of systolic contraction velocity, and a regression of hypertrophy. Advanced stages with massive hypertrophy, left ventricular dysfunction, and fibrosis (delayed enhancement) will not benefit from enzyme replacement therapy.[22] MRI studies show that the right ventricle is also affected by glycosphingolipid deposition and becomes hypertrophic.

Endomyocardial Diseases

Endomyocardial diseases are causally related to the toxic effects of compounds in eosinophilic granules. On the whole, they are considered a frequent cause of restrictive cardiomyopathies. Two main types are distinguished:

- Endomyocardial fibrosis
- Löffler endocarditis

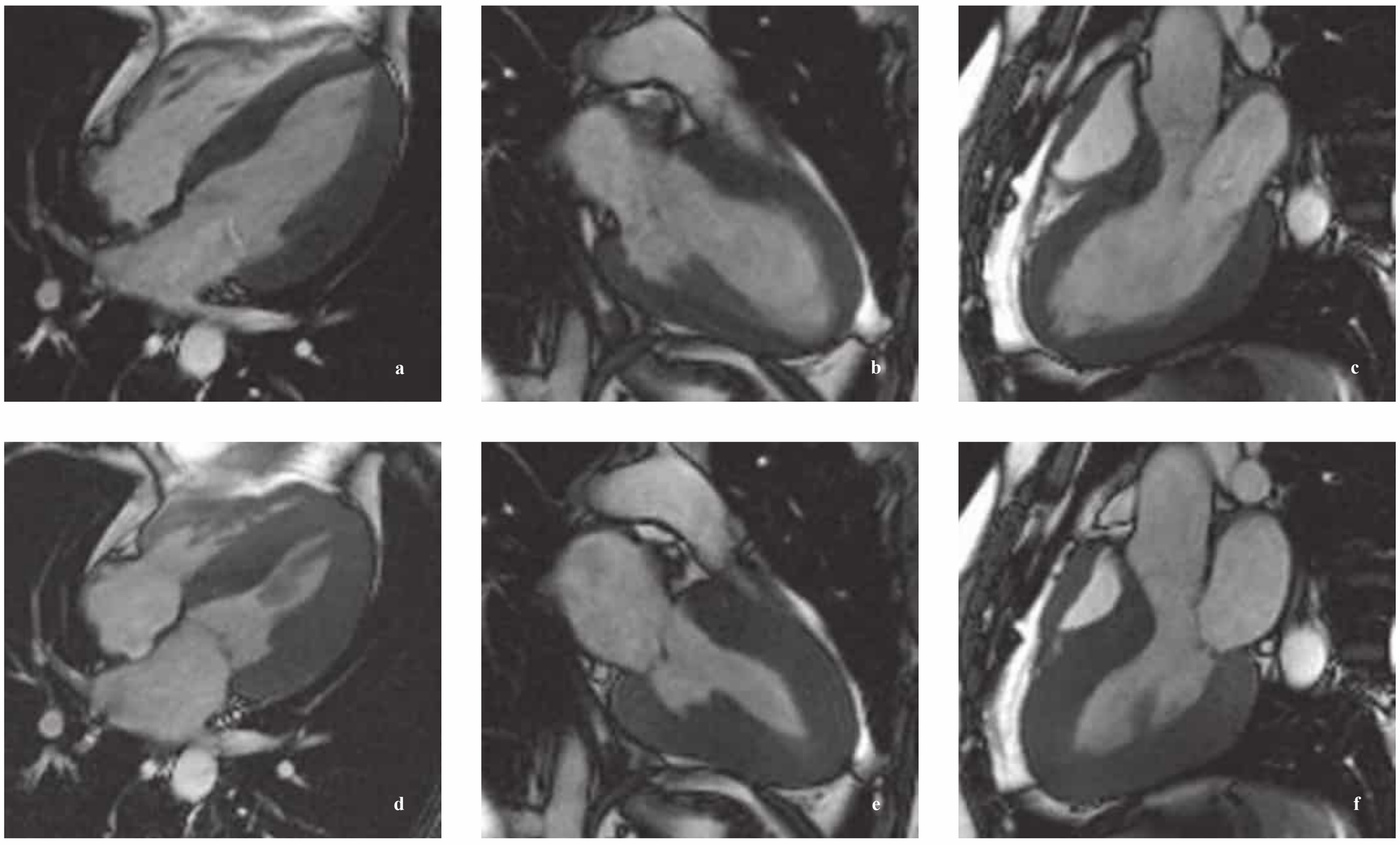

Fig. 9.12 a–f Pronounced concentric left ventricular hypertrophy with preservation of systolic function in Anderson—Fabry disease (end-diastolic volume 156 mL, end-systolic volume 66 mL, ejection fraction 57 %, LV mass 230 g).

a, d End-diastolic and end-systolic four-chamber view.
b, e End-diastolic and end-systolic two-chamber view.
c, f End-diastolic and end-systolic three-chamber view.

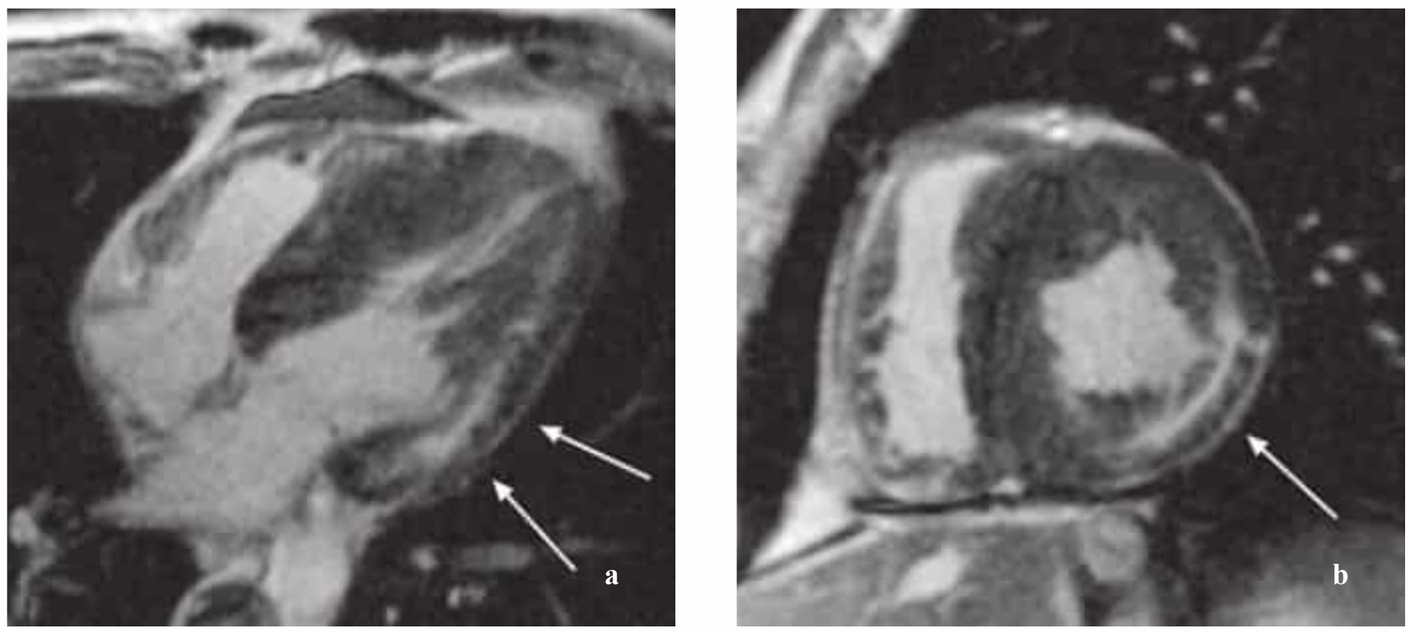

Fig. 9.13 a, b Typical inferolateral, midmyocardial delayed enhancement in a patient with known Anderson–Fabry disease (arrows).
a Horizontal long-axis image.
b Sagittal short-axis image.

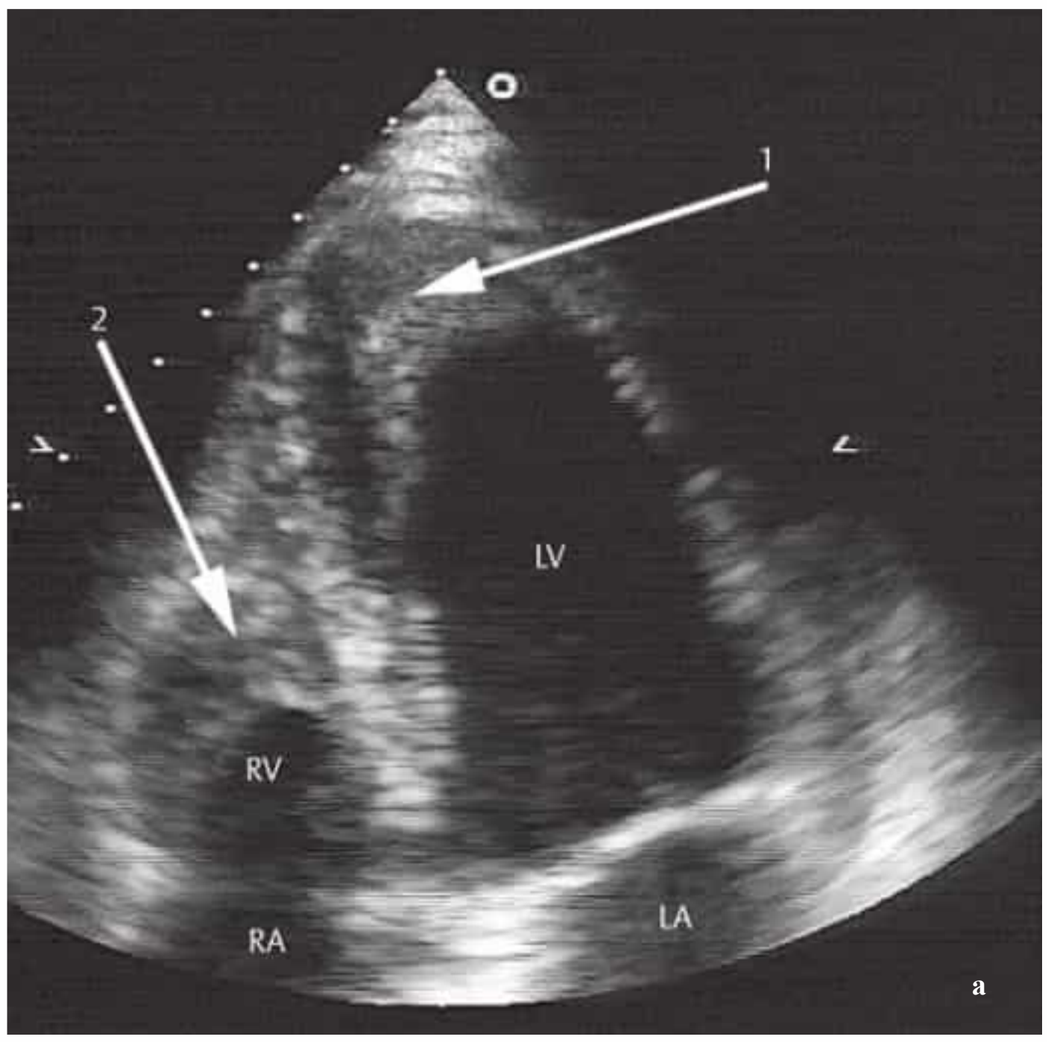

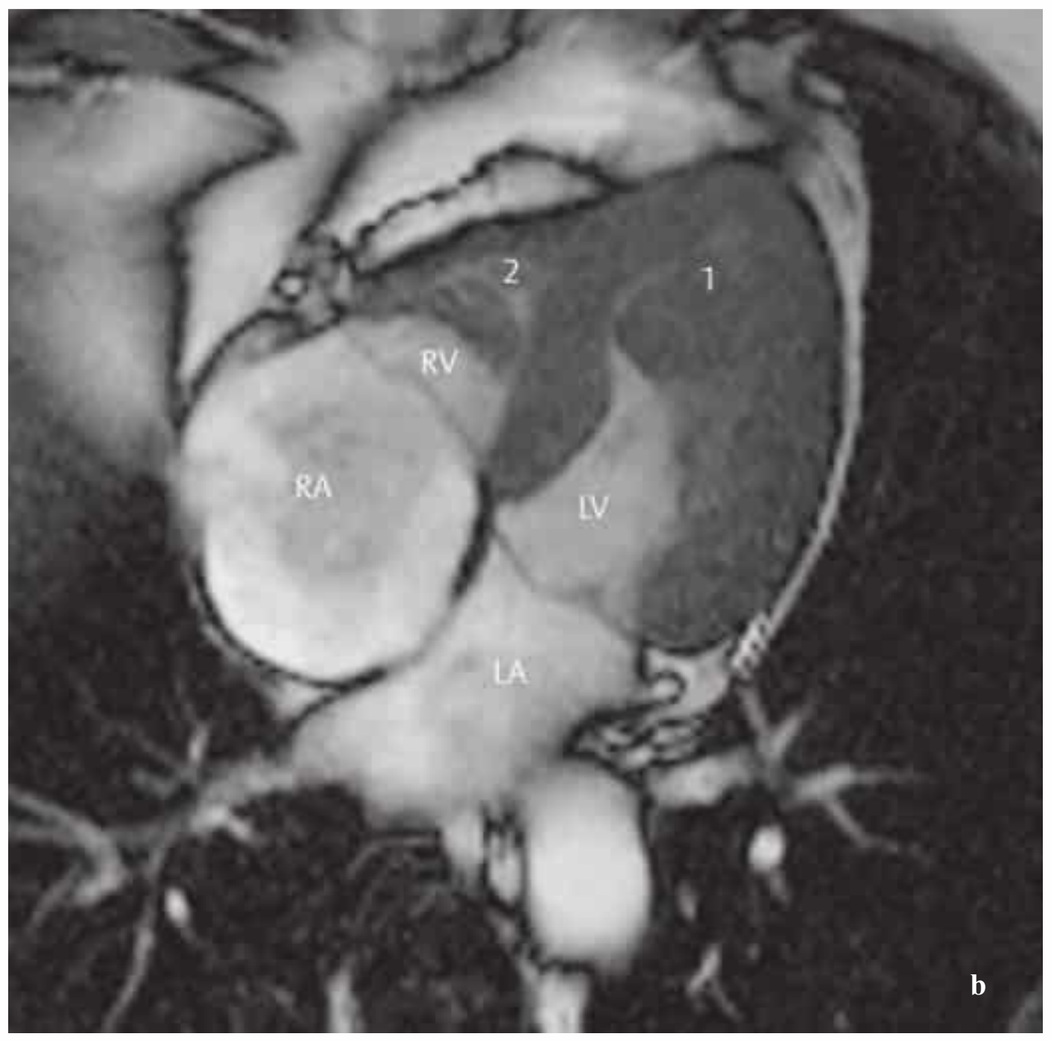

Fig. 9.14 a, b Endomyocardial fibrosis.
a Typical echocardiographic findings in endomyocardial fibrosis. Four-chamber view shows "apical truncation" of the right and left ventricular cavities (arrows).
b Correlative cine MRI.
1 Apex of the left ventricle
2 Apex of the right ventricle

Endomyocardial fibrosis is an endemic cardiomyopathy that is most prevalent in equatorial Africa and less so in the equatorial regions of Brazil, India, and Sri Lanka, accounting for one-fourth of all heart failure cases in those regions. Involvement may be biventricular or confined to the right or left ventricle, with corresponding variations in the clinical picture. As in Löffler endocarditis at middle latitudes, advanced cases exhibit dense endomyocardial fibrosis with thrombi occluding the apical ventricular cavity and causing restriction of diastolic filling.

Löffler endocarditis is part of the hypereosinophilic syndrome, which is characterized by a hypereosinophilia of unknown cause affecting numerous organs such as the brain, bone marrow, and lung. Cardiac involvement is generally present. An acute eosinophilic myocarditis, which also affects the endocardium, incites a pronounced fibrosis of the endocardium and myocardium with massive thrombosis of the ventricles. All imaging studies typically show a "truncated" apex, usually in the right ventricle, as a result of endomyocardial fibrosis (**Fig. 9.14**). Endomyocardial fibrosis as well as thrombus formation are best demonstrated by delayed-enhancement MRI but are still difficult to differentiate.

Essential Point
Typical representatives of this group are the infiltrative cardiomyopathies, which present echocardiographic features of left ventricular hypertrophy, restrictive-type diastolic dysfunction, and atrial enlargement. Typical delayed enhancement patterns (Anderson–Fabry disease, amyloidosis, sarcoidosis) are seen on postcontrast MRI.

Arrhythmogenic Right Ventricular Cardiomyopathy

Epidemiology, Pathophysiology, and Clinical Features

A rare cardiomyopathy of unknown etiology, arrhythmogenic right ventricular cardiomyopathy (ARVC) is characterized by a progressive, fatty or fibrofatty degeneration of the right ventricular myocardium and, less commonly, of the left ventricular myocardium. Apoptosis is the presumptive cause of myocardial

Table 9.4 Diagnostic criteria for ARVC (after McKenna WJ et al., 1994[30]). ARVC is diagnosed if two major criteria, one major and two minor criteria, or four minor criteria are present

Criteria	Major	Minor
Global and segmental function, structural alterations	• Severe RV dilatation and dysfunction without left ventricular involvement • Circumscribed RV aneurysms • Severe RV segmental dilatation	• Mild RV dilatation and dysfunction • Mild RV segmental dilatation • Segmental RV hypokinesia
Tissue characterization of the RV myocardium	• Fibrofatty infiltration of the RV myocardium by endomyocardial biopsy	–
Repolarization abnormalities	–	• T-wave inversion in right precordial leads (V2, V3) in patients >12 years of age • No right bundle branch block
Depolarization and AV conduction abnormalities	• Epsilon waves in V1–V3 • Localized widening of QRS complex (>110 ms) in V1–V3	• Late potentials
Arrhythmias	–	• Ventricular tachycardia with LBBB morphology • >1000 VES/24 hours
Family history	• Family disease confirmed histologically by surgery or autopsy	• Sudden cardiac death in family members (<35 years) with suspicion of ARVC • Suspected family history of ARVC based on available criteria

cell loss. The function of the right ventricle is impaired as a result of dilatation, increased trabeculation, and regional wall-motion abnormalities (dyskinesia). In rare, severe cases the left ventricle is also affected.

ARVC requires differentiation from Uhl anomaly, which features massive generalized thinning of the right ventricular wall due to congenital aplasia of the myocardium. The cause of ARVC is still poorly understood. Approximately one-third of cases show a familial occurrence with autosomal dominant inheritance and an identifiable genetic mutation.

The structural changes in the right ventricle predispose to stress-induced ventricular reentry tachycardia with a left bundle branch block configuration, which may lead to sudden cardiac death. The spectrum of clinical, electrophysiological, and morphological changes is extremely broad. According to the Task Force Report,[30] the diagnosis is based on a combination of major and minor criteria (**Table 9.4**). The following symptoms may occur (in descending order of frequency):

- Palpitations
- Syncope
- Atypical angina pectoris
- Dyspnea

ARVC should be suspected in all patients with stress-related syncopal events, patients resuscitated from sudden cardiac death, and young patients who experience episodes of ventricular tachycardia. MRI is the only imaging modality that can meet this challenge owing to its capabilities for right ventricular visualization and myocardial tissue characterization.

Imaging

The **MRI criteria** for ARVC are as follows:

- Regional right ventricular wall-motion abnormalities, sometimes in the form of circumscribed dyskinetic bulges ("microaneurysms")
- Right ventricular dilatation not referable to other causes (shunt lesion, pulmonary hypertension, tricuspid insufficiency)
- Increased right ventricular trabeculation ("stack of dishes" sign)
- Circumscribed increase of signal intensity in the right ventricular myocardium in T1-weighted spin-echo sequences (with or without a fat saturation prepulse, consistent with fatty infiltration)
- Delayed enhancement of the right ventricular myocardium after contrast administration (**Fig. 9.15**)

Study populations to date have been small owing to the low incidence of ARVC, and the MRI criteria for the disease have not all been met in these populations.[31] The detection of fatty infiltration is particularly challenging, and the proportion of fat in the myocardium of ARVC patients is very small at histopathology. Fibrous transformation of the myocardium is the dominant finding in most patients. The fatty infiltrates are so small that even high-resolution spin-echo sequences reach the limit of their spatial resolution. The most reliable criteria in our experience are localized dyskinetic right ventricular contraction abnormalities and the detection of delayed enhancement indicating fibrotic transformation of the right ventricular myocardium.[32]

ARVC is difficult to distinguish from the wall-motion abnormalities that occur in the right ventricular outflow tract (RVOT) of most patients with RVOT tachycardia.[33]

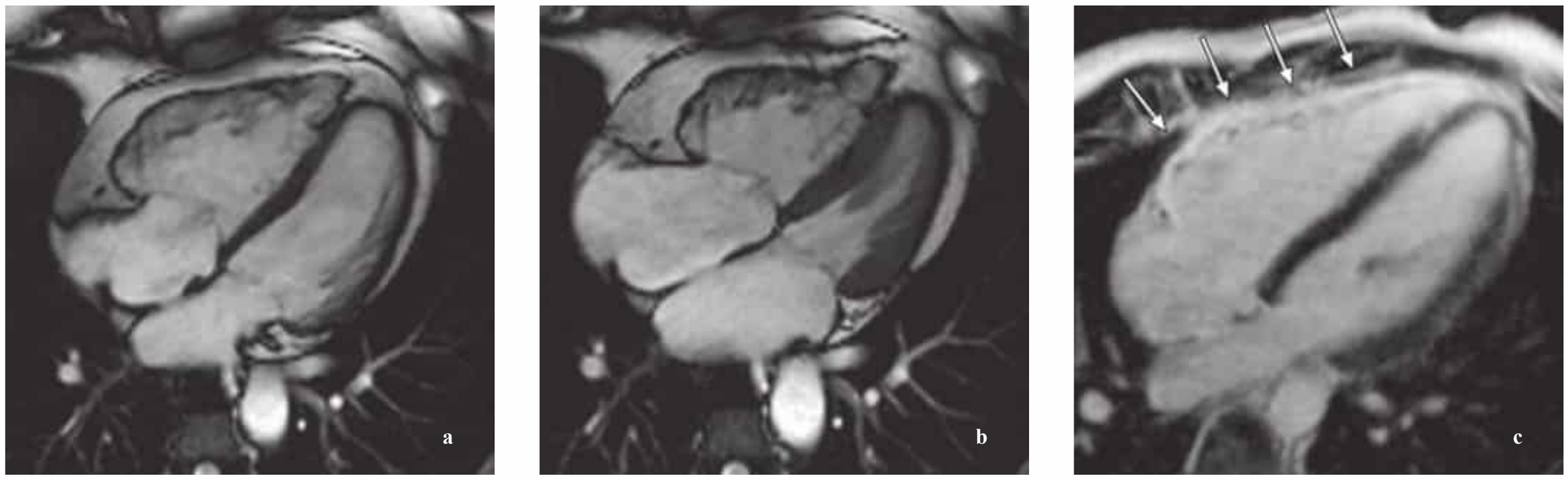

Fig. 9.15 a–c Arrhythmogenic right ventricular cardiomyopathy in a young male. Cine images show dyskinesia of the free wall of the right ventricle accompanied by increased myocardial trabeculation (arrow). Postcontrast image shows marked delayed enhancement consistent with fibrotic transformation of the myocardial tissue.

a Horizontal long-axis image at end diastole.
b Horizontal long-axis image at end systole.
c Delayed enhancement image.

Advanced ARVC is characterized by marked, progressive right ventricular dilatation with involvement of the left ventricle, generally sparing the septum. Rare cases that involve only the left ventricle have also been described (arrhythmogenic left ventricular cardiomyopathy). They have a familial occurrence with autosomal dominant inheritance and relate to a mutation of the desmoplakin gene.

■ Unclassified Cardiomyopathies

Unclassified cardiomyopathies include isolated left ventricular noncompaction and Tako-Tsubo cardiomyopathy.

Increasing clinical attention has focused on Tako-Tsubo cardiomyopathy in recent years. Synonyms are stress cardiomyopathy, neurocardiogenic stunning, and apical ballooning syndrome. The pathophysiology may involve the overactivation of plasma catecholamines and neuropeptides, coronary spasms, microvascular abnormalities, or direct myocytic injury.[34]

Females are predominantly affected. Patients complain of severe angina pectoris following an emotional stress such as a death in the family, and ECG shows changes typical of myocardial infarction (ST segment elevation). Most patients are initially admitted to the ICU and undergo invasive coronary angiography, which generally shows no evidence of coronary disease, although coronary spasms are common. Ventriculography, echocardiography, and cardiac MRI show extensive dyskinesia affecting almost all midventricular and apical segments and encompassing the territories of multiple coronary arteries. Contraction of the basal segments is unimpaired, but there is severe impairment of global left ventricular function. Tako-Tsubo (Japanese for "octopus trap") describes the amphora-like shape of the left ventricle at end systole, with a narrow neck (basal segments) and greatly distended apex. Differentiation from acute myocardial infarction is based on a typical history of emotional distress and the pathognomonic ventricular morphology. The prognosis is favorable for a complete recovery of left ventricular function within a period of days or weeks (**Fig. 9.16**).

Myocarditis

Epidemiology, Pathophysiology, and Clinical Features

Despite the simple clinical and pathological definition of myocarditis as an "inflammation of the myocardium," a presumptive diagnosis of myocarditis presents the clinician with a formidable diagnostic and therapeutic challenge.

The incidence of myocarditis is difficult to estimate. Current data based on prospective postmortem analyses suggest that myocarditis is responsible for 8.6–12% of all sudden cardiac deaths in young adults.[35,36] Underlying dilated cardiomyopathy is present in 9% of all patients with chronic progressive myocarditis.[37]

Myocarditis has a very broad etiological spectrum (**Table 9.5**). The most frequent cause is viral infection, usually with enteroviruses, parvovirus, hepatitis C, or human immunodeficiency viruses. Less frequent causes are drug hypersensitivity reactions and myocardial involvement by systemic diseases.

The Dallas criteria published in 1986 are still considered valid for the histopathological classification of myocarditis.[38] Active myocarditis is characterized by the presence of inflammatory infiltrates and associated myocyte necrosis. Borderline myocarditis is characterized by inflammatory infiltrates with no evidence of myocyte necrosis on light-microscopic examination of endomyocardial biopsy.

The main limitation of endomyocardial biopsy is its sampling error. The usual clinical standard for endomyocardial biopsy is four to six specimens. In one postmortem simulation, more than 17 specimens were needed to achieve a sensitivity higher than 80% in patients with confirmed myocarditis.[15] In another study, fewer than 10% of all patients with high clinical suspicion of myocarditis could be confirmed by biopsy based on the Dallas criteria.[39] Moreover, the Dallas criteria are compromised by high interobserver variability.[40] A more comprehensive clinicopathological classification has been described but has not yet been widely adopted.[41] At present, myocarditis is investigated mainly by virological testing of the myocardium, which is superior to conventional serological testing.

Table 9.5 Principal causes of myocarditis

Viruses	Adenovirus, coxsackievirus, HCV, HIV, Parvovirus B19
Bacteria	Mycobacteria, streptococci, Mycoplasma, Treponema pallidum, Tropheryma whipplei (Whipple disease)
Fungi	Aspergillus, Candida, Coccidioides, Cryptotoccus, Histoplasma
Protozoa	Trypanosoma cruzi, Toxoplasma
Parasites	Schistosomiasis, larva migrans
Toxins	Anthracyclines, cocaine, interleukin-2
Hypersensitivity	Sulfonamides, cephalosporins, diuretics, digoxin, tricyclic antidepressants, dobutamine
Immunological syndromes	Churg–Strauss, inflammatory bowel diseases, giant-cell arteritis, diabetes mellitus, sarcoidosis, systemic lupus erythematosus, thyrotoxicosis, Wegener granulomatosis, Takayasu arteritis

The clinical presentation ranges from transient ECG changes in asymptomatic patients during a pandemic influenza to fulminant heart failure following viral prodromal symptoms such as fever, myalgia, gastroenteritis, or respiratory symptoms. Besides heart failure, acute coronary syndromes with ischemic-type ECG changes and troponin activation in predominantly young patients with a low cardiovascular risk profile are frequent clinical manifestations of acute myocarditis.

Imaging

Several techniques are available for myocardial imaging: echocardiography, scintigraphy (using gallium 67 [^{67}Ga]- or indium 111 [^{111}In]-labeled antimyosin antibodies), and cardiac MRI.

Numerous studies document the value of transthoracic echocardiography in the initial imaging assessment of acute myocarditis.[42] In one retrospective analysis of biopsy-confirmed myocarditis, echocardiograms showed predominantly segmental (64%) and global (69%) impairment of left ventricular systolic function. Most cases showed little or no enlargement of left ventricular diameters. Right ventricular dysfunction was noted in only 23% of the patients. Reversible left ventricular hypertrophy was also uncommon (15%).[42] With its high avail-

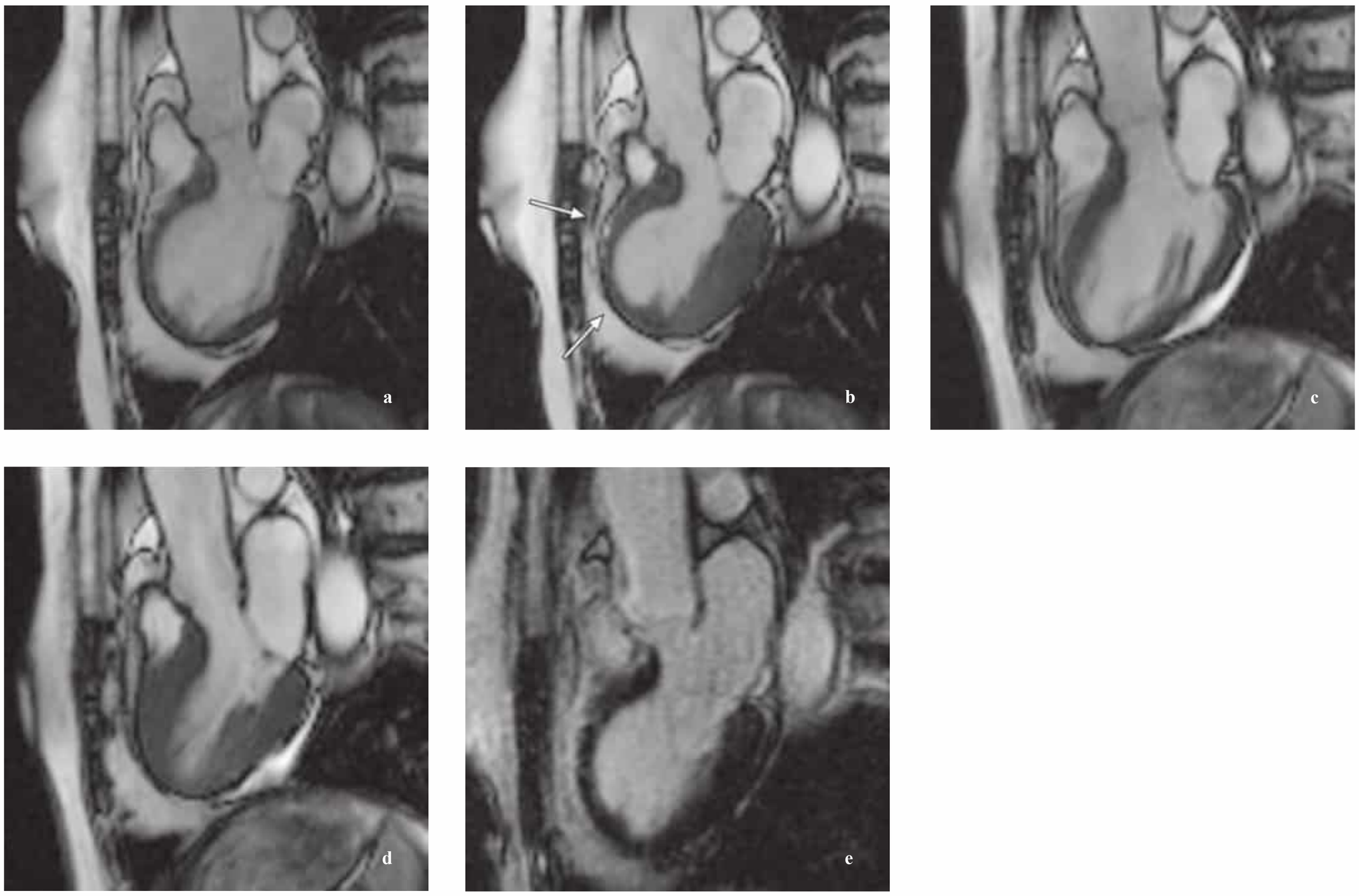

Fig. 9.16 a–e A woman 70 years of age presented with typical angina pectoris and anterior ST-segment elevation typical of myocardial infarction following a dispute with her husband. Cine MRI, performed immediately after angiographic exclusion of coronary heart disease, shows extensive anterior wall dyskinesia (apical ballooning, arrows) and a marked reduction of systolic left ventricular global function. Images taken 7 days after the event document complete recovery of LV function (**c** end-diastolic, **d** end-systolic) with an absence of delayed enhancement (**e**). Diagnosis: takotsubo cardiomyopathy!

a, b Three-chamber views at end diastole and end systole during initial examination.

c, d Three-chamber views at end diastole and end systole 7 days later show normalization of findings.

e Delayed-enhancement image.

ability and convenience, echocardiography is also the modality of first choice for the serial follow-up of myocarditis. For example, the normalization of concentric left ventricular hypertrophy in response to corticosteroid therapy has been described in patients with eosinophilic myocarditis. The reflection and absorption of ultrasound energy depends on tissue properties such as density, elasticity, and acoustic impedance. Although echocardiographic tissue characterization can distinguish healthy myocardium from inflammatory myocardium with reasonably high confidence, it cannot differentiate between active myocarditis and idiopathic dilated cardiomyopathy. Tissue Doppler techniques are better suited for this purpose but have not yet been adequately evaluated clinically. The detection of pericardial effusion is helpful in differential diagnostic classification.

Indium 111-labeled monoclonal antibody fragments bind to myosin when the integrity of the sarcolemmal membrane is disrupted. Unlike ^{67}Ga, which images myocardial inflammation, antimyosin imaging with ^{111}I defines the presence and extent of cell necrosis. Imaging with radionuclide-labeled antimyosin antibodies is more sensitive than endomyocardial biopsy (83%) but is less specific (53%). In terms of clinical use, it is interesting to note that antimyosin imaging has a high negative predictive value (92%). Moreover, a positive antimyosin scan with a normal-sized left ventricle has a high predictive value for the biopsy detection of myocarditis. Myocardial scintigraphy is not currently used in the routine clinical work-up of myocarditis, however.

Contrast-enhanced cardiac MRI shows promise for resolving the diagnostic dilemma of myocarditis. Myocardium that has undergone inflammatory change offers several specific targets for MR imaging in the form of myocyte necrosis, cell membrane damage, tissue and cellular edema, and hyperemia. As early as 1998, Friedrich et al.[43] noted myocardial hyperenhancement in patients with viral myocarditis using free-breathing T1-weighted spin-echo sequences with a 1.0-T system and an average acquisition time of 9 minutes. They also documented the regression of hyperenhancement over time. Both focal and global relative enhancement were described in this study using skeletal muscle as an internal reference standard. Inflammatory tissue edema can also be detected with the aid of newer, fast, fat-suppressed T2-weighted turbo spin-echo sequences using breath-hold technique (**Fig. 9.17**).

Mahrholdt et al.[44] used delayed-enhancement imaging to direct myocardial biopsy in 32 patients with clinical suspicion of myocarditis. Myocarditis could be diagnosed histologically in 19 of 21 patients by "MR-guided" biopsy. Histology in the remaining two patients indicated hypertrophic cardiomyopathy based on the septal location of delayed enhancement. Delayed enhancement in myocarditis was subepicardial and occurred predominantly in the lateral wall of the left ventricle (**Fig. 9.17**). A subendocardial pattern typical of myocardial infarction was not found in any of the myocarditis patients. On follow-up at 3 months, the areas of delayed enhancement had decreased in size or disappeared, accompanied by improvement or complete recovery of left ventricular function. A recent study by the same

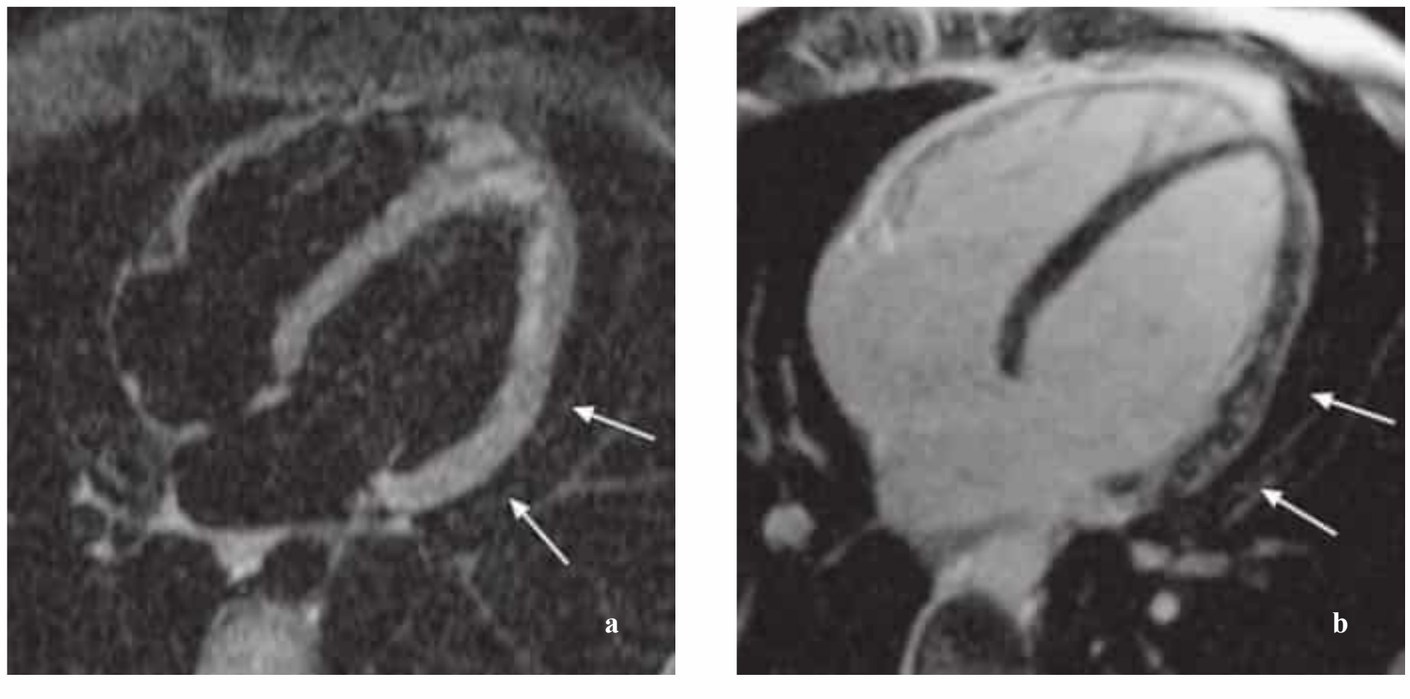

Fig. 9.17 a–d Acute viral myocarditis in a 25-year-old man. There was no impairment of global left ventricular function under resting conditions.
a Fat-suppressed STIR image shows edema of the left ventricular myocardium predominantly affecting the lateral wall, which appears thickened (arrows) relative to the septum.
b Postcontrast image reveals typical patchy subendocardial delayed enhancement (arrows).
c Sagittal short-axis view (arrow).
d Follow-up 3 months after diagnosis shows significant regression of delayed enhancement areas in the lateral wall of the left ventricle.

author even suggest that clinical presentation, type of virus and pattern of delayed enhancement are related to the clinical course.[45]

Presumably, the mechanisms responsible for delayed enhancement in myocarditis are comparable to the pathophysiology of delayed enhancement in acute myocardial infarction. Inflammatory damage to the cell membranes allows gadolinium molecules to diffuse into the affected myocytes. This increases the distribution volume of the "extracellular" contrast agent, resulting in higher T1-weighted signal intensity compared with healthy myocardium. Unlike the homogeneous necrosis that occurs in acute myocardial infarction, the necrotic areas in myocarditis are relatively small and have a focal distribution. One focus contains islands of necrotic cells interspersed with viable myocytes, with the result that delayed enhancement in myocarditis has a lower overall signal intensity. Inflammatory edema and hyperemia in myocarditis also play a role. Much as in infarctions, inflammatory areas are replaced by fibrotic tissue that has a smaller volume than the acute area owing to scar retraction. "Myocarditis scars" become smaller over time, and scars smaller than the voxel size can no longer be resolved as areas of delayed enhancement.

Essential Point

Given the low diagnostic yield of undirected endomyocardial biopsy, an algorithm based on clinical suspicion, ECG, serum troponin activity, echocardiography, and delayed enhancement MRI-guided endomyocardial biopsy is the most promising diagnostic strategy at present.

Myocarditis should be considered in patients who develop heart failure or angina pectoris after an influenza-like infection or gastroenteritis.

Transthoracic echocardiography supplies initial diagnostic information on a segmental or global abnormality of left ventricular systolic function and can detect even small pericardial effusions.

The diagnosis is established by the detection of myocyte necrosis and/or inflammatory infiltrates and a positive PCR for cardiotropic viruses in an endomyocardial biopsy.

Inflammatory infiltrates and necrosis in the left ventricular myocardium are detectable by MRI as areas of delayed enhancement. Delayed-enhancement imaging can also direct the biopsy of these sites and monitor their regression over time. They differ from infarction-type changes in their location, signal intensity, and reversibility.

References

1. Braunwald E, Seidman CE, Sigwart U. Contemporary evaluation and management of hypertrophic cardiomyopathy. Circulation 2002;106: 1312–1316
2. Konstam MA. Progress in heart failure management? Lessons from the real world. Circulation 2000;102:1076–1078
3. Richardson P, McKenna W, Bristow M, et al. Report of the 1995 World Health Organization/International Society and Federation of Cardiology Task Force on the Definition and Classification of cardiomyopathies. Circulation 1996;93:841–842
4. Simonetti OP, Kim RJ, Fieno DS, et al. An improved MR imaging technique for the visualization of myocardial infarction. Radiology 2001;218:215–223
5. Wagner A, Mahrholdt H, Holly TA, et al. Contrast-enhanced MRI and routine single photon emission computed tomography (SPECT) perfusion imaging for detection of subendocardial myocardial infarcts: an imaging study. Lancet 2003;361:374–379
6. Braunwald E, Bristow MR. Congestive heart failure: fifty years of progress. Circulation 2000;102:IV14–IV23
7. Seidman JG, Seidman C. The genetic basis for cardiomyopathy: from mutation identification to mechanistic paradigms. Cell 2001;104:557–567
8. Bax JJ, Abraham T, Barold SS, et al. Cardiac resynchronization therapy: Part 1 – issues before device implantation. J Am Coll Cardiol 2005;46: 2153–2167
9. Barkhausen J, Ruehm SG, Goyen M, et al. MR evaluation of ventricular function: true fast imaging with steady-state precession versus fast low-angle shot cine MR imaging: feasibility study. Radiology 2001; 219:264–269
10. Strohm O, Schulz-Menger J, Pilz B, et al. Measurement of left ventricular dimensions and function in patients with dilated cardiomyopathy. J Magn Reson Imaging 2001;13:367–371
11. Doherty NE III, Fujita N, Caputo GR, et al. Measurement of right ventricular mass in normal and dilated cardiomyopathic ventricles using cine magnetic resonance imaging. Am J Cardiol 1992;69:1223–1228
12. Hunold P, Schlosser T, Vogt FM, et al. Myocardial late enhancement in contrast-enhanced cardiac MRI: distinction between infarction scar and non-infarction-related disease. AJR Am J Roentgenol 2005;184: 1420–1426
13. McCrohon JA, Moon JCC, Prasad SK, et al. Differentiation of heart failure related to dilated cardiomyopathy and coronary artery disease using gadolinium-enhanced cardiovascular magnetic resonance. Circulation 2003;108:54–59
14. Assomull RG, Prasad SK, Lyne J, et al. Cardiovascular magnetic resonance, fibrosis, and prognosis in dilated cardiomyopathy. J Am Coll Cardiol 2006;48:1977–1985
15. Hauck AJ, Kearney DL, Edwards WD. Evaluation of postmortem endomyocardial biopsy specimens from 38 patients with lymphocytic myocarditis: implications for role of sampling error. Mayo Clin Proc 1989;64:1235–1245
16. Maron BJ, Gardin JM, Flack JM, et al. Prevalence of hypertrophic cardiomyopathy in a general population of young adults. Echocardiographic analysis of 4111 subjects in the CARDIA Study. Coronary Artery Risk Development in (Young) Adults. Circulation 1995;92:785–789
17. Maron MS, Olivotto I, Betocchi S, et al. Effect of left ventricular outflow tract obstruction on clinical outcome in hypertrophic cardiomyopathy. N Engl J Med 2003;348:295–303
18. Ho CY, Sweitzer NK, McDonough B, et al. Assessment of diastolic function with Doppler tissue imaging to predict genotype in preclinical hypertrophic cardiomyopathy. Circulation 2002;105:2992–2997
19. Rickers C, Wilke NM, Jerosch-Herold M, et al. Utility of cardiac magnetic resonance imaging in the diagnosis of hypertrophic cardiomyopathy. Circulation 2005;112:855–861
20. Moon JC, Reed E, Sheppard MN, et al. The histologic basis of late gadolinium enhancement cardiovascular magnetic resonance in hypertrophic cardiomyopathy. J Am Coll Cardiol 2004;43:2260–2264
21. Gross CM, Schulz-Menger J, Kramer J, et al. Percutaneous transluminal septal artery ablation using polyvinyl alcohol foam particles for septal hypertrophy in patients with hypertrophic obstructive cardiomyopathy: acute and 3-year outcomes. J Endovasc Ther 2004;11:705–711
22. Beer M, Weidemann F, Breunig F, et al. Impact of enzyme replacement therapy on cardiac morphology and function and late enhancement in Fabry's cardiomyopathy. Am J Cardiol 2006;97:1515–1518

23. Rybicki BA, Major M, Popovich J Jr, et al. Racial differences in sarcoidosis incidence: a 5-year study in a health maintenance organization. Am J Epidemiol 1997;145:234–241
24. Sekiguchi M, Numao Y, Imai M, et al. Clinical and histopathological profile of sarcoidosis of the heart and acute idiopathic myocarditis. Concepts through a study employing endomyocardial biopsy. I. Sarcoidosis. Jpn Circ J 1980;44:249–263
25. Silverman KJ, Hutchins GM, Bulkley BH. Cardiac sarcoid: a clinicopathologic study of 84 unselected patients with systemic sarcoidosis. Circulation 1978;58:1204–1211
26. Hiraga H[6], Yuwai K, Hiroe M. Guideline for diagnosis of cardiac sarcoidosis: study report on diffuse pulmonary diseases from the Japanese Ministry of Health and Welfare. Tokyo: Japanese Ministry of Health and Welfare; 1993.
27. Smedema JP, Snoep G, van Kroonenburgh MP, et al. Evaluation of the accuracy of gadolinium-enhanced cardiovascular magnetic resonance in the diagnosis of cardiac sarcoidosis. J Am Coll Cardiol 2005;45:1683–1690
28. Vignaux O, Dhote R, Duboc D, et al. Detection of myocardial involvement in patients with sarcoidosis applying T2-weighted, contrast-enhanced, and cine magnetic resonance imaging: initial results of a prospective study. J Comput Assist Tomogr 2002;26:762–767
29. Moon JC, Sachdev B, Elkington AG, et al. Gadolinium enhanced cardiovascular magnetic resonance in Anderson-Fabry disease. Evidence for a disease specific abnormality of the myocardial interstitium. Eur Heart J 2003;24:2151–2155
30. McKenna WJ, Thiene G, Nava A, et al. Diagnosis of arrhythmogenic right ventricular dysplasia/cardiomyopathy. Task Force of the Working Group Myocardial and Pericardial Disease of the European Society of Cardiology and of the Scientific Council on Cardiomyopathies of the International Society and Federation of Cardiology. Br Heart J 1994;71:215–218
31. Midiri M, Finazzo M, Brancato M, et al. Arrhythmogenic right ventricular dysplasia: MR features. Eur Radiol 1997;7:307–312
32. Hunold P, Wieneke H, Bruder O, et al. Late enhancement: a new feature in MRI of arrhythmogenic right ventricular cardiomyopathy? J Cardiovasc Magn Reson 2005;7:649–655
33. White RD, Trohman RG, Flamm SD, et al. Right ventricular arrhythmia in the absence of arrhythmogenic dysplasia: MR imaging of myocardial abnormalities. Radiology 1998;207:743–751
34. Wittstein IS, Thiemann DR, Lima JA, et al. Neurohumoral features of myocardial stunning due to sudden emotional stress. N Engl J Med 2005;352:539–548
35. Doolan A, Langlois N, Semsarian C. Causes of sudden cardiac death in young Australians. Med J Aust 2004;180:110–112
36. Fabre A, Sheppard MN. Sudden adult death syndrome and other non-ischaemic causes of sudden cardiac death. Heart 2006;92:316–320
37. Felker GM, Hu W, Hare JM, et al. Takotsubo cardiomyopathy. The Johns Hopkins experience with 1,278 patients. Medicine (Baltimore) 1999;78:270–283
38. Aretz HT. Diagnosis of myocarditis by endomyocardial biopsy. Med Clin North Am 1986;70:1215–1226
39. Jin O, Sole MJ, Butany JW, et al. Detection of enterovirus RNA in myocardial biopsies from patients with myocarditis and cardiomyopathy using gene amplification by polymerase chain reaction. Circulation 1990;82:8–16
40. Shanes JG, Ghali J, Billingham ME, et al. Interobserver variability in the pathologic interpretation of endomyocardial biopsy results. Circulation 1987;75:401–405
41. Lieberman EB, Hutchins GM, Herskowitz A, et al. Clinicopathologic description of myocarditis. J Am Coll Cardiol 1991;18:1617–1626
42. Pinamonti B, Alberti E, Cigalotto A, et al. Echocardiographic findings in myocarditis. Am J Cardiol 1988;62:285–291
43. Friedrich MG, Strohm O, Schulz-Menger J, et al. Contrast media-enhanced magnetic resonance imaging visualizes myocardial changes in the course of viral myocarditis. Circulation 1998;97:1802–1809
44. Mahrholdt H, Goedecke C, Wagner A, et al. Cardiovascular magnetic resonance assessment of human myocarditis: a comparison to histology and molecular pathology. Circulation 2004;109:1250–1258
45. Mahrholdt H, Wagner A, Deluigi CC, et al. Presentation, patterns of myocardial damage, and clinical course of viral myocarditis. Circulation 2006;114:1581–1590

Further Reading

Bleeker GB, Kaandorp TA, Lamb HJ, et al. Effect of posterolateral scar tissue on clinical and echocardiographic improvement after cardiac resynchronization therapy. Circulation 2006;113:969–976

Fifer MA, Aroney CN, Semigran MJ, et al. Techniques for assessing inotropic effects of drugs in patients with heart failure: application to the evaluation of nicardipine. Am Heart J 1990;119:451–456

Maron BJ, Shirani J, Poliac LC, et al. Sudden death in young competitive athletes. Clinical, demographic, and pathological profiles. JAMA 1996;276:199–204

Vignaux O, Dhote R, Duboc D, et al. Clinical significance of myocardial magnetic resonance abnormalities in patients with sarcoidosis: a 1-year follow-up study. Chest 2002;122:1895–1901

10 Cardiac Tumors

J. Barkhausen and H. Eggebrecht

Primary cardiac tumors are extremely rare, with a reported prevalence of 0.001–0.3 % in autopsy studies. Approximately 75 % of primary cardiac tumors are benign, while malignancies account for just 25 % of cases. The most common benign tumor is myxoma, which constitutes ~50 % of all benign cardiac tumors.[1–3] Although benign tumors are not locally invasive and do not metastasize, they may cause significant morbidity and mortality due to arrhythmias, embolism, or obstruction of blood flow. Malignant primary cardiac tumors are almost always sarcomas, consisting mainly of angiosarcomas and rhabdomyosarcomas.

Metastatic tumors to the heart and pericardium are ~20–40 times more common than primary cardiac tumors and are detectable in 0.6–1.5 % of patients with an underlying malignant disease. Metastases occur chiefly in the pericardium and myocardium; valvular and endocardial involvement is extremely rare.

The first step in the differentiation of cardiac tumors is to characterize the tumor as a paracardiac, pericardial, myocardial, or intracavitary mass. **Fig. 10.1** illustrates various sites of tumor occurrence, and **Table 10.1** reviews the sites of the most common benign and malignant cardiac tumors. **Table 10.2** lists diagnostic criteria that have proved useful in differentiating between benign and malignant tumors.

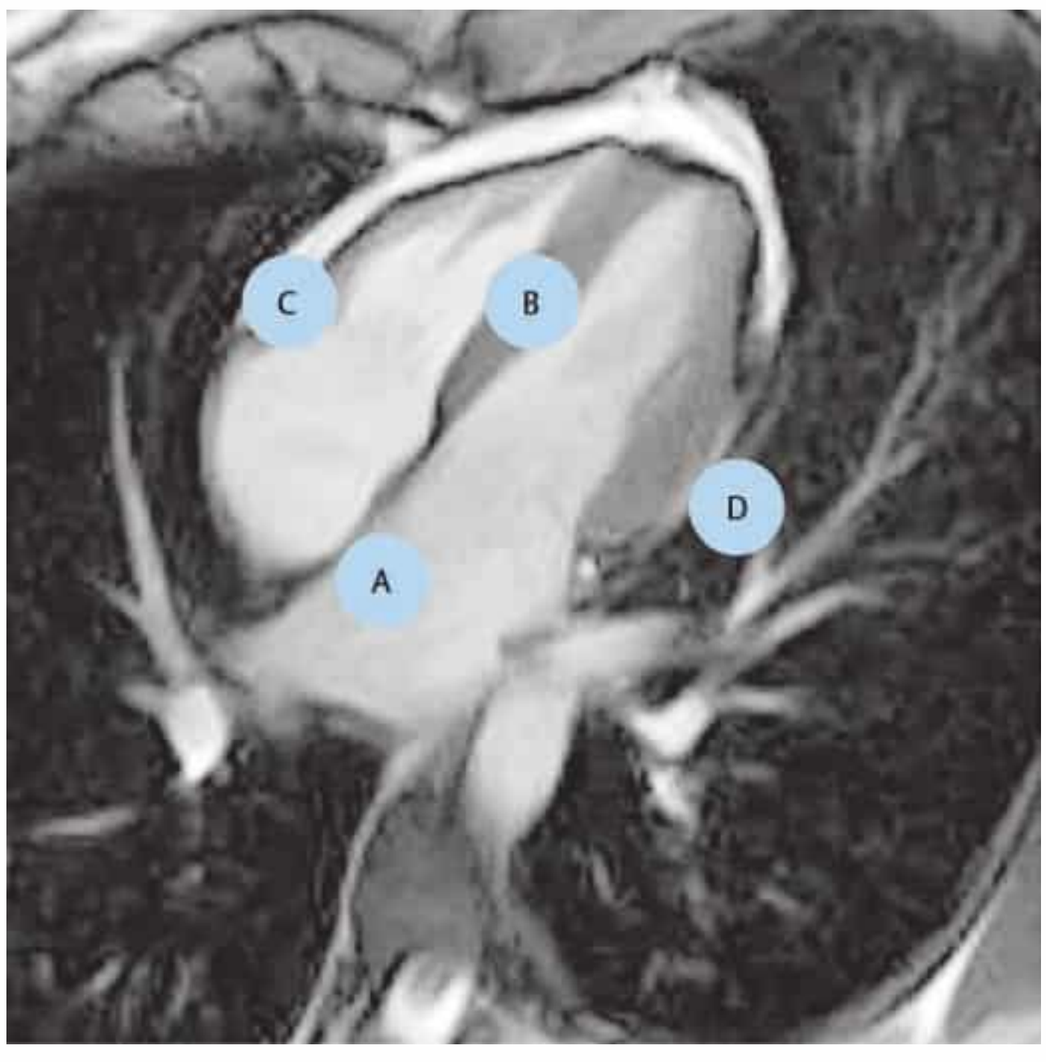

Fig. 10.1 Localization of cardiac tumors: intracavitary (A), intramyocardial (B), intrapericardial (C), and paracardiac (D).

Essential Point

Three-fourths of all cardiac tumors are benign, and the most common benign tumor is myxoma. Among malignancies, metastases are 20–40 times more common than primary cardiac tumors.

Table 10.1 Sites of occurrence of the most common benign and malignant cardiac tumors[a]

	Malignant	Benign
Endocardial, intracavitary	• Angiosarcoma • Other sarcomas • Metastases • Rhabdomyosarcoma*	• Thrombus • Myxoma • Lipoma • Papillary fibroelastoma • Hemangioma
Intramyocardial	• Metastases • Angiosarcoma • Other sarcomas • Rhabdomyosarcoma*	• Lipoma • Hemangioma • Rhabdomyoma* • Fibroma*
Pericardial	• Metastases • Mesothelioma • Lymphoma	• Pericardial cyst • Lipoma • Hemangioma • Lymphangioma • Pheochromocytoma • Teratoma*
Paracardiac	• Lymphoma • Bronchial carcinoma • Pleural mesothelioma • Malignant teratoma	• Bronchogenic cyst • Hemangioma • Teratoma*

[a] Tumors marked with an asterisk occur predominantly in children.

Table 10.2 Morphological criteria for the differentiation of benign and malignant cardiac tumors

	Benign	Malignant
Internal structure	Homogeneous	Inhomogeneous owing to necrosis and intratumoral hemorrhage
Attachment to myocardium	Pedunculated	Sessile
Extent	Limited to one chamber	Involves multiple chambers, extends beyond the heart
Pericardial effusion	Absent	Frequent, occasionally hemorrhagic
Other		Vascular invasion, pulmonary metastases

Diagnostic Techniques

The clinical presentation of cardiac tumors is usually nonspecific and is often more suggestive of a systemic disease than a cardiovascular problem. As a result, cardiac tumors were extremely difficult to diagnose before the modern imaging era, and in many cases the diagnosis was only made post mortem. On the other hand, cardiac tumors may present with symptoms such as heart failure, arrhythmias, or arterial emboli that suggest a cardiovascular problem.

Echocardiography, including transesophageal echocardiography, is the current imaging modality of first choice in patients with a suspected cardiac mass. Echocardiography has serious limitations, however, owing to its inability to clearly define mediastinal and paracardiac structures and the potential for poor image quality in patients with obesity or pulmonary emphysema.

For these reasons, sectional imaging techniques such as CT and MRI are routinely employed for the further investigation of cardiac tumors. Both modalities can evaluate the heart, mediastinum, and lung, but MRI is particularly useful for tissue characterization owing to its excellent soft-tissue contrast. The protocol for cardiac masses includes T1- and T2-weighted sequences, with and without fat suppression, and T1-weighted sequences after intravenous contrast administration (see Chapter 6). The signal characteristics of the most common cardiac tumors are summarized in **Tables 10.3–10.5.**

Essential Point

Following administration of Gd-based contrast agents, some tumors can be excellently visualized using inversion-recovery gradient-echo sequences. But if the signal from the tumor is inadvertently nulled, it can mimic an absence of enhancement. For this reason, the protocol for cardiac tumors should always include T1-weighted sequences without an inversion pulse before and after contrast administration.

Benign Primary Cardiac Tumors

Myxoma

Myxomas are the most common primary cardiac tumors and comprise ~50% of all primary cardiac masses. Ninety percent of patients are between 30 and 60 years of age, with a slight female preponderance.[4,5] Myxomas tend to occur sporadically, but rarely they occur in the setting of Carney complex—an autosomal dominant condition that includes myxomas, hyperpigmentation of the skin, and extracardiac tumors (pituitary adenomas, fibroadenomas of the breast, schwannomas).

Myxomas often become symptomatic by embolizing to the central nervous system or causing hemodynamic obstruction. Myxomas of the left atrium may produce symptoms of mitral stenosis, while right atrial tumors can mimic the features of tricuspid stenosis on clinical examination.

Additionally, patients with myxomas often have nonspecific clinical symptoms such as fatigue, joint pain, weight loss, and anemia. The cause of these systemic manifestation is unknown.

Cardiac myxomas typically arise from the interatrial septum, with 75% of tumors occurring in the left atrium and ~20% in the right atrium.[5] Echocardiography typically demonstrates mobile tumors attached to the interatrial septum by a pedicle. Large tumors may occupy almost the entire atrium, however, and may be in broad contact with the atrial wall (**Fig. 10.2**). Some tumors prolapse through the AV valve into the ventricle during diastole.

Myxomas often present a homogeneous internal structure on echocardiography, but intratumoral hemorrhage, necrosis, or calcifications may produce an inhomogeneous internal echo pattern. Calcifications are best demonstrated by CT and are found in ~20% of all myxomas. On MRI, myxomas appear isointense to myocardium on T1-weighted images. Normally they are hyperintense to myocardium on T2-weighted images, but heterogeneous lesions may rarely have lower signal intensity

Table 10.3 MRI signal characteristics of the most common benign tumors: typical signal intensity on T1-weighted turbo spin-echo (T1-TSE) images, T2-weighted turbo spin-echo (T2-TSE) images, and gradient-echo (GE) images relative to myocardium, and enhancement characteristics[a]

	Site of predilection	T1-TSE	T2-TSE	GE	Contrast enhancement
Myxoma	Left atrium	→	↑	↓	Yes
Lipoma	None	↑	↑	↑	No
Fibroelastoma	On the valves	→	↑	→	Yes
Hemangioma	Ventricle	→	↑	→	Yes
Pheochromocytoma	Pericardial	→	↑	→	Yes
Rhabdomyoma	Ventricle	→ / ↑	→ / ↑	→	Same as myocardium
Fibroma	Ventricle	→ / ↑	→ / ↓	→	Slight
Lymphangioma	Pericardial	Variable	↑	Variable	Rim enhancement
Teratoma	Pericardial	Variable	Variable	Variable	Inhomogeneous

[a] ↑ hyperintense, → isointense, ↓ hypointense.

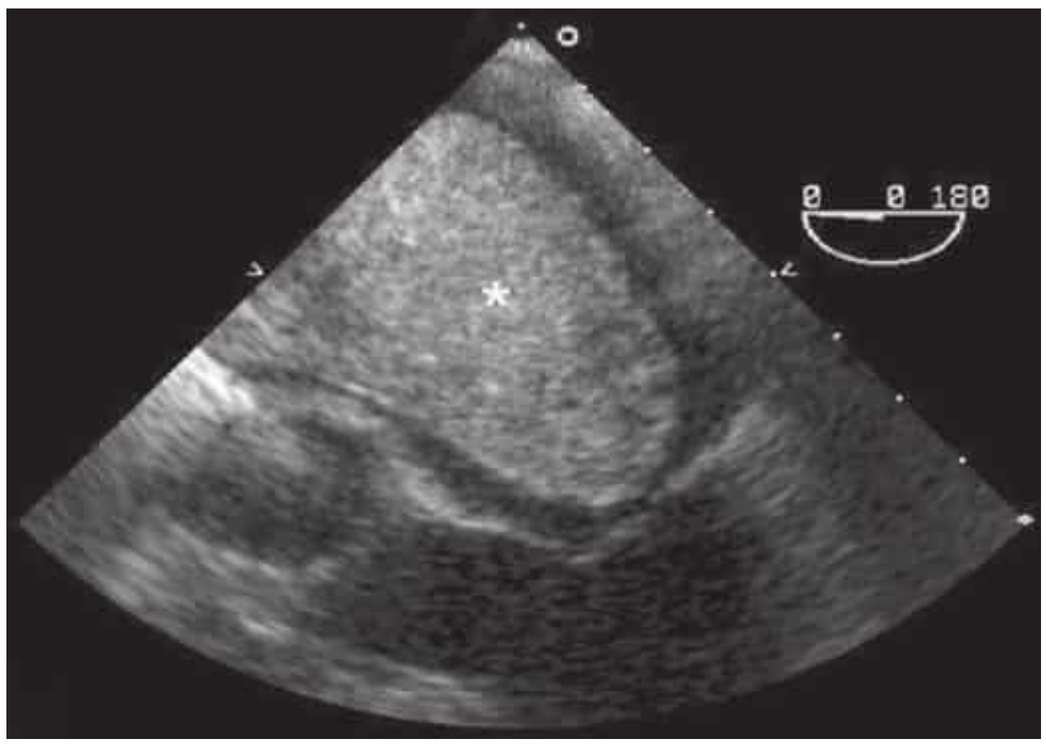

Fig. 10.2 Echocardiogram of a giant myxoma (asterisk) that occupies almost the entire left atrium.

than the myocardium. Intratumoral hemorrhage in particular may shorten the T2 relaxation time of the mass, causing it to appear hypointense to myocardium. Myxomas show marked, often inhomogeneous enhancement after intravenous contrast administration (**Fig. 10.3**). Cine MRI can demonstrate tumor mobility in much the same way as echocardiography.

Cardiac Lipoma

There is considerable variation in published reports on the incidence of cardiac lipomas. Some authors call it the second most common tumor in adults,[6] while others describe it as extremely rare.[7] A potential reason may be the difficulty of detecting small epicardial lipomas. Moreover, some authors do not distinguish between lipomas and lipomatous hypertrophy of the interatrial septum. Cardiac lipomas may occur in any age group but are most prevalent in middle-aged and elderly individuals. Cardiac lipomas are generally asymptomatic and are not associated with clinical syndromes, although there have been a few published cases of multiple cardiac lipomas in children with tuberous sclerosis.

Lipomas are most commonly located in the right atrium or atrial septum but may occur in any heart chamber. Echocardiograms typically show a sharply circumscribed, hypoechoic mass that is broadly apposed to the adjacent wall. Lipomas have a homogeneous CT appearance with an attenuation of approximately –50 HU. Lipomas have high signal intensity in T1-weighted sequences and intermediate signal intensity on T2-weighted images. Cardiac lipomas do not contain foci of calcification, hemorrhage, or necrosis. Lipomas can be positively identified on fat-suppressed MR images (**Fig. 10.4**). They do not enhance after IV contrast administration.

Table 10.4 MRI signal characteristics of the most common malignant tumors: typical signal intensity on T1-weighted turbo spin-echo (T1-TSE) images, T2-weighted turbo spin-echo (T2-TSE) images, and gradient-echo images relative to myocardium, and enhancement characteristics[a]

	Site of predilection	T1-TSE	T2-TSE	GE	Contrast enhancement
Angiosarcoma	Right atrium	Inhomogeneous	Inhomogeneous	Inhomogeneous	Yes
Other sarcomas	None	Variable	Variable	Variable	Yes
Lymphoma	Right atrium, ventricle	→	→	→	Inhomogeneous
Mesothelioma	Pericardial	→	↑	→ / ↓	Inhomogeneous
Rhabdomyosarcoma	None	Variable	Variable	Variable	Inhomogeneous
Metastases	Pericardial	Variable	Variable	Variable	Inhomogeneous

[a] ↑ hyperintense, → isointense, ↓ hypointense.

Table 10.5 MRI signal characteristics of the most common nonneoplastic cardiac masses: typical signal intensity on T1-weighted turbo spin-echo (T1-TSE) images, T2-weighted turbo spin-echo (T2-TSE) images, and gradient-echo images relative to myocardium, and enhancement characteristics[a]

	Site of predilection	T1-TSE	T2-TSE	GE	Contrast enhancement
Thrombi	Atrial appendage, ventricle	→ / ↑	→ / ↑	↓	No (rarely in chronic thrombi)
Valvular vegetations	Valves	Not visible	Not visible	↓	No
Fatty hyperplasia of atrial septum	Atrial septum	↑	↑	→	No
Aneurysms	Sinus of Valsalva, atrial septum	↓	↓	↑	Yes

[a] ↑ hyperintense, → isointense, ↓ hypointense.

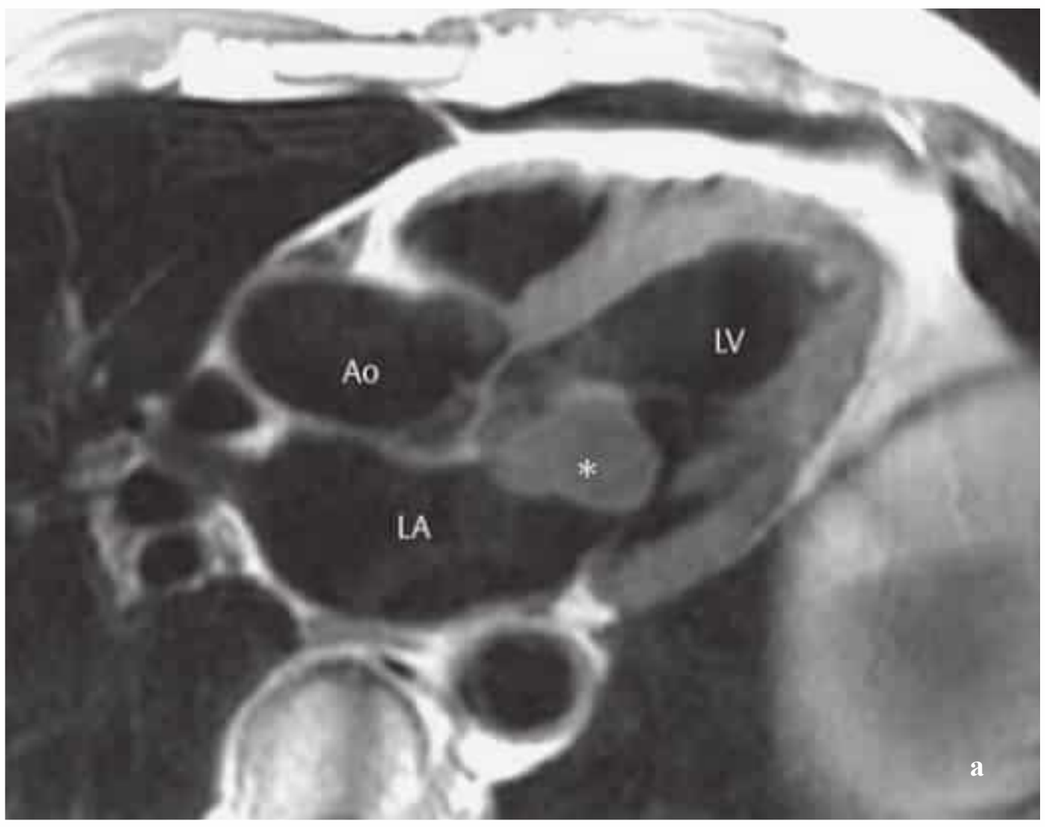

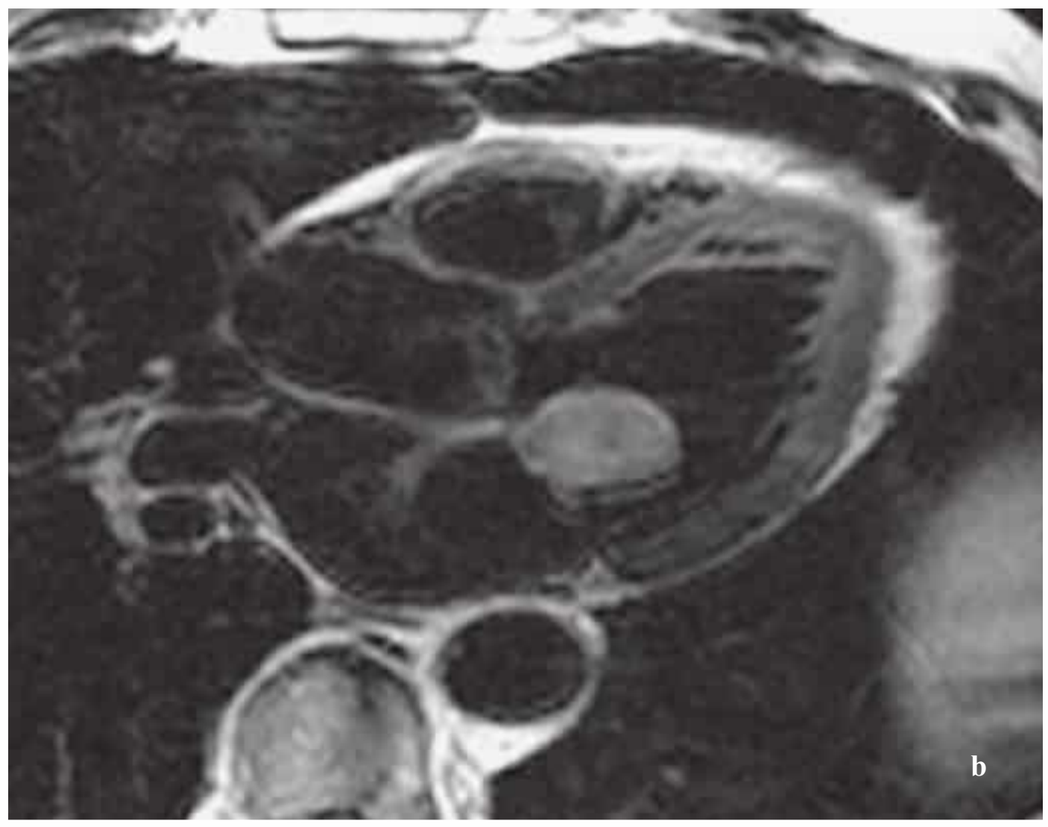

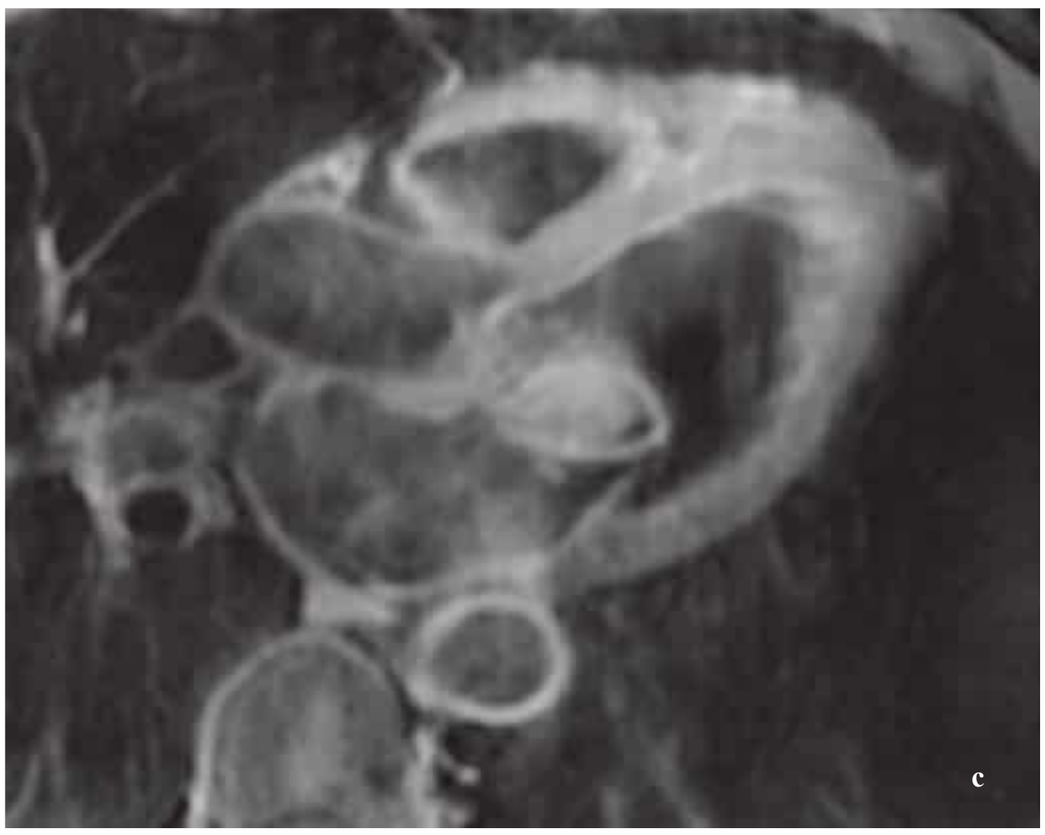

Fig. 10.3a–c Myxoma (asterisk) that prolapses into the left ventricle in diastole. T1-weighted image (**a**), T2-weighted image (**b**), and fat-suppressed T1-weighted image after intravenous contrast injection (**c**).

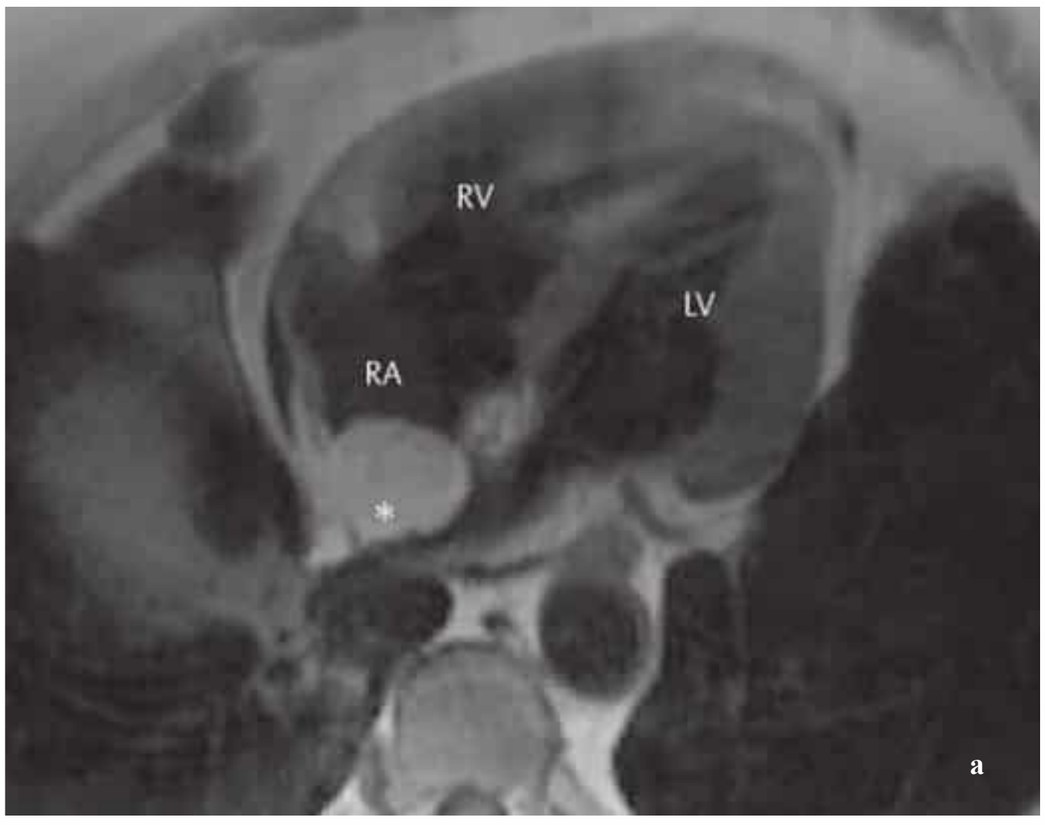

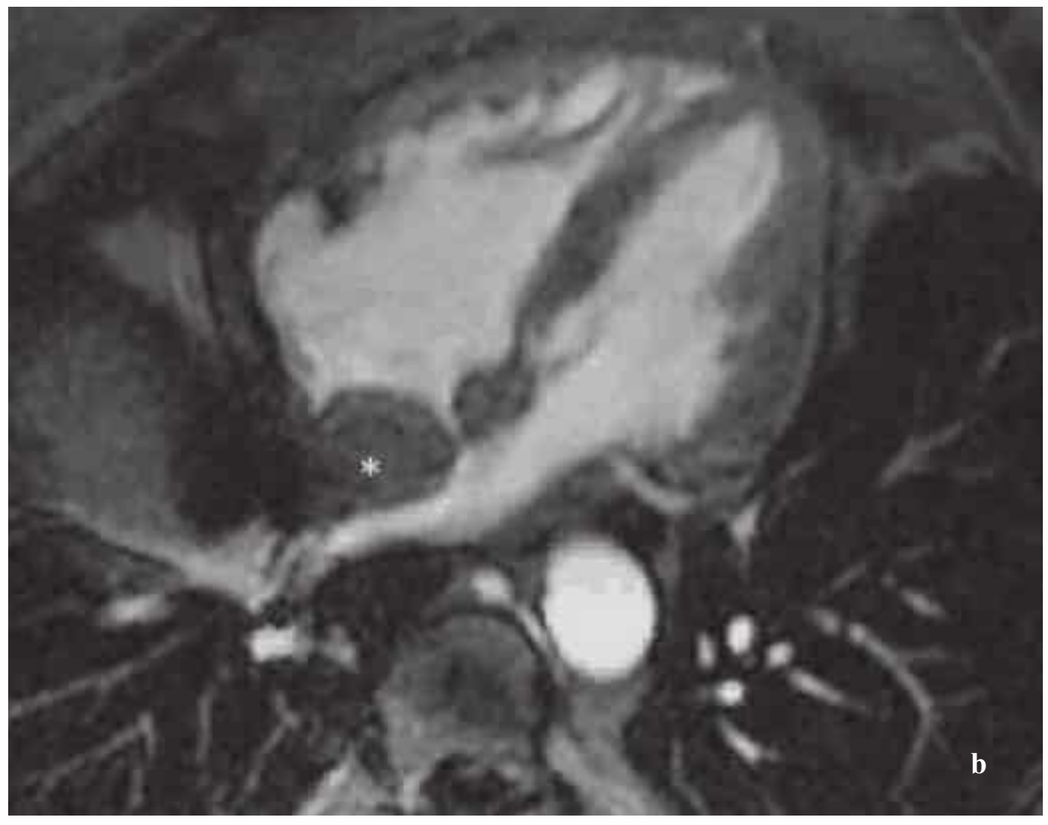

Fig. 10.4a, b Lipoma in the right atrium (asterisk). T1-weighted image before contrast administration (**a**) and fat-suppressed T1-weighted image after contrast administration (**b**). The tumor has high, homogeneous signal intensity on the precontrast image. It does not enhance after contrast administration and has very low signal intensity in the fat-suppressed image (**b**).

Differentiation is required from lipomatous hypertrophy of the interatrial septum, which is more common than cardiac lipoma and may precipitate supraventricular arrhythmias. Lipomatous hypertrophy of the interatrial septum is defined as an area of fat deposition in the atrial septum that is larger than 2 cm in transverse diameter and spares the fossa ovalis.

Essential Point
Cardiac lipoma mainly requires differentiation from lipomatous hypertrophy of the interatrial septum.

Papillary Fibroelastoma

Papillary fibroelastomas account for ~10% of primary benign cardiac tumors. They are most prevalent in the elderly population. Tumors located in the right cardiac chambers are asymptomatic, whereas tumors in the left heart may rarely become symptomatic owing to embolization.[6,7]

Papillary fibroelastomas are usually attached to a cardiac valve, most commonly the aortic or mitral valve. Only ~10% of papillary fibroelastomas do not involve the heart valves. Fibroelastoma is easily detected by echocardiography, appearing as a small mass less than 1 cm in diameter that is attached to a heart valve by a short pedicle. No reports have yet been published on the CT detection of these tumors, but this situation is likely to change through the increased use of ECG-triggered multislice CT. Calcifications are rarely found in pathological examinations of tissue specimens. On MRI, papillary fibroelastomas are best demonstrated by cine imaging because of their small size and rapid motion (**Fig. 10.5**). Their tissue composition cannot always be characterized in T1- and T2-weighted sequences.

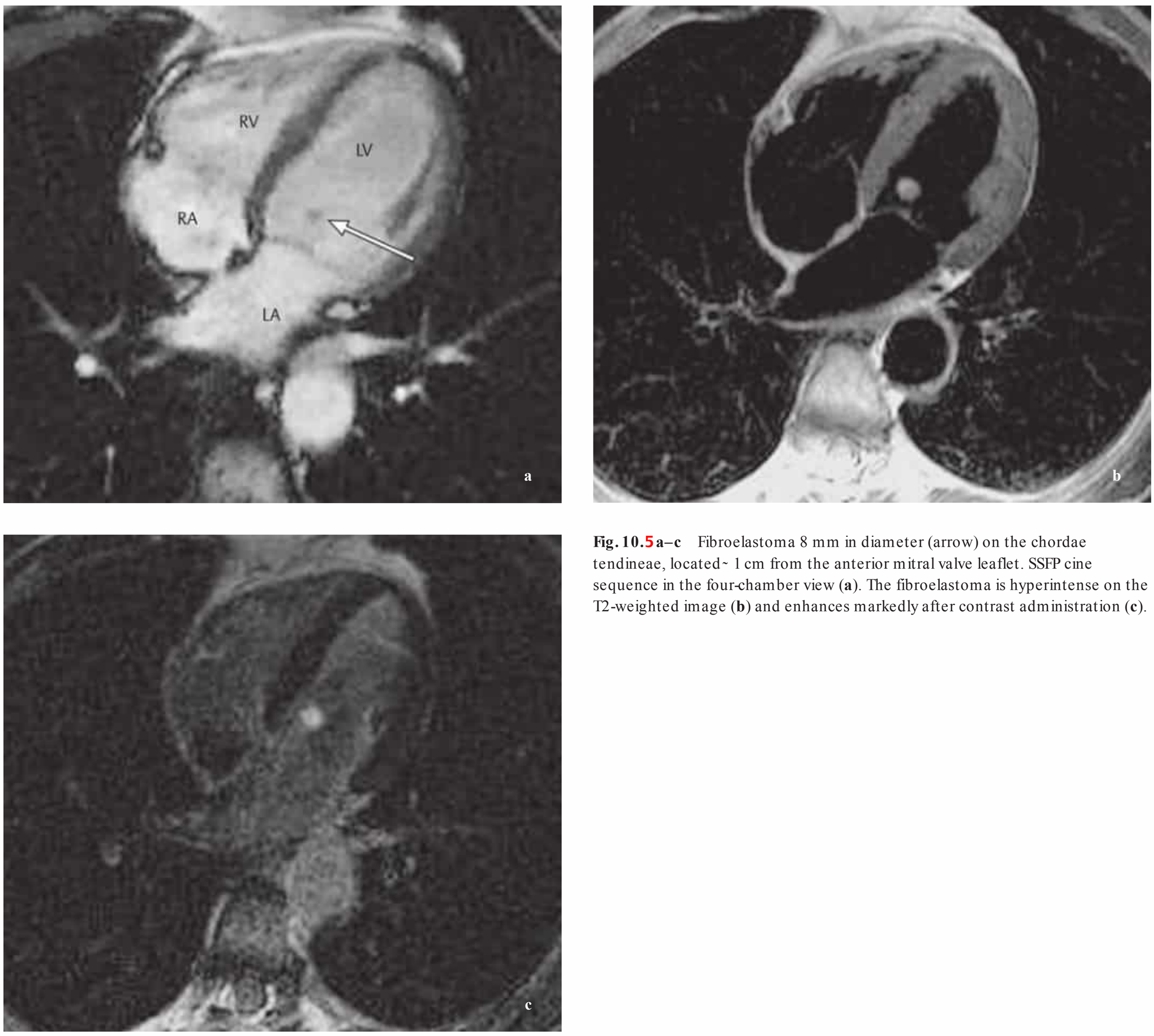

Fig. 10.5 a–c Fibroelastoma 8 mm in diameter (arrow) on the chordae tendineae, located ~ 1 cm from the anterior mitral valve leaflet. SSFP cine sequence in the four-chamber view (**a**). The fibroelastoma is hyperintense on the T2-weighted image (**b**) and enhances markedly after contrast administration (**c**).

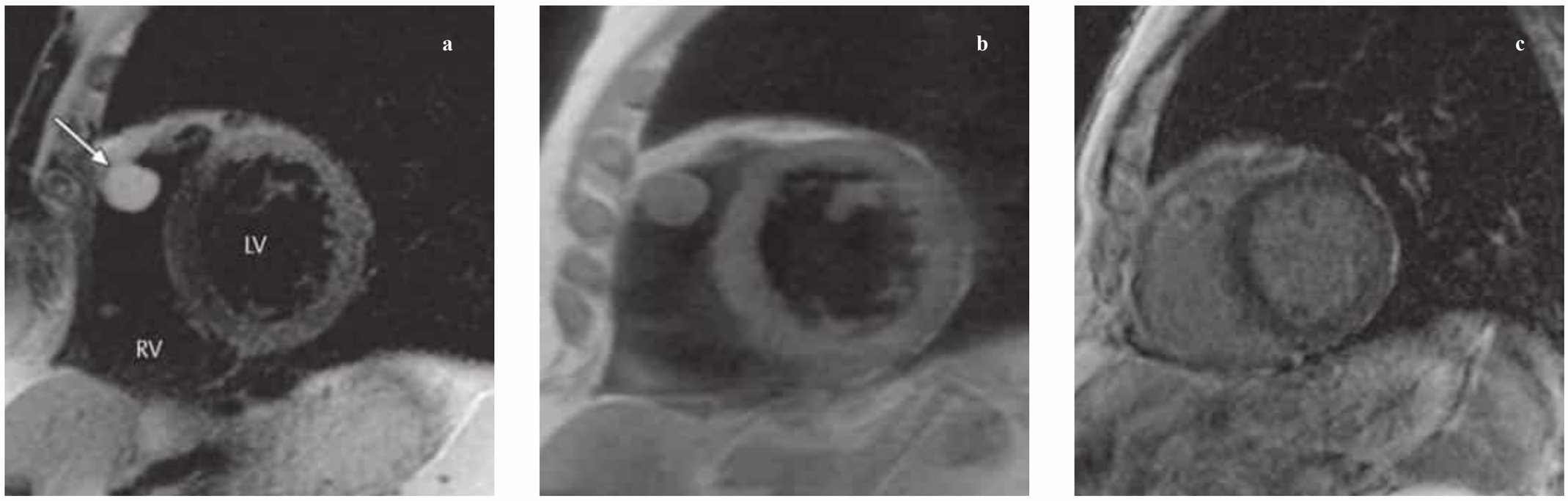

Fig. 10.6a–c Well-circumscribed hemangioma (arrow) in the right ventricular outflow tract has high signal intensity on the T2-weighted image (**a**) and is isointense to myocardium on the T1-weighted image (**b**). It shows marked contrast enhancement (**c**).

Cardiac Hemangioma

Hemangioma is a rare primary cardiac tumor that comprises ~5 %of all benign cardiac tumors. It may occur in the setting of Kasabach–Meritt syndrome, which is characterized by multiple systemic hemangiomas, recurrent thrombocytopenia, and coagulopathy. Most cardiac hemangiomas are asymptomatic, but some may cause dyspnea, chest pain, or arrhythmias.[7]

Cardiac hemangiomas may occur in any cardiac chamber and may arise from the endocardium, myocardium, or epicardium. They may also have a pericardial or paracardiac location. Hyperechoic masses are typically seen at echocardiography. CT often demonstrates calcified lesions that enhance intensely after contrast administration. Hemangiomas usually have intermediate signal intensity on T1-weighted images and high signal intensity on T2-weighted images. Calcifications or flow voids may produce an inhomogeneous appearance. Hemangiomas typically show intense enhancement after intravenous contrast injection (**Fig. 10.6**).

Pheochromocytoma

Cardiac pheochromocytomas are an extremely rare benign tumor occurring in adults. Most of these tumors produce catecholamines and present clinically with hypertension, headache, and flushing. Twenty percent of patients also have pheochromocytomas at other sites.

Cardiac pheochromocytomas most commonly occur in the posterior wall of the left atrium, followed by the roof of the left atrium, the lumen of the atria, the interatrial septum, and the ventricles. Echocardiography typically demonstrates a large echogenic mass in the left atrium. The tumors may contain calcifications at CT and enhance after contrast administration, often showing central low density owing to necrosis. They are isointense to myocardium on T1-weighted MR images and are hyperintense on T2-weighted images. They show intense, inhomogeneous enhancement after IV contrast administration.

Rhabdomyoma

Rhabdomyoma is the most common benign cardiac tumor in children. Approximately 50 %occur in patients with tuberous sclerosis.[7] Most tumors are asymptomatic and are detected by antenatal or postpartum echocardiography. They may cause arrhythmias or a heart murmur, however, and may lead to cardiac failure. Cardiac rhabdomyomas often undergo spontaneous regression.

Given the intramural location of the tumors, echocardiography shows circumscribed wall thickening of the left and/or right ventricle. Multifocal lesions are common. Rhabdomyomas are typically isointense to myocardium on T1-weighted images and are sometimes delineated as hyperintense masses on T2-weighted images (**Fig. 10.7**). Most cardiac rhabdomyomas are isointense to myocardium after IV contrast administration, but may show slightly increased enhancement.

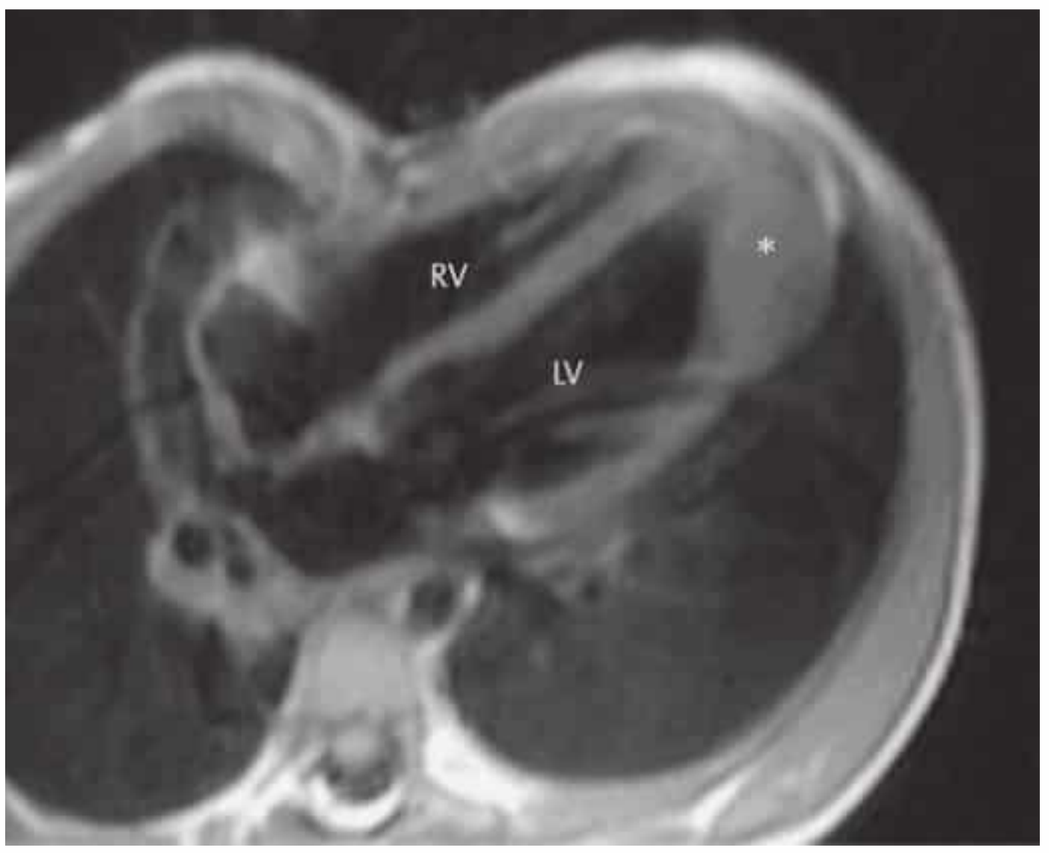

Fig. 10.7 Rhabdomyoma in the apical lateral wall. T2-weighted MRI displays the tumor as a well-circumscribed homogeneous mass that is isointense to myocardium.

Fibroma

Fibroma is the second most common benign cardiac tumor in children. The average age at diagnosis is 13 years, but patients show a broad age range from birth to 56 years. Cardiac fibromas are particularly common in patients with Gorlin syndrome, an autosomal dominant condition characterized by multiple basal cell carcinomas, multiple jaw cysts, rib anomalies, glaucoma, and cataracts. Cardiac fibromas may be asymptomatic or may present with a cardiac murmur, heart failure, or arrhythmias.[5,6]

Cardiac fibromas invariably involve the ventricles. Sites of predilection are the interventricular septum and the free wall of the left ventricle. Most of these tumors are large, ranging from 2 to 5 cm in diameter. Fibromas appear on echocardiography as noncontractile solid masses in the ventricular wall. They appear on CT as homogeneous masses of soft-tissue attenuation, although calcifications are frequently detected. Fibromas are isointense or hyperintense to myocardium on T1-weighted MR images and hypointense on T2-weighted images. They show little or no enhancement after IV contrast administration.

Lymphangioma

Lymphangiomas are extremely rare, benign primary cardiac tumors that occur predominantly in children. Most lymphangiomas are clinically silent, but patients may become symptomatic owing to arrhythmias.

Most cardiac lymphangiomas are located in the pericardium, where they may incite a chylous pericardial effusion. At echocardiography, lymphangiomas appear as cystic masses that may contain septations. They do not contain calcifications, hemorrhagic areas, or necrosis. The tumors have a heterogeneous CT appearance with septations and low attenuation values. Lymphangiomas are hyperintense on T2-weighted images and have variable signal intensity on T1-weighted images. They show inhomogeneous enhancement after IV contrast administration.

Teratoma

Teratoma is a rare, benign primary cardiac tumor in children that is almost always located in the pericardium. Patients often present clinically with shortness of breath or cyanosis due to pericardial tamponade or the compression of right-sided vascular structures.

Pericardial teratomas may already be detectable by prenatal ultrasound, appearing as multifocal cystic masses with an associated pericardial effusion. The chest radiograph shows cardiac enlargement and may demonstrate teeth or other calcified structures. Echocardiography shows a heterogeneous intrapericardial mass with multiple cystic elements, typically located adjacent to the right heart. Concomitant pericardial effusion is often present. CT and MRI show a large, heterogeneous tumor that enhances after IV contrast administration.

Malignant Primary Cardiac Tumors

Angiosarcoma

Angiosarcoma is the most common primary malignant cardiac tumor and accounts for ~40 % of all malignant cardiac tumors. Males are predominantly affected. The peak incidence is between 20 and 50 years of age, but the tumor may occur in any age group. The most common site of occurrence is the right atrium (**Fig. 10.8a**). The right atrial location of the tumor and its frequent infiltration of the pericardium produce clinical signs of right heart failure and pericardial effusion, which may lead to pericardial tamponade. Patients may also have systemic manifestations such as fever or weight loss.[1]

Conventional radiographs show cardiomegaly caused by the tumor itself or the accompanying pericardial effusion. Echocardiography shows an inhomogeneous mass, which may be only partially visualized if it extends beyond the heart. CT shows an extensive mass with a heterogeneous internal structure owing to hemorrhage and necrosis. Angiosarcomas typically show

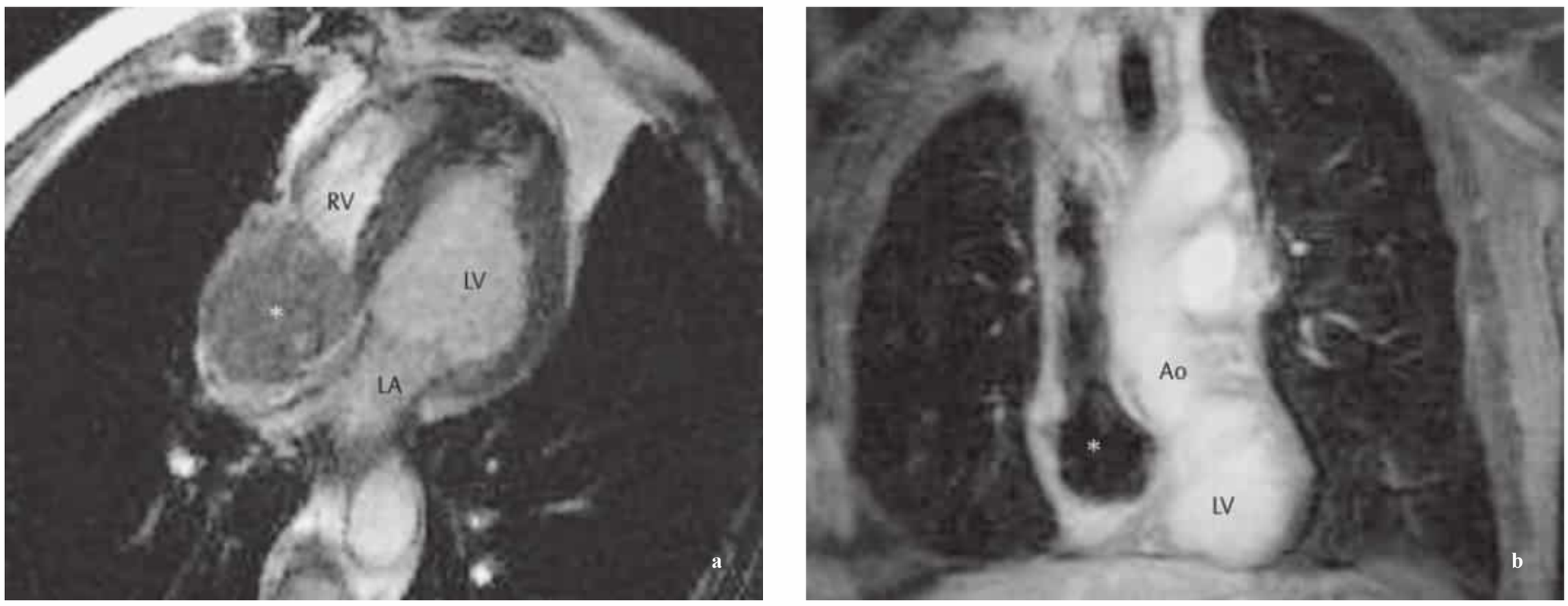

Fig. 10.8 a, b Large angiosarcoma (asterisk) in the right atrium (cine SSFP). After contrast administration (IR-GRE), the tumor appears predominantly hypointense and should not be mistaken for a thrombus.

contrast enhancement. They have inhomogeneous signal intensity on T1- and T2-weighted MR images. Areas of intratumoral hemorrhage have high signal intensity on T1-weighted images, while cystic or necrotic tumor components appear hyperintense on T2-weighted images. The tumors show inhomogeneous enhancement after IV contrast injection. The entire pericardium may show marked enhancement owing to diffuse pericardial invasion.

Essential Point
Large angiosarcomas may completely fill the vena cava. These lesions are difficult to distinguish from vena cava thrombi based on their imaging features.

Other Primary Cardiac Sarcomas

This group includes various tumor entities, which are listed below in descending order of frequency:

- Undifferentiated sarcoma
- Osteosarcoma
- Leiomyosarcoma
- Fibrosarcoma
- Liposarcoma

While the peak age incidence and clinical symptoms are the same as for angiosarcoma, tumors of this group occur predominantly in the left atrium, although they also occur at other sites (**Fig. 10.9**). These tumors usually have imaging features that are indistinguishable from angiosarcoma. Osteosarcoma is the only entity that can be differentiated by the presence of calcifications. It should be added that liposarcoma rarely contains lipomatous elements, and this simplifies its differentiation from lipoma.

Primary Cardiac Lymphoma

The majority of these tumors are non-Hodgkin lymphomas. By definition, primary cardiac lymphoma is not associated with extracardiac manifestations. Primary cardiac lymphoma is much less common than cardiac involvement by generalized lymphomatous disease. Cardiac lymphomas develop with increased incidence in immunocompromised patients, especially in association with AIDS. The peak incidence is at ~60 years of age, but patients may range in age from 13 to 90 years. The incidence appears to be slightly higher in males. Cardiac lymphoma may present clinically with:

- Rapidly progressive heart failure
- Arrhythmias
- Chest pain
- Pericardial tamponade
- Compression of the superior vena cava[1,6]

The most common site of occurrence is the right atrium. The chest radiograph demonstrates cardiomegaly. Echocardiography shows a hypoechoic mass with an associated pericardial effusion. CT shows large, inhomogeneous masses that are iso- or hypointense to myocardium and enhance markedly after IV contrast injection. MRI shows poorly demarcated, often heterogeneous tumors that are usually isointense to myocardium on T1-weighted images and slightly hyperintense on T2-weighted images (see **Fig. 6.10**, p. 99). They often show inhomogeneous enhancement after IV contrast administration.

Pericardial Mesothelioma

Although primary pericardial mesotheliomas make up less than 1% of all malignant mesotheliomas, they are responsible for ~50% of all primary pericardial tumors. Pericardial mesothelio-

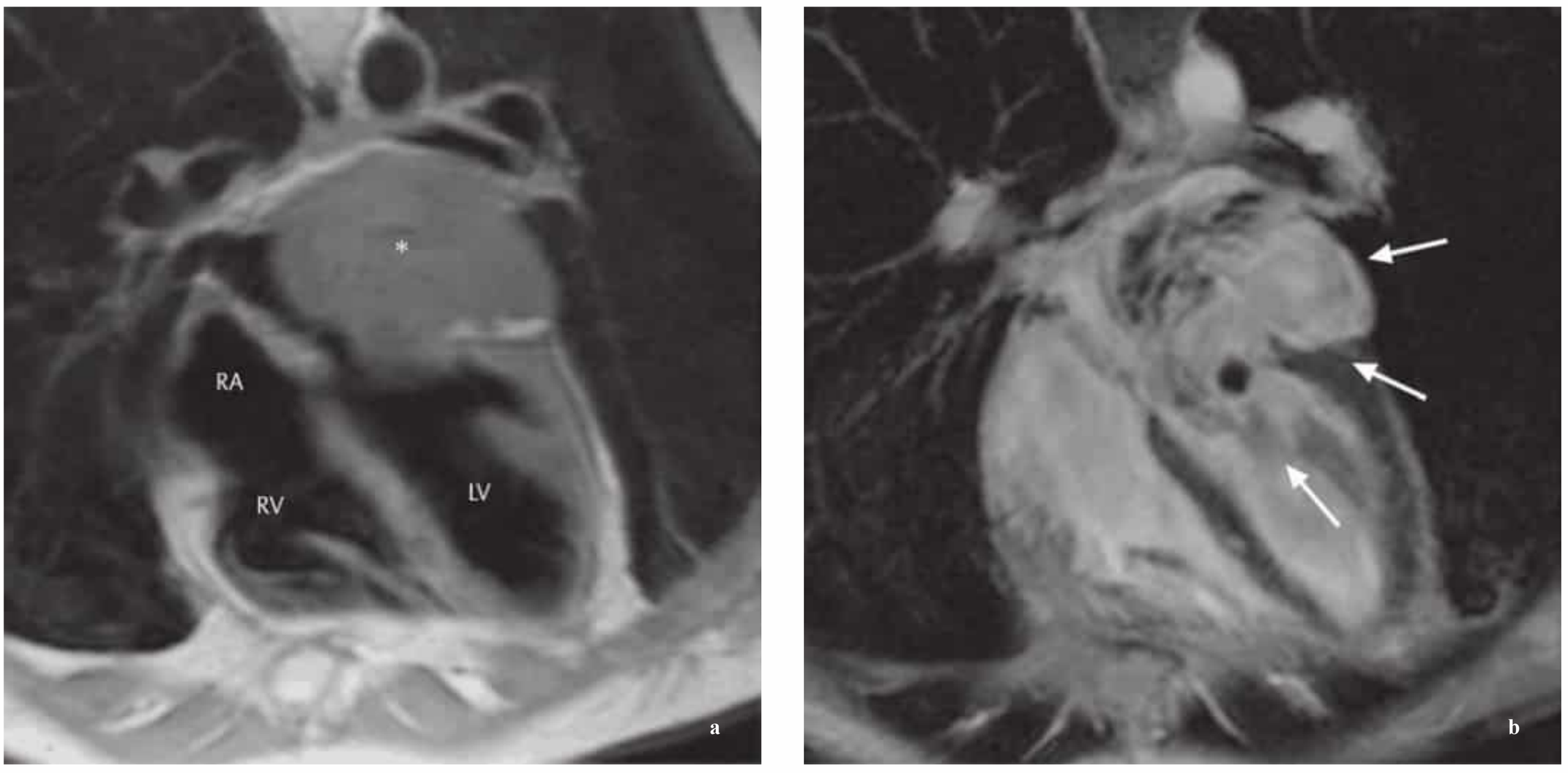

Fig. 10.9 a, b Undifferentiated sarcoma (asterisk) occupies almost the entire left atrium and extends beyond the atrial cavity. It has a homogeneous appearance in the precontrast T1-weighted image (**a**) and shows marked inhomogeneous contrast enhancement (**a**) (arrows).

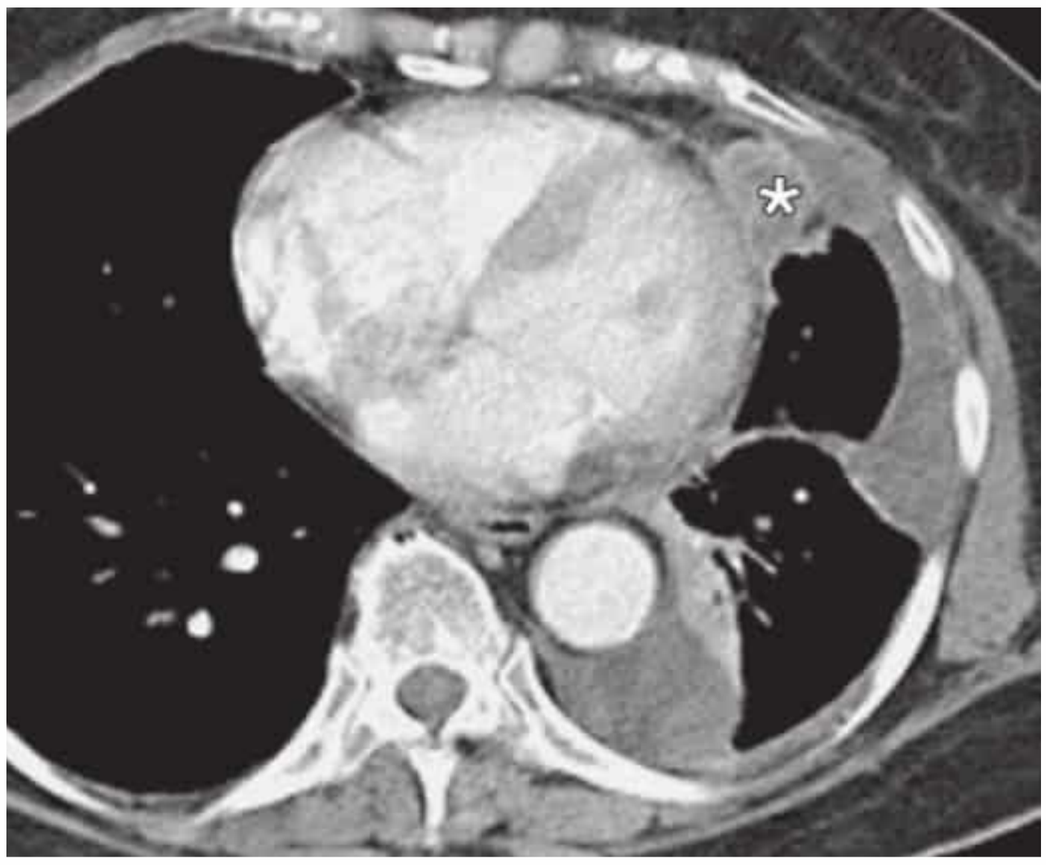

Fig. 10.10 Pericardial metastasis from breast carcinoma (asterisk). Contrast-enhanced CT.

mas may occur at any age, and males predominate by a ratio of about 2:1. Patients frequently complain of chest pain, cough, dyspnea, or cardiac arrhythmias. The clinical manifestations often resemble those of pericarditis.

Chest radiographs typically show marked cardiac enlargement caused by the tumor and concomitant pericardial effusion. The films may also show irregular cardiac borders and diffuse mediastinal widening. CT reveals irregular, diffuse pericardial thickenings, and pericardial effusion. The pericardial masses and entire pericardium may show diffuse contrast enhancement. MRI also shows significant pericardial effusion and pericardial masses that are isointense to myocardium on plain T1-weighted images and enhance intensely after contrast administration.

Rhabdomyosarcoma

Rhabdomyosarcoma is the most common primary malignant cardiac tumor in children. Boys are affected somewhat more frequently than girls. The tumor may arise from any portion of the myocardium, and rhabdomyosarcomas are often multiple. CT typically shows a large mass of soft-tissue attenuation that does not contain calcifications. The MR signal intensity is variable. Rhabdomyosarcomas may appear isointense to myocardium on T1- and T2-weighted images, but necrotic areas can produce a heterogeneous pattern. They show patchy enhancement after IV contrast injection. Vascular invasion is common and can be reliably detected by CT and MRI.

Secondary Cardiac Tumors

Metastases

Melanoma, bronchial carcinoma, and breast carcinoma are tumors that frequently metastasize to the heart. The pericardium is a common site of predilection (**Fig. 10.10**), but diffuse myocardial metastasis may also occur, especially with malignant melanoma (**Fig. 10.11**). Endocardial or intracavitary metastasis occurs in only 5 % of cases.

Direct Extension

As well as cardiac metastasis, malignant tumors of the lung or mediastinum may invade the heart by direct extension. The most common tumors are:

- Lymphoma
- Bronchial carcinoma
- Pleural mesothelioma
- Malignant teratoma

Tumors may also invade the heart through large venous vessels. In particular, renal cell carcinoma may invade the right atrium by extension along the renal vein and inferior vena cava.

Nonneoplastic Cardiac Masses

Intracardiac Thrombi

Thrombi are the most common intracavitary cardiac masses. Most are located in the left ventricle or left atrium. Thrombi in the left atrium are typically associated with:

- Atrial enlargement
- Mitral valve disease
- Atrial fibrillation

Thrombi in the left ventricle occur almost exclusively in akinetic or dyskinetic areas following a myocardial infarction or in left ventricular aneurysms.

It has been reported that ~30 % of patients who have sustained a myocardial infarction go on to develop left ventricular thrombi, although that figure may be lower today as a result of modern therapies for acute myocardial infarction including thrombolytic and anticoagulant therapy. Thrombi in the left cardiac chambers are often manifested clinically by strokes or other systemic emboli. Approximately 30 % of all strokes are caused by cardiac thrombi.

Thrombi are much less common in the right heart and usually represent transit thrombi in patients with deep venous thrombosis and pulmonary embolism (**Fig. 10.12**). The following rare diseases are associated with an increased incidence of cardiac thrombi:

- Behçet syndrome
- Löffler endocarditis
- Churg–Strauss syndrome
- Coagulation disorders
- Aneurysms of the right cardiac chambers

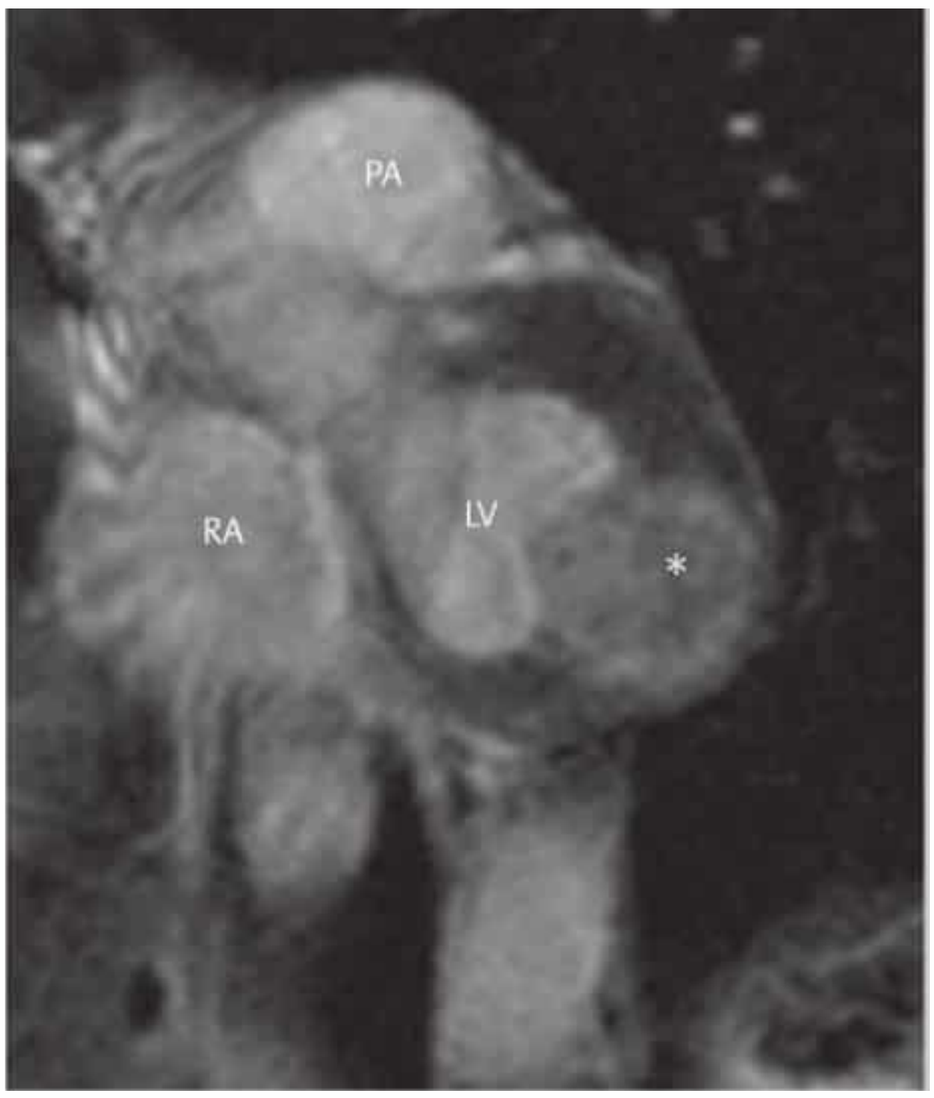

Fig. 10.11 Metastasis (asterisk) from renal cell carcinoma in the inferolateral wall of the left ventricle. IR-GRE sequence after contrast administration.

Thrombi appear on echocardiography as intracavitary masses with irregular or lobulated margins. Transesophageal echocardiography is considered the method of first choice for the detection of left atrial thrombi. In most cases these thrombi, which are frequently small, cannot be reliably detected or excluded by MRI. Cardiac CT would seem to be a more promising approach, but data from large studies are not yet available. Thrombi appear on CT as homogeneous filling defects after IV contrast administration.

Disadvantages of echocardiography are that it cannot completely visualize all the cardiac chambers, and it cannot reliably distinguish between acute and organized thrombi. The MRI detection and characterization of intraventricular thrombi with dark-blood T1- and T2-weighted turbo spin-echo sequences is limited because of slow-flow artifacts, since thrombi are most likely to occur in areas where blood flow velocity is reduced. Thrombi are predominantly isointense to myocardium when imaged in steady-state free-precession (SSFP) sequences. Thus, larger intracavitary thrombi can be positively identified with this technique, whereas small thrombi layered along the wall are not detectable because they are not delineated from the myocardium. As a result, intravenous contrast administration is necessary for the reliable detection and characterization of intracardiac thrombi.[8,9]

Inversion recovery-gradient-echo (IR-GRE) sequences have proved particularly useful owing to their robust image quality. In images acquired immediately after IV contrast administration, thrombi appear as hypointense masses that are clearly delineated from the myocardium and its cavity (**Fig. 10.13**). Most intracardiac thrombi are nonenhancing, but chronic organized thrombi may show a centripetal pattern of enhancement. MRI has higher sensitivity and specificity than echocardiography in the detection of left ventricular thrombi.[10]

Essential Point

MRI is the method of choice for ventricular thrombi, while transesophageal echocardiography is the method of first choice for thrombi in the atria and especially in the atrial appendage.

When cardiac thrombi are suspected, 2D or preferably 3D IR–GRE sequences with a long TI (300–400 ms) should be acquired immediately after contrast administration. Owing to the long TI and early timing of the acquisition, the myocardium will show intermediate signal intensity (not nulled) while thrombi appear as low-signal masses that contrast sharply with the myocardium and the hyperintense cavity (**Fig. 10.13**).

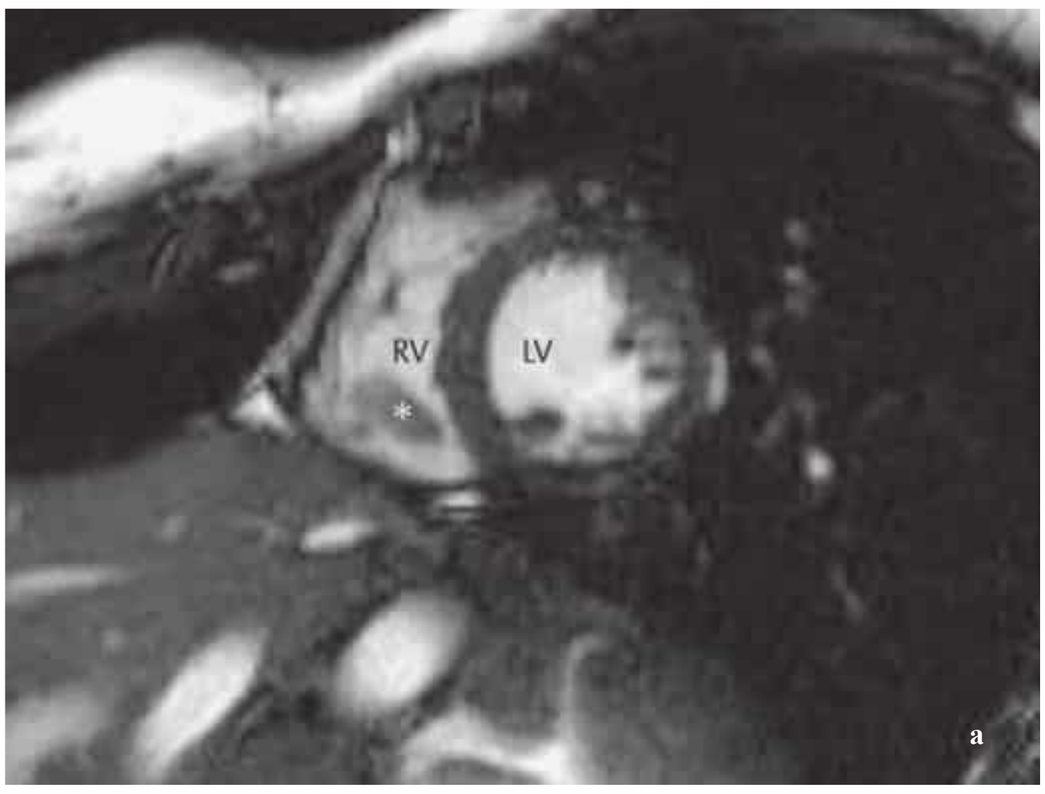

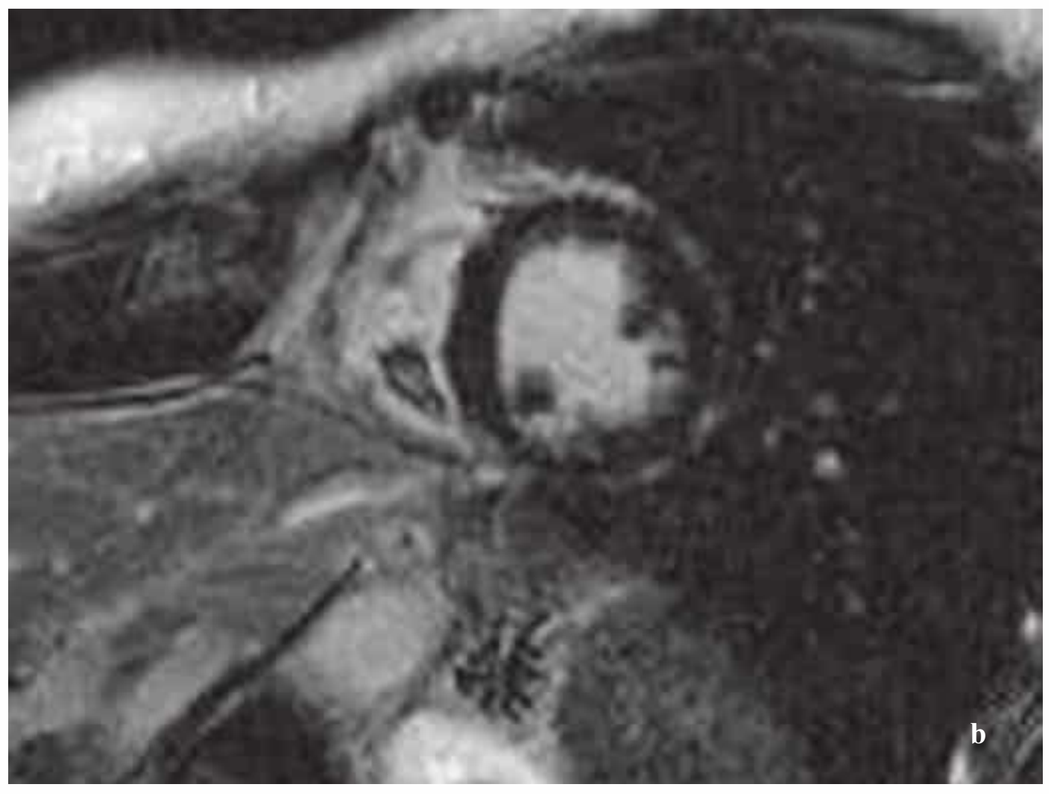

Fig. 10.12 a, b Thrombus in the right ventricle (asterisk) is well delineated in the cine SSFP sequence (**a**) and in the IR-GRE sequence after contrast administration (**b**).

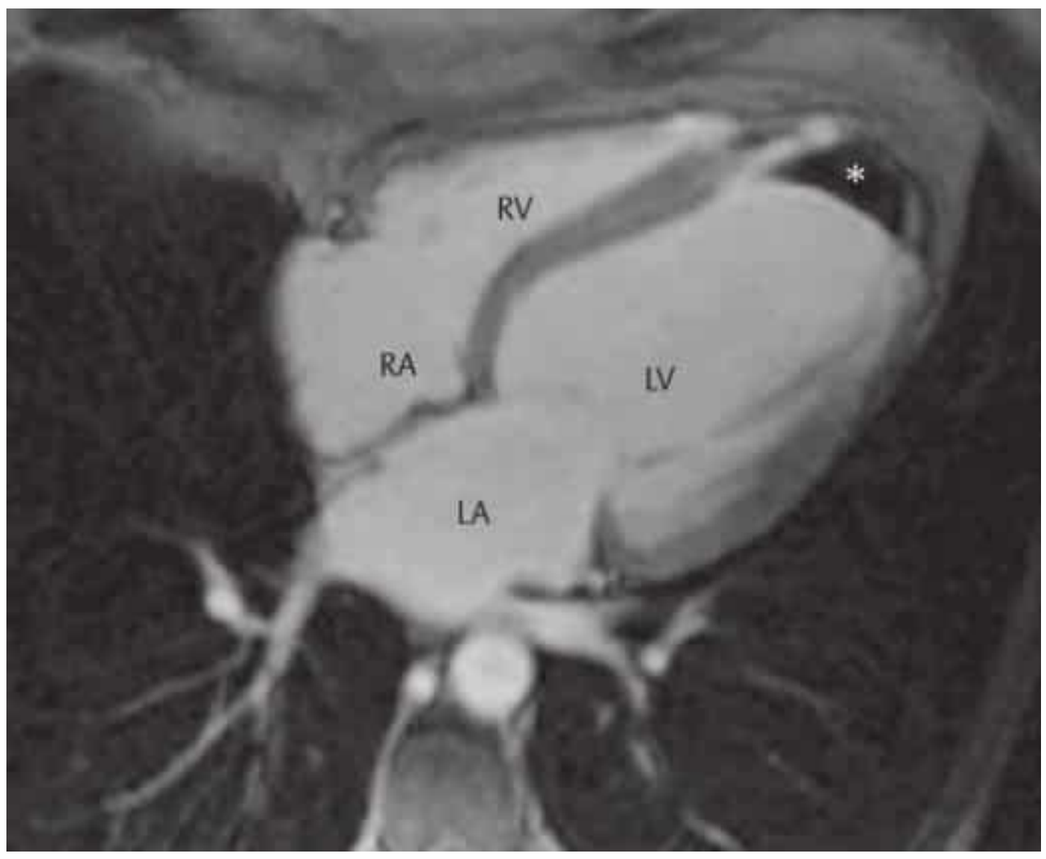

Fig. 10.13 IR-GRE sequence with an inversion time of 300 ms. Four-chamber view immediately after contrast administration reveals a hypointense thrombus in the apex of the left ventricle (asterisk).

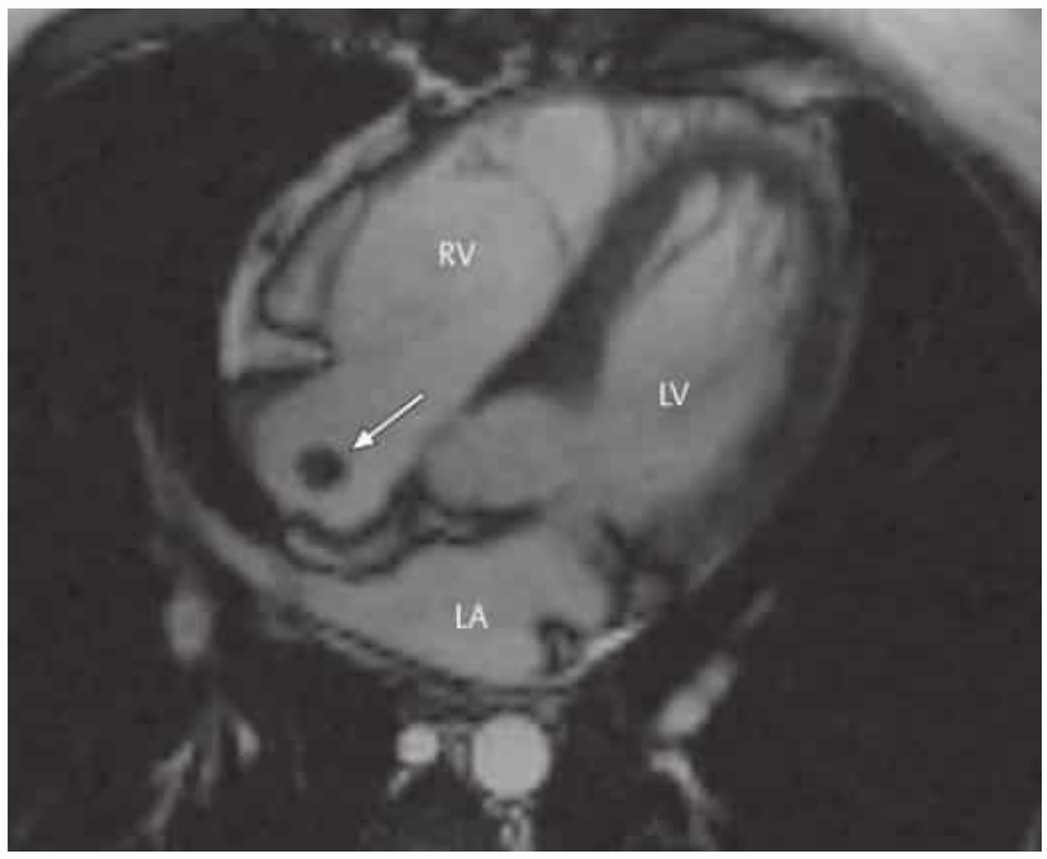

Fig. 10.14 Nodular thickening of the crista terminalis (arrow). This finding should not be mistaken for a mass.

Aneurysms

Aneurysms that arise from cardiac structures can mimic intracardiac thrombi. They have two typical sites of occurrence: the sinus of Valsalva and the atrial septum. Sinus of Valsalva aneurysms are most commonly located in the right coronary sinus. Most are congenital, but a small percentage may be acquired as a result of endocarditis. The most frequent complication is rupture of the aneurysm, usually occurring into the right ventricular outflow tract, right ventricular cavity, or right atrium. Initial diagnosis relies on echocardiography, and MRI may be helpful in defining the communication between the aorta and cardiac chambers.

The second main site of occurrence is the atrial septum. An atrial septal aneurysm is defined as a diffuse or localized protrusion of the interatrial septum into the right atrium, left atrium, or both. These aneurysms may be associated with atrial septal defects, a patent foramen ovale (PFO) and may give rise to arrhythmias or emboli. Usually the diagnosis is established by echocardiography. Atrial septal aneurysms can mimic tumors on MRI, but cine imaging will usually provide an accurate diagnosis (see Chapter 7, **Fig. 7.6**).

Anatomical Variants

Cardiac tumors require differentiation from anatomical variants that resemble cardiac masses. One such mimic is the crista terminalis, a remnant of the septum spurium that forms a fibromuscular ridge on the posterior wall of the right atrium between the orifices of the superior and inferior venae cavae.

Other anatomical structures that can mimic a right atrial mass are the eustachian valve and the Chiari network. The Chiari network is attached to the area of the crista terminalis and extends toward the inferior vena cava and coronary sinus. Sometimes these structures may have a nodular appearance (**Fig. 10.14**), but an awareness of these variants and their typical locations should prevent their misinterpretation as cardiac masses.

Essential Point
Anatomical variants in the atrium may be mistaken for tumors at echocardiography, but most ambiguities can be resolved by MRI.

References

1. Araoz PA, Eklund HE, Welch TJ, Breen JF. CT and MR imaging of primary cardiac malignancies. Radiographics 1999;19:1421–1434
2. Lam KY, Dickens P, Chan AC. Tumors of the heart. A 20-year experience with a review of 12,485 consecutive autopsies. Arch Pathol Lab Med 1993;117:1027–1031
3. McAllister HA Jr. Primary tumors of the heart and pericardium. Pathol Annu 1979;14(Pt 2):325–355
4. Amano J, Kono T, Wada Y, et al. Cardiac myxoma: its origin and tumor characteristics. Ann Thorac Cardiovasc Surg 2003;9:215–221
5. Araoz PA, Mulvagh SL, Tazelaar HD, Julsrud PR, Breen JF. CT and MR imaging of benign primary cardiac neoplasms with echocardiographic correlation. Radiographics 2000;20:1303–1319
6. Krombach GA, Spuentrup E, Buecker A, et al. Herztumoren: MRT und Mehrschicht-Spiral-CT. Rofo. 2005;177:1205–1218
7. Grebenc ML, Rosado de Christenson ML, Burke AP, Green CE, Galvin JR. Primary cardiac and pericardial neoplasms: radiologic-pathologic correlation. Radiographics. 2000;20:1073–1103; quiz 1110–1011, 1112.
8. Barkhausen J, Hunold P, Eggebrecht H, et al. Detection and characterization of intracardiac thrombi on MR imaging. AJR Am J Roentgenol 2002;179:1539–1544
9. Mollet NR, Dymarkowski S, Volders W, et al. Visualization of ventricular thrombi with contrast-enhanced magnetic resonance imaging in patients with ischemic heart disease. Circulation 2002;106:2873–2876
10. Bruder O, Waltering KU, Hunold P, et al. Detektion und Charakterisierung linksventrikulärer Thromben mittels MRT im Vergleich zur transthorakalen Echokardiographie. Fortschr Roentgenstr. 2005;177:344–349

11 Diseases of the Pericardium

C. U. Herborn, C. Bruch, and R. Erbel

Anatomy

The pericardium is a fluid-filled, double-walled fibrous sac ~1 mm thick that encloses the heart. Like the pleura and peritoneum, it consists of an outer, parietal pericardial layer and an inner, visceral epicardial layer that covers the heart.

Normally these two layers are separated by a fluid film of ~20 to 50 mL that allows smooth movement of the heart during systole and diastole. The parietal layer of the pericardium is attached anteriorly to the chest wall, posteriorly to the thoracic spine, and inferiorly to the diaphragm. Superiorly, the pericardium extends onto the proximal portions of the great vessels, forming a broad fold close to the ascending aorta at the level of the tracheal bijurcation. The pericardium is innervated by the vagal and phrenic nerves, and it drains to the mediastinal and axillary lymph nodes by small pericardial lymph vessels.[1,2] Both the outer and epicardial surfaces of the pericardium are surrounded by copious fat, making it easier to identify the pericardium as a thin, fat-embedded membrane on CT and MR images. Healthy pericardium is almost never delineated from the epicardium on echocardiograms because it has the same echogenicity as surrounding structures.

Imaging Modalities

Chest Radiographs

The normal pericardium cannot be identified as a separate structure on frontal and lateral chest radiographs[3] (see Pericardium, p. 25). Plain films may, however, show tent- or bottle-shaped widening of the cardiac silhouette as evidence of pericardial effusion. This may be indistinguishable from global cardiac enlargement in heart failure, although this condition is associated with enlarged central pulmonary vessels and interstitial fluid accumulation in the lung, allowing differentiation from pericardial effusion.[4] Calcifications of the pericardium are easily identified on chest films and do not necessarily indicate a constrictive disease of the pericardium. Finally, a circumscribed bulge in the cardiac outline on the chest film may indicate herniation of myocardial tissue through a pericardial defect.[5] With left-sided aplasia of the pericardium, the heart will be displaced toward the left side and will show increased mobility.

Echocardiography

Echocardiography is the first diagnostic test for evaluation of the pericardium, especially in patients with suspected pericardial effusion. The dynamic information provided by real-time M-mode, B-mode and Doppler imaging allows for detection of pathological changes in the setting of pericardial diseases. The diagnosis of effusion in the pleural or pericardial space was one of the first major applications of M-mode echocardiography. Two-dimensional echocardiography has improved the diagnosis and quantification of pericardial effusions.

A pericardial effusion appears on echocardiography as a hypoechoic zone between the epicardium and pericardium. A circumferential effusion can be distinguished from a localized effusion with reasonably high confidence. Difficulties may arise in differentiating between a pleural and pericardial effusion. This can be aided by noting how the effusion is projected relative to the descending aorta in the parasternal view. A posterior pericardial effusion is typically projected between the left atrium and descending aorta in this view, while a pleural effusion is not.[1] In the absence of an effusion, however, it may be impossible to delineate the pericardium by echocardiography. It is also difficult to detect pericardial defects. Pericardial calcifications increase the echogenicity of the pericardium, causing the pericardial echo to appear brighter than the surrounding tissue. This finding is relatively nonspecific, however.

Computed Tomography

CT is also used in the diagnosis of pericardial diseases. The pericardial fold close to the ascending aorta should not be misinterpreted as an enlarged lymph node. The pericardium is clearly distinguished from surrounding fat by the difference in attenuation values. This makes it easy to detect focal areas of wall thickening,[6] although these sites may be difficult to distinguish from loculated areas of pericardial effusion. When imaged by CT, a pericardial effusion appears as a hypodense stripe that generally encircles the heart. CT is the most accurate imaging modality for the detection of pericardial calcifications.[7] Moreover, the use of iodinated contrast media can not only differentiate between cardiac chambers, great vessels, and coronary arteries but can also detect inflammations and circumscribed neoplasms by their increased contrast uptake, although this enhancement is not a specific sign.

Magnetic Resonance Imaging

MRI is most favorable for pericardial imaging owing to its intrinsically high soft-tissue contrast and its high temporal and spatial resolution for structural delineation and functional analysis.[4] As in CT, ECG triggering should be used for data acquisition. It should be noted, however, that pleural and pericardial effusions may cause a decreased or wavy amplitude of the QRS complex (electrical alternans), which may hamper detection of the ECG signal for optimal data acquisition.

Large pericardial effusions can be detected even without ECG gating in examinations of the chest or abdomen for noncardiac indications. In most cases this can be done with T2-weighted sequences, in which an effusion appears hyperintense within the pericardium. However, pericardial effusion may also have low signal intensity or produce a signal void on T2-weighted images when turbo spin-echo sequences are used and especially in sequences with dark-blood preparation. The low signal intensity in these images results from fluid motion driven by cardiac pulsations. The signal characteristics of pericardial effusions may vary in the case of encapsulated effusions, blood collections, or proteinaceous effusions. Calcifications appear as signal voids on MRI and are detected less sensitively than by CT.[8] Dynamic cine sequences (SSFP) can document cardiac and pericardial movements. Also, Gd-based contrast agents make it possible to detect inflammatory and neoplastic changes owing to increased contrast uptake in those areas.

Essential Point
Echocardiography is the initial imaging study used in case of suspected pericardial disease, whereas the chest radiograph contributes only little information. Sectional imaging modalities like CT and MRI, however, permit the most accurate morphological analysis of pericardial diseases.

Specific Diseases

Pericardial Cysts and Diverticula

Anatomy and Pathophysiology

While pericardial cysts may be congenital or acquired, pericardial diverticula develop as a result of increased intracardiac pressure or adhesions. Both cysts and diverticula are located in immediate proximity to the pericardium. Cysts are often located in the right cardiophrenic angle, while diverticula often occur over the right atrium on the outer cardiac surface or in the left cardiophrenic angle.[9] Pericardial cysts are fluid-filled cavities that do not communicate with normal pericardial fluid and may be encapsulated by pericardium (**Figs. 11.1, 11.2**). Pericardial diverticula result from increased pressure in the pericardial cavity or from scar traction (e.g., after trauma or surgery) sufficient to cause a fluid-filled outpouching of the pericardium. Pericardial cysts and diverticula have no hemodynamic effects and do not interfere with cardiac filling.

Most pericardial cysts and diverticula are detected incidentally at imaging. Aside from an occasional retrosternal pressure sensation, patients are asymptomatic. Whereas diverticula are definitely benign and rarely cause incarceration of cardiac structures, surgical removal may be considered for pericardial cysts to exclude other potentially malignant cystic tumors.

Imaging

Chest radiographs may demonstrate a round paracardiac opacity (**Fig. 11.2**), which can be further analyzed fluoroscopically for its mobility and deformation during respiratory excursions.[4]

M-mode echocardiography is of little importance in the detection of cysts or diverticula. On 2D imaging, cysts and diverticula usually appear as extraneous cavities on the pericardium that contain low-level internal echoes and undergo pulsatile movements. Intracardiac and extracardiac masses can be differentiated by administering a transpulmonary ultrasound contrast agent. The agent will opacify the cardiac chambers while sparing extracavitary masses.[1]

Pericardial cysts and diverticula have the following CT features:

- Smooth-walled, hypodense mass bordering the pericardium
- Homogeneous (simple) or inhomogeneous density (complicated)
- Typically no contrast enhancement
- Occasional wall calcifications

MRI of simple pericardial cysts shows a rounded, smooth-walled mass with a uniformly hyperintense internal structure on T2-weighted images (**Fig. 11.1**). Complicated cysts have in-

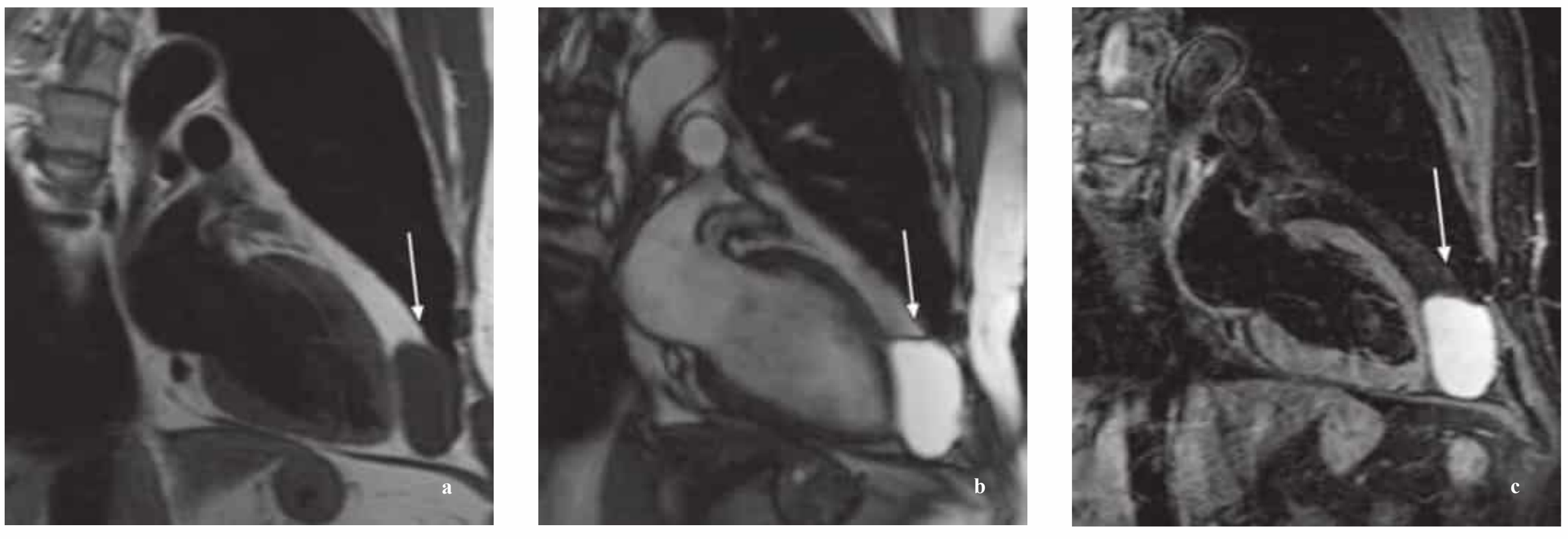

Fig. 11.1 a–c Vertical long-axis MRI in a patient with a pericardial cyst. Anterior to the cardiac apex a well-circumscribed mass (arrow) with low signal intensity on the T1-weighted image (**a**) and homogeneous high signal intensity on the SSFP sequence (**b**) can be detected. The lesion is isointense to fluid on the fat-suppressed T2-weighted image (**c**).

homogeneous signal intensity owing to intracystic hemorrhage, septa, or protein-rich fluid. Complicated cysts may enhance after IV contrast administration, making them difficult to distinguish from other cystic tumors.[7,9] As a sectional imaging modality, MRI can additionally demonstrate locoregional lymph nodes and changes in the lung parenchyma.

Differential Diagnosis

- Pericardial and paracardiac fat pads or lipomas
- Bronchogenic cysts
- Aneurysms
- Hernias, especially hiatal hernias and "upside-down stomach"
- Achalasia
- Other mainly cystic tumors arising from the mediastinum, diaphragm, pericardium, or pleura

Pericarditis

Pathophysiology and Clinical Features

The causes of chronic and acute pericarditis are diverse. Possible causes include viral and bacterial infections, previous cardiac surgery, previous myocardial infarction, neoplasms, systemic diseases, chronic renal failure, and many others.[7–9] The various causes of acute and chronic pericarditis are summarized in **Table 11.1**. A fibrinous (dry) form is distinguished from an exudative (wet) form that is associated with effusion. In fibrinous pericarditis, adhesions may form between the pericardial layers, restricting the motion of the pericardium and interfering with cardiac filling. Chronic forms are characterized by recurrent effusions, adhesive plaques, calcifications, and an audible pericardial friction rub. The diagnosis of pericarditis is based on typical clinical symptoms, ST segment changes, and the presence of a pericardial friction rub. A pericardial effusion is not always detected initially but will usually develop during the course of the disease. Pericardial effusion in pericarditis initially forms in the posterior portion of the pericardium. It then spreads across the anterior wall to the base of the heart and eventually fills the space behind the left atrium (late stage). The distance from the pericardial effusion to the chest wall should be measured, as it may be important in planning a safe ultrasound-guided pericardiocentesis, for example.

The acute form of pericarditis may become life-threatening owing to the rapid development of pericardial tamponade with sudden obstruction of venous return to the heart (**Fig. 11.3**). The development of tamponade depends on the volume of the pericardial effusion and on the morphology and functional sta-

Table 11.1 Causes of pericarditis

- Idiopathic
- Infectious (bacterial, viral, fungal, parasitic, tuberculous)
- Myocardial infarction
- Allergic
- Rheumatic
- Autoimmune systemic diseases (especially collagen diseases: chronic rheumatoid arthritis, Reiter disease, ankylosing spondylitis, Sjögren disease, Felty disease, lupus erythematosus, scleroderma, dermatomyositis, panarteritis nodosa)
- Sarcoid
- Metabolic (renal failure, hypothyroidism, Addison disease, diabetes mellitus, hypercholesterolemia)
- Posttraumatic, postoperative
- Neoplastic (including leukemia and myeloma)
- Dissecting aneurysm of the ascending aorta
- Postradiogenic
- Chylogenic (e.g., due to fistula formation)

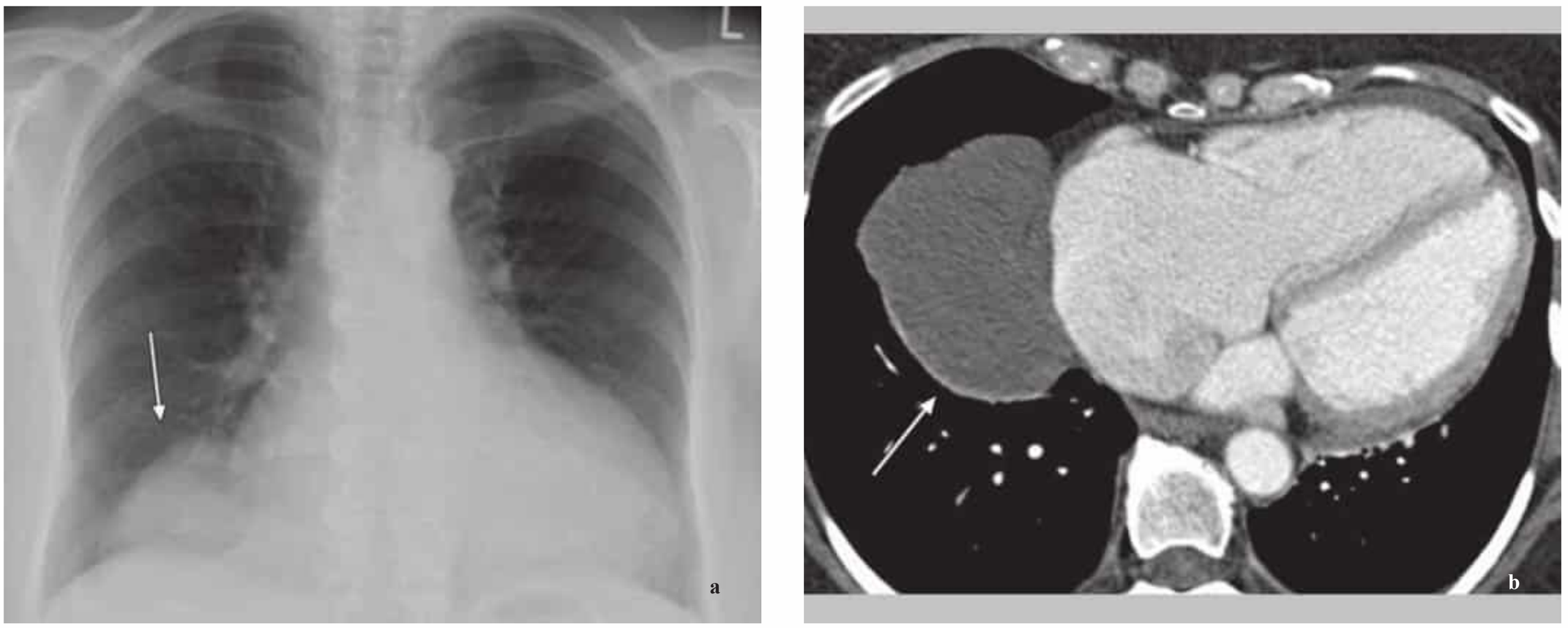

Fig. 11.2 a, b Large pericardial cyst appears on the chest radiograph as a well-circumscribed mass projected over the right cardiophrenic angle (**a**). Contrast-enhanced CT (**b**) demonstrates the cystic mass (arrow) next to the right atrium.

tus of the heart. Its clinical manifestations are dyspnea and a feeling of pressure and tightness in the chest accompanied by tachycardia and a fall in blood pressure. Typically the pulse diminishes in amplitude during inspiration (paradoxical pulse), though this may be absent in patients with preexisting heart disease. Auscultation reveals diminished heart sounds in the presence of a large effusion. The ECG shows low QRS voltages with possible electrical alternans.

Imaging

Chest radiographs are unrewarding in pericarditis without significant pericardial effusion because the cardiac shape is essentially unchanged. At least 200—300 mL of fluid must be present to cause typical globular or triangular enlargement of the cardiac silhouette (see **Fig. 1.26a**). The lateral chest film shows obliteration of the retrosternal space and blunting of the cardiophrenic angle. Indirect signs of significant pericardial effusion are widening of the superior vena cava and a general reduction of pulmonary vascular calibers. In some cases the epicardial–myocardial interface is clearly delineated by the effusion. A retrosternal double contour and crescent sign are visible in the lateral radiograph (see Pericardium, p. 25).

Echocardiograms may be normal in acute pericarditis without an associated effusion. Consequently, a normal echocardiogram does not exclude acute pericarditis (clinical presentation, ECG, and laboratory findings suggest the correct diagnosis).

Separation of the pericardium and epicardium is noted at ultrasound and always occurs when more than 15–35 mL of pericardial fluid is present (**Fig. 11.3**). Various types of pericardial effusion can be distinguished in M-mode echocardiography based on the Horowitz criteria. When effusion is present, diastolic collapse of the right ventricle or right atrium (depending on the principal site of the effusion) provides the most compelling evidence of tamponade. It should be noted, however, that this sign is dependent on preexisting right ventricular and right atrial pressures and on the volume status of the patient. The Doppler interrogation of hepatic venous flow may provide additional information. When tamponade is present, Doppler shows respiration-dependent flow variations with markedly decreased systolic/diastolic antegrade flow during inspiration and a reversal of flow during atrial contraction. Two-dimensional echocardiography in large effusions shows an overall increase in cardiac mobility ("swinging heart").

Two-dimensional echocardiography can also determine the quantity and extent of pericardial effusion in transthoracic and subcostal parasternal scans. The pericardial space is hypoechoic in the presence of an acute pericardial effusion (**Fig. 11.4**).

The volume of a pericardial effusion in diastole can be determined echocardiographically by using the formula:

$$V = \square\, \pi\, (D_p^3 - D_v^3)$$

where V=pericardial effusion volume, D_p=diameter of the pericardium, and D_v=diameter of the epicardium.

Both M-mode echocardiography and two-dimensional echocardiography can be used for the quantification of effusion. A linear relationship exists in the range 250–600 mL and declines above 600 mL. A correlation coefficient of 0.97 has been found for two-dimensional echocardiography. As fluid is withdrawn percutaneously from the pericardial sac, the regression of the effusion can be observed in real time.

A semiquantitative three-part scale is also available for the assessment of pericardial effusion volume:

- Small pericardial effusion: <10 mm separation of the pericardium and epicardium in systole
- Moderate pericardial effusion: 10–20 mm
- Large pericardial effusion: >20 mm separation of the epicardium and pericardium

It should be considered, however, that a 10-mm effusion layer in a normal heart makes up less of the total volume than in a dilated heart, and so the effusion volume may be underestimated unless cardiac size is taken into account. It should also be noted that subcostal scans often display tangential sections that may overestimate the pericardial volume.

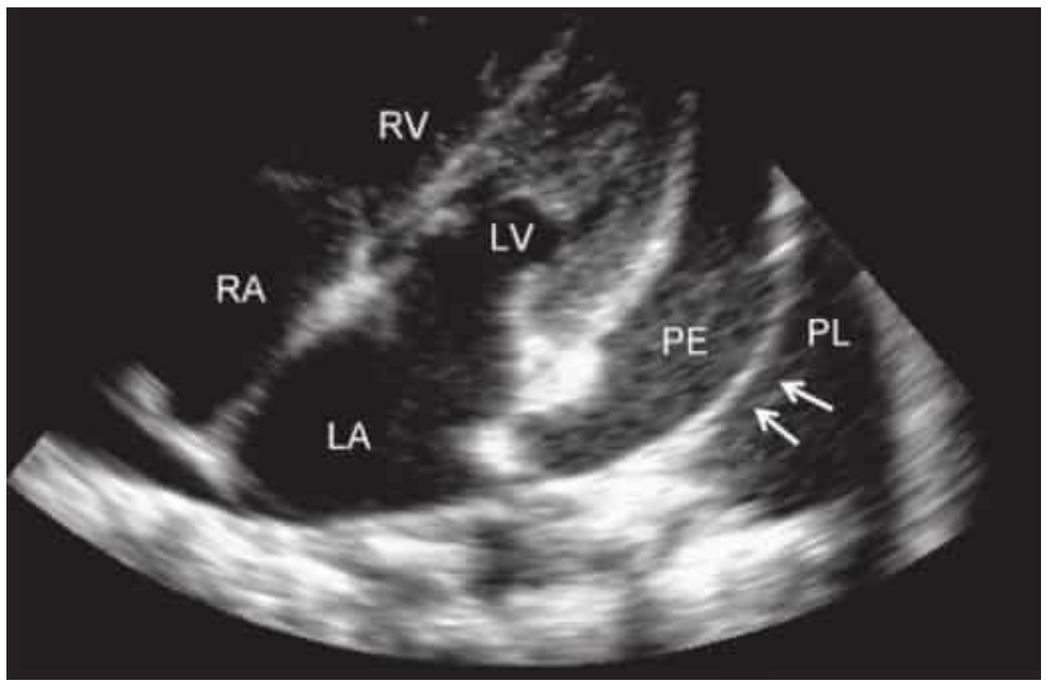

Fig. 11.3 Subcostal scan in a patient with pericardial effusion. The echogenic parietal pericardium (arrows) clearly separates the pericardial effusion from the pleural effusion.

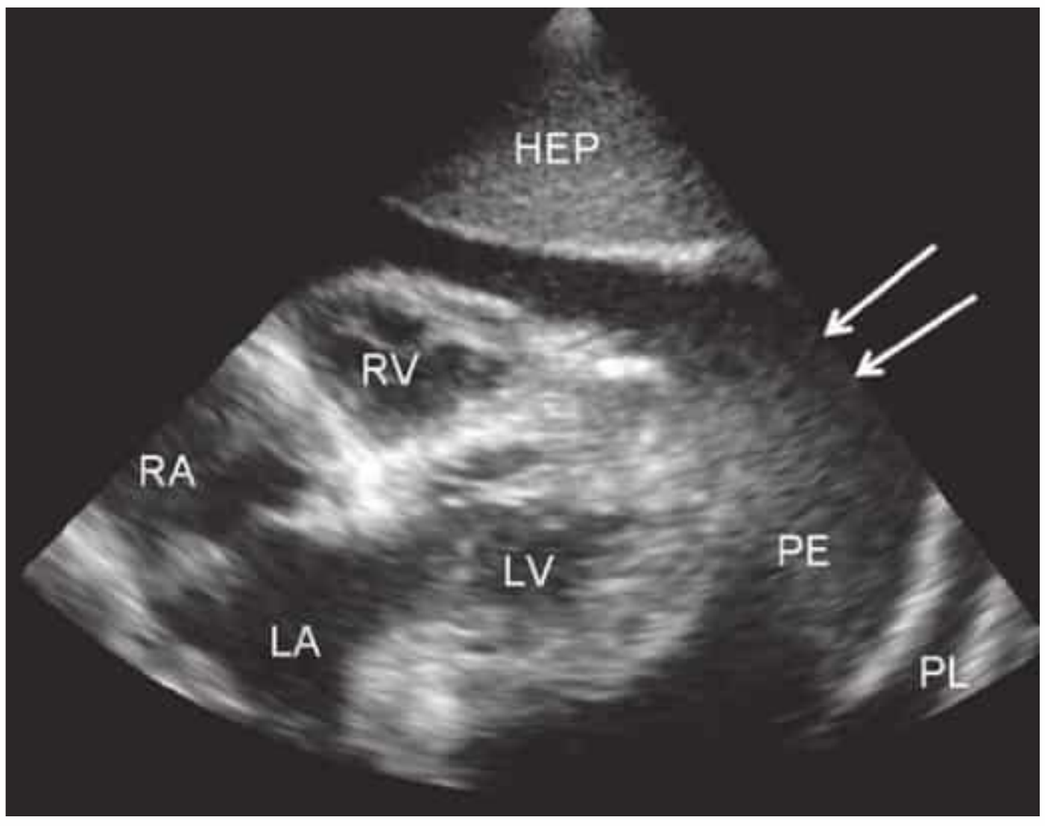

Fig. 11.4 Subcostal scan demonstrates a 3-cm-wide fluid collection (arrows) over the left ventricular apex, large enough for pericardiocentesis.

Pericardial tamponade is rarely found in patients with less than 100 mL of fluid. An effusion volume between 100 and 400 mL leads to tamponade in 13 % of patients, and a volume greater than 400 mL leads to tamponade in 39 %

A very large pericardial effusion may cause a "swinging heart" phenomenon, in which the heart swings back and forth within the pericardial space while tethered by the base and great vessels (**Fig. 11.5**). ECG shows varying R-wave amplitudes that decline when the heart moves away from the chest wall and increase when it moves toward the chest wall.[1]

An effusion layer in pericarditis is very clearly demonstrated by CT. Also, attenuation measurements can be performed to differentiate among hydro-, hemo- and chylopericardium. Post-contrast scans show marked enhancement of the thickened pericardium. Pathological changes in the surrounding mediastinum and in the lung tissue can also be identified.[7]

MRI is useful for the more precise differentiation of pericardial effusions. A transudative effusion has long T1 and T2 relaxation times, with the result that transudates appear dark in T1-weighted sequences and bright in T2-weighted sequences. Protein-rich exudates, on the other hand, tend to have short T1 and T2 relaxation times, resulting in high T1-weighted signal intensity and low T2-weighted signal intensity.[9–11] MRI also permits a dedicated analysis of pericardial changes.

Differential Diagnosis

Akute:

- Myocarditis
- Left- or right-sided heart failure (e.g., due to acute myocardial ischemia in infarction)
- Pulmonary embolism
- Aortic dissection

Chronic:

- Ischemic or nonischemic cardiomyopathy with right or left ventricular failure
- Pulmonary hypertension with cor pulmonale
- Valvular pathologies with cardiac failure (e.g., mitral stenosis)
- Late sequelae of uncorrected congenital heart disease

Constrictive Pericarditis

Anatomy, Pathophysiology, and Clinical Features

Fibrotic scarring of the pericardium may occur after a clinically mild course of viral and/or bacterial inflammatory pericarditis, after previous radiotherapy, in the setting of tuberculosis, or after a traumatic intrapericardial hemorrhage[12] (**Fig. 11.6**). However, the most common cause of constrictive pericarditis is open-heart surgery. The scarring reduces the compliance of the pericardial layers, resulting in constrictive pericarditis. Constrictive pericarditis may also develop without a discernible cause. A detailed list of possible causes is given in **Table 11.2**. An "armored heart" develops when fibrotic scarring is associated with calcium deposition (**Fig. 1.27, Figs. 11.7, 11.8**).

During diastole, the constrictive effect of the disease causes decreased filling of the cardiac chambers with a reduction in stroke volume. In most cases the initial clinical effect is decreased inflow into the right heart, which may lead to portal venous hypertension and ascites.

The decreased return to the left heart causes a pressure rise in the pulmonary vascular bed, with possible development of interstitial or intra-alveolar pulmonary edema. Generally the stroke volume of the heart is markedly reduced.

The clinical manifestations depend on whether right-sided or left-sided heart failure is predominant. Predominant right-sided failure leads to peripheral dependent edema, epigastric pressure due to hepatomegaly and/or ascites, and dyspnea due to pleural effusion. Other manifestations are distended neck veins, possible muffled heart sounds, and a diminished pulse. Predominant left-sided heart failure leads to decreased exercise tolerance and dyspnea on mild exertion or even at rest. Dizziness and peripheral cyanosis are occasionally present owing to increased peripheral oxygen extraction.

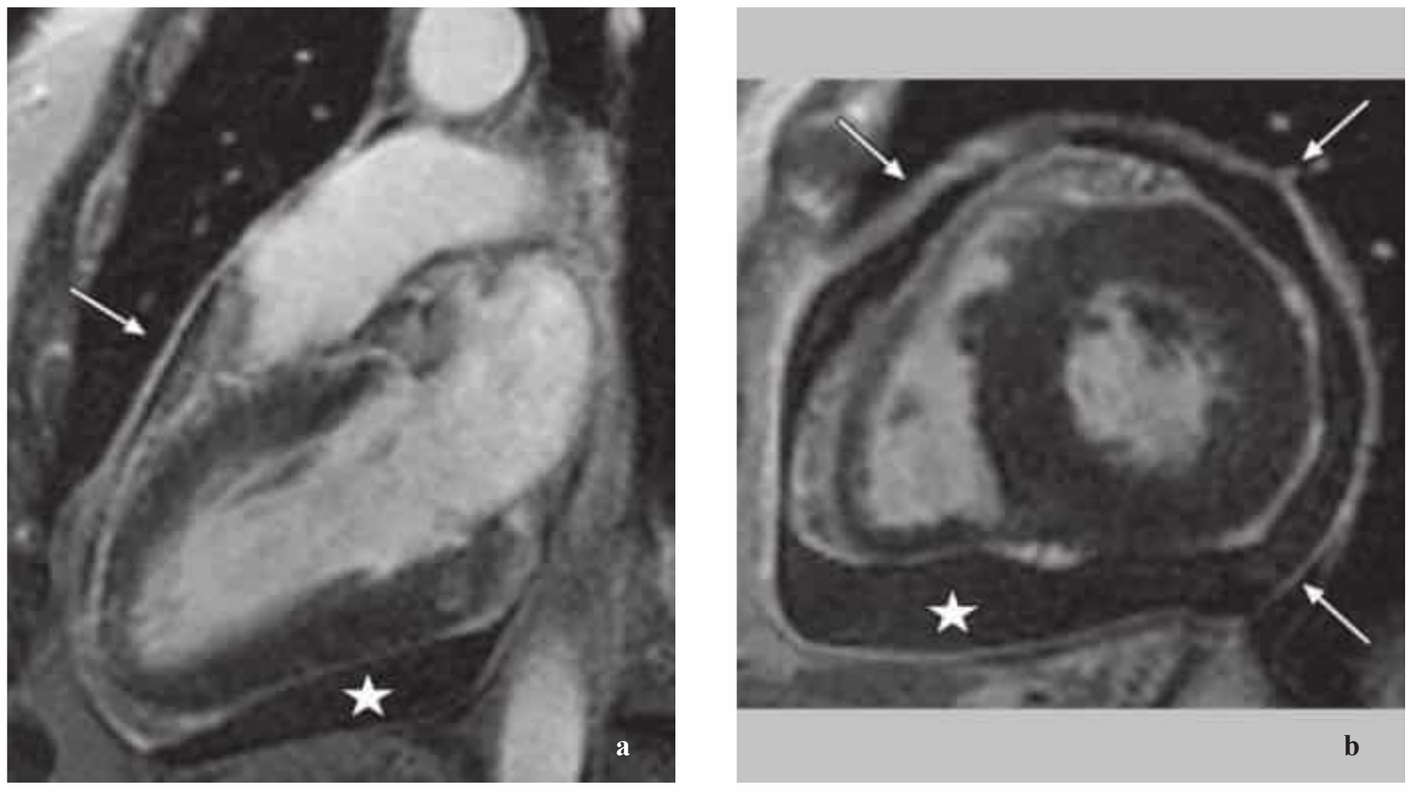

Fig. 11.5 a, b Contrast-enhanced T1-weighted MR images of a large pericardial effusion (star) in acute pericarditis. Note the contrast enhancement in the pericardium (arrows).
a Vertical long-axis view.
b Basal short-axis view.

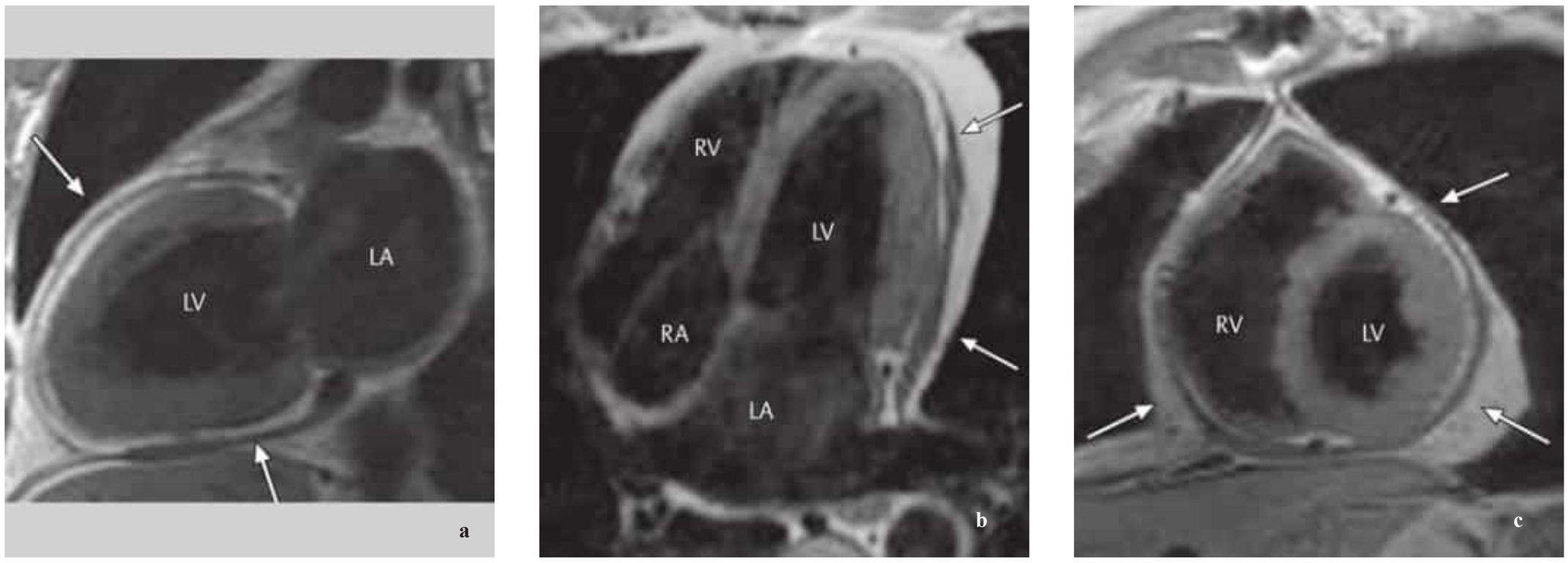

Fig. 11.6 a–c Massive thickening of the pericardium (arrows) in a patient with constrictive pericarditis.

a T1-weighted TSE image, vertical long-axis view.
b T1-weighted TSE image, horizontal long-axis view.
c T1-weighted TSE image, short-axis view.

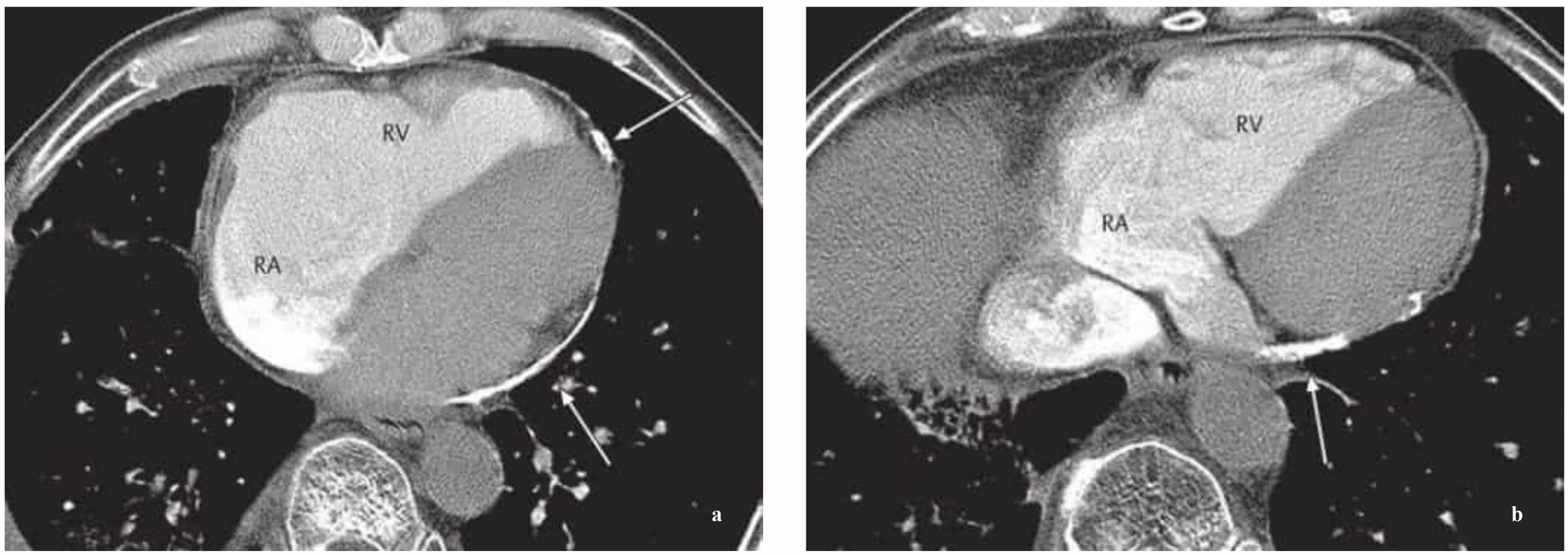

Fig. 11.7 a, b Pericardial calcification (arrow) in constrictive pericarditis, depicted by CT. Note the enlargement of the right atrium.

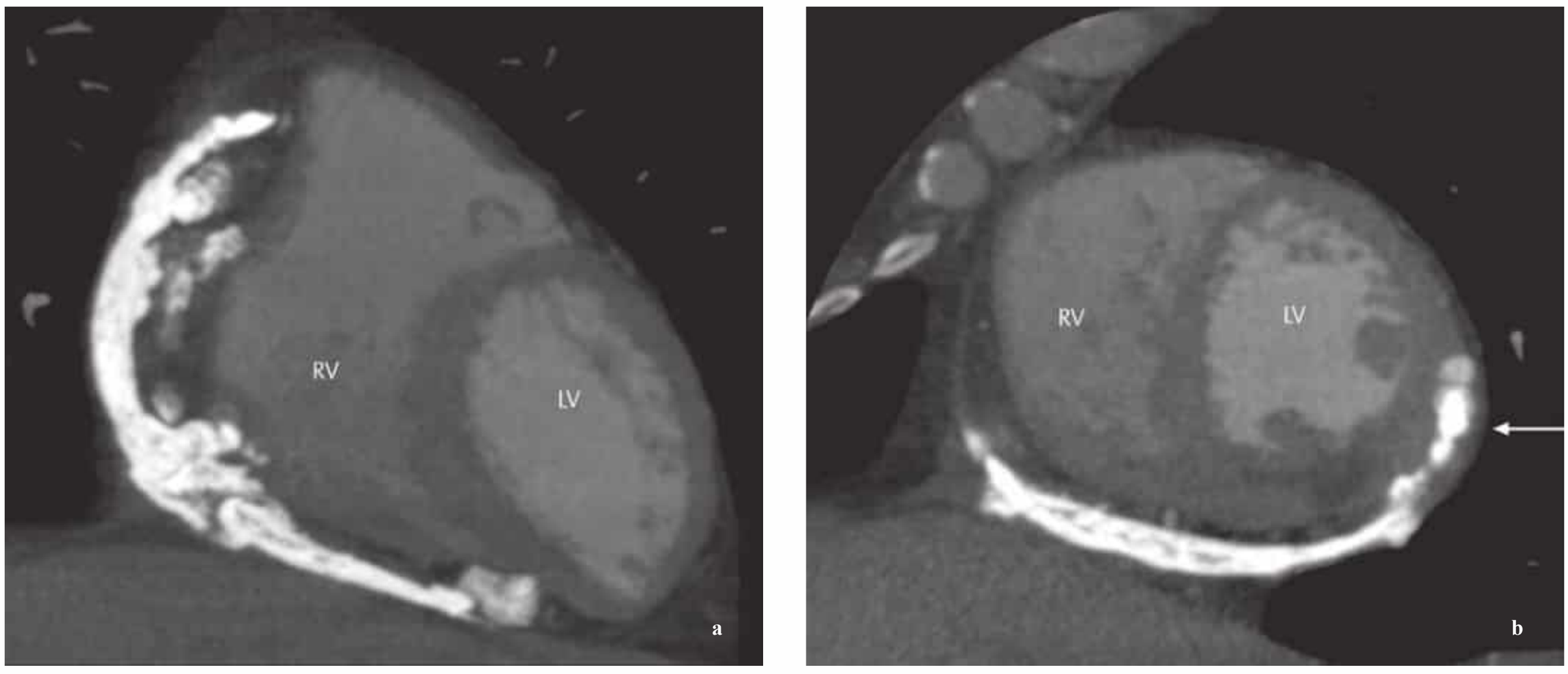

Fig. 11.8 a, b Patient with posttraumatic constrictive pericarditis years after sustaining a knife wound. CT was done in preparation for a pericardial resection and coronary artery revascularization. Note the extensive, flocculent pericardial calcifications, which have spread to the lateral wall of the left ventricular myocardium (arrow).
a Coronal reconstruction of CT dataset. **b** Short-axis view.

Table 11.2 Causes of constrictive pericarditis

- Previous cardiac or thoracic surgery (common)
- Postinflammatory (bacterial, viral, fungal, parasitic)
- Idiopathic
- Collagen diseases
- Posttraumatic
- Postradiogenic
- Hypercholesterolemia
- Chronic renal failure
- Recurrent hemopericardium
- Cardiac and pericardial tumors

Imaging

Chest radiographs in uncalcified forms of constrictive pericarditis often show a normal cardiac silhouette or may demonstrate global enlargement. Peripheral calcifications are most clearly appreciated when projected onto the right atrium and atrioventricular junctional zone, especially in the lateral projection[3,4] (see Pericardium, p. 25).

Constrictive pericarditis can be diagnosed in most patients by a combination of 2D M-mode and Doppler echocardiography. The 2D image shows pericardial thickening, calcifications, and localized adhesions (tethering) of the atria and ventricles. The classic M-mode sign of constrictive pericarditis is septal "bouncing," an early diastolic septal excursion in parasternal scans caused by an abrupt cessation of ventricular filling in early diastole. Doppler echocardiography demonstrates the pathophysiological changes of constrictive pericarditis and is a mainstay of echocardiographic assessment.[1] The principal findings are reciprocal, respiration-dependent variations of mitral and tricuspid inflow resulting from a state of increased interventricular dependence. Tissue Doppler supplies important additional information by demonstrating normal or increased early diastolic excursion of the mitral annulus in constrictive pericarditis. This contrasts with the markedly decreased early diastolic excursion of the mitral annulus seen in restrictive cardiomyopathy.

In typical cases of constrictive pericarditis, echocardiography shows thickening of the pericardium to more than 4 mm. It should be noted, however, that constrictive pericarditis may occur in the absence of pericardial thickening. Diagnosis in these cases is based on typical hemodynamic changes. Enlargement of the atria occurs in response to constrictive pericarditis. This is particularly apparent in the four-chamber view. Indirect signs of constrictive pericarditis are typical early diastolic outward and inward motion of the interventricular septum, corresponding to the dip–plateau waveform in pressure tracings (see below). The diameter of the left ventricle is not increased. The ventricle does not enlarge during the late diastolic filling phase. The septum and posterior wall produce a horizontal trace on M-mode echocardiography. The size of the left ventricle increases only during the early filling phase and during atrial contraction.

The differential diagnosis includes dilatation of the right heart due to pulmonary embolism, right-sided myocardial infarction, pleural effusion, and chronic obstructive pulmonary disease (COPD). Constrictive pericarditis mainly requires differentiation from COPD, which is characterized by a decreased flow velocity across the mitral valve and an increased flow velocity during expiration, showing a range of variation of almost 100 % The highest flow velocity is recorded at end-expiration. This is opposite to the pattern seen in constrictive pericarditis, where peak flow velocity occurs at the start of expiration. The best differentiation is achieved by scanning the superior vena cava. In COPD, flow in the superior vena cava increases during inspiration, while in constrictive pericarditis it does not show a detectable increase.

Differential diagnosis is more difficult in patients with atrial fibrillation. Diastolic flow reversal may be observed in the hepatic veins during expiration, even if the flow velocity cannot be diagnostically evaluated.

When cardiac catheterization is performed in constrictive pericarditis, pressure measurements in the left and right heart show an almost complete equalization of diastolic pressures in all four cardiac chambers. Typically the end-diastolic pressure is elevated. Other important hemodynamic signs are a rapid early diastolic pressure rise followed by a plateau phase in the ventricles ("dip and plateau phenomenon" or "square root sign") and W-shaped atrial pressure curves with a preserved *x* descent and prominent *y* descent. The hemodynamic criteria for a diagnosis of constrictive pericarditis are as follows:

- A difference of less than 5 mmHg between the pressure in the left ventricle at end diastole (PLVED) and the pressure in the right ventricle at end diastole (PRVED)
- A low systolic pulmonary artery pressure of ~30 mmHg
- A high end-diastolic filling pressure in the right ventricle, equal to more than 30 %of the systolic pressure wave[1]

CT is superior to echocardiography for the detection of pericardial thickening and calcifications, which can be accurately localized (**Figs. 11.7, 11.8**). Additionally, CT typically demonstrates global enlargement of the cardiac chambers with predominant atrial enlargement. Indirect signs of pericardial constriction are enlarged hepatic veins with possible retrograde flow of contrast medium into the hepatic veins. Chronic constrictive pericarditis leads to changes in the pulmonary vascular bed, which can be appreciated in high-resolution scans. Ascites may be detectable in the upper abdomen.

Similarly, MR images demonstrate enlarged cardiac chambers with predominant atrial dilatation.[7,9–11,13,14] Indirect signs such as enlarged hepatic veins and upper abdominal ascites are also clearly visualized. A key advantage of MRI is the ability to analyze cardiac motion using cine sequences (SSFP). On functional MRI of the heart in constrictive pericarditis, early diastolic images show a paradoxical motion pattern with bowing of the septum into the left ventricle. Fibrous thickening of the pericardium is also detectable by MRI. Postcontrast images show not only rapid enhancement in the acute stage of pericarditis but also delayed enhancement, which may allow differentiation between acute and chronic changes.[15] Myocardial involvement can also be evaluated. The good soft-tissue contrast

permits a morphological analysis of the heart with fast T1- and T2-weighted sequences and the detection of myocardial edema on fat-suppressed images (STIR or fat-suppressed T2-weighted TSE).

Differential Diagnosis

- Calcifications due to other causes (pleural thickening, cardiac valves, coronary arteries, cardiac thrombi or aneurysms)
- Restrictive cardiomyopathies (e.g., endomyocardial fibrosis)
- Differential diagnosis of chronic pericarditis with respect to right- and left-sided heart failure

Malignant Pericardial Diseases

Pathophysiology and Clinical Features

Malignant pericardial masses most commonly result from the direct spread of malignant disease from nearby structures (e.g., pleural mesothelioma) and the metastatic spread of breast cancer, lung cancer, lymphoma, or melanoma[9,16,17] (**Fig. 11.9**). Cardiac masses may also infiltrate the pericardium. Primary pericardial malignancies may be mesotheliomas, angiosarcomas, or fibrous tumors (e.g., fibrosarcomas).

In the great majority of cases, malignant pericardial masses have no primary hemodynamic effects and do not impair cardiac filling. Occasionally, however, massive tumor invasion of the pericardium may lead to pericardial constriction.

As a rule, cardiac masses are detected incidentally in staging examinations of patients with malignant diseases. When questioned, patients occasionally describe a feeling of retrosternal tightness. Symptoms of chronic pericarditis are observed when a concomitant effusion is present (see above).

Imaging

The great majority of pericardial malignancies produce no detectable abnormalities on chest radiographs. Expansile tumors may occasionally cause a bulge in the cardiac outline.

On 2D echocardiography, pericardial malignancies usually appear as hypoechoic masses projected over the pericardium. Again, contrast echocardiography may provide important localizing information based on improved delineation of the pericardium and cardiac chambers. Doppler scanning is helpful in detecting the possible functional effects of malignant infiltration.

CT is very useful for the accurate localization of masses and for determining their origin and local extent. It can also provide information on the internal structure of a lesion and its enhancement characteristics after intravenous contrast. Calcified areas can be clearly identified.

Besides the localization of pericardial masses, MRI is useful for evaluating mobility and contrast dynamics. The high soft-tissue contrast of MRI also permits an analysis of tumor composition and the differentiation of intratumoral hemorrhage, necrosis, and solid tumor elements.

Differential Diagnosis

- Pericardial cyst or diverticulum

Pericardial Aplasia

Anatomy and Pathophysiology

Complete integrity of the pericardium is not essential for life. The pericardium may be deficient as a result of congenital aplasia, or an iatrogenic defect may result from pericardial resection for constrictive pericarditis or pericardial fenestration for recurrent effusions. The defects may be partial or complete. Partial congenital pericardial aplasia is commonly found at the ventricular apex.

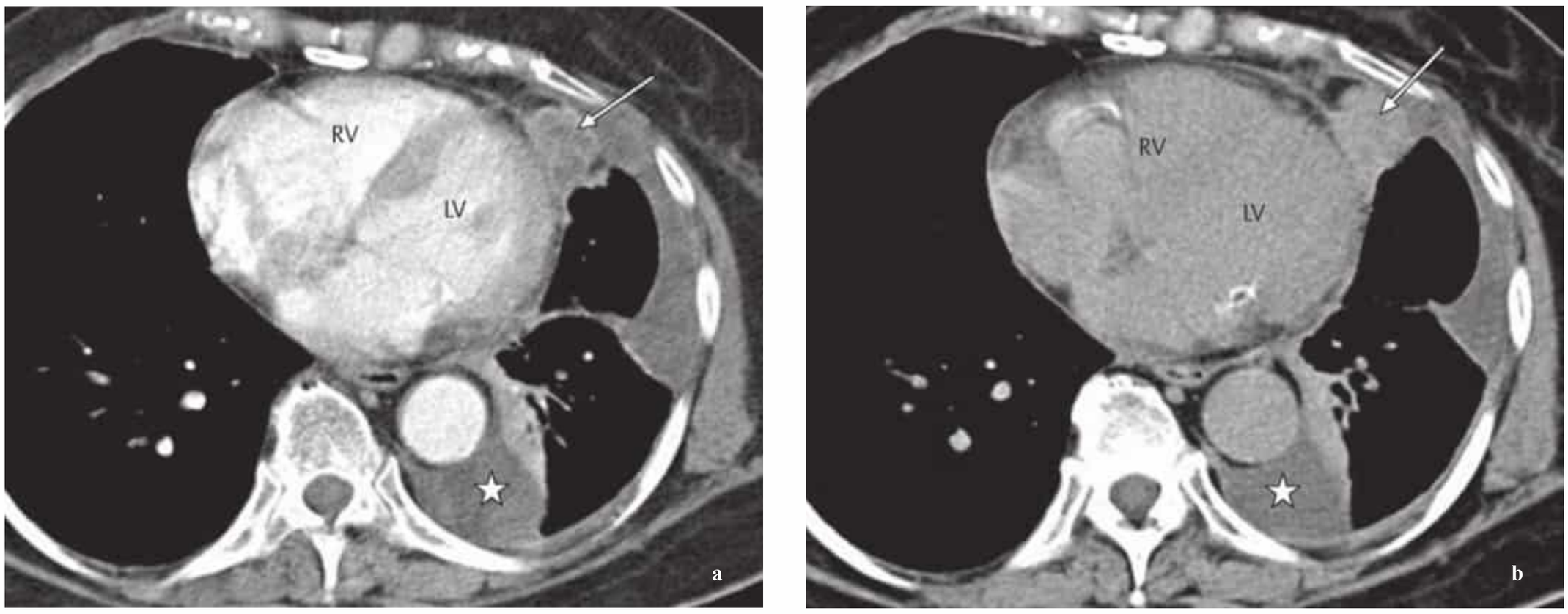

Fig. 11.9 a, b Contrast-enhanced CT of a pericardial metastasis (arrow) anterolateral to the left ventricle shows mainly peripheral enhancement in the early phase (**a**) and soft-tissue attenuation in the late phase (**b**). CT also shows a loculated posterior pleural effusion on the left side (star) and hypoventilated areas in the adjacent lung.

Congenital pericardial aplasia is often incomplete, especially about the left ventricle, and occasionally shows a communication with the pleural space. This type has no impact on cardiac filling and is asymptomatic. Herniation and incarceration of the atrial appendages may occasionally develop, with an associated risk of thrombus formation.

There are no typical clinical manifestations of complete or partial pericardial aplasia. With a partially aplastic pericardium that communicates with the pleura, air may accumulate between the heart and pericardium (pneumopericardium).

Imaging

Chest radiographs show a predominantly left-sided bulge in the cardiac silhouette and an elevated, curved, and broadened cardiac apex.

In many cases echocardiography can provide initial evidence of pericardial aplasia only when the heart is scanned from an unusually far lateral site. Echocardiography also shows a marked overall increase in the amplitude of cardiac motions. The posterior left ventricular wall in particular shows increased mobility in congenital pericardial aplasia.

CT may show a discontinuity in the pericardium in patients with copious epicardial fat. Otherwise it shows a general broadening of the cardiac outline that is most pronounced at the apex.

Besides showing a possible pericardial discontinuity, MRI may detect atrial appendage herniation through the pericardial defect. Like CT, it shows a broadened cardiac outline with an accentuated apex. Cine MRI documents abnormal mobility of the heart.

Differential Diagnosis

- Pericarditis
- Congenital heart defects

Essential Point

The pericardium can be imaged with various modalities. Echocardiography, CT, or MRI may be used, depending on the clinical situation. Conventional radiographs and cardiac catheterization are of minor importance. Echocardiography should be the initial imaging study in patients with suspected pericardial disease. In experienced hands, transthoracic or transesophageal echocardiography can accurately investigate the majority of pericardial diseases.
Further imaging tests are reserved for cases with equivocal echo findings, especially for suspected constrictive pericarditis or a pericardial mass.

References

1. Maisch B, Seferovic PM, Ristic AD, et al. Guidelines on the Diagnosis and Management of Pericardial Diseases Executive Summary; The Task Force on the Diagnosis and Management of Pericardial Diseases of the European Society of Cardiology. Eur Heart J 2004;25:587–610
2. Spodick DH. Macrophysiology, microphysiology, and anatomy of the pericardium: a synopsis. Am Heart J 1992;124:1046–1051
3. Lipton MJ, Boxt LM. How to approach cardiac diagnosis from the chest radiograph. Radiol Clin North Am 2004;42:487–495
4. Duerinckx AJ. Plain film/MR imaging correlation in heart disease. Radiol Clin North Am 2004;42:515–541
5. Boxt LM, Reagan K, Katz J. Normal plain film examination of the heart and great arteries in the adult. J Thorac Imaging 1994;9:208–218
6. Bull RK, Edwards PD, Dixon AK. CT dimensions of the normal pericardium. Br J Radiol 1998;71:923–925
7. Rienmüller R, Groll R, Lipton MJ. CT and MR imaging of pericardial disease. Radiol Clin North Am 2004;42:587–601
8. Glockner JF. Imaging of pericardial disease. Magn Reson Imaging Clin N Am 2003;11:149–162
9. Sechtem U, Tscholakoff D, Higgins CB. MRI of the abnormal pericardium. AJR Am J Roentgenol 1986;147:245–252
10. Sechtem U, Tscholakoff D, Higgins CB. MRI of the normal pericardium. AJR Am J Roentgenol 1986;147:239–244
11. Wang ZJ, Reddy GP, Gotway MB, Yeh BM, Hetts SW, Higgins CB. CT and MR imaging of pericardial disease. Radiographics 2003;23:S167–S180
12. Cameron J, Oesterle SN, Baldwin JC, Hancock EW. The etiologic spectrum of constrictive pericarditis. Am Heart J 1987;113:354–360
13. Masui T, Finck S, Higgins CB. Constrictive pericarditis and restrictive cardiomyopathy: evaluation with MR imaging. Radiology 1992;182:369–373
14. Yousem D, Traill TT, Wheeler PS, Fishman EK. Illustrative cases in pericardial effusion misdetection: correlation of echocardiography and CT. Cardiovasc Intervent Radiol 1987;10:162–167
15. Taylor AM, Dymarkowski S, Verbeken EK, Bogaert J. Detection of pericardial inflammation with late-enhancement cardiac magnetic resonance imaging: initial results. Eur Radiol 2006;16:569–574
16. Ferguson ER, Blackwell GG, Murrah CP, Holman WL. Evaluation of complex mediastinal masses by magnetic resonance imaging. J Cardiovasc Surg (Torino) 1998;39:117–119
17. Klatt EC, Heitz DR. Cardiac metastases. Cancer 1990;65:1456–1459

12 Diseases of the Great Pulmonary Vessels

S. Ley, K.-F. Kreitner, and G. Horstick

The right ventricular outflow tract opens into the pulmonary trunk, which then divides into the right and left main pulmonary arteries. The pulmonary arteries (PA) undergo further branching out to the level of the subpleural space. After the blood has passed through the alveolar capillary bed, the pulmonary veins (PV) return the oxygenated blood to the left atrium. Various diseases may cause an interruption of blood flow on both the arterial and venous sides of the circulation. Besides intravascular causes, primary extravascular pathologies may also lead to a reduction of blood flow. Over time a decrease in the cross-sectional area of the PA or PV leads to an increased resistance in the pulmonary vascular bed, causing the development of **pulmonary hypertension** (PH). As a result, even primary vascular changes are frequently associated with cardiac changes (e.g., right ventricular hypertrophy, paradoxical septal motion; see Pulmonary Arterial Hypertension, p. 25). This right heart strain usually leads to **delayed contrast wash-in**, making it necessary to administer a test bolus or use individual bolus timing to achieve a high image quality e.g., in contrast-enhanced CT or MR angiography.

Echocardiography is excellent for detection of the increase in pressure in the pulmonary arterial system. It can also be used for the quantification of pulmonary arterial systolic pressure. The advantage of **CT** and **MRI**, on the other hand, is their ability to image all the arterial and venous components of the pulmonary vascular bed.[1] These modalities can provide an accurate diagnosis of intravascular changes to the subsegmental level as well as extravascular abnormalities.

Pulmonary Arterial Disorders

Acute Pulmonary Embolism

Pulmonary embolism is defined as the embolic occlusion of central or peripheral (segmental to subsegmental) pulmonary arteries. The principal cause is **venous thrombosis**. Almost all pulmonary emboli originate from thrombi in the iliac veins or deep lower extremity veins, and so both diseases should be viewed as a common entity. Lower extremity venous thrombosis has an annual incidence of about three cases per 1000 population, while pulmonary embolism has a reported incidence of 0.5 cases per 1000 population in Western industrialized countries. It is reasonable to assume, however, that a substantially higher number of clinically silent cases remain undiagnosed.[2] From 8 %to 12 %of symptomatic patients die from the sequelae of acute pulmonary thromboembolism.

Risk Factors

Numerous risk factors for venous thromboembolism have been identified. They include specific coagulopathies such as factor V Leiden (APC resistance) and hyperhomocysteinemia as well as general risk factors such as age, obesity, and sedentary lifestyle.

Clinical Features

The clinical complaints associated with acute pulmonary embolism are nonspecific and range from an asymptomatic course to a fulminant, acutely life-threatening condition, depending on severity and location. Frequent clinical symptoms may include:

- Dyspnea
- Tachypnea
- Tachycardia
- Chest pain
- Syncope

Diagnosis

Given the nonspecific clinical presentation, imaging studies are particularly important in differentiating pulmonary embolism from other cardiopulmonary diseases such as myocardial infarction, pneumothorax, pneumonia, heart failure, and aortic dissection. An efficient diagnostic work-up must include an analysis of the overall clinical presentation and individual factors (e.g., outpatient or in-patient, age, underlying diseases, etc.). Several studies have shown that an accurate assessment of the clinical likelihood of an acute pulmonary embolism (pretest clinical probability) can make the diagnostic evaluation more cost-effective and easier for the patient to tolerate (e.g., less need for invasive pulmonary angiography).[3]

An effective diagnostic algorithm for acute pulmonary embolism also depends on factors such as the local availability of imaging procedures (pulmonary angiography, CT, scintigraphy) and operator expertise.

Pathophysiology

Embolic occlusion of the pulmonary arteries has immediate effects on the cardiovascular and respiratory system. The effects include a sudden rise in pulmonary artery pressure with an overload on the right heart. This may progress to an acute decompensation of the right heart with myocardial ischemia, depending on the severity of the embolism and the presence of preexisting disease. The hemodynamic stress may also cause dilatation of the pulmonary artery and right heart, paradoxical

systolic motion of the septum toward the left ventricle, possible tricuspid regurgitation, and absence of inspiratory collapse of the inferior vena cava. A decline in left ventricular stroke volume and fall in blood pressure have also been reported.[2] Additionally, the ventilation–perfusion imbalance in the lung and the development of intrapulmonary shunts lead to hypoxemia and respiratory insufficiency.

Clinical Classification

Pulmonary embolism is classified into four grades of clinical severity: **Grade I** involves peripheral pulmonary arteries and is clinically silent in 80 % of cases. **Grade II** is characterized by vascular obliteration at the level of the segmental arteries. The clinical complaints (dyspnea of acute onset, tachypnea, chest pain) overlap with **grade III**, in which a main branch of the pulmonary artery (left or right PA) or multiple lobar arteries are occluded. The difference between the two grades lies in the blood pressure, which is normal to low in grade II and low in grade III. The mean PA pressure is usually normal in grade II and is normal or slightly elevated (25–30 mmHg) in grade III. **Grade IV** is an occlusion of the pulmonary trunk or of a main pulmonary branch and multiple lobar arteries leading to cardiac arrest.

Echocardiography

Echocardiography is a simple, noninvasive, fast, and cost-effective imaging study whose main role in pulmonary embolism is the assessment of right cardiac function. It is the procedure of choice for patients with right heart failure whose life depends on immediate thrombolytic therapy or emergency surgery. Echocardiography is also useful for detecting thrombi in the pulmonary trunk. In principle, direct visualization of the embolus can be accomplished only in the central pulmonary arteries (trunk and main arteries), depending on the mode of use (transthoracic or transesophageal). In most cases the pulmonary arteries cannot be adequately evaluated because of the limited acoustic window. Signs of pulmonary embolism can be found when at least 30 % of the pulmonary vascular tree has become occluded. Indirect signs result from the acute pressure load on the right ventricle and the corresponding hemodynamic signs (see above).

CT Angiography

Multislice CT scanners are becoming increasingly available and can provide an excellent assessment of central and subsegmental pulmonary arteries. Besides **confirming or excluding pulmonary embolism**, CT angiography (CTA) is also useful in estimating the **age of the thrombotic material**.

Fresh thromboembolic material typically appears on CTA as an intravascular filling defect that partially obstructs the vessel lumen (**Fig. 12.1**, **Table 12.1**). The thrombus may occupy the center of the lumen or may be partially adherent to the vessel wall. Complete luminal obstruction appears as an abrupt cut-off, often with no direct evidence of a thrombus. As the thrombotic material ages and anticoagulant or thrombolytic therapy is instituted, the thrombus becomes layered along the vessel wall. Its shape changes over time from convex to concave. Thrombus age in a complete vascular occlusion is much more difficult to assess. Dilatation of the occluded vessel beyond its normal diameter is suggestive of a fresh pulmonary embolism (or intraluminal neoplasm), whereas a reduction in vascular diameter is typical of a chronic embolism. Thromboembolic wall thickening, irregular wall contours, and intraluminal webs and bands are consistent with a diagnosis of chronic recurrent pulmonary embolism. Calcifications of the thromboembolic material occur in ~10 % of cases.[4]

Changes in the lung parenchyma and cardiac morphology[5] provide indirect evidence of pulmonary embolism. These changes include the presence of round or oval pleural-based densities in the lung parenchyma, which represent pulmonary infarctions. Associated hemodynamic changes can be quantified by ECG-triggered multislice CT. The thrombus burden itself does not indicate the severity of the hemodynamic stress.[6] Taken together, the following four criteria are useful in assessing the severity of pulmonary embolism by CTA:

- Vascular obstruction index
- Minimum diameter of the left ventricle
- Ratio of the smallest diameters of the right and left ventricles
- Diameter of the central pulmonary arteries[7]

Pleural effusion, pericardial effusion, and/or ascites may also be present in various combinations.

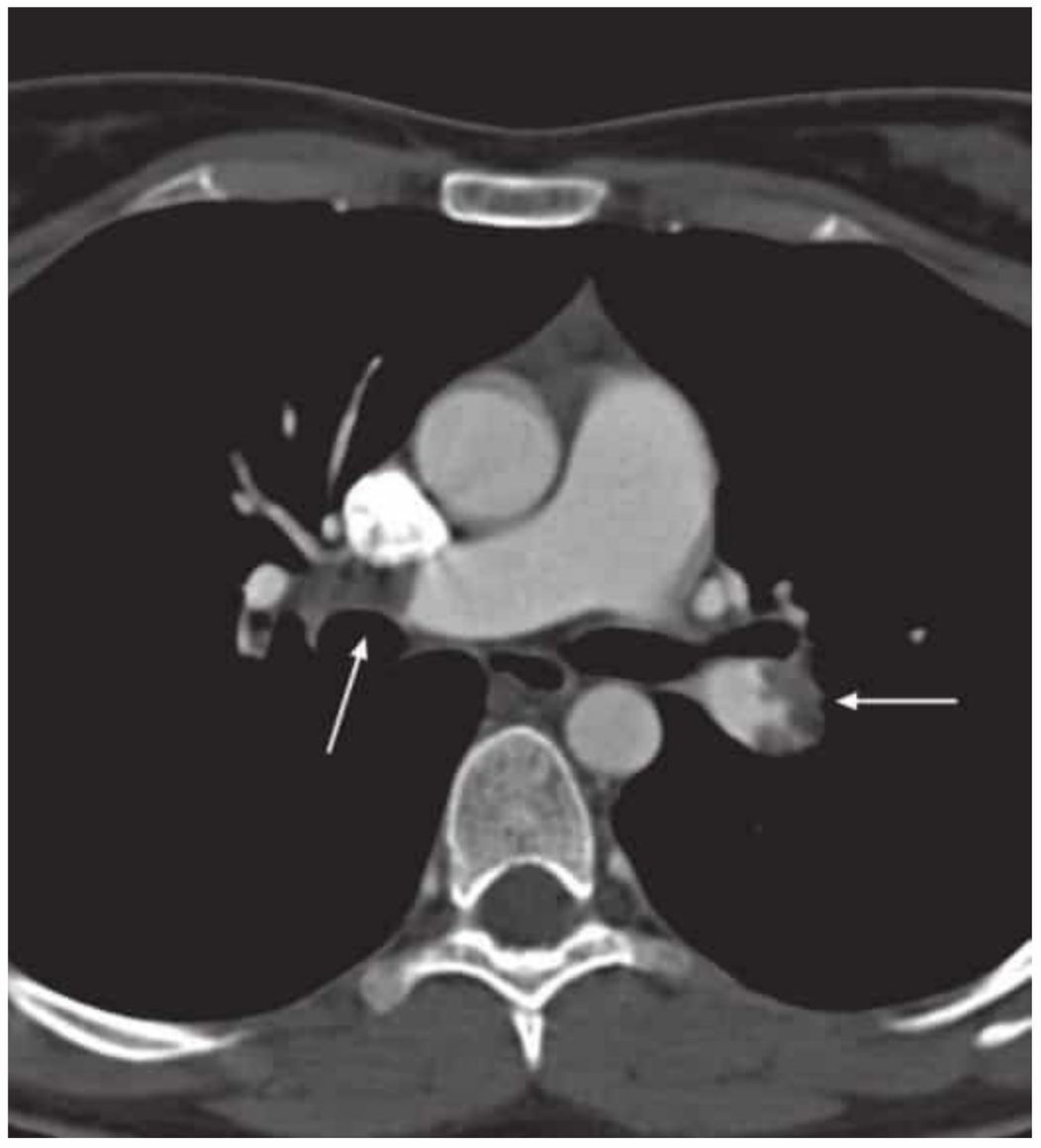

Fig. 12.1 CT angiogram in acute pulmonary embolism demonstrates mural thrombi in the left lower lobe artery (arrow) and right central pulmonary artery (arrow).

Limitations and Difficulties of Interpretation

The basis for an accurate diagnosis, of course, is a complete examination that provides images of acceptable quality. In particular, the pulmonary arteries should be well opacified and completely visualized.

Respiratory artifacts are a significant obstacle to image interpretation, but in most cases the central portions of the pulmonary arteries can be evaluated. Approximately 10 %of all examinations are nondiagnostic as a result of **technical errors**.

Multiplanar reformatted (MPR) images are often helpful in making an accurate assessment. In some cases the peribronchovascular tissue may enhance after IV contrast administration, making it more difficult to distinguish between an intraluminal and extraluminal filling defect.

Pulmonary veins that are **not completely opacified** can mimic an intraluminal arterial filling defect. The pulmonary artery can be identified in these cases on the basis of its parallel relationship to the bronchi.

MPR images should also be used for the assessment of horizontal oriented pulmonary arteries (lingula, middle lobe, segments 3 and 6). Otherwise, partial volume effects in these vessels could mimic intraluminal filling defects. This problem is less significant in modern multislice CT imagers with an appropriate thin collimation.

The presence of pulmonary embolism can be accurately confirmed or excluded in 91 %of examinations when both direct and indirect signs are interpreted. Initial data from studies performed with a 16-slice CT scanner document the increased potential of CT. With a slice thickness of 0.75 mm, the subsegmental pulmonary arteries could be directly visualized in 92 %of the patients examined.

Contraindications

CTA is contraindicated in ~12 %of cases. One reason is risk of **acute renal failure** in response to intravenous contrast medium, for example, in diabetics who take metformin-containing drugs.[8] Also, iodinated contrast media should not be used in patients with hyperthyroidism owing to the risk of symptomatic hyperthyroidism or thyrotoxic crisis.

Perfusion CT

Special postprocessing algorithms are available in CT that can map lung perfusion by providing a 3D representation of parenchymal lung enhancement. This requires the acquisition of two complete datasets, the first without contrast medium and the second after IV contrast administration. To date this has been done only for illustrative purposes and is not yet part of the routine postprocessing of CT datasets.

Magnetic Resonance Imaging

In the past, MRI has had only a **minor role** in the investigation of acute pulmonary embolism. This has been due to the poorer spatial resolution of MRI compared with multislice CT, the longer acquisition times, and problems related to scanner design and the magnetic field making it difficult to handle critically ill patients. But with constant improvements in scanner technology and pulse sequences, the spatial resolution and image quality of MR angiography (MRA) have improved significantly in recent years, making MRA a possible alternative to CTA in the investigation of acute pulmonary embolism especially in cases where CTA is contraindicated.[9]

Several studies comparing contrast-enhanced (CE-)MRA with conventional pulmonary angiography have documented the high sensitivity and specificity of the technique (**Table 12.2**). A recent study found that the accuracy of MRA was still limited in the diagnosis of isolated subsegmental emboli (40 %sensitivity).[10] Nevertheless, MRA is indicated in selected patient groups owing to its capacity for functional measurements and the absence of radiation exposure and iodinated contrast media. These indications include the following:

- Cases in which radiographic contrast material are contraindicated
- The follow-up of acute pulmonary embolism in patients on anticoagulant therapy
- Preoperative imaging in patients with chronic thromboembolic pulmonary hypertension[11]

Table 12.1 Direct and indirect signs of pulmonary embolism (PE) at different stages

Acute PE	Central intraluminal filling defects Parenchyma: rounded pleural-based densities, pleural effusion
Subacute PE	Convex mural filling defects Parenchyma: oval pleural-based densities, pleural effusion
Chronic PE	Concave mural filling defects, intraluminal "rope ladder" Irregular wall thickening, abnormal vascular tapering, variation in size of segmental vessels Parenchyma: translobular lines, mosaic perfusion, pleural effusion

Table 12.2 Sensitivity and specificity of MRA in the detection of acute pulmonary embolism

Reference	N	Sensitivity (%)	Specificity (%)
Meaney et al. (1997)[37]	30	87	97
Gupta et al. (1999)[38]	36	85	96
Oudkerk et al. (2002)[10]	141	77	95
Blum et al. (2005)[39]	89	71	92
Pleszewski et al. (2006)[40]	48	82	100
Kluge et al (2006)[41]	62	81	100

Image Display and Interpretation

As in CTA, the diagnosis of CE-MRA is based on the source images. Viewing images digitally on a monitor is advantageous for reading the images and reporting findings. MPR and MIP reconstructions can also be obtained as an adjunct to source image analysis.

Fresh thromboembolic material in MRA typically appears as a filling defect that occupies the center of the lumen or is partially adherent to the vessel wall (**Fig. 12.2**). Depending on its extent, the thrombus may completely occlude the vessel and produce a peripheral cutoff sign. Older thrombi appear as irregular mural deposits that contrast with the enhancing vessel lumen. Changes associated with pulmonary embolism, such as pleural effusion and atelectasis, can also be visualized.

Limitations and Difficulties of Interpretation

Good contrast enhancement is the key to the accurate interpretation of MR images. Because MRI is more susceptible to motion artifacts, difficulties may arise in dyspneic patients, especially during the evaluation of peripheral vascular segments. It may be more difficult to distinguish mural thrombi from the vessel wall in MRA than in CTA owing to the strong suppression of background signals.

A significant advantage of MRI over other imaging modalities is the ability to supplement morphological assessment of the pulmonary vascular system with functional measurements. This includes the analysis of lung perfusion, assessment of hemodynamics, and right cardiac function.[12]

Essential Point

Multislice CT is the imaging procedure of choice in the diagnosis of acute pulmonary embolism and can define the pulmonary arteries down to the subsegmental level. The isotropic voxels make it possible to create artifact-free 3D reconstructions that further improve diagnostic sensitivity. MRI does not match the quality of CT because of its lower spatial resolution. For the present, then, the use of MRI is limited to cases in which CT is contraindicated.

Chronic Recurrent Pulmonary Embolism

In the chronic recurrent form of pulmonary embolism, there is a progressive reduction in the cross-sectional area of the pulmonary vascular bed owing to the recurrence or incomplete resolved pulmonary emboli. Over time this leads to **chronic thromboembolic pulmonary hypertension** (CTEPH).

An incidence of 0.4–3.8 %has been reported for the development of CTEPH as a complication of acute pulmonary embolism.[13,14] Bilateral surgical pulmonary endarterectomy (PEA) is a curative therapeutic option that effects an immediate and permanent reduction of pulmonary artery pressure and pulmonary vascular resistance.[15,16]

Besides confirming the diagnosis of CTEPH, a major goal of imaging is to assess technical operability. Technical operability is given if the disease involves a central obstruction located at or proximal to the origin of the segmental arteries. In both CTA and MRA, the diagnosis of CTEPH is based on the detection of dilated central pulmonary arteries, the direct visualization of mural wall-adherent thrombus (**Figs. 12.3, 12.4**), the detection of vascular cutoffs and rapid tapering, and the presence of intraluminal filling defects and localized constrictions (intralu-

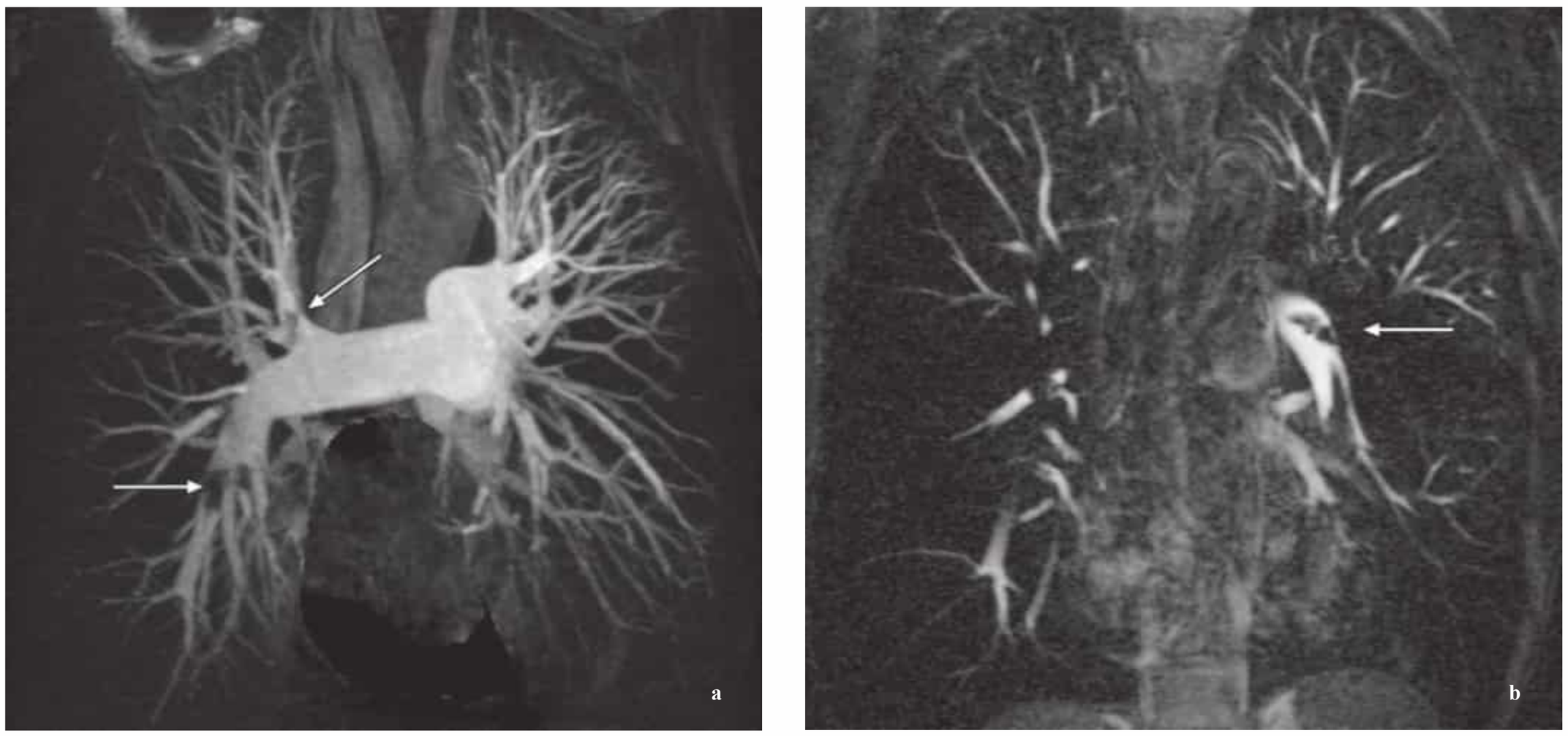

Fig. 12.2 a, b MRA of acute pulmonary embolism.
a MIP of an MRA data set shows thrombotic material in the right upper lobe artery (upper arrow) and lower lobe artery (lower arrow).
b Single slice from a coronary MRA data set. Thrombus appears as an intraluminal filling defect in the left lower lobe artery (arrow).

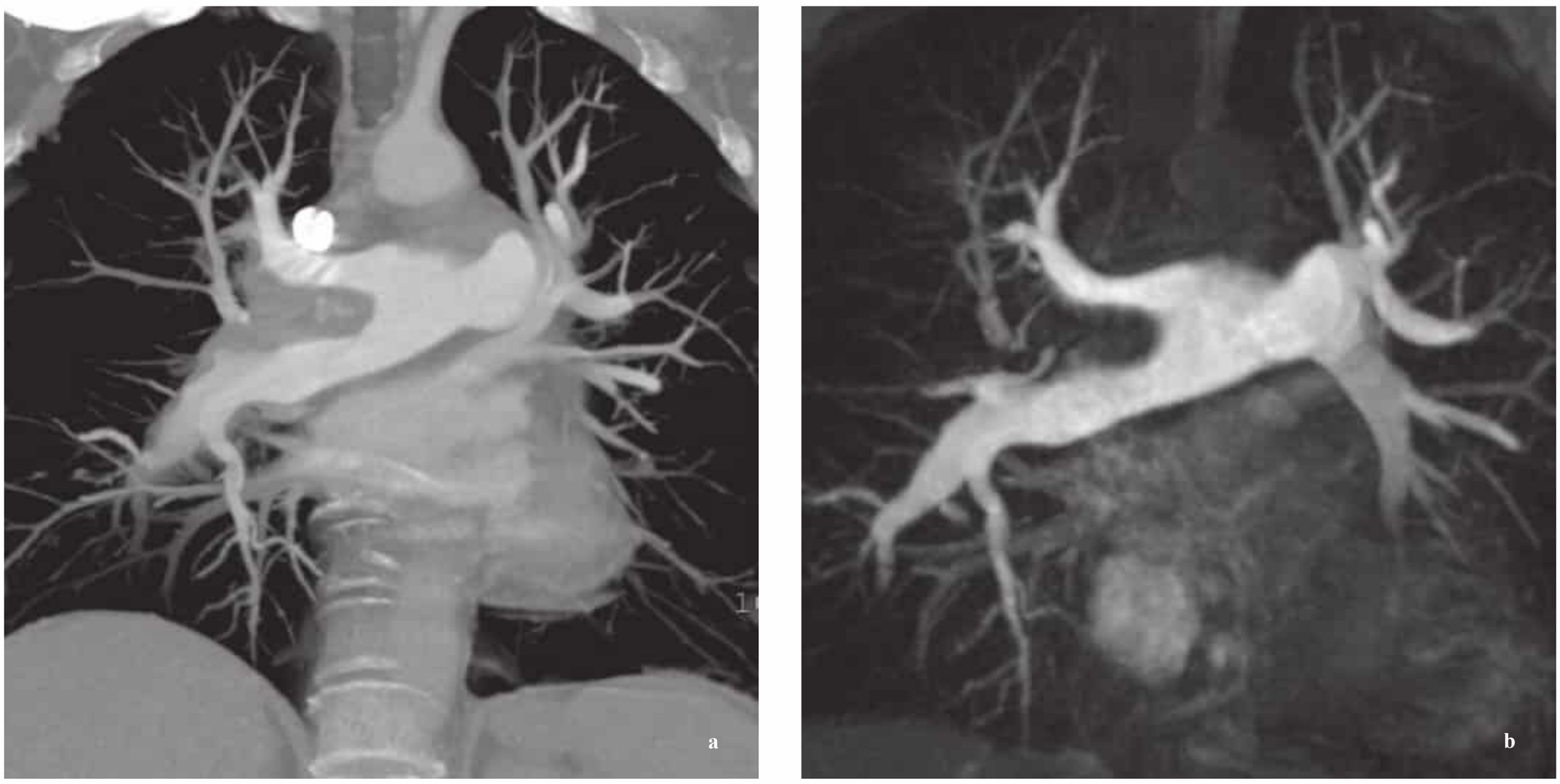

Fig. 12.3 a, b Chronic thromboembolic pulmonary hypertension (CTEPH): CTA and MRA findings.

a Coronal reformatted image from multislice CTA reveals mural thrombotic material at the bifurcation of the right upper and lower lobe arteries.

b MRA (MIP view) of the same patient also defines the begin and peripheral extent of the wall adherent thrombus.

minal webs). In our own study, we found very good agreement between selective findings of digital subtraction angiography (DSA) and the findings at operation. MRA even proved superior to DSA in the direct visualization of central thrombotic occlusive material. MRA and CTA were equivalent in evaluating the central pulmonary arteries, but CTA was superior to MRA in evaluating the subsegmental arteries.[4,17]

Imaging in CTEPH frequently shows an inhomogeneous or "mosaic" pattern of parenchymal perfusion with thickening of the interlobular septa. Chronic cases present with dilated bronchial arteries that extend from the aorta through the mediastinum to the lung parenchyma. The presence of dilated bronchial arteries is an important sign that should be specifically looked for, as it predicts a positive outcome of PEA.

Other Forms of Pulmonary Arterial Hypertension

Chronic obstructive pulmonary disease (COPD) is the third leading cause of death, with secondary changes such as PH contributing significantly to its mortality.

Dilatation of the central pulmonary arteries provides an indirect sign for estimating the pressure in the pulmonary vascular bed. It is not useful as a quantitative parameter, because the individual pressure is strongly dependent on cardiac function. If the diameter of the pulmonary trunk is greater than 28.6 mm, it is highly probable that PH is present. Furthermore, CTA and MRA detect no other intravascular abnormalities (**Fig. 12.5**). Instead, the hyperinflated condition of the lung parenchyma leads to a generalized decrease in peripheral vascularity, marked particularly by an absence of subsegmental vessels at the subpleural level. Segmental artery cutoffs may also be seen when bullous changes of the lung parenchyma are present. CT is better for demonstrating the morphological correlate of this finding, the destruction of lung parenchyma (**Fig. 12.6**).

Essential Point

CT and MRI are both excellent for diagnosing the typical changes that occur in chronic pulmonary vascular diseases. Multislice CT is preferred is patients with severe dyspnea.

Tumors of the Pulmonary Vessels

Leiomyosarcoma is the most frequent tumor of the pulmonary arteries and veins (pulmonary artery sarcomas [PASs] and pulmonary vein sarcomas [PVSs]). It arises from the smooth-muscle cells of the media (**Fig. 12.7**).

Primary PASs affect both sexes equally and occur at a slightly earlier average age (50 years) than the venous forms. The incidence ratio of PAS to PVS is ~20:1. Only 17 cases of PVS have been described in the literature. The median age at radiological diagnosis was ~48 years (six men, 11 women).

PASs most commonly involve the main pulmonary artery and may spread from there toward the peripheral arterial branches or may extend back into the right ventricle. Tumor growth may be completely extravascular (62%), completely intravascular (5%), or both extra- and intravascular (33%).[18] Other studies indicate that ~50% of PASs are intravascular when diagnosed. The remaining half demonstrate a transmural spread into the lung parenchyma.[19,20]

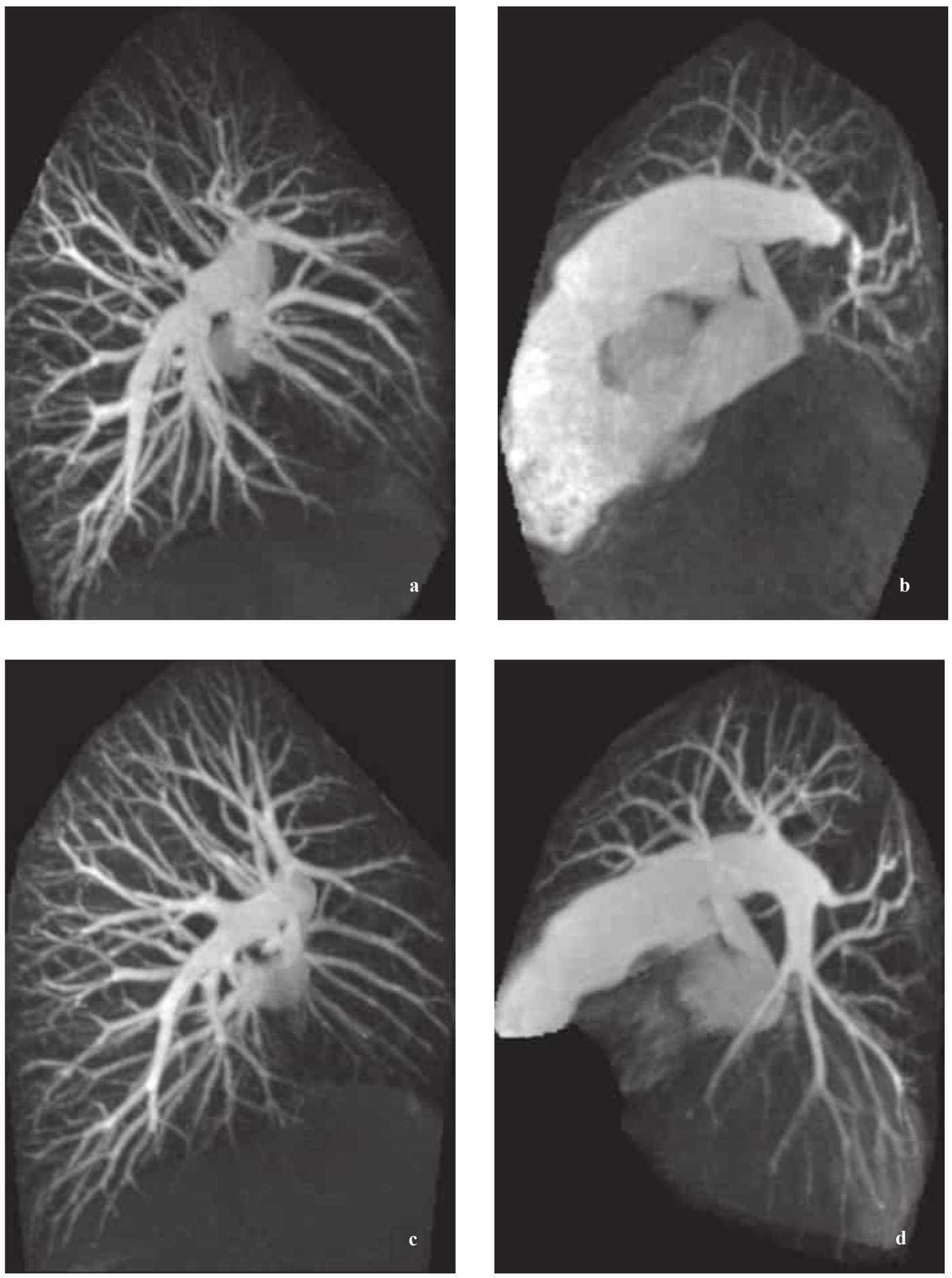

Fig. 12.4 a–d CTEPH before and after surgery.
a, b Preoperative MRA of the right and left pulmonary arterial systems. MIP views show typical vascular changes with occlusion of numerous segmental arteries on the left side and typical intraluminal webs at the junction of lobar and segmental arteries on the right side.
c, d MRA 20 days after successful pulmonary endarterectomy shows that the right pulmonary arterial tree is almost normal while multiple segmental arteries have been reopened on the left side, particularly in the lower lobe.

PVSs have a tendency to spread into the left atrium (**Fig. 12.8**).[21]

Clinical Features

The clinical manifestations of PAS are nonspecific and may include dyspnea, chest pain, cough, hemoptysis, and signs of right heart failure. Because these tumors are often intraluminal, they may embolize and cause peripheral infarctions, producing clinical symptoms similar to those of acute or chronic recurrent pulmonary embolism.

Venous sarcomas are generally larger than arterial sarcomas. They remain asymptomatic until their growth interferes with pulmonary venous return. The most frequent clinical manifestations are dyspnea, hemoptysis, cough, chest pain, and weight loss.

Diagnosis

Pulmonary artery sarcomas appear on CT and MR images as a **convex intraluminal mass** that usually begins in the pulmonary trunk and spreads in a peripheral or occasionally central fashion. Both primary and metastatic tumors of the pulmonary arteries may cause intraluminal filling defects that are similar in appearance to chronic recurrent pulmonary emboli. Delayed imaging after contrast administration shows a highly variable degree of tumor enhancement, which is an important feature that allows for differentiation from CTEPH.

The tumors may be inhomogeneous as a result of hemorrhage, necrosis, or different tissue components. Thrombi may adhere to intraluminal tumor components and may in turn be infiltrated by tumor.[22] Thus, delayed T1-weighted images after contrast administration are an essential part of the MR imaging protocol. Tumor enlargement over time may lead to vascular expansion with complete obliteration of the lumen. A convex shape of the filling defect does not support a diagnosis of

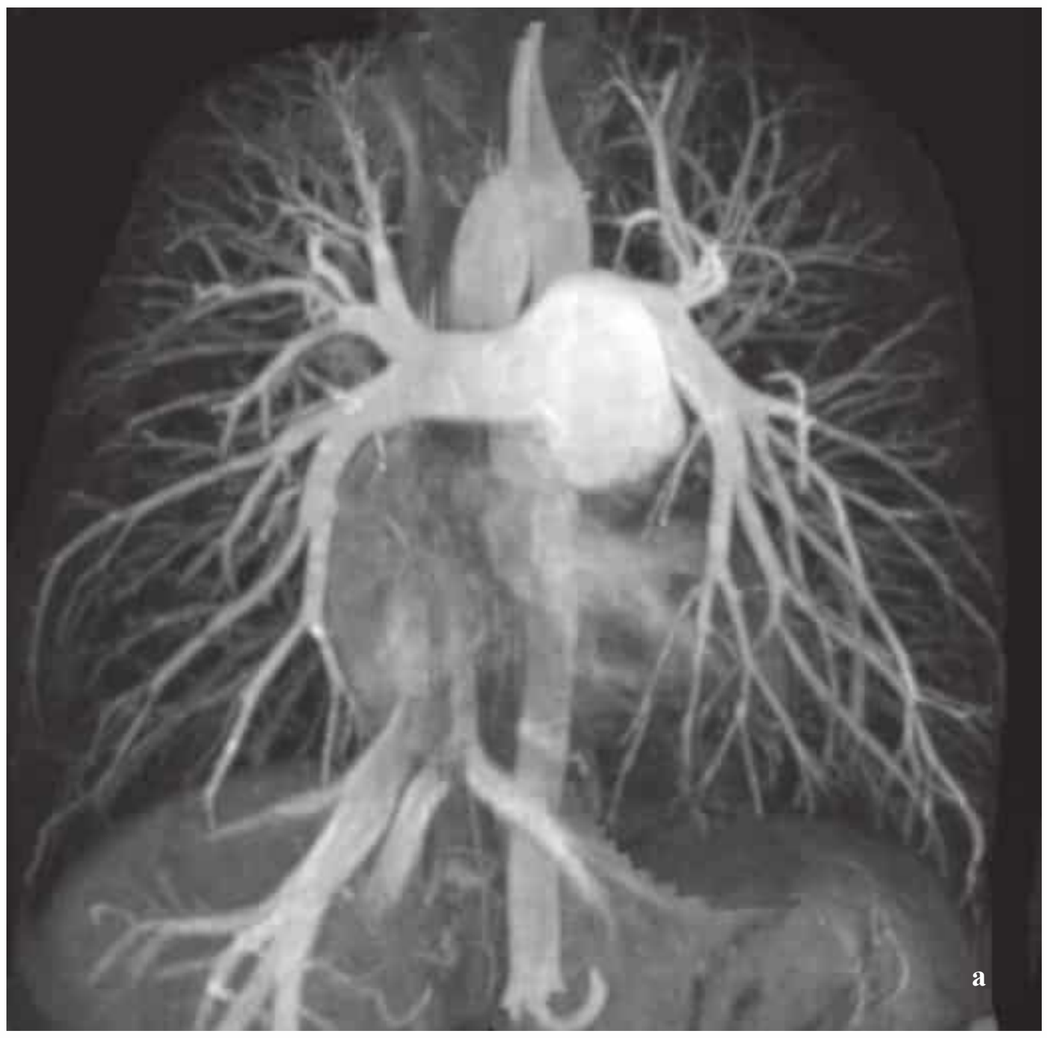

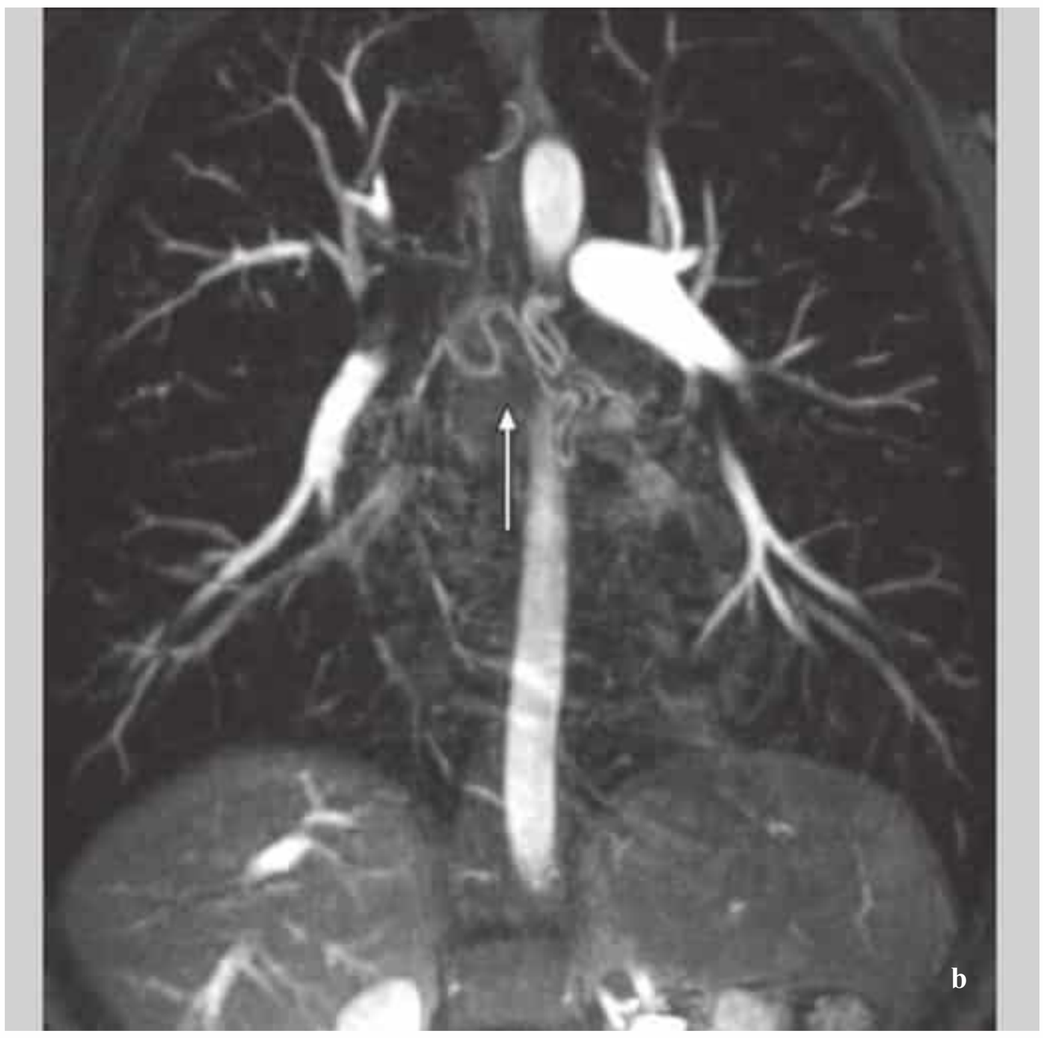

Fig. 12.5 a, b Secondary pulmonary arterial hypertension in a man who underwent partial surgical correction of tetralogy of Fallot in childhood. Incomplete closure of the ventricular septal defect with the development of an Eisenmenger reaction, and pulmonary hypertension due to an absence of right ventricular outflow tract obstruction.

a MRA shows a dilated pulmonary trunk with an almost normal pulmonary vessel course in the periphery. At most, a slight pruning of the peripheral pulmonary arteries is observed.

b Another sign of pulmonary hypertension is dilated bronchial arteries arising from the descending aorta (arrow). MRA has sufficient resolution to bring out these fine anatomical details.

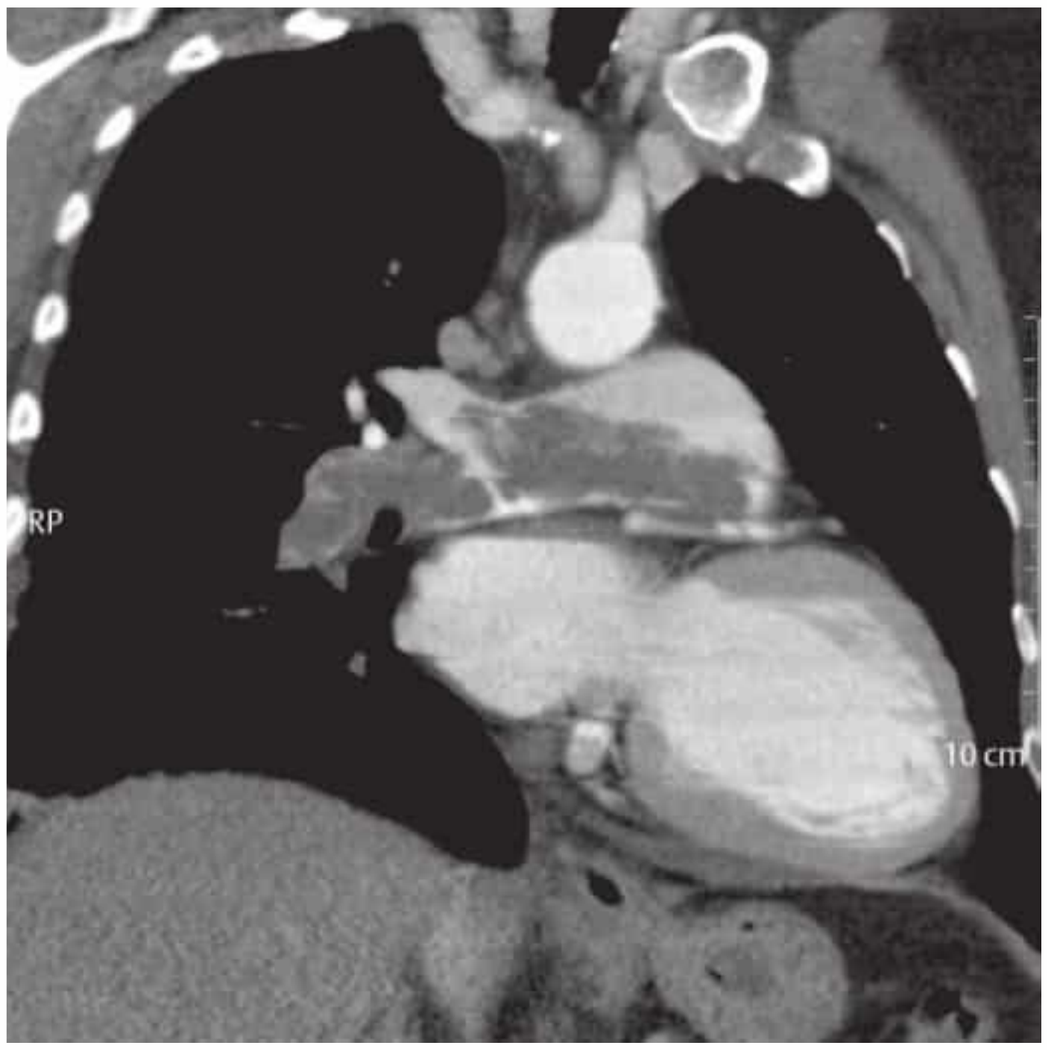

Fig. 12.7 Tumor of the pulmonary artery. Coronal reformatted CTA image. The hypodense material in the central pulmonary arteries, with extension into the right pulmonary artery, is easily misinterpreted as thrombotic material. The material in this case is a pulmonary artery sarcoma. Differentiation is aided by contrast medium enhancement of the sarcoma on delayed postcontrast images.

chronic pulmonary embolism. Contrast enhancement on MRI is another indicator of intravascular tumor growth.

Completely intravascular leiomyosarcomas are usually nodular, polypoid tumors that are fixed to the inner vessel wall. Intraluminal tumor growth expands the vessel diameter, and intracardiac tumor extension occasionally occurs.

Besides leiomyosarcoma, the differential diagnosis of intrathoracic sarcomas should include angiosarcoma, rhabdomyosarcoma, and the sarcomatoid variant of mesothelioma.

Treatment

The treatment of choice is complete tumor resection based on an early preoperative diagnosis. Modern surgical techniques can be used to reconstruct the vascular defect with prosthetic material. Even if curative treatment is not an option, it appears that palliative surgery can significantly prolong the patient's life.

■ Pulmonary Capillary Hemangioma

Most cases of pulmonary capillary hemangioma (PCH) involve **bilateral disease with an unknown origin**. Capillaries proliferate into the alveolar septa and other structures such as bronchial walls, pleura, and regional lymph nodes. Extrathoracic growth or metastasis has not previously been described. The disease is most prevalent in the third and fourth decades, with a range from 6 to 71 years, and affects males and females equally. Life expectancy after onset of symptoms is 2–12 years in untreated cases.

Clinical Features

Typical clinical manifestations are progressive shortness of breath, pleuritic chest pain, and frequent hemoptysis, often prompting a misdiagnosis of CTEPH. With the progression of disease, patients develop clinical signs of cor pulmonale with elevated pulmonary artery pressures (PAP) but normal pulmonary capillary wedge pressures on right heart catheterization.

Diagnosis

To date, CT is the only sectional imaging modality that has been investigated in the literature. The principal CT findings are enlarged pulmonary arteries and numerous small, bilateral, ill-defined densities.[23] Compared with idiopathic pulmonary artery hypertension, perfusion scanning shows increased perfusion in the hemangiomatous tissue and decreased perfusion in occluded vessels, resulting in an inhomogeneous perfusion pattern.

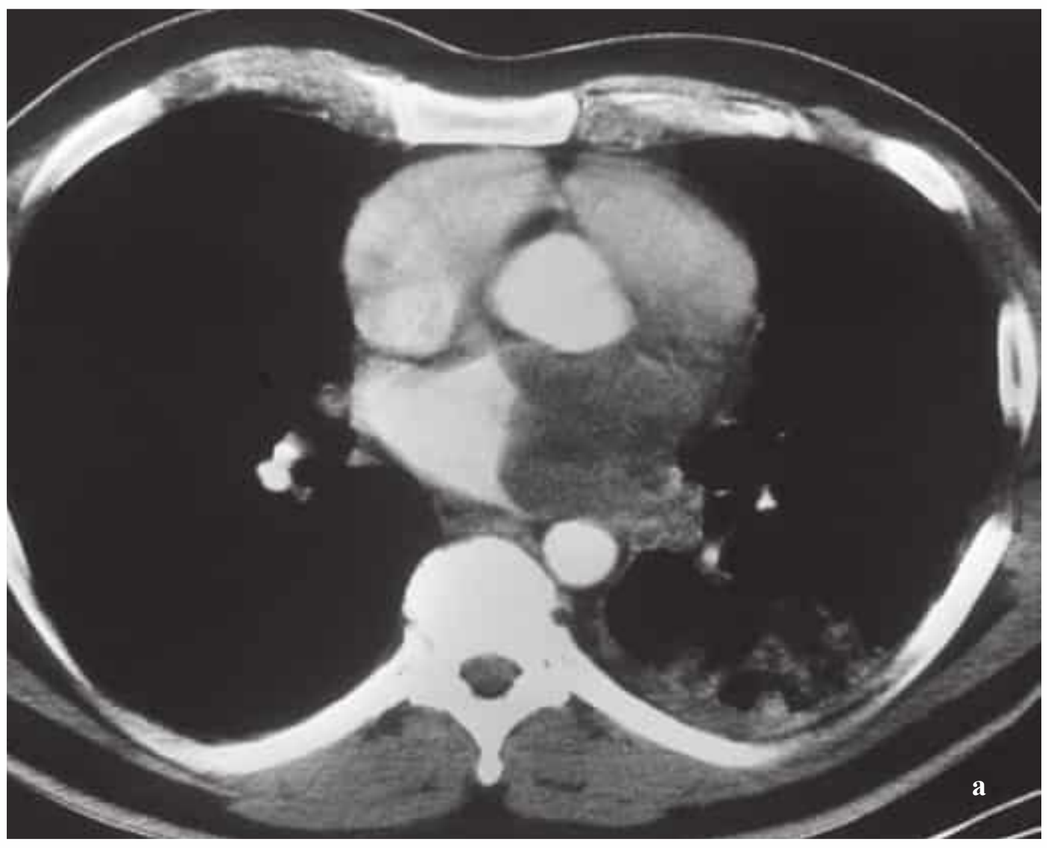

Fig. 12.8 a, b Tumor of the pulmonary vein (CT and MRI). CT (**a**) and MRI (**b**) of a pulmonary vein sarcoma extending into the left atrium. The relationship of the tumor to the other cardiac chambers and vessels is clearly demonstrated by CT. Invasion of these structures is difficult or impossible to detect, however. Coronal MRI (HASTE) provides assessment of invasion of adjacent structures by clear delineation of different signal intensities.

The only curative treatment is bilateral lung transplantation, for which patients must be selected at a very early stage.

Essential Point
Primary or metastatic tumors of the pulmonary arteries and veins appear as intraluminal filling defects that resemble chronic recurrent pulmonary emboli. Delayed imaging after contrast administration shows a highly variable degree of tumor enhancement, which is an important differentiating feature from CTEPH. Primary tumors of the pulmonary arteries and veins consist of leiomyosarcomas and other entities.

Arteriovenous Malformations

Pulmonary arteriovenous malformations (PAVMs) result from fistula formation between the pulmonary arteries and veins. Blood flow bypasses the pulmonary capillary bed, giving rise to a functional right-to-left shunt. The prevalence of PAVM is ~2–3 per 100 000 population. The great majority of PAVMs (80 %) are congenital. Within this group, PAVMs are present in 47–80 % of patients with autosomal dominant Osler–Weber–Rendu syndrome (hereditary hemorrhagic telangiectasia).[24] Other cases are not referable to a specific syndrome, although a genetic link to the 9q3 chromosome has been suggested.

Acquired AV shunts may have various causes:

- Trauma
- Infection
- Metastatic carcinoma
- Mitral stenosis
- Hepatic cirrhosis[25]

AV shunts may develop owing to metastatic involvement of the lung parenchyma. This possibility should be considered in patients who develop sudden hemoptysis following successful chemotherapy.[25]

A large, long-term follow-up study documented the superiority of sectional imaging modalities over conventional angiography. CTA (incremental and single-slice spiral CT) achieved a detection rate of 98 % of all PAVMs, while angiography detected only 60 %[26] In a study comparing DSA and MRA, MRA correctly defined the location of the PAVMs in 16 of 16 cases. The origin and the size of the feeding vessel could be accurately determined in 14 of 16 cases (**Fig. 12.9**). In two cases the feeding vessels were not contained in the volume slab.[27] This limitation no longer exists with the current generation of MR scanners, and both sectional imaging modalities may be considered equivalent in the evaluation of PAVMs.

Pulmonary Venous Disorders

Generally there are a total of four pulmonary veins (PVs), with one pair of veins opening into the left atrium on each side.

Congenital Anomalies

Anomalous pulmonary venous drainage may be **partial** or **complete**. The complete form, known as total anomalous pulmo-

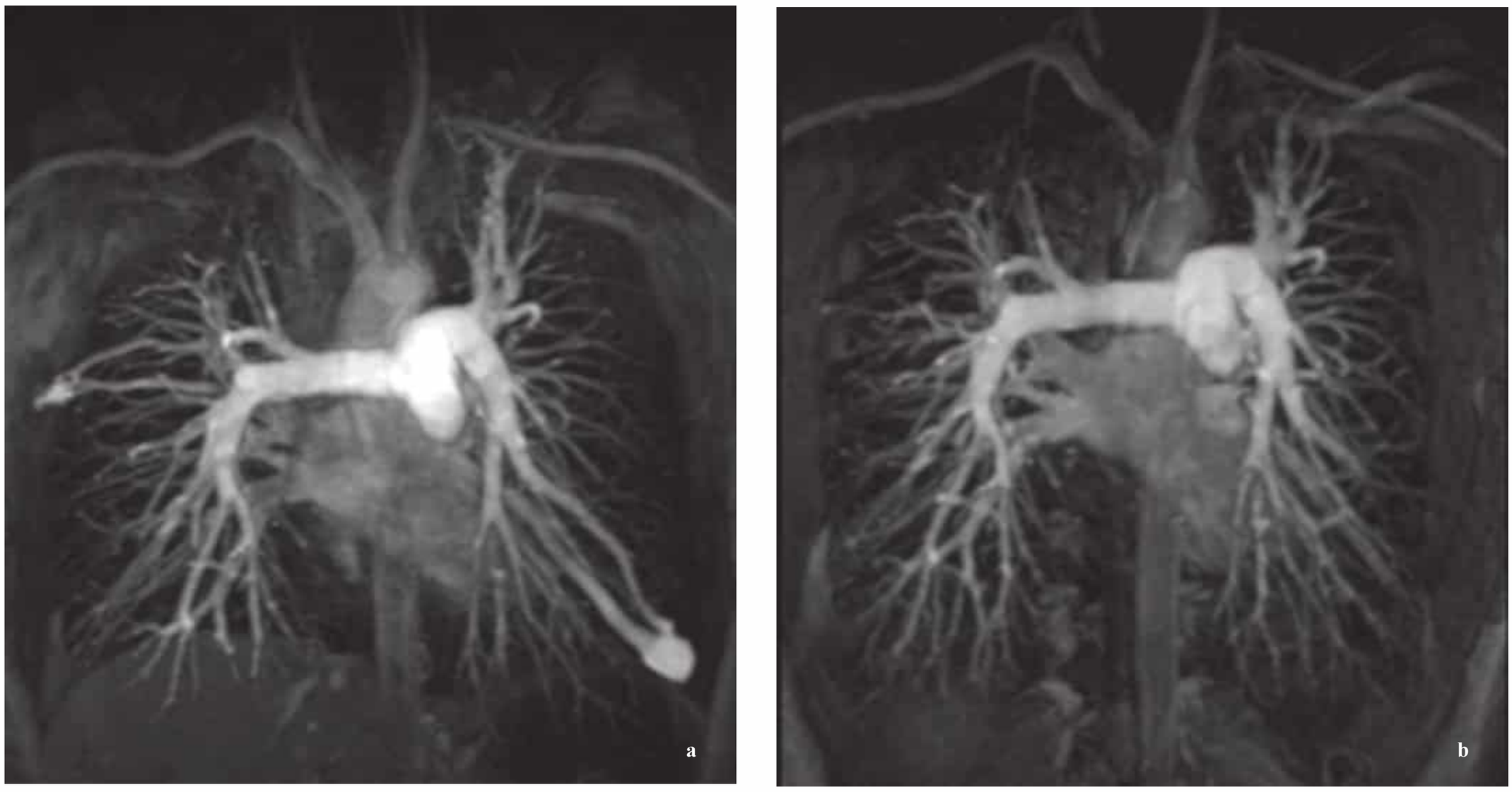

Fig. 12.9 a, b Arteriovenous malformation (MRI).
a MRA in a young woman with a family history of AVMs. Like her father, she had AVMs of the pulmonary vessels. The temporal resolution of MRA provides clear visualization of the feeding arteries and draining veins. The diagnostic quality is sufficient to eliminate the need for further preinterventional imaging.
b MRA several days after interventional closure of the AVM confirms complete occlusion with no residual abnormalities.

nary venous connection (TAPVC), is compatible with life only in patients with a coexisting atrial septal defect or patent foramen ovale. Three main types are differentiated in descending order of frequency:

- **Supracardiac type:** The anomalous PVs unite posterior to the atria and drain into a left ascending vessel that opens into a persistent superior vena cava. The blood then enters the right atrium by way of the left innominate vein and right superior vena cava.
- **Intracardiac type:** The anomalous PVs unite to form a short vessel that opens into the coronary sinus.
- **Infracardiac type:** The anomalous PVs drain into the portal vein, hepatic vein, left gastric vein, directly into the inferior vena cava, directly into the right atrium, or into the right atrium by way of a collecting vessel.

In partial anomalous pulmonary venous connection (PAPVC) some of the PVs are connected to the right atrium (RA), and in few cases only one single vein communicates with that chamber. In the most common configuration, the right superior pulmonary vein opens into the superior vena cava or RA. A special form is the scimitar syndrome, with a hypoplastic right lung and partial or total anomalous drainage of the right pulmonary vein into the inferior vena cava.[28]

The **relative frequency** of PAPVC is ~0.6 % of all congenital anomalies, while TAPVC accounts for 0.4 %[29]

Clinical Features

Anomalous pulmonary venous drainage imposes a volume overload on the pulmonary circulation with subsequent volume loading and dilatation of the right ventricle. PAPVC is usually asymptomatic and is often detected incidentally.

Echocardiography

Anomalous pulmonary venous connections are not well demonstrated by transthoracic echocardiography in many cases, and transesophageal echocardiography is more commonly used for this purpose.

Computed Tomography

CT is well suited for the detection of anomalous pulmonary venous drainage. Partial anomalous connections are particularly well displayed by CT, followed if necessary by MPR images in oblique coronal planes.

Magnetic Resonance Imaging

Generally the PVs are adequately visualized in axial T1-weighted SE sequences. Adding thin-slice acquisitions or a dynamic GE sequence with bright-blood vascular imaging may allow for visualization in patients with more complex vascular anatomy. Additionally, contrast-enhanced MRA followed by 3D MIP reconstructions can define the course of the PVs as an aid to preoperative planning (**Fig. 12.10**).[30] The shunt volume can be quantified by performing flow measurements in the ascending aorta and pulmonary trunk. MRI can aid in noninvasive patient selection for the surgical treatment of PAPVC. The heart can also be examined with cine sequences to check for concomitant septal defects. These capabilities make MRI the imaging modality of choice for the investigation of anomalous pulmonary venous drainage.

Essential Point

Congenital TAPVC of the pulmonary veins (relative frequency 0.4 %) is classified as supracardiac, intracardiac, or infracardiac. With PAPVC (relative frequency 0.6 %), not all the PVs are connected to the RA, and only one vein may communicate with it. MRI is the modality of choice (axial T1-weighted SE sequences and MRA) for imaging the pulmonary veins.

Acquired Pulmonary Venous Disorders

In the absence of congenital anomalies, there is rarely an indication for diagnostic imaging of the pulmonary veins. The most frequent indication at present is pre- and postinterventional imaging of the pulmonary veins before and after radiofrequency ablation.

Atrial fibrillation is the most common cardiac arrhythmia, with a prevalence of ~5 % in persons over 65 years of age.[31] Percutaneous catheter ablation using radiofrequency ablation or cryoablation is a minimally invasive procedure for destroying arrhythmogenic foci. Because the origin of the pulmonary vein exhibits slight variations due to the rotation of the left atrium during embryonic development, preinterventional imaging is recommended (also to exclude previously undetected normal variants or anomalous origin). 3D imaging is useful for planning the optimum size of the catheter balloon.

The most frequent complication of catheter ablation (prevalence of 1.5–42 %) is stenosis of the pulmonary veins. Other possible complications are thrombosis or dissection. Pulmonary vein stenosis develops during the first few days after the procedure, as initial tissue swelling is followed by the development of fibrotic changes. Clinical manifestations are progressive dyspnea, orthopnea, nonproductive cough, infection, and hemoptysis.[32] Again, CTA or MRA can detect the pulmonary vein stenosis and quantify the degree of narrowing. Time-resolved angiographic techniques with adequate in-plane resolution should be used to achieve optimum timing of the contrast bolus for pulmonary vein imaging. Optimum bolus timing varies in different patients (and in different PV segments), especially in the presence of pulmonary vein stenosis.

Extravascular Disorders

MRA and CTA are equally sensitive in detecting invasion of the central pulmonary arteries by bronchial carcinoma, but studies have documented the value of MRI in the detection and evaluation of mediastinal and arterial invasion. This information is critical in planning the resection of the carcinoma. When vascular invasion is present, the patient must be placed on a heart–lung machine during the operation and a suitable vascular in-

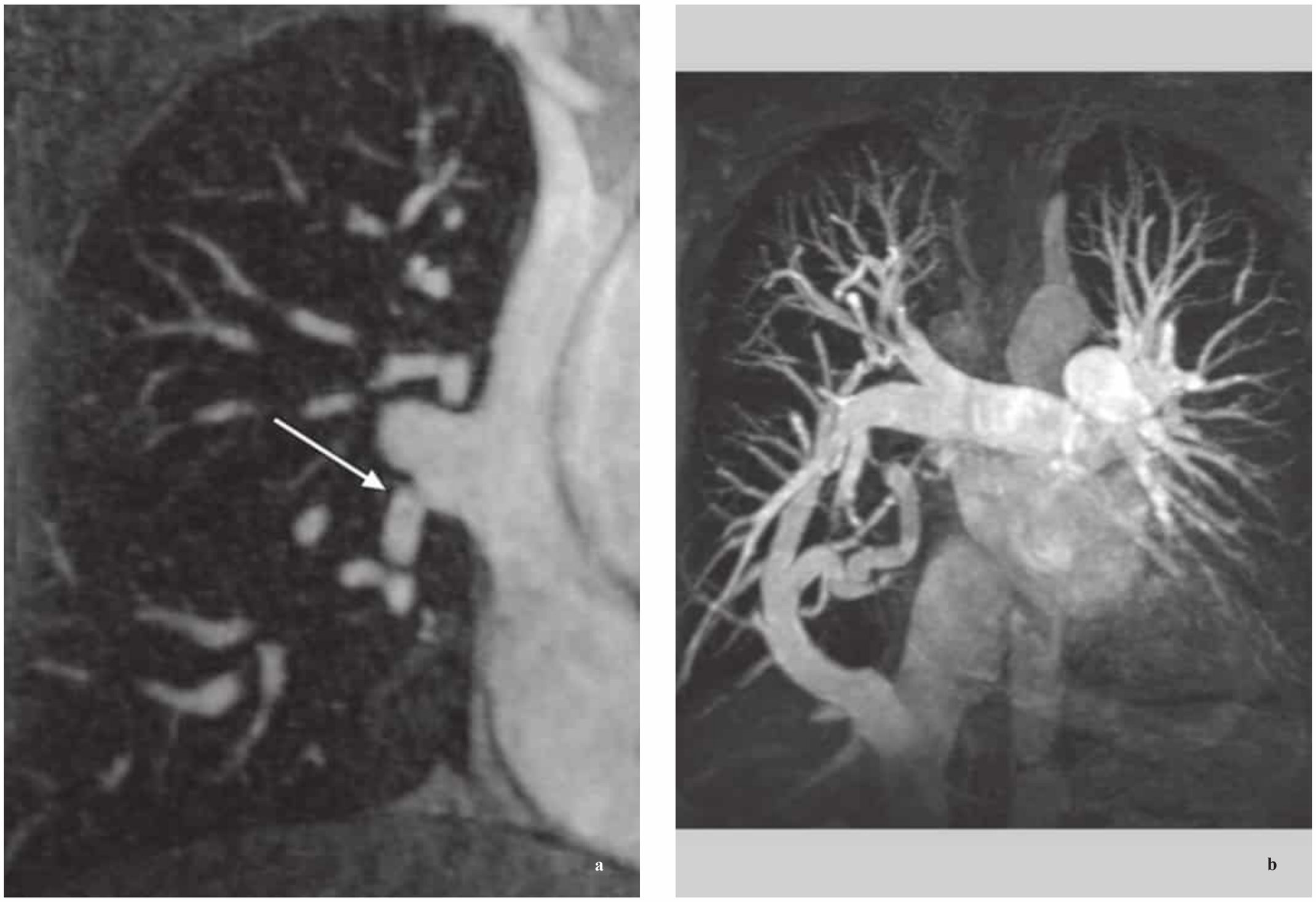

Fig. 12.10 a, b Anomalous pulmonary venous drainage (MRI).
a Coronal-acquisition 3D MRA in an adult patient shows anomalous drainage of a right pulmonary vein into the superior vena cava (arrow). The patient presented clinically with exertional dyspnea.
b Aberrant subdiaphragmatic termination of the right pulmonary vein in a patient with scimitar syndrome.

terposition graft should be ready for use. The long-term survival rate is significantly reduced in patients with pulmonary vascular invasion.[33,34] The lung parenchyma should also be evaluated during preoperative staging.

The presence of aneurysms in the setting of Behçet disease or Hughes–Stovin syndrome[35,36] and involvement by vasculitis are relatively rare indications for CTA or MRA of the pulmonary vessels. The primary sectional imaging modality in these cases is still spiral CT, the capabilities of which have been greatly augmented by the advent of multidetector technology. MRA should be considered in cases where CT is contraindicated because of renal failure or thyroid dysfunction.

References

1. Ley S, Kreitner KF, Fink C, Heussel CP, Borst MM, Kauczor HU. Assessment of pulmonary hypertension by CT and MR imaging. Eur Radiol 2004;14:359–368
2. Walther A, Bottiger BW. Akute Lungenembolie. Anaesthesist 2002;51: 427–443 quiz 444–5
3. Michiels JJ. Rational diagnosis of pulmonary embolism (RADIA PE) in symptomatic outpatients with suspected PE: an improved strategy to exclude or diagnose venous thromboembolism by the sequential use of a clinical model, rapid ELISA D-dimer test, perfusion lung scan, ultrasonography, spiral CT, and pulmonary angiography. Semin Thromb Hemost 1998;24:413–418
4. Ley S, Kauczor HU, Heussel CP, et al. Value of contrast-enhanced MR angiography and helical CT angiography in chronic thromboembolic pulmonary hypertension. Eur Radiol 2003;13:2365–2371
5. Roberts HC, Kauczor H-U, Schweden F, Thelen M. Spiral CT of pulmonary hypertension and chronic thromboembolism. J Thorac Imaging 1997;12:118–127
6. Mastora I, Remy-Jardin M, Masson P, et al. Severity of acute pulmonary embolism: evaluation of a new spiral CT angiographic score in correlation with echocardiographic data. Eur Radiol 2003;13:29–35
7. Collomb D, Paramelle PJ, Calaque O, et al. Severity assessment of acute pulmonary embolism: evaluation using helical CT. Eur Radiol 2003; 13:1508–1514
8. Morcos SK, Thomsen HS. Adverse reactions to iodinated contrast media. Eur Radiol 2001;11:1267–1275
9. Fink C, Ley S, Schoenberg SO, Reiser MF, Kauczor HU. Magnetic resonance imaging of acute pulmonary embolism. Eur Radiol 2007;17: 2546–2553
10. Oudkerk M, van Beek EJ, Wielopolski P, et al. Comparison of contrast-enhanced magnetic resonance angiography and conventional pulmo-

nary angiography for the diagnosis of pulmonary embolism: a prospective study. Lancet 2002;359:1643–1647
11. Kauczor H-U, Heussel CP, Thelen M. Update on diagnostic strategies of pulmonary embolism. Eur Radiol 1999;9:262–275
12. Rominger MB, Bachmann GF, Pabst W, Rau WS. Right ventricular volumes and ejection fraction with fast Cine MR imaging in breath-hold technique: applicability, normal values from 52 volunteers, and evaluation of 325 adult cardiac patients. J Magn Reson Imaging 1999;10:908–918
13. Pengo V, Lensing AW, Prins MH, et al. Incidence of chronic thromboembolic pulmonary hypertension after pulmonary embolism. N Engl J Med 2004;350:2257–2264
14. Kreitner KF, Kunz RP, Ley S, et al. Chronic thromboembolic pulmonary hypertension – assessment by magnetic resonance imaging. Eur Radiol 2007;17:11–21
15. Klepetko W, Mayer E, Sandoval J, et al. Interventional and surgical modalities of treatment for pulmonary arterial hypertension. J Am Coll Cardiol 2004;43:73S–80S
16. Jamieson SW, Kapelanski DP, Sakakibara N, et al. Pulmonary endarterectomy: experience and lessons learned in 1,500 Cases. Ann Thorac Surg 2003;76:1457–1464
17. Kreitner KF, Ley S, Kauczor HU, et al. Chronic thromboembolic pulmonary hypertension: pre- and postoperative assessment with breath-hold MR imaging techniques. Radiology 2004;232:535–543
18. Kreft B, Flacke S, Zhou H, Textor J, Remig J, Schild HH. Diagnostic imaging of vascular leiomyosarcomas. Fortschr Roentgenstr. 2004;176:183–190
19. Bressler EL, Nelson JM. Primary pulmonary artery sarcoma: diagnosis with CT, MR imaging, and transthoracic needle biopsy. AJR Am J Roentgenol 1992;159:702–704
20. Fasse A, Kauczor HU, Mayer E, Kreitner KF, Heussel CP, Thelen M. Das Pulmonalarteriensarkom – Prä- und postoperative radiologische Befunde bei der Tumormanifestation und beim Rezidiv. Rofo 1999;170:112–118
21. Yi ES. Tumors of the pulmonary vasculature. Cardiol Clin 2004;22:431–440
22. Kauczor HU, Schwickert HC, Mayer E, Kersjes W, Moll R, Schweden F. Pulmonary artery sarcoma mimicking chronic thromboembolic disease: computed tomography and magnetic resonance imaging findings. Cardiovasc Intervent Radiol 1994;17:185–189
23. Eltorky MA, Headley AS, Winer-Muram H, Garrett HE Jr, Griffin JP. Pulmonary capillary hemangiomatosis: a clinicopathologic review. Ann Thorac Surg 1994;57:772–776
24. Khurshid I, Downie GH. Pulmonary arteriovenous malformation. Postgrad Med J 2002;78:191–197
25. Choi SH, Goo JM, Kim HC, Im JG. Pulmonary arteriovenous fistulas developed after chemotherapy of metastatic choriocarcinoma. AJR Am J Roentgenol 2003;181:1544–1546
26. Remy J, Remy-Jardin M, Wattinne L, Deffontaines C. Pulmonary arteriovenous malformations: evaluation with CT of the chest before and after treatment. Radiology 1992;182:809–816
27. Mohrs OK, Voigtlander T, Heussel CP, Bardeleben S, Düber C, Kreitner KF. Morphologische und funktionelle Evaluation pulmonaler Gefäßanomalien mittels schneller MR-Techniken. Fortschr Roentgenstr. 2002;174:467–473
28. Holt PD, Berdon WE, Marans Z, Griffiths S, Hsu D. Scimitar vein draining to the left atrium and a historical review of the scimitar syndrome. Pediatr Radiol 2004;34:409–413
29. Moos A. Heart Disease in Infants, Children and Adolescents. Including the Fetus and Yound Adult. Philadelphia: Lippincott Williams & Wilkins; 2001.
30. Kivelitz DE, Scheer I, Taupitz M. Scimitar Syndrome: diagnosis with MR angiography. AJR Am J Roentgenol 1999;172:1700
31. Falk RH. Atrial fibrillation. N Engl J Med 2001;344:1067–1078
32. Ghaye B, Szapiro D, Dacher JN, Rodriguez LM, Timmermans C, Devillers D, Dondelinger RF. Percutaneous ablation for atrial fibrillation: the role of cross-sectional imaging. Radiographics 2003;23 Spec No:S19–33; discussion S48–50.
33. Chunwei F, Weiji W, Xinguan Z, Qingzen N, Xiangmin J, Qingzhen Z. Evaluations of bronchoplasty and pulmonary artery reconstruction for bronchogenic carcinoma. Eur J Cardiothorac Surg 2003;23:209–213
34. Ohno Y, Adachi S, Motoyama A, et al. Multiphase ECG-triggered 3D contrast-enhanced MR angiography: utility for evaluation of hilar and mediastinal invasion of bronchogenic carcinoma. J Magn Reson Imaging 2001;13:215–224
35. Kindermann M, Wilkens H, Hartmann W, Schafers HJ, Bohm M. Images in cardiovascular medicine. Hughes-Stovin syndrome. Circulation 2003;108:e156
36. Oliver TB, Stevenson AJ, Gillespie IN. Pulmonary artery pseudoaneurysm due to bronchial carcinoma. Br J Radiol 1997;70:950–951
37. Meaney JF, Weg JG, Chenevert TL, Stafford-Johnson D, Hamilton BH, Prince MR. Diagnosis of pulmonary embolism with magnetic resonance angiography. N Engl J Med 1997;336:1422–1427
38. Gupta A, Frazer CK, Ferguson JM, et al. Acute pulmonary embolism: diagnosis with MR angiography. Radiology 1999;210:353–359
39. Blum A, Bellou A, Guillemin F, Douek P, Laprévote-Heully MC, Wahl D. GENEPI study group. Performance of magnetic resonance angiography in suspected acute pulmonary embolism. Thromb Haemost 2005;93:503–511
40. Pleszewski B, Chartrand-Lefebvre C, Qanadli SD, et al. Gadolinium-enhanced pulmonary magnetic resonance angiography in the diagnosis of acute pulmonary embolism: a prospective study on 48 patients. Clin Imaging 2006;30:166–172
41. Kluge A, Luboldt W, Bachmann G. Acute pulmonary embolism to the subsegmental level: diagnostic accuracy of three MRI techniques compared with 16-MDCT. AJR Am J Roentgenol 2006;187:W7–14

Further Reading

Fink C, Bock M, Puderbach M, Schmähl A, Delorme S. Partially parallel three-dimensional magnetic resonance imaging for the assessment of lung perfusion—initial results. Invest Radiol 2003;38:482–488

13 Diseases of the Thoracic Aorta

H. Eggebrecht, J. Barkhausen, and K.-F. Kreitner

Besides congenital anomalies, the most common diseases of the thoracic aorta are acquired, usually degenerative diseases that affect the aortic wall. Atherosclerotic wall changes, disorders of connective-tissue metabolism (e.g., in Marfan syndrome), or inflammatory infiltration of the vessel wall can lead to thickening of the aortic wall, aortic dilatation (ectasia), dissection, or aneurysm formation. Acute aortic syndrome often takes a fulminating course. This requires a rapid diagnostic evaluation to provide an immediate basis for making therapeutic decisions that will critically affect the prognosis.

Anatomy of the Thoracic Aorta

The aorta begins at the aortic valve and extends distally to the aortic bifurcation. The aorta is divided into four parts:

- Ascending aorta
- Aortic arch
- Supradiaphragmatic descending thoracic aorta
- Infradiaphragmatic descending abdominal aorta

The **ascending aorta** originates in the supravalvular part of the left ventricle. The annulus of the ascending aorta bears the aortic valve. The initial portion of the ascending aorta, the aortic root, forms a bulbous expansion (the aortic bulb) that bears three dilatations corresponding to the cusps of the aortic valve. The left and right coronary sinuses (of Valsalva) give origin to the left and right coronary arteries, respectively, and are accompanied by a third, acoronary, sinus. The aortic bulb tapers at the sinotubular junction to become continuous with the ascending aorta.

The aortic arch runs upward, backward, and to the left, passing over the right pulmonary artery and left main bronchus. The aortic arch gives off the supra-aortic arteries. This region should be closely scrutinized for any variants in the origins of the arch vessels.

The **descending thoracic aorta** lies just to the left of the vertebral column and descends to the aortic hiatus of the diaphragm. The descending aorta gives off the bronchial arteries, spinal arteries, and smaller arterial branches. The descending aorta may show considerable elongation and tortuosity, especially in older individuals, but usually this does not cause clinical complaints. The descending aorta is smaller in diameter than the ascending aorta and tapers only slightly in its course. The part below the aortic hiatus is called the **abdominal aorta**.

Congenital Anomalies

Right Descending Aorta

A right descending aorta in the absence of visceral transposition is a very rare developmental anomaly. It involves a mirror-image reversal of anatomy in which the brachiocephalic trunk supplies the left side, followed in turn by the right subclavian artery and right carotid artery. A very high percentage of patients have a coexisting cardiac anomaly, usually a tetralogy of Fallot or a truncus arteriosus. The most common clinical manifestation of a right descending aortic arch is dyspnea due to tracheal compression by the left subclavian artery, which passes behind the trachea and esophagus.

Double Aortic Arch

In a double aortic arch, the ascending aorta is divided into two parts that run to the right and left of the esophagus and trachea. In most cases this division occurs just anterior to the trachea. The two limbs of the aortic arch pass around the trachea and reunite behind it and the esophagus, or rarely in front of the esophagus, to form a central or left-sided descending aorta. Hence this anomaly is also called the "vascular ring." Normally, one of the aortic arches is small or rudimentary (**Fig. 13.1**). A double aortic limbs is not usually associated with other cardiovascular anomalies. In most cases, however, it produces early clinical manifestations because the ring around the trachea causes extrinsic tracheomalacia and dyspnea.[1]

Aortic Arch Anomalies

A far posterior origin of the left subclavian artery may signify a coarctation or other aortic anomaly. Among the many possible variants in vessel origins, the aberrant right subclavian artery has the greatest clinical importance (prevalence of 0.5–1 % in the general population). It arises behind and below the apex of the aortic arch and runs to the right, passing behind the trachea and esophagus. This vessel may cause dysphagia because of its retroesophageal course (**Fig. 13.2**).

Congenital hypoplasia of the aortic arch, known also as Williams–Beuren syndrome, is very rare.

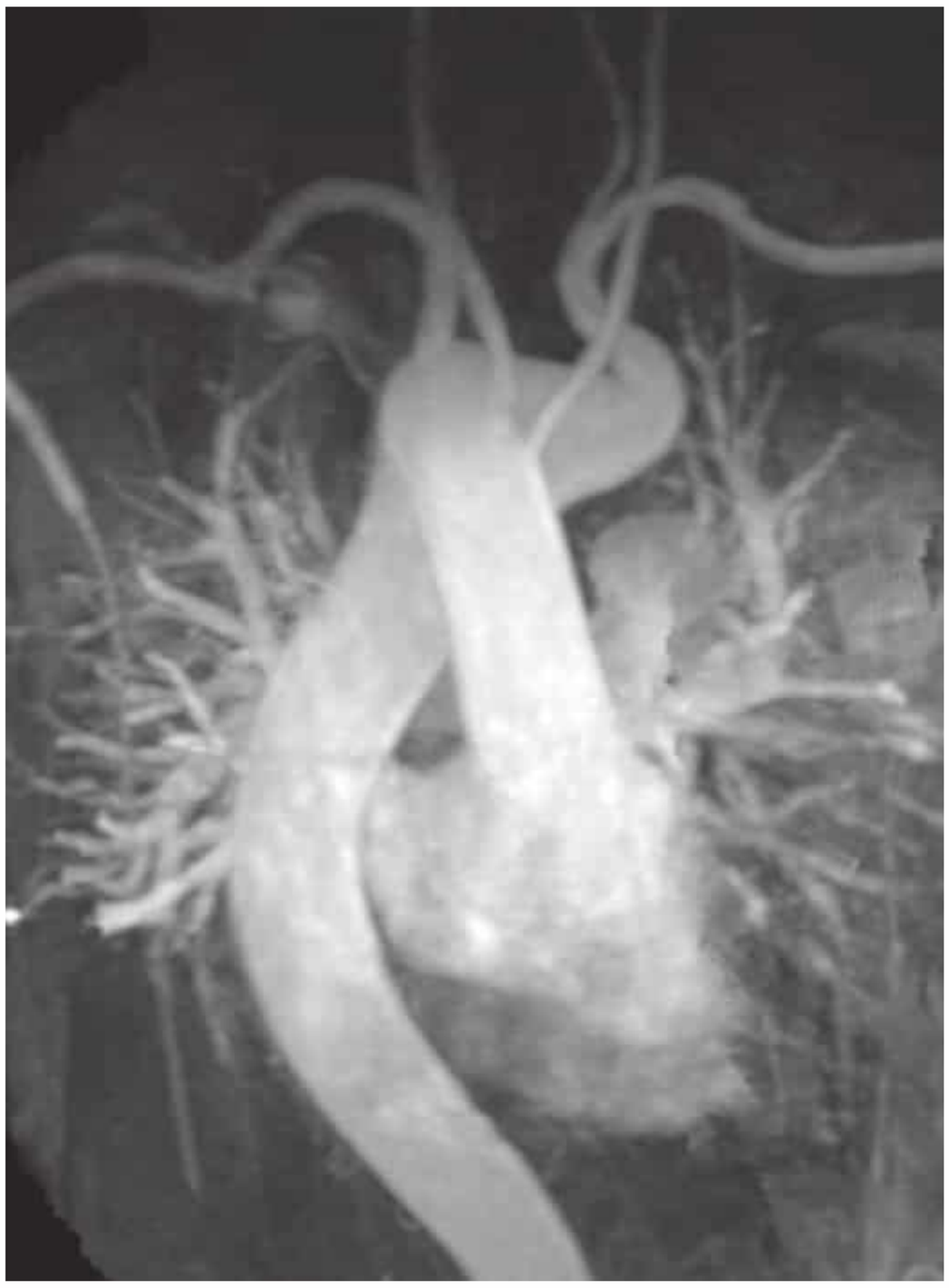

Fig. 13.1 Aortic arch anomaly in a 45-year-old man with a right-sided aortic arch and rudimentary left aortic arch, a right descending aorta, and separate origins of all supra-aortic vessels (sequence: left common carotid artery, right common carotid artery, right subclavian artery, and left subclavian artery).

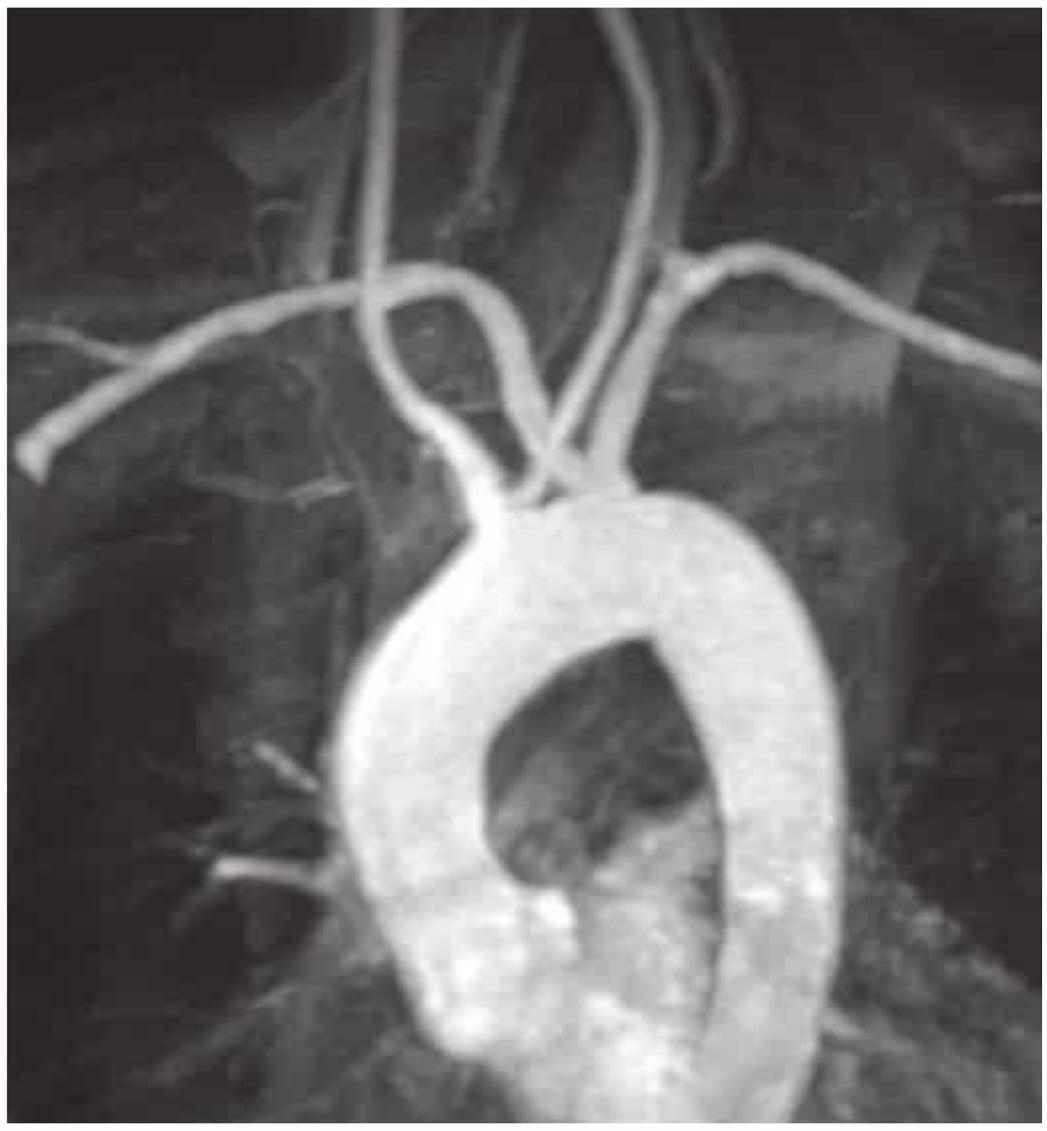

Fig. 13.2 Aberrant right subclavian artery, which is the last vessel arising from the aortic arch. All the supra-aortic vessels arise separately from the aortic arch.

Coarctation of the Aorta

Coarctation is the most common congenital anomaly of the thoracic aorta. It has an incidence of ~4.1 in 10000 newborns and is present in ~7%of patients with congenital heart disease. Preductal and postductal forms are distinguished. The preductal form, which is symptomatic in the neonatal period, is associated with prestenotic hypoplasia of the transverse aortic arch in ~80%of cases (**Fig. 13.3**). Only 10–16%of patients with the postductal form become symptomatic during infancy. As a rule, these patients are free of subjective complaints in childhood. They go on to develop early arterial hypertension, however, and this finding plus absent or diminished pulses in the lower half of the body suggest the correct diagnosis[1] (see Aorta, p. 28).

Both multislice-CT and MRI are useful in the morphological assessment of coarctation. MRI additionally provides functional information on the condition and is therefore preferred in younger patients. Besides evaluating the length and degree of stenosis, it is necessary to determine the pre- and poststenotic diameters, the minimum diameter at the level of the stenosis, and the relationship of the stenosis to the ligamentum arteriosum. The collateral vessels in the chest wall should also be evaluated, as the degree of collateralization correlates with the hemodynamic significance of the stenosis (see **Fig. 1.28**). Phase-contrast flow measurements can also be performed just distal to the coarctation and at the level of the diaphragm to determine the flow volume through chest-wall collaterals. Determination of the maximum flow velocity just distal to the stenosis permits an estimation of the systolic pressure gradient. MRI can also be used for the morphological and functional evaluation of re-stenosis following open surgical repair or transluminal intervention (**Fig. 13.4**).

Pseudocoarctation has to be differentiated from coarctation of the aorta. The former is caused by a kink in the aorta at the level of the ligamentum arteriosum. Examination in most of these cases will not indicate significant pressure gradients or a poststenotic increase in flow velocities.

Acquired Aortic Diseases

Degenerative Aortic Diseases

Aortic Sclerosis

Atherosclerotic wall changes occur predominantly in the descending aorta and aortic arch. Atherosclerotic plaques are found less commonly in the ascending aorta but may be a source of cerebral and peripheral emboli. The initial step in the pathogenesis of aortic sclerosis is atherosclerotic thickening of the aortic wall. With the progression of sclerosis, circumscribed plaques form that may bear thrombotic deposits or mobile components that pose a significant embolic risk (**Figs. 13.5, 13.6**).

Aortic sclerosis is classified into five grades of severity:

- Grade I: minimal intimal thickening <4 mm
- Grade II: pronounced intimal thickening >4 mm

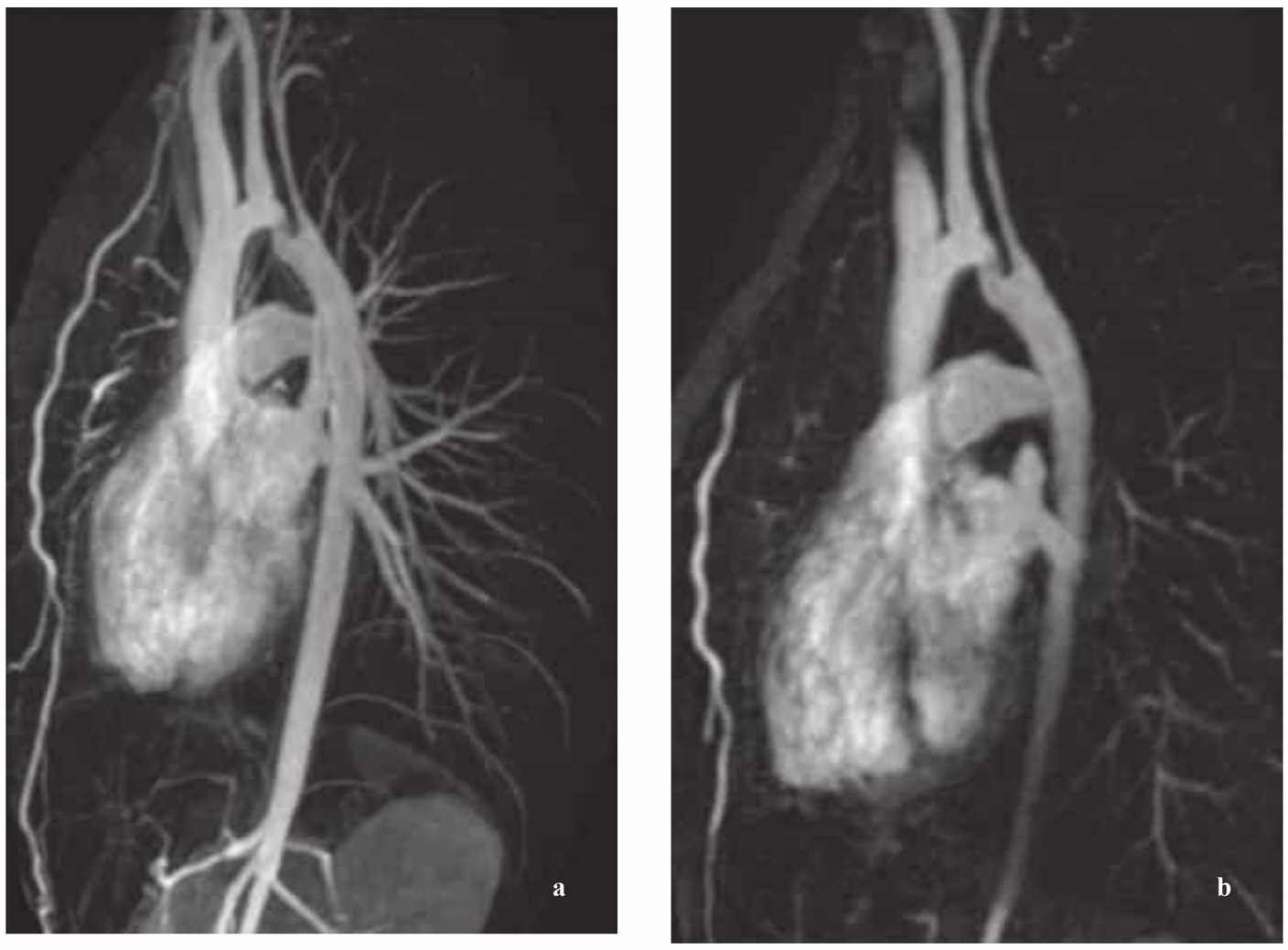

Fig. 13.3 a, b A 12-year-old girl with preductal coarctation of the aorta after PTA. Hypoplastic posterior aortic arch segment and hypoplastic left subclavian artery.
a MIP reconstruction of contrast-enhanced MRA.
b MPR of the same dataset.

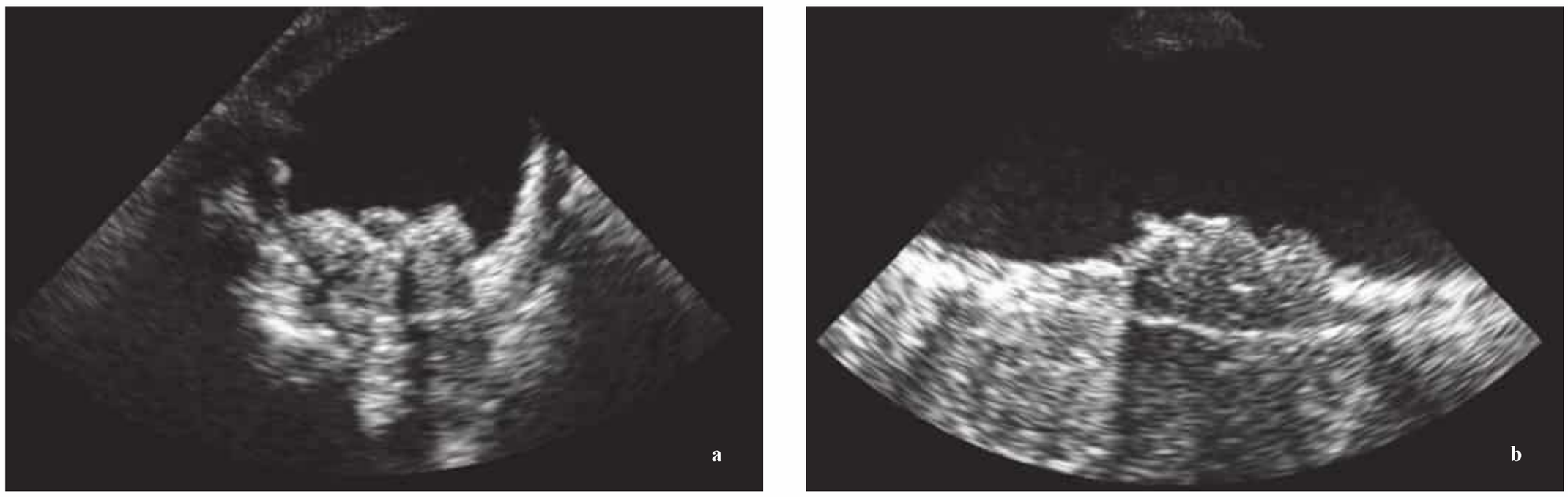

Fig. 13.5 a, b Detection of a complicated plaque with mobile components (grade V) projecting far into the aortic lumen.

a Short-axis TEE view of the midthoracic descending aorta at 35 cm from the incisor teeth.
b Corresponding long-axis TEE view.

- Grade III: circumscribed atheroma without intraluminal protrusion
- Grade IV: atheroma with intraluminal protrusion
- Grade V: plaque formation with fissures and mobile material (intima or thrombotic deposits)

Aortic Aneurysm

The normal diameter of the aorta varies with the site of the measurement and the age and sex of the patient. Normal values are 2.3–3 cm for the aortic annulus, 3–3.7 cm for the sinus of Valsalva, and 2.5–3.5 cm for the proximal ascending aorta.[2,3] The normal wall thickness is less than 4 mm. The normal values in women are ~10 % lower than in men. Besides sex-specific differences, the aortic diameter also depends on physical activity. Persons engaged in strenuous physical labor have larger aortic diameters than more sedentary individuals.[2] Aortic diameters should be stated in relation to body surface area. The normal range of values for the ascending aorta is 1.4–2.1 cm/m^2 body surface area. The normal range for the descending aorta is 1.0–1.6 cm/m^2 body surface area.[2,3]

With aging, the aortic tube undergoes a continuous, physiological enlargement of ~1–2 mm over a 10-year period. If the aortic diameter is larger than normal (>3.5 cm for the ascending aorta, >3 cm for the descending aorta), it is initially described as aortic ectasia. Dilatation past 4 cm is classified as an aortic aneurysm.[2–4]

A true aneurysm involves a fusiform (spindle-shaped) or saccular (pouch-shaped) dilatation of all the aortic wall layers, usually as a result of aortic sclerosis. Pseudoaneurysms have at least partially penetrated the vessel wall and are often stabilized only by a fibrous capsule. Pseudoaneurysms frequently have a saccular configuration.[4] They may have a traumatic, infectious, or iatrogenic cause or may develop as a complication of penetrating aortic ulcer. Approximately one-third of aortic aneurysms are located in the thoracic aorta, the rest in the abdominal aorta.[5] Risk factors for aneurysm formation include the classic atherosclerotic risk factors, especially arterial hypertension, congenital disorders of connective-tissue metabolism

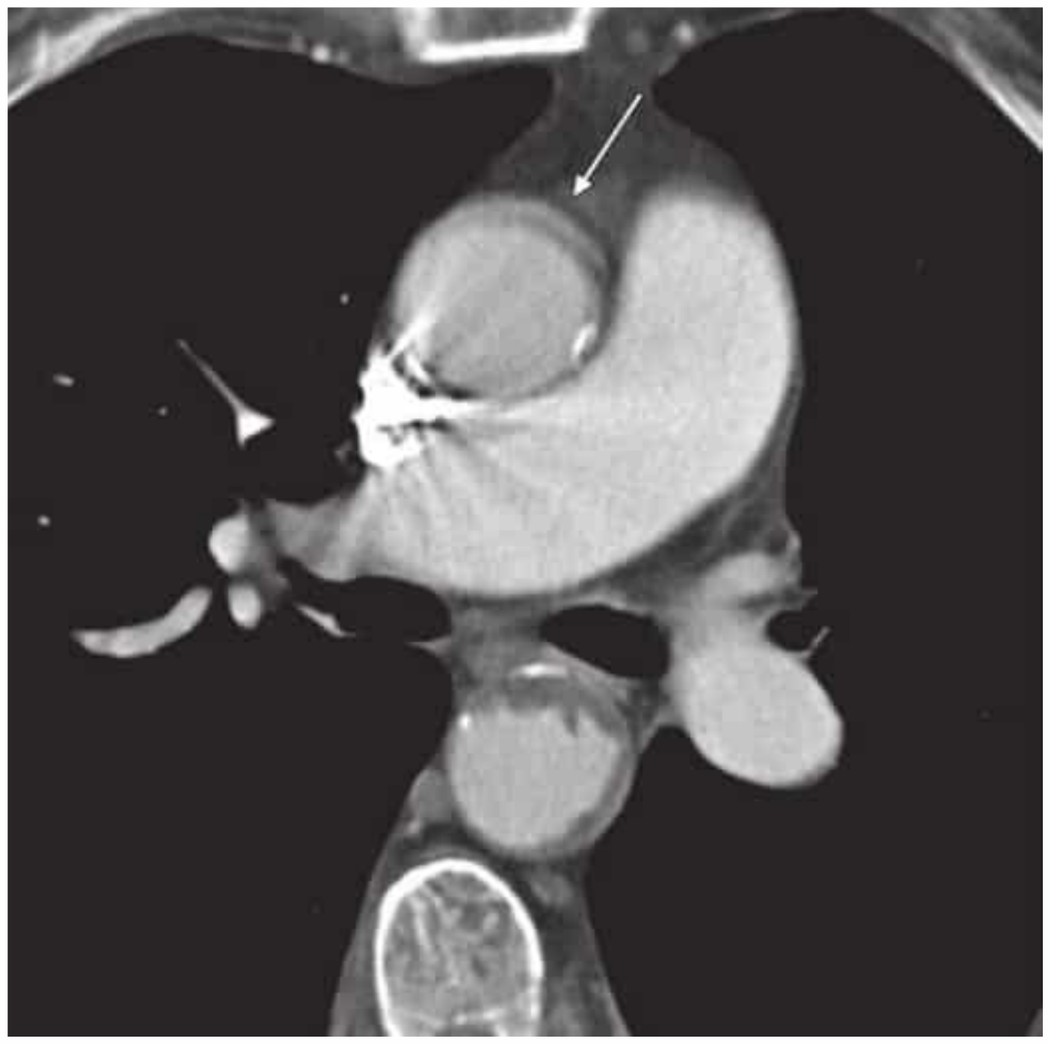

Fig. 13.6 Contrast-enhanced CT at the level of the main pulmonary trunk demonstrates a calcified plaque with thrombotic deposits in the descending thoracic aorta due to severe atherosclerosis. A pulsation artifact in the ascending aorta mimics an intimal flap (arrow).

in Marfan syndrome or Ehlers–Danlos syndrome, and a bicuspid aortic valve.

As a rule, an ascending aortic aneurysm should be treated surgically if its maximum diameter exceeds 5.5 cm or if it enlarges by more than 1 cm per year. If associated changes are present (e.g., severe aortic regurgitation with left ventricular dilatation), it may be appropriate to proceed with surgical replacement of the ascending aorta for aneurysms smaller than 5.5 cm.[2,3] Prophylactic aortic replacement is generally recommended earlier in patients with Marfan syndrome, usually when the diameter of the ascending aorta exceeds 4.5 cm.[2,3] An aneurysm of the descending aorta requires greater operative

trauma, and so surgical treatment is withheld until the aneurysm exceeds 6.5 cm in maximum diameter or enlarges by more than 1 cm per year. Endovascular aortic stent grafting provides a new, minimally invasive alternative to open surgery in the management of these cases.[6] Aneurysms smaller than the critical diameter should be followed at regular intervals. The follow-up interval depends on the size of the aneurysm. Aneurysms >5 cm should be followed at relatively close intervals, such as every 3 months.[3] If no size change is noted, the follow-up interval may be gradually increased. In all follow-up examinations, the maximum diameter of the aneurysm should be measured at the same site as in previous examinations.

Essential Point

- Aortic ectasia: maximum aortic diameter >3.5 cm (ascending aorta) or >3 cm (descending aorta) and <4 cm.
- Aortic aneurysm: aortic diameter >4 cm.
- Indications for surgical treatment: ascending aorta >5.5 cm (>4.5 cm in Marfan patients), descending aorta >6.5 cm.
- Follow-up intervals depend on maximum aneurysm diameter.

Imaging of Aortic Aneurysms

Aortic aneurysms often remain clinically silent for many years and are detected fortuitously on chest radiographs (**Fig. 13.7**). Aneurysms of the aortic bulb and proximal ascending aorta can be imaged noninvasively by transthoracic echocardiography. The parasternal long-axis scan can demonstrate the aortic valve and the first 2–4 cm of the ascending aorta and is particularly useful for follow-up examinations (e.g., of the aortic bulb in patients with Marfan syndrome) as it is a rapid, cost-effective procedure that does not require any contrast agent or involve any radiation exposure (**Fig. 13.8**).

Transesophageal echocardiography (TEE) can demonstrate ~5–7 cm of the proximal ascending aorta (**Fig. 13.9**). Generally it can define the descending aorta from the distal aortic arch (origin of the left subclavian artery) to the thoracoabdominal junction (**Fig. 13.10**). The distal ascending aorta and the aortic arch itself are obscured by the overlying left main bronchus. This portion of the aorta constitutes a "blind spot" in TEE. Often this procedure is inaccurate in determining maximum aortic diameter because of aortic elongation, which results in tangential sections that overestimate the maximum diameter. CT can image the entire aorta in a matter of seconds. Administration of IV contrast medium should be used in patients evaluated for aortic disease, as it is the only way to provide an adequate assessment of aortic wall pathology (**Fig. 13.11**). A current serum creatinine should be obtained before the examination owing to the nephrotoxicity of CT contrast medium.

It is good practice to image the entire aorta from the annulus to the iliac vessels because of the frequent presence of multilevel disease. Examination of the entire aorta is also important for treatment planning (e.g., identifying the iliac axis as an access site for endovascular aortic stent grafting). Multislice CT technology has made it possible to examine the entire aorta during a single breath hold.

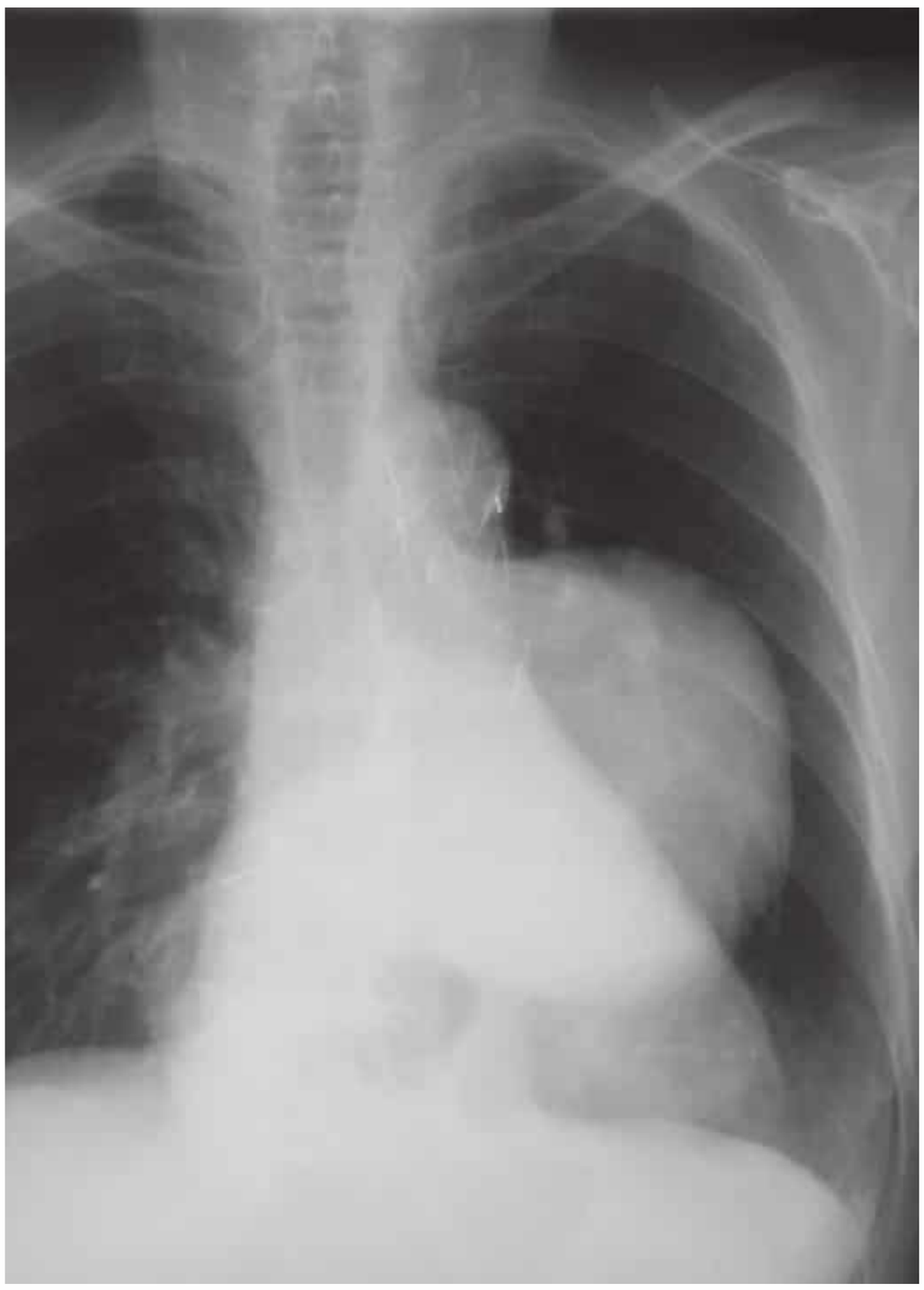

Fig. 13.7 PA chest radiograph of a large thoracic aortic aneurysm, which was successfully managed by the previous insertion of an endovascular stent graft.

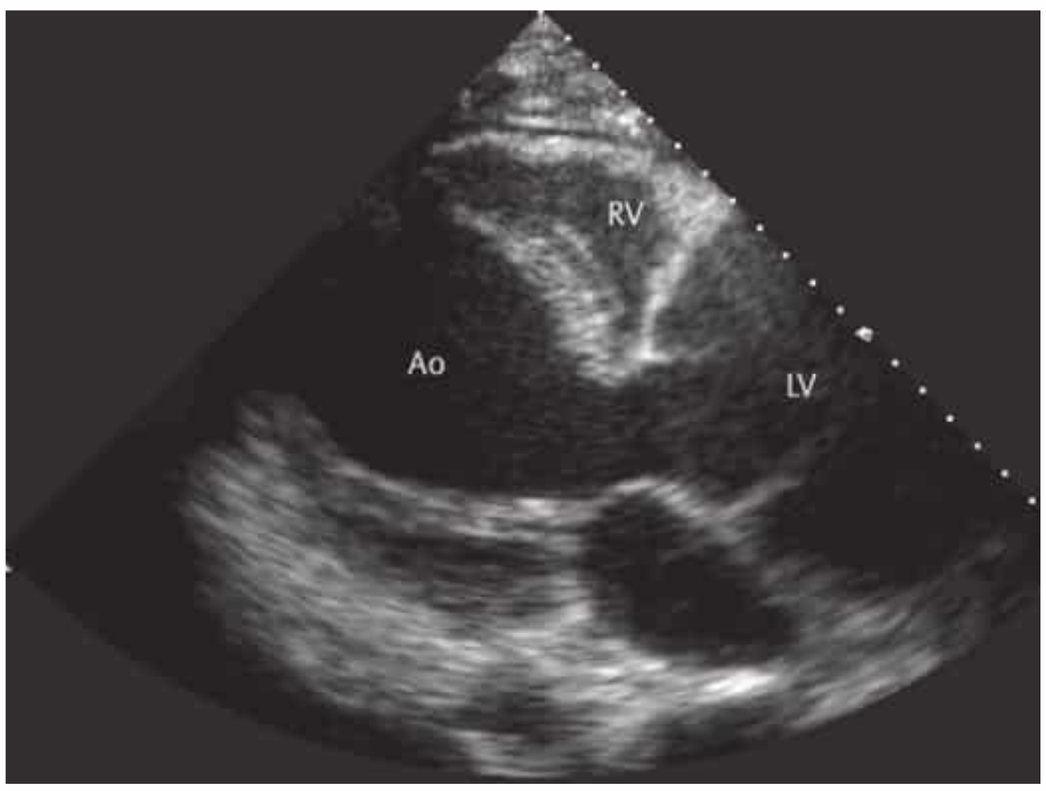

Fig. 13.8 TEE. Parasternal long-axis view shows a conspicuous aneurysm of the aortic bulb in a patient with Marfan syndrome.

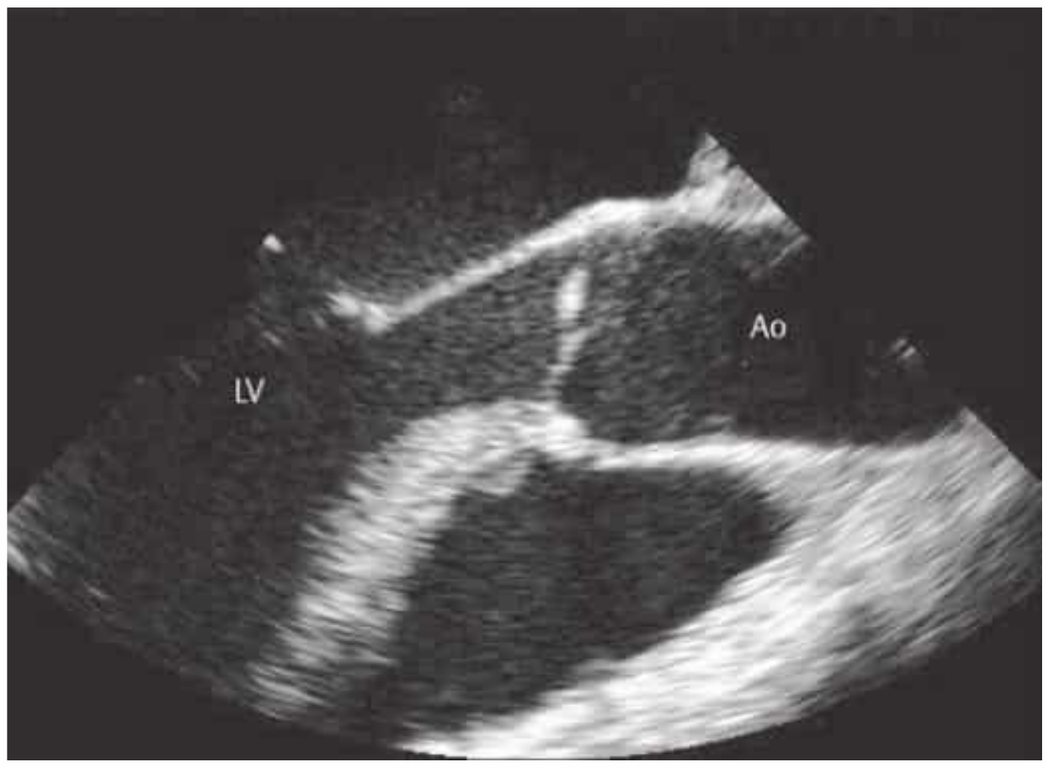

Fig. 13.9 TEE long-axis view of a normal ascending aorta.

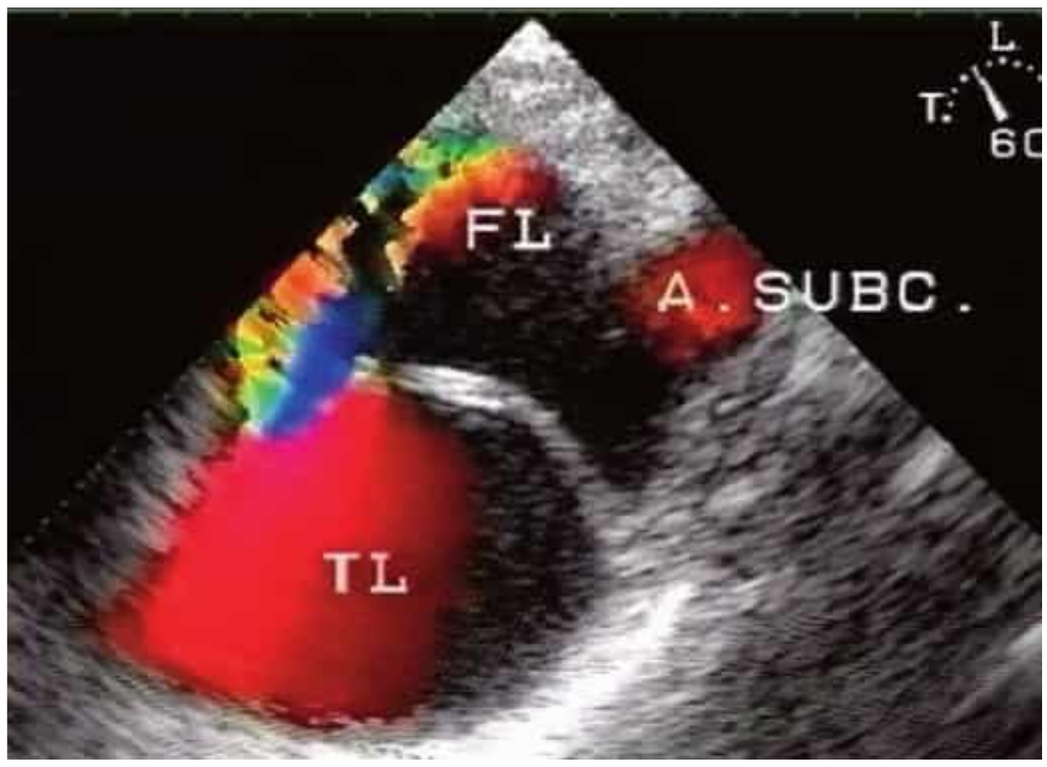

Fig. 13.10 TEE image of a type B aortic dissection demonstrates the proximal intimal tear near the origin of the left subclavian artery.

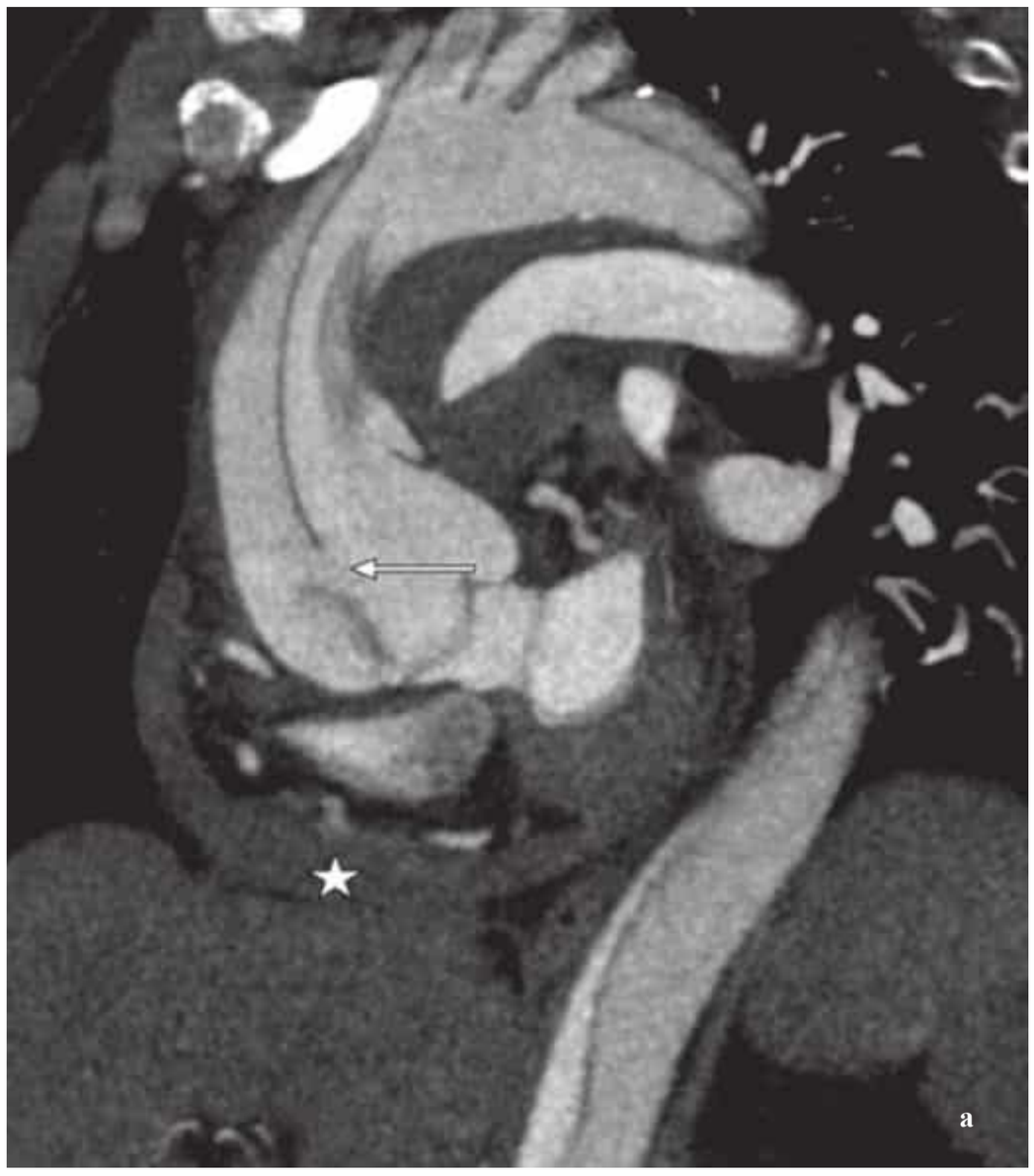

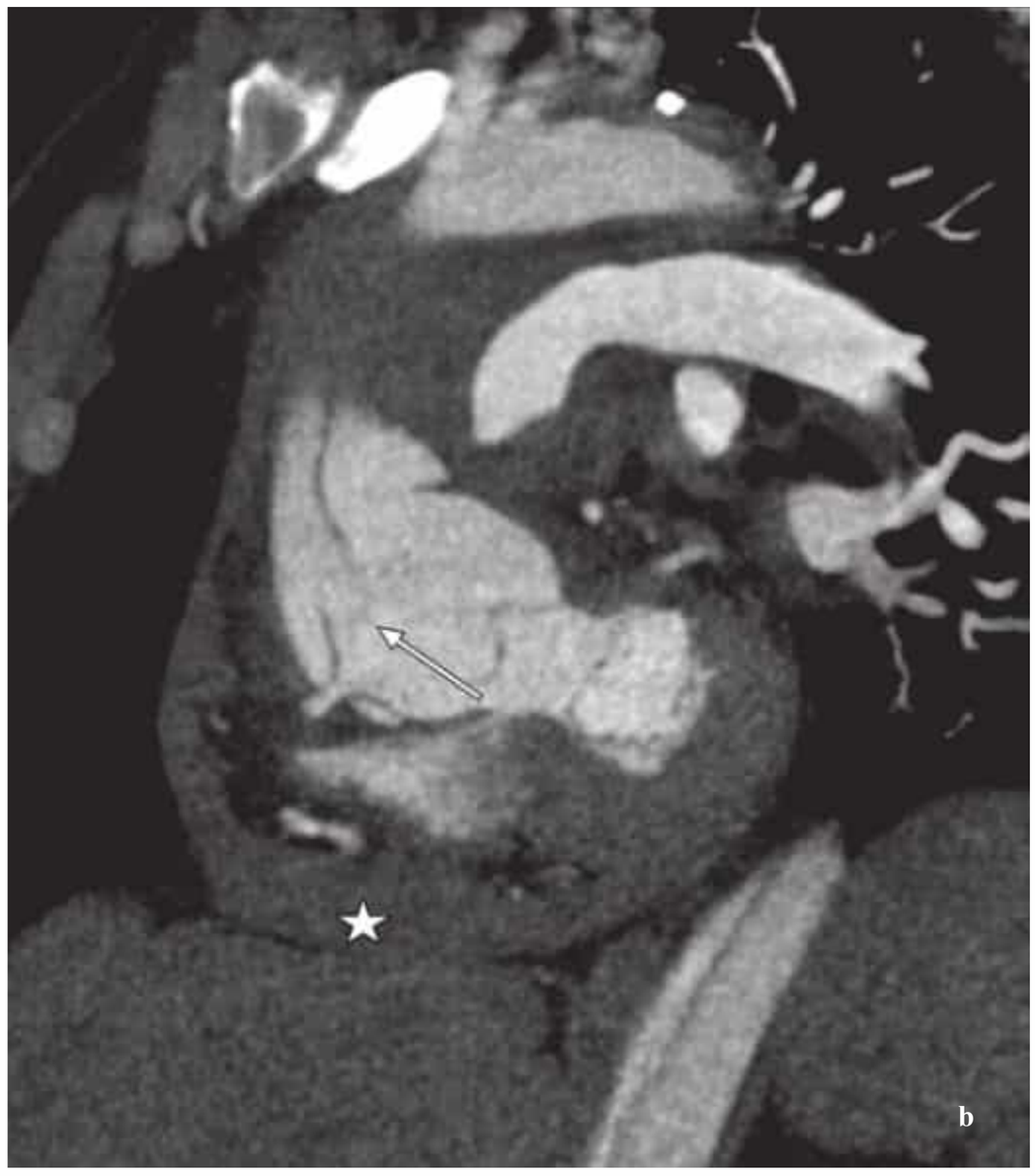

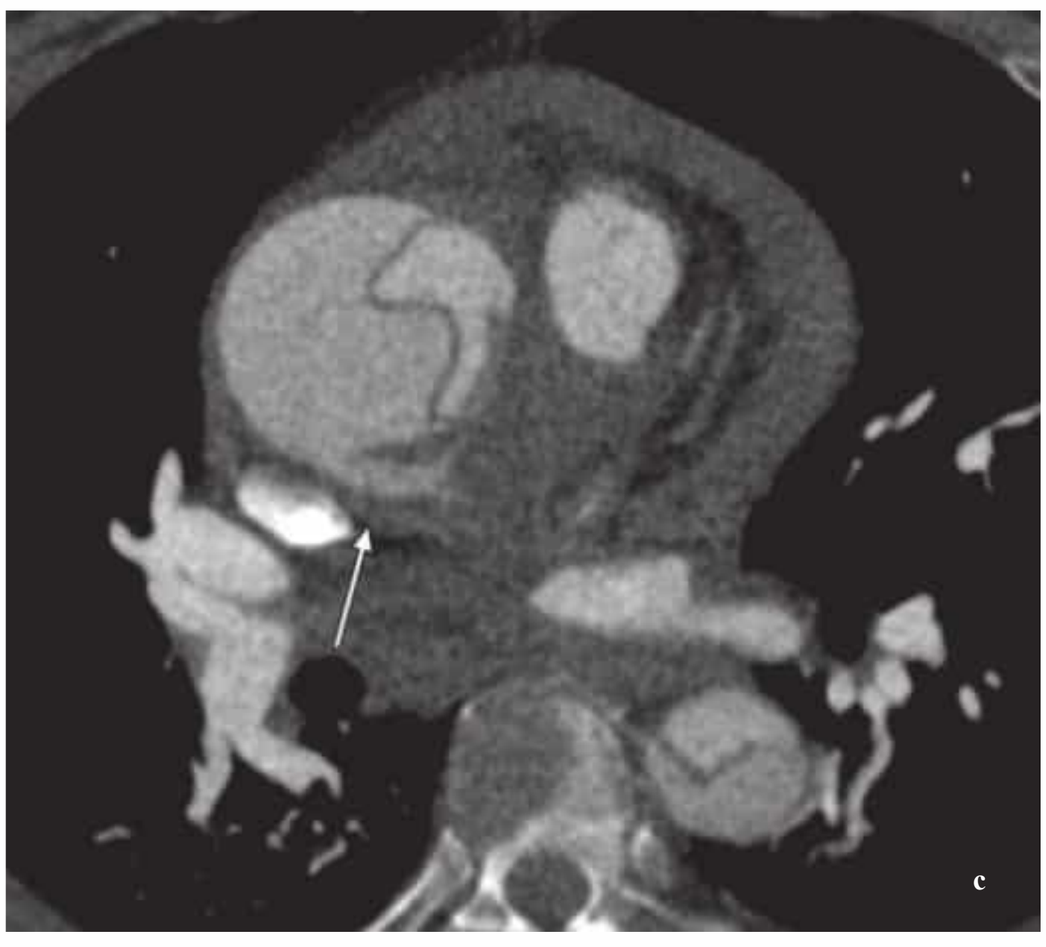

Fig. 13.11 a–c Contrast-enhanced ECG-gated multislice CT in a patient with an acute type A dissection, rupture of the aorta, and pericardial effusion. The patient survived emergency surgery despite the aortic rupture.

a, b Multiplanar reformatting from the 3D dataset show the entry (arrow), retrograde extension of the dissection down to the origin of the right coronary artery, and a pericardial effusion (star).

c Rupture site in the ascending aorta (arrow) with subsequent bleeding into the mediastinum and pericardium.

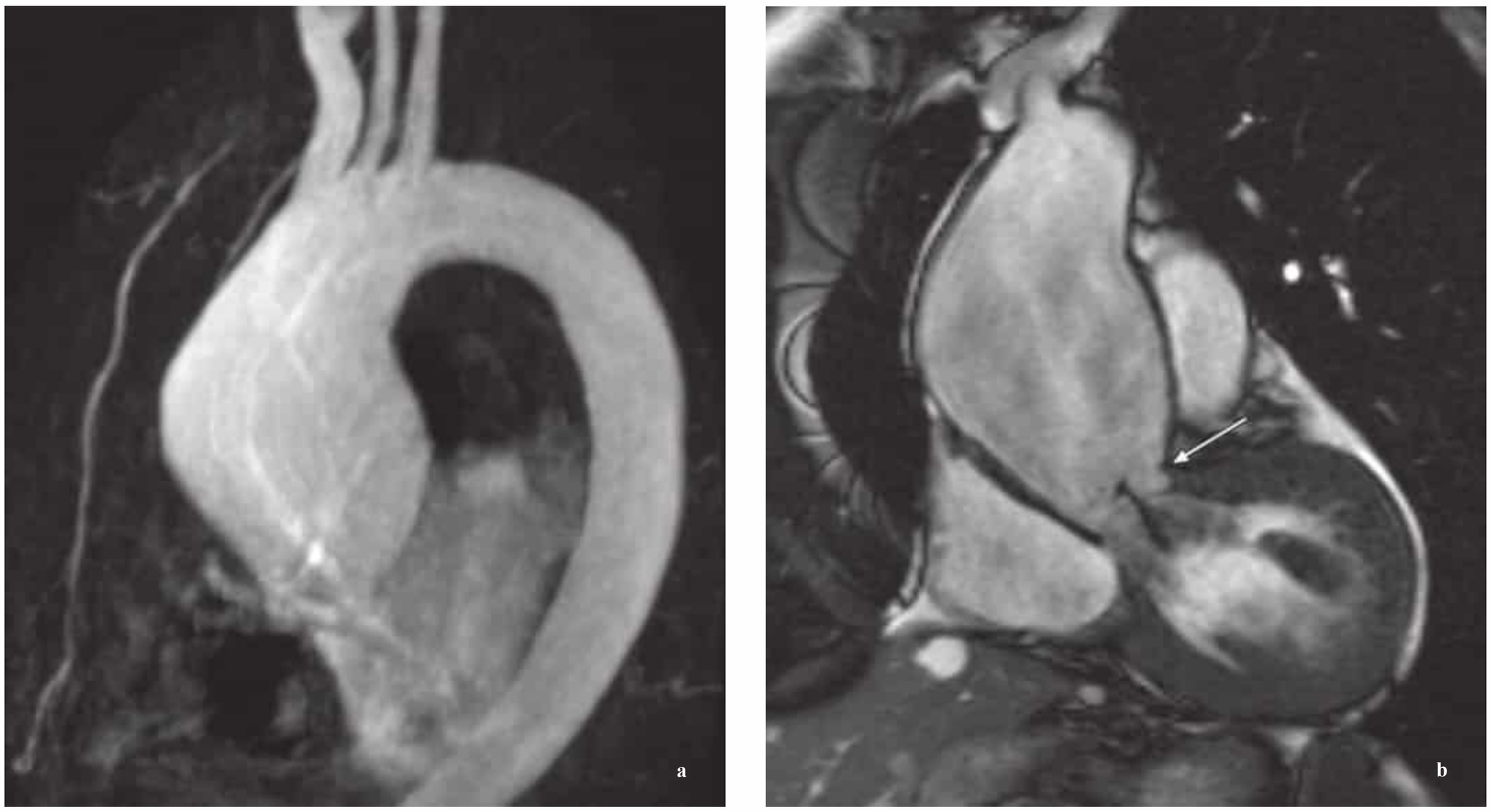

Fig. 13.12 a, b Aneurysm of the ascending aorta with consequent enlargement of the aortic annulus and aortic regurgitation.

a MIP of contrast-enhanced 3D MRA.
b Cine sequence demonstrates the regurgitant jet (arrow).

MRI makes it possible to examine the aorta noninvasively without contrast medium or radiation exposure. As in CT, all portions of the aorta should be evaluated. Accurate caliber measurements can be performed on black-blood images. One disadvantage of black-blood imaging is its susceptibility to slow-flow artifacts, which can sometimes mimic thrombus and intimal flaps. For this reason, a bright-blood sequence (e.g., SSFP sequence) should be added so that an accurate assessment can be made (**Fig. 13.12**). Contrast-enhanced MRA permits three-dimensional visualization of the aorta and has almost completely replaced conventional angiography in aortic investigations. It should be noted, however, that MRA is a luminographic technique and, as such, can image only the perfused lumen; it cannot evaluate the aortic wall or mural thrombosis. For this reason, MRA should always be performed in conjunction with black- or bright-blood sequences.

When the diameter of the aorta is enlarged, the maximum diameter should be measured perpendicular to the main direction of blood flow using the centerline method. This can be difficult in the presence of aortic elongation and kinking, and errors may result owing to measurements made in tangential scans. The slow blood-flow velocities in the aneurysm lumen may lead to spontaneous echo contrast as well as mural thrombus formation. The presence of spontaneous echo contrast and thrombi constitutes a significant risk factor for peripheral embolism. Luminographic techniques alone (conventional angiography and MRA) cannot accurately assess the maximum aortic diameter when mural thrombus is present. Often in the aorta it is difficult to distinguish between mural thrombus and intramural hematoma. This can be facilitated by evaluating wall thickening in relation to the aortic intima, which is frequently

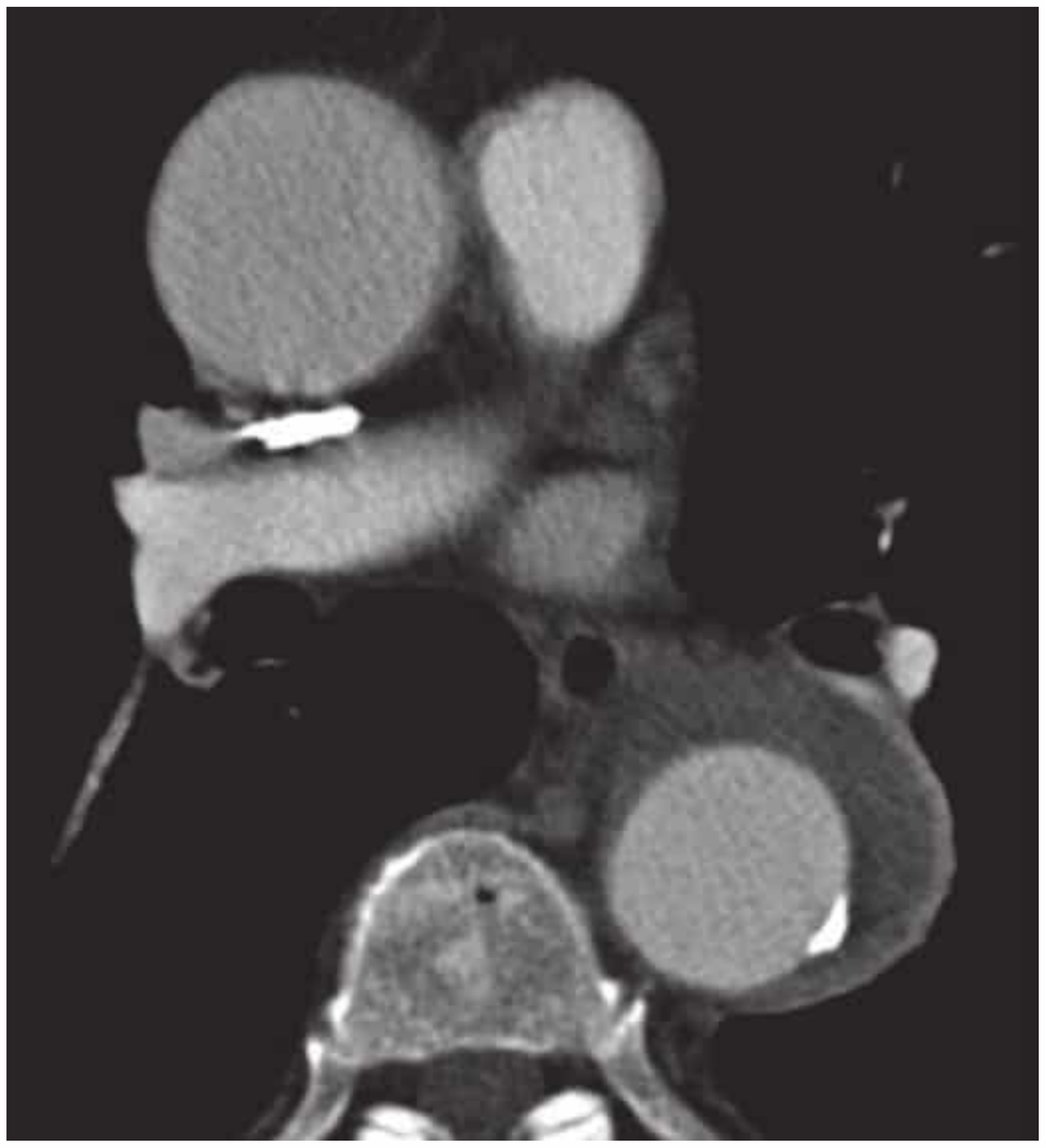

Fig. 13.13 Contrast-enhanced CT in a patient with an intramural hematoma of the descending aorta. The intramural hemorrhage has caused luminal displacement of the calcified intima.

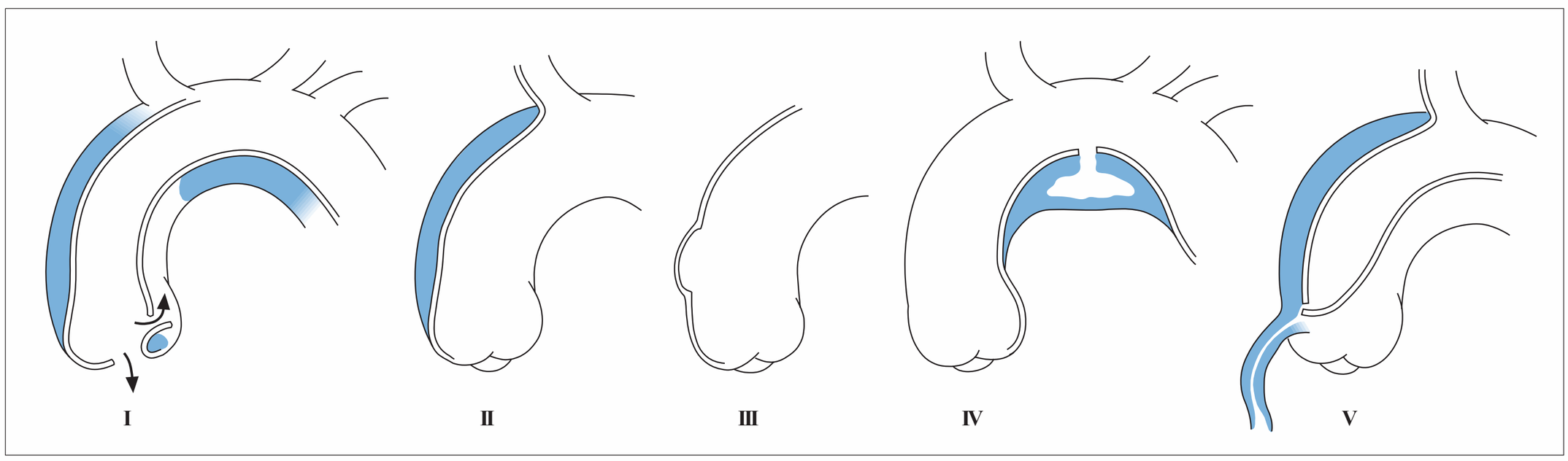

Fig. 13.14 Schematic drawing of the Svensson classification of the acute aortic syndrome.

calcified or thickened in these patients. With mural thrombus, the calcified intima is located on the side opposite the aortic lumen. With intramural hematoma, on the other hand, bleeding into the media shifts the calcified intima toward the vessel lumen (luminal displacement of intimal calcium, **Fig. 13.13**).

Essential Point

- Mural thrombus and intramural hematoma can often be differentiated by evaluating the relationship of the calcified aortic intima to the lumen (luminal displacement of intimal calcium).
- Tangential scans may lead to incorrect measurement of maximum aortic diameter.
- The "blind spot" in TEE precludes evaluation of the aortic arch.
- Respiratory or triggering artifacts in CT scans can mimic an aortic dissection owing to the pulsations of the aortic wall. Therefore, ECG gating should be used with modern multislice CT scanners.
- Luminographic techniques (conventional angiography and MRA) underestimate the maximum aortic diameter in the presence of mural thrombus.

Acute Aortic Syndrome

Chest pain is frequently caused by acute diseases of the aorta. It is estimated that one patient in 80–300 admitted to the ER with suspicion of an acute coronary symptom has an acute aortic syndrome.[5] In a list of conditions that may cause chest pain, acute aortic syndrome is the most frequent acutely life-threatening condition after acute coronary syndrome and before pulmonary embolism.[4,5]

The previous decade has witnessed important advances in the diagnosis and management of these diseases. A new concept in this regard is the acute aortic syndrome, which is enabling physicians to apply an increasingly consistent diagnostic and therapeutic approach. With optimum management, an 80 %survival rate can be achieved in patients with acute aortic syndrome. Even so, this syndrome still has up to an 80 %mortality rate owing to the lack of an accurate diagnosis in vivo.[5] Consequently, an aortic syndrome should always be considered in patients who present with acute chest pain following the exclusion of acute myocardial ischemia.

The clinical presentation of acute aortic syndrome is based on several etiologically diverse, acutely life-threatening diseases of the thoracic aorta. Besides a classic aortic dissection with the formation of a true and false lumen (class I dissection), the **Svensson classification**[7] recognizes intramural hematoma (class 2 dissection, IMH), circumscribed dissection (class 3 dissection), penetrating aortic ulcer (class 4 dissection, PAU), and a traumatic/iatrogenic dissection (class 5 dissection) as pathological variants or precursors of a classic aortic dissection (**Table 13.1**, **Fig. 13.14**).

While the Svensson classification is based on pathoanatomical changes, the **Stanford classification** describes the location and extent of the dissection (**Fig. 13.15**). The DeBakey classification, which distinguishes three types, is less widely used today. In the Stanford classification, any involvement of the ascending aorta is classified as a type A dissection.[8] Generally, a type A dissection will spread distally along the descending aorta, often reaching the aortic bifurcation (**Fig. 13.11**).

A type B dissection in the Stanford classification is confined to the descending aorta. This classification has major clinical and prognostic implications, because every **type A dissection** is at high risk for acute rupture and should therefore be referred for emergency surgical replacement of the ascending aorta.[4] A **type B dissection**, on the other hand, can usually be managed with rigorous antihypertensive therapy, reserving surgery for the treatment of complications.[4] Endovascular aortic stent grafting is also available as a new option for patients with dissections confined to the descending aorta.[6]

Table 13.1 Svensson classification of aortic dissection[7] (see **Fig. 13.14**)

Class 1 dissection	Classic aortic dissection with true and false lumina
Class 2 dissection	Intramural hematoma (IMH)
Class 3 dissection	Circumscribed dissection
Class 4 dissection	Penetrating aortic ulcer (PAU)
Class 5 dissection	Iatrogenic/traumatic transection/dissection

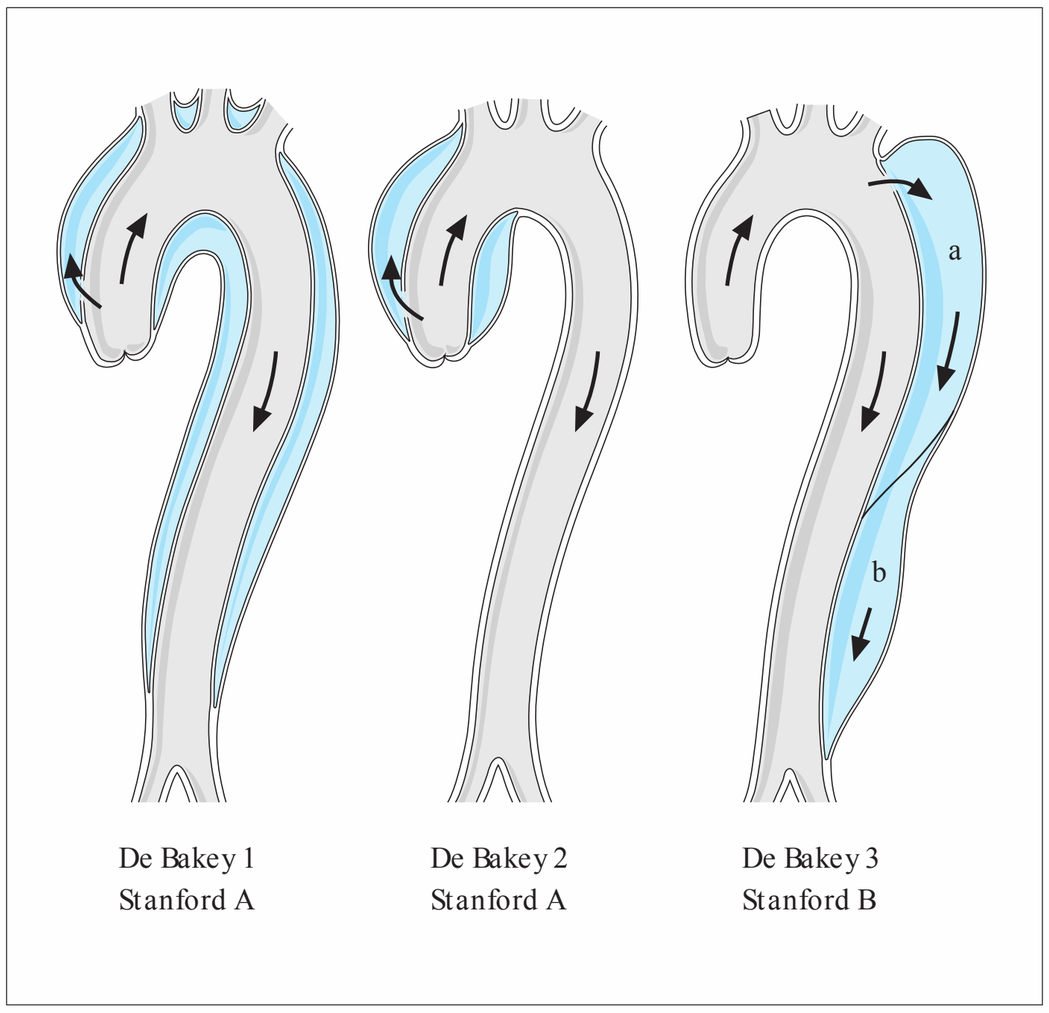

Fig. 13.15 Schematic drawing of the Stanford and DeBakey classification of aortic dissection.

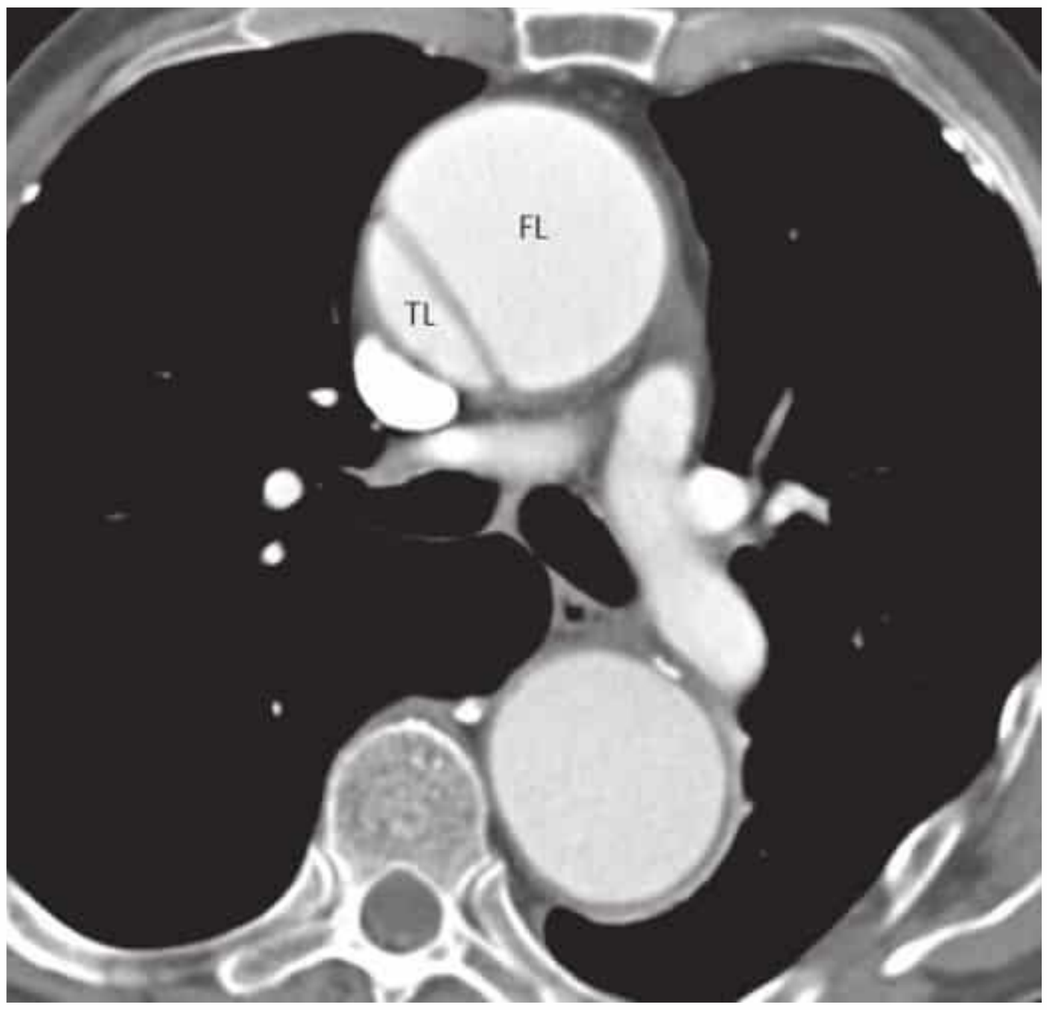

Fig. 13.16 Contrast-enhanced CT of an aortic dissection confined to the ascending aorta (Stanford type A or DeBakey type 2). Dissection is absent in the descending aorta.

Aortic Dissection (Svensson Class 1 Dissection)

Classic aortic dissection is the most common and most malignant variant of acute aortic syndrome.[5] It involves a **longitudinal separation** of the aortic wall layers with the **formation of a false lumen** between the intima and adventitia. Acute aortic dissection has a reported incidence of 5–15 per 100 000 population per year, or 10–20 cases per 1 million population.[4,9] Except in Marfan syndrome, the peak age of occurrence is between 50 and 70 years with a 3:1 preponderance of males.[10,11]

The prime **risk factor** for aortic dissection is arterial hypertension, which is detectable in more than 75 % of patients. Congenital abnormalities of connective-tissue metabolism (Marfan or Ehlers-Danlos syndrome) and a bicuspid aortic valve also predispose to aortic dissection.[4,10,11]

Aortic dissection may result from **increased wall tension** that develops owing to enlargement of the aortic diameter.[2] The older term "dissecting aneurysm" should be avoided, however, because a dissection may develop in an aorta with a normal caliber. It has been suggested that aortic dissection may result from rupture of the vasa vasorum with the initial formation of an intramural hematoma and the secondary development of a communicating dissection. The proximal intimal tear exposes the aortic media to pulsatile blood flow, creating a false lumen that spreads distally along the vessel. The intimal tears occur at sites where the flowing blood exerts the strongest shear forces and the blood pressure variations are most pronounced. In ~65 % of cases, the proximal (entry) tear is located in the ascending aorta and will almost always culminate in a fatal rupture without immediate operative treatment (proximal aortic dissection, type A in the Stanford classification) (**Figs. 13.11, 13.16**).[5]

Essential Point

The type A aortic dissection is an absolute indication for emergency surgical treatment.

Dissections that do not involve the ascending aorta are less common. The entry tear is usually located distal to the origin of the left subclavian artery, just past the ligamentum arteriosum.[5] Most patients will survive this Stanford type B dissection without surgical intervention, and the treatment of first choice is rigorous antihypertensive therapy (**Fig. 13.17**).[4] The location of the entry tear is unimportant in the Stanford classification. The key consideration is which portion of the aorta is affected. Thus, a (retrograde) dissection of the ascending aorta with a single entry tear in the descending aorta is also classified as a type A dissection.

The classic clinical manifestation of aortic dissection is a sudden, stabbing or tearing pain in the chest or back that may migrate distally, depending on the extent of the dissection ("aortic pain").[4] The severe pain almost always evokes strong vasovagal reactions such as profuse sweating, nausea, and vomiting. Often the excruciating pain may precipitate syncope. The dissection may also be painless in up to 15 % of patients.[4,10,11]

Typical complications of classic dissections are aortic rupture with pericardial tamponade and shock (especially in type A dissections) and severe aortic regurgitation due to the disruption of aortic root geometry with acute left-sided heart failure. Up to 30 % of patients present with malperfusion syndrome leading to infarction or ischemia of the myocardium, spinal cord, mesentery, kidneys, or extremities.[4,5,10,11] Untreated, a classic aortic dissection has a mortality rate of 1–2 % per hour during the initial hours after onset of symptoms.[9]

Imaging of Aortic Dissection

Given the high acute mortality of aortic dissection, the primary goal of imaging is to establish a diagnosis as quickly as possible using all necessary means. Procedures such as TEE, CT, and MRI have assumed critical importance in the modern diagnostic imaging of aortic dissection.[3,12–17] The Task Force of the European Society of Cardiology has stated that contrast-enhanced CT and TEE are equally rewarding in the primary acute diagnosis of aortic dissection.[4] Transthoracic echocardiography (TTE) can evaluate only the initial part of the ascending aorta but not the descending aorta, and at best can provide clues to the presence of an aortic dissection. TTE cannot establish a definitive diagnosis.[17] Similarly, chest radiographs alone are of little value in many cases but may provide important clues in patients with mediastinal widening combined with clinical signs such as aortic pain and a peripheral pulse deficit.[5]

The visualization of an intimal flap or a dissection membrane confirms the diagnosis of aortic dissection (**Figs. 13.11, 13.16–13.19**). TEE and contrast-enhanced CT, like MRI, have better than 95 % accuracy in the detection of aortic dissection.[13,16,18] MRI with phase-contrast imaging can supply hemodynamic information as well as morphological data. On the other hand, the role of MRI in acute diagnosis is compromised by its limited 24-hour availability and the limitation of intensive care options in critically ill patients.[4] The dissection membrane should be imaged in at least two, preferably orthogonal, planes of section, because TEE, for example, may yield false-positive findings owing to reverberation artifacts.[4,13,16,18]

The imaging investigation of an aortic dissection should cover the entire aorta from the aortic valve to the iliac arteries.[4] TEE, unlike CT or MRI, cannot define the abdominal part of the aorta or the aortic arch. Nevertheless, TEE is useful for the diagnosis and classification of aortic dissection based on the criteria of

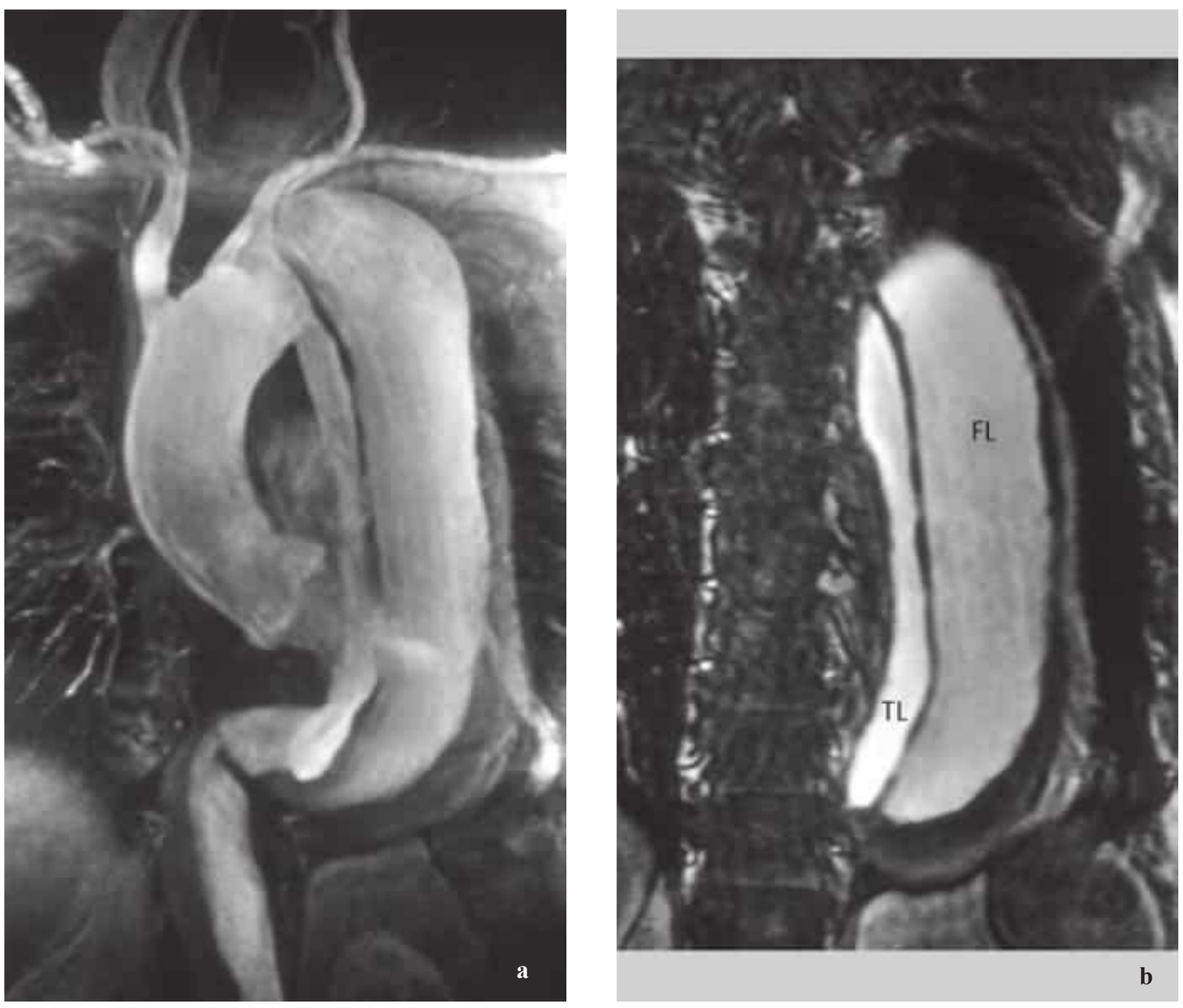

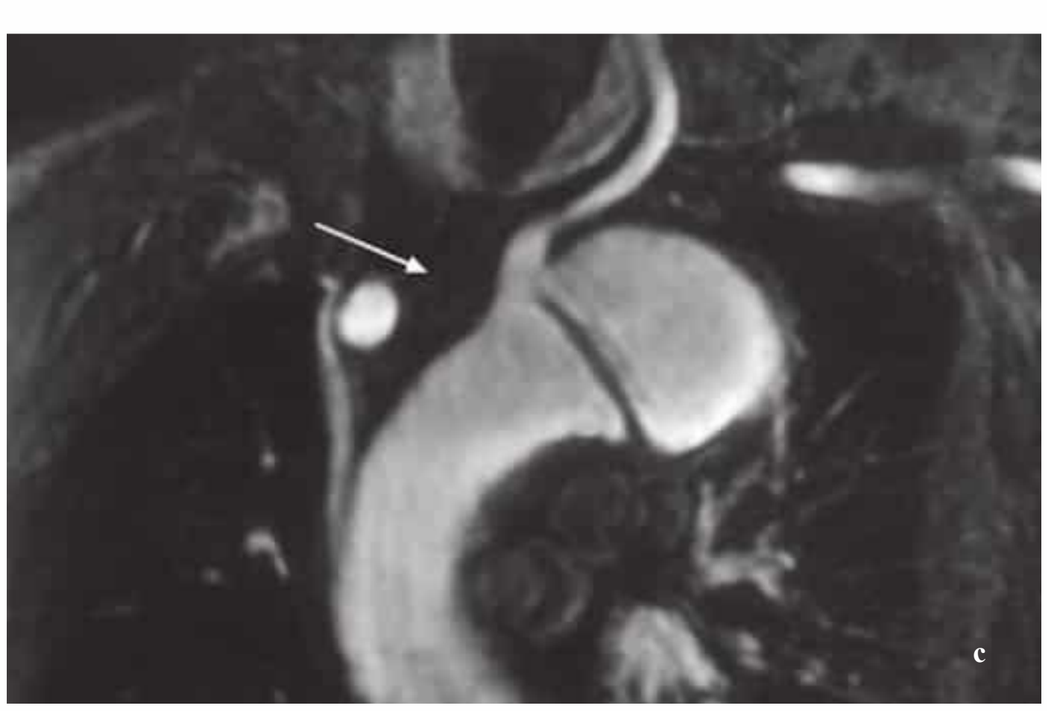

Fig. 13.17 a–c Contrast-enhanced 3D MRA in a patient with a type B aortic dissection.

a MIP view reveals extension of the dissection into the abdominal aorta.

b Multiplanar reformatting shows a large, partially thrombosed false lumen (FL) and a smaller true lumen (TL).

c MPR reveals an entry tear (arrow) just behind the origin of the left subclavian artery.

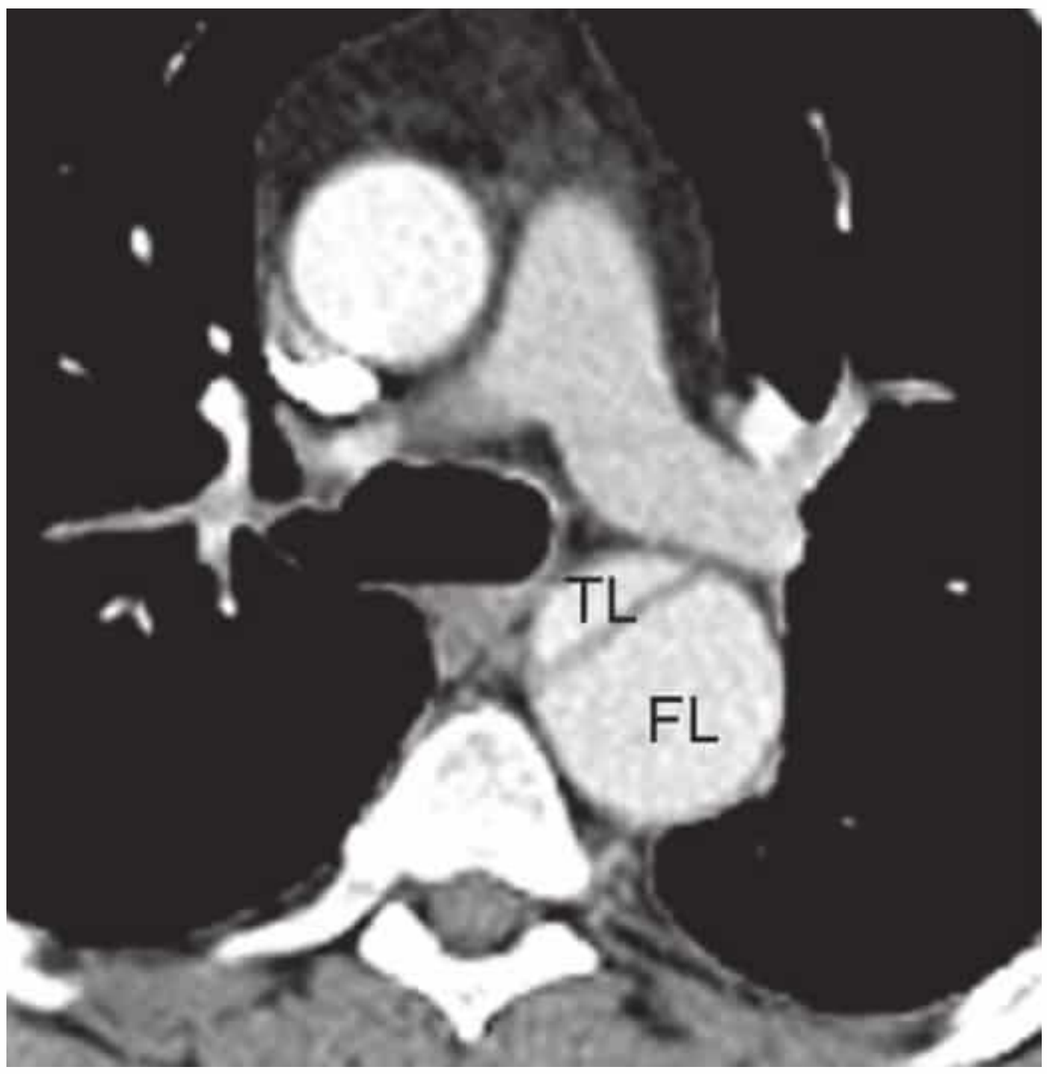

Fig. 13.18 Contrast-enhanced CT demonstrates an intimal flap in the descending thoracic aorta with the development of true (TL) and false (FL) lumina.

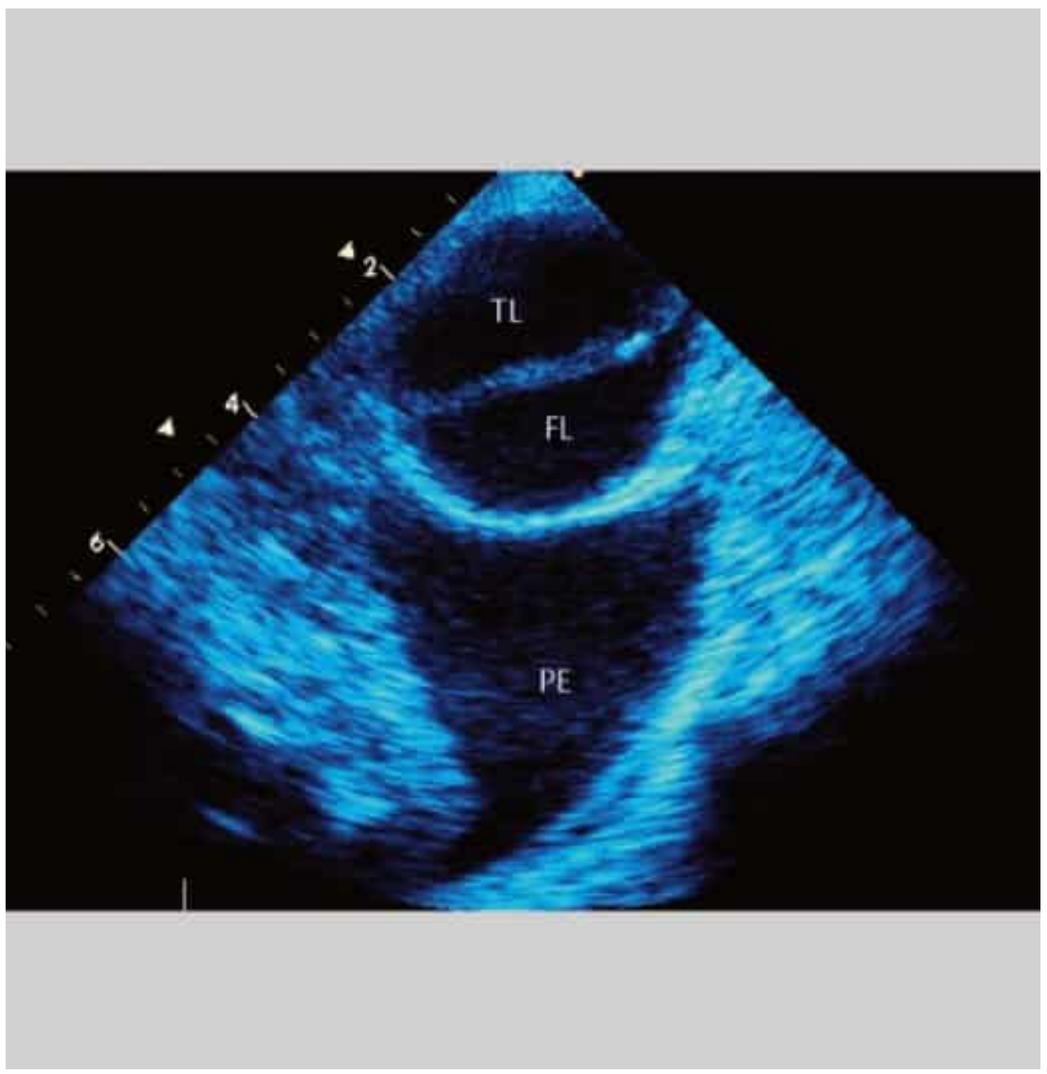

Fig. 13.19 TEE short-axis scan reveals an intimal flap in the descending aorta 38 cm from the incisor teeth, with the development of true (TL) and false (FL) lumina. A left-sided pleural effusion (PE) is present as a sign of impending rupture

the Stanford classification. As a result, **TEE** can be used to select patients for emergency surgery, provided the examiner has adequate experience in the evaluation of aortic dissections. The Task Force of the European Society of Cardiology recommends that conventional angiography be used only in the planning of interventional procedures (e.g., aortic stent grafting or intimal flap fenestration) (**Fig. 13.20**).[4] Studies by the International Registry of Acute Aortic Dissection (IRAD) show that **contrast-enhanced multislice CT** is the imaging procedure of first choice in clinical settings.[19]

Essential Point
In many cases the diagnosis is established by a combination of several imaging studies because of the complementary nature of the information supplied by different modalities.[19]

The dissection membrane divides the aortic lumen into a true lumen (TL) and a false lumen (FL). Frequently the true lumen is compressed by the higher pressure in the false lumen, causing it to appear narrower than the false lumen, and has an oval cross-sectional appearance. The true lumen expands with the systolic pulse wave, causing it to present a periodic convex interface with the adjacent false lumen. In diastole the false lumen may compress the true lumen to the point of complete collapse, especially in an acute dissection. This collapse of the true lumen may lead to visceral or peripheral hypoperfusion, necessitating further therapeutic interventions such as percutaneous balloon fenestration of the dissection membrane or aortic stent grafting. Surgical procedures for the treatment of acute visceral ischemia are associated with a significant mortality rate.

Dynamic collapse of the true lumen often cannot be demonstrated with contrast-enhanced CT (**Fig. 13.21**). TEE and MRI with use of cine sequences, and conventional angiography can provide evidence of a dynamic, compression-induced malperfusion syndrome owing to their high temporal resolution. A malperfusion syndrome may also result from static occlusion of the origin of a visceral artery by the intimal flap or from clotting of the false lumen at the origin of a visceral artery. It is important, therefore, to evaluate how the visceral arteries are supplied by the true and false lumina (**Fig. 13.22**). This assessment is clearly the domain of **noninvasive imaging** by CTA or MRI and, in rare cases, conventional angiography. TEE is unrewarding for this application. Multiplanar reformatting in CT and MRI are helpful in determining which lumen supplies the branch arteries, whether the dissection extends into the branch origins, and whether a distal reentry tear is present.[3]

Differentiation of the true and false lumina is sometimes difficult and can generally be accomplished if the true lumen can be traced over the full extent of the dissection. As a rule, the true lumen is located along the inner curve of the aortic arch, while the false lumen lies along the outer curve. Because flow is usually diminished in the false lumen, this channel may show spontaneous echo contrast or (partial) thrombosis (**Fig. 13.17b**).

Once a dissection has been diagnosed, the main goal of imaging is to determine the **location and extent of the dissection** based on the criteria of the Stanford classification. Another imaging goal is to **locate the intimal tears**. In a type A dissection, the entry tear is usually located directly above the valvular annulus (**Fig. 13.11a, b**). In a type B dissection, an entry tear is typically found in close proximity to the origin of the left subclavian artery, at the level of the aortic isthmus (**Fig. 13.17c**). It

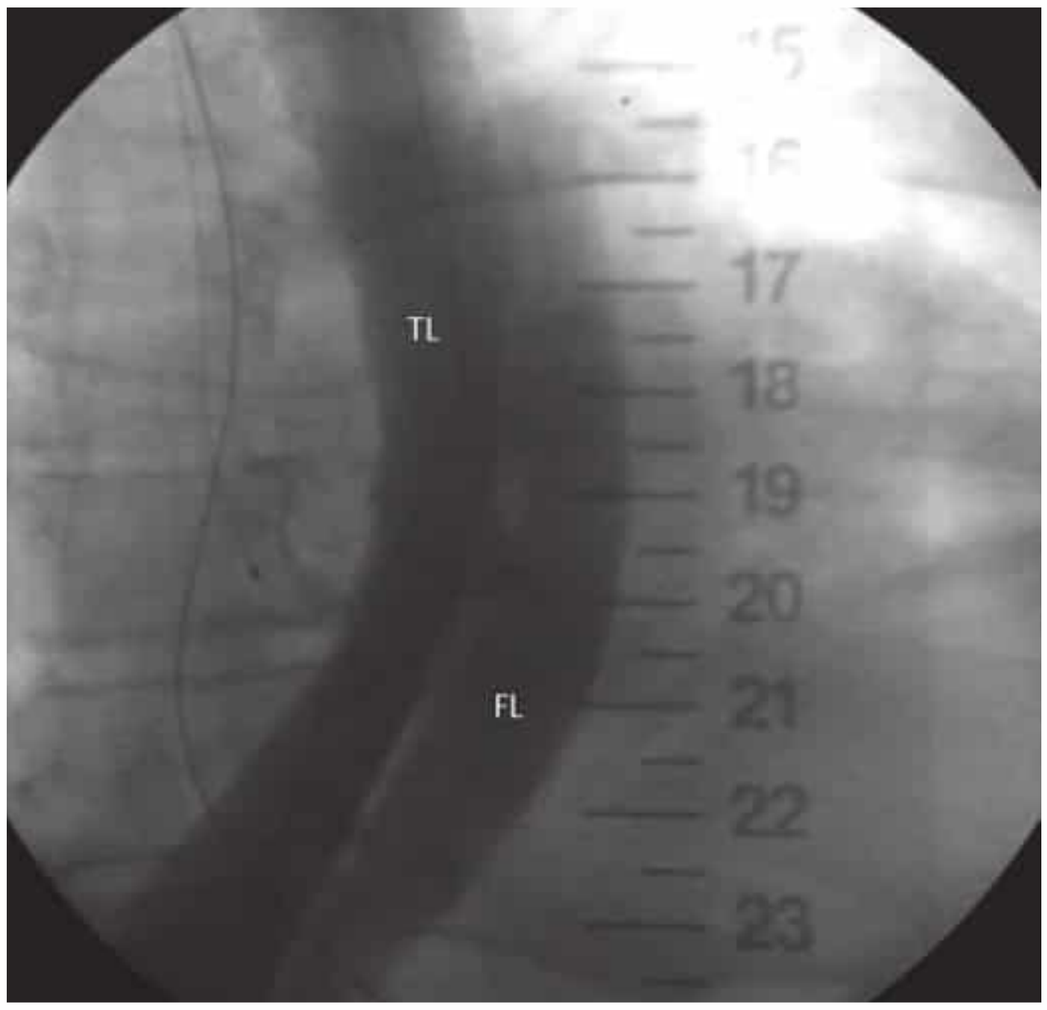

Fig. 13.20 Conventional angiogram of a thoracic aortic dissection reveals the communication between the true (TL) and false (FL) lumina in the midthoracic aorta (at ~ 20 cm).

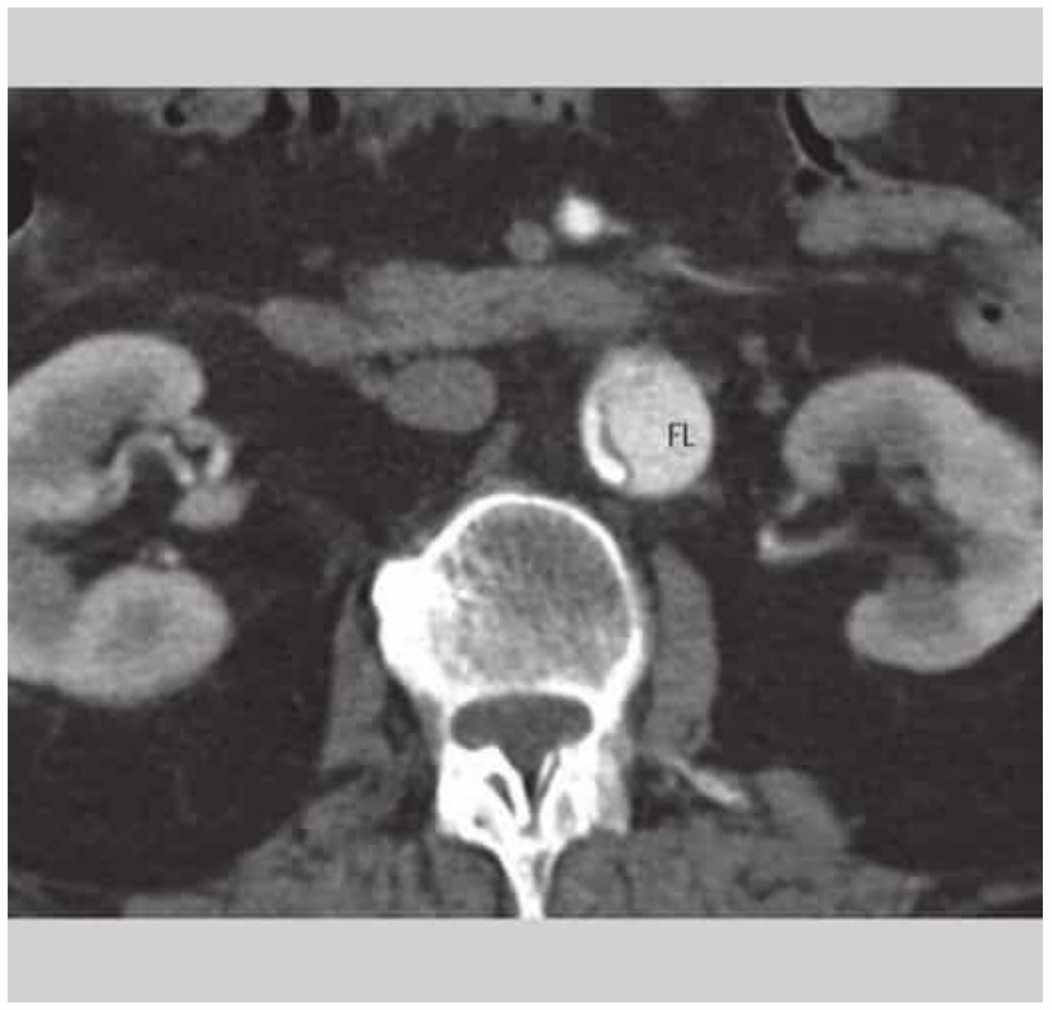

Fig. 13.21 The true lumen of the abdominal aorta is greatly compressed by the higher pressure in the false lumen (FL) ("true lumen collapse").

is common to find multiple tears, however, particularly in the abdominal aorta. **TEE** and conventional **angiography** are superior to CT for entry site detection owing to their higher temporal resolution. An entry tear appears on CT only as a morphological defect in the intimal flap (**Fig. 13.23**).[4]

Color Doppler echocardiography can detect even the smallest communications between the true and false lumina (**Fig. 13.24**). CW Doppler echocardiography can provide spectral analysis for flow characterization. Scans generally show a multiphasic Doppler waveform with a systolic–diastolic flow reversal corresponding to the varying pressure differential between the true and false lumina (**Fig. 13.25**).[12]

Additional goals in the acute diastolic work-up of aortic dissection are the **assessment of left ventricular function** and the **morphological and functional evaluation of the aortic valve**.[4] This is definitely the domain of **TEE**. CT is of little help in this regard, although it may reveal some indirect signs (e.g., LV dilatation due to severe aortic regurgitation). MRI can also detect concomitant aortic regurgitation, though it may be difficult to quantify with MRI. The aortic valve may have a bicuspid anatomy. The dissection may disrupt the geometry of the aortic bulb, causing incomplete coaptation of the valve cusps and leading to severe aortic regurgitation with acute left heart decompensation and pulmonary edema. Aortic regurgitation is found in up to 70% of patients with a type A aortic dissection.[5] Prolapse of the intimal flap into the left ventricular outflow tract may also lead to severe, acute aortic regurgitation. Visualization of the **pathogenic mechanism** of the aortic regurgitation is essential for surgical treatment planning, as valve-preserving surgery is preferable to valve replacement in terms of long-term results. Valve replacement is still necessary, however, in cases where primary annular ectasia is the cause of aortic regurgitation.

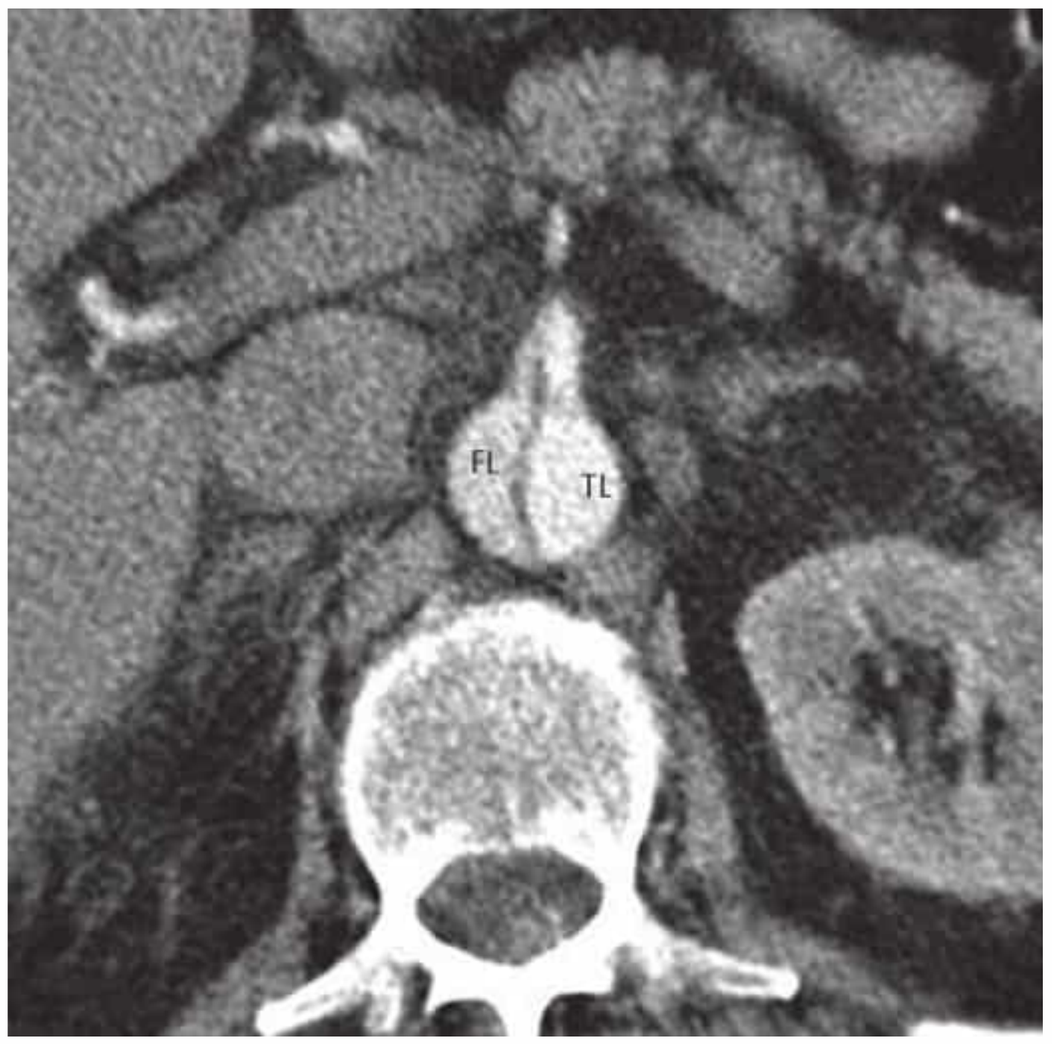

Fig. 13.22 Contrast-enhanced CT scan at the level of the origin of the superior mesenteric artery. The intimal flap in this type B aortic dissection extends into the origin of the superior mesenteric artery.

Pericardial effusion should be taken as an immediate warning sign of an impending rupture or a confined rupture that has already taken place. If there are no signs of pericardial tamponade, the effusion should not be removed by pericardiocentesis.[4] Similarly, a predominantly left-sided, hemorrhagic **pleural effusion** should be taken as a warning sign of impending perforation. Other high risk indicators are streaky mediastinal densi-

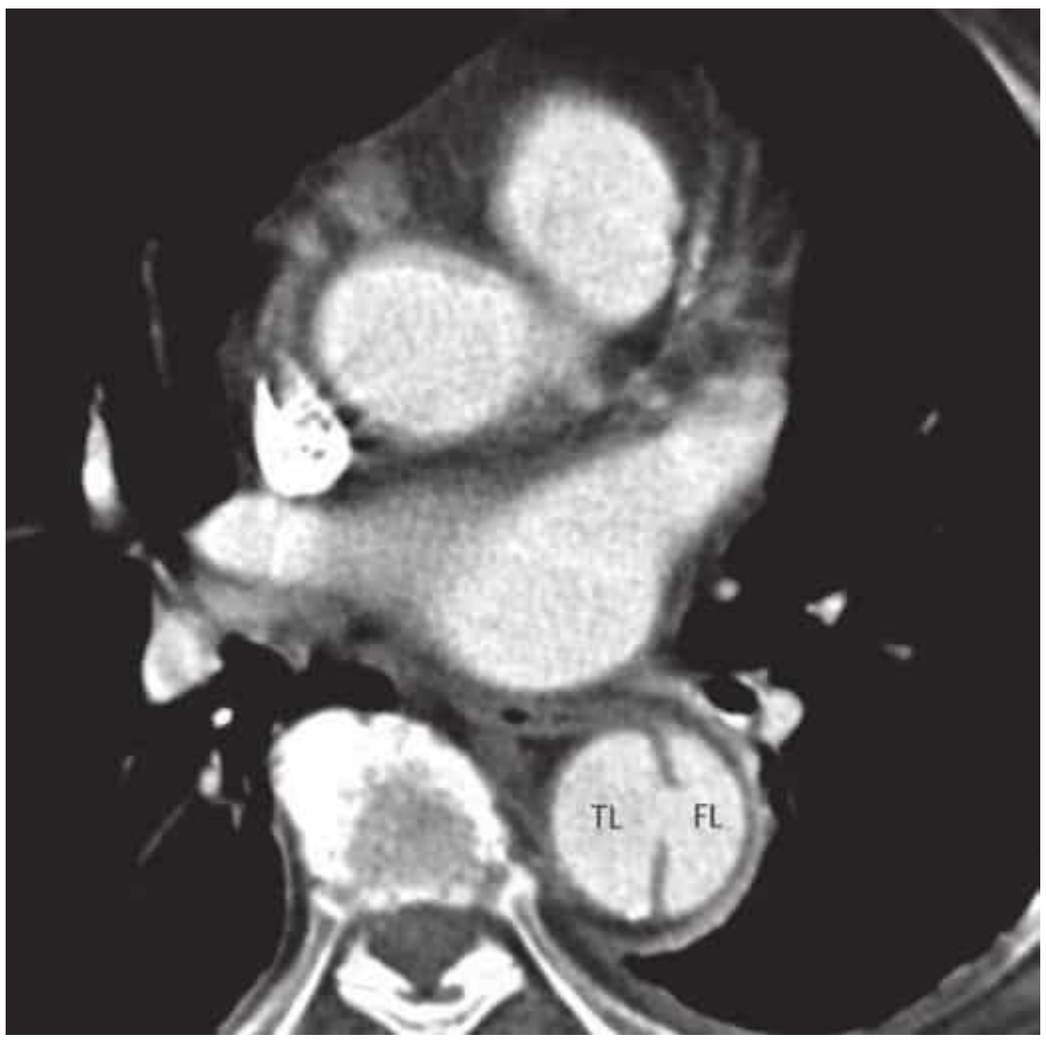

Fig. 13.23 Contrast-enhanced CT reveals a large entry between true (TL) and false (FL) lumina.

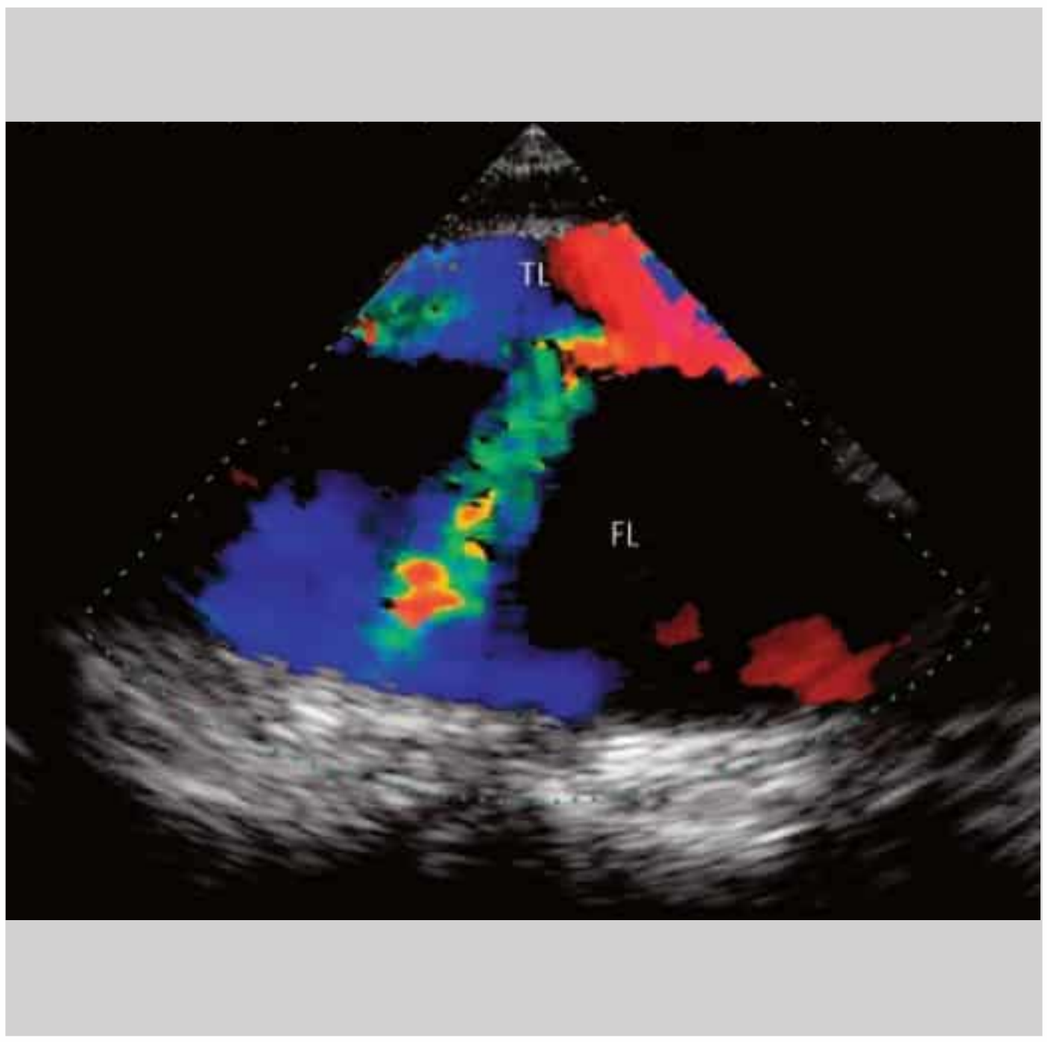

Fig. 13.24 Contrast-enhanced TEE shows a large entry between true (TL) and false (FL) lumina.

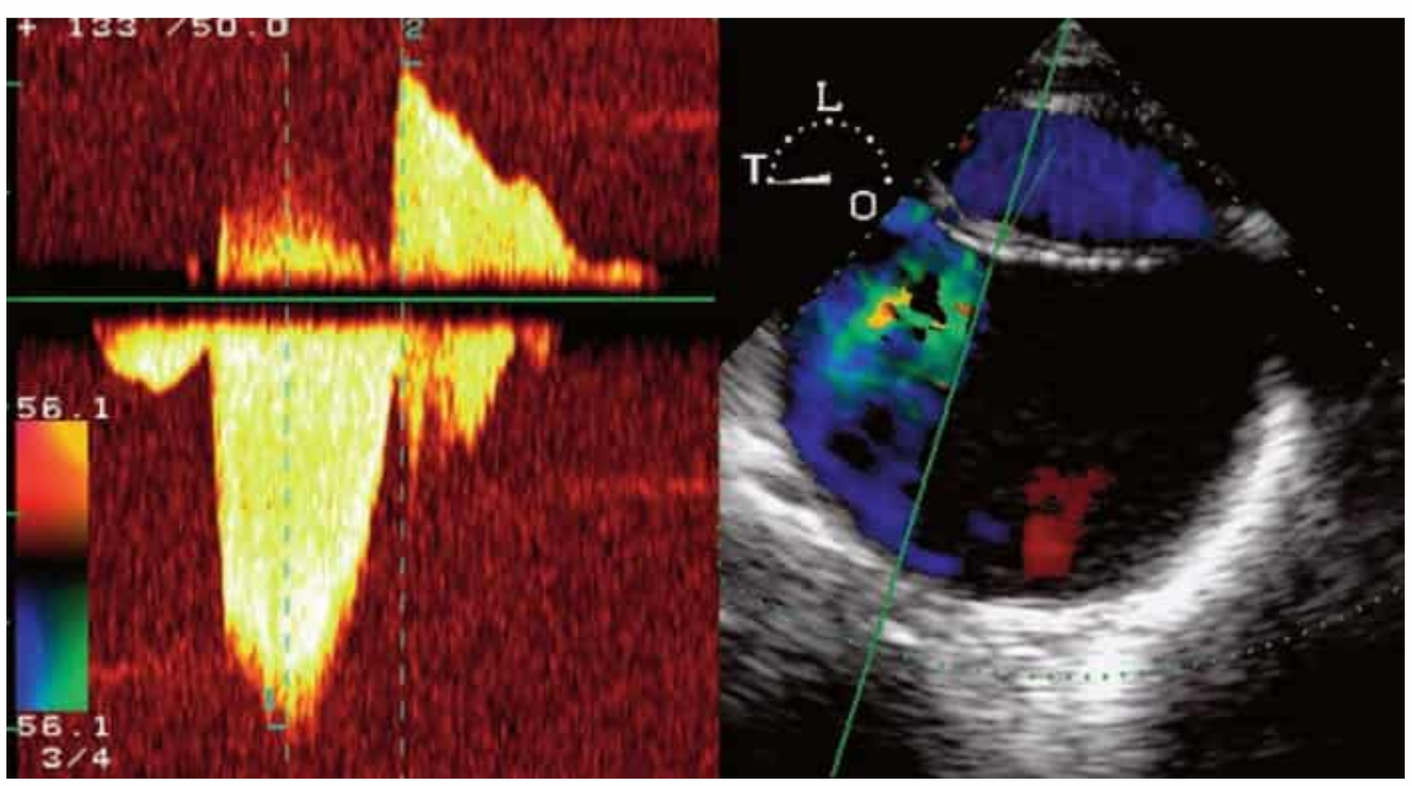

Fig. 13.25 Transesophageal CW Doppler echocardiography for characterizing flow across the entry during systole and diastole. The Doppler spectrum shows that flow is directed from the true to the false lumen during systole and that flow reversal occurs during diastole.

ties or hematomas. A particularly high mortality rate has been reported in patients with mediastinal hematoma.[4,13]

MRI is particularly useful for the follow-up of chronic aortic dissection (>14 days after the initial event) because of the absence of radiation exposure.[16] The first follow-up should be scheduled for ~3–6 months after discharge. The follow-up intervals can be gradually lengthened if there is no evidence of enlargement. Yearly follow-ups are recommended for patients with a stable chronic dissection >1 year and for patients with Marfan syndrome.

Essential Point

- Contrast-enhanced CT and TEE are the most important tools for the acute diagnosis of aortic dissection in clinically suspicious cases.
- Malperfusion syndrome may result from dynamic compression of the true lumen or static occlusion of visceral aortic branches by the intimal flap.
- The diagnostic accuracy of TEE depends critically on the experience of the examiner.
- Reverberation artifacts in the aortic lumen may cause false-positive findings.

Intramural Hematoma of the Aorta (Svensson Class 2 Dissection)

Intramural hematoma (IMH) may be a precursor of classic aortic dissection. It is caused by acute bleeding from ruptured vasa vasorum in the aortic media, which usually have been diseased by preexisting hypertension.[4,5,7] By definition, IMH does not communicate with the aortic lumen and is not perfused by blood flow. The IMH may be localized or may extend the full length of the aorta, similarly to a classic aortic dissection. The bleeding has a fulminating onset and generally causes excruciating pain ("aortic apoplexy").[20] Clinically, IMH is indistinguishable from a classic dissection. Typical complications of IMH are progression to a classic aortic dissection or aneurysm and aortic rupture.[14,21–24] Risk factors for progression are involvement of the ascending aorta and an ectatic aortic diameter at the time of diagnosis.[14,21–24] Rupture of the aorta often occurs during progression to a classic dissection. Malperfusion syndromes are less common than with classic dissections. The prevalence of IMH in patients with acute aortic syndrome is estimated at 10–30%[5]

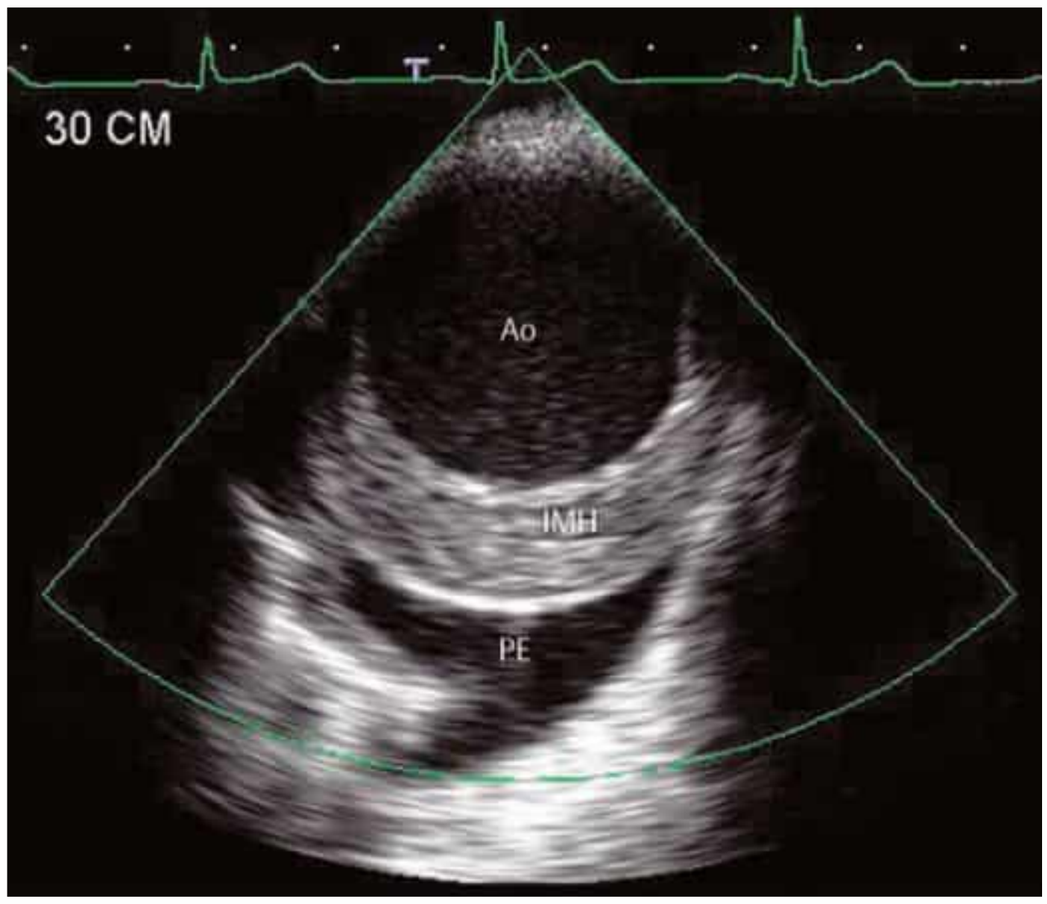

Fig. 13.26 TEE short-axis scan at 30 cm from the incisor teeth demonstrates an extensive intramural hematoma (IMH) in the midthoracic descending aorta.

Imaging of Intramural Hematoma

The hallmark of IMH is a circular or crescent-shaped thickening of the aortic wall to more than 7 mm in cross-sectional images (**Figs. 13.26, 13.27**).[20,23,24] TEE often shows hypoechoic zones in the thickened wall consistent with acute intramural bleeding. By definition, however, these hypoechoic zones do not communicate with the aortic lumen. But since IMH progresses to a classic communicating dissection in 16–36% of cases, very close attention should be given to possible entry sites that would signify an incipient dissection. CT is excellent for imaging fresh intramural blood, which appears on plain scans as a hyperdense crescent (60–70 HU) that contrasts sharply with the aortic wall layers. MRI is also useful for estimating the age of an intramural hemorrhage. While fresh intramural blood has high signal intensity in T2-weighted sequences, subacute intramural hemorrhages can be identified by their high T1-weighted and T2-weighted signal intensity due to methemoglobin formation.

As with a classic aortic dissection, patients diagnosed with aortic IMH should be evaluated further to determine whether the ascending aorta is involved. Based on current data and recommendations, surgical replacement of the ascending aorta is indicated in patients with a type A IMH, analogous to a classic aortic dissection. Cases with spontaneous regression of type A IMH have also been described, however.[14,21–24]

IMH may be difficult to distinguish from complicated atherosclerotic plaque, mural thrombus, and aortic dissection with a clotted false lumen. Atherosclerotic plaque often has an irregular luminal surface, contrasting with the smooth luminal surface of IMH. Moreover, IMH tends to extend over a longer segment of the aorta. The location of the sclerotic or calcified intima is a feature helpful in differentiating from mural thrombus. The intramural blood in IMH displaces the sclerotic or calcified intima toward the vessel lumen, while a mural thrombus displaces the intima outward toward the adventitia. Contrast-enhanced CT is particularly helpful in making this assessment (**Figs. 13.13, 13.27**). In many cases TEE can also localize the thickened, sclerotic intima in relation to the thickened hypoechoic wall. Conventional angiography contributes little to the diagnosis of IMH because, like MRA, it is a luminographic technique that cannot demonstrate mural pathology.

Attention should also be given to possible risk signs, as with a classic dissection. A concomitant left-sided pleural effusion should alert the examiner to the risk of impending perforation.[4]

Essential Point

- IMH often progresses to a classic dissection, aneurysm, or rupture, particularly when it involves the ascending aorta (type A IMH).
- Type A IMH generally warrants emergency surgical replacement of the ascending aorta.
- Contrast-enhanced CT and TEE are helpful in differentiating IMH from mural thrombus.

Circumscribed Dissection (Svensson Class 3 Dissection)

Circumscribed aortic dissections are of relatively minor importance in clinical practice. Often they go undetected until operation and are most commonly found in patients with Marfan syndrome. The dissection appears grossly as a stellate or linear tear in the aortic wall, frequently covered over by thrombus. This type of tear may give rise to a classic dissection with a false lumen, or it may resolve without treatment. The diagnosis of a circumscribed dissection is often difficult and relies on conventional angiography, which shows a circumscribed bulging of the aortic lumen through the tear.

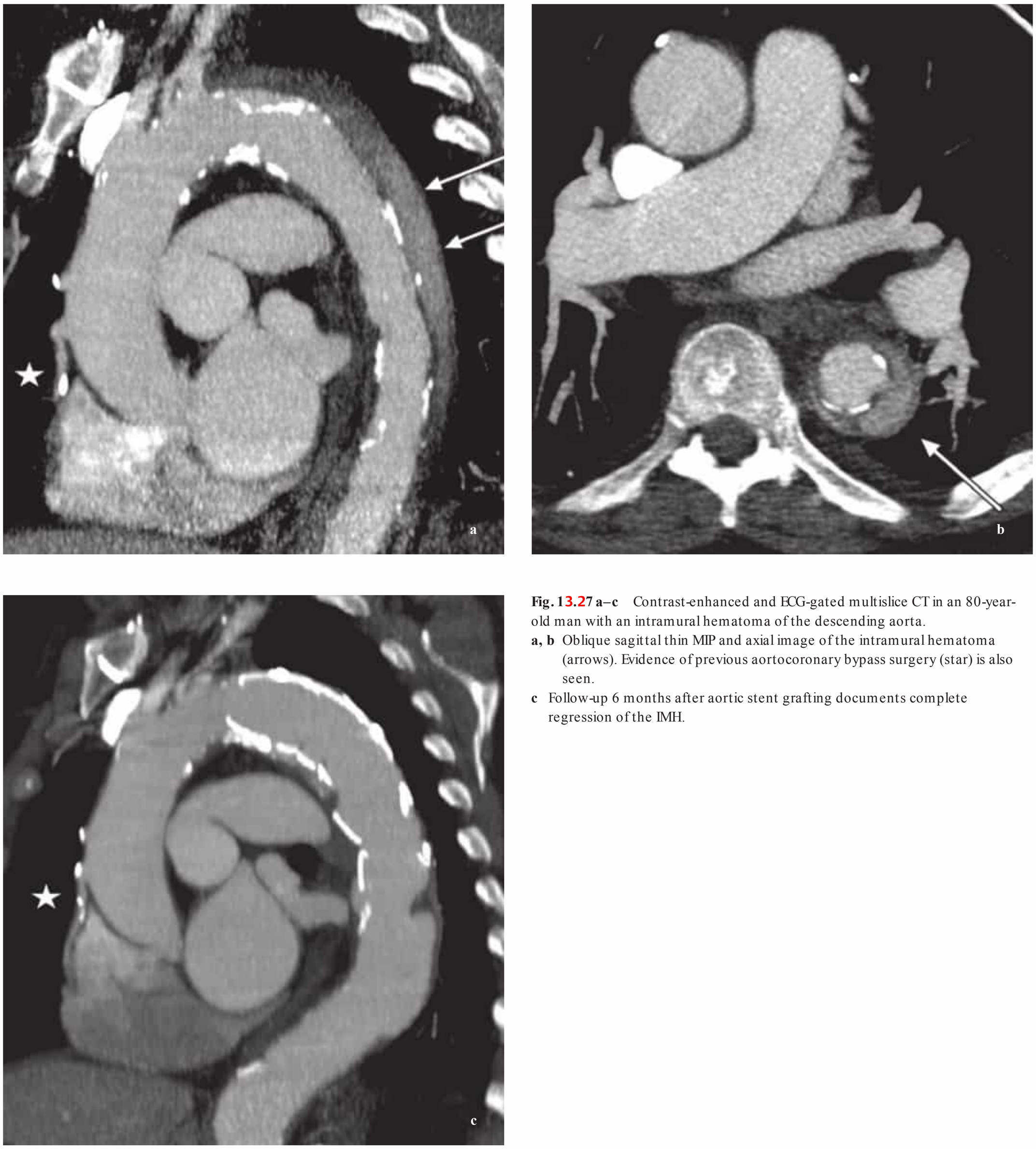

Fig. 13.27 a–c Contrast-enhanced and ECG-gated multislice CT in an 80-year-old man with an intramural hematoma of the descending aorta.

a, b Oblique sagittal thin MIP and axial image of the intramural hematoma (arrows). Evidence of previous aortocoronary bypass surgery (star) is also seen.

c Follow-up 6 months after aortic stent grafting documents complete regression of the IMH.

Penetrating Aortic Ulcer (Svensson Class 4 Dissection)

Atheromatous plaques may progressively erode the aortic wall, creating a central ulcer that may penetrate the internal elastic membrane and extend into the media and adventitia.[5,25–27] Complications of penetrating aortic ulcer (PAU) include progression to wall dissection, the development of rapidly progressive pseudoaneurysms, or a (confined) aortic rupture.[5,25–27] It has been found that PAU has an even higher association with aortic ruptures than does a classic type B aortic dissection.[25] Erosion of the vasa vasorum by the ulcer may lead to intramural hemorrhage. Unlike an actual intramural hematoma, this hemorrhage is usually localized and almost never leads to a classic dissection, although it is an unfavorable prognostic sign.[5,27]

Penetrating aortic ulcers usually develop only in association with massive aortic sclerosis. Frequently, then, clinical manifestations do not appear until after 70 years of age.[4,5,27] PAUs are most commonly located in the descending thoracic aorta.

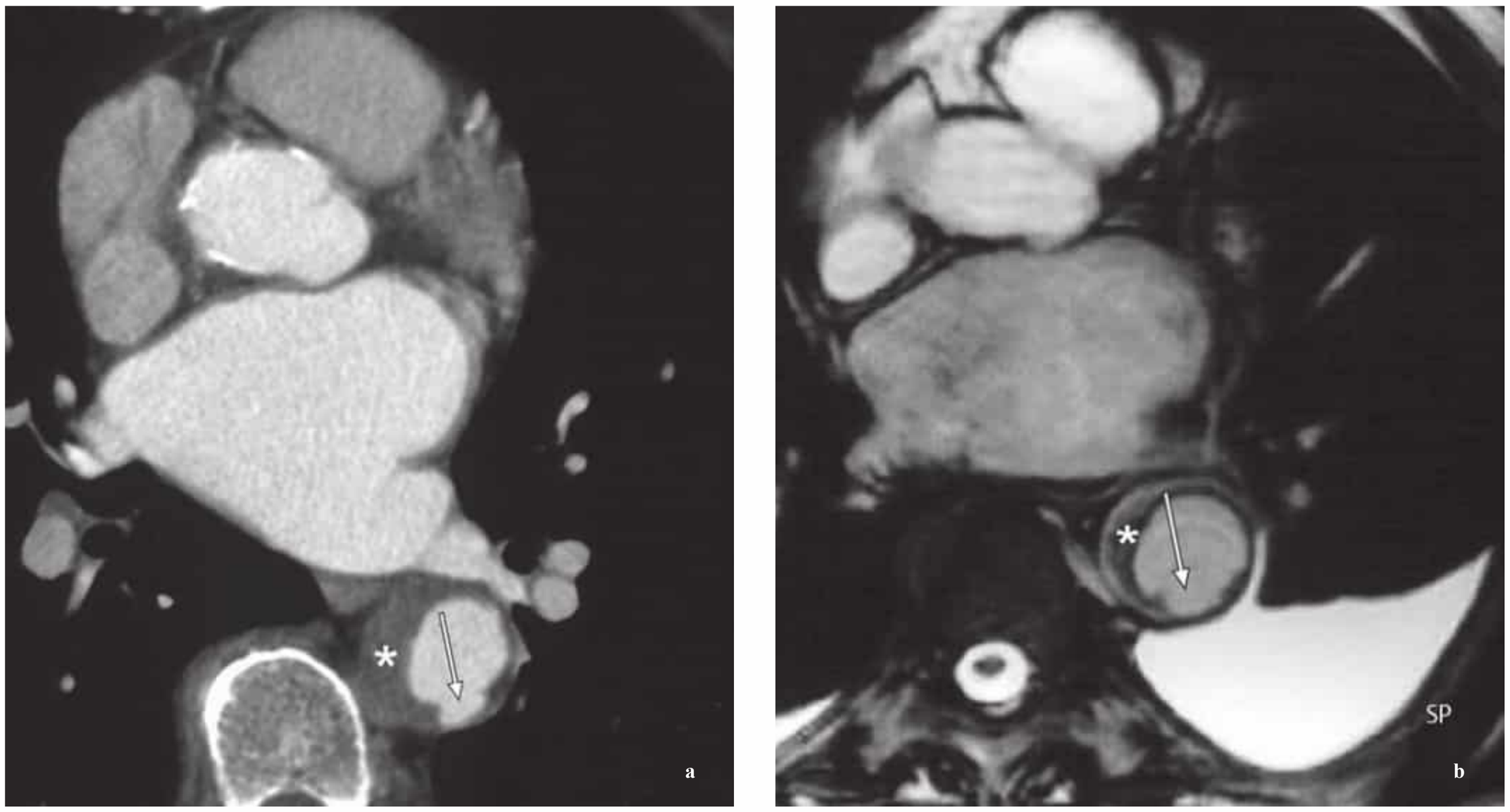

Fig. 13.28 a, b Penetrating aortic ulcer (arrow) with an associated intramural hematoma based on vascular erosion by the ulcer (star).

a Contrast-enhanced CT.
b Correlative MRI shows a large pleural effusion signifying an impending rupture.

Ulcers of the ascending aorta have a poor prognosis but are relatively rare. PAU is also associated with an increased incidence of infrarenal aortic aneurysms.

Imaging of Penetrating Aortic Ulcer

The imaging appearance of PAU is that of a contrast-filled crater located outside the boundaries of the aortic lumen and not associated with a mobile intimal flap or detectable false lumen (**Figs. 13.28, 13.29**). Generally the ulcer is accompanied by significant atherosclerosis of the aorta. Pseudoaneurysms often have a mushroom-shaped configuration in the parasagittal plane that can mimic a dissection in axial views. Usually this "dissection flap" is localized, markedly thickened or calcified, and does not visibly oscillate with the pulse. To date, no data have been published on the diagnostic accuracy of TEE, CT, MRI, or conventional angiography in the detection of PAU.

It is good practice to image the entire aorta in stable patients, since PAU tends to involve multiple aortic sites. Contrast-enhanced CT is preferred for whole-aorta imaging, as it permits the noninvasive evaluation of concomitant fresh intramural hemorrhage (see above), the direct detection of aortic calcium, and the visualization of thrombosed pseudoaneurysms. It should be noted, however, that patients with generalized atherosclerosis often have chronic renal failure that would contraindicate the use of nephrotoxic contrast media. MRI is preferred over contrast-enhanced CT in this subset of patients.

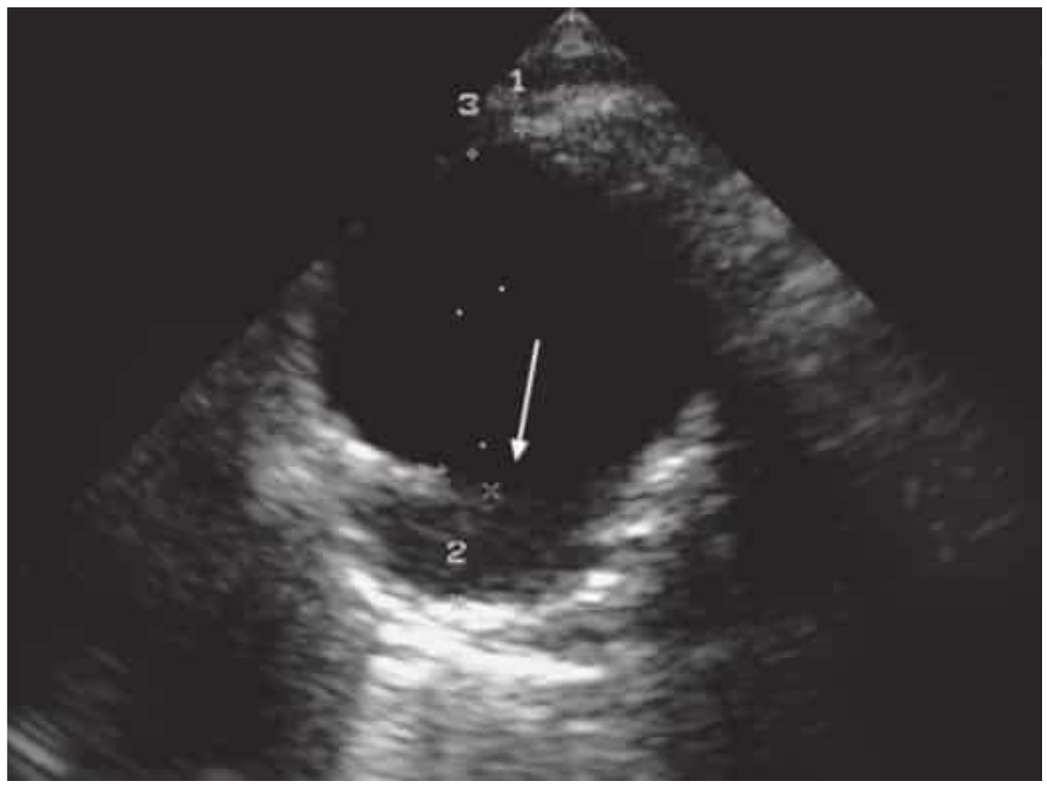

Fig. 13.29 Transesophageal echocardiogram of a penetrating aortic ulcer (arrow, probe at 36 cm from incisor teeth).

Iatrogenic/Traumatic Transection or Dissection (Svensson Class 5 Dissection)

Aortic injuries may result from blunt chest trauma and from severe deceleration trauma or falls from a great height.[4] These injuries most commonly affect the aortic isthmus, which is exposed anatomically to exceptionally high shear forces, but the ascending aorta may also be affected. Aortic dissections may have an iatrogenic cause, occurring in the setting of diagnostic cardiac catheterizations, coronary interventions, the angioplastic treatment of coarctation, the introduction of an intra-aortic balloon pump, or open cardiac surgery.[4]

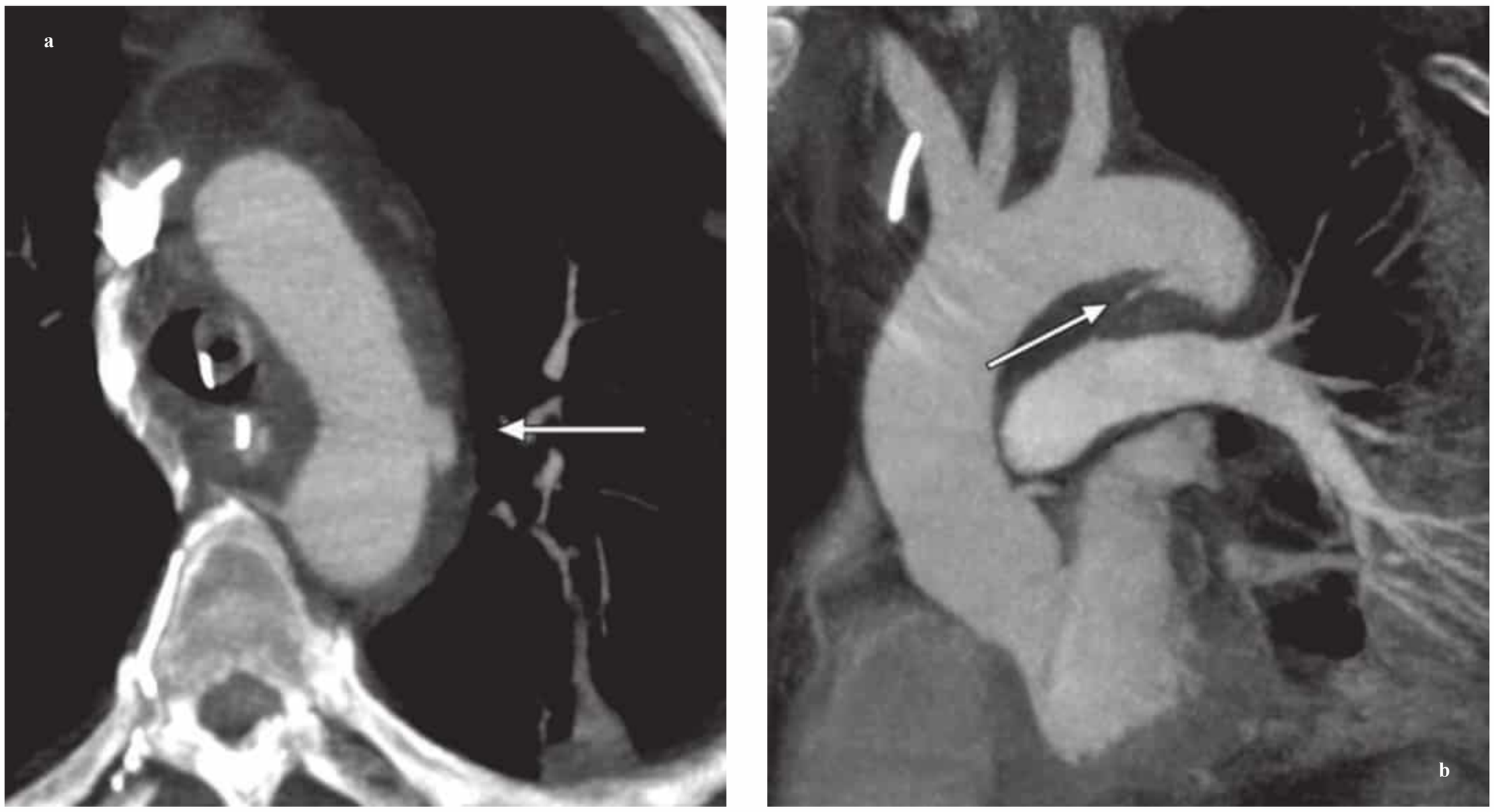

Fig. 13.30 a, b Multislice CT of traumatic aortic rupture (arrow) in a 25-year-old motorcyclist. The rupture occurred in the aortic isthmus and caused bleeding into the mediastinum.

a Axial scan through the lower portion of the aortic arch.
b Oblique sagittal reformatted image.

Imaging of Traumatic Aortic Dissection

The spectrum of traumatic aortic injuries ranges from intimal laceration and intimal hemorrhage to classic aortic dissection and complete aortic rupture (transection) (**Fig. 13.30**). Thus, it is important to check for injuries to the thoracic aorta in polytraumatized patients, who routinely undergo thoracic CT scanning for the detection of thoracic injuries. Subtle aortic injuries are common and may be missed if the interslice gap is too large. Additionally, the examination should be performed with the application of a contrast medium. The presence of a pericardial or pleural effusion may suggest a traumatic aortic injury. Mediastinal hematoma is also a common finding. If a traumatic aortic dissection is suspected and CT findings are equivocal, TEE should be performed. The detection of echogenic material protruding into the aortic lumen is a typical finding at TEE.

Inflammatory Aortic Diseases

Aortitis

Aortitis is characterized by inflammatory infiltration of the aortic wall. Three main forms are distinguished:

- Infectious syphilitic aortitis
- Infectious nonsyphilitic aortitis
- Noninfectious aortitis based on vasculitis of the great vessels[4]

Infectious syphilitic aortitis has become rare as a result of widespread penicillin use. Even today, however, aortitis may develop in the setting of tertiary syphilis in immunosuppressed patients (e.g., HIV). Infectious nonsyphilitic aortitis is caused mainly by *Staphylococcus aureus* or Gram-negative bacteria (*Salmonella* and *Proteus* species) and most commonly affects sites of least resistance such as preexisting (abdominal aortic) aneurysms. Noninfectious aortitis may occur in the setting of Takayasu arteritis or giant-cell arteritis as well as several autoimmune and rheumatological disorders such as Behçet disease and systemic lupus erythematosus.

Imaging of Aortitis

The imaging hallmark of aortitis is inflammatory wall thickening that enhances after IV contrast administration. Differentiation from intramural hematoma may be difficult, but the overall clinical picture with signs of an inflammatory reaction in the absence of acute pain often suggests the correct diagnosis. Contrast-enhanced CT is the classic modality for the detection of aortitis. MRI with edema-sensitive sequences can narrow the differential diagnosis and is particularly useful for follow-up (**Fig. 13.31**). PET imaging can be combined with CT, for example, to assess the activity of aortitis in response to therapy. The initial wall thickening in aortitis may progress to aortic stenosis or high-grade proximal stenosis of aortic side branches (e.g., coronary arteries, cerebral arteries) with consequent ischemia. This is particularly common in Takayasu arteritis. The typical proximal stenoses of the supra-aortic vessels can be demonstrated by conventional angiography and MRA. Inflammatory infiltration may also weaken the aortic wall, leading to "mycotic" aneurysms with an atypical configuration that may be indolent and often undergo rapid enlargement.

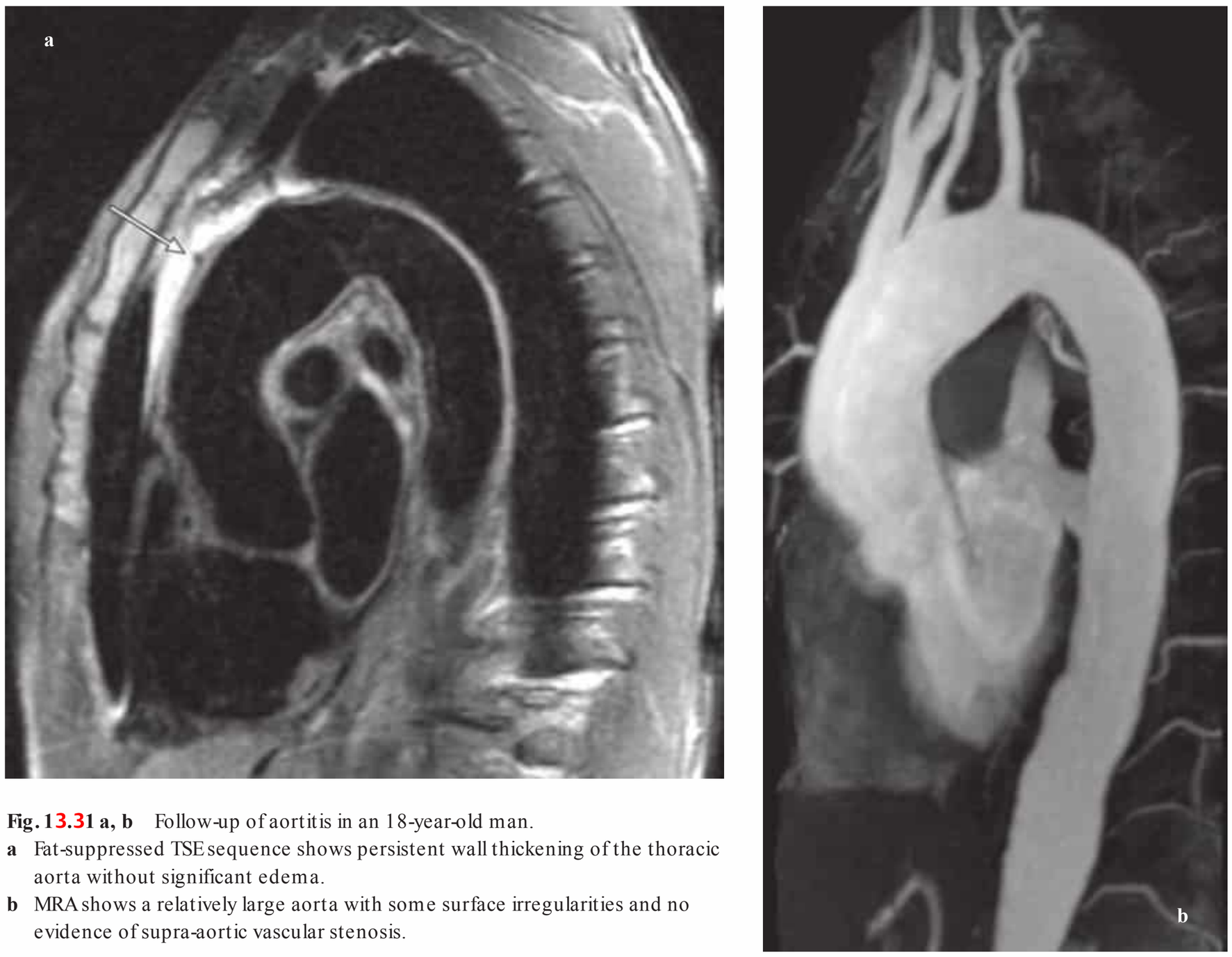

Fig. 13.31 a, b Follow-up of aortitis in an 18-year-old man.
a Fat-suppressed TSE sequence shows persistent wall thickening of the thoracic aorta without significant edema.
b MRA shows a relatively large aorta with some surface irregularities and no evidence of supra-aortic vascular stenosis.

References

1. Russo V, Renzulli M, La Palombara C, Fattori R. Congenital diseases of the thoracic aorta. Role of MRI and MRA. Eur Radiol 2006;16:676–684
2. Erbel R, Eggebrecht H. Aortic dimensions and the risk of dissection. Heart 2006;92:137–142
3. Fattori R, Nienaber CA. MRI of acute and chronic aortic pathology: preoperative and postoperative evaluation. J Magn Reson Imaging 1999; 10:741–750
4. Erbel R, Alfonso F, Boileau C, et al; Task Force on Aortic Dissection, European Society of Cardiology. Diagnosis and management of aortic dissection. Eur Heart J 2001;22:1642–1681
5. von Kodolitsch Y, Baumgart D, Eggebrecht H, et al. Das akute Aortensyndrom. Dtsch Arztebl 2003;100:A326–A333
6. Eggebrecht H, Nienaber CA, Neuhauser M, et al. Endovascular stent-graft placement in aortic dissection: a meta-analysis. Eur Heart J 2006; 27:489–498
7. Svensson LG, Labib SB, Eisenhauer AC, Butterly JR. Intimal tear without hematoma: an important variant of aortic dissection that can elude current imaging techniques. Circulation 1999;99:1331–1336
8. Crawford ES, Svensson LG, Coselli JS, Safi HJ, Hess KR. Surgical treatment of aneurysm and/or dissection of the ascending aorta, transverse aortic arch, and ascending aorta and transverse aortic arch. Factors influencing survival in 717 patients. J Thorac Cardiovasc Surg 1989;98: 659–673
9. Meszaros I, Morocz J, Szlavi J, et al. Epidemiology and clinicopathology of aortic dissection. Chest 2000;117:1271–1278
10. Nienaber CA, Eagle KA. Aortic dissection: new frontiers in diagnosis and management: Part I: from etiology to diagnostic strategies. Circulation 2003;108:628–635
11. Nienaber CA, Eagle KA. Aortic dissection: new frontiers in diagnosis and management: Part II: therapeutic management and follow-up. Circulation 2003;108:772–778
12. Erbel R, Engberding R, Daniel W, Roelandt J, Visser C, Rennollet H. Echocardiography in diagnosis of aortic dissection. Lancet 1989;1:457–461
13. Erbel R, Oelert H, Meyer J, et al. Effect of medical and surgical therapy on aortic dissection evaluated by transesophageal echocardiography. Implications for prognosis and therapy. The European Cooperative Study Group on Echocardiography. Circulation 1993;87:1604–1615
14. Evangelista A, Avegliano G, Elorz C, Gonzalez-Alujas T. Garcia dC, Soler-Soler J. Transesophageal echocardiography in the diagnosis of acute aortic syndrome. J Card Surg 2002;17:95–106
15. Keren A, Kim CB, Hu BS, et al. Accuracy of biplane and multiplane transesophageal echocardiography in diagnosis of typical acute aortic dissection and intramural hematoma. J Am Coll Cardiol 1996;28:627–636
16. Nienaber CA, Spielmann RP, von Kodolitsch Y, et al. Diagnosis of thoracic aortic dissection. Magnetic resonance imaging versus transesophageal echocardiography. Circulation 1992;85:434–447
17. Kodolitsch Y, Krause N, Spielmann R, Nienaber CA. Diagnostic potential of combined transthoracic echocardiography and x-ray computed tomography in suspected aortic dissection. Clin Cardiol 1999;22:345–352
18. Nienaber CA, von Kodolitsch Y, Nicolas V, et al. The diagnosis of thoracic aortic dissection by noninvasive imaging procedures. N Engl J Med 1993;328:1–9
19. Moore AG, Eagle KA, Bruckman D, et al. Choice of computed tomography, transesophageal echocardiography, magnetic resonance imaging, and aortography in acute aortic dissection: International Registry of Acute Aortic Dissection (IRAD). Am J Cardiol 2002;89:1235–1238
20. von Kodolitsch Y, Nienaber CA. Die intramurale Hämorrhagie der thorakalen Aorta: Diagnostik, Therapie und Prognose bei 209 in vivo diagnostizierten Fällen. Z Kardiol 1998;87:797–807
21. Evangelista A, Dominguez R, Sebastia C, et al. Prognostic value of clinical and morphologic findings in short-term evolution of aortic intramural haematoma. Therapeutic implications. Eur Heart J 2004;25:81–87
22. Evangelista A, Mukherjee D, Mehta RH, et al; International Registry of Aortic Dissection (IRAD) Investigators. Acute intramural hematoma of the aorta: a mystery in evolution. Circulation 2005;111:1063–1070

23. Mohr-Kahaly S, Erbel R, Kearney P, Puth M, Meyer J. Aortic intramural hemorrhage visualized by transesophageal echocardiography: findings and prognostic implications. J Am Coll Cardiol 1994;23:658–664
24. von Kodolitsch Y, Csosz SK, Koschyk DH, et al. Intramural hematoma of the aorta: predictors of progression to dissection and rupture. Circulation 2003;107:1158–1163
25. Coady MA, Rizzo JA, Elefteriades JA. Pathologic variants of thoracic aortic dissections. Penetrating atherosclerotic ulcers and intramural hematomas. Cardiol Clin 1999;17:637–657
26. Coady MA, Rizzo JA, Hammond GL, Pierce JG, Kopf GS, Elefteriades JA. Penetrating ulcer of the thoracic aorta: what is it? How do we recognize it? How do we manage it? J Vasc Surg 1998;27:1006–1015
27. von Kodolitsch Y, Nienaber CA. Das Ulkus der thorakalen Aorta: Diagnostik, Therapie und Prognose. Z Kardiol 1998;87:917–927

Further Reading

Isselbacher EM. Thoracic and abdominal aortic aneurysms. Circulation 2005;111:816–828

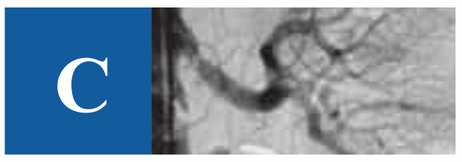

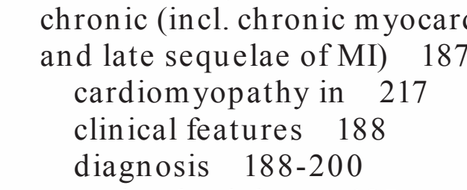

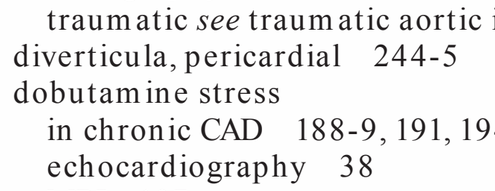

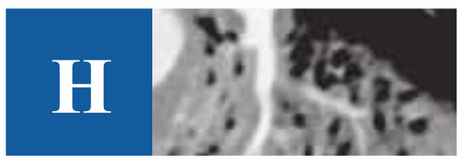

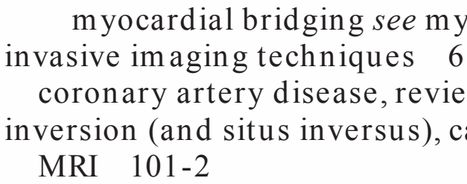

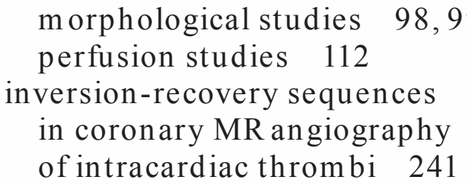

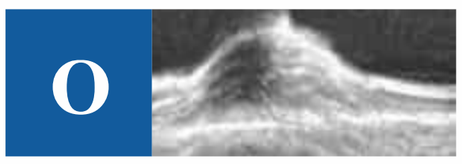

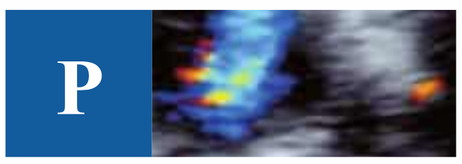

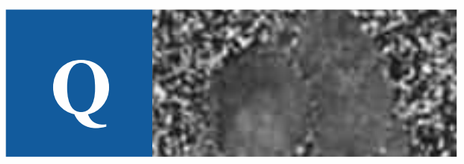

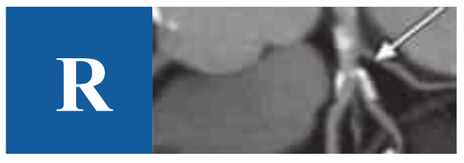

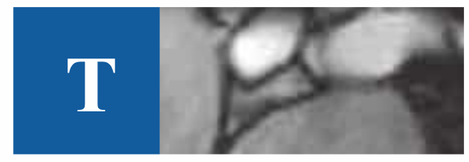

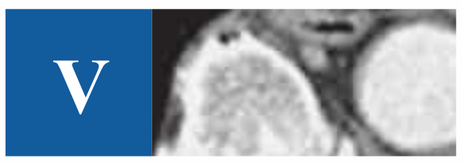

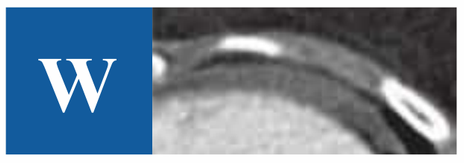

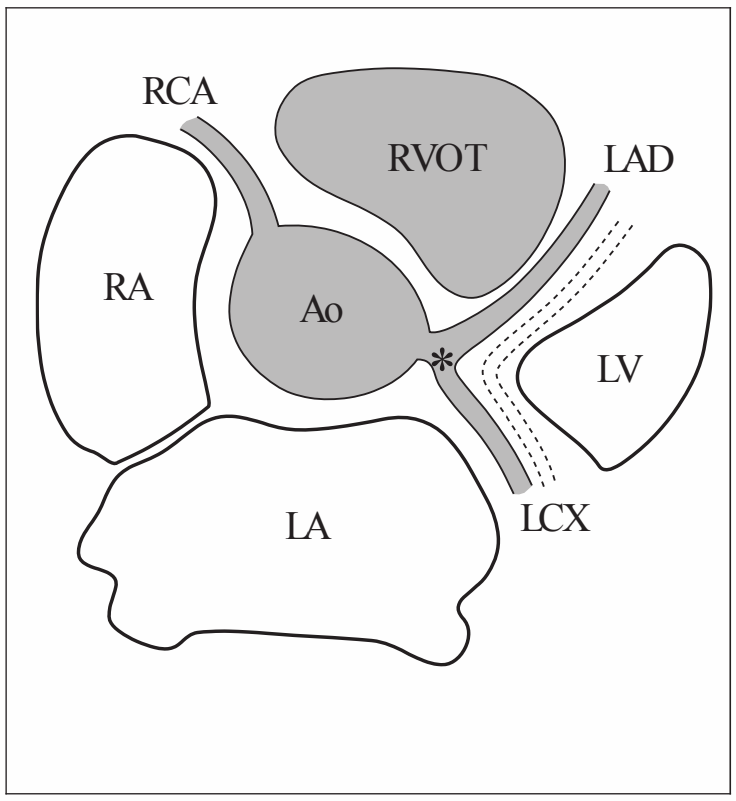

Fig. 12.9 Normal anatomy of the coronary origins.
RCA Right coronary artery
RVOT Right ventricular outflow tract
LAD Left anterior descending artery
RA Right atrium
Ao Aorta
LV Left ventricle
* Left coronary artery (left main trunk)
LCX Circumflex branch of LCA
LA Left atrium

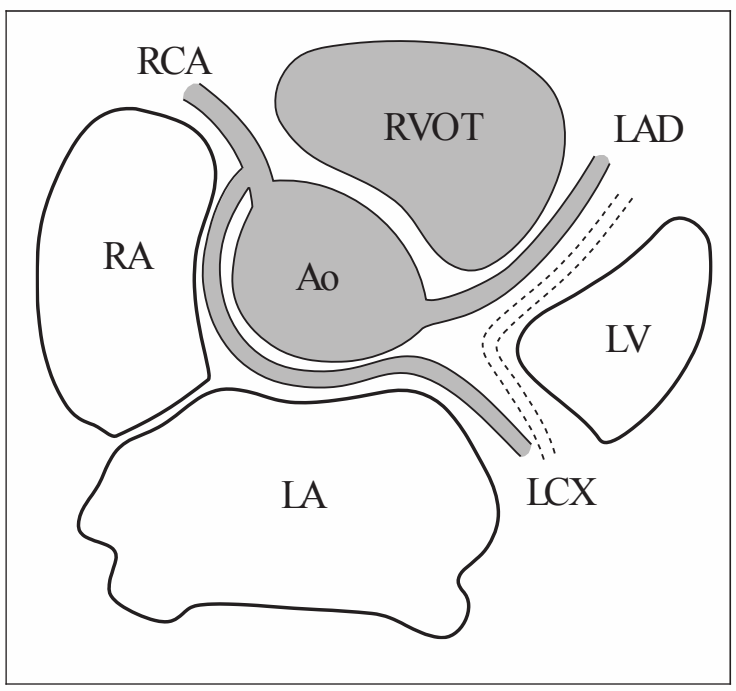

Fig. 12.10 Normal variant with the LCX arising from the RCA.

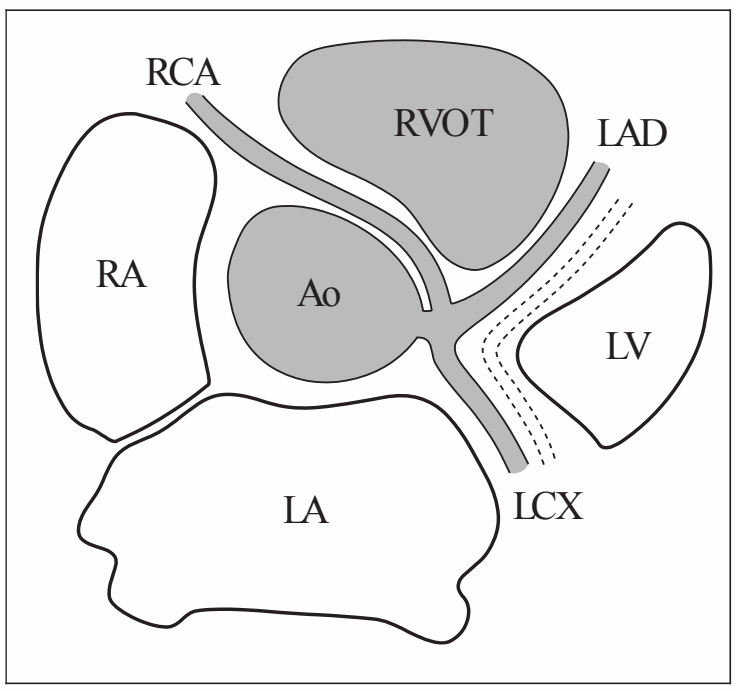

Fig. 12.11 Normal variant with the RCA arising from the LCA. Malignant variant in which the RCA runs between the aorta and RVOT.

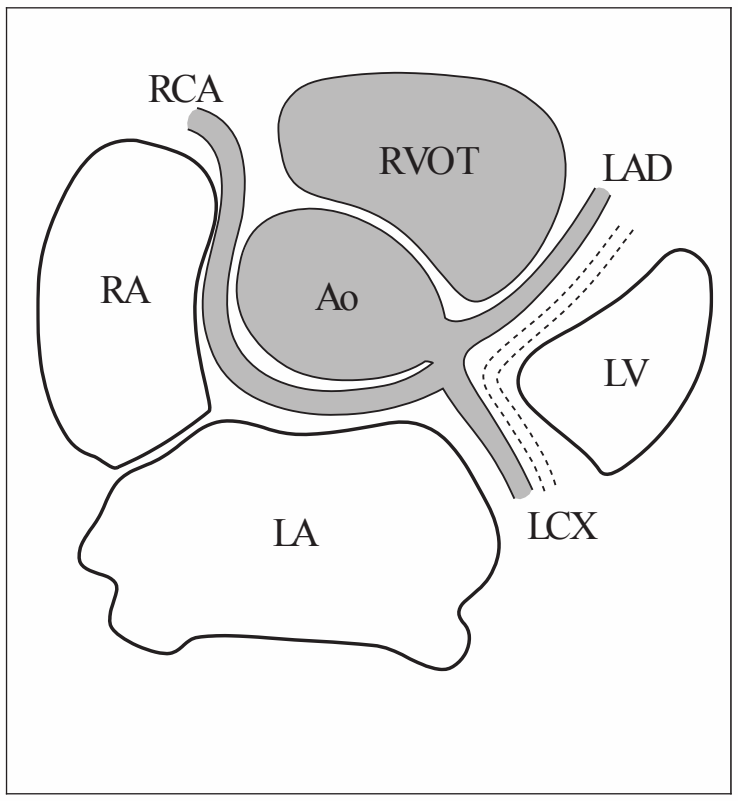

Fig. 12.12 Normal variant with the RCA arising from the LCA. Benign variant in which the RCA runs between the aorta and the LA and RA.

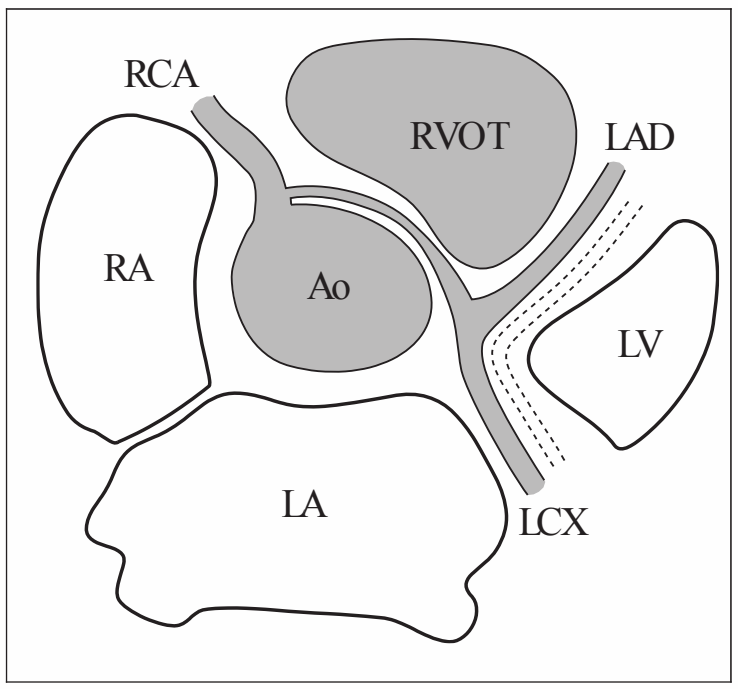

Fig. 12.13 Normal variant with the LCA arising from the RCA. Malignant variant in which the LCA runs between the aorta and RVOT.

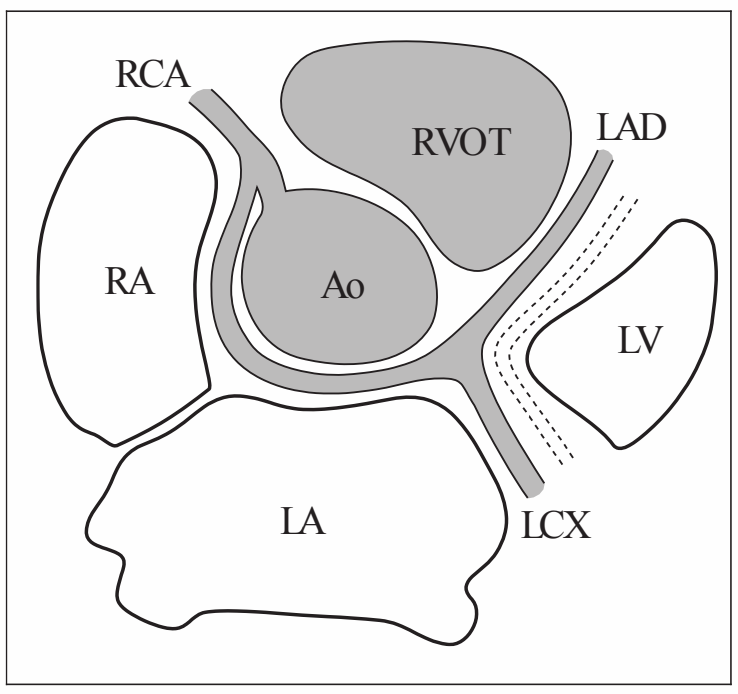

Fig. 12.14 Normal variant with the LCA arising from the RCA. Benign variant in which the LCA runs between the aorta and the LA and RA.

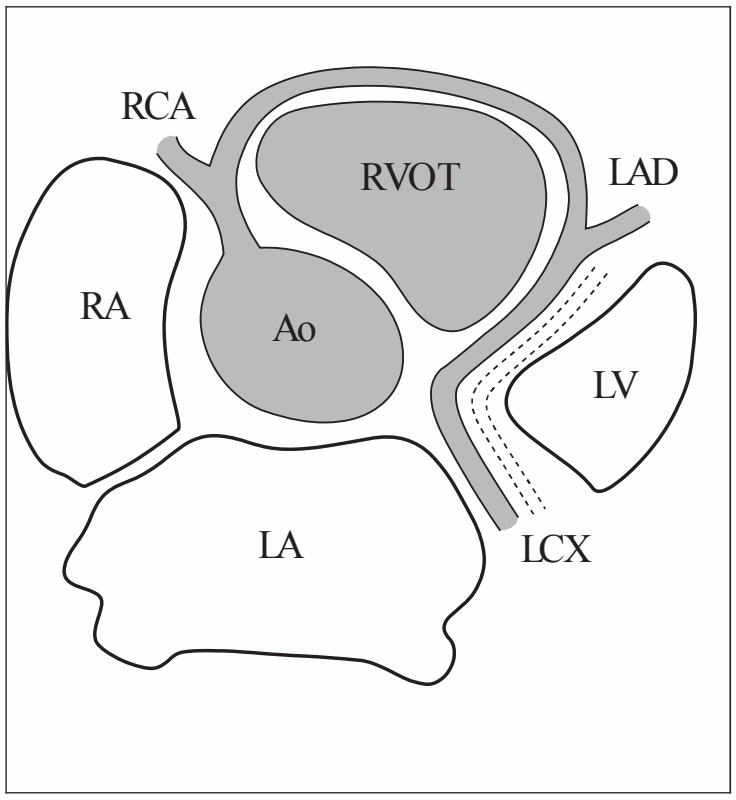

Fig. 12.15 Normal variant with the LCA arising from the RCA. Potentially malignant variant in which the LCA runs between the RVOT and LV.

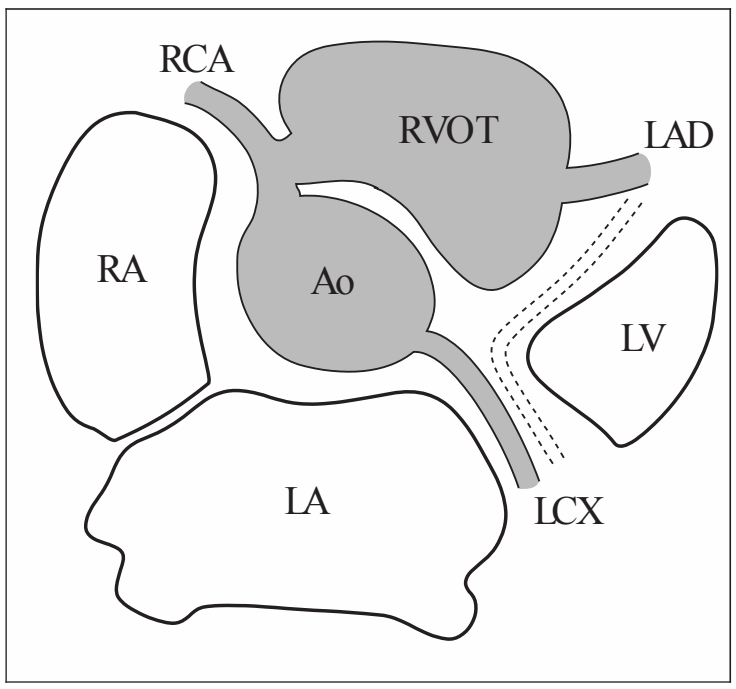

Fig. 12.16 Normal variant with the LAD arising from the RVOT and a coronary fistula between the RVOT and the RCA. The LCX arises directly from the aorta.

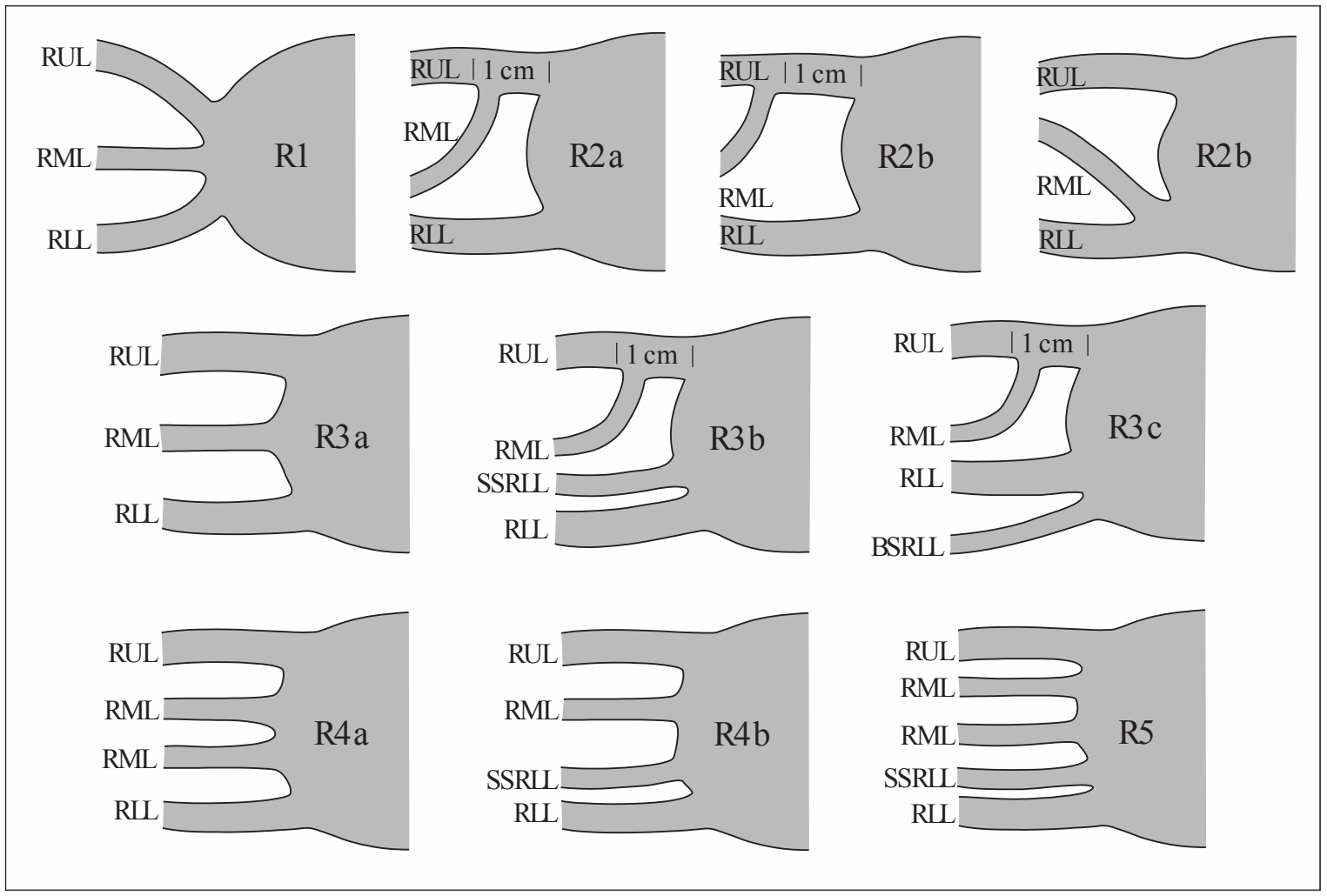

Fig. 12.17 Right pulmonary venous system.
RUL Right upper lobe vein
RML Right middle lobe vein
RLL Right lower lobe vein
SSRLL Right lower lobe vein, superior (apical) segment
BSRLL Right lower lobe vein, basal segment

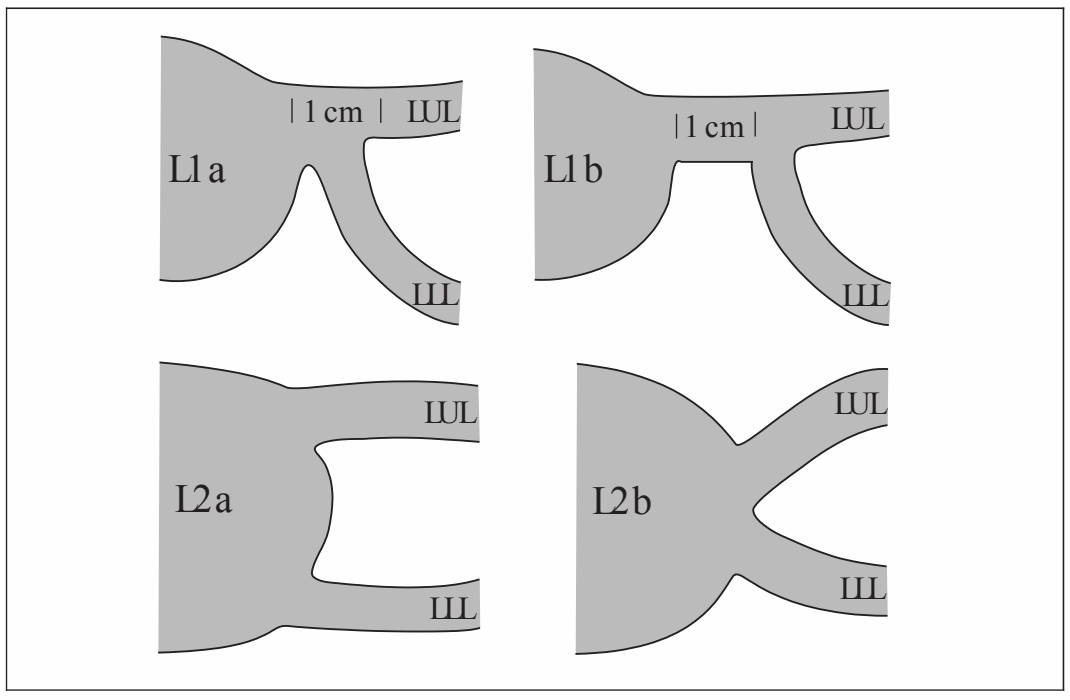

Fig. 12.18 Left pulmonary venous system.
LUL
Left upper lobe vein
LLL
Left lower lobe vein

References

Marom et al. Variations in Pulmonary Venous Drainage to the Left Atrium: Implications for Radiofrequency Ablation. Radiology 2004; 230: 824–829

NYHA Classification of Heart Failure

Class I	No limitation of physical activity; ordinary activities do not cause symptoms.
Class II	Mild limitation of physical activity; no symptoms at rest or with mild exertion.
Class III	Marked limitation of physical activity; asymptomatic only at rest.
Class IV	Symptomatic even at rest.

Primary cardiomyopathies
• DCM • HCM/HOCM • RCM • ARVC

Secondary cardiomyopathies
• Inflammatory (autoimmune, viral) • Toxic: alcohol, anthracyclines, cyclophosphamide, lithium, etc. • Ischemic, valvular, hypertensive • Induced by tachycardia • Metabolic: hypo- or hyperthyroidism, uremia, diabetes mellitus, nutritional deficiency, electrolyte imbalance, etc. • Systemic diseases: amyloidosis, lupus erythematosus, scleroderma, sarcoidosis, leukemias, rheumatoid arthritis, ankylosing spondylitis • Neuromuscular diseases (Friedrich ataxia), muscular and myotonic dystrophies (Duchenne disease, Becker–Kiener disease, Curschmann–Steinert disease) • Radiogenic • Perinatal

Unclassified cardiomyopathies
• ILNC • Fibroelastosis • Systolic dysfunction with minimal dilatation • Apical ballooning syndrome, identical with Tako–Tsubo syndrome • Mitochondrial diseases

Diagnostic Criteria of ARVC

I	**Global or regional dysfunction or structural changes**	
	Major criteria	• Severe RV dilatation and reduction of the RV EF with little or no impairment of LV function • Localized RV aneurysms • Severe segmental RV dilatation
	Minor criteria	• Mild RV dilatation and reduction of the RV EF with normal LV function • Mild segmental RV dilatation • Regional RV hypokinesia • Trabecular hypertrophy*
II	**Tissue characterization of the cardiac wall**	
	Major criterion	• Fibrolipomatous transformation of the myocardium, detectable by myocardial biopsy
III	**Repolarization abnormalities**	
	Minor criterion	• Inverted T waves in right precordial leads (V_2–V_3) (age > 12 years, no RBBB)
IV	**Depolarization and conduction abnormalities**	
	Major criterion	• Epsilon waves or localized prolongation (> 110 ms) of the QRS complex in the right precordial leads (V_1–V_3)
	Minor criterion	• Late potentials
V	**Arrhythmias**	
	Major criteria	• Ventricular tachycardia with LBBB morphology (ECG, ambulatory ECG, stress ECG) • Frequent ventricular extrasystoles (> 1000/24h, ambulatory ECG)
VI	**Family history**	
	Major criterion	• Family history with anatomic confirmation (autopsy, surgery)
	Minor criteria	• Sudden cardiac death in family members < 35 years of age with suspected ARVC • Evidence of ARVC in family members based on clinical criteria

Diagnosis requires two major criteria, one major plus two minor criteria, or four minor criteria.
* Not considered a valid criterion by all authors.

Crawford Classification

Type I	Involves all of the descending thoracic aorta and proximal abdominal aorta, but without involving the renal or visceral arteries.
Type II	Involves all of the descending thoracic aorta and abdominal aorta.
Type III	Involves the middle and distal descending thoracic aorta and abdominolumbar aorta.
Type IV	Involves the thoracoabdominal junction and abdominolumbar aorta.
Type V	Involves only the abdominal aorta, including the renal arteries.

Capabilities of Different Imaging Modalities

	Chest radio-graph	TTE, TEE	Invasive diagnos-tic pro-cedures	Multi-detec-tor CT	MRI	SPECT, PET
Morphology of cardiac chambers, pericardium	III	Ib	III	Ib	Ia	III
Morphology of coronary arteries	IV	IV	Ia	Ib	III	IV
Morphology of cardiac valves	IV	Ia	III	Ib	II	IV
Morphology of great vessels	III	III	III	Ia	Ia	IV
Qualitative myo-cardial function	IV	Ia	II	inv	Ib	III
Quantitative myo-cardial function	IV	Ib	III	inv	Ia	III
Qualitative valve function	IV	Ia	II	inv	II	IV
Quantitative valve function	IV	Ia	III	inv	II	IV
Myocardial perfusion	IV	inv	IV	inv	Ib	Ia
Myocardial metabo-lism	IV	IV	IV	IV	inv	Ia
Myocardial viability	IV	III*	III	inv	Ia	Ib
Structural tissue changes	IV	IV	Ia†	III	Ib	III‡
Volume and flow assessment	IV	Ib	Ia	IV	Ib	IV
Pressure relationships	IV	II	Ia	IV	III	IV
Impulse conduction	IV	IV	Ia	inv	inv	III

Ia First choice modality.
Ib Alternative to Ia as a first-line study.
II Often used and well established but provides information that can also be obtained with other modalities.
III Used occasionally, provides information that is generally obtained with other modalities.
IV Does not provide clinically relevant information.
inv Investigative, probably yields relevant information, still undergoing trials.
Invasive diagnostic procedures = cardiac catheterization studies including coronary angiography and electrophysiologic test procedures.
CT, computed tomography; MRI, magnetic resonance imaging; TTE, transthoracic echocardiography; TEE, transesophageal echocardiography; SPECT, single photon emission computed tomography; PET, positron emission tomography.
* Stress echocardiography; † myocardial biopsy; ‡ of limited usefulness.

A

Page numbers in italics refer to illustrations.

D

E

F

G

H

I

R

S

T

U

V

W

Flexibook Pocket Atlases

2006/233 pp./
444 illus./softcover

American continents
ISBN 978-1-58890-433-1/
US$44.95

All other continents
ISBN 978-3-13-141241-6/
€39.95

Pocket Atlas of Echocardiography

Thomas Boehmeke, MD, and Ralf Doliva, MD

The pocket atlas presents all of the information you need to navigate the numerous imaging planes that transect the heart. It provides a practical overview of patient management and uses more than 400 illustrations, including sharp, clear echocardiograms, full-color schematic diagrams, and 3-D images to convey key aspects of examination and diagnostic techniques, and diseases and abnormalities of the heart. You will learn imaging and patient positioning techniques that will help you achieve the best possible echocardiogram to detect cardiac diseases and conditions including valvular heart disease, coronary heart disease, cardiomyopathies, and more.

HIGHLIGHTS

- Hundreds of vivid mnemonic devices and useful tips to help you locate, identify, and remember all anatomical structures and features
- All major diseases depicted in B-mode, M-mode, Doppler, and color Doppler
- 444 high-quality illustrations integrated into succinct text
- Detailed descriptions of all the acoustic windows and imaging planes for every echocardiogram

Radiology

Differential Diagnosis

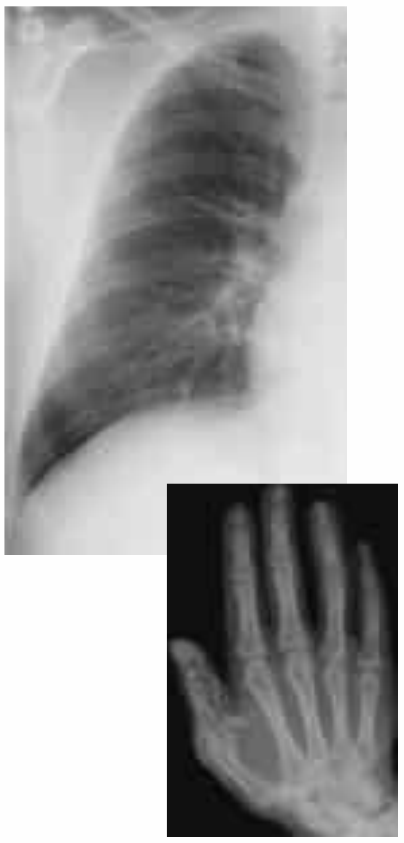

NEW

Differential Diagnosis in Conventional Radiology

Third Edition

Francis A. Burgener, MD, Martti Kormano, MD,
and Tomi Pudas, MD

Here is the long-awaited third edition of a standard reference for diagnostic radiology. This edition guides the radiologist through the process of determining differential diagnoses for the most common clinical problems.

HIGHLIGHTS

- New sections address the increasing importance of sectional imaging techniques.
- Easy-to-reference tables organize the possible differential diagnoses.
- Clear, concise descriptions of commonly associated radiologic findings and pertinent clinical data.
- Nearly 2,000 high-quality radiographs illustrate all the imaging findings.

2007/874 pp./
1,870 illus./hardcover/

American continents
ISBN 978-1-58890-275-7/
US$249.95

All other continents
ISBN 978-3-13-656103-4/
€229.95

Easy ways to order:
Visit our homepage www.thieme.com

Thieme